APPLICATION OF NUMERICAL LIMIT ANALYSES FOR UNDRAINED STABILITY PROBLEMS IN CLAY

by

BOONCHAI UKRITCHON

B. Eng. Civil Engineering (1992)
Chulalongkorn University

Master of Science Civil and Environmental Engineering (1996)
Massachusetts Institute of Technology

SUBMITTED TO THE DEPARTMENT OF
CIVIL AND ENVIRONMENTAL ENGINEERING
IN PARTIAL FULFILLMENT OF THE REQUIREMENTS
FOR THE DEGREE OF

DOCTOR OF SCIENCE IN GEOTECHNICAL ENGINEERING

at the

MASSACHUSETTS INSTITUTE OF TECHNOLOGY

May 1998
[June 1998]

Signature of Author_____
Department of Civil and Environmental Engineering
May 1998

Certified by_____
Professor Andrew J. Whittle
Thesis Supervisor

Accepted by_____
Professor Joseph M. Sussman
Chairman, Departmental Committee on Graduate Students

APPLICATION OF NUMERICAL LIMIT ANALYSES FOR UNDRAINED STABILITY PROBLEMS IN CLAY

by

BOONCHAI UKRITCHON

Submitted to the Department of Civil and Environmental Engineering
on May 20, 1998 in partial fulfillment of the requirements for the degree of
Doctor of Science in Geotechnical Engineering

ABSTRACT

This thesis describes the development and application of numerical limit analyses for planar, undrained stability problems in geotechnical engineering. The proposed analyses formulate upper and lower bound theorems for perfectly plastic, cohesive-frictional soils as linear programming problems, with spatial variations of the unknown velocities and stresses approximated by standard finite element interpolation functions. The thesis includes three substantial modifications of the pre-existing software: 1) inclusion of structural beam and joint elements, that enable the program to model failure in combined bending, shear and axial loading; 2) implementation of functions to represent the undrained strength anisotropy of soft clays; and 3) representation of pore water pressures and effective stress strength parameters for stability analyses that include free draining soil layers. In all of the examples presented in this thesis, the proposed numerical limit analyses are able to bracket the true collapse load within ±5%.

The stability of surface footings under combined effects of vertical, horizontal and moment (V, H, M) loading is solved in the form of three-dimensional failure envelopes, that include effects of underbase suction and non-homogeneous undrained strength profiles. Existing empirical bearing capacity factors for inclined, eccentric loading are shown to be conservative, often underestimating the exact collapse solutions for footings on homogeneous clay by more than 25%. However, the same correction factors can become completely unreliable when there is a significant undrained strength gradient. The numerically-derived failure envelope for footings on homogeneous clay is described approximately by curve fitting techniques using relatively simple functions that can be used to update the existing bearing capacity factors.

The undrained (short-term) pullout capacity of a single caisson cell in clay is initially investigated as a planar problem. Limit analyses show that the capacity can be presented as a normalized function of the undrained strength gradient in the clay, and interior surface area of the caisson. The results show that there are significant errors in limit equilibrium calculations which assume mechanisms of reverse end-bearing. Pullout predictions are compared with measured data from 1) small scale laboratory element tests on miniature caissons, 2) centrifuge models and 3) field tests on a four-cell caisson unit. These comparisons introduce approximations in the scaling of the planar solutions to axisymmetric cell geometries, and inclined loading cases. Good agreement is obtained with all three sets of experiments, and confirms that the proposed limit analyses are at

least comparable in predictive capability to the limit equilibrium calculations currently used in practice.

The limit analyses represent the undrained strength anisotropy of soft clays using a yield function originally proposed by Davis and Christian (1970). Undrained strength anisotropy is found to have a major influence on the stability and failure mechanisms for unbraced vertical cuts in clay. In contrast, there is minimal effect on the failure mechanisms for kinematically constrained problems such as the lateral load capacity of deeply embedded pile or pipe sections.

Applications of limit analyses for braced excavations show important errors in existing calculations of basal stability. The analyses also provide the first theoretical solutions that quantify effects of wall embedment and bending strength on the stability of well-braced cuts. The results have also been compared with previous displacement-based finite element calculations based on the anisotropic MIT-E3 soil model. Good matching is obtained using the limit analyses together with anisotropic strength parameters mobilized at shear strains, $\gamma = 0.6$ - 1.0%, corresponding to failure conditions in the finite element solutions.

Limit analyses have been used to re-assess the stability of tied-back walls at Bird Island Flats in East Boston. Detailed analyses were carried out for two cases 1) estimated excavation and support geometry at an unstable section; and 2) at final excavated grade after placement of a remedial buttress constructed by deep soil-mixing and jet grouting. Reliability analyses show that uncertainties in the undrained strength profile represent the major factor affecting predictions of stability. Successful performance of the improved cross-section is not consistently explained by strength parameters derived from the unstable cross-section. Additional calculations compare the stabilizing effects of different designs for the wall, tiebacks and remedial buttress.

The failure of an offshore breakwater in Brazil was analyzed extensively using conventional slope stability methods in a recent Ph.D thesis by Lee (1995). Limit analyses, using the same soil parameters, shows similar mechanisms of failure controlled by the undrained shear strength of the underlying Sergipe clay. However, the factors of safety computed by Spencer's method are shown to be unrealistically low due to the assumed directions of interslice forces in the overlying sand and rockfill layers.

Thesis Supervisor: Prof. Andrew J. Whittle
Title: Associate Professor of Civil and Environmental Engineering

ACKNOWLEDGMENTS

This work would have not been possible without the collaboration of many individual and institutions; and I would like to express my thanks to them.

First, I am indebted to my thesis supervisor, Professor Andrew J. Whittle, for supporting my work, and providing technical insights and superior intellectual challenges during all the research. I would also like to thank him for his meticulous review of my thesis. It has been priceless and rewarding experience working with him.

I would like to thank my thesis committee members: Professor Charles C. Ladd for providing input, careful review and guidance for this thesis, particularly for case studies of a tieback excavation in East Boston and an offshore breakwater in Brazil; and Professor John C. Connor for devoting his valuable time to serve my committee.

Prof. Scott Sloan of the University of Newcastle, Australia for providing the numerical lower and upper bound programs for this research.

I am grateful to the Anada Mahidol Foundation, Thailand, for supporting all my Master and Doctoral studies at M.I.T.

I would also like to thank the following individuals:

Dr. John T. Germaine for his teaching in geotechnical laboratory. Prof. Robert V. Whitman for his teaching in soil dynamics. Prof. Hobert H. Einstein for his teaching in geology and rock mechanics

Prof. Mark F. Randolph of the University of Western Australia for attending my doctoral thesis defense. It is a great honor for me to have one of the most renown geotechnical professor in my defense.

The following Thai students: Twarath Sutabutr, Suchatwee Suwansawat, and Manasa Muttamra for helping me in many areas and for their great friendships.

Cynthia Stewart, an academic programs administrator, for helping me several academic and bureaucratic problems.

Other geotechnical students for providing a much lighter and enjoyable working atmosphere at MIT: Marika Santagata, Joe Sinfield, Guoping Zhang, Shoamin Wang, Catalina Marulanda, Ariel Martinez, Thomas Meyer. Special thanks to Yo-Ming Hsieh for setting up Pentium-II for me to perform computer simulations.

This thesis is dedicated to my parents whom I owe the most. They have provided unconditional support, love, and sacrifice throughout my five years studies at MIT.

Boonchai "Lek" Ukritchon.

TABLE OF CONTENTS

LIST OF TABLES

LIST OF FIGURES

Chapter 1. Introduction

Stability analyses or collapse calculations are important in geotechnical engineering to ensure that foundations and earthworks have adequate factors of safety against all possible modes of failure (ultimate limit states). Examples of stability problems include bearing capacity of foundations, lateral earth pressures, and stability of natural and man made slopes and cuts.

The available techniques for solving stability problems in design are all based on the theory of rigid-perfectly plastic material behavior and include limit equilibrium method, slip-line analyses, and limit analysis[1]. Limit equilibrium methods (LEM) are most commonly used in geotechnical practice as they can handle complex stratification and variations in strength properties. However, it is very difficult to assess the accuracy of limit equilibrium solutions due to ad hoc assumptions used in selecting the shape of the failure surface, search procedures to locate the critical surface, and approximations in the equilibrium calculations (e.g. in method of slices used for slope stability).

Slip-line and limit analyses are based on powerful bound theorems (Drucker et al. 1952) that compute rigorous upper and lower bound estimates collapse load. However, these methods are difficult to apply for practical stability problems involving non-homogeneous profiles, complex loading and geometries. Conventional methods that solve associated fields by numerical integration along characteristics have been applied to relatively simple soil profile (e.g. Davis and Booker, 1973). In principle, non-linear finite element methods can provide complete analysis of deformation and stability. However, in practice, it is difficult to perform numerically accurate non-linear finite element analyses, while the reliability of the predictions are largely dependent on the ability of the constitutive model to describe generalized stress-strain-strength properties of soil (c.f. Whittle, 1987; Pestana, 1994).

More reliable calculations of stability can now be achieved by optimizing upper and lower bound analyses using (linear) programming methods, while spatial discretization of the field variables is accomplished using finite element interpolation

[1] Stability can also be evaluated by non-linear finite element methods. However, these require more sophisticated constitutive assumptions and are rarely used in design as the primary method of stability calculations.

methods. This approach combines the advantages of finite element methods for handling complex geometric and loading conditions with the power of the plastic limit theorems for bounding the true solution. Although these techniques were first proposed by Lysmer (1970) and Bottero et al. (1980), their applications were limited to relatively simple problems due to excessive computational times to solve large scale linear programming optimization using simplex or revised simple algorithms. This efficiency problem was resolved by Sloan (1988a) using a steepest edge active set algorithm (Best & Ritter, 1985) that has now been implemented in linear programming forms of both lower bound (Sloan, 1988b) and upper bound (Sloan & Kleeman, 1995) formulations.

The current numerical limit analyses consider plane strain conditions with the yield of the soil described by an isotropic Mohr-Coulomb or Tresca criterion. The programs do not consider pore water pressure and hence, are restricted to undrained total stress analyses ($\phi = 0$), or fully drained stability analyses with zero pore pressure. Anisotropic undrained shear strength of clay is also not considered in the current program. In addition, the analyses are limited to simple stress boundary conditions, thus there is no option for applied inclined or moment loading. Finally, the programs can not handle failure of both soil and structure. The objective of this thesis is to extend the capabilities of the numerical limit analyses and to apply and demonstrate the techniques in various practical stability problems that include complex loading and geometry, soil-structure interaction, and generalized soil profiles.

Chapter 2 applies numerical limit analyses to compute the undrained stability of surface strip footings under the combined action of vertical, horizontal, and moment (V, H, M) loading. The chapter reviews briefly the numerical lower and upper bound limit analyses for plane strain problems (based on Ukritchon, 1996; Sloan, 1988b, and Sloan and Kleeman, 1995). Results are presented for a wide range of eccentricity ratios, inclination angles, and undrained shear strength profiles of the clay. The analyses focus on the geometry of three-dimensional failure surface of (V, H, M) and illustrate the effects of underbase suction and non-homogeneous undrained strength profiles that are characteristics of offshore gravity base structures. Solutions of numerical limit analyses are also compared with published empirical factors for inclined and eccentric loading.

The chapter proposes an empirical curve fitting equation for combined loading of footings on homogeneous clay.

Chapter 3 describes the formulation of numerical upper and lower bound limit analyses for structural elements. The proposed formulation is evaluated by: i) comparison with analytical closed-form solutions for a series of 2-D structural frame problems published in the literature; and ii) analyses of a laterally loaded wall embedded in clay. The formulation of structural elements represents the first step toward the use of limit analyses for problems of soil-structure interaction described in Chapters 6 and 7.

Chapter 4 reviews the existing interpretation of undrained strength anisotropy and proposed yield functions. The formulation selected for the limit analyses is based on the work on Davis and Christian (1971). The chapter applies numerical limit analyses with undrained strength anisotropy for two example problems: 1) the bearing capacity of a rigid footing on clay; and 2) lateral load capacities of deeply-embedded pile and pipe cross sections.

Chapter 5 presents the application of the numerical limit analyses for computing the undrained tensile capacity of a rigid-planar caisson in non-homogeneous clay. Solutions of limit analyses are compared with limit equilibrium calculations for planar caissons. The chapter also proposes a simple method for applying the solutions for the planar caisson geometries to estimate the capacity of axisymmetric caissons. The scaling results are then compared with displacement-based finite element analyses (FE) using the MIT-E3 soil model (Whittle et al., 1996). Numerical limit analyses are also compared with pullout measurements for: 1) miniature caisson in laboratory tests on miniature caissons in BBC (Cauble, 1996); 2) centrifuge tests performed by EPR in kaolin (Clukey and Morrison, 1993); and 3) field experiments performed by NGI (Andersen et. al., 1993). The centrifuge and field experiments include data for inclined loading.

Chapter 6 describes the application of numerical limit analyses for computing undrained stability of braced excavations in clay. New components of these analyses include the definition of the objective function and factor of safety for layered soil profiles. The analyses present the results of stability for braced excavations and embedded walls in a homogenous clay layer. Stability numbers of excavations from numerical limit analyses are compared with conventional basal heave methods as well as

existing modifications dealing with wall embedment. Empirical curve fitting techniques are used together with the dimensional analysis to interpret predictions of stability for braced excavations in deep layers of homogeneous clay. The analyses also assess the role of undrained strength anisotropy for the stability of unsupported and supported vertical cuts. The chapter compares predictions of failure using numerical limit analyses with results obtained previously from finite element analyses with the MIT-E3 soil model (Hashash and Whittle, 1996; Jen, 1998).

Chapter 7 describes the application of numerical limit analyses to analyze the stability of tied-back walls associated with construction of Section D007A of the Central Artery/Third Harbor Tunnel (CA/T) Project in East Boston. The analyses consider two sections: 1) cross-section at which instability occurred during construction (East wall); and 2) the final excavation grade at a section, where deep soil mixing and jet grouting were used to stabilize the base of the excavation. Factors of safety calculated by limit analysis are compared with deep rotational stability calculations using limit equilibrium method (O'Rourke and O'Donnell, 1997a, 1997b). Reliability analysis with First Order Second Moment Method (FOSM) were also carried out to investigate the uncertainty in calculated factor of safety due to soil properties and geometries of excavation for the unstable East wall. Further analyses are used to evaluate possible re-designs of the wall and ground improvement system.

Chapter 8 describes modification of the numerical limit analyses to include pore water pressure and effective stress, strength parameters. The proposed formulation is evaluated by comparisons with analytical upper bound solutions and limit equilibrium calculations for homogeneous slopes: 1) subjected to uniform ratio of pore pressure to total overburden stress; and 2) submerged under water. The chapter also applies the new formulation to predict upper and lower bounds on the stability of an offshore breakwater in Brazil (Lee, 1995; Ladd & Lee, 1993; Ladd et. al. 1993). Factors of safety from numerical limit analyses are compared with solutions from limit equilibrium calculations using Spencer method of slices (as solved by UTEXAS3, Wright, 1991).

Chapter 9 summarizes the main results of the thesis and proposes further research and other applications on numerical limit analyses.

1.1 References

Andersen, K.H., Dyvik, R., Schroder, K., Hansteen, O.E. and Bysveen, S. (1993). "Field tests of anchors in clay. II: Predictions and interpretation" J. of Geotech. Engrg., ASCE, 119(10), 1532-1549.

Best, M. J., and Ritter, K. (1985). *Linear Programming: Active Set Analysis and Computer Programs*, Prentice-Hall, New Jersey.

Bottero, A., Negre, R., Pastor, J., and Turgeman, S. (1980). "Finite element method and limit analysis theory for soil mechanics problems." Comp. Meth. Appl. Mech. Eng., 22 131-149.

Cauble, D.F. (1996). "Experimental measurements for a model suction caisson" PhD Thesis, Dept. of Civil Engrg., MIT, Cambridge, MA.

Clukey, E.C. and Morrison, M.J. (1993). "A centrifuge and analytical study to evaluate suction caissons for TLP applications in the Gulf of Mexico." Design and Performance of Deep Foundations: Piles and Piers in Soil and Soft Rock, ASCE, NY, 141-156.

Davis, E. H., and Booker, J. R. (1973). "The effect of increasing strength with depth on the bearing capacity of clays." Géotechnique, 23 (4), 551-563.

Davis, H. E., and Christian, T. J. (1971). "Bearing capacity of anisotropic cohesive soil". J. Soil Mech. Found. Div., ASCE, 97(5), 753-769.

Drucker, D. C., Greenberg, H. J., and Prager, W. (1952). "Extended limit design theorems for continuous media." Q. Appl. Math., 9, 381-389.

Geer, M. (1996). "Analysis of pile and suction caisson behavior in axial loading." PhD Thesis in progress, MIT, Cambridge, MA.

Hashash, Y. M. A., and Whittle, A. J. (1996). "Ground movement prediction for deep excavations in soft clay.". J. of Geotech. Engrg. ASCE, 122(6), 474-486.

Ladd, C. C., and Lee, S-M. (1993). "Engineering properties of the Sergipe Clay." TPS Progress Report No. 4, Research Report 93-07, March 19, 1993, Dept. of Civil and Environmental Engineering, MIT, Cambridge, MA.

Ladd, C. C, Lee, S-M, and Whelan, M. P. (1993). "Backanalyses of the Reinder Failure." TPS Progress Report No. 5, Research Report 93-10, May 29, 1993, Dept. of Civil and Environmental Engineering, MIT, Cambridge, MA.

Lee, S-M (1995). "Stability and deformation during staged construction of an offshore breakwater on soft clay." PhD thesis, Dept. of Civil and Environmental Eng., Massachusetts Institute of Technology, Cambridge, MA.

Lysmer, J. (1970). "Limit analysis of plane problems in soil mechanics." J. Soil Mech. Found. Div., ASCE., 96(SM4), 1311-1334.

Pestana-Nascimento, J. M. (1994). "A unified constitutive model for clays and sands." ScD thesis, Dept. of Civil and Environmental Eng., Massachusetts Institute of Technology, Cambridge, MA.

Sloan S. W. (1988a). "A steepest edge active set algorithm for solving sparse linear programming problems." Int. J. Numer. Anal. Methods in Geomech., 26(12), 2671-2685.

Sloan S. W. (1988b). "Lower bound limit analysis using finite elements and linear programming." Int. J. Numer. Anal. Methods in Geomech., 12(1), 61-77.

Sloan S. W., and Kleeman, P. W. (1995). "Upper bound limit analysis using discontinuous velocity fields." Computer Methods in Applied Mechanics & Engineering, 127, 293-314.

Ukritchon, B. (1996). "Evaluation of numerical limit analyses by finite elements and linear programming." MS Thesis, Department of Civil & Environmental Engineering, MIT, Cambridge, MA.

Whittle, A. J. (1987). "A constitutive model for over-consolidated clays with application to the cyclic loading of friction piles." ScD thesis, Dept. of Civil and Environmental Eng., Massachusetts Institute of Technology, Cambridge, MA.

Whittle, A. J., Germaine, J. T., Cauble, D. F., Geer, M. A. (1996). "Behavior of suction caisson foundations: Final Report." report submitted to MIT Sea Grant and Joint Oil Industry Consortium, Cambridge , MA.

Wrigth, S. G. (1991). "UTEXAS3, A computer program for slope stability calculations." Shinoak Software, Austin, TX, Revised Sept. 1991.

Chapter 2. Undrained Limit Analyses for Combined Loading of Strip Footings On Clay[1]

2.1 Summary

This chapter applies numerical limit analyses to evaluate the undrained stability of surface footings on non-homogeneous and layered clay deposits under the combined effects of vertical, horizontal and moment (V, H, M) loading. The analyses are able to resolve the true collapse loads to within ±5% by computing rigorous upper and lower bound solutions for these plane strain problems using linear programming methods and finite element discretization. The results focus on the geometry of the three-dimensional failure envelope and illustrate the effects of underbase suction and non-homogeneous undrained strength profiles. The existing empirical bearing capacity factors for inclined, eccentric loading are conservative, often underestimating the exact collapse solutions for footings on homogeneous clay by more than 25%. However, the same correction factors can become completely unreliable when there is a significant undrained strength gradient. The numerically-derived failure envelope for footings on homogeneous clay is described approximately by curve fitting techniques using relatively simple functions that can be used to update the existing bearing capacity factors.

2.2 Introduction

The undrained stability of a shallow foundation on clay is conventionally computed using the bearing capacity equation of Terzaghi (1943). The core of this equation is the slip line solution of Prandtl (1920) for a vertically loaded surface strip footing, which was later shown to be an exact solution satisfying upper and lower bound theorems of plasticity theory (Drucker et al., 1952). This basic solution is then modified using empirical or semi-empirical correction factors in order to account for the embedment depth, foundation shape, load inclination, eccentricity etc. (after Meyerhof, 1953; Brinch Hansen, 1970; Vesic, 1975). The accuracy of these correction factors is of particular interest for structures which are subject to large lateral and moment loading

[1] This chapter was published in J. of Geotech. Engrg, ASCE, Vol. 124, No. 3, March, 1998, p265-276.

including offshore breakwaters (Sekiguchi & Ohmaki, 1992), gravity base platforms (Janbu, 1985; Andersen & Lauritzen, 1988; Bransby & Randolph, 1997), and spud-can foundations for jack-up rigs (Houlsby & Martin, 1992; Gottardi & Butterfield, 1993; Dean et al., 1992; Murff, 1994). Much of this recent research has focused on the development of more reliable failure criteria for shallow foundations under combined vertical, horizontal and moment loading (V, H and M; Fig. 2.1), based either on direct experimental measurements (1-g and centrifuge models), or computed by non-linear finite element analyses or approximate limit equilibrium methods.

This chapter applies techniques of numerical (upper and lower bound) limit analyses to establish the generalized, undrained failure criterion for combined loading of a surface strip footing. Rigorous upper and lower bound failure loads are solved by linear programming methods, while spatial discretization and interpolation of the field variables are accomplished using finite element methods. This approach combines the advantages of finite element methods for handling complex geometric and loading conditions, with the power of the limit theorems for bounding the exact collapse load. Although these techniques were first proposed by Lysmer (1970) and Bottero et al. (1980), their subsequent development was hampered by the excessive computation times required to solve large systems of sparse linear equations (originally carried out using simplex or revised simplex algorithms). This efficiency problem was resolved by Sloan (1988a) using a steepest edge active set algorithm (Best & Ritter, 1985) that has now been implemented in both lower bound (Sloan, 1988b) and upper bound (Sloan & Kleeman, 1995) formulations. Full details of the numerical algorithms are given in these source papers, while Assadi and Sloan (1991) have demonstrated the application of these analyses for undrained stability of shallow tunnels. This chapter gives a very brief summary of the two formulations emphasizing only those aspects of the analyses that were developed for the current study of surface foundations.

Figure 2.1 summarizes the problem notation. Combined loading of a footing of width, B, can be represented either by a resultant force, Q, at eccentricity, e, and inclination angle, α or by three statically equivalent forces V, H and M (Fig. 2.1c). Loading conditions where Q is directed towards the centerline, Mode I ('backward

eccentricity', Fig. 2.1a), can also be distinguished from Mode II condi'ions ('forward eccentricity', Fig. 2.1b) where the resultant force acts towards the edge of the footing. These modes correspond to different combinations of horizontal and moment loading (M-H plane, Fig. 2.1d). For notation purposes, the horizontal load component always points towards the "leading edge" and away from the "trailing edge" of the footing.

The two most commonly used calculations used to compute the maximum value of Q for combined loading of a surface strip footing on level ground are as follows:

For $\alpha \le \alpha_0$: $$\frac{Q}{Bs_u} = N_{c0}\left(1-\frac{2e}{B}\right)\left(\frac{1}{\cos\alpha}\left[1-\frac{\alpha^\circ}{90}\right]^2\right)$$ Meyerhof (1953) (2.1a)

$$\frac{Q}{Bs_u} = N_{c0}\left(1-\frac{2e}{B}\right)\left(\frac{1}{\cos\alpha + 2\sin\alpha}\right)$$ Vesic (1975) (2.1b)

For $\alpha > \alpha_0$: $$\frac{Q}{Bs_u} = \left(1-\frac{2e}{B}\right)\frac{1}{\sin\alpha}$$ Interface Sliding (2.1c)

where s_u is the undrained, plane strain shear strength of the (homogeneous) clay layer, N_{c0} is the theoretical bearing capacity factor for vertical loading (for homogeneous clay, $N_{c0} = [2+\pi]$, while analytical solutions for non-homogeneous layers are given by Davis & Booker, 1973), and α_0 is the inclination angle at which the undrained strength is mobilized at all points along the horizontal soil-footing interface ($\alpha_0 = 15.99°$, $17.59°$ in eqns. 2.1a and 2.1b, respectively).

Both methods compute the capacity under combined loading as the product of two terms representing the effects of load eccentricity and inclination. For eccentric loading, the calculations assume a reduced area of contact between the soil and foundation, corresponding to the effective width, B' = B-2e (Meyerhof, 1953), where it is implicitly assumed that e > 0. Hence, eqns. 2.1a and 2.1b do not recognize differences in capacity between combined loading in Modes I and II.

2.3 Numerical Limit Analyses

2.3.1 Lower Bound Formulation

The lower bound theorem states that any *statically admissible stress field* will provide a lower bound (or "safe") estimate of the exact limit load. A statically admissible

stress field is one which satisfies the equilibrium equations, stress boundary conditions, and must not violate the yield criterion of the material.

The numerical implementation of the lower bound analysis for plane strain problems discretizes the soil mass into 3-noded triangular elements and assumes a linear variation of the unknown stresses (σ_x, σ_y, τ_{xy}) within each element (Fig. 2.2):

$$\sigma_x = \sum_{i=1}^{3} N_i \sigma_{xi} \quad ; \quad \sigma_y = \sum_{i=1}^{3} N_i \sigma_{yi} \quad ; \quad \tau_{xy} = \sum_{i=1}^{3} N_i \tau_{xyi} \tag{2.2}$$

where N_i are standard linear shape functions (e.g., Zienkiewicz, 1983), and (σ_{xi}, σ_{yi}, τ_{xyi}) are the stresses at node i.

In contrast to conventional displacement based finite element methods, each node is unique to a particular element such that stress discontinuities can occur along shared edges between elements (defined by pairs of nodes, e.g., 2, 4 and 3, 6, Fig. 2.2). The conditions of static admissibility are then derived as a series of linear constraints on the nodal stresses.

For plane strain analyses, the lower bound stress field must satisfy the following equations of equilibrium:

$$\frac{\partial \sigma_x}{\partial x} + \frac{\partial \tau_{xy}}{\partial y} = 0 \quad ; \quad \frac{\partial \tau_{xy}}{\partial x} + \frac{\partial \sigma_y}{\partial y} = \gamma \tag{2.3}$$

where γ is the unit weight of the soil, and compressive stresses are positive.

Equilibrium of the nodal point stresses is then achieved by differentiating eqn. 2.2 and substituting into eqn. 2.3, generating a set of linear equalities in the form:

$$\mathbf{A_1 \sigma_l} = \mathbf{B_1} \tag{2.4}$$

where σ_l is the vector of nodal point stresses for each element.

The shear and normal tractions must also be in equilibrium at all points along the discontinuities between elements. This condition can be satisfied by matching traction components at the nodal pairs (e.g., 2, 4 and 3, 6 in Fig. 2.2; and 1, a etc., for the soil-footing interface in Fig. 2.3):

$$\sigma_{n2} = \sigma_{n4} \quad \text{and} \quad \tau_2 = \tau_4 \tag{2.5a}$$

$$\sigma_{n3} = \sigma_{n6} \quad \text{and} \quad \tau_3 = \tau_6 \tag{2.5b}$$

For each interface, these relations can be rewritten as a series of equality constraints on the nodal point stresses by introducing standard transformation equations between surface tractions (σ_n, τ) and Cartesian stress components (σ_x, σ_y, τ_{xy}):

$$\mathbf{A_2}\sigma_2 = \mathbf{B_2} \tag{2.6}$$

where σ_2 is the vector of nodal point stresses for the two pairs of nodes at either end of the discontinuity.

These same types of constraint can be used to represent all stress controlled boundary conditions.

The present analyses assume that the undrained shear strength of the clay can be represented by the isotropic Tresca yield criterion. Hence for plane strain problems, the locus of admissible stress states can be written as:

$$F = X^2 + Y^2 - R^2 \leq 0 \tag{2.7}$$

where $X = (\sigma_y - \sigma_x)$ and $Y = 2\tau_{xy}$ are transformed stress components, defined such that the Tresca yield criterion ($F = 0$) plots as a circular surface with radius, $R = 2s_u$ (Fig. 2.4).

Following Lysmer (1970), this single non-linear function can be approximated by an interior polygon, with p sides of equal length (Fig. 2.4). The locus of statically admissible stress states must then satisfy a series of linear inequality constraints of the form:

$$F_k = A_k\sigma_x + B_k\sigma_y + C_k\tau_{xy} - D \leq 0 \tag{2.8}$$

where $k = 1...p$, and the linear coefficients A_k, B_k, and C_k are defined from the vertices of the polygon, and $D = 2s_u\cos(\pi/p)$.

As the stresses vary linearly within the element, the yield condition can be satisfied by enforcing a series of linear inequality constraints on the nodal point stresses, $F_{ki} \leq 0$, where F_{ki} is the k^{th} side of the linearized yield function at node i. Thus, the linearized yield surface introduces p constraints on the stresses at each nodal point, written in matrix form as:

$$\mathbf{A_3}\sigma_3 \leq \mathbf{B_3} \tag{2.9}$$

where σ_3 is the vector of stress components at each node in the mesh.

It should be noted that the analyses can be readily modified to simulate foundations which have no uplift capacity by truncating the yield function using a no-tension cut-off criterion (Fig. 2.5).

Finally, the vertical, horizontal and moment equilibrium for the footing itself impose two additional constraints on the interface tractions (Fig. 3b):

$$\sin\alpha\int_s \sigma_n dx - \cos\alpha\int_s \tau\, dx = 0 \tag{2.10a}$$

$$\int_s x\sigma_n dx = 0 \tag{2.10b}$$

where x is the distance measured from the point of the resultant load application (Fig. 2.3). As the stresses vary linearly across each element, the integrals in eqns. 2.10a, b can also be assembled in matrix form:

$$\mathbf{A_4}\sigma_4 = \mathbf{B_4} \tag{2.11}$$

where σ_4 is the vector of stresses at nodes along the soil-footing interface.

Equations 2.4, 2.6, 2.9 and 2.11 summarize the constraints on the nodal point stresses which ensure static admissibility. Lower bound estimates of the collapse load for surface footings are then obtained by maximizing the resultant force, Q (per unit width):

$$\text{Max.}\{Q\} = \text{Max.}\left\{\frac{1}{\cos\alpha}\int_s \sigma_n\, dx\right\} \tag{2.12}$$

Using the stress transformation relations, this objective function can be written as:

$$\text{Max. } \mathbf{C}^T\sigma \quad \text{or} \quad \text{Min. } -\mathbf{C}^T\sigma \tag{2.13}$$

Hence, by assembling the coefficients for the complete finite element mesh, the lower bound analysis can be formulated as a linear programming problem that can be solved efficiently by an active set algorithm (Table 2.1; Sloan, 1988a).

2.3.2 Upper Bound Formulation

An upper bound on the exact collapse load can be obtained by equating the power dissipated in a *kinematically admissible velocity field* with the power expended by the external loads (Drucker et al., 1952). A kinematically admissible velocity field is one

which satisfies the compatibility equations, velocity boundary conditions and the flow rule. During plastic flow, power is dissipated by plastic yielding of the soil mass, and by sliding along velocity discontinuities, where jumps in the normal and tangential velocities can occur.

The upper bound analysis for plane strain problems is solved numerically using three-noded triangular finite elements. Velocity discontinuities can occur along shared edges between elements, while the unknown soil velocities (u_x, u_y) vary linearly within each element:

$$u = \sum_{i=1}^{3} N_i u_i \quad ; \quad v = \sum_{i=1}^{3} N_i v_i \tag{2.14}$$

where (u_i, v_i) are the components of the nodal point velocities, and N_i are the linear shape functions.

In order to satisfy the conditions of kinematic admissibility, the plastic strain rates within each element must be compatible with the velocity field and satisfy the associated flow rule:

$$\dot{\varepsilon}_x = -\frac{\partial u}{\partial x} = \dot{\lambda}\frac{\partial F}{\partial \sigma_x} \; ; \; \dot{\varepsilon}_y = -\frac{\partial v}{\partial y} = \dot{\lambda}\frac{\partial F}{\partial \sigma_y} \; ; \; \dot{\gamma}_{xy} = -\left(\frac{\partial u}{\partial y} + \frac{\partial v}{\partial x}\right) = \dot{\lambda}\frac{\partial F}{\partial \tau_{xy}} \tag{2.15}$$

where $\dot{\varepsilon}_x, \dot{\varepsilon}_y, \dot{\gamma}_{xy}$ are the plastic strain rates (positive in compression), $\dot{\lambda}$ is the plastic multiplier and F is the (Tresca) yield function of the clay.

For the upper bound calculation, the Tresca yield surface is represented by a p-sided polygon that externally circumscribes the exact function (eqn. 2.8 with $D = 2s_u$). Hence, the conditions for a kinematically admissible velocity field within each element can be expressed as a series of linear constraints on the nodal point velocities and unknown plastic multiplier rates (for each of the p sides of the yield polygon) by combining eqns. 2.14, 2.15 and 2.8:

$$\begin{aligned} &\sum_{i=1}^{3} \frac{\partial N_i}{\partial x} u_i + \sum_{k=1}^{p} \dot{\lambda}_k A_k = 0 \; ; \; \sum_{i=1}^{3} \frac{\partial N_i}{\partial y} v_i + \sum_{k=1}^{p} \dot{\lambda}_k B_k = 0 \\ &\sum_{i=1}^{3} \frac{\partial N_i}{\partial x} v_i + \sum_{i=1}^{3} \frac{\partial N_i}{\partial y} u_i + \sum_{k=1}^{p} \dot{\lambda}_k C_k = 0 \end{aligned} \tag{2.16}$$

where $\dot{\lambda}_k \geq 0$.

These relations can be re-written in a compact matrix form as:

$$\mathbf{A}_{11}\mathbf{u}_1 + \mathbf{A}_{12}\lambda = 0 \tag{2.17}$$

where $\mathbf{u}_1$ and λ are vectors of nodal point velocities and plastic multipliers, respectively, for each element.

The upper bound formulation allows velocity discontinuities to occur along shared edges between elements. The discontinuity can be characterised by a jump in the normal and tangential velocity components (Δu, Δv) between pairs of nodes (i, j) (e.g., 2, 4 or 3, 6 in Figure 2.2).

$$\begin{aligned} \Delta u_{ij} &= (u_j - u_i)\cos\theta + (v_j - v_i)\sin\theta \\ \Delta v_{ij} &= (u_i - u_j)\sin\theta + (v_j - v_i)\cos\theta \end{aligned} \tag{2.18}$$

where θ describes the orientation of the discontinuity.

In order to maintain kinematic admissibility, the velocity jump must satisfy the flow rule. For the Tresca yield condition, this requires that plastic deformation occurs at constant volume with no jump in the normal velocity component, i.e.,:

$$\Delta v_{ij} = 0 \tag{2.19}$$

There is no restriction on the sign of the tangential velocity jump. However, its value can be constrained according to the requirements of standard linear programming methods, by introducing two subsidiary non-negative variables (Δu^+, Δu^-) such that:

$$\begin{aligned} &\Delta u_{ij} = u_{ij}^+ - u_{ij}^- \\ &\text{subject to: } u_{ij}^+ \geq 0 \,;\, u_{ij}^- \geq 0 \end{aligned} \tag{2.20}$$

Equations 2.18, 2.19 and 2.20 can be combined to form a series of linear constraints, written in matrix form as:

$$\mathbf{A}_{21}\mathbf{u}_2 + \mathbf{A}_{22}\mathbf{u}^{\pm} = 0 \tag{2.21}$$

where $\mathbf{u}_2$ is the vector of nodal velocities for the matched pairs (e.g., 2, 4 and 3, 6 in Fig. 2.2), and , $\mathbf{u}^{\pm}$ is the vector of subsidiary variables (u_{12}^+ etc.).

The total internal power, W_i, can be computed by summing the dissipation that occurs due to plastic deformation within each of the soil elements and by shearing along

the velocity discontinuities between elements. The components of internal power dissipation are as follows:

Within each element: $$W_c=\int_A \left(\sigma_x\dot{\varepsilon}_x+\sigma_y\dot{\varepsilon}_y+\tau_{xy}\dot{\gamma}_{xy}\right)\ dA=2\sum_{k=1}^{p}\dot{\lambda}_k\int_A s_u dA=\mathbf{C}_2^T\lambda \qquad (2.22a)$$

Along each discontinuity: $$W_d=\int_L s_u|\Delta u_t|\,dL=\int s_u\left(\Delta u_t^+ +\Delta u_t^-\right)\,dL=\mathbf{C}_3^T\mathbf{u}^{\pm} \qquad (2.22b)$$

The motions of a rigid footing under combined loading can be represented by two unknown velocities, u_c, v_c, and an angular rotation, ω_c, defined about a fixed reference point at the center of the base (Fig. 2.3c). The external work done by the applied load is then:

$$W_e = Q\{u_c\sin\alpha - v_c\cos\alpha + \omega_c e\cos\alpha\} \qquad (2.23)$$

An upper bound on the true collapse load can then be obtained by equating the total internal power dissipation and the external work, W_e:

$$Q\{u_c\sin\alpha - v_c\cos\alpha + w_c e\cos\alpha\} = W_i \qquad (2.23a)$$

Hence, the resultant force, Q, can be obtained from eqn. 2.23a by constraining movements of the footing such that:

$$u_c\sin\alpha - v_c\cos\alpha + \omega_c e\cos\alpha = 1 \qquad (2.24)$$

This result can be combined with other velocity boundary conditions to form a set of constraints on the nodal point velocities:

$$\mathbf{A}_3\mathbf{u}_l=\mathbf{B}_3 \qquad (2.25)$$

The objective function for these upper bound analyses seeks to minimize the external applied load (i.e., Min.{Q}) which is equivalent to minimizing the total rate of internal power dissipation, Min.{W_i} (from eqns. 2.23a, 2.24).

Table 2.1 summarizes the formulation of the upper bound analysis in a standard linear programming form. Sloan and Kleeman (1995) give full details of the condensation of these equations into the canonical form used by the steepest edge active set algorithm.

2.4 Typical Results

One of the principal advantages of the numerical limit analyses is that the true collapse load is always bracketed by results from the upper and lower bound calculations. However, careful mesh refinement is essential in order to achieve numerically accurate solutions, where the error bounds on the exact load are within a prescribed tolerance, say $\pm 5\%$. Figure 2.6 shows typical finite element meshes used for computing the undrained stability of footings on clay (after Ukritchon, 1996). The mesh for the lower bound analysis uses a high element density (mesh refinement) close to the stress singularities at the edges of the footing. Extension elements are introduced in order to ensure statically admissible solutions at all points in the deep clay layer (half-space). These elements require special forms of the constraint equations for equilibrium and yield (cf. eqns. 2.4, 2.9; Sloan, 1988b). Most of the analyses reported in this chapter consider that the base of the footing is rough (i.e., the interface shear traction, $|\tau| \leq s_u$), and assume there is either no tensile stress between the footing and soil ($\sigma_n \geq 0$; zero underbase suction) or that the normal stress is constrained only by the shear strength of the soil (full suction with no cavitation). Validation calculations for vertically loaded footings have also considered smooth bases ($\tau = 0$).

The mesh for the upper bound analysis is based on a uniform squares each subdivided into four triangular elements. There is apparently no advantage in more complex geometric arrangements, presumably due to the large number of velocity discontinuities permitted in the analysis. The size of the discretized domain must be sufficient to contain potential failure mechanisms, such that the far field boundaries can be represented as zero velocity conditions. Rigid body motions of the footing constrain the surface velocities at points along the interface. The analyses assume that separation can occur under combined loading if there is no suction at the interface. Figure 2.5 shows how the flow directions are affected by the introduction of a tension cut-off in the yield criterion. This condition imposes the constraint that the normal velocity jump, $\Delta u_n \leq 0$, at points along the soil-footing interface.

Both upper and lower bound calculations assume a constant value, p = 24, for the yield surface linearization. Typical computation times for the analyses reported in this chapter range from 10 -30mins of CPU on a DEC workstation (Alpha 3000-300x).

Figure 2.7 summarizes the computed upper and lower bound estimates of the bearing capacity for vertically loaded footings on soil profiles where the undrained shear strength increases linearly with depth ($s_u = s_{u0}+\rho z$). The numerical solutions are compared with analytical results reported by Davis and Booker (1973) for smooth and rough bases. For the homogeneous case ($\rho B/s_{u0} = 0$), the interface shear strength has no effect on the bearing capacity, and the numerical solutions provide very tight bounds on the exact collapse load (3.7% difference between the upper and lower bound). For non-homogeneous strength profiles with $\rho B/s_{u0} \leq 20$ the true collapse load is bounded within 5 - 6%, and very good estimates of failure can be obtained by averaging the computed upper and lower bound loads ($Q_A = 1/2[Q_L + Q_U]$; the error on the exact load is then bounded within $\pm 1.5\%$). For small values of the ratio $s_{u0}/\rho B$ (0.005 - 0.05) the difference in computed bounds increases to 10%. Comparisons with the analytical solutions suggest that this range can be reduced by further mesh refinement for the lower bound calculation. In all cases, Q_A is within $\pm 4.5\%$ of the true collapse load. The mechanism of failure for $s_{u0}/\rho B = 0$ involves horizontal displacement of a surface veneer of soil beneath the footing, and cannot be simulated accurately by the numerical upper bound calculation.

Figure 2.8 illustrates the character of the statically admissible stress fields by comparing lower bound predictions for smooth bases, and soil profiles with $\rho B/s_{u0} = 0$ and 3. As expected for the homogeneous case ($\rho B/s_{u0} = 0$), the major principal stress remains constant throughout a large zone of active shearing ($\delta = 0°$; Fig. 2.8b) beneath the footing. The region of principal stress rotation is well defined by a series of radial stress discontinuities (Fig. 2.8a), and passive shearing occurs in the surrounding soil ($\delta = 90°$; Fig. 8b). The analysis predicts uniform vertical contact stresses across the width of the footing (Fig. 2.8e). In contrast, lower bound calculations for $\rho B/s_{u0} = 3$ show that contact stresses increase towards the center of the footing (the results match analytical

solutions from Davis & Booker, 1973; Fig. 2.8f), while the zone of principal stress rotation extends to all points beneath the footing (Fig. 2.8d). The results of upper bound analyses for the same two examples are shown in Figure 2.9, and provide information on the location of the plastic zone and failure mechanisms (interpreted from velocity vectors, Figs. 2.9b, d; and mesh deformations, Figs. 2.9a, c). Although the results for the homogeneous case are very similar to the mechanism proposed by Prandtl, the numerical analyses predict some lateral spreading in the soil beneath the smooth base, and a slightly larger plastic failure zone. For the non-homogeneous strength profile ($\rho B/s_{u0} = 3$; Figs. 2.9c, d), the plastic failure zone is greatly reduced in size, and the mechanism is dominated by lateral spreading towards the edge of the footing.

2.5 Predictions For Combined Loading

2.5.1 Eccentric and Inclined Loading

Figures 2.10 and 2.11 summarize the results of lower and upper bound analyses for footings on homogeneous soil with a) vertical, eccentric loading (H = 0), and b) inclined central loading (M = 0). These calculations all assume a rough interface with no underbase suction (i.e., tension cut-off is in effect; Fig. 2.5). Lower bound calculations confirm that the reduction in footing capacity for vertical eccentric loading (Fig. 2.10a) is related to the loss of contact pressure at the trailing edge of the footing. At an eccentricity e/B = 0.25, approximately 50% of the footing remains in contact with the soil. For inclined central loading, full mobilization of the horizontal shear resistance occurs at relatively small inclination angles (e.g., at $\alpha = 15°$, $\tau/s_u \geq 0.90$ over most of the footing; Fig. 2.10b). The upper bound calculations for the same loading conditions (Fig. 2.11a-c) show clearly the transition in failure mechanisms from a vertically penetrating active wedge at $\alpha = 0°$, to a sliding wedge at $\alpha = 15°$ and full interface sliding at $\alpha = 45°$. As the eccentricity of the applied vertical load increases (e/B = 0, 0.1, 0.25; Figs. 2.11a, d, e), there is an overall reduction in the volume of the failure zone. At the leading edge of the footing, the mechanism of failure closely resembles the sliding wedge from Fig. 2.11b. The pivot point for rotation is located close to the ground surface and migrates towards the centerline as the load eccentricity increases. At e/B = 0.25, separation occurs at the

trailing edge of the footing (for $x/B < 0.15$) and the rotational mechanism is fully contained beneath the base (note that the onset of separation occurs at $e/B = 0.20$).

2.5.2 Combined Loading

The preceding upper and lower bound calculations have been extended for selected combinations of inclination angle, $\alpha = 0° - 90°$, and eccentricity, $-0.35 \leq e/B \leq 0.35$. Figure 2.12 shows the computed collapse loads as contour lines, corresponding to constant values of α and e/B, projected in two orthogonal planes $[V/(Bs_u), M/(B^2s_u)]$ and $[V/(Bs_u), H/(Bs_u)]$. In all cases, the upper and lower bound calculations are able to estimate the true collapse load within $\pm$4-5%. More precise bounds ($\pm$0.5%) occur for cases dominated by interface sliding, where $|H/(Bs_u)| \rightarrow 1$ (Fig. 2.12b). The maximum moment for both loading modes can be well estimated by $|M/(B^2s_u)| = N_{c0}/8 = 0.643$ [at $V/(Bs_u) = N_{c0}/2$, where $N_{c0} = (2 + \pi)$], as predicted using the effective width concept of Meyerhof (1953). The reduction in moment capacity for values of $V/(Bs_u) < 2.0 - 3.0$ is caused by the assumption that there is no underbase suction and hence, the area of contact between the footing and soil reduces to zero as $|e/B| \rightarrow 0.5$. The effects of eccentricity mode (I vs II) can be seen from the lack of symmetry of the projected contour lines in Figures 2.12a, b. The most pronounced differences occur for $e/B > 0.25$, and $\alpha = 15° - 30°$, where footing capacity in Mode II loading is up to 20 - 25% less than that in Mode I.

Figure 2.13 compares the predicted limit loads $(Q/[Bs_u])$ with conventional bearing capacity calculations using the empirical correction factors given in equation 2.1. In general, the empirical calculations are conservative and underestimate the limit loads for combined loading by up to 25%. More detailed observations show that a) the concept of effective width matches the lower bound solutions for vertical eccentric loading ($\alpha = 0°$, Fig. 2.13a); and b) the empirical inclination factors proposed by Meyerhof (1953) are in better agreement with predicted limit loads for inclined central loading ($e/B = 0$), than those introduced by Vesic (1975).

2.5.3 Effects of Underbase Suction

For certain types of offshore foundation, such as gravity bases with short skirt piles, underbase suction can contribute significantly to the short-term undrained stability. Figure 2.14 compares 3-D failure envelopes (defined in terms of the statically equivalent loads V, H and M) for footings with zero underbase suction (derived from Fig. 2.13) and with full suction. In this representation, it is convenient to report the best estimate of the true collapse load as the average of the upper and lower bound predictions. Underbase suction preserves the moment capacity of the footing at low vertical load ratios, V/V_0 (where the maximum vertical capacity, $V_0 = N_{c0}s_u$), but has no effect on the predicted failure conditions for $V/V_0 > 0.65$.

Differences between Mode I and Mode II loading can be seen most clearly in cross-sections of the failure surfaces at constant values of V/V_0 (H-M planes), Figure 2.15. For both modes of loading, the maximum horizontal load capacity is constrained by $H/Bs_u \leq 1.0$. At large vertical load ratios, $V/V_0 > 0.875$, the maximum moment capacity occurs when $H/Bs_u = 0$ and the failure locus is approximately symmetric. As the vertical load ratio decreases from $V/V_0 = 0.825$ to 0.5, the failure surface becomes increasingly skewed with the maximum moment capacity occurring for Mode I combinations of H and M. For $V/V_0 < 0.5$, the vertical load has minimal effect on Mode II failure conditions (with full suction), while Mode I produces a maximum moment capacity, $M/(B^2s_u) = 0.8$ [at $H/(Bs_u) \approx 0.8$] for $V/V_0 \leq 0.25$. At these same sections, the failure envelope for Mode I loading is truncated by the constraint of maximum horizontal load capacity.

Figures 2.16 and 2.17 present more detailed results of the upper and lower bound analyses, respectively, for three loading conditions labelled A, B and C in Figure 2.15 [all at $V/V_0 = 0.5$, with $|H/(Bs_u)| = 0.7$; i.e., $\alpha = 55°$]. The comparisons between A and B show the role of underbase suction in Mode I; while the results for C are typical of Mode II combined loading (and are not affected by the underbase suction). There is a large reduction in the interface contact area for case A (zero suction, Fig. 2.16a). The failure mechanism can be characterized by an active zone that rotates about a pivot point located below the detachment point on the base of the footing (at $x/B \approx -0.125$, $y/B \approx 0.5$), connecting to a rotational shear zone and a passive wedge. Very similar failure

mechanisms have been assumed in upper bound analyses by Salencon and Pecker (1995a, b) and in limit equilibrium calculations (Lauritzen & Schjetne, 1976). The lower bound calculations (Fig. 2.17a) show that the maximum vertical bearing pressures ($N_{c0}s_u$) are mobilized at the leading edge of the footing, while shear tractions are fully mobilized from the trailing edge to the centerline.

With full underbase suction (case B, Fig 2.16b) there is a rotational failure mechanism contained beneath the base of the footing (centered close to the ground surface and slightly offset from the centerline), and a failure wedge at the leading edge of the footing (this is similar to the scoop-wedge mechanism proposed by Bransby & Randolph, 1997). The lower bound calculations predict that tensile stresses occur towards the trailing edge of the footing ($x/B < -0.6$), however, underbase suction has little effect on the distribution of the shear tractions (τ/s_u, Figs. 2.16b, a). Failure in Mode II involves a single scoop mechanism extending slightly beyond the leading edge of the footing. The normal stress varies linearly across the base from a maximum bearing pressure at the trailing edge to zero at the leading edge of the footing (hence, the direction of the major principal stress also varies from $\delta = 0° - 45°$).

2.5.4 Effect of Non-Homogeneous Strength Profile

Limit analyses have also been carried out for combined loading of non-homogeneous clay profiles where the undrained shear strength increases linearly with depth for $0 \leq \rho B/s_{u0} \leq 12$ (cf. Fig. 2.7), assuming zero underbase suction. Figures 2.18a, b summarize the results for cases of vertical, eccentric and inclined, central loading. As expected, the maximum horizontal shear resistance is controlled by the strength of the surficial soil ($H/[Bs_{u0}] \leq 1$), while the maximum moment capacity occurs at a vertical load ratio, $V/V_0 = 0.5$, and ranges from $M/[B^2s_{u0}] = 0.65$ to 1.35 for $\rho B/s_{u0} = 0$, 12, respectively. Figure 2.18c illustrates the effects of the undrained strength gradient on the shape of the yield envelope in the H-M plane at $V/V_0 = 0.5$. The yield surface remains non-symmetric as the profile parameter $\rho B/s_{u0}$ rises, while increases in the moment capacity are more pronounced for Mode II than for Mode I.

There are no published solutions specifically for combined loading of footings on non-homogeneous clay layers. However, it is conventional practice (e.g., Det Norske Veritas, 1992) to apply the correction factors given in eqn. 2.1 together with analytical solutions for N_{c0} (Davis & Booker, 1973). Figure 2.19 compares the predicted limit loads with these empirical calculations. It is clear that the empirical calculations can greatly overestimate the actual limit load especially at small inclination angles ($\alpha \leq 10°$; Fig. 2.19b), and/or large eccentricities ($|e/B| > 0.1$; Fig. 2.19a).

2.6 Empirical Equations For Failure Envelope

The failure envelopes for combined loading have relatively complex geometries, that are most clearly illustrated by the H-M cross-sections shown in Figures 2.15 and 2.18c. In part, this reflects the transition in failure mechanisms for different combinations of loading, underbase suction, undrained strength profiles etc. Although undrained stability can be estimated directly from the results presented in this chapter (or evaluated through further computation), it is more convenient if the solutions can be computed reliably using simple functions. Approximate empirical equations have been developed to describe the failure envelope for footings on homogeneous clay with zero underbase suction. The curve fitting procedure is based on a dimensional analysis which shows that:

For $e/B \geq 0$

$$\tilde{V} = a_1\left\{1 - a_2\left(\frac{2e}{B}\right) - a_3\left(\frac{2e}{B}\right)^2\right\} \tag{2.26}$$

where $\tilde{V} = V/(Bs_u)$, and the eccentricity ratio, $e/B = \tilde{M} / \tilde{V}$ ($\tilde{M} = M/[B^2 s_u]$), and a_1, a_2 and a_3 are all functions of $\tilde{H} = H/(Bs_u)$. For inclined, central loading, eqn. 2.16 reduces to $\tilde{V} = a_1$.

The functions a_1, a_2 and a_3 are determined by empirical curve fitting of the numerical failure envelope:

For $-1 \leq \tilde{H} \leq 1$

$$a_1 = 1 + \pi - 0.8761 \sin^{-1}\left|\tilde{H}\right| + \sqrt{1 - \tilde{H}^2} \tag{2.27a}$$

Mode I, $0 \leq \tilde{H} \leq 1$:

$$a_2 = 1 - \tilde{H} + 0.8\tilde{H}^2 \quad ; \quad a_3 = 1 - a_2 \tag{2.27b}$$

Mode II, $-1 \leq \tilde{H} \leq 0$:

$$a_2 = (2 + \pi)/a_1 \quad ; \quad a_3 = 0 \tag{2.27c}$$

Figure 2.20 compares the empirical equations with the numerically-derived failure envelope. For vertical eccentric loading, eqn. 2.26 is identical to the equation proposed by Meyerhof (1953) using the effective width concept, and matches closely the lower bound limit analyses. For inclined central loading, the function a_I (eqn. 2.27a) is similar to an equation proposed by Bolton (1979) and corresponds to an average of the numerical bounds. Figure 2.20 shows that eqn. 2.27b gives an excellent match to the Mode I failure envelope, while eqn. 2.27c gives a conservative estimate of the Mode II collapse loads (especially at high V/V_0).

The use of separate functions for Modes I and II (eqns. 2.27b, c) is a limitation of the present curve fitting solution. For example, the equations do not guarantee convexity of the failure envelope and this may restrict the application of the empirical functions in further structural stability applications (cf. Murff, 1994).

2.7 Conclusions

The recent numerical formulation of upper and lower bound limit analyses, using finite element discretization and linear programming methods, provides a practical, efficient and accurate method for estimating the undrained stability of foundations on clay. The exact failure conditions for combined loading of surface strip footings can be estimated within $\pm 5\%$ for all of the numerical limit analyses presented in this chapter. The calculations for combined vertical, horizontal and moment loading are summarized in the form of convex failure envelopes for homogeneous clays and profiles where the undrained shear strength increases linearly with depth. The results clarify differences in failure mechanisms between two modes of combined loading (Fig. 2.1), and identify the additional stability provided by underbase suction (which can be mobilized for offshore shallow foundations). Empirical bearing capacity correction factors (for load eccentricity and inclination) are conservative, and can underestimate the true combined collapse load on homogeneous clay by more than 20%. However, the same correction factors are completely unreliable (and non-conservative) for situations where there is an undrained strength gradient ($\rho B/s_{u0} > 0$). The undrained stability for combined loading of surface

foundations can be either be estimated directly from results presented in this chapter, or computed using the proposed curve fitting functions, based on dimensional analysis.

2.8 References

Andersen, K. H., and Lauritzen, R. (1988). "Bearing capacity for foundations with cyclic loads." ASCE Journal of Geotechnical Engineering, 114(5), 540-555.

Assadi, A., and Sloan, S. W. (1991). "Undrained stability of shallow square tunnel." ASCE Journal of Geotechnical Engineering, 117(8), 1152-1173.

Best, M. J., and Ritter, K. (1985). *Linear Programming: Active Set Analysis and Computer Programs*, Prentice-Hall, New Jersey.

Bolton, M. D. (1979). *A guide to soil mechanics*, Macmillan, London.

Bottero, A., Negre, R., Pastor, J., and Turgeman, S. (1980). "Finite element method and limit analysis theory for soil mechanics problems." Comp. Meth. Appl. Mech. Eng., 22 131-149.

Bransby, M. F. and Randolph, M. F. (1997). "Shallow foundations subject to combined loadings." Proc. ISOPE'97, Honolulu.

Brinch Hansen, J. (1970). "A revised and extended formula for bearing capacity." *DGI, Bulletin No. 28*, Danish Geotechnical Institute, 5-11.

Davis, E. H., and Booker, J. R. (1973). "The effect of increasing strength with depth on the bearing capacity of clays." Géotechnique, 23 (4), 551-563.

Dean, E. T. R., James, R. G., Schofield, A. N., Tan, F. S. C., and Tsukamoto, Y. (1992). "The bearing capacity of conical footings on sand." *Predictive Soil Mechanics*, Thomas Telford, London, 230-253.

Det Norske Veritas (1992). "Foundations." Classification Notes No. 30.4, Det Norske Veritas, Hovik, Norway.

Drucker, D. C., Greenberg, H. J., and Prager, W. (1952). "Extended limit design theorems for continuous media." Q. Appl. Math., 9, 381-389.

Gottardi, G., and Butterfield, R. (1993). "On the bearing capacity of surface footings on sand under general planar loads." Soils and Foundations, 33(3), 68-79.

Houlsby, G. T., and Martin, C. M. (1992). "Modelling of the behaviour of jack-up units on clay." *Predictive Soil Mechanics*, Thomas Telford, London, 339-358.

Janbu, N. (1985). "Soil models in offshore engineering." Géotechnique, 35(3), 239-283.

Lauritzen, R., and Schjetne, K. (1976). "Stability calculations for offshore gravity structures." Proc. 8th Offshore Technology Conference, Houston, Paper No. OTC 2431.

Lysmer, J. (1970). "Limit analysis of plane problems in soil mechanics." J. Soil Mech. Found. Div., ASCE., 96(SM4), 1311-1334.

Meyerhof, G. G. (1953). "The bearing capacity of foundation under eccentric and inclined loads." Proc. Third International Conference on Soil Mechanics and Foundation Engineering, Zurich, 1, 440-445.

Murff, J. D. (1994). "Limit analysis of multi-footing foundation systems." Proc. 8th IACMAG, Morgantown, WVa., 1, 233-244.

Prandtl, L. (1920). *Über die Harte plastischer Körper*, Nachr. K. Ges. Wiss. Gott., Math-Phys. Kl., 74-85.

Salencon, J. and Pecker, A. (1995a). "Ultimate bearing capacity of shallow foundations under inclined and eccentric loads. Part I: Purely cohesive soil." Eur. J. Mech. A/Solids, 14(3), 349-375.

Salencon, J. and Pecker, A. (1995b). "Ultimate bearing capacity of shallow foundations under inclined and eccentric loads. Part I: Purely cohesive soil without tensile strength." Eur. J. Mech. A/Solids, 14(3), 377-396.

Sekiguchi, H. and Ohmaki, S. (1992). "Overturning of caissons by storm wave." Soils and Foundations, 32(3), 144-155.

Sloan S. W. (1988a). "A steepest edge active set algorithm for solving sparse linear programming problems." Int. J. Numer. Anal. Methods in Geomech., 26(12), 2671-2685.

Sloan S. W. (1988b). "Lower bound limit analysis using finite elements and linear programming." Int. J. Numer. Anal. Methods in Geomech., 12(1), 61-77.

Sloan S. W., and Kleeman, P. W. (1995). "Upper bound limit analysis using discontinuous velocity fields." Computer Methods in Applied Mechanics & Engineering, 127, 293-314.

Terzaghi, K. (1943). *Theoretical Soil Mechanics*. John Wiley and Sons, New York.

Ukritchon, B. (1996). "Evaluation of numerical limit analyses by finite elements and linear programming." MS Thesis, Department of Civil & Environmental Engineering, MIT, Cambridge, MA.

Vesic, A. S. (1975). "Bearing capacity of shallow foundations." *Foundation Engineering Handbook*, H. F. Winterkorn and H. Y. Fang (Ed.) Van Nostrand Reinhold Company, 121-145.

Zienkiewicz, O.C. (1983). *The finite element method*, McGraw-Hill.

Lower Bound	Upper Bound
MIN.$\{-\mathbf{C}^T\sigma\}$	MIN. $\left\{\mathbf{C}_2^T\Lambda+\mathbf{C}_3^T\mathbf{U}^{\pm}\right\}$
Subject To:	Subject To:
$\mathbf{A}_1\Sigma_1 = \mathbf{B}_1$	$\mathbf{A}_{11}\mathbf{U}_1 + \mathbf{A}_{12}\Lambda = 0$
$\mathbf{A}_2\sigma_2 = \mathbf{B}_2$	$\mathbf{A}_{21}\mathbf{U}_2 + \mathbf{A}_{22}\mathbf{U}^{\pm} = 0$
$\mathbf{A}_3\sigma_3 \leq \mathbf{B}_3$	$\mathbf{A}_{31}\mathbf{U}_1 = \mathbf{B}_3$
$\mathbf{A}_4\sigma_4 = \mathbf{B}_4$	$\Lambda \geq 0$
	$\mathbf{U}^{\pm} \geq 0$
Where Σ is the global vector of nodal stresses.	Where $\mathbf{U}_1$, Λ and $\mathbf{U}^{\pm}$ are global vectors of nodal velocities, plastic multipliers and subsidiary tangential velocity jumps

Table 2.1 Solution of Limit Analyses as Linear Programming Problems

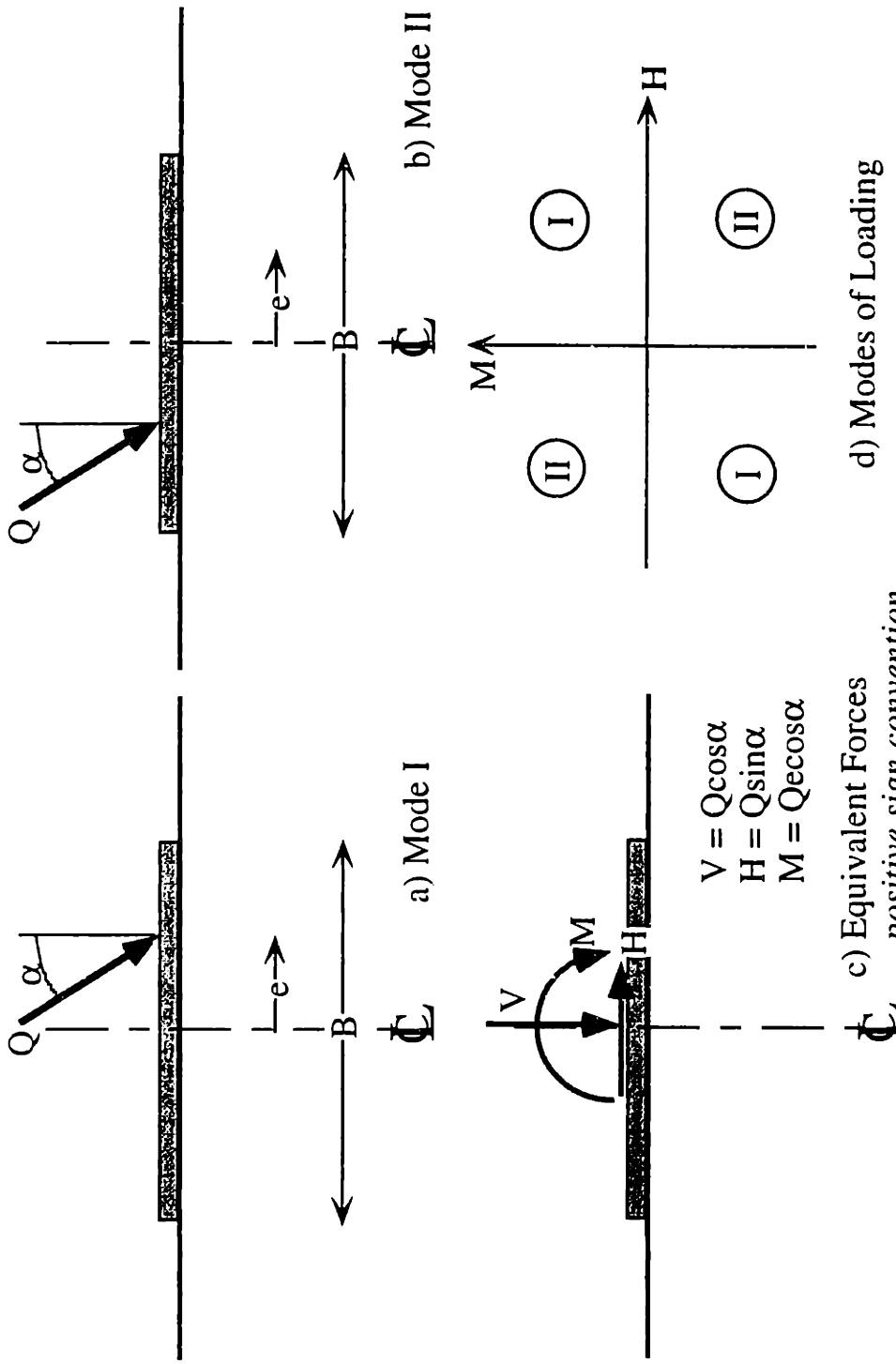

Figure 2.1 Problem notation

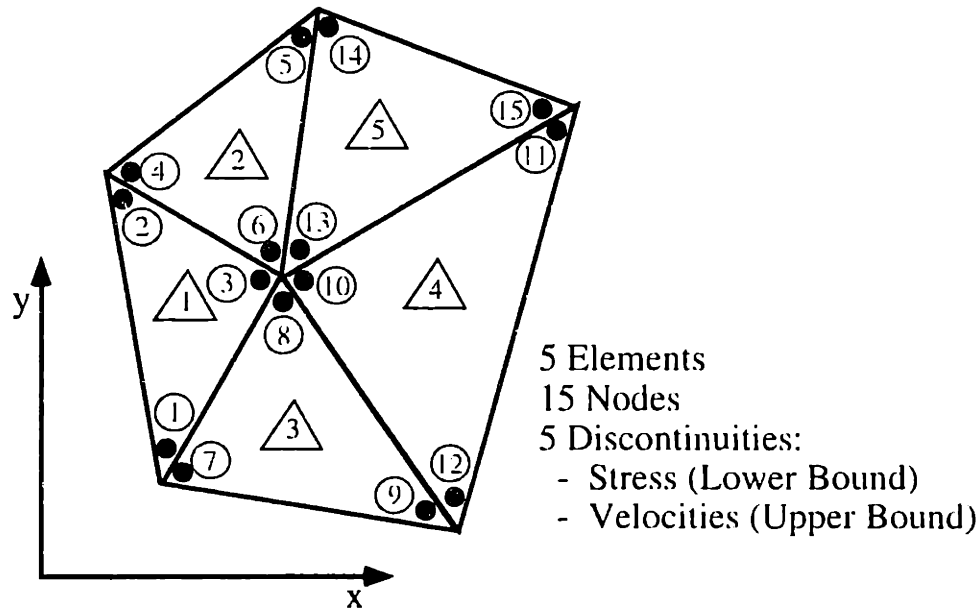

Figure 2.2 Finite element discretization of soil mass

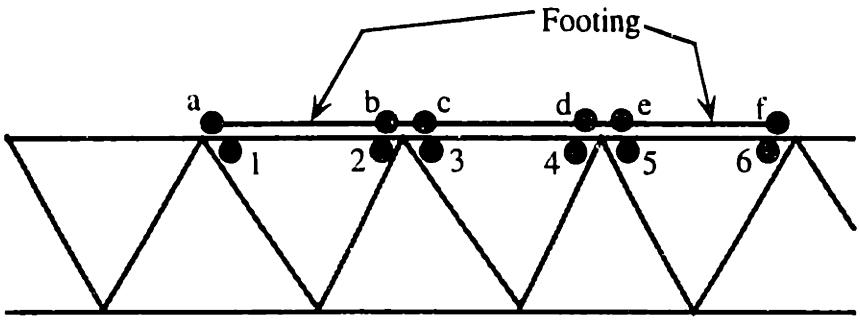

a) Representation of Rigid Footing

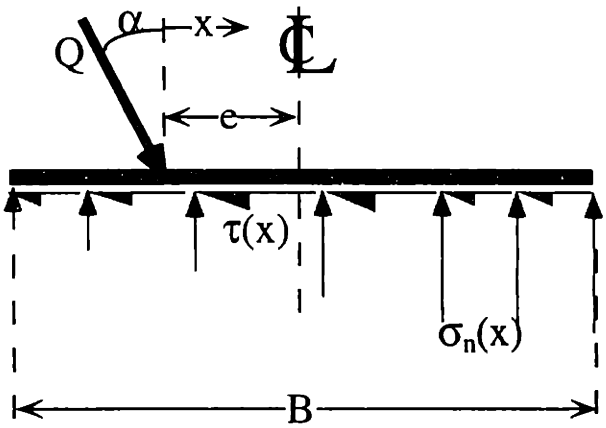

b) Equilibrium of Footing

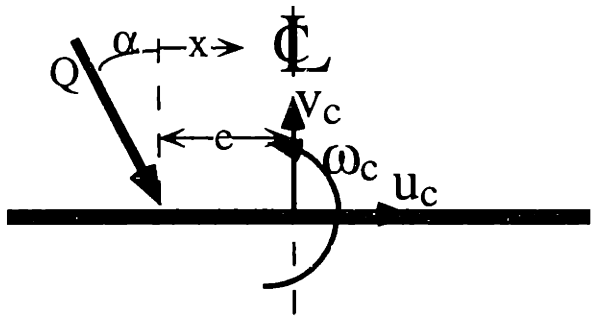

c) Kinematics of Rigid Footing

Figure 2.3 Representation of rigid footing in limit analyses

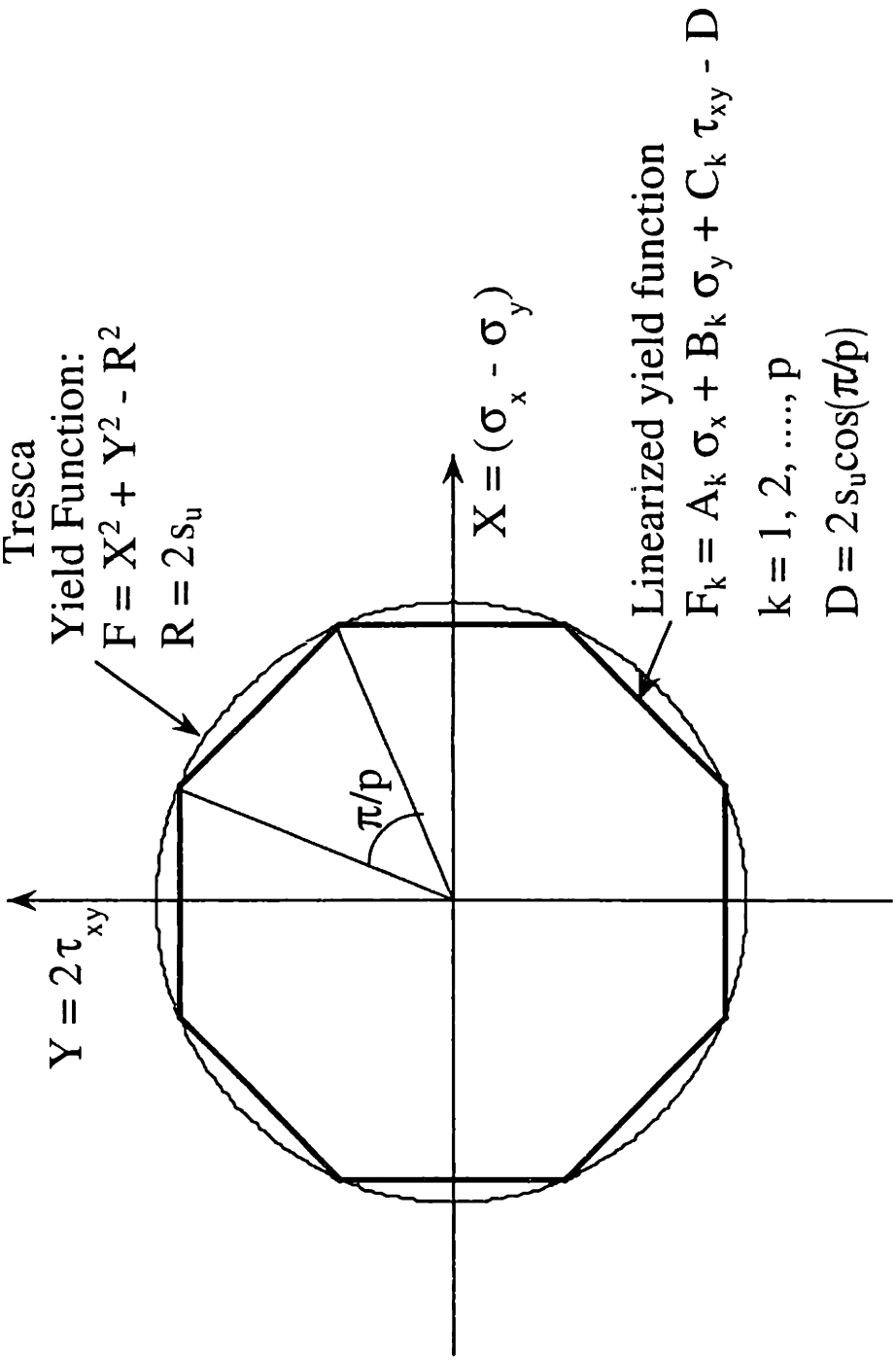

Figure 2.4 Polygonal representation of Tresca yield criterion for lower bound analysis

(after Sloan, 1988b)

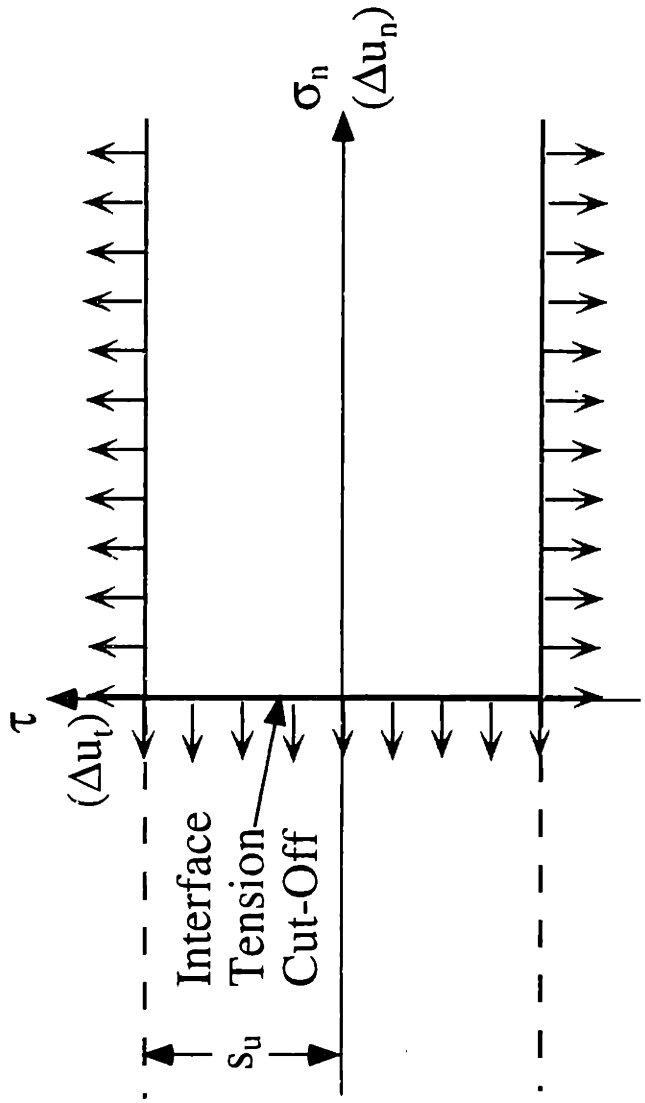

Figure 2.5 Yield and flow directions for soil-footing interface with zero underbase suction

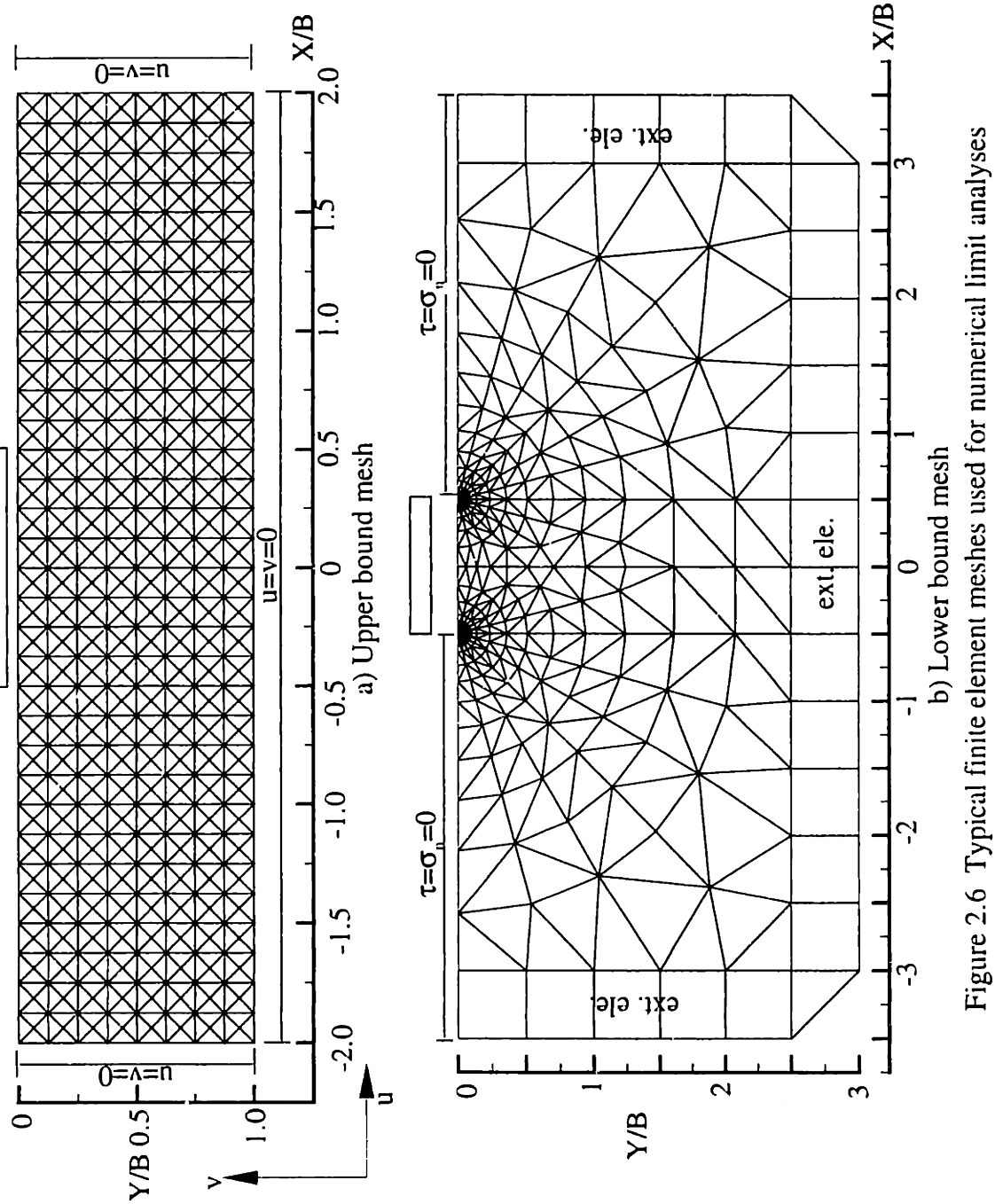

Figure 2.6 Typical finite element meshes used for numerical limit analyses

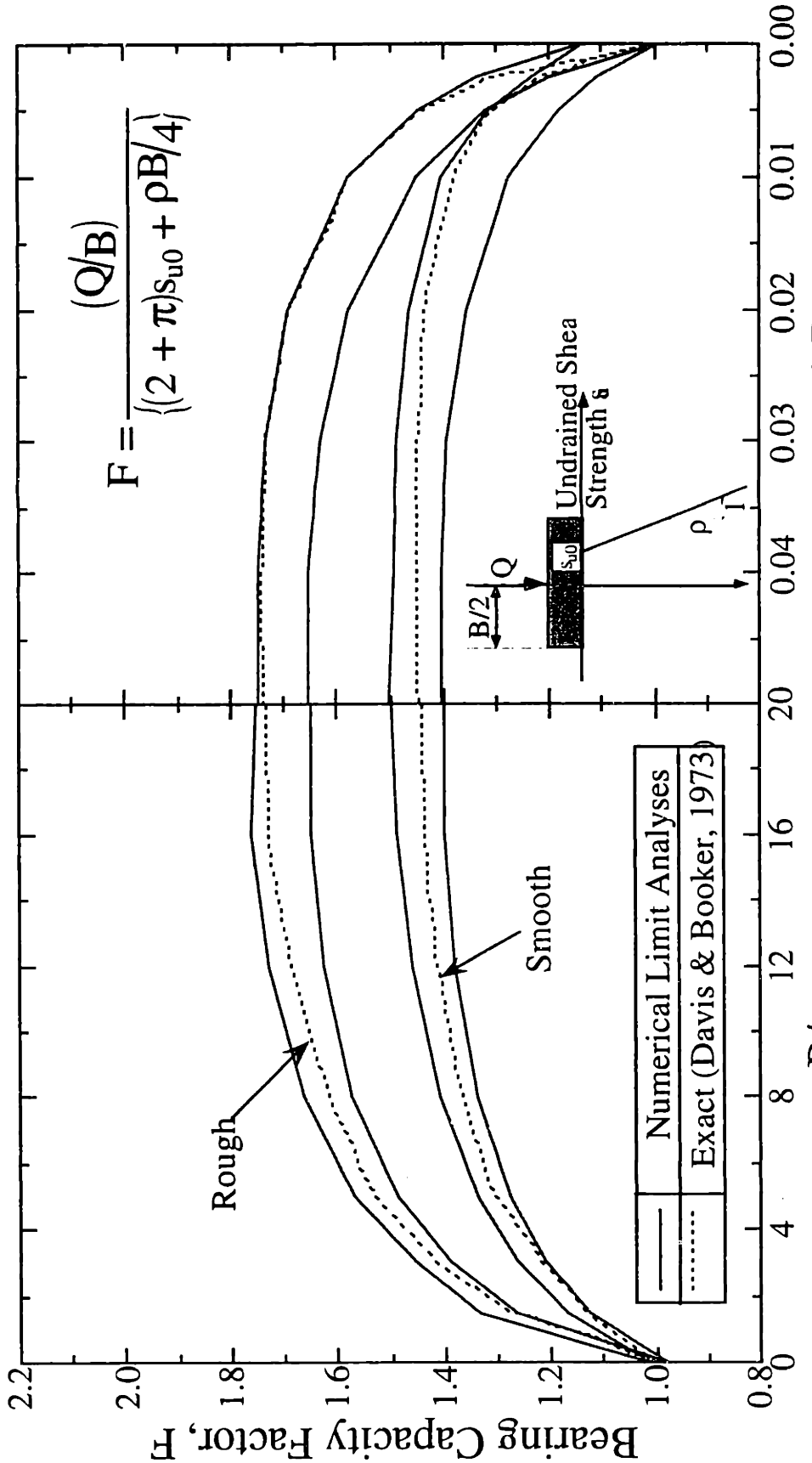

Figure 2.7 Evaluation of numerical limit analyses for vertically loaded footings on non-homogeneous clay layers

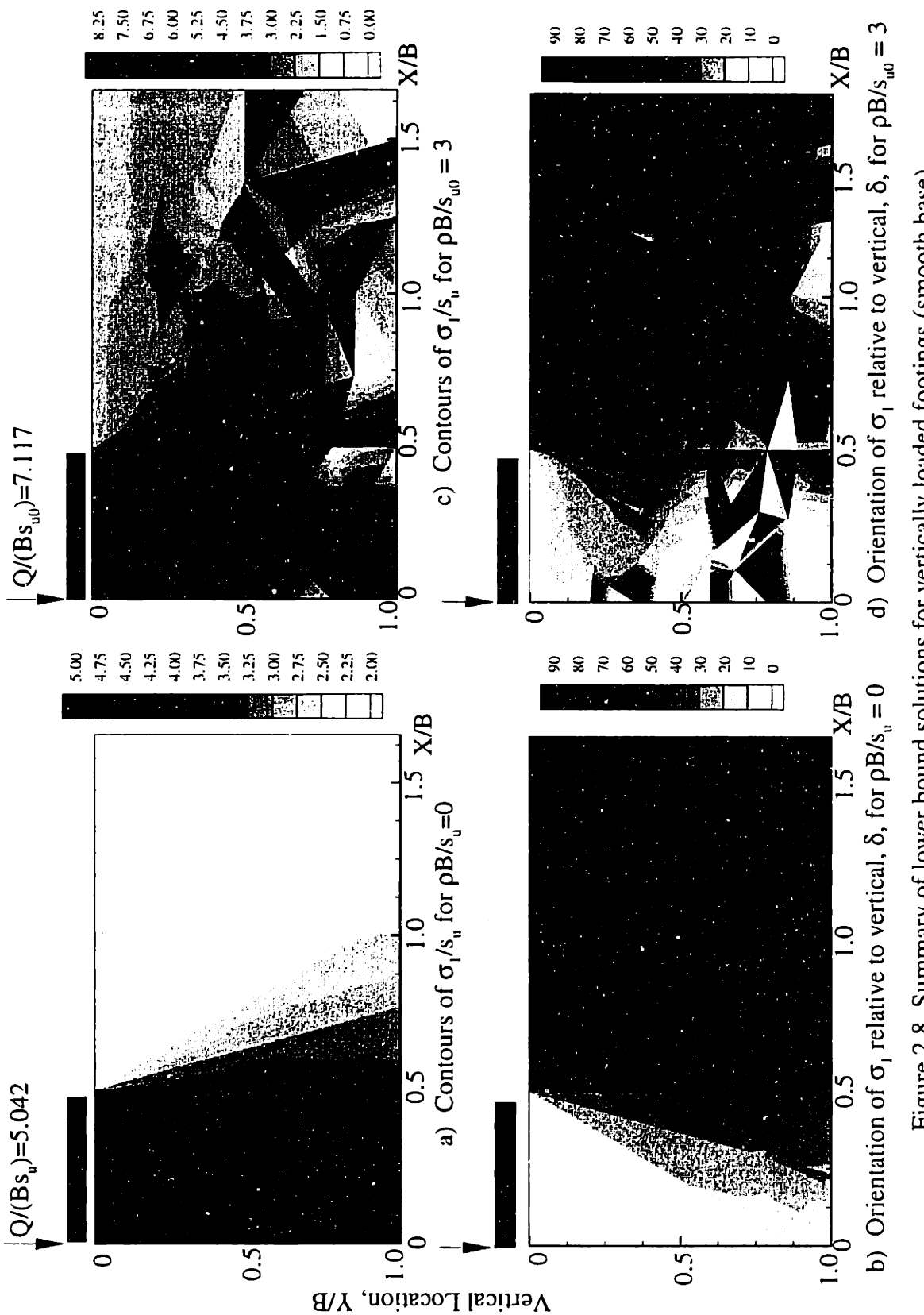

Figure 2.8 Summary of lower bound solutions for vertically loaded footings (smooth base)

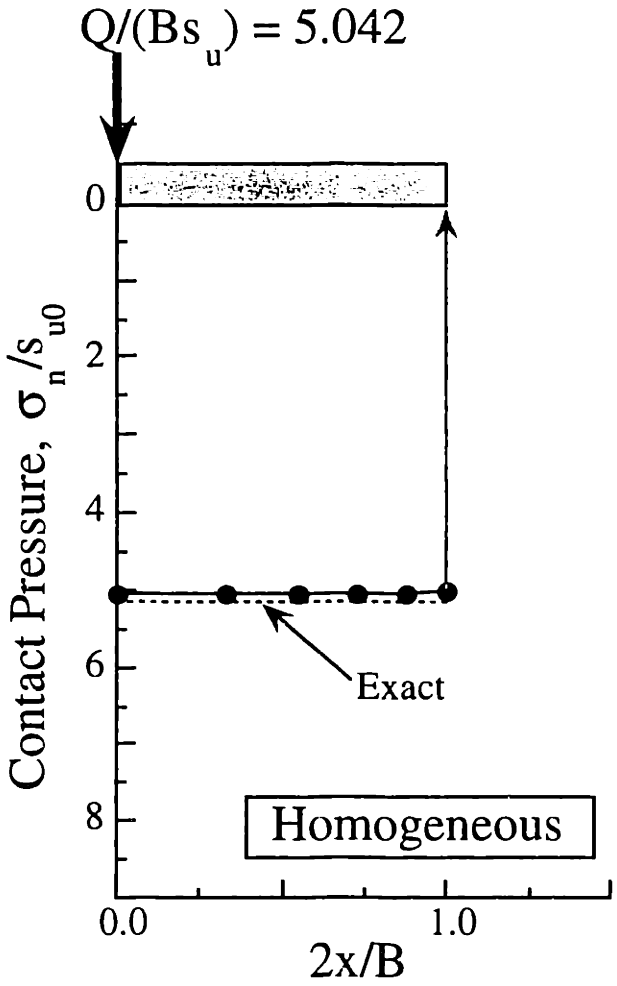

e) Contact pressures, $\rho B/s_u = 0$

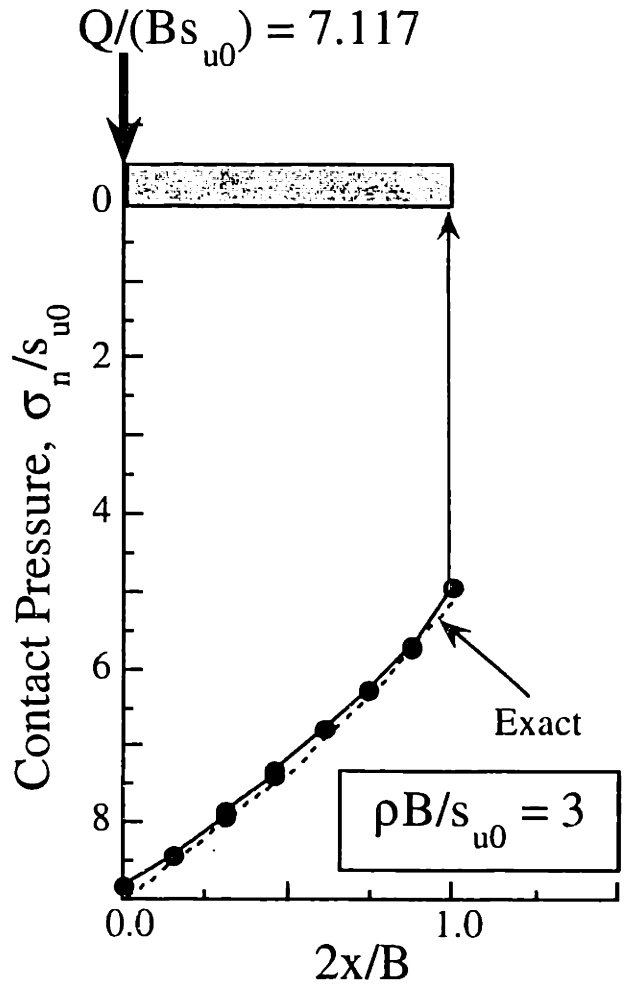

f) Contact pressures, $\rho B/s_{u0} = 3$

Figure 2.8 Summary of lower bound solutions for vertically loaded footings (smooth base)

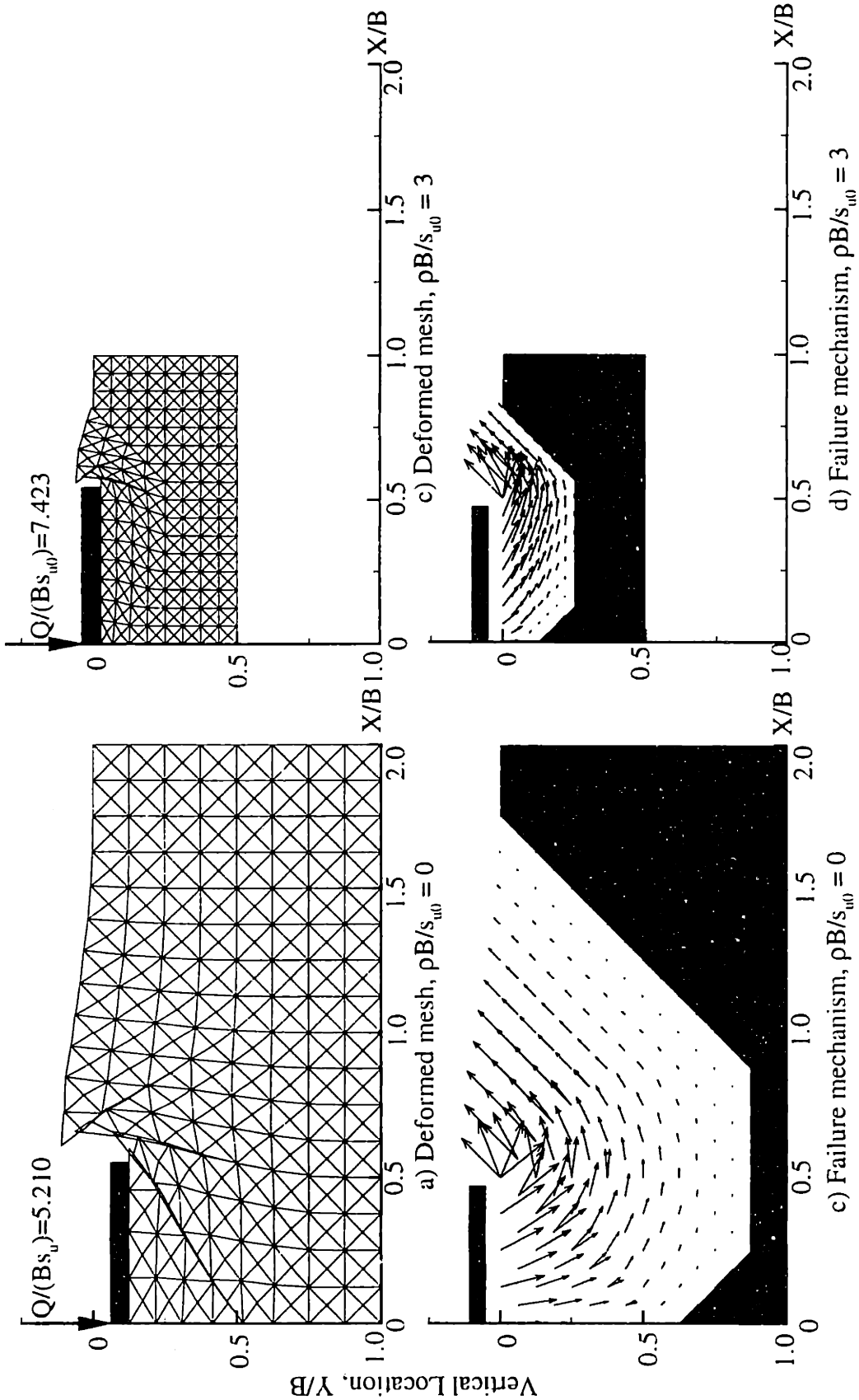

Figure 2.9 Summary of upper bound solutons for vertically loaded footings with smooth base
(Note: light shading - plastic zone)

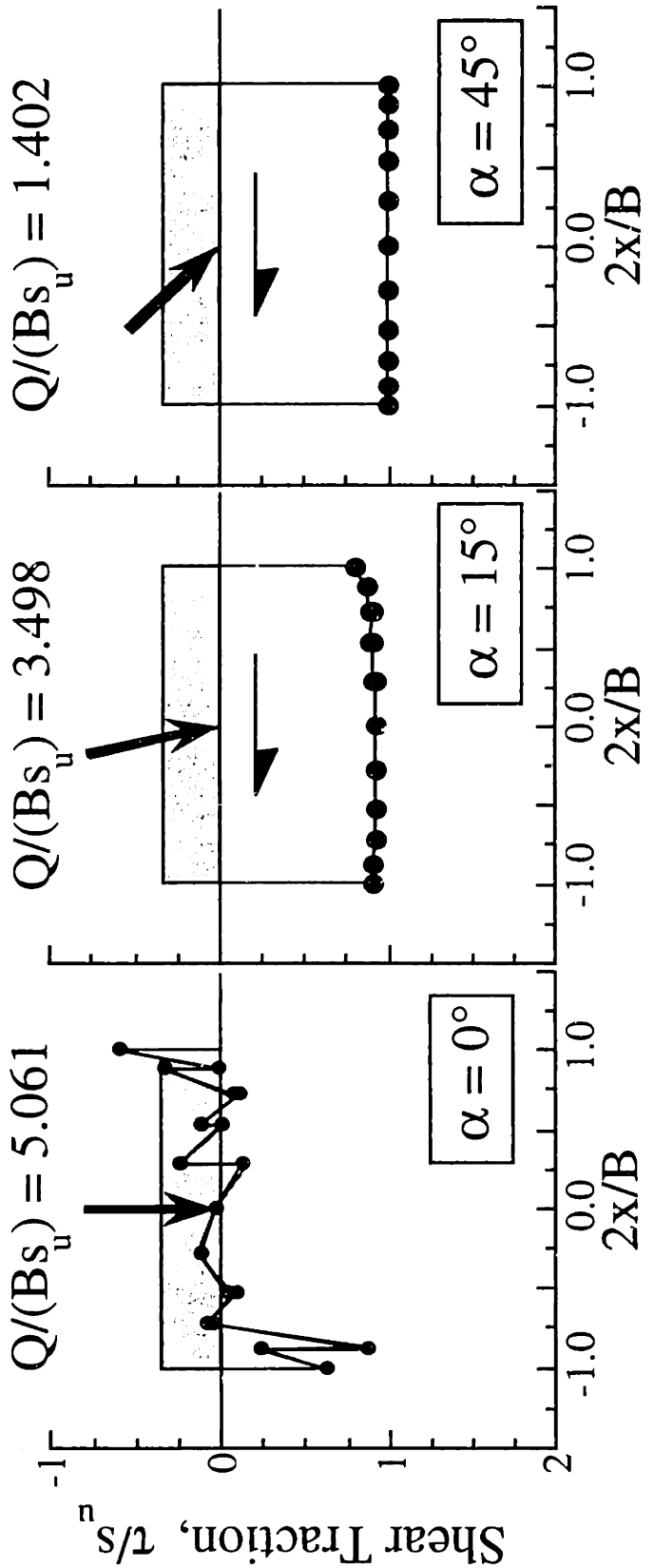

a) Vertical eccentric loading

Figure 2.10 Footing interface tractions from lower bound analyses

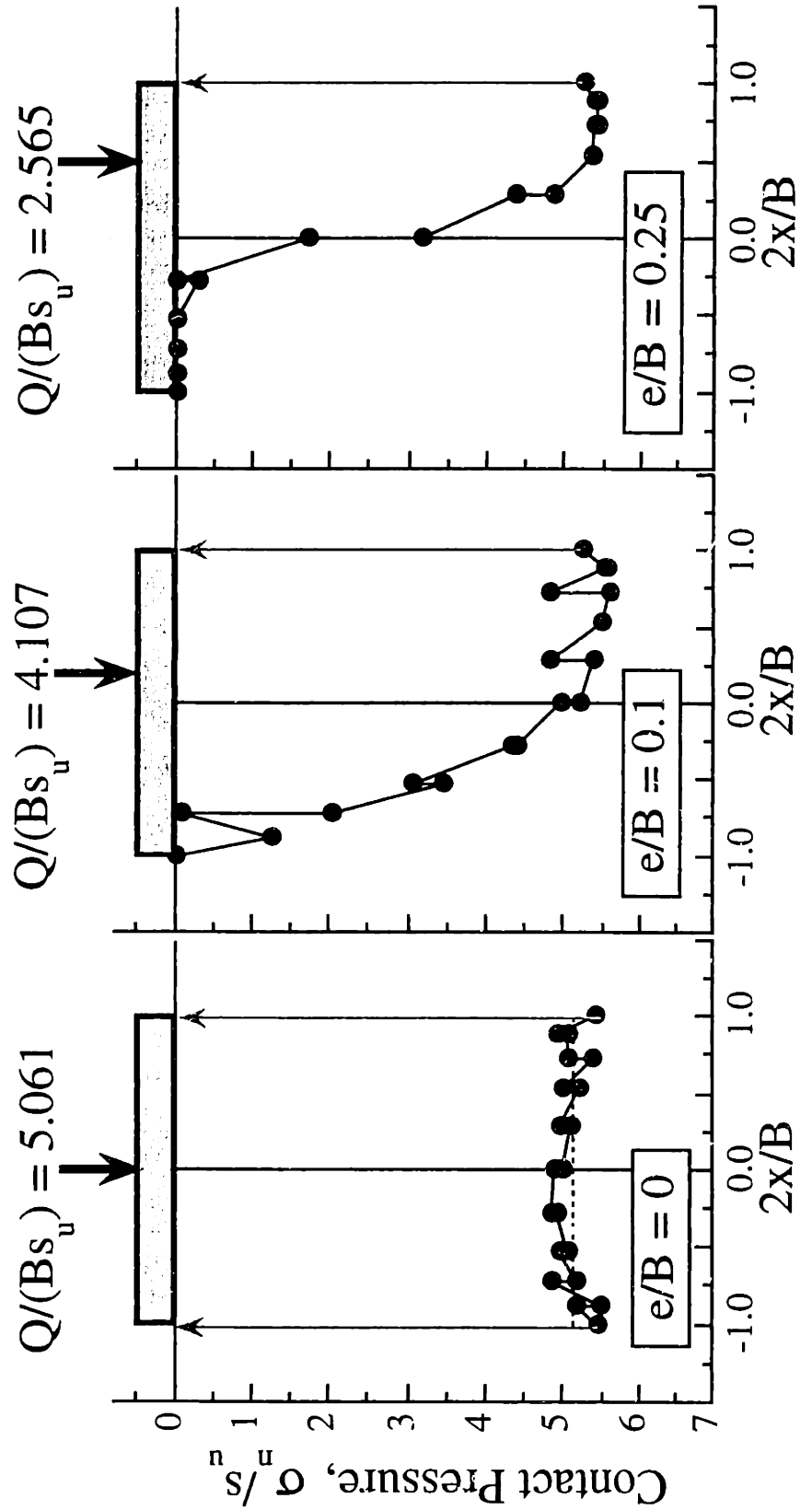

b) Inclined, central loading

Figure 2.10 Footing interface tractions from lower bound analyses

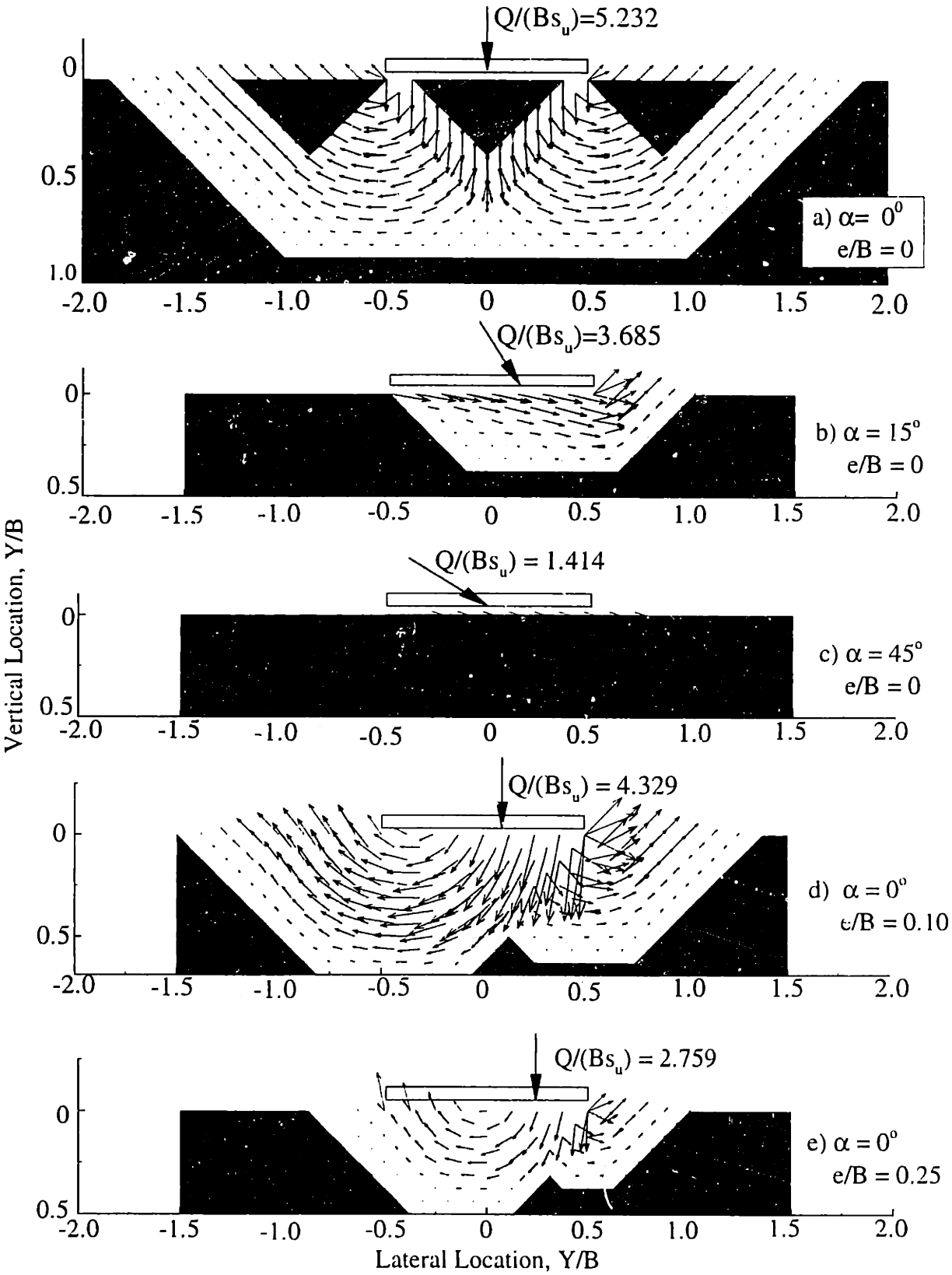

Figure 2.11 Summary of upper bound mechanisms for vertical, eccentric and inclined, central loading

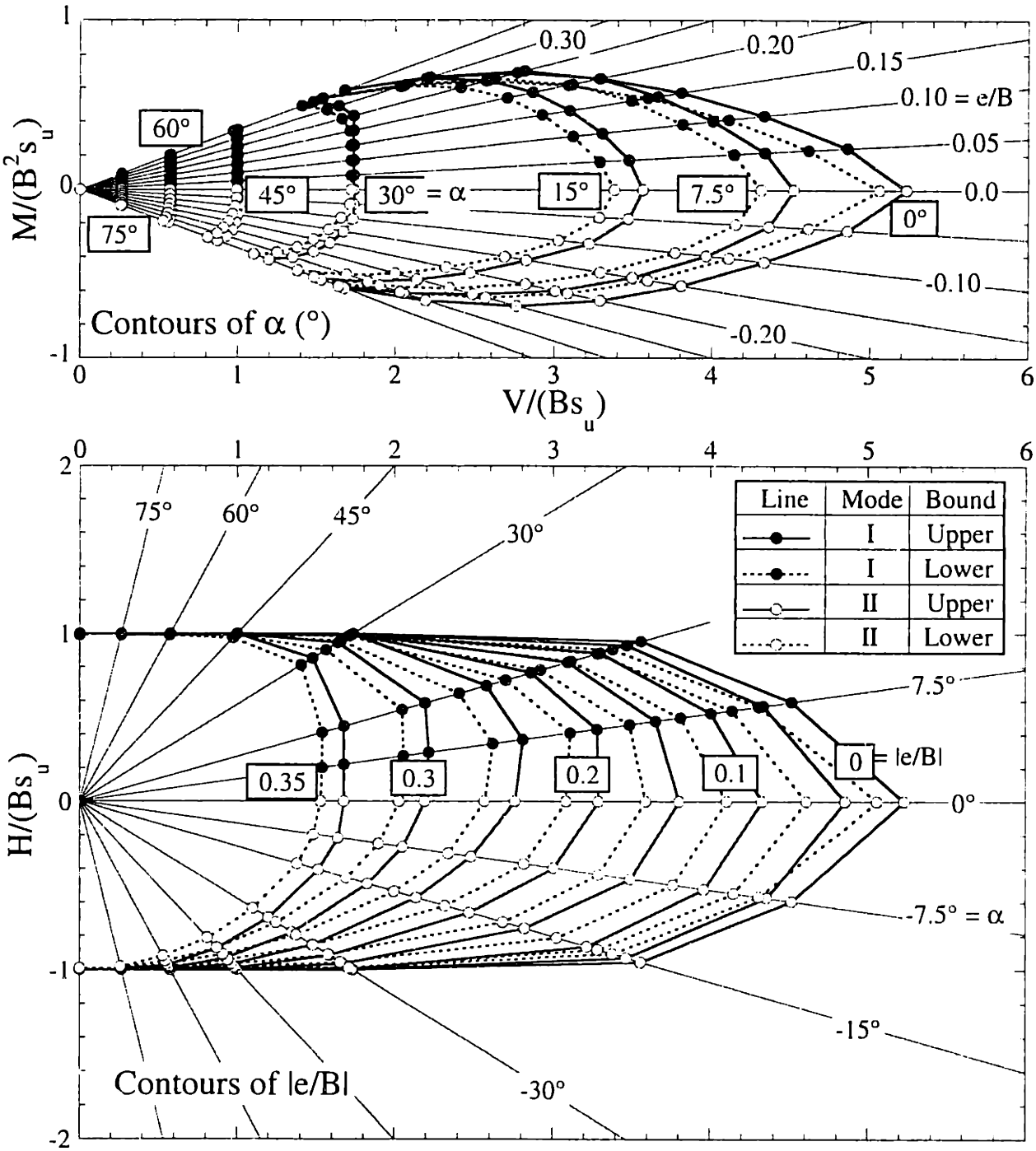

Figure 2.12 Projection of failure surface for combined loading of footing on homogeous clay

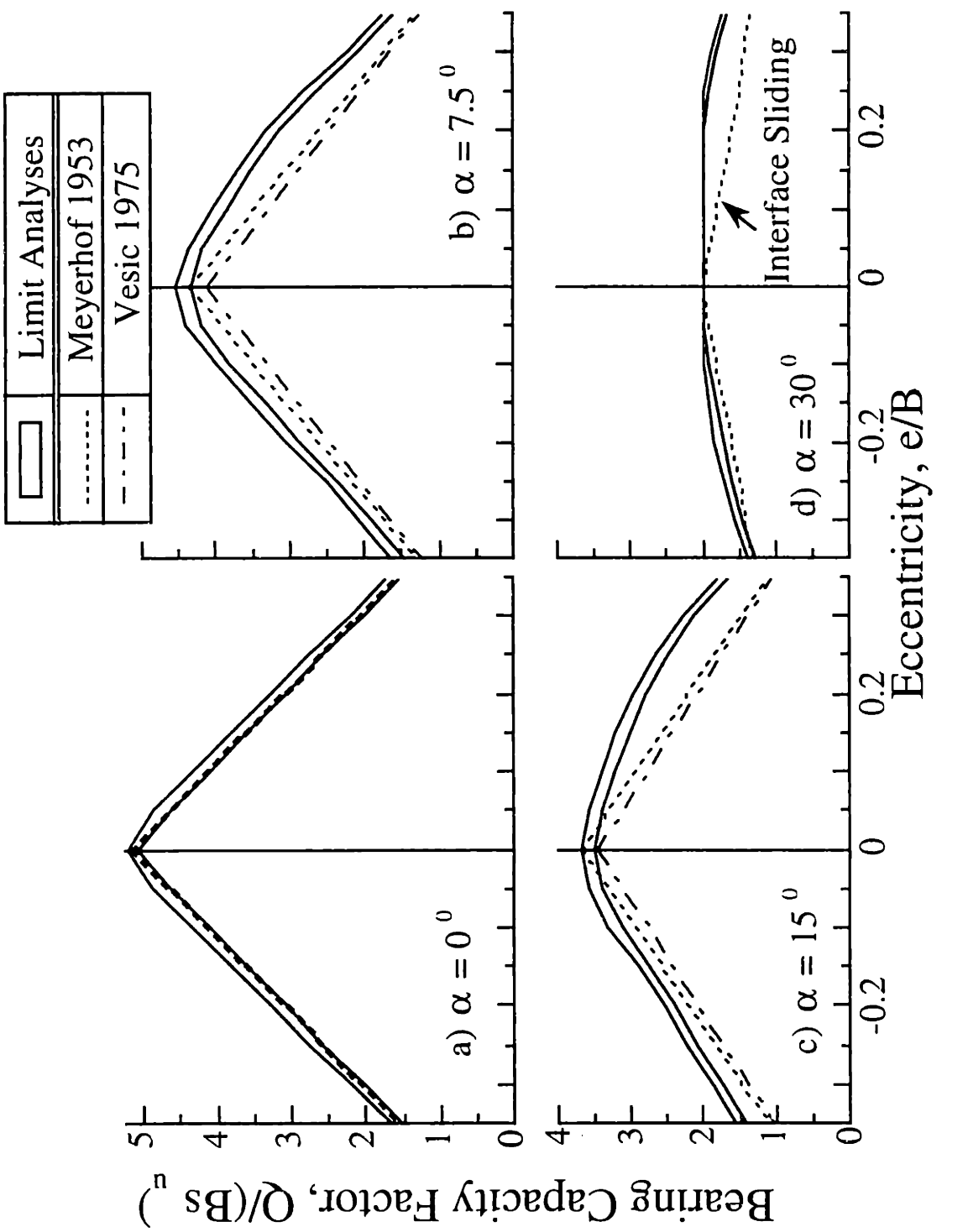

Figure 2.13 Evaluation of empirical bearing capacity factors for combined loading on homogeneous clay

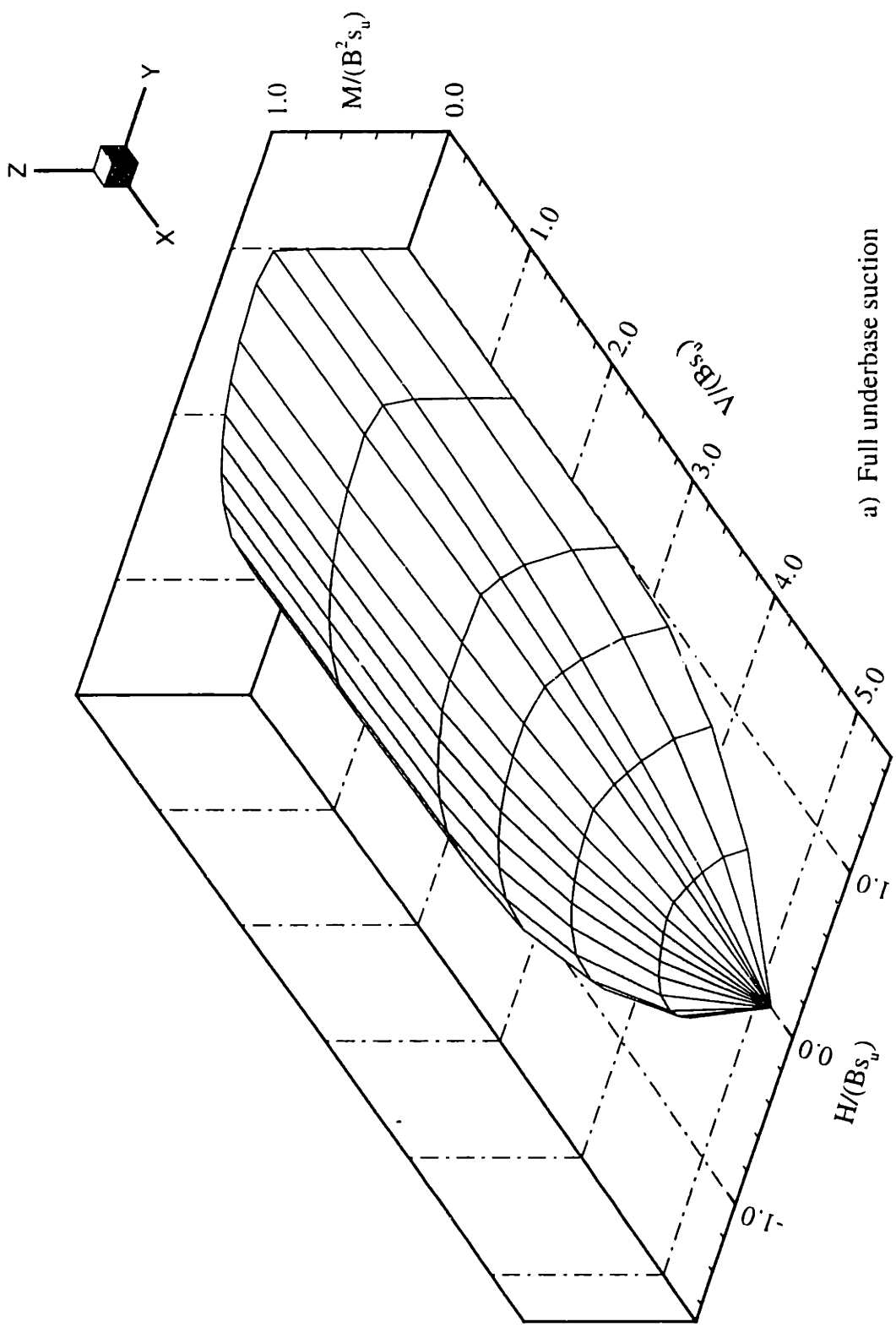

a) Full underbase suction

Figure 2.14 Three-dimensional failure envelopes for footings on homogenesous clay

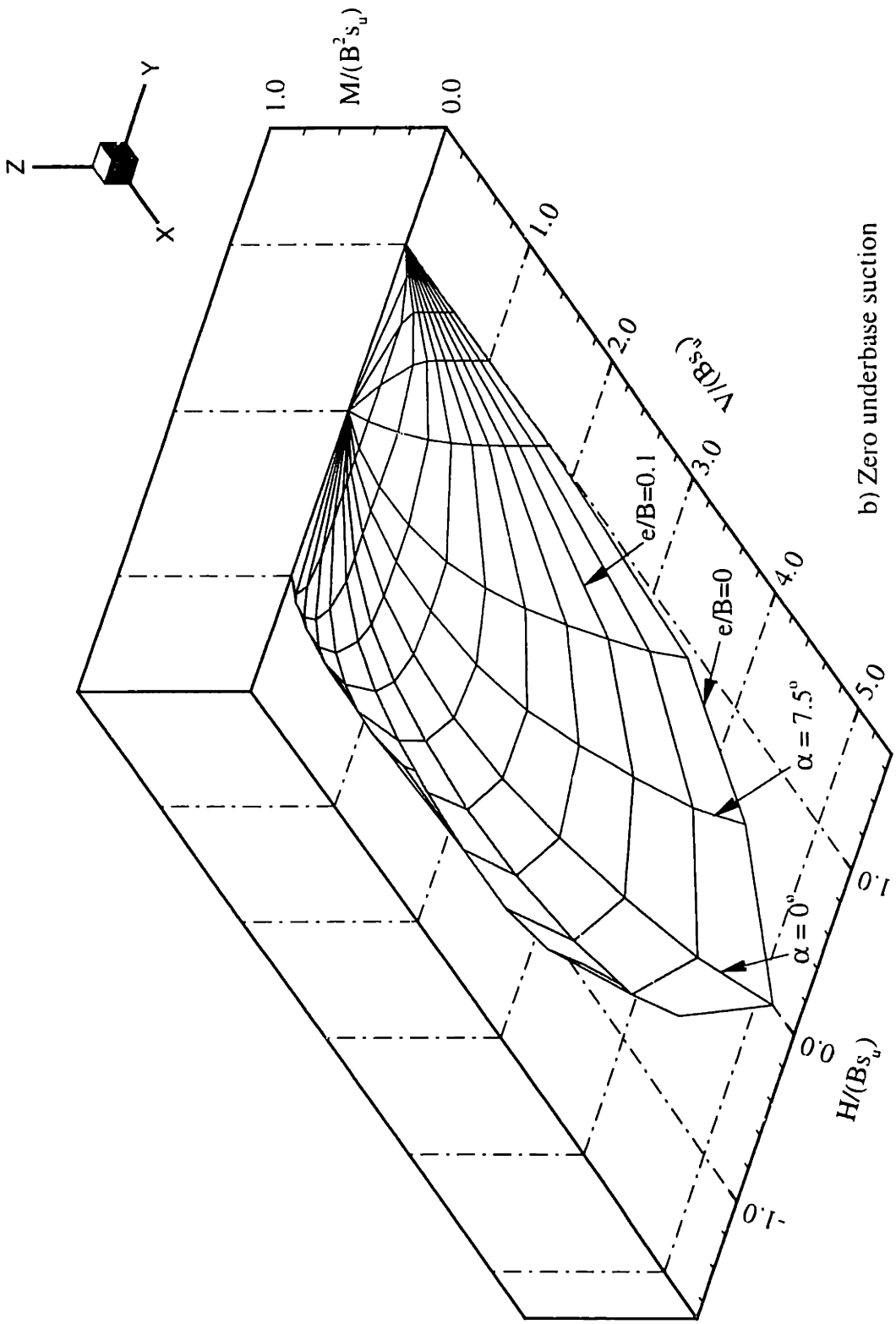

b) Zero underbase suction

Figure 2.14 Three-dimensional failure envelopes for footings on homogenesous clay

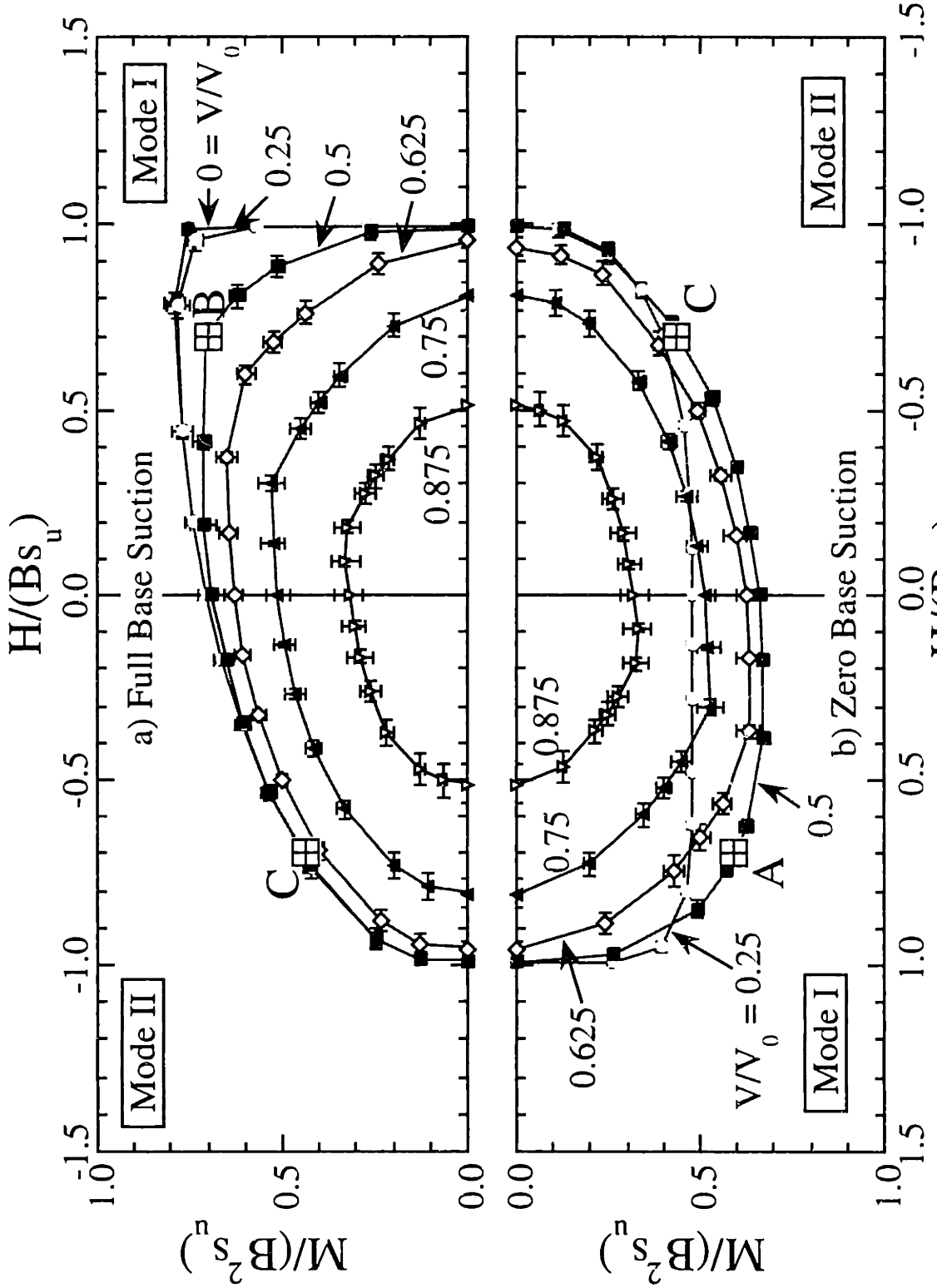

Figure 2.15 Cross-sections of failure envelopes for footings on homogeneous clay

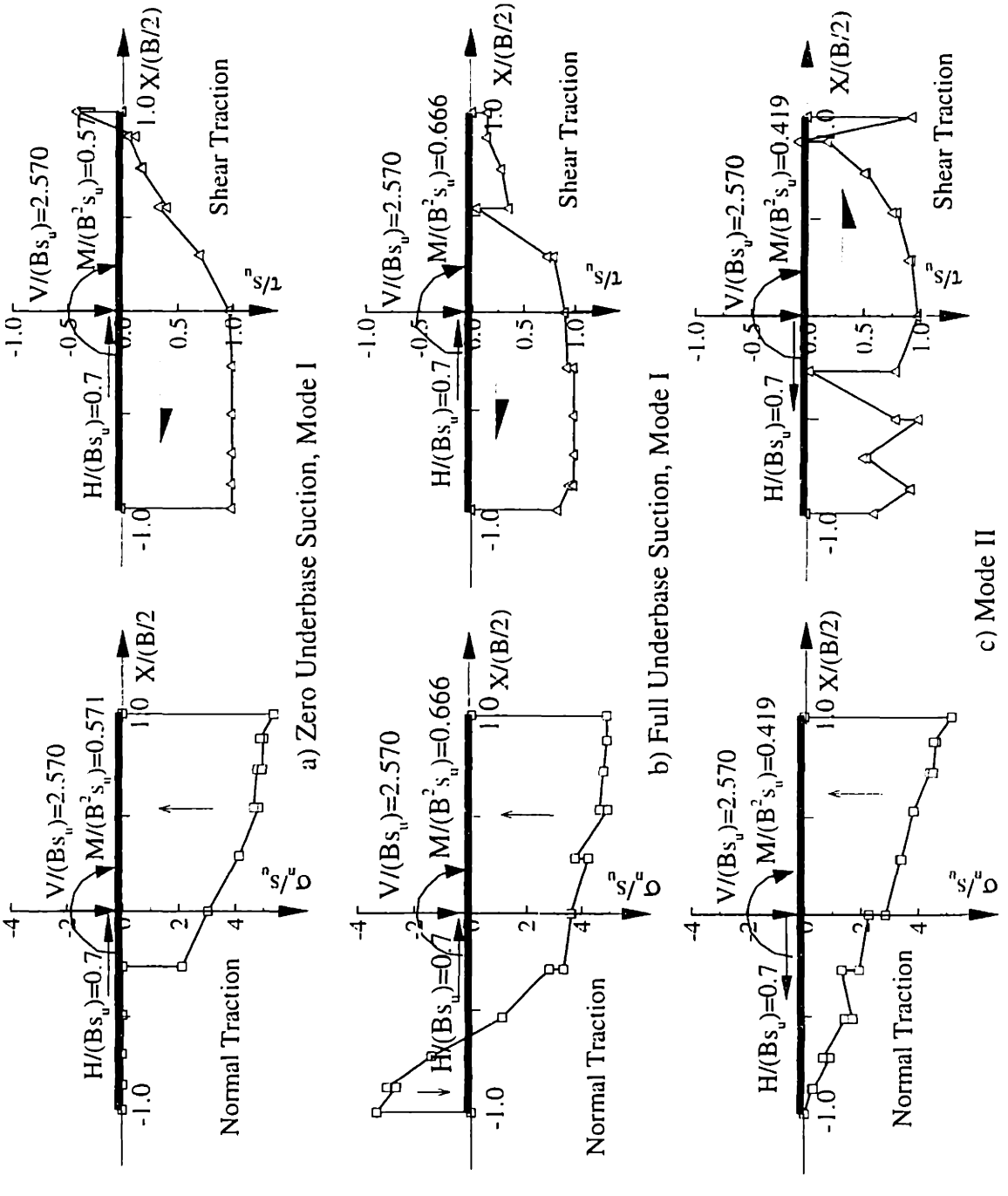

Figure 2.16 Examples of lower bound solutions for combined loading of footings on homogeneous clay

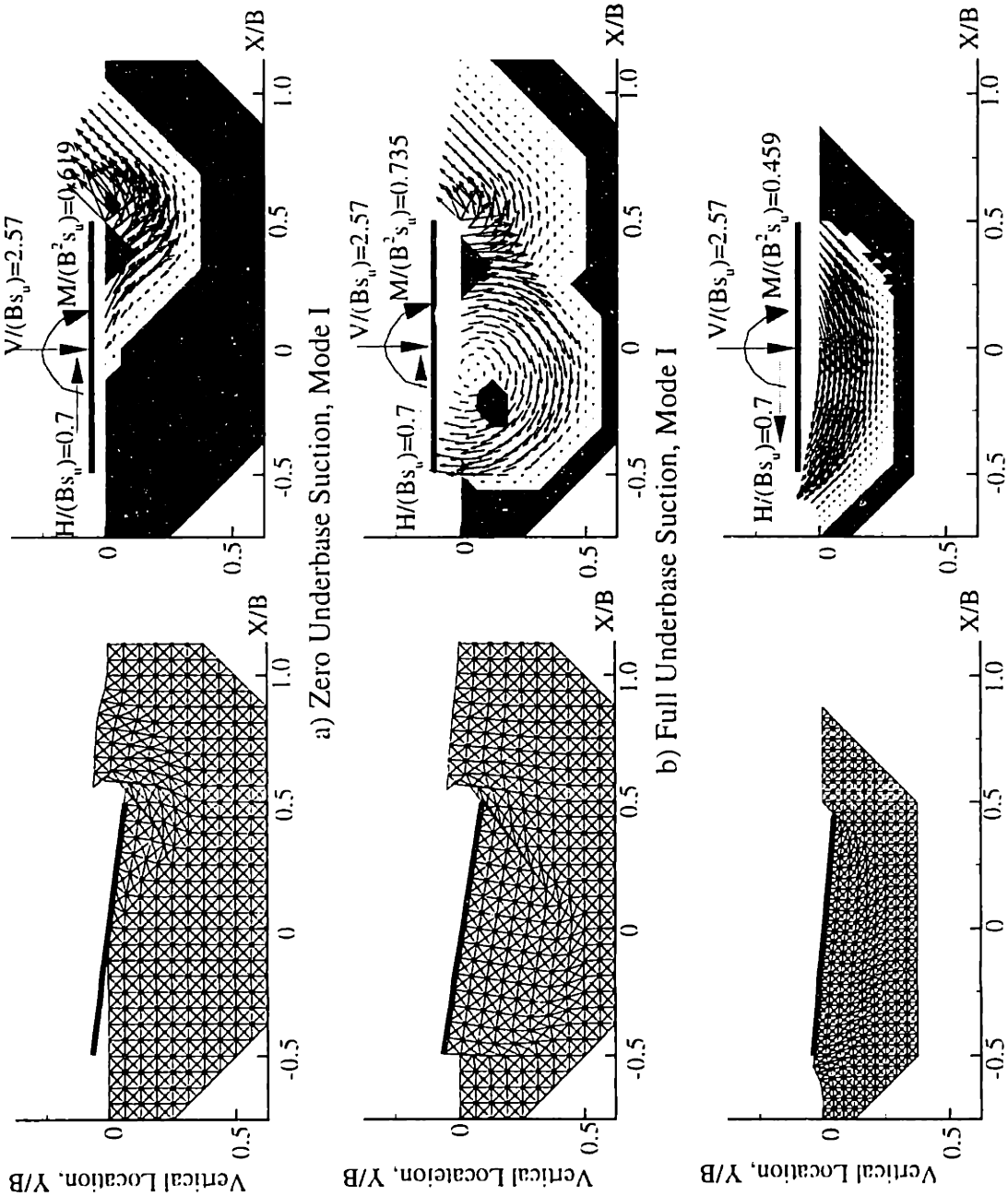

Figure 2.17 Examples of upper bound solutions for combined loading of footings on homogeneous clay

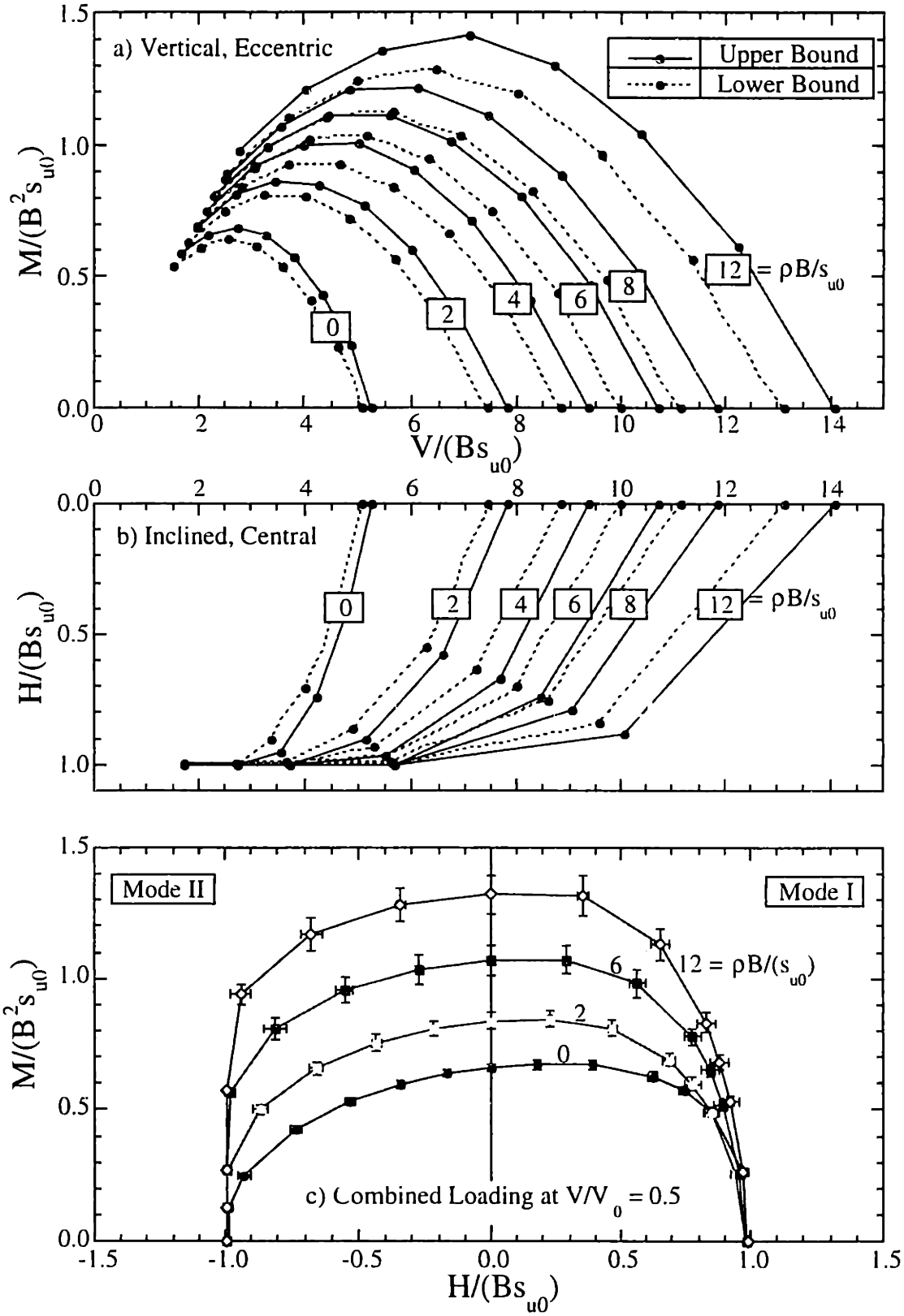

Figure 2.18 Failure envelopes for footings on clay layers with undrained strength gradient: a) Vertical, eccentric loading, b) Inclined, central loading, c) Combined loading at $V/V_0 = 0.5$ (Note: Vertical scales are exaggerated in a, b)

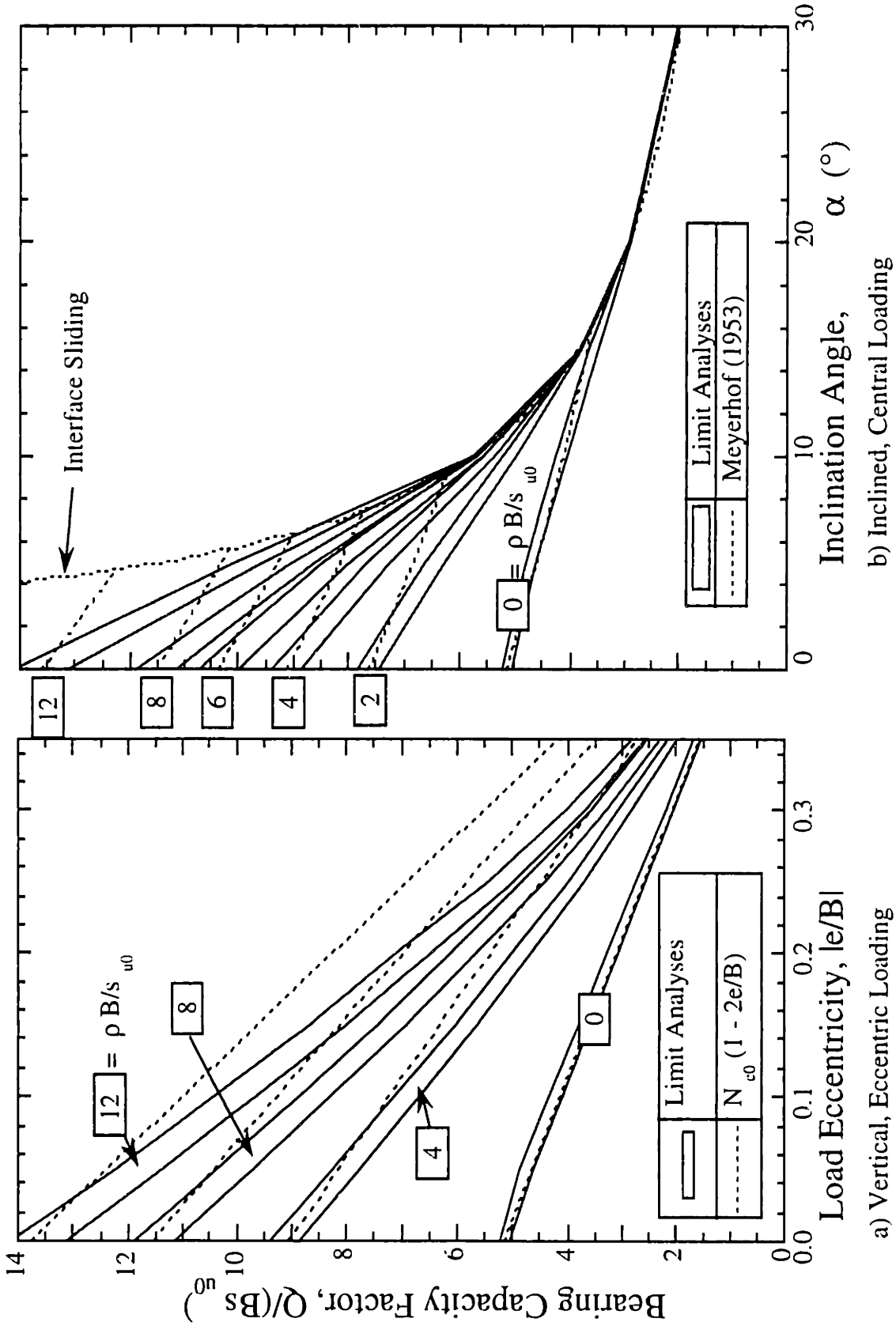

a) Vertical, Eccentric Loading

b) Inclined, Central Loading

Figure 2.19 Evaluation of bearing capacity factors for footings on non-homogeneous clay layers

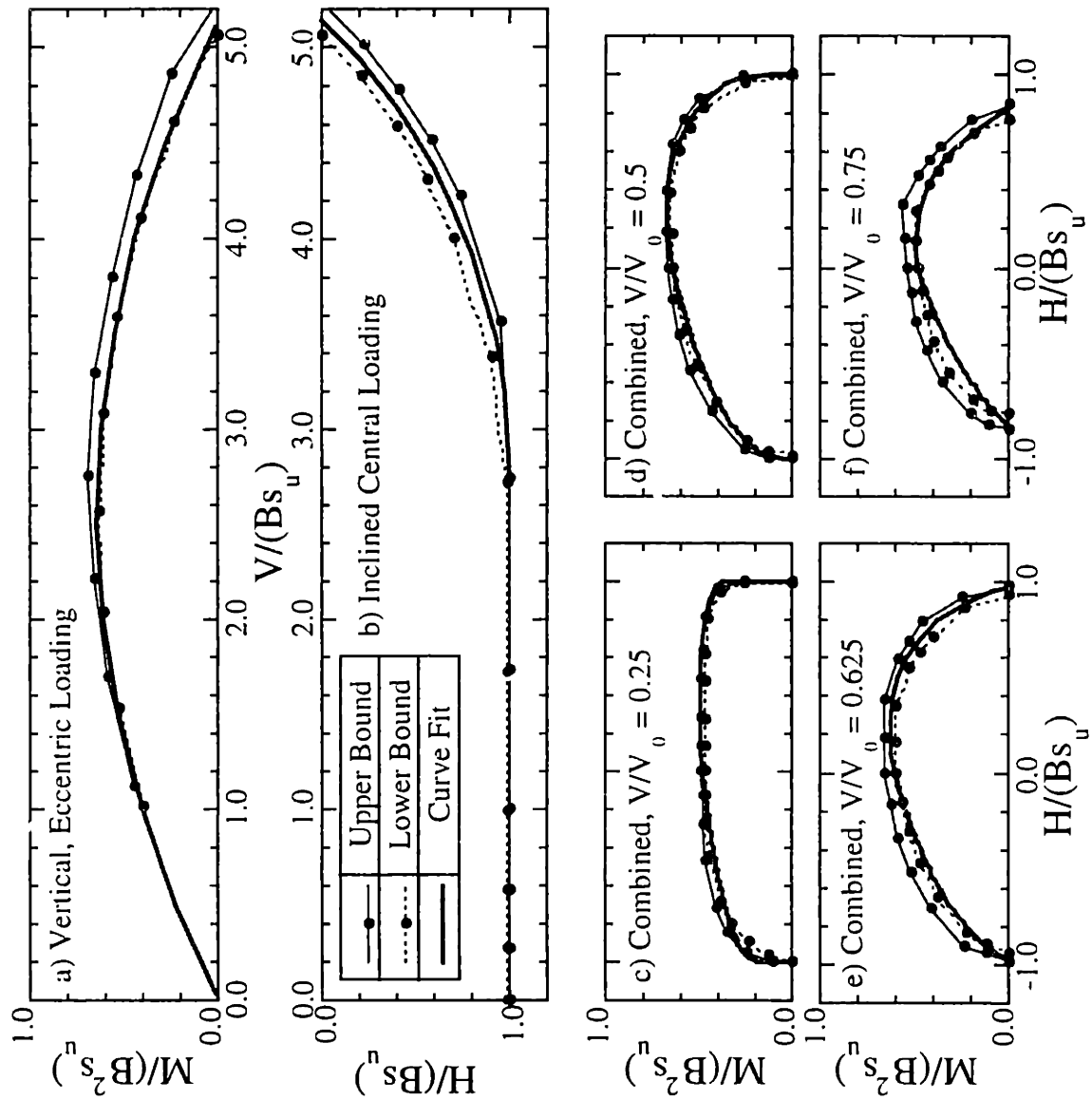

Figure 2.20 Evaluation of proposed curve fit for combined loading of footings on homogeneous clay

Chapter 3. Development and Validation of Finite Element Limit Analyses for Structural Elements

3.1 Introduction

This chapter describes the formulation of numerical upper and lower bound limit analyses for structural elements. The proposed formulation is evaluated by: i) comparison with analytical closed-form solutions for a series of 2-D structural frame problems published in the literature; and ii) analyses of a laterally loaded wall embedded in clay. The formulation of structural elements represents the first step toward the use of limit analyses for problems of soil-structure interaction described in subsequent chapters.

Section 3.2 and 3.3 describe the formulation of lower and upper bound methods for structural elements, respectively. In Section 3.4, the proposed formulation is evaluated through analyses of two-dimensional frame structures. Section 3.5 presents the first application of numerical limit analyses combining the structural elements with plane strain soil elements (Sloan 1988a; Sloan and Kleeman,1995) to predict collapse loads of a laterally loaded wall embedded in the soil.

3.2 Lower Bound Formulation

This section describes the formulation of the numerical lower bound method for structural elements. The structure is discretized into beam and joint elements. The beam element has two nodes (one at each end), while the joint element has one node. Each node has three unknown degrees of freedom (2 forces and 1 moment). The lower bound analysis is formulated as linear programming problem whose objective function is the maximization of the external applied load subject to the constraints of a static admissibility, including equilibrium of the beam and joint elements, traction (or force) boundary conditions, and no-violation of the yield criterion. Finally, the lower bound load is solved by the method of linear programming problem using the active set algorithm (Sloan 1988b).

3.2.1 Finite Element Discretization

Two dimensional frame or beam structures are discretized into 2-noded beam and 1-noded joint elements, as shown in Figure 3.1. Each node at the end of the beam is associated with two unknown forces, F_x (x-direction), F_y (y-direction) and one moment, F_z (z-direction) in the global Cartesian frame of reference. The beam nodes are unique to each particular element.

The joint element has one node and is also associated with two unknown forces (F_{xj}, F_{yj}) and one moment (F_{zj}) similar to those of the beam element. It should be noted that joint elements do not have any physical dimension. The formulation assumes that beam elements carry only distributed tractions (normal and shear), while joint elements carry only point forces, including moments. The incorporation of joint element and uniqueness of beam nodes allows force discontinuities (axial, shear and moments) to occur at beam nodes adjacent to the joint considered.

Force variations along beam element are controlled by element equilibrium and the assumption of distributed tractions.

3.2.2 Beam Element Equilibrium

Figure 3.2 shows the positive sign convention for the beam element with nodal forces in the global (x, y) and local (t, n) frames of reference. The nodal forces in the global axis are two forces in x and y directions (F_x, F_y) and moment (F_z in z-dir), while those in the local axis are axial force, H; shear force, V; and moment M. The axial force, shear force and moment in the local axis at nodes 1 and 2 can be written in terms of nodal forces in the global axis as:

Node 1:

$$H_1 = -\cos\theta\, F_{x1} - \sin\theta\, F_{y1} \tag{3.1}$$

$$V_1 = \sin\theta\, F_{x1} - \cos\theta\, F_{y1}$$

$$M_1 = -F_{z1}$$

Node 2:

$$H_2 = \cos\theta\, F_{y2} + \sin\theta\, F_{y2} \tag{3.2}$$

$$V_2 = -\sin\theta\, F_{x2} + \cos\theta\, F_{y2}$$

$$M_2 = F_{z2}$$

where H_1, V_1, M_1 are axial force, shear force, and moment at node 1, respectively

H_2, V_2, M_2 are axial force, shear force, and moment at node 2, respectively

F_{x1}, F_{y1}, F_{z1} are forces in x, y direction and moment (z-dir.) at node 1, respectively

F_{x2}, F_{y2}, F_{z2} are forces in x, y direction and moment (z-dir.) at node 2, respectively

θ is the orientation angle of the beam element (defined positive in an anticlockwise direction from the x-axis).

The lower bound theorem states that the force distribution along the beam element must satisfy the static equilibrium equation. Figure 3.3 shows a free body diagram of an infinitesimal element, dt, along the beam element. This element is subjected to the normal traction, σ_n and the shear traction, τ. The internal forces on the left hand cross section are the axial force, H, the shear force, V and the moment, M. The changes of these forces over the distance, dt are expressed as: $\frac{\partial H}{\partial t}$ (axial), $\frac{\partial V}{\partial t}$(shear), and $\frac{\partial M}{\partial t}$ (moment). By using the first order Taylor's expansion, the internal forces on the right hand cross section can be expressed as: $H+ \frac{\partial H}{\partial t}dt$ (axial), $V + \frac{\partial V}{\partial t}dt$ (shear), and $M + \frac{\partial M}{\partial t}dt$ (moment). The equilibrium of forces and moment give rise to the following expressions:

$$\Sigma F_t = 0: \qquad \tau_n = -\frac{\partial H}{\partial t} \tag{3.3}$$

$$\Sigma F_n = 0: \qquad \sigma_n = -\frac{\partial V}{\partial t} \tag{3.4}$$

$$\Sigma M = 0: \qquad V = -\frac{\partial M}{\partial t} \tag{3.5}$$

It can be seen from these equations that the selection of traction distribution governs the mathematical function of internal forces (axial, shear, and moment) along beam element. In order to be compatible with the formulation of lower bound method for plane strain problems, which uses the linear stress variation, it is assumed that the beam element is loaded with a linear distributed shear and normal tractions. This assumption allows the formulation of structural elements to be used together with plain strain soil elements (Sloan, 1988a) for analyzing problems involving soil-structure interaction.

It follows from the assumption of a linear traction distribution (c.f. eqn. 2.6) and equations 3.3-3.5 that the moment varies as a cubic function, while the axial and shear forces vary quadratically along beam elements. The expressions of internal forces are given as:

Moment: $M(t) = a_1t^3 + a_2t^2 + a_3t + a_4$ (3.6)

Shear Force: $V(t) = -(3a_1t^2 + 2a_2t + a_3)$ (3.7)

Axial Force: $H(t) = a_5t^2 + a_6t + a_7$ (3.8)

where a_1-a_7 are the coefficients

t = distance from the node 1 to a point considered

Appendix 3A presents the derivation of parameters, a_1-a_7 in terms of axial force, shear force and moment at both end nodes. The expressions of these coefficients are given as:

$$a_1 = \frac{2}{L^3}M_1 - \frac{1}{L^2}V_1 - \frac{2}{L^3}M_2 - \frac{1}{L^2}V_2 \quad (3.9)$$

$$a_2 = -\frac{3}{L^2}M_1 + \frac{2}{L}V_1 + \frac{3}{L^2}M_2 + \frac{1}{L}V_2$$

$$a_3 = -V_1$$

$$a_4 = M_1$$

$$a_5 = \frac{(\tau_1 - \tau_2)}{2L}$$

$$a_6 = -\tau_1$$

$$a_7 = H_1$$

where L is the length of beam element

τ_1 and τ_2 are the shear traction at nodes 1 and 2, respectively

The equilibrium constraints of beam elements in terms of axial force, shear force and moment at both end nodes are given as:

$$\sigma_{n1} = -\frac{6}{L^2}M_1 + \frac{4}{L}V_1 + \frac{6}{L^2}M_2 + \frac{2}{L}V_2 \quad (3.10)$$

$$\sigma_{n2} = \frac{6}{L^2}M_1 - \frac{2}{L}V_1 - \frac{6}{L^2}M_2 - \frac{4}{L}V_2$$

$$H_2 - H_1 = -\frac{(\tau_1 - \tau_2)}{2}L$$

where σ_{n1} and σ_{n2} are the normal tractions at nodes 1 and 2, respectively

Substituting equations 3.1 and 3.2 into 3.10 gives rise to the equilibrium constraints in terms of nodal forces in the global axis as:

$$[A_{equi,\,beam}]\,\{F_{beam}\} = \{b_{equi,\,beam}\} \tag{3.11}$$

where

$$\{A_{equi.beam}\} = \frac{1}{L^2}\begin{bmatrix} 4L\sin\theta & -4L\cos\theta & 6 & -2L\sin\theta & 2L\cos\theta & 6 \\ -2L\sin\theta & 2L\cos\theta & -6 & 4L\sin\theta & -4L\cos\theta & -6 \\ L^2\cos\theta & L^2\sin\theta & 0 & L^2\cos\theta & L^2\sin\theta & 0 \end{bmatrix}$$

$$\{F_{beam}\}^T = \{\, F_{x1} \quad F_{y1} \quad F_{z1} \quad F_{x2} \quad F_{y2} \quad F_{z2} \,\}$$

$$\{b_{equi,\,beam}\}^T = \{\sigma_{n1} \quad \sigma_{n2} \quad -(\tau_1 + \tau_2)/(2L) \,\}$$

Thus, by enforcing constraint 3.11, the equilibrium along the beam element is satisfied.

3.2.3 Joint Element Equilibrium

Figure 3.4 shows the joint element and adjacent nodes of beam elements. The nodal forces of the joint element must be in equilibrium with the nodal forces of adjacent beam nodes:

$$\Sigma F_x = 0: \qquad F_{xj} = \Sigma(F_{x,i}) \tag{3.12}$$

$$\Sigma F_y = 0: \qquad F_{yj} = \Sigma(F_{y,i})$$

$$\Sigma M = 0: \qquad F_{zj} = \Sigma(F_{z,i})$$

where F_{xj} , F_{yj} , F_{zj} are nodal forces of joint element in x, y directions and moment,

F_{xi}, F_{yi}, F_{zi} are forces in x, y directions and moment of node i adjacent to the joint, and the summation is taken for all nodes (i = 1,..,n) adjacent to joint element considered.

This constraint may rewritten in matrix form as:

$$[A_{equi,\,joint}]\,\{F_{joint}\} = \{b_{equi,\,joint}\} \tag{3.13}$$

where

$$[A_{equi,joint}] = [\, I \quad -I \quad \ldots. \quad -I \,]; \; I = \begin{bmatrix} 1 & 0 & 0 \\ 0 & 1 & 0 \\ 0 & 0 & 1 \end{bmatrix}$$

$$\{F_{joint}\}^T = \{\, F_{xj} \; F_{yj} \; F_{zj} \quad F_{x1} \; F_{y1} \; F_{z1} \ldots. \quad F_{xn} \; F_{yn} \; F_{zn} \,\}$$

$$\{b_{equi,joint}\}^T = \{\, 0 \quad 0 \quad 0 \,\}$$

3.2.4 Force Boundary Conditions

Equation 3.11 ensures that beam elements satisfy the applied normal and shear tractions along element. In addition, unknown forces and moment at joint element must satisfy prescribed force boundary conditions. Consider a joint element i subjected to the applied forces, F_{xja} , F_{yja} and moment F_{zja} , leading to force boundary conditions as follows:

$$F_{xj} = F_{xja} \tag{3.14}$$

$$F_{yj} = F_{yja}$$

$$F_{zj} = F_{zja}$$

These constraints may be written in matrix form as:

$$[A_{bound}] \{F_{joint,bound}\} = \{b_{bound}\} \tag{3.15}$$

where

$$[A_{bound}] = \begin{bmatrix} 1 & 0 & 0 \\ 0 & 1 & 0 \\ 0 & 0 & 1 \end{bmatrix}$$

$$\{F_{joint,bound}\}^T = \{\, F_{xj} \; F_{yj} \; F_{zj} \,\}$$

$$\{b_{bound}\}^T = \{\, F_{xja} \quad F_{yja} \quad F_{zja} \,\}$$

3.2.5 Yield Criterion

Appendix 3B describes the generalized yield surface of the structural element, whose a section is loaded with axial force, shear force, and moment. For a rectangular cross section, the generalized yield surface, F(H, M, V) can be expressed as (Mrázik et al., 1987):

$$F(H,M,V) = \left(\frac{M}{M_p}\right)^2 \{1-\left(\frac{V}{V_p}\right)^2\} - \{1-\left(\frac{H}{H_p}\right)^2 - \left(\frac{V}{V_p}\right)^2\}^2 = 0 \qquad (3.16)$$

where H, V, M = axial and shear forces and moment at a cross section, respectively

H_p, V_p, M_p = plastic axial and shear forces and plastic moment of a rectangular section, respectively

$H_p = \sigma_0(bd)$; $V_p = \sigma_0(bd)$; $M_p = \sigma_0(bd^2)/4$

σ_0 = the uniaxial yield stress of material

b, d = the width and depth of a rectangular section

According to the lower bound theorem, the internal forces - axial force, shear force, and moment at any section - must not violate the yield criterion. That means F(H, M, V) $\leq$ 0 along the beam element. Since the lower bound method is formulated as a linear programming problem, equation 3.16, which is a single non-linear function of the unknown internal forces, H, M, V, must be linearized. For the special case where the effects of plastic axial and shear forces are neglected (i.e. the values of H_p and V_p are very large compared to M_p), the actual yield surface becomes a linear function. Thus, linearization is not necessary in this case, and the yield criterion reduces to a simple form as:

$$F(H,M,V) = \left(\frac{M}{M_p}\right)^2 - 1 = 0 \qquad (3.17a)$$

Equation 3.17 represents two horizontal planes in the three dimensional H-M-V space:

$$(M/M_p)-1 = 0; \text{ and } -(M/M_p)-1 = 0 \qquad (3.17b)$$

Appendix 3C presents lower bound linearizations of the yield surface for four cases: 1) pure bending moment; 2) axial force and moment; 3) shear and moments; and 4) combined axial force, shear, and moment loading (equation 3.16). In general, the linearized yield criterion can be written as a set of inequality constraints as follows:

$$F_k(H, M, V) = A_kH + B_kM + C_kV - D_k \leq 0 \ ; k = 1,2,...,p \qquad (3.18)$$

where F_k = the k^{th} side of the linearized yield surface

A_k, B_k, C_k and D_k = coefficients of the linearized plane derived in Appendix 3C

p = the number of linearized planes of yield surface

Linearization must also be performed for the internal forces along the beam element (H, V and M) because these variables have non-linear functions, according to equations 3.6-3.8. This linearization is done by dividing the beam element into n-internal nodes (including both end nodes). The spacing of each internal node is equal to L/(n-1), where L is the length of beam. Thus, the distance from node 1 to an internal node i is given by:

$$t_i = \frac{(i-1)}{n-1} L \quad ; i = 1,2,...,n \tag{3.19}$$

The linearized internal forces - axial, shear and moment - at the internal node i are expressed as:

$$H_i = a_5 t_i^2 + a_6 t_i + a_7 \tag{3.20}$$

$$M_i = a_1 t_i^3 + a_2 t_i^2 + a_3 t_i + a_4$$

$$V_i = -(3a_1 t_i^2 + 2a_2 t_i + a_3)$$

Thus, the set of inequality constraints to be enforced are as:

$$F_k(H_i, M_i, V_i) = A_k H_i + B_k M_i + C_k V_i - D_k \leq 0 \tag{3.21}$$

where i =1,2,...,n and k = 1,2,...,p

Substituting equation 3.20 and the expression of a_1-a_7 (equation 3.9) into 3.21 generates inequality constraints of the matrix form as:

$$[A_{yield}^{k,i}]\{F_{beam}\} \leq \{b_{yield}^{k,i}\}; k = 1,2,..,p \text{ ; and } i = 1,2,...,n \tag{3.22}$$

where

$$\{F_{beam}\}^T = \{ F_{x1} \quad F_{y1} \quad F_{z1} \quad F_{x2} \quad F_{y2} \quad F_{z2} \}$$

The expressions of $[A_{yield}^{k,i}]$ and $\{b_{yield}^{k,i}\}$ are given in Appendix 3D.

3.2.6 Assembly of Constraint Equations

The statically admissible forces of structural elements are satisfied by assembling the following constraints:

1. Beam element equilibrium

$$[A_{equi,\,beam}]\{F_{beam}\} = \{b_{equi,\,beam}\} \tag{3.11}$$

2. Joint element equilibrium

$$[A_{equi,\,joint}]\,\{F_{joint}\} = \{b_{equi,\,joint}\} \tag{3.13}$$

3. Force boundary conditions

$$[A_{bound}]\,\{F_{joint,bound}\} = \{b_{bound}\} \tag{3.15}$$

4. Linearized yield criterion

$$[A^{k,i}_{yield}]\{F_{beam}\} \le \{b^{k,i}_{yield}\};\ k = 1,2,..,p\ ;\ \text{and}\ i = 1,2,...,n \tag{3.22}$$

All of the equality and inequality constraints can be summarized in a compact form as:

$$\begin{aligned} [A_1]\{F\} &= \{b_1\} \\ [A_2]\{F\} &\le \{b_2\} \end{aligned} \tag{3.23}$$

where

$[A_1]$ is the constraint matrix of equilibrium of beam and joint elements, and force boundary condition, while

$[A_2]$ is the constraint matrix of the linearized yield criterion

$\{F\}$ is nodal forces of beam and joint elements

3.2.7 Objective Function

The objective function of the lower bound method maximizes the externally applied load, $Q_{applied}$. For beam and structure problems, the external applied load is one of the forces at the joint. For example, if we wish to find the maximum vertical load at joint #5, the objective function can be written as matrix form as:

$$Q_{applied} = \{c\}^T\{F\}$$

where $\{c\}^T = \{\,0\ \ 0\ \ 0\ \ ...\ \ 1\ ...\ \ 0\ \ 0\ \ 0\}$, and

the non-zero index corresponds to the force in y-direction of joint #5.

In general, the lower bound linear programming problem has the form:

$$\begin{aligned} &\text{Maximize: } \{c\}^T\{F\} \\ &\text{Subject to: } [A_1]\{F\} = \{b_1\} \\ &\qquad\qquad\ [A_2]\{F\} \le \{b_2\} \end{aligned} \tag{3.24}$$

The solution of this form is solved by using the active set algorithm based on Sloan (1988b).

3.3 Upper Bound Formulation

This section describes the formulation of numerical upper bound method for structural elements. The formulation is analogous to that of the lower bound method (described in Section 3.2) and involves discretizing the structure into beam and joint elements, but introducing nodal velocities (translational and rotational rates) as the unknown variables. Each node of a beam element has two unknown velocities in x and y directions, whereas a joint element has three unknown velocities (two velocities in x and y directions and one angular velocity). The beam element is assumed to be a rigid element while the plastic failure mechanisms are permitted to develop at adjacent nodes of beam and joint elements. Linearization of the non-linear yield criterion results in additional sets of unknown variables (plastic multiplier rates) associated with each linearized yield constraint. Kinematically admissible solutions are defined by the constraints of rigid movement of beam elements, associated plastic flow, and velocity boundary conditions. The upper bound formulation leads to a linear programming problem whose objective function is the minimization of the external applied load subject to the constraints of kinematic admissibility. Finally, the upper bound load is solved by applying the active set algorithm of linear programming (Sloan, 1988b).

3.3.1 Finite Element Discretization

Two dimensional frame or beam structures are discretized into 2-noded beam and 1-noded joint elements, as shown in Figure 3.5. The beam element has two nodes (one at each end), each of which is associated with two unknown velocities, u (x-direction), v (y-direction) in the global Cartesian frame of reference. It is assumed that the velocities varies linearly along beam element, and the beam element is rigid. It should be noted that the assumption of a rigid beam element eliminates the need for an additional degree of freedom (angular velocity) at the end nodes. Rigid body movement of beam elements is governed by the movement of their nodes. Also, note that beam nodes are unique to a particular element.

The joint element has one node and is associated with three unknown velocities, u_j (x-direction) , v_j (y-direction) and w_j (angular velocity). It should be noted joint elements

do not have any physical dimension. Plastic failure is allowed to occur at adjacent nodes of beam and joint elements.

The formulation assumes that beam elements carry only distributed tractions (normal and shear), while joint elements carry only point forces, including moments.

3.3.2 Constraints for Rigid Beam Movement

Figure 3.6 shows a beam element in the global and local axes. The velocities in the local axis (t,n) can be expressed as those in the global axis (x, y) as:

Node 1:
$$u_{1t} = \cos\theta\, u_1 - \sin\theta\, v_1 \tag{3.25}$$
$$u_{1n} = -\sin\theta\, u_1 + \cos\theta\, v_1$$

Node 2:
$$u_{2t} = \cos\theta\, u_2 - \sin\theta\, v_2 \tag{3.26}$$
$$u_{2n} = -\sin\theta\, u_2 + \cos\theta\, v_2$$

where u_1, v_1 = velocities of node 1 in x and y directions (global axis), respectively

u_{1t}, u_{1n} = velocities of node 1 in t and n directions (local axis), respectively

u_2, v_2 = velocities of node 2 in x and y directions (global axis), respectively

u_{2t}, u_{2n} = velocities of node 2 in t and n directions (local axis), respectively

θ = the orientation angle of beam element (defined positive in an anticlockwise direction from the x-axis)

In the local axis, the velocities also vary linearly along beam element according to:

$$u_t = u_{1t}\left(1 - \frac{t}{L}\right) + u_{2t}\left(\frac{t}{L}\right) \tag{3.27}$$

$$u_n = u_{1n}\left(1 - \frac{t}{L}\right) + u_{2n}\left(\frac{t}{L}\right) \tag{3.28}$$

where L = the length of beam element

The rigid movement of beam element specifies that there is no change in the velocity in the t-direction:

$$\dot{\varepsilon}_t = \frac{\partial u_t}{\partial t} = 0 \tag{3.29}$$

Thus, differentiating equation 3.27 with respect to t-direction gives rise to:

$$u_{1t} = u_{2t} \tag{3.30}$$

Substituting equations 3.25 and 3.26 into 3.30 generates the constraint of rigid beam element as:

$$[A_{\text{rigid, beam}}]\ \{u_{\text{beam}}\} = \{b_{\text{rigid, beam}}\} \tag{3.31}$$

where

$$[A_{\text{rigid, beam}}] = [\ \cos\theta \quad \sin\theta \quad -\cos\theta \quad -\sin\theta\ ]$$

$$\{u_{\text{beam}}\}^T = \{\ u_1 \quad v_1 \quad u_2 \quad v_2\ \}$$

$$\{b_{\text{rigid, beam}}\} = \{\ 0\ \}$$

Note that the angular velocity of beam element is defined by the derivative of the velocity in the n-direction:

$$w_{1-2} = \frac{\partial u_n}{\partial t} \tag{3.32}$$

where w_{1-2} = the angular velocity between node 1 and 2

Thus, differentiating equation 3.28 with respect to n-direction gives rise to:

$$w_{1-2} = \frac{(u_{2n} - u_{2n})}{L} \tag{3.33}$$

Substituting equation 3.25, and 3.26 into 3.33 gives the expression of the angular velocity as a function of nodal velocities as:

$$w_{1-2} = \frac{1}{L}\{-u_2 \sin\theta + v_2 \cos\theta + u_1 \sin\theta - v_1 \cos\theta\} \tag{3.34}$$

3.3.3 Constraints of Plastic Failure at Joint Elements

Plastic failure is allowed to occur at all adjacent nodes shared by beam and joint elements. Figure 3.7 show a typical plastic failure defined by the joint element, and adjacent nodes 1 and 4. Three types of plastic failure are permitted: 1) plastic axial failure; 2) plastic shear failure; and 3) plastic moment failure or so called "plastic hinge".

Considering joint element and adjacent node 1, plastic failure mechanisms are defined by:

$$\Delta u_{1j,t} = u_{1t} - u_{jt} \tag{3.35}$$

$$\Delta u_{1j,n} = u_{1n} - u_{jn}$$

$$\Delta w_{1j} = w_{1\text{-}2} - w_j$$

where $\Delta u_{1j,t}$, $\Delta u_{1j,n}$ = axial and shear velocity jump between joint element and node 1

Δw_{1j} = angular velocity jump between joint element and node 1

u_{1t}, u_{1n} = tangential and normal velocities of node 1

$w_{1\text{-}2}$ = angular velocity between node 1 and 2

u_{jt} , u_{jn} , w_j = tangential, normal and angular velocities of joint element

Referring to Figure 3.7, the tangential and normal velocities of joint j can be expressed in terms of those in the global axis as:

$$u_{jt} = \cos\theta\, u_j - \sin\theta\, v_j \tag{3.36}$$

$$u_{jn} = -\sin\theta\, u_j + \cos\theta\, v_j$$

where u_j, v_j = velocities in x and y directions of joint element.

According to the upper bound theorem, plastic failure mechanisms must satisfy the associated flow equation given by:

$$\Delta u_{1j,t} = \dot{\lambda}\frac{\partial F}{\partial H} \tag{3.37}$$

$$\Delta u_{1j,n} = \dot{\lambda}\frac{\partial F}{\partial V}$$

$$\Delta w_{1j} = \dot{\lambda}\frac{\partial F}{\partial M}$$

where F = the yield function

H, V, M = axial force, shear force, and moment at a cross section, respectively

For a beam having the rectangular section and subjected to axial force, shear force, and moment, the generalized yield surface can be expressed as (see Appendix 3B):

$$F(H,M,V) = \left(\frac{M}{M_p}\right)^2\left\{1-\left(\frac{V}{V_p}\right)^4\right\} - \left\{1-\left(\frac{H}{H_p}\right)^2 - \left(\frac{V}{V_p}\right)^2\right\}^2 = 0 \tag{3.17, bis}$$

H_p, V_p, M_p = plastic axial and shear forces, and plastic moment

$H_p = \sigma_0(bd)$; $V_p = \sigma_0(bd)$; $M_p = \sigma_0(bd^2)/4$

σ_0 = the yield stress of material

b, d = the width and depth of a rectangular section

Since the upper bound method is formulated as a linear programming problem, equation 3.17 must be linearized using a polygonal approximation which describes the forces as a series of linear functions. In addition, in order to ensure that the solution obtained is a strict upper bound on the true collapse load, the polygon must circumscribe the actual yield surface. Appendix 3E describes the upper bound linearization for four cases: 1) pure moment; 2) axial force and moment; 3) shear and moment; and 4) combined loading.

In general, a set of equality constraints which linearizes the actual yield criterion can be written as:

$$F_k (H, M, V) = A_k H + B_k M + C_k V - D_k = 0 \quad ; k = 1,2,...,p \tag{3.38}$$

where F_k = the k^{th} side of a linearized yield surface

A_k, B_k, C_k and D_k = coefficients of a linearized plane (derived in Appendix 3E)

p = the number of linearized yield planes

For the linearized yield function defined by equation 3.38, the associated flow rule of equation 3.37 can then be written in term of the unknown plastic multiplier rates and the linearizing coefficients, A_k, B_k, and C_k:

$$\Delta u_{1j,l} = \sum_{k=1}^{p} \dot{\lambda}_k A_k \tag{3.39}$$

$$\Delta u_{1j,n} = \sum_{k=1}^{p} \dot{\lambda}_k C_k$$

$$\Delta w_{1j} = \sum_{k=1}^{p} \dot{\lambda}_k B_k$$

where $\dot{\lambda}_k$ is the non-negative plastic multiplier rate associated with the k^{th} side of the linearized yield plane.

Finally, equating equation 3.39 and 3.35, and substituting the expression of u_{1l}, u_{1n}, and w_{1-2}, the flow rule constraint of plastic failure can be expressed by constraint matrix as:

$$[A_{comp}]\{u\} - [A_{flow}]\{\dot{\lambda}\} = \{0 \quad 0 \quad 0\}^T \tag{3.40}$$

$$\{\dot{\lambda}\} \geq 0$$

where

$$[A_{comp}]=\begin{bmatrix} \cos\theta & \sin\theta & 0 & 0 & -\cos\theta & -\sin\theta & 0 \\ -\sin\theta & \cos\theta & 0 & 0 & \sin\theta & -\cos\theta & 0 \\ \sin\theta & -\cos\theta & -\sin\theta & \cos\theta & 0 & 0 & -1 \end{bmatrix}$$

$$[A_{flow}]=\begin{bmatrix} A_1 & A_2 & A_3 & \dots & A_p \\ C_1 & C_2 & C_3 & \dots & C_p \\ B_1 & B_2 & B_3 & \dots & B_p \end{bmatrix}$$

$$\{u_{12,j}\}^T = \{u_1 \quad v_1 \quad u_2 \quad v_2 \quad u_j \quad v_j \quad w_j\}$$

$$\{\dot{\lambda}\}^T = \{\dot{\lambda}_1 \quad \dot{\lambda}_2 \quad \dot{\lambda}_3 \quad \dots \dot{\lambda}_p\}$$

3.3.4 Velocity Boundary Conditions

As stated in the upper bound theorem, the velocity field must satisfy prescribed velocity boundary conditions. Consider a joint element where the prescribed velocities in x and y directions and angular velocity are ($\bar{u}$, $\bar{v}$, $\bar{w}$). Thus, the nodal velocities of joint element (u_j, v_j, w_j) must satisfy the following equalities:

$$u_j = \bar{u} \tag{3.41}$$

$$v_j = \bar{v}$$

$$w_j = \bar{w}$$

These constraints may be written in matrix form as:

$$[A_{vel,bound}]\{u_j\} = \{b_{vel,bound}\} \tag{3.42}$$

where

$$[A_{vel,bound}]=\begin{bmatrix} 1 & 0 & 0 \\ 0 & 1 & 0 \\ 0 & 0 & 1 \end{bmatrix}$$

$$\{u_j\}^T = \{u_j \quad v_j \quad w_j\}$$

$$\{b_{vel,bound}\}^T = \{\bar{u} \quad \bar{v} \quad \bar{w}\}$$

3.3.5 Objective Function

The upper bound analysis is a minimization problem. Thus, the objective function is to minimize the external applied load, $Q_{applied}$. For beam and structure problems, the external applied load is one of the forces at the joint. In general, the linear programming of the upper bound analysis has the form:

Minimize: $Q_{applied}$ (3.43)

Subject to: constraints of kinematically admissible velocity

The external load, $Q_{applied}$ is linked with nodal velocities by equating the rate of work done by external loads with the internal power dissipated at plastic failure of adjacent nodes of beam and joint elements:

$$W_{ext} = W_{int} \tag{3.44}$$

where

W_{ext} = the external rate of work done by the external loads

W_{int} = the internal dissipation of power at plastic failure of adjacent nodes

3.3.6 Internal Dissipation of Power

Since the beam element is assumed to be rigid, the internal dissipation of power only occurs at the plastic failure of adjacent nodes. Referring to Figure 3.7, the power dissipated by the plastic failure mechanisms is given by:

$$W_{int} = H\Delta u_{1j,t} + V\Delta u_{1j,n} + M\,\Delta w_{1j} \tag{3.45}$$

Substituting equation 3.39 gives rise to the following equation:

$$W_{int} = \sum_{k=1}^{p}[\dot{\lambda}_k (A_k H + B_k M + C_k V_k)] \tag{3.46}$$

The expression $(A_kH + B_kM + C_kV_k) = D_k$, hence the force terms can be eliminated from equation 3.45:

$$W_{int} = \sum_{k=1}^{p}[\dot{\lambda}_k D_k] \tag{3.47}$$

This equation can be written in matrix form as follows:

$$W_{int} = \{c_{int}\}^T\{\dot{\lambda}\} \tag{3.48}$$

where

$$\{c_{int}\}^T = \{ D_1 \quad D_2 \quad D_3 \quad \ldots \quad D_P \}$$

$$\{\dot{\lambda}\}^T = \{\dot{\lambda}_1 \quad \dot{\lambda}_2 \quad \dot{\lambda}_3 \quad \ldots \quad \dot{\lambda}_p \}$$

It should be noted that the power dissipated by plastic mechanism at adjacent nodes is guaranteed to be non-negative as the plastic multiplier rates are constrained so that $\{ \dot{\lambda} \} \geq 0$, and other terms also have positive values. Thus, the internal dissipation of power is calculated correctly.

3.3.7 External Rate of Work

As mentioned earlier, it is assumed that the beam element is subjected with distributed tractions (normal and shear), while the joint element is subjected to point forces and moment. Thus, the external rate of work can occur at beam and joint elements.

Figure 3.8a shows the beam element subjected to the applied distributed shear traction, τ, and normal traction σ_n. Thus, the work done at this beam element is given as:

$$W_{ext,beam} = \int_0^L (u_t \tau + u_n \sigma_n) dt \tag{3.49}$$

It is assumed that the applied shear and normal tractions vary linearly along beam element:

$$\tau = \tau_1 (1 - \frac{t}{L}) + \tau_2 (\frac{t}{L}) \tag{3.50}$$

$$\sigma = \sigma_{n1} (1 - \frac{t}{L}) + \sigma_{n2} (\frac{t}{L})$$

where τ_1, σ_{n1} = values of shear and normal tractions at node 1, respectively

τ_2, σ_{n1} = values of shear and normal tractions at node 2, respectively

Substituting equations 3.27 and 3.50 into 3.49 and integrating, the external work done by applied tractions can be found:

$$W_{ext,beam} = \sum_{i=1}^{4} c_i Q_i \tag{3.51}$$

where

$$c_1 = L(\frac{u_1\cos\theta}{3}+\frac{v_1\sin\theta}{3}+\frac{u_2\cos\theta}{6}+\frac{v_2\sin\theta}{6})\ ;\ Q_1 = \tau_1$$

$$c_2 = L(\frac{u_1\cos\theta}{6}+\frac{v_1\sin\theta}{6}+\frac{u_2\cos\theta}{3}+\frac{v_2\sin\theta}{3})\ ;\ Q_2 = \tau_2$$

$$c_3 = L(-\frac{u_1\sin\theta}{3}+\frac{v_1\cos\theta}{3}-\frac{u_2\sin\theta}{6}+\frac{v_2\cos\theta}{6})\ ;\ Q_3 = \sigma_{n1}$$

$$c_4 = L(-\frac{u_1\sin\theta}{6}+\frac{v_1\cos\theta}{6}-\frac{u_2\sin\theta}{3}+\frac{v_2\cos\theta}{3})\ ;\ Q_4 = \sigma_{n2}$$

Figure 3.8b shows the joint element, j subjected to the applied forces, F_{xj} (x-dir.), F_{yj} (y-dir.), and moment F_{zj} (z-dir). Thus, the work done by these forces is given as:

$$W_{ext,joint} = F_{xj}\,u_j + F_{yj}\,v_j + F_{zj}\,w_j \tag{3.52}$$

This equation can be expressed in the matrix form as:

$$W_{ext,beam} = \sum_{i=5}^{7} c_i Q_i \tag{3.53}$$

where

$c_5 = u_j\ ;\ Q_5 = F_{xj}$

$c_6 = v_j\ ;\ Q_6 = F_{yj}$

$c_7 = w_j\ ;\ Q_7 = F_{zj}$

Thus, the total external work is obtained by summing that of beam and joint elements:

$$W_{ext} = W_{ext,beam} + W_{ext,joint} = \sum_{i=1}^{7} c_i Q_i \tag{3.54}$$

3.3.8 Constraint Generated by Objective Function

After equating the internal dissipation of work to the external work, it can be seen that:

$$\sum_{i=1}^{7} c_i Q_i = \{c_{int}\}^T\{\dot{\lambda}\} \tag{3.55}$$

The objective function also generates an equality constraint, depending on what variable will be optimized. For example, if we want to optimize the horizontal load applied at joint j, F_{xj} or Q_5, the equality constraint due to this objective function is $c_5 = 1$. Thus, the objective function obtained from equation 3.55 is:

$$\text{Min. } [Q_5] = \text{Min. } [\{c_{int}\}^T \{\dot{\lambda}\} - \sum_{i=1,\, i\neq 5}^{7} c_i Q_i]$$

On the other hand, if we want to optimize the normal traction applied at node 1, σ_{n1} or Q_3, the equality constraint due to this objective function becomes $c_3 = 1$. Thus, the objective function obtained from equation 3.55 is:

$$\text{Min. } [Q_3] = \text{Min. } [\{c_{int}\}^T \{\dot{\lambda}\} - \sum_{i=1,\, i\neq 3}^{7} c_i Q_i]$$

In general, if Q_a denotes the external applied load/traction being optimized, the objective function are given by:

$$\text{Min. } [Q_a] = \text{Min. } [\{c_{int}\}^T \{\dot{\lambda}\} - \sum_{i=1,\, i\neq a}^{7} c_i Q_i] \tag{3.56}$$

and the associated constraint generated by the objective function is:

$$c_a = 1 \tag{3.57}$$

It should be noted that constraint 3.57 is also a function of nodal velocities of either beam or joint elements because the expressions of c_1-c_7 are consisted of these unknown variables.

3.3.9 Assembly of Constraint Equations and Objective Function

The kinematically admissible nodal velocities are defined by assembling the following constraint equations:

1. Rigid movement of beam elements:

$$[A_{\text{rigid, beam}}] \{u_{\text{beam}}\} = \{b_{\text{rigid, beam}}\} \tag{3.31}$$

2. Flow rule equation of plastic failure of adjacent nodes:

$$[A_{comp}]\{u\} - [A_{flow}]\{\dot{\lambda}\} = \{0\} \tag{3.40}$$

3. Velocity boundary conditions:

$$[A_{vel,bound}]\{u_j\} = \{b_{vel,bound}\} \tag{3.42}$$

4. Additional constraint due to the objective function

$$c_a = 1 \tag{3.57}$$

5. Non-negative constraints on the plastic multiplier rates:

$$\{\dot{\lambda}\} \geq 0$$

Objective function:

$$\text{Min. } [Q_a] = \text{Min. } [\{c_{int}\}^T\{\dot{\lambda}\} - \sum_{i=1,\, i\neq a}^{7} c_i Q_i \,] \tag{3.56}$$

Assembling those constraints gives rise to a linear programming problem of the form:

$$\text{Minimize: } \{C_1\}^T\{X_1\} + \{C_2\}^T\{X_2\} \tag{3.58}$$

Subject to:

$$[A_1]\{X_1\} + \{A_2\}\{X_2\} = \{B\}$$

$$\{X_2\} \geq 0$$

where $\{X_1\}$ and $\{X_2\}$ are vectors of nodal velocities and plastic multipliers, respectively.

The solution of this form is solved by using the active set algorithm to the dual problem of equation 3.24. More details of the active set algorithm may be found in Sloan (1988b).

3.4 Validation of Structural Element Formulation: Analyses of Collapsed Loads of Two-Dimensional Frame Structures

This section evaluates the proposed formulation of numerical limit analyses for structural elements described in the previous section, by analyzing collapse loads of two dimensional frame structures, whose exact solutions are known. The known collapse loads for these structured problems provide a useful basis for evaluating the accuracy of the proposed numerical procedure.

Five examples of two dimensional frame structures were analyzed with the proposed formulation and the results are summarized in Table 3.1. The examples range from a relatively simple structure such as a one-bay-one-story frame (Figure 3.9), to more complicated structures, such as the 2-bay-3-story frame (Figure 3.15) or the Veirendeel

truss (Figure 3.17). It should be noted that all of these calculations consider only the failure of structural elements in bending (i.e. neglecting the effects of plastic axial and shear forces causing failure). The upper and lower bound results are also presented through Figures 3.9-3.18. The lower bound analysis generates the moment diagram, while the upper bound analysis presents the collapse mechanism.

In all five cases, the upper and lower bound analyses bracket the true collapse load very accurately(<< 1% error). In addition, computed collapse mechanisms from upper bound analyses are in excellent agreement with the exact solutions.

3.5 A Numerical Example of Soil-Structure Interaction: Analysis of Laterally Loaded Walls

3.5.1 Introduction

This section describes the first application of numerical limit analyses combining the structural elements (beam and joint), together with plane strain soil elements. Chapter 2 describes modifications of the original codes to incorporate complex loading and boundary conditions in order to simulate combined inclined and eccentric loading of footing and generalized soil-structure interfaces. Thus, the formulations of plane strain elements used in this thesis are based on the modified version presented by Ukritchon (1996).

The numerical limit analyses of structural and plane strain elements can be applied to analyze a wide range of stability problems involving soil-structure interaction. In this section, the application is illustrated through the collapse load calculation of a laterally loaded wall embedded in a homogeneous clay layer. This problem is complicated and difficult to analyze because failure of the system can occur due to shear distortion in the soil mass and/or plastic collapse of the structural wall. This application represents the first step toward the use of numerical limit analyses for basal stability of braced excavations in clay, presented in Chapter 6.

Section 3.5.2 summarizes a modification of lower and upper bound programs to handle soil-structure interfaces. Section 3.5.3 describes the results of analyses for laterally loaded walls with free and fixed head boundary conditions. Section 3.5.4 gives further

analyses for a failure envelope of free head walls loaded with horizontal force and moment. Upper and lower bound solutions are compared with existing analytical solutions. Finally, Section 3.5.5 describes parametric studies of free head walls for a practical range of the relative strength parameters, and eccentricity ratios of horizontal load.

3.5.2 Modeling of Soil-Structure Interfaces

When a wall embedded in a clay layer is subjected to a horizontal load at its top, failure may be caused by the separation between the soil and the wall, because the soil cannot sustain tensile stress across the interface. In order to model the mechanism of separation correctly, it is necessary to enforce additional constraints at soil-structure interfaces. The procedure for modeling the separation used in this study follows the same procedure proposed by Ukritchon (1996) who applied to the undrained loading of footings on clay with inclined and eccentric loads. In addition to the separation, there are two possible boundary conditions at soil-structure interfaces: 1) rough interfaces; and 2) smooth interfaces.

Figure 3.19a summarizes the numerical model of a laterally loaded wall embedded in a clay layer. The soil mass is discretized into 3-noded triangular elements (Figure 3.19b), while the wall is discretized into 2-noded beam and 1-noded joint elements (Figure 3.19c). Nodes are unique to a particular element. The following paragraphs summarize the procedure for modeling lower and upper bound methods with soil-structure interfaces:

3.5.2.1 Lower Bound Method

a) Plane Strain Elements: Each node of a triangular element has three unknown stresses (σ_x, σ_y, τ_{xy}). The stress components are assumed to vary linearly within each element.

b) Structural Elements: Each node of the beam and joint elements have two unknown forces (F_x, F_y) and one moment (F_z).

c) Soil-Structure Interfaces:

- Contact Stresses: Figure 3.19d shows a soil-structure interface in the lower bound discretization. The contact tractions from both sides of triangular elements acting to adjacent beam element are (σ_{nL}, τ_L) and (σ_{nR}, τ_R). The lower bound modeling of the interface requires that the net shear and normal tractions are applied to the adjacent beam element:

$$\text{Net shear traction, } \Sigma\tau = \tau_L - \tau_R \qquad (3.59)$$

$$\text{Net normal traction, } \Sigma\sigma_n = \sigma_{nL} - \sigma_{nR}$$

where

τ_L, τ_R = shear tractions along the left and right sides of soil-structure interfaces

σ_{nL}, σ_{nR} = normal tractions along the left and right sides of soil-structure interfaces

- Separation: Separation between the soil and a beam element can be modeled using the yield envelope. Assuming that no tension can be sustained across the interface, the Tresca yield criterion must be modified to include a tension cutoff, shown in Figure 3.20a. The stresses along soil-structure interfaces must satisfy the modified Tresca yield criterion as:

$$\text{Tresca yield criterion: } |\tau_L| \le s_i \; ; \; |\tau_R| \le s_i \qquad (3.60)$$

$$\text{Tension cutoff: } \sigma_{nL} \ge 0 \; ; \; \sigma_{nR} \ge 0$$

where s_i = the soil-structure adhesion at interfaces

Note that constraint eqn. 3.60 is not activated when full suction is permitted along interfaces.

- Rough Interfaces: For a perfectly rough interface, it is reasonable to assume that the interface adhesion is equal to the undrained shear strength of the clay:

$$s_i = s_u \qquad (3.61)$$

where s_u = undrained shear strength of clay.

Equation 3.61 is substituted into equation 3.60 when enforcing this boundary condition.

- Smooth Interfaces: The stress boundary conditions of a smooth interface corresponds to zero shear tractions along both sides:

$$\tau_L = 0 \; ; \; \tau_R = 0 \tag{3.62}$$

3.5.2.2 Upper Bound Method

a) Plane Strain Elements: Each node of a triangular element has two unknown velocities (u, v). The velocity components are assumed to vary linearly within each element.

b) Structural Element: Each node of beam element has two unknown velocities (u,v), while the joint element has two unknown velocities (u_j,v_j) and an angular velocity, (w_j).

c) Soil-Structure Interfaces:

- Separation: The upper bound method treats a soil-structure interface as a velocity discontinuity. The separation mechanism can be modeled by enforcing the flow rule at soil-structure interfaces. To be kinematically admissible at interfaces, the velocity jumps must remain associated with the modified Tresca yield criterion, shown in Figure 3.20b. The constraints of normal velocity jumps at soil-structure interfaces are:

$$\Delta u_{nL} \leq 0 \; ; \; \Delta u_{nR} \leq 0 \tag{3.63}$$

where Δu_{nL}, Δu_{nR} = normal velocity jumps on the left and right sides of interfaces, respectively

Conceptually, these constraints specify that the soil elements on the left or right sides can either remain in contact with the beam element ($\Delta u_n = 0$) or separate from it ($\Delta u_n < 0$). It should be noted that no constraint is required for the tangential velocity jump at interfaces because the soil element can slip either up or down, or may stick to the beam element. Note that if the separation is not permitted along interfaces, it is not necessary to enforce this constraint.

- Rough Interfaces: For the upper bound modeling, the interface adhesion is set to be equal to the undrained shear strength of clay when computing the internal dissipation of energy at rough interfaces.
- Smooth Interfaces: The representation of smooth interfaces in the upper bound method requires that the interface adhesion is zero ($s_i = 0$). As a result, the internal dissipation of energy for smooth interfaces becomes zero.

3.5.3 Analysis of Laterally Loaded Wall in Clay

Broms (1964) analyzed the ultimate resistance of piles in clay and proposed two boundary conditions at the pile head: 1) an unrestrained or free-head pile; and 2) a restrained or fixed-head pile. The free-head pile allows both translation and rotation to occur at its top, whereas a fixed-head pile allows only translation. As a result, the fixed-head pile allows a plastic hinge to develop at the top due to the restrained condition, while there is zero moment at the top of a free-head pile. Possible failure mechanisms of these two piles are shown in Figure 3.21. The first failure mechanism involves failure of the soil only, while bending moments along the pile are below the plastic moment. This is termed the "short piles" failure and the lateral capacity is dependent only on the soil resistance. The other extreme failure mechanism occurs for long piles, where the failure of the system includes plastic hinges in the pile itself (either at the top of a fixed head pile and/or at a certain distance below the ground surface. In this case, the lateral load capacity depends on both the strength of the soil and of the pile.

Even though the laterally loaded wall corresponds to a plane strain geometry, it is expected that the same failure mechanisms (described above for axi-symmetric piles) should occur. Therefore, the objective of this section is to demonstrate the capability of numerical limit analyses to be able to generate combined failure mechanisms of the wall and soil elements.

Figure 3.22 shows the problem geometry of a laterally loaded wall. The wall with length L, embedded in a homogeneous clay layer, is loaded at the top by a horizontal force, H, and moment M. The wall is discretized by structural beam and joint elements

with a plastic moment, M_p, while the soil is modeled using plane strain triangular elements with a constant undrained shear strength, s_u. The analyses do not consider the weight of soil (i.e. $\gamma = 0$). Note that the wall has no thickness and the width effects are represented in the strength criterion of plastic moment.

Figure 3.23 shows the typical meshes used in the lower and upper bound analyses, respectively. In this section, boundary conditions along all soil-structure interfaces correspond to the case of rough interfaces and also allow the possibility of separation.

3.5.3.1 Results for Free-Head Walls

It can be shown that the capacity of a laterally loaded wall, $H/(s_uL)$, is a function of the relative strength parameter, $M_p/(s_uL^2)$. Analyses have been carried out for two cases: 1) $M_p/(s_uL^2) = 1.0$; and 2) $M_p/(s_uL^2) = 0.2$. The first case corresponds to a relatively strong wall that remains rigid, while the latter represents the case where wall failure occurs. For both cases, the upper and lower bound analyses bracket the true lateral limit load, $H/(s_uL)$ within ±5% as follows:

For $M_p/(s_uL^2) = 1.0$: $H/(s_uL) = 1.085 - 1.190$, Bound = ±4%

For $M_p/(s_uL^2) = 0.2$: $H/(s_uL) = 1.009 - 1.031$, Bound = ±1%

Figures 3.24-3.26 show complete results of the upper and lower bound analyses for $M_p/(s_uL^2) = 1.0$, while Figures 3.27-3.29 show similar results for $M_p/(s_uL^2) = 0.2$. The lower bound results include the contact stresses on both side of the wall (e.g. Figure 3.24), the net tractions and the internal forces (e.g. Figure 3.25). The upper bound results (e.g. Figure 3.26) include the failure mechanism, the plastic failure zone, and velocity field and characteristics. In order to illustrate the relative strength parameter, $M_p/(s_uL^2)$, the same results (Figures 3.24-3.29) are replotted again in Figures 3.30-3.31.

Figure 3.30 compares the contact normal traction, σ_n/s_u and moment diagram, M/M_p of these two cases. For $M_p/(s_uL^2) = 1.0$, the maximum moment along the wall, $|M_{max}|/M_p \approx 0.23$ occurs at about the mid-depth of the pile. In contrast, for $M_p/(s_uL^2) = 0.2$, $|M_{max}|/M_p = 1.0$, indicating failure of the wall at a depth $z/L \approx 0.4$. For both cases, the lower bound analysis predict zero contact normal pressure over a large portion on the left

side of the wall. There is also a loss of contact pressure on the right had side towards the base of the wall.

Figure 3.31 compares the failure mechanism, plastic failure zone, and velocity characteristics for those cases. For $M_p/(s_uL^2) = 1.0$, the failure mechanism occurs such that the wall rotates rigidly to the right side and pushes the soil to failure. The results also show the physical separation between the soil and the wall on the left side, which agrees with zones of zero contact normal pressure (Figure 3.30a). When the relative pile-soil strength is reduced [$M_p/(s_uL^2) = 0.2$], the size of failure zone decreases significantly and the failure occurs due to soil distortion, and formation of a plastic hinge of the wall located at $z/L \approx 0.4$ below the ground surface. This agrees very well with the location of M_{max}/M_p from the lower bound analyses (Figure 3.30b). Furthermore, $M_p/(s_uL^2) = 0.2$ still generates physical separation on the left side of the wall.

Clearly, the failure mechanisms given by the upper bound analyses for $M_p/(s_uL^2) =$ 1.0 and 0.2 are in excellent agreement with the failure behavior of "short piles" and "long piles" as described by Broms (1964), respectively.

3.5.3.2 Results of Fixed-Head Walls

The analyses of fixed-head walls are performed for three relative strength parameters, $M_p/(s_uL^2) = 3.33$, 1.0, and 0.125. For a physical meaning, the case of rigid wall corresponds to $M_p/(s_uL^2) = 3.33$, while the case of weak wall corresponds to $M_p/(s_uL^2) = 0.125$ ($M_p/(s_uL^2) = 1.0$ is an intermediate case). For all cases, the true collapse loads can be bracketed by limit analyses to within ±5% as follows:

For $M_p/(s_uL^2) = 3.33$: $H/(s_uL) =$ 2.544 - 2.655, Bound = ±2.1%

For $M_p/(s_uL^2) = 1.0$: $H/(s_uL) =$ 2.253 - 2.306, Bound = ±1.1%

For $M_p/(s_uL^2) = 0.125$: $H/(s_uL) =$ 1.128 - 1.156, Bound = ±1.2%

Figures 3.32 through 3.40 show the complete results of upper and lower bound analyses for those parameters. Comparisons between different values of $M_p/(s_uL^2)$ are given in Figures 3.41-3.42.

Figures 3.41 compares the lower bound contact normal pressure and moment diagrams for the three selected relative strength parameters. The results show that as

$M_p/(s_uL^2)$ decreases from 3.33 to 1.0, the maximum moment M_{max}/M_p, which occurs at the top, increases from 0.381 to 1.0 (the wall fails by plastic bending moment). As $M_p/(s_uL^2)$ continues to decrease to 0.125, a second hinge develops at z/L = 0.44 below the ground surface. Notice that for all cases, the maximum contact pressure on the right side of the wall, $\sigma_n(R)/s_u \approx 2.5$, which is the same value as in the free-head case. Moreover, for $M_p/(s_uL^2) = 3.33$, the contact normal pressure on the left side, $\sigma_n(L)/s_u$ is zero over the entire length of the wall. As $M_p/(s_uL^2)$ decreases from 3.33 to 0.125, $\sigma_n(L)/s_u$ begins to develop from the tip over a certain length. These results make sense because as the soil strength increases, it has more resistance to hold the tip of the wall in place.

The corresponding upper bound results in Figure 3.43 show a significant reduction of plastic failure zone with decreasing values of $M_p/(s_uL^2)$. For $M_p/(s_uL^2)$ = 3.33, the failure occurs due to the wall translating horizontally and pushing the soil to the right side. As the soil becomes stronger [$M_p/(s_uL^2) = 1.0$], the wall is loaded to failure at the top, where the first plastic hinge occurs. With further decreases in $M_p/(s_uL^2)$ (= 0.125), the second plastic hinge occurs at the location, $z/L \approx 0.4$ below the ground surface. The distance of the second plastic hinge agrees very well with the distance of second $M_{max}/M_p = 1.0$ at 0.44L reported by lower bound analyses (Figure 3.14c). Notice that physical separation between the soil and wall can be seen in all cases. This is particularly for $M_p/(s_uL^2) = 3.33$, where separation occurs over the entire length of the left side of the wall. This result is also in an excellent agreement with the lower bound result (Figure 3.14a), where there is no adhesion between soil and wall over the entire length on the left side.

It can be seen that the failure mechanisms for $M_p/(s_uL^2)$ = 3.33, 1.0, and 0.2 generated by upper bound analyses correspond to the mechanism of failure for short, intermediate, and long piles, proposed by Broms (1964), respectively.

Therefore, the results of free-head and fixed walls clearly show that the numerical limit analyses for plane strain and structural elements are able to simulate correctly stability problems involving soil-structure interaction.

3.5.4 Results of Free-Head Walls with Combined Horizontal Load and Moment

The analyses are extended to study the case, where a free-head wall is subjected to combined horizontal, H, and moment, M, loading at the top. The analyses were performed for two loading modes: I) H = +ve, M = +ve; and II) H = -ve and M= +ve (see Figure 3.22b). For each loading, the analyses were simulated for three relative strength parameters, $M_p/(s_uL^2)$ = 2.0, 1.0, and 0.2, and also for smooth and rough interfaces conditions.

Tables 3.2, 3.3 and 3.4 summarize the lower and upper bound loads, $H/(s_uL)$ and moment, $M/(s_uL^2)$ obtained from the numerical limit analyses at each of the three relative strength parameters, $M_p/(s_uL^2)$ = 2.0, 1.0, and 0.2, respectively. The data are plotted in Figures 3.43-3.45, as failure envelopes of free-head walls subjected combined loadings of horizontal force and moment. For all cases, the upper and lower bound analyses are able to bracket the true collapse load within ±6%, where in some cases the calculations give negligible difference between computed upper and lower bound collapse loads.

Figure 3.46 compares the failure envelopes for different values of $M_p/(s_uL^2)$, assuming the average of lower bound and upper bound data provides a best estimate of collapse. For both rough and smooth interfaces, the results clearly show the size of failure envelope reduces significantly with the relative strength parameter. Notice that all three failure envelopes have similar lateral load capacities at a given applied moment, but the maximum moment capacity is controlled by the relative strength parameter decreasing from $M/(s_uL^2)$ = 1.5, 1.0, and 0.2 for a rough wall, and $M/(s_uL^2)$ = 2.0, 1.0, and 0.2 for a smooth wall.

Figure 3.47 compares the failure envelopes for smooth and rough interfaces. For the case of a rigid wall [$M_p/(s_uL^2)$ = 2.0], the wall capacity for a rough interface is higher than a smooth interface. For lower relative strengths [$M_p/(s_uL^2)$ = 0.2], the failure envelope is independent of wall roughness. Note that the maximum moment, $M_{max}/(s_uL^2)$ applied at the top of rigid wall has an average of 1.43, and 1.35, for smooth and rough walls, respectively.

Figures 3.48 and 3.49 provide comparisons of contact normal pressure and failure mechanism between smooth and rough interfaces of free head walls for the case of rigid

wall and $M_p/(s_uL^2) = 1.0$. Note that the lower and upper bound solutions of these cases are as follows:

Rough walls: $H/(s_uL) = 1.085 - 1.190$, Bound = ±4.1%

Smooth walls: $H/(s_uL) = 0.900 - 0.953$, Bound = ±2.9%

For smooth walls, it is expected that contact normal pressure on the right side should reach the passive failure, $\sigma_n(R)/s_u = 2$. This assumption agrees very well with the contact pressure from lower bound analyses given in Figure 3.48b, which shows $\sigma_n(R)/s_u$ remains constant at the value of 2.0. The results clearly show the rough interfaces increases $\sigma_n(R)/s_u$ from 2.0 to 2.5. On the contrary, the average contact pressure on the left side is two times higher than that of passive failure: $\sigma_n(L)/s_u = 4.3$ for smooth walls; and $\sigma_n(L)/s_u = 4.1$ for rough walls. There are also significant differences in failure mechanism from upper bound analyses between smooth and rough interfaces, as shown in Figure 3.49. For smooth walls, velocity characteristics on the right side correspond to a passive wedge failure, while those on the left side are similar to the Terzaghi bearing capacity failure. This explains why the lower bound solution gives a value of $\sigma_n(L)/s_u$ higher than that of passive failure. It should be noted that these observations are similar to the interpretation of Davis (1961).

Davis (1961) obtained upper and lower bound solutions for a rigid wall in a purely-cohesive weightless soil with plane strain geometry. Figure 3.50 shows the failure envelope of free head walls by Davis (1961) for smooth and rough interfaces. His analyses assume that there is no tension between the soil and wall. At failure, Davis assumes the pressure on AB is $2s_u$, while that on BC is $5.14s_u$, the solution of Terzaghi bearing capacity. Comparison of failure envelope between Davis (1961)'s solutions and numerical limit analyses are illustrated in Figure 3.51. It can be seen that the shape pattern of failure envelopes given by Davis (1961) is very consistent with that of numerical limit analyses. For rough walls, numerical lower bound solutions are more accurate than those of Davis. On the other hand, both Davis (1961)'s LB and UB solutions match almost exactly with numerical upper and lower bound solutions for smooth walls.

3.5.5 Parametric Studies of Free Head Wall, Smooth Interfaces

The analyses can be readily extended to study the ultimate lateral load capacity of free head (smooth) walls, where the horizontal force, H is applied at an elevation, e above the ground surface. These simulations study practical ranges of elevation ratio, e/L = 0.0 - 0.5, and relative strength parameters, $M_p/(s_uL^2)$ = 0.01 - 2.0. Table 3.5 summarizes the results of parametric studies and corresponding data are plotted in Figure 3.52. In all cases, the upper and lower bound solutions provide bound on true collapse load within 6%. Figure 3.52a summarizes the ultimate lateral load, $H/(s_uL)$ as a function of e/L and $M_p/(s_uL^2)$, while Figure 3.52b shows the maximum moment M_{max}/M_p in the wall from lower bound analyses. It can be seen that for $M_p/(s_uL^2) < 0.5$, $H/(s_uL)$ decreases almost linearly with $M_p/(s_uL^2)$, and $M_{max}/M_p = 1.0$ indicating bending failure of the wall. For $M_p/(s_uL^2) > 0.5$, $H/(s_uL)$ remains constant for all values of e/L. These results correspond to a failure of the soil with no plastic hinge in the wall, and $M_{max}/M_p < 1.0$. Note that ultimate lateral resistance decreases with increasing the value of e/L.

3.6 References

Baker, J. and Heyman J. (1969). *Plastic Design of Frames 1.* Cambridge University Press.

Broms, B. B. (1964). "Lateral Resistance of Piles in Cohesive Soils." J.S.M.F.D., ASCE, Vol. 90, SM2, 27-63.

Davis, E. H. (1961). "The Application of the Theory of Plasticity to Foundation Problem - Limit Analysis." Post-Grad. Course on Fndn. Eng., Univ. of Sydney, Aust.

Hodge, P. G. (1959). *Plastic Analysis of Structures.* McGraw-Hill, New York.

Horne, R. M. (1971). *Plastic Theory of Structures.* The M.I.T Press, Cambridge, Massachusetts.

Neal, B. G. (1977). *The Plastic Methods of Structural Analysis.* John Wiley & Sons, New York.

Mrázik, A., Škaloud, M., and Tochácek, M. (1987). *Plastic Design of Steel Structures.* John Wiley & Sons, New York.

Sloan, S. W. (1988a). "Lower bound limit analysis using finite elements and linear programming." Int. J. Numer. Anal. Methods in Geomech., 12(1), 61-77.

Sloan, S. W. (1988b). "A steepest edge active set algorithm for solving sparse linear programming problems." Int. J. Numer. Anal. Methods in Geomech., 26(12), 2671-2685.

Sloan, S. W., and Kleeman, P. W. (1994). "Upper bound limit analysis using discontinuous velocity fields." Computer Methods in Applied Mechanics and Engineering., 127, 293-314.

Ukritchon, B. (1996). "Evaluation of Numerical Limit Analyses by Finite Elements and Linear Programming, M.S. Thesis, Dept. of Civil and Environmental Eng., Massachusetts Institute of Technology, Cambridge, MA.

Two-Dimensional Frames	Loading Factor by Limit Analyses λ_{LB} - λ_{UB}	Exact Solution λ_{exact}	References
1st Example 1-bay-1-story Frame	1.5 - 1.5	1.5	Neal (1977)
2nd Example 1-bay-1-story Frame	1.645 - 1.646	1.645	Neal (1977)
3rd Example 1-bay-2-story Frame	1.341 - 1.357	1.342	Neal (1977)
4th Example 2-bay-3-story Frame	1.938 - 1.949	1.940	Baker & Heyman (1969)
5th Example Veirendeel Truss	1.714 - 1.714	1.714	Hodge (1959)

Table 3.1 Validation of the Proposed Formulation for Stuctural Elements through Collapse Calculations of Two-Dimensional Frames

β	tan(β)	Rough wall					Smooth wall				
		Upper bound		Lower bound		% Bound	Upper bound		Lower bound		% Bound
(deg.)	M/(HL)	$H/(Ls_u)$	$M/(s_uL^2)$	$H/(Ls_u)$	$M/(s_uL^2)$		$H/(Ls_u)$	$M/(s_uL^2)$	$H/(Ls_u)$	$M/(s_uL^2)$	
0	0.000	1.190	0.000	1.085	0.000	9.2	0.953	0.000	0.899	0.000	5.8
15	0.268	0.873	0.234	0.799	0.214	8.9	0.723	0.194	0.677	0.181	6.5
30	0.577	0.669	0.386	0.607	0.351	9.6	0.560	0.324	0.517	0.299	8.0
45	1.000	0.505	0.505	0.454	0.454	10.5	0.429	0.429	0.391	0.391	9.1
60	1.732	0.354	0.612	0.323	0.559	9.1	0.305	0.528	0.277	0.481	9.4
75	3.732	0.193	0.721	0.175	0.653	9.9	0.165	0.614	0.153	0.570	7.5
90	-	0.000	0.846	0.000	0.764	10.2	0.000	0.722	0.000	0.670	7.4
105	-3.732	-0.270	1.008	-0.242	0.903	10.9	-0.232	0.867	-0.214	0.799	8.1
120	-1.732	-0.731	1.265	-0.651	1.127	11.6	-0.615	1.065	-0.555	0.962	10.2
135	-1.000	-1.536	1.536	-1.372	1.372	11.3	-1.302	1.302	-1.186	1.186	9.3
140	-0.839	-1.878	1.576	-1.693	1.420	10.4	-1.606	1.348	-1.468	1.232	9.0
145	-0.700	-2.261	1.583	-2.045	1.432	10.0	-1.913	1.339	-1.778	1.245	7.3
150	-0.577	-2.572	1.485	-2.378	1.373	7.8	-2.000	1.155	-1.950	1.126	2.5
152.5	-0.521	-2.631	1.369	-2.445	1.273	7.3	-2.000	1.041	-1.983	1.032	0.9
155	-0.466	-2.447	1.141	-2.359	1.100	3.7	-1.874	0.874	-1.842	0.859	1.7
160	-0.364	-2.053	0.747	-1.928	0.702	6.3	-1.572	0.572	-1.515	0.551	3.7
165	-0.268	-1.753	0.470	-1.621	0.434	7.8	-1.361	0.365	-1.296	0.347	4.9
170	-0.176	-1.513	0.267	-1.397	0.246	8.0	-1.188	0.210	-1.130	0.199	5.1
175	-0.087	-1.333	0.117	-1.223	0.107	8.6	-1.058	0.093	-1.001	0.088	5.6
180	0.000	-1.190	0.000	-1.085	0.000	9.2	-0.953	0.000	-0.899	0.000	5.8

Notes: All symbols are referred to the following figures.

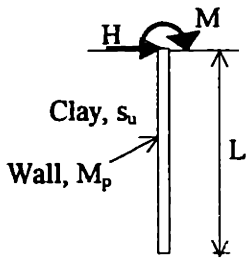

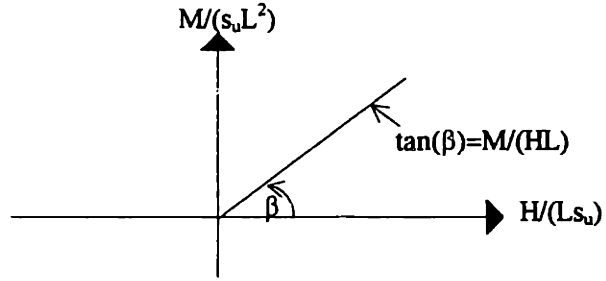

Table 3.2 Summary of lower and upper bound analyses for a laterally loaded free head wall, where $M_p/(s_uL^2) = 2.0$

β	tan(β)	Rough wall					Smooth wall				
		Upper bound		Lower bound		% Bound	Upper bound		Lower bound		% Bound
(deg.)	M/(HL)	$H/(Ls_u)$	$M/(s_uL^2)$	$H/(Ls_u)$	$M/(s_uL^2)$		$H/(Ls_u)$	$M/(s_uL^2)$	$H/(Ls_u)$	$M/(s_uL^2)$	
0	0.000	1.190	0.000	1.085	0.000	9.2	0.953	0.000	0.899	0.000	5.8
15	0.268	0.873	0.234	0.799	0.214	8.9	0.723	0.194	0.677	0.181	6.5
30	0.577	0.669	0.386	0.607	0.351	9.6	0.560	0.324	0.517	0.299	8.0
45	1.000	0.505	0.505	0.454	0.454	10.5	0.429	0.429	0.391	0.391	9.1
60	1.732	0.354	0.612	0.323	0.559	9.1	0.305	0.528	0.277	0.481	9.4
75	3.732	0.193	0.721	0.175	0.653	9.9	0.165	0.614	0.153	0.570	7.5
90	-	0.000	0.846	0.000	0.764	10.2	0.000	0.722	0.000	0.670	7.4
105	-3.732	-0.268	1.000	-0.242	0.903	10.2	-0.232	0.867	-0.214	0.799	8.1
120	-1.732	-0.577	1.000	-0.577	1.000	0.0	-0.577	1.000	-0.555	0.962	3.9
135	-1.000	-1.000	1.000	-1.000	1.000	0.0	-1.000	1.000	-1.000	1.000	0.0
150	-0.577	-1.732	1.000	-1.732	1.000	0.0	-1.732	1.000	-1.732	1.000	0.0
155	-0.466	-2.145	1.000	-2.145	1.000	0.0	-1.874	0.874	-1.842	0.859	1.7
160	-0.364	-2.053	0.747	-1.928	0.702	6.3	-1.572	0.572	-1.515	0.551	3.7
165	-0.268	-1.753	0.470	-1.621	0.434	7.8	-1.361	0.365	-1.296	0.347	4.9
170	-0.176	-1.513	0.267	-1.397	0.246	8.0	-1.188	0.210	-1.130	0.199	5.1
175	-0.087	-1.333	0.117	-1.223	0.107	8.6	-1.058	0.093	-1.001	0.088	5.6
180	0.000	-1.190	0.000	-1.085	0.000	9.2	-0.953	0.000	-0.899	0.000	5.8

Notes: All symbols are referred to the following figures.

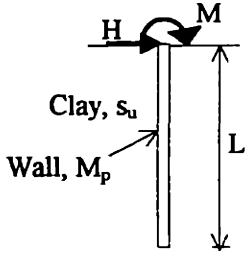

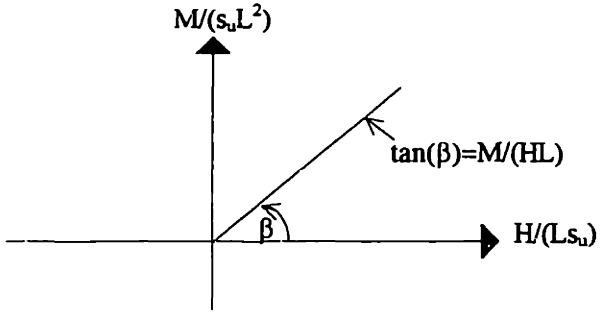

Table 3.3 Summary of lower and upper bound analyses for a laterally loaded free head wall, where $M_p/(s_uL^2) = 1.0$

β	tan(β)	Rough wall					Smooth wall				
		Upper bound		Lower bound		% Bound	Upper bound		Lower bound		% Bound
(deg.)	M/(HL)	$H/(Ls_u)$	$M/(s_uL^2)$	$H/(Ls_u)$	$M/(s_uL^2)$		$H/(Ls_u)$	$M/(s_uL^2)$	$H/(Ls_u)$	$M/(s_uL^2)$	
0	0.00000	1.031	0.000	1.009	0.000	2.1	0.900	0.000	0.891	0.000	1.0
5	0.08749	0.846	0.074	0.811	0.071	4.3	0.738	0.065	0.734	0.064	0.6
10	0.17633	0.675	0.119	0.656	0.116	3.0	0.625	0.110	0.607	0.107	2.8
15	0.26795	0.543	0.146	0.536	0.144	1.3	0.513	0.137	0.506	0.136	1.4
20	0.36397	0.451	0.164	0.443	0.161	1.6	0.426	0.155	0.425	0.155	0.2
25	0.46631	0.381	0.178	0.371	0.173	2.8	0.360	0.168	0.359	0.167	0.3
30	0.57735	0.327	0.189	0.313	0.153	4.3	0.309	0.178	0.306	0.153	1.0
45	1.00000	0.200	0.200	0.193	0.193	3.7	0.200	0.200	0.191	0.191	4.7
60	1.73205	0.115	0.200	0.115	0.200	0.0	0.115	0.200	0.115	0.200	0.0
90	-	0.000	0.200	0.000	0.200	0.0	0.000	0.200	0.000	0.200	0.0
120	-1.73205	-0.115	0.200	-0.115	0.200	0.0	-0.115	0.200	-0.115	0.200	0.0
150	-0.57735	-0.346	0.200	-0.346	0.200	0.0	-0.346	0.200	-0.346	0.200	0.0
170	-0.17633	-1.134	0.200	-1.134	0.200	0.0	-1.134	0.200	-1.130	0.199	0.4
175	-0.08749	-1.314	0.115	-1.223	0.107	7.2	-1.058	0.093	-1.001	0.088	5.6
177.5	-0.04366	-1.158	0.051	-1.127	0.049	2.7	-1.003	0.044	-0.947	0.041	5.8
180	0.00000	-1.031	0.000	-1.009	0.000	2.1	-0.900	0.000	-0.891	0.000	1.0

Notes:

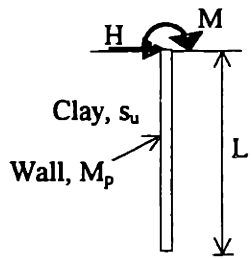

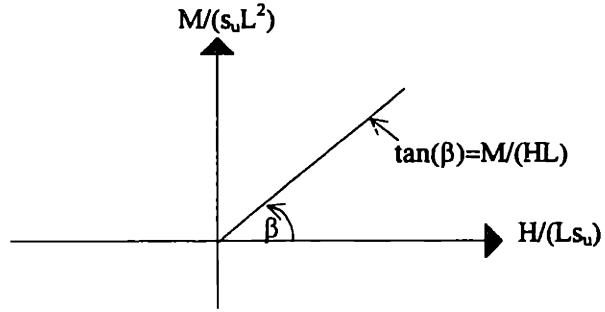

Table 3.4 Summary of lower and upper bound analyses for a laterally loaded free head wall, where $M_p/(s_uL^2) = 0.2$

$M_p/(s_uL^2)$ / e/L		0.01	0.05	0.1	0.2	0.5	1	2
0.0	UB	0.200	0.450	0.650	0.900	0.953	0.953	0.953
	LB	0.199	0.445	0.630	0.891	0.899	0.899	0.899
0.1	UB	0.083	0.300	0.467	0.720	0.853	0.853	0.853
	LB	0.083	0.289	0.462	0.714	0.804	0.804	0.804
0.2	UB	0.050	0.200	0.350	0.600	0.771	0.771	0.771
	LB	0.047	0.200	0.348	0.578	0.726	0.726	0.726
0.5	UB	0.020	0.100	0.183	0.343	0.594	0.594	0.594
	LB	0.020	0.095	0.183	0.341	0.550	0.550	0.550

a) Ultimate lateral resistance, $H/(s_uL)$

$M_p/(s_uL^2)$ / e/L	0.01	0.05	0.1	0.2	0.5	1	2
0	0.4	1.0	3.2	1.0	5.8	5.8	5.8
0.1	0.7	3.7	1.0	0.8	5.9	5.9	5.9
0.2	5.8	0.1	0.7	3.7	6.1	6.1	6.1
0.5	1.0	4.7	0.1	0.5	7.6	7.6	7.6

b) % bounds of $H/(s_uL)$ between UB. and LB.

$M_p/(s_uL^2)$ / e/L	0.01	0.05	0.1	0.2	0.5	1	2
0	1.000	1.000	1.000	1.000	0.407	0.204	0.102
0.1	1.000	1.000	1.000	1.000	0.487	0.244	0.122
0.2	1.000	1.000	1.000	1.000	0.556	0.278	0.139
0.5	1.000	1.000	1.000	1.000	0.703	0.351	0.176

c) Maximum moment in wall (LB. solution), M_{max}/M_p

Notes:
LB = Lower bound, UB = Upper bound

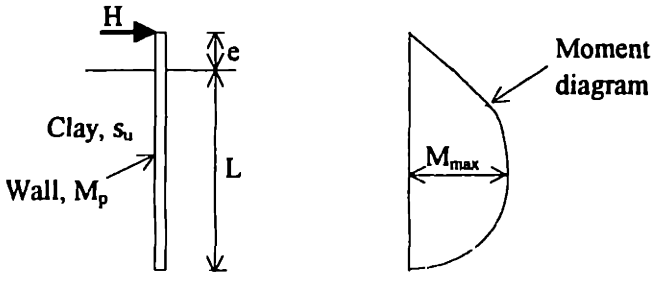

Table 3.5 Ultimate lateral resistance of a free head wall in clay, smooth interface

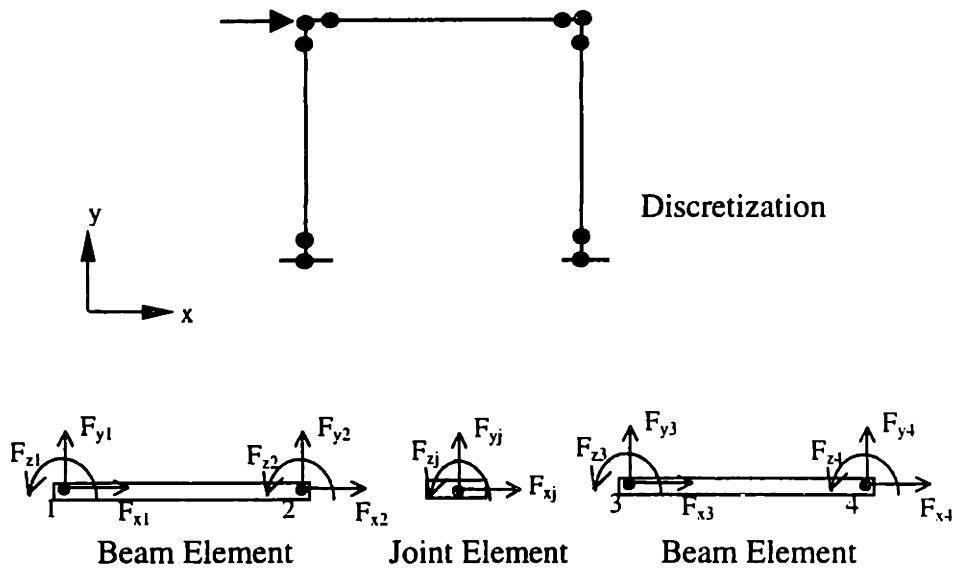

Figure 3.1 Lower bound discretization - 2D structural problems

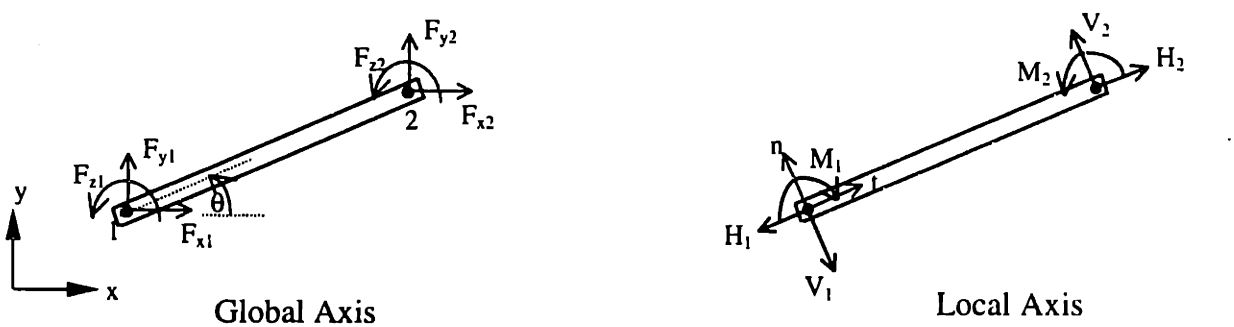

Figure 3.2 Positive sign convention of nodal forces in the global and local axis

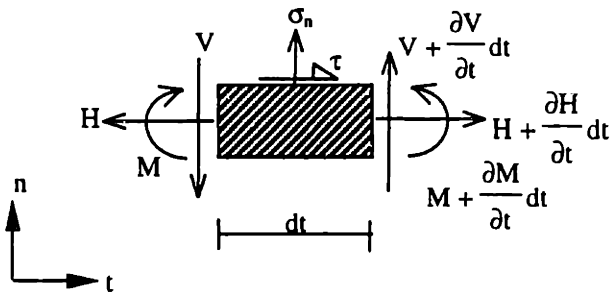

Figure 3.3 Equilibrium of beam element

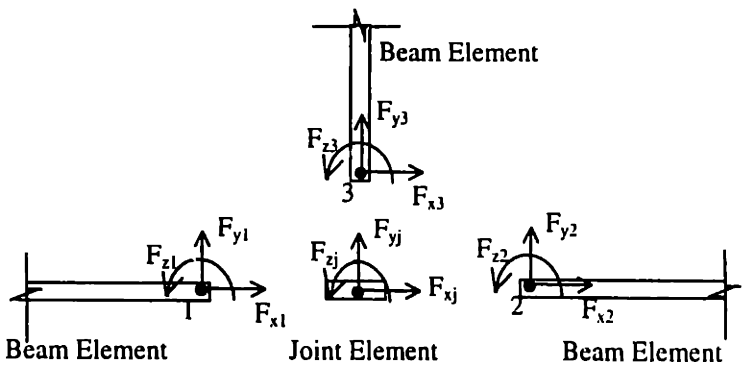

Figure 3.4 Equilibrium of joint element

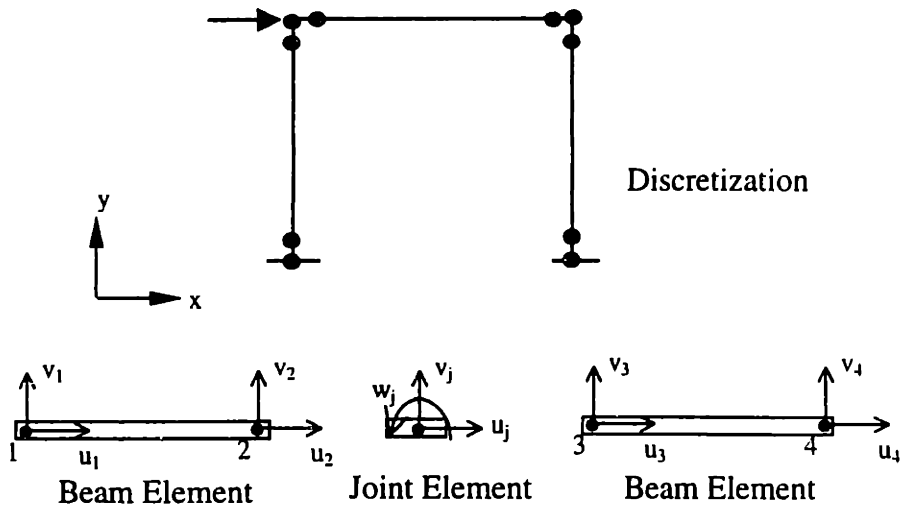

Figure 3.5 Upper bound discretization - 2D structural problems

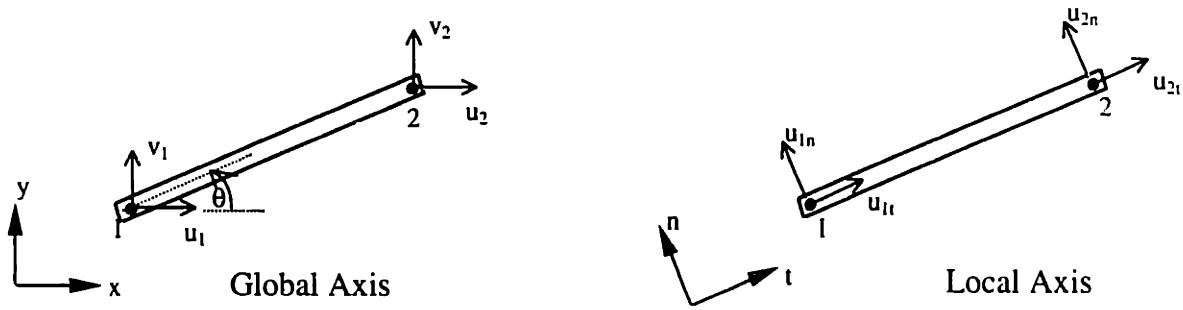

Figure 3.6 Beam element in the global and local axes

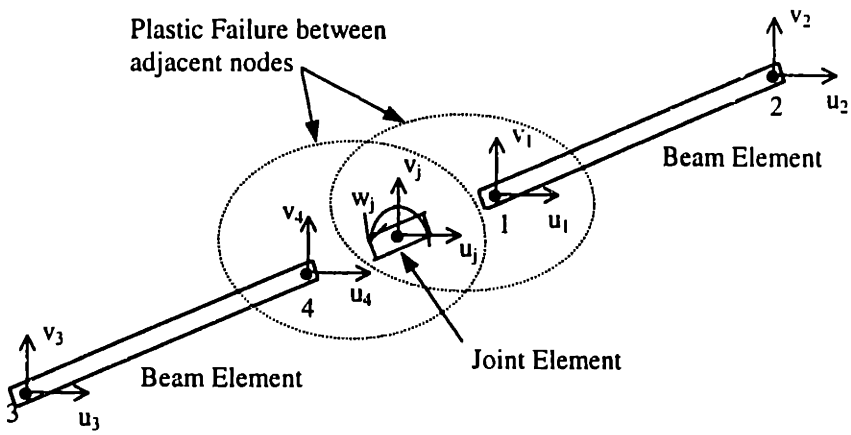

Figure 3.7 Plastic failure at adjacent nodes between beam and joint elements

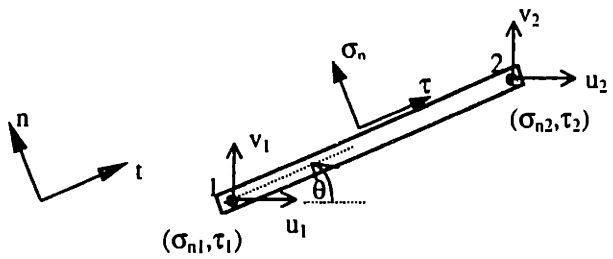

a) Beam element loaded with shear and normal tractions

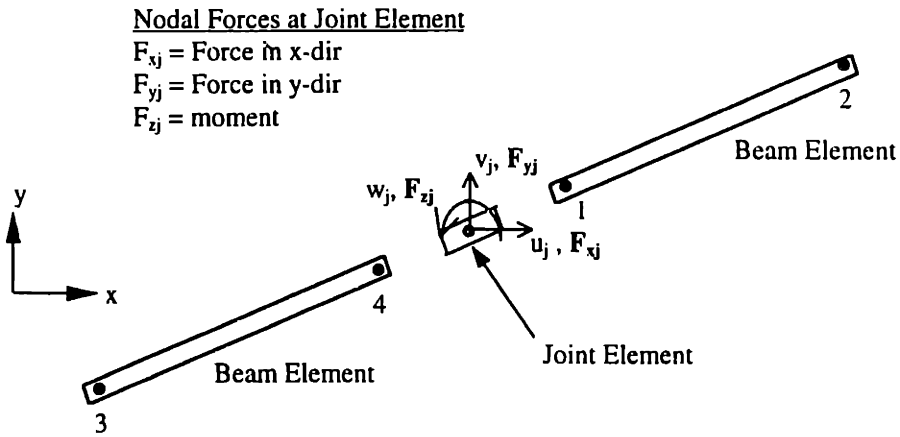

b) Joint element loaded with point forces and moment

Figure 3.8. External applied loads at beam and joint elements

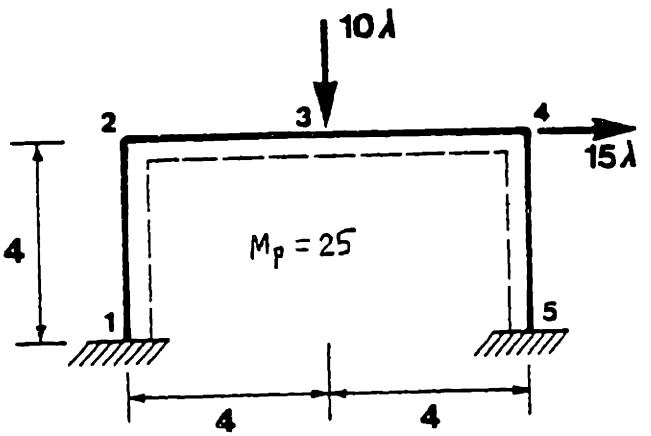

a) Problem Geometry

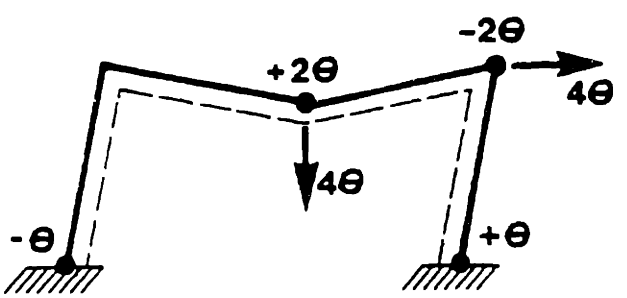

b) Collapse Mechanism, $\lambda_{exact} = 1.5$

Figure 3.9 1st Example: 1-bay-1-story Frame (Neal, 1977)

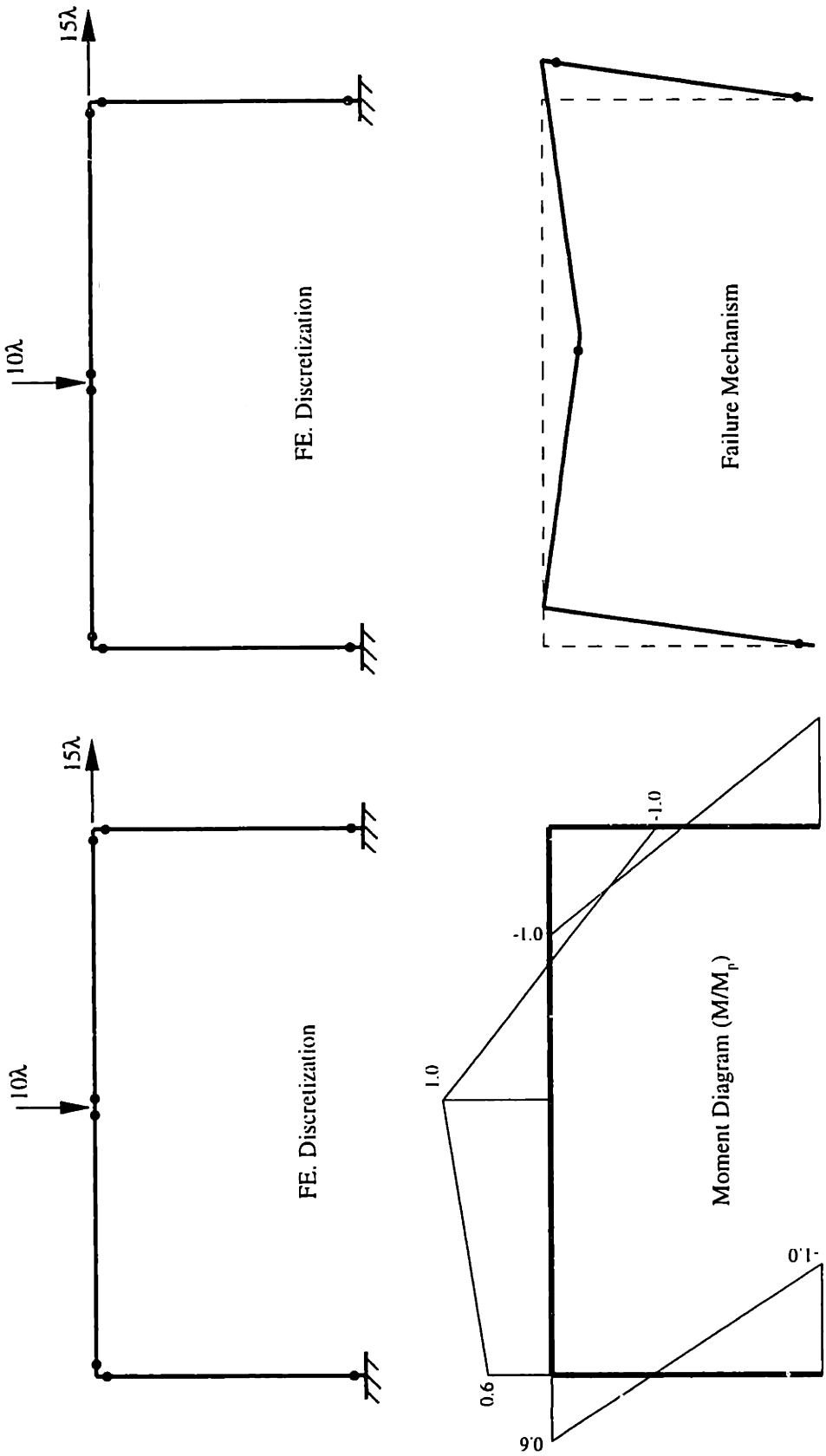

a) LB Analysis: $\lambda_{LB} = 1.5$

b) UB Analysis: $\lambda_{UB} = 1.5$

Figure 3.10 LB and UB results for an analysis of 1st example: 1-bay-1-story frame , $\lambda_{exact} = 1.5$

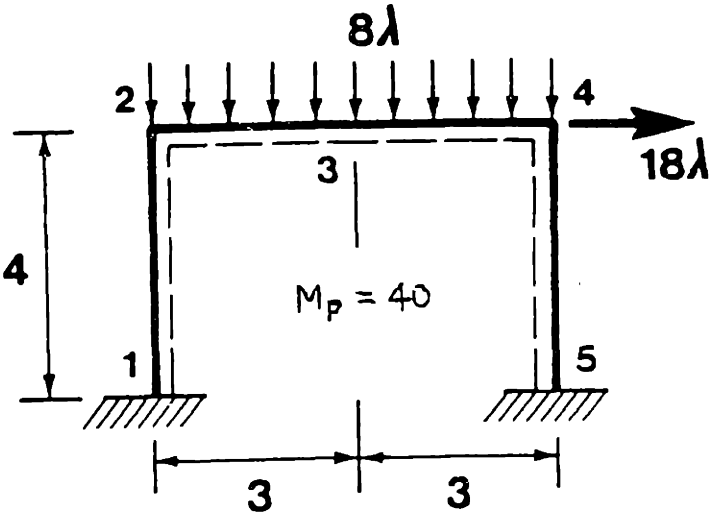

a) Problem Geometry

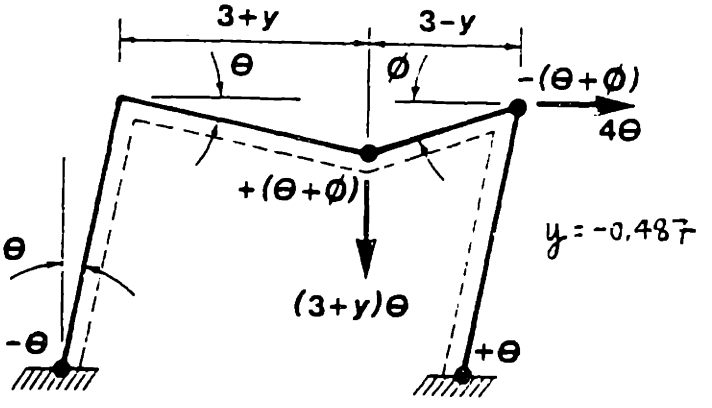

b) Collapse Mechanism, $\lambda_{exact} = 1.645$

Figure 3.11 2nd Example: 1-bay-1-story Frame (Neal, 1977)

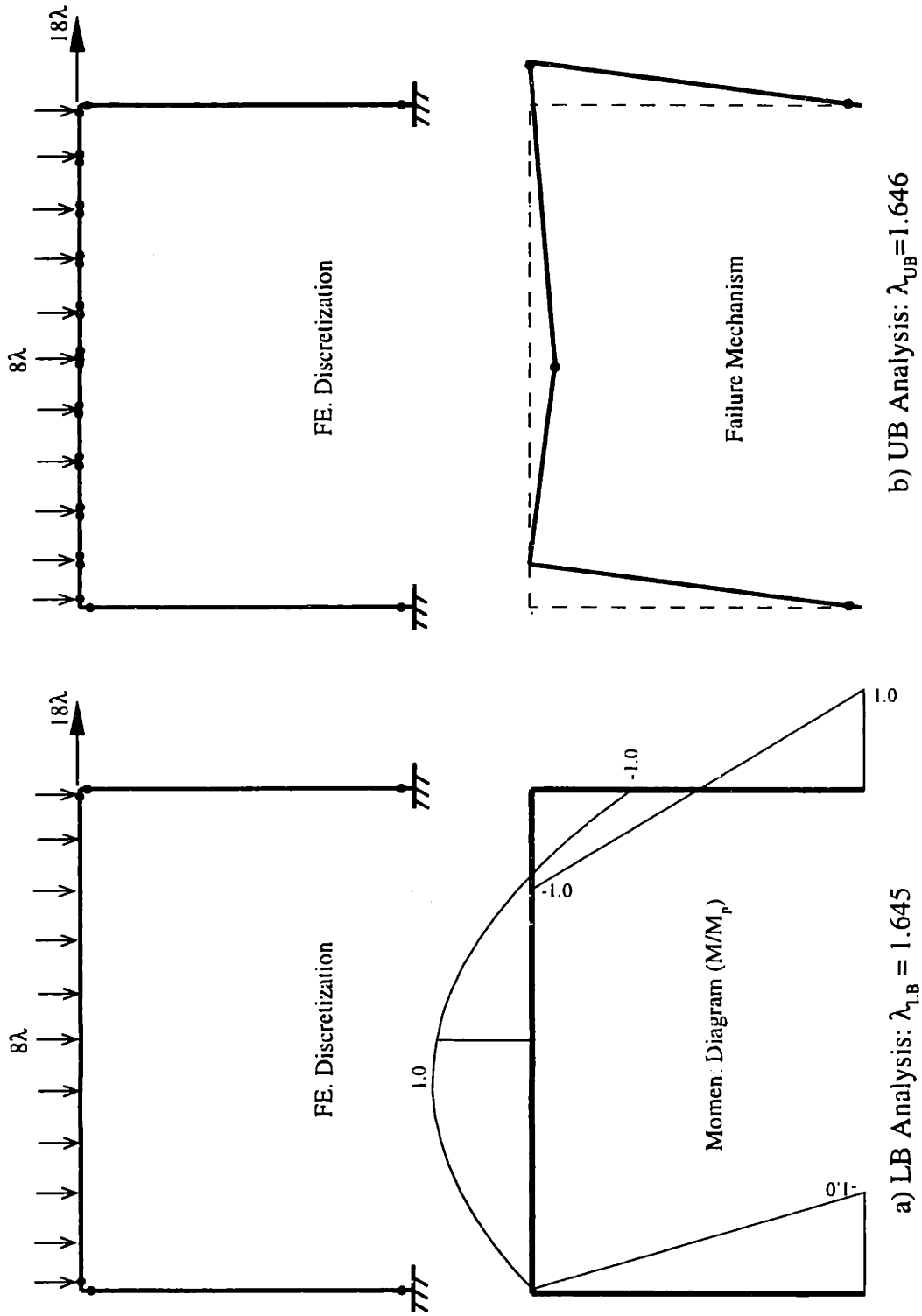

a) LB Analysis: λ_{LB} = 1.645

b) UB Analysis: λ_{UB}=1.646

Figure 3.12 LB and UB results for an analysis of 2nd example: 1-bay-1-story frame, λ_{exact} = 1.645

(Broken Arrow = Total value of uniformly distributed load)

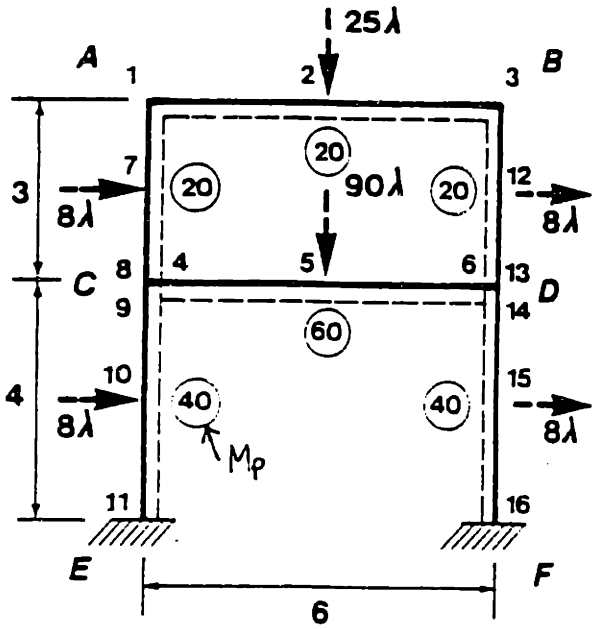

a) Problem Geometry

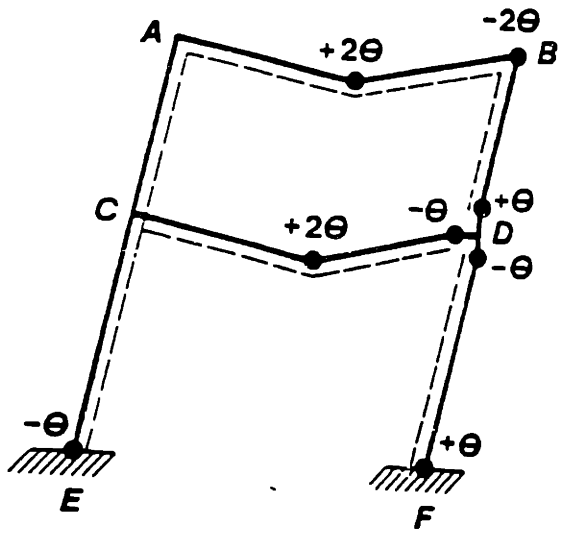

b) Collapse Mechanism, $\lambda_{exact} = 1.342$

Figure 3.13 3rd Example: 1-bay-2-story Frame (Neal, 1977)

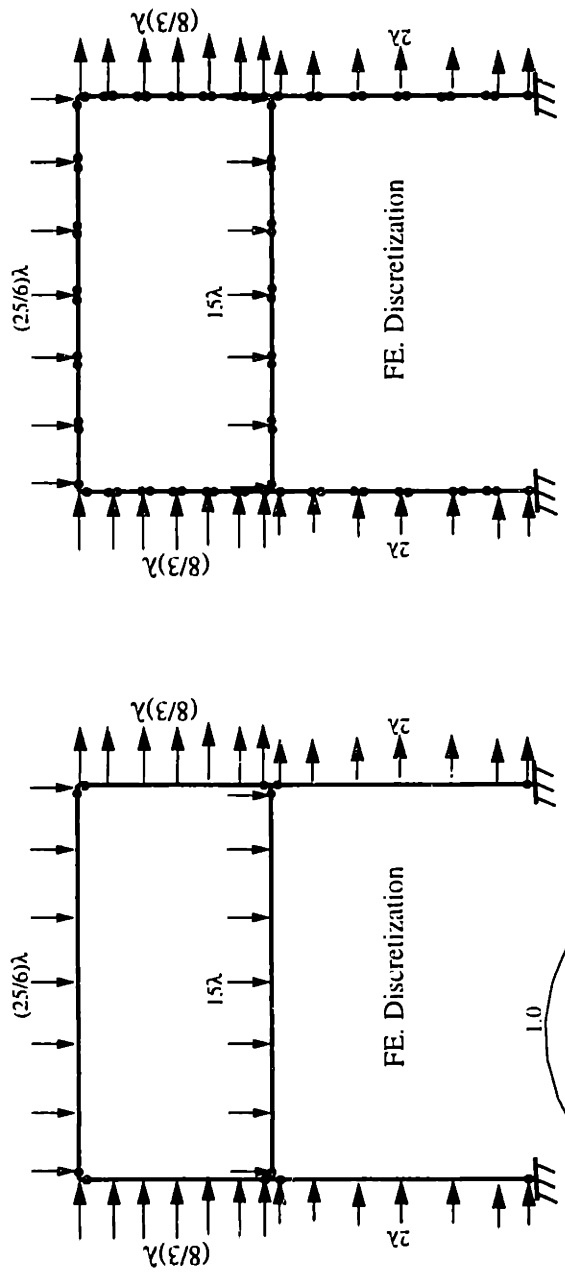

a) LB Analysis: λ_{LB}=1.341

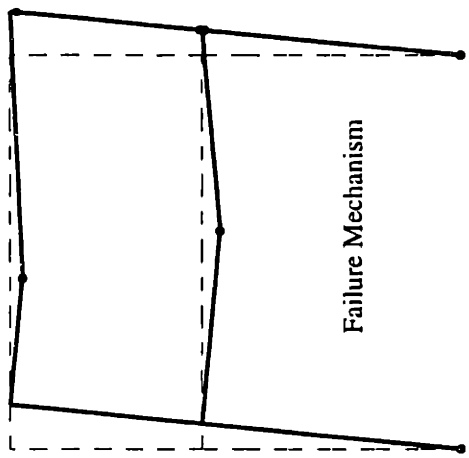

b) UB Analysis: λ_{UB}=1.357

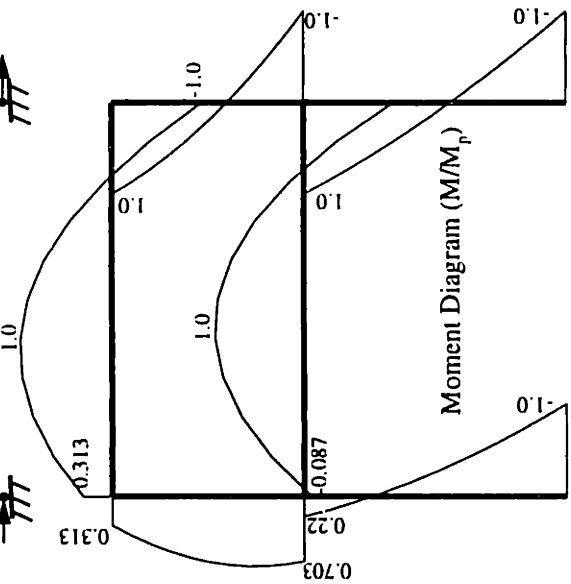

Figure 3.14 LB and UB results for an analysis of 3rd example: 1-bay-2-story frame, λ_{exact} = 1.342

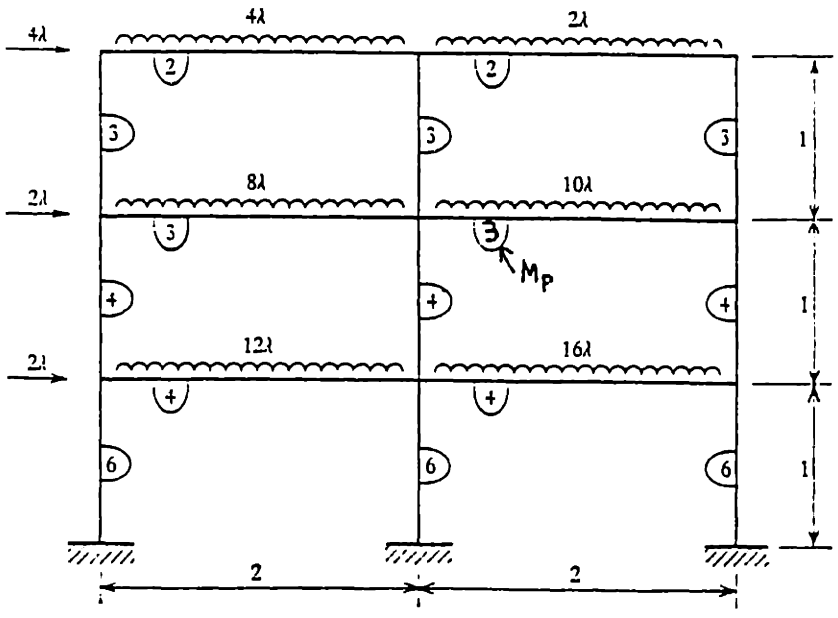

a) Problem Geometry

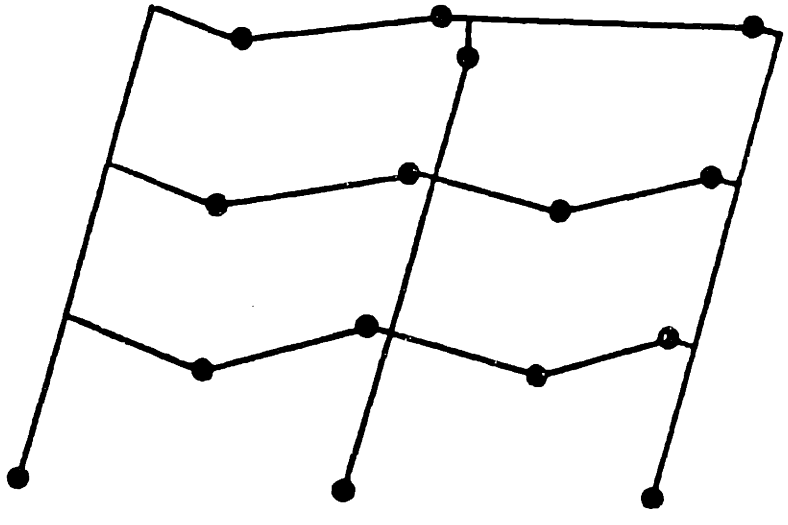

b) Collapse Mechanism, $\lambda_{exact} = 1.940$

Figure 3.15 4th Example: 2-bay-3-story Frame (Baker & Heyman, 1969)

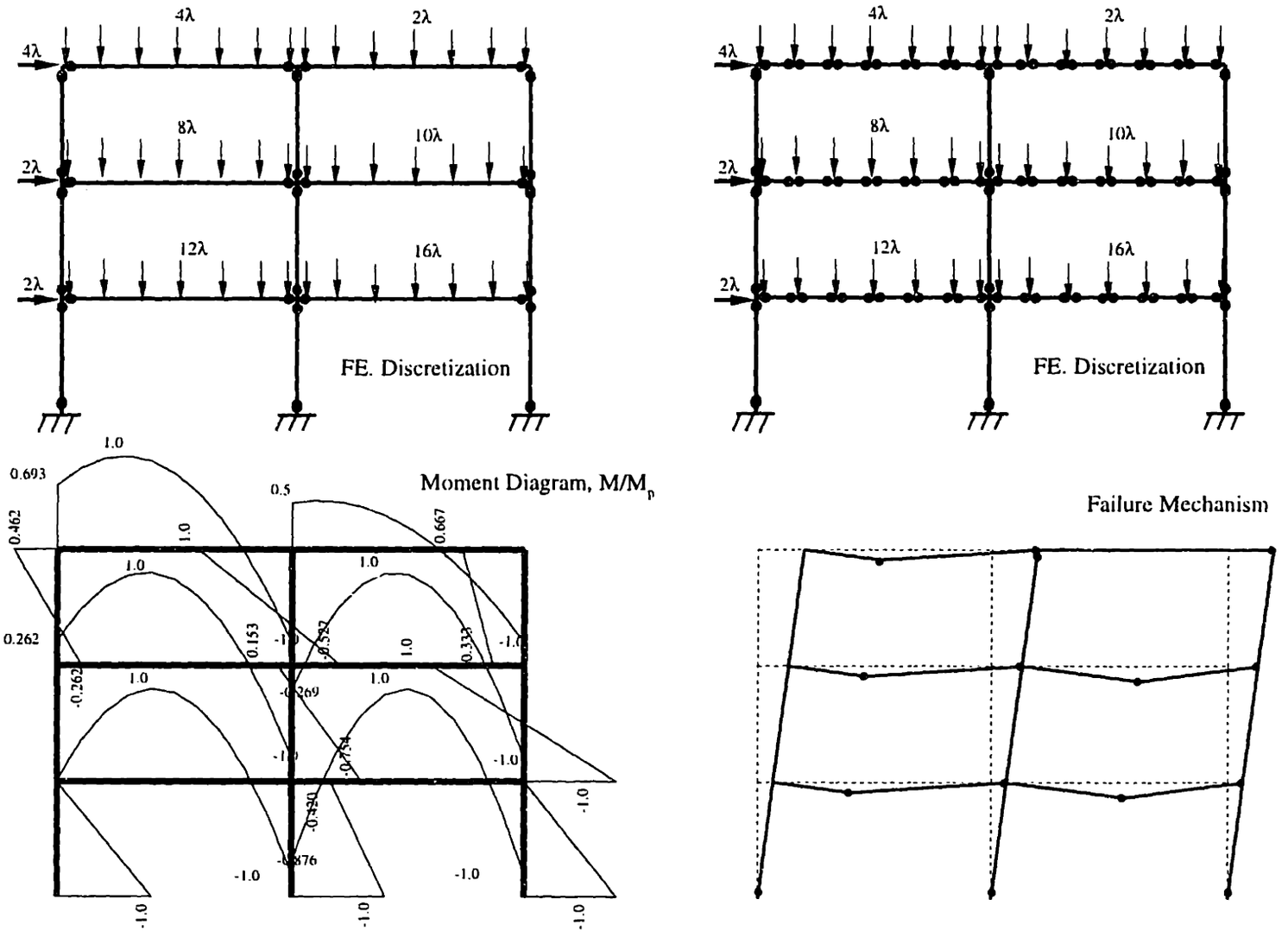

a) LB Analysis: $\lambda_{LB} = 1.938$

b) UB Analysis: $\lambda_{UB} = 1.949$

Figure 3.16 LB and UB results for an analysis of 4th example: 2-bay-3-story frame, $\lambda_{exact} = 1.940$)

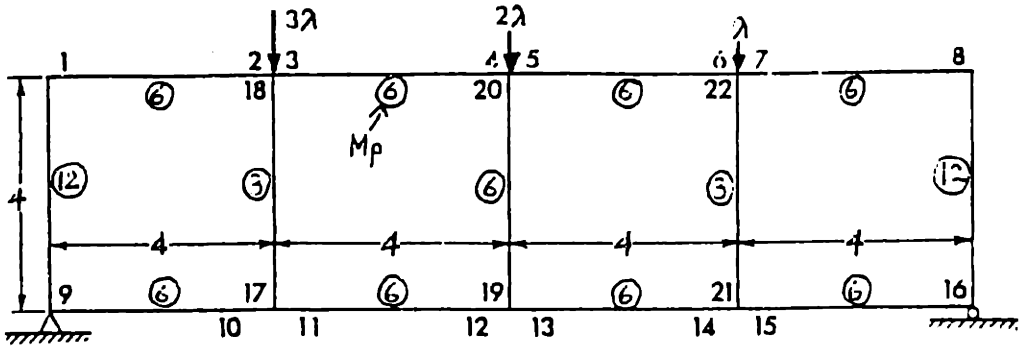

a) Problem Geometry

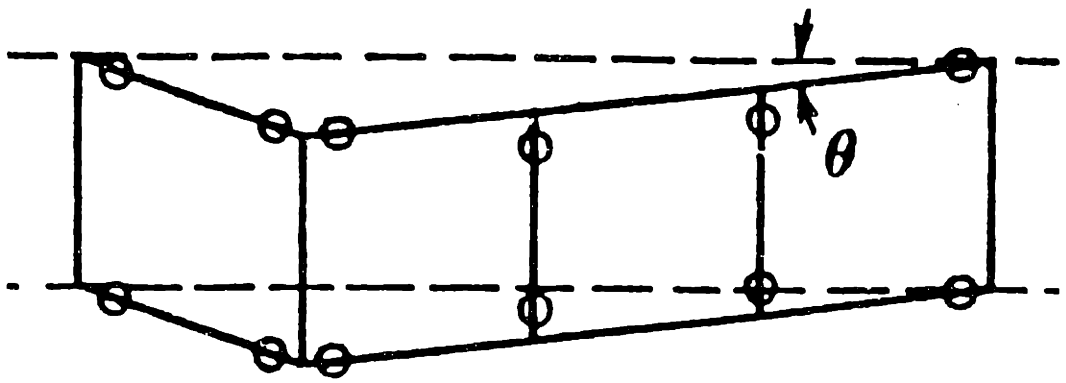

b) Collapse Mechanism, $\lambda_{exact} = 1.714$

Figure 3.17 5th Example: Veirendeel Truss (Hodge, 1959)

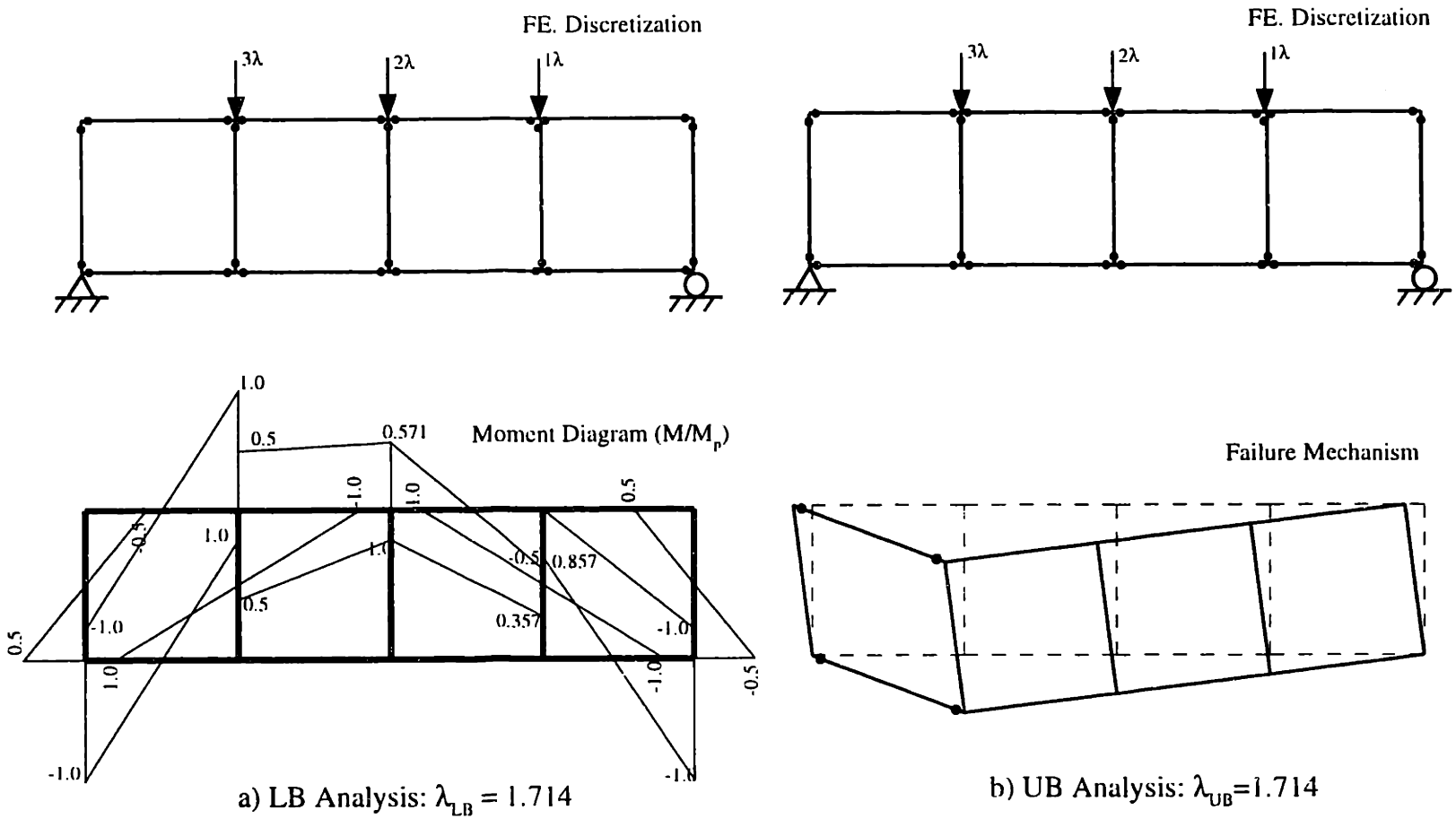

a) LB Analysis: $\lambda_{LB} = 1.714$

b) UB Analysis: $\lambda_{UB}=1.714$

Figure 3.18 LB and UB results for an analysis of 5th example: Veirendeel truss, $\lambda_{exact} = 1.714$

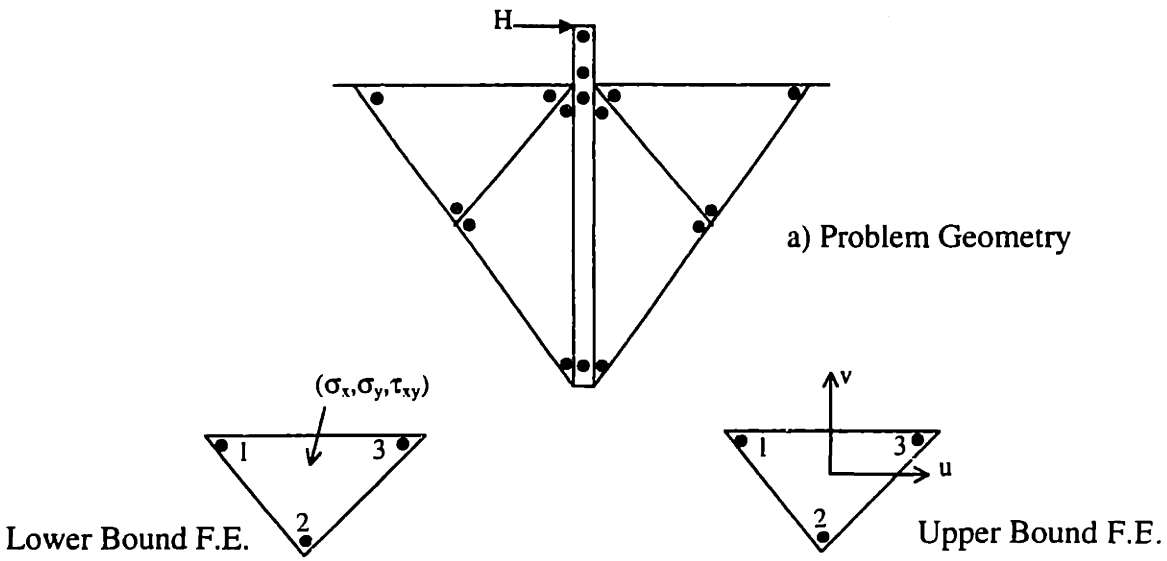

b) Plane strain elements of limit analyses

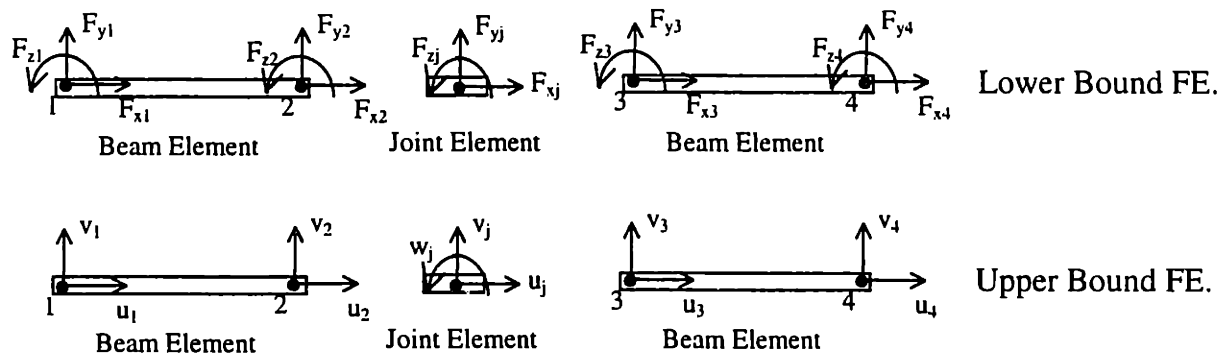

c) Structural element of limit analyses

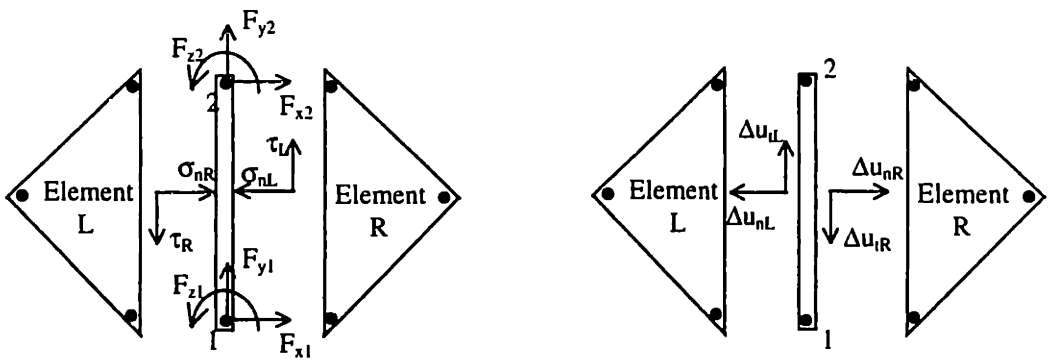

d) Modeling for soil-structure interfaces

Figure 3.19 Summary of numerical limit analyses for plain strain and structural elements

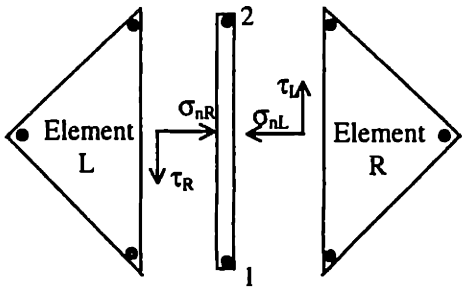

Interface for lower bound method

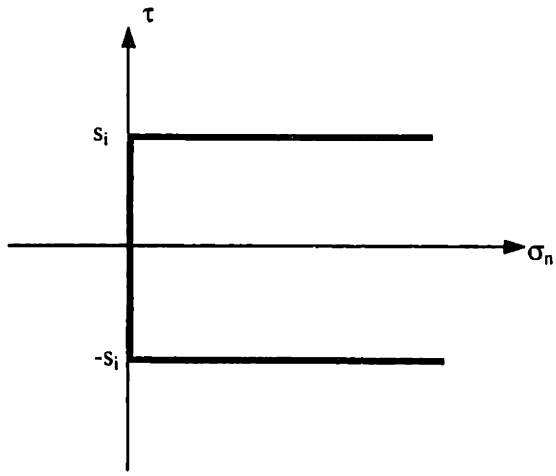

Modified Tresca yield criterion
with tension cutoff

a) Lower bound modeling of separation

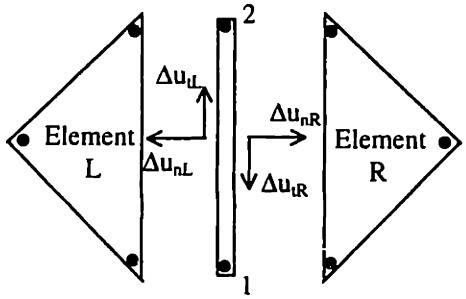

Interface for upper bound method

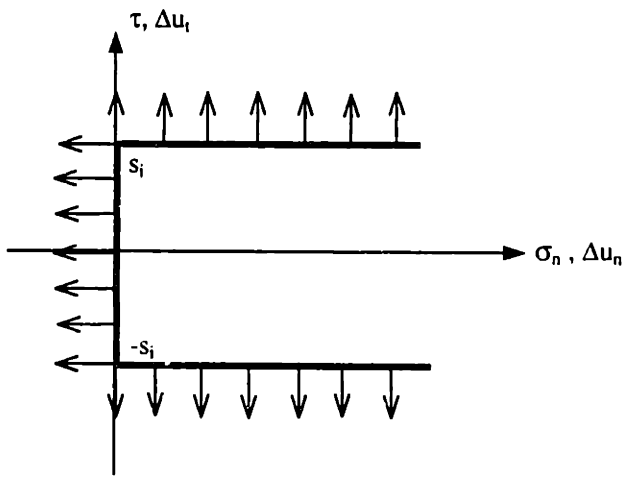

Associated plastic flow direction of
modified Tresca yield criterion
with tension cut-off

b) Upper bound modeling of separation

Figure 3.20 Lower and upper bound modeling for separation of soil-structure interfaces

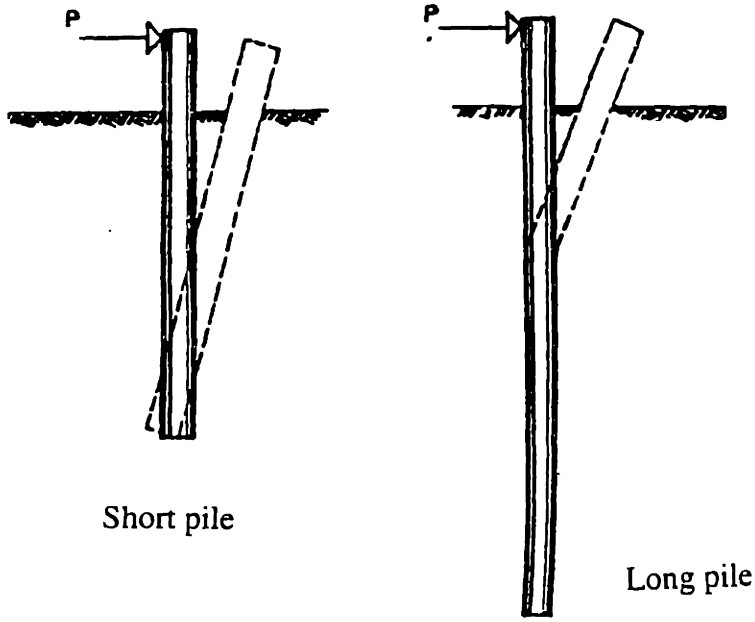

a) Free head pile

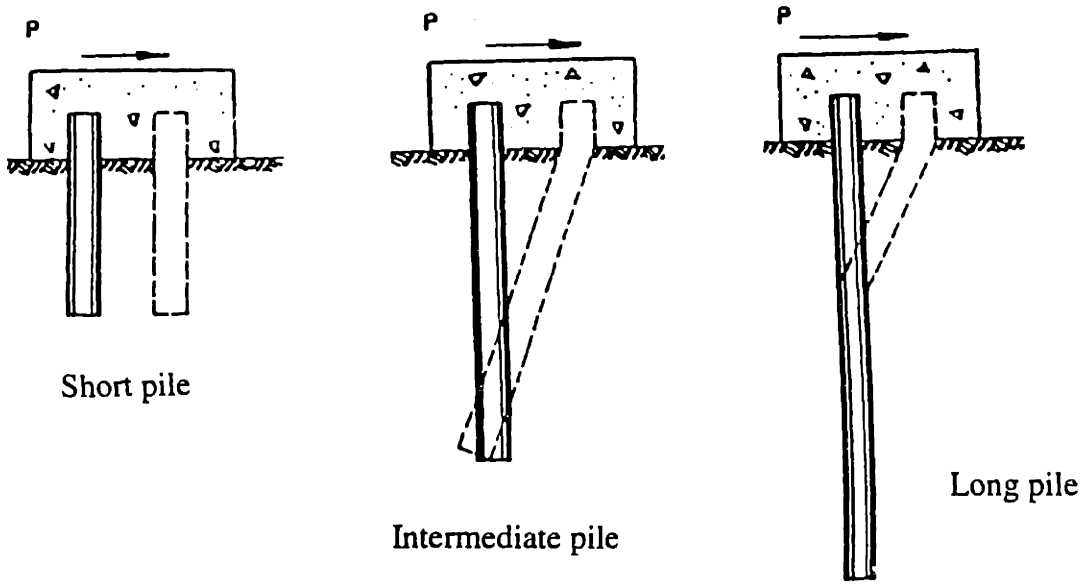

b) Fixed head pile

Figure 3.21 Failure mechanisms of free head and fixed head piles in clay (after Broms, 1964)

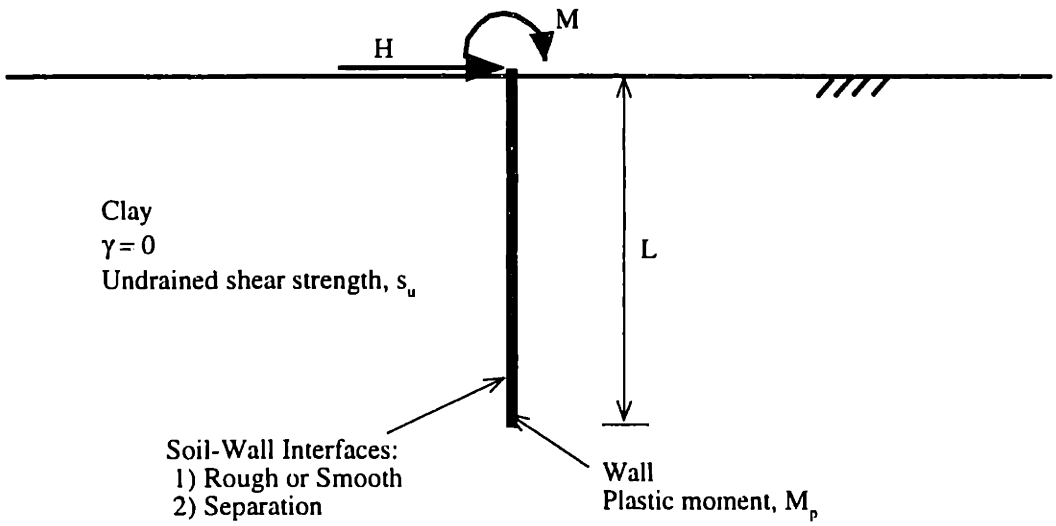

a) Problem geometry and positive sign convention

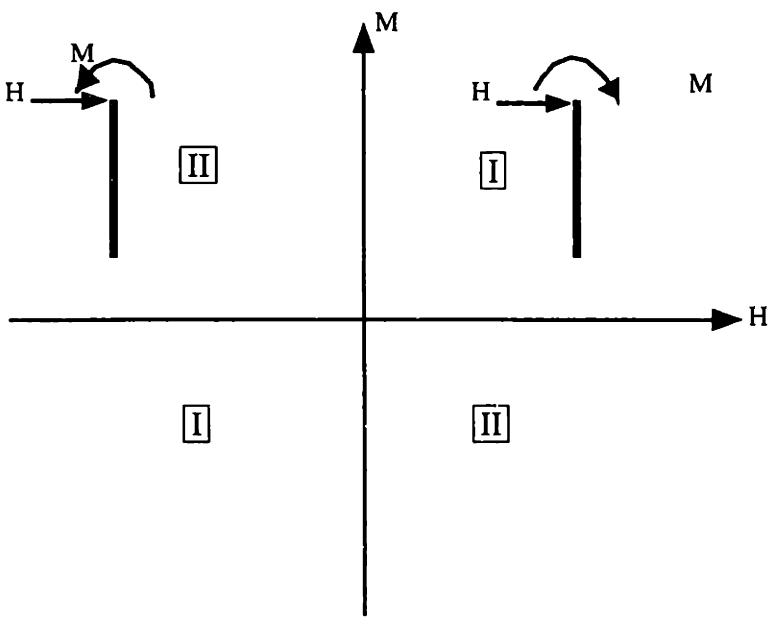

b) Mode of loading

Figure 3.22 Problem notation of laterally loaded free head walls

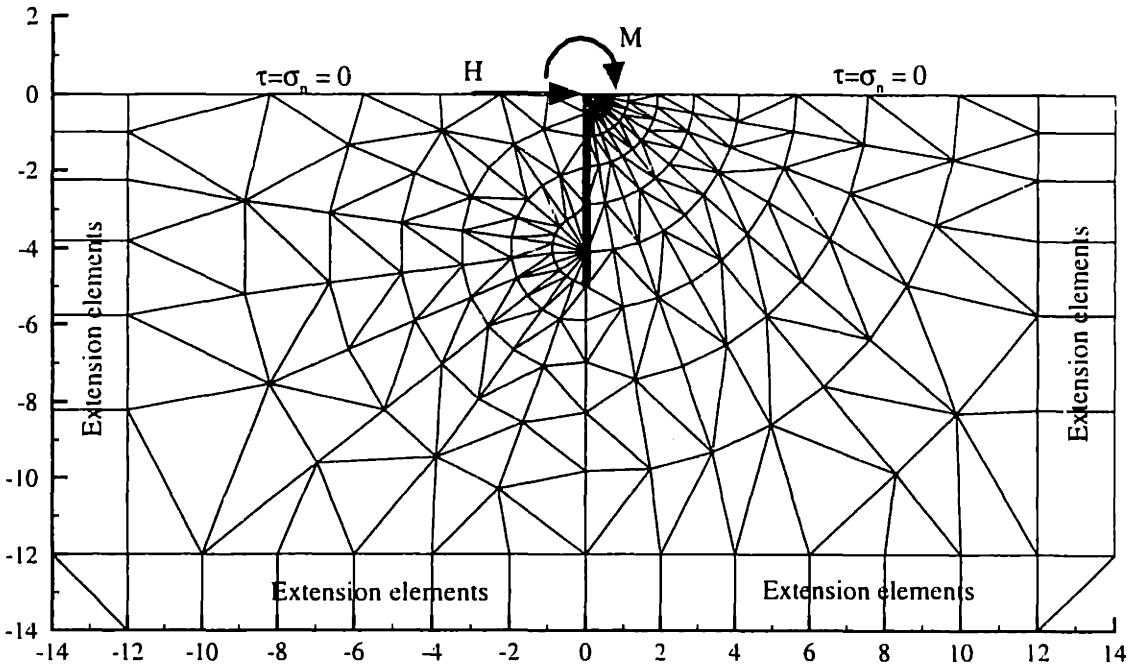

a) Lower bound mesh

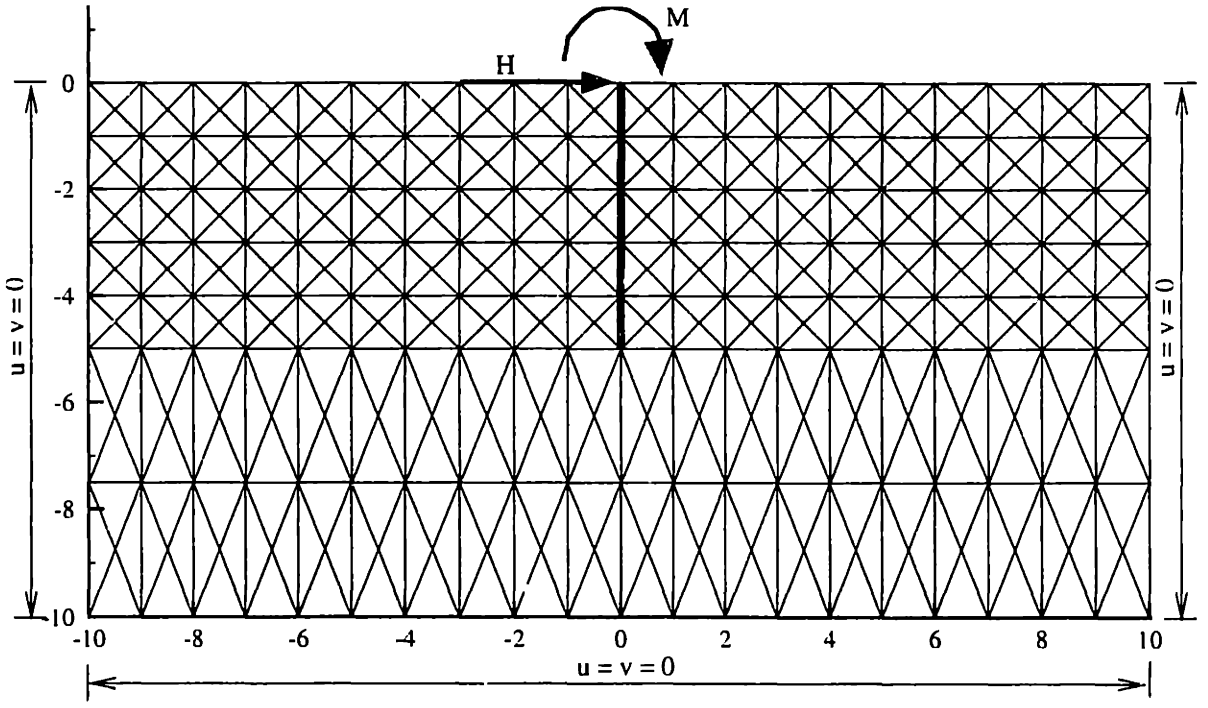

b) Upper bound mesh

Figure 3.23 Lower and upper bound meshes used for analyses of laterally loaded walls

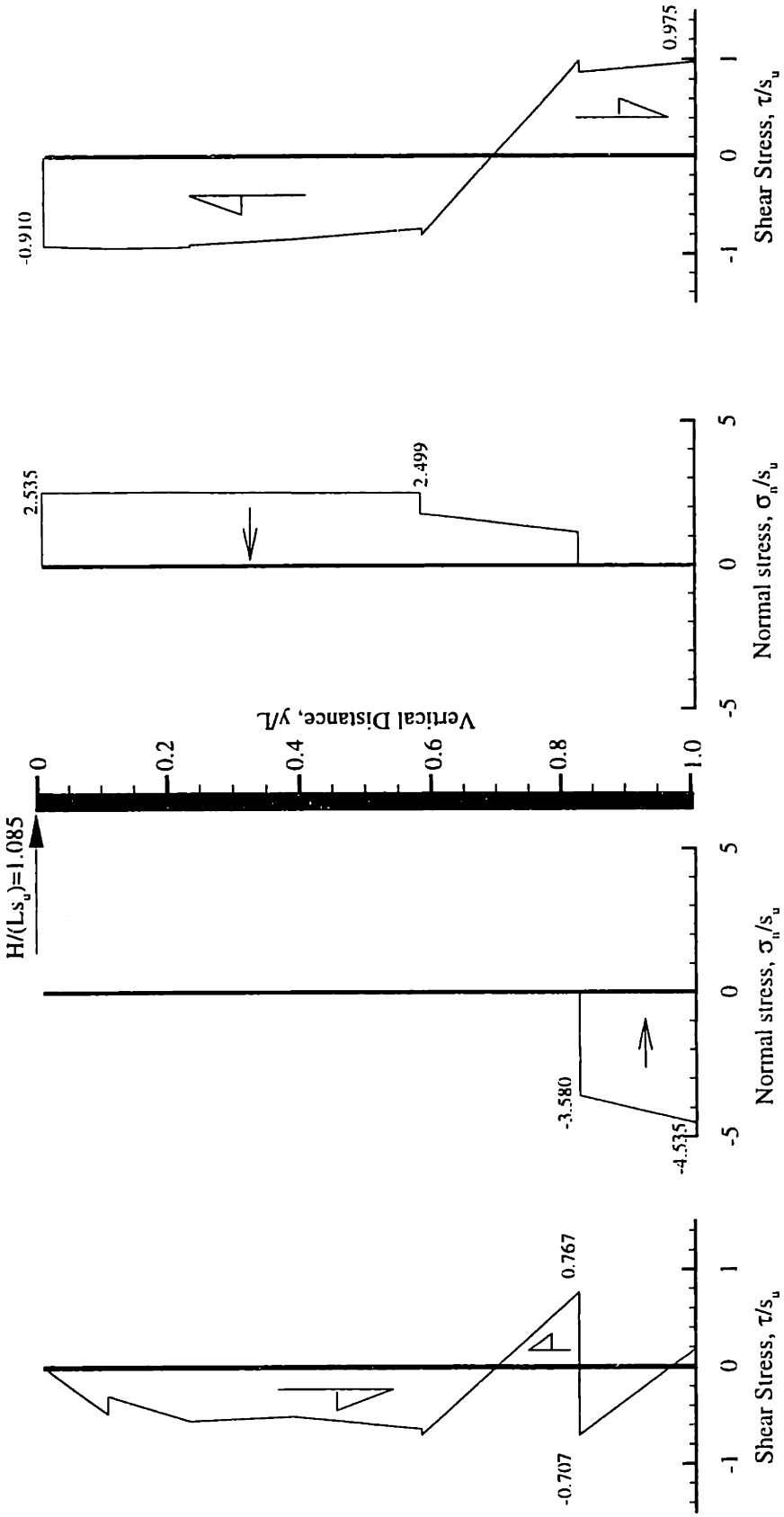

Figure 3.24 Contact stresses on a free head wall, where $M_p/(s_u L^2) = 1.0$

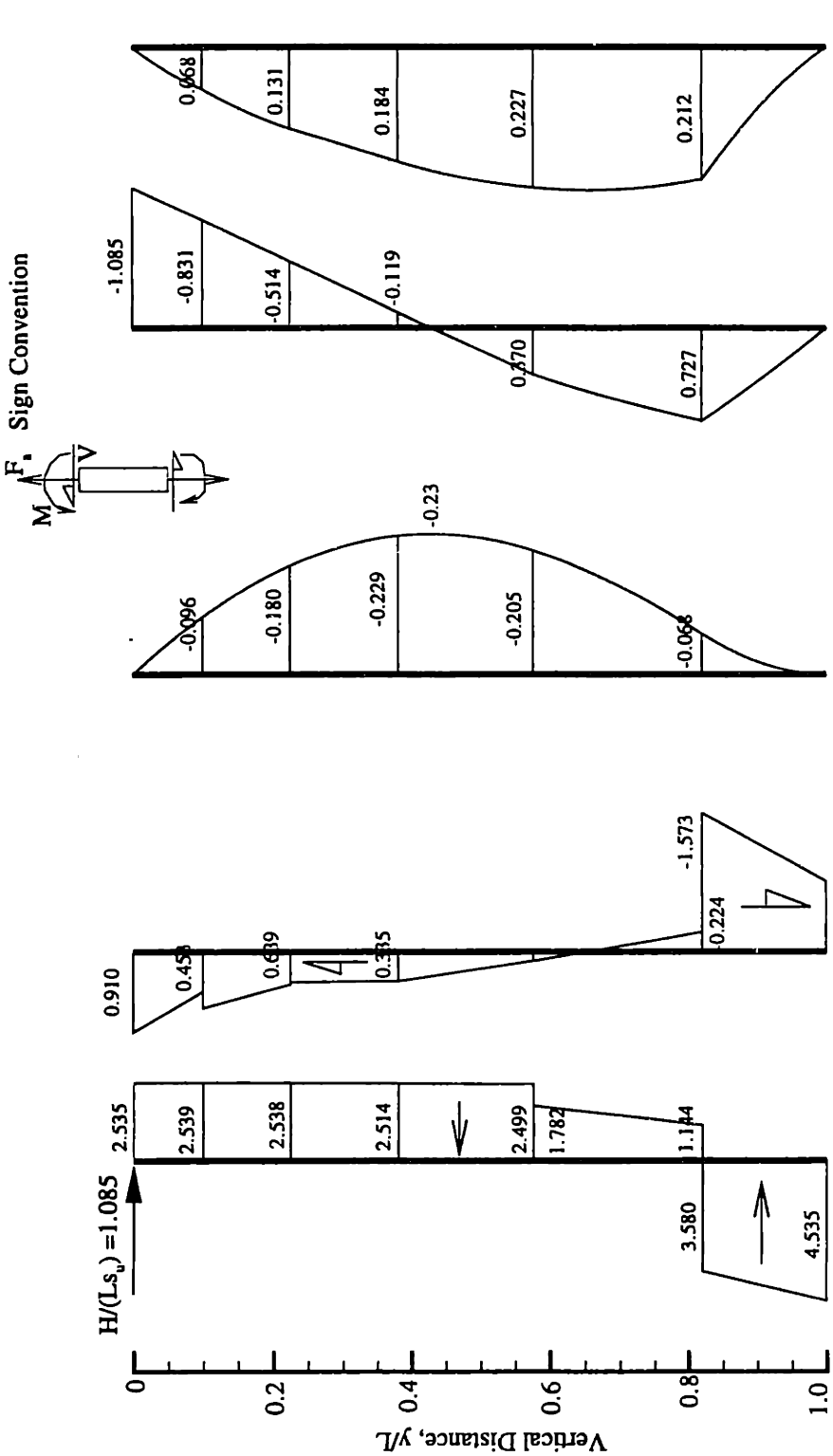

Figure 3.25 Net tractions and force diagram for a free head wall, where $M_p(s_uL^2) = 1.0$

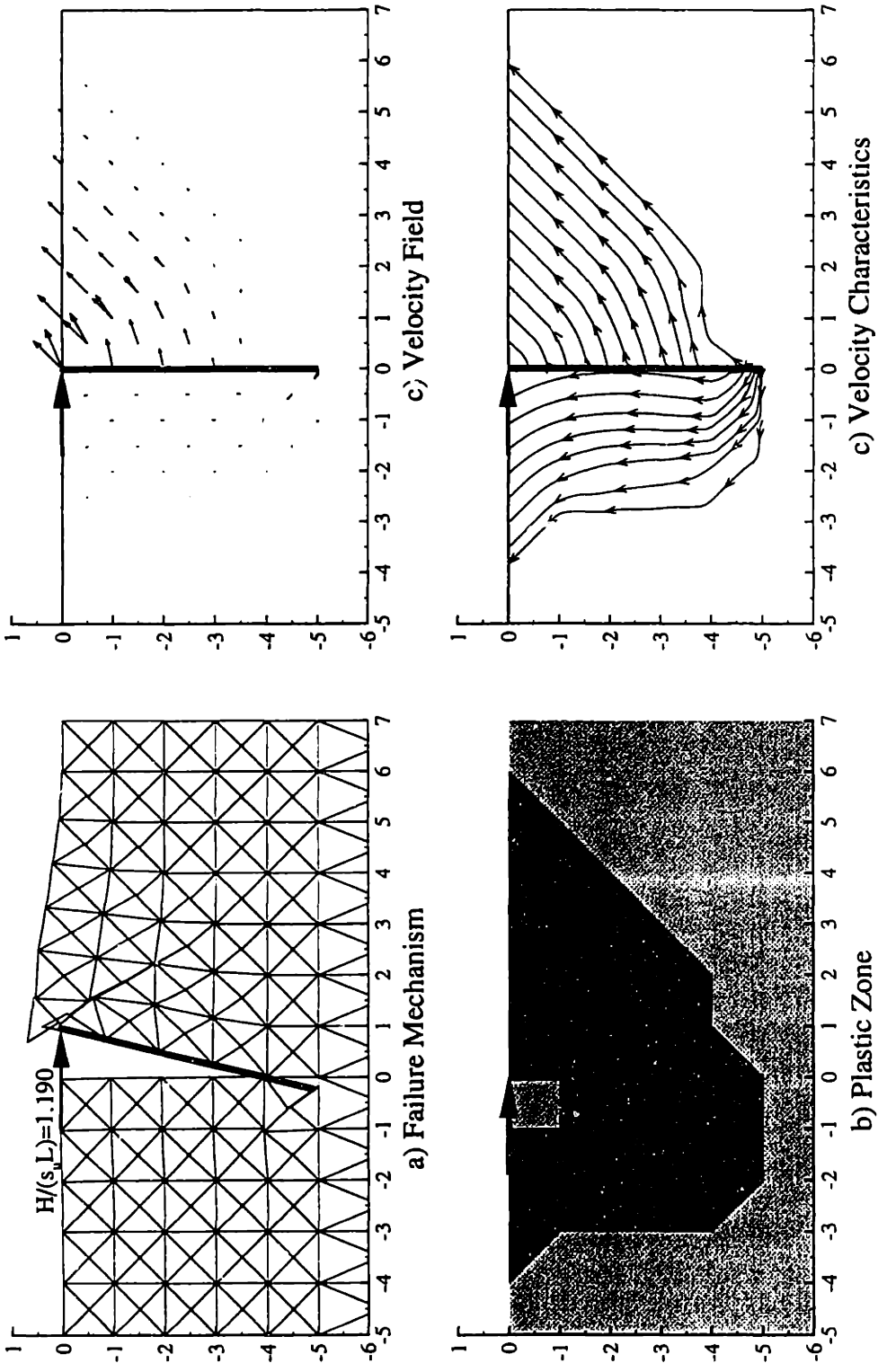

Figure 3.26 Upper bound results of a free head wall, where $M_p/(s_u L^2) = 1.0$

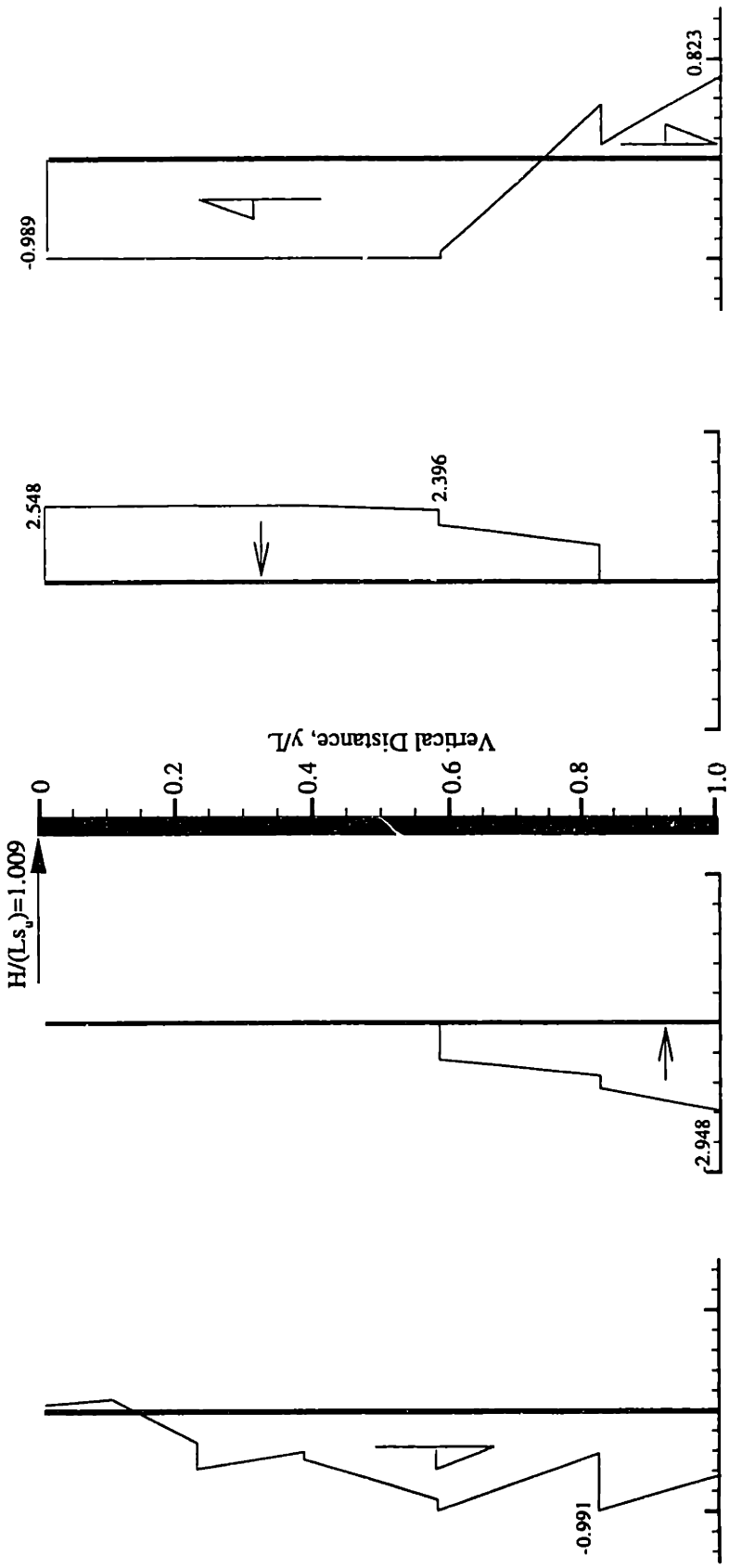

Contact Stresses on the left side

Contact Stresses on the right side

Figure 3.27 Contact stresses on a free head wall, where $M_p/(s_u L^2) = 0.2$

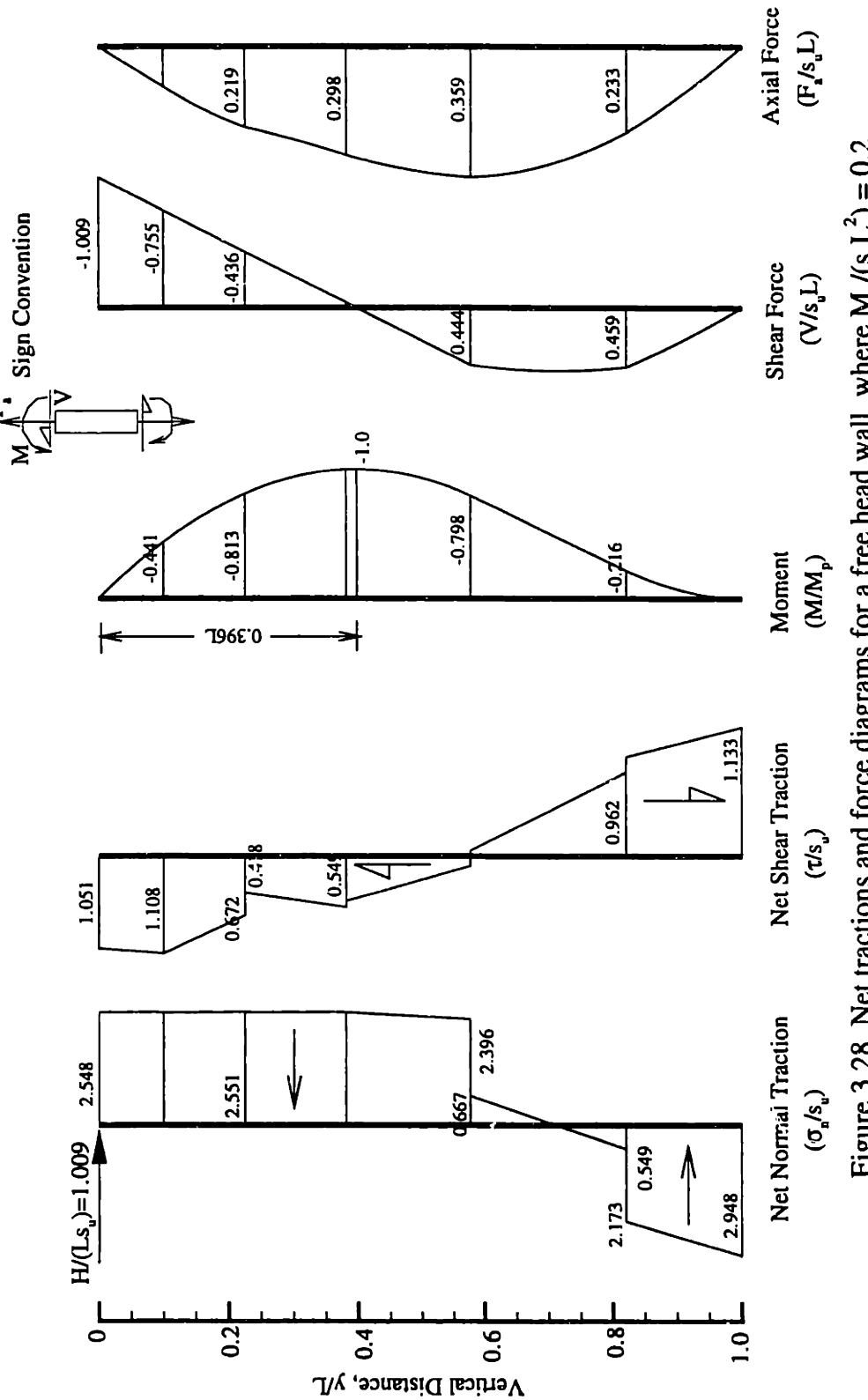

Figure 3.28 Net tractions and force diagrams for a free head wall, where $M_p/(s_u L^2) = 0.2$

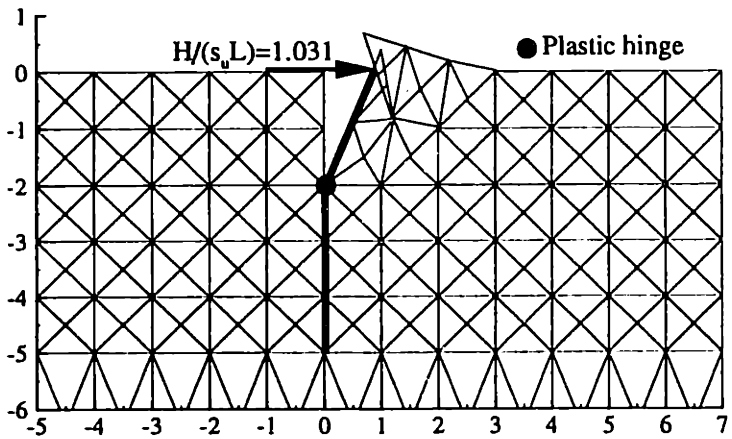

a) Failure Mechanism

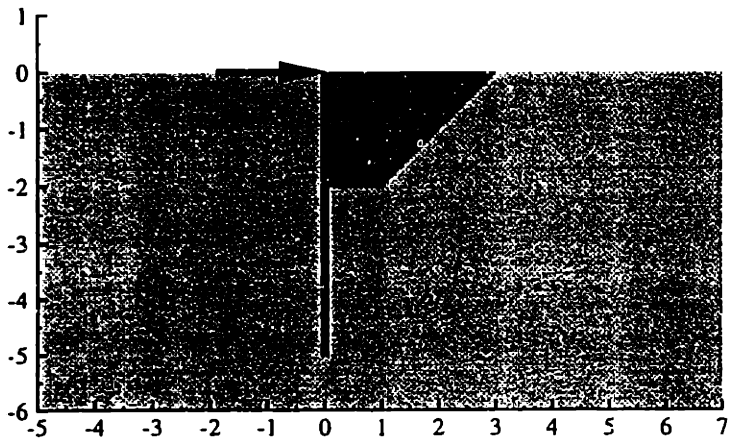

b) Plastic Zone

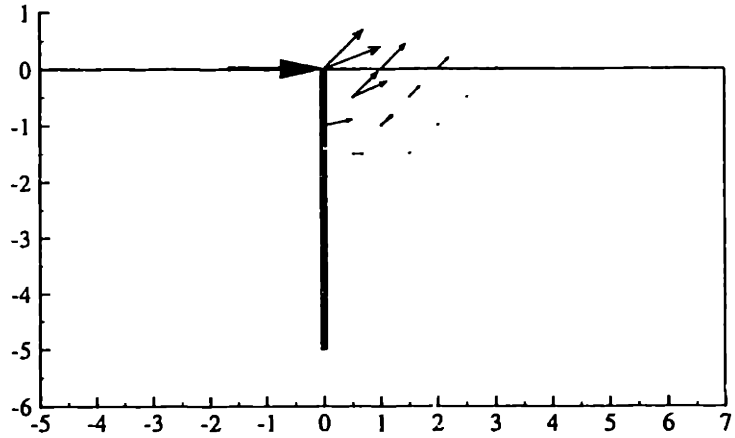

c) Velocity Field

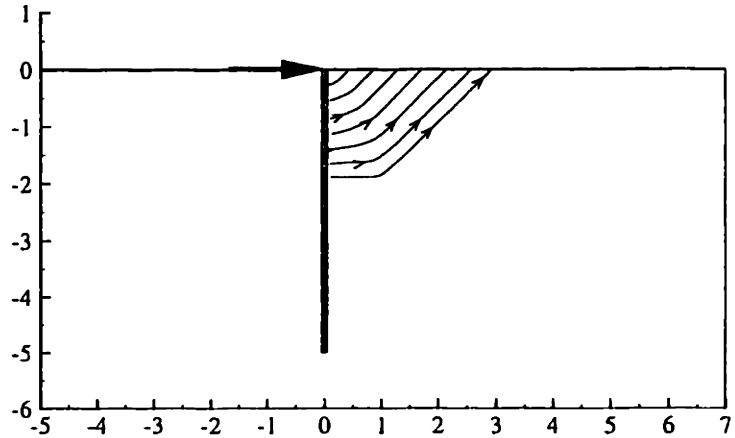

c) Velocity Characteristics

Figure 3.29 Upper bound results of a free head wall, where $M_p(s_uL^2) = 0.2$

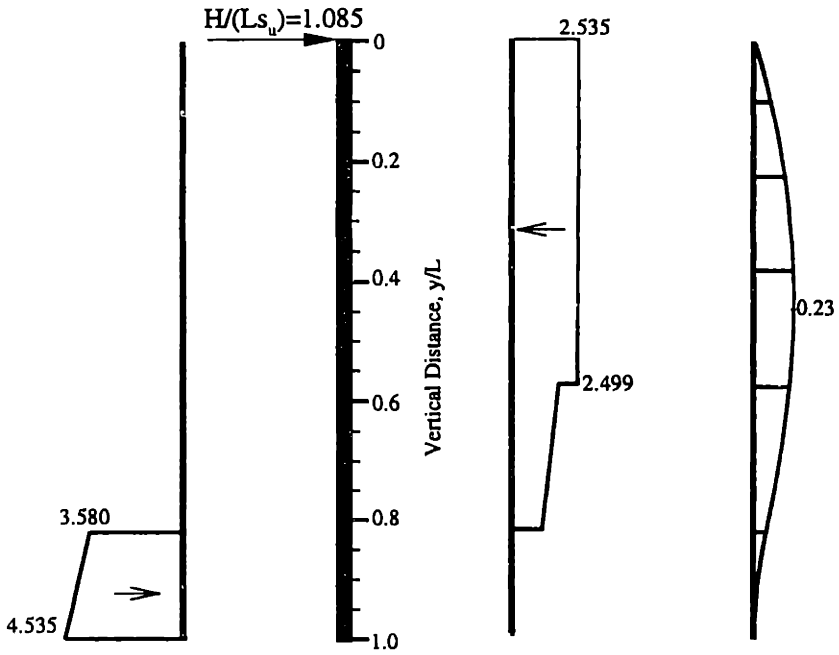

a) $M_p/(s_uL^2) = 1.0$

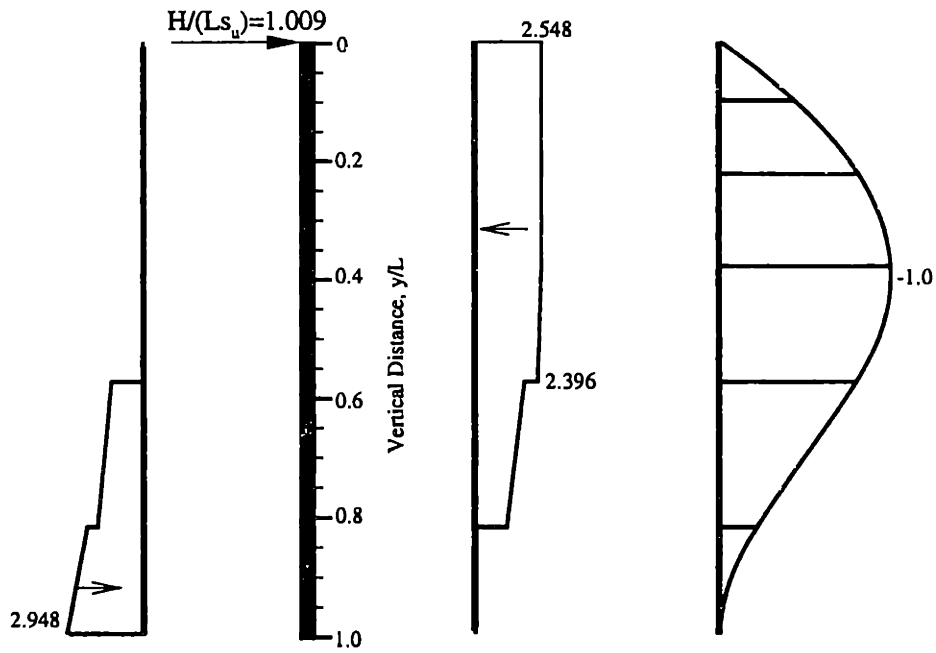

b) $M_p/(s_uL^2) = 0.2$

Figure 3.30 Comparisons of contact pressure and moment diagram from LB analyses of free head walls at two strength parameters, $M_p/(s_uL^2)$

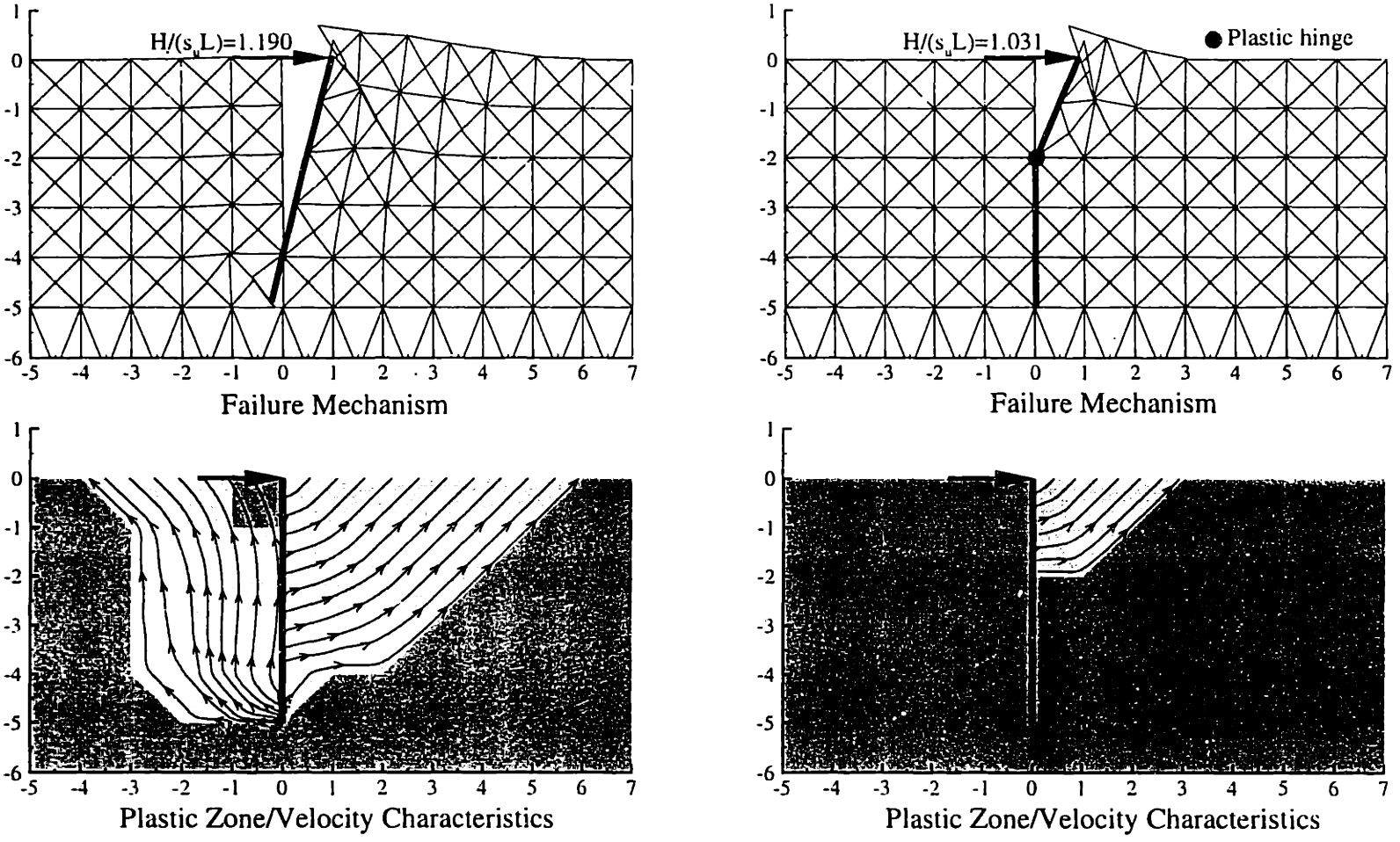

a) $M_p/(s_uL^2) = 1.0$

b) $M_p/(s_uL^2) = 0.2$

Figure 3.31 Comparisons of upper bound results of free head walls at two strength parameters, $M_p/(s_uL^2)$

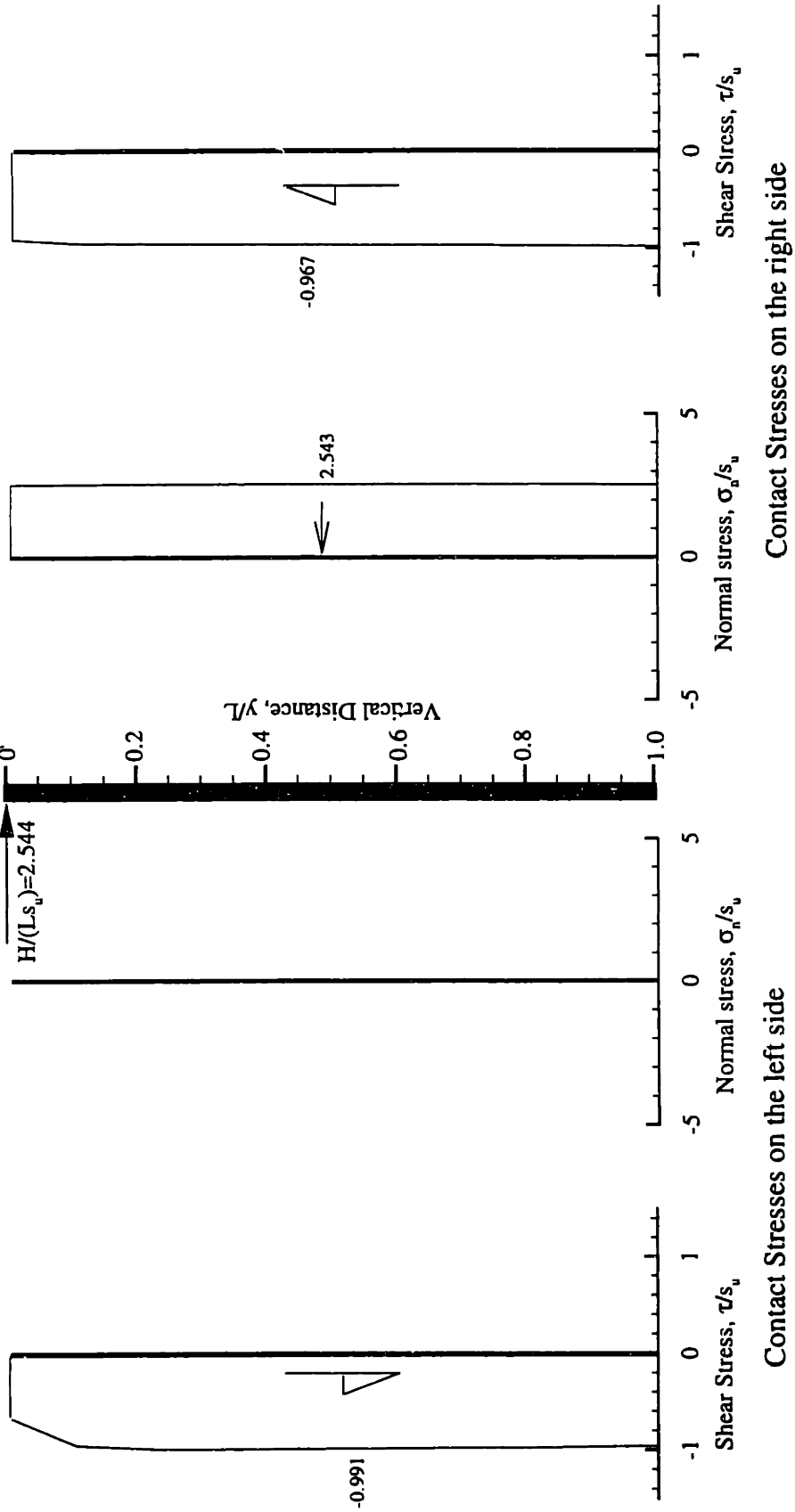

Figure 3.32 Contact stresses on a fixed head wall, where $M_p/(s_u L^2) = 3.33$

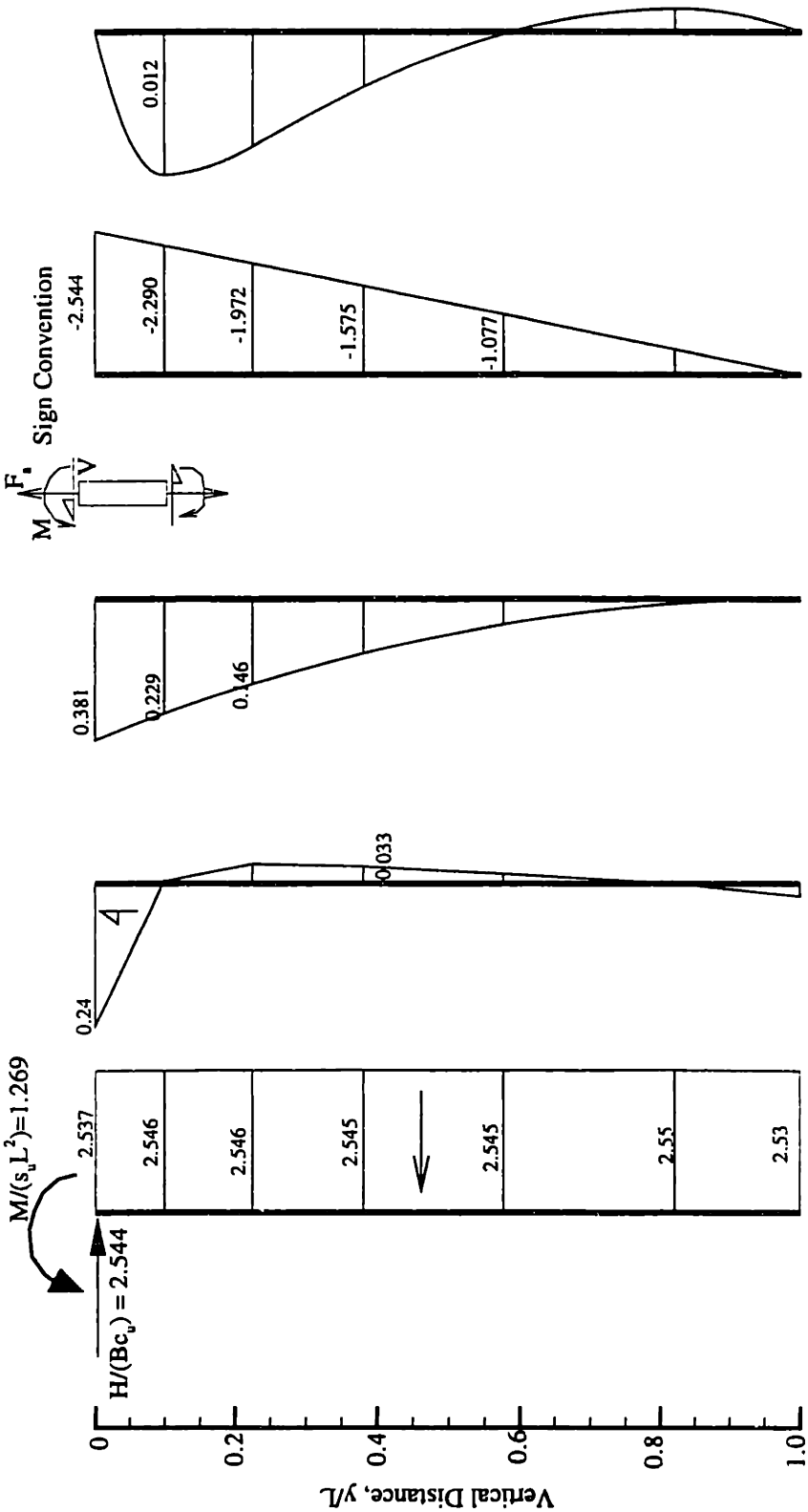

Figure 3.33 Net tractions and force diagram for a fixed head wall, where $M_p/(s_uL^2) = 3.33$

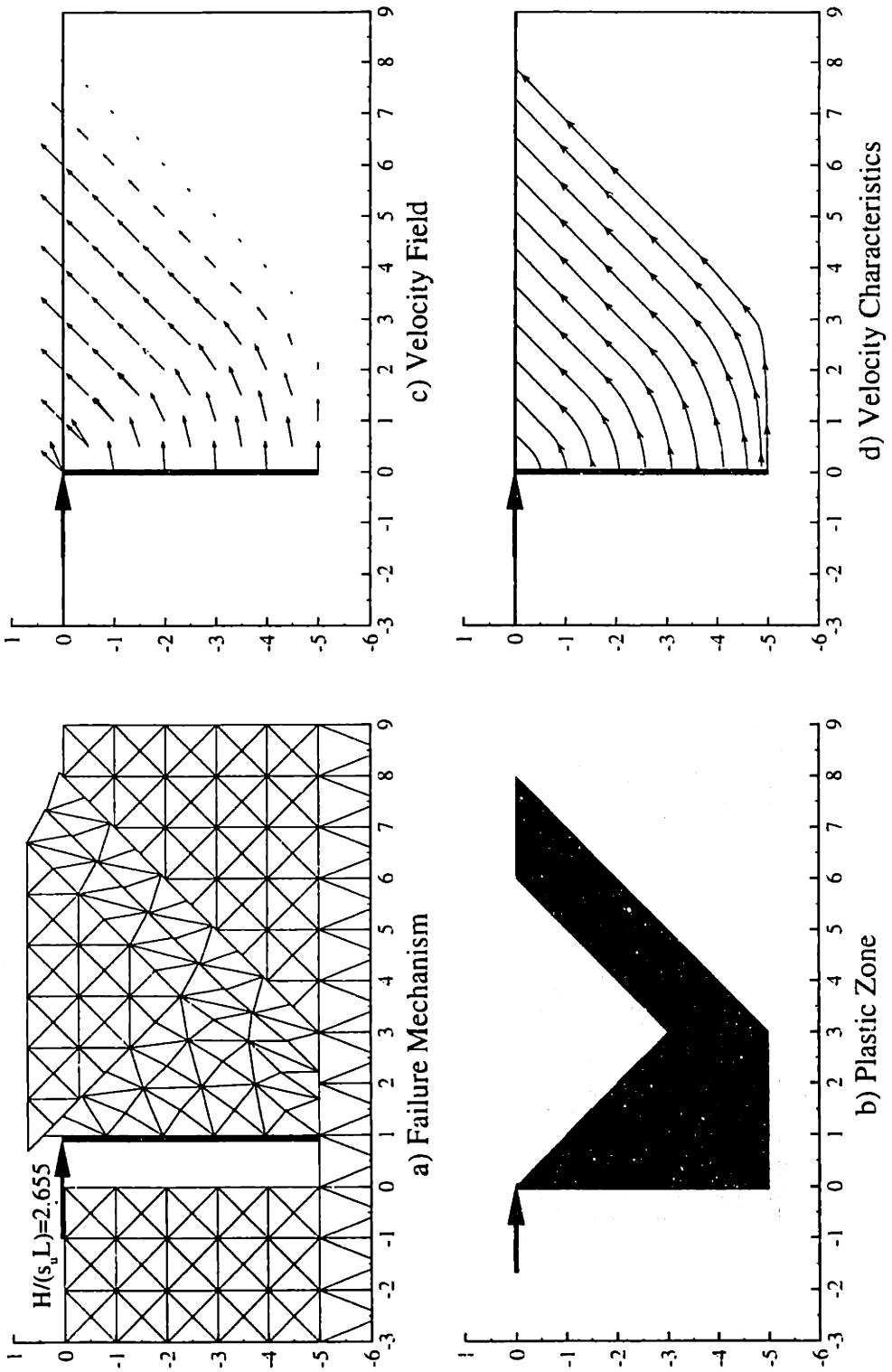

Figure 3.34 Upper bound results of a fixed head wall, where $M_p/(s_u L^2) = 3.33$

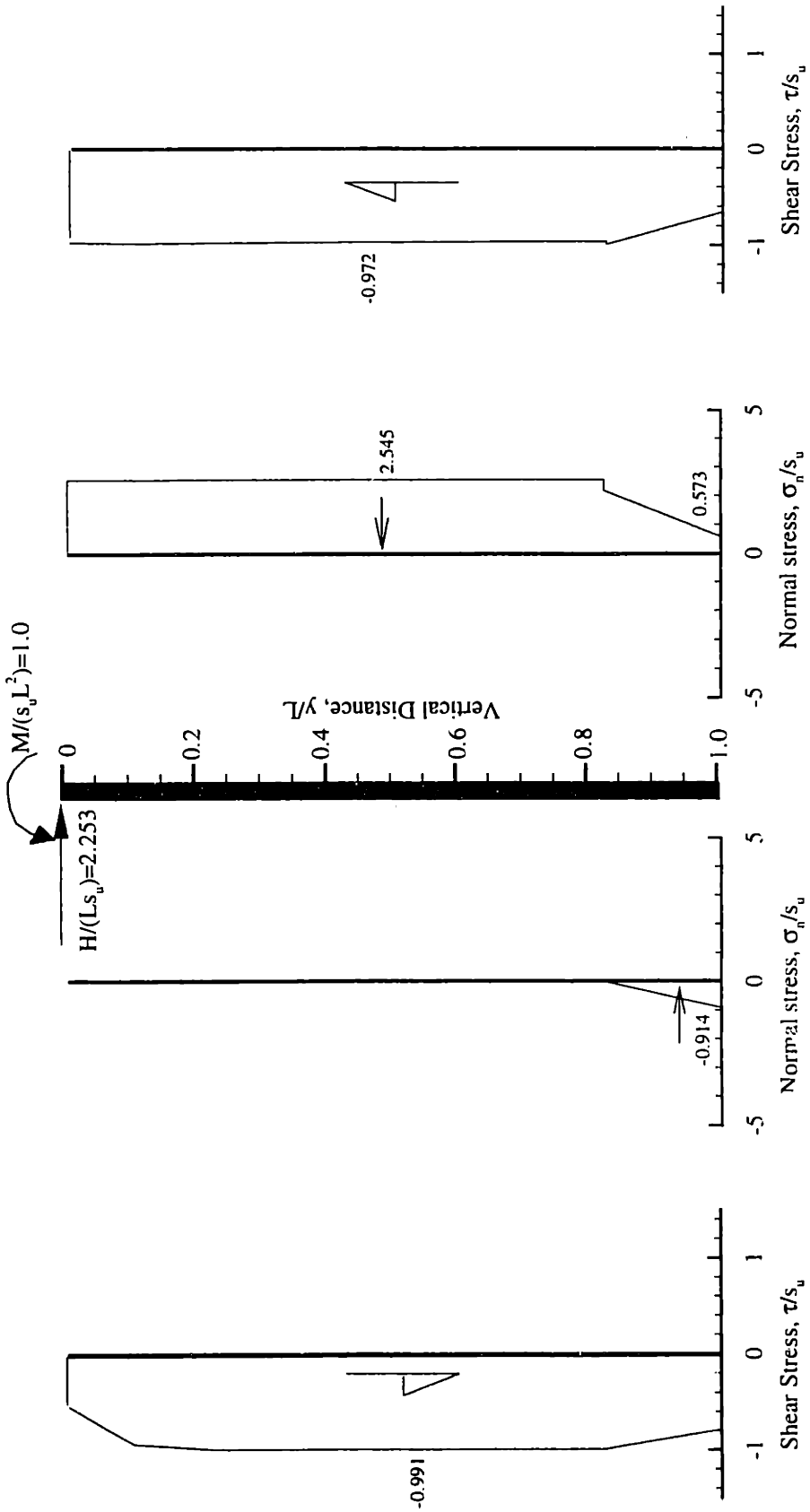

Contact Stresses on the left side

Contact Stresses on the right side

Figure 3.35 Contact stresses on a fixed head wall, where $M_p/(s_uL^2) = 1.0$

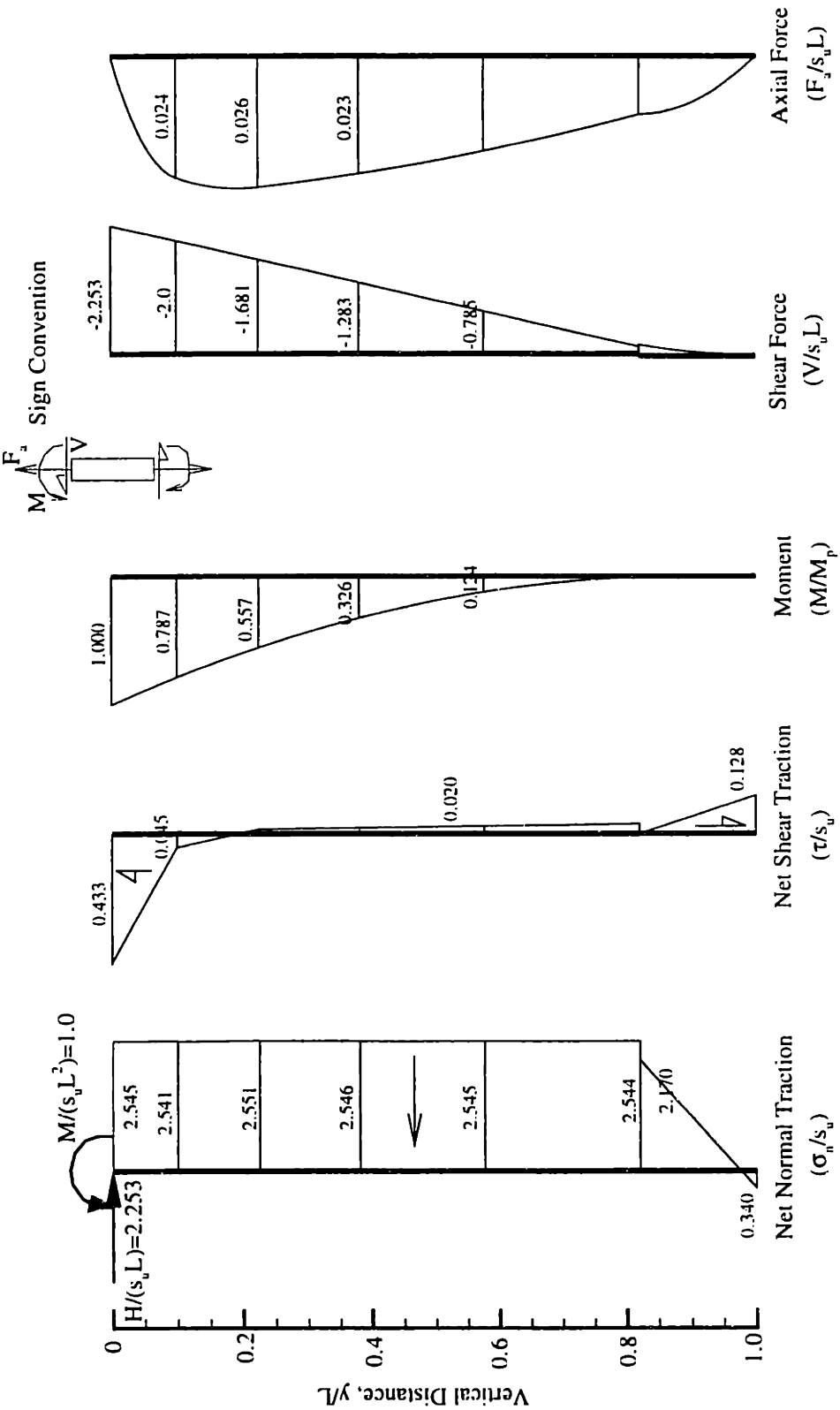

Figure 3.36 Net tractions and forces diagrams for a fixed head wall, where $M_p/(s_u L^2) = 1.0$

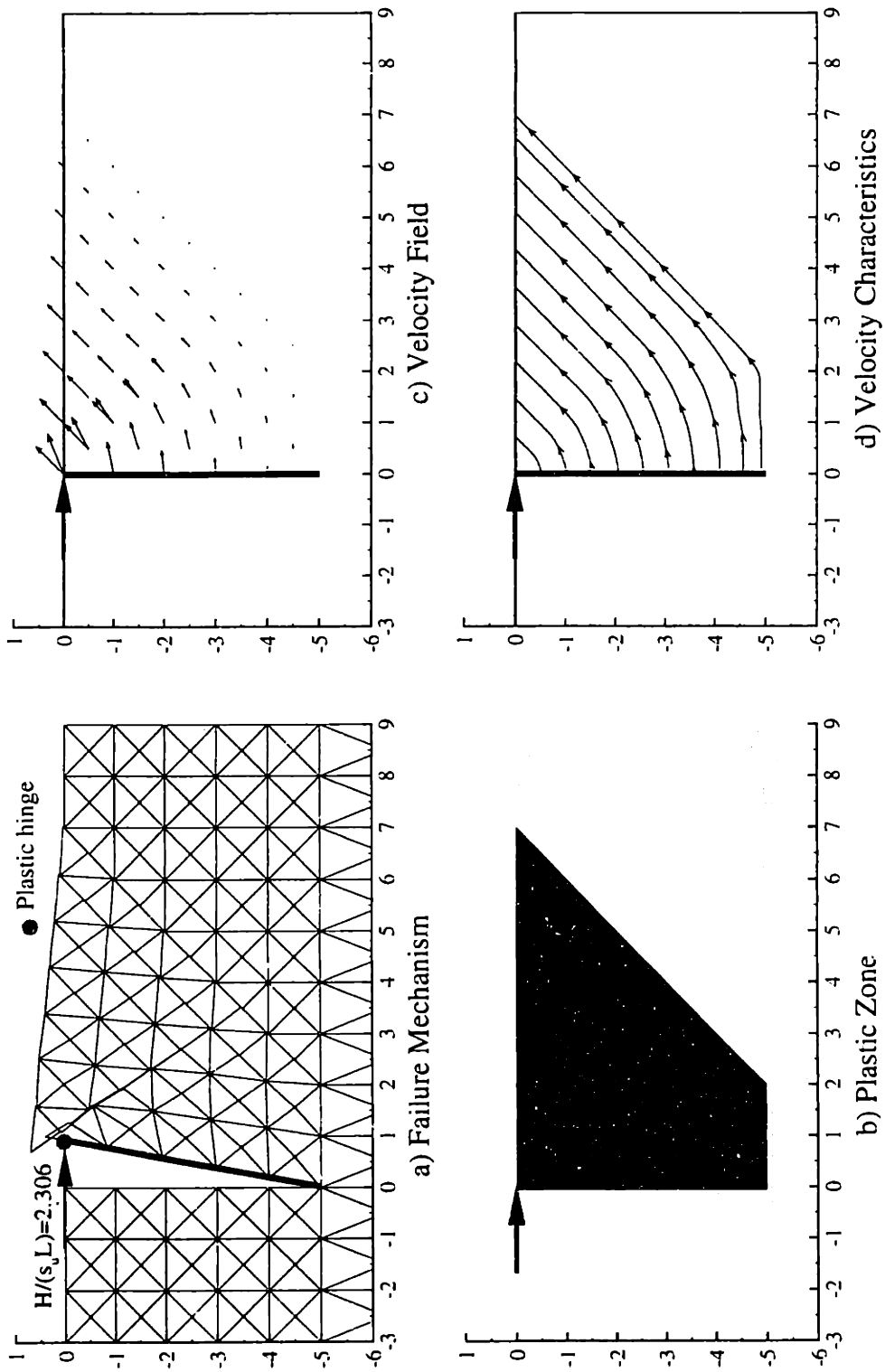

Figure 3.37 Upper bound results of a fixed head wall, where $M_p/(s_u L^2) = 1.0$

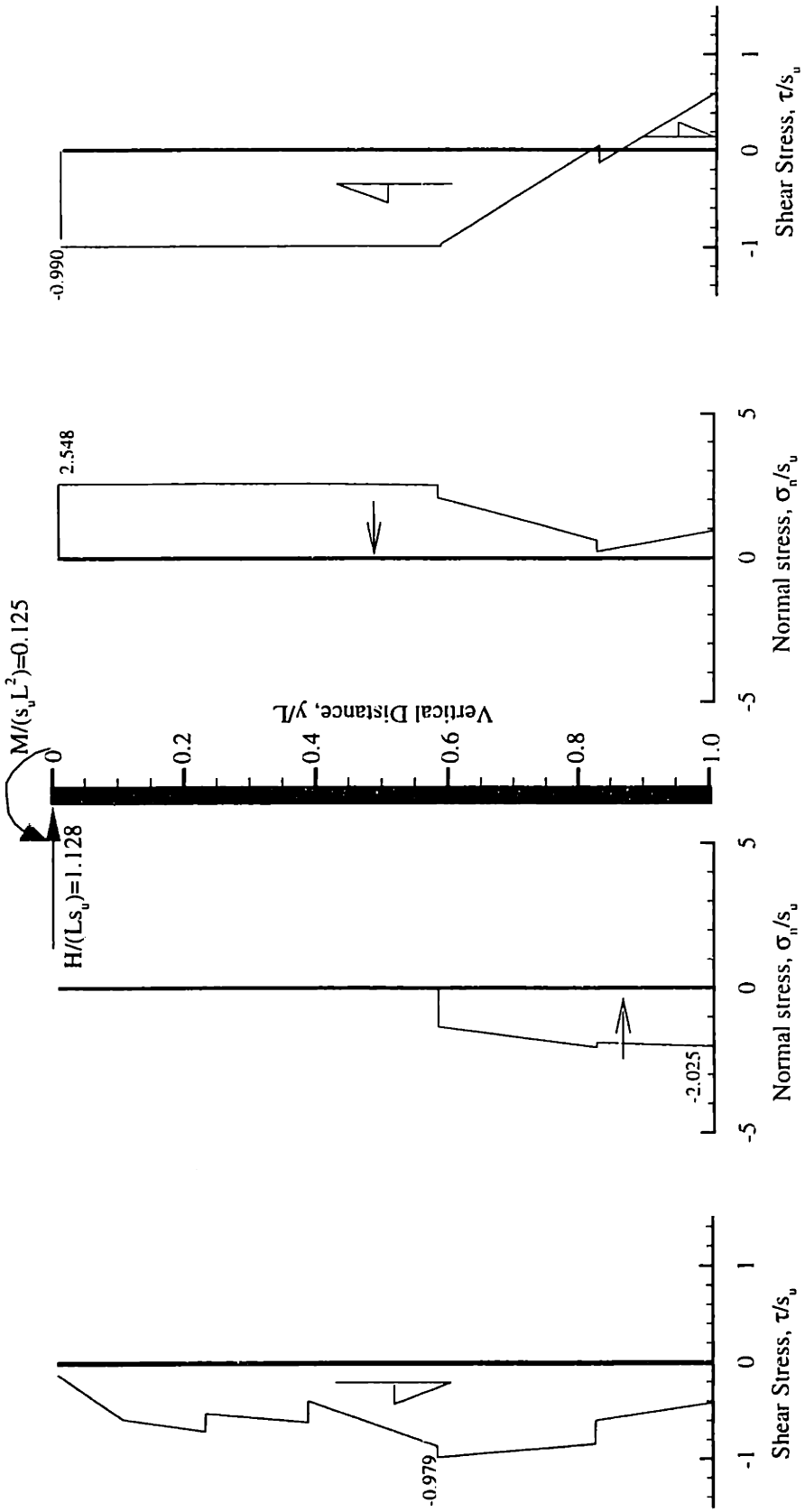

Contact Stresses on the left side

Contact Stresses on the right side

Figure 3.38 Contact stresses on a fixed head wall, where $M_p/(s_u L^2) = 0.125$

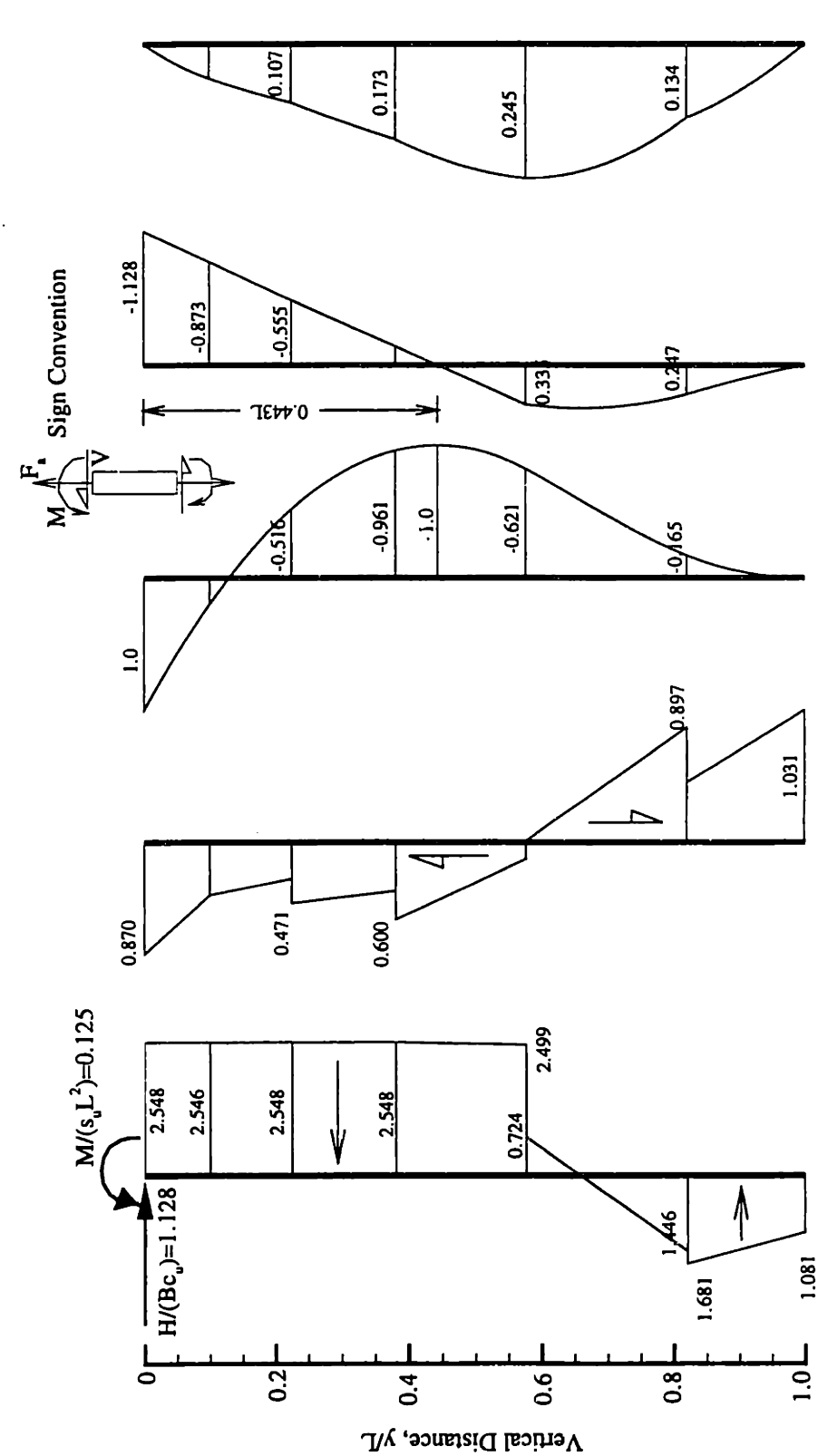

Figure 3.39 Net tractions and force diagram for a fixed head wall, where $M_p/(s_u L^2) = 0.125$

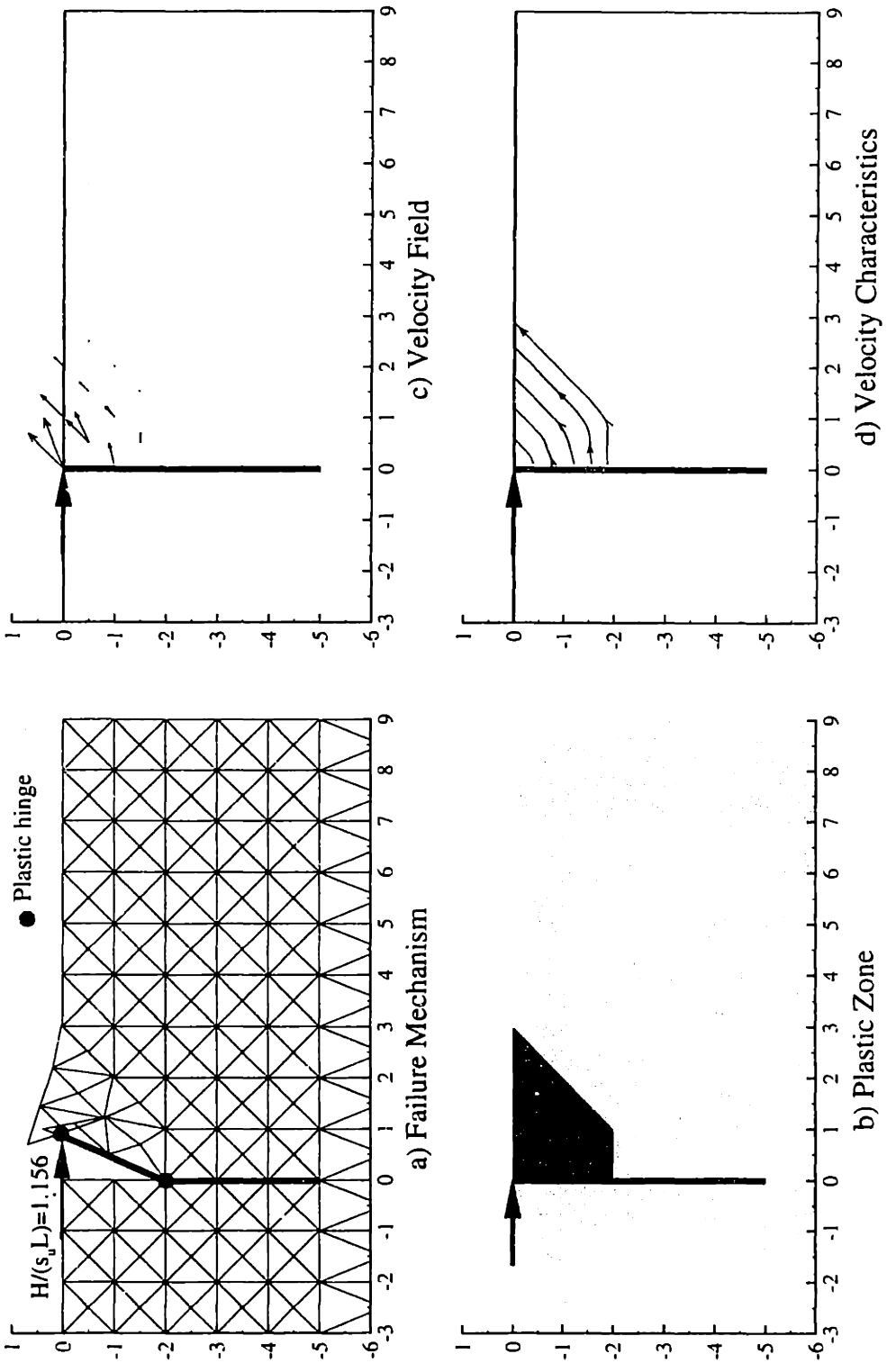

Figure 3.40 Upper bound results of a fixed head wall, where $M_p/(s_uL^2) = 0.125$

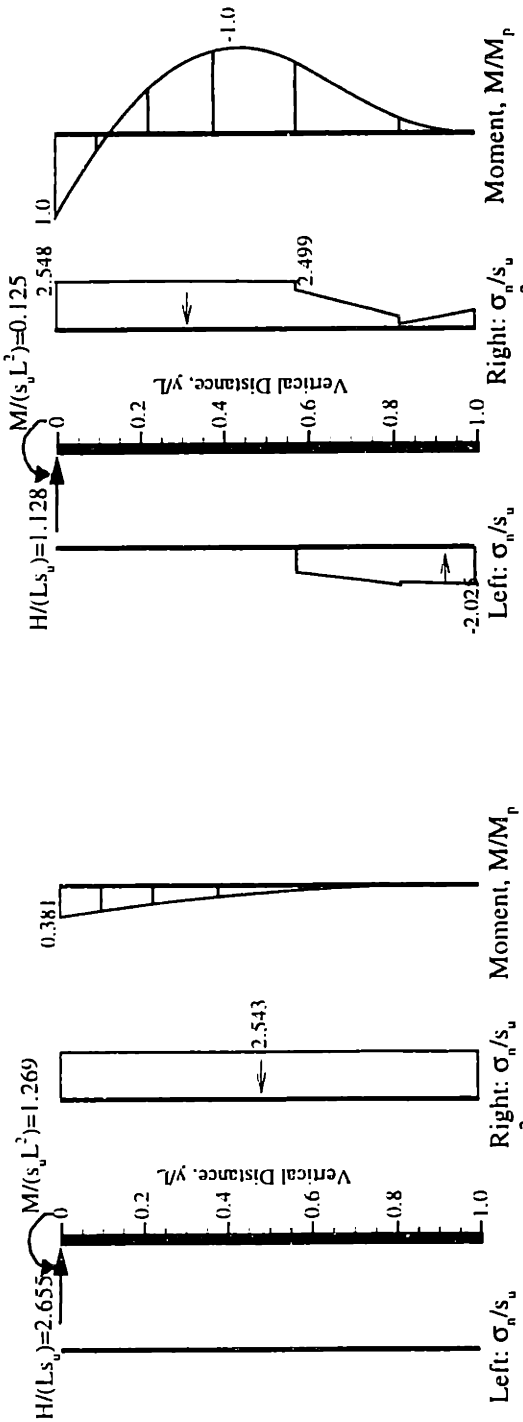

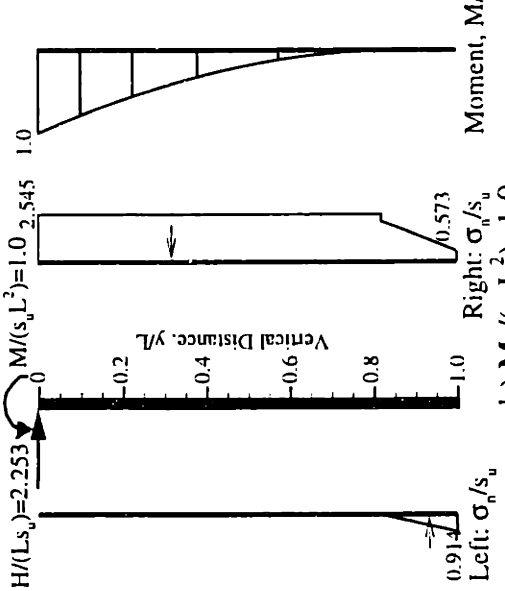

Figure 3.41 Comparisons of contact pressure and moment diagram from LB analyses of fixed head walls at three strength parameters, $M_p/(s_uL^2)$

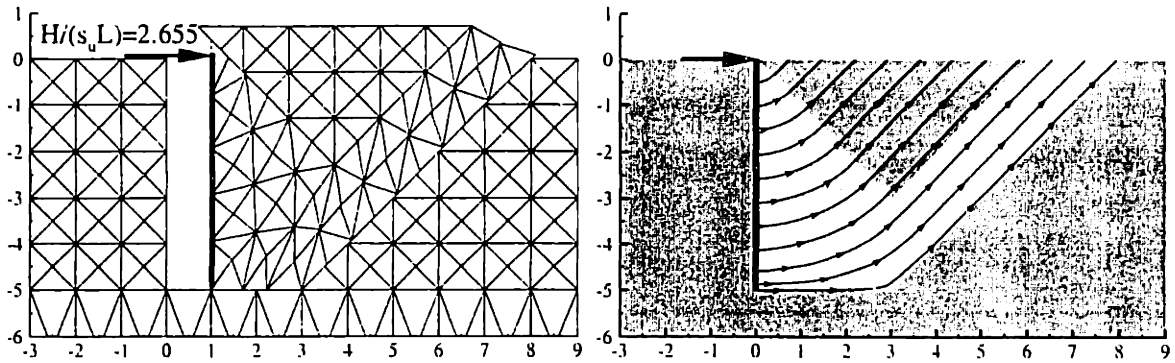

a) $M_p/(s_uL^2) = 3.33$

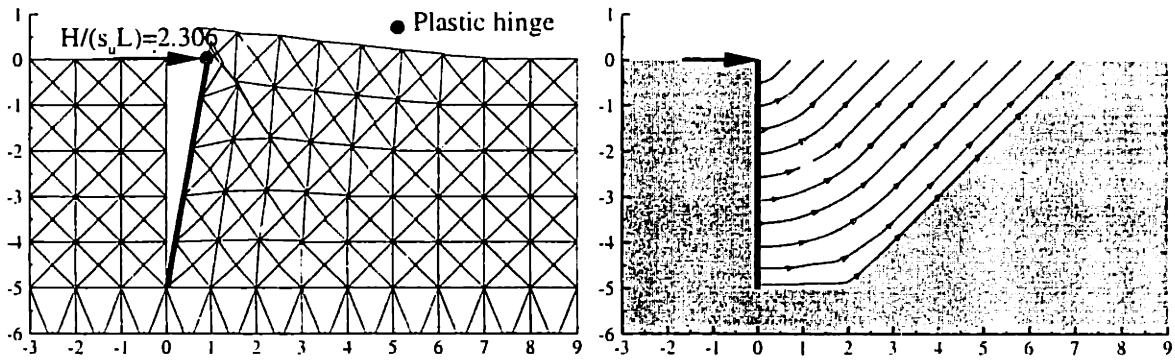

b) $M_p/(s_uL^2) = 1.0$

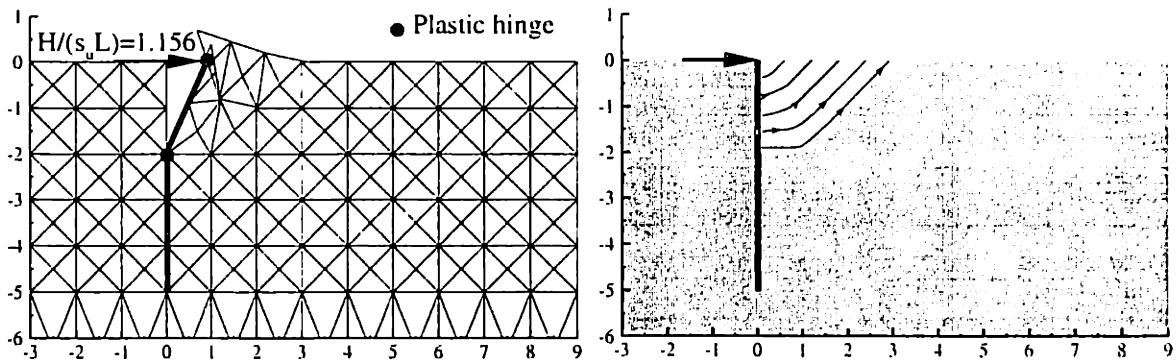

c) $M_p/(s_uL^2) = 0.125$

Figure 3.42 Comparison of upper bound results of fixed head walls at three strength parameters, $M_p/(s_uL^2)$

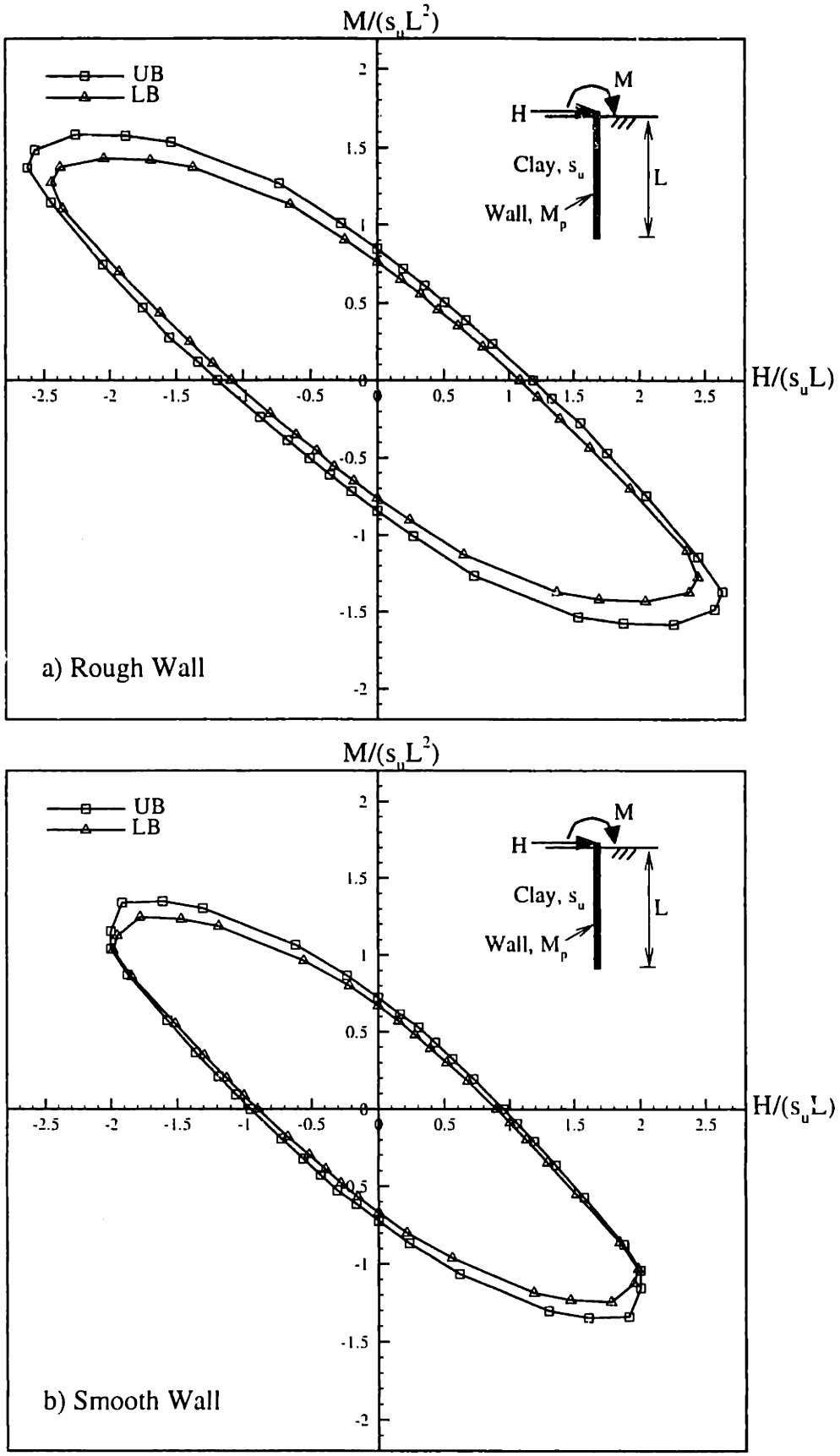

Figure 3.43 Failure envelope of free head walls under horizontal load and moment, where $M_p/(s_uL^2)=2.0$

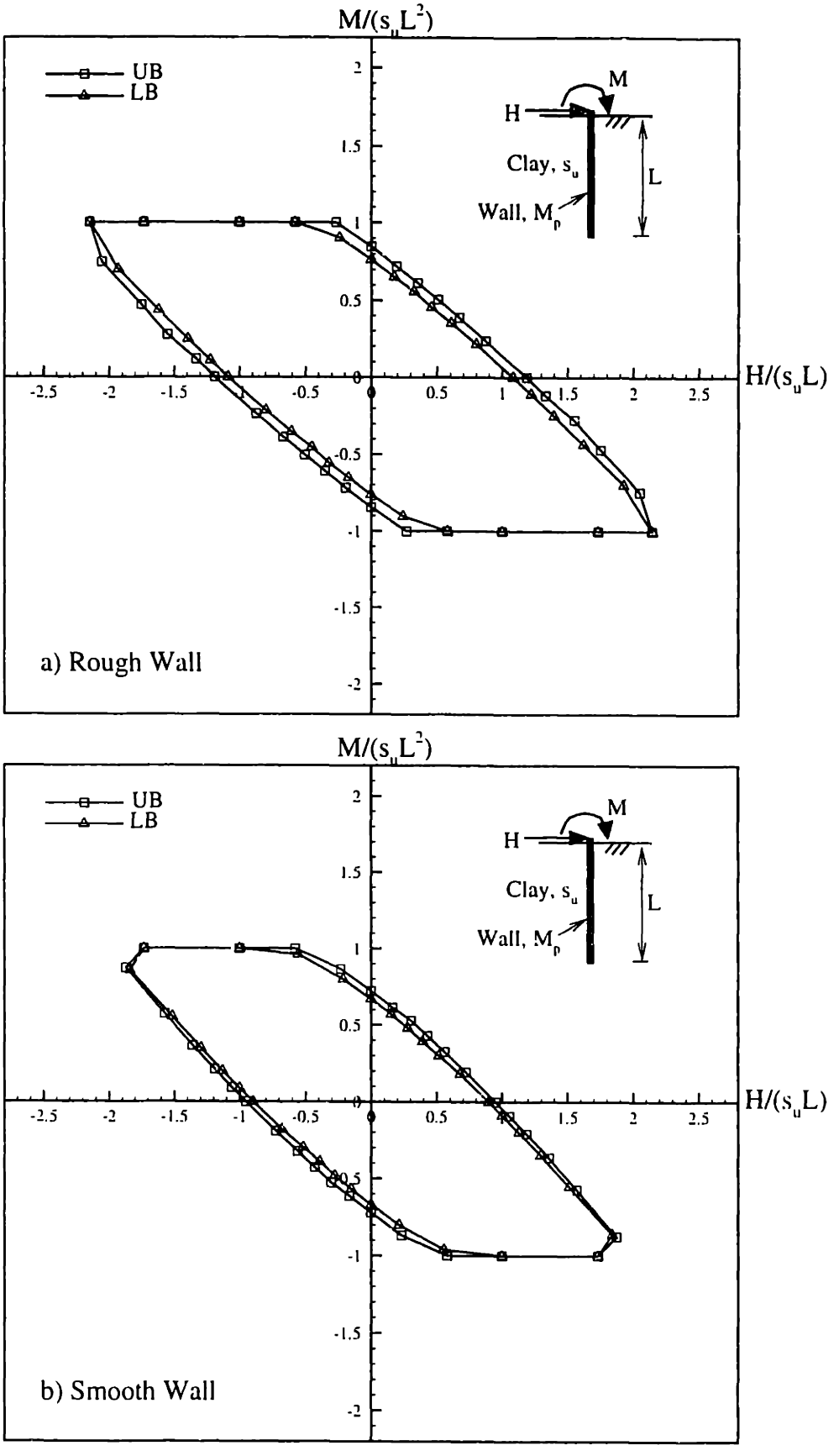

Figure 3.44 Failure envelope of free head walls under horizontal load and moment, where $M_p/(s_u L^2)=1.0$

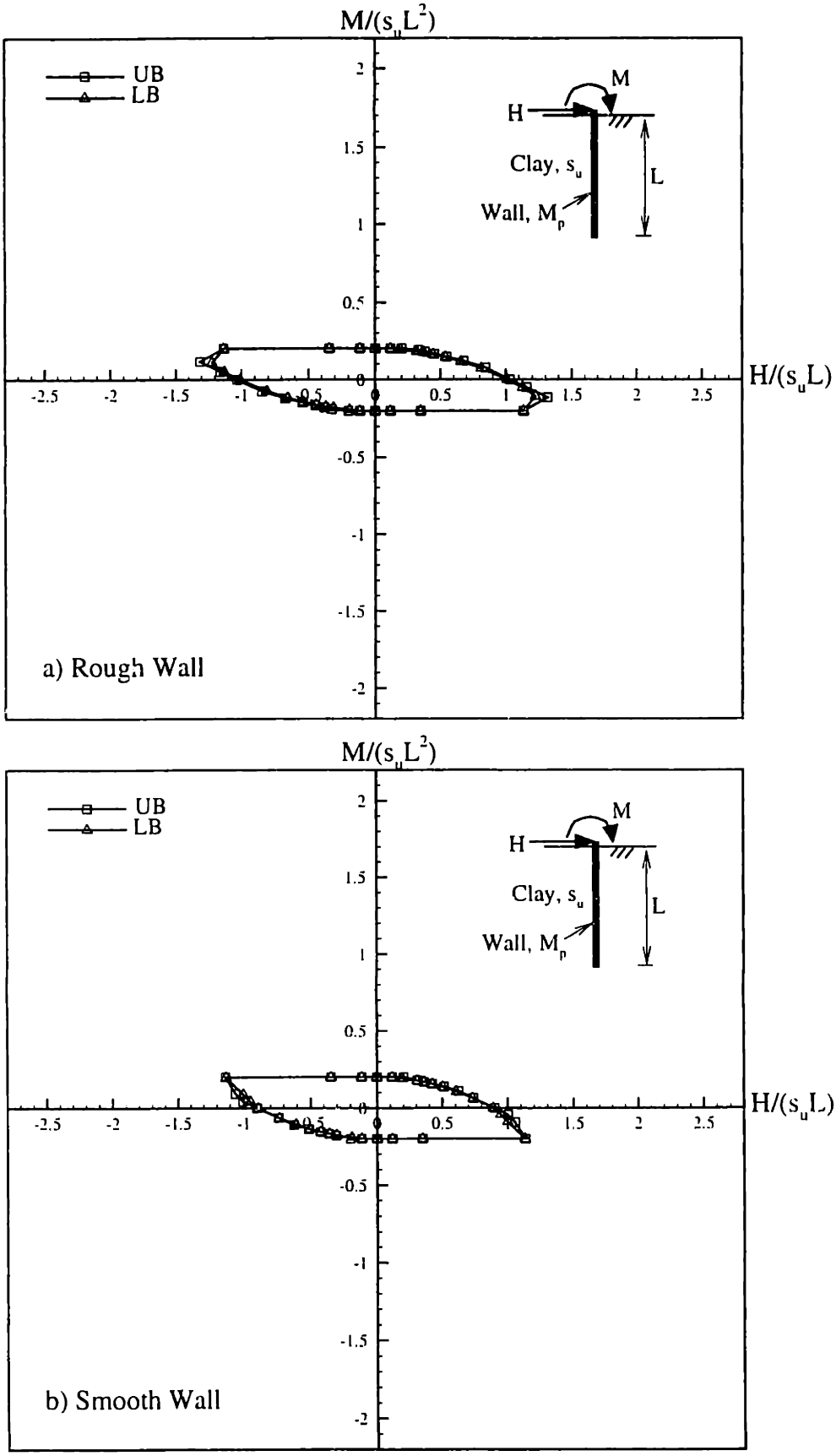

Figure 3.45 Failure envelope of free head walls under horizontal load and moment, where $M_p/(s_u L^2)=0.125$

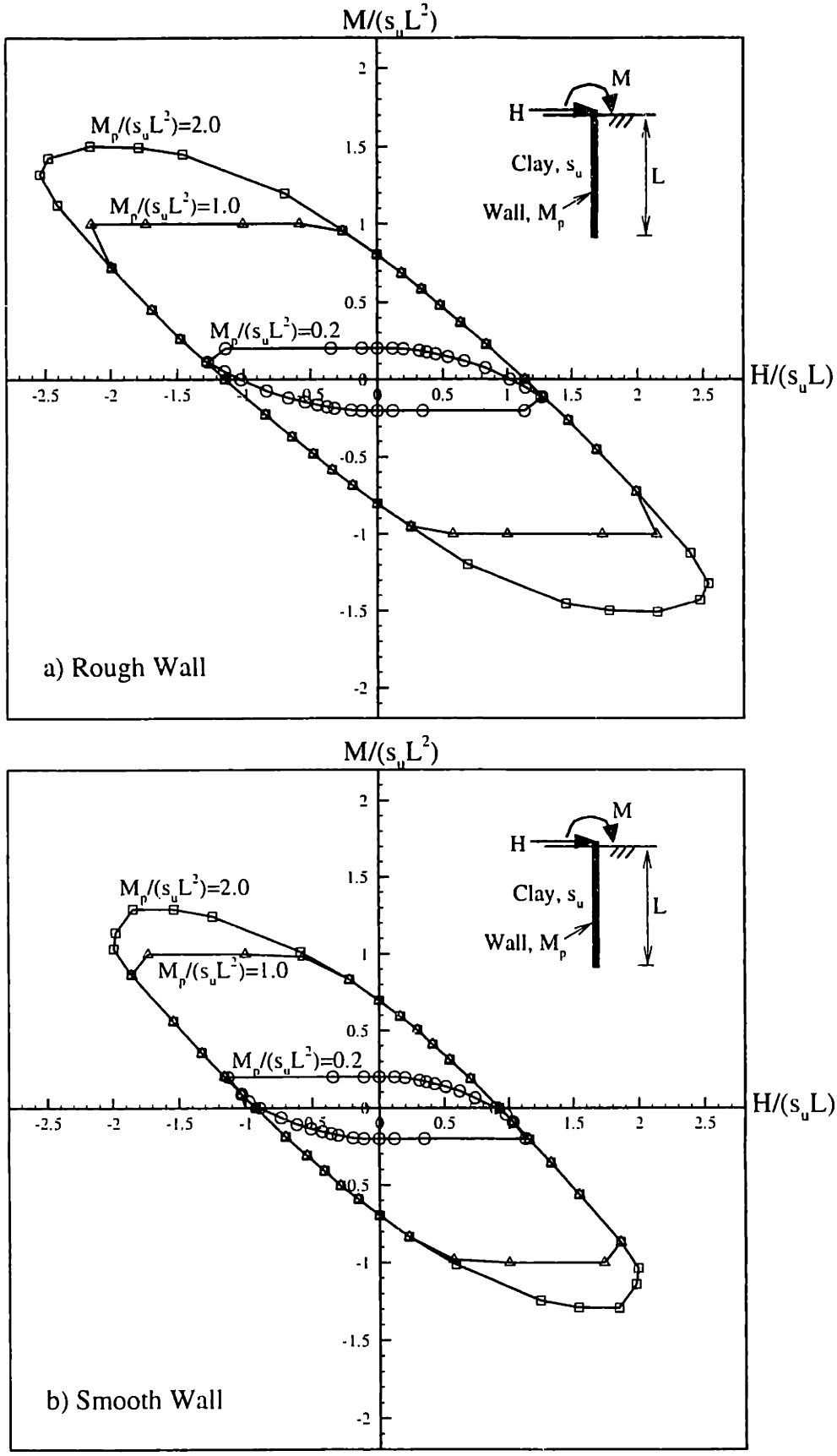

Figure 3.46 Comparisons of failure envelopes of free head walls at three different strength parameters, $M_p/(s_uL^2)$

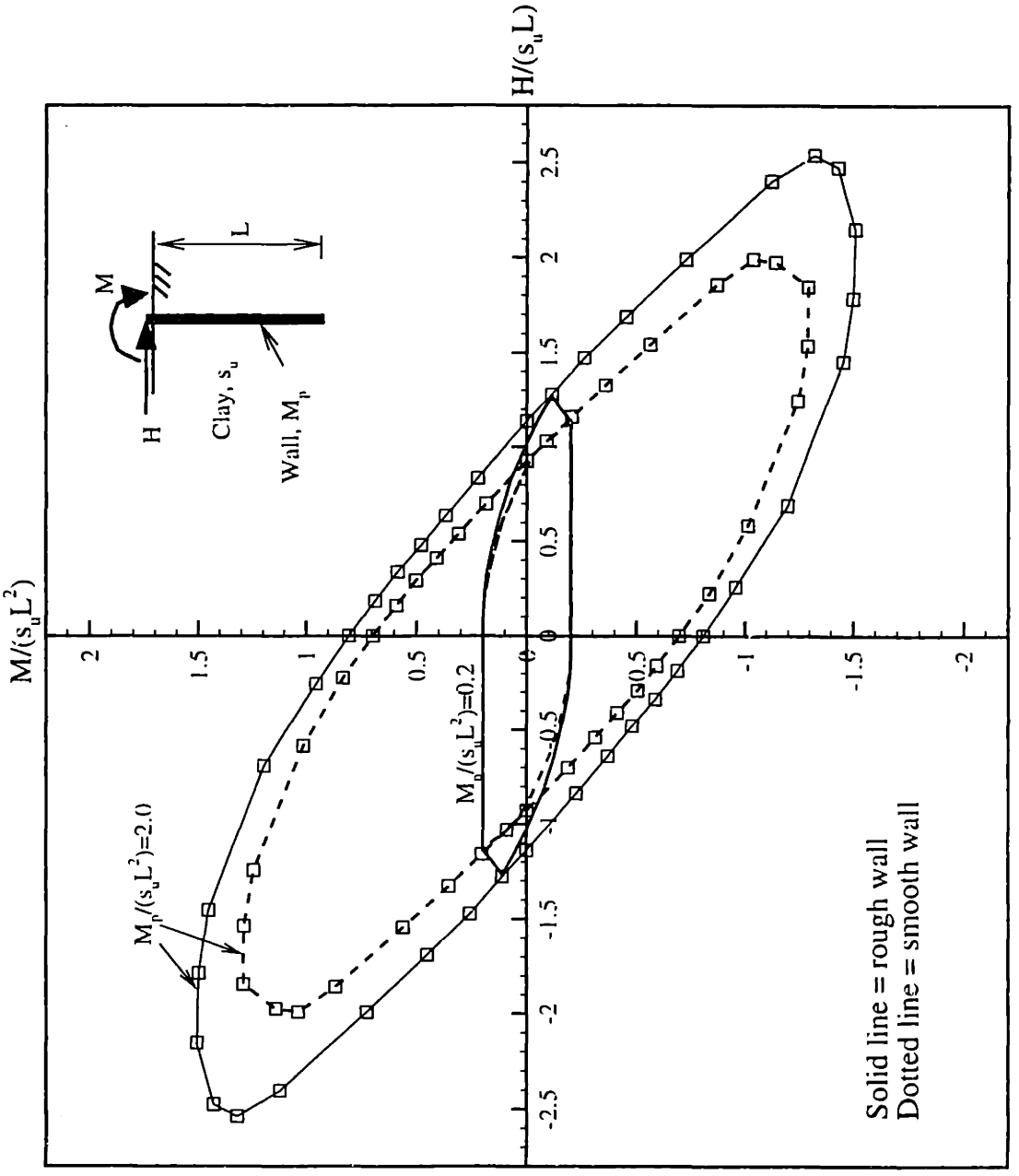

Figure 3.47 Comparisons of failure envelopes of free head walls between smooth and rough walls

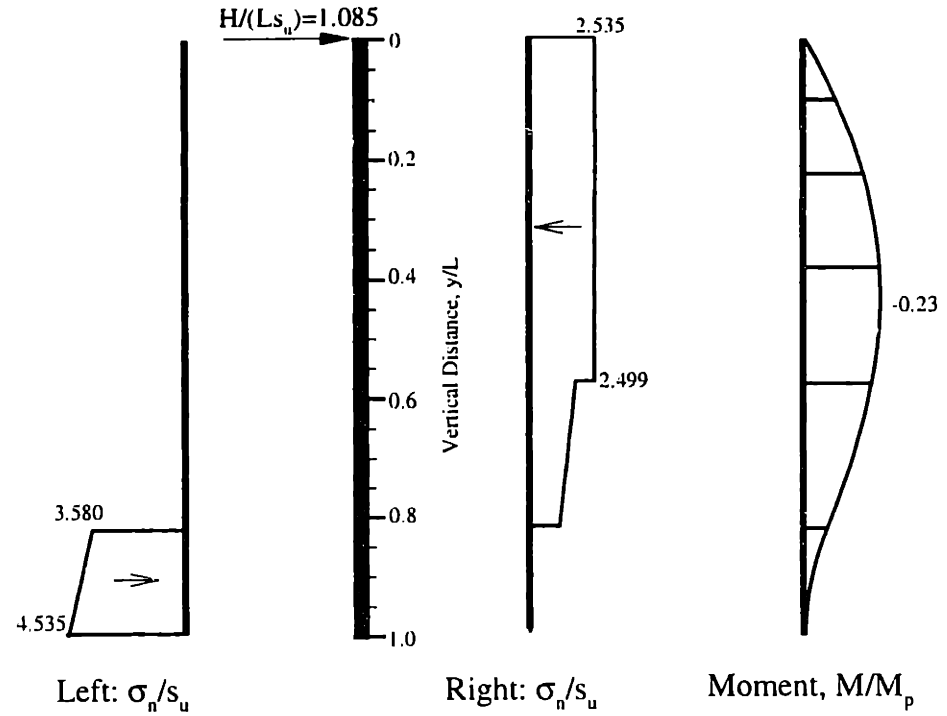

a) Rough interface

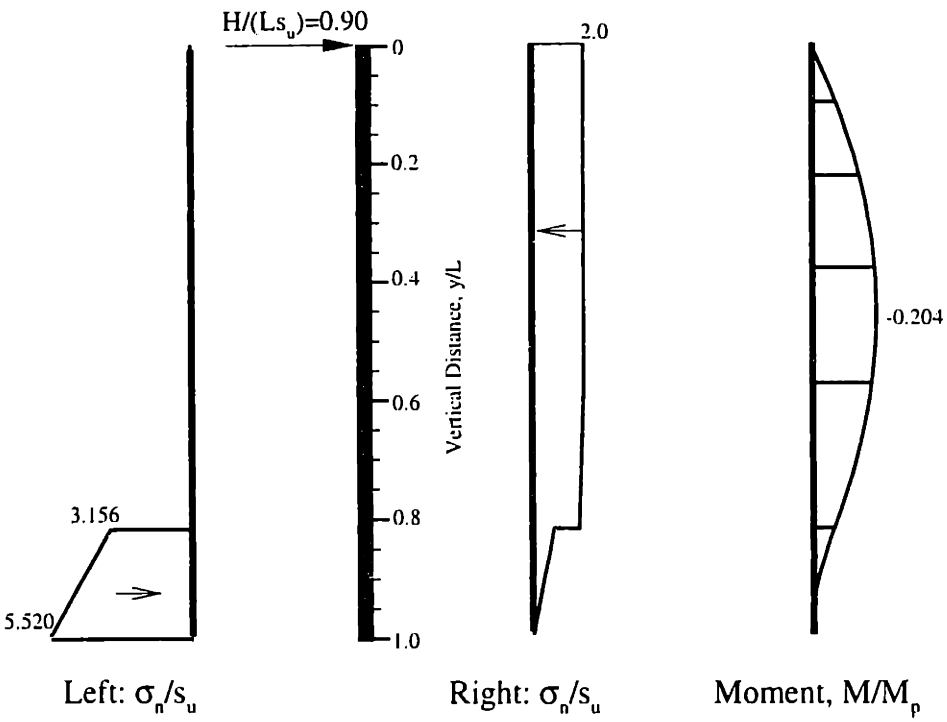

b) Smooth interface

Figure 3.48 Comparisons of contact pressure and moment diagram between smooth and rough interfaces of free head walls, Rigid wall [$M_p/(s_u L^2) = 1.0$]

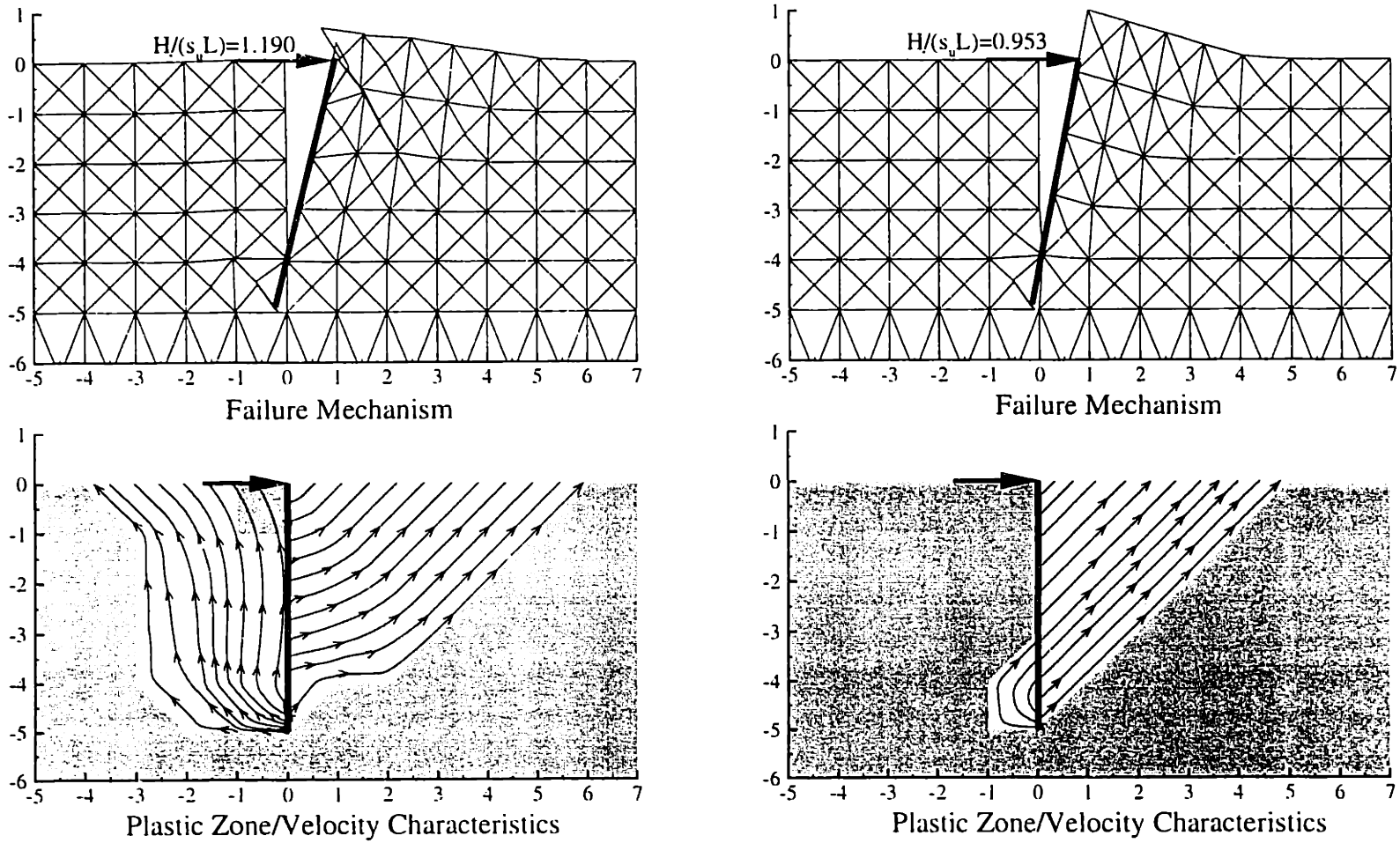

Figure 3.49 Comparisons of upper bound results between smooth and rough interfaces of free head walls, Rigid wall [$M_p/(s_uL^2) = 1.0$]

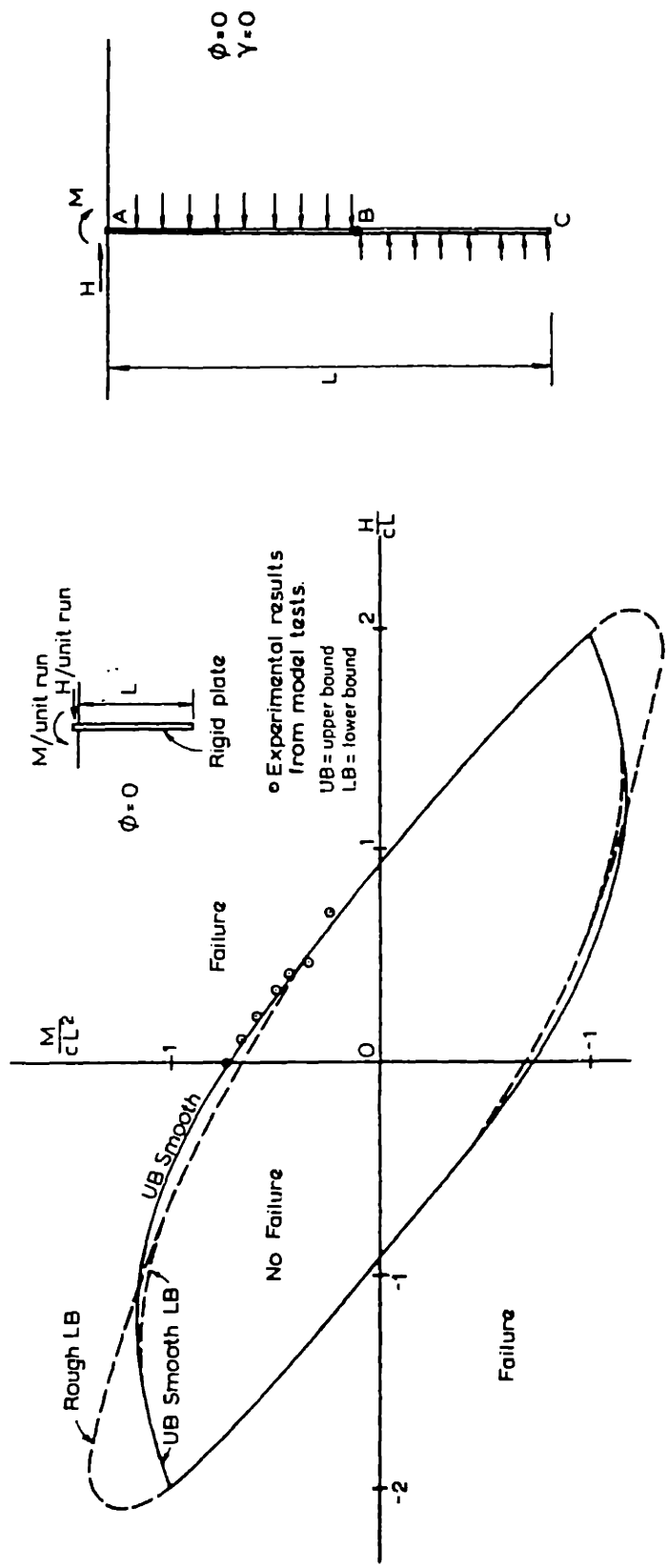

Figure 3.50 Failure envelope of a free head wall derived by Davis (1961)

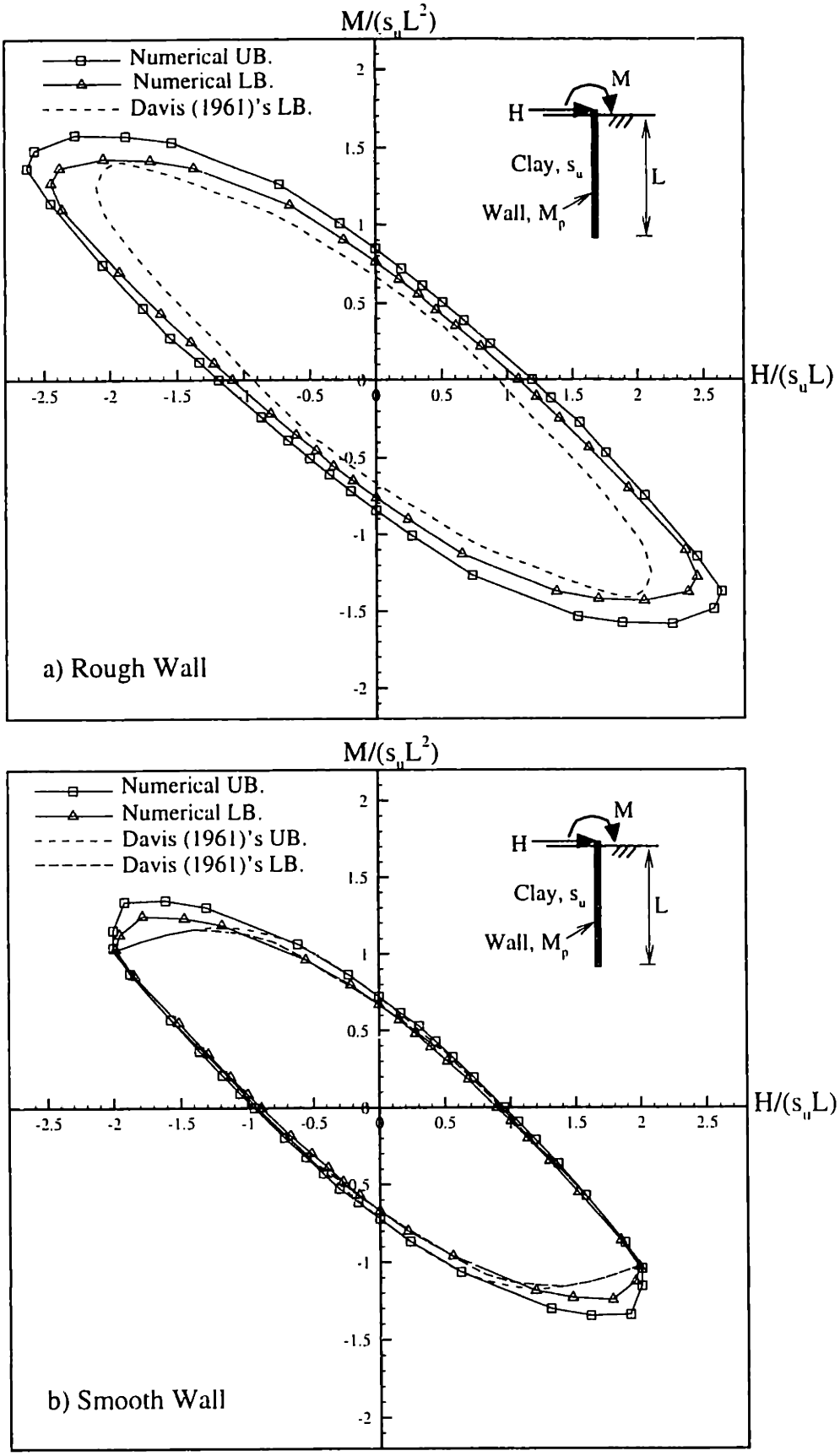

Figure 3.51 Comparisons of failure envelope of free head walls between numerical limit analyses and Davis(1961) solutions: Rigid wall

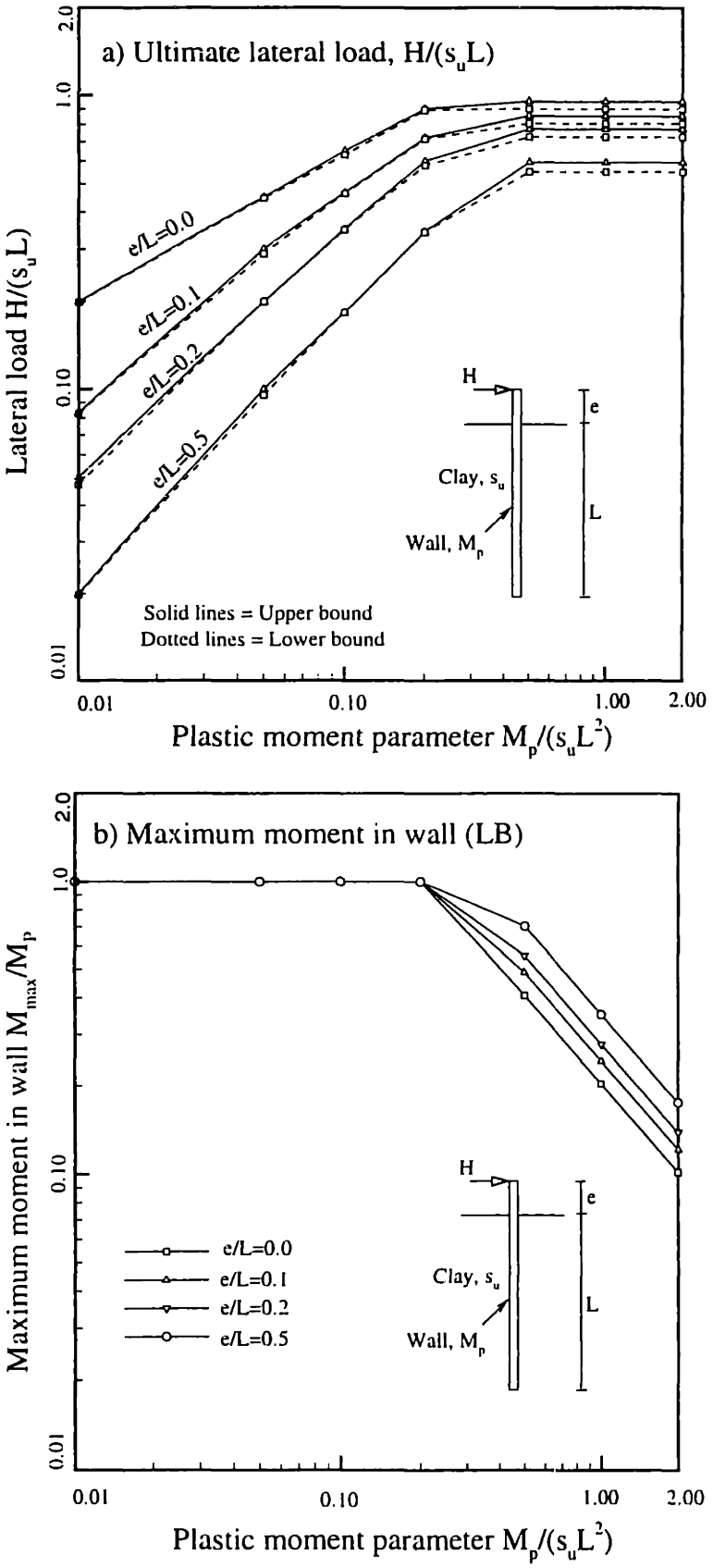

Figure 3.52 Design chart for an ultimate lateral resistance of a free head wall in clay, smooth walls

Appendix 3A: Derivation of Equilibrium Constraints of Beam Elements

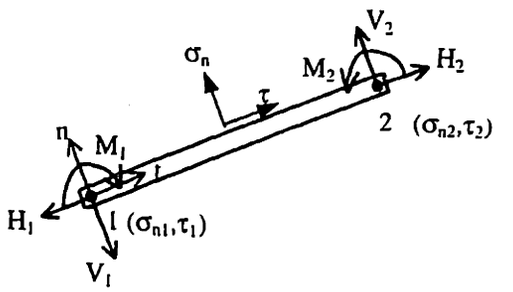

Figure 3A.1 Nodal forces of beam element in the local frame of reference (t,n)

Figure 3A.1 shows a beam element whose nodal forces at nodes 1 and 2 are axial force (H), shear force (V), and moment (M). The shear traction τ, and normal traction, σ_n, acting on the beam element are assumed to vary linearly (following eqn. 2.6). Their positive sign conventions follow the local frame of reference (t, n). According to the equilibrium equation, the moment varies as a cubic function, and the axial and shear forces vary quadratically along the element:

$$M(t) = a_1t^3 + a_2t^2 + a_3t + a_4 \qquad (3A.1)$$

$$V(t) = -(3a_1t^2 + 2a_2t + a_3) \qquad (3A.2)$$

$$H(t) = a_5t^2 + a_6t + a_7 \qquad (3A.3)$$

where

t = distance measure from node 1 along the beam to point considered

a_1-a_7 = coefficients

Equations 3A.1 and 3A.2 must satisfy the force boundary conditions:

At node 1: $M(0) = M_1$ and $V(0) = V_1$ (3A.4)

At node 2: $M(L) = M_2$ and $V(L) = V_2$ (3A.5)

where L is the length of the beam element

Substituting equation 3A.1 and 3A.2 and collecting terms, we obtain a system of linear equations for a_1-a_4 as follows:

$$\begin{bmatrix} L^3 & L^2 & L & 1 \\ -3L^2 & -2L & -1 & 0 \\ 0 & 0 & 0 & 1 \\ 0 & 0 & -1 & 0 \end{bmatrix} \begin{Bmatrix} a_1 \\ a_2 \\ a_3 \\ a_4 \end{Bmatrix} = \begin{Bmatrix} M_2 \\ V_2 \\ M_1 \\ V_1 \end{Bmatrix} \tag{3A.6}$$

From which a_1- a_4 can be derived as:

$$a_1 = \frac{2}{L^3}M_1 - \frac{1}{L^2}V_1 - \frac{2}{L^3}M_2 - \frac{1}{L^2}V_2 \tag{3A.7}$$

$$a_2 = -\frac{3}{L^2}M_1 + \frac{2}{L}V_1 + \frac{3}{L^2}M_2 + \frac{1}{L}V_2$$

$$a_3 = -V_1$$

$$a_4 = M_1$$

Equilibrium constraints result from the boundary conditions of normal traction at nodes 1 and 2 as:

Node 1: $\sigma_n(0) = \sigma_{n1}$ (3A.8)

Node 2: $\sigma_n(L) = \sigma_{n2}$

According to the equilibrium equation of beam element (see equation 3.4), the normal traction is given by:

$$\sigma_n = -\frac{\partial V}{\partial t} \tag{3A.9}$$

Substituting equations 3A.2, and 3A.9, and coefficients a_1-a_4 into equation 3A.8, we obtain two equilibrium constraints as:

$$\sigma_{n1} = -\frac{6}{L^2}M_1 + \frac{4}{L}V_1 + \frac{6}{L^2}M_2 + \frac{2}{L}V_2 \tag{3A.10}$$

$$\sigma_{n2} = \frac{6}{L^2}M_1 - \frac{2}{L}V_1 - \frac{6}{L^2}M_2 - \frac{4}{L}V_2$$

According to equation (3.3), the expression of shear traction along the beam element is given as:

$$\tau = -\frac{\partial H}{\partial t} \tag{3A.11}$$

Substituting into equation 3A.3, we obtain:

$$\tau(t) = -(2a_5 t + a_6) \tag{3A.12}$$

It is assumed that the shear traction along the beam element varies linearly from node 1, $\tau(0) = \tau_1$, to node 2, $\tau(L) = \tau_2$ as:

$$\tau(t) = \tau_1(1 - \frac{t}{L}) + \tau_2(\frac{t}{L}) \tag{3A.13}$$

Equating equation 3A.12 to equation 3A.13 gives the coefficient a_5 and a_6 as:

$$a_5 = \frac{(\tau_1 - \tau_2)}{2L} \tag{3A.14}$$

$$a_6 = -\tau_1$$

The coefficient a_7 is obtained by enforcing the force boundary condition at node 1 as:

$$H(0) = H_1 \tag{3A.15}$$

Substituting equation 3A.3, we get:

$$a_7 = H_1 \tag{3A.16}$$

The equilibrium equation in the t-direction results from the force boundary condition at node 2 as:

$$H(L) = H_2 \tag{3A.17}$$

Substituting equation 3A.3 and coefficients a_5-a_7 gives rise to:

$$H_2 - H_1 = -\frac{(\tau_1 + \tau_2)}{2}L \tag{3A.18}$$

Constraints 3A.10 and 3A.18 summarize the equilibrium equations of beam element in terms of axial force, shear force, and moment in the lo :al coordinate frame.

Appendix 3B: General Yield Surface of Beam Element

This Appendix presents a calculation of yield surface for a beam having a rectangular cross section. For other sections, readers may refer to Mrázik et al. (1987); Baker and Heyman (1969); and Horne (1971).

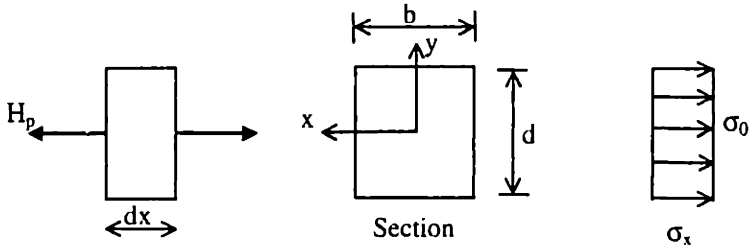

Figure 3B.1 Plastic axial load

1. Element Loaded in Pure Tension or Compression

Figure 3B.1 shows a rectangular section loaded by concentric pure tension or compression, H_p. At the fully plastic state, the axial stress reaches the yield stress in one-dimensional loading, σ_0, and is distributed uniformly over the cross section. Thus, the plastic axial load, H_p is given by:

$$H_p = \sigma_0 A \tag{3B.1}$$

where A = the cross section area = bd

b, d = the width of rectangular section

2. Element Loaded in Pure Shear

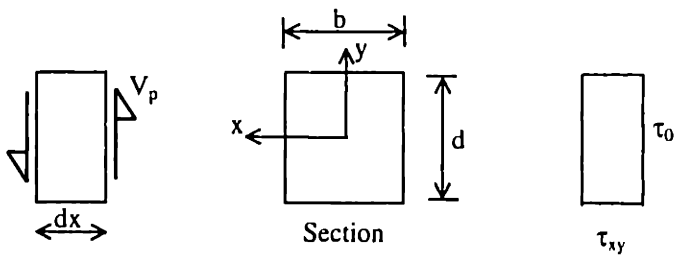

Figure 3B.2 Plastic shear load

Figure 3B.2 shows a rectangular section loaded by pure shear force, V_p. At the fully plastic state, it is assumed that the plastic shear stress, τ_0 is distributed uniformly

over the section. It should be noted that the state of stress of this idealization does not satisfy the boundary condition; that is the shear stress is not equal to zero at the top and bottom levels. According to Mrázik et al. (1987), there is no exact solution for this case. Thus, the assumed shear stress distribution is just an approximate solution.

The plastic shear strength, τ_0 for the case of Von-Mises and Tresca yield criteria are as:

Von Mises: $\tau_0 = \sigma_0/\sqrt{3}$ (3B.2)

Tresca: $\tau_0 = \sigma_0/2$

Consequently, the plastic shear force, V_p is given as:

$$V_p = \tau_0 A \quad (3B.3)$$

3. Element Loaded in Pure Bending

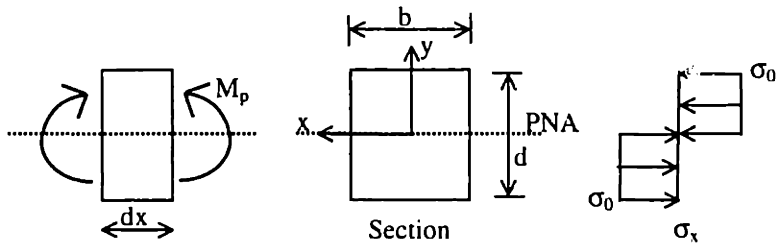

Figure 3B.3 Plastic moment

Figure 3B.3 shows a rectangular section loaded by pure bending moment, M_p. At the fully plastic state, all level of axial stress reaches yield stress, σ_0. The upper half of section undergoes compression and the lower half undergoes tension. The plastic neutral axis (PNA) is located at the middle of the rectangular section (x-axis) and divides a section into two equal areas. The plastic moment, M_p can be calculated by taking the moment about PNA:

$$M_p = \sigma_0 Z_p \quad (3B.4)$$

where Z_p = the plastic section modulus = $bd^2/4$

4. Element Loaded in Axial and Bending

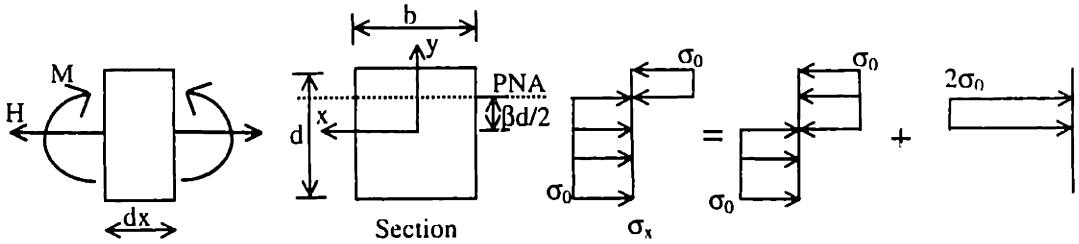

Figure 3B.4 Analysis of axial and moment

Figure 3B.4 shows a rectangular section loaded by an axial force, H and, moment M at the central axis, x. In the presence of axial load (either tensile or compressive), the plastic neutral axis no longer divides a section into two equal areas. The moment which causes the whole section to fully plastified is reduced by the presence axial force.

In order that there will be a net resultant force, H across the section, the plastic neutral axis, PNA must shift from the centroidal axis, x, by an amount βd/2 say. The axial stress over the section reaches the yield stress, σ_0, and its distribution is in compression above PNA, and in tension below PNA. The interaction between the bending moment and the axial force is determined by the equilibrium of force and moment.

From Figure 3B.4, it can be seen that the fully plastic stress distribution may be decomposed into two parts; that is, the original fully plastic distribution in the absence of axial load (see Figure 3B.3) is superimposed with a fictitious distribution involving compressive stress of magnitude, $2\sigma_0$. The axial and moment equilibrium equations give rise to:

$$\Sigma F_x = 0 ; \qquad H = 2\sigma_0(\frac{\beta d}{2})b = \beta H_p \tag{3B.5}$$

$$\Sigma M = 0 ; \qquad M = M_p - H(\frac{\beta d}{4}) = (1-\beta^2)M_p \tag{3B.6}$$

where H_p and M_p are given in equations 3B.1, and 3B.4, respectively.

Combining these equations gives the expression of the yield criterion for the interaction between axial force and moment:

$$(\frac{H}{H_p})^2 + (\frac{M}{M_p}) = 1 \qquad (3B.7)$$

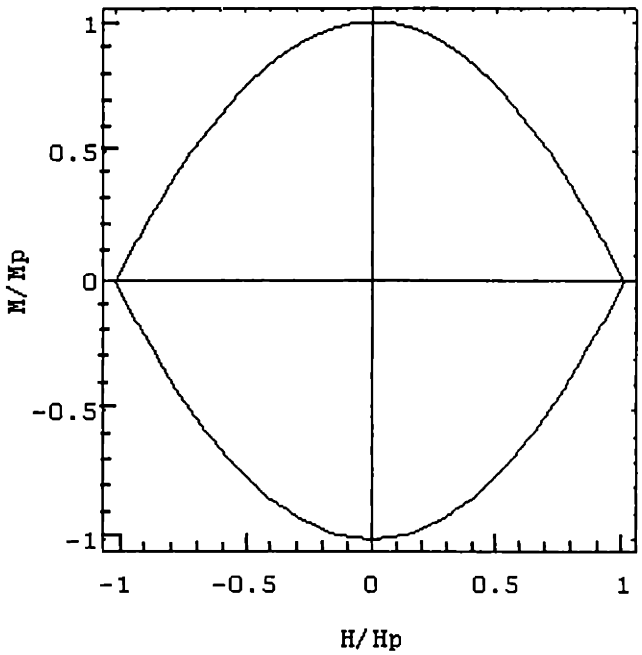

Figure 3B.5 Yield envelope for H and M

Note that this envelope has two axes of symmetry; that is the analysis of compressive load is exactly the same as that of the tensile load, and for the bending moment in the reversed direction. Thus, the complete yield envelope can be obtained using these symmetries, as shown in Figure 3B.5. It should be noted that for a small value of axial load, there is very little reduction in the value of M_P.

5. Element Loaded in Shear and Bending

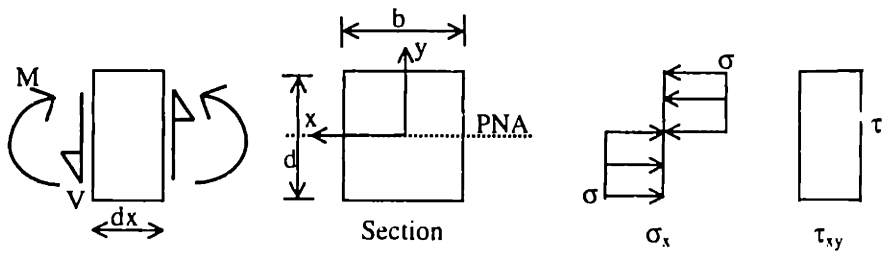

Figure 3B.6 Analysis of shear and moment

The effect of shear force on a beam is much more complex than that of axial load. With the latter, the resulting stresses can be superimposed directly on the bending stress, since they were all axial stress. However, shear force combined with bending moment gives rise to a two-dimensional stress system and thus, it is necessary to use the two-dimensional stress yield criterion such as Tresca or Von Mises, in order to determine the interaction.

Figure 3B.6 shows a rectangular cross section subjected to shear force and bending moment, and the stress distribution at the fully plastic state. The plastic neutral axis is located at the centrodial axis. The assumed stress distribution are: the axial stress, $\sigma_x = \sigma$; and the shear stress $\tau_{xy} = \tau_0$. Recalling the Tresca and Von Mises yield criteria:

$$\text{Tresca:} \qquad \sigma_x^2 + 4\tau_{xy}^2 = \sigma_0^2 \tag{3B.8}$$

$$\text{Von Mises:} \qquad \sigma_x^2 + 3\tau_{xy}^2 = \sigma_0^2$$

Both criteria can be rewritten as:

$$(\frac{\sigma}{\sigma_0})^2 + (\frac{\tau}{\tau_0})^2 = 1 \tag{3B.9}$$

where $\sigma_x = \sigma$, $\tau_{xy} = \tau$

$\tau_0 = \sigma_0/\sqrt{3}$, $\sigma_0/2$ for Von Mises and Tresca Yield Criteria, respectively

Referring to Figure 3B.6, the moment and shear force can be expressed as:

$$\Sigma M = 0: \qquad M = \sigma(bd^2)/4 = (\sigma/\sigma_0)M_p \tag{3B.10}$$

$$\Sigma F_y = 0: \qquad V = \tau(bd) = (\tau/\tau_0)V_p$$

Substituting equation 3B.10 into 3B.9 gives the expression of yield function for combined shear force and moment:

$$(\frac{V}{V_p})^2 + (\frac{M}{M_p})^2 = 1 \tag{3B.11}$$

, which has the circular envelope as shown in Figure 3B.7.

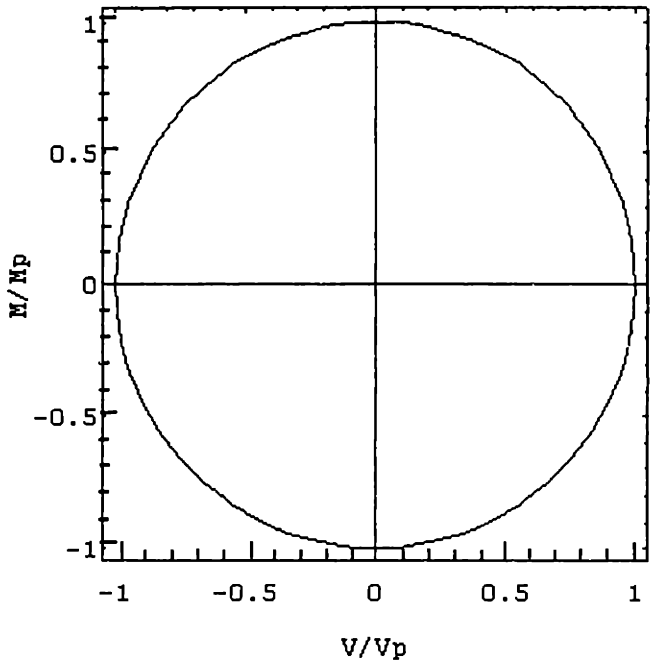

Figure 3B.7 Yield envelope for V and M

6. Element Loaded in Axial, Shear and Bending

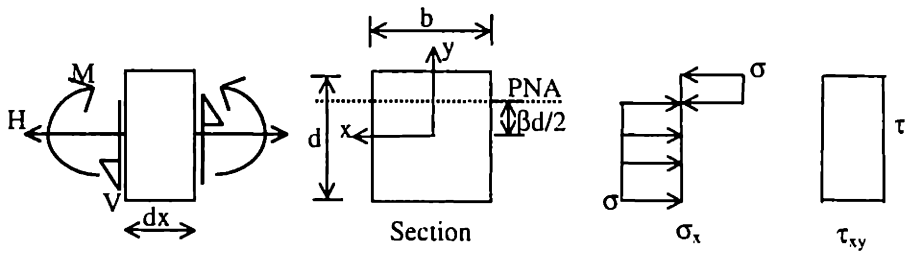

Figure 3B.8 Analysis of H, V and M

This case corresponds to the generalized loading of axial force H, shear force V, and moment M. The generalized yield criterion can be determined following the procedure used for combined shear and bending. The shear and axial stress distributions, shown in Figure 3B.8 are similar to the one in Figures 3B.2, and 3B.4. The only difference is that the shear stress, τ_{xy}, and the axial stress, σ_x, do not reach their yield values; instead, $\tau_{xy} = \tau$ and $\sigma_x = \sigma$. Thus, force and moment equilibrium give rise to the expression of H, M and V as:

$$\Sigma F_x = 0 ; \qquad H = 2\sigma(\frac{\beta d}{2})b = \sigma\beta(bd) \tag{3B.12}$$

$$\Sigma M = 0 ; \qquad M = \sigma\frac{bd^2}{4} - H(\frac{\beta d}{4}) \tag{3B.13}$$

$$\Sigma F_y = 0 : \qquad V = \tau(bd) \tag{3B.14}$$

Combining these three equations and substituting into equation 3B.9 gives the expression of the generalized yield criterion of H, V, M as:

$$(\frac{M}{M_p})^2 \{1-(\frac{V}{V_p})^2\} = \{1-(\frac{H}{H_p})^2-(\frac{V}{V_p})^2\}^2 \tag{3B.15}$$

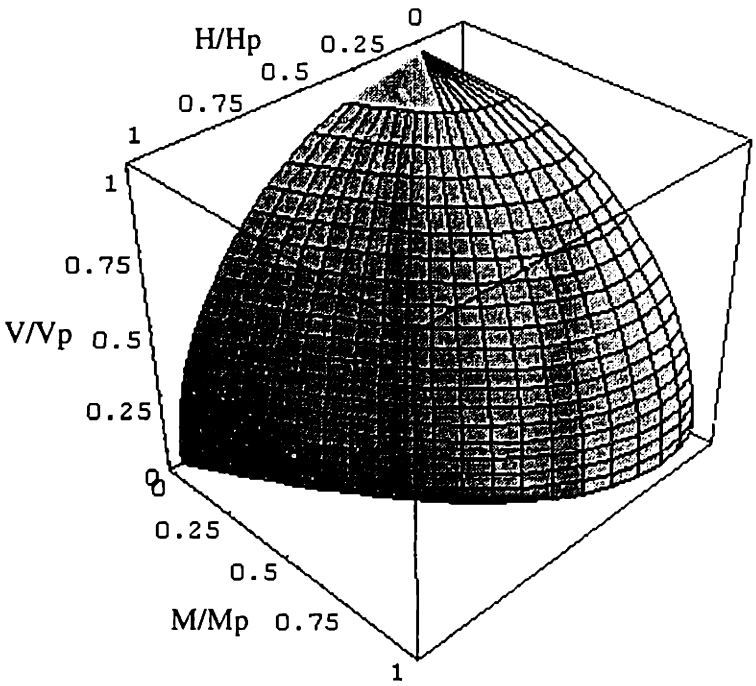

Figure 3B.9 Yield envelope for H,V and M

The three-dimensional representation of the generalized yield surface is shown in Figure 3B.9. The cross section parallel to a H-M plane gives a quadratic envelope, while that parallel to V-M or V-H plane gives a circular envelope. It should be noted that this yield surface is convex, and has three planes of symmetry: 1) M-H; 2) M-V; and 3) V-H. The complete yield surface can be obtained using these symmetries.

Appendix 3C: Lower Bound Linearization of Yield Surface for Structural Elements

In general, an inequality constraint which describes the convex region of the linearized yield surface can be expressed as:

$$A_kH + B_kM + C_kV - D_k \leq 0 \qquad (3C.1)$$

where

H, V, M = axial force, shear force, moment applied at a section

A_k, B_k, C_k, D_k = coefficients of the linearized plane

Note that the plastic properties of a rectangular section - the axial force, H_p, shear force, V_p, and moment M_p, are derived in Appendix 3B.

In order to ensure that the solution obtained is a strict lower bound on the true collapse load, the linearized yield surface must be inside or on the actual yield surface. Four cases has been considered:

1.) Element subjected to pure moment

2.) Element subjected to axial and moment

3.) Element subjected to shear and moment

4.) Element subjected to axial, shear, and moment

Case 1: Element subjected to pure moment

The exact yield surface of a beam subjected to pure bending moment is simply given as:

$$|M| - M_p = 0 \qquad (3C.2)$$

The linearized plane which gives the convexity of this yield surface are as:

$$M - M_p \leq 0 \text{ and } -M - M_p \leq 0 \qquad (3C.3)$$

Thus, it can be seen that the linearization requires only two planes to obtain the actual yield surface:

Plane 1: $A_1 = 0, B_1 = 1, C_1 = 0, D_1 = -M_p$ (3C.4)

Plane 2: $A_2 = 0, B_2 = -1, C_2 = 0, D_2 = -M_p$

Case 2: Element subjected to axial force and moment

The exact yield surface of a beam subjected to axial and moment is given as (see equation 3B.7) :

$$(\frac{H}{H_p})^2 + (\frac{M}{M_p}) - 1 = 0 \qquad (3C.5)$$

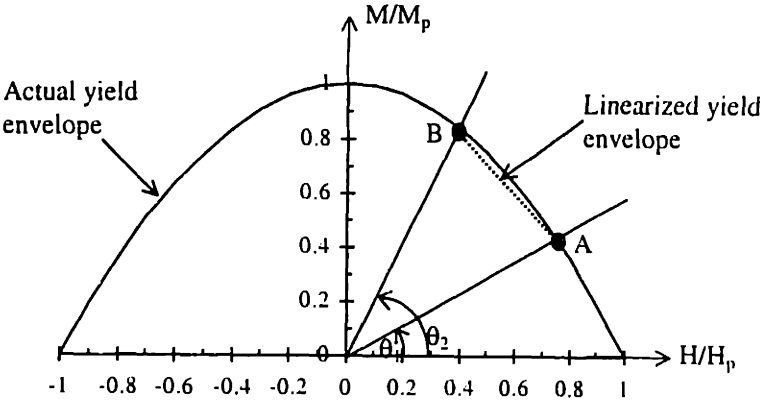

Figure 3C.1 Schematic internal linearization of H-M

The concept of internal linearization is to determine a series of lines, each of which connects two points located on the actual yield envelope, as shown in Figure 3.C1. For a given θ_1 and θ_2, we can obtain points A and B and solve for the equation of line A-B. The coefficients of a linearized plane are:

$$A_k = \frac{a\cos^2\theta_1}{H_p} \qquad (3C.6)$$

$$B_k = \frac{b\cos^2\theta_1}{M_p}$$

$$C_k = 0$$

$$D_k = ax_1\cos\theta_1 + bx_1\sin\theta_1$$

where $a = x_2\sin\theta_2\cos^2\theta_1 - x_1\sin\theta_1\cos^2\theta_2$

$b = (x_1\cos\theta_2 - x_2\cos\theta_1)\cos\theta_1\cos\theta_2$

$$x_1 = \frac{1}{2}(-\sin\theta_1 + \sqrt{4\cos^2\theta_1 + \sin^2\theta_1})$$

$$x_2 = \frac{1}{2}(-\sin\theta_2 + \sqrt{4\cos^2\theta_2 + \sin^2\theta_2})$$

Case 3: Element subjected to shear and moment

The exact yield surface of a beam subjected to shear and moment is given as (see equation 3B.11) :

$$(\frac{V}{V_p})^2 + (\frac{M}{M_p})^2 - 1 = 0 \qquad (3C.7)$$

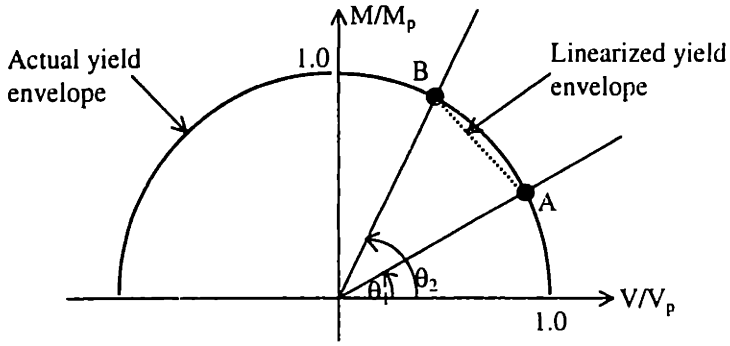

Figure 3C.2 Schematic internal linearization of V-M

Figure 3C.2 shows a schematic internal linearization of V-M, which follows the same concept as the previous case. Thus, for a given θ_1 and θ_2, we can get the coefficients of a linearized plane as:

$$A_k = 0 \qquad (3C.8)$$

$$B_k = \frac{\cos\theta_1 - \cos\theta_2}{M_p}$$

$$C_k = \frac{\sin\theta_2 - \sin\theta_1}{V_p}$$

$$D_k = \sin(\theta_2 - \theta_1)$$

Case 4: Element subjected to axial, shear and moment

The exact yield surface of a beam subjected to axial, shear and moment is given as (see equation 3B15) :

$$(\frac{M}{M_p})^2\{1-(\frac{V}{V_p})^2\} = \{1-(\frac{H}{H_p})^2-(\frac{V}{V_p})^2\}^2 \qquad (3C.9)$$

The internal linearization of the three-dimensional yield surface is more complicated than the two-dimensional cases above. The linearization can be done as shown in Figure 3C.3.

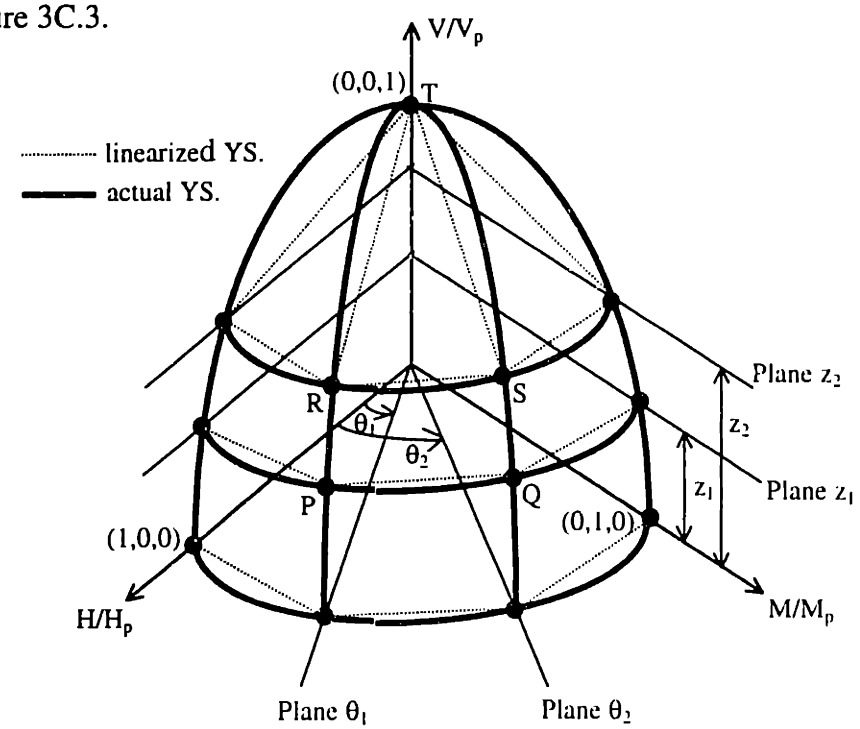

Figure 3C.3 Schematic internal linearization of H-M-V

Conceptually, the actual yield surface is linearized by a series of rectangular and triangular planes. The rectangular plane (e.g. PQSR) is defined by the intersection of the two vertical planes, θ_1 and θ_2, passing (0,0,0) and (0,0,1), and two horizontal plane, z_1 and z_2. The triangular plane (e.g. TRS) is defined by the intersection of two vertical planes, θ_1 and θ_2, one horizontal plane, z_2 and a vertex point (0,0,1). It is only used at the top of actual yield surface.

For a given θ_1, θ_2, z_1 and z_2, we can obtain the expression of coefficients of a linearized yield surface as:

$$A_k = \frac{ad_3}{H_p} \qquad (3C.10)$$

$$B_k = \frac{bd_3}{M_p}$$

$$C_k = \frac{-bd_2 - ad_1}{V_p}$$

$$D_k = r_1 k_1 d_3 (a \cos\theta_1 + b \sin\theta_1) - z_1(bd_2 + ad_1)$$

where

$$r_1 = \frac{x_1}{\cos^2 \theta_1}$$

$$k_1 = \sqrt{1 - z_1^2}$$

$$k_2 = \sqrt{1 - z_2^2}$$

$$d_1 = r_1 \cos\theta_1 (k_2 - k_1)$$

$$d_2 = r_1 \sin\theta_1 (k_2 - k_1)$$

$$d_3 = z_2 - z_1$$

Expressions for x_1, x_2, a, and b are the same as given in Case 2.

The expressions for A_k, B_k, C_k and D_k are applied both rectangular and triangular linearized planes. For the latter, the value of z_2 is set to one.

Appendix 3D: Inequality Constraints for Convexity of Linearized Yield Criterion

Inequality constraints for convexity of linearized yield criterion can be written in the matrix form as:

$$[A^{k,i}_{yield}]\{F_{beam}\} \le \{b^{k,i}_{yield}\};\ k = 1,2,..,p\ ;\ \text{and}\ i = 1,2,...,n \qquad (3.22)$$

where

p = the number of linearized planes of yield criterion

n = the number of internal nodes along beam elements (including both end nodes)

$$[A^{k,i}_{yield}] = [Y^{k,i}_{x1} \quad Y^{k,i}_{y1} \quad Y^{k,i}_{z1} \quad Y^{k,i}_{x2} \quad Y^{k,i}_{y2} \quad Y^{k,i}_{z2}]$$

$$\{F_{beam}\}^T = \{F_{x1} \quad F_{y1} \quad F_{z1} \quad F_{x2} \quad F_{y2} \quad F_{z2}\}$$

$$\{b^{k,i}_{yield}\} = \{Y^{k,i}_{\tau 1} + Y^{k,i}_{\tau 2}\}$$

$$Y^{k,i}_{x1} = -A_k\cos\theta + C_k\sin\theta - B_k\sin\theta\, t_i - \frac{4C_k\sin\theta\, t_i}{L} + \frac{3C_k\sin\theta\, t_i^2}{L^2} + \frac{2B_k\sin\theta\, t_i^2}{L} - \frac{B_k\sin\theta t_i^3}{L^2}$$

$$Y^{k,i}_{y1} = -C_k\cos\theta - A_k\sin\theta + B_k\cos\theta\, t_i + \frac{4C_k\cos\theta\, t_i}{L} - \frac{3C_k\cos\theta\, t_i^2}{L^2} - \frac{2B_k\cos\theta\, t_i^2}{L} + \frac{B_k\cos\theta t_i^3}{L^2}$$

$$Y^{k,i}_{z1} = -B_k - \frac{6C_k\, t_i}{L^2} + \frac{6C_k\, t_i^2}{L^3} + \frac{3B_k\, t_i^2}{L^2} - \frac{2B_k t_i^3}{L^3}$$

$$Y^{k,i}_{x2} = \frac{2C_k\sin\theta\, t_i}{L} - \frac{3C_k\sin\theta\, t_i^2}{L^2} - \frac{B_k\sin\theta\, t_i^2}{L} + \frac{B_k\sin\theta t_i^3}{L^2}$$

$$Y^{k,i}_{y2} = -\frac{2C_k\cos\theta\, t_i}{L} + \frac{3C_k\cos\theta\, t_i^2}{L^2} + \frac{B_k\cos\theta\, t_i^2}{L} - \frac{B_k\cos\theta t_i^3}{L^2}$$

$$Y^{k,i}_{z2} = -\frac{6C_k\, t_i}{L^2} + \frac{6C_k\, t_i^2}{L^3} + \frac{3B_k\, t_i^2}{L^2} - \frac{2B_k t_i^3}{L^3}$$

$$Y^{k,i}_{\tau 1} = -A_k t + \frac{A_k\, t_i^2}{2L}$$

$$Y^{k,i}_{\tau 2} = -\frac{A_k\, t_i^2}{2L}$$

A_k, B_k, C_k are coefficients of a linearzied yield function based on Appendix 3C.

t_i = the distance from node #1 to an internal node, i; $t_i = \frac{(i-1)}{n-1} L$

L = the length of the beam element

θ = the orientation angle of the beam element (defined positive in an anticlockwise direction from the horizontal)

F_{x1}, F_{y1}, F_{z1} are forces in x, y directions and moment (z-dir.) at node 1, respectively

F_{x2}, F_{y2}, F_{z2} are forces in x, y directions and moment (z-dir.) at node 2, respectively

Appendix 3E: Upper Bound Linearization of Yield Surface for Structural Elements

In general, the linearized yield surface can be expressed as:

$$A_kH + B_kM + C_kV - D_k = 0 \qquad (3E.1)$$

where

H, V, M = axial force, shear force, moment applied at a section

A_k, B_k, C_k, D_k = coefficients of a linearized plane

Note that the plastic properties of a rectangular section - the plastic axial force, H_p, plastic shear force, V_p, and plastic moment M_p, are derived in Appendix 3B.

In order to ensure that the solution obtained is a strict upper bound on the true collapse load, the linearized yield surface must circumscribe the actual yield surface. Four cases are considered here:

1.) Element subjected to pure moment

2.) Element subjected to axial and moment

3.) Element subjected to shear and moment

4.) Element subjected to axial, shear, and moment

Case 1: Element subjected to pure moment

The exact yield surface of a beam subjected to only pure bending moment is simply given by:

$$|M| - M_p = 0 \qquad (3E.2)$$

Thus, the linearized planes are as:

$$M - M_p = 0 \text{ and } -M - M_p = 0 \qquad (3E.3)$$

It can be seen that the linearization requires only two planes to obtain the actual yield surface:

Plane 1: $A_1 = 0, B_1 = 1, C_1 = 0, D_1 = -M_p$ (3E.4)

Plane 2: $A_2 = 0, B_2 = -1, C_2 = 0, D_2 = -M_p$

Case 2: Element subjected to axial force and moment

The exact yield function of a beam having a rectangular section subjected to axial force and moment is given by (see equation 3B.7) :

$$(\frac{H}{H_p})^2 + (\frac{M}{M_p}) - 1 = 0 \qquad (3E.5)$$

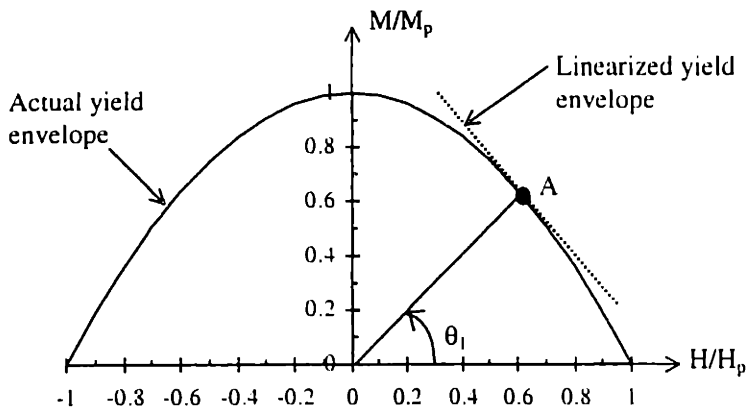

Figure 3E.1 Schematic external linearization of H-M

The concept of external linearization is to determine a series of envelopes tangential to the actual yield envelope. For a given θ_l, we can obtain a linearized yield envelope, as shown in Figure 3E.1. The coefficients of the linearized plane are:

$$A_k = \frac{2x_l \cos\theta_l}{H_p} \qquad (3E.6)$$

$$B_k = \frac{\cos^2\theta_l}{M_p}$$

$$C_k = 0$$

$$D_k = 2\cos^2\theta_l - x_l \sin\theta_l$$

where

$$x_l = \frac{1}{2}(-\sin\theta_l + \sqrt{4\cos^2\theta_l + \sin^2\theta_l})$$

Case 3: Element subjected to shear force and moment

For a rectangular section, the yield function of a beam subjected to shear force and moment is given as (see equation 3B.11) :

$$(\frac{V}{V_p})^2 + (\frac{M}{M_p})^2 - 1 = 0 \qquad (3E.7)$$

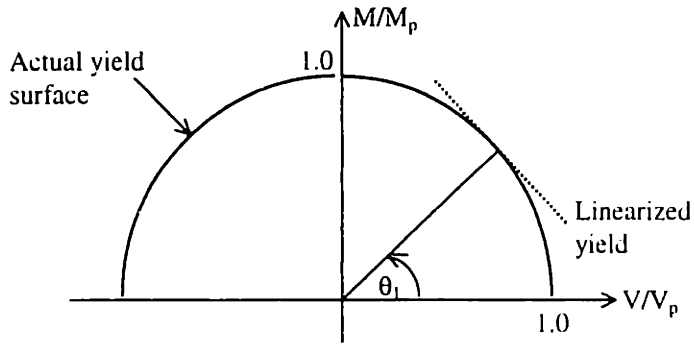

Figure 3E.2 Schematic external linearization of V-M

Figure 3E.2 shows a schematic external linearization of V-M, which follows the same concept as the previous case. Thus, for a given θ_l, we can get the coefficients of a linearized plane as:

$$A_k = 0 \qquad (3E.8)$$

$$B_k = \frac{\sin\theta_l}{M_p}$$

$$C_k = \frac{\cos\theta_l}{V_p}$$

$$D_k = 1$$

Case 4: Element subjected to axial, shear and moment

For a rectangular section, the yield surface of a beam subjected to axial force, shear force and moment is given as (see equation 3B.15) :

$$(\frac{M}{M_p})^2\{1-(\frac{V}{V_p})^2\} = \{1-(\frac{H}{H_p})^2-(\frac{V}{V_p})^2\}^2 \qquad (3E.9)$$

External linearization of the three-dimensional yield surface follows the same concept as that of two-dimensional yield envelope. That is to determine a series of planes which are tangential to the actual yield surface, as shown in Figure 3E.3.

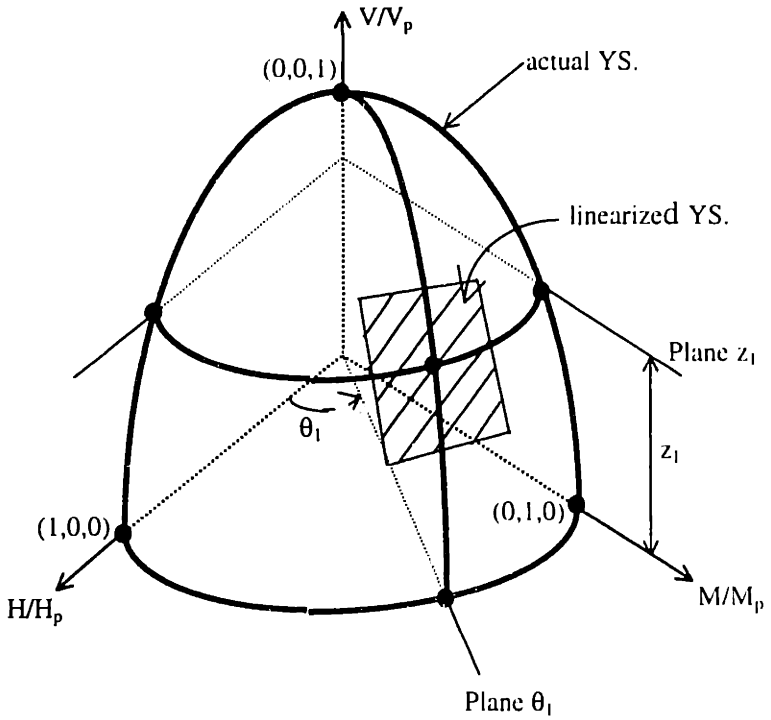

Figure 3E.3 Schematic external linearization of H-M-V

Conceptually, a point on the actual yield surface is defined by the intersection of: 1) a vertical plane passing V-axis and making an angle of θ_l with H-M plane; and 2) a horizontal plane, z_l. Thus, for a given θ_l, and z_l, we can obtain the linear coefficients of tangential plane as:

$$A_k = \frac{2k_1 x_1}{H_p} \tag{3E.8}$$

$$B_k = \frac{k_1}{M_p}$$

$$C_k = \frac{z_1(1+x_1^2)}{V_p}$$

$$D_k = 1+x_1^2$$

where

$$k_1 = \sqrt{1-z_1^2}$$

$$x_1 = \frac{1}{2}(-\sin\theta_1 + \sqrt{4\cos^2\theta_1 + \sin^2\theta_1})$$

Chapter 4. Development and Validation of Anisotropic Undrained Strength

4.1 Introduction

This chapter describes the formulation of an anisotropic yield function for representing the undrained strength of clays in numerical limit analyses. Sections 4.2 and 4.3 review the existing mechanical interpretation of undrained strength anisotropy and proposed anisotropic yield functions. Section 4.4 presents modifications of the lower and upper bound programs to include an anisotropic yield function for undrained strength based on the work of Davis and Christian (1971). Section 4.5 illustrates the selection undrained strength parameters for K_0-normally consolidated Boston Blue Clay (BBC) based on results of laboratory Directional Shear Cell and discusses the relationship between strain and strength mobilization. Sections 4.6 and 4.7 apply numerical limit analyses with undrained strength anisotropy for two example problems: 1) the bearing capacity of a rigid footing on clay; and 2) the lateral load capacity of embedded piles (for selected cross-sectional geometries).

4.2 Undrained Strength Anisotropy

It is generally accepted that the strength parameters of natural clay are anisotropic. Ladd (1991) describes the "initial" anisotropy as the anisotropic behavior (stress-strain-strength) measured during monotonic loading (shearing) of a soil. This may be subdivided into: a) inherent anisotropy, which is the anisotropy caused by one dimensional deposition and subsequent K_0-consolidation; and b) initial shear stress anisotropy which occurs whenever the soil exists under non-hydrostatic stress conditions. In general, using these definitions, it is very difficult to separate the effects of inherent and initial shear stress anisotropy. Kavvadas (1982) introduces a much clearer definition of anisotropic behavior which consists of: a) history preferred direction which describes the memory of the soil has of its previous load history; and b) current stress state preferred directions which are the directions imposed by the current principal stress directions. These definitions separate the influence of geological history from anisotropic behavior that evolves during subsequent loading.

Anisotropic behavior of clay can be illustrated by the results of standard laboratory triaxial compression (CK_0UC), extension (CK_0UE), and direct simple shear tests (CK_0DSS). Figure 4.1 summarizes the peak undrained shear strength ratios of normally consolidated clays and silts (but excluding varved deposits) from these three standard modes of shearing. The data show the following: 1) the highest undrained strength ratio occurs in the triaxial compression mode with $s_u/\sigma'_{vc} \approx 0.32$ (and is independent of I_p), while the triaxial extension ratios, s_{uTE}/σ'_{vc} increase from 0.12-0.15 for $I_p < 10\%$ to 0.22-0.24 for high plasticity clays ($I_p > 70\%$); 2) the peak shear resistance in direct simple shear test τ_f/σ'_{vc} (assumed to be s_{uDSS}/σ'_{vc}) generally lie between the compression and extension strength ratios, exhibiting a small increase with I_p. These data clearly demonstrated that most OCR = 1 soils exhibit significant undrained strength anisotropy that generally becomes most important in lean (low plasticity) clays, especially those which are also sensitive (s_t > 3-7). Varved clays represent a special case (not shown in Fig. 4.1) wherein horizontal (DSS) shearing gives an unusually low peak $\tau_h/\sigma'_{vc} = 0.16$ based on data from several deposits in the northeastern US (Ladd, 1987).

Figure 4.2 plots peak undrained shear strength ratios of two clays as functions of the overconsolidation ratio, for $1 \leq OCR \leq 10$. For the medium plasticity, insensitive AGS clay (Fig. 4.2a), the undrained strength anisotropy (s_{uTC}/s_{uTE}, s_{uDSS}/σ'_{vc}) decreases slightly with increasing OCR, that is accompanied by a significant increase in the shear strain at failure (γ_f) for the triaxial compression shearing mode. In contrast, Figure 4.2b results for the high sensitive, low plasticity of James Bay clay, where s_{uTC} is much higher than either s_{uDSS} or s_{uTE}, and exhibits a very small strain to failure for $1 \leq OCR \leq 3$.

Figure 4.3 compares the incremental shear stress-strain response of CK_0U plane strain compression, extension, and direct simple shear tests on AGS clay (OCR = 1.0). The compression data show a small strain to failure, followed by significant strain softening (undrained brittleness). In contrast, the extension behavior is ductile and strain hardening, requiring a very large strain to mobilize the peak strength, while the DSS curve (τ_d) falls between these extremes. These data indicate that the soil undergoing a compression mode (element C) will be strained beyond its peak strength and lose

resistance before the strengths of the soil undergoing the DSS (element D) and extension modes (element E) can be fully mobilized, leading to the potential for a progressive failure mechanism. Hence, using peak undrained strength at different modes of shearing for computing undrained stability can lead to unsafe design. Ladd (1975) proposed a *strain compatibility* technique to account for progressive failure when selecting undrained strengths for use in stability analyses. The technique assumes that the shear strain along a potential surface is approximately uniform at the moment of actual failure. According to Ladd (1991), the strain level to determine the corresponding undrained strengths is selected in such a way that give $s_{u,ave}$ values near the collective maximum for stress histories representative of critical stability conditions, but also yields reasonable anisotropic strength ratios, i.e. $s_{uTC} > s_{uDSS} > s_{uTE}$.

The above evidences clearly demonstrate the importance of undrained strength anisotropy, but also highlight the difficulty in selecting representative strengths to use in a stability analysis based on rigid plasticity.

4.3 Representation of Anisotropic Undrained Strength

For plane strain conditions, undrained failure of the clay is most commonly described by the isotropic Tresca failure criterion (cf. Chapter 2) and can be written in terms of principal stresses as:

$$F = \left| \frac{\sigma_1 - \sigma_3}{2} \right| - s_u = 0 \qquad (4.1)$$

where σ_1, σ_3 = the major and minor principal stresses

s_u = an undrained shear strength of clays

In terms of the Cartesian stress system, equation 4.1 can be re-written:

$$F = \left(\frac{\sigma_y - \sigma_x}{2} \right)^2 + \tau_{xy}^2 - s_u^2 = 0 \qquad (4.2)$$

where σ_x, σ_y = normal stresses in x and y directions, respectively

τ_{xy} = shear stress in the x-y axis

Equation 4.1 represents a circle in $[(\sigma_y-\sigma_x)/2, \tau_{xy}]$ stress space, with radius, s_u as shown in Figure 4.4. Strength isotropy implies that s_u is independent of the principal

stress orientation, δ (Fig. 4.4).

The directional shear cell (DSC, Arthur et al., 1977) is a plane strain, stress controlled device that is able to apply both normal and shear forces to four faces of a cubical sample and hence can control principal stress direction in the plane of loading. Figure 4.5 illustrates an idealized test procedure for using the DSC to evaluate the anisotropic stress-strain properties of clay in undrained shearing that developed due to a one-dimensional consolidation stress history. Soil specimens are first consolidated under K_0-conditions to the prescribed OCR (i.e. no lateral strains in the x-z plane) and are then sheared by imposing principal stress increments oriented at angle, δ_{inc}[1], to the original direction of deposition. Tests performed at $\delta_{inc} = 0°$ and 90° correspond to the undrained plane strain active (compression) and passive (extension) modes of shearing. Figure 4.6 shows the undrained strength envelope (at failure) for Boston Blue Clay (BBC) at OCR = 1.0 (Seah, 1990) and 4.0 (O'Neill, 1985). DSC tests are performed at δ = 0°, 45°, 60°, 75°, 90°, for OCR = 1.0 and δ = 0°, 20°, 40°, 65°, 75°, 90°. For both cases, the envelopes of undrained shear strengths $s_u(\delta)$ can be approximated by an elliptical locus. For OCR = 1.0 (Figure 4.6a), $s_u(\delta)/\sigma'_{vc}$ ranges from 0.34 (active) to 0.17 (passive). For OCR = 4.0 (Figure 4.6b), $s_u(\delta)/\sigma'_p$ ranges from 0.25 (active) to 0.15 (passive).

Figure 4.6 also includes the initial K_0-consolidation shear stress and the isotropic undrained strength envelope by Tresca yield criterion using s_{uDSS}[2]. For OCR = 1.0, there is a significant difference between isotropic and anisotropic strength envelopes and an inconsistency between the consolidation K_0 condition and the isotropic strength criterion, wherein the initial K_0-stress mobilizes a high shear stress than is permitted by the isotropic strength criterion. For OCR = 4.0, the clay becomes less anisotropic and K_0 stress is located inside the isotropic envelope.

The plane strain, undrained strength envelope of clays can be described by anisotropic yield using functions proposed by the following: Davis and Christian (1971);

---

[1]The angle δ can be prescribed at $K_0 = 1$, corresponding to OCR 4 (after Germaine, 1982; O'Neill, 1985). For tests with δ_{inc} = const, there is continuously rotation of the principal stress direction, δ.

[2]For OCR = 1.0, where $K_0 = 0.53$, and $s_{uDSS}/\sigma'_{vc} = 0.21$, initial stresses are: $(\sigma_y-\sigma_x)/2\sigma'_{vc} = 0.235$, $\tau_{xy}/\sigma'_{vc} = 0$. For OCR = 4.0, where $K_0 = 1.0$, and $s_{uDSS}/\sigma'_p = 0.16$, initial stresses are: $(\sigma_y-\sigma_x)/2\sigma'_p = \tau_{xy}/\sigma'_p = 0$.

Casagrande and Carrillo (1944); Bishop (1966); Hill (1950); and Yu and Sloan (1994). Figures 4.7-4.11 show schematically each of these yield graphical envelopes in $[(\sigma_y-\sigma_x)/2, \tau_{xy}]$ stress space.

4.3.1 Davis and Christian (1971)

Davis and Christian (1971) proposed a yield function representing an anisotropic strength envelope as:

$$F=\left(\frac{(\sigma_y-\sigma_x)/2-h}{a}\right)^2+\left(\frac{\tau_{xy}}{b}\right)^2-1=0 \tag{4.3a}$$

where $h = [s_u(0°)-s_u(90°)]/2$ (4.3b)

$a = [s_u(0°)+s_u(90°)]/2$

$$b=\frac{a\times s_u(45°)}{\sqrt{s_u(0°)\times s_u(90°)}}$$

and $s_u(0°)$, $s_u(45°)$, $s_u(90°)$ are the undrained strengths at δ = 0°, 45°, and 90°, respectively.

As shown in Figure 4.7, equation 4.3 describes an elliptical strength envelope, where h is the center of the ellipse, a and b are its major and minor semi-axes. Equation 4.3a can be rewritten in terms of undrained strength at any direction as (c.f. Whittle et al. 1994):

$$s_u(\delta)=\frac{c_1}{c_2}+\sqrt{\left(\frac{c_1}{c_2}\right)^2+\frac{s_u(0°)s_u(90°)}{c_2}} \tag{4.4}$$

where $c_1=\cos(2\delta)\sqrt{a^2-s_u(0°)s_u(90°)}$

$c_2=\cos^2(2\delta)+(a/b)^2\sin^2(2\delta)$

4.3.2 Casagrande-Carrilo (1944)

Undrained strength envelope proposed by Casagrande-Carrilo (1944) is given as:

$$s_u(\delta)=s_u(90°)+[s_u(0°)-s_u(90°)]\cos^2\delta \tag{4.5}$$

Figure 4.8 plots this envelope. The model requires only two parameters, $s_u(0°)$, and $s_u(90°)$ and inherently assumes that $s_u(45°) = [s_u(0°) + s_u(90°)]/2$. Thus, the accuracy

of this representation depends on the ratio of $s_u(0°)/s_u(90°)$ of real clays.

Note that equation 4.5 is similar to the anisotropic yield function proposed by Lo (1965).

4.3.3 Bishop (1966)

To account for the dependency in $s_u(45°)$, Bishop (1966) proposed a modification of Casagrande-Carrilo (1944)'s equation as:

$$s_u(\delta) = s_u(0°)(1 - m\sin^2\delta)(1 - n\sin^2 2\delta) \tag{4.6}$$

where $s_u(90°) = s_u(0°)(1 - m)$

$s_u(45°) = s_u(0°)(1 - m/2)(1 - n)$

Bishop's equation is very similar to an elliptical locus as illustrated in Figure 4.9. The equation requires 3 input parameters, $s_u(0°)$, $s_u(45°)$, and $s_u(90°)$ similar to Davis and Christian's (1971) equation. However, the latter gives a much simpler expression of anisotropic failure envelope in $[(\sigma_y-\sigma_x)/2, \tau_{xy}]$ stress space.

4.3.4 Hill (1950)

Hill (1950) proposed an anisotropic failure criterion for metal, which Scott (1963) recommended for clays as:

$$F = \frac{[(\sigma_y - \sigma_x)/2]^2}{1 - C} + \tau_{xy}^2 - T^2 = 0 \tag{4.7}$$

where C, T = constants

Hill's equation yields an ellipse, where the center is at the origin as shown in Figure 4.10. Thus, the major drawback of this model is that it implies $s_u(0°) = s_u(90°)$, which is contradicted by experimented results illustrated in Figures 4.1, 4.2 and 4.6.

4.3.5 Yu and Sloan (1994)

Yu and Sloan (1994) proposed an anisotropic strength based on an assumption that the cohesion for a given plane varies with direction as:

$$c(\theta) = c_h + (c_v - c_h)\sin^2\theta \tag{4.8}$$

where c_h, c_v = cohesion on the horizontal and vertical planes, respectively

θ = an angle orientation of a plane to the horizontal (see Figure 4.11)

They solved for the critical orientation angle, giving rise to the following anisotropic yield criterion as:

$$F = \left(\frac{\sigma_y - \sigma_x}{2} \right)^2 + \left(\tau_{xy} - (\frac{c_h - c_v}{2}) \right)^2 - \left(\frac{c_h + c_v}{2} \right)^2 = 0 \qquad (4.9)$$

Figure 4.11 shows that this equation is a circle whose center is on the τ_{xy} axis. This is contradicted by the results of DSC tests on K_0-consolidated BBC in Figure 4.6, where the undrained strength envelope is symmetrical in the plane, $\tau = 0$.

A suitable representation of undrained strength envelope must be able to distinguish between undrained strengths in different modes of shearing. Anisotropic strength envelope given by Yu and Sloan (1994) is completely uncorrelated with DSC results, while that given by Hill (1950) fails to differentiate between $s_u(0°)$ and $s_u(90°)$. Casagrande-Carrilo's (1944) equation is also inadequate because it implies that $s_u(45°) = [s_u(0°) + s_u(90°)]/2$. Thus, only the yield criteria proposed by Davis and Christian (1971) and Bishop (1966) are valid for representing the undrained strength anisotropy of K_0-consolidated BBC. Figure 4.12 shows that both functions fit very well with the undrained strength locus (failure) derived from DSC tests.

In this thesis, the author selects the anisotropic yield function proposed by Davis and Christian (1971) to implement in numerical limit analyses due to its simplicity in the $[(\sigma_y-\sigma_x)/2, \tau_{xy}]$ stress space.

4.4 Implementation of Anisotropic Undrained Strength Envelope

4.4.1 Lower Bound Implementation

Modification of the lower bound analysis to incorporate anisotropic yield is quite straightforward. For plane strain conditions with positive stresses in tension, the anisotropic yield criterion by Davis and Christian (1971) can be expressed as:

$$F = \left(\frac{q_{xy} - h}{a} \right)^2 + \left(\frac{\tau_{xy}}{b} \right)^2 - 1 = 0 \qquad (4.10)$$

where $q_{xy} = (\sigma_x - \sigma_y)/2$

$h = [s_u(0°)-s_u(90°)]/2$

$a = [s_u(0°)+s_u(90°)]/2$

$$b = \frac{a \times s_u(45°)}{\sqrt{s_u(0°) \times s_u(90°)}}$$

$s_u(0°)$, $s_u(45°)$, $s_u(90°)$ = undrained strengths when $\delta = 0°, 45°, 90°$

According to the lower bound theorem, the stress field must not violate this anisotropic yield criterion, and hence $F \leq 0$ at all points. Since the lower bound method is formulated as a linear programming problem, equation 4.10 must be linearized. In order to ensure that the solution obtained is a strict lower bound on the true collapse load, the actual anisotropic yield surface must circumscribe the linearized yield surface. The linearization is accomplished by transforming Davis and Christian (1971)'s yield criterion using the following variables:

$$X = \left(\frac{(\sigma_x - \sigma_y)/2 - h}{a} \right); \quad Y = \left(\frac{\tau_{xy}}{b} \right); \quad R = 1 \tag{4.11}$$

Thus, Davis and Christian (1971)'s yield criterion then becomes:

$$F = X^2 + Y^2 - R^2 = 0 \tag{4.12}$$

Equation 4.11 represents a circle in X, Y stress space, with radius R. The lower bound linearization is approximated by an interior polygon with p sides and p vertices as shown in Figure 4.13. The convexity of linearized anisotropic yield criterion generates a set of inequality constraints as:

$$F_k = A_k\sigma_x + B_k\sigma_y + C\tau_{xy} - D_k \leq 0 \quad , k = 1,2,...,p \tag{4.13}$$

where $A_k = \cos(2\pi k/p)$; $B_k = -\cos(2\pi k/p)$ (4.14)

$C_k = 2(a/b)\sin(2\pi k/p)$; $D_k = 2a\cos(\pi/p) + 2h\cos(2\pi k/p)$

p = the number of linearized planes

Note that the same coefficients A_k, B_k and C_k are also applied for triangular and extension elements.

4.4.2 Upper Bound Implementation

To implement an anisotropic yield criterion in the upper bound method, modifications are required for the plastic flow and internal work dissipation associated with the anisotropic yield criterion in the triangular elements and along the velocity discontinuities.

4.4.2.1 Modifications in Triangular Elements

In order to ensure that the solution obtained is a strict upper bound on the true collapse load, the linearized yield function must circumscribe the actual yield one. Thus, the transformed Davis and Christian (1971)'s criterion according to equation 4.12 is approximated by an exterior polygon with p sides and p vertices, shown in Figure 4.14. The convexity of external linearized yield function can be expressed as:

$$F_k = A_k\sigma_x + B_k\sigma_y + C\tau_{xy} - D_k = 0 \quad , k = 1,2,...,p \tag{4.15}$$

where $A_k = \cos(2\pi k/p)$; $B_k = -\cos(2\pi k/p)$ (4.16)

$C_k = 2(a/b)\sin(2\pi k/p)$; $D_k = 2a + 2h\cos(2\pi k/p)$

p = the number of linearized planes

F^k = the k^{th} side of external linearized yield function

The first modification for plastic flow is to apply the linearizing coefficients A_k, B_k, and C_k to the compatibility and associated flow equation given by:

$$\dot{\varepsilon}_x = \sum_{k=1}^{p} \dot{\lambda}_k \frac{\partial F_k}{\partial \sigma_x} = \sum_{k=1}^{p} \dot{\lambda}_k A_k \tag{4.17}$$

$$\dot{\varepsilon}_y = \sum_{k=1}^{p} \dot{\lambda}_k \frac{\partial F_k}{\partial \sigma_y} = \sum_{k=1}^{p} \dot{\lambda}_k B_k$$

$$\dot{\gamma}_{xy} = \sum_{k=1}^{p} \dot{\lambda}_k \frac{\partial F_k}{\partial \tau_{xy}} = \sum_{k=1}^{p} \dot{\lambda}_k C_k$$

where $\dot{\lambda}_k$ is the non-negative plastic multiplier rates associated with F_k

The second modification is to modify the calculation of internal power dissipation in each triangular element as follows:

$$
\begin{aligned}
W_{ele} &= \int_A (\sigma_x \dot{\varepsilon}_x + \sigma_y \dot{\varepsilon}_y + \tau_{xy} \dot{\gamma}_{xy}) dA \\
&= \int_A \sum_{k=1}^{p} [\dot{\lambda}_k (A_k \sigma_x + B_k \sigma_y + C_k \tau_{xy})] dA \\
&= \int_A \sum_{k=1}^{p} [\dot{\lambda}_k D_k] dA \\
&= A \sum_{k=1}^{p} [\dot{\lambda}_k D_k]
\end{aligned}
\tag{4.18}
$$

where A = the area of each triangular element

4.4.2.2 Modifications in Velocity Discontinuities

Consider the discontinuity which is defined by nodal pairs (i,j) as shown in Figure 4.15 (e.g. nodes (1,2) and (3,4)), the velocity jump in any direction with respect to node i is equal to the velocity of node j minus that of node i in the same direction. Therefore, the tangential and normal velocity jumps of nodal pair (i,j) are defined by (c.f. equation 2.18):

$$\Delta u_{ij,t} = (u_j - u_i) \cos\theta + (v_j - v_i) \sin\theta \tag{4.19}$$

$$\Delta u_{ij,n} = -(u_j - u_i) \sin\theta + (v_j - v_i) \cos\theta \tag{4.20}$$

where

$\Delta u_{ij,t}$, $\Delta u_{ij,n}$ = the tangential and normal velocity jumps between nodal pairs (i, j)

u_i, u_j = nodal velocities in x-direction of nodes i and j, respectively

v_i, v_j = nodal velocities in y-direction of nodes i and j, respectively

θ = the angle of the discontinuity to the x-axis measured in a positive anticlockwise direction

According to the upper bound theorem, the tangential and normal velocity jumps must be associated with the anisotropic yield function corresponding to the local t-n axis (Fig. 4.15). Recalling Davis and Christian's (1971) yield criterion:

$$F = \left(\frac{q_{xy} - h}{a} \right)^2 + \left(\frac{\tau_{xy}}{b} \right)^2 - 1 = 0 \tag{4.10, bis}$$

where $q_{xy} = (\sigma_x - \sigma_y)/2$

$h = [s_u(0°) - s_u(90°)]/2$

$a = [s_u(0°) + s_u(90°)]/2$

$$b = \frac{a \times s_u(45°)}{\sqrt{s_u(0°) \times s_u(90°)}}$$

Deviatoric stress (q_{xy}) and shear stress (τ_{xy}) in the x-y axis can be related to those in the t-n axis as:

$$q_{xy} = q_{tn}\cos 2\theta - \tau_{tn}\sin 2\theta \tag{4.21}$$

$$\tau_{xy} = q_{tn}\sin 2\theta + \tau_{tn}\cos 2\theta$$

where $q_{tn} = (\sigma_{tt} - \sigma_{nn})/2$

σ_{tt}, σ_{nn} = normal stresses in t and n directions, respectively

τ_{tn} = shear stress in the t-n axis

Substituting equation 4.21 into 4.10 gives the anisotropic yield criterion in terms of stresses in the t-n axis as:

$$F = \left(\frac{q_{tn}\cos 2\theta - \tau_{tn}\sin 2\theta - h}{a}\right)^2 + \left(\frac{q_{tn}\sin 2\theta + \tau_{tn}\cos 2\theta}{b}\right)^2 - 1 = 0 \tag{4.22}$$

In (q_{tn}, τ_{tn}) stress space, equation 4.22 represents an ellipse rotated 2θ anti-clockwise with the q_{tn} (or τ_{tn}) axis, as illustrated in Figure 4.16a.

The associated flow rule at the velocity discontinuity are given by:

$$\frac{(\dot{\varepsilon}_{tt} - \dot{\varepsilon}_{nn})}{2} = \dot{\lambda}\frac{\partial F}{\partial q_{tn}} \tag{4.23a}$$

$$\Delta u_t = \dot{\lambda}\frac{\partial F}{\partial \tau_{tn}} \tag{4.23b}$$

where Δu_t = tangential velocity jump or slip

$\dot{\varepsilon}_{tt}$, $\dot{\varepsilon}_{nn}$ = normal strain rates in the t and n directions

Along velocity discontinuity, the normal velocity jump, Δu_n must be equal to zero due to undrained conditions (incompressibility), giving rise to the following constraints:

$$\Delta u_{ij,n} = \dot{\varepsilon}_{nn} = 0 \tag{4.24a}$$

$$\dot{\varepsilon}_{nn} + \dot{\varepsilon}_{tt} = 0 \;\; ; \dot{\varepsilon}_{tt} = 0 \tag{4.24b}$$

$$\frac{(\dot{\varepsilon}_{tt} - \dot{\varepsilon}_{nn})}{2} = 0 \tag{4.24c}$$

Thus, the flow direction at the velocity discontinuity must be equal to the tangential velocity jump or slip (Δu_t) whose direction is parallel to the τ_{tn} axis, as shown in Figure 4.16a. It can be seen that there are two possible points which can satisfy this condition. Point 1, where $\tau_{tn} = |\tau_1|$, corresponds to the slip in the positive direction, while Point 2 where $\tau_{tn} = -|\tau_2|$, corresponds to the slip in the negative direction. Figure 4.16b shows the positive sign convention of the slip at a velocity discontinuity. For a given orientation of velocity discontinuity, the magnitudes of τ_1 and τ_2 can be found as:

$$|\tau_1| = \left| h\sin 2\theta - \sqrt{\frac{a^2+b^2-a^2\cos 4\theta+b^2\cos 4\theta}{2}} \right| \tag{4.25}$$

$$|\tau_2| = \left| h\sin 2\theta + \sqrt{\frac{a^2+b^2-a^2\cos 4\theta+b^2\cos 4\theta}{2}} \right|$$

Two yield envelopes associated with point 1 and 2 are:

$$\text{Point 1 :} \qquad F_1 = \tau_{tn} - |\tau_1| = 0 \tag{4.26}$$

$$\text{Point 2 :} \qquad F_2 = -\tau_{tn} - |\tau_2| = 0$$

Thus, the flow direction of these yield envelopes are given by:

$$\Delta u_t = \Sigma \dot{\lambda}_i \frac{\partial F_i}{\partial \tau_{tn}} = \dot{\lambda}_1 - \dot{\lambda}_2 \tag{4.27}$$

$$\Delta u_n = 0$$

where $\dot{\lambda}_1$, $\dot{\lambda}_2$ = non-negative plastic multiplier rates associated with the yield envelope, F_1 and F_2, respectively

The internal dissipation of work along the velocity discontinuity are given by:

$$\begin{aligned} W_{dis} &= \int_0^L \tau_{tn}\Delta u_t dt \\ &= \int_0^L \tau_{tn}(\dot{\lambda}_1 - \dot{\lambda}_2)dt \\ &= \int_0^L (|\tau_1|\dot{\lambda}_1 + |\tau_2|\dot{\lambda}_2)dt \end{aligned} \tag{4.28}$$

where L = the length of the discontinuity, and $0 \le t \le L$

The physical interpretation of equations 4.27 and 4.28 is that only tangential velocity jumps (Δu_t) can occur along interface between elements ($\Delta u_n = 0$). However, there is no restriction on the sign of the tangential velocity on either side of the discontinuity ($\Delta u_t > 0$ or $\Delta u_t < 0$ or $\Delta u_t = 0$). The calculation of plastic dissipation per unit shear then varies with the direction of slip according to:

For $\Delta u_t > 0$, $|\tau_{tn}| = |\tau_1|$ $\qquad W_{dis} = \int_0^L |\tau_1| \Delta u_t dt$ (4.29a)

For $\Delta u_t < 0$, $|\tau_{tn}| = |\tau_2|$ $\qquad W_{dis} = \int_0^L |\tau_2| \Delta u_t dt$ (4.29b)

Internal dissipation of work along discontinuity is zero ($W_{dis} = 0$) if there is no slip ($\Delta u_t = 0$). It can be seen that at a velocity discontinuity, the mechanical behavior of anisotropic clay is completely different from that of isotropic clay, where the shear stress on the slip plane, $|\tau_{tn}|$ corresponds to the undrained shear strength, s_u, regardless of slip direction and its orientation.

The above results can be further illustrated by looking at the undrained strength envelope (failure) of normally consolidated BBC (OCR = 1.0, Fig. 4.5a). The three parameters defining Davis and Christian (1971)'s yield criterion are: $s_u(0°)/\sigma'_{vc} = 0.34$, $s_u(45°)/\sigma'_{vc} = 0.23$, $s_u(90°)/\sigma'_{vc} = 0.17$ ($h/\sigma'_{vc} = 0.085$, $a/\sigma'_{vc} = 0.255$, $b/\sigma'_{vc} = 0.244$). Figure 4.17 plots the magnitude of shear stress, $|\tau_{tn}|$ along the slip plane as a function of the orientation of discontinuity, according to equation 4.25. $|\tau_{tn}| = |\tau_1|$ when $\Delta u_t > 0$, while $|\tau_{tn}| = |\tau_2|$ when $\Delta u_t < 0$. Note that for $\theta = 0°$ and 90°, $|\tau_{tn}| = |\tau_1| = |\tau_2| = b = s_u(\delta = 40.11°)$, regardless of slip direction.

Figures 4.18a, b show slip along discontinuities oriented at $\theta = 45°$ and 135°, respectively. For each orientation, there are two possible slip directions. Slip directions in Figures 4.18ai and 4.18bi correspond to the passive failure, where $|\tau_{tn}| = s_u(90°)$, while those in Figures 4.18aii and 4.18bii correspond to the active failure, where $|\tau_{tn}| = s_u(0°)$. Using the graph in Figure 4.17 and the positive sign convention for Δu_t in Figure 4.16b, it can be seen that the value of $|\tau_{tn}|$ on the slip plane is determined correctly with its corresponding slip direction for all cases. Hence, these examples verify equations 4.27

and 4.28.

The flow direction constraints (eqn. 4.27) are applied at nodal pairs (i, j) of each velocity discontinuity as: (c.f. 4.19 and 4.20):

$$\Delta u_{ij,t} = (u_j - u_i)\cos\theta + (v_j - v_i)\sin\theta = \dot{\lambda}_{(i,j),1} - \dot{\lambda}_{(i,j),2} \qquad (4.30)$$

$$\Delta u_{ij,n} = -(u_j - u_i)\sin\theta + (v_j - v_i)\cos\theta = 0$$

where $\dot{\lambda}_{(i,j),1}, \dot{\lambda}_{(i,j),2}$ are the plastic multiplier rates associated with F_1, and F_2 at nodal pairs (i, j) (F_1, F_2 defined in Fig. 4.16)

Since the tangential velocity field varies linearly along the discontinuity, the term, $\dot{\lambda}_1$, and $\dot{\lambda}_2$ also follow the same linear variation and can be expressed as:

$$\dot{\lambda}_1 = \dot{\lambda}_{(1,2)1}(1 - t/L) - \dot{\lambda}_{(3,4)1}(t/L) \qquad (4.31a)$$

$$\dot{\lambda}_2 = \dot{\lambda}_{(1,2)2}(1 - t/L) - \dot{\lambda}_{(3,4)2}(t/L)$$

where $\dot{\lambda}_{(1,2),1}, \dot{\lambda}_{(1,2),2}$ are the plastic multiplier rates associated with F_1, and F_2 at nodal pairs (1,2)

$\dot{\lambda}_{(3,4),1}, \dot{\lambda}_{(3,4),2}$ are the plastic multiplier rates associated with F_1, and F_2 at nodal pairs (3,4)

Substituting these two equations into 4.28 and integrating, the power dissipated in each discontinuity can be found:

$$W_{dis} = (L/2)|\tau_1|(\dot{\lambda}_{(1,2),1} + \dot{\lambda}_{(3,4),1}) + (L/2)|\tau_2|(\dot{\lambda}_{(1,2),2} + \dot{\lambda}_{(3,4),2}) \qquad (4.31b)$$

Equations 4.29 and 4.31b represents the modifications necessary to include the proposed anisotropic yield criterion along velocity discontinuities in the upper bound formulation.

4.5 Mobilization of Anisotropic Shear Undrained Strength for BBC

Figure 4.19 summarizes the undrained shear stress-strain behavior measured in laboratory directional shear cell tests on K_0-normally consolidated BBC (after Seah, 1990). It can be seen that there are large differences in the strain required to mobilize the peak undrained strength for different directions of shearing. For example, in the compression mode, the peak strength is mobilized at a small strain, $\gamma \approx 0.6\%$. In contrast,

for $\delta = 0°$, the shear strain required to mobilize peak shear strength, $\gamma > 6$-7%. Therefore, it is clear that a complete constitutive model of anisotropic stress-strain response (such as MIT-E3; Whittle and Kavvadas, 1994) will be able to simulate progressive failure associated with different rates of strength mobilization. The effects of these anisotropic stress-strain properties can be approximated in the numerical limit analyses by assuming that failure mechanisms can be characterized by uniform mobilization of shear strain (strain compatibility approach, Ladd, 1991). In this approach, anisotropic shear resistance is represented by yield surfaces at selected shear strain level. For example, Figure 4.20 compares the yield surfaces corresponding to a) peak undrained shear strength, and b) $\gamma =$ 0.6% and 1.0% iso-shear strain. The case $\gamma = 0.6\%$ corresponds (approximately) to the strain required to mobilize the maximum undrained shear strength ratio (in compression), while $\gamma = 1\%$ represents the average shear strain observed in finite element analyses of deep excavation stability (Hashash and Whittle, 1996).

Table 4.1 summarizes mobilized shear resistance at $\gamma = 0.6$ %, 1.0%, and the peak undrained strength ratios using the proposed Davis and Christian (1971) yield criterion. For each strain level, strength ratios are selected such that $s_u(0°) > s_u(45°) > s_u(90°)$, according to Ladd (1991)'s recommendation. For $\delta = 0°$, there is very small strain softening after reaching the peak resistance when $\gamma < 1.0\%$; hence, it is assumed that $s_u(0°)$ corresponding to those strain levels are the same as its peak strength. Figure 4.20 shows that Davis and Christian (1971) yield criterion fits very well with the undrained strength envelope obtained from DSC tests. These strength ratios will be used to study the effects of anisotropic strength to collapse loads for two examples in subsequent sections.

4.6 Anisotropic Bearing Capacity of Surface Strip Footings

This section evaluates the implementation of anisotropic undrained strength envelope in evaluating the bearing capacity of a rigid strip footing. The exact collapse loads for a smooth rigid footing on an anisotropic clay have been solved by the method of characteristics (Davis and Christian, 1971), leading to a revised bearing capacity factor, N'_c as:

$$q = N'_c\left(\frac{s_u(0°)+s_u(90°)}{2}\right) \tag{4.32}$$

where N'_c is a function of $b/a = s_u(45°)/\sqrt{s_u(0°)s_u(90°)}$ as shown in Figure 4.21. When b = a, N'_c reduces to the conventional Prandtl solution, $N'_c = N_c = 2 + \pi$. The stress and velocity characteristics used by Davis and Christian (1971) for the bearing capacity problem are shown in Figure 4.21a. The construction of the characteristics for the anisotropic case is very similar to that for the isotropic case (Prandtl, 1920).

Numerical limit analyses have been carried out for a footing on homogeneous clay with anisotropic undrained strength ratios given in Figure 4.20 at γ = 0.6%, 1.0% and peak strength (Table 4.1). In addition, the analyses also consider smooth and rough interface conditions. Figures 4.22a and b show the meshes used in the numerical lower bound and upper bound analyses. Due to symmetry, only one-half of the problem is represented in the analyses. Table 4.2 summarizes the bearing capacity factors, $N_c = Q/[Bs_{uDSS}]$, where B is the width of the footing, s_{uDSS} = the undrained shear strength of clays from CK_0UDSS tests, and $s_{uDSS}/\sigma'_{vc} = 0.21$, for normally consolidated BBC. The results show the following:

1. For isotropic and all anisotropic cases, the lower and upper bound solutions bracket the true collapse pressure within an accuracy of ±3-4%. The error in predicting the collapse pressure (the average of both lower and upper bounds) is less than 2%. There is an excellent agreement between the numerical limit solutions and the analytical results of Davis and Christian (1971).
2. For both isotropic and anisotropic strengths, the lower bound analyses predict that the collapse pressure of smooth footings is identical to that of rough footings, while the upper bound analyses predict very small differences in collapse pressure between smooth and rough footings.
3. For the anisotropic peak strength, the bearing capacity increases by about 20%, compared to the isotropic case based on capacity calculations using the direct simple shear tests as the reference strength. In comparison, mobilized shear resistance parameters at γ = 0.6%, 1% generates a 15% and 4% reductions in bearing capacity, respectively, compared to the isotropic capacity.

These results suggest that the isotropic and anisotropic bearing capacity solutions match at a mobilized shear strain slightly higher than 1%. In comparison, experiments on model footings show settlement ratios, s/B ≈ 30 – 40% are required to mobilize the undrained strength capacity (Kenny and Andrawes, 1997). This indicates that the maximum shear strain that is necessary to cause failure of footings should be significantly higher than 1%, and hence the mobilized shear resistance parameter at 1% provides a conservative estimate of bearing capacity on anisotropic clays.

Figures 4.23 and 4.24 show the failure mechanism, velocity field and plastic zone of the upper bound analyses for a smooth footing. It can be seen that those results for anisotropic cases at different strain levels are very similar to those for isotropic case. Figure 4.25 and 4.26 compare the contours of the major principal stress, σ_1, and its orientation to the vertical, δ, from the lower bound analyses of isotropic and anisotropic cases. For both cases, the stress field can be divided into three zones (Figure 4.26). The first zone corresponds to the active failure occurring beneath footings, where $\delta = 0°$. The second zone forms a radial shear fan around the edge of the footing, where the major principal stress rotates from the vertical to the horizontal direction ($\delta = 0° \rightarrow 90°$). The third zone consists of passive shearing extending along a line at 45° from the edge of the footing to the ground surface, where $\delta = 90°$. Even though those zones of isotropic case are similar to those of anisotropic case, there are significant differences in the magnitude and distribution of σ_1 (Figure 4.25) due to different mobilized shear resistance for each mode of shearing. Figure 4.27 shows the contact pressure beneath the footings. For isotropic and all anisotropic cases, these results indicate that the lower bound analyses correctly predict a uniform contact pressure beneath the footing with the magnitude very close to the exact solutions given by Davis and Christian (1971).

Figures 4.28 through 4.31 illustrate the upper and lower bound results for rough footings. Similarly, there is very small difference in the failure mechanism, velocity field and plastic zone between isotropic and all anisotropic cases. Note that even though the upper bound analyses predict a very small difference in the collapse pressure between smooth and rough footings, there are significant differences in those results. Slip only occurs when there is a smooth interface between the footing and the soil. The principal

stress contours between isotropic and anisotropic cases are similarly as described earlier.

The excellent agreement in the collapse pressure between numerical limit analyses and Davis and Christian (1971)'s solutions validates the proposed development of anisotropic undrained strength in numerical limit analyses.

4.7 Ultimate Undrained Lateral Resistance of Deeply-Embedded Sections

This section applies numerical limit analyses for computing the undrained lateral resistance of deeply-embedded sections in clay. Figure 4.32 shows the problem definition. The analyses consider three cross sections: 1) centrally-loaded flat plate; 2) diagonally-loaded square section; and 3) a pipe section. The analyses assume that sections are long and embedded within a deep clay layer. Hence, the stability calculations assume plane strain conditions within a full space of clay. Each section is also assumed to be rigid so that there is no plastic failure of the structure (in bending, axial or shear). Isotropic strength conditions can be assumed where the plane of shearing is normal to the direction of deposition (K_0-consolidation).

The ultimate lateral capacity can be written as:

$$N_p = P/(s_u D) \tag{4.33}$$

where P is the applied lateral load, D is the characteristic dimension (Figure 4.32), and s_u is the undrained shear strength of clay

Analytical solutions of the ultimate lateral resistance of sections were reported by Broms (1964) as shown in Figure 4.33. Plate sections give the largest ultimate lateral resistance, followed by pipe and square sections. In addition, the collapse load for rough surfaces is generally larger than that of smooth surfaces. It should be noted that the ultimate lateral resistance in the figure may not represent the exact solutions since they were derived from the assumed slip line pattern.

For pipe sections, Randolph and Houlsby (1984) obtained analytical lower and upper bound solutions by the method of characteristics as illustrated in Figures 4.34a, b. They reported the exact solution as:

$$N_p = \pi + 2\Delta + 4\cos\left(\frac{\pi}{4} - \frac{\Delta}{2}\right)\left(\sqrt{2} + \sin\left(\frac{\pi}{4} - \frac{\Delta}{2}\right)\right) \tag{4.34}$$

where $\sin\Delta = f_s/s_u$ is interface roughness ratio

f_s is the limiting shear stress at the interface

There is an error in the derivation of upper bound solutions by Randolph and Houlsby (1984), which includes some negative work in all values of f_s/s_u except the fully rough pipe (i.e. f_s/s_u = 1) (Randolph, Pers. Comm., 1998). Thus, equation 4.34 corresponds only for lower bound solutions. Figure 4.34c show their analytical lower and corrected upper bound solutions for pipe sections for all interface roughness ratios, f_s/s_u = 0 – 1. Generally, the differences between their lower and upper bound solutions are less than ±2%. Both solutions only coincide for the fully rough cases (f_s/s_u = 1.0). The ultimate lateral resistance of pipe sections ranges from 9 for smooth surface (f_s/s_u = 0) to 12 for rough surface (f_s/s_u = 1.0). Notice that for smooth surfaces, the lateral resistance of pipe given by Broms (1964) is identical to the lower bound solution by Randolph and Houlsby (1984).

4.7.1 Results of Numerical Limit Analyses

The analyses first consider the case of isotropic strength and the effects of surface roughness of sections. The studies are then extended for the case of vertical penetration where undrained strengths are anisotropic and results are presented for mobilized strain levels, γ = 0.6%, 1.0%, and at peak strength (Table 4.1). Figures 4.35-4.37 show the lower and upper bound meshes used to analyze each of the three section geometries. Due to symmetry, only one-half of each problem is represented in the analyses. To simulate the infinite full space, the lower bound analyses are performed with extension elements all around the boundary, while the upper bound analyses are performed with larger discretized domains to ensure that zero boundary velocities (u, v) do not affect the computed upper bound limit loads. The structural sections are simulated using rigid structural elements.

Table 4.3 summarizes the computed ultimate lateral resistance of sections, N_p in the isotropic clay[3]. The lower and upper bound solutions bracket the true collapse load to within 3% for plate sections, 4% for square sections, and 4-8% for pipe sections. For all

[3]These results apply for cases of lateral loading of K_0-consolidated soils in the horizontal plane.

cases except rough surfaces of plate sections, the ultimate lateral capacity given by Broms (1964) and Randolph and Houlsby (1984) fall in between the computed lower and upper bound solutions, again confirming the quality of the numerical limit predictions. The upper bound analysis of the rough plate (Broms, 1964) uses an approximate field and hence represents an upper bound on the true collapse load which is less accurate than the present calculations.

Figure 4.38 and Table 4.4 summarize the effects of surface roughness on the computed ultimate lateral capacity of pipe sections. There is excellent agreement between the computed N_p by numerical limit analyses and analytical solutions by Randolph and Houlsby (1984). The figure shows that the load factor, N_p increases by about 30% as the interface strength ratio, f_s/s_u increases from 0 (smooth) to 1 (fully adhesive).

4.7.2 Results of Plate Sections

Figures 4.39 compares the upper bound results of plate sections with smooth and rough interfaces, respectively. Although, the difference in collapse loads for these two cases is very small, there are important differences in the predicted failure mechanisms. The rough surface generates a larger failure zone in the soil, and also forms a rigid body displacement of the plate and attached rectangular zone of soil. For smooth surfaces, the soils in the front face of the plate slips outward toward the edge of the plate, while material on the back side (unloading) slips inwards center. For both cases, there is a radial shear fan around the edge of the plate bounded by lines extending ±45° from the edge to the centerline. Note that the slip line pattern reported by Broms (1964) in Figure 4.33 agrees very well with the upper bound velocity fields for the smooth interface, but does not correspond closely with the results for the rough surface. This explains why N_p of plate sections by Broms (1964) for rough surfaces is higher than N_p by the numerical upper bound analysis.

Figures 4.40 and 4.41 show contours of the major principal stresses for smooth and rough surfaces, respectively. The soil in the front contact undergoes the active failure ($\delta = 0°$), while that below the rear surface undergoes passive failure ($\delta = 90°$); Figures 4.40c, 4.41c. In both cases, the stress field is characterized by three radial shear fans,

where δ = 0° -> 90°, 90° -> 0°, and 0° -> 90° moving from the front to the rear of the plate. It can be seen that the contour of δ is anti-symmetric about a horizontal line extending from the edge of the plate. For both cases, the major principal stress reduces from $\sigma_1/s_u = 6$ on the front side to -3 on the rear surface, while the minor principal stress decreases from $\sigma_3/s_u = 4$ to -5. Figure 4.42 shows the contact stress distribution on both sides of the plate. The lower bound analysis predicts that normal traction is nearly constant along both surfaces for smooth surfaces. The contact normal traction on the rear surface is tensile, with the average magnitude of 5.1, which is equal to the Terzaghi bearing capacity. On the other hand, that on the front side is a compressive stress with the average value of 6. For rough surfaces, the shear resistance is not fully mobilized ($|\tau|/s_u \leq 1.0$) on either side of the plate and thus, no slip takes place. This result corresponds by the upper bound analysis described earlier.

4.7.3 Results of Square Sections

Figures 4.43a and b show the upper bound results for square sections with rough and smooth interfaces. The velocity field and failure mechanisms show large differences depending on interface roughness. The rough interface generates a much larger zone of soil distortion than the smooth case, as illustrated by their plastic zones. The effect of roughness can also be seen by the direction of soil movement along the contact surfaces. The soil along both edges of the square sections moves almost normal to the rough interface, but displaces laterally for the smooth surface. For both cases, there is a net downward displacement of soil along both edges. Notice that for rough surfaces, the upper bound velocity field for the square sections is very similar to previous results for the plate section (Figure 4.39a). The velocity field from numerical upper bound analyses for both cases correspond very well with the slip line solutions given by Broms (1964) (see Figure 4.34).

Figures 4.44 - 4.46 summarize the lower bound results for square sections. There are significant differences in the directions and magnitude of the major principal stress for smooth and rough surfaces. Notice that there is the symmetry between the major and minor principal stresses on the front and rear edges of the section.

Smooth surfaces: $\sigma_1/s_u = 4$ (front) -> -2 (back), $\sigma_3/s_u = 2$ (front) -> -4 (back)

Rough surfaces: $\sigma_1/s_u = 5.5$ (front) -> -3.5 (back) , $\sigma_3/s_u = 3.5$ (front)-> -5.5 (back)

The difference in N_p between smooth and rough surfaces is best illustrated by the contact tractions in Figure 4.46. For both cases, the lower bound analyses predict almost constant normal stress on both edges of the square section, with magnitude of $\sigma_n/s_u = 4.6$. The normal traction on the front edge is compressive, while that on the back edge is tensile. The higher N_p for rough surfaces results from the presence of downward shear tractions, where $|\tau|/s_u \approx 1.0$ on both edges. These downward shear forces generate an additional lateral resistance of sections. Note that $|\tau|/s_u$ -> 1.0 suggests that the slip between soil and section will take place, which accords with the upper bound results described previously.

4.7.4 Results of Pipe Sections

Figure 4.47 illustrates the upper bound results for pipe sections. As expected, rough surfaces produce a much larger plastic zone than smooth surfaces. There is also a significant difference in velocity field between these two cases, particularly along the pipe-soil interface. Note that the velocity characteristics given by Randolph and Houlsby (1984) shown in Figure 4.34 agree very well with the velocity field from the numerical upper bound calculation for both interfaces. Figures 4.48 and 4.49 show the lower bound contours of major and minor principal stresses and their directions for rough and smooth surfaces, respectively. The direction of major principal stress (δ) rotates around the mid points of the pipe for rough surfaces, but it points to the center of the pipe for smooth surfaces. Figure 4.50 compares the contact normal and shear tractions for smooth and rough surfaces. The results show that the upper half of the pipe experiences large compressive pressure with $\sigma_n/s_u \approx 6.7$ (crown) to 3.9 (center); and tensile pressure $\sigma_n/s_u \approx$ -1.8 (center) to -4.8 (bottom). For rough surfaces, the shear traction, τ/s_u builds up from 0 (crown) to 1.0 (center) and decreases to 0 (bottom). The presence of downward shear traction results in a higher lateral resistance for the rough interface analysis.

4.7.5 Results of Analyses for Anisotropic Undrained Strength of Clays

Numerical limit analyses have been performed for sections embedded in a clay layer with undrained strengths anisotropy using parameters for BBC at OCR = 1.0. The analyses include calculations based on peak strength and mobilized strength at $\gamma = 0.6\%$, 1.0% (see Table 4.1), and the results are summarized in Table 4.5. These calculations correspond to limiting pressures on vertically loaded sections in K_0-consolidated deep clay layers. Note that the lateral resistance for all cases is normalized by the undrained shear strength from the direct simple shear test, where $s_{uDSS}/\sigma'_{vc} = 0.21$. The lower and upper bound solutions bracket the true collapse load to within 4% for plate sections, 7% for square sections, and 8% for pipe sections. Generally, numerical limit analyses predict that the ultimate lateral capacity for anisotropic strengths reduces by about 15-20% for $\gamma =$ 0.6%, and 5% for $\gamma = 1$ % from the isotropic case, but increases by 15-20% for peak strength.

Figures 4.51 - 4.59 compares upper and lower bound results between isotropic and peak anisotropic strengths for plate, square and pipe sections. Generally, there is no difference in predicted upper bound failure mechanisms between anisotropic strength and isotropic strengths (e.g. Figures 4.51, 4.54, 4.57). In contrast, the lower bound results (Figures 4.53, 4.56, 4.59) show that the magnitude of contact shear and normal tractions along sections for peak anisotropic strength is typically higher than the isotropic case, giving rise to a higher lateral resistance of the former. The larger magnitude of tractions is mainly due to the a substantial shear resistance for compression mode of shearing [$s_u(0°)/\sigma'_{vc} = 0.34$), compared to the direct simple shear mode [$s_{uDSS}/\sigma'_{vc} = 0.21$].

4.8 References

Arthur, J. R. F., Chua, K. S., and Dunstan, T. (1977). "Induced anisotropy in a sand." Géotechnique, 37(1), 1-25.

Bishop, A. W. (1966). "The strength of soils as engineering materials." Géotechnique, 16(2), 89-130.

Broms, B. B. (1964). "Lateral Resistance of Piles in Cohesive Soils." J. Soil Mech. Found. Div., ASCE, 90(2), 27-63.

Casagrande, A., and Carrillo, N. (1944). "Shear failure of anisotropic soils." Contribution to Soil Mechanics, BSCE, 1941-1953, 122-135.

Davis, E. H., and Christian, T. J. (1971). "Bearing capacity of anisotropic cohesive soil". J. Soil Mech. Found. Div., ASCE, 97(5), 753-769.

Germaine, J. T. (1982). "Development of the directional shear cell for measuring cross-anisotropic clay properties." ScD thesis, Massachusetts Inst. of Tech., Cambridge, Mass.

Hill, R. (1950). The mathematical theory of plasticity. Clarendon Press, Oxford, 317-340.

Kenny, M. J., and Andrawes, K. Z. (1966). "The bearing capacity of footings on a sand layer overlying soft clay" Géotechnique, 47(2), 339-345.

Ladd, C. C. (1987). "Characteristics and engineering properties of Northeastern varved clay." Notes for Foundations and Soil Mechanics Group, Metropolitan Section of ASCE, New York, N.Y.

Ladd, C. C. (1975). "Foundation design of embankments constructed on Connecticut Valley varved clays." Research Report R75-7, Dept. of Civil Engrg., MIT, Cambridge, MA, 439 p.

Ladd, C. C. (1991). "Stability evaluation during staged construction." The Twenty-Second Terzaghi Lecture, J. of Geotech. Engrg. Div., ASCE, 117(4), 537-615.

Lo, K. Y. (1965). "Stability of slopes in anisotropic soils." J. Soil Mech. Found. Div., ASCE, 91(4), 85-106.

O'Neill, D. A. (1985). "Undrained shear anisotropy of an overconsolidated thixotropic clay." SM thesis, Massachusetts Inst. of Tech., Cambridge, Mass.

Prandtl, L. (1920). Über die Harte plastischer Körper. Nachr. K. Ges. Wiss. Gott., Math-Phys. Kl., 74-85.

Randolph and Houlsby (1984). "The limiting pressure on a circular pipe loaded laterally in cohesive soil." Géotechnique, 34(4), 613-623.

Seah, T. H. (1990) . "Anisotropy of normally consolidated Boston blue clay.", ScD thesis, Massachusetts Inst. of Tech., Cambridge, Mass.

Scott, R. S. (1963). Principles of soil mechanics. Addison-Wesley Publishing Co., Reading, Massachusetts, p 440.

Hashash, Y.M.A, and Whittle, A. J (1992). "Analysis of braced diaphragm walls in deep deposits of clay." Res. Rep. R92-19, Dept. of Civil. Engrg., Massachusetts Inst. of Tech., Cambridge, Mass.

Whittle, A. J., and Kavvadas, M. J. (1994). "Formulation of the MIT-E3 constitutive model for overconsolidated clays" J. of Geotech. Engrg. Div., ASCE, 120(1), 173-198.

Whittle, A. J., DeGroot, D. J., Ladd, C. C., and Seah, T. H. (1994). "Model prediction of anisotropic behavior of Boston Blue Clay " J. of Geotech. Engrg. Div., ASCE, 120(1), 199-224.

Yu. H. S. and Sloan, S. W. (1994). "Limit analysis of anisotropic soils using finite elements and linear programming.", Mech. Research Commun., 21(6), 545-554.

	Mobilized shear strength, $s_u(\delta^o)/\sigma'_{vc}$				
Maximum shear strain, γ	0°	45°	60°	75°	90°
0.6%	0.340	0.282	0.216	0.120	0.030
1.0%	0.340	0.291	0.228	0.138	0.075
Peak strength	0.340	0.302	0.257	0.204	0.170

a) Mobilized shear strength at different shear strain levels, $K_0 = 0.53$

	$\gamma = 0.6\%$	$\gamma = 1.0\%$	Peak Strength
$s_u(0^o)/\sigma'_{vc}$	0.34	0.34	0.34
$s_u(45^o)/\sigma'_{vc}$	0.09	0.15	0.23
$s_u(90^o)/\sigma'_{vc}$	0.03	0.075	0.17
h/σ'_{vc}	0.155	0.132	0.085
a/σ'_{vc}	0.185	0.207	0.255
b/σ'_{vc}	0.165	0.195	0.244

Notes:

$h = [s_u(0^o) - s_u(90^o)]/2$

$a = [s_u(0^o) + s_u(90^o)]/2$

$$b = \frac{a \times s_u(45^o)}{\sqrt{s_u(0^o) \times s_u(90^o)}}$$

b) Input parameters for anisotropic undrained strength envelope given by Davis and Christian (1971)

Table 4.1 Mobilized undrained shear strength ratios from Directional Shear Cell tests for K_0-normally consolidated Boston Blue Clay (BBC)

Ultimate bearing capacity $N_c = Q/(Bs_{uDSS})$	Numerical limit analyses		Davis and Christian (1971)
	Smooth footings LB –UB	Rough footings LB – UB	Smooth footings
Isotropic Strength	5.042 – 5.210	5.042 – 5.232	5.141
Anisotropic Strength (Table 4.1)			
1. $\gamma = 0.6\%$	4.300 – 4.782	4.300 – 4.452	4.381
2. $\gamma = 1.0\%$	4.892 – 5.053	4.892 – 5.071	4.986
3. Peak Strength	6.043 – 6.243	6.043 – 6.266	6.161

Notes:

1) $s_u(DSS)/\sigma'_{v0} = 0.21$ for normally-consolidated Boston Blue Clay (BBC)

Table 4.2 Ultimate bearing capacity of a rigid footing on a homogeneous clay layer

Plate Sections	Ultimate lateral resistance $N_p = P/(s_u D)$	
	Numerical limit analyses LB - UB	Broms (1964)
Smooth surfaces	11.285 – 11.623	11.42
Rough surfaces	11.294 – 11.654	12.56

Square Sections	Ultimate lateral resistance $N_p = P/(s_u D)$	
	Numerical limit analyses LB - UB	Broms (1964)
Smooth surfaces	8.194 – 8.531	8.28
Rough surfaces	11.294 – 11.661	11.42

Pipe Sections	Ultimate lateral resistance $N_p = P/(s_u D)$	
	Numerical limit analyses LB - UB	Randolph & Houlsby (1984) LB - UB
Smooth surfaces	9.016 – 9.756	9.142 – 9.975
Rough surfaces	11.747 – 12.271	11.940 (exact sol.)

Table 4.3 Ultimate lateral resistance of a deeply-embedded section in a clay layer, isotropic strength

Roughness ratio f_s/s_u	Ultimate lateral resistance $N_p = P/(s_u D)$	
	Numerical limit analyses LB – UB	Randolph & Houlsby (1984) LB[a] – UB[b]
0.0 (smooth)	9.016 – 9.756	9.14 – 9.66
0.1	9.038 – 10.100	9.53 – 9.96
0.2	9.413 – 10.420	9.89 – 10.24
0.3	9.768 – 10.712	10.22 – 10.51
0.4	10.102 – 10.986	10.53 – 10.76
0.5	10.416 – 11.240	10.82 – 11.00
0.6	10.720 – 11.476	11.09 – 11.22
0.7	11.000 – 11.700	11.34 – 11.42
0.8	12.272 – 11.903	11.56 – 11.61
0.9	11.522 – 12.095	11.77 – 11.79
1.0 (rough)	11.747 – 12.271	11.94 (exact solution)

[a]Equation 4.34
[b]Corrected UB (Randolph, Pers. Comm., 1998)

Table 4.4 Effects of surface roughness ratio on ultimate lateral resistance of pipe sections

Plate Sections	Ultimate lateral resistance $N_p = P/(Ds_{uDSS})$	
	Smooth surfaces LB –UB	Rough surfaces LB – UB
Isotropic Strength	11.285 – 11.623	11.294 – 11.654
Anisotropic Strength		
1. $\gamma = 0.6\%$	9.503 – 9.782	9.506 – 9.802
2. $\gamma = 1.0\%$	10.875 – 11.198	10.880 – 11.223
3. Peak Strength	13.461 – 13.861	13.468 – 13.894

Square Sections	Ultimate lateral resistance $N_p = P/(Ds_{uDSS})$	
	Smooth surfaces LB –UB	Rough surfaces LB – UB
Isotropic Strength	8.194 – 8.531	11.294 – 11.661
Anisotropic Strength		
1. $\gamma = 0.6\%$	6.225 – 6.640	9.506 – 9.808
2. $\gamma = 1.0\%$	7.471 – 7.888	10.880 – 11.230
3. Peak Strength	9.574 – 10.016	13.468 – 13.903

Pipe Sections	Ultimate lateral resistance $N_p = P/(Ds_{uDSS})$	
	Smooth surfaces LB –UB	Rough surfaces LB – UB
Isotropic Strength	9.016 – 9.756	11.747 – 12.271
Anisotropic Strength		
1. $\gamma = 0.6\%$	7.374 – 7.945	9.840 – 10.279
2. $\gamma = 1.0\%$	8.566 – 9.231	11.287 – 11.791
3. Peak Strength	10.688 – 11.551	13.982 – 14.607

Table 4.5 Effects of anisotropic undrained strengths of clays on ultimate lateral resistance of embedded sections

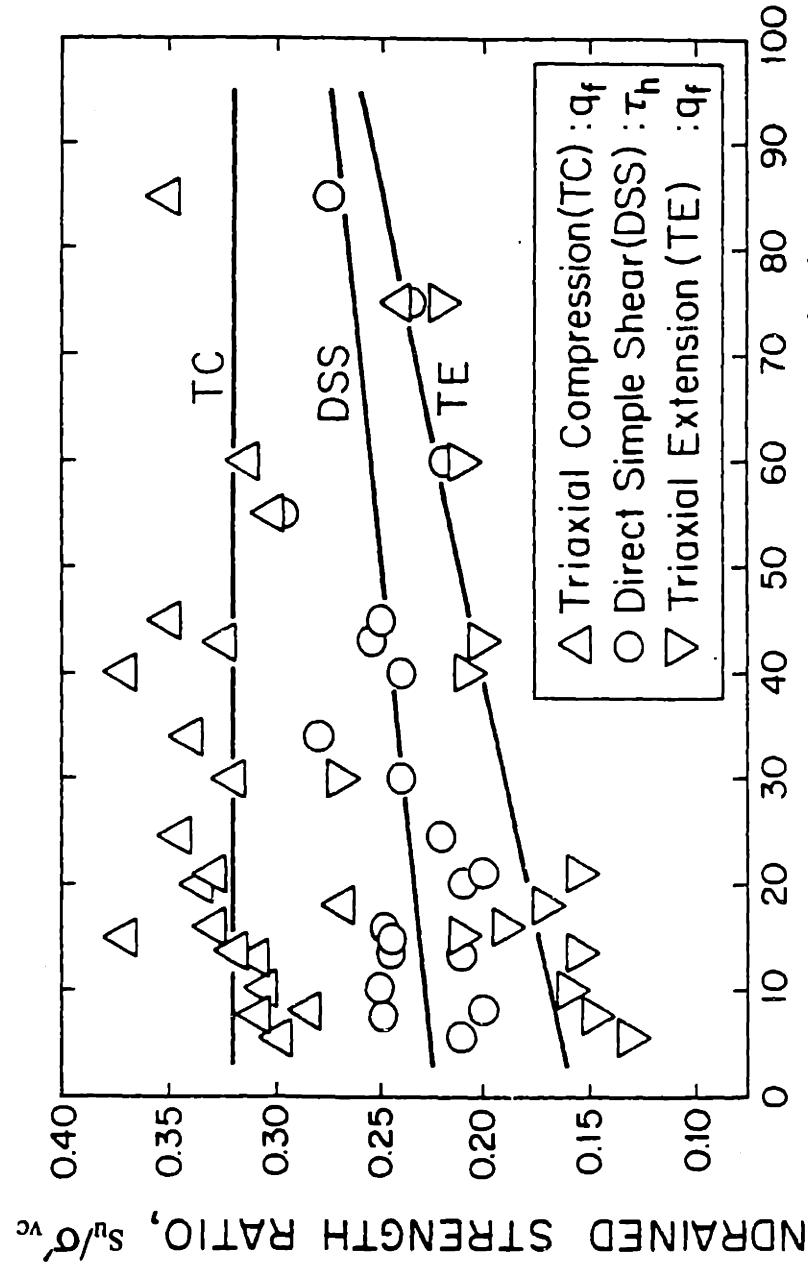

Figure 4.1 Undrained strength anisotropy from CK_0U Tests on Normally Consolidated Clays and Silts (after Ladd, 1991)

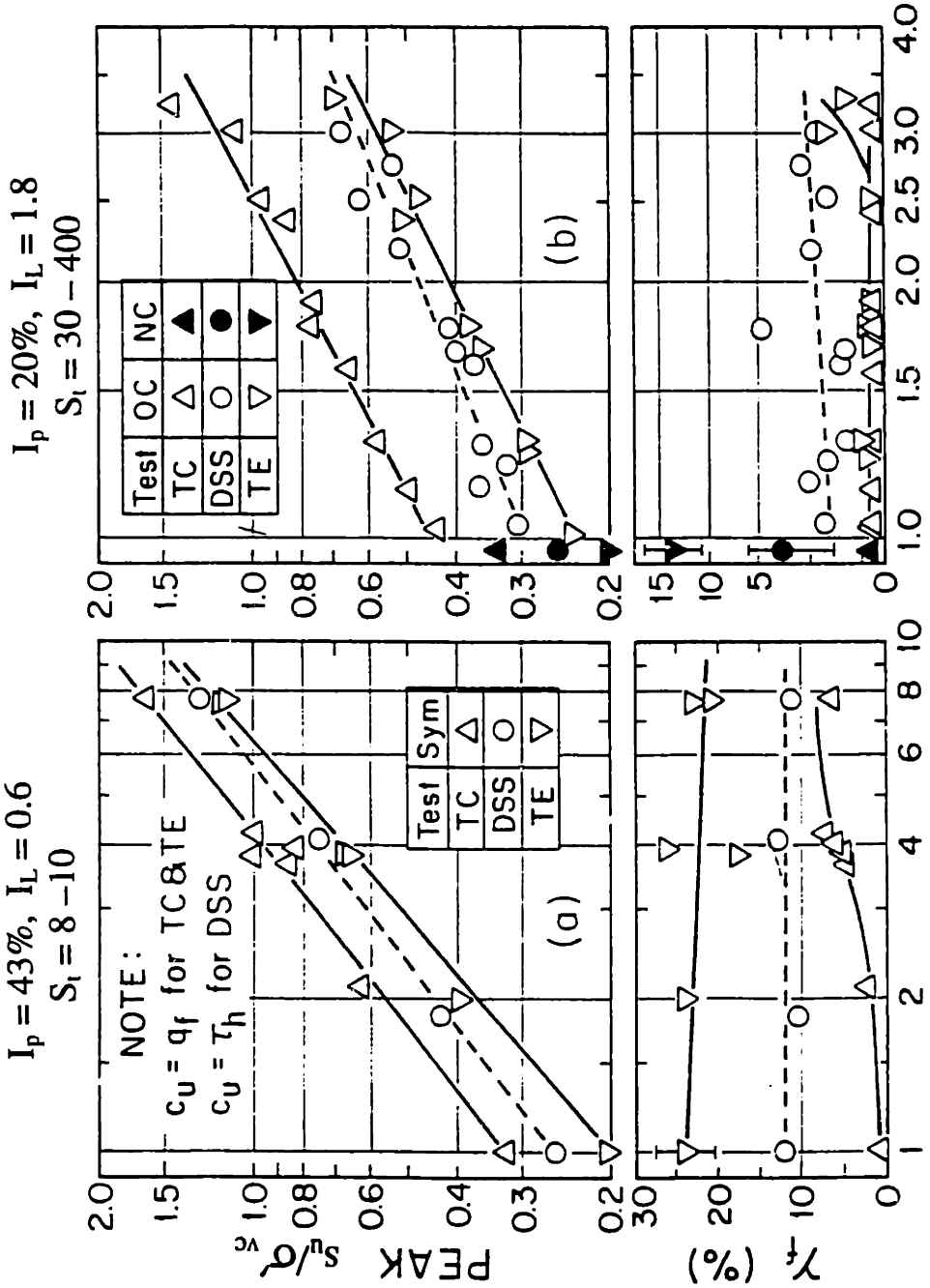

Figure 4.2 OCR versus undrained strength ratio and shear strain at failure from CK_0U Test: a) AGS clay via SHANSEP; and b) James Bay clay via Recompression (after Ladd, 1991)

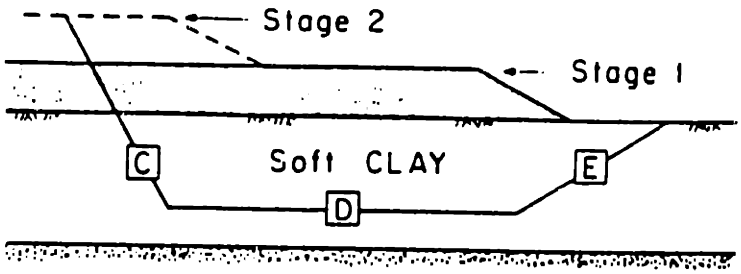

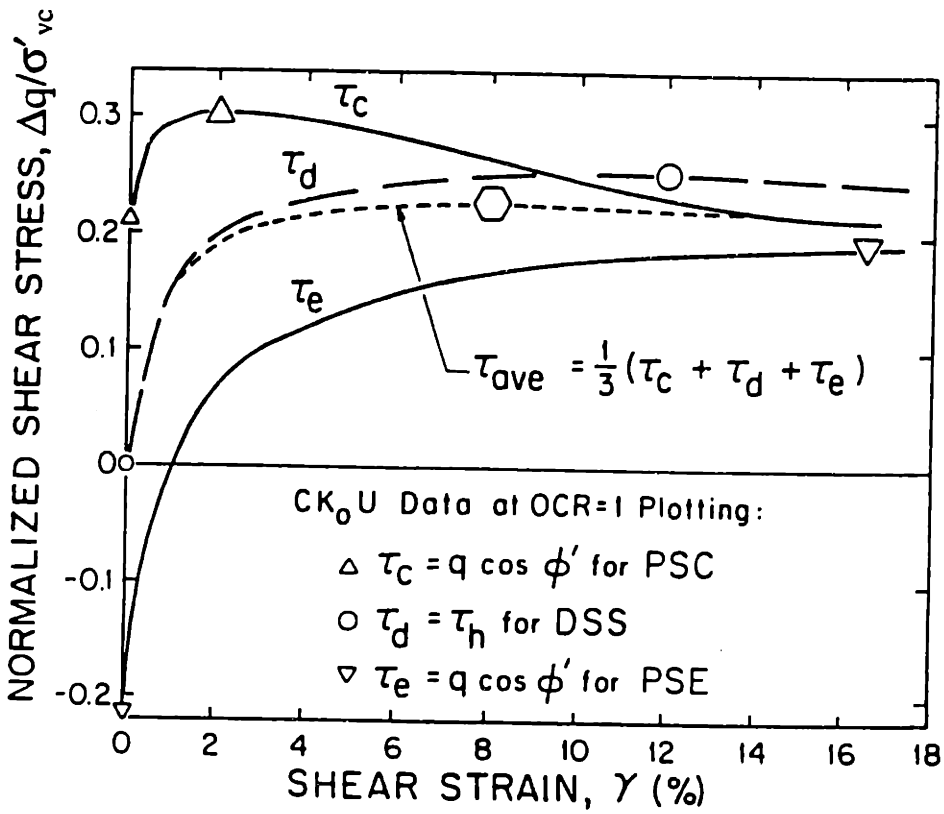

Figure 4.3 Normalized stress-strain curve for AGS clay illustrating progressive failure (after Ladd, 1991)

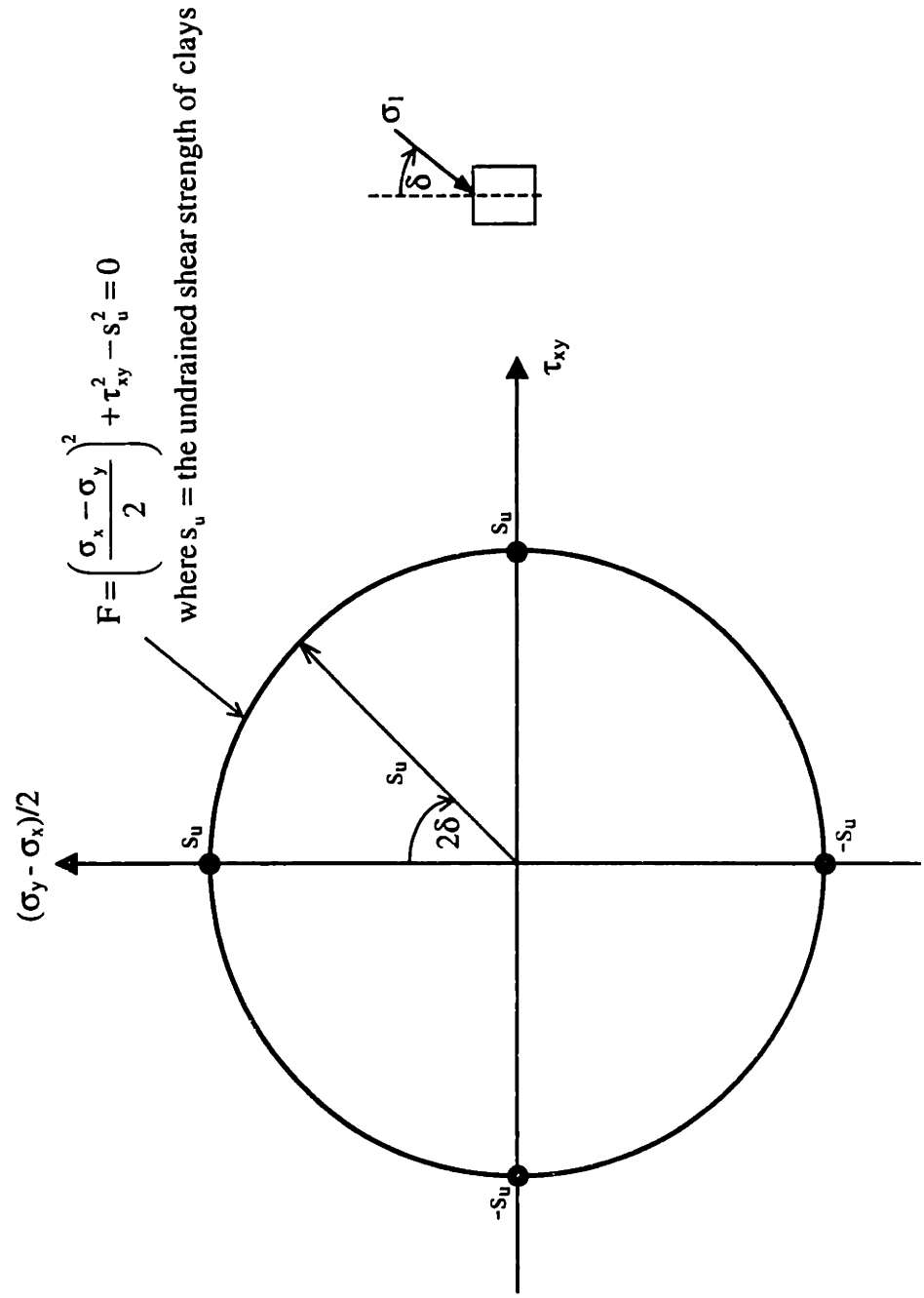

Figure 4.4 Isotropic strength envelope by Tresca yield criterion in $[(\sigma_y - \sigma_x)/2, \tau_{xy}]$ stress space

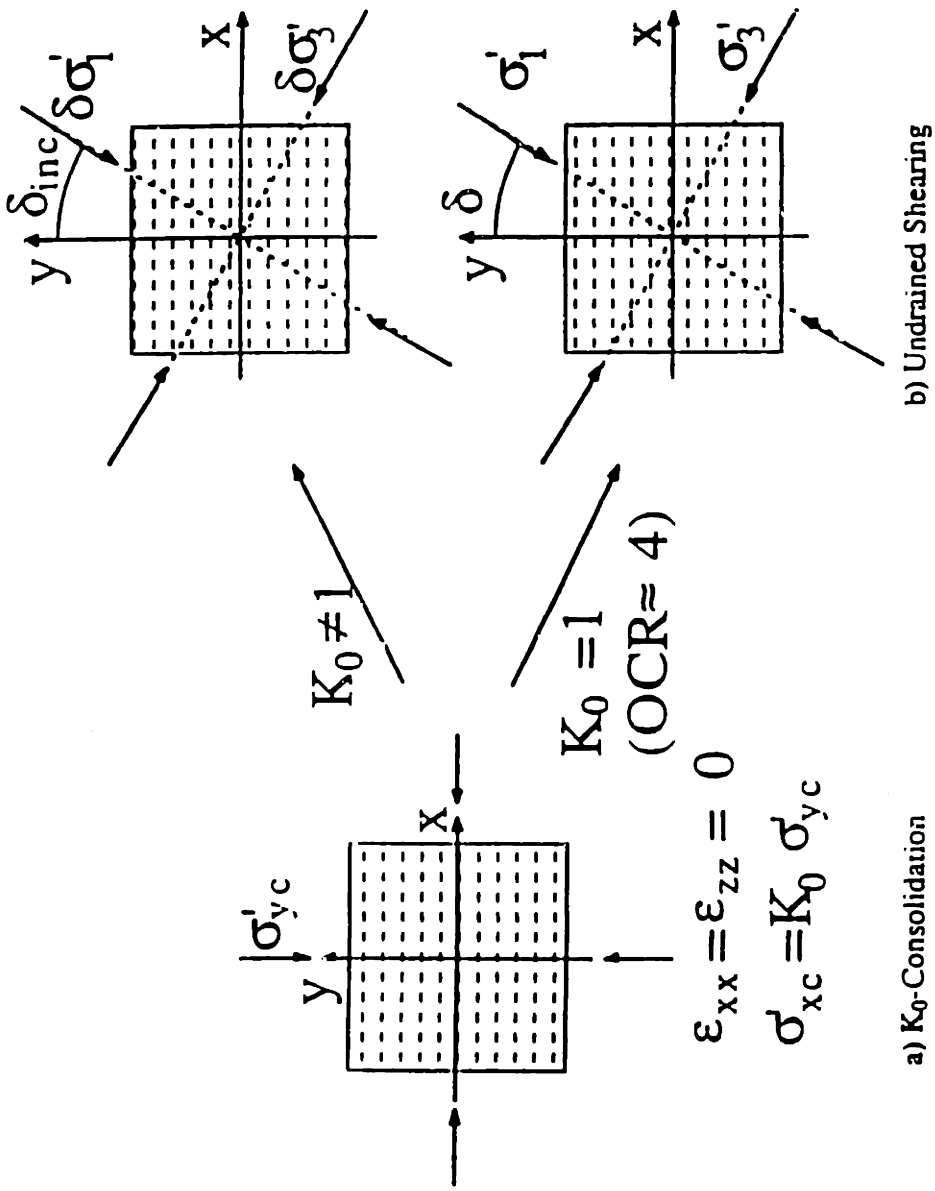

Figure 4.5 Experimental procedure used to study anisotropy in undrained shearing using Directional Shear Cell (after Whittle et al., 1994)

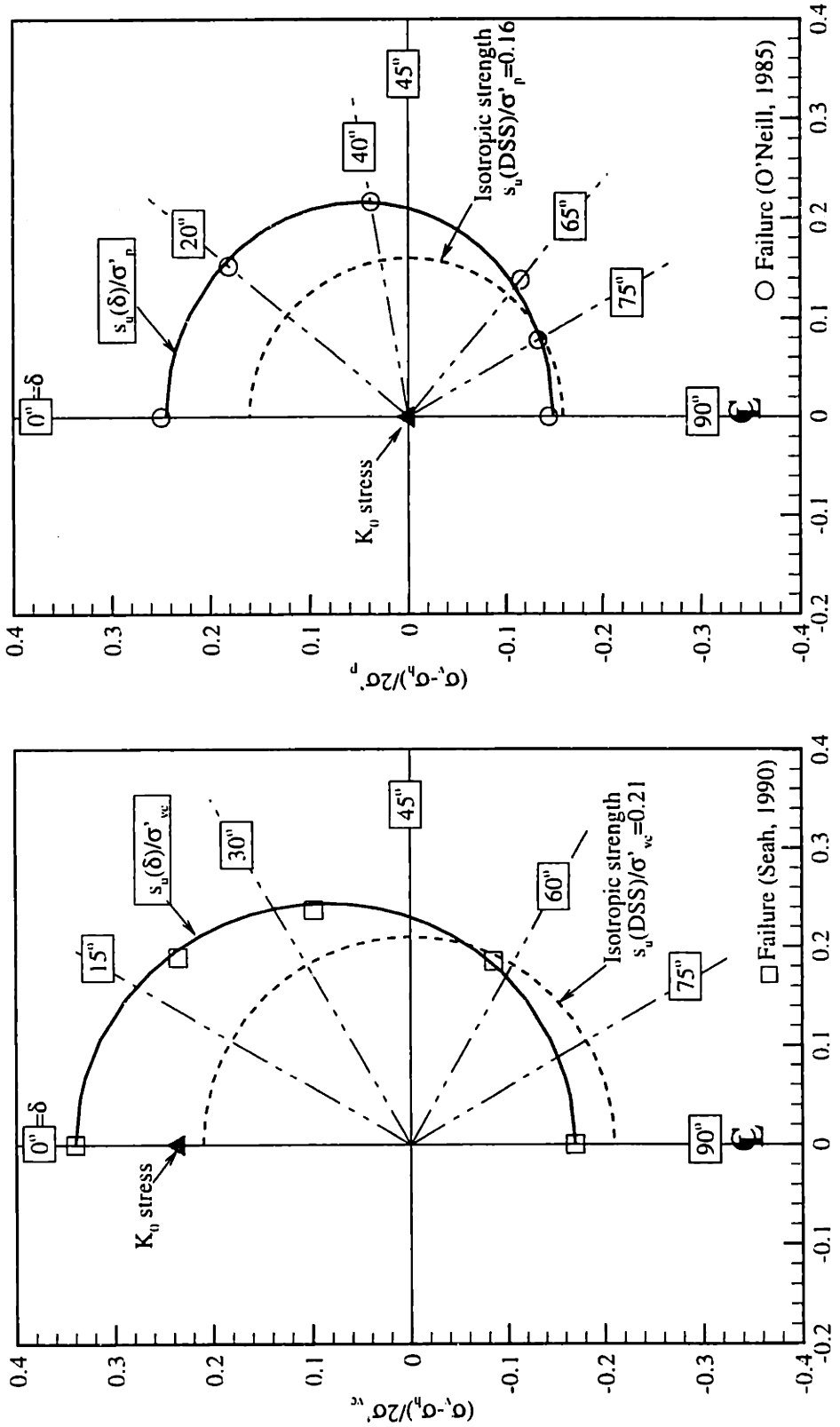

a) OCR = 1: K_0 = 0.53

b) OCR = 4: K_0 = 1.0

Figure 4.6 Undrained strength envelope (failure) of Boston Blue Clay from Directional Shear Cell

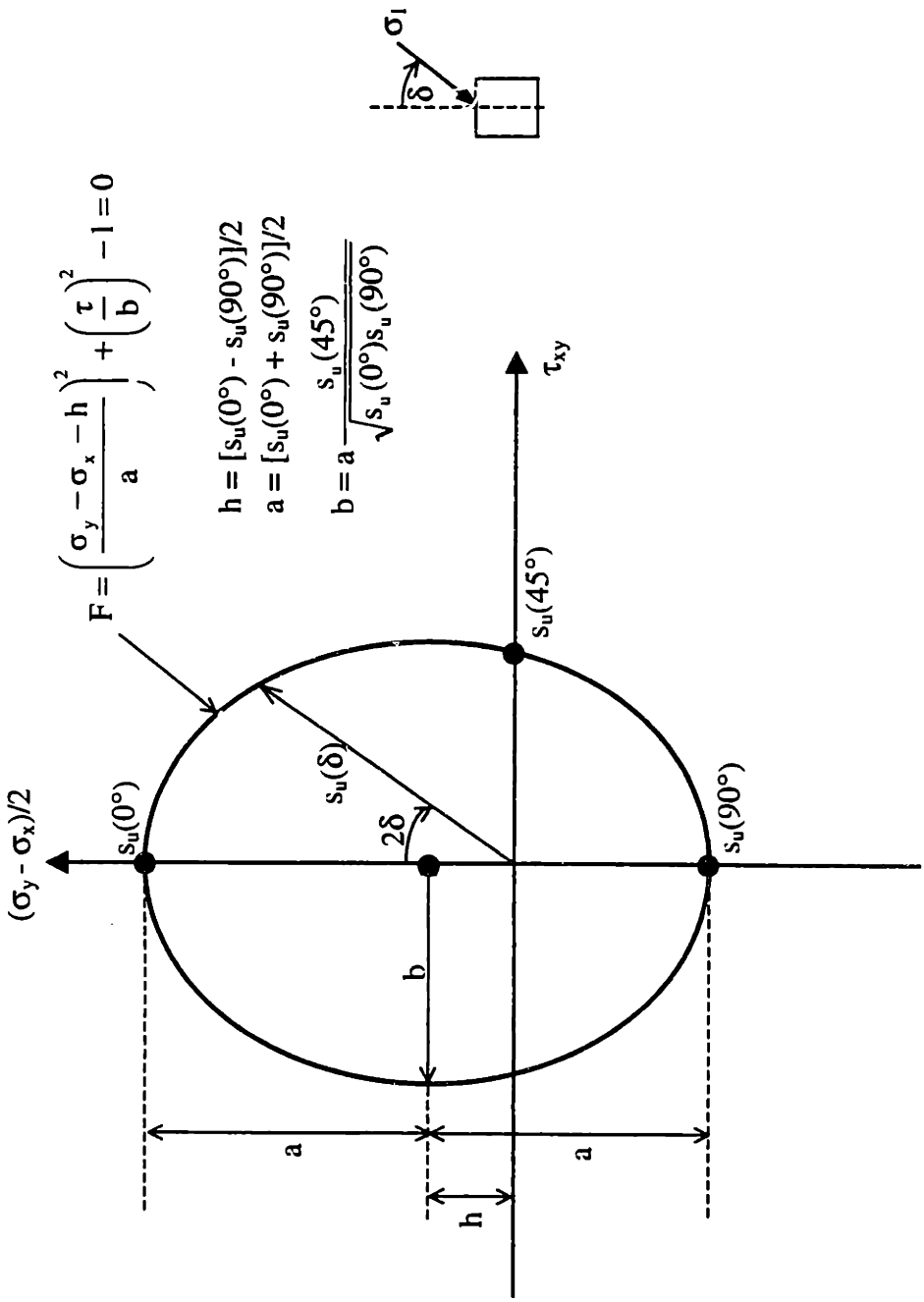

Figure 4.7 Undrained strength envelope by Davis and Christian (1971) in $[(\sigma_y - \sigma_x)/2, \tau_{xy}]$ stress space

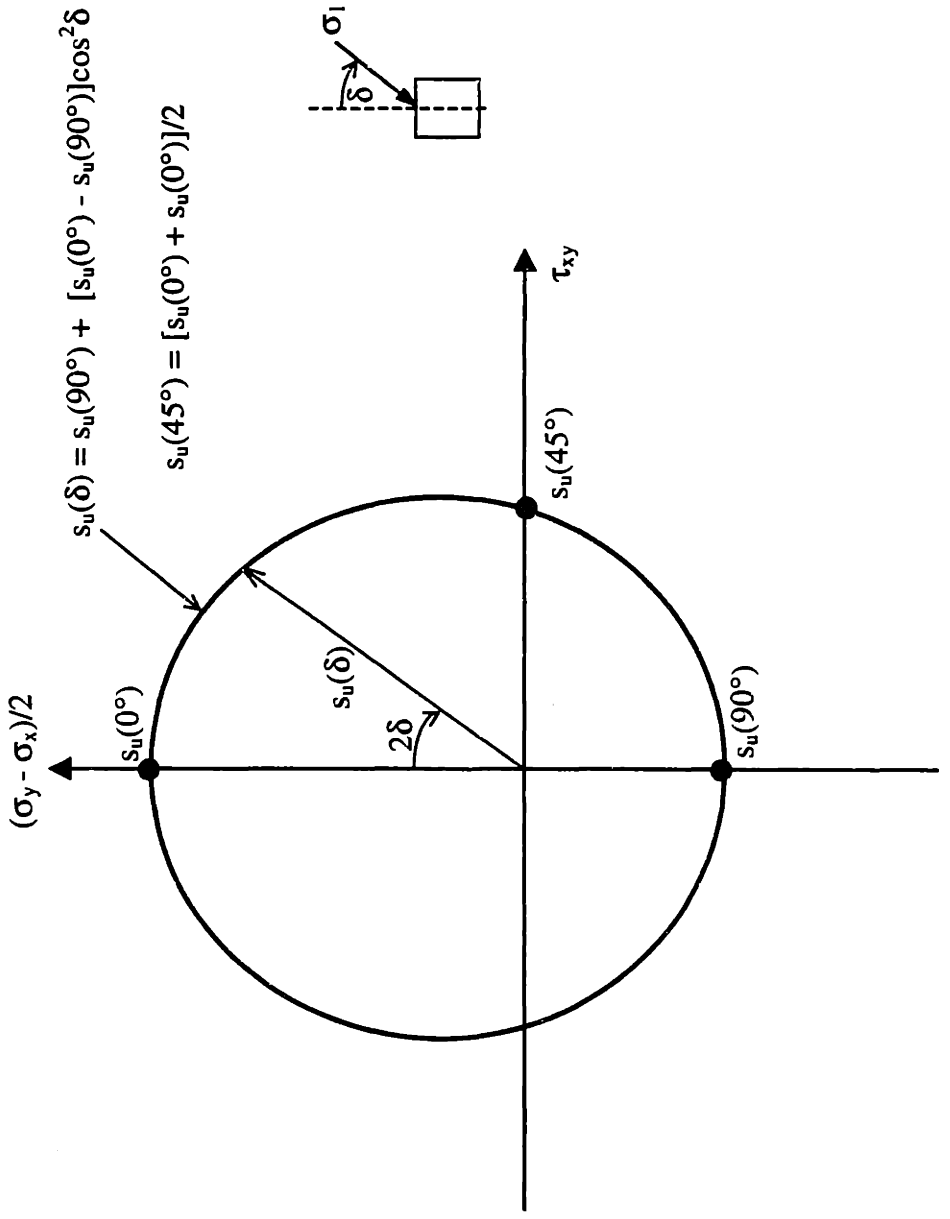

Figure 4.8 Undrained strength envelope by Casagrande-Carrillo (1944) in $[(\sigma_y - \sigma_x)/2, \tau_{xy}]$ stress space

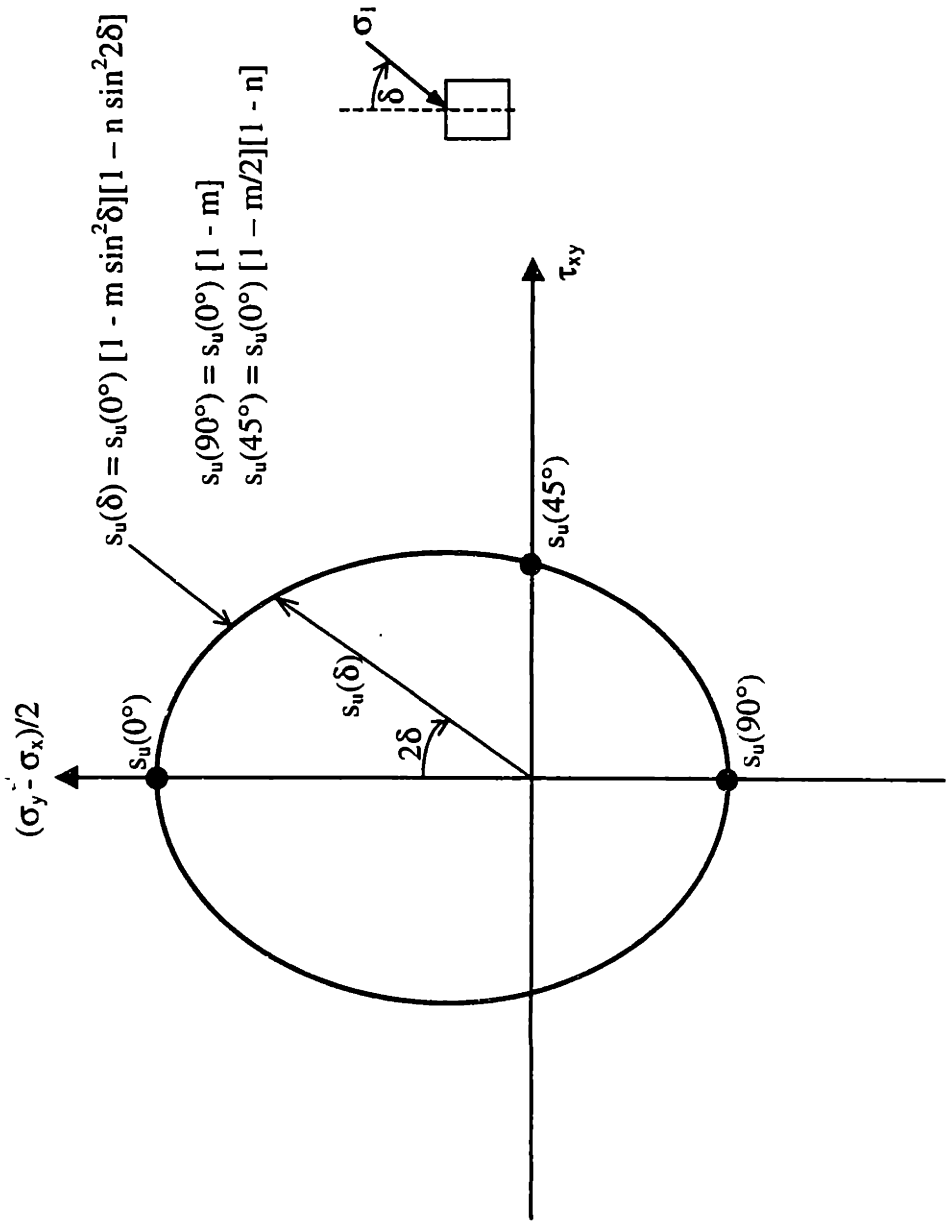

Figure 4.9 Undrained strength envelope by Bishop (1966) in $[(\sigma_y - \sigma_x)/2, \tau_{xy}]$ stress space

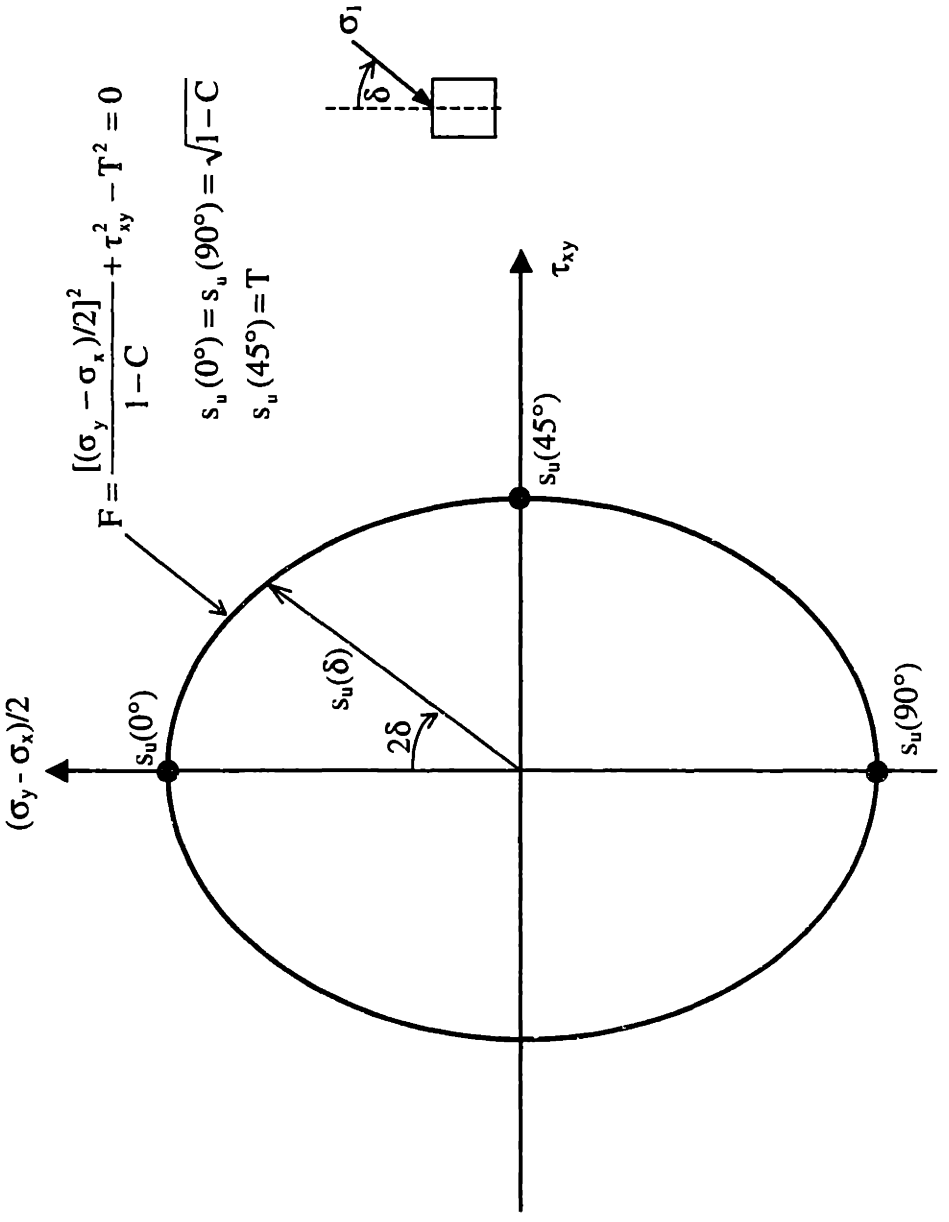

Figure 4.10 Undrained strength envelope by Hill (1950) in $[(\sigma_y - \sigma_x)/2, \tau_{xy}]$ stress space

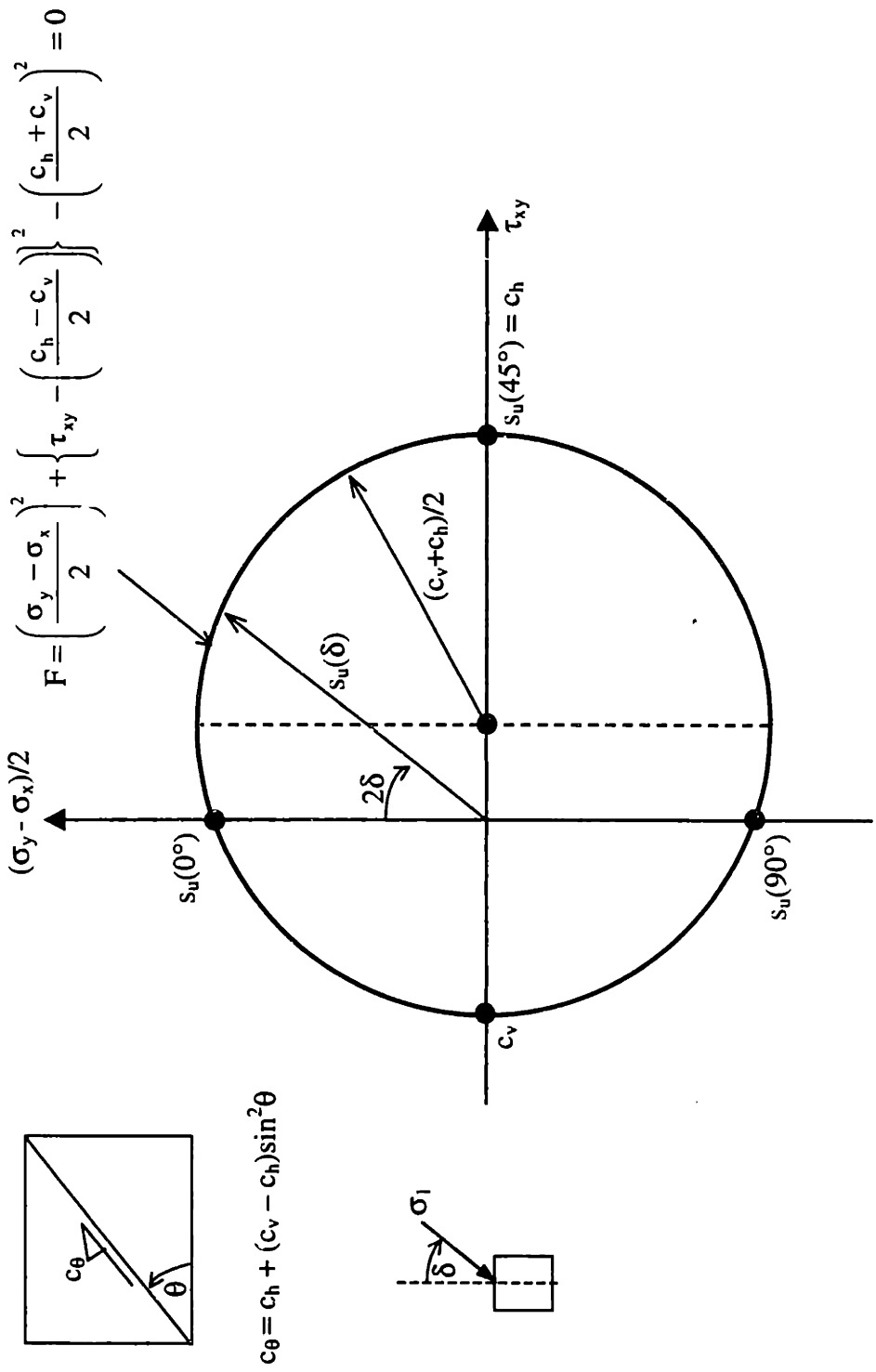

Figure 4.11 Undrained strength envelope by Yu and Sloan (1994) in $[(\sigma_y - \sigma_x)/2, \tau_{xy}]$ stress space

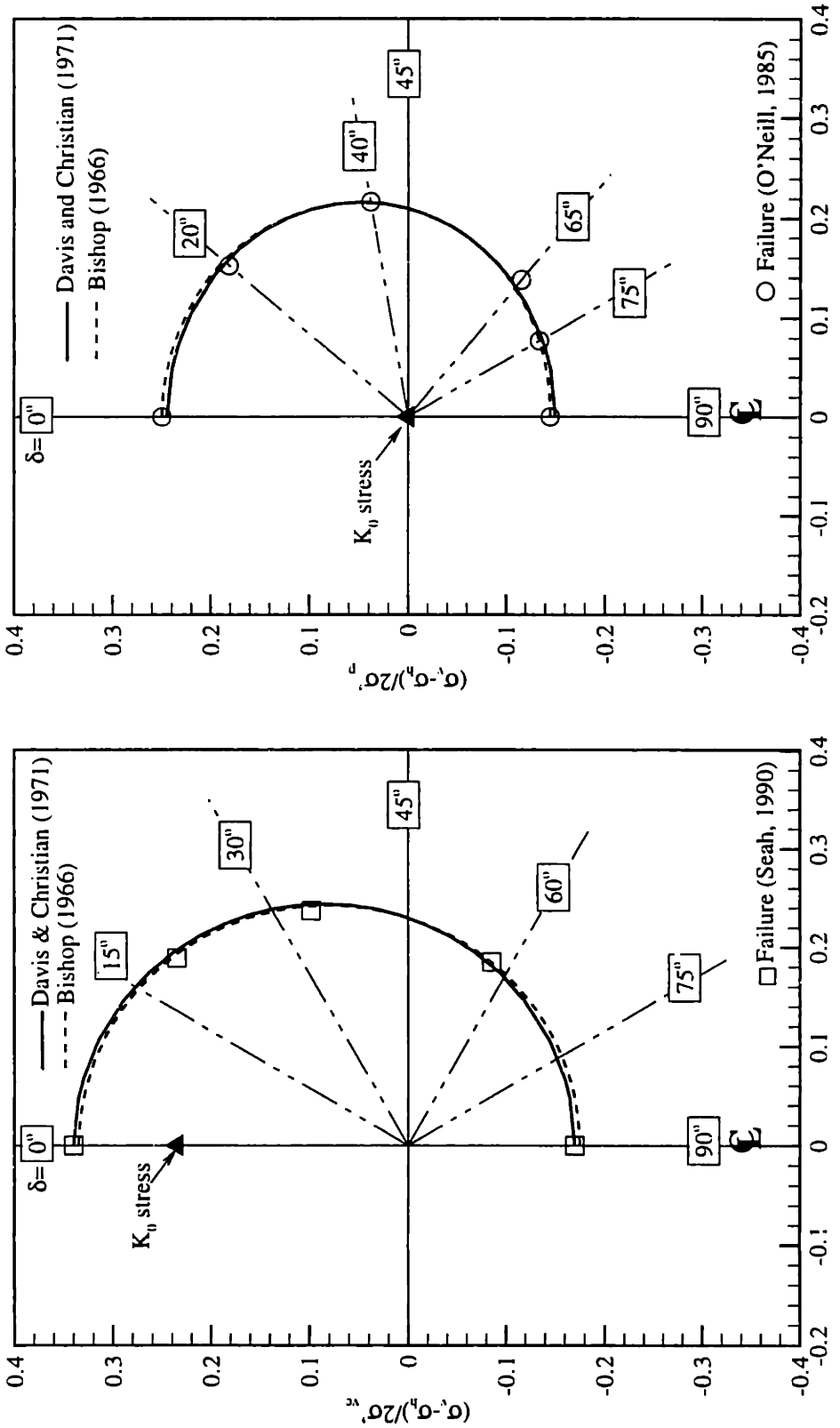

a) OCR = 1: K_0 = 0.53

b) OCR = 4: K_0 = 1.0

Figure 4.12 Comparisons of undrained strength envelope (failure) between Davis and Christian (1971) and Bishop (1966) (Data of Boston Blue Clay from Directional Shear Cell)

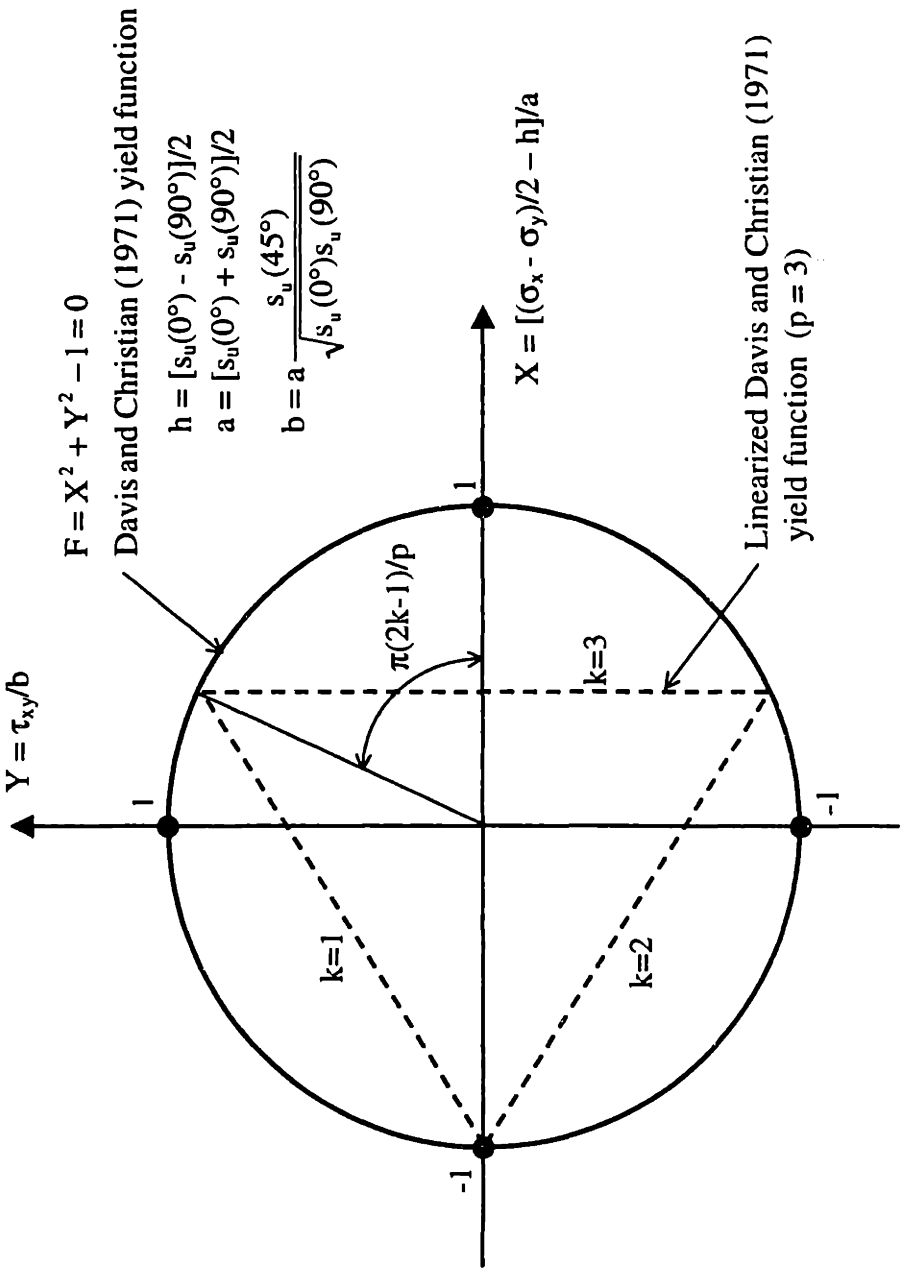

Figure 4.13 Internal linear approximation to Davis and Christian (1971) yield criterion (p = number of sides in yield polygon = 3)

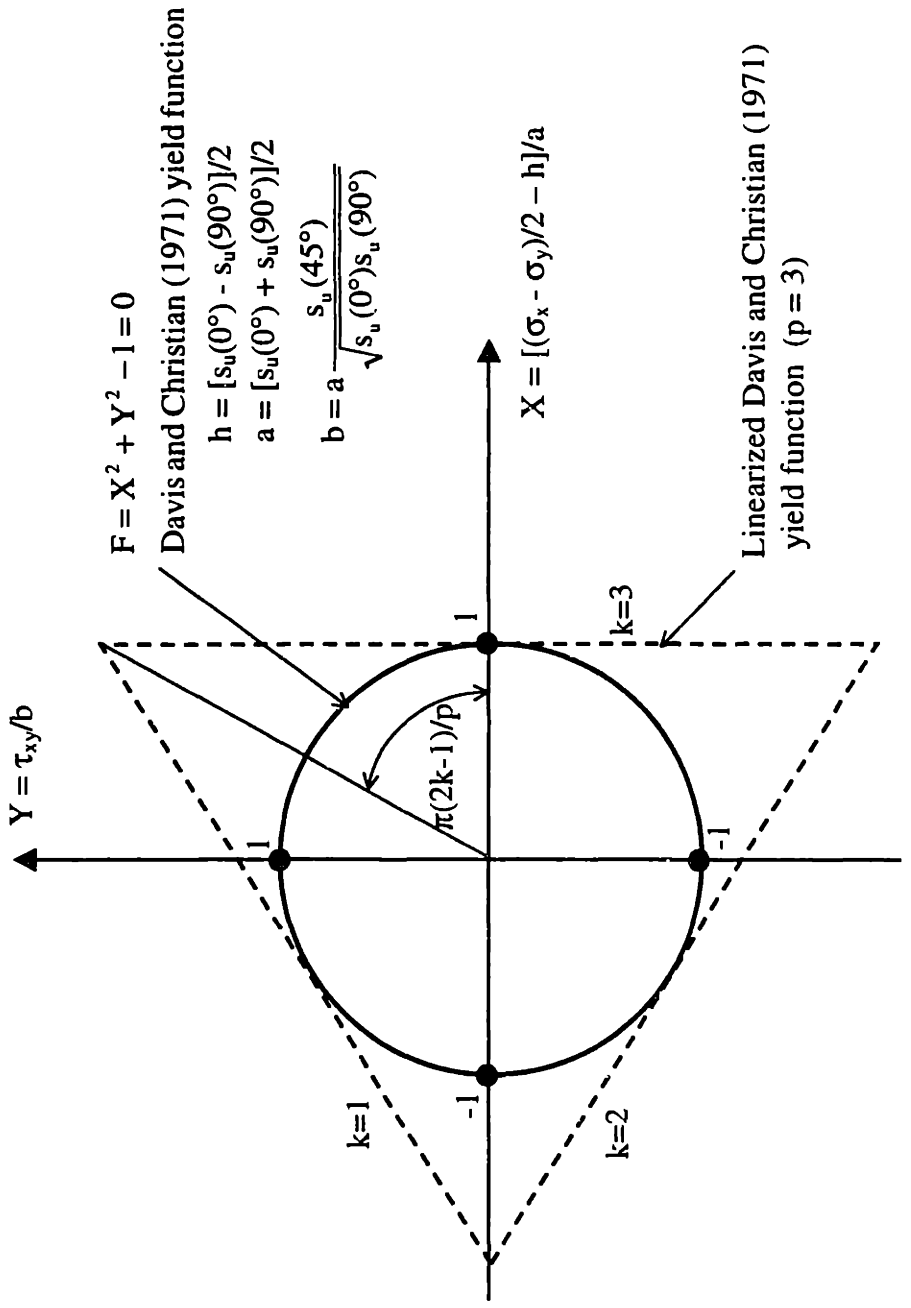

Figure 4.14 External linear approximation to Davis and Christian (1971) yield criterion (p = number of sides in yield polygon = 3)

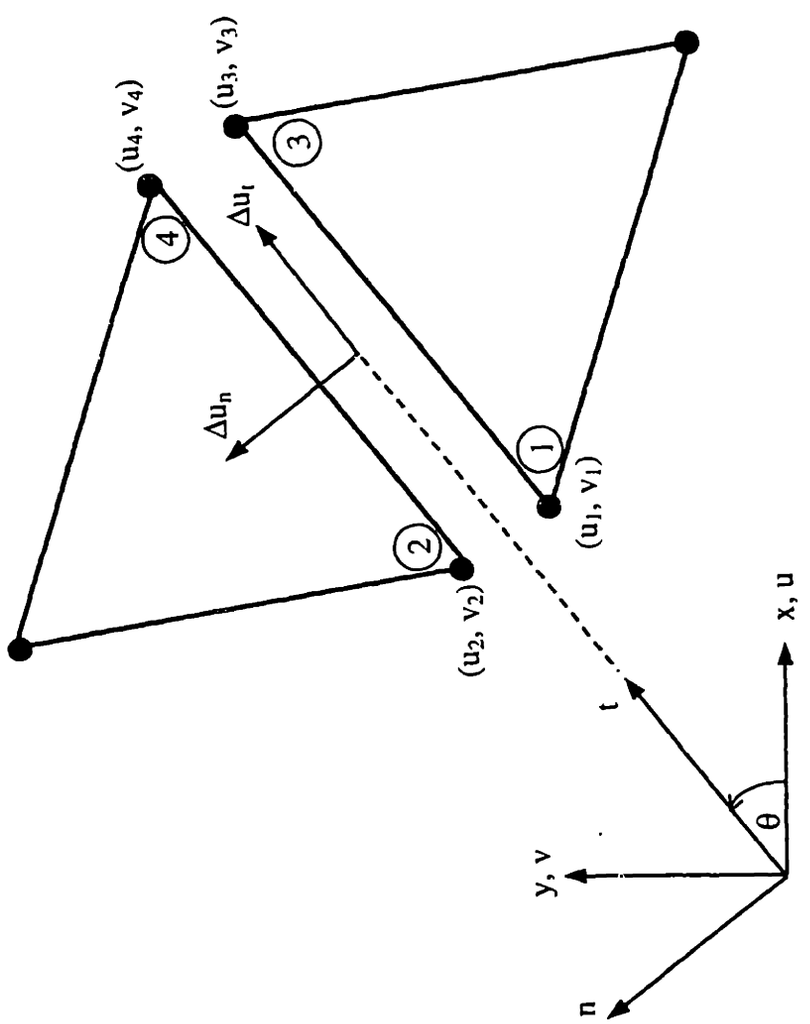

Tangential velocity jump, $\Delta u_t = (u_j - u_i)\cos\theta + (v_j - v_i)\sin\theta$

Normal velocity jump, $\Delta u_n = -(u_j - u_i)\sin\theta + (v_j - v_i)\cos\theta$

Figure 4.15 Velocity discontinuity for the upper bound calculation

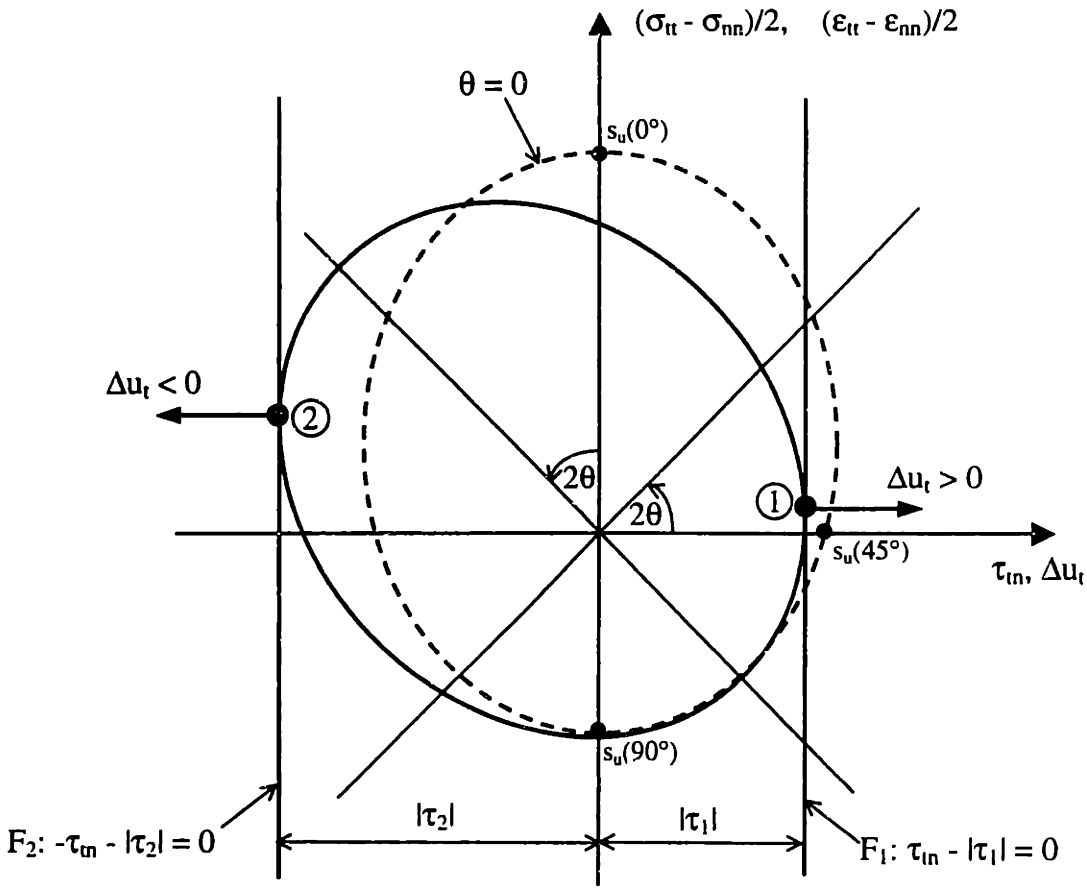

a) Anisotropic yield envelope and flow direction at velocity discontinuity

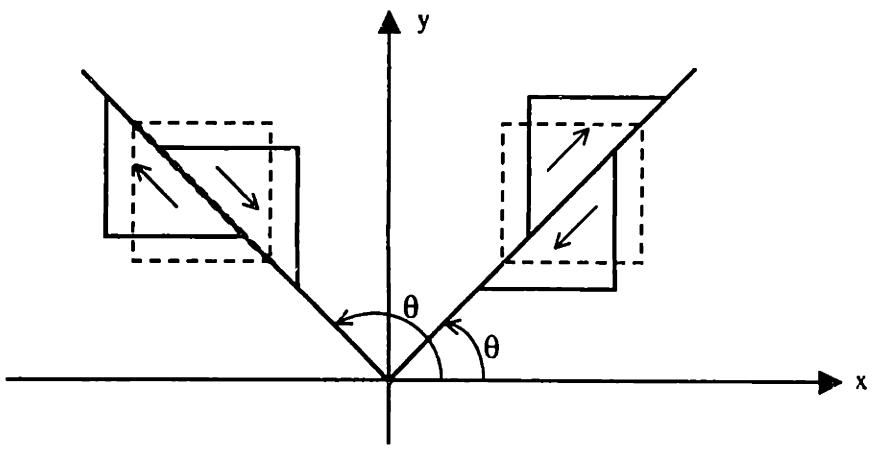

b) Positive sign convention for slip (Δu_t) at velocity discontinuity

Figure 4.16 Plastic flow of velocity discontinuities for anisotropic clays

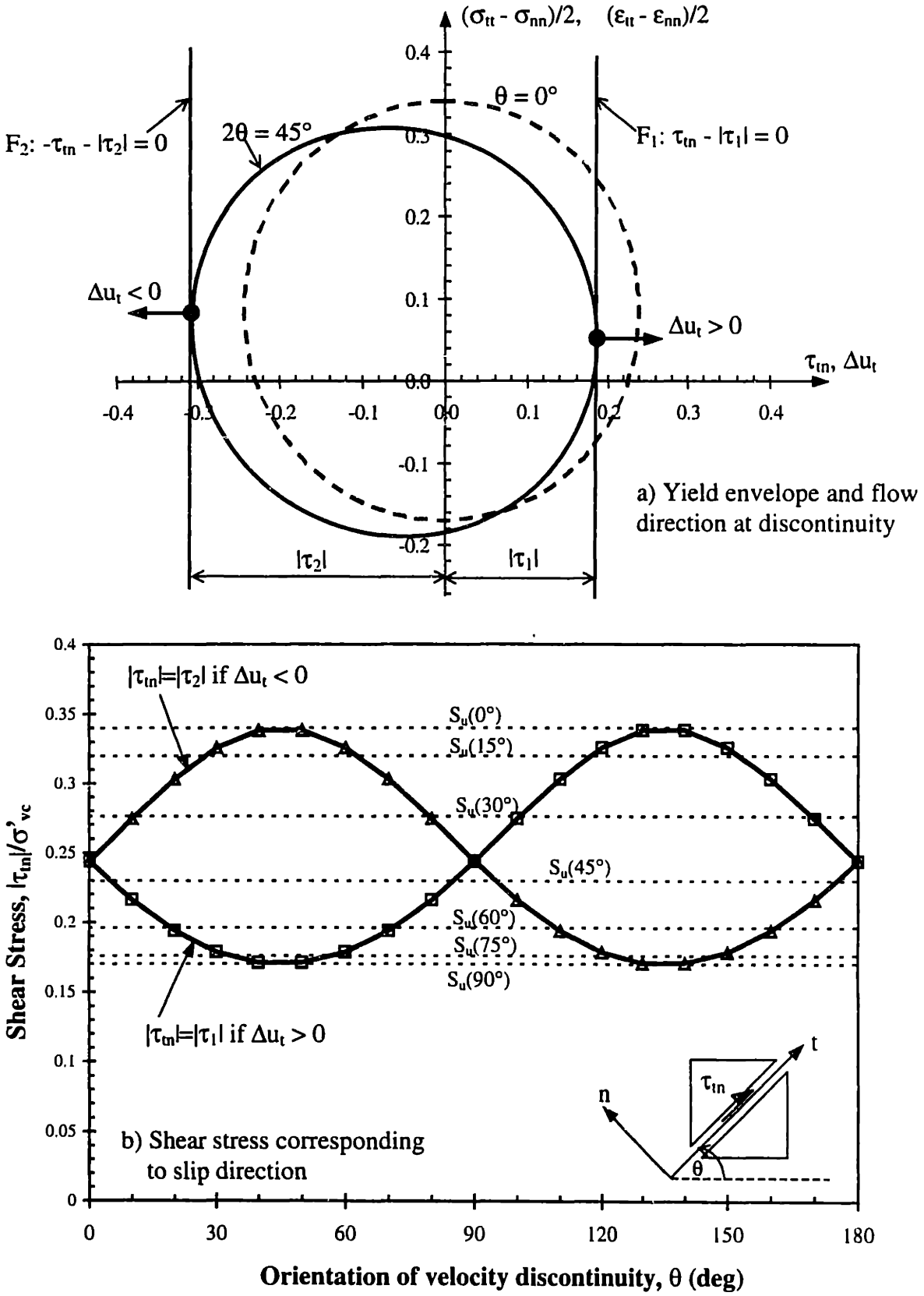

Figure 4.17 Magnitude of shear stress at velocity discontinuities for BBC, OCR = 1.0 (undrained strength ratios at failure)

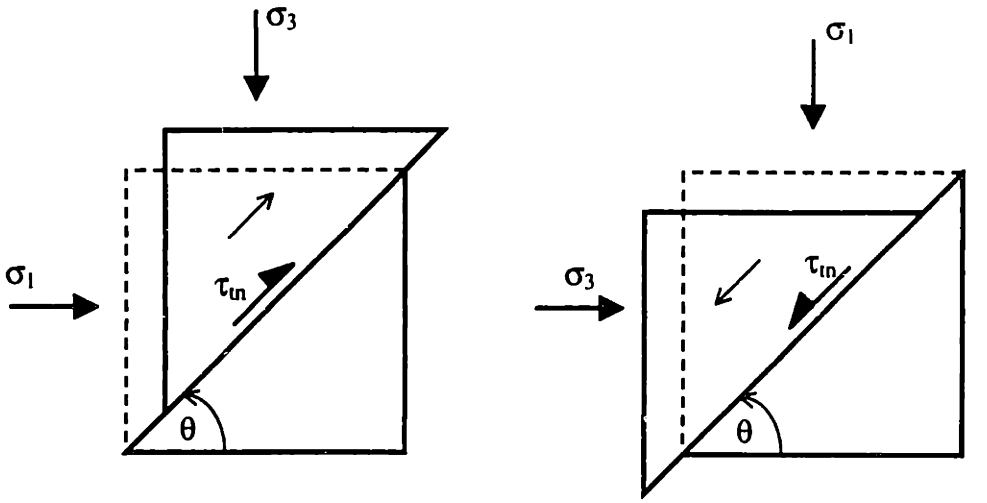

i) Positive slip ($\delta = 90°$)
$\Delta u_t > 0$, $|\tau_{tn}| = |\tau_1| = s_u\ (90°)$

ii) Negative slip ($\delta = 0°$)
$\Delta u_t < 0$, $|\tau_{tn}| = |\tau_2| = s_u\ (0°)$

a) Discontinuity for $\theta = 45°$

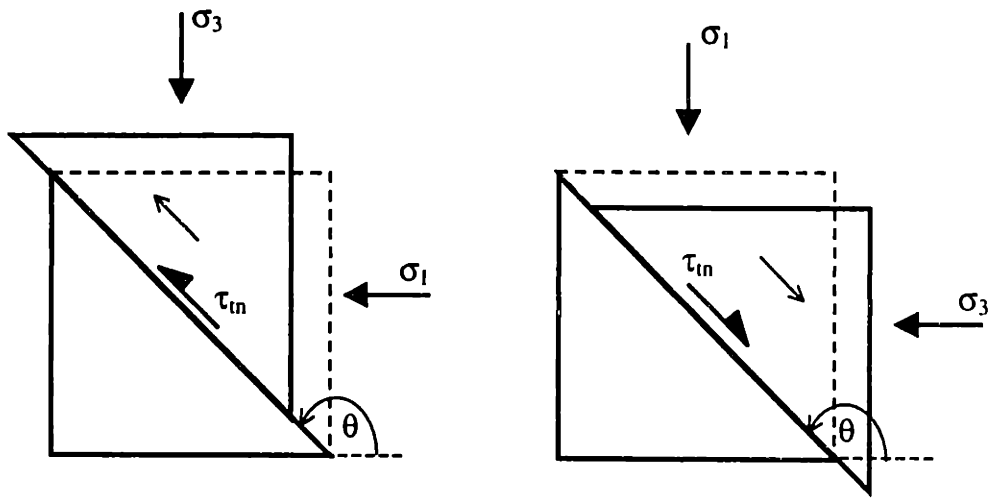

i) Negative slip ($\delta = 90°$)
$\Delta u_t < 0$, $|\tau_{tn}| = |\tau_2| = s_u\ (90°)$

ii) Positive slip ($\delta = 0°$)
$\Delta u_t > 0$, $|\tau_{tn}| = |\tau_1| = s_u\ (0°)$

b) Discontinuity for $\theta = 135°$

Figure 4.18 Verification of upper bound modification at velocity discontinuities to include anisotropic strengths of clays

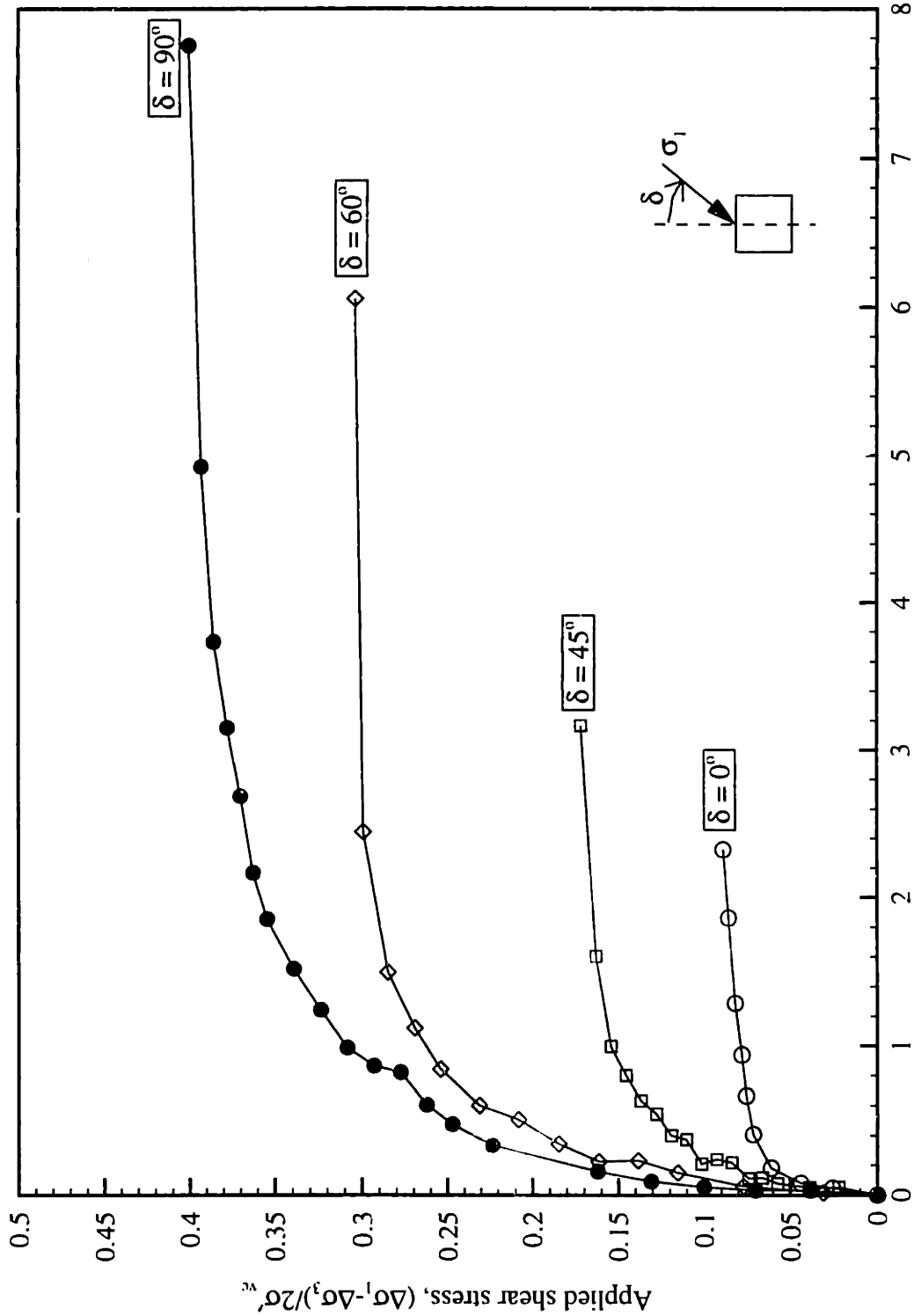

Figure 4.19 Shear stress-strain response for K_0-normally consolidated BBC in directional shear cell tests (after Seah, 1990)

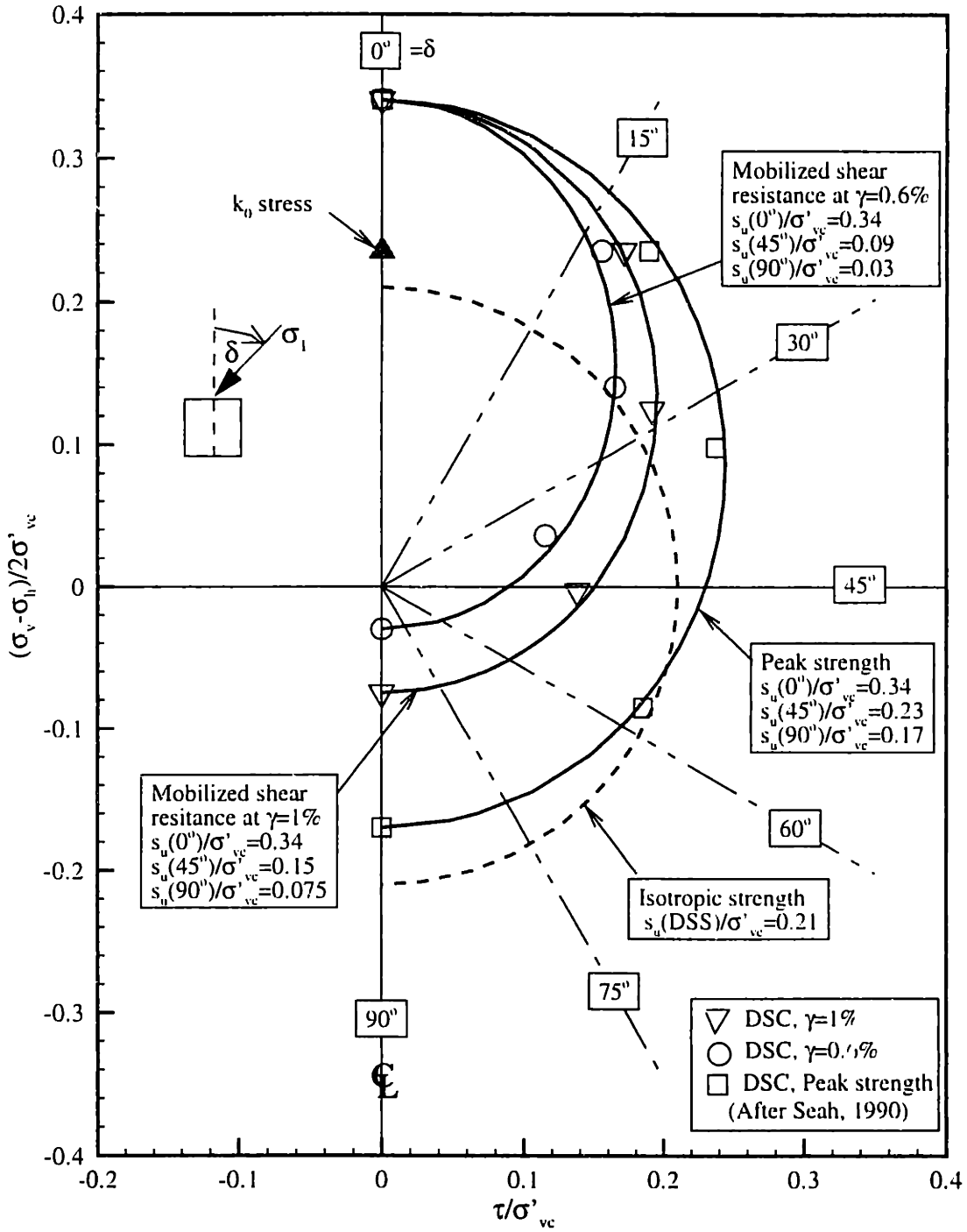

Figure 4.20 Undrained strength envelope of K_0-normally consolidated BBC by Davis and Christian (1971) for different strain levels

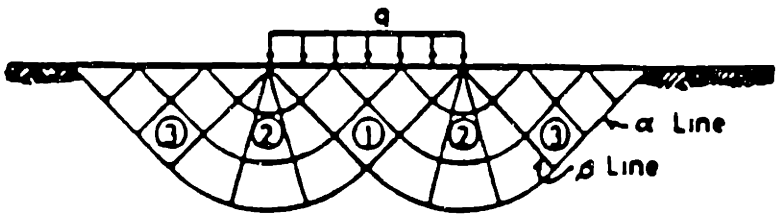

a) Slip-line field

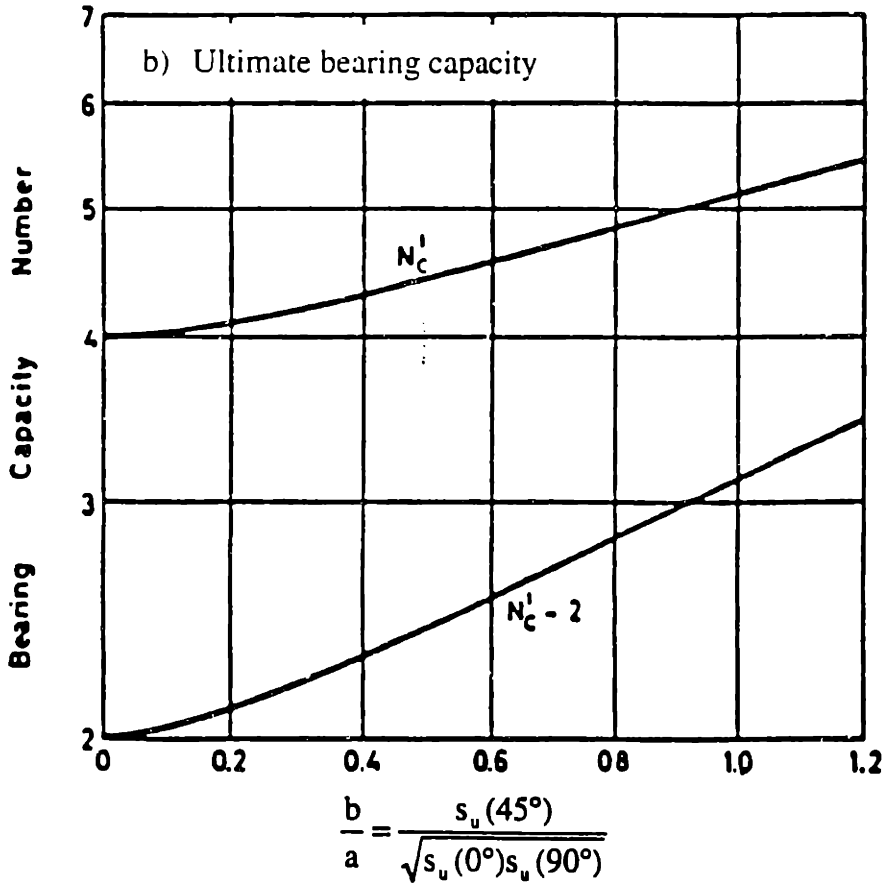

Figure 4.21 Davis and Christian (1971) solutions for ultimate bearing capacity of a rigid footing on a clay layer, where undrained strength is anisotropic

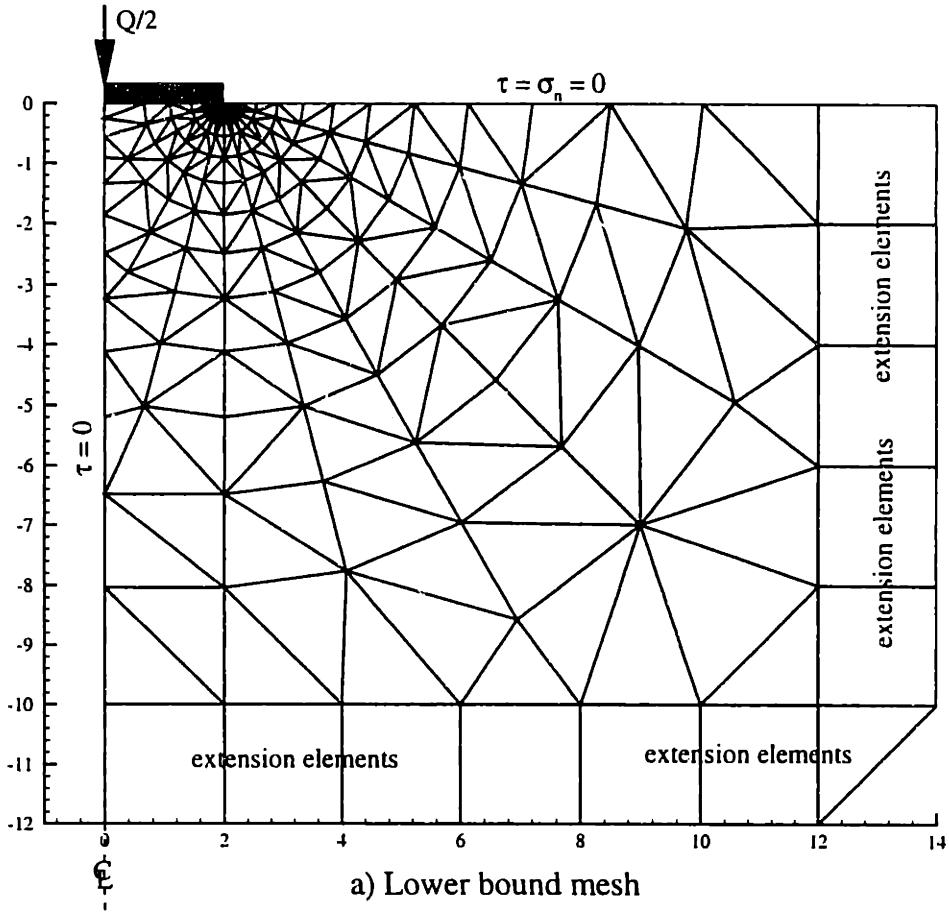

a) Lower bound mesh

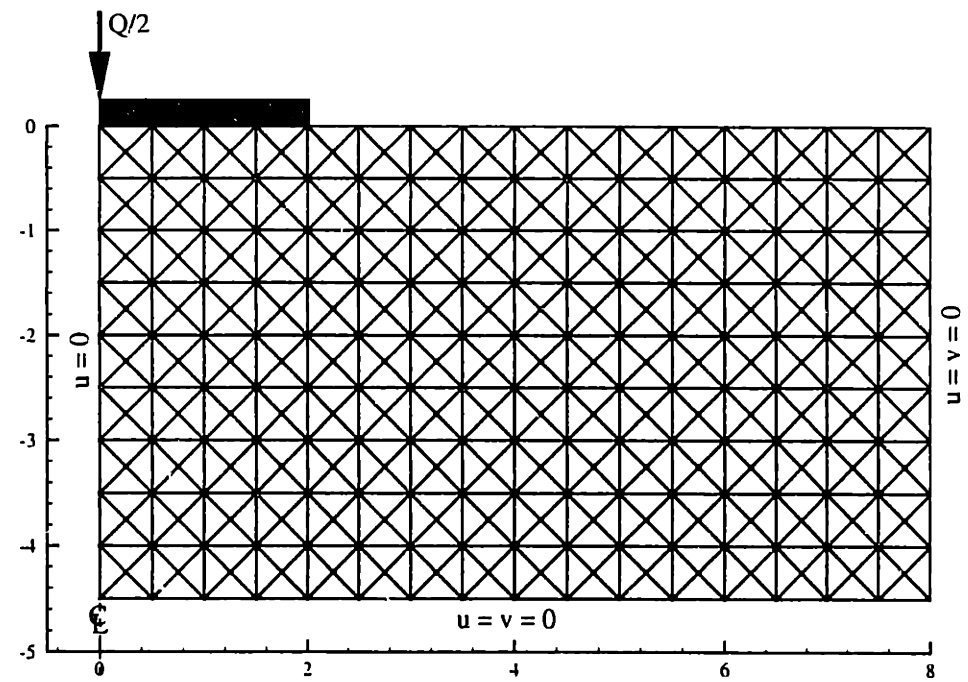

Figure 4.22 Meshes used in a rigid footing on homogenous clay, where strength is isotropic and anisotropic

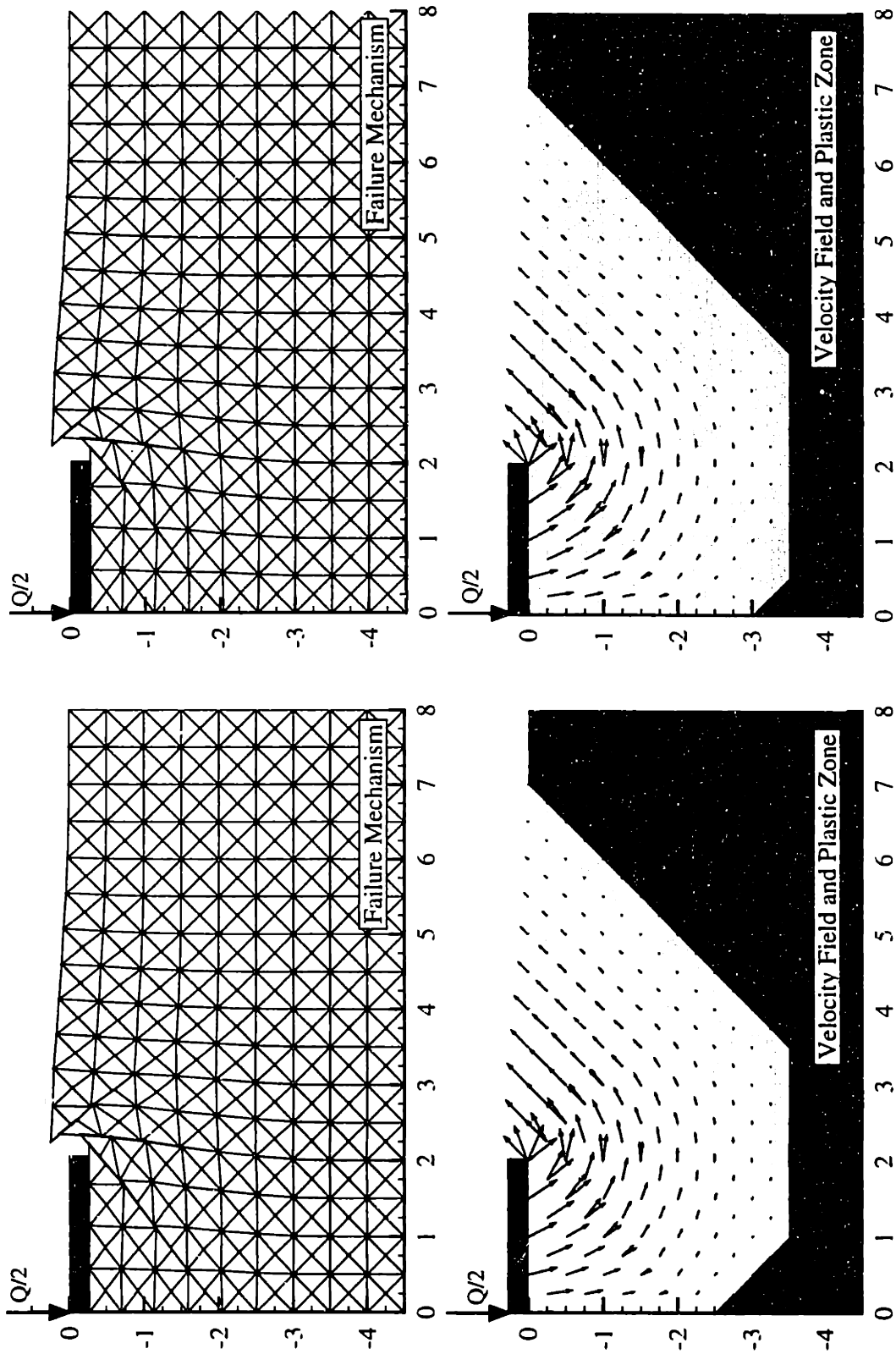

a) Isotropic strength, N_c = 5.042 - 5.210

b) Anisotropic strength at γ = 1%, N_c = 4.892 - 5.053

Figure 4.23 Comparison of upper bound results between istropic and anisotropic strengths, smooth footings

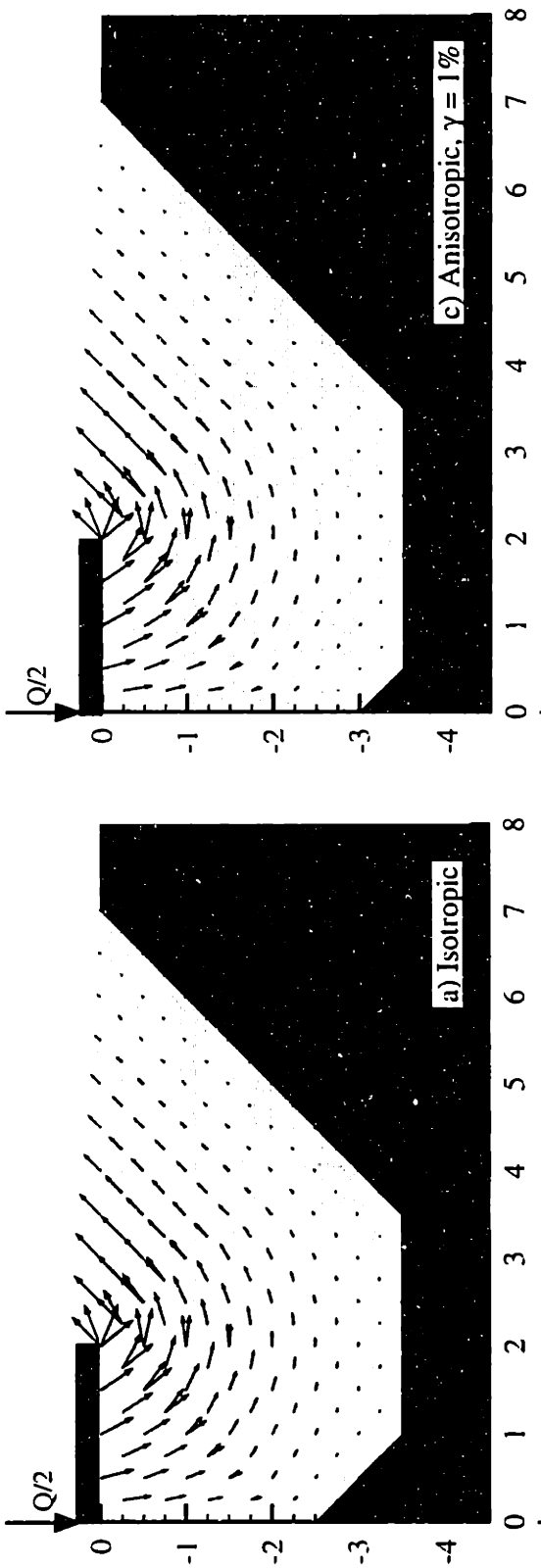

Figure 4.24 Comparison of velocity fields and plastic zone between isotropic and anisotropic strengths, smooth footings

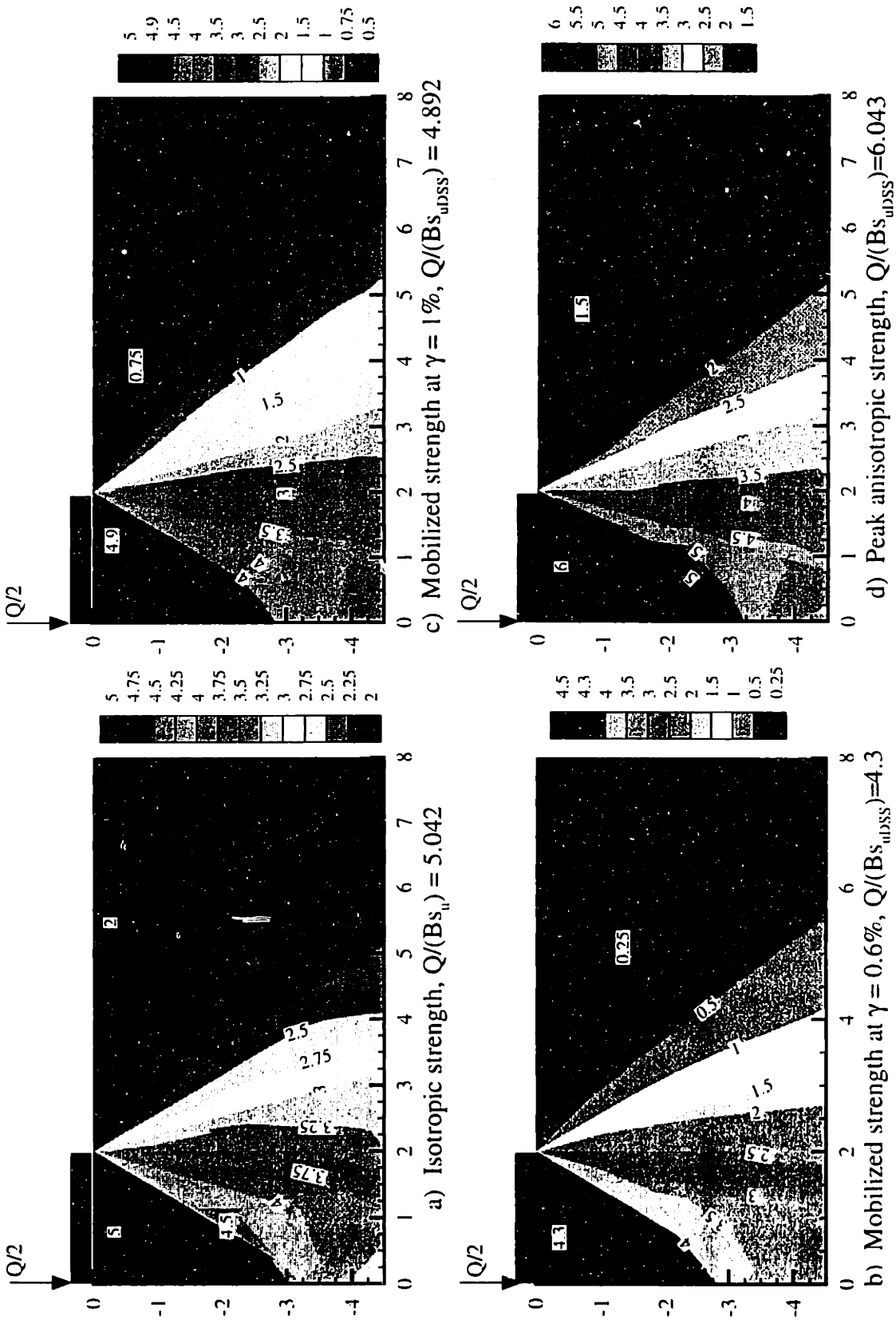

Figure 4.25 Contours of σ_1/s_{uDSS} from lower bound analyses of smooth footings

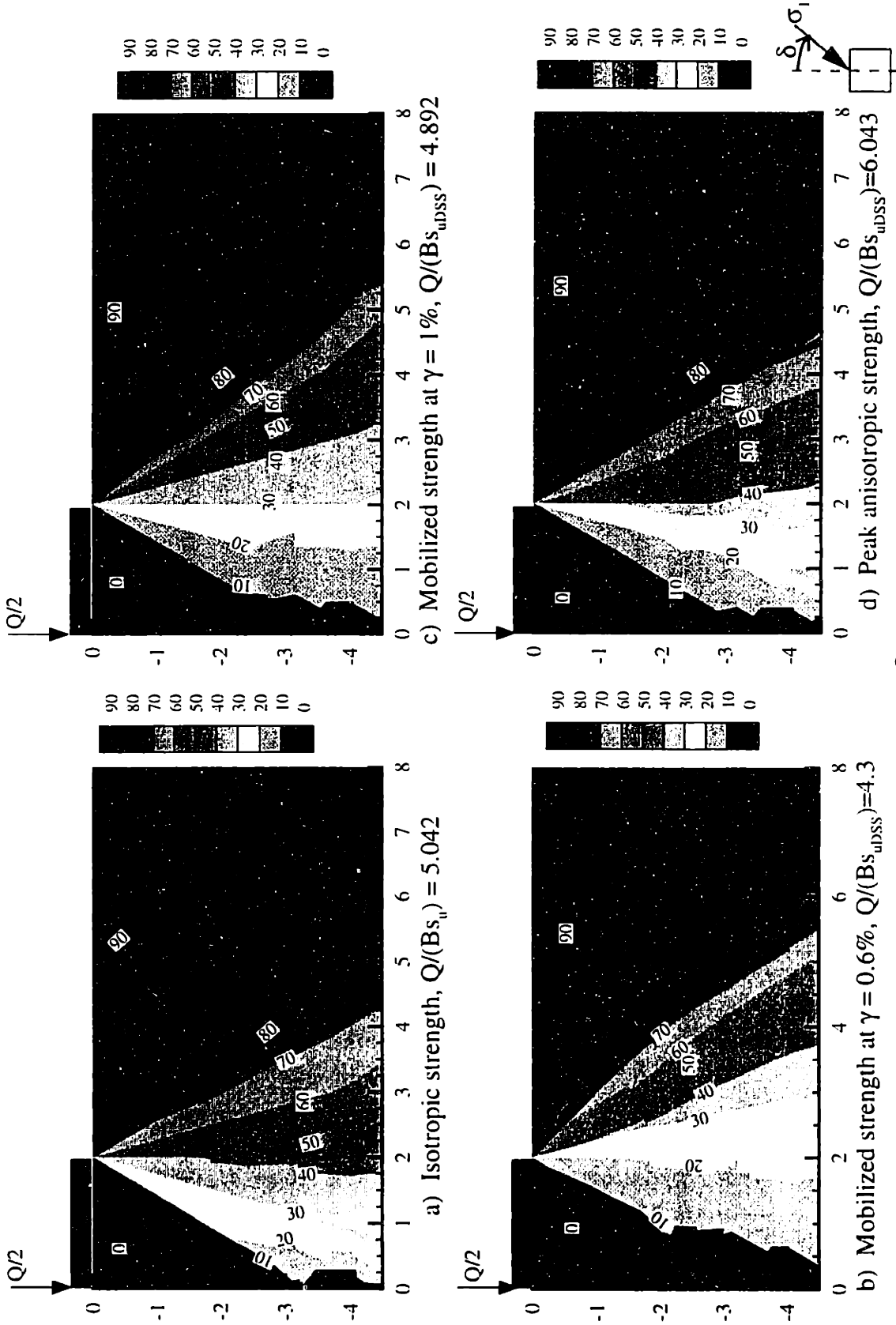

a) Isotropic strength, $Q/(Bs_u) = 5.042$

c) Mobilized strength at $\gamma = 1\%$, $Q/(Bs_{uDSS}) = 4.892$

b) Mobilized strength at $\gamma = 0.6\%$, $Q/(Bs_{uDSS}) = 4.3$

d) Peak anisotropic strength, $Q/(Bs_{uDSS}) = 6.043$

Figure 4.26 Contours of orientation of σ_1 to the vertical, δ (deg.) from lower bound analyses of smooth footings

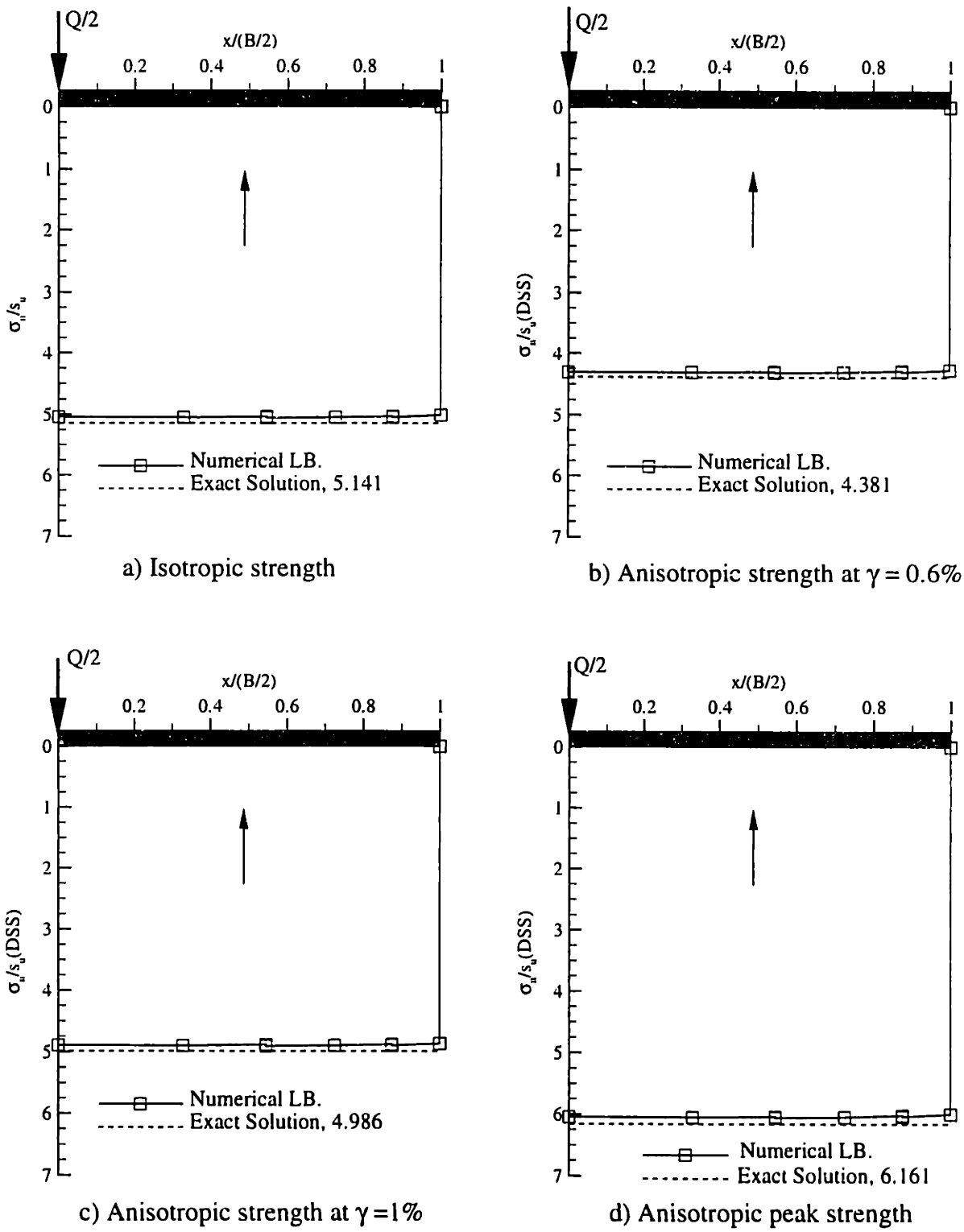

a) Isotropic strength

b) Anisotropic strength at $\gamma = 0.6\%$

c) Anisotropic strength at $\gamma = 1\%$

d) Anisotropic peak strength

Figure 4.27 Contact pressure beneath smooth footings from lower bound analyses

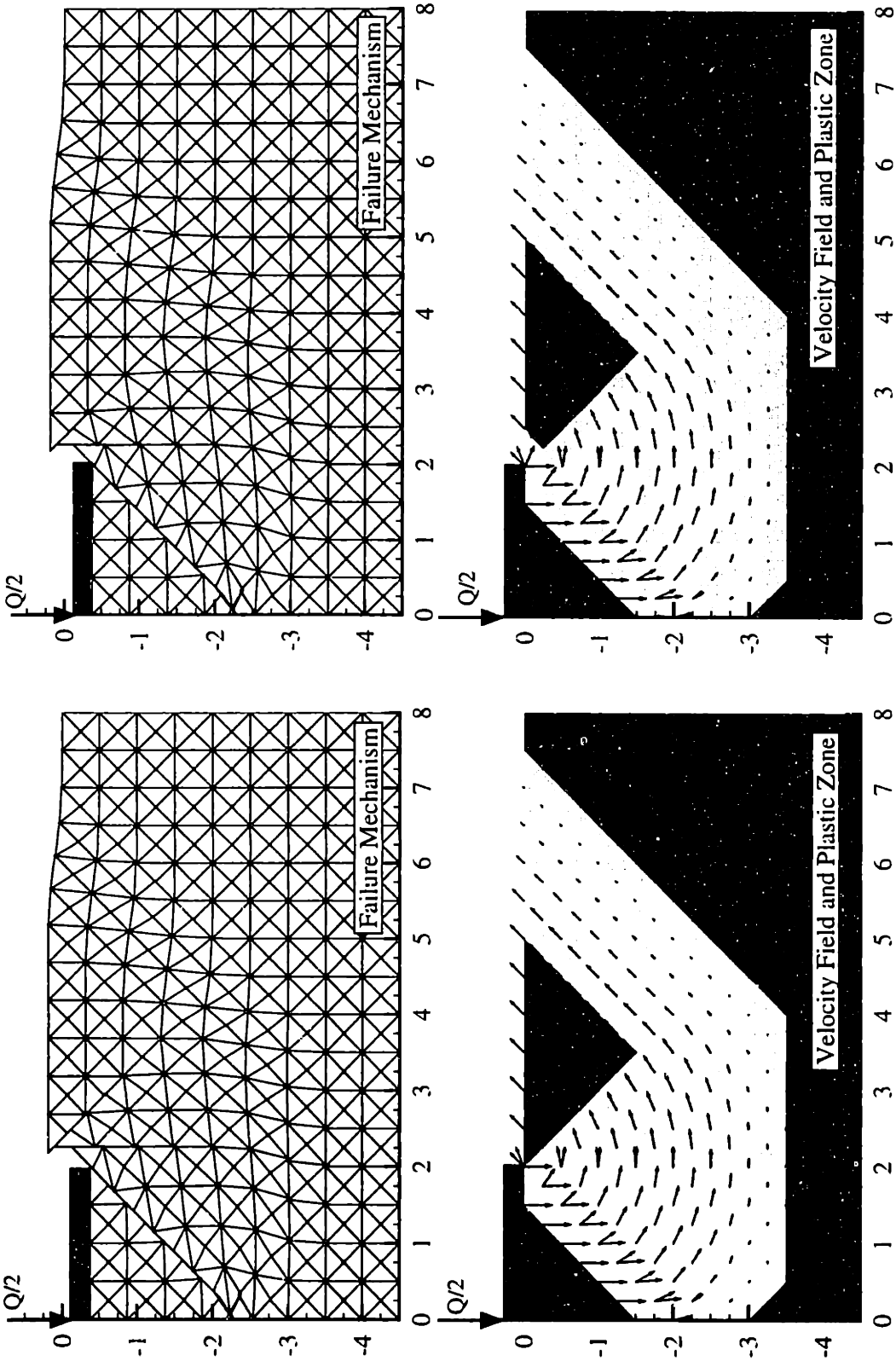

a) Isotropic strength, $N_c = 5.042 - 5.232$

b) Anisotropic strength at $\gamma = 1\%$, $N_c = 4.892 - 5.071$

Figure 4.28 Comparison of upper bound results between istropic and anisotropic strengths, rough footings

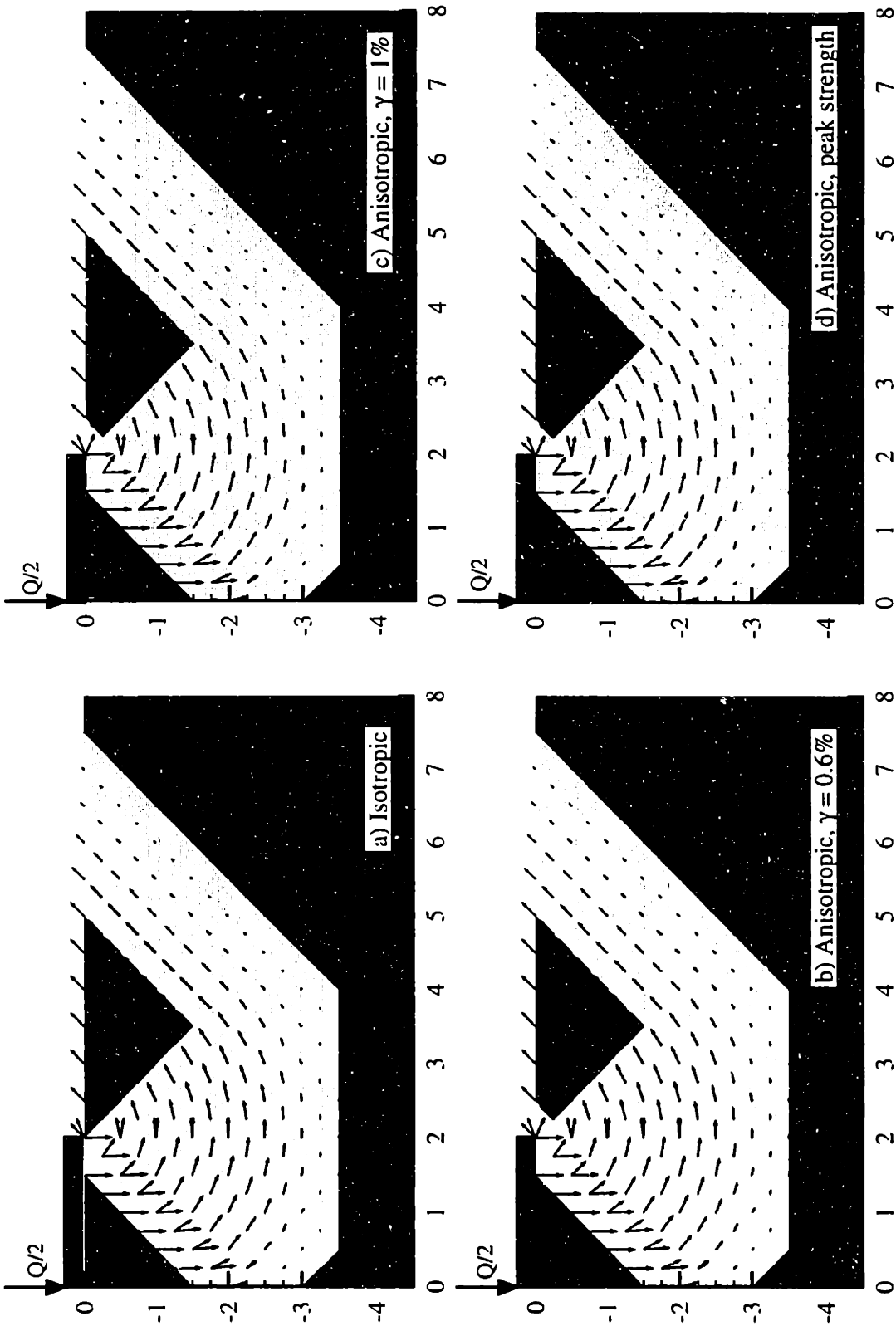

Figure 4.29 Comparisons of velocity fields and plastic zone between istropic and anisotropic strengths, rough footings

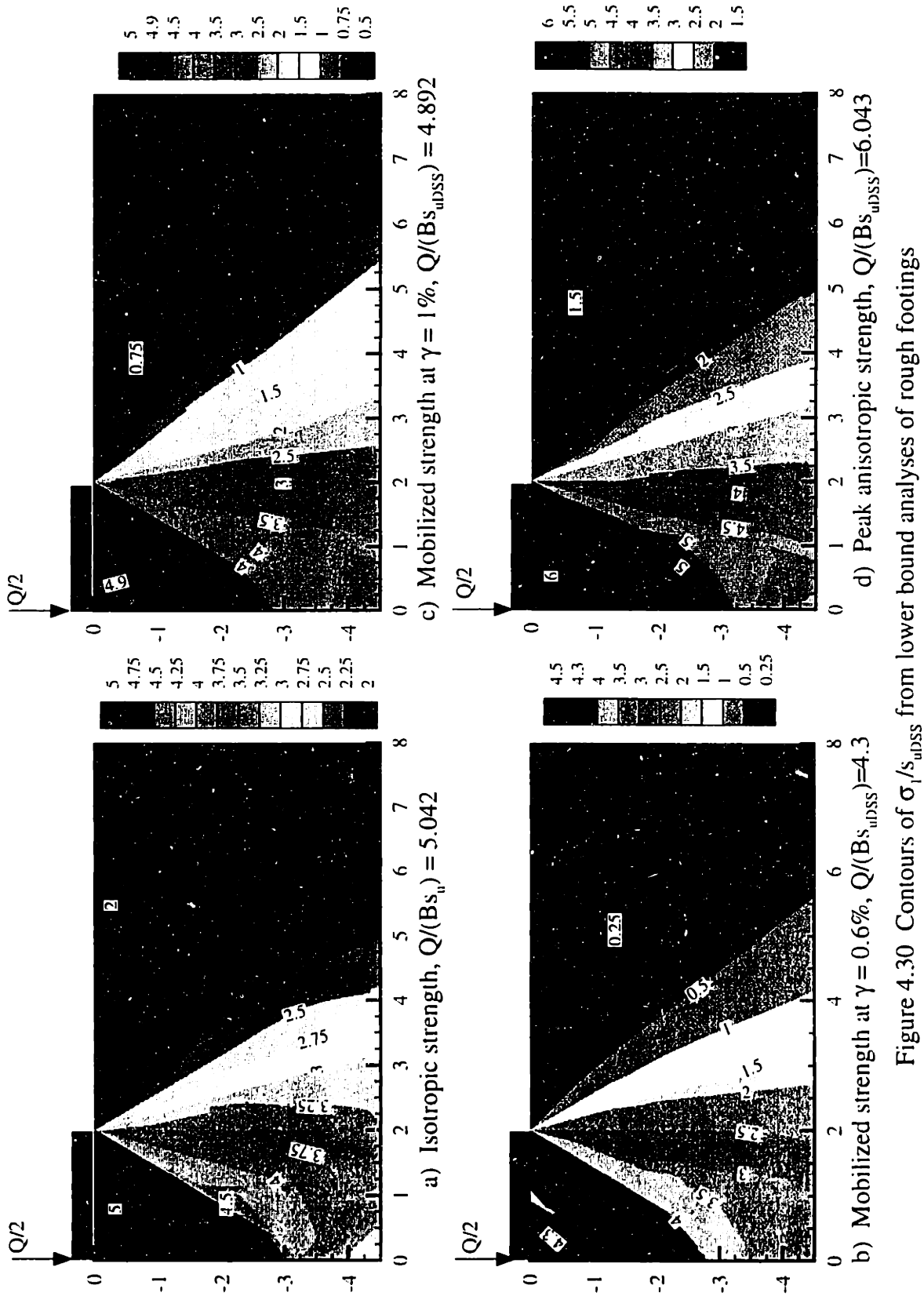

Figure 4.30 Contours of σ_1/s_{uDSS} from lower bound analyses of rough footings

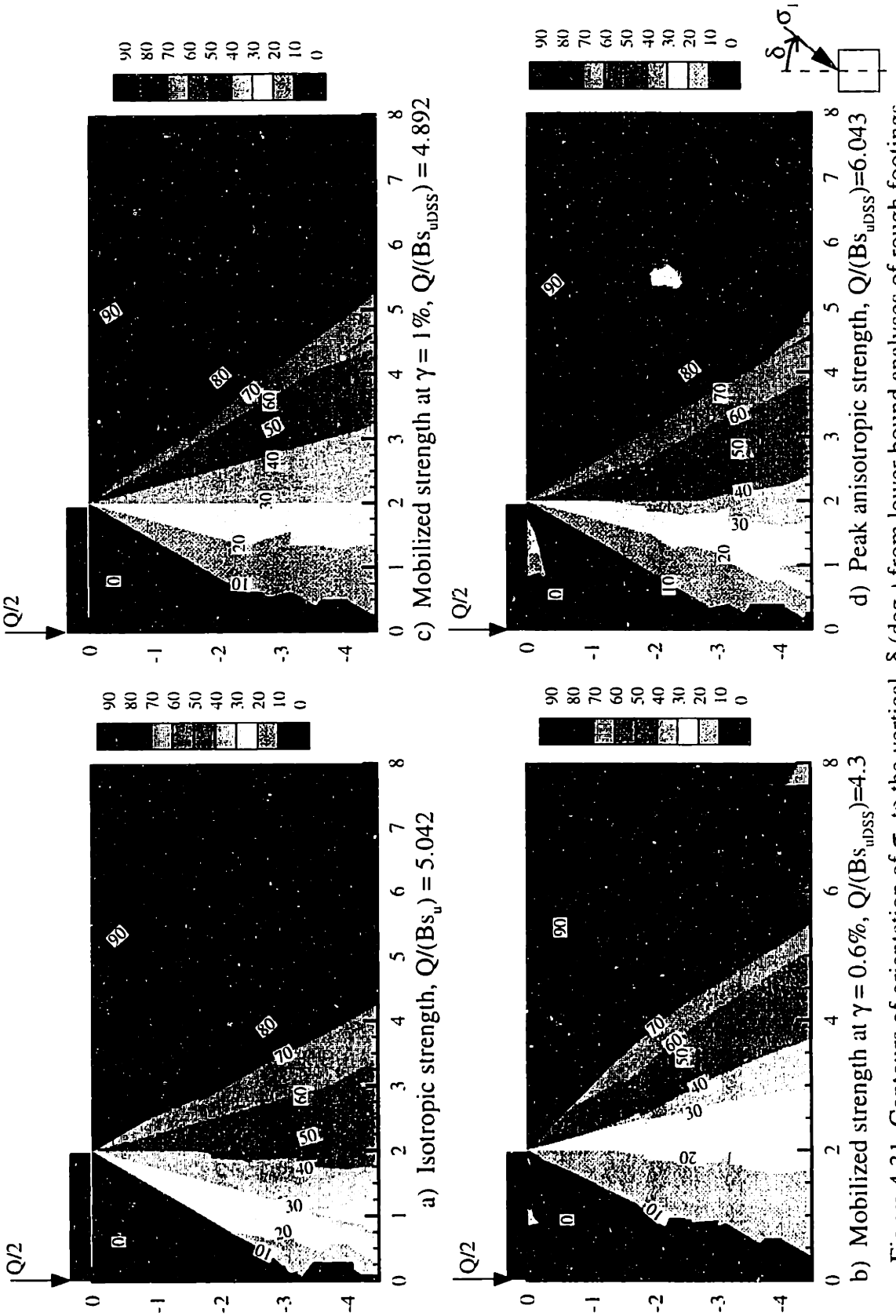

a) Isotropic strength, $Q/(Bs_u) = 5.042$

c) Mobilized strength at $\gamma = 1\%$, $Q/(Bs_{uDSS}) = 4.892$

b) Mobilized strength at $\gamma = 0.6\%$, $Q/(Bs_{uDSS})=4.3$

d) Peak anisotropic strength, $Q/(Bs_{uDSS})=6.043$

Figure 4.31 Contours of orientation of σ_1 to the vertical, δ (deg.) from lower bound analyses of rough footings

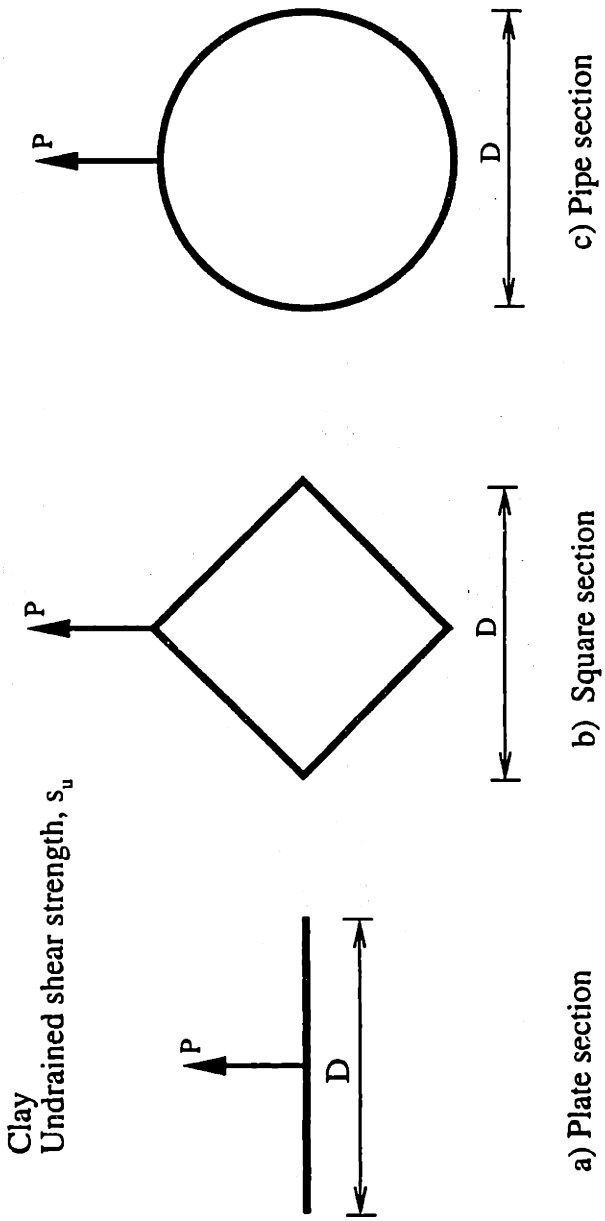

Figure 4.32 Ultimate lateral resistance of deeply-embeded sections in a clay layer (undrained)

SLIP FIELD PATTERN	SURFACE	ULTIMATE LATERAL RESISTANCE, q_{ult}/c_u
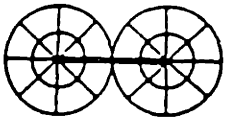	ROUGH	12.56
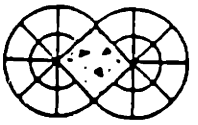	ROUGH	11.42
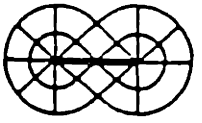	SMOOTH	11.42
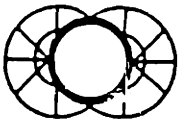	SMOOTH	9.14
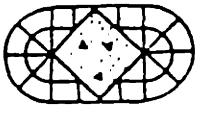	SMOOTH	8.28

Figure 4.33 Ultimate lateral resistance of sections given by Broms (1964)

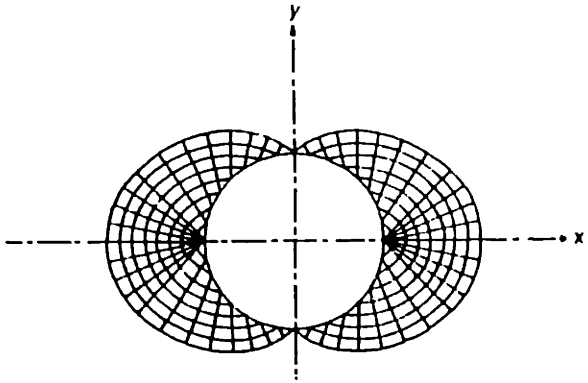

a) Characteristics for smooth surfaces

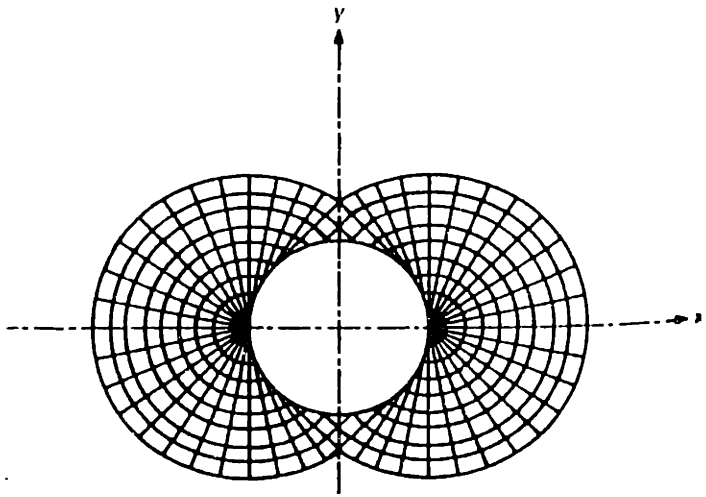

b) Characteristics for rough surfaces

Roughness ratio, f_s/s_u	Lower Bound Solutions (equation 4.34)	Upper Bound Solutions (Randolph. Pers. Comm., 1998)
0.0 (smooth)	9.14	9.66
0.1	9.53	9.96
0.2	9.89	10.24
0.3	10.22	10.51
0.4	10.53	10.76
0.5	10.82	11.00
0.6	11.09	11.22
0.7	11.34	11.42
0.8	11.56	11.61
0.9	11.77	11.79
1.0 (rough)	11.94	11.94

c) Analytical lateral resistance, N_p

Figure 4.34 Ultimate lateral resistance of pipe sections given by Randolph and Houlsby (1984)

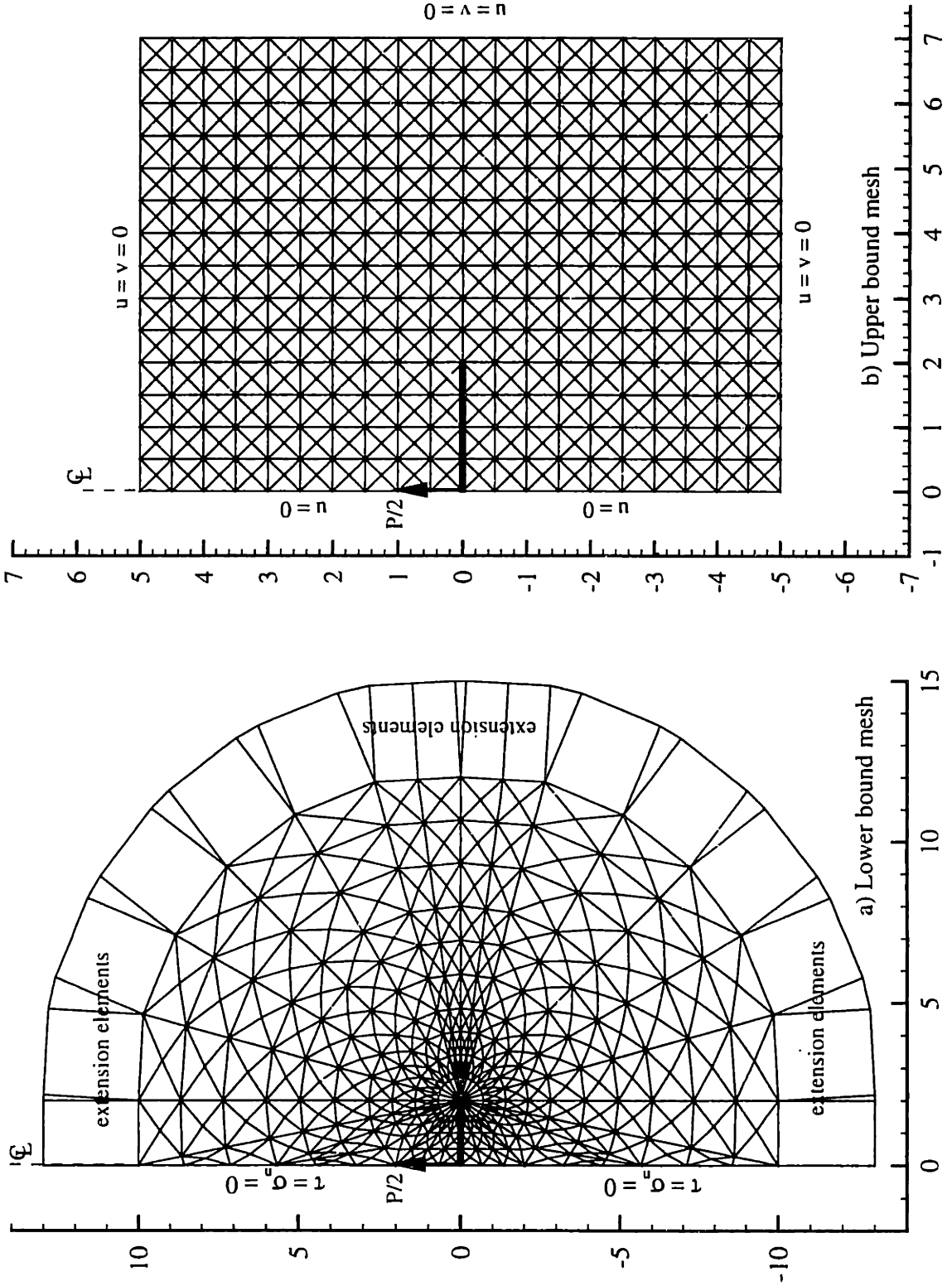

Figure 4.35 Meshes used for limit analyses of plate sections

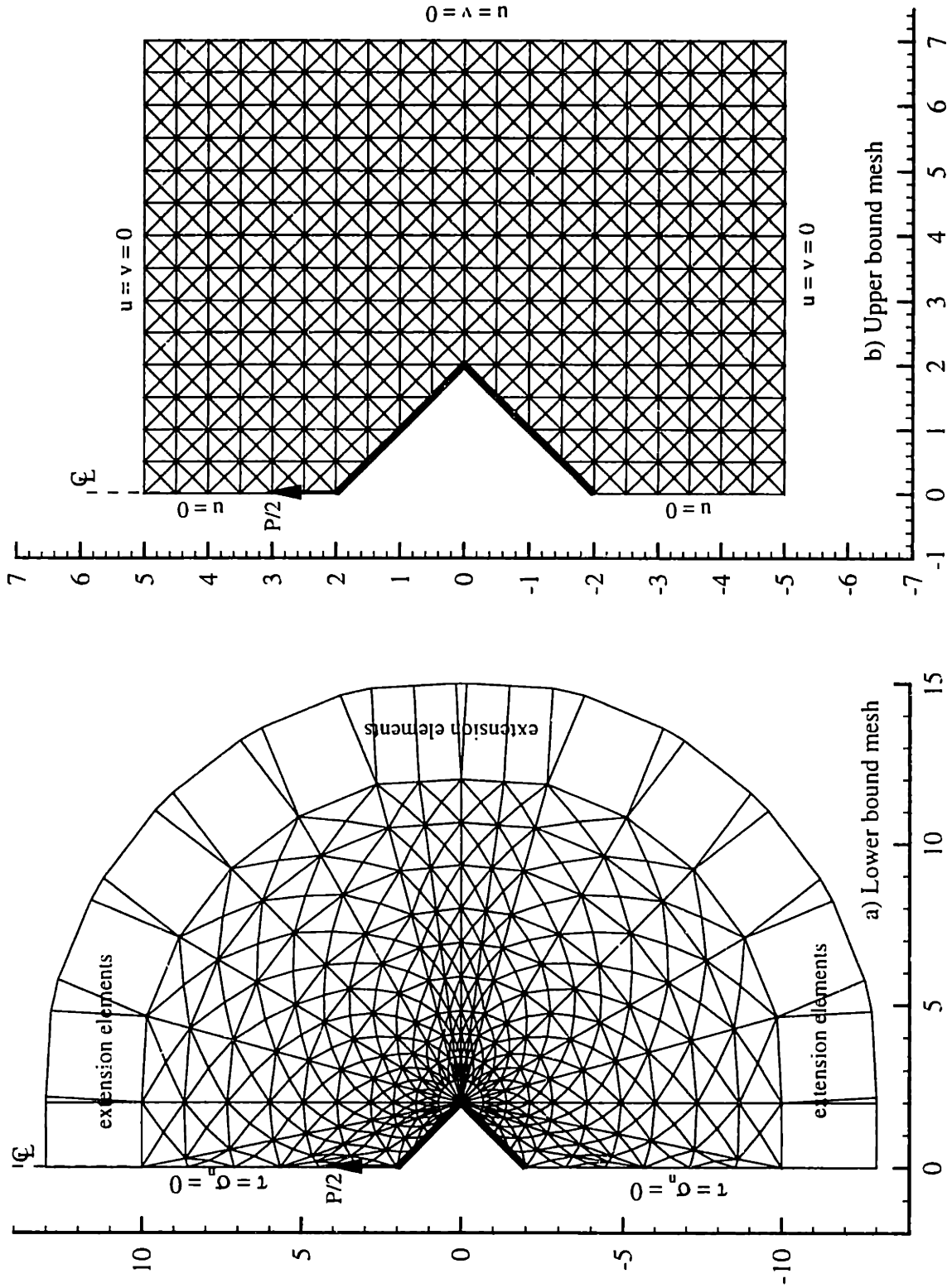

Figure 4.36 Meshes used for limit analyses of square sections

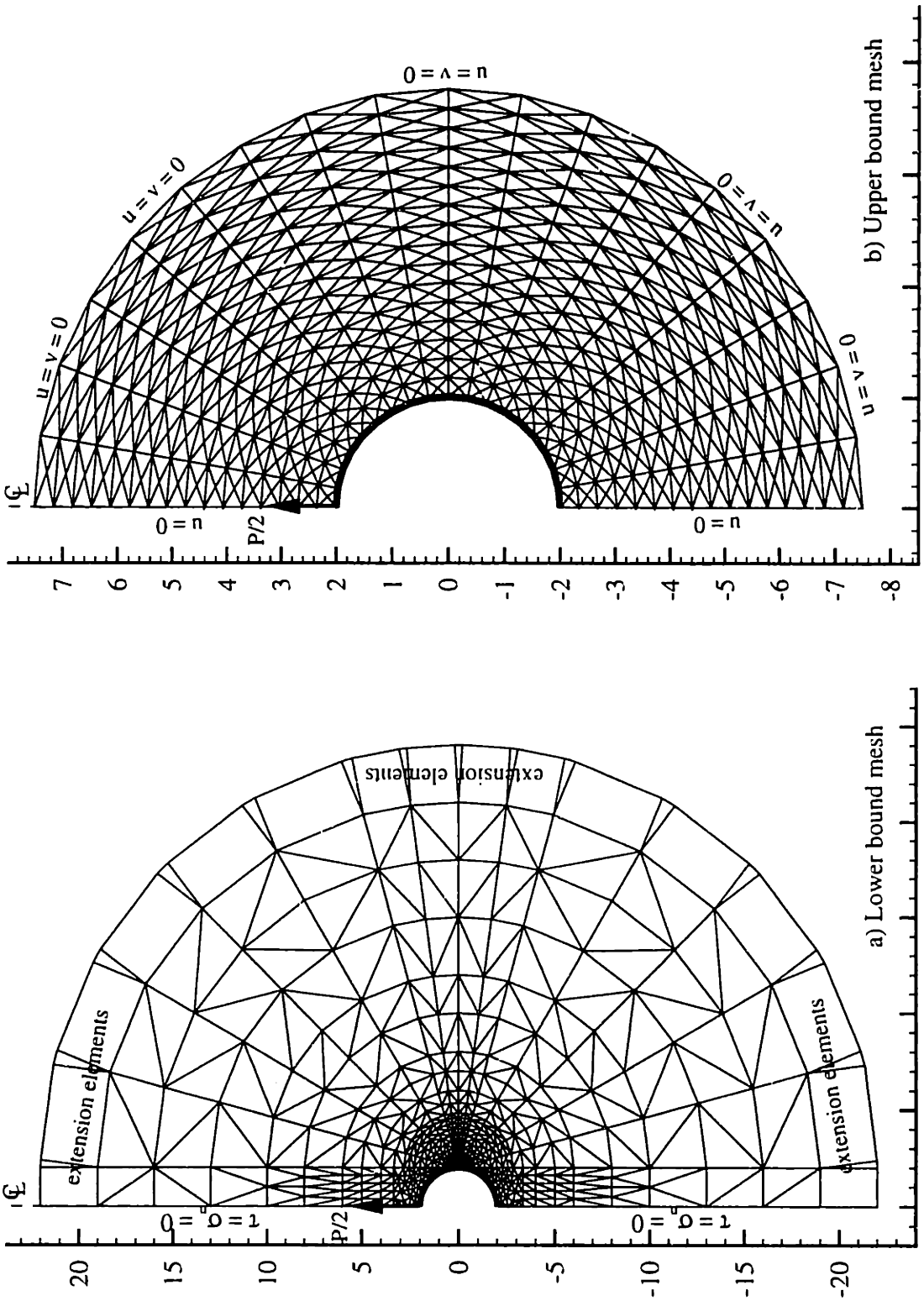

Figure 4.37 Meshes used for limit analyses of pipe sections

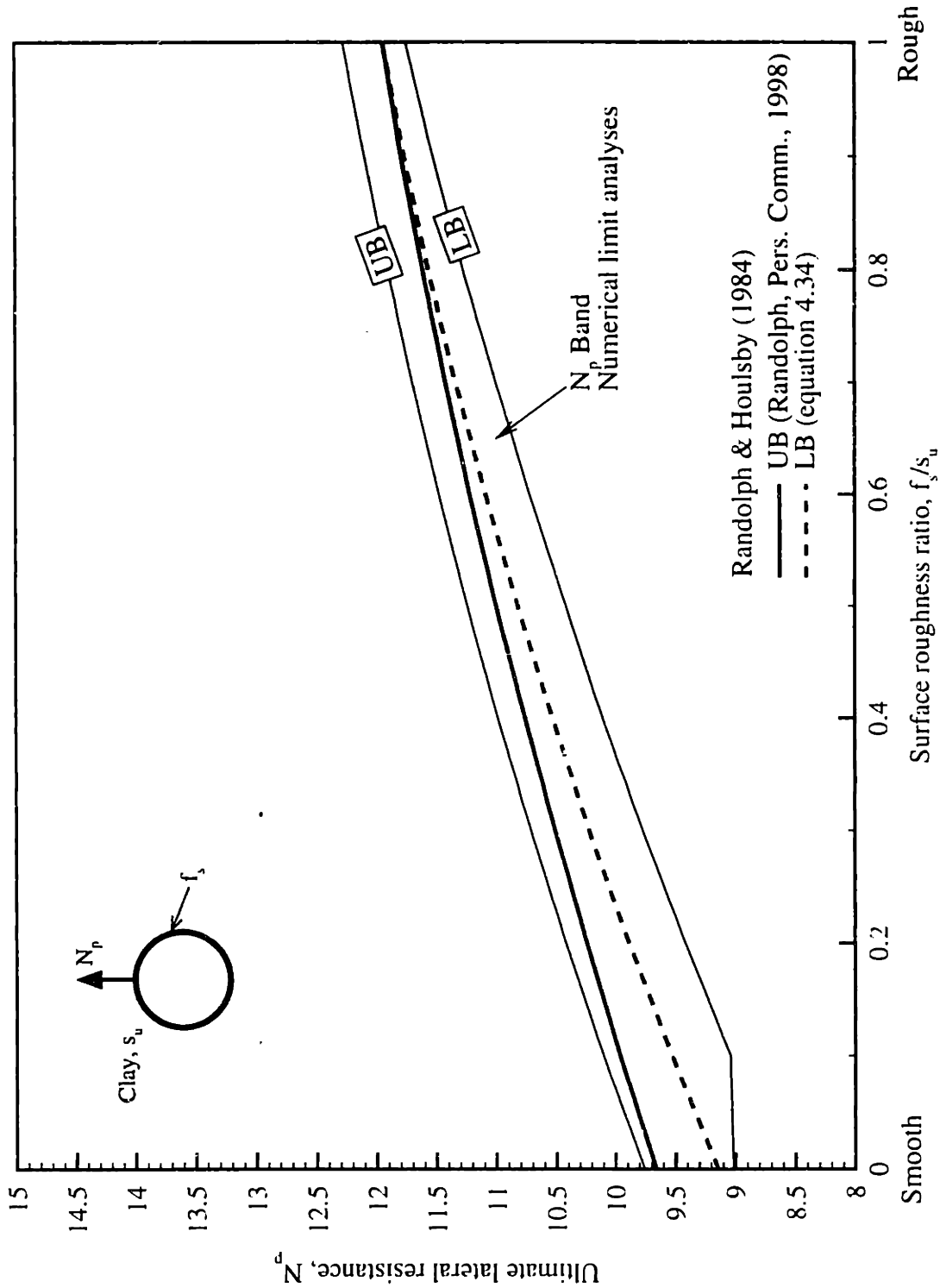

Figure 4.38 Effects of surface roughness ratios to ultimate lateral resistance of pipe sections

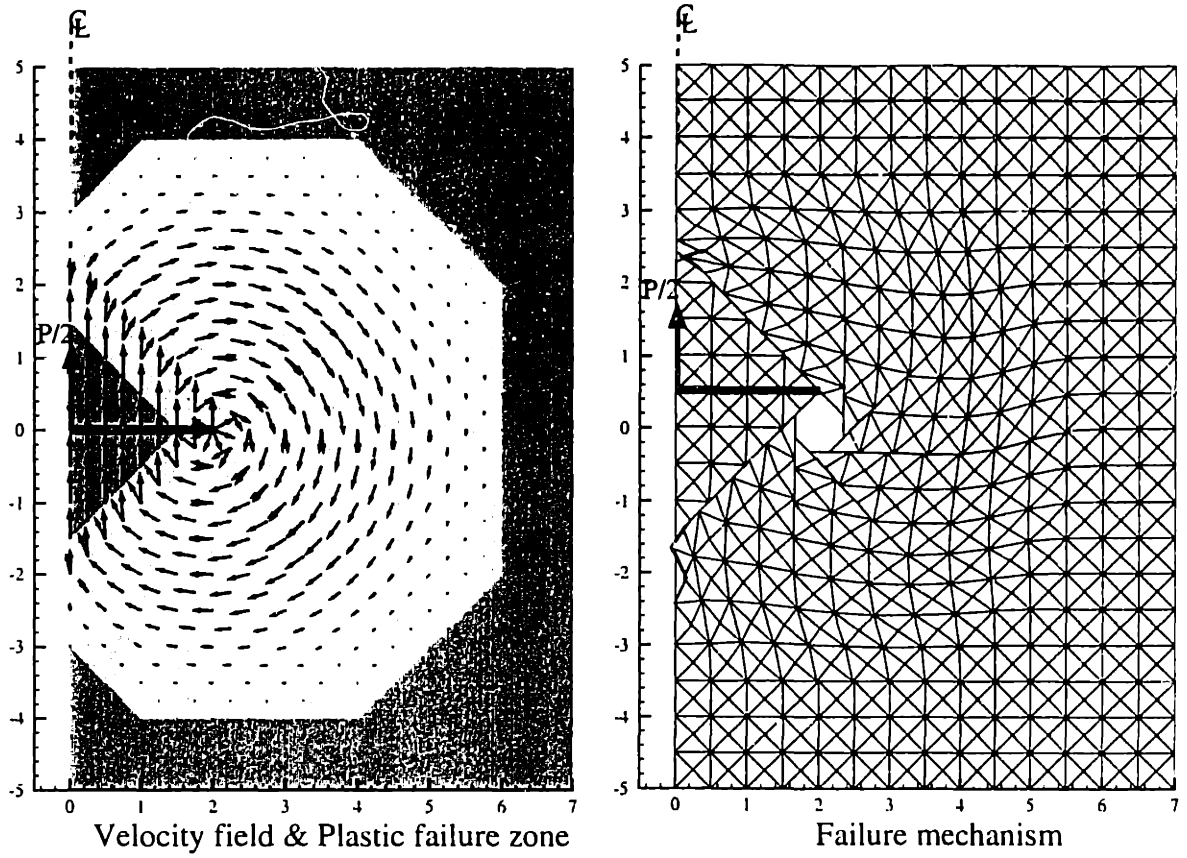

a) Rough interfaces: N_p = 11.294 - 11.654

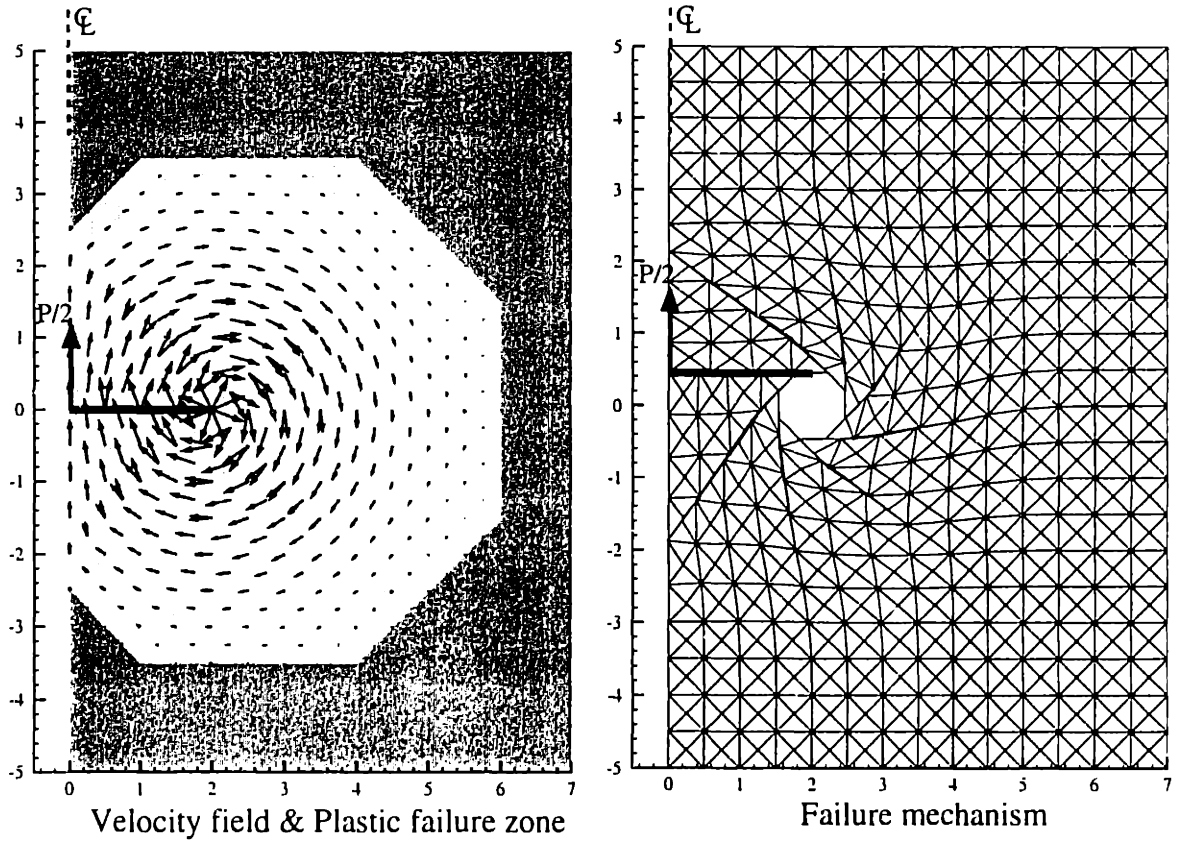

b) smooth interfaces: N_p = 11.285 - 11.623

Figure 4.39 Upper bound results of ultimate lateral resistance of plate sections

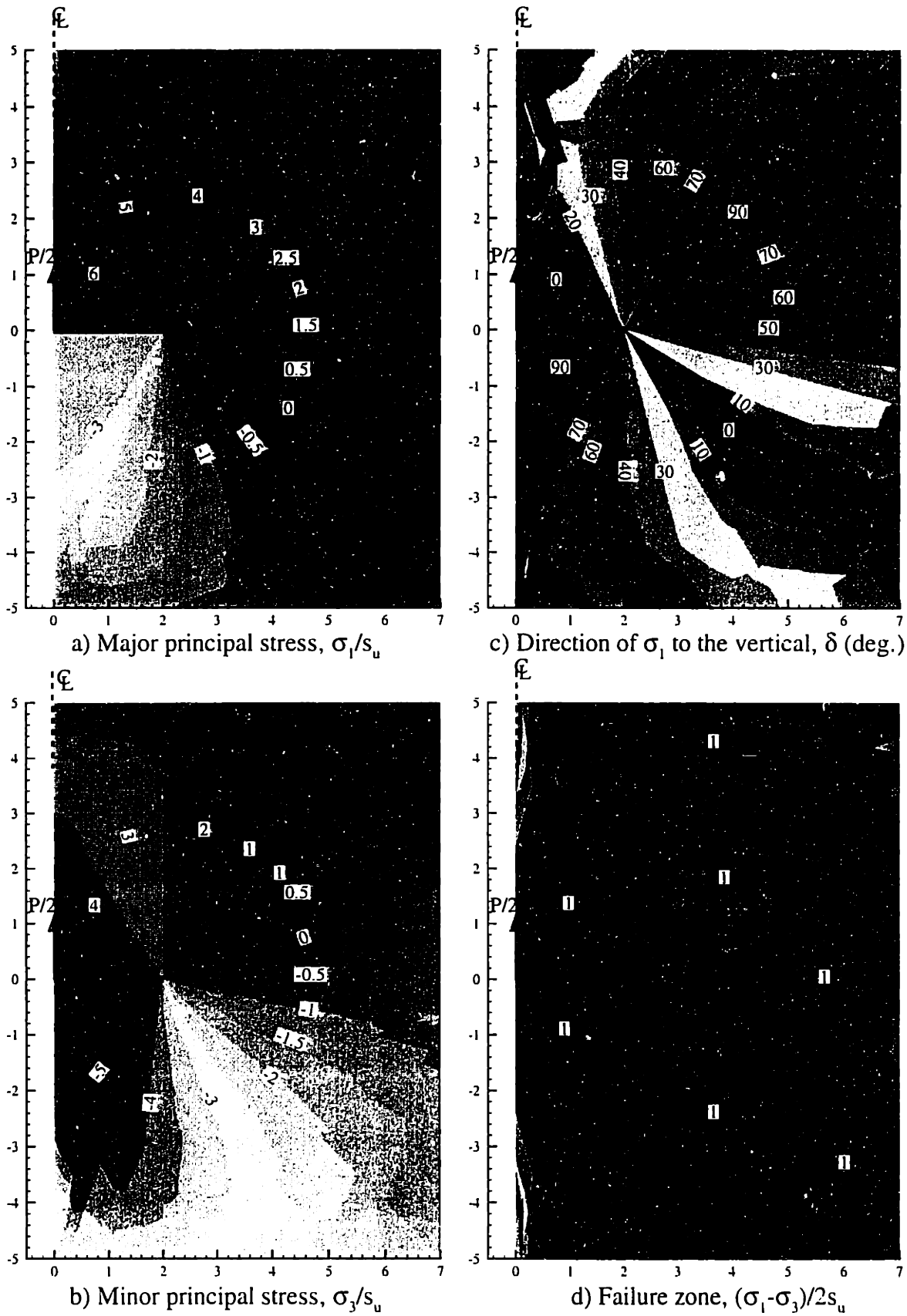

Figure 4.40 Lower bound results of ultimate lateral resistance of plate sections, smooth surfaces: N_p = 11.285 - 11.623

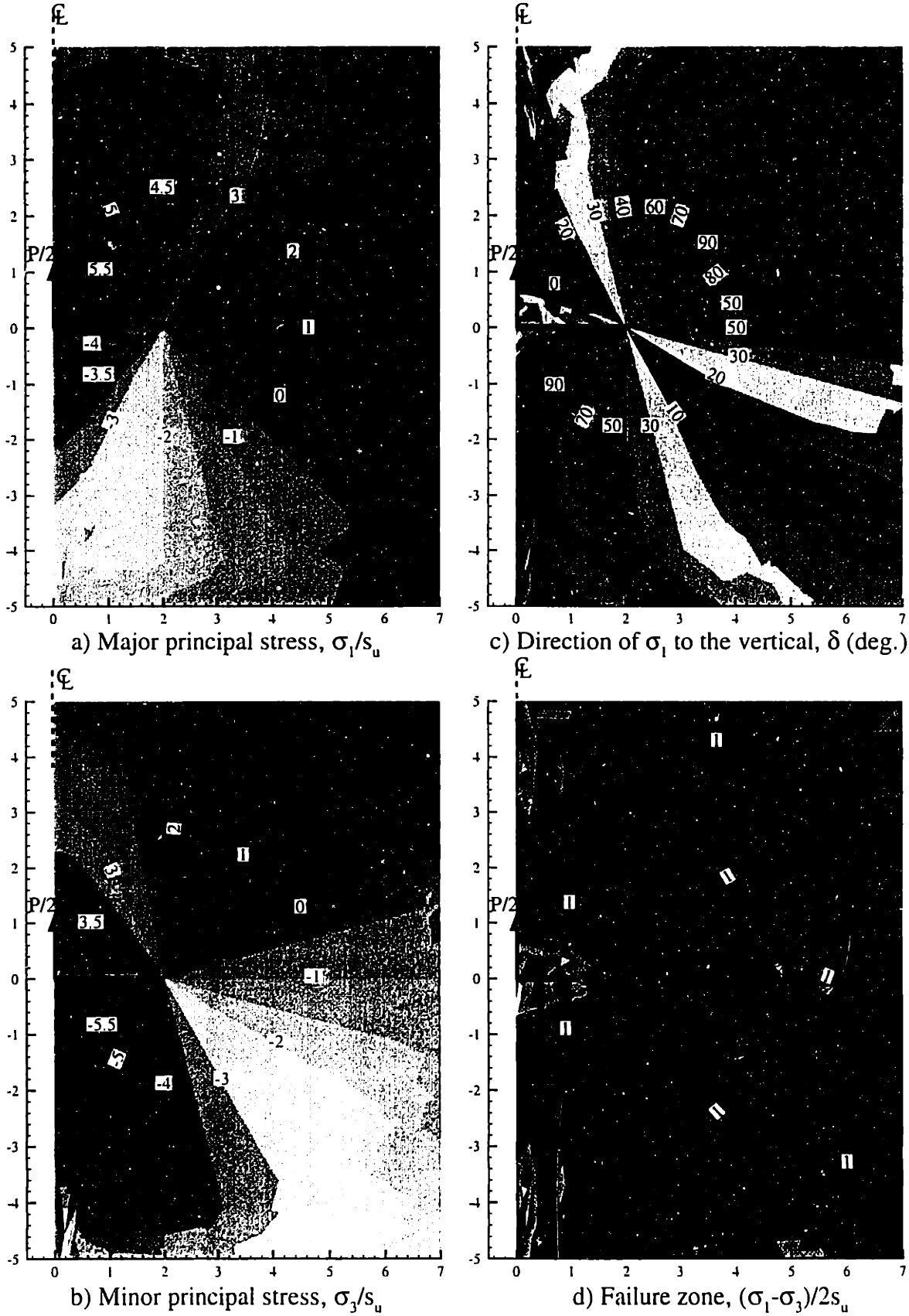

a) Major principal stress, σ_1/s_u

c) Direction of σ_1 to the vertical, δ (deg.)

Figure 4.41 Lower bound results of ultimate lateral resistance of plate sections, rough surfaces: N_p = 11.294 - 11.654

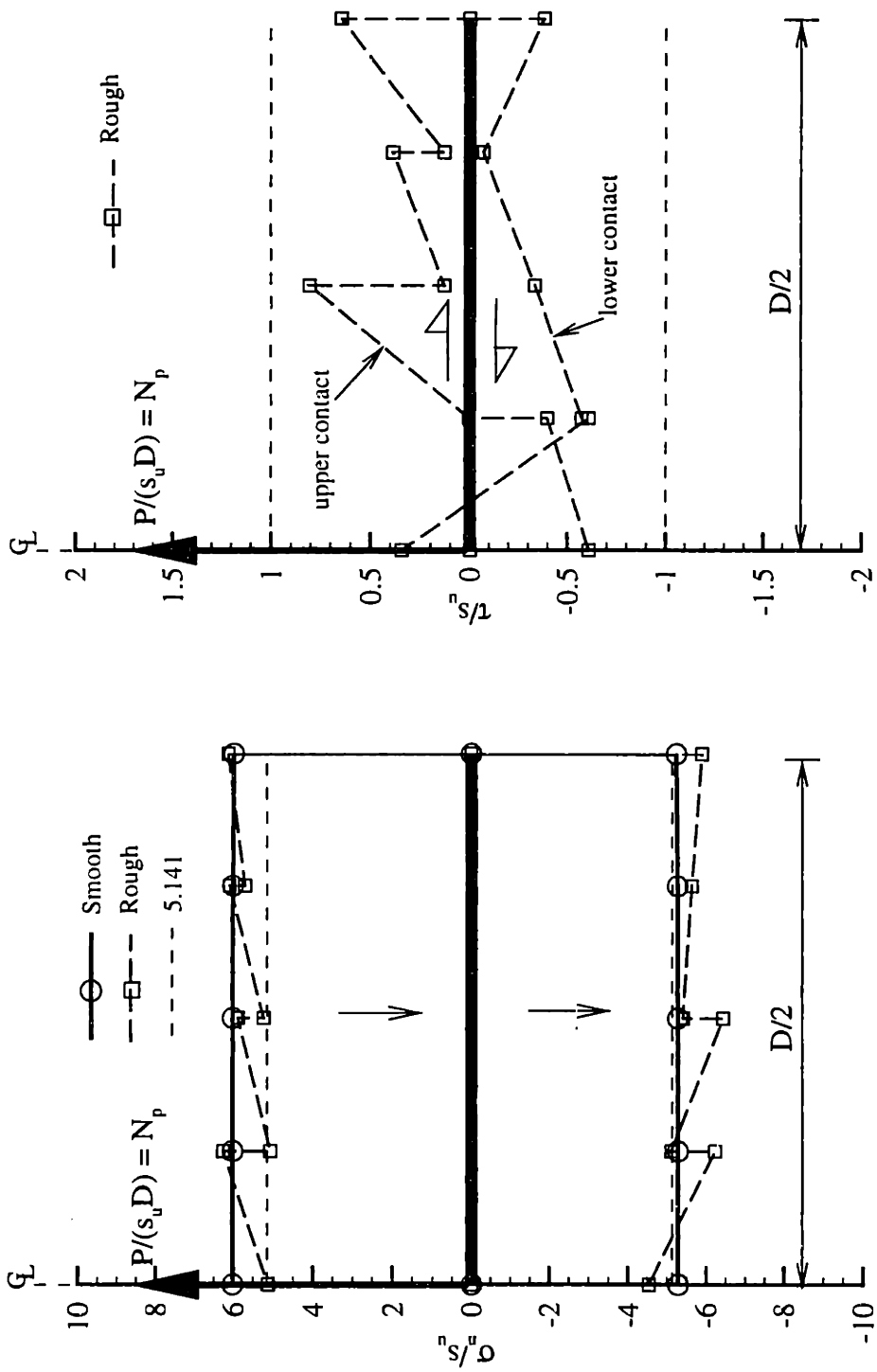

Figure 4.42 Contact stresses from lower bound results of lateral resistance of plate sections
Rough: N_p = 11.294 - 11.654 Smooth: N_p = 11.285 - 11.623

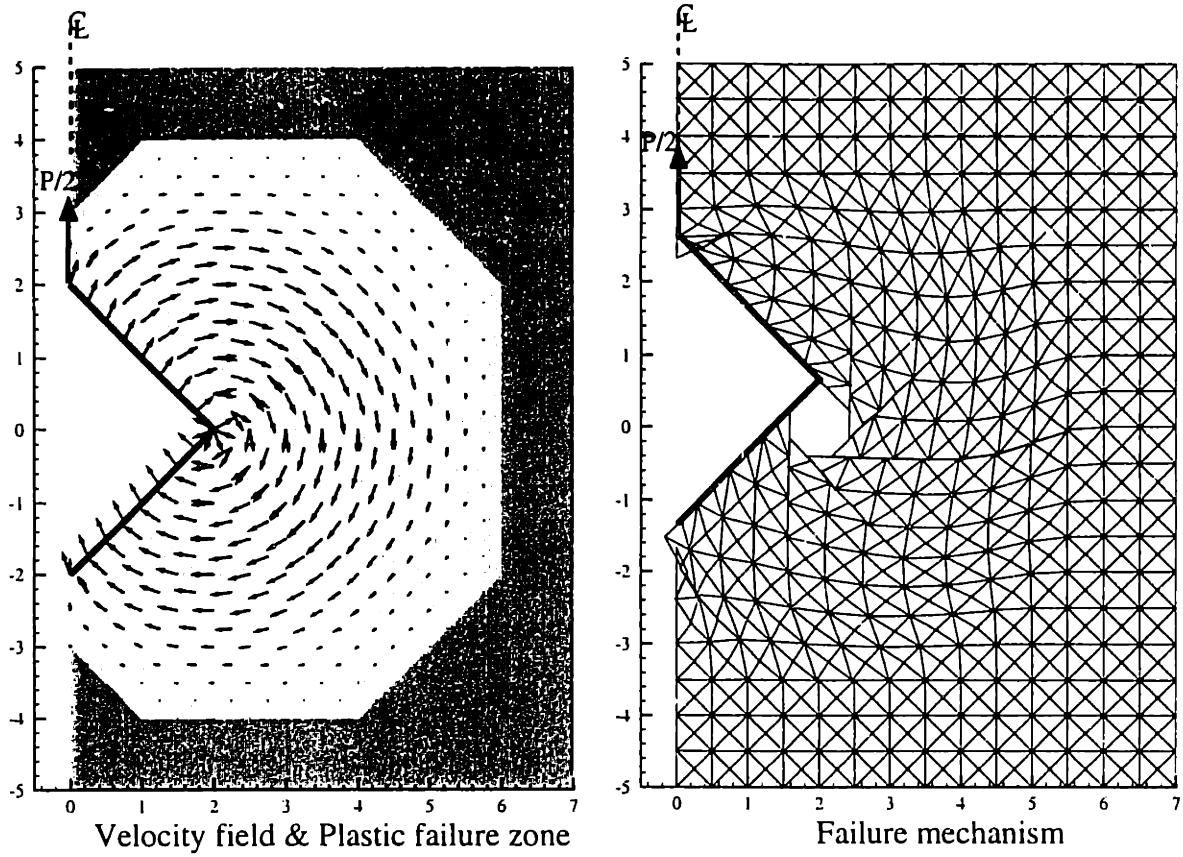

a) Rough interfaces: N_p = 11.294 - 11.661

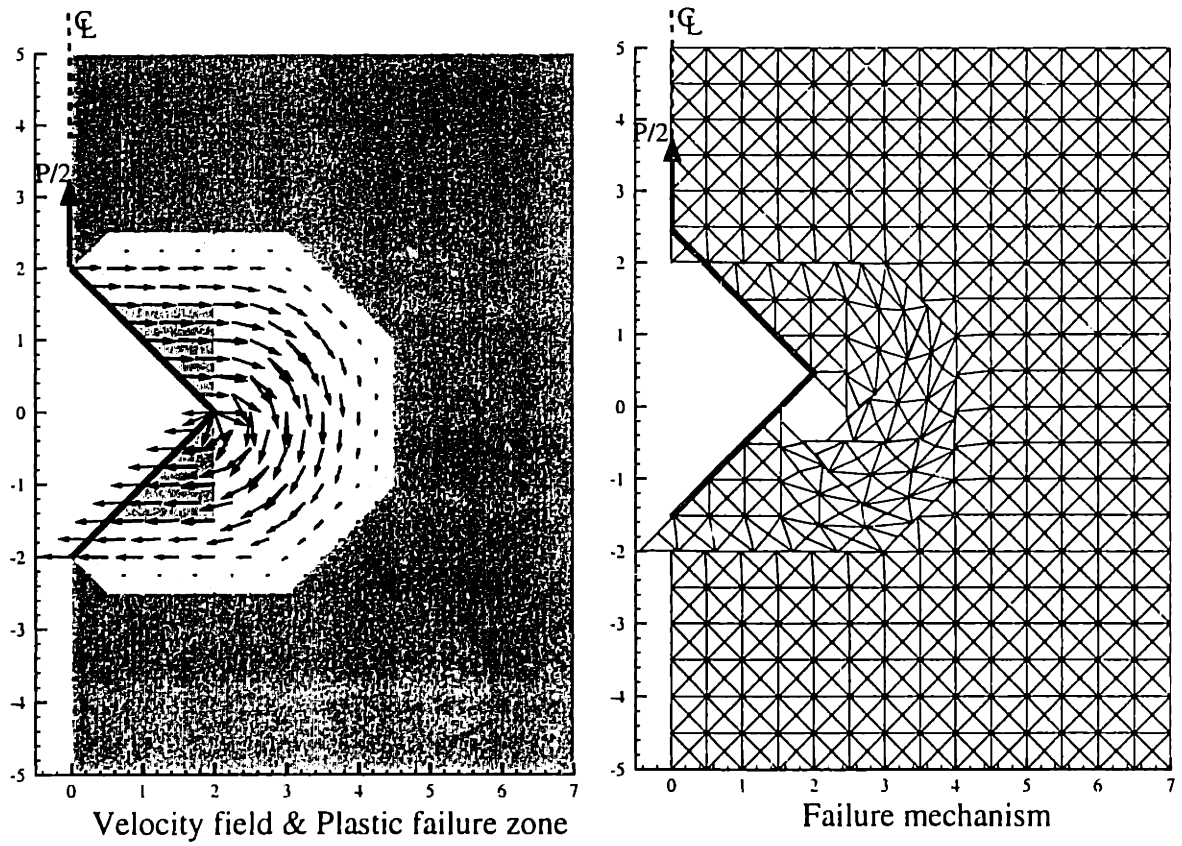

b) smooth interfaces: N_p = 8.194 - 8.531

Figure 4.43 Upper bound results of ultimate lateral resistance of square sections

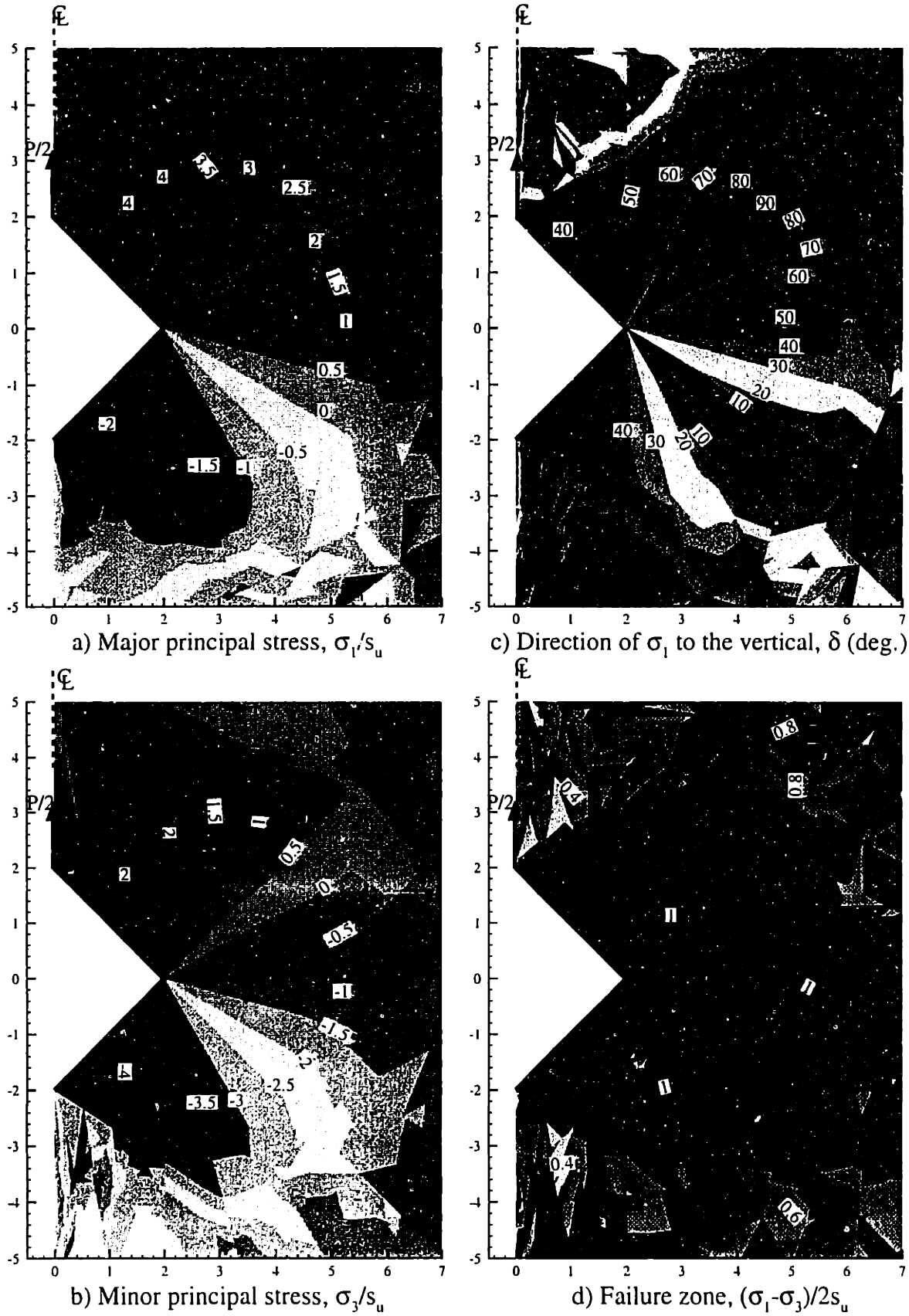

a) Major principal stress, σ_1/s_u

c) Direction of σ_1 to the vertical, δ (deg.)

b) Minor principal stress, σ_3/s_u

d) Failure zone, $(\sigma_1-\sigma_3)/2s_u$

Figure 4.44 Lower bound results of ultimate lateral resistance of square sections, smooth surfaces: N_p = 8.194 - 8.531

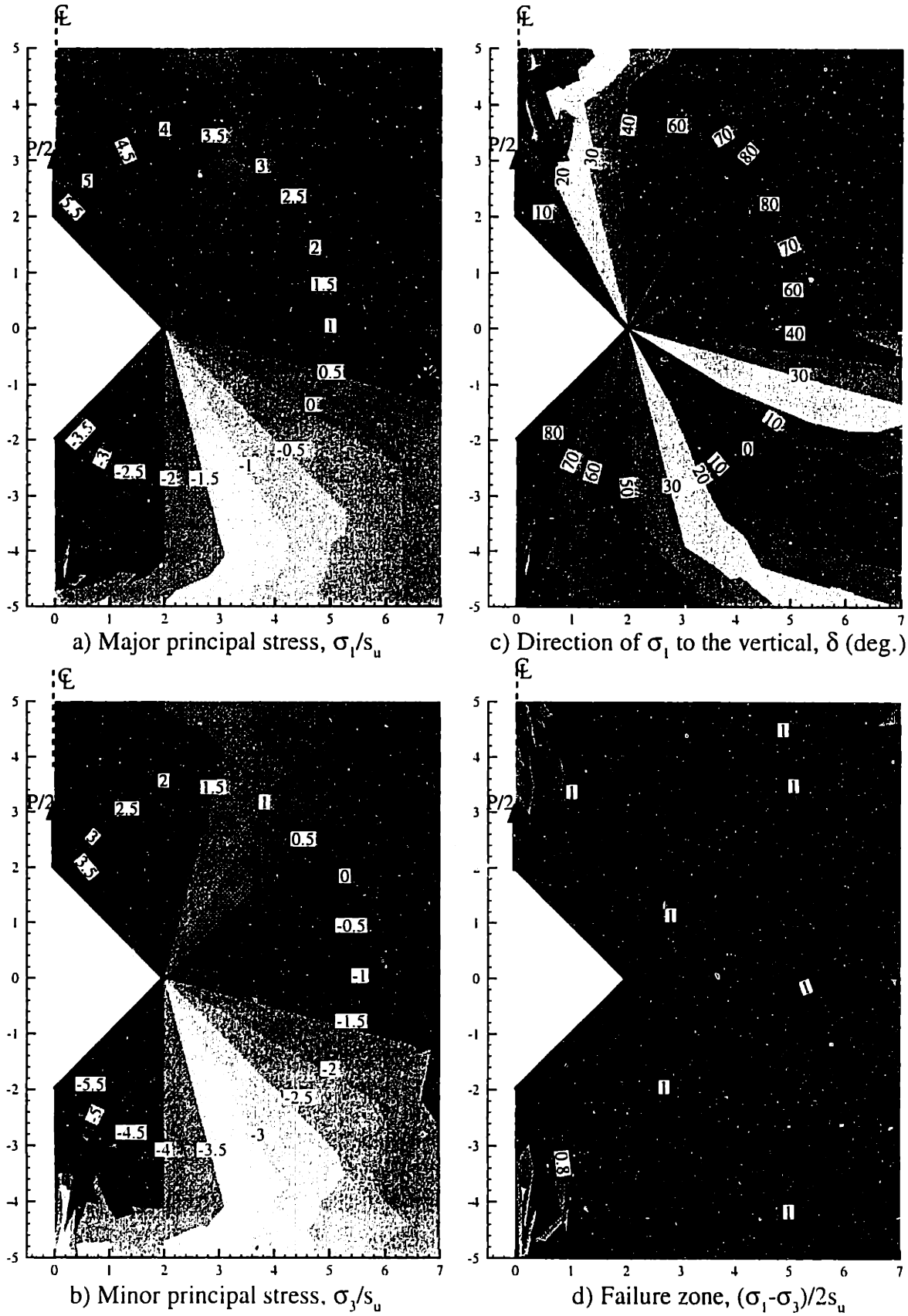

Figure 4.45 Lower bound results of ultimate lateral resistance of square sections, rough surfaces: N_p = 11.294 - 11.661

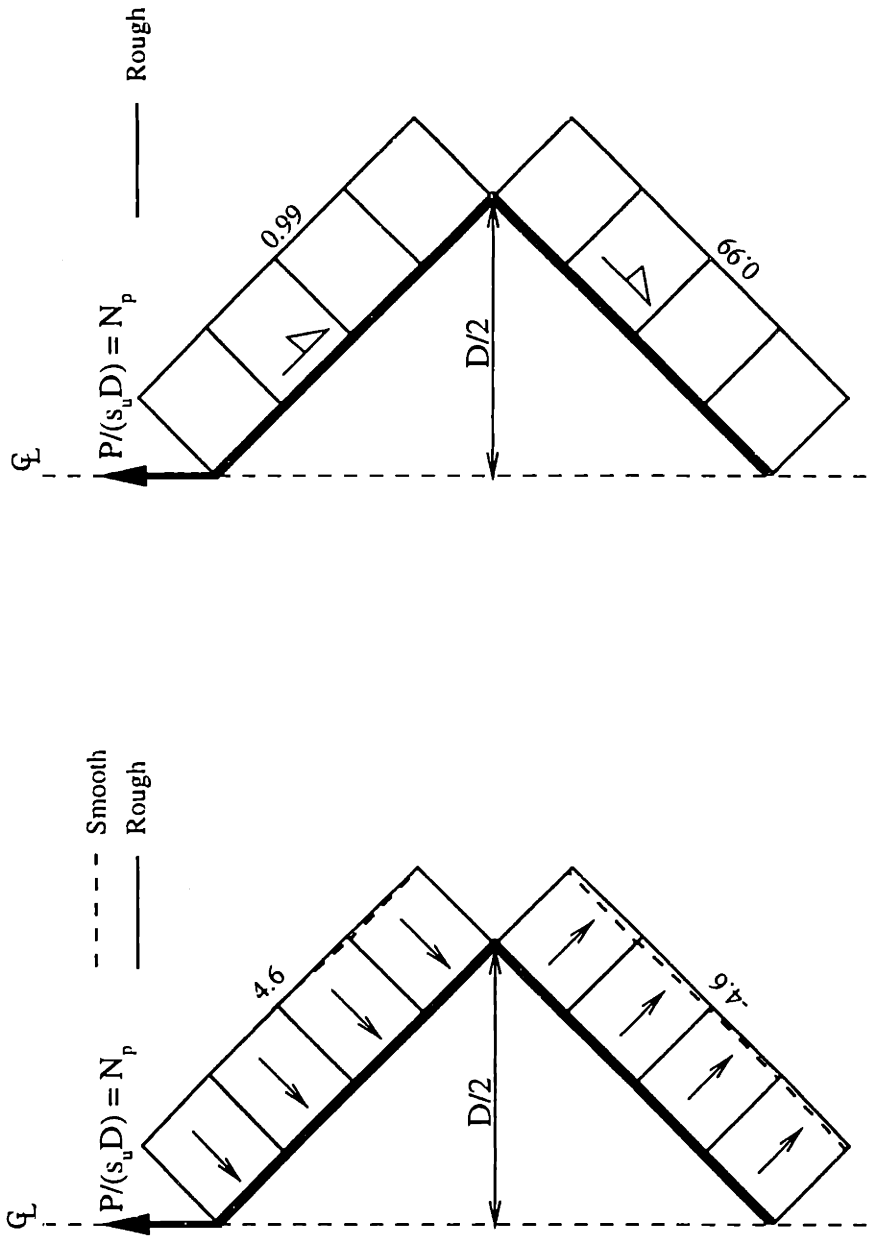

a) Contact normal traction, σ_n/s_u

b) Contact shear traction, τ/s_u

Figure 4.46 Contact stresses from lower bound results of lateral resistance of square sections

Rough: N_p = 11.294 - 11.661 Smooth: N_p = 8.194 - 8.531

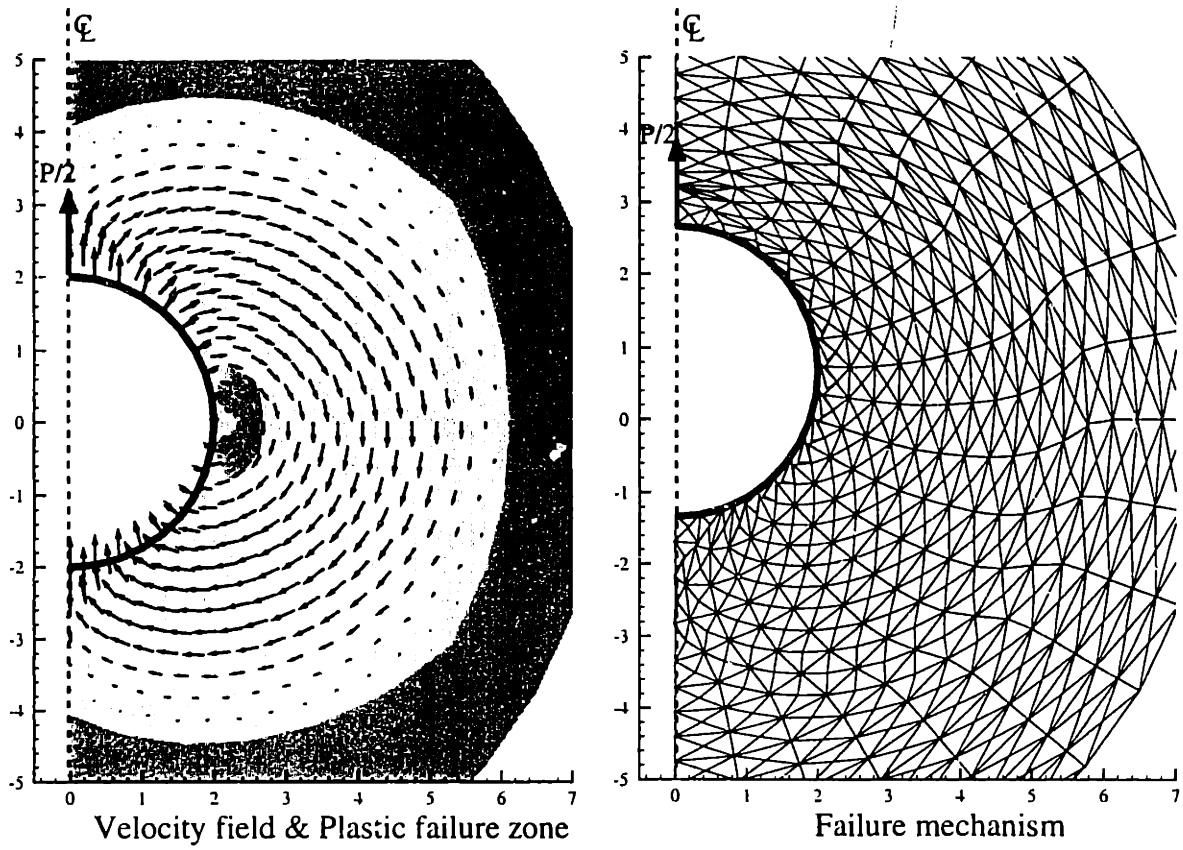

Velocity field & Plastic failure zone Failure mechanism

a) Rough interfaces: N_p = 11.747 - 12.271

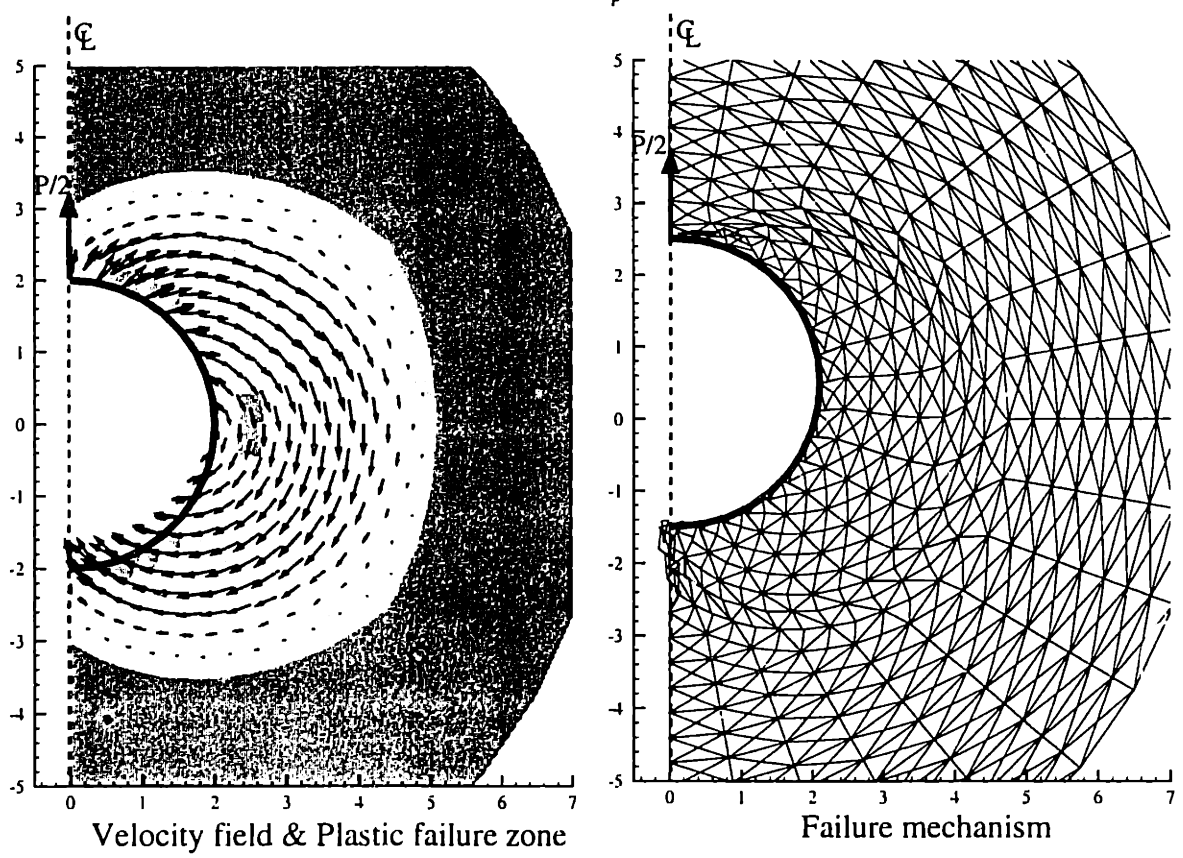

Velocity field & Plastic failure zone Failure mechanism

b) smooth interfaces: N_p = 9.016 - 9.756

Figure 4.47 Upper bound results of ultimate lateral resistance of pipe sections

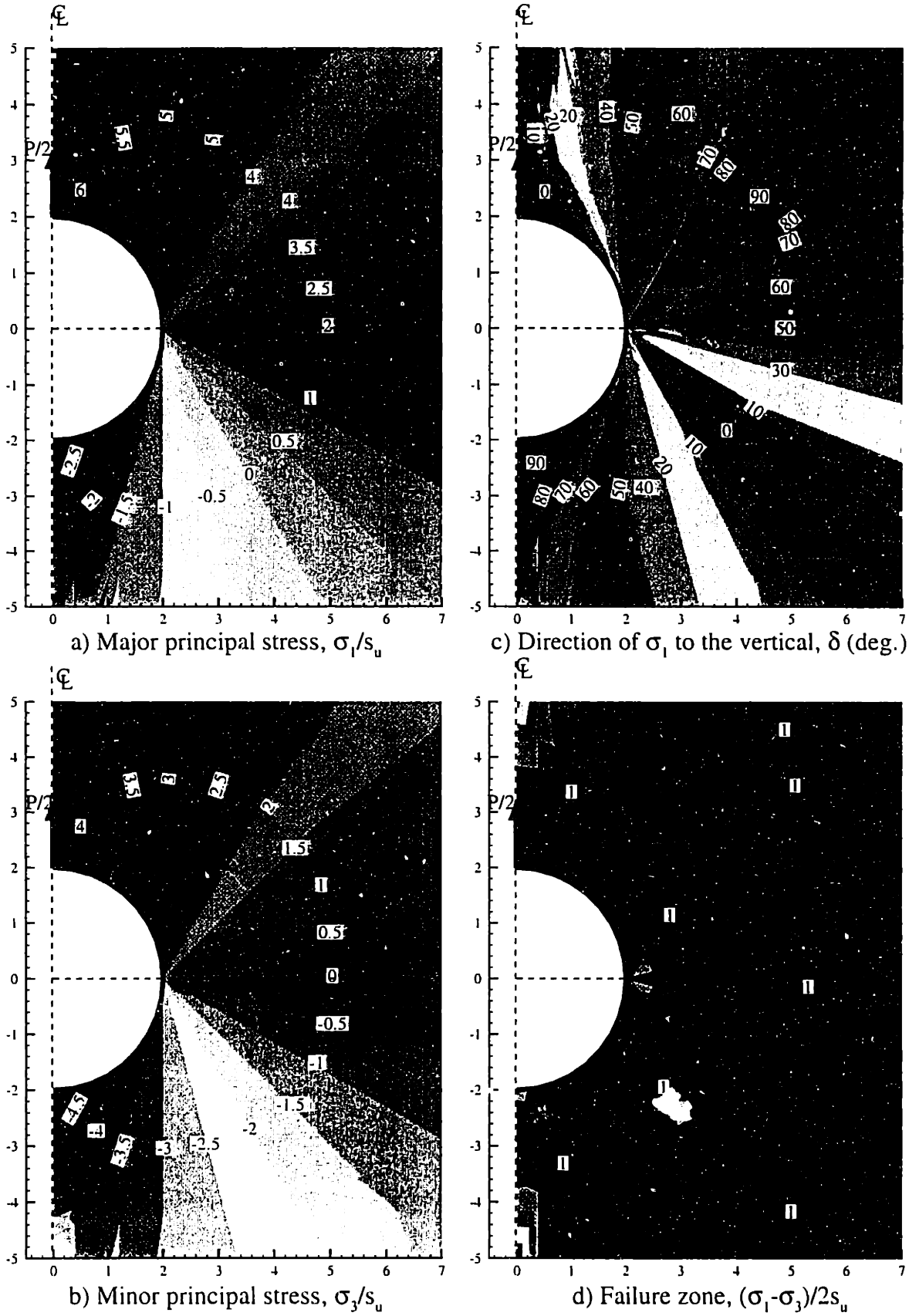

a) Major principal stress, σ_1/s_u

c) Direction of σ_1 to the vertical, δ (deg.)

b) Minor principal stress, σ_3/s_u

d) Failure zone, $(\sigma_1-\sigma_3)/2s_u$

Figure 4.48 Lower bound results of ultimate lateral resistance of pipe sections, rough surfaces: N_p = 11.747 - 12.271

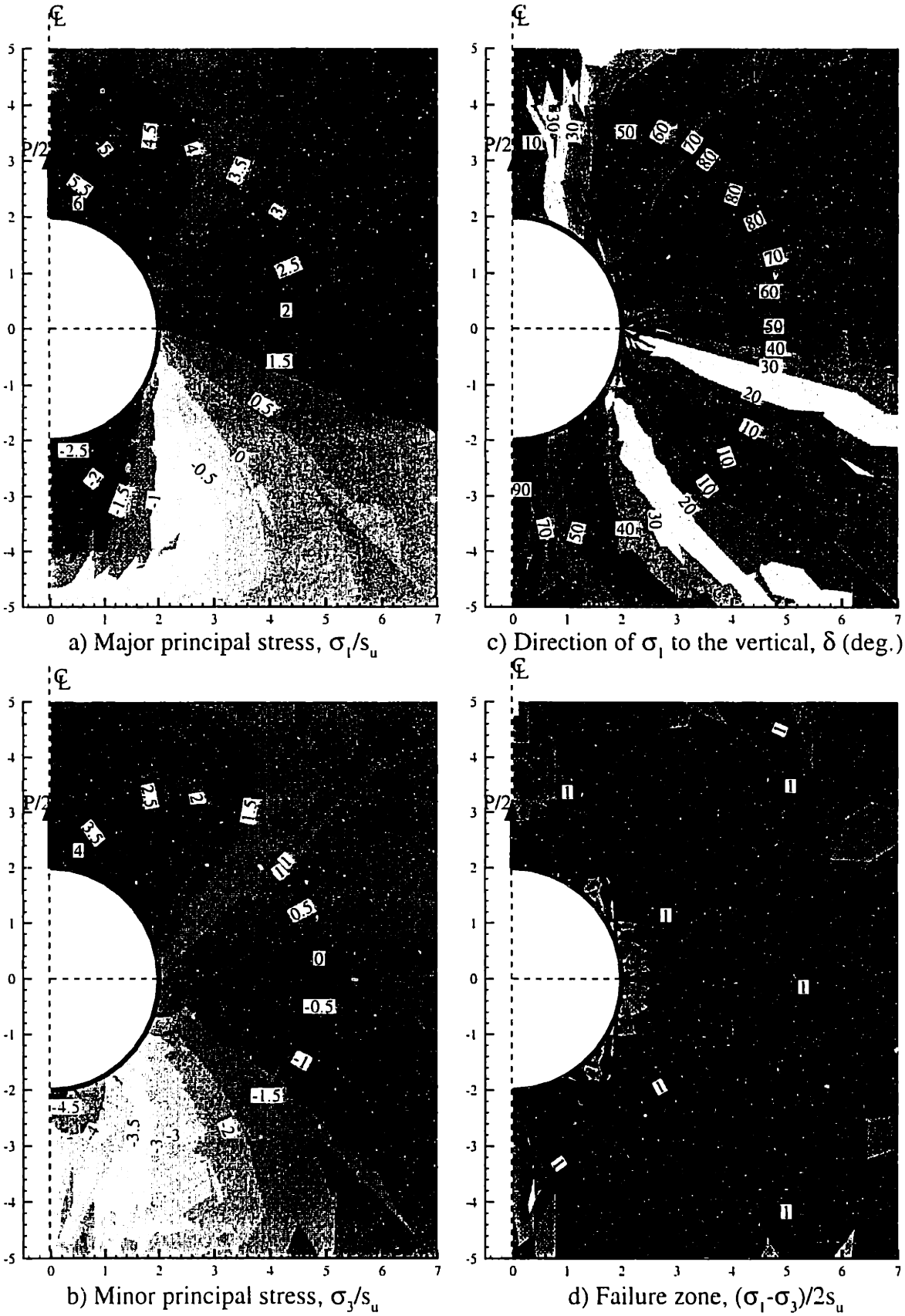

Figure 4.49 Lower bound results of ultimate lateral resistance of pipe sections, smooth surfaces: $N_p = 9.016 - 9.756$

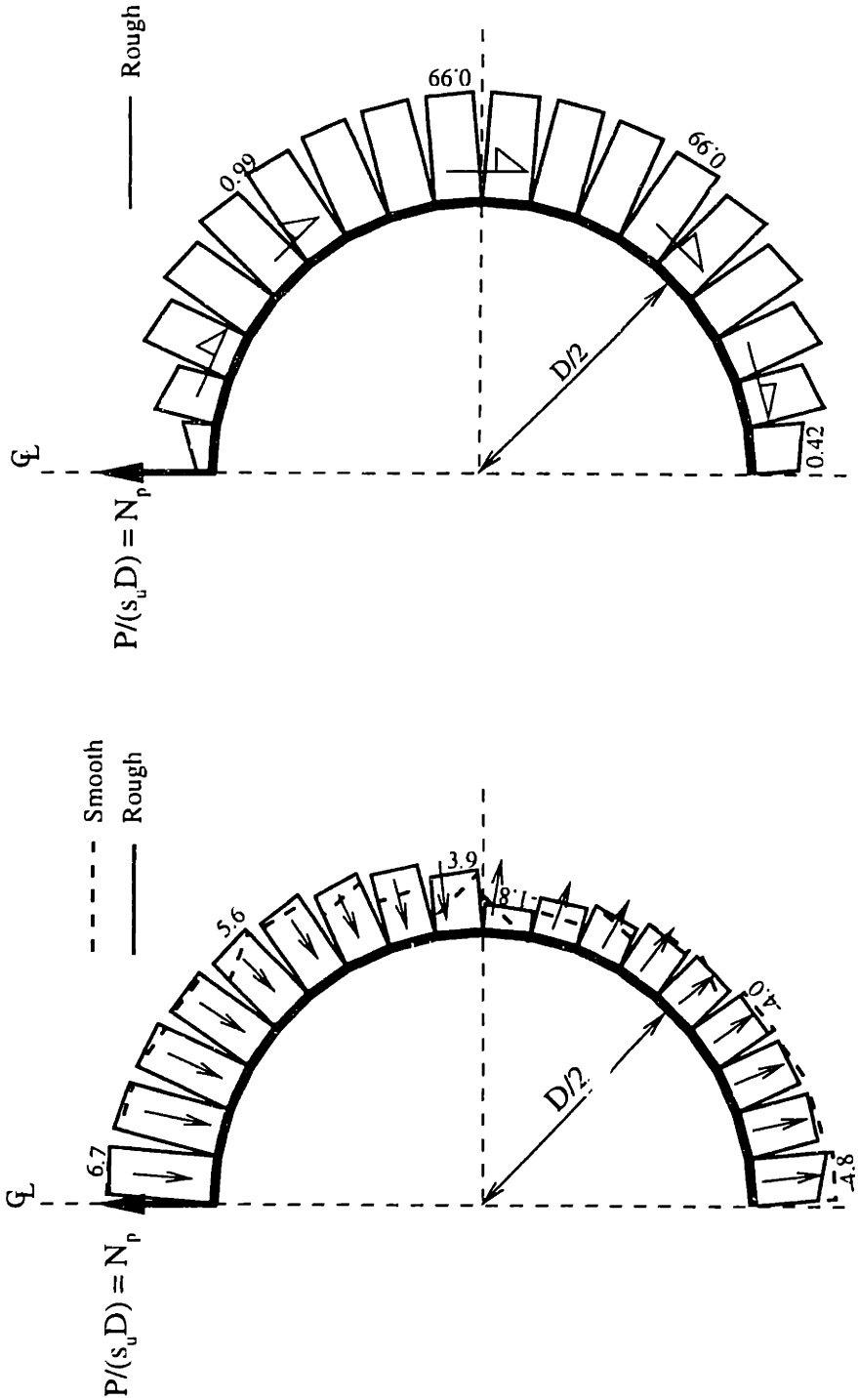

b) Contact shear traction, τ/s_u

a) Contact normal traction, σ_n/s_u

Figure 4.50 Contact stresses from lower bound results of lateral resistance of pipe sections

Rough: N_p = 11.747 - 11.271 Smooth: N_p = 9.016 - 9.756

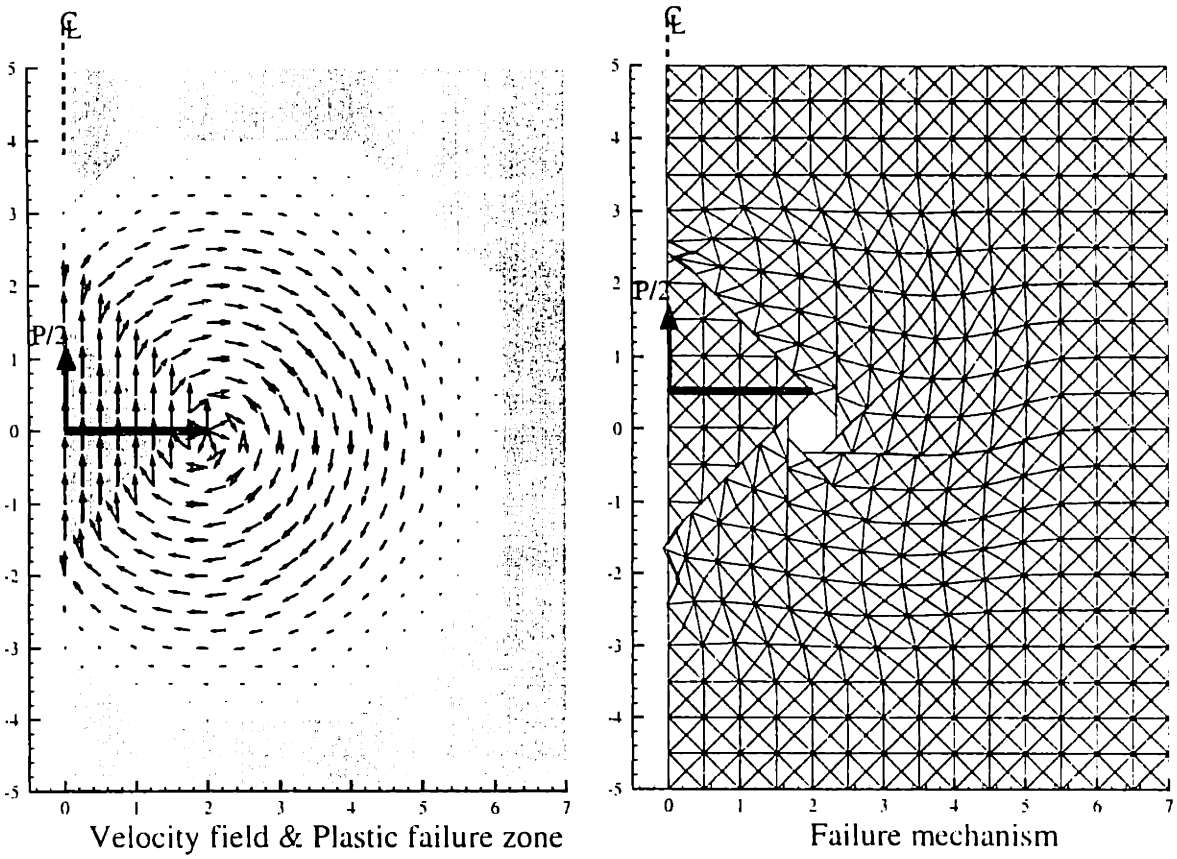

a) Isotropic strength: N_p = 11.294 - 11.654

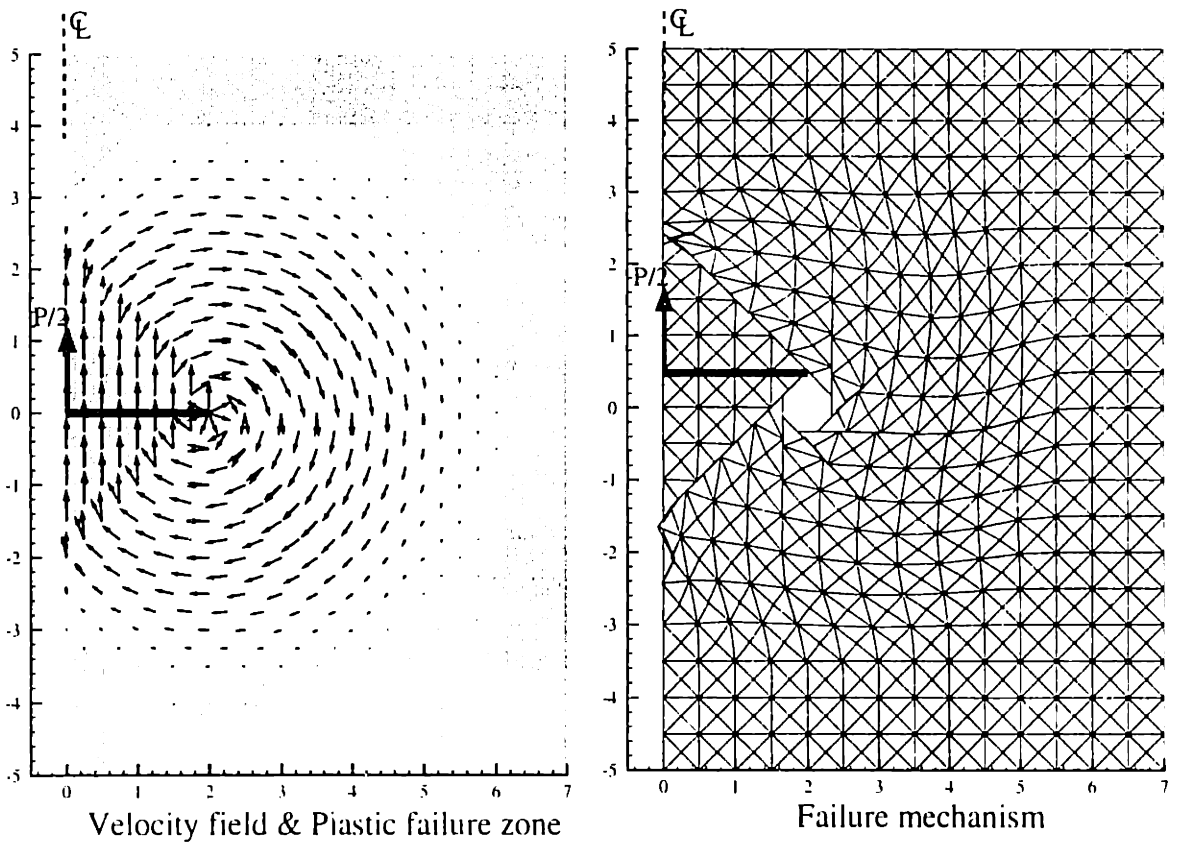

b) Peak anisotropic strength: N_p = 13.468 - 13.894

Figure 4.51 Comparisons of UB results between isotropic and anisotropic strength: pipe section, rough surfaces

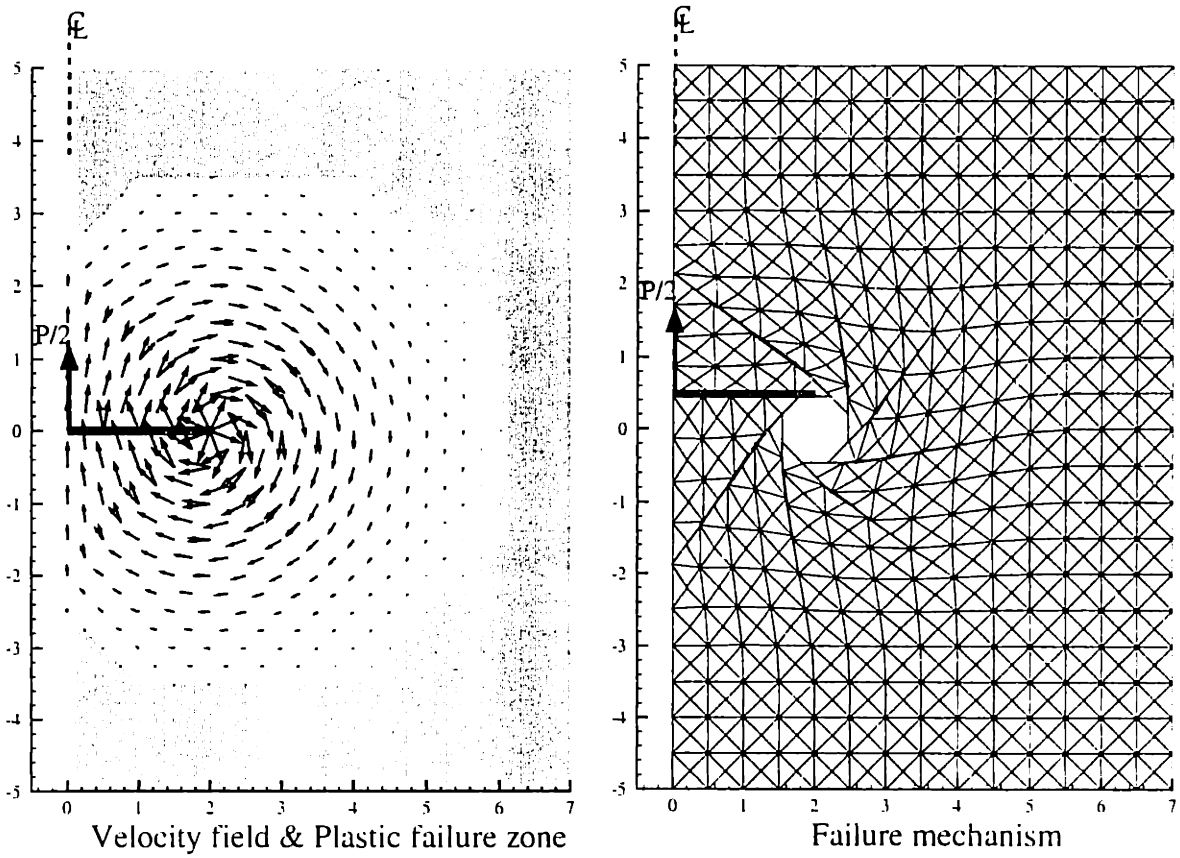

a) Isotropic strength: N_p = 11.285 - 11.623

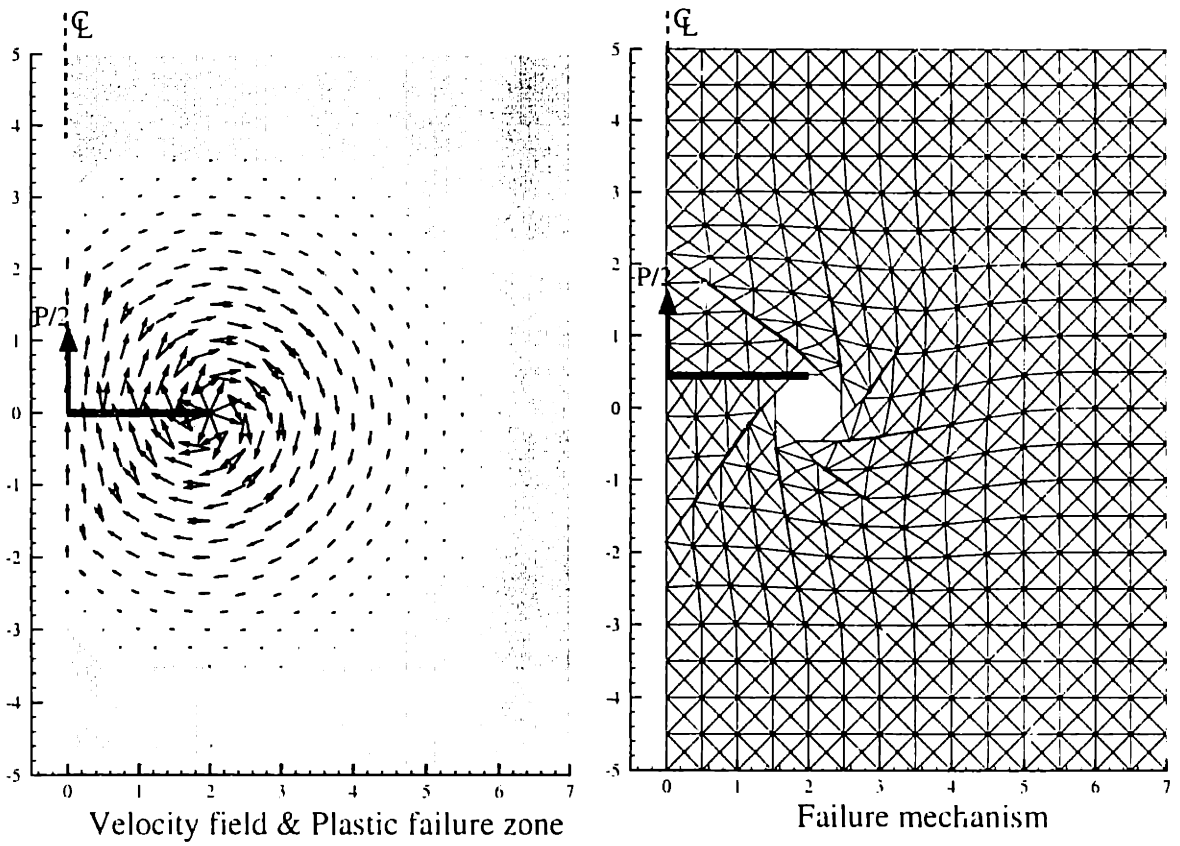

b) Peak anisotropic strength: N_p = 13.461 - 13.861

Figure 4.52 Comparisons of UB results between isotropic and anisotropic strength: pipe section, smooth surfaces

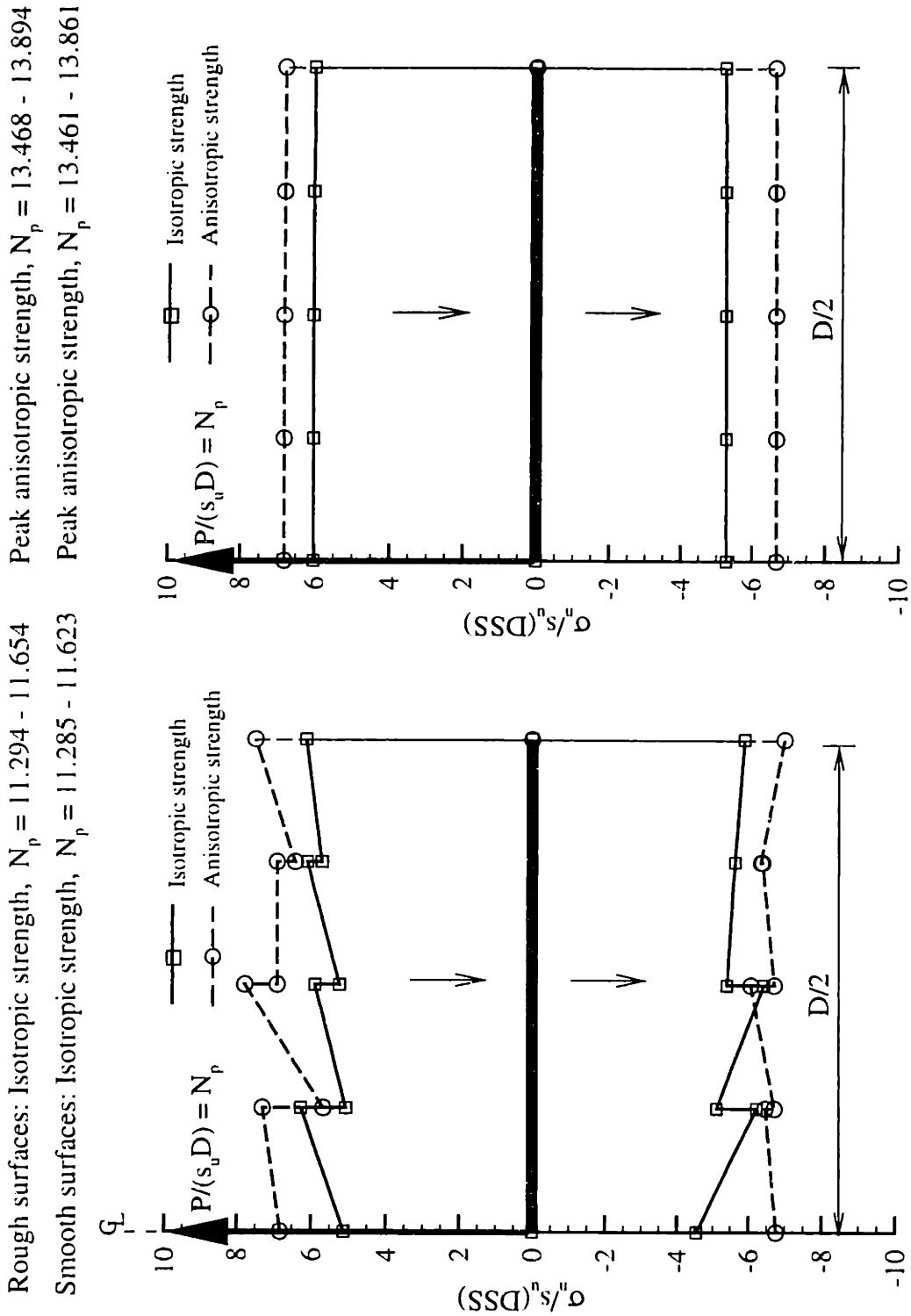

Figure 4.53 Comparisons of contact stresses between isotropic and anisotropic strength: plate section

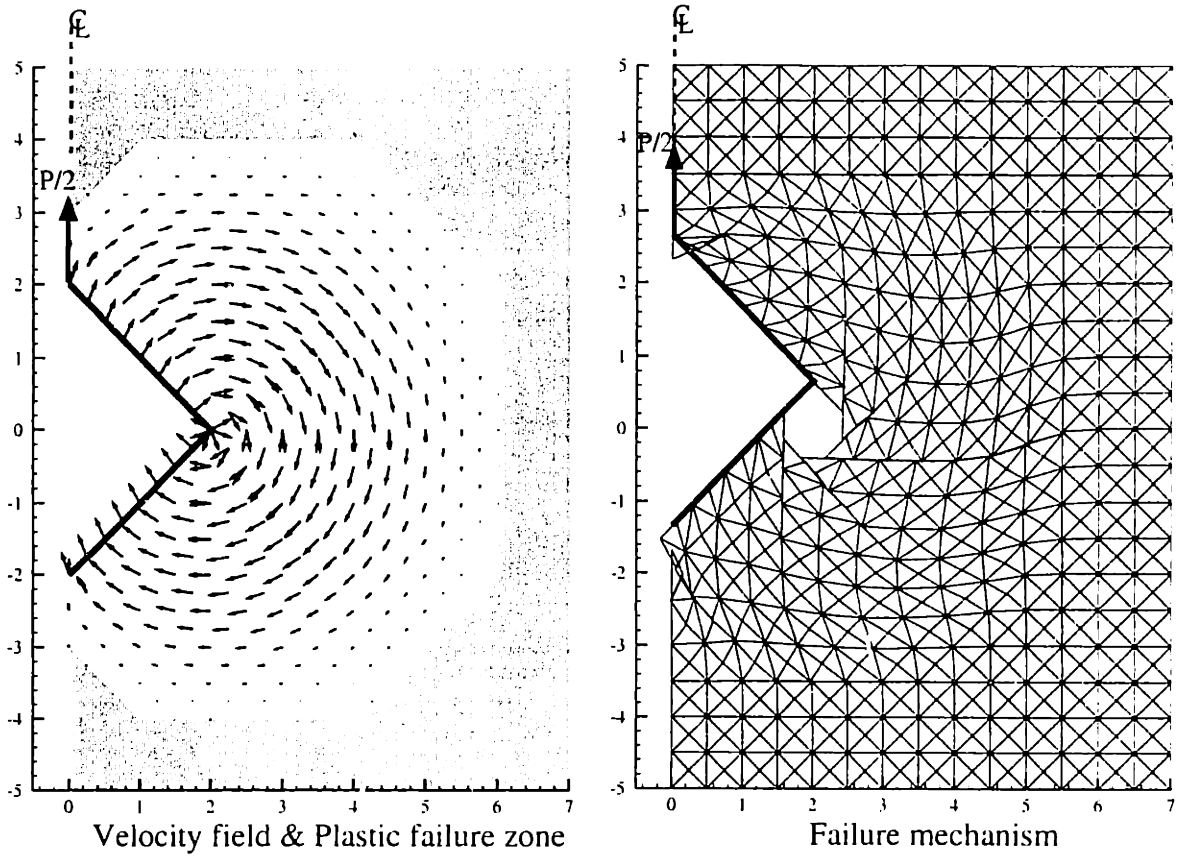

a) Isotropic strength: N_p = 11.294 - 11.661

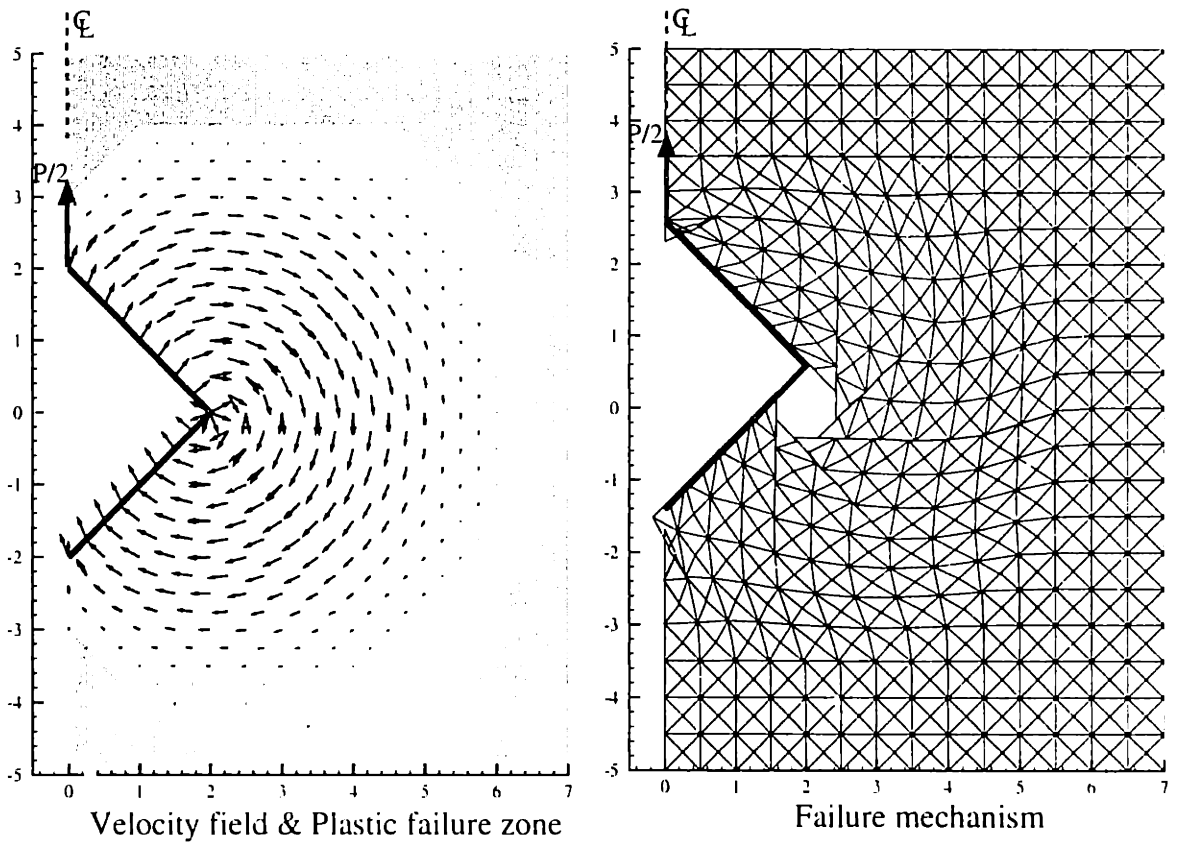

b) Peak anisotropic strength: N_p = 13.468 - 13.903

Figure 4.54 Comparisons of UB results between isotropic and anisotropic strength for square sections, rough surfaces

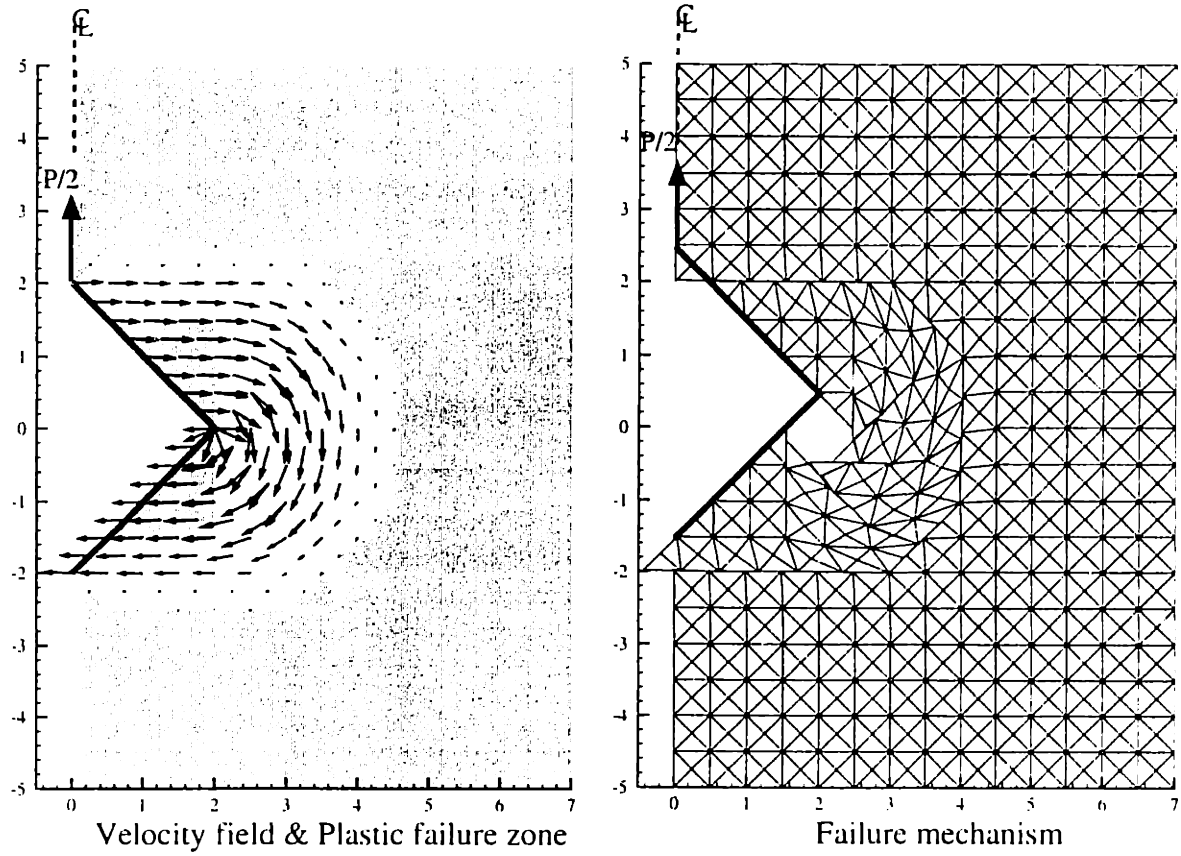

a) Isotropic strength: N_p = 8.194 - 8.531

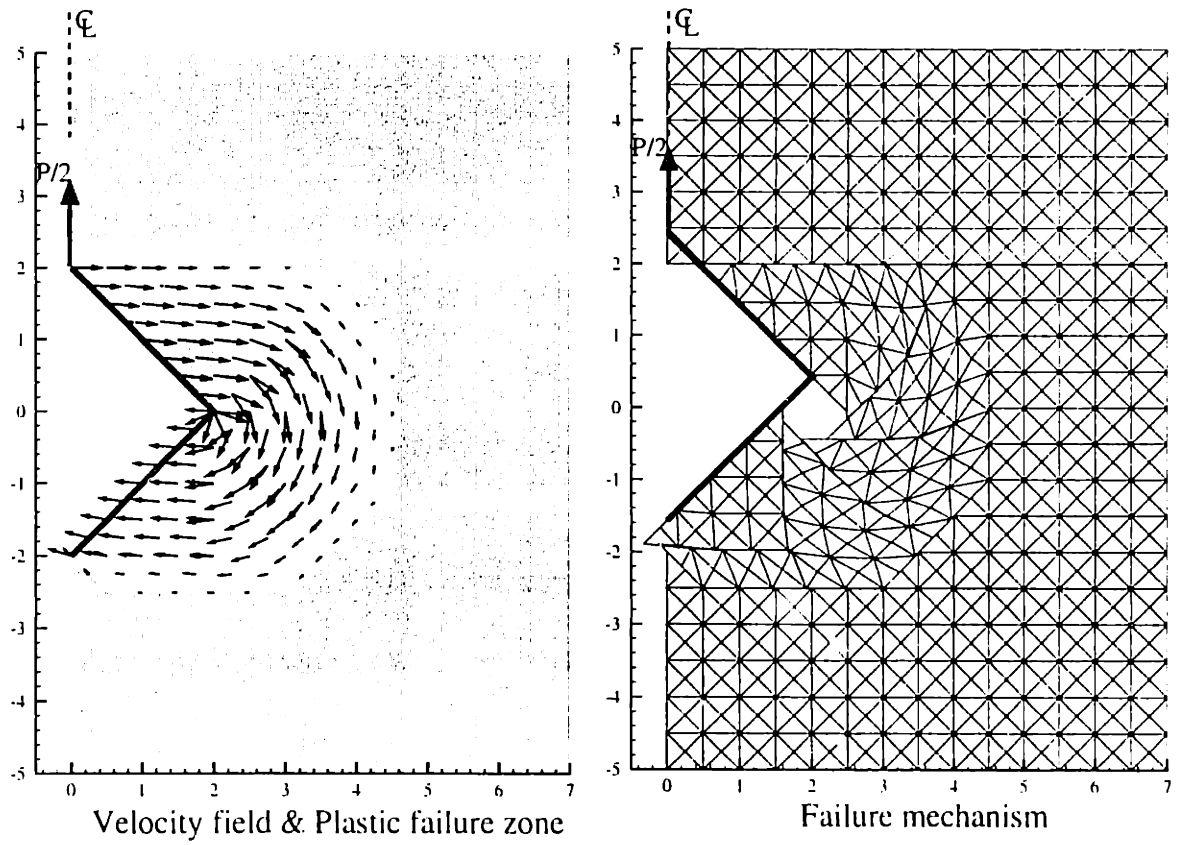

b) Peak anisotropic strength: N_p = 9.574 - 10.016

Figure 4.55 Comparisons of UB results between isotropic and anisotropic strength for square sections, smooth surfaces

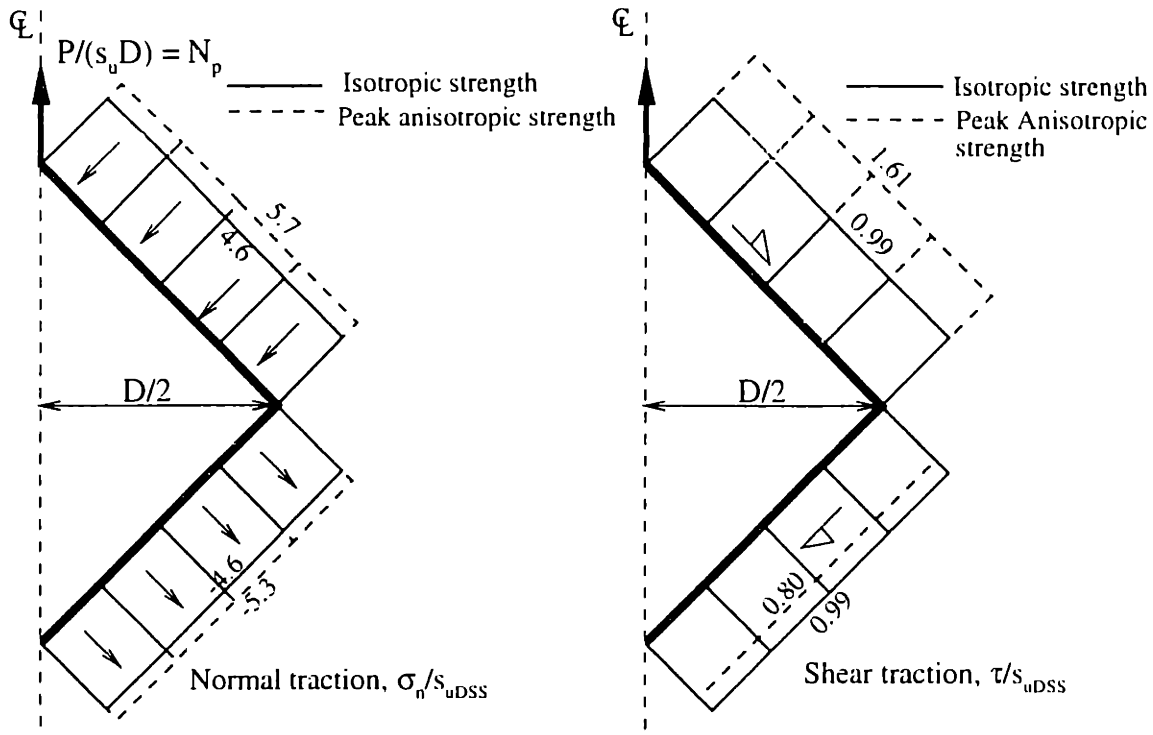

a) Rough surfaces:

Isotropic strength, N_p = 11.294 - 11.661 Peak anisotropic strength, N_p = 13.468 - 13.903

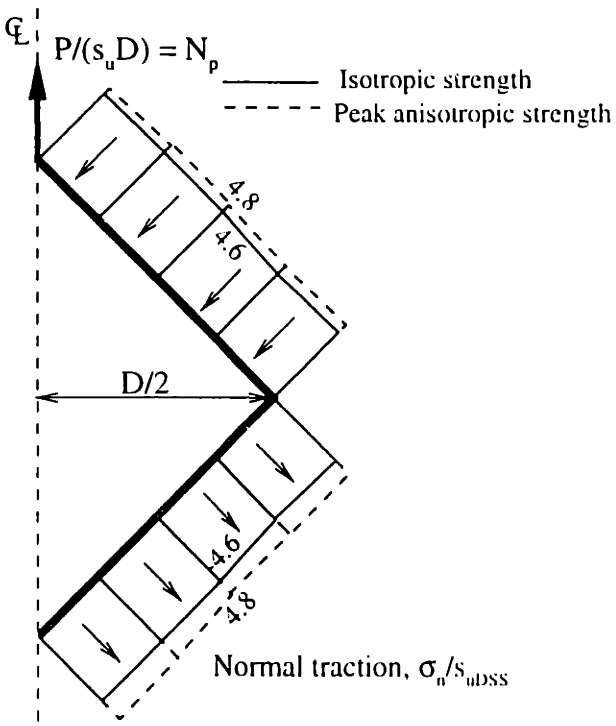

b) Smooth surfaces

Isotropic strength, N_p = 8.194 - 8.531 Peak anisotropic strength, N_p = 9.574 - 10.016

Figure 4.56 Comparisons of contact tractions between isotropic and anisotropic strength: square sections

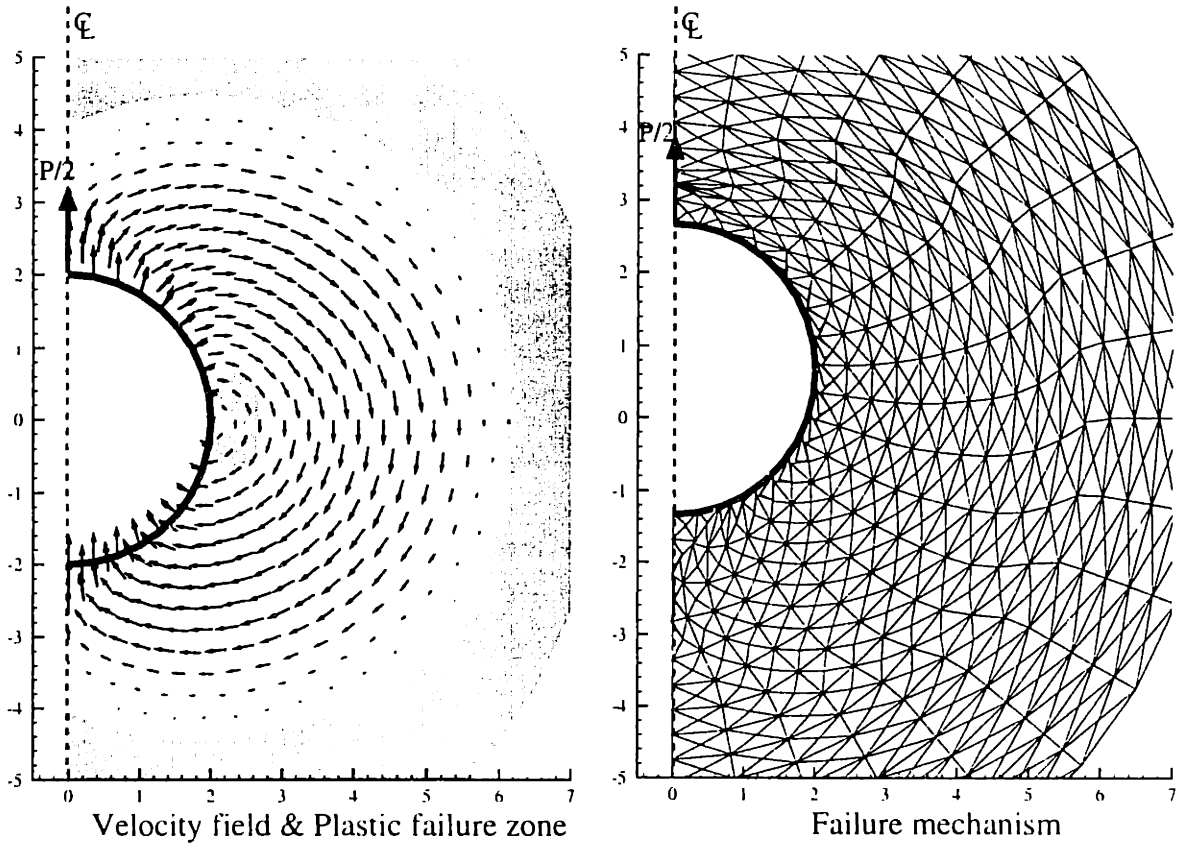

a) Isotropic strength: N_p = 11.747 - 12.271

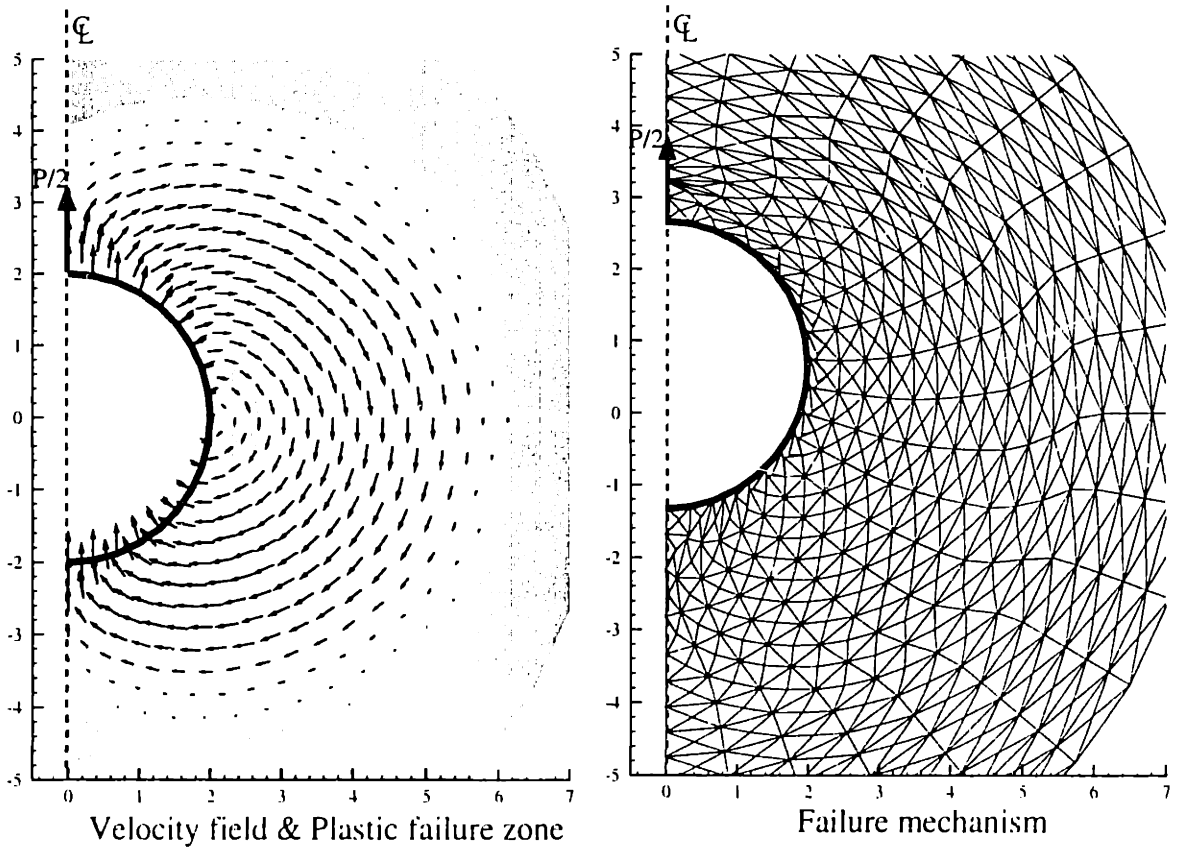

b) Peak anisotropic strength: N_p = 13.982 - 14.607

Figure 4.57 Comparisons of UB results between isotropic and anisotropic strength for pipe sections, rough surfaces

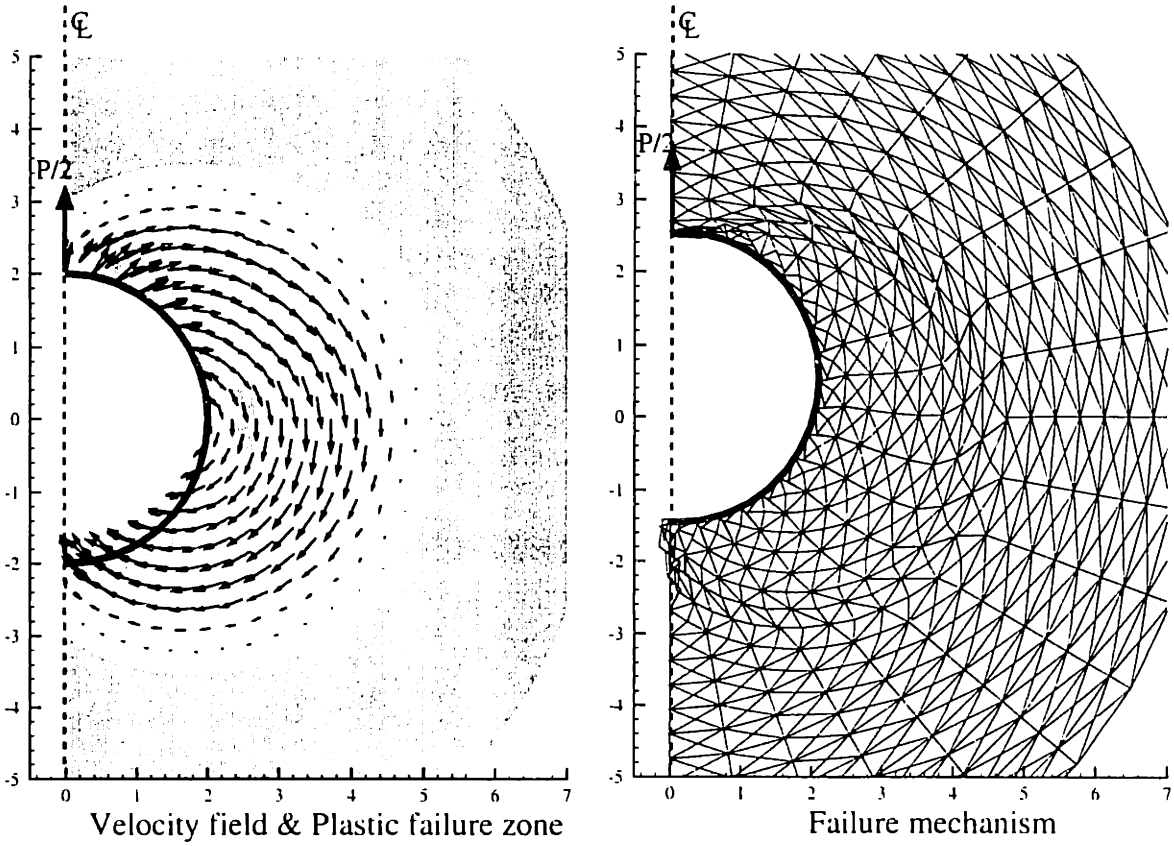

a) Isotropic strength: N_p = 9.016 - 9.756

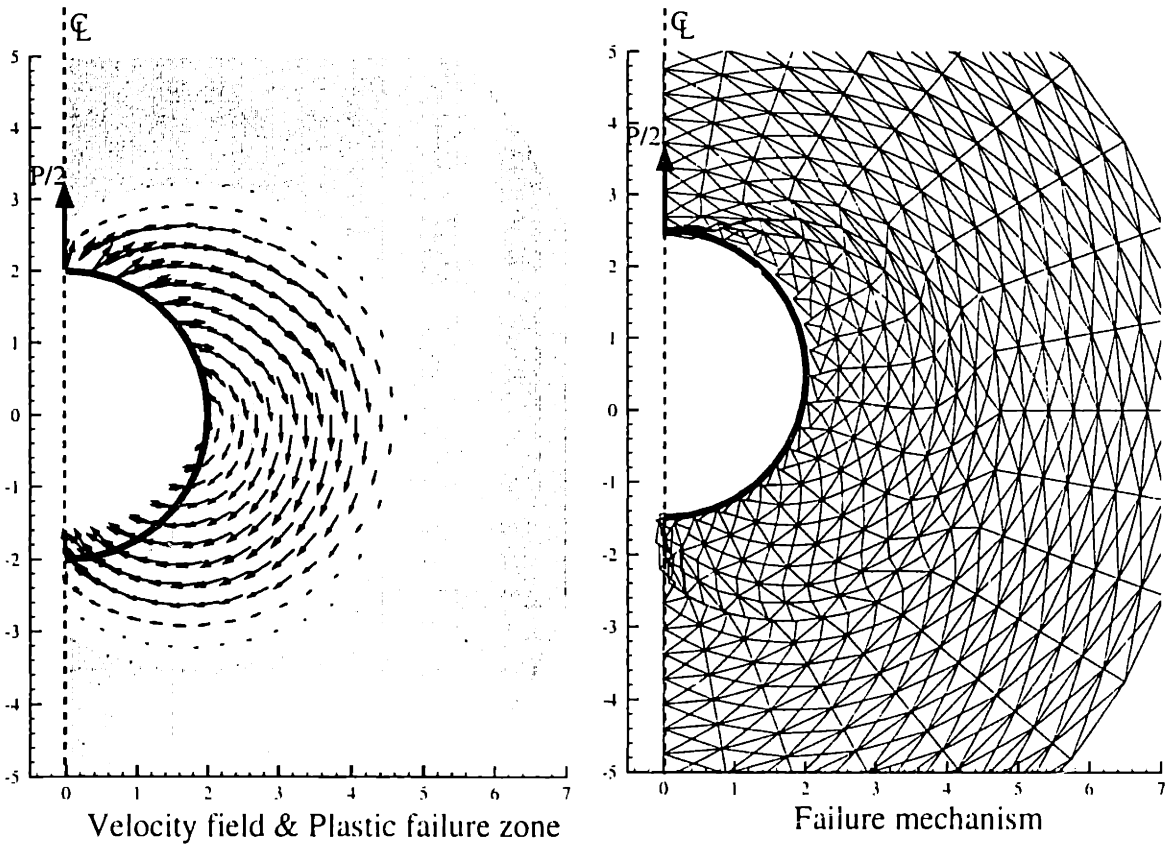

b) Peak anisotropic strength: N_p = 10.688 - 11.551

Figure 4.58 Comparisons of UB results between isotropic and anisotropic strength for pipe sections, smooth surfaces

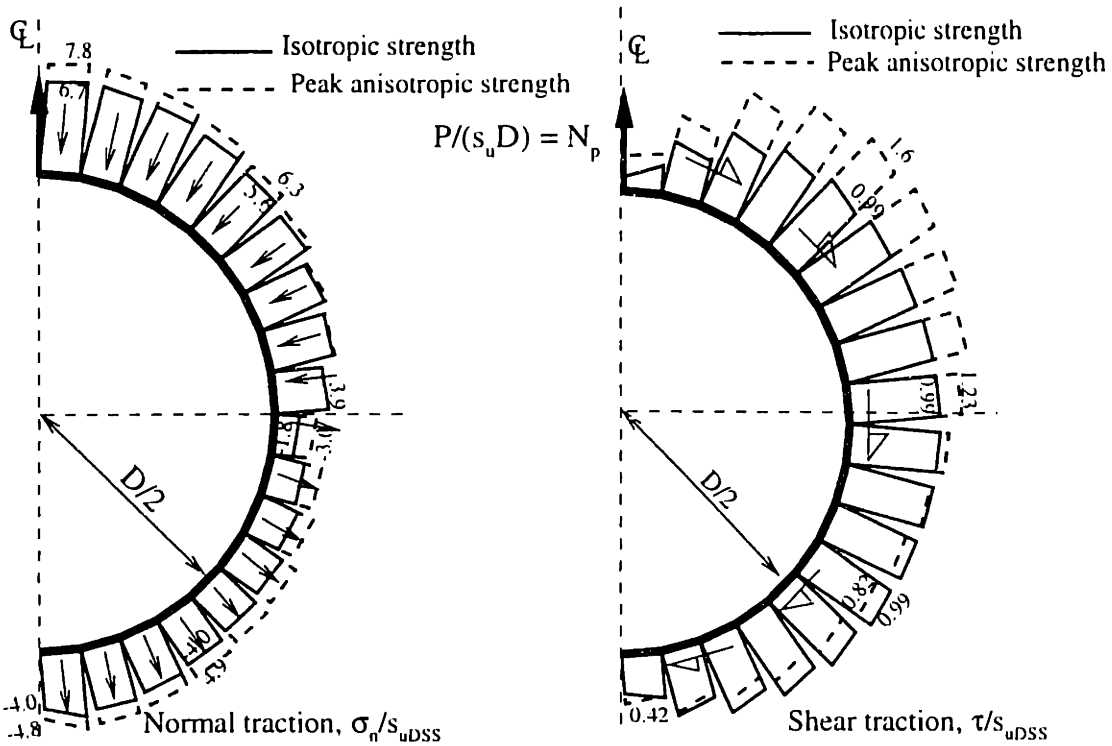

a) Rough surfaces

Isotropic strength, N_p = 11.747 - 12.271 Peak anisotropic strength, N_p = 13.982 - 114.607

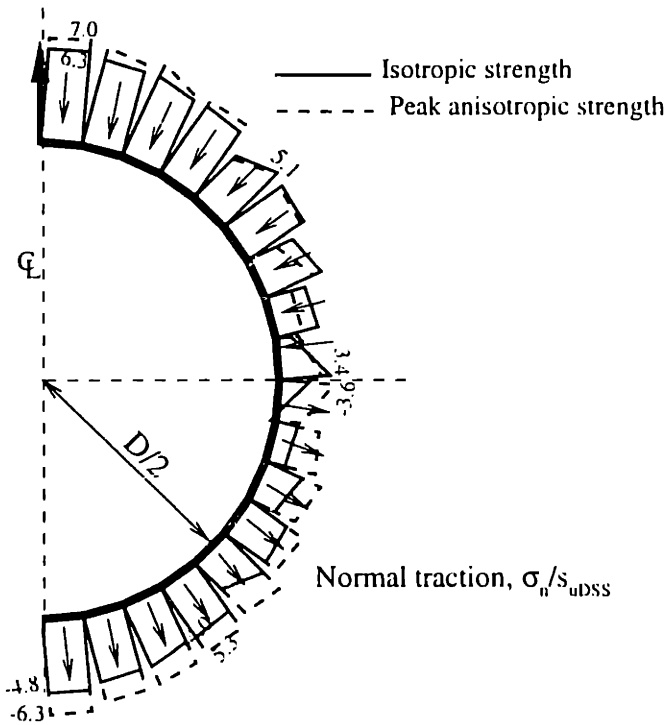

b) Smooth surfaces

Isotropic strength, N_p = 9.016 - 9.756 Peak anisotropic strength, N_p = 10.688 - 11.551

Figure 4.59 Comparisons of contact tractions between isotropic and anisotropic strength: pipe sections

Chapter 5. Undrained Tensile Loading for a Rigid-Planar Caisson

5.1 Introduction

This chapter describes the application of the numerical limit analyses for computing the undrained tensile capacity of a rigid planar caisson in clay. Previous experiment data and finite element predictions focus on the performance of cylindrical caissons and hence, approximate methods are necessary to apply the proposed upper and lower bound limit solutions for these axisymmetric problem geometries.

Section 5.2 presents results of the planar limit analyses for caissons embedded in a non-homogeneous clay layer, where undrained shear strength increases linearly with depth, and show how the mechanisms of pullout are related to the caisson cell geometry. The section also proposes a simple method for applying the solutions of planar caisson geometries to estimate the capacity of axisymmetric caissons. Limit analysis solutions are then compared with conventional limit equilibrium calculations (also based on theoretical plane strain solutions) and with displacement-based finite element analyses using the MIT-E3 soil model (Whittle et. al, 1996). Sections 5.3 to 5.5 illustrate predictions of axial pullout for: 1) the miniature caisson in laboratory Caisson Element Tests (Cauble, 1996); 2) centrifuge experiments performed by EPR (Clukey and Morrison, 1993); and 3) field experiments performed by NGI (Andersen et al., 1993). The centrifuge and field experiments include data for inclined loading and hence, correspond to 3-dimensional problem geometries that are only modeled approximately using the current limit analyses.

5.2 Undrained Capacity of Suction Caissons

5.2.1 Numerical Limit Analysis for Planar Caissons

This section presents results of numerical limit analyses that predict the undrained, axial tensile capacity of a wished-in-place planar caisson. Figure 5.1 shows the problem geometry with a point load, Q, applied centrally at the top of the caisson cell of width, B, and length, L. The caissons is embedded in a deep clay layer, with undrained shear strength increasing linearly with depth: $s_u = \rho z$, where ρ is the strength gradient of the clay, and z is the depth below the mudline. Figure 5.2 shows typical meshes used in

these analyses. The soil is discretized using the standard plane strain elements, while the caissons are represented by a series of rigid structural elements (no structural failure considered). Full adhesion is allowed along all soil-structure interfaces. All of the analyses assume that there is no separation between the cap and underlying soil (no cavitation).

In order to cover the full ranges of caisson embedment ratios, B/L, the undrained tensile capacity of caisson can be generalized as:

$$N_{ca} = \frac{Q}{\rho(B/2 + L)^2} \tag{5.1}$$

where (B/2 + L) corresponds to half the interior surface area of the planar caisson.

The collapse loads presented in this normalized format converge to the exact solutions of Davis and Booker (1973) for a surface footing (L/B -> 0), and to the limiting skin friction of a deep wall (B/L -> 0). Figure 5.3 plots the computed lower and upper bound collapse loads as a function of caisson embedment ratio, B/L (Table 5.1 tabulates these values). For all values of B/L, the true collapse load can be bounded within an error of ±5-6%. Table 6.2 and Figure 5.4 summarize the limiting wall (Q_w) and cap forces (Q_c) obtained from the lower bound stress analyses at selected embedment ratios. For shallow caissons, where L/B < 0.3, the cap force represents almost 100% of the total caisson resistance. As caissons become deeper, the wall force builds up gradually and represents about 20% of the total capacity at B/L = 1.0. For a relatively-deep caisson, where B/L > 0.2, more than 70% of the total capacity is due to the wall resistance.

5.2.1.1 Upper and Lower Bound Results

Figures 5.3 to 5.13 show upper and lower bound predictions for the planar caisson at three embedment ratios, L/B = 1.0, 3.0, 0.25. All of the examples assume B = 20m. The clay has a buoyant unit weight, γ_b = 8.2 kN/m^3, an average undrained strength ratio, s_u/σ'_{v0} = 0.20, and hence the strength gradient of the clay, ρ = 1.64 kPa/m. The upper bound results include the predicted failure mechanism, plastic failure zone and velocity field (e.g. Fig. 5.5), while the lower bound solutions comprise contours of vertical and horizontal stresses, mobilized shear strength, and direction of the major principal stress, δ

(e.g. Fig. 5.6). The distribution of contact tractions along the cap and wall (e.g. Fig. 5.7) can also be interpreted from lower bound calculations.

For L/B = 1.0 and 3.0, the upper bound calculations show that there is no failure within the plug, while the zone of basal failure extends to a maximum depth, z = 35m and 85m, respectively (i.e. $z_f \approx 1.2[B/2 + L]$, Figs. 5.5, 5.8). Outside the caisson, the failure mechanism indicates a local zone of shear along the wall, which is separated from movements associated with the basal failure mechanism. There is a large failure zone extending laterally to a distance x = 55m for L/B = 1.0 and 115m for L/B = 3.0 (i.e. $x_f \approx 1.2[B/2 + L]$). In contrast, the failure extends inside the shallow caisson at low embedment ratio (L/B = 0.25; Fig. 5.11), with a much smaller failure zone in the surrounding soil (x_f = 25m).

For L/B = 1.0 (Fig. 5.6), the lower bound results show that the soil below the tip of caisson fails in an extension mode of shearing (passive), where the direction of major principal stress to the vertical, $\delta = 90°$. There is a radial shear failure around the tip of caisson, where principal stresses rotate from $\delta = 90° \rightarrow 0°$. The soil fails in an compression mode of shearing ($\delta = 0°$) in planes extending 45° away from the caisson tip. It can be seen that these three zones are similar to 'reverse end bearing failure' (Clukey and Morrison, 1993). Along the external wall, the clay fails in a direct simple shear, with $\delta = 45°$-$50°$. These failure characteristics are similar for the deep caissons (L/B = 3.0, Fig. 5.9). Notice that there is a suction pressure (tensile) developed inside the top half of the soil plug, while the pressure in the other half below is compressive due to the self-weight of the soil plug. For shallow caissons (L/B = 0.25, Fig. 5.12), tensile stresses occur throughout the entire soil plug. For all cases, the lower bound analyses predict that the normal underbase tractions are tensile and uniformly distributed (Figs. 5.7a, 5.10a 5.13a). For deep caissons (L/B = 3.0, Fig. 5.10b), the full shear resistance is mobilized ($\tau/s_u \rightarrow 1.0$) along both the inside and outside caisson walls. However, this happens for only the external wall at L/B = 1.0 (Fig. 5.7b). For shallow caissons (Fig. 5.13b), the shear traction are less than the undrained strength of the surrounding soil, indicating that failure does not occur at the soil-caisson wall interface.

5.2.1.2 Scaling results of planar analysis to axisymmetric geometries

In order to apply the results of planar caissons for a cylindrical caisson, the results must be scaled to account for the axisymmetric geometry. Two alternative (approximate) methods for doing this scaling are as follows:

1. Assume that the caisson acts as a planar structure with width, B. Thus, the collapse load can be estimated as:

   Upper Bound: $F_{TOT,UB} = (B)(Q_{TOT,UB})$ (5.2)

   Lower Bound: $F_{TOT,LB} = (B)(Q_{TOT,LB})$

   Note that the symbol F [F] is introduced to represent the forces for axisymmetric geometries in order to distinguish from the forces per unit width Q, [F/l] used in the preceding calculations for planar caissons.

2. Scale the wall and cap forces from the lower bound analyses separately in order to account for differences in the relative surface areas of the cap and side walls. Thus, the lower bound estimates of forces in an axisymmetric geometry are:

   Wall force: $F_{w,LB} = (\pi B/2)(Q_{w,LB})$ (5.3)

   Cap force: $F_{c,LB} = (\pi B/4)(Q_{c,LB})$

   Total force: $F_{TOT,LB} = F_{w,LB} + F_{c,LB}$

   where $(\pi B/4)$ and $(\pi B/2)$ are the scaling dimensions for the cap and wall, respectively

   $Q_{c,LB}$, $Q_{w,LB}$ are limiting cap and wall forces from lower bound analyses of planar caissons (Figure 5.4, Table 5.2)

The capacity of axisymmetric geometries from the upper bound results can be estimated by assuming that the ratio of the upper bound and lower bound collapse loads is not affected by the caisson geometry:

$$\frac{F_{c,UB}}{F_{c,LB}} = \frac{F_{w,UB}}{F_{w,LB}} = \frac{F_{TOT,UB}}{F_{TOT,LB}} = \frac{Q_{TOT,UB}}{Q_{TOT,LB}} \quad (5.4)$$

For an axial pullout of caisson, the second procedure is more reliable because it takes the effect of relative surface areas of the caisson cap and wall. However, for an inclined pullout loading, it is difficult to use the second procedure to scale the results of planar limit analyses because the lateral wall resistance constitutes a significant fraction

of the total caisson capacity. Thus, the first method which scales the results by the width, B is used in these cases (see Section 5.5).

These procedures will be used to estimate reference caisson capacities for comparisons with the results of finite element analysis (FE) and model tests in subsequent sections.

5.2.2 Limit Equilibrium Calculations for Pullout Capacity

Caisson capacity is usually estimated by limit equilibrium methods (cf. Clukey & Morrison, 1993; Andersen et al., 1993; Fuglsang & Steensen-Bach, 1991). For undrained axial loading, the conventional assumption is that the soil plug moves with caisson. Hence, the ultimate capacity of the caisson can be obtained as the sum of the external wall friction and the reverse end bearing acting over the full basal area (footprint) of the caisson (Figure 5.14). Following the notation of Clukey and Morrison (1993), this is written as:

$$F_{TOT} = F_{ESF} + F'_{REB} \tag{5.5}$$

where F_{TOT} = the total capacity of caisson

F_{ESF} = the external wall force

F'_{REB} = the reverse end bearing force

The usual procedure for estimating F_{ESF} is to assume that: 1) the caisson wall is relatively inextensible, such that the total resistance is provided by f_s, the limiting skin friction; 2) the skin friction f_s is equated with the undrained shear strength of the soil adjacent to the soil-wall interface[1]; and 3) the clay fails in a mode of undrained direct simple shear, s_{uDSS}. Thus, the resulting equation for external skin friction for caissons is given by:

$$F_{ESF} = A_{ew} f_s \tag{5.6}$$

where A_{ew} = the external surface area of the caisson $= \pi BL$

$f_s = s_{uDSS}$

[1] This is equivalent to $\alpha = 1$ used in the design of friction plies, and also implies no installation disturbance.

There are no closed-form analytical expressions for the reverse end bearing capacity of an embedded cylinder in a homogenous clay layer. However, the reverse end bearing can be estimated based on the conventional Terzaghi bearing capacity formula for strip footings together with empirical factors to account for the embedment and axisymmetric geometry of the caisson. Clukey and Morrison (1993) follow design equations given by Kulhawy et al. (1983):

$$F'_{REB} = A_c q = A_c N_c s_u \alpha_c \alpha_d \tag{5.7}$$

where A_c = the area of cap = $\pi B^2/4$

$N_c = (2 + \pi)$

s_u= the undrained shearing strength in triaxial extension

α_c = empirical factor for cylindrical geometry = 1.2

α_d = depth factor by Kulhawy et al. (1983) = $1 + 0.33\tan^{-1}(B/L)$

For an embedded cylinder in a non-homogenous clay layer, where the undrained strength increases linearly with depth, Clukey and Morrison (1993) recommended that F'_{REB} can be estimated from the plasticity solutions for a surface strip footing given by Davis and Booker (1973), together with modified empirical depth factor as follows:

$$F'_{REB} = A_c F\{ (2 + \pi)s_{ub} + \rho B/4) \}\alpha_c \alpha_d \tag{5.8}$$

where F = solutions by Davis and Booker (1973) from Figure 5.15

s_{ub} = undrained strength in triaxial extension average over a depth of B/2 below the tip of caisson

ρ = the strength variation with depth

α_c = empirical factor for cylindrical geometry = 1.2

α_d = depth factor by Clukey and Morrison (1993) = $1 + 0.18\tan^{-1}(B/L)$

More complex limit equilibrium calculations have been used by Andersen et al. (1993) to interpret caisson capacity with inclined and cyclic loading. The procedures were developed by the Norwegian Geotechnical Institute (NGI) and were originally proposed for the design of offshore gravity structures as shown in Figure 5.16 (Andersen et al., 1988; Andersen & Lauritzsen, 1988). These calculations assume specified distributions of

undrained shear strength, which account for anisotropy and cyclic loading and search for a composite critical failure surface (c.f. Fig. 5.16).

Although limiting equilibrium calculations are very simple and easy to perform, there is no way of validating the accuracy of the solutions other than physical model testing. Indeed, the correction factors represent a significant factor in the calculation, while the selection of the reference undrained strength for equation 5.7 is backfitted to available model test data. These types of problem are common to limit equilibrium methods, which generally involve a search procedure to locate the critical failure surface.

5.2.3 Comparison of Limit Equilibrium and Limit Analyses for Planar Caisson

This section evaluates limit equilibrium calculations for undrained capacity presented in the previous section through a comparison with numerical limit analyses for planar caissons. For cases where the undrained strength increases linearly with depth, the pullout loads according to equations 5.5, 5.6, and 5.8 from limit equilibrium calculations can be written:

$$Q_{TOT} = Q_{ESF} + Q'_{REB} \tag{5.9}$$

where Q_{ESF} [F/l] $= \rho L^2$

Q'_{REB} [F/l] $= BF\{ (2 + \pi)\, s_{ub} + \rho B/4) \}\alpha_d$

$s_{ub} = \rho(L + B/4)$

$\alpha_d = 1 + 0.18\tan^{-1}(B/L)$

Note that the symbol Q represent for plane strain conditions and the correction factor, $\alpha_c = 1.0$ in equation 5.8.

Equation 5.9 has been applied to several caissons with, embedment ratios, L/B = 0.25 - 3.0. Figure 5.17 compares the collapse loads from numerical limit analyses with the limit equilibrium calculations (LEM). The assumption of the reverse end bearing mechanism leads to unsafe estimates of cap force, especially for shallow caissons, where L/B < 1. For example, Q'_{REB} is larger than the cap force predicted from limit analyses by 38% at L/B = 0.5. The upper bound results for L/B = 0.25 (Figure 5.11) also confirm that the assumption of reverse end bearing is no loner valid for shallow caissons, where there is a failure inside the soil plug. When combined Q_{ESF} and Q'_{REB}, the total force from

LEM is conservative for only deep planar caissons, where L/B > 1. These results show clearly an important theoretical limitation of the limit equilibrium calculations for handling undrained capacity of suction caissons.

5.2.4 Pullout Capacity by Non-Linear Finite Element Analysis

This section presents the results of finite element analysis (FE) to predict the undrained axial loading of cylindrical caissons, together with comparisons from numerical limit analysis and limit equilibrium calculations. Finite element analysis requires a generalized soil model in order to achieve reliable solutions. The calculations of pullout loads for caissons presented here were simulated with non-linear finite element analyses (Whittle et. al, 1996) using the generalized effective stress soil model MIT-E3 (Whittle, 1987; Whittle and Kavvadas, 1994) with input parameters for K_0-normally consolidated BBC. This soil model describes accurately many features of the behavior of normally and overconsolidated clay ($1 \leq OCR \leq 8$) observed in laboratory element tests including: a) anisotropic stress-strain strength; b) small strain non-linearity; and c) strain softening in certain modes of shear deformation. Figure 5.18 shows that the MIT-E3 matches closely the measured stress-strain-strength properties in triaxial compression, extension, and direct simple shear tests. The FE analyses of monotonic axial loading include a base case reference geometry (B/L = 1; B = 20m) as well as a parametric study which examines the effect of wall length (L) and cell diameter (B).

Figure 5.19 shows a detail of finite element model of the caisson for the base case reference cell geometry, with wall length, L = 20m, outside diameter, B = 20m, and wall thickness, 2w = 0.5m (i.e. aspect ratio R/w = 40, and embedment ratio L/B = 1.0). The soil is discretized using high order triangular elements (Sloan and Randolph, 1982) with mixed interpolation of displacement and pore pressure (15-3), while the wall is modeled as an elastic material (the cap is rigid). The analyses assume that caisson installation causes no disturbance of the surrounding soil (i.e. wished-in-place). There is no separation between the lid and soil surface inside the plug and no slippage allowed between the caisson walls and the adjacent soils (i.e. no special interface elements are

used in the analysis). Undrained conditions are approximated by using an artificial time frame for the loading sequence.

Mechanical properties of the soil are described by the MIT-E3 model. Due to model assumptions of normalized soil behavior, the shear stiffness and undrained shear strength are proportional to the in-situ vertical effective stress, σ'_{v0} (= $\gamma_b z$) for a given OCR of the clay. Figure 5.19 also shows the undrained shear strength profiles s_{uTC}, s_{uDSS}, s_{uTE} for the MIT-E3 soil model, based on input parameters for K_0-normally consolidated BBC.

5.2.4.1 Comparison for Base Case Geometry

Figure 5.20 plots the load-displacement response of the caisson together with the wall and cap forces and their contribution to the total resistance for the base case geometry, where B = L = 20m. There is a distinct yield in the total force-displacement response beyond which the total force continues to increase almost linearly with displacement, reaching a value of F_{TOT} = 98.1 MN at a cap displacement of δ_v = 0.5m. The wall and cap forces also show a very stiff initial response, with a yield occurring at $\delta_v \approx$ 0.05m. Thereafter, the wall force reaches a limiting values, F_w = 30 MN at $\delta_v \geq$ 0.1m and all subsequent changes in the total resistance are due to increases in the cap force. The analyses do not reach a limiting capacity at the maximum cap displacement used in the calculations.

For B = L = 20m, and ρ = 1.64 kPa/m (s_{uDSS}/σ'_{v0} = 0.20), the true collapse load for planar caissons can be bounded by the numerical limit analyses, $-5993 \leq Q \leq -6510$ kN/m width (using Table 5.1); while the lower bound analysis gives forces on the cap and side walls, Q_c = 4950 kN/m, Q_w = 1043 kN/m (using Table 5.2). The total resistance for the axisymmetric cell geometry can be estimated by scaling the wall and cap forces separately as described in Section 5.2.1.2 such that; $-110.5 \leq F_{TOT} \leq -120$ MN. Furthermore, the numerical limit analysis are also able to give estimates of the limiting wall and cap force, $-32.8 \leq F_w \leq -35.6$ MN, and $-77.8 \leq F_c \leq -84.5$ MN. These calculations cannot be expected to match exactly the results of the axisymmetric finite element analyses (which include anisotropic stress-strain-strength properties of BBC

using the MIT-E3 model). However, Figure 5.20 shows the estimated collapse loads do appear to tie in with the finite element solutions. According to the limit analysis estimates, the caisson has mobilized 85% of its ultimate capacity in the finite element calculation at δ_v = 0.5m. There is also an good agreement between the predicted wall force from limit analysis and the results of FE analysis, where F_w = 30 MN. Figure 5.20 also illustrates that it is difficult to estimate the caisson capacity reliably from non-linear finite element analyses, because relatively large cap displacements are necessary to mobilize the full capacity of caisson in undrained, axial loading (pullout) conditions.

5.2.4.2 Comparisons for Effects of Wall Length and Caisson Diameter

Figure 5.21 shows the load-deformation response of caissons from the FE analysis for a series of different wall lengths, L = 10, 20, 30, 40, 60m, and B = 20 m. In all cases, the analyses do not reach the limiting load at a vertical cap displacement, δ_v = 0.5 m. The cap response is initially highly non-linear, with stiffness similar to the wall, but continues to harden almost linearly with displacement, $\delta_v > 0.1$. The cap forces do not reach a maximum resistance in any of these calculations, however, the wall forces are fully mobilized for cases, where, $L \leq 30$m.

Figure 5.22 summarizes effects of wall length on caisson resistance mobilized in the FE analysis at δ_v = 0.1m and 0.5m and compares these results with the numerical limit loads (scaling from planar caisson). The results suggest that 85-90% of the total capacity is mobilized at δ_v = 0.5m for caissons with shallow wall embedment ($L \leq 20$ m), but this ratio drops to less than 70% for L = 60m. One of the underlying reasons for this trend is that the lower bound calculations predicts much higher wall forces than are computed by the finite element analysis. Another explanation for this trend is that the wall forces from the latter are not fully mobilized at L = 60m (as suggested by results for $\delta_v > 0.3$m in Fig. 5.21). However, Figure 5.22 shows that there is consistent agreement between the lower bound calculations and finite element analysis of limiting cap resistance. The figure also compares the reverse end bearing, F'_{REB}, and the external skin friction, F_{ESF}, from limit equilibrium calculation as explained in Section 5.2.2. It can be seen that limit equilibrium

calculations predict a maximum cap force F'_{REB}, that is significantly higher than the limit analyses[2], while the wall force mobilized in the FE calculations exceeds F_{ESF} at δ_v = 0.5m.

Figure 5.23 compares effects of cap diameter, B = 10, 20, and 40m, L = 20m in finite element analysis, numerical limit analyses (scaling from planar caissons) and limit equilibrium calculations. The limit analyses predict that the wall forces are in the same range as the FE analysis, but suggest that the caisson can sustain much higher cap forces for B > 30m than are computed in the FE analyses at δ_v = 0.5m. Limit equilibrium calculations predict a limiting cap that is much larger than the range predicted by limit analyses. In all cases, the computed wall force from FE analysis is larger than F_{ESF} due to shear tractions inside the soil plug.

5.3 Pullout Capacity for the CET Model Caisson by Limit Analyses

This section compares pullout capacity of CET model caisson with predictions from planar limit analyses, limit equilibrium calculations, and non-linear finite element analyses.

The Caisson Element Test (CET) cell was developed by Cauble (1996) in order to study the behavior of a suction caisson in a homogeneous clay element through successive phases of installation by underbase suction, set-up, and monotonic (undrained) and sustained axial tensile loading. Figures 5.24 and 5.25 show the layout and instrumentation of the CET cell and the geometry of the two-piece miniature caisson. The CET cell comprises a miniature cylindrical caisson in a homogeneous, saturated clay with a controlled stress history. The model has an outside diameter, D_0 = 5.08 cm, and a wall thickness, t_w = 0.145 cm, and penetrates to a depth, L = 5.1cm. The experiments can measure or control the force and displacement of the caisson cap and wall components, while cell instrumentation includes additional data on surface settlements, pore pressures within the clay, etc. Tests were conducted on K_0-normally consolidated resedimented

[2] It is not expected that F'_{REB} from limit equilibrium calculations and F_c from limit analyses tie each other, because the analyses consider different free body equilibrium (see Fig. 5.1, 5.14).

Boston Blue Clay (RBBC) samples, at a consolidation stress, σ'_{vc} = 0.75ksc. After the installation, the caisson is allowed to equilibrate at least 24hrs prior to pullout test.

Figure 5.26 summarizes the best estimate of the total, wall and cap force-displacement responses derived from monotonic pullout tests. The model caissons have a well defined tensile load capacity, F_{TOT} = -23±1 kg, which is mobilized at a cap displacement, δ_c = 0.2±0.05cm (comparable to the wall thickness, t_w = 0.145cm). Tensile loading generates a maximum wall resistance, F_w = -13.5±1.5 kg (i.e. 60% of the total capacity), which also occurs at $\delta_c \approx$ 0.2cm. The cap force reaches the maximum value of F_c = -8±2 kg.

The measured data in the CET cell do not take account of the confining pressure acting on top of the caisson (cap and wall)[3]. The measured data can be amended to account for these pressures as follows:

$$\overline{F}_c = -(8 + A_c\sigma_{vo}) = -[8 + 0.75(16.98)] = -20.7\text{kg}$$
$$\therefore F_c = -20.7 \pm 2\text{kg}$$

$$\overline{F}_w = -[13.5 + (A_{TOT} - A_c)\sigma_{vo}] = -[13.5 + 0.75(3.29)] = -15.5\text{kg}$$
$$\therefore F_c = -15.5 \pm 1.5\text{kg}$$

where A_c and A_{TOT} are given in Figure 5.25.

$$\text{Hence, } F_{TOT} = -[20.7 + 15.5] = -36.2\text{kg}$$
$$\therefore F_{TOT} = -36.2 \pm 1\text{kg}$$

Figure 5.27 shows the spatial discretization and boundary conditions used to represent the CET model caisson in numerical limit analyses. The analysis assumes that the geometry of caisson is B = 50.8mm and L = 51mm, and there is no transfer of shear force or bending moment at the junction of the caisson cap and wall. The soil is assigned an average undrained shear strength equivalent, $s_u = s_{uDSS} = 0.205(\sigma'_{vc})$ = 0.15 ksc, with full adhesion permitted along all soil-wall interfaces. Due to the consolidation stress, there is also a surcharge, σ_{vo} = 0.75 ksc, acting on the clay surface and the on the lid of the caisson.

---

[3] All of the subsequent analyses assume uniform pressures, σ_v = 0.75 ksc acting at all points on the surface of the caisson and soil.

Figure 5.28 summarizes the total resistance from lower and upper bound limit analyses. According to the lower bound calculation, the total vertical force acting on the cap and wall, Q_L = -0.64 kg/mm width. This resistance comprises: 1) forces on the inside and outside surface of the wall, $Q_w = (Q_{wi} + Q_{wo}) = -(0.146 + 0.133) = -0.259$ kg; 2) the surcharge pressure on the lid of the caisson, $Q_s = -\sigma_{v0}B = -0.381$ kg/mm; and 3) the underbase reaction force on the soil on the cap, $Q_{c,soil} = 0.02$ kg/mm. The upper bound collapse load is Q_U = -0.70 kg/mm width. Thus, the true collapse load, Q is bounded by $-0.64 \leq Q \leq -0.70$ kg/mm (i.e. a 9% range of uncertainty).

Figure 5.29 shows the mechanism of failure predicted by the upper bound analysis together with velocity field and the zone of plastic failure within the CET cell. These results show that there is no failure within the soil plug and a conical region beneath the wall tip. However, the zone of plastic failure covers most of the CET cell extending to both the base and side walls. Slip occurs at the external wall-soil interface, and most of the soil surface moves downwards in the computed failure mechanism.

Figures 5.30 and 5.31 show the stress contours computed by the lower bound analysis. The vertical stress (Figure 5.30a) is tensile throughout most of the soil plug, and the stress field mobilizes the full shear strength of the soil at most points within the CET cell (Figure 5.31d, $(\sigma_1-\sigma_3)/2s_u = 1$). The lowest suction pressures occur close to the base of the caisson where the clay fails in an extension mode of shearing (Figure 5.31c, δ = 90°). Reverse end bearing failure can be seen around the tip of caisson (where principal stresses rotate for δ = 90°->0°). Failure in undrained direct simple shear (δ = 45°-50°) occurs at points along the outside wall of the caisson and extends to the base of the cell. Figure 5.32 shows the contact normal traction beneath the cap and the shear traction along the inside and outside walls. The lower bound analysis predicts that the shear traction is fully mobilized ($\tau/s_u = 1.0$) along both inner and outer walls of the caisson.

In order to estimate the collapse load of the CET model caisson, the results of the planar limit analyses must be scaled to account for the axisymmetric geometry. The wall and cap forces (from the lower bound analysis) are scaled separately to account for the relative surface areas of the caisson cap and wall (internal and external surfaces) as described in Section 5.2.1.2. In this calculation, the lower bound wall force, F_{wL} =

$Q_w(\pi B/2)$ = -19.5 kg; and the cap force, $F_{cL} = (Q_s + Q_{c,soil})(\pi B/4)$ = -15.8 kg; and hence, F_{TOTL} = -35.3 kg. Assuming that the ratio Q_U/Q_L is unaffected by the geometry, then the estimated wall, cap and total forces for the CET model caisson can be summarized as follows:

	Limit Analyses (kg) LB → UB	Experiments (kg)
Wall	-19.5 → -21.3	-15.5 ± 1.5
Cap	-15.8 → -17.3	-20.7 ± 2
Total	-35.3 → -38.6	-36.2 ± 1

It can be seen that the numerical limit analyses predict collapse loads that are in good agreement with the measured capacity of the CET model caisson. However, the analyses tend to underestimate the measured cap force, while overestimating the measured wall force. These differences may be explaind by a number of factors including: 1) the analyses consider a wall of infinitesimal thickness; 2) the scaling procedures used to estimate axisymmetric behavior are approximate; and 3) installation disturbance occurs in the experiments, but is not considered in the analyses.

Similar calculations of undrained pullout capacity can be made using limit equilibrium methods based on the approach proposed by Clukey and Morrison (1993). In this case, the capacity of the caisson estimated from external wall force, F_{ESF} and the reverse end bearing, F'_{REB} as:

$$F_{ESF} = -(\pi BL)s_{uDSS} = -12.5 \text{ kg} \tag{5.10}$$

where B = 5.08 cm, L = 5.1 cm,

assuming $s_{uDSS}/\sigma'_{vc} = 0.2$ (Ladd, 1991); σ'_{vc} = 0.75 ksc

and:

$$Q'_{REB} = -N_c s_u \alpha_c \alpha_d (\pi BL) A_b = -18.9 \rightarrow -23.6 \text{ kg} \tag{5.11}$$

where N_c = 5.14, α_c = 1.2, α_d = 1.26, $A_b = \pi B^2/4$

assuming $s_{uTE} \leq s_u \leq s_{uDSS}$ (where $s_{uTE}/\sigma'_{vc} = 0.16$)

Thus, the total caisson capacity, F_{TOT} = -31.4 → -36.1 kg, also ties in closely with the measured caisson capacity, and tends to underestimate the actual wall force in the CET experiments.

Geer (1996) performed finite element analyses to simulate an axial loading of CET model caisson, as shown in Figure 5.33. These analyses assume that the caisson is initially wished-in-place, such that there are no changes in stresses and soil properties associated with the installation process. The caisson wall is modeled as a very stiff, elastic material, while the cap is assumed to be perfectly rigid, with no transfer of shear force or bending moment between the cap and the side wall. The calculations simulate a rigid top cap by imposing uniform increments of vertical displacements to both the cap and side wall. There is no separation between the lid and soil surface inside the plug and no slippage allowed between the caisson walls and the adjacent soil. The analyses use the MIT-E3 soil model to represent the stress-strain-strength properties of K_0-normally consolidated BBC. The calculations approximate undrained conditions using an artificial time frame for the axial loading procedure, with no flow occurring at either the surface or base of the clay element.

Figure 5.34 shows the finite element prediction of the axial load-displacement response of CET model caisson using the MIT-E3 soil model. The total force does not reach a limiting value over the range of displacements imposed in the analysis, but increases to F_{TOT} = -31kg at δ_v = 0.1 cm. In contrast, the wall force reaches a maximum resistance, F_w = -14.5kg at $\delta_v \approx$ 0.04 - 0.05cm and remains almost constant with continued loading of the caisson. The total and cap forces increase almost linearly with displacement of the caisson for δ_v > 0.06cm. The analysis does not predict the limit load. It can be seen that the finite element analysis predicts very well the maximum wall forces measured in the CET experiment (F_w = -15.5 ± 1.5kg). As expected, the predictions show a mobilized cap force of F_c = -16.5kg at δ_v = 0.1m, and are lower than the maximum cap force measured in the experiments (F_c = -20.7 ± 2kg).

In summary, numerical limit analysis, limit equilibrium calculations, and finite element analyses all provide good predictions of the undrained pullout capacity of the vertically loading CET miniature caissons.

5.4 Pullout Capacity for the EPR Centrifuge Model by Limit Analyses

This section compares pullout capacity of a centrifuge model caisson with predictions from numerical limit analyses and non-linear finite element analyses.

The EPR centrifuge model caissons were performed by the Laboratoire Central des Ponts et Chausées in Nantes (Clukey & Morrison, 1993). By imposing a centrifugal force of 100g on a model caisson with characteristic dimension [L], these experiments replicate the in-situ stress field expected around a prototype offshore caisson of length scale [100L]. Figure 5.35 shows the geometry at the scale of the prototype caisson, which has a total wall length L = 31.2m, outside radius R = 7.6m and wall thickness 2w = 6cm. Note that the centrifuge model caisson has a relatively large embedment ratio, L/B = 2.05, compared to the CET experiment (L/B = 1). After consolidation, the clay layer has an overall depth of 50m, while the water depth is maintained at approximately 32.5m. After installation, the stresses and pore pressures were allowed to equilibrate for a period of 24 hours prior to loading.

Figure 5.36 summarizes the measured axial load-deformation response in test f8, where a maximum pullout resistance, F_{TOT} = -110 MN occurs at a vertical displacement δ_v = 1.5m with a total time to failure, $t_f \approx$ 4hrs at prototype scale (t_f = 150 secs at model scale). Also shown in this figure are the results of the finite element analysis by (Whittle et. al, 1996) which predicts a mobilized resistance, F_{TOT} = -78 MN at δ_v = 0.2m, but do not reach the limit load.

Figure 5.37 shows a spatial discretization of the EPR centrifuge model caisson used in numerical lower and upper bound limit calculations. The analyses assume an isotropic undrained strength ratio for the clay, s_u/σ'_{vc} = 0.20 and hence, simulate a profile in which the undrained shear strength increases linearly with depth (γ_b = 8.9 kN/m^3). The water depth of 35 m is treated as a surcharge σ_{vo} = 343 kPa, acting on the clay surface and the cap of caisson. The caisson wall and cap are rigidly connected together (in contrast to the CET model caisson).

Figure 5.38 summarizes the lower and upper bound limit load for the EPR model caisson. The true collapse load is well bounded, -6.44 $\leq$ Q $\leq$ -6.90 MN/m (6.7% accuracy). The lower bound limit load, Q_L = -6.44 MN/m, includes a limiting wall

resistance, Q_w = -2.47 MN/m, and a net cap force, Q_c = -3.97 MN/m. To estimate the pullout load of cylindrical caisson, the cap and wall forces are scaled separately to account for the relative surface areas of the caisson cap and wall. In this calculation, the lower bound wall force, $F_{WL} = Q_w(\pi B/2)$ = -2.47(23.88) = -59.0 MN; and the cap force, $F_{CL} = Q_c(\pi B/4)$ = -3.97(11.94) = -47.4MN and hence, the lower bound collapse load for the caisson, F_{TOT} = -106.4MN. Assuming that the ratio of Q_U/Q_L is unaffected by the geometry, then the total caisson capacity is in the range $-106.4 \leq F_{TOT} \leq -113.5$MN. Figure 5.36 confirms that these calculations give excellent predictions of the measured caisson capacity in test f8.

Figure 5.39 shows the results of upper bound analysis for axial pullout of the EPR centrifuge caisson. The upper bound analysis predicts a failure mechanism across the base of caisson, extending across the full width of the test chamber. There is no failure within the soil plug and slips occur at the external wall-soil interface. The stress contours from lower bound analysis are shown in Figures 5.40 and 5.41. The vertical stress within the soil plug is compressive (Figure 5.40a). Figure 5.41c shows that the clay fails in an extension mode of shearing at the tip of caisson ($\delta = 90°$), while the reverse end bearing failure can be observed around the base of caisson (where principal stresses rotate for δ = 90° -> 0°). The soil along the external wall fails in direct simple shear ($\delta \approx 50°$) and the shear strength is fully mobilized along both inside and outside walls (τ/s_u = 1.0, Figure 5.42b). The full shear strength of the clay is also mobilized in the entire chamber ($[\sigma_1-\sigma_3]/2s_u$ = 1.0, Figure 5.41d).

5.5 Caisson Capacity with Inclined Loading

Inclined loading represents a major challenge for non-linear finite element analysis as it requires either a full three-dimensional model or a Fourier-series two-dimensional (Lai & Booker, 1991; Ganendra, 1995) to model the complete load-deformation response. In principle, there are similar geometric problems for the numerical limit analyses. However, it has been conventional practice in geotechnical engineering to use planar limit equilibrium calculations to compute collapse loads for

generalized loading conditions (e.g. Andersen et al., 1993). This section illustrates predictions of collapse load for inclined static loading of the EPR centrifuge model caissons and the NGI field tests with 4 caisson units using planar limit analyses.

5.5.1 Inclined Pullout of EPR Centrifuge Model

Figure 5.43 shows the meshes used in planar limit analyses for the EPR centrifuge model loaded at an inclination angle, i = 6° to the vertical. Loading is applied through a pin connection at the top of the cap approximately 8.5m above the ground surface (at prototype scale). The analysis assume that there is no yielding of the caisson structure and hence, it is modeled by a series of rigid structural beam and joint elements. Figure 5.44 summarizes the results of collapse loads. The computed lower and upper bound loads for the planar section define the collapse load within ±6%, $-5.39 \leq Q \leq -6.06$MN.

It is difficult to scale separately the cap and wall force from planar limit analyses for the case where the lateral wall resistance constitutes a significant of the total caisson capacity. Thus, it is assumed that the cylindrical caisson is approximated as a planar structure with width, B = 15.2m. Hence, the estimated inclined pullout capacity is $-81.93 \leq Q \leq -92.11$MN. The measured static capacity of the EPR model caisson at i = 6° ranges from 92.3MN (test 2II - Clukey & Morrison, 1993) to 108.5 MN, 120.4 MN (for tests L19 and g10; Whittle et. al, 1996). Part of this data scatter is due to differences in the embedment depth. The predictions from numerical limit analyses match the lowest of these three tests.

Figure 5.45 shows the results of upper bound analysis for the EPR model caisson loaded at an inclination angle, i = 6° to the vertical. The failure mechanism involves a rigid body rotation centered at a point on the front wall of the caisson at a depth of 22m. The ground surface in front of the caisson heaves, while the trailing edge settles. Stress contours from lower bound analysis are shown in Figures 5.46 and 5.47. A high horizontal stress of 900 kPa is developed at the tip of the back wall (Figure 5.46b). The lower bound analysis predict that there is a zone of passive failure (δ = 90°) occurring at the middle of front wall while the direction of major principal stress, δ ranges from 10° - 60° along the back wall (Figure 5.47c). The full shear strength of the clay is mobilized

almost everywhere in the chamber ($[\sigma_1-\sigma_3]/2s_u$ = 1.0, Figure 5.47d). Contact normal and shear traction along the cap and the side wall are shown in Figure 5.48.

5.5.2 Inclined Pullout of NGI Field Tests

Figure 5.49 shows the plan view and vertical cross-section of a 4-cell caisson model tested by NGI as part of the Snorre designed project. The static 1-g field tests were performed by NGI at the Lysaker site (test no. 1; Dyvik et al., 1993; Andersen et al., 1993). The outside diameter of each cell is 91.4 cm and the penetrated depth of skirt is 82 cm. In test no.1, the loading is applied at i = 10° to the vertical, through a point centrally located on the caisson lid 49cm above the ground surface. Figure 5.50 shows the in-situ vane shear strength profile at the Lysaker site. Note that the upper 1.8 m of soil at the site was removed before the installation of the caisson.

Figure 5.51 shows the spatial discretization of numerical limit analysis for inclined pullout of NGI model caisson. The analysis considers a planar section, with two rigidly connected cells, each of width 85 cm and embedded to a total depth of 82 cm. The clay is assigned the average undrained strength profile as shown in Figure 5.50, where s_u increases linearly with depth from the excavated surface, s_{u0} = 5.8 kPa, ρ = 1.645 kPa/m[4].

Figure 5.52 summarizes the collapse loads predicted by the numerical limit analysis. The collapse is bounded within ±4-5%, and $-0.782 \leq F_{TOT} \leq -0.852$ kN/cm width. The simplest method for applying the planar solutions is to scale the results by the width, B = 170cm, such that the estimate collapse load for the 4-cell assembly, $-133 \leq F_{TOT} \leq -145$ kN. These results provide excellent bounds on the measured caisson capacity of 137.7 kN. Figure 5.53 shows the failure surface from the limit equilibrium method (LEM) reported by Andersen et al. (1993), who predicted collapse loads, F = -138 kN, -128 kN at i = 7.5° and 10°, respectively. The mechanism is in reasonable agreement with estimated locations of the failure surface based on distortions of epoxy columns within the clay.

[4] The total unit weight of the clay is 16 kN/m^3 reported by Andersen et al. (1993).

The upper bound failure mechanism (Figure 5.54) involves a rigid body rotation of the caisson about a point located at the base of the caisson, close to the inside face of the leading wall. The zone of soil failure extends to a total depth of approximately 2.25m and up to 4.0m laterally in the trailing direction from the point of load application. The predicted failure mechanism differs significantly from the critical limit equilibrium failure surface reported by Andersen et al. (1993) but appears to provide an equally valid representation of the measured horizontal deformations of (vertical) epoxy columns within the clays (Figure 5.53). Figure 5.55 shows the stress contours from the lower bound analysis. It can be seen that both vertical and horizontal stresses are tensile inside the soil plug and also extend to a depth of 1.5m from the ground surface. The suction pressure inside the left cell is higher than that inside the right one. The clay along the front outside wall fails in the passive mode of shearing (δ = 90°), but that along the trailing outside wall fails in the direct simple shear mode (δ = 45°). Figures 5.56 and 5.57 show the contact normal and shear traction on both cells.

The planar limit analyses for inclined pullout of NGI model caisson are extended to include the situation, where the loading inclination, i varies from 0° to 90°. Figure 5.58 plots the lower and upper bound limit loads for inclined pullout as a function of loading inclination (Table 5.3 tabulates the data). For all inclination angles, the numerical limit analyses are able to bracket the true collapse load to within ±6% accuracy. The results show that there is a significant reduction in caisson capacity for inclined pullout, where the resistance decreases by 30% and 65% and at i = 15° and 45°, respectively. It is worth noting here that the limitation of these analyses is the plane strain approximation, which may have significant influence on lateral resistance of cylindrical caissons (c.f. Chapter 4)[5].

Figures 5.59 through 5.64 summarize the upper and lower bound results for inclined pullout at three loading inclinations, i = 0°, 45°, and 90°. For i = 0°, the upper bound results in Figure 5.59 show that there is no failure within the soil plug inside both

[5] For example, plane strain case, the passive lateral earth pressure, $\sigma_h = \sigma_v + 2s_u$, while axisymmetric case, $\sigma_h = \sigma_v + N_p s_u$, where the value of N_p is typically of 9.

cells, together with a conical rigid zone beneath the wall tip. The failure mechanism is symmetrical on both sides about the centerline, where the plastic zone extends 4.5m laterally. Slip also occurs at the external wall-soil interface. The lower bound results in Figure 5.60 show that the soil fails in an extension mode of shearing (δ=90°) below the base of both cells. Furthermore, a reverse end bearing failure can be observed around the caisson tip of the front and back walls (δ = 90°->0°). Suction pressures also occur inside both cells. For i = 45°, the failure mechanisms involve the rigid body rotation about a point located on the front cell, near the middle wall (Figure 5.61). The lower bound calculations (Figure 5.62c) predict that the soil fails in an extension mode of shearing (δ=90°) at the base of the back cell, but fails in a compression mode of shearing at the base of front cell (δ = 0°). Note that there are tensile pressures in the left cell, but compressive pressures in the right cell. For i = 90°, the upper bound results show that there is a significant reduction in the plastic zone and the rigid body rotation of caisson occurs about a point located at the middle wall near the tip (Figure 5.63). The failure mechanism is anti-symmetrical on both sides about the panel of the middle wall, where the ground surface heaves in front of the leading wall of the caisson and settles behind the back wall. The lower bound results (Figure 5.64d) show an active failure zone behind the back of the wall (δ = 0°) and a passive failure zone in front of the leading wall (δ = 90°).

5.6 Summary

For all model caissons (CET, EPR, NGI), planar limit analyses provide a good estimate of undrained pullout load for cylindrical cell caissons. The chapter also demonstrates the application of limit analyses to generate the design chart of generalized failure load for caissons in normally consolidated clay, where the results are useful for offshore engineering. Results of limit analyses indicate that the empirical mechanism of reverse end bearing assumed in the limit equilibrium method is only valid for deep caissons, where L/B > 0.8.

The limitation of the method is restrict to plane strain analyses, where the results has to be scaled to approximate the capacity of actual geometry of caisson. Another limitation of this method can be seen from comparison with CET caissons, where scaling

results of planar analyses fail to match the measured wall and cap forces. However, the results still give a good prediction for the total pullout load. In practice, design engineers are interested in estimating the total capacity of the caisson, particularly where caissons consist of multi cells and subjected to inclined loads, and hence this restriction may not be of primary importance. The other limitation is that the method can not take into account of caisson installation, which may constitute important parameter in practice.

5.7 References

Andersen, K.H., and Lauritzsen, R. (1988). "Bearing capacity for foundations with cyclic loads" J. of Geotech. Engrg., ASCE, 114(5), 540-555.

Andersen, K.H., Kleven, A., and Heien, D. (1988). "Cyclic soil data for design of gravity structures." J. of Geotech. Engrg., ASCE, 114(5).

Andersen, K.H., Dyvik, R., Schroder, K., Hansteen, O.E. and Bysveen, S. (1993). "Field tests of anchors in clay. II: Predictions and interpretation" J. of Geotech. Engrg., ASCE, 119(10), 1532-1549.

Cauble, D.F. (1996). "Experimental measurements for a model suction caisson" PhD Thesis, Dept. of Civil Engrg., MIT, Cambridge, MA

Clukey, E.C. and Morrison, M.J. (1993). "A centrifuge and analytical study to evaluate suction caissons for TLP applications in the Gulf of Mexico." Design and Performance of Deep Foundations: Piles and Piers in Soil and Soft Rock, ASCE, NY, 141-156.

Davis, E.H. and Booker, J. R. (1973). "The effect of increasing strength with depth on the bearing capacity of clays." Géotechnique, 23(4), 551-563.

Dyvik, R., Andersen, K.H., Hansen, S.B. and Christophersen, H.P. (1993). "Field tests of anchors in clay. I: Description." J. of Geotech. Engrg., ASCE, 119(10), 1515-1531.

Fuglsang, L.D. and Steensen-Bach (1991). "Breakout resistance of suction piles in clay." Proc. Centrifuge'91, Boulder, CO., Balkema, 153-159.

Ganendra D. (1995). "Finite element analysis of laterally loaded pile." PhD. Thesis, Imperial College of Science, Technology and Medicine, University of London, London.

Geer, M. (1996). "Analysis of pile and suction caisson behavior in axial loading." PhD Thesis in progress, MIT, Cambridge, MA.

Kulhawy, F.H., Trautmann, C.H., Beech, J.F., O'Rourke, T.D, and Mcguire, W. (1983). "Transmission line structure foundations for uplift-compression loading." EPRI Report EL-2870, Electric Power Research Institute, Palo Alto, CA.

Ladd, C. C. (1991). "The Twenty-Second Terzaghi Lecture: Stability evaluation during staged construction." J. of Geotech. Engrg., ASCE, 117(4), 537-615.

Lai, J. Y. and Booker, J. R. (1991). "Application of discrete Fourier-series to the finite-element stress-analysis of axisymmetrical solids." International Fournal for Numerical Methods in Engineering, 31(4), 619-647.

Sloan S. W., and Randolph M. F. (1982). "Numerical prediction of collapse loads using finite element methods." Int. J. for Numerical and Analytical Methods in Geomechanics, 6(1), 47-76.

Whittle, A. J. (1987). "A constitutive model for overconsolidated clays with application to the cyclic loading of friction piles." Sc.D. Thesis, Dept of Civil Engrg., MIT, Cambridge, MA.

Whittle, A.J. and Kavvadas, M. (1994). "Formulation of the MIT-E3 constitutive model for over consolidated clays." J. of Geotech. Engrg., ASCE, 120(1), 173-198.

Whittle, A. J., Germaine, J. T., Cauble, D. F., Geer, M. A. (1996). "Behavior of suction caisson foundations: Final Report." report submittted to MIT Sea Grant and Joint Oil Industry Consortium, Cambridge , MA.

L/B	$\frac{Q}{\rho(B/2+L)^2}$		Bound
	Lower bound	Upper bound	(%)
0.0	0.980	1.020	4.0
0.125	3.117	3.507	11.8
0.25	4.313	4.704	8.7
0.5	4.553	4.999	9.3
0.75	4.331	4.687	7.9
1.0	4.060	4.411	8.3

B/L	$\frac{Q}{\rho(B/2+L)^2}$		Bound
	Lower bound	Upper bound	(%)
1	4.060	4.411	8.3
0.667	3.562	3.856	7.9
0.5	3.167	3.443	8.4
0.333	2.656	2.915	9.3
0.2	2.240	2.382	6.2
0.125	1.850	2.004	8.0
0	0.991	1.000	0.9

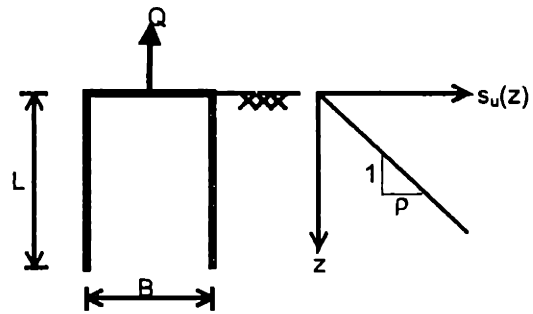

Table 5.1 Summary of collapse loads for vertically loaded planar caissons

L/B	Total force $\frac{Q}{\rho(B/2+L)^2}$	Force on the cap $\frac{Q_c}{\rho(B/2+L)^2}$	Force on the side wall $\frac{Q_w}{\rho(B/2+L)^2}$	Q_c/Q (%)	Q_w/Q (%)
0	0.980	0.980	0.000	100.0	0.0
0.125	3.117	3.112	0.005	99.8	0.2
0.25	4.313	4.296	0.018	99.6	0.4
0.5	4.553	4.244	0.310	93.2	6.8
0.75	4.331	3.823	0.508	88.3	11.7
1	4.060	3.354	0.705	82.6	17.4

B/L	Total force $\frac{Q}{\rho(B/2+L)^2}$	Force on the cap $\frac{Q_c}{\rho(B/2+L)^2}$	Force on the side wall $\frac{Q_w}{\rho(B/2+L)^2}$	Q_c/Q (%)	Q_w/Q (%)
1	4.060	3.354	0.705	82.6	17.4
0.667	3.562	2.539	1.023	71.3	28.7
0.5	3.167	2.004	1.163	63.3	36.7
0.333	2.656	1.335	1.321	50.3	49.7
0.2	2.240	0.644	1.596	28.7	71.3
0.125	1.850	0.155	1.694	8.4	91.6
0	0.991	0.000	0.991	0.0	100.0

Table 5.2 Summary of wall and cap forces from lower bound analyses of planar caisson

Loading inclination i (deg)	Limit load, Q		Bound
	Lower bound (kN/cm)	Upper bound (kN/cm)	(%)
0	0.9183	1.0001	8.5
7.5	0.8274	0.8998	8.4
10	0.7826	0.8522	8.5
15	0.6929	0.7602	9.3
30	0.4855	0.5477	12.0
45	0.3655	0.4114	11.8
60	0.3016	0.3407	12.2
75	0.2707	0.3055	12.1
90	0.2617	0.2924	11.1

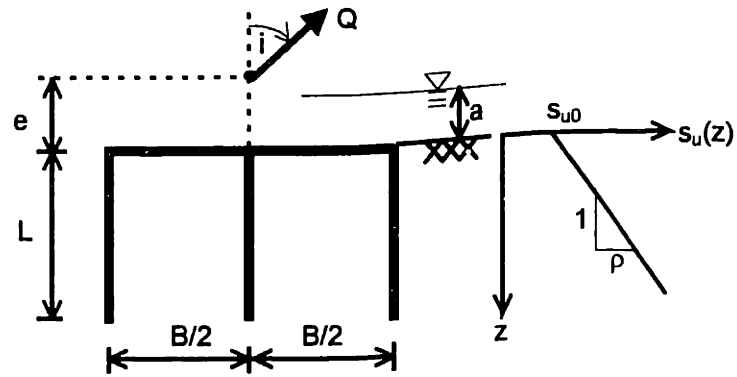

Dimension

B = 170 cm., L = 82 cm., e = 49 cm., a = 35 cm.

Clay

γ_t = 16 kN/m^3 , s_{u0} = 5.8 kPa, ρ = 1.645 kPa/m

Table 5.3 Collapse loads for an inclined pullout of NGI model caissons

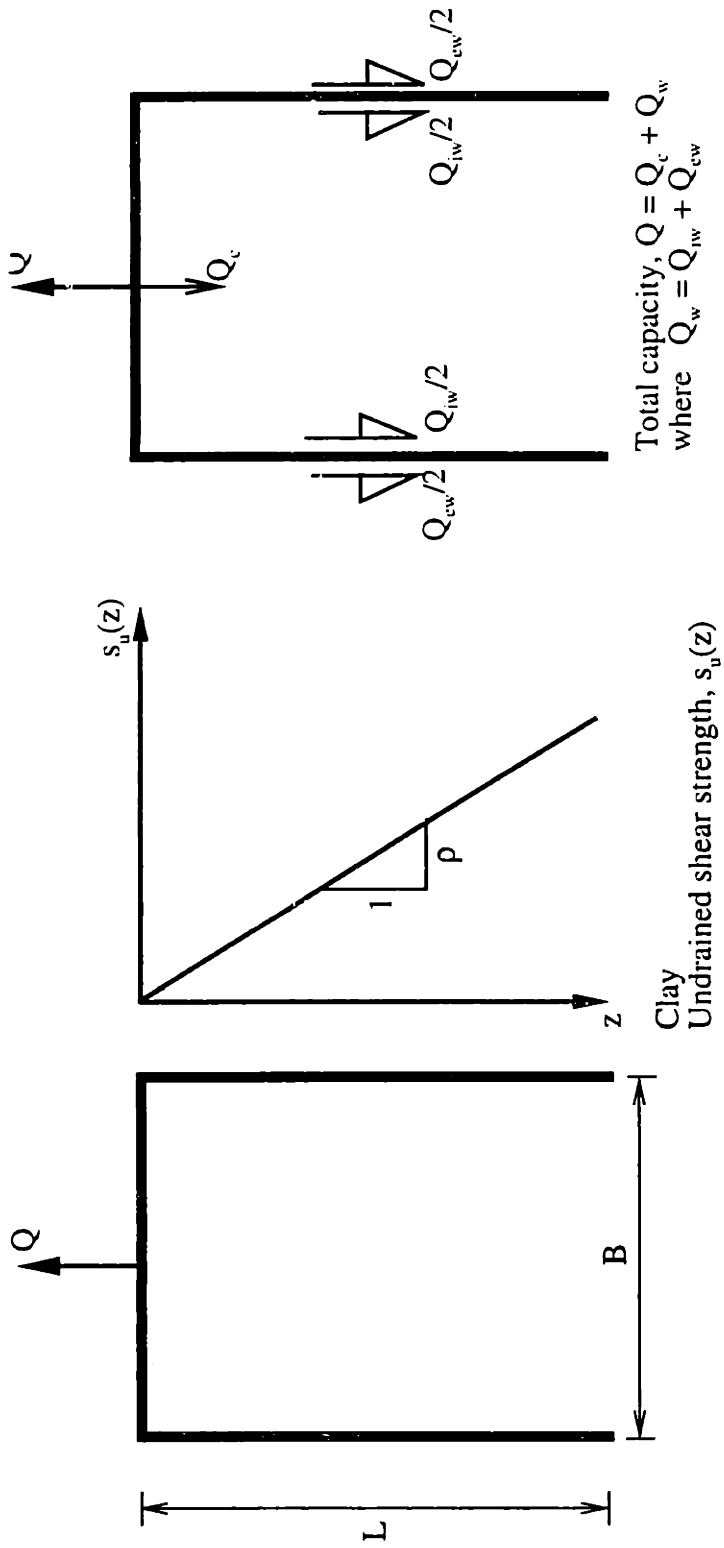

Figure 5.1 Problem notation for an ultimate tensile loading of a rigid-planar caisson

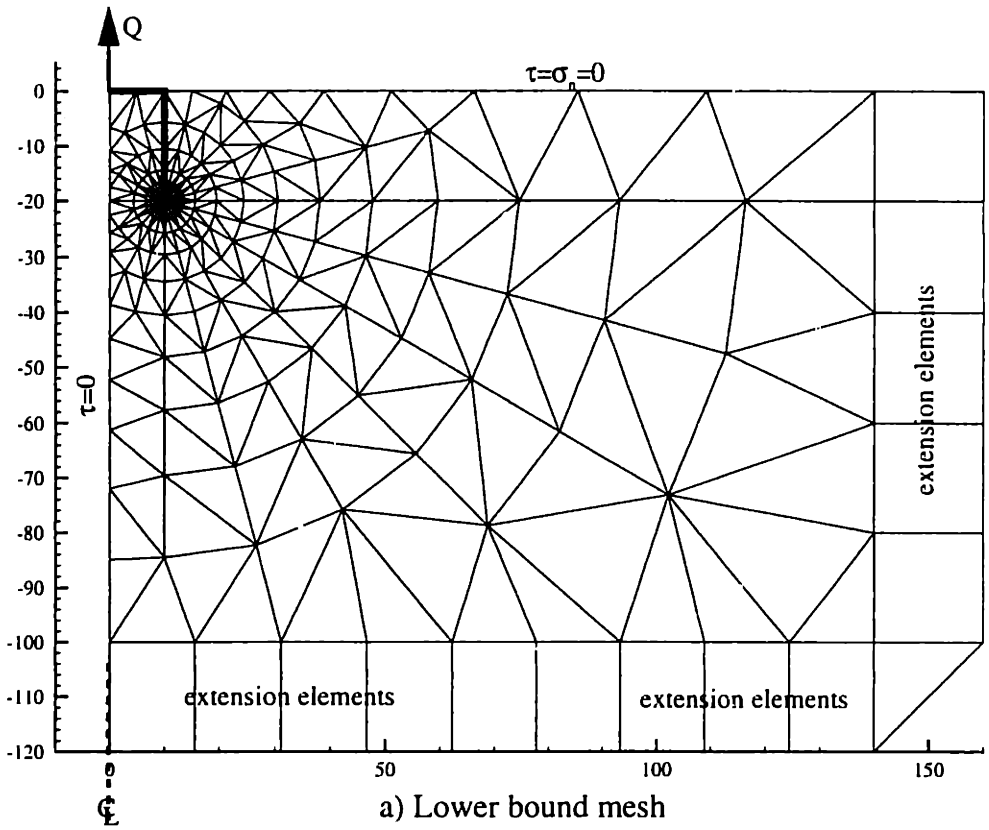

a) Lower bound mesh

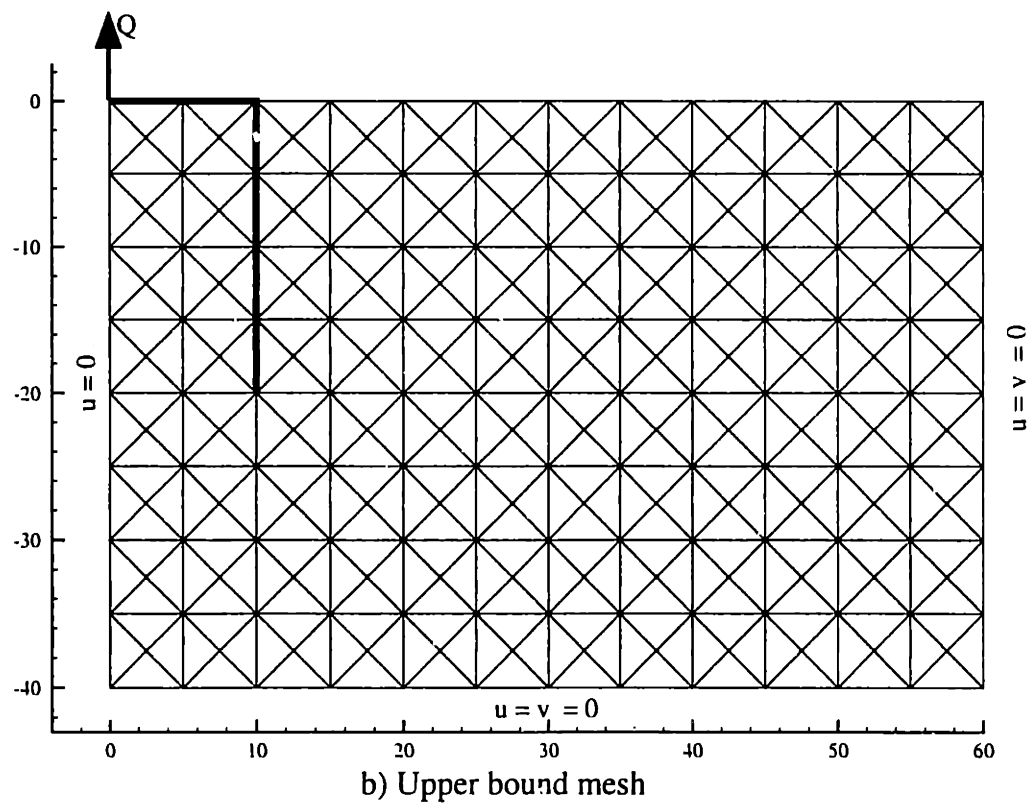

b) Upper bound mesh

Figure 5.2 Meshes used in axial tensile loading of rigid-plannar caissons

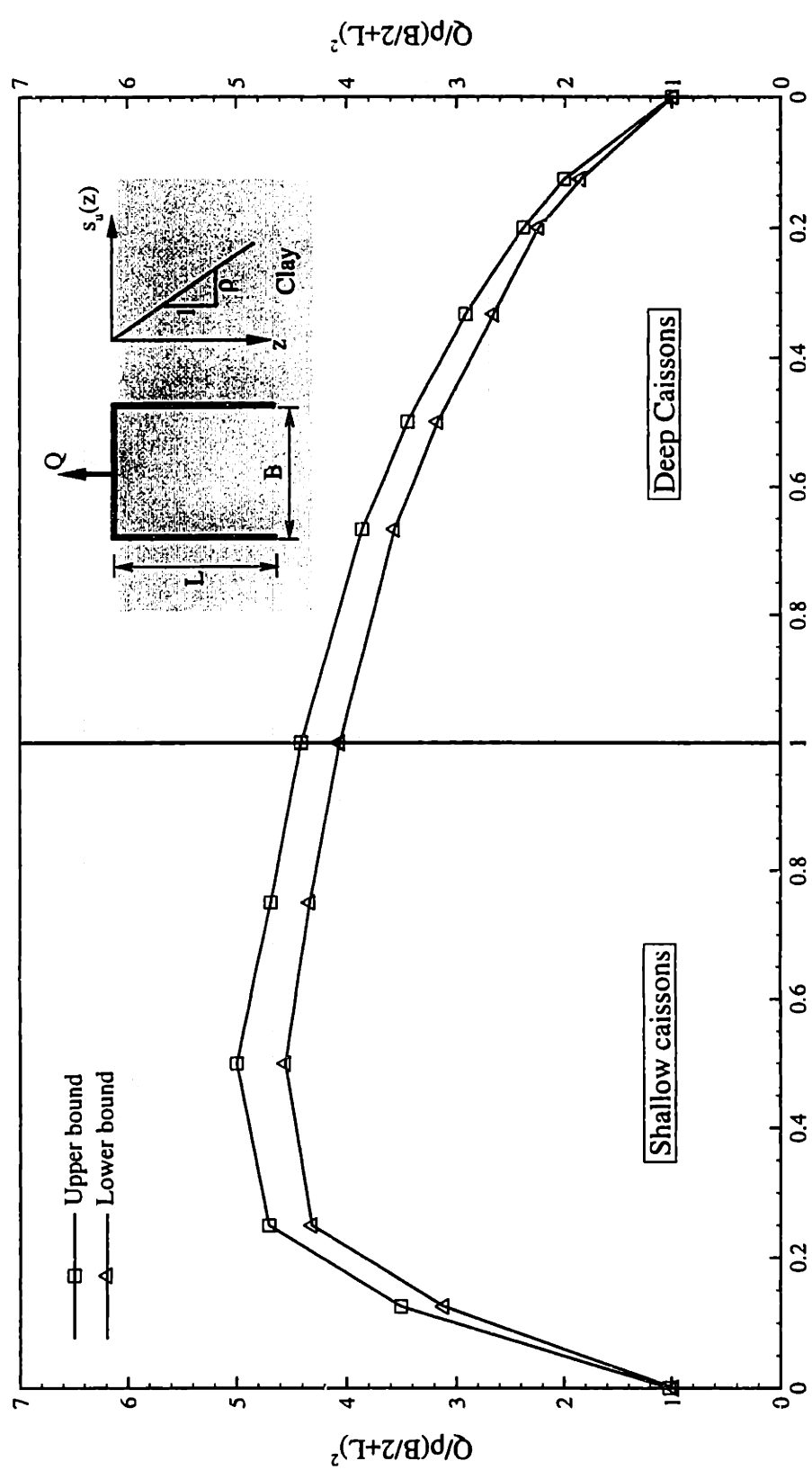

Figure 5.3 Pullout loads from planar limit analyses of caissons in non-homogeneous clay

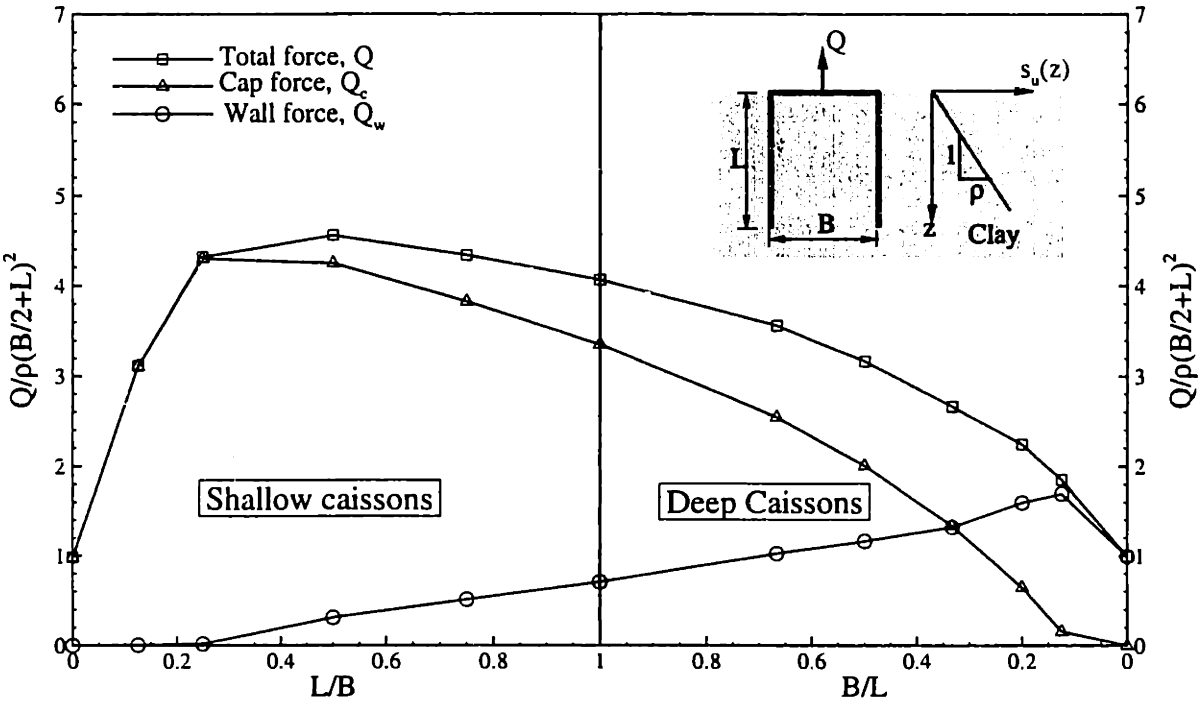

a) Total, cap and side wall forces

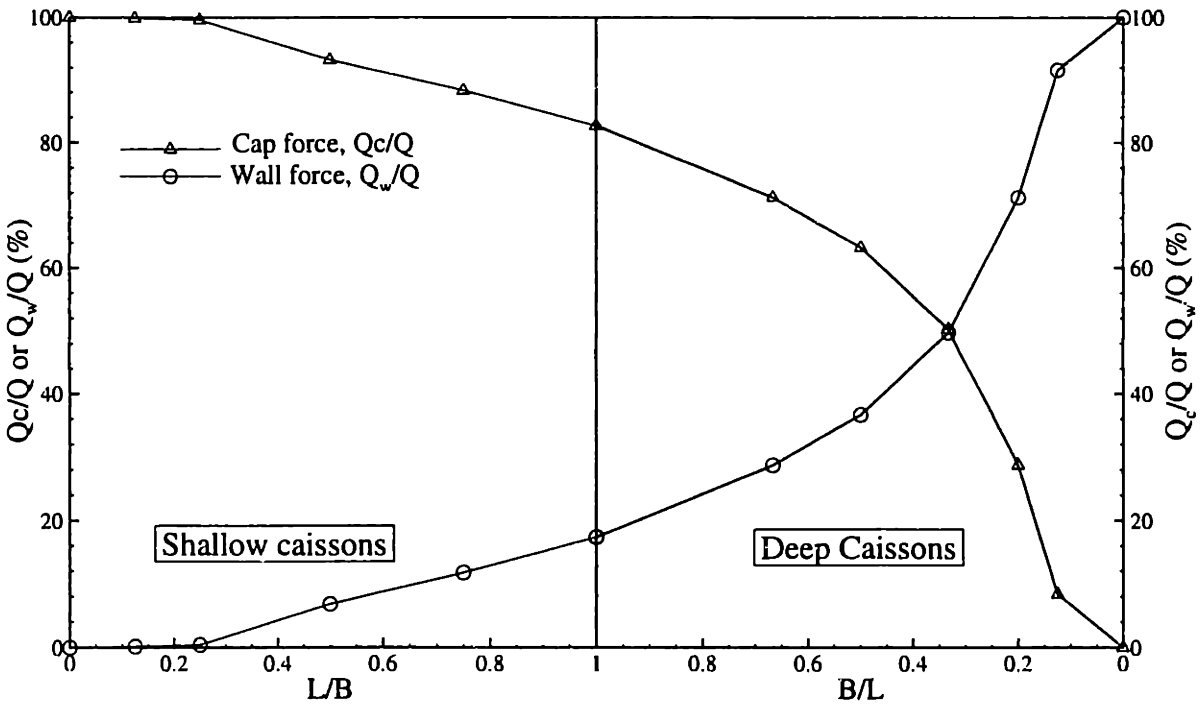

b) Percentage of cap and side wall forces

Figure 5.4 Lower bound calculations of wall and cap forces for planar caissons in non-homogeneous clay

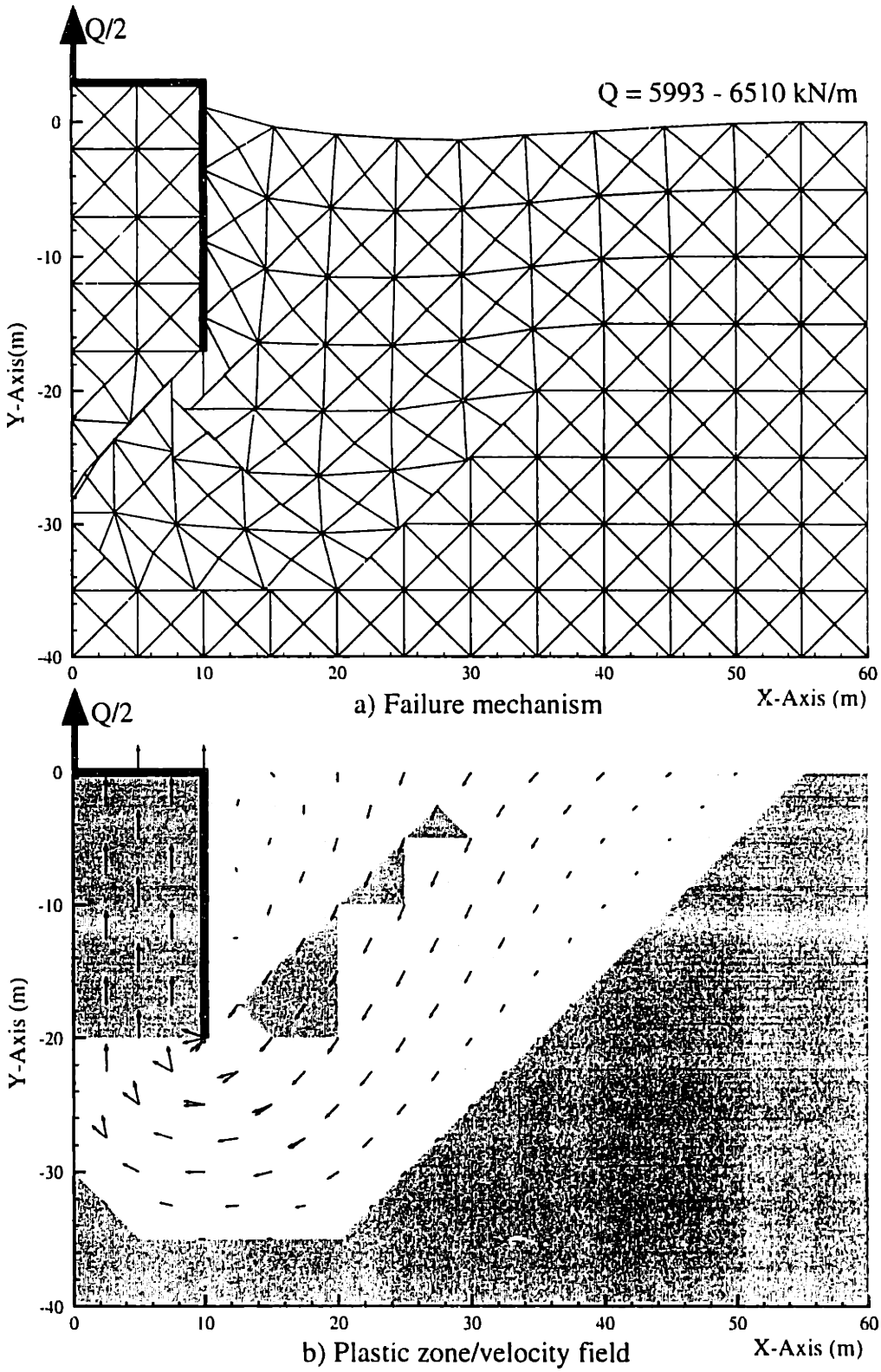

Figure 5.5 Upper bound results for tensile loading of planar caissons, where B/L =1

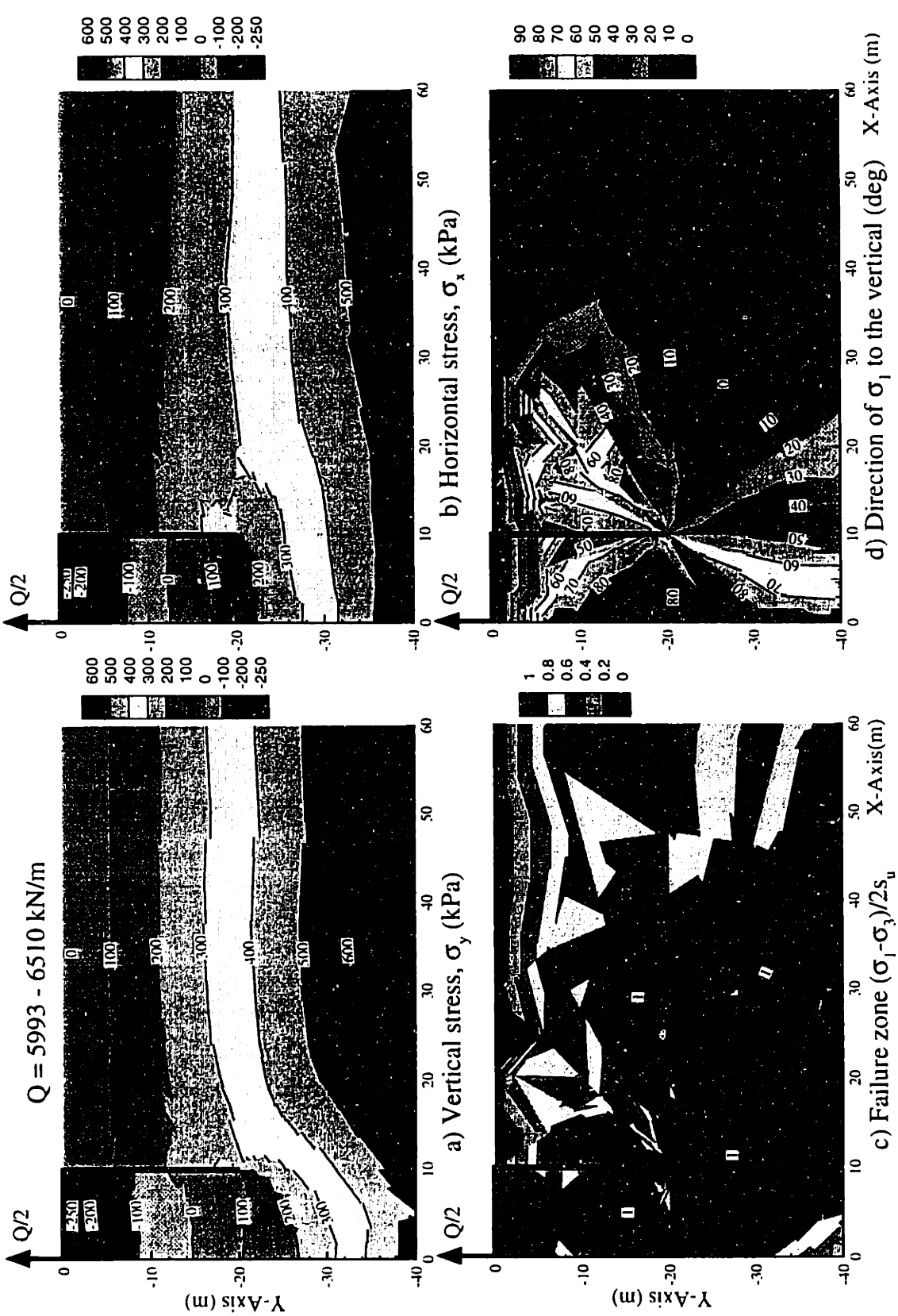

Figure 5.6 Lower bound results for tensile loading of planar caissons, where B/L = 1

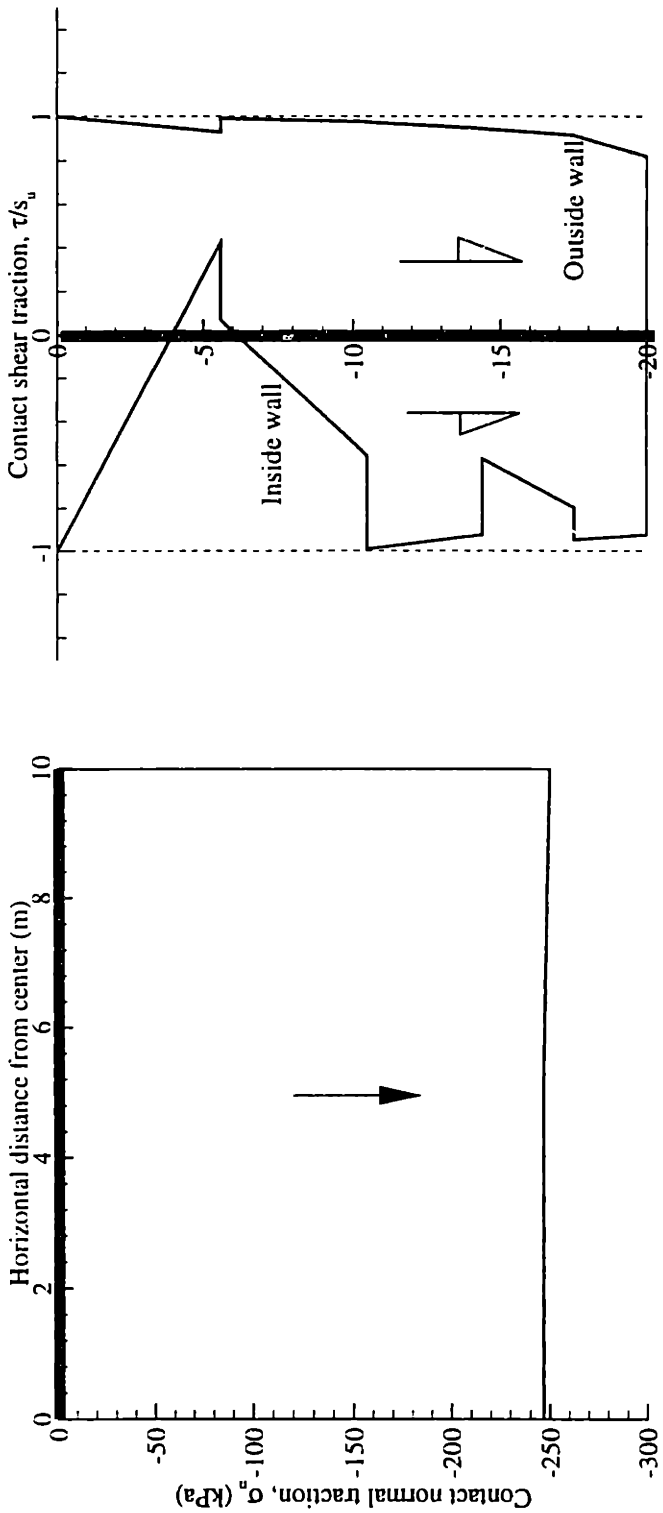

a) Contact normal traction on the cap, σ_n

b) Contact shear tractions on the wall, τ/s_u

Figure 5.7 Contact tractions on the cap and wall from lower bound analyses of planar caissons, where B/L = 1

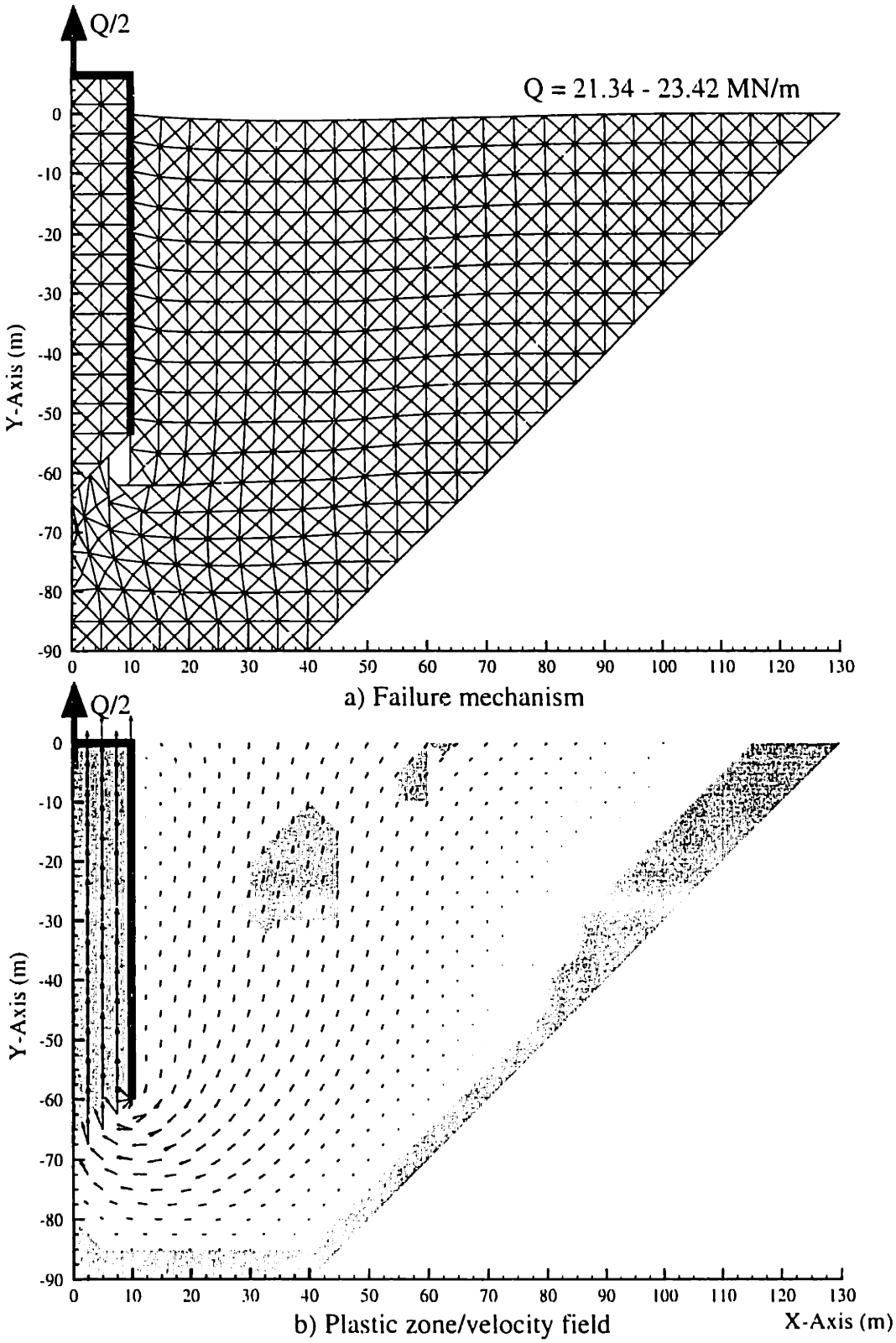

Figure 5.8 Results of upper bound analysis of a deep caisson with embedment ratio, L/B=3

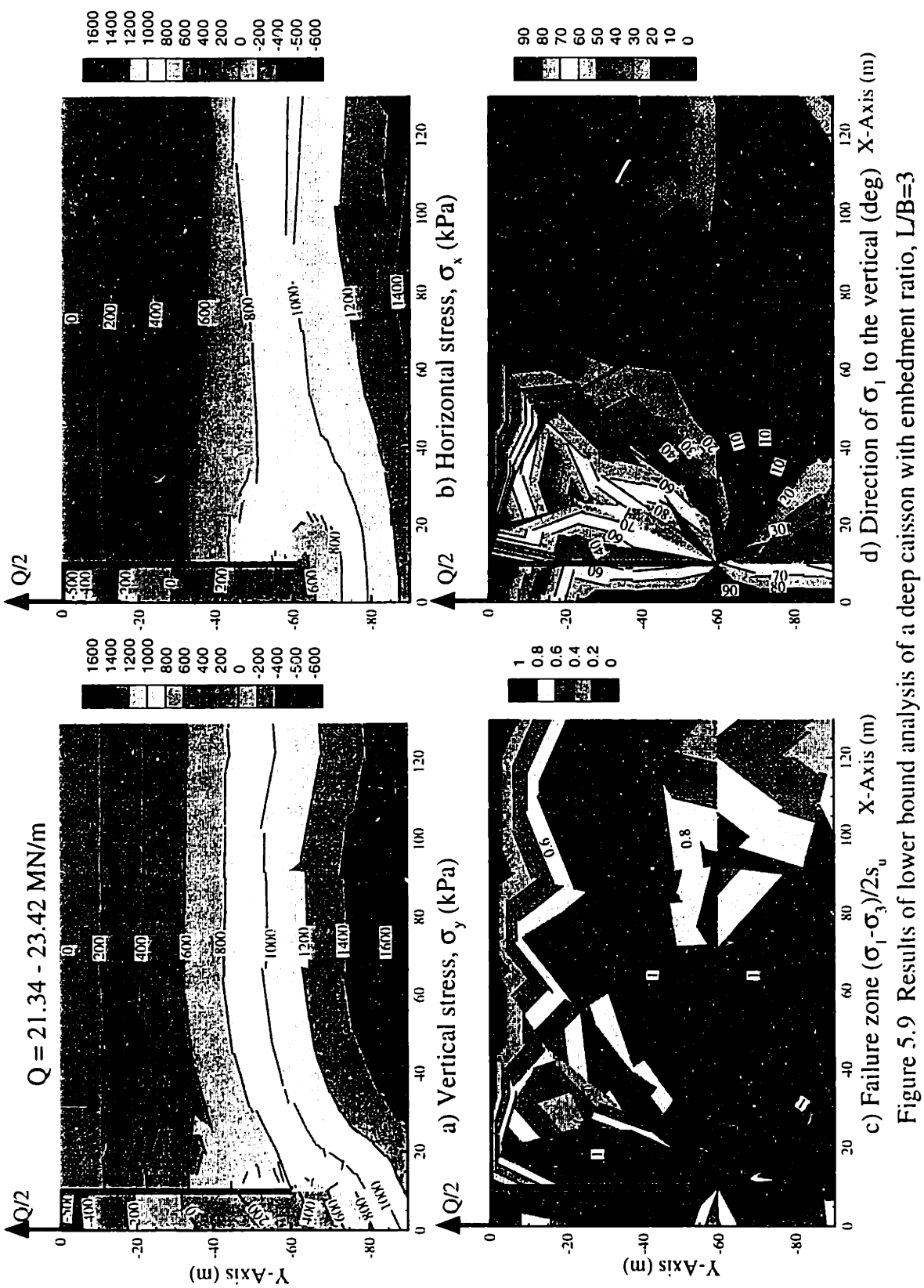

Figure 5.9 Results of lower bound analysis of a deep caisson with embedment ratio, L/B=3

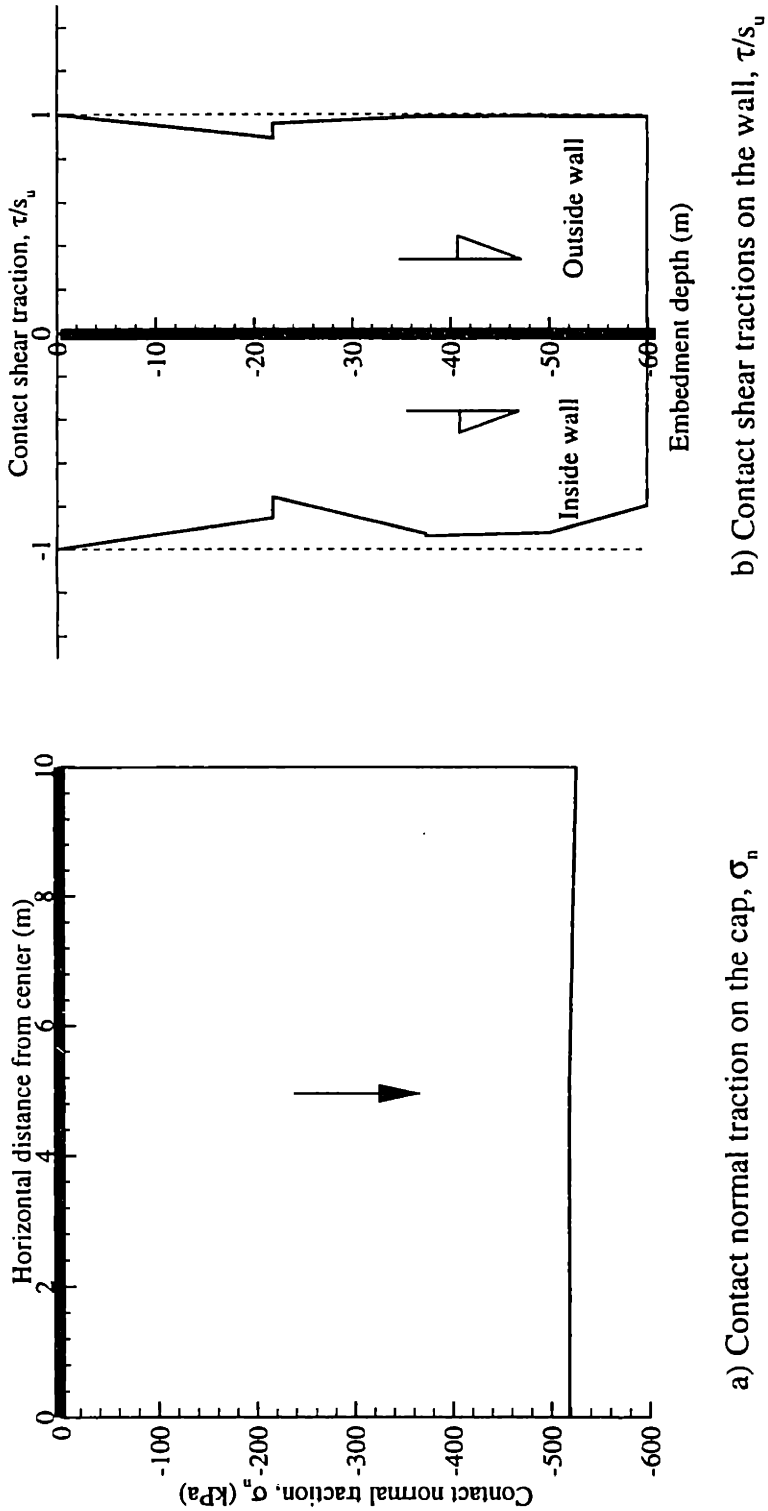

a) Contact normal traction on the cap, σ_n

b) Contact shear tractions on the wall, τ/s_u

Figure 5.10 Contact tractions on the cap and wall from lower bound analyses of deep planar caissons, where $L/B = 3.0$

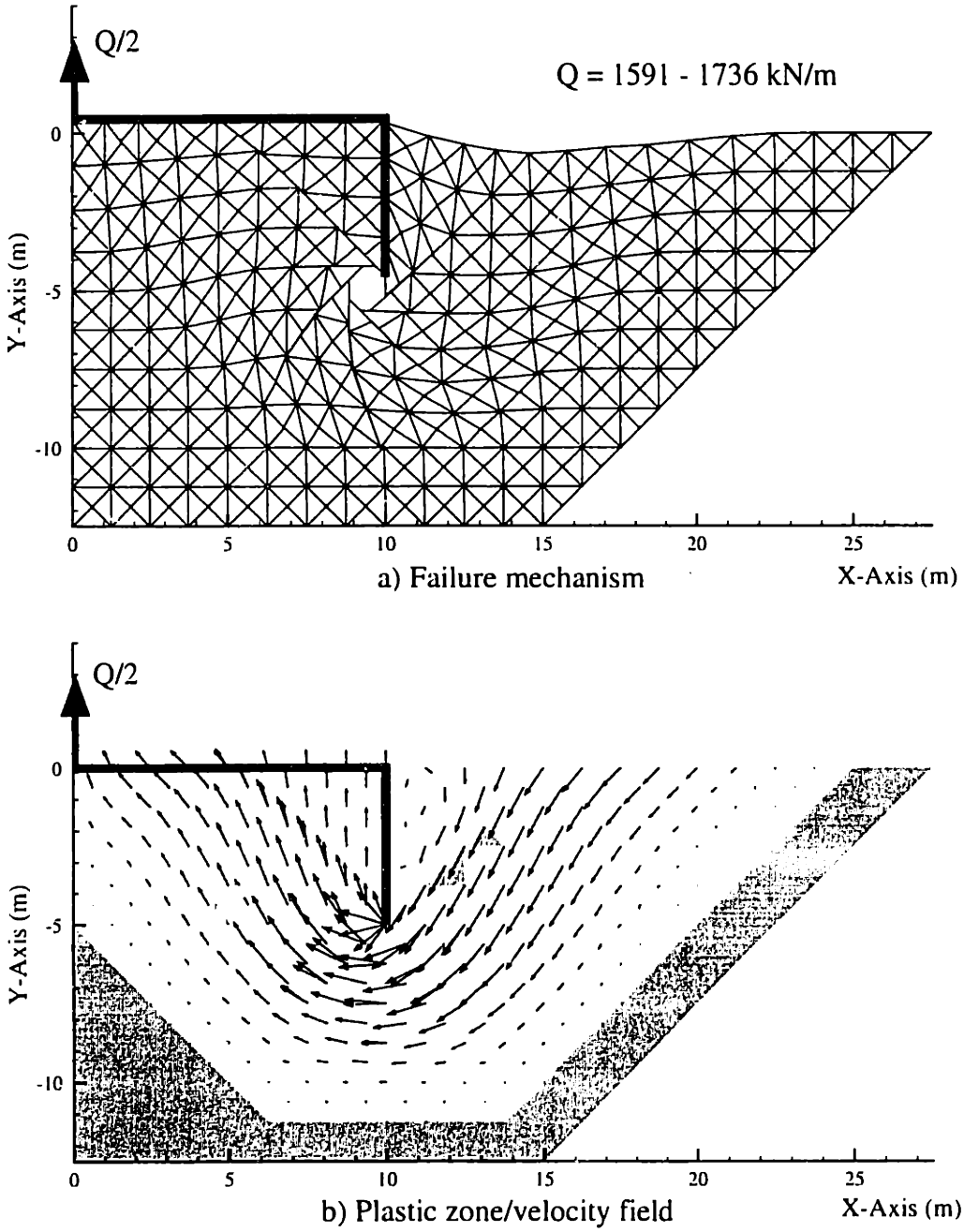

Figure 5.11 Results of upper bound analysis of a shallow caisson with embedment ratio, L/B = 0.25

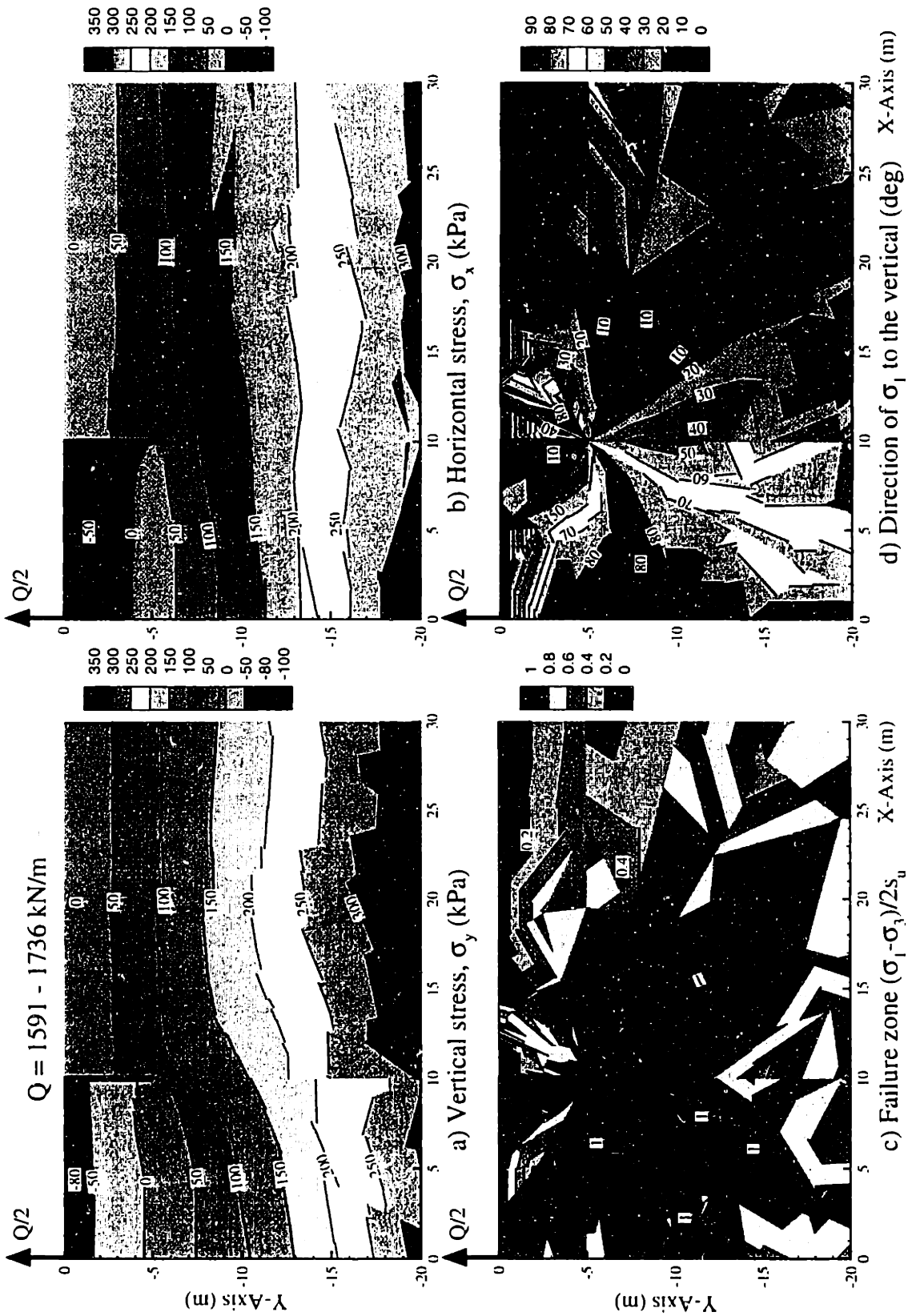

Figure 5.12 Results of lower bound analysis of a shallow caisson with embedment ratio, L/B=0.25

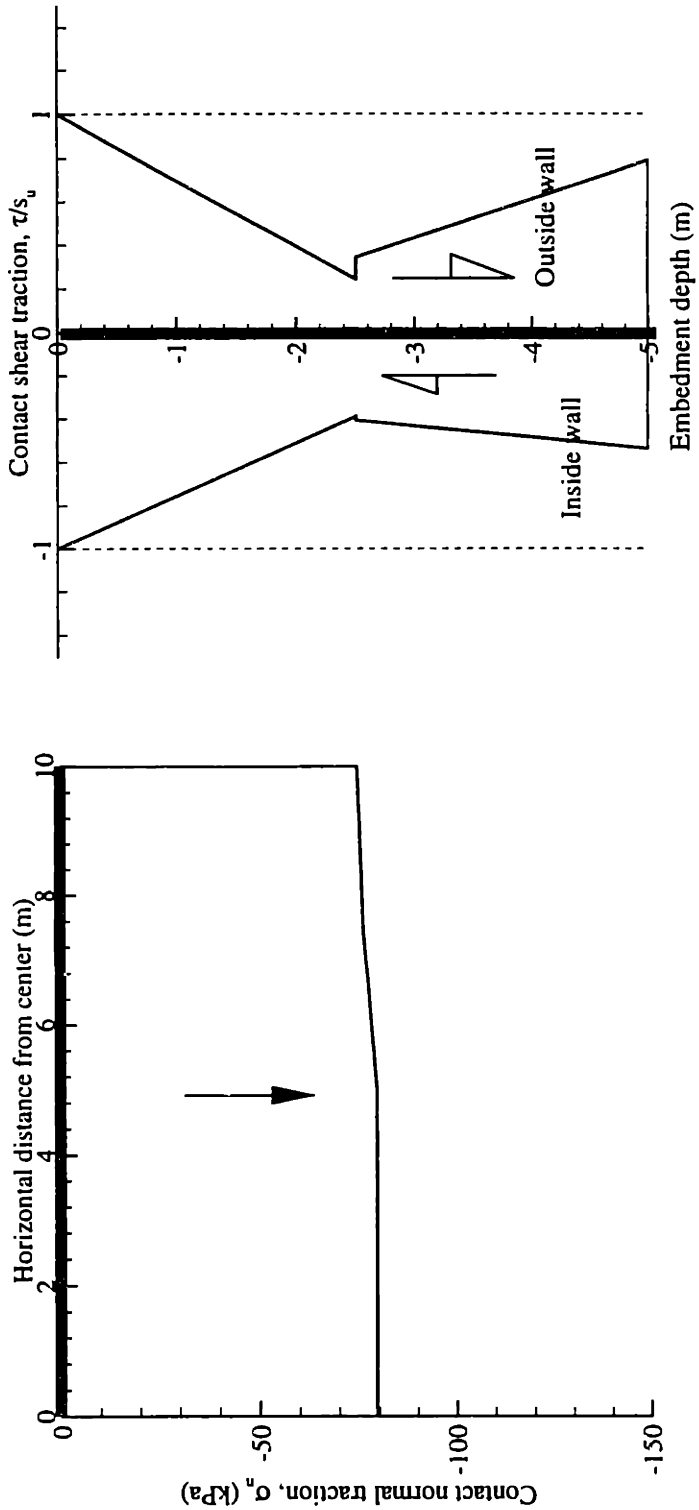

a) Contact normal traction on the cap, σ_n

b) Contact shear tractions on the wall, τ/s_u

Figure 5.13 Contact tractions on the cap and wall from lower bound analyses of shallow planar caissons, where $L/B = 0.25$

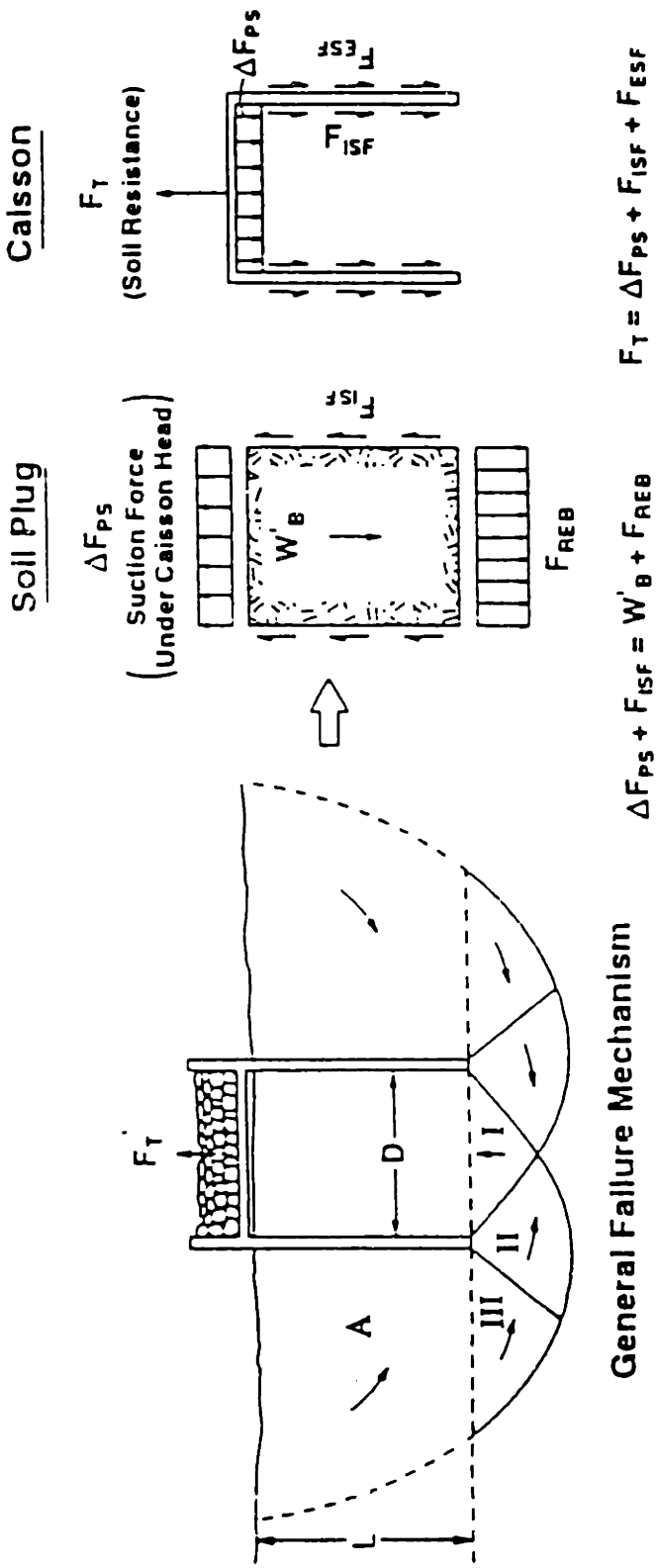

Figure 5.14 Limit equilibrium calculations for vertically loaded suction caissons (after Clukey and Morrison, 1993)

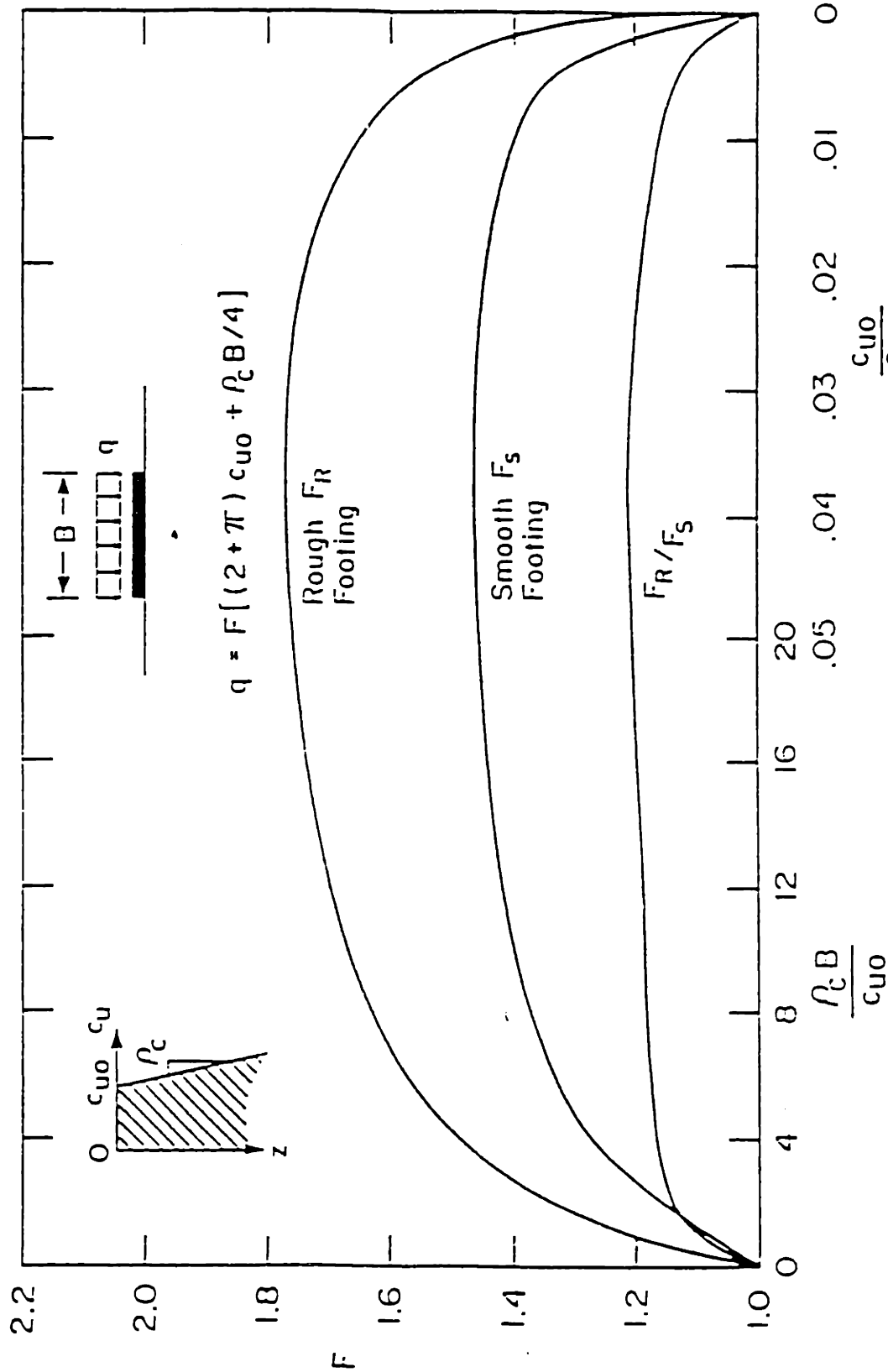

Figure 5.15 Bearing capacity factors for footings on non-homogeneous clay (after Davis and Booker, 1973)

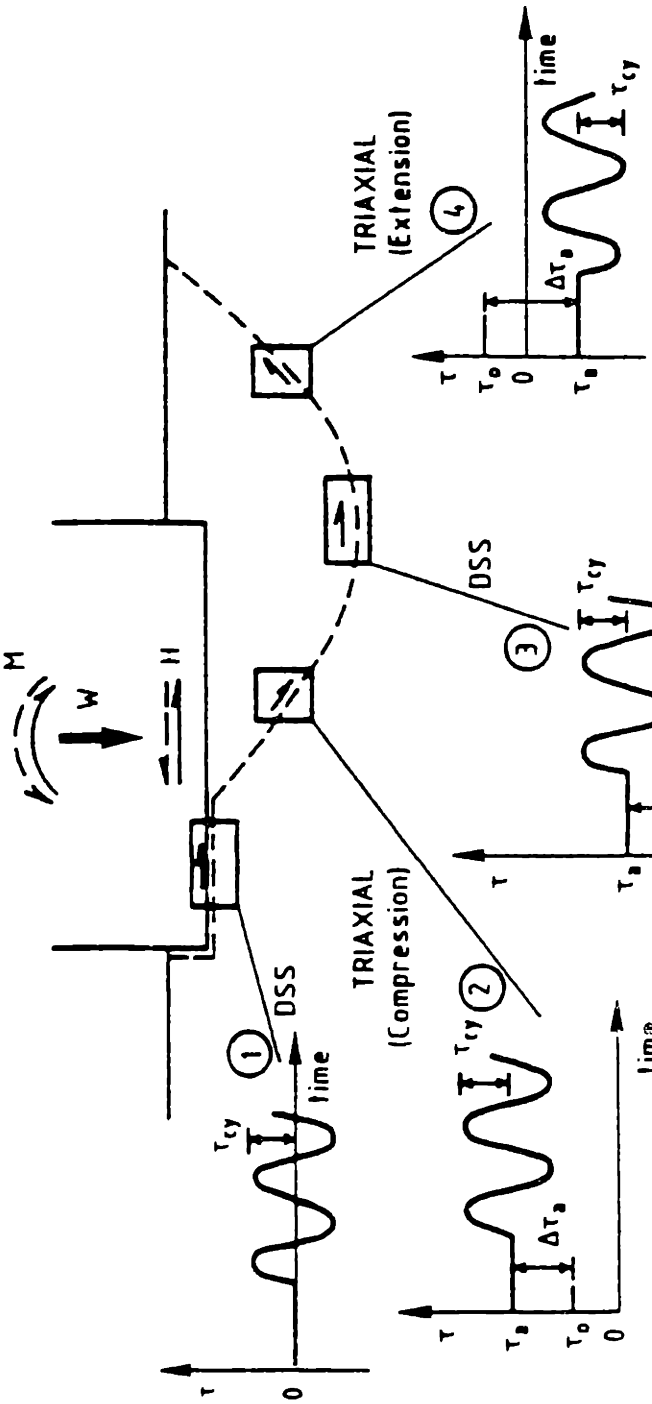

Figure 5.16 Limit equilibrium methods for an offshore gravity platform (after Andersen and Lauritzen, 1988)

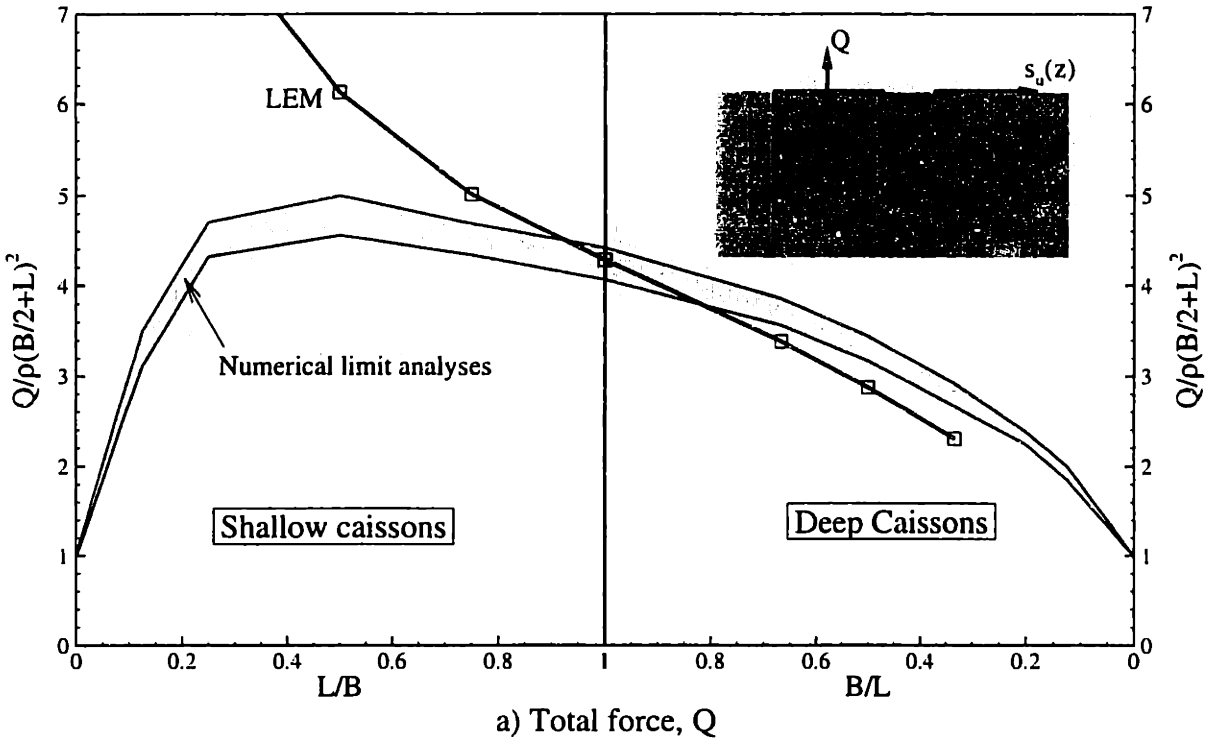

a) Total force, Q

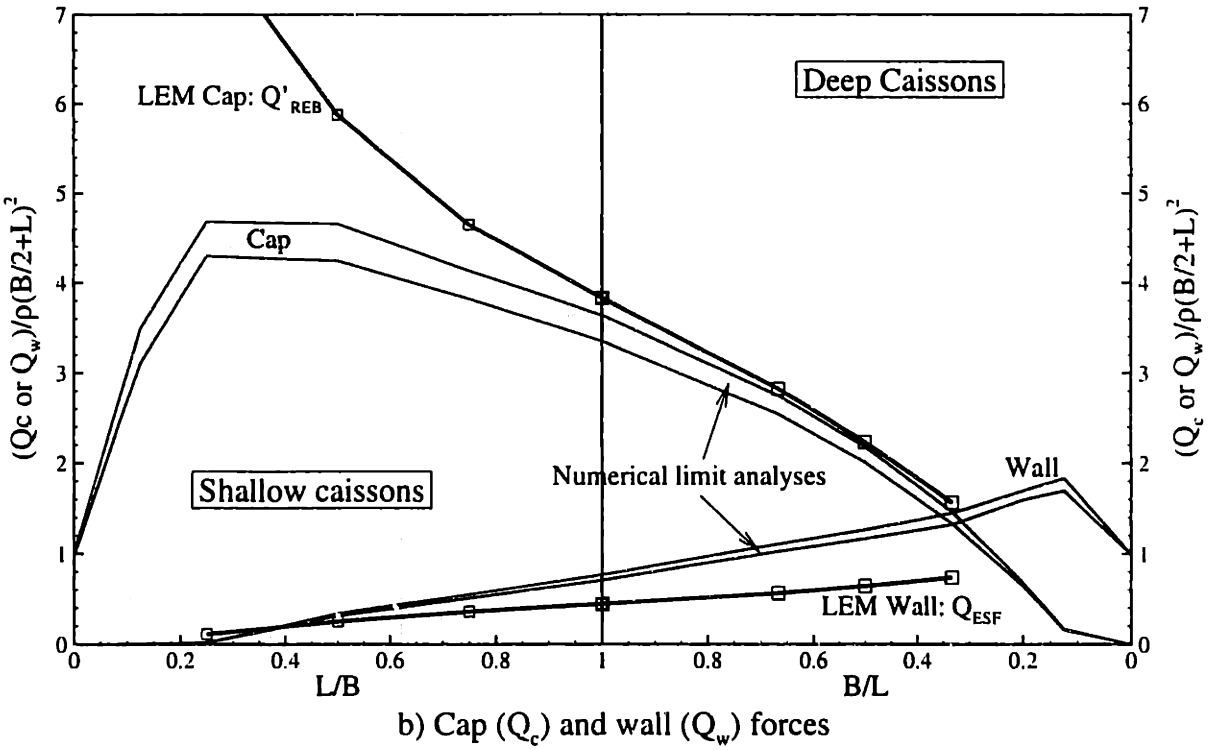

b) Cap (Q_c) and wall (Q_w) forces

Figure 5.17 Comparisons of pullout loads between limit analysis and limit equilibrium calculations (LEM) for planar caissons in non-homogeneous clay

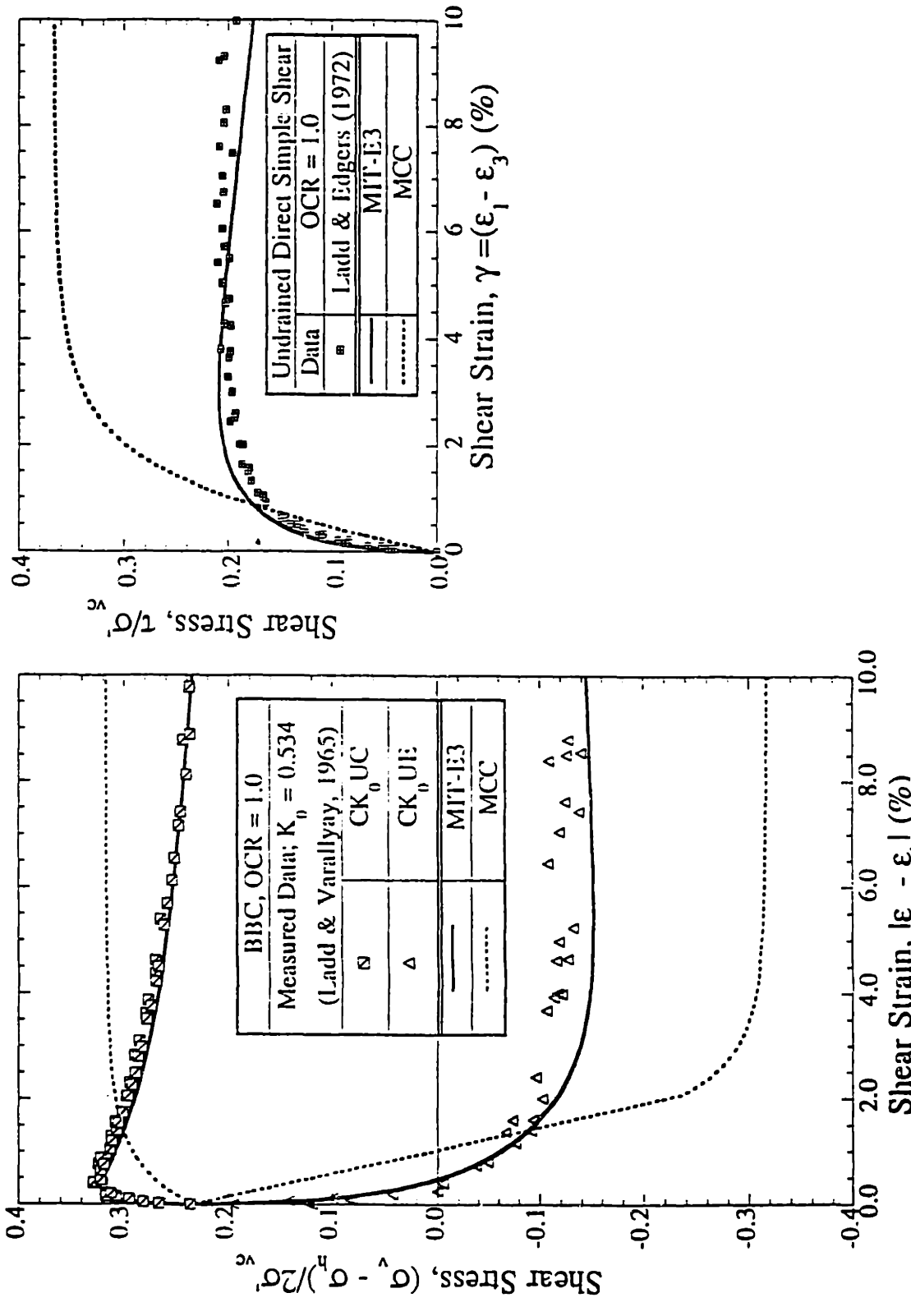

Figure 5.18 Comparison of predicted and measured undrained shear behavior of K_0-normally consolidated BBC (after Whittle et al., 1996)

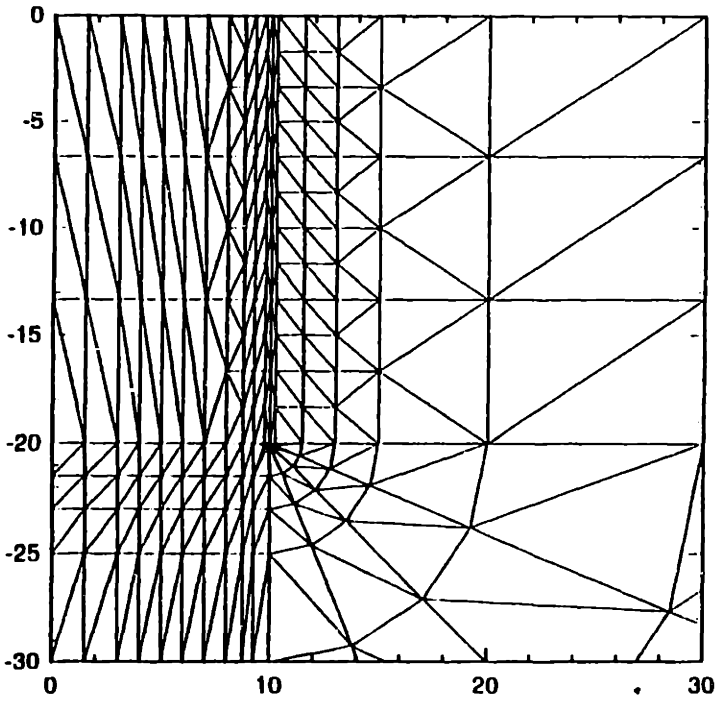

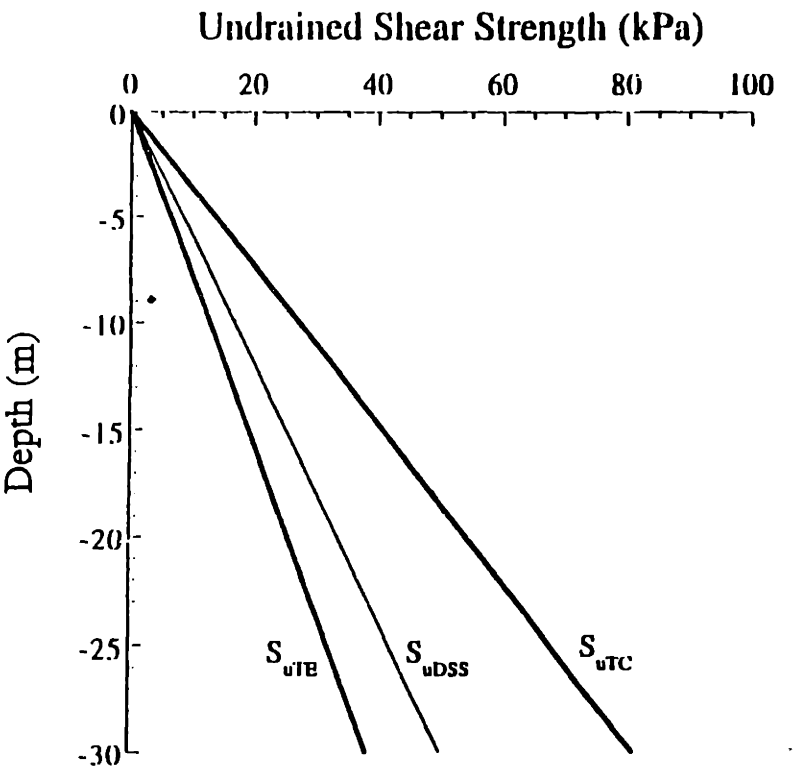

Suction Caisson Material Properties:
$E = 3.4 \times 10^4$ MPa
$\nu = 0.2$
$\gamma = 18 kN/m^3$

Finite Element Mesh:
491 Elements (15-noded triangles)
404 Soil Elements, 87 Caisson Elements
4272 Nodes
8600 DOF

Element Types:
Caisson: UEL type U18, 15-noded triangles, 15 displacement nodes, 0 pore pressure nodes, 16 integration points
Soil: UEL type U17, 15-noded triangles, 15 displacement nodes, 3 pore pressure nodes, 16 integration points

Figure 5.19 Details of finite element mesh and shear strength profile of clay for base case analyses (after Whittle et al., 1996)

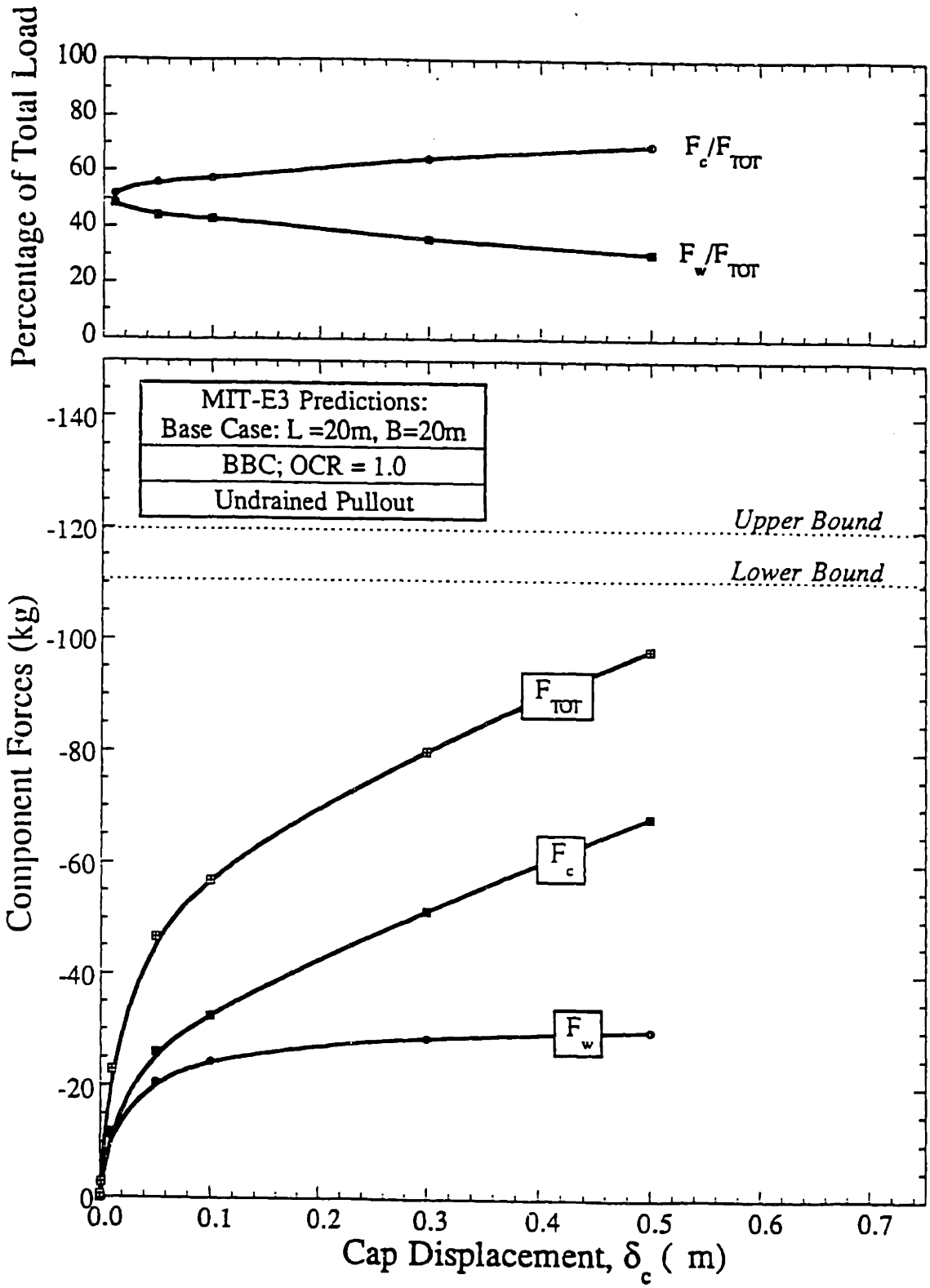

Figure 5.20 Predictions of load-deformation response for base case geometry using the MIT-E3 soil model (after Whittle et al., 1996)

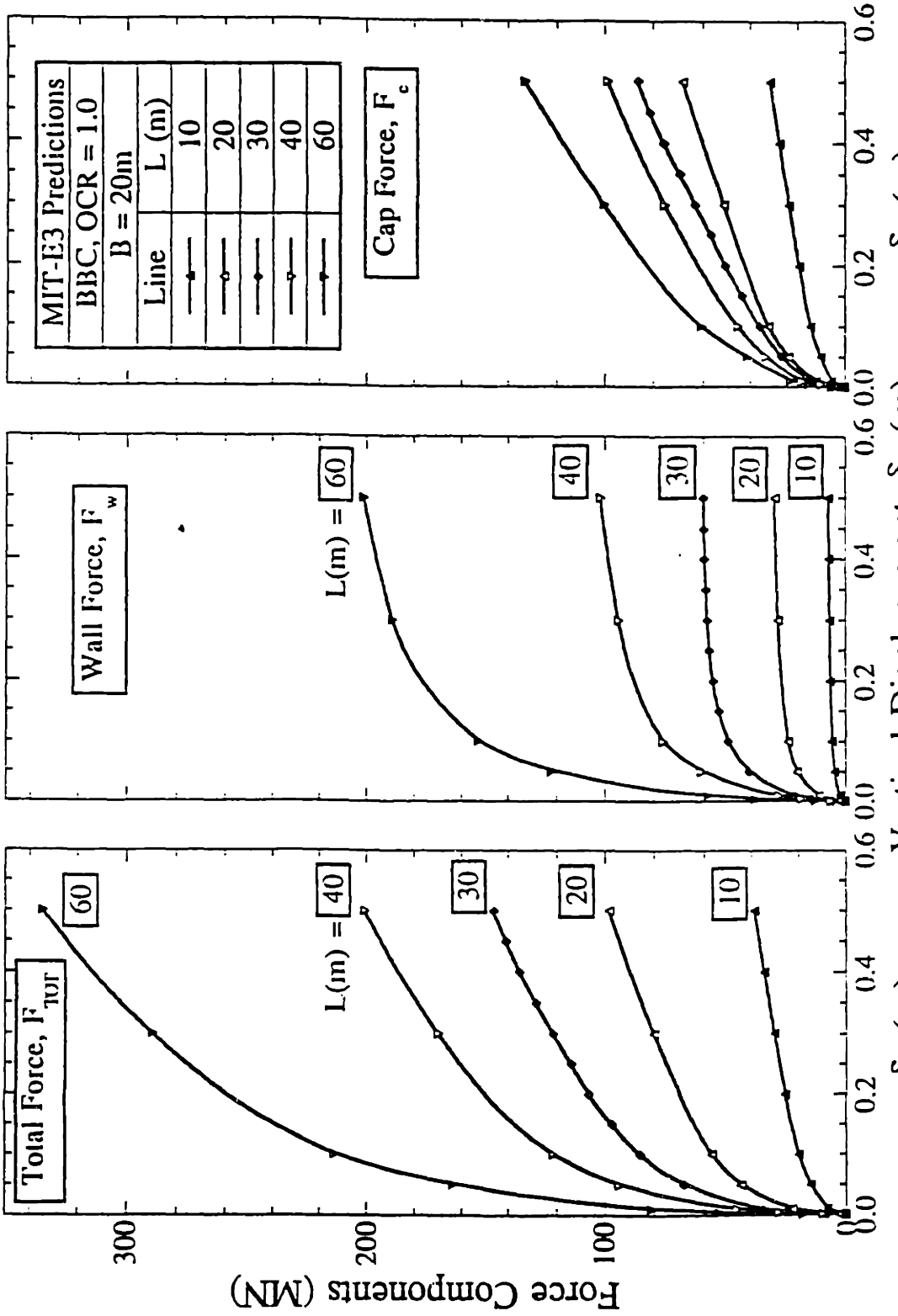

Figure 5.21 Effect of wall length on predicted load-deformation response using the MIT-E3 soil model (after Whittle et al., 1996)

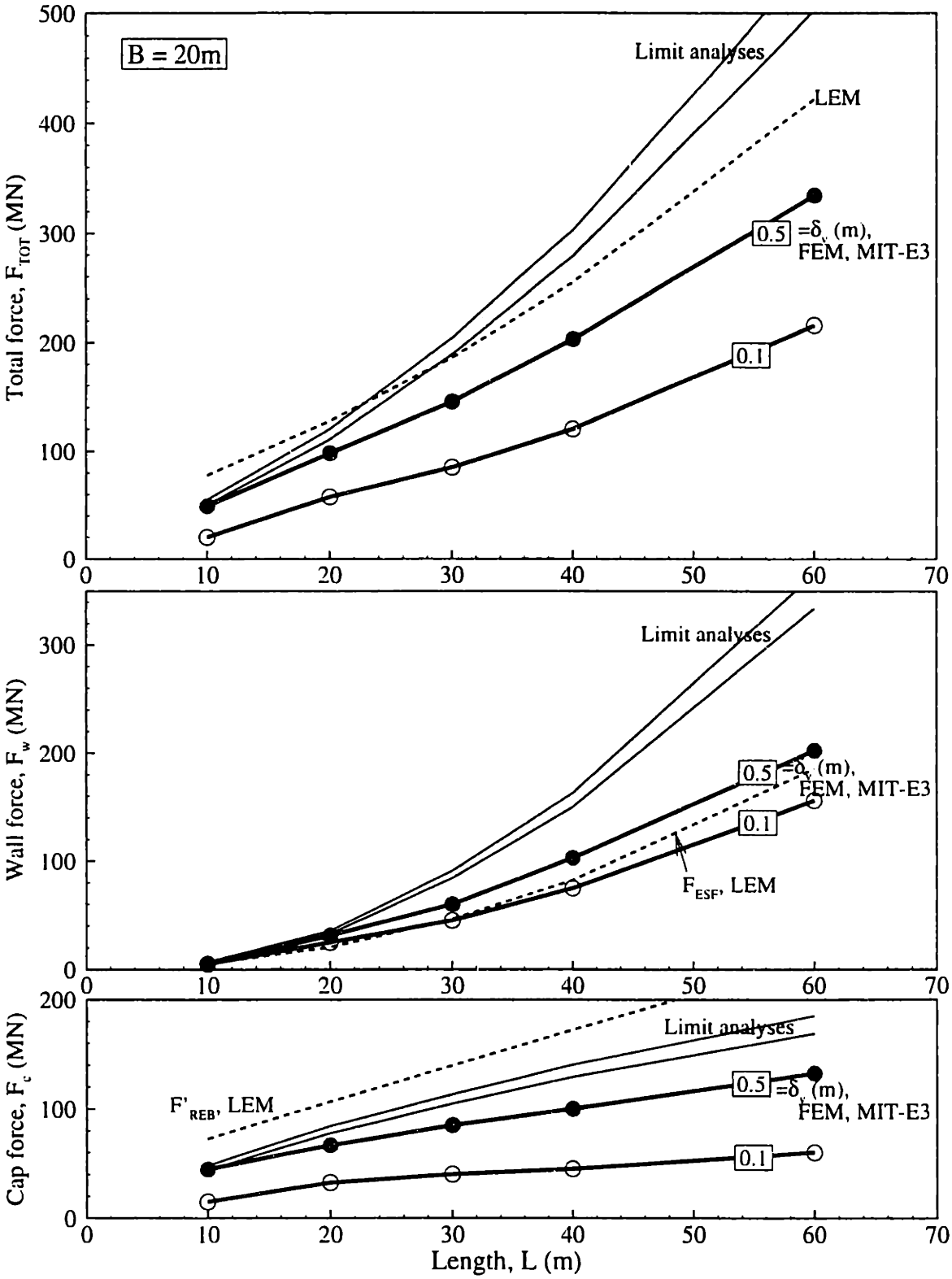

Figure 5.22 Effect of wall length on mobilization of total, wall and cap forces

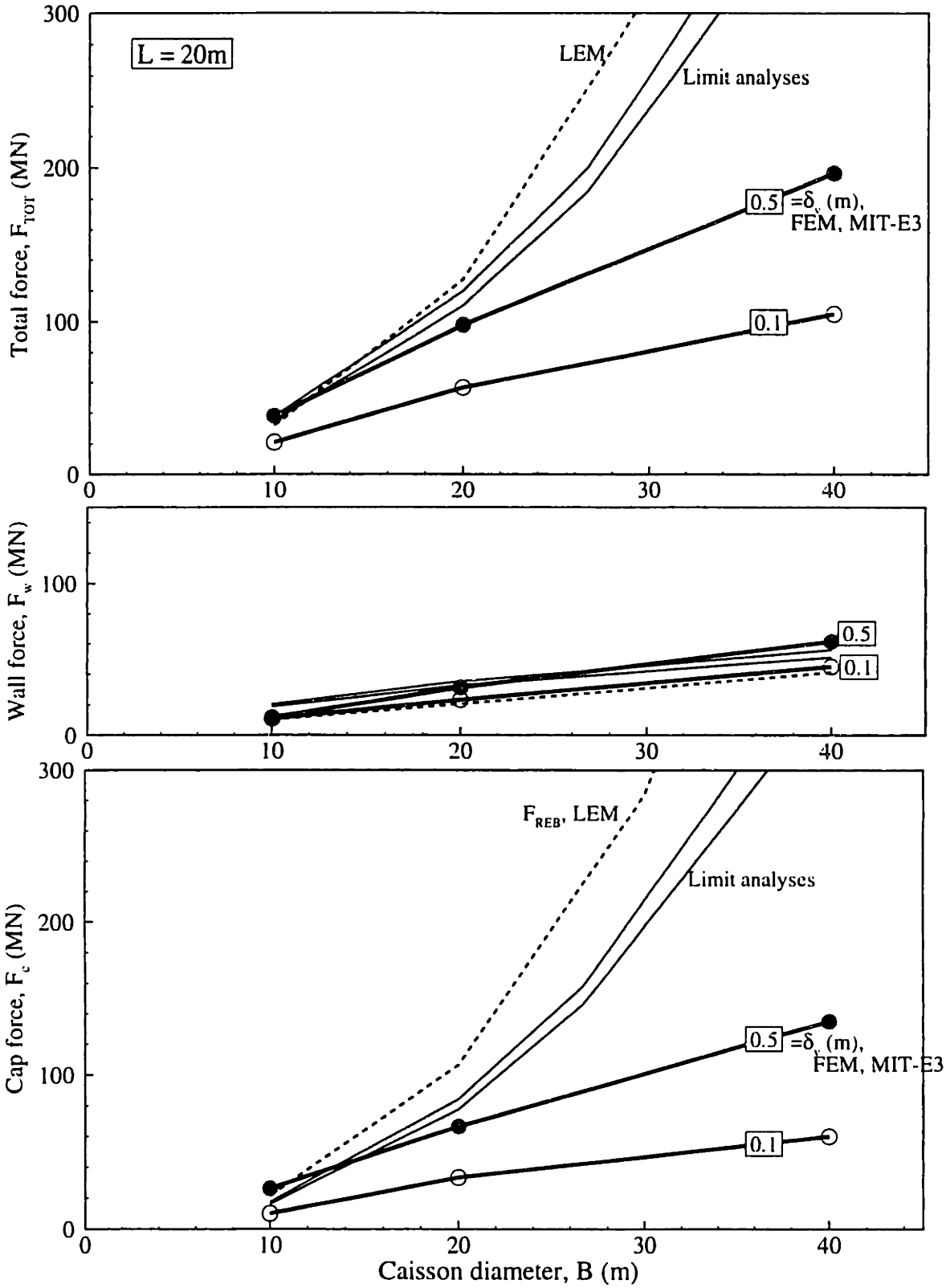

Figure 5.23 Effect of caisson diameter on mobilization of total, wall and cap forces

I.D. #	Instrument	Radial Location (cm) from centerline
CP	Cap Pore Pressure	0.00
AP	Chamber Air Pressure	(cover plate)
P1	Pore Pressure Probe	0.00
P2	" " "	1.78
P3	" " "	3.18
P4	" " "	4.45
S1	Surface Displacement	4.2
S2	" "	5.2
S3	" "	7.7
S4	" "	9.8
S5	" "	12.1
σ_H	Total Stress	(chamber sidewall)

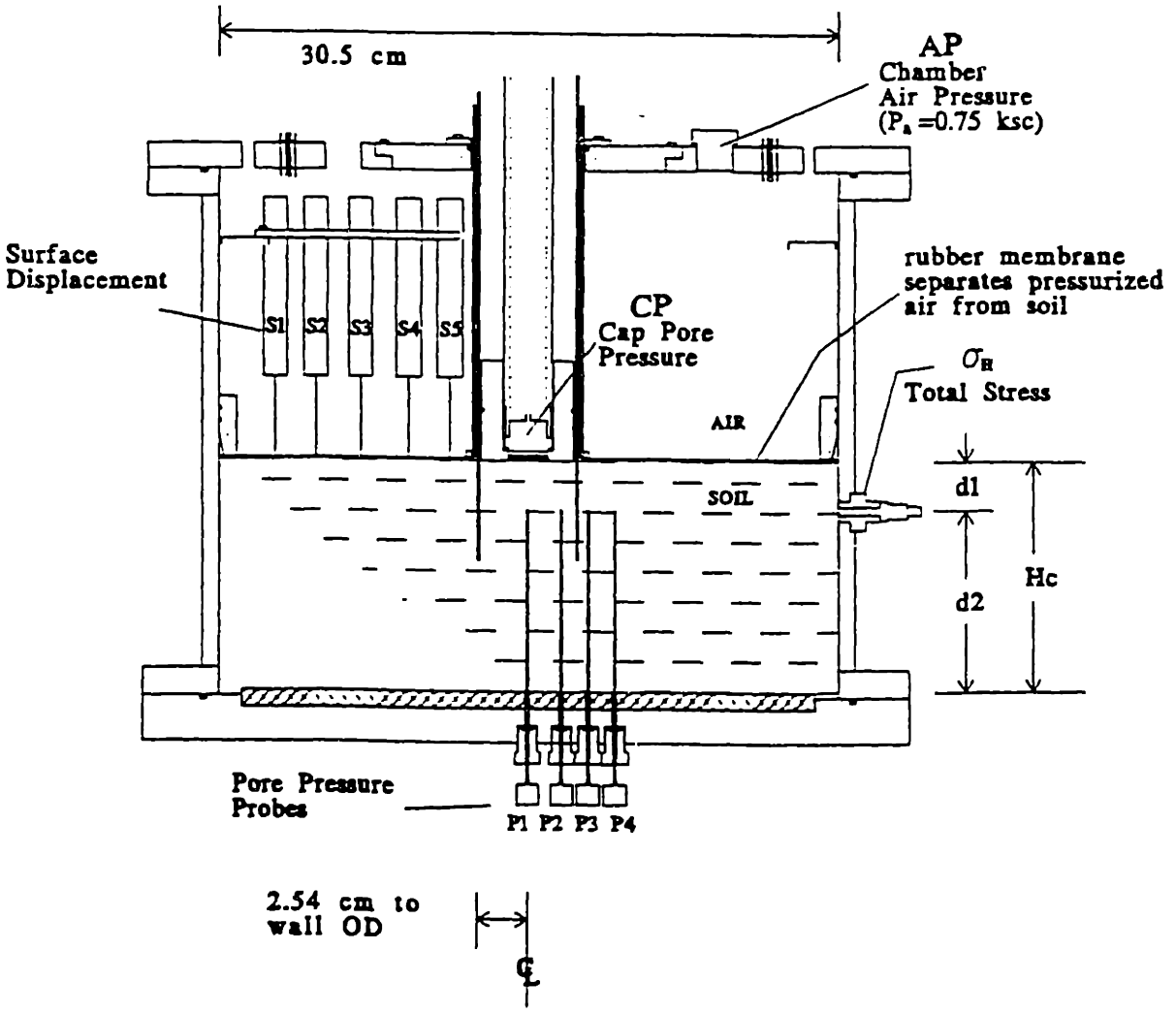

Figure 5.24 Geometry and instrumentation for the CET model caisson experiments (after Cauble, 1996)

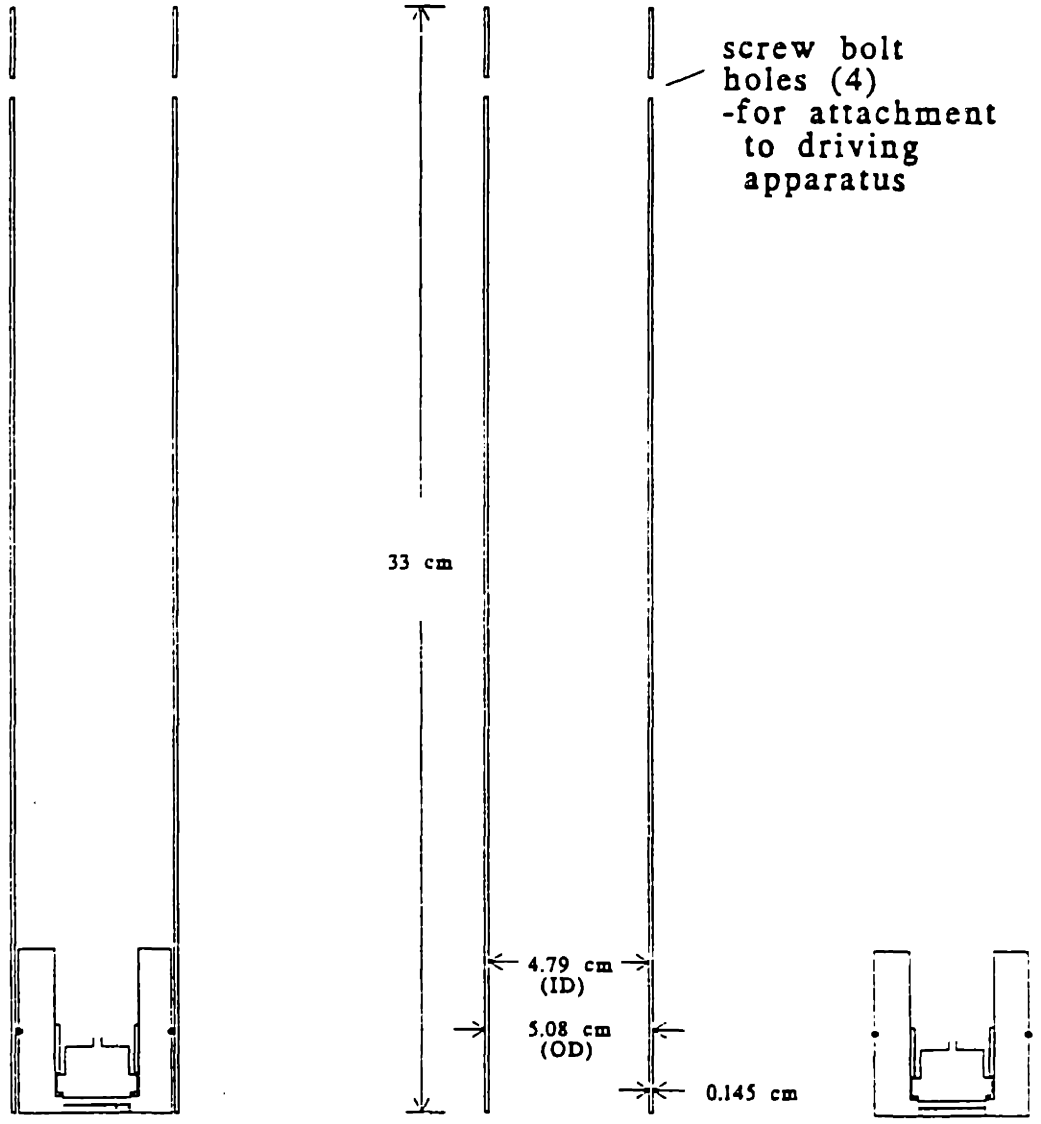

Area of cap, $A_c = 16.98\ cm^2$
Total area, $A_{TOT} = 20.27\ cm^2$

Model Caisson Caisson Wall Caisson Cap

Figure 5.25 Cross sectional side views of wall and cap components for the CET model caisson: (after Cauble, 1996)

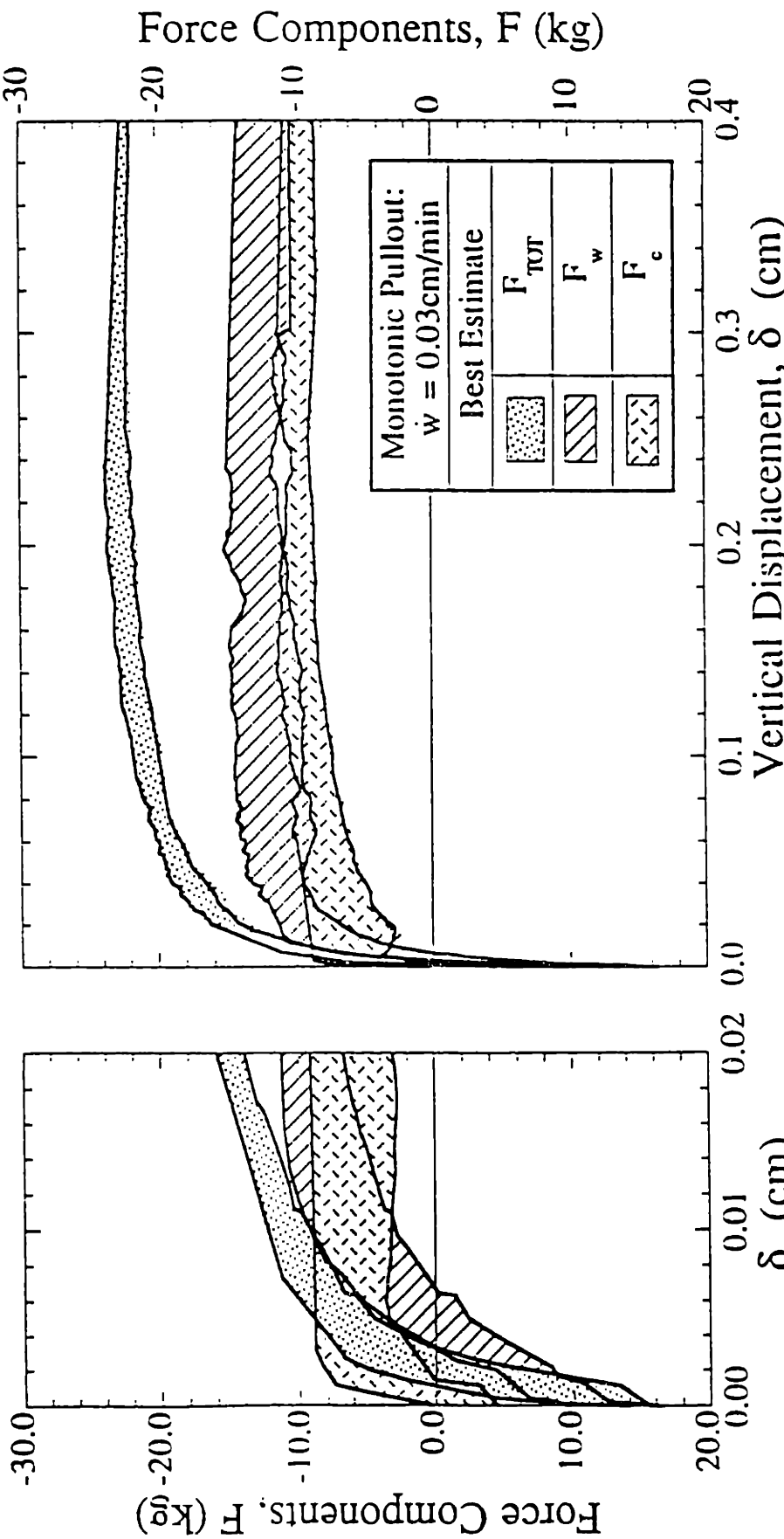

Figure 5.26 Best estimate of force-displacement response in first time axial pullout tests for the CET model caisson (after Cauble, 1996)

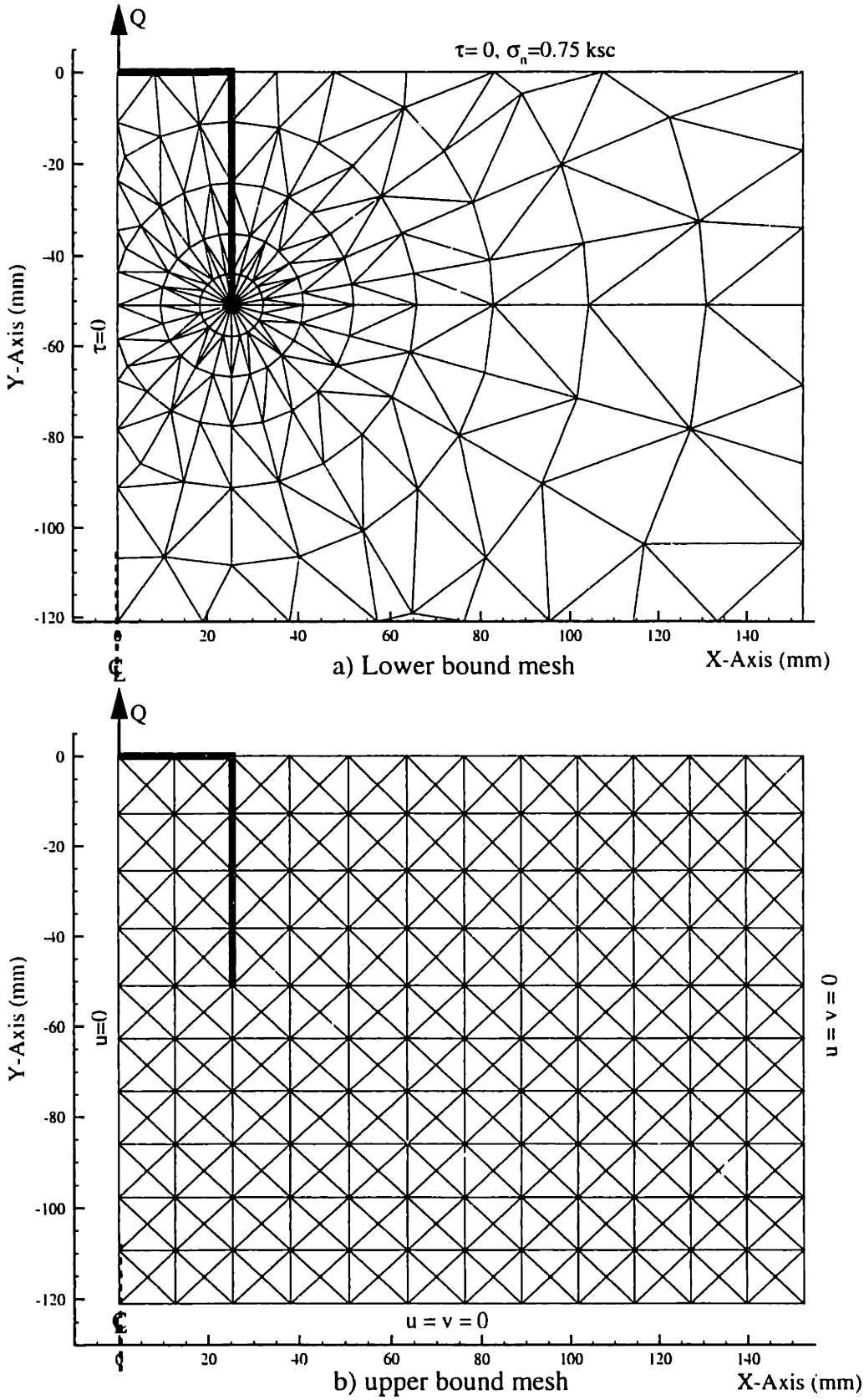

Figure 5.27 Spatial discretization of CET cell for numerical limit analyses

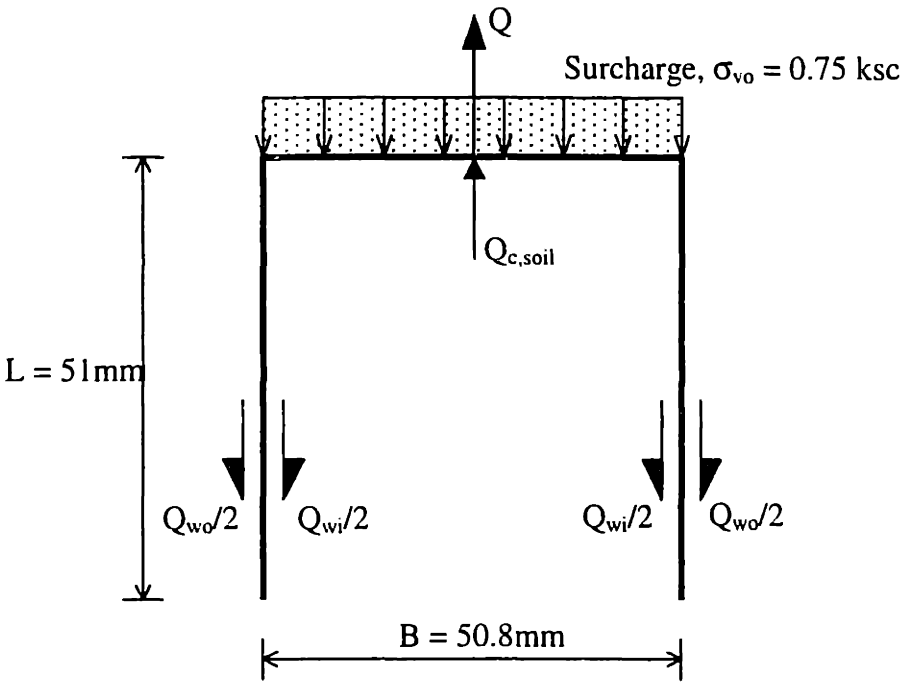

Solutions of Planar Limit Analyses
Upper bound: Q_U = 0.70 kg/mm width
Lower Bound: Q_L = 0.64 kg/mm width
Bound = 8.9%

Components of forces from lower bound analysis
Cap forces Surcharge, $Q_s = (\sigma_{vo})(B)$ = 0.381 kg/mm Soil, $Q_{c,soil}$ = 0.02 kg/mm Net cap force, Q_c = 0.361 kg/mm
Wall forces Inside wall, Q_{wi} = 0.1462 kg/mm Outside wall, Q_{wo} = 0.1328 kg/mm Net wall force, Q_w = 0.279 kg/mm
Total forces, Q_L = 0.64 kg/mm

Figure 5.28 Summary of pullout loads from planar limit analyses for the CET model caisson

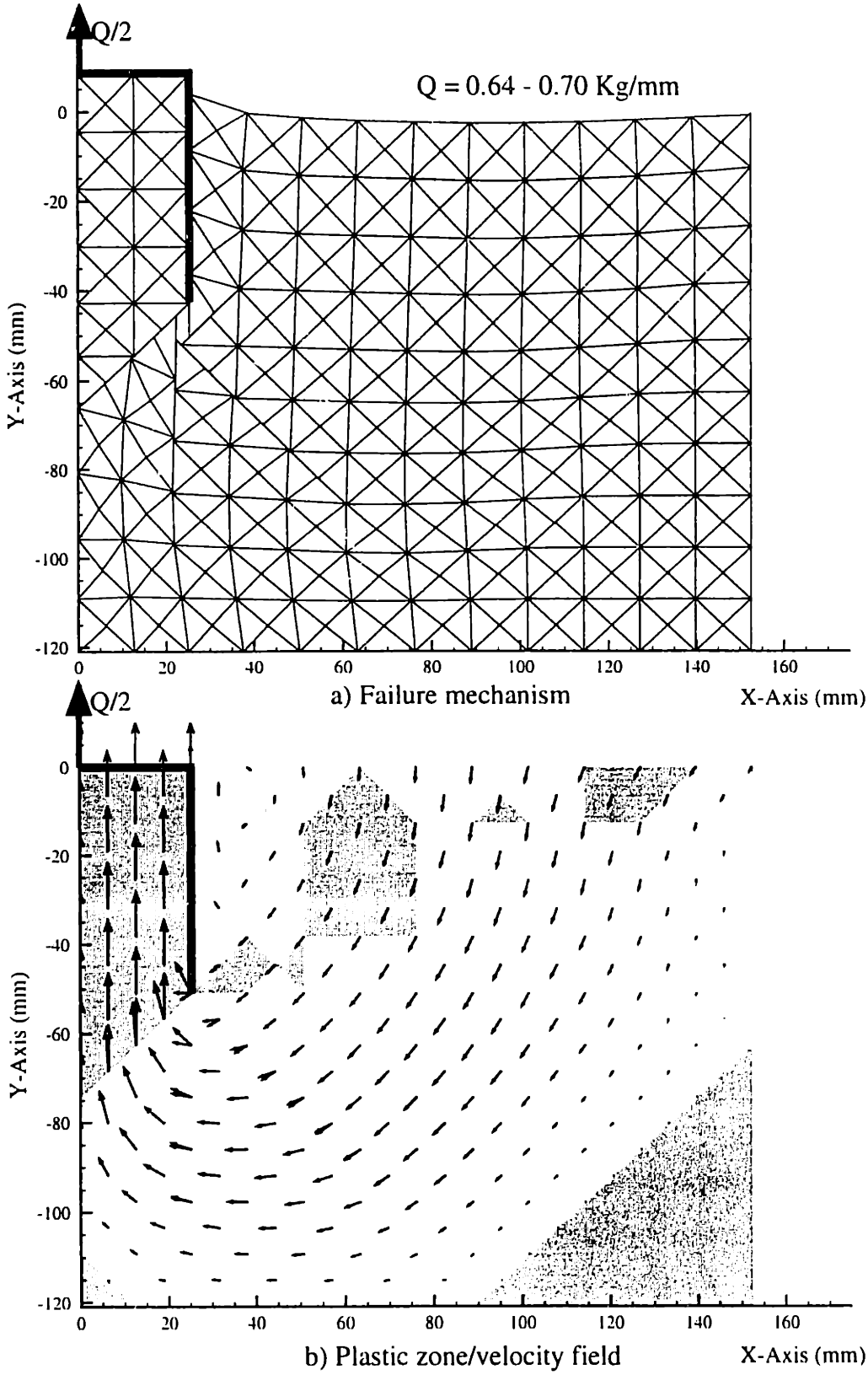

Figure 5.29 Results of upper bound analysis for CET model caisson

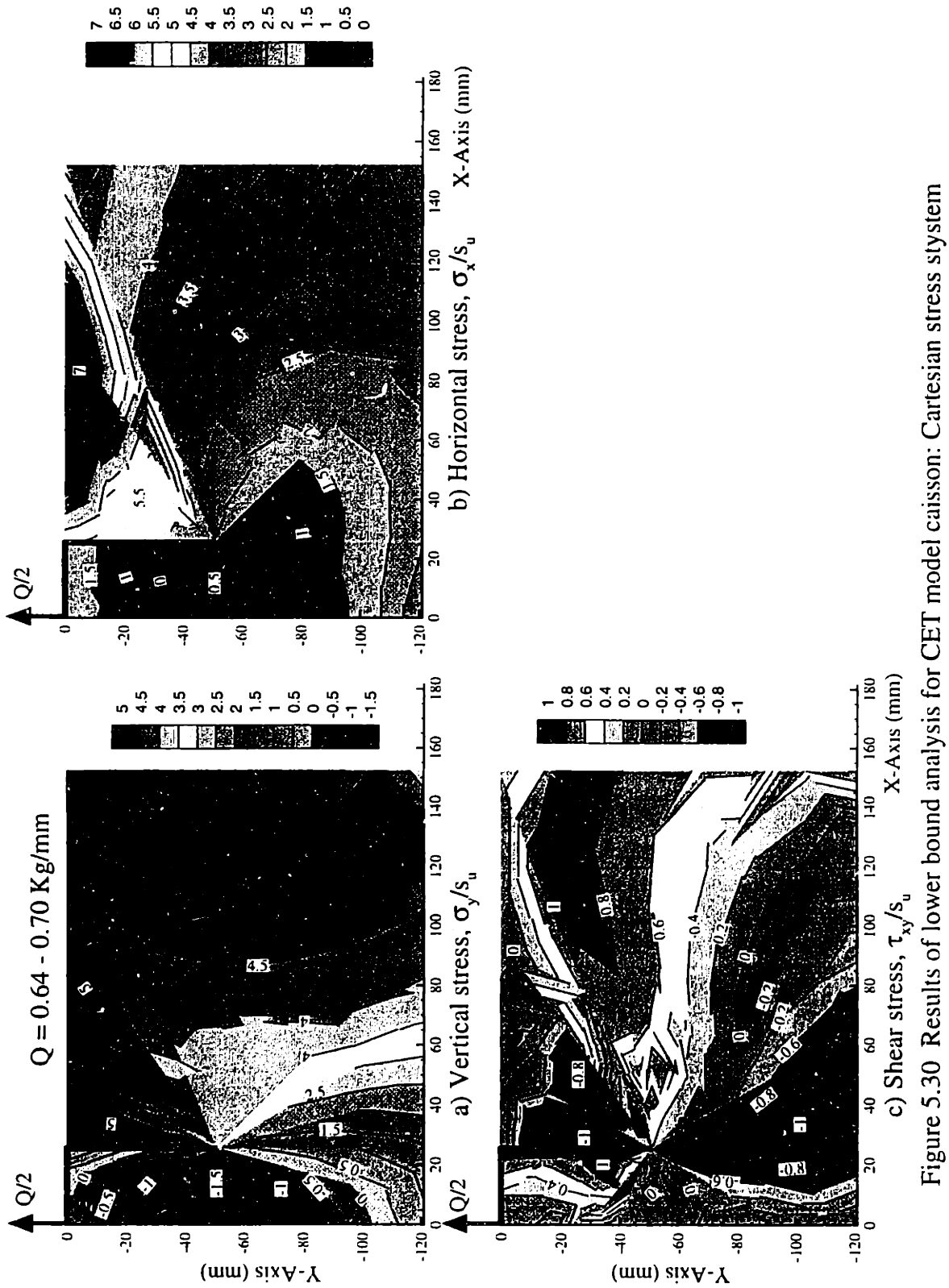

Figure 5.30 Results of lower bound analysis for CET model caisson: Cartesian stress stystem

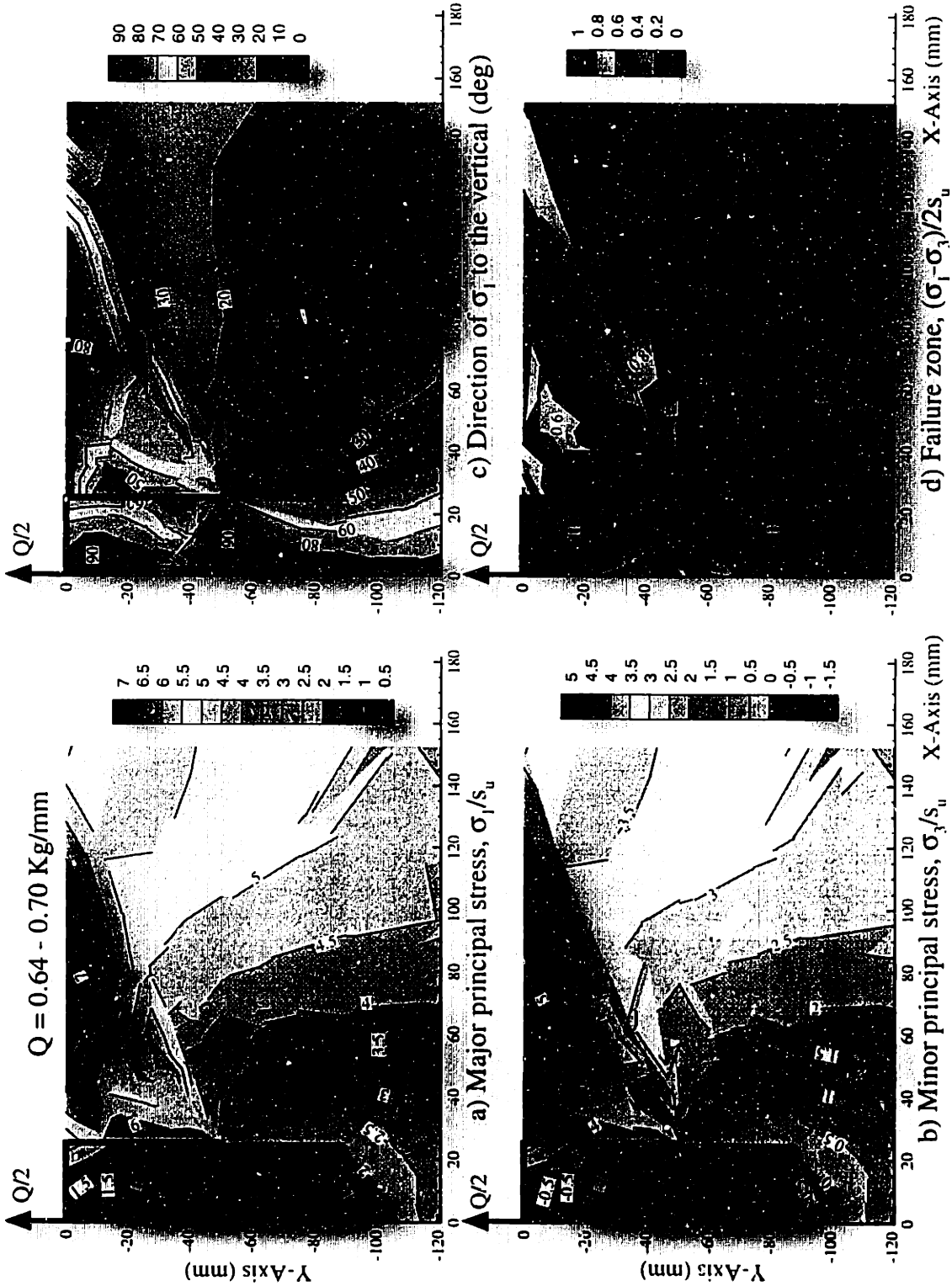

Figure 5.31 Results of lower bound analysis for CET model caisson: Principal stress stystem

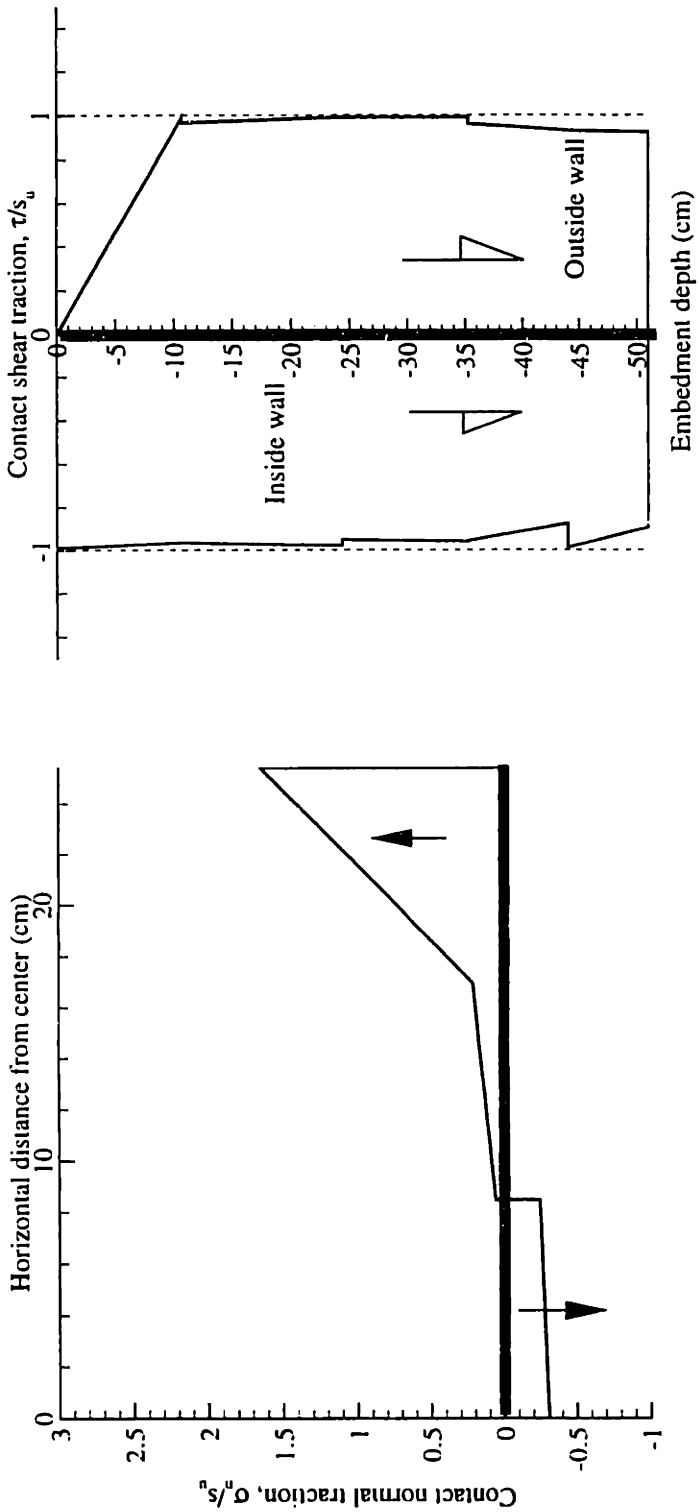

a) Contact normal traction on the cap, σ_n/s_u b) Contact shear tractions on the wall, τ/s_u

Figure 5.32 Contact tractions on the cap and wall from lower bound analyses of CET model caissons

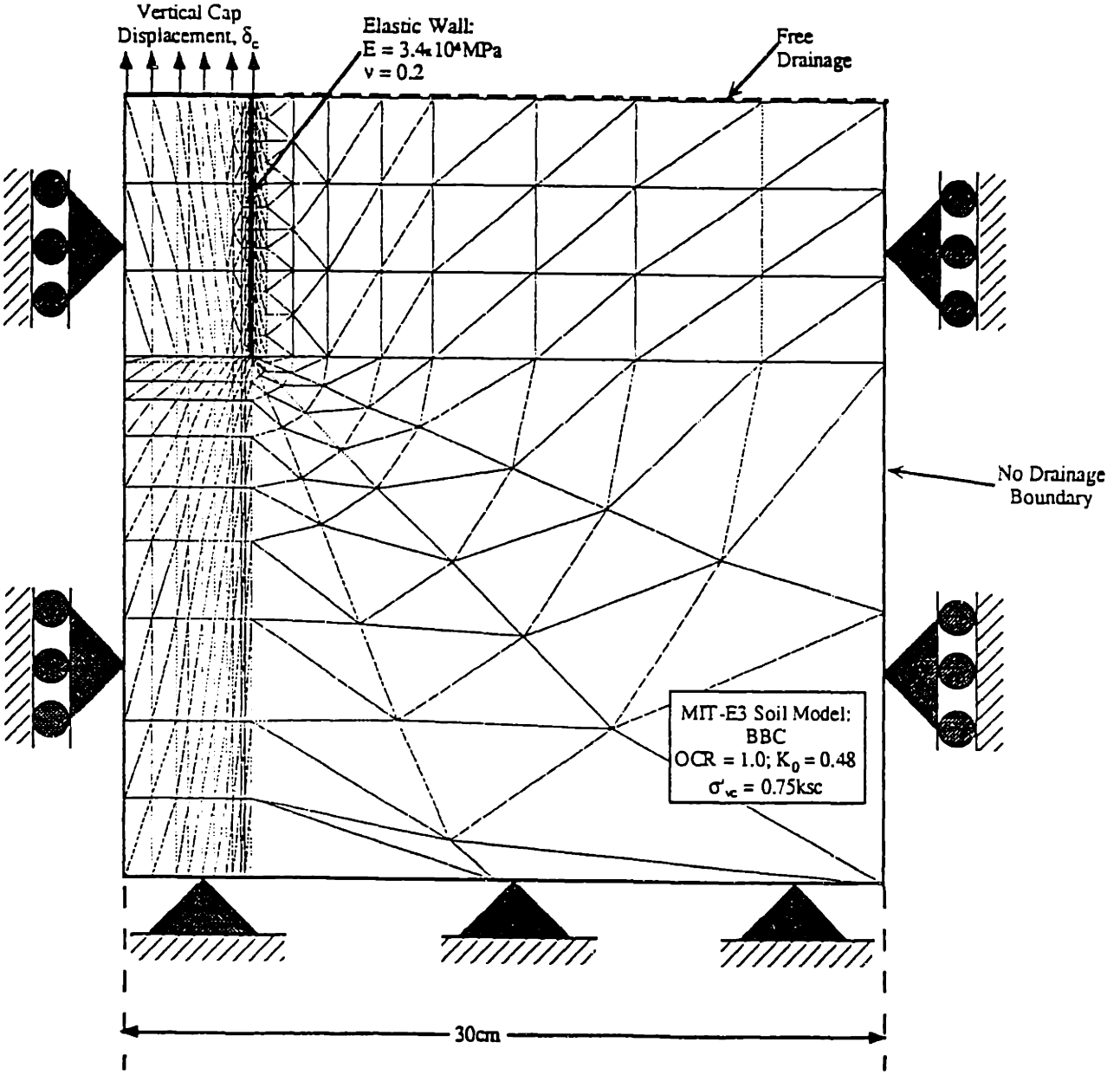

Figure 5.33 Finite element mesh for finite element analysis of CET test (after Whittle et al., 1996)

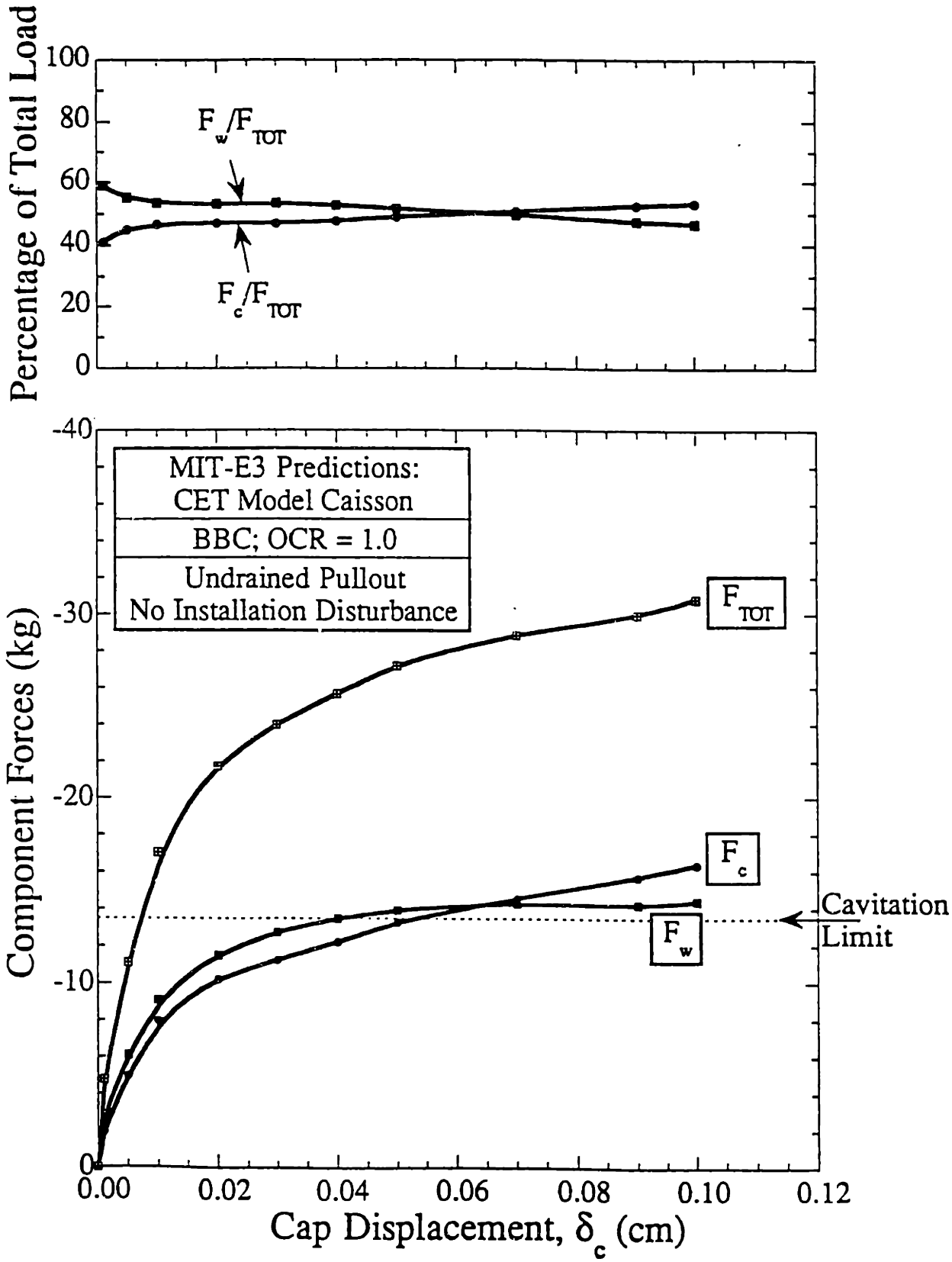

Figure 5.34 Finite element predictions of undrained axial load-deformation response for CET model caisson (after Whittle et al., 1996)

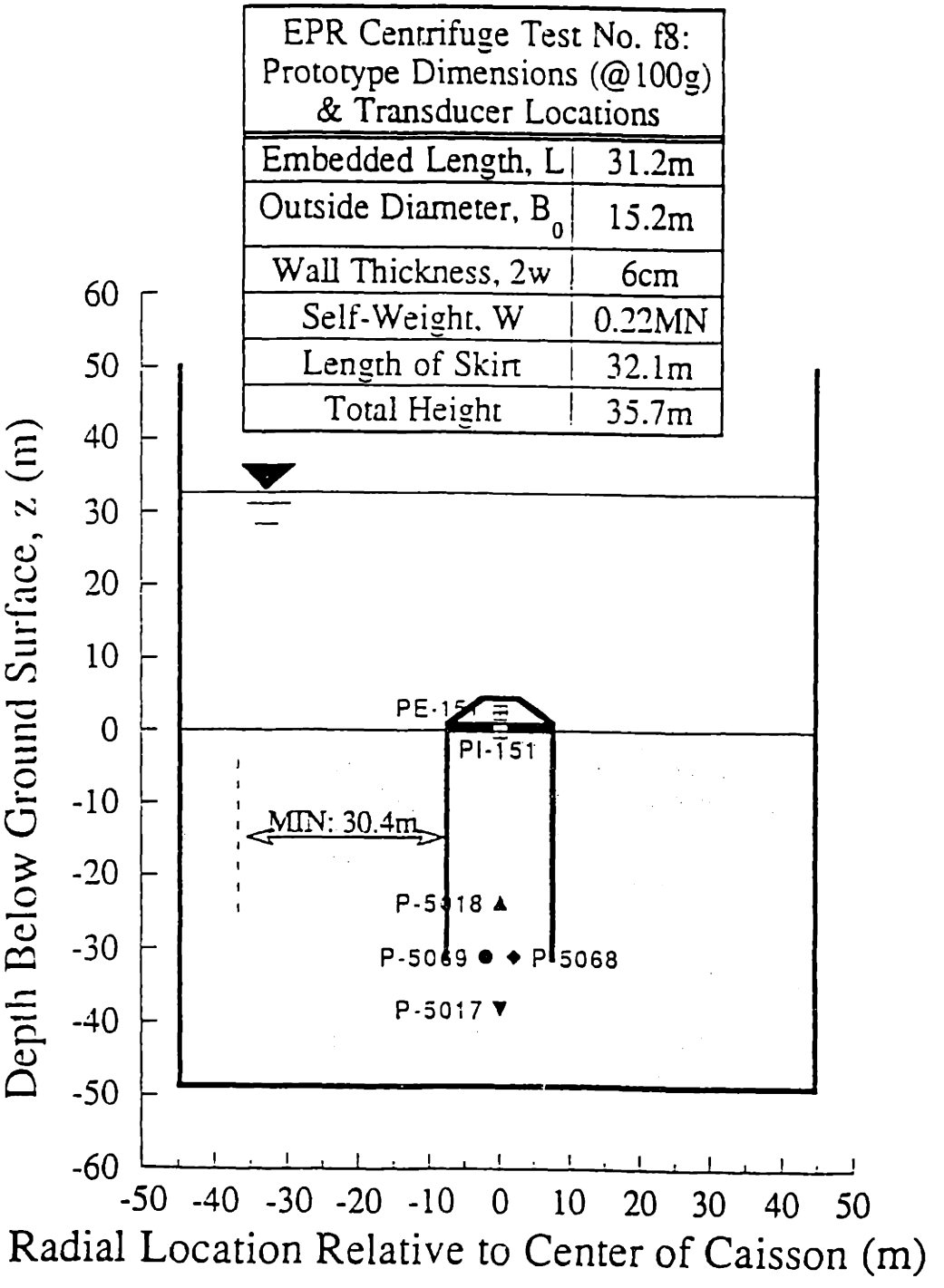

Figure 5.35 Geometry and instrumentation for EPR centrifuge model caisson experiment (after Clukey and Morrison, 1993)

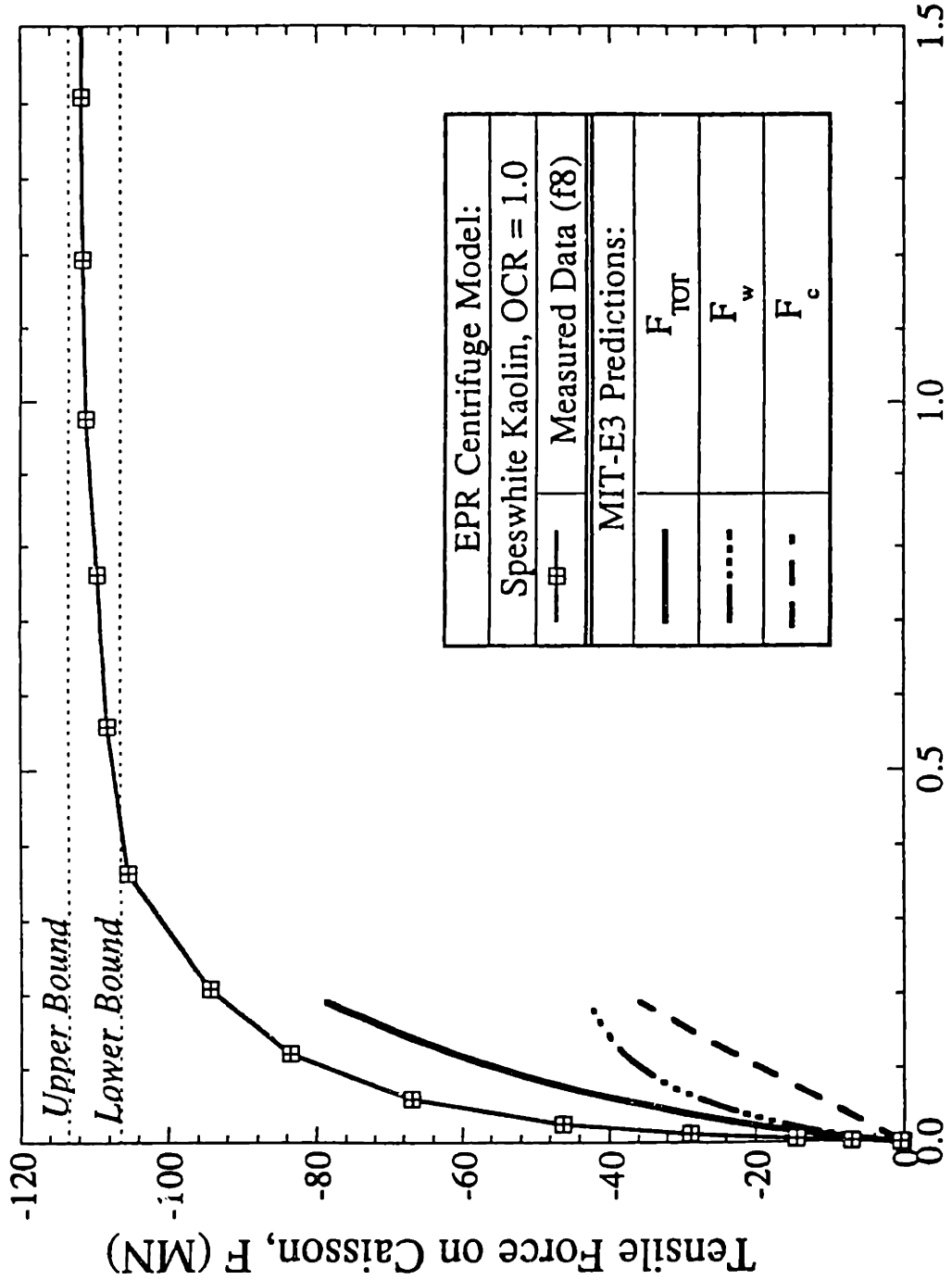

Figure 5.36 Comparisons of predicted and measured behavior for axial pullout of EPR centrifuge model caisson (after Whittle et al., 1996)

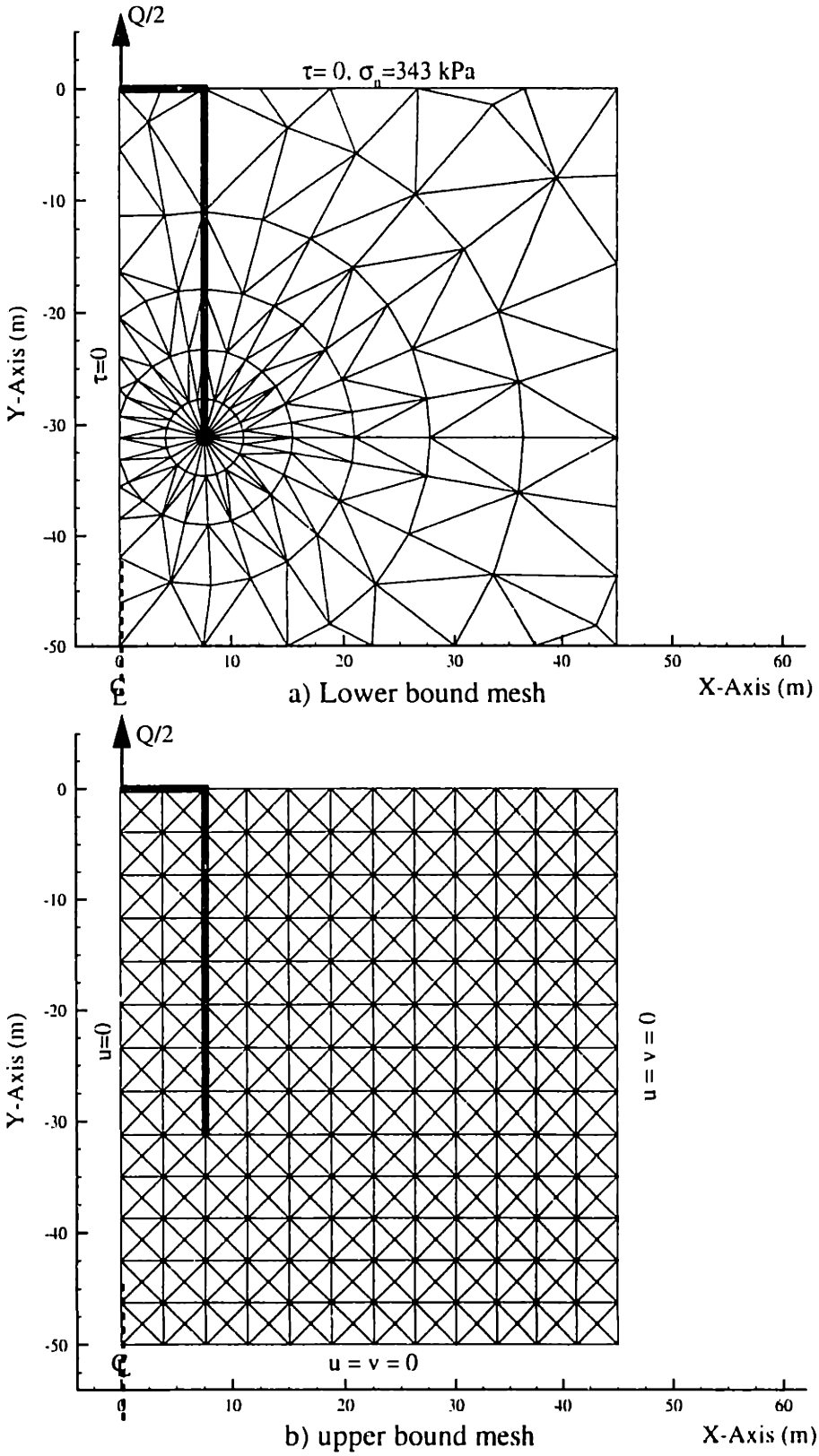

Figure 5.37 Spatial discretization of EPR Centrifuge Model Caisson for numerical limit analyses

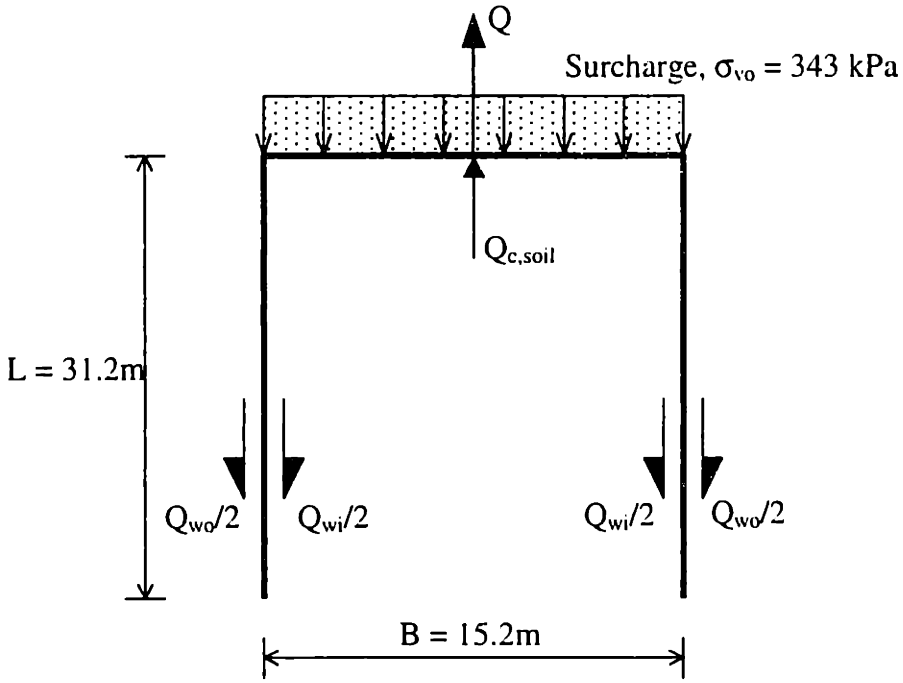

Solutions of Planar Limit Analyses
Upper bound: Q_U = 6.89 MN/m width
Lower Bound: Q_L = 6.44 MN/m width
Bound = 6.7%

Components of forces from lower bound analysis
Cap forces Surcharge, $Q_s = (\sigma_{vo})(B)$ = 5.22 MN/m Soil, $Q_{c,soil}$ = 1.25 MN/m Net cap force, Q_c = 3.97 MN/m
Wall forces Inside wall, Q_{wi} = 1.22 MN/m Outside wall, Q_{wo} = 1.25 MN/m Net wall force, Q_w = 2.47 MN/m
Total forces, Q_L = 6.44 MN/m

Figure 5.38 Summary of pullout loads from planar limit analyses for the EPR model caisson

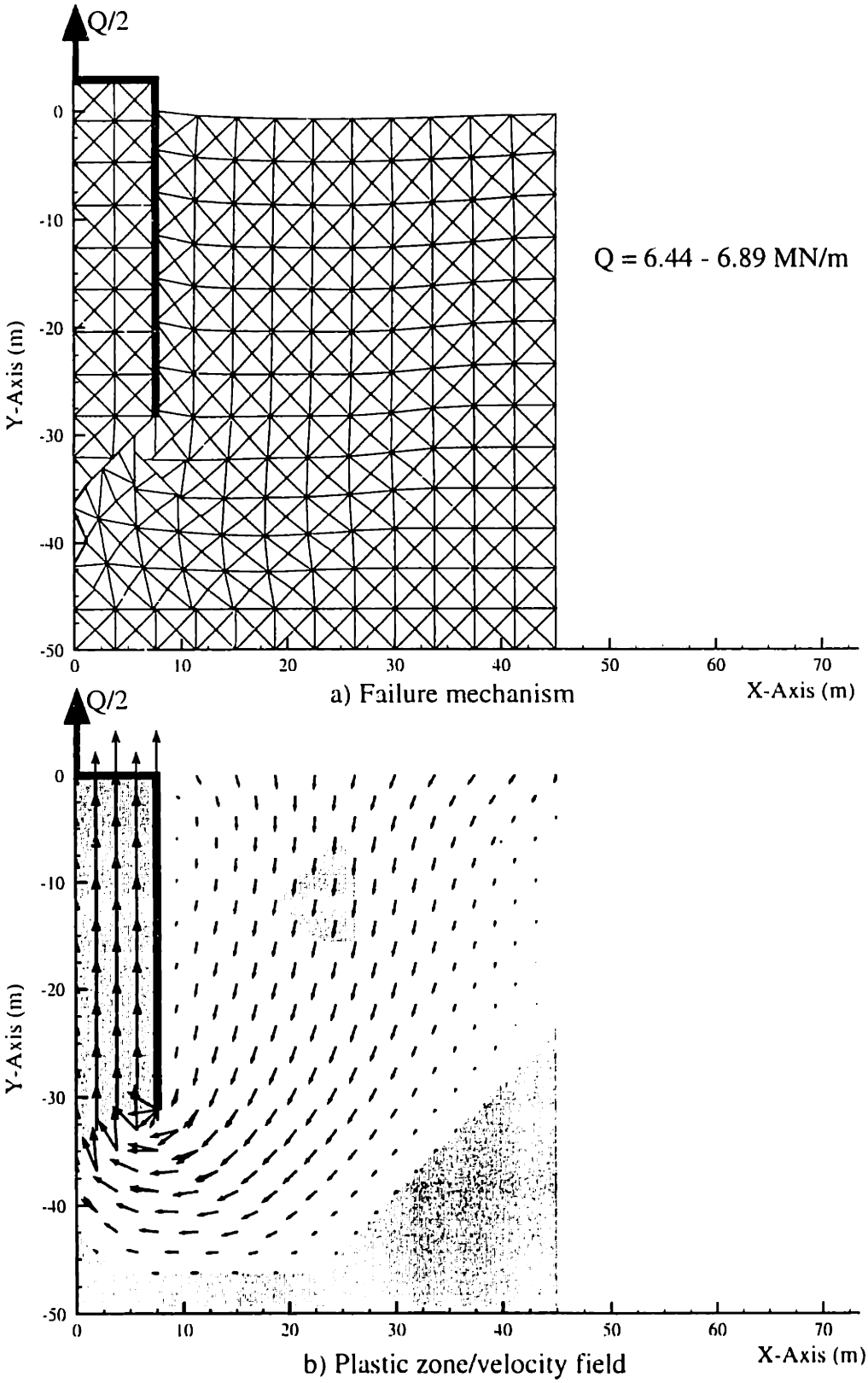

Figure 5.39 Upper bound limit analysis for axial pullout of EPR centrifuge caisson model

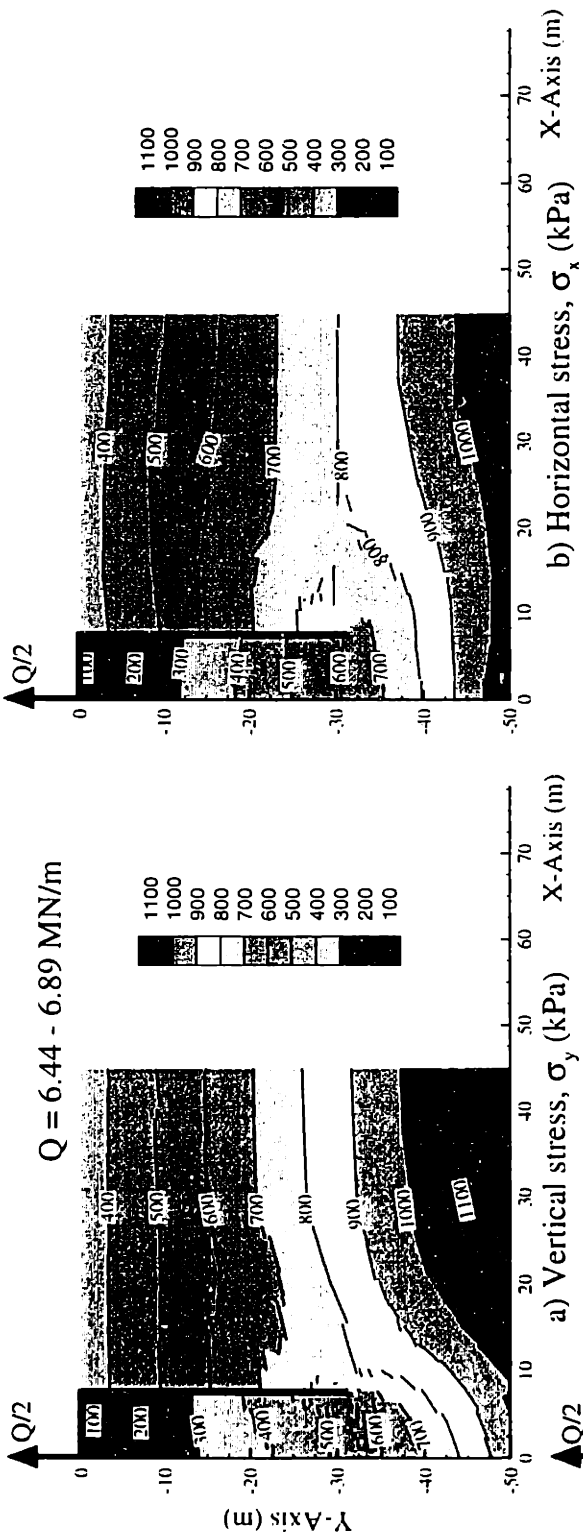

Figure 5.40 Lower bound limit analysis for EPR centrifuge model caisson: Cartesian stress system

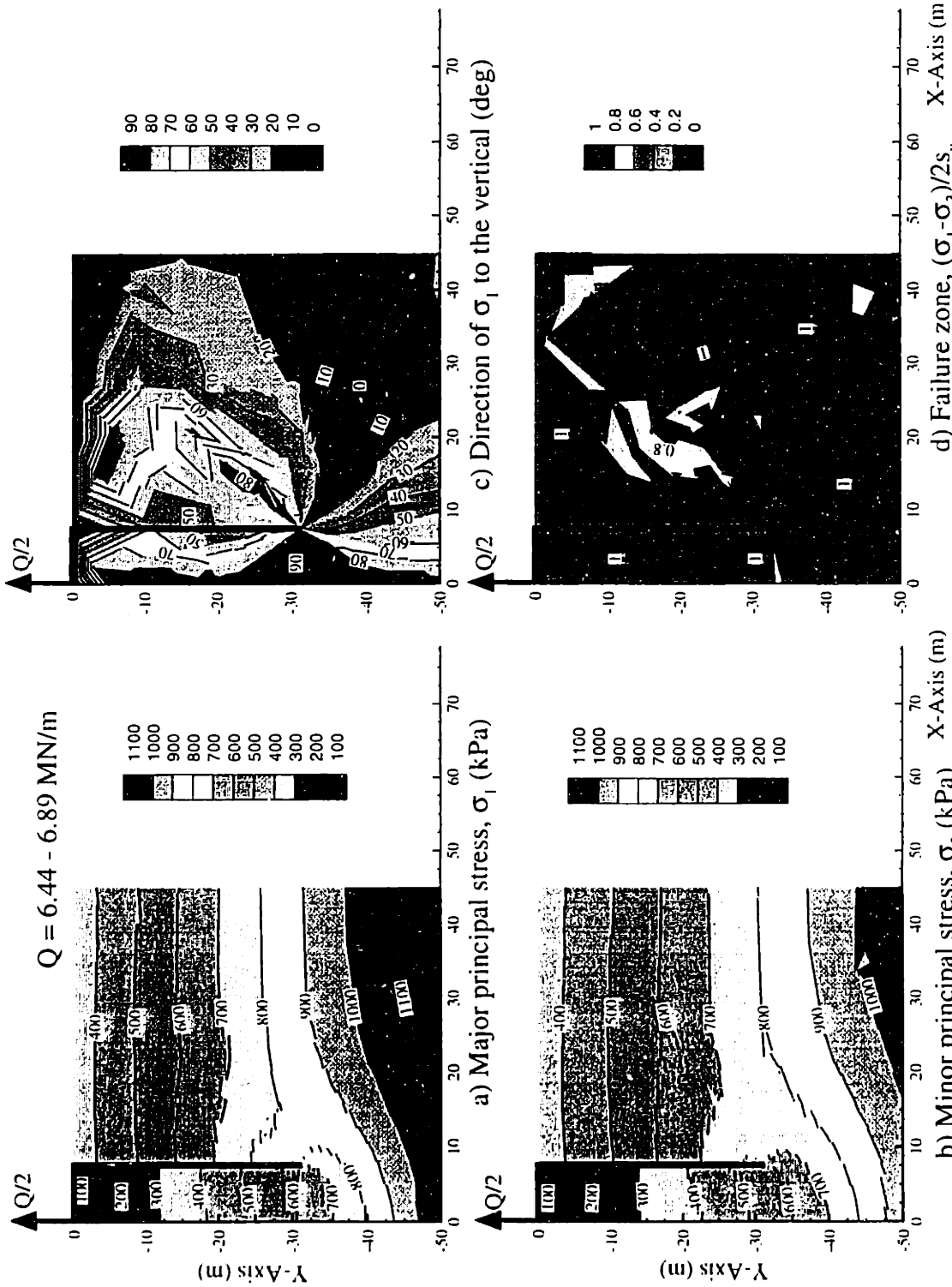

Figure 5.41 Lower bound limit analysis for EPR centrifuge model caisson: Principal stress system

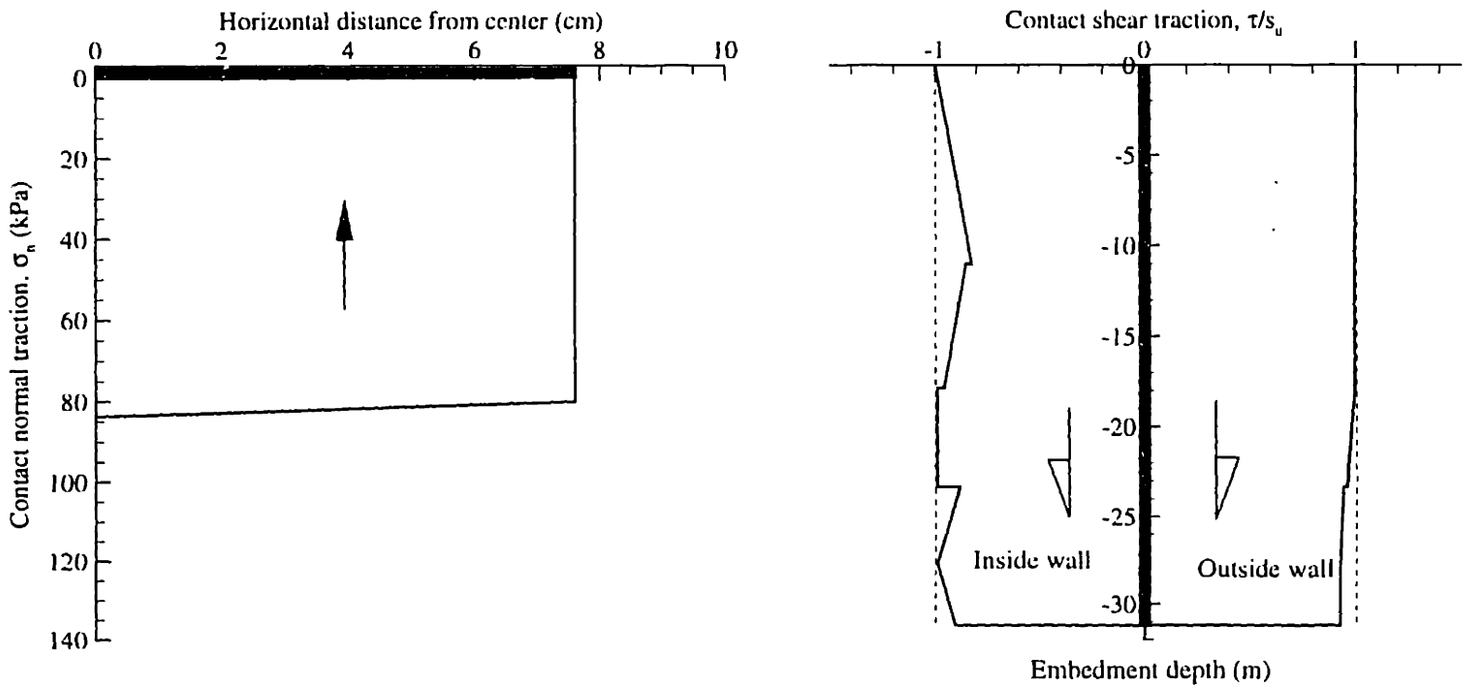

a) Contact normal traction on the cap, σ_n

b) Contact shear tractions on the wall, τ/s_u

Figure 5.42 Contact tractions on the cap and wall from lower bound analyses of axial pullout for EPR centrifuge model caisson

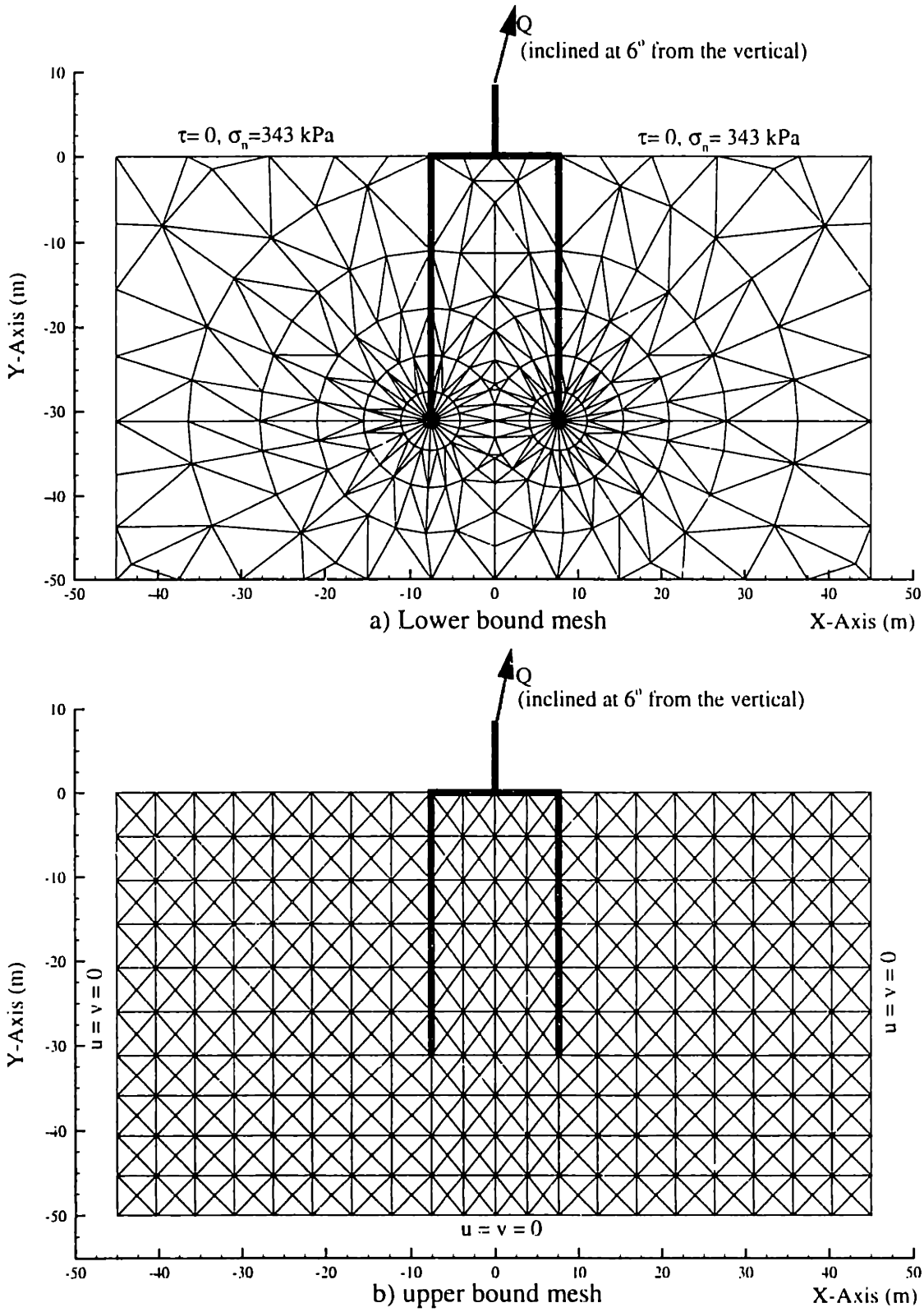

Figure 5.43 Spatial discretization of an inclined pullout of EPR centrifuge model caisson

Planar Limit Analyses

Upper Bound	Q_U = 6056 kN/m
Lower Bound	Q_L = 5387 kN/m
Bound	11.70%

Net Reaction Forces on Caisson (Lower Bound Results)

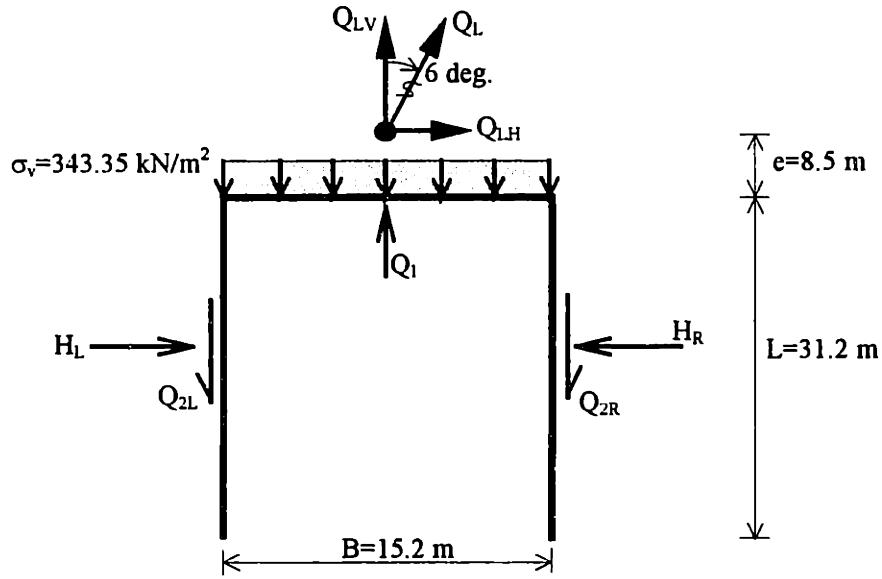

Vertical Components

Q_{LV} =	5357 kN/m
Q_1 =	1888 kN/m
Q_{2L} =	1163 kN/m
Q_{2R} =	864 kN/m
σ_v (B) =	5218 kN/m

Horizontal Components

Q_{LH} =	563 kN/m
H_L =	6250 kN/m
H_R =	6813 kN/m

Figure 5.44 Collapse loads from numerical limit analyses for inclined pullout of EPR centrifuge model caisson

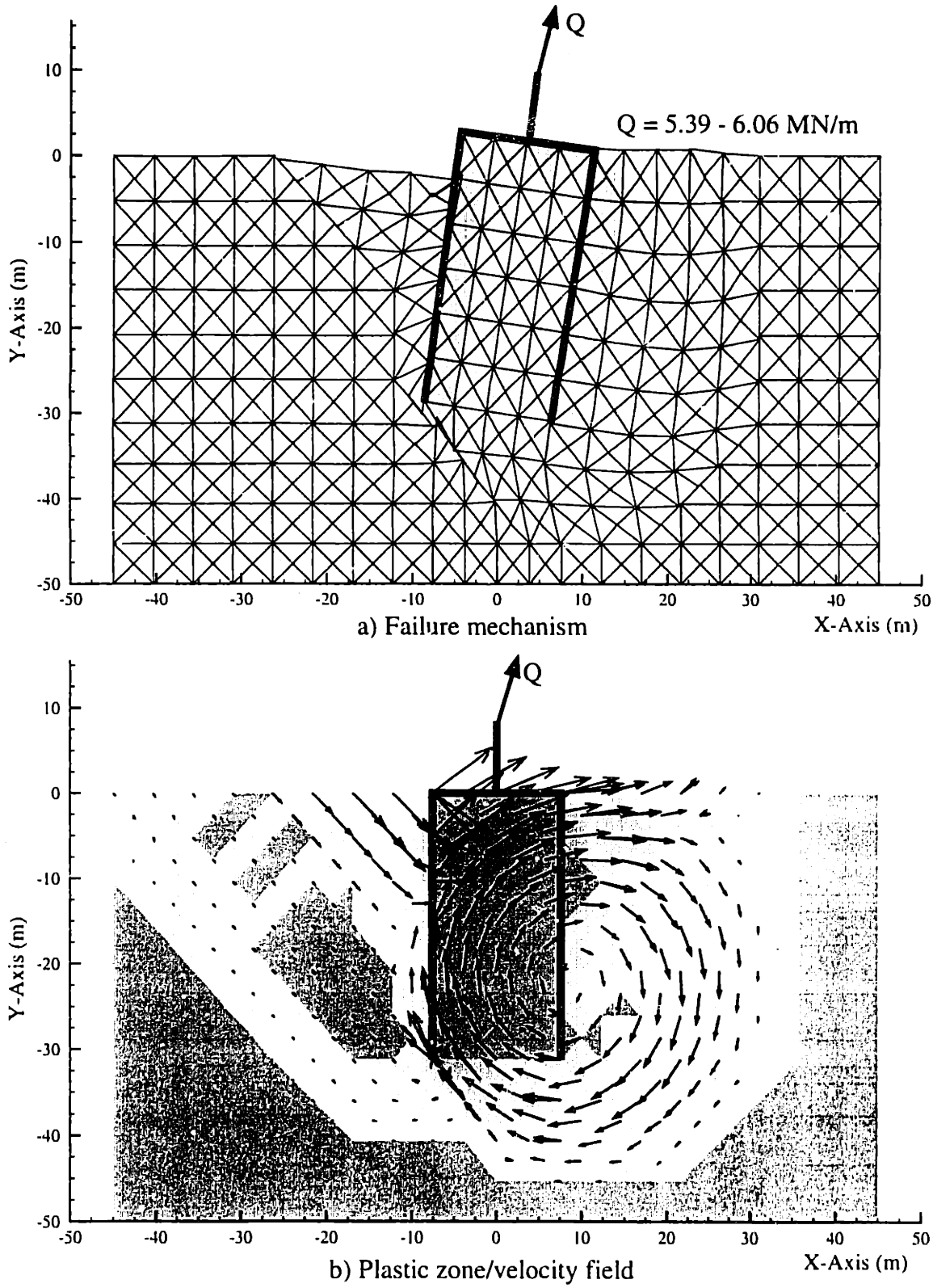

Figure 5.45 Results of upper bound limit analysis for inclined pullout of EPR centrifuge model caisson

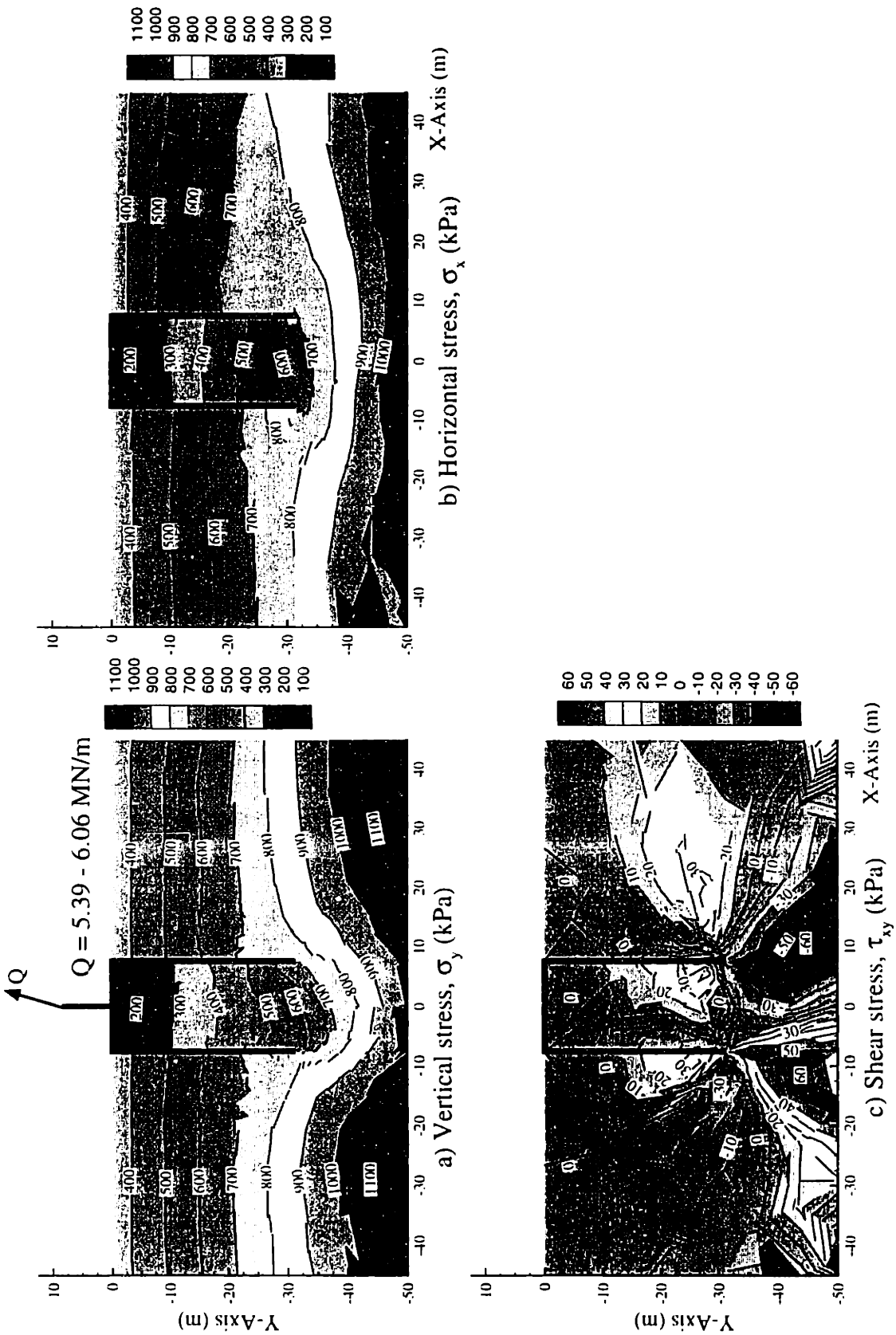

Figure 5.46 Lower bound limit analysis for inclined pullout of EPR centrifuge model caisson: Cartesian stress system

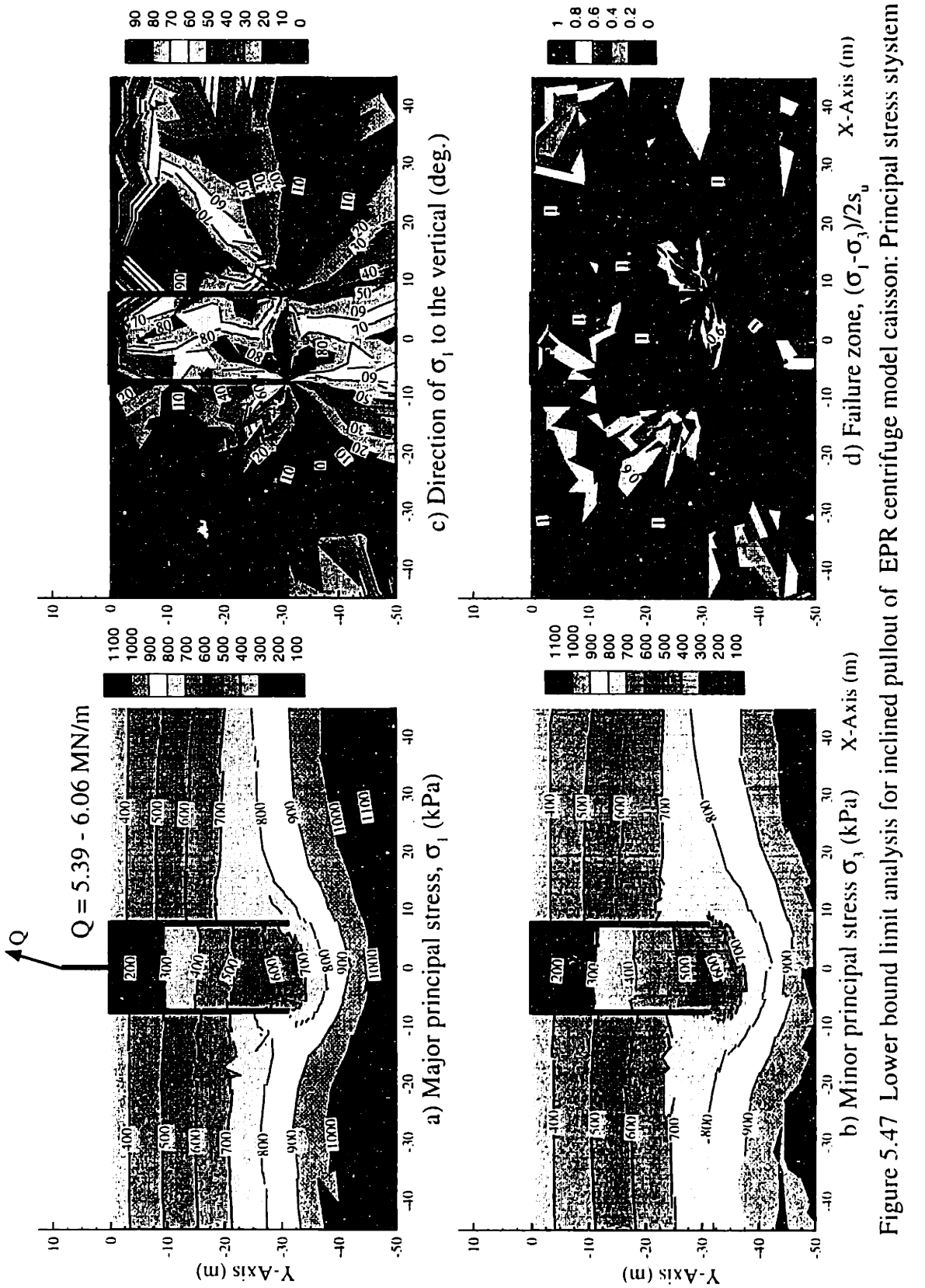

Figure 5.47 Lower bound limit analysis for inclined pullout of EPR centrifuge model caisson: Principal stress system

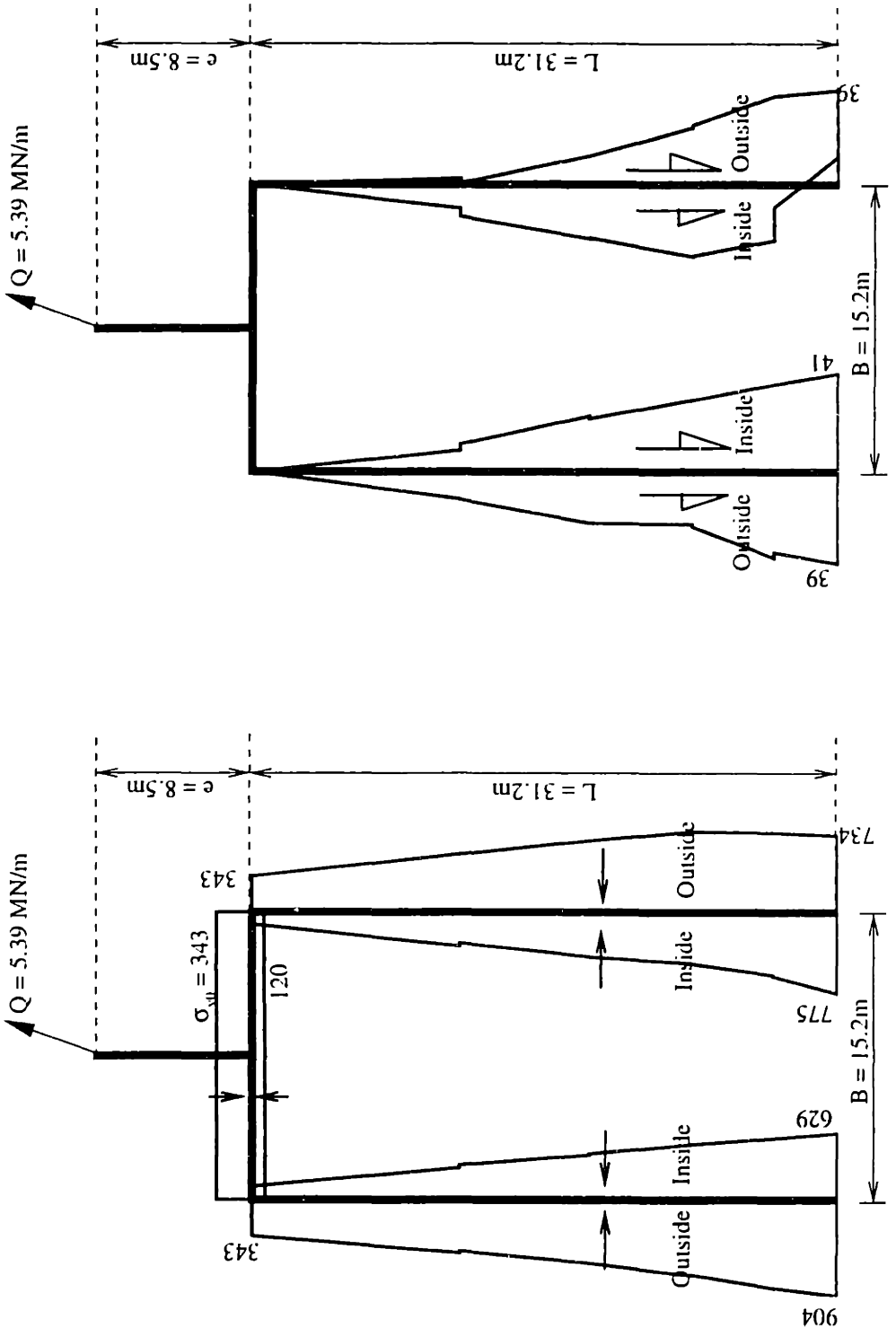

a) Shear traction (kPa)

a) Normal traction (kPa)

Figure 5.48 Contact tractions for inclined pullout of EPR centrifuge model caisson (Lower bound analysis)

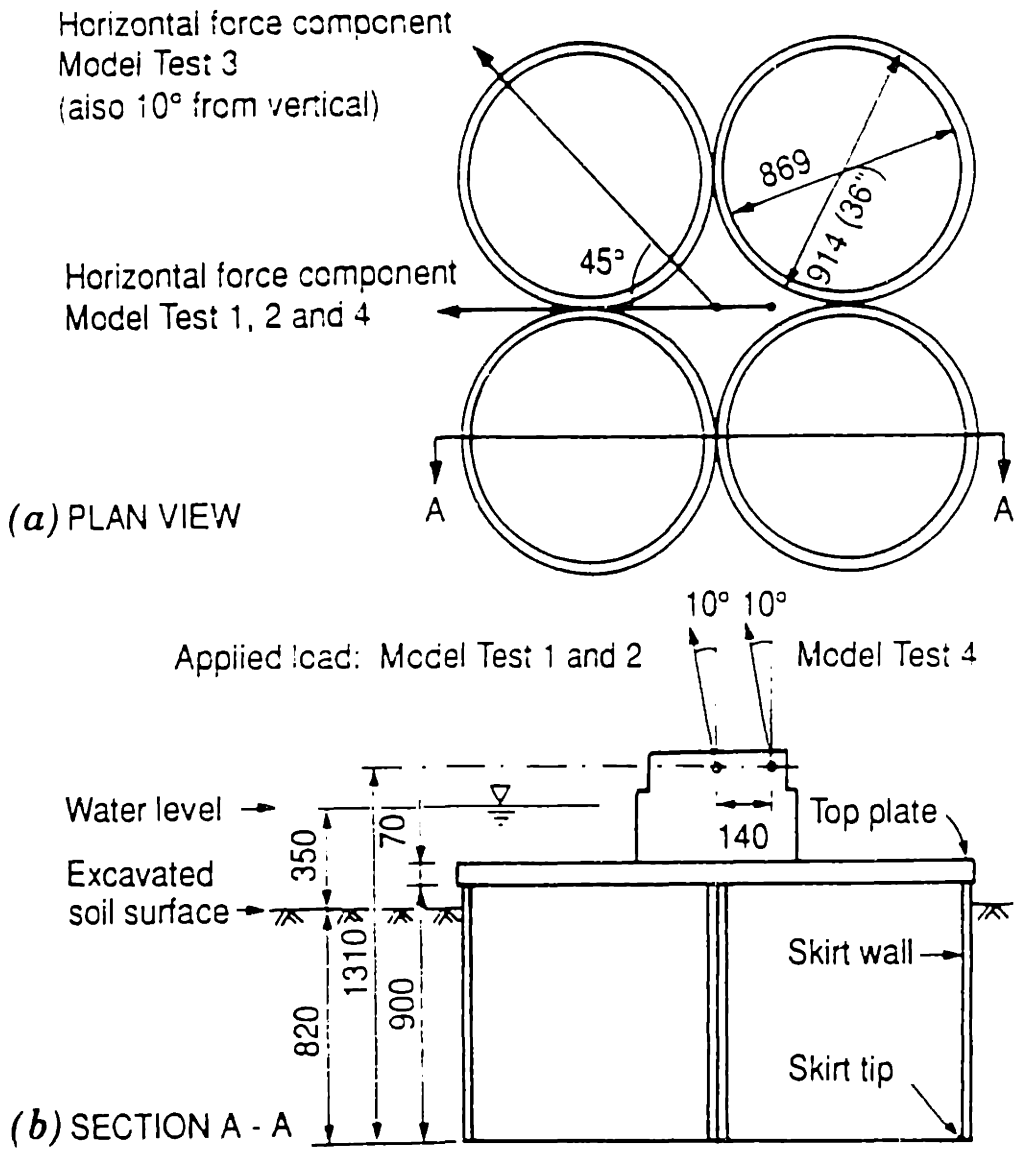

Characteristics of Model Tests

Model test (1)	Test type (2)	Loading point (3)	Load orientation (degrees) (4)
1	Static	Center	0
2	Cyclic	Center	0
3	Cyclic	Center	45
4	Cyclic	Off-center	0

Figure 5.49 NGI four cell caisson model (after Dyvik et al., 1993)

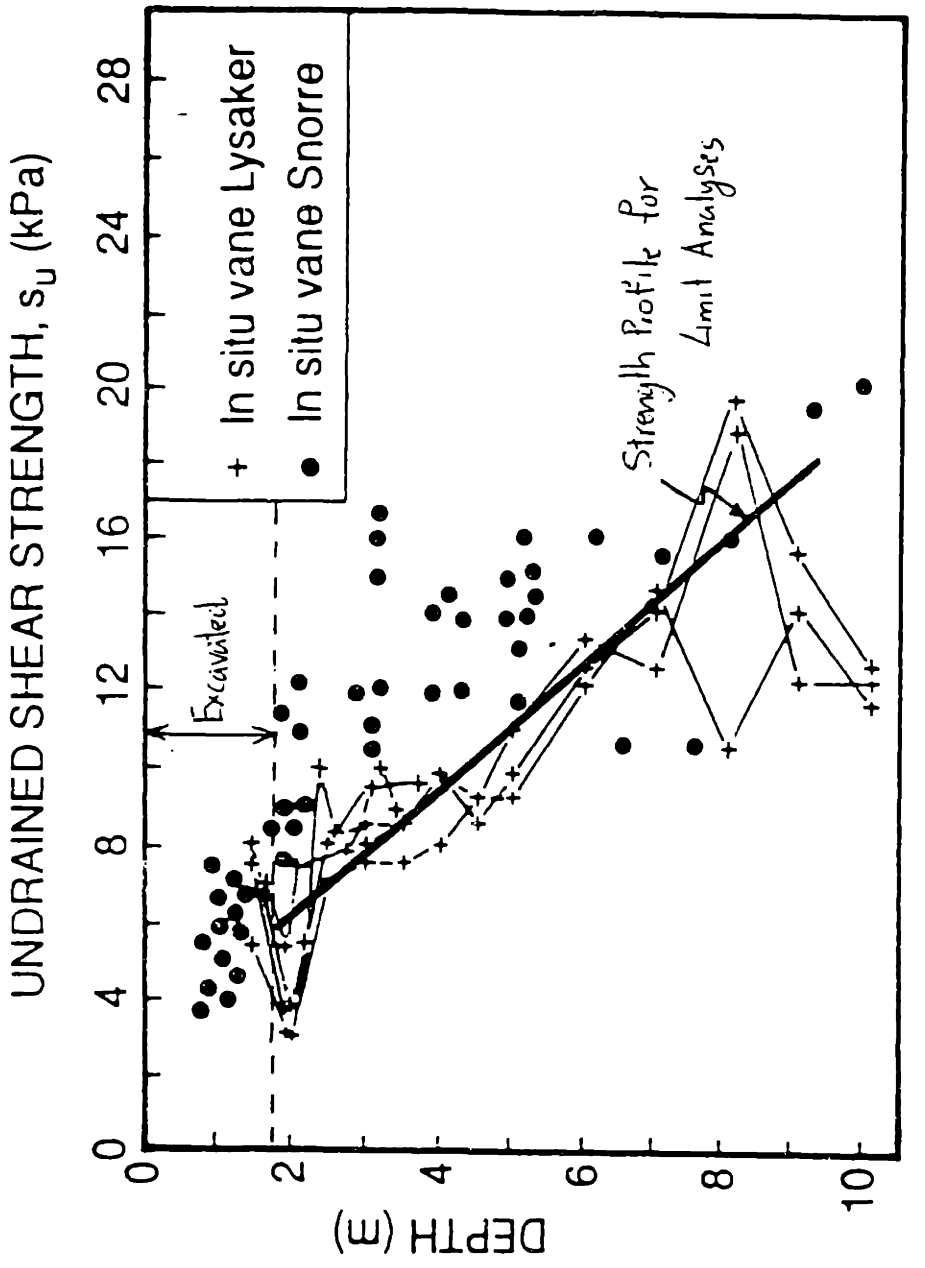

Figure 5.50 In-situ vane shear strength profile for Lysaker and Snorre clays (after Dyvik et al., 1993)

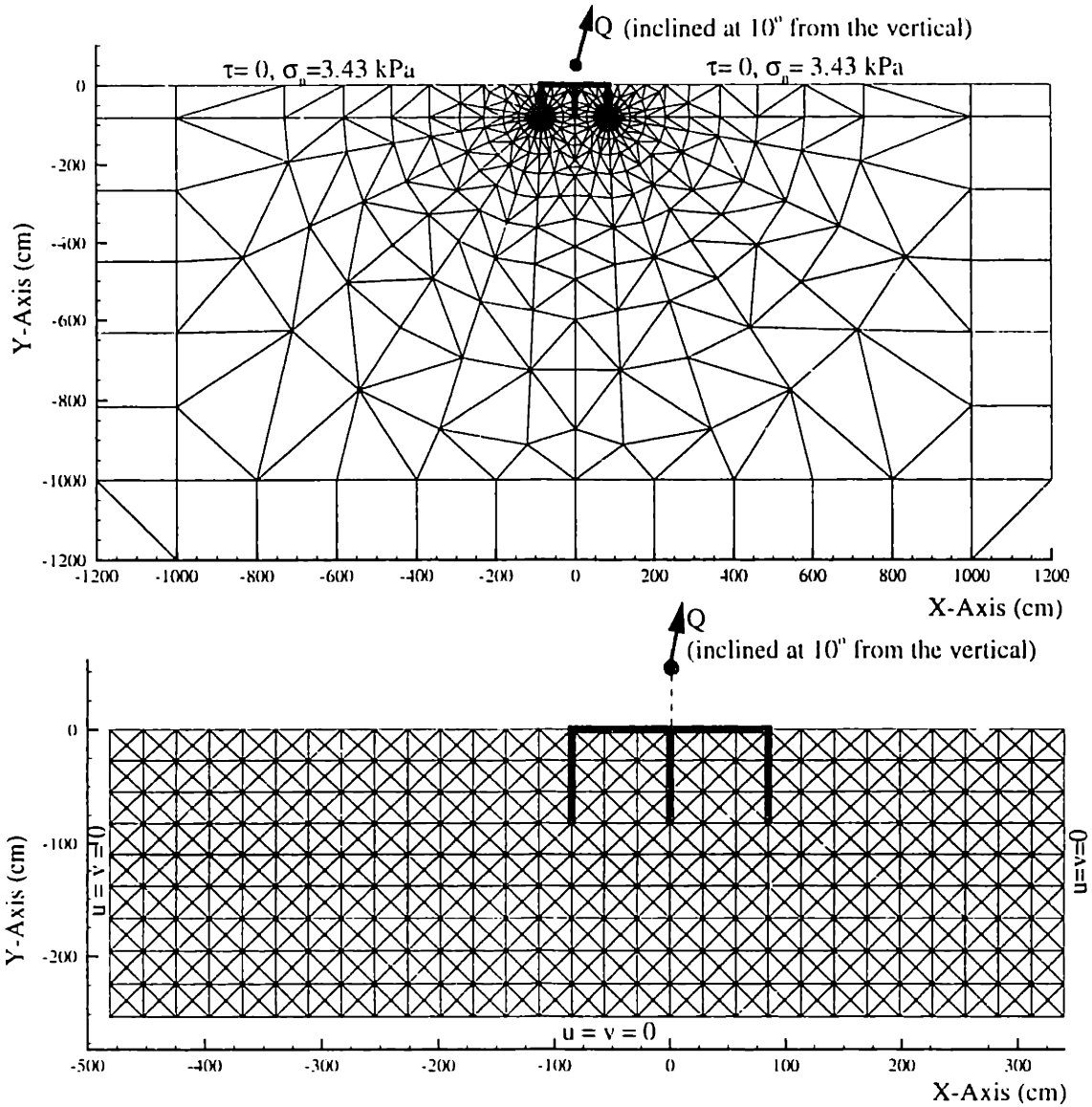

Figure 5.51 Spatial discrtization of NGI model caisson for numerical limit analyses

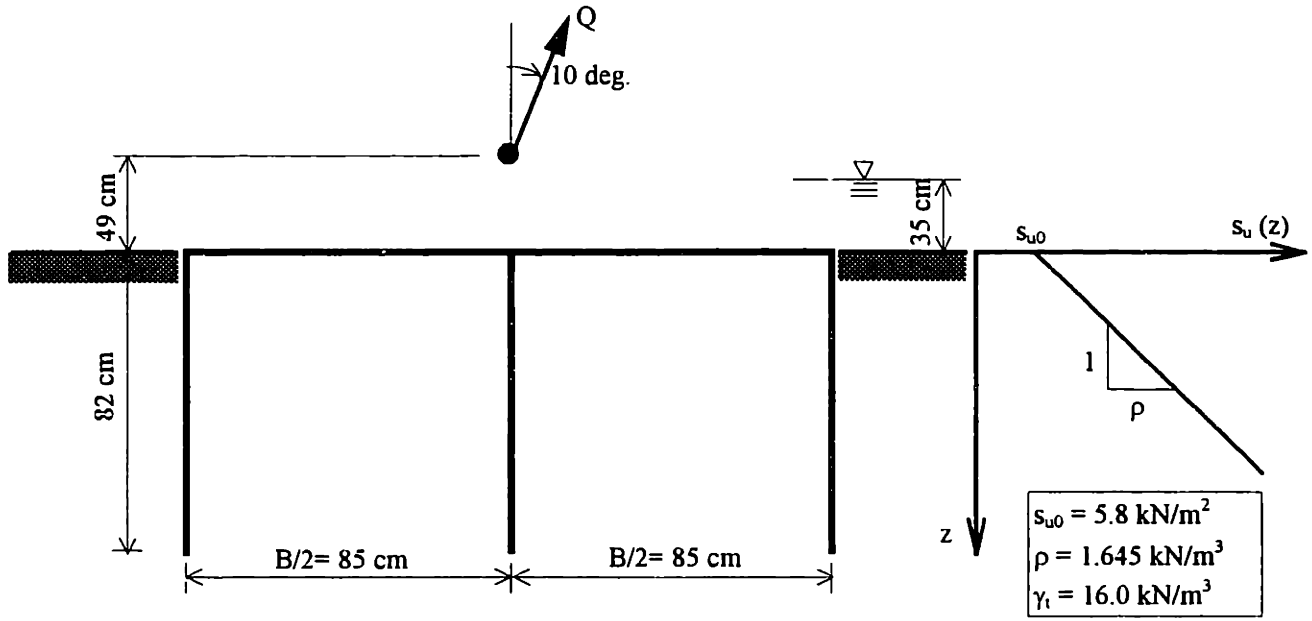

Numerical Solutions	
Upper Bound	Q_U = 0.852 kN/cm
Lower Bound	Q_L = 0.782 kN/m
Bound	8.50%
Axisymmetric Approximation	
Upper Bound	$F_U = Q_U$ (B) = 145 kN
Lower Bound	$F_L = Q_L$ (B) = 133 kN

NGI Results	
Field Test	F = 137.7 kN
LEM, i = 7.5°	F = 138 kN
LEM, i = 10.0°	F = 128 kN

Figure 5.52 Collapse loads from numerical limit analysis for inclined pullout of NGI field tests

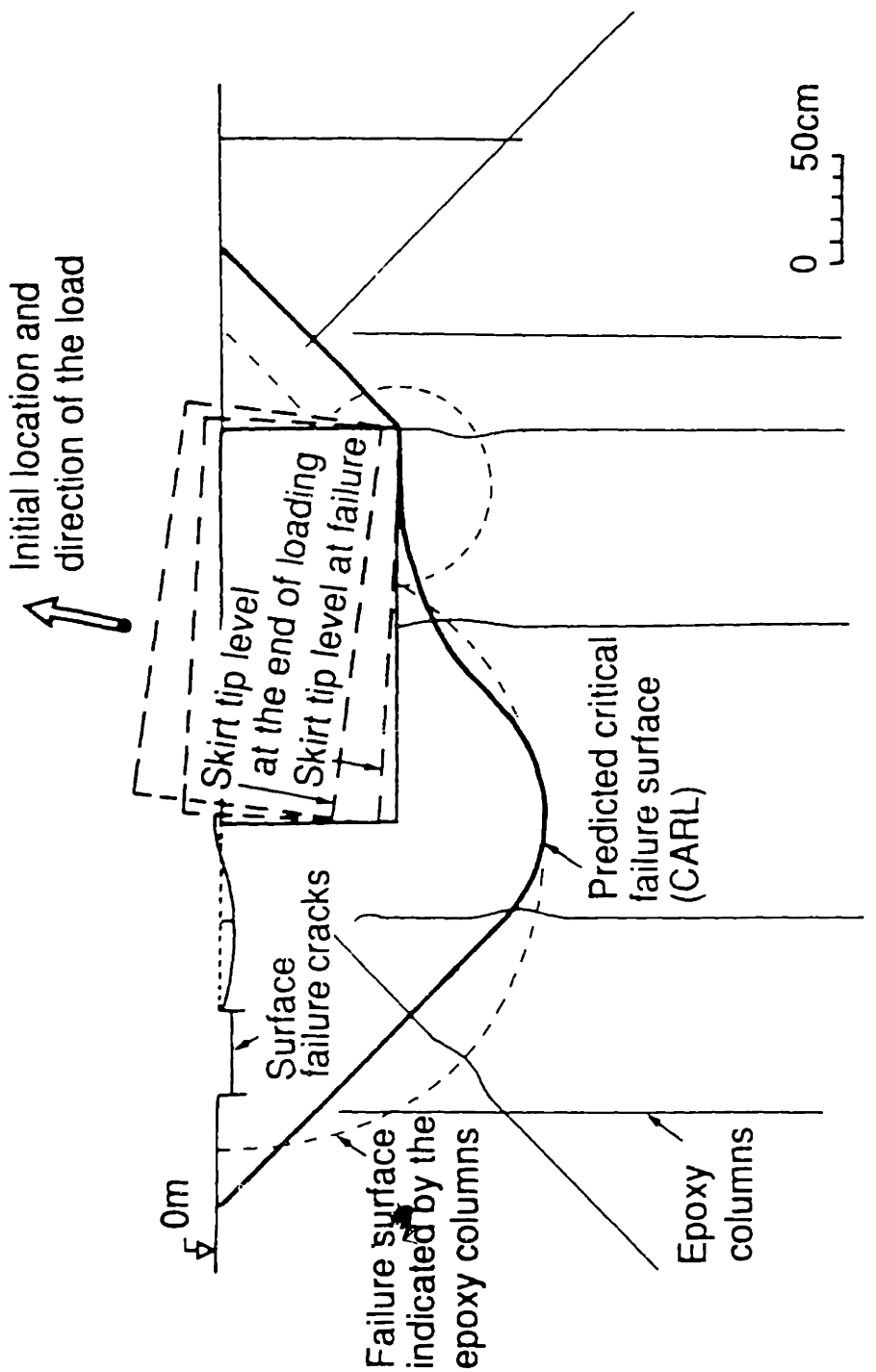

Figure 5.53 Prediction from limit equilibrium method and observation of failure in NGI caisson test (after Andersen et al., 1993)

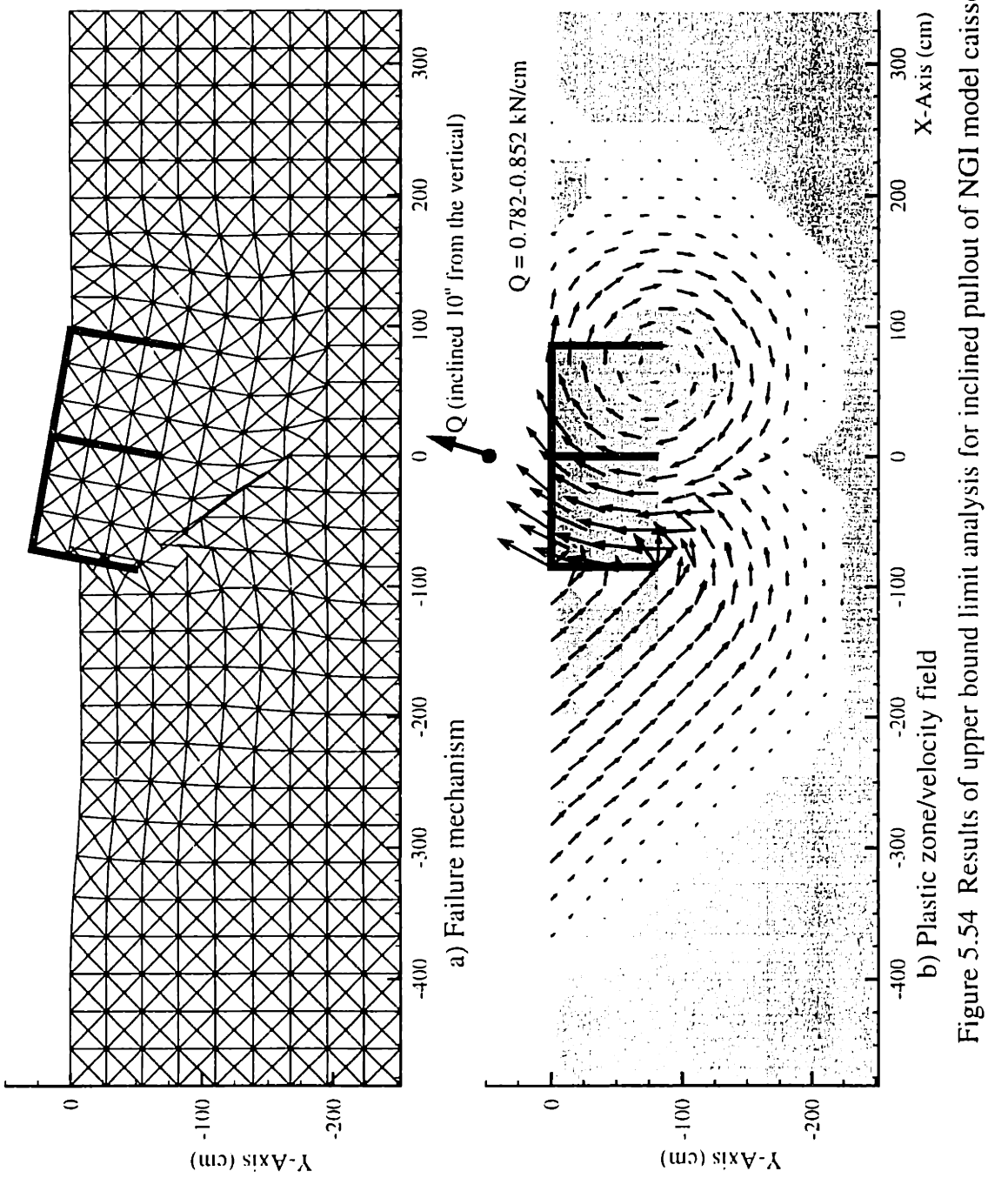

Figure 5.54 Results of upper bound limit analysis for inclined pullout of NGI model caisson

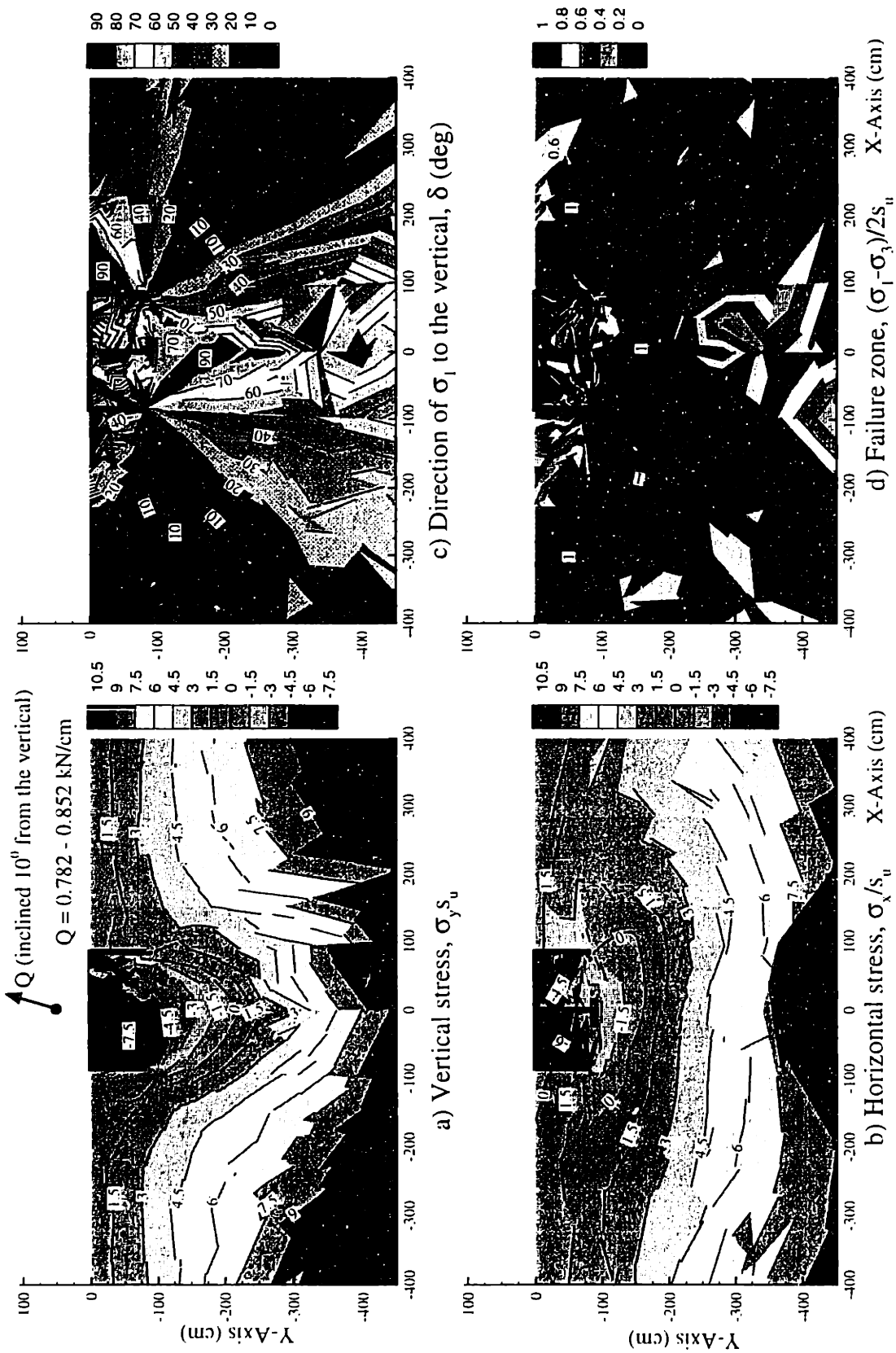

Figure 5.55 Lower bound limit analysis for inclined pullout of NGI model caisson

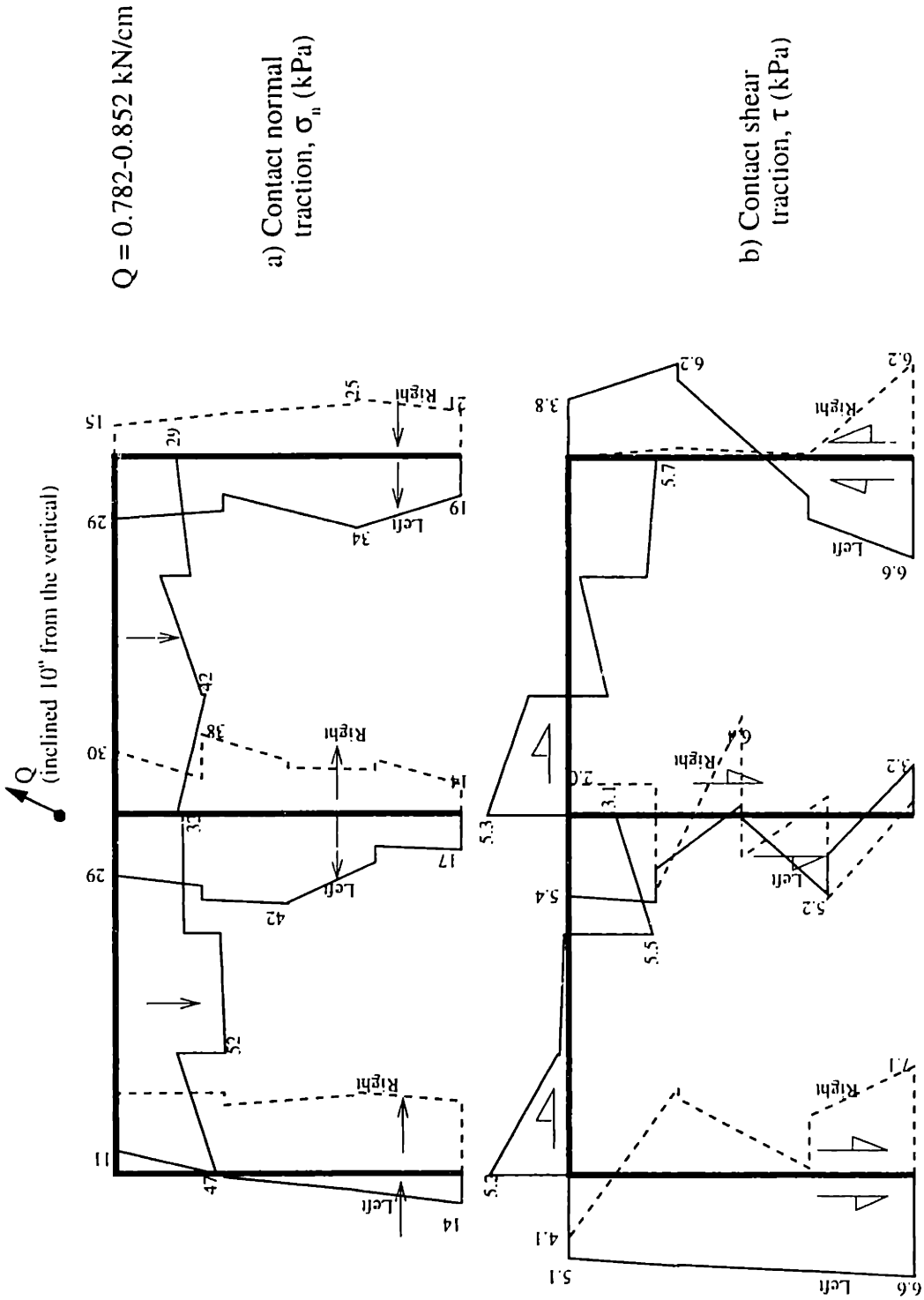

Figure 5.56 Contact tractions from lower bound analysis for inclined pullout of NGI model caisson

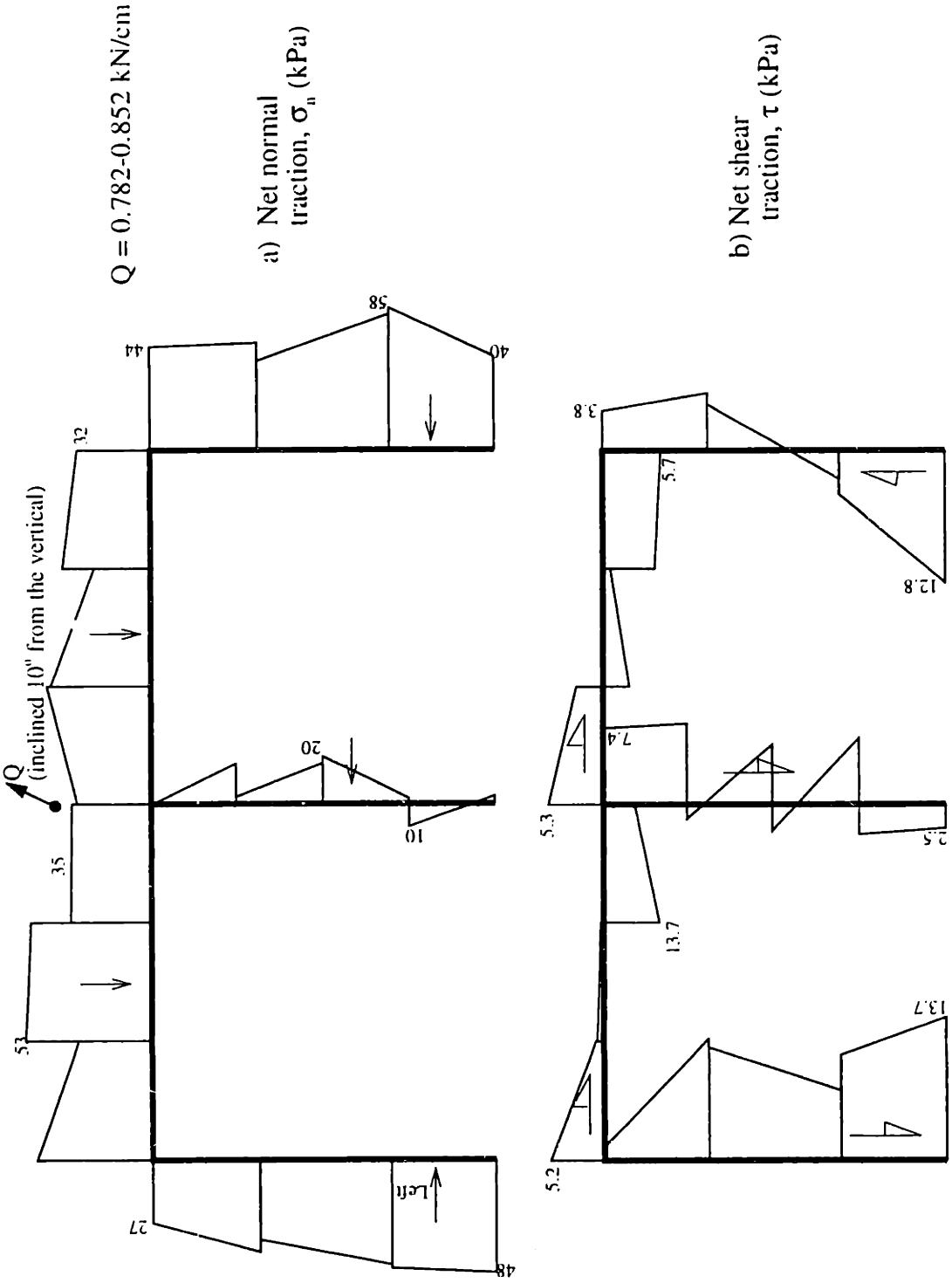

Figure 5.57 Net tractions from lower bound analysis for inclined pullout of NGI model caisson

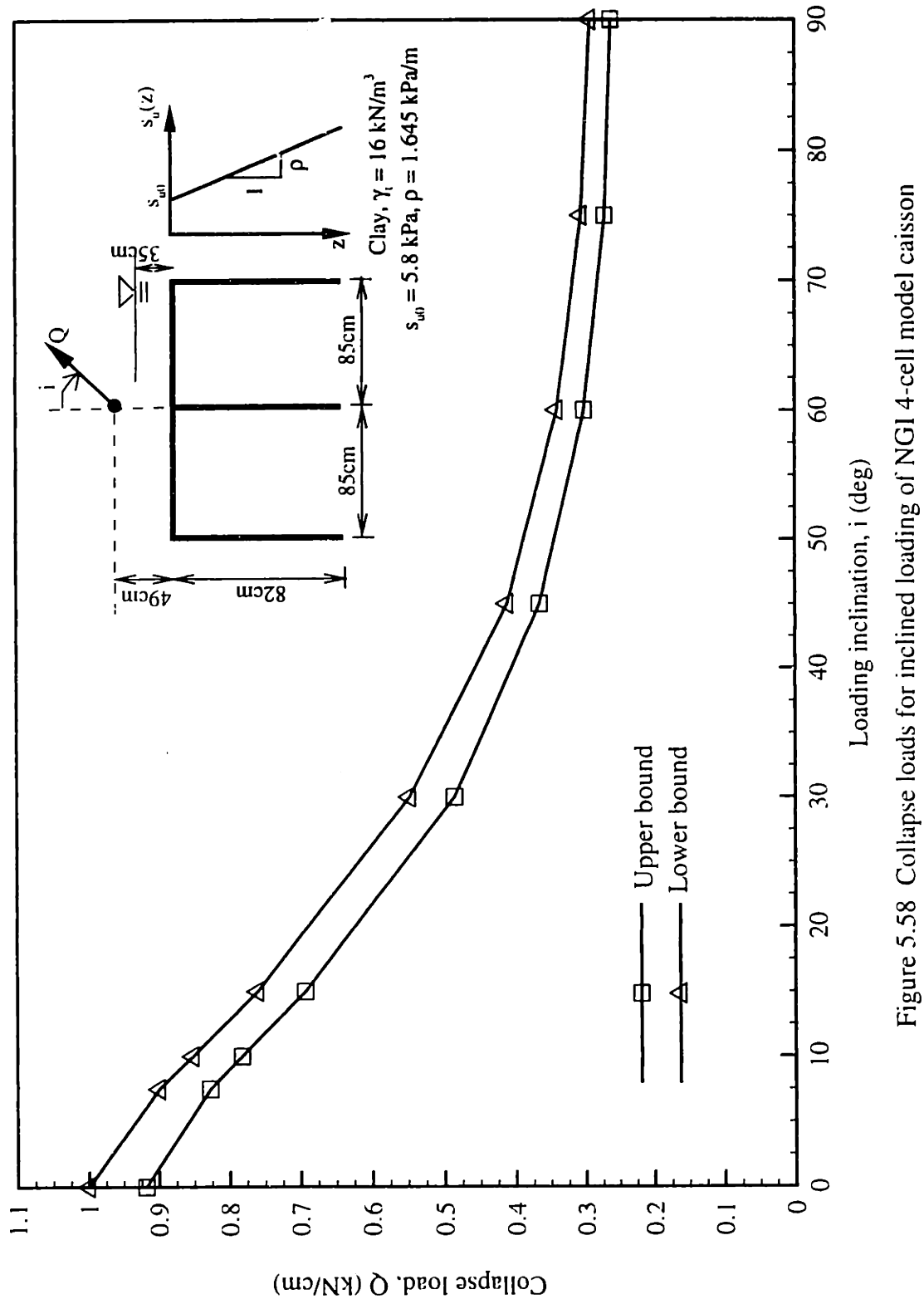

Figure 5.58 Collapse loads for inclined loading of NGI 4-cell model caisson

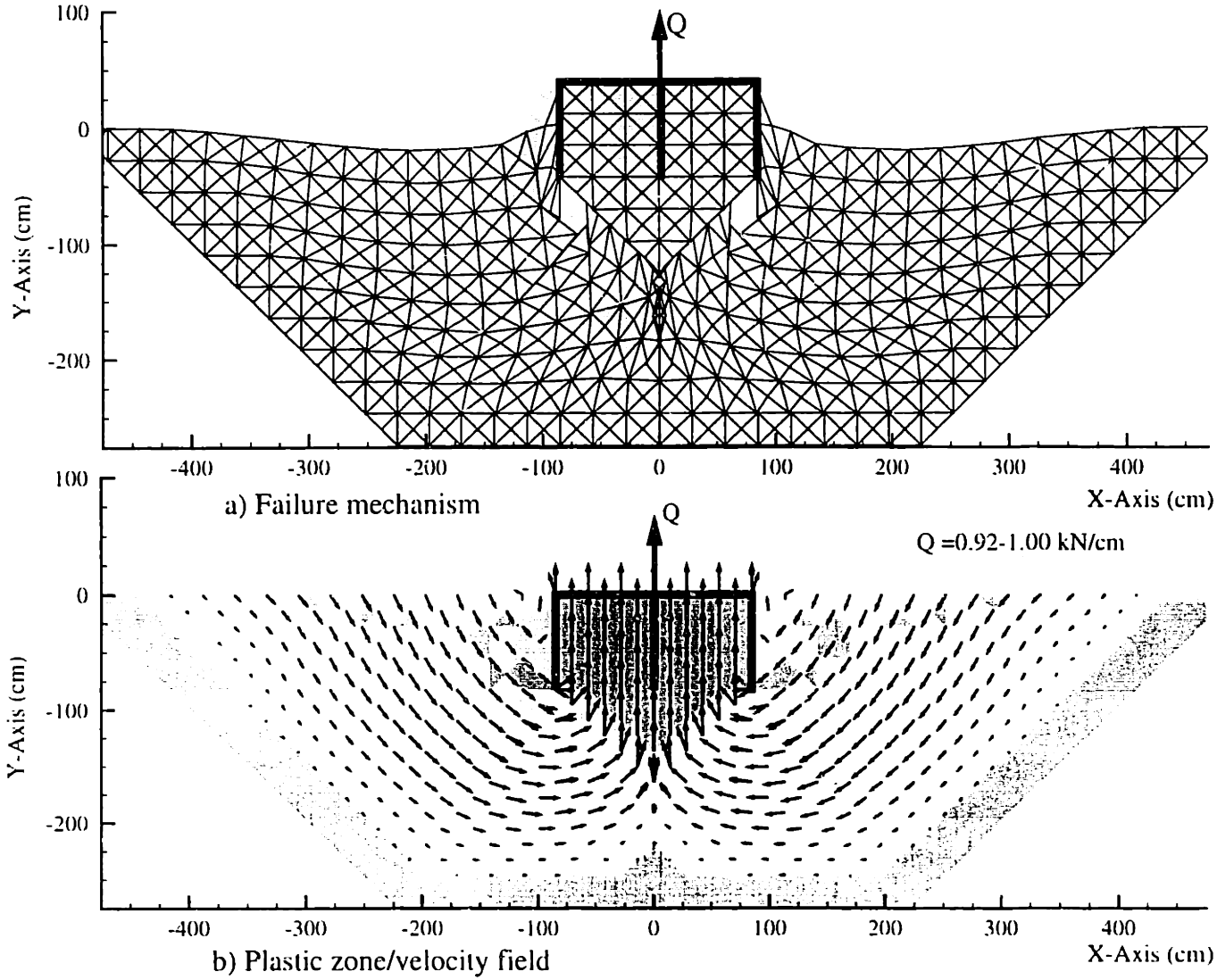

Figure 5.59 Results of upper bound limit analysis for axial pullout of NGI model caisson

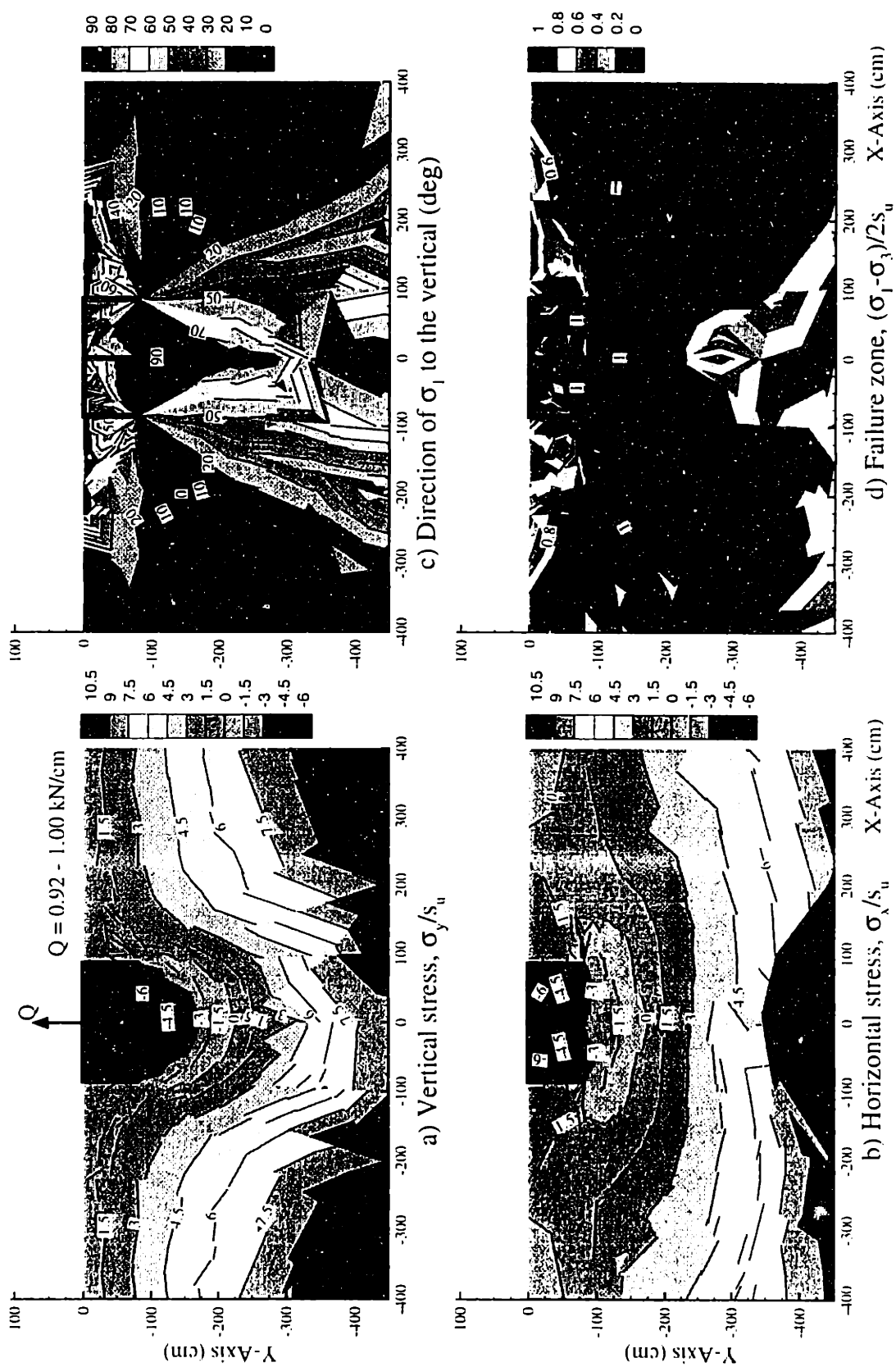

Figure 3.60 Lower bound limit analysis for axial pullout of NGI model caisson

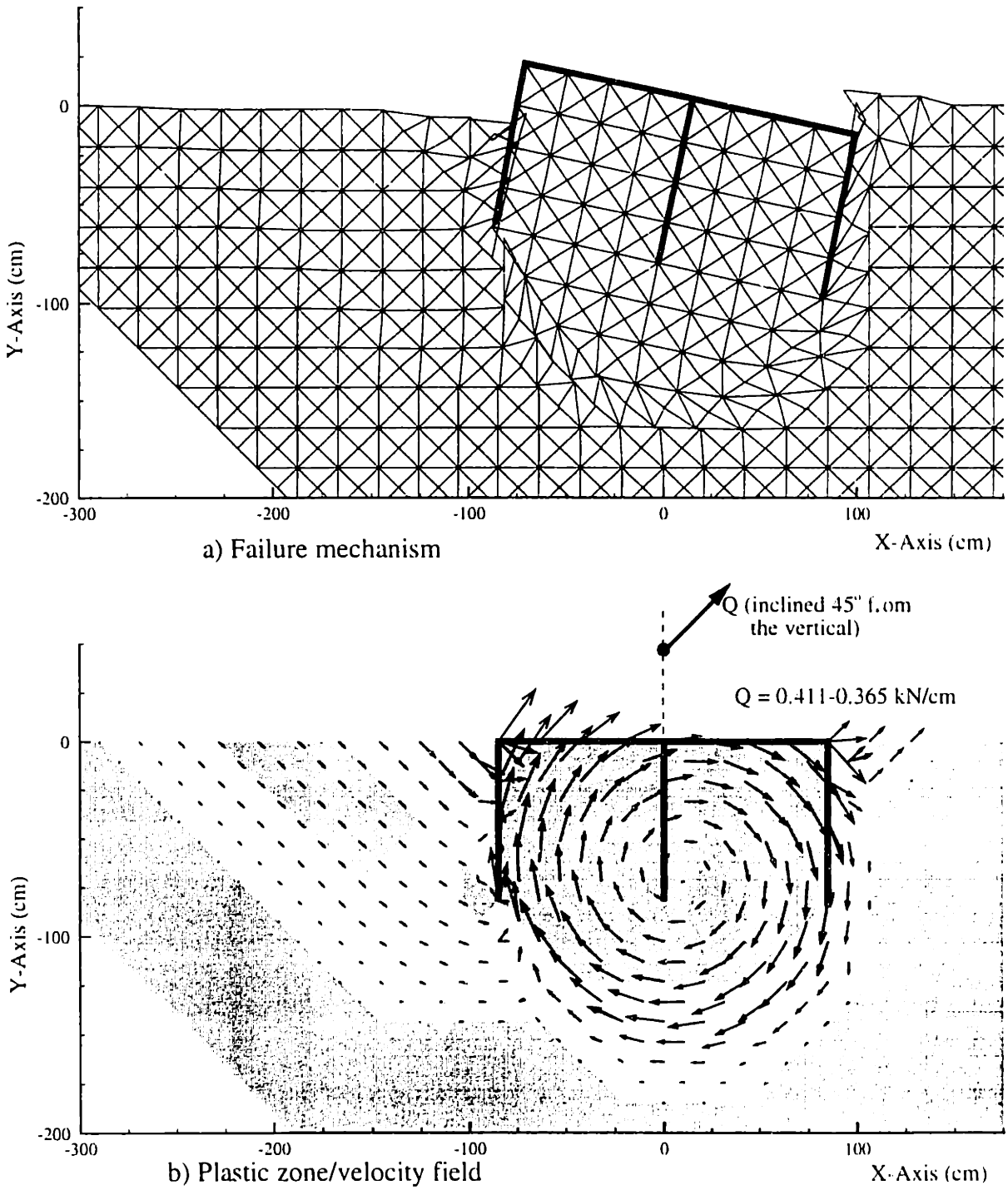

Figure 5.61 Results of upper bound limit analysis for inclined pullout of NGI model caisson, where loading inclination, i = 45°

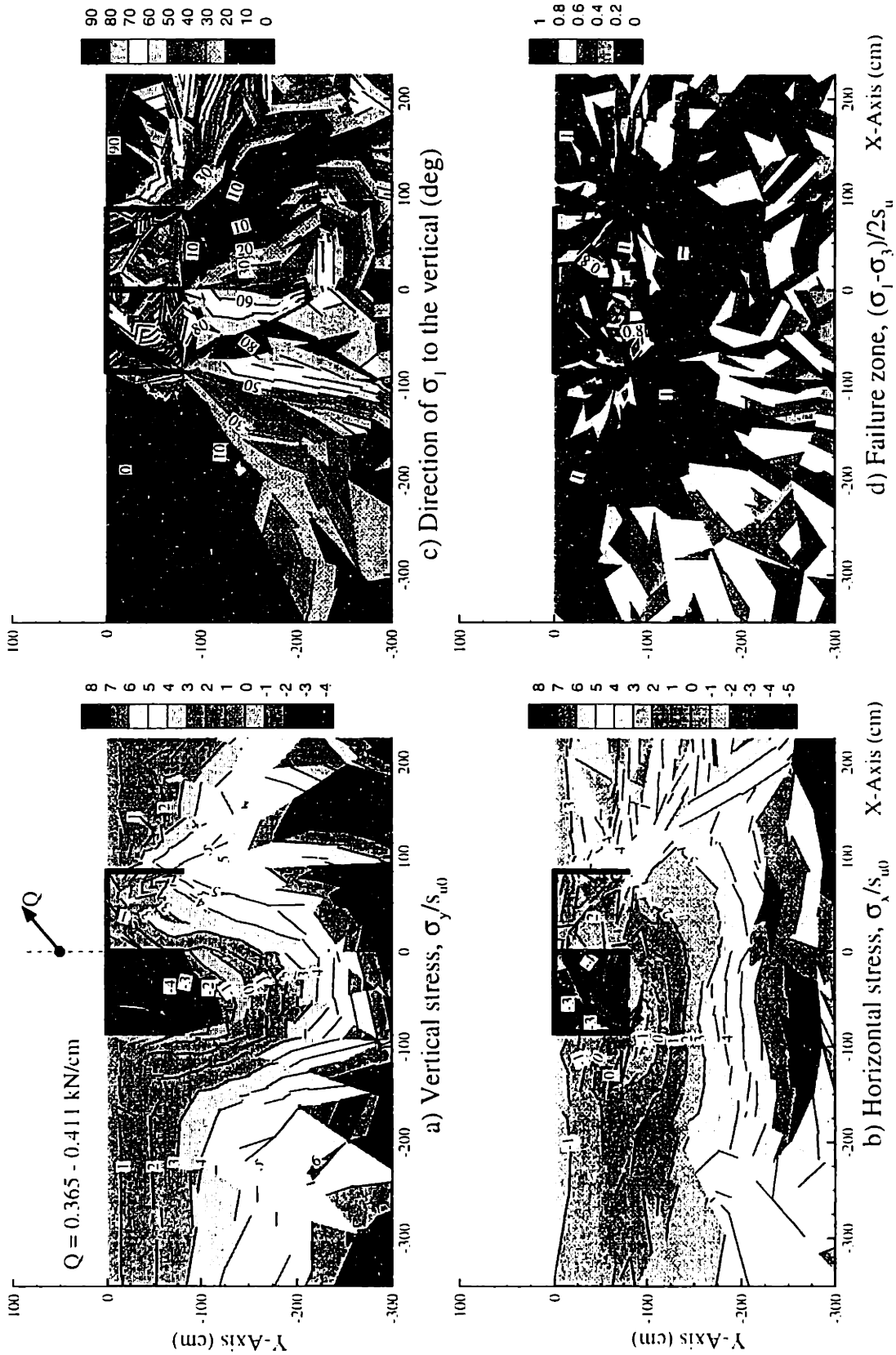

Figure 5.62 Lower bound limit analysis for inclined pullout of NGI model caisson, where loading inclination, i = 45°

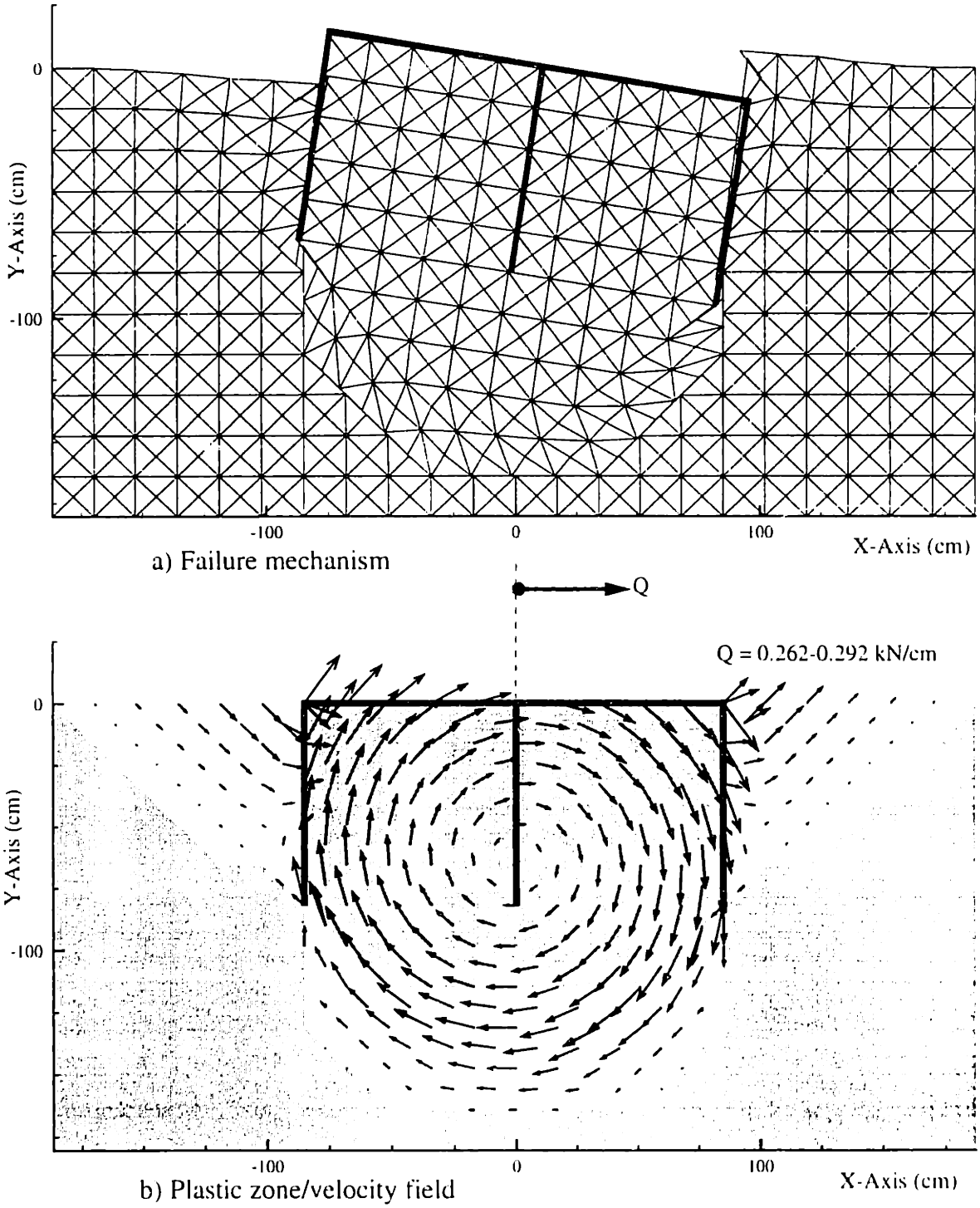

Figure 5.63 Results of upper bound limit analysis for inclined pullout of NGI model caisson, where loading inclination, i = 90°

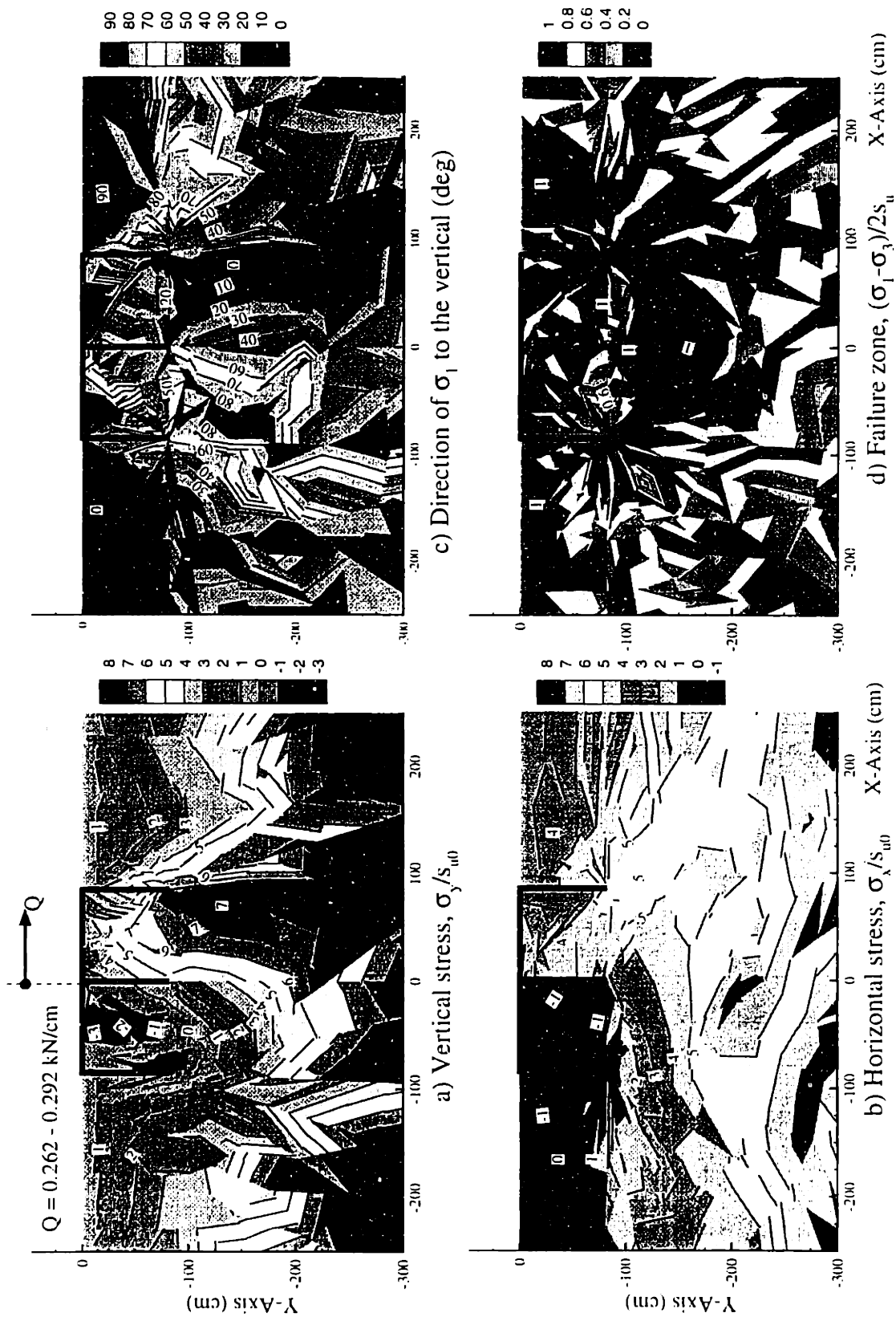

Figure 5.64 Lower bound limit analysis for inclined pullout of NGI model caisson, where loading inclination, i = 90°

Chapter 6. Undrained Stability of Braced Excavations

6.1 Introduction

Non-linear finite element methods are now routinely used in the design of braced and tieback excavations. In principle, these analyses offer a comprehensive framework which can evaluate multiple facets of excavation performance ranging from the design of the wall and support system, to predictions of ground movements and the effects of construction activities such as dewatering, ground improvement etc. In practice, the accuracy of finite element predictions is often limited by uncertainties in site investigations and in the representation of soil properties (Whittle et al. 1993).

For deep excavations in soft clays, the design of the lateral earth support system is often controlled by stability requirements, which are difficult to compute reliably, due to limitations in the constitutive models used in most existing finite element codes (Hashash and Whittle, 1996). Instead, stability calculations are usually performed using limit equilibrium methods (LEM) as implemented in conventional slope stability programs. Separate hand calculations of basal stability (after Terzaghi, 1943; or Bjerrum and Eide, 1956) are also widely used in the US for preliminary estimation of ground deformations (after Mana and Clough, 1981).

Although limit equilibrium stability calculations are widely used and very simple, it is difficult to assess their accuracy and validity due to the lack of theoretical background. In addition, the inaccuracies in LEM are related to the selected shape of the failure surface and the search procedure used to locate the critical surface.

More reliable calculations of stability can now be achieved through numerical solutions of upper and lower bound limit analyses. Rigorous upper and lower bound collapse loads are solved by linear programming methods, while spatial discretization and interpolation of the field variables are accomplished using finite element methods. This approach combines the advantages of finite element methods for handling complex geometric and loading conditions, with the power of the plastic limit theorems for bounding the exact collapse load. This chapter presents results from numerical limit analyses which calculate the undrained stability of braced excavations in clay.

Section 6.2 describes the objective function and factor of safety used for limit analyses of braced excavations. Section 6.3 illustrates typical results for an unsupported vertical cuts in clay. Section 6.4 presents the results of stability for braced excavations and embedded walls in a homogenous clay layer. Stability numbers from numerical limit analyses are compared with conventional basal heave methods as well as existing modifications dealing with wall embedment. The results of wall embedment demonstrate the capability of numerical limit analyses to predict combined failure of soil and support structures. Empirical curve fitting methods are used together with the dimensional analyses to interpret predictions of stability for braced excavations in deep homogeneous clay. The design chart generated by this equation reveals the relative importance of parameters which control the stability of excavations. Section 6.5 assesses the role of undrained strength anisotropy on the stability of unsupported and supported vertical cuts. Section 6.6 compares predictions of failure using numerical limit analyses with results obtained previously (in non-homogeneous clay) from finite element analyses with the MIT-E3 soil model (Hashash and Whittle, 1996; Jen, 1998).

6.2 Objective Function and Factor of Safety

Figure 6.1 illustrates the definition of the objective function for numerical limit analyses of braced excavations in homogeneous and layered soil profiles. For an excavation of depth, H, in homogeneous clay (Figure 6.1a), the vertical pressure of the retained soil, γH is the driving force which causes failure of the excavation, where γ is the total unit weight of the clay. Thus, the objective function for numerical upper and lower bound analyses optimizes the driving pressure, γH as follows:

Upper bound (UB):	Maximize (γH)	(6.1)
Lower bound (LB):	Minimize (γH)	

For excavations consisting of several soil layers as shown in Figure 6.1b, the vertical pressure of the entire retained soil (driving pressure) is equal to the sum of vertical pressure of each layer, $\Sigma\gamma_i h_i$, where γ_i is the unit weight of the i^{th} soil layer, with thickness h_i. Thus, the resulting objective functions for the non-homogeneous profile are:

Upper bound (UB): $\text{Maximize}(\sum_i \gamma_i h_i)$ (6.2)

Lower bound (LB): $\text{Minimize}(\sum_i \gamma_i h_i)$

Based on these definitions, the factor of safety (FS) for excavations can be specified as the ratio of the vertical pressure in the retained soil which causes failure to that occurring at the design excavation depth. Thus, the factors of safety for the excavation shown in Figure 6.1 are:

Homogeneous soil profile

Upper Bound (UB): $$FS_{UB} = \frac{(\gamma H)_{UB}}{(\gamma H)_{actual}} \quad (6.3)$$

Lower Bound (LB): $$FS_{LB} = \frac{(\gamma H)_{LB}}{(\gamma H)_{actual}}$$

Non-homogeneous soil profile

Upper Bound (UB): $$FS_{UB} = \frac{\sum(\gamma_i h_i)_{UB}}{\sum(\gamma_i h_i)_{actual}} \quad (6.4)$$

Lower Bound (LB): $$FS_{LB} = \frac{\sum(\gamma_i h_i)_{LB}}{\sum(\gamma_i h_i)_{actual}}$$

6.3 Unsupported Vertical Cuts in Homogenous Clay

Figure 6.2 shows an unsupported vertical cut in a homogeneous clay layer. The undrained stability number of this problem is defined as:

$$N = \gamma H/s_u \quad (6.5)$$

where γ = total unit weight of clay

H = height of vertical cut

s_u = undrained shear strength of clay

Figure 6.3 shows simple upper and lower bound solutions for a vertical cut in clay (Atkinson, 1981). The upper bound failure mechanism consists of a single straight slip surface at an angle of 45° to the vertical, generating a collapse load, $\gamma H/s_u = 4$. The crude lower bound stress field estimates, $\gamma H/s_u = 2$. Thus, the lower and upper bound stability calculations bracket the true collapse load with a range as, $2 \leq \gamma H/s_u \leq 4$ (i.e. solution is

bounded within ±33%). Surprisingly, it is difficult to obtain accurate solutions of this simple problem. Chen (1975) obtained a better upper bound solution using a logarithmic spiral failure surface, resulting in an estimate, $\gamma H/s_u = 3.83$; while the lower bound solutions have been improved by Heyman (1973) through the selection of more complex statically admissible stress fields, leading to an improved estimate, $\gamma H/s_u = 2.83$. Thus, even using improved upper and lower bound calculations, the true collapse load is bounded by, $2.83 \leq \gamma H/s_u \leq 3.83$.

Figure 6.4 shows the spatial discretization for numerical limit analyses of the undrained stability vertical cut in clay. The numerical lower and upper bound calculations give stability numbers, $\gamma H/s_u = 3.634$ and 3.902, respectively. Thus, the true collapse load is very well bounded with a maximum of ±3.5%. Clearly, numerical lower bound analyses are able to achieve a much more accurate lower bound solution than Heyman (1973), while upper bound solutions are in good agreement with results of Chen (1975).

Figures 6.5 and 6.6 summarize the upper and lower bound results for the vertical cut, respectively. The upper bound results include the predicted velocity field, plastic failure zone, and the failure mechanism; while the lower bound results comprise contours of principal stresses and their orientations. The upper bound failure mechanism (Figure 6.5a) involves an overlying rigid wedge of soil which slides at approximately 45° to the vertical, while plastic shear distortion occurs within a thin band (controlled by element size). These results also agree very well with the simple collapse mechanism shown in Figure 6.3. The lower bound analysis (Figure 6.6c) predicts that the soil in the retained side fails in an active mode of shearing ($\delta = 0°$). In addition, the major principal stress rotates from the vertical to the horizontal direction at the base of the cut ($\delta = 0°\text{->}90°$). The quality of the lower bound solution is most clearly shown by the high proportion of the soil mass, where $(\sigma_1 - \sigma_3)/2s_u \text{ -> } 1$.

6.4 Braced Excavations in Homogenous Clay

6.4.1 Braced Vertical Cut

This section studies the undrained stability of a well braced vertical cut in clay as shown in Figure 6.7a. The most widely used methods for assessing basal stability of braced excavations in homogeneous clay are based on limit equilibrium methods by Terzaghi (1943) and Bjerrum and Eide (1956), Figure 6.8. These calculations assume that unloading caused by an excavation is analogous to the failure of a wide footing such that the bearing capacity expressions can be applied directly to the calculations of a basal stability factor. The bearing capacity mechanism is approximated as the block of retained soil of a certain width whose weight is sufficient to push a wedge of soil upwards in the excavation area, through a rotational shear zone passing below the support wall. The mechanism may be constrained by an underlying stiff soil or bedrock as indicated in Figure 6.8. The factor of safety against basal heave (FS) according to Terzaghi (1943) is given as:

Deep clay: $$FS = \frac{5.7 s_u}{H(\gamma - \sqrt{2} s_u / B)} \quad , \text{for } d_b > B/\sqrt{2} \qquad (6.6a)$$

Effect of underlying rock: $$FS = \frac{5.7 s_u}{H(\gamma - s_u / d_b)} \quad , \text{for } d_b < B/\sqrt{2} \qquad (6.6b)$$

where H = excavation height

B = excavation width

s_u = undrained shear strength of clay

γ = total unit weight of clay

d_b = depth from base of excavation to bedrock

Note that the term, $N_c = 5.7$, corresponds to the bearing capacity factor for a rough footing assumed by Terzaghi (1943), while the denominator of both cases represents the net vertical pressure during the failure mechanism (i.e. self weight of retained soil minus the shear resistance on the vertical slip plane through the retained soil).

Bjerrum and Eide (1956) proposed a modified version of the basal stability. The block of retained soil is assumed to have a width of B instead of $B/\sqrt{2}$ (c.f. Fig. 6.8); while the bearing capacity factor, N_c is modified to account for the effect of excavation

width-depth ratio, as shown in Figure 6.9. The factor of safety against basal heave based on Bjerrum and Eide (1956) is given by:

$$FS = \frac{N_c}{\gamma H / s_u} \tag{6.7}$$

where N_c = bearing capacity factor according to Figure 6.9

Setting FS = 1, ones can obtain the stability number of excavations at failure as follows:

Stability number by Terzaghi (1943)

Deep clay: $$N = \frac{\gamma H}{s_u} = 5.7 + \sqrt{2}\left(\frac{H}{B}\right) \quad \text{,for } d_b > B/\sqrt{2} \tag{6.8a}$$

With underlying rock: $$N = \frac{\gamma H}{s_u} = 5.7 + \sqrt{2}\left(\frac{H}{d_b}\right) \quad \text{,for } d_b < B/\sqrt{2} \tag{6.8b}$$

Stability number by Bjerrum and Eide (1956)

Deep clay: $$N = \frac{\gamma H}{s_u} = N_c \tag{6.9}$$

The major disadvantage for calculations of basal stability by these limit equilibrium methods is that it is difficult to check the accuracy of solutions due to their assumptions about the width of the failure zone in the retained soil, the magnitude of bearing capacity factor, the effect of excavation depth, and the treatment of shear resistance along the vertical slip plane. Numerical limit analyses eliminate these uncertainties and hence provide a reliable estimate of stability.

6.4.1.1 Results for Deep Clay Layer

Figures 6.10 and 6.11 show the spatial discretization used in lower and upper bound analyses of a supported vertical cut, respectively. The calculations assume that the vertical cut is supported by a rigid wall and bracing system. The wall is represented by a series of rigid beam and joint elements. The shear at the wall-soil interface can range from $f_s = 0$ (smooth) to $f_s = s_u$ (rough). In this section, the analyses use an isotropic strength (Tresca criterion). Figure 6.12 presents results of lower (LB) and upper bound (UB) predictions of the stability number, $N = \gamma H/s_u$, for braced excavations in deep homogeneous deposits of clay (Table 6.1 tabulates the results). The calculations consider

a wide range of width to depth aspect ratios, B/H, and in all cases bound the true collapse load within ±5%. For narrow excavations (H/B->3), the interface roughness causes a 15% increase in the predicted value of N, but has minimal effect on the stability of wide excavations (B/H->5). Figure 6.12 also shows the stability numbers computed by the methods of Terzaghi (1943) and Bjerrum and Eide (1956) (according to equations 6.8a and 6.9). The basal stability mechanism proposed by Terzaghi(1943) corresponds to an upper bound on the actual stability of a wide excavation, but significantly overestimates the stability of narrow excavation. In contrast, the empirical mechanism of Bjerrum and Eide (1956) is conservative for all excavation aspect ratios.

Figures 6.13 through 6.25 show upper and lower bound results for three excavation ratios, H/B = 1.0, 3.0, and B/H = 5.0, with smooth and rough wall interfaces. For H/B = 1, the failure mechanisms (smooth and rough walls, Figures 6.13 and 6.14) comprise a rigid wedge of soil that is pushed upward inside the excavation, together with a rotational shear zone passing below the wall. Wall roughness increases the zone of plastic failure in the retained soil. The failure zone extends laterally to $(x-B/2)/B \approx 3.75$ and 2.75 behind the retained soil for rough and smooth walls, respectively, and downward $y/H \approx 1.75$ and 1.5 below the bottom of excavation. It can be seen that the failure mechanisms assumed by Terzaghi (1943) and Bjerrum and Eide (1956) differ significantly from the upper bound predictions. The lower bound analysis (Figures 6.15c and 6.16c) predict that the soil below the bottom of excavation fails in an extension mode of shearing ($\delta = 90°$), together with a radial shear zone below the tip of the wall ($\delta = 90°->0°$). The retained soil behind the wall fails between the direct simple shear and a passive shearing ($\delta = 45\text{-}90°$). A passive stress state occurs in the retained soil above the base of the excavation. Similar stress distributions were observed in excavation analyses using the finite element method by Hashash (1992).

For narrow excavations, where H/B = 3 (Figures 6.17 and 6.18), the failure zone extends the base of the excavation $y/H \approx 1.0$, and laterally behind the wall $(x-B/2)/B \approx 8.0$. Rough walls generate a much larger zone of failure than smooth walls. The types of failure (Figures 6.19c and 6.20c) predicted by lower bound analysis are similar to the case of H/B = 1. For a wide excavation (B/H = 5,) there is no difference in failure mechanism

and plastic between smooth and rough walls (Figures 6.21 and 6.22). The failure zone extends laterally (x-B/2)/B ≈ 1.9B behind the wall, and vertically y/H ≈ 5.5 below the excavation grade. Notice that the empirical mechanism assumed by Terzaghi (1943) and Bjerrum and Eide (1956) correspond to the upper bound solution for a wide excavation.

Figure 6.25 shows the vertical, σ_v, and horizontal, σ_h, pressure distributions on the smooth wall from the lower bound stress analyses. It can be seen that for all values of H/B, horizontal pressure, $\sigma_h \approx \sigma_v + 2s_u$, which means that the passive shear resistance is fully mobilized along the wall. For wide excavation (B/H = 5.0), vertical stress is approximately equal to the vertical overburden pressure (i.e. $\sigma_v \approx \gamma z$). As the excavation approaches the narrow excavation (H/B = 3.0), vertical stress is much smaller than γz for z/H > 0.5.

6.4.1.2 Effect of Underlying Bedrock

Figure 6.26 summarizes lower and upper bound predictions of the stability number for braced excavations in a clay layer underlain by bedrock (Table 6.2 tabulates these data), for the case where $d_b/H = 1.0$ (where d_b = depth from bottom of excavation to bedrock). Note that the bedrock is assumed to be a rigid stratum. For all excavation ratios, B/H, the numerical limit analysis bounds the stability number within ±5%. The results show that the depth to bedrock increases the stability by 20-25% for wide excavations (B/H ≥ 2) (compared to the deep clay layer), but has no effect for stability of narrow excavations (H/B ≥2). The figure also shows the stability numbers computed by Terzaghi (1943) with $d_b/H = 1$ (see equation 6.8b). Terzaghi's mechanism matches exactly with the lower bound stability number for wide excavations (B/H ≥ 2), but is again non-conservative for narrow excavations (H/B > 1.5)

Figures 6.27-6.29 compare upper bound results of braced excavation between deep clay layer and clay underlying with bedrock. For narrow excavations (H/B = 3, Figure 6.27), the plastic failure zone extends below the base of the excavation approximately to y/H ≈ 1, and hence the bedrock contact ($d_b/H = 1.0$) does not affect the stability number at all. However, for B/H = 1 and 5, the failure mechanism and plastic

zone are greatly constrained by the underlying bedrock in the vertical direction (Figures 6.28 and 6.29). As a result, there is a significant decrease in the size of plastic zone, especially for wide excavation (B/H = 5, Figure 6.29)

6.4.2 Embedded Walls

This section studies the effect of wall penetration below the base of excavation as illustrated in Figure 6.7b. The excavation is well braced wall above the excavated grade, while the wall extends to a depth, D, below the base of the excavation. Empirical design methods described in Section 6.4.1 (Terzaghi, 1943; and Bjerrum and Eide, 1956) are only applicable for bases where D = 0m. One of the most widely used modifications to account for wall embedment was proposed by Terzaghi (1943) as shown in Figure 6.30. According to Terzaghi's suggestion, "the simplest procedure is to compute the vertical pressure on a horizontal section through the lower edge of the sheet piles. The heave of the bottom is resisted not only by the weight of the soil located between the buried parts of the sheet piles but also by the adhesion between this body of earth and the adjoining sheet piles". Following this suggestion, one can obtain a modified version of the factor of safety from the conventional Terzaghi (1943) in equation 6.6a as:

$$FS = \frac{5.7s_u}{[\gamma(H+D) - \sqrt{2}s_u(H+D)/B] - [\gamma D + 2s_u D/B]} \tag{6.10}$$

Note that the second term of denominator represents the weight of the soil plug and the shear resistance adjacent to the wall.

Setting FS = 1, the modified Terzaghi (1943) stability number including wall embedment can be written as:

$$N = \frac{\gamma H}{s_u} = 5.7 + \sqrt{2}\left(\frac{H+D}{B}\right) + 2\left(\frac{D}{B}\right) \tag{6.11}$$

An alternative modification to account for wall embedment was proposed by O'Rourke (1993), who incorporated the elastic strain energy for an assumed wall deflection. According to O'Rourke (1993), the modified stability number can be written:

$$N_{OR} = N_{c,B\text{-}E} + U_w \tag{6.12}$$

where $N_{c,B\text{-}E}$ = stability number computed by Bjerrum and Eide (1956) for D = 0

$U_w = M_y\pi^2/(8DLs_{ub})$ for a free end wall

$U_w = M_y\pi^2/(2DLs_{ub})$ for a fixed end wall

$U_w = 9M_y\pi^2/(32DLs_{ub})$ for a sliding end wall

s_{ub} = undrained strength of basal clay

M_y = the yield moment (per unit width of wall)

D = wall embedment below base of excavation

L = the wall length beneath the lowest level of support (see Figure 6.31)

Note that the term U_w represents the elastic strain energy of an embedded wall, whose deflection (δ) is approximated by a cosine function (see Figure 6.31); while the maximum wall deflection (δ_m) is related to the yield moment of the wall, M_y. More details of the derivation for U_w can be found in O'Rourke (1993).

Even though these modifications take into account for the increase in basal stability associated with wall embedment, none of the existing solutions consider the failure of the wall. The modified Terzaghi method corresponds to the case of a rigid wall, while O'Rourke's method relies on the assumed deflection mode shape. In reality, the failure of braced excavation can occur due to shear distortion in the soil mass and/or bending of the structural wall pile. The problem of soil-structure failure interaction can be handled correctly by numerical limit analyses, which incorporate structural elements into the calculation. The following section presents the results of numerical limit analyses for a braced excavation with wall embedment in the homogeneous clay.

6.4.2.1 Effect of Wall Embedment

A series of numerical experiments have been performed in order to consider the effects of wall embedment, D on the stability of a well braced excavation with depth, H = 15m and width, B = 40m (H/B = 0.375). This section focuses on results for two cases: 1) D/H = 2/3 (D = 10m, shallow embedment); and 2) D/H =2 (D = 30m, deep embedment). Figures 6.32 and 6.33 show the spatial discretization of lower and upper bound calculations for these analyses. The undrained strength profile, s_u is constant and isotropic. The wall is simulated with a series of beam and joint elements, whose strength is controlled by the plastic bending moment, M_p (i.e., failure of the wall is permitted to occur only due to plastic bending). Dimensional analysis shows that the stability number

of the excavation can be written as a function of the relative strength parameter, $M_p/(s_uD^2)$, and the embedment ratio, D/H. Figure 6.34 shows the lower and upper bound predictions of stability number for these studies (Table 6.3 tabulates these data). For all values of $M_p/(s_uD^2)$, the true stability number is bounded within ±5% by numerical limit analyses. The results show that the stability number increases with embedment ratio D/H, and with the relative strength parameter $M_p/(s_uD^2)$, but remains constant for $M_p/(s_uD^2) \geq 6$. This limiting condition corresponds to the case where there is no bending failure of the wall.

Comparisons have been made between O'Rourke's stability number N_{OR}, and predictions of the numerical limit analyses. For H/B = 0.375, Bjerrum and Eide's stability number, $N_{c,B\text{-}E} = 5.7$ (see Figure 6.9). Considering a rectangular section of a unit width of wall, the yield moment, $M_y = M_p/1.5$. Substituting these parameters into equation 6.12, N_{OR} for the embedded wall with free end is given by:

$$N_{OR} = 5.7 + M_p\pi^2/(12s_uD^2) \qquad (6.13)$$

These results have been plotted in Figure 6.34. It is clear from equation 6.13 that N_{OR} fails to identify the increase in stability of excavations due to the embedment ratio, D/H. Furthermore, the results in Figure 6.34 show that O'Rourke's calculation method underestimates the stability of flexible walls, while greatly overestimating it for rigid cases.

Stability numbers from the numerical the limit analyses have also been compared with the conventional and modified Terzaghi method. Without wall embedment (D = 0m), numerical limit analyses provide a stability number for H/B = 0.375 as: $5.91 \leq N \leq 6.26$, while the Terzaghi's method (equation 6.8a) give N = 6.23, which agrees very well with the upper bound calculations. For the case of wall embedment, the modified Terzaghi's approach predicts stability numbers, N = 7.08 and 8.79 for D/H = 2/3, and 2, respectively. Figure 6.34 clearly shows that these calculations are in very good agreement with upper bound stability calculations for the case of rigid wall [$M_p/(s_uD^2) = 6$] for both embedment ratios.

Figures 6.37 through 6.40 summarize the upper and lower bound results of wall embedment, D/H = 2/3 for three selected relative strength parameters, $M_p/(s_uD^2) = 0.1$,

0.5, and 6.0 (Figures 6.35 and 6.36 show the upper and lower bound results for D = 0m). It should be noted that $M_p/(s_uD^2)$ = 0.1 represents the case of a flexible wall, whereas $M_p/(s_uD^2)$ = 6.0 corresponds to a rigid wall. For $M_p/(s_uD^2)$ = 0.1, the upper bound analysis predicts that the soil in the retained side causes rotation of the embedded wall with plastic hinges forming at two locations: 1) at the excavated grade; and 2) 5m below the base of excavation (Figure 6.37a). The failure of the soil extends laterally more than 100m behind the wall and 55m below the base of the excavation. As the value of $M_p/(s_uD^2)$ increases to 0.5, only one plastic hinge occurs at the excavated grade (Figure 6.37b). For $M_p/(s_uD^2)$ = 6.0, the upper bound results show that the wall is rigid, and failure occurs with flow of soil around the toe of the wall, and upward displacement of a rigid soil plug (Figure 6.37c). As a result, the plastic zone extends 70 m below the base of the excavation. Figure 6.39 shows the direction of the major principal stress to the vertical, δ predicted from the lower bound analysis. It can be seen that the rotational shear zone (δ = 0°->90°) moves downward from the level of excavated height to the tip of the wall as the values of $M_p/(s_uD^2)$ increases from 0.1 to 6.0. Figure 6.40 shows the lateral earth pressure and bending moment diagrams for the wall. For $M_p/(s_uD^2)$ = 0.1, the lower bound analysis predicts that there are two locations, where bending failure occurs, $|M/M_p|$ = 1.0; 1) at the level of excavated height; and 2) 4m below the bottom of excavation. For $M_p/(s_uD^2)$ = 0.5, $|M/M_p|$ = 1.0 occurs at only the excavation grade. For $M_p/(s_uD^2)$ = 6.0, the bending moment along the wall is less than its plastic moment, and hence there is no failure in the wall. Clearly, the lower bound predictions of wall failure correspond very well with the upper bound failure mechanism.

Figures 6.41-6.44 summarize the lower and upper bound results of wall embedment ratio, D/H = 2 for $M_p/(s_uD^2)$ = 0.05, 0.5, and 6.0. It can be seen that the failure mechanisms for deep embedment case (Figures 6.41, 6.42) are very similar to those for shallow embedment (D/H = 2/3). Figure 6.41a corresponds to a wall bulging failure mode, where plastic hinges form at the excavated grade and within the embedded wall section. Figure 6.41b ($M_p/(s_uD^2)$ = 0.5) corresponds to a rotational failure (one plastic hinge at the excavated grade). The stability number of these two types of failure is dependent on the relative strength parameter $M_p/(s_uD^2)$. Figure 6.41c corresponds to the

case of rigid wall, where the stability number is dependent only to the undrained strength of the clay. Notice that the failure mechanism for the case of rigid wall is similar to the modified Terzaghi's mechanism. Figure 6.43 compares the contours of the direction of the major of principal stress to the vertical. These comparisons show that as the value of $M_p/(s_uD^2)$ increases from 0.05 to 6.0, the rotational shear zone (δ = 0°->90°) occurring right at the excavated grade moves down to the toe of the wall. The locations of $|M/M_p|$ = 1.0 predicted from lower bound analysis (Figure 6.44) agree very well with the location of plastic hinges from the upper bound results (Figure 6.41).

6.4.3 Design Charts for Stability of Braced Excavations in Deep Homogeneous Clay

Based on the results of analyses in Section 6.4.1 and 6.4.2, the stability number $\gamma H/s_u$ for braced excavations is governed by three parameters:

1. Excavation aspect ratio, H/B
2. Wall embedment, D/H
3. Relative strength parameter, $M_p/(s_uD^2)$

Hence, additional numerical limit analyses have been carried out to assess the stability for combinations of these parameters 1) D/H = 2/3, $0.2 \le H/B \le 3$, and $0.001 \le M_p/(s_uD^2) \le 6$; and 2) H/B = 1; $0 \le D/H \le 2$, and $0.001 \le M_p/(s_uD^2) \le 6$. An ad-hoc empirical technique of curve fitting based on dimensional analysis has been carried out to interpret the numerical results. Table 6.4 summarizes a proposed empirical equation of stability number for braced excavations as a dimensional function of H/B, D/H and $M_p/(s_uD^2)$. There are 7 constants used in this equation. For the data of numerical upper, lower and average solutions, the values of r^2 fitness are higher than 99%, which indicates that this empirical equation fits very well these numerical solutions. For the special case, where there is no wall embedment (D = 0), the empirical equation of stability number reduces to a simple form:

$$\frac{\gamma H}{s_u} = \frac{5.141(B/H) + b_2}{(B/H) + a_2} \qquad (6.14)$$

where b_2 = 6.10 and a_2 = 0.61 (average of lower and upper bound data)

Figure 6.45 shows the excellent agreement between this proposed equation and the best estimate of the stability number without wall embedment. Figures 6.46 through 6.49 show further comparisons between the proposed empirical equation and computed stability numbers. These figures include the effects of different wall embedment ratios (D/H) at selected relative strength parameters, $M_p/(s_uD^2)$. In all cases, the proposed equation matches very well with results of the average of numerical upper and lower bound limit analyses and hence, the maximum errors in computed stability number is ±5%.

Figures 6.50 to 6.52 present examples of design charts for braced excavations in deep homogeneous clay. Each design chart is generated by the proposed empirical equation using the coefficients corresponding to the average of lower and upper bound data at a selected value of the bending strength of the wall (M_p = 1, 2, 3 MNm/m, respectively). The charts assume a typical (total) unit weight of clay, γ = 18.0 kN/m^3. Results are presented for undrained shear strengths of clay, s_u = 30, 50, and 70 kPa with wall embedments, D = 0 - 40m. Given the width of excavation (B), undrained strength of clay (s_u), and wall embedment depth (D), the chart shows the excavation depth that will cause failure, H_f. Thus, the factor of safety against basal heave, FS can be evaluated as: $FS = H_f/H$, where H is the actual excavation depth in the field.

The design charts clearly show that the undrained shear strength of the clay is the dominant parameter affecting stability, while B, D, M_p, all have secondary effects. For example, each of the charts shows that to a first order approximation, the critical excavation depth is proportional to the undrained strength, while embedment depth increasing from D = 0 to 40m may only cause a 5m increase in H_f. Wall embedment has a minimal effect on stability in these calculations when D > 10m.

6.5 Effect of Strength Anisotropy of Clay

The numerical results presented in Section 6.4 are based on the assumption that the undrained shear strength of the clay is isotropic. In reality, the undrained shear strength of soft clays is anisotropic. Figure 6.53 summarizes the undrained shear strength of K_0-normally consolidated clays from CK_0U compression (CK_0UC)/extension (CK_0UE)

and direct simple shear (CK_0UDSS) tests. The results show that s_{uTE}/s_{uTC} = 0.50 to 0.75, and s_{uDSS}/s_{uTC} = 0.65 to 0.85[1]. Table 6.5 shows further results of mobilized undrained strength ratios selected to represent progressive failure of anisotropic clays using the strain compatibility technique (Ladd, 1991). For these data, s_{uTE}/s_{uTC} = 0.35 - 0.92, while s_{uDSS}/s_{uTC} = 0.67 to 0.96.

This section assumes that $s_{u45} = 0.5(s_{u0} + s_{u90})$, and the strength anisotropy of clay is controlled by the anisotropic undrained strength ratio, $K_s = s_{u90}/s_{u0}$. Based on the anisotropic strength data from Figure 6.53 and Table 6.5, K_s is approximated as, $K_s \approx s_{uTC}/s_{uTE}$, ranging from 0.35 to 1.0 (isotropic) for most clays except varved clays and fissured clays. Figure 6.54 plots the undrained strength ratio, $s_{u\delta}/s_{u0}$ as a function of the angle of major principal stress to the vertical, δ, using the anisotropic strength function given by Davis and Christian (1971) as described in Section 4.2.

Hence, by varying the values of the parameter K_s, the effect of strength anisotropy on excavation stability can be examined. The next two sections present the results of numerical limit analyses for vertical unsupported cuts and braced excavation in anisotropic clay (homogeneous strength profile).

6.5.1 Unsupported Vertical Cuts

Figure 6.55 shows the lower and upper bound predictions of the stability number, $N = \gamma H/s_{u45}$ for an unsupported vertical cut in homogeneous clay, where the undrained strength is anisotropic (Table 6.6 tabulates these data). The numerical limit analyses bound the true stability number within ±5% for all values of anisotropic undrained strength ratios, K_s. The results show that the analysis using s_{u45} with isotropic strength gives a conservative estimate of the stability number for actual vertical cuts in anisotropic clay. The stability number for K_s = 0.5 is about 20% higher than that of isotropic strength (K_s = 1). The figure also shows good agreement between the analyses and solutions by Chen (1975), while conventional mechanisms with planar surface overestimate the stability number.

---

[1] Assuming $s_{uDSS} = \tau_{hmax}$

Figures 6.56 and 6.57 compare the upper bound results of vertical cuts between isotropic strength (K_s = 1) and two ratios of anisotropic undrained strength, K_s = 0.5, and 0.35. These comparisons clearly show important differences in predicted failure mechanisms due to undrained strength anisotropy. In contrast to the isotropic case where plastic shear distortion occurs in a band extending at 45° from the toe of the slope, anisotropic failure extends below the toe of the cut. For K_s = 0.5, failure occurs in a much broader band in the retained soil, and the failure zone extends slightly below the base of the cut (Figure 6.56). For very low anisotropic strength ratio (K_s = 0.35, Figure 6.57), the failure mechanism involves a deep-seated failure, more closely resembling a bearing capacity problem. The plastic failure zone extends behind the cut to a distance of 4H, and to a depth of 2H below the excavated grade, and emerges into the excavation 2.5H from the cut face.

6.5.2 Braced Excavations without Wall Embedment

Figures 6.58 and 6.59 compare the upper and lower bound predictions of the stability number, $N = \gamma H/s_{u45}$ for well braced excavations in a deep layer of isotropic (K_s = 1) and strongly anisotropic strength (K_s = 0.35) for rough ($f_s = s_u$) and smooth walls (f_s = 0), respectively. Table 6.7 tabulates these results. For all excavation-width ratios, H/B, the numerical limit analyses bound the true stability number with ±5% in both cases. The results shows that the stability number of anisotropic strength ratio of K_s = 0.35 is approximately 4-6% higher than for isotropic strength (K_s = 1) for all geometric aspect ratios, H/B.

Clough and Hansen (1981) proposed a modification of the Terzaghi (1943)'s basal heave calculation, which takes into account of anisotropic strength of the clay, as shown in Figure 6.60. Along the vertical plane extending through the retained soil, the undrained strength for 45°, s_{u45} is applicable. Below the bottom of excavation, a shallow bearing failure occurs and the major principal stress varies from 0°-90°. Thus, the modified bearing capacity factor given by Davis and Christian (1971) can be used to represent the resistance of the bottom of excavation. According to these assumptions,

Clough and Hansen (1981) proposed a modified factor of safety accounting for shear strength:

$$FS = \frac{N'_c \frac{1}{2}(s_{u0} + s_{u90})}{H(\gamma - \sqrt{2}s_{u45}/B)} \tag{6.15}$$

where N'_c = bearing capacity factor by Davis and Christian (1971, Figure 6.61)

The modified stability number based on Clough and Hansen (1981) can be obtained by setting FS = 1 as:

$$N = \frac{\gamma H}{s_{u45}} = N'_c \frac{1}{2}\left(\frac{s_{u0} + s_{u90}}{s_{u45}}\right) + \sqrt{2}\left(\frac{H}{B}\right) \tag{6.16}$$

In this study, it is assumed that $s_{u45} = 0.5(s_{u0} + s_{u90})$ and the anisotropic strength of clay is controlled by the parameter $K_s = s_{u90}/s_{u0}$. Thus, the resulting stability number based on the modification of Clough and Hansen (1981) can be written as:

$$N = \frac{\gamma H}{s_{u45}} = N'_c + \sqrt{2}\left(\frac{H}{B}\right) \tag{6.17}$$

where $N'_c = 5.141$ when $K_s = 1$; and $N'_c = 5.367$ when $K_s = 0.35$

This equation is also plotted in Figures 6.58 and 6.59. Even though the modifications by Clough and Hansen (1981) do show a 4-6% increase in the stability number for $K_s = 0.35$ from isotropic strength, their overall predictions do not match with those from numerical limit analyses. For smooth walls, modified solutions are conservative for aspect ratios, $B/H \geq 1$, but can overestimate the basal stability of narrow excavations ($H/B > 2$).

Figures 6.62 through 6.64 illustrate comparisons of upper bound results between isotropic strength ($K_s = 1$) and anisotropic strength, $K_s = 0.35$ for three excavation width ratios, H/B = 0.2, 1, and 3. For all cases, there is very small difference in velocity field, plastic failure zone, and failure mechanism for isotropic and anisotropic strength criteria.

6.6 Comparisons of Failure Depth of Braced Excavations with Finite Element Analyses

6.6.1 Numerical Experiments by Hashash and Whittle (1996)

This section presents the predictions of excavation height at failure in a deep non-homogeneous clay, where the undrained strength increases linearly with depth. The predictions from numerical limit analyses are compared with those from non-linear finite element analyses.

Figure 6.65 shows numerical experiments reported by Hashash and Whittle (1996) who used non-linear finite element analyses to study the effects of wall embedment depth, support conditions, and stress history profile on the undrained deformations around a braced diaphragm wall in a deep clay deposit. The analyses use a comprehensive effective stress soil model, MIT-E3 (Whittle and Kavvadas, 1994), to describe the anisotropic stress-strain strength of the clay, with input parameters selected to represent Boston Blue Clay (BBC) (Whittle et al, 1994). Their calculations consider an excavation with half-width, B/2= 20m, supported by a 0.9-m-thick diaphragm wall, and simulate a simplified construction sequence (Figure 6.65b) comprising the following steps:

1) the soil is initially excavated to a depth, h_u, without lateral support;
2) the wall is propped at the surface and excavation proceeds (in 2.5 steps) to a depth, h_e;
3) a second level of support is installed at a spacing, h ($h \leq h_e$), and soil is then removed over a further interval h_e; and
4) step 3 is repeated unit either failure occurs (or the excavation reaches a total depth H = 40m).

More details of these analyses can be found in Hashash (1992).

According to Hashash and Whittle (1996), the reported failure depth H_f from the numerical experiments of BBC at OCR = 1 profile can be related to wall length, L, as follows:

a) L =12.5m, H_f = 10-12.5m
b) L =20m, H_f = 15-17.5m
c) L =40m, H_f = 22.5-25m
d) L =60m, H_f = 30-32.5m

where L = the total length of diaphragm wall

Failure in the non-linear finite element analysis occurs when numerical convergence is not achieved during an increment of excavation (Hashash, 1992)[2].

The factor of safety for each step of excavation is evaluated using numerical limit analyses. To be comparable with the strength profile predicted by MIT-E3 soil model for OCR = 1, the analyses assume that the undrained strength of clay varies linearly from the ground surface with constant OCR such that, s_u/σ'_{v0} = const (σ'_{v0} [kPa] = 8.19z [m] + 24.5). For isotropic limit analyses, the undrained strength ratio is based on direct simple shear strength ratio, s_{uDSS}/σ'_{v0} = 0.21. Thus, the undrained strengths increase linearly with depth from 5.15 kPa at the ground surface with a gradient, ρ = 1.72 kPa/m. The wall is simulated by structural elements, with failure permitted in bending using plastic moment, M_p = 2.0 MNm/m for a heavily reinforced, 0.9m thick diaphragm wall.

6.6.1.1 Results of Isotropic Strength

Figure 6.66 compares predictions of the factor of safety (FS) against basal heave at each step of excavation depth using numerical limit analysis with failure depths reported in the FE analyses (FS = 1). For all excavation heights and diaphragm wall lengths, the factors of safety are bounded within ±5%. The calculations of limit analysis can not be expected to match exactly with the results of the finite element analysis which include anisotropic-stress-strain-strength properties of clay using the MIT-E3 model. However, the predicted failure depths from numerical limit analyses using isotropic strengths do tie in closely with the finite element analyses for L = 12.5m → 60m. Closer inspection shows an overestimate of H_f for L = 20m and 40m cases, but excellent matching at L = 12.5m and 60m.

Comparisons are also be made for the factor of safety based on the conventional Terzaghi (1943, see Equation 6.6a) and the modified Terzaghi (1943, see Equation 6.10) which takes into account of the wall embedment and the soil plug. Since the undrained strength profile is not constant, the factor of safety according to equation 6.6a and 6.10

[2] The analyses use 2.5m excavation steps, based on the selected finite element discretization. Hence, the reported failure can only be reported to a resolution of 2.5m.

must be revised to include the effect of undrained strength increasing linearly width depth, as follows:

Conventional Terzaghi (1943):

$$FS = \frac{5.7 s_{ub1}}{H(\gamma - \sqrt{2} s_{uu1} / B)} \qquad (6.19a)$$

where s_{ub1} = undrained strength at $z = H + B/(2\sqrt{2})$

s_{uu1} = undrained strength at $z = H/2$

Modified Terzaghi(1943):

$$FS = \frac{5.7 s_{ub2}}{[\gamma(H+D) - \sqrt{2} s_{uu2}(H+D)/B] - [\gamma D + 2 s_{up} D / B]} \qquad (6.19b)$$

where

s_{ub2} = undrained strength at $z = L + B/(2\sqrt{2})$

s_{uu1} = undrained strength at $z = L/2$

s_{up} = undrained strength at $z = H + D/2$

D = wall embedment = L - H

Figure 6.66 also plots the conventional and modified factor of safety of Terzaghi (1943) from equations 6.19a and 6.19b. It can be seen that the failure height predicted by Terzaghi's method does not correlate well with either the finite element analyses or the numerical limit analyses. The conventional Terzaghi (1943) predicts the failure height, H_f = 23 at FS =1, regardless of any length of the diaphragm wall. If ones take the effect of wall embedment based on the modified Terzaghi (1943), the results are: 1) no failure is predicted for L = 12.5, and 20m; 2) H_f = 35m for L = 40m; 3) H_f = 51m for L = 60m. The two latter overpredict the failure height by approximately 40% and 70% based on the finite element results. These comparisons clearly show the limitation of standard basal heave calculations.

6.6.1.2 Effects of Undrained Strength Anisotropy in Limit Analyses

In principle, one would expect improved agreement between results of FE calculations (using MIT-E3) and numerical limit analyses when undrained strength

anisotropy is included in the calculations. However, comparison of results requires further correlation of the shear resistance mobilized in the different shear directions (see Section 4.5). This section presents results for undrained strength anisotropy for three cases: 1) strengths mobilized at a shear strain, $\gamma = 0.6\%$; 2) strengths mobilized at a shear strain, $\gamma = 1\%$; and 3) peak anisotropic strength. The strain compatibility levels were selected by observing shear strain contours at failure in the non-linear finite element analyses (Hashash, 1992). The strain level, $\gamma = 0.6\%$, corresponds to an average shear strain at failure for the short wall, L = 12.5m, while $\gamma = 1\%$ corresponds to the case of longest wall, L = 60m. Figure 6.67 shows measurements of the mobilized undrained strength envelope for all three cases (after Seah, 1990; Whittle et al, 1994) together with isotropic strength based on direct simple shear test ($s_{uDSS}/\sigma'_{v0} = 0.21$). The anisotropic strength criterion of Davis and Christian (1971) fits the experimental results very closely for all three cases.

Figure 6.68 through 6.71 shows the predicted factor of safety from numerical limit analyses using the mobilized anisotropic strengths at $\gamma = 0.6\%$, 1% and peak resistance for L = 12.5m, 20m, 40m and 60m. In all of the analyses, the factors of safety are bounded within ±5%. The predicted failure height at FS = 1 are summarized in Table 6.8 and plotted in Figure 6.72. The results show the following:

1. Mobilized anisotropic strengths at $\gamma = 0.6\%$ give a better prediction of failure depth, H_f, than the isotropic strength for L = 12.5m and 20m, but tends to underestimate the failure depth for long diaphragm walls, L = 40m, and 60m.

2. Anisotropic peak strengths significantly overestimate the failure height for all lengths of diaphragm walls.

3. Isotropic strengths and mobilized anisotropic strengths at $\gamma = 1\%$ give excellent estimates H_f for cases where $L \geq 25$m.

4. Conventional Terzaghi (1943) method does not show any improvement of failure height when increasing the length of diaphragm wall.

5. Modified Terzaghi (1943) method gives an unsafe prediction of failure height for all lengths of diaphragm wall.

The above result confirms that limit analyses and FE analyses can generate similar estimate of stability in anisotropic clays but shows the importance of shear strain level γ in mobilized strength calculations as these are related to failure mechanisms in FE calculations. The difficulty in applying anisotropic strength in limit analyses is to select the strain level, γ to be used for particular stability problems. In design, this selection may be less problematic, as engineers will select γ based on allowable ground movements. Note that it is surprising that numerical limit analyses with isotropic strength provide reasonable estimates of critical excavated depths, compared to the non-linear finite element analyses.

6.6.2 Other Factors Affecting Undrained Stability

Jen (1998) has extended the FE analyses reported by Hashash (1992) to investigate study several parameters affecting ground movements for deep excavation, including: 1) excavation width; 2) depth to bedrock; 3) OCR profiles; 4) sand layers overlying clay; and 5) stiffness of bracing and diaphragm wall. Numerical limit analyses have been performed to check the failure height for the following cases from Jen's analyses:

1) Case 1: Effects of Clay Stress History

Figure 6.73 show the Group D FE analyses which study the effects of clay strength/OCR profile of the clay layer. The excavation width, B = 80m, supported by the diaphragm wall with length, L = 25, 30, 35, 40m. Five stress history profiles were selected in the FE calculations, OCR = 1.0, 1.15, 1.25, 1.7 and 2.0. The bedrock is located 100m below the ground surface. Note that the FE analyses limit the excavated depth to 20-22.5m.

From analyses of Group D, the author has selected to re-evaluate the stability of excavations with L = 25m at OCR = 1.0, and 1.15. The FE analyses predict failure depths as:

OCR = 1.0: $H_f = 17.5 - 20$m

OCR = 1.15: $H_f = 20 - 22.5$m

In numerical limit analyses, undrained (isotropic) shear strength profile of the clay is estimated based on the SHANSEP equation as: $s_u/\sigma'_{v0} = s(OCR)^m$, where s = 0.21 = undrained strength in the direct simple shear mode for OCR = 1, and m = 0.8. The plastic bending moment of the diaphragm wall, M_p = 2MNm/m. Figure 6.76 compares the predicted factor of safety as a function of excavated depth from numerical limit analyses with failure depths reported in the FE analyses (FS = 1). Limit analyses predict failure depth at FS = 1 as, H_f = 21 – 22m, and 23 - 24m for OCR = 1.0 and 1.15, respectively. It can be seen that for both OCR profiles, failure predictions from limit analyses do tie closely with the FE analyses.

2) Effect of Clay Crust and Strength of Wall

Figure 6.74 shows the Group F FE analyses which investigate the effects of clay crust layer for an excavation with B = 40m, L = 25m. The author selects to check failure of excavations in the soil profile F4 (see Figure 6.75), supported by diaphragm wall and sheet pile wall, PZ-38. This soil profile consists of 5m layer of sand, underlain by 12.5m thickness of the clay crust with decreasing OCR from = 2.4 to 1.0, and 32.5m of normally consolidated clay. The bedrock is located 50m below the ground surface. The FE analyses predict failure depths for different types of wall as:

Diaphragm wall: H_f = 20 – 22.5m

Sheet pile wall, PZ-38: H_f = 15 – 17.5m

In limit analyses, the strength of sand layer is controlled by the Mohr-Coulomb yield criterion with frictional angle, ϕ = 30°; while the undrained strength of clay crust and normally consolidated clay is controlled by Tresca (isotropic) yield criterion. The shear strength profile of clay is approximated using the SHANSEP equation as explained in the previous case. The plastic moment of diaphragm wall and sheet pile wall, M_p = 2 and 0.76 MNm/m, respectively.

Figure 6.77 shows the predicted factor of safety for effects of clay crust and wall strengths from numerical limit analyses. The differences of FS between the lower and upper bound calculations are within ±5% for all calculations. Limit analyses predict failure at FS = 1 as, H_f = 21-22m and 19.5-21.5m for diaphragm wall and sheet pile,

respectively. There is an excellent agreement in predicted failure depths for the case of diaphragm wall between numerical limit analyses and the finite element analyses. However, limit analyses overestimate the failure depth for the case of the sheet pile wall by approximately 5m.

6.6.3 Factor of Safety Versus Wall Deflection

Several researchers have proposed empirical methods for estimating ground movements using the factor of safety against basal heave failure. For example, Mana and Clough (1981) and Clough and O'Rourke (1990) have shown that measurements of maximum lateral wall deflection, δ_{wmax} can be correlated with the factor of safety against basal heave as defined by Terzaghi (1943), Figure 6.78. They report large deflections (δ_{wmax} > 0.02H-0.03H) for walls embedded in soft clays with factors of safety less than 1.5. Although these results provide initial guidance on the expected magnitudes of deformations, most of the existing data were obtained from excavations less than 15m deep, with relatively flexible lateral earth support systems (i.e., sheet pile and soldier pile walls).

Figure 6.79 plots the factor of safety predicted from the numerical limit analyses as a function of maximum wall deflection (δ_{wmax}/H) reported by the finite element analyses (Hashash and Whittle, 1996; Jen, 1998). Although there is clearly a correlation between FS and δ_w/H, the large scatter in this theoretically derived band suggests that other parameters such as excavation width, wall length and strength, and soil profiles are also important.

6.7 References

Atkinson, J. H. (1981). Foundations and Slopes, McGraw-Hill.

Bjerrum, L., and Eide, O. (1956). "Stability of strutted excavations in clay." Géotechnique, 6, 115-128.

Clough, G. W., and Hansen, L. A. (1981). "Clay anisotropy and braced wall behavior." J. of Geotech. Engrg., ASCE, 107(7), 893-913.

Clough, G. W. and O'Rourke, T. D. (1990). "Construction induced movements of insitu walls." Design and performance of earth retaining structures, Geotech. Spec. Publ. No. 25, ASCE, N.Y., 439 – 470.

Davis, E. H., and Christian, T. J. (1971). "Bearing capacity of anisotropic cohesive soil.". J. Soil Mech. Found. Div., ASCE, 97(5), 753-769.

Hashash, Y. M. A (1992). "Analysis of deep excavations in clay.", PhD thesis, Massachusetts Inst. of Tech (MIT)., Cambridge, Mass.

Hashash, Y. M. A., and Whittle, A. J. (1996). "Ground movement prediction for deep excavations in soft clay.". J. of Geotech. Engrg, ASCE, 122(6), 474-486.

Heyman, J. (1973). "The stability of a vertical cut." Int. J. Mech. Sci., 15, 845-854.

Ladd, C. C. (1991). The Twenty-Second Terzaghi Lecture "Stability evaluation during staged construction.", J. of Geotech. Engrg., ASCE, 117(4), 537-615.

Jen, L. C. (1998). "The design and performance of deep excavations in clay.", PhD thesis, Massachusetts Inst. of Tech. (MIT), Cambridge, Mass.

Mana, A. I., and Clough, G. W. (1981). "Prediction of movements for braced cuts in clay.". J. of Geotech. Engrg, ASCE, 107(6), 759-777.

O'Rourke, T. D. (1993). "Base stability and ground movement prediction for excavations in soft clay." Proc. ICE Conf. on Retaining Structures, Cambridge, Thomas Telford, 131-139.

Seah, T. H. (1990). "Anisotropy of normally consolidated Boston blue clay.", ScD thesis, Massachusetts Inst. of Tech. (MIT), Cambridge, Mass.

Terzaghi, K. (1943). Theoretical Soil Mechanics, John Wiley & Sons, New York.

Whittle, A. J., Hashash, Y.M.A., and Whitman, R.V. (1993). "Analysis of a deep excavation in Boston." J. of Geotech. Engrg., ASCE, 119(1), 69-90.

Whittle, A. J., DeGroot, D. J., Ladd, C. C., and Seah, T. H. (1994). "Model prediction of anisotropic behavior of Boston Blue Clay " J. of Geotech. Engrg. Div., ASCE, 120(1), 199-224.

Whittle, A.J. and Kavvadas, M. (1994). "Formulation of the MIT-E3 constitutive model for over consolidated clays." J. of Geotech. Engrg., ASCE, 120(1), 173-198.

H/B	Stability Number from numerical limit analysis, $N = \gamma H/s_u$						Terzaghi (1943)	Bjerrum & Eide (1956)
	Rough wall			Smooth wall				
	LB.	UB.	Bound (%)	LB.	UB.	Bound (%)	$\gamma H/s_u$	$\gamma H/s_u$
1.0	6.684	7.169	7.0	6.353	6.748	6.0	7.114	6.333
1.5	7.129	7.767	8.6	6.640	7.190	8.0	7.821	6.700
2.0	7.480	8.127	8.3	6.908	7.443	7.5	8.528	7.000
2.5	7.764	8.427	8.2	7.103	7.668	7.7	9.235	7.233
3.0	8.024	8.683	7.9	7.263	7.865	8.0	9.942	7.367

B/H	Stability Number from numerical limit analysis, $N = \gamma H/s_u$						Terzaghi (1943)	Bjerrum & Eide (1956)
	Rough wall			Smooth wall				
	LB.	UB.	Bound (%)	LB.	UB.	Bound (%)	$\gamma H/s_u$	$\gamma H/s_u$
1.0	6.684	7.169	7.0	6.353	6.748	6.0	7.114	6.333
2.0	6.056	6.520	7.4	5.993	6.339	5.6	6.407	5.833
3.0	5.863	6.174	5.2	5.833	6.098	4.4	6.171	5.633
4.0	5.696	5.973	4.7	5.689	5.934	4.2	6.054	5.500
5.0	5.595	5.868	4.8	5.591	5.836	4.3	5.983	5.400

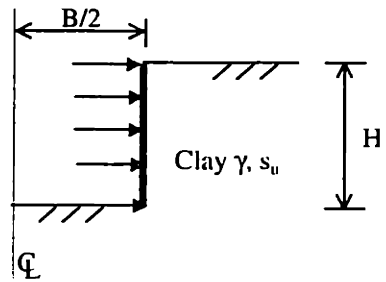

Table 6.1 Numerical limit analysis for a braced excavation in deep homogeneous clay - without wall embedment

H/B	Stability Number from numerical limit analysis, $N = \gamma H/s_u$						Terzaghi (1943)	
	Deep clay layer			$d_b/H=1.0$			Deep clay layer	$d_b/H=1.0$
	LB.	UB.	Bound (%)	LB.	UB.	Bound (%)	$\gamma H/s_u$	$\gamma H/s_u$
1.0	6.684	7.169	7.0	6.808	7.432	8.8	7.114	7.114
1.5	7.129	7.767	8.6	7.161	7.884	9.6	7.821	7.821
2.0	7.480	8.127	8.3	7.497	8.163	8.5	8.528	8.528
2.5	7.764	8.427	8.2	7.765	8.435	8.3	9.235	9.235
3.0	8.024	8.683	7.9	8.025	8.685	7.9	9.942	9.942

B/H	Stability Number from numerical limit analysis, $N = \gamma H/s_u$						Terzaghi (1943)	
	Deep clay layer			$d_b/H=1.0$			Deep clay layer	$d_b/H=1.0$
	LB.	UB.	Bound (%)	LB.	UB.	Bound (%)	$\gamma H/s_u$	$\gamma H/s_u$
1.0	6.684	7.169	7.0	6.808	7.432	8.8	7.114	7.114
2.0	6.056	6.520	7.4	6.683	7.332	9.3	6.407	6.700
3.0	5.863	6.174	5.2	6.698	7.232	7.7	6.171	6.700
4.0	5.696	5.973	4.7	6.698	7.232	7.7	6.054	6.700
5.0	5.595	5.868	4.8	6.698	7.232	7.7	5.983	6.700

Notes: Numerical results correpond to rough walls.

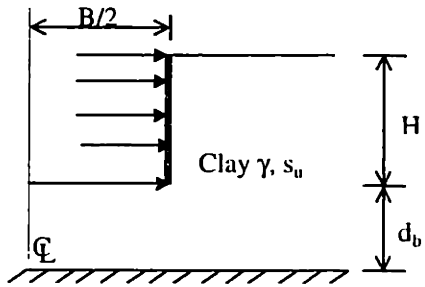

Table 6.2 Numerical limit analysis for a braced excavation in a finite depth of clay - without wall embedment

Without Wall Embedment, D = 0m

Numerical Limit Analysis	Existing Solutions
UB: $\gamma H/s_u = 6.258$	Terzaghi (1943): $\gamma H/s_u = 6.230$
LB: $\gamma H/s_u = 5.913$	Bjerrum & Eide (1959): $\gamma H/s_u = 5.667$
Bound = 5.7%	O'Rourke (1993): $\gamma H/s_u = 5.667$

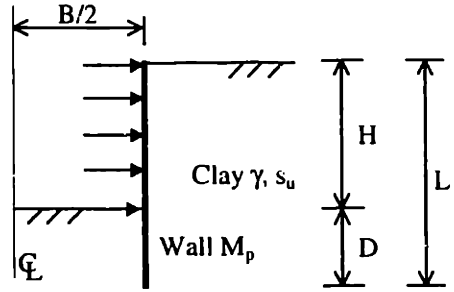

H=15m., B/2= 20m. [H/B = 0.375]

With Wall Embedment

Relative Strength Parameter $M_p/(s_uD^2)$	Numerical Limit Analysis, D = 10 m. (D/H = 2/3)			Numerical Limit Analysis, D = 30 m. (D/H = 2)			O'Rourke (1993)
	Stability Number, $\gamma H/s_u$		Bound (%)	Stability Number, $\gamma H/s_u$		Bound (%)	$\gamma H/s_u$
	LB	UB		LB	UB		
0.01	5.867	6.448	9.4	5.976	6.537	9.0	5.675
0.025	5.908	6.461	8.9	6.104	6.619	8.1	5.688
0.05	5.957	6.481	8.4	6.240	6.733	7.6	5.708
0.10	6.001	6.516	8.2	6.405	6.894	7.4	5.749
0.25	6.020	6.580	8.9	6.590	7.085	7.2	5.873
0.50	6.147	6.649	7.8	6.824	7.302	6.8	6.078
1.00	6.245	6.766	8.0	7.203	7.667	6.2	6.489
1.50	6.317	6.864	8.3	7.494	7.955	6.0	6.901
2.00	6.371	6.948	8.7	7.713	8.184	5.9	7.312
3.00	6.442	7.086	9.5	8.049	8.535	5.9	8.134
4.00	6.473	7.169	10.2	8.261	8.751	5.8	8.957
6.00	6.474	7.176	10.3	8.272	8.759	5.7	10.602
10.00	6.474	7.176	10.3	8.272	8.759	5.7	13.892

Notes:

O'Rourke (1943): $\gamma H/s_u = 5.667 + (M_y\pi^2)/(8s_uD^2)$, where $M_p/M_y = 1.5$ for a rectangular section

Table 6.3 Stability number for a braced excavation with wall embedment

$$\frac{\gamma H}{s_u} = \frac{5.141\left(\frac{B}{H}\right) + b_2 + b_3\sqrt{\frac{M_p}{s_u D^2}}\left(\frac{D}{H}\right) + \left(\frac{M_p}{s_u D^2}\right)\left(\frac{D}{H}\right)^2\left\{c_2\left(\frac{D}{H}\right)\left(\frac{H}{B}\right)^2 + c_3\sqrt{\frac{(D/H)}{(H/B)}}\right\}}{\frac{B}{H} + a_2 + \sqrt{\frac{M_p}{s_u D^2}}\left(\frac{D}{H}\right)\left\{a_3\left(\frac{D}{H}\right) + a_4\sqrt{\left(\frac{D}{H}\right)}\right\}}$$

where

B = excavation width

H = excavation depth

D = embedded length of wall

γ = unit weight of clay

s_u = undrained shear strength

M_p = plastic moment of wall

a_2, a_3, a_4, b_2, b_3, c_2, c_3 = coefficients

Coefficients	Upper Bound	Lower Bound	Average
a_2	0.72073	0.48241	0.60787
a_3	0.22389	0.17722	0.20780
a_4	-0.23154	-0.21965	-0.22420
b_2	7.38059	4.79973	6.10244
b_3	2.42912	1.68233	2.08235
c_2	0.17324	0.08319	0.14663
c_3	0.18978	0.12951	0.17204
r^2 curve fit	99.25%	99.38%	99.36%

Special Case: $M_p = 0$ or $D = 0$ (Braced Excavation without wall embedment)

$$\frac{\gamma H}{s_u} = \frac{5.141\left(\frac{B}{H}\right) + b_2}{\frac{B}{H} + a_2}$$

Table 6.4 Proposed equation of stability number of braced excavations in homogeneous clay

Number	Soil	Index Properties			Peak s_u/σ'_{vc}		Strain Compatibility, s_u/σ'_{vc}					C/E testing[b]	Tests by	$K_s = \tau_e/\tau_c$
		USC	I_p (%)	I_L	q_f(TC)	τ_h(DSS)	γ^a (%)	τ_c	τ_d	τ_e	τ_{ave}			
1	B2 marine clay	CL	8.5	2.6	0.31	0.23	1.5	0.26	0.22	0.09	0.19	TX	SEBJ	0.35
2	B6 marine clay	CL	13	1.9	0.33	0.24	2	0.26	0.225	0.16	0.215	TX	SEBJ	0.62
3	Resedimented BBC	CL	21	1.0	0.33	0.20	6	0.265	0.20	0.135	0.20	PS	MIT	0.51
4	Connecticut Valley varved clay	CL CH	12 39	-	0.25	0.16	6	0.21	0.15	0.20	0.185	PS	MIT	0.95
5	Great Salt Lake clay	CH	40	1.1	0.37	0.24	8	0.27	0.24	0.16	0.225	TX	MIT	0.59
6	AGS marine clay	CH	43	0.6	0.325	0.255	8	0.265	0.25	0.16	0.225	PS	MIT UBC	0.60
7	Omaha, Nebr. Clay	CH	60	0.7	0.315	0.22	10	0.23	0.21	0.20	0.215	TX[c]	MIT	0.87
8	Arctic silt A	ML	15	0.3	0.37	0.245	12	0.305	0.24	0.18	0.24	TX	MIT	0.59
9	Arctic silt B	MH	30	0.7	0.32	0.24	12	0.27	0.24	0.20	0.235	TX	MIT	0.74
10	EABPL clay	CH	75	0.85	0.24	0.235	15	0.24	0.23	0.22	0.23	PS/TX[d]	MIT	0.92

[a] Design shear strain selected for strain compatibility
[b] TX = triaxial and PS = plane strain
[c] Triaxial τ_c increased by 5%
[d] Approximate mean of plane strain and triaxial data

Table 6.5 Normally consolidated undrained strength ratios from CK_0U compression, direct simple shear and extension tests accounting for strain compatibility (After Ladd, 1991)

Anisotropic Undrained Strength Ratio $K_s = s_{u90}/s_{u0}$	Stability Number by Numerical Limit Analyses $N = \gamma H/s_{u45}$ LB – UB	Upper Bound Solutions by Chen (1975) $N = \gamma H/s_{u45}$
0.35	5.242 – 5.469	-
0.40	5.055 – 5.376	-
0.50	4.736 – 5.096	5.013
0.60	4.449 – 4.809	4.725
0.70	4.202 – 4.543	4.459
0.80	3.969 – 4.308	4.233
0.90	3.793 – 4.096	4.021
1.0 (Isotropic)	3.634 – 3.902	3.830

Note: $s_{u45} = 0.5(s_{u0} + s_{u90})$

Table 6.6 Stability number of vertical cuts in anisotropic homogeneous clay

H/B	Stabilty Number from numerical limit analysis, $N = \gamma H/s_{u45}$						Clough & Hansen (1981) $\gamma H/s_{u45}$
	Rough wall			Smooth wall			
	LB.	UB.	Bound (%)	LB.	UB.	Bound (%)	
1.0	7.048	7.572	7.2	6.765	7.185	6.0	6.781
1.5	7.565	8.229	8.4	7.090	7.676	7.9	7.488
2.0	7.981	8.642	8.0	7.370	7.959	7.7	8.195
2.5	8.284	8.976	8.0	7.587	8.204	7.8	8.902
3.0	8.564	9.260	7.8	7.782	8.418	7.9	9.610

B/H	Stabilty Number from numerical limit analysis, $N = \gamma H/s_{u45}$						Clough & Hansen (1981) $\gamma H/s_{u45}$
	Rough wall			Smooth wall			
	LB.	UB.	Bound (%)	LB.	UB.	Bound (%)	
1.0	7.048	7.572	7.2	6.765	7.185	6.0	6.781
2.0	6.364	6.840	7.2	6.321	6.712	6.0	6.074
3.0	6.138	6.456	5.1	6.117	6.405	4.6	5.838
4.0	5.953	6.237	4.7	5.950	6.211	4.3	5.720
5.0	5.840	6.130	4.8	5.838	6.102	4.4	5.650

Note:
$K_s = s_{u90}/s_{u0}$
$s_{u45} = 0.5(s_{u0} + s_{u90})$

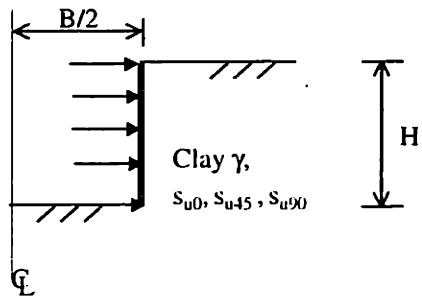

Table 6.7 Numerical limit analysis for a braced excavation in anisotropic homogeneous clay, where $K_s = 0.35$

Predicted Excavation Depth at Failure	Length of Diaphragm Wall, L (m)			
	12.5	20.0	40.0	60.0
Finite Element Method (FEM) Hashash & Whittle (1996)	**10-12.5 m**	**15-17.5 m**	**22.5-25 m**	**30-32.5 m**
Numerical Limit Analyses				
Isotropic Strength	12.0-12.5 m	18.5-19.0 m	24.5-29.5 m	27.5-34 m
Anisotropic Strength, $\gamma = 0.6$ %	10.5-11.5 m	14.5-16.5 m	17.5-20 m	19.5-22.5
Anisotropic Strength, $\gamma = 1$ %	11.5-12.0m	18.0-18.5 m	22.5-26.5 m	25.0-30.5 m
Peak Anisotropic Strength	no failure	20 m	35.5-39 m	46.5-56.5 m
Conventional Terzaghi (1943)				
$s_u(DSS)/\sigma'_{v0} = 0.21$	23 m	23 m	23 m	23 m
$s_u(TE)/\sigma'_{v0} = 0.17$	14.5 m	14.5 m	14.5 m	14.5 m
Modified Terzaghi (1943)				
$s_u(DSS)/\sigma'_{v0} = 0.21$	no failure	no failure	35 m	51 m
$s_u(TE)/\sigma'_{v0} = 0.17$	no failure	17 m	29 m	43 m

Notes:

1) $s_u(DSS)/\sigma'_{v0} = 0.21$ for NC clay (BBC)

2) Anisotropic undrained strength ratios for NC clay (BBC)

	$s_u(0°)/\sigma'_{v0}$	$s_u(45°)/\sigma'_{v0}$	$s_u(90°)/\sigma'_{v0}$
$\gamma = 0.6\%$	0.34	0.09	0.03
$\gamma = 1.0\%$	0.34	0.15	0.075
Peak Strength	0.34	0.23	0.17

Table 6.8 Comparisons of basal heave analyses by FEM and numerical limit analyses

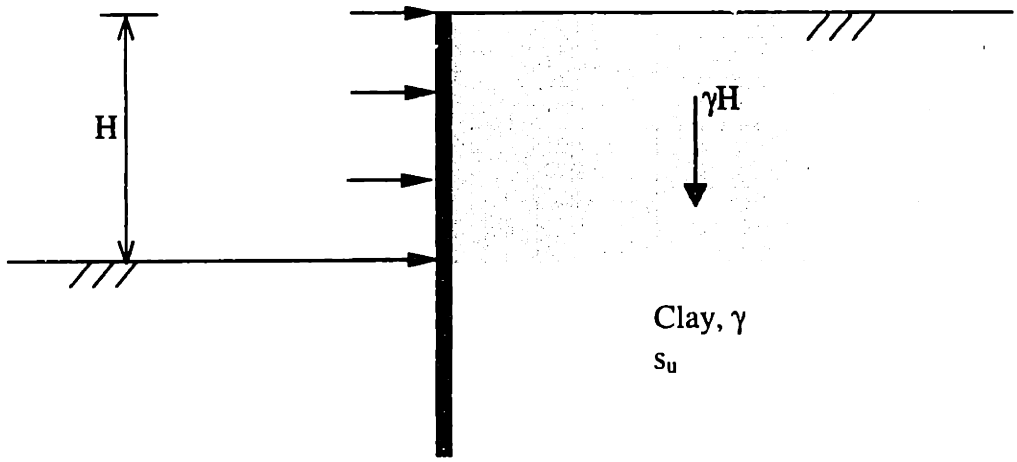

a) Homogeneous soil profile: Optimize (γH)

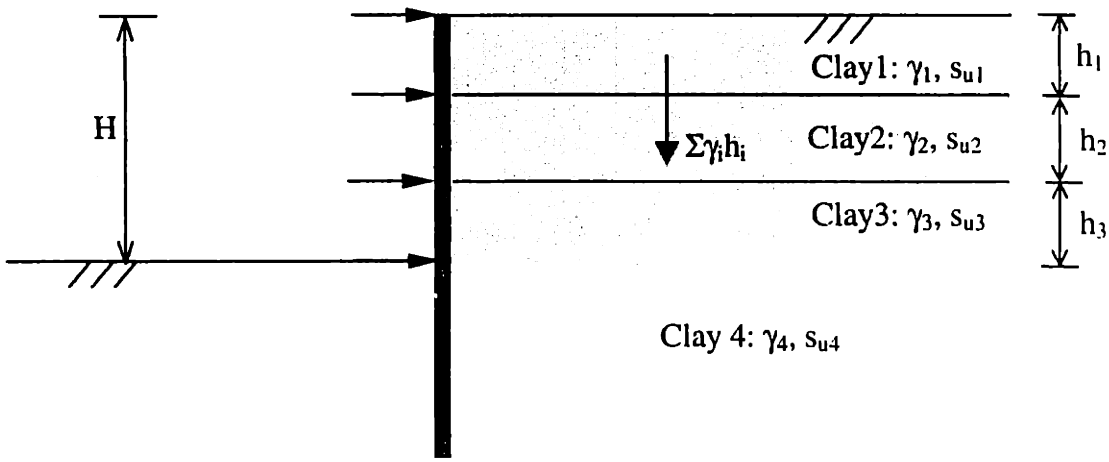

b) Non-homogeneous soil profile: Optimize ($\Sigma\gamma_i h_i$)

Figure 6.1 Objective function of braced excavations in numerical limit analyses

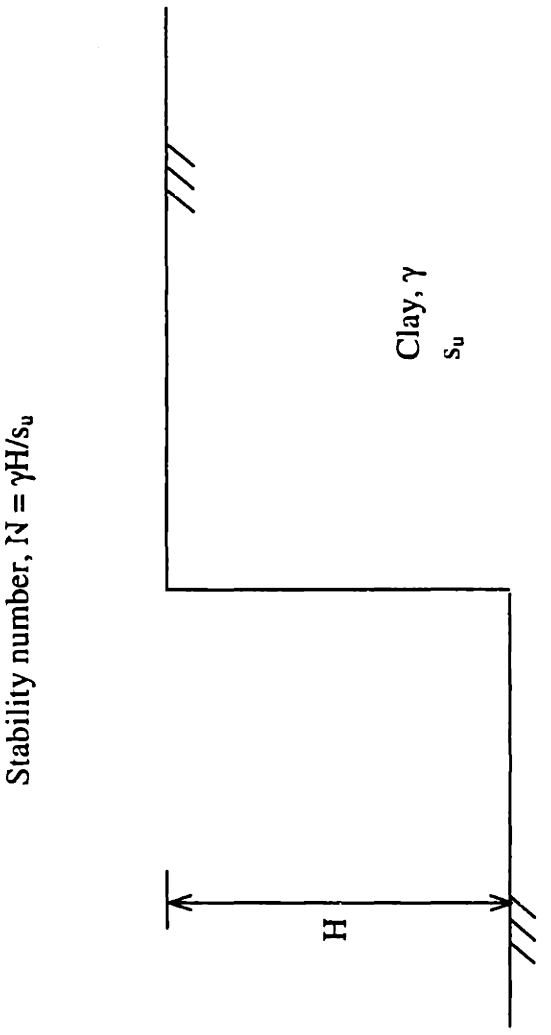

Figure 6.2 Stability of an unsupported vertical cut in homogeneous clay

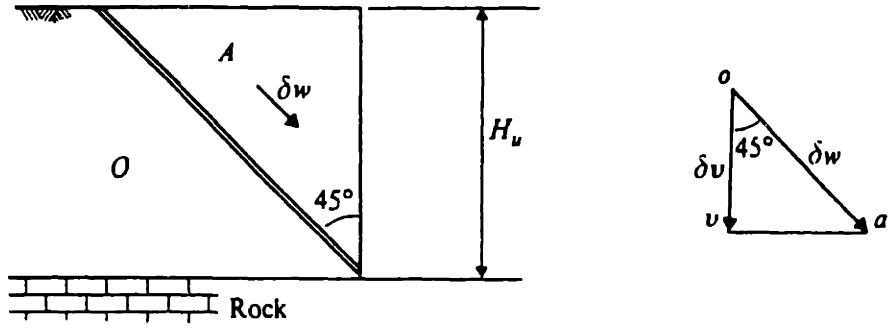

a) Upper bound solution

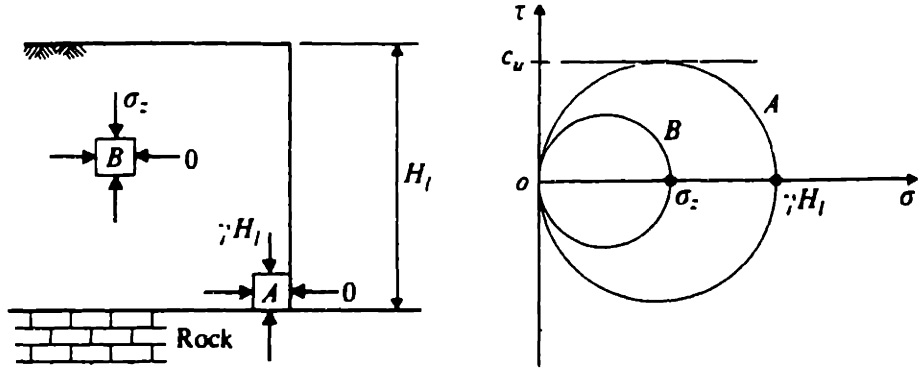

b) Lower bound solution

Figure 6.3 Lower and upper bound solutions for a vertical cut in a homogeneous clay (After Atkinson, 1981)

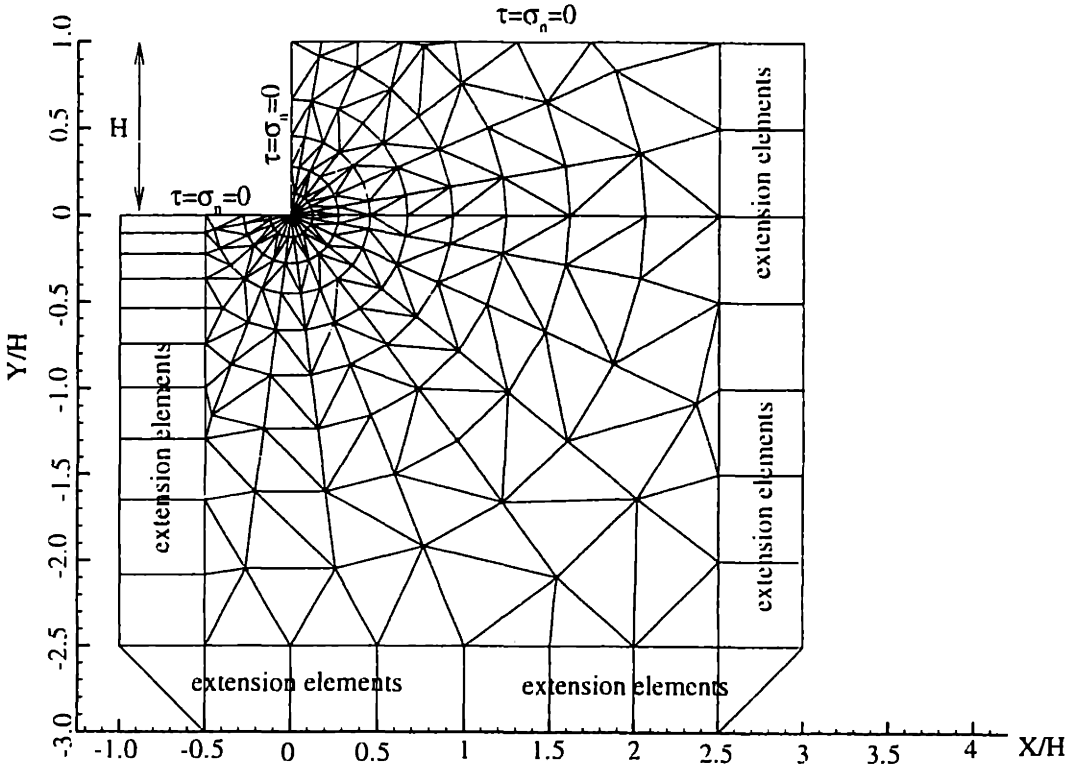

a) Lower bound mesh

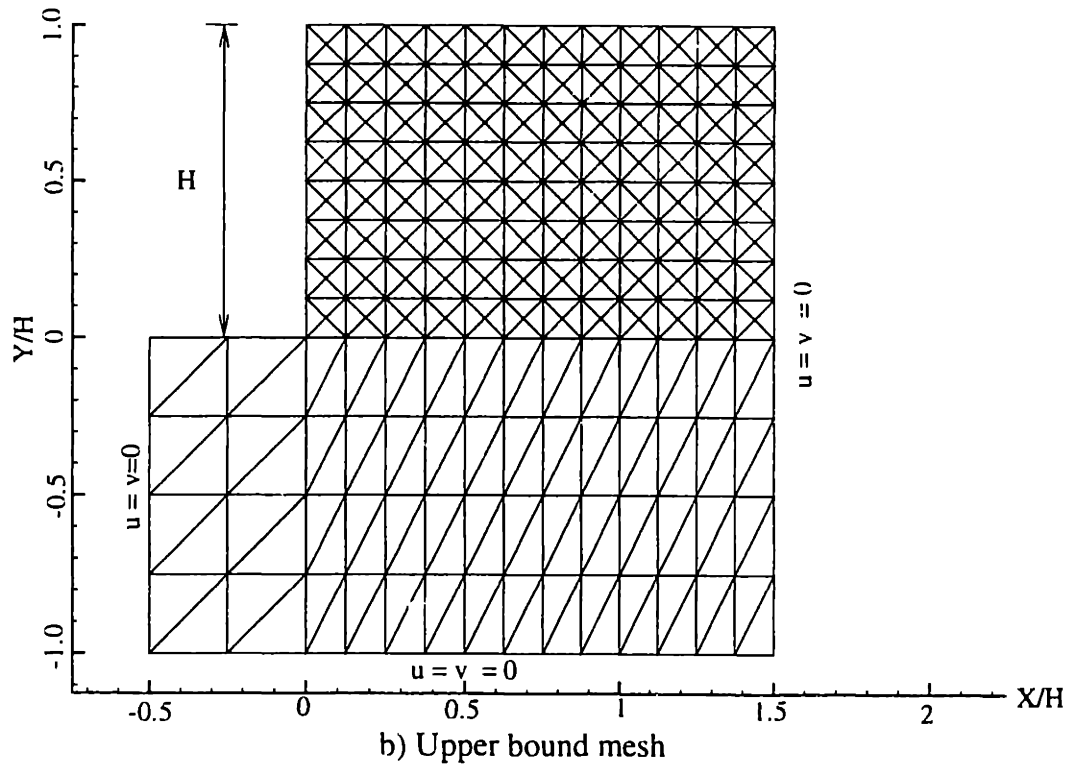

b) Upper bound mesh

Figure 6.4 Spatial discretization of vertical cuts in clay for numerical limit analyses

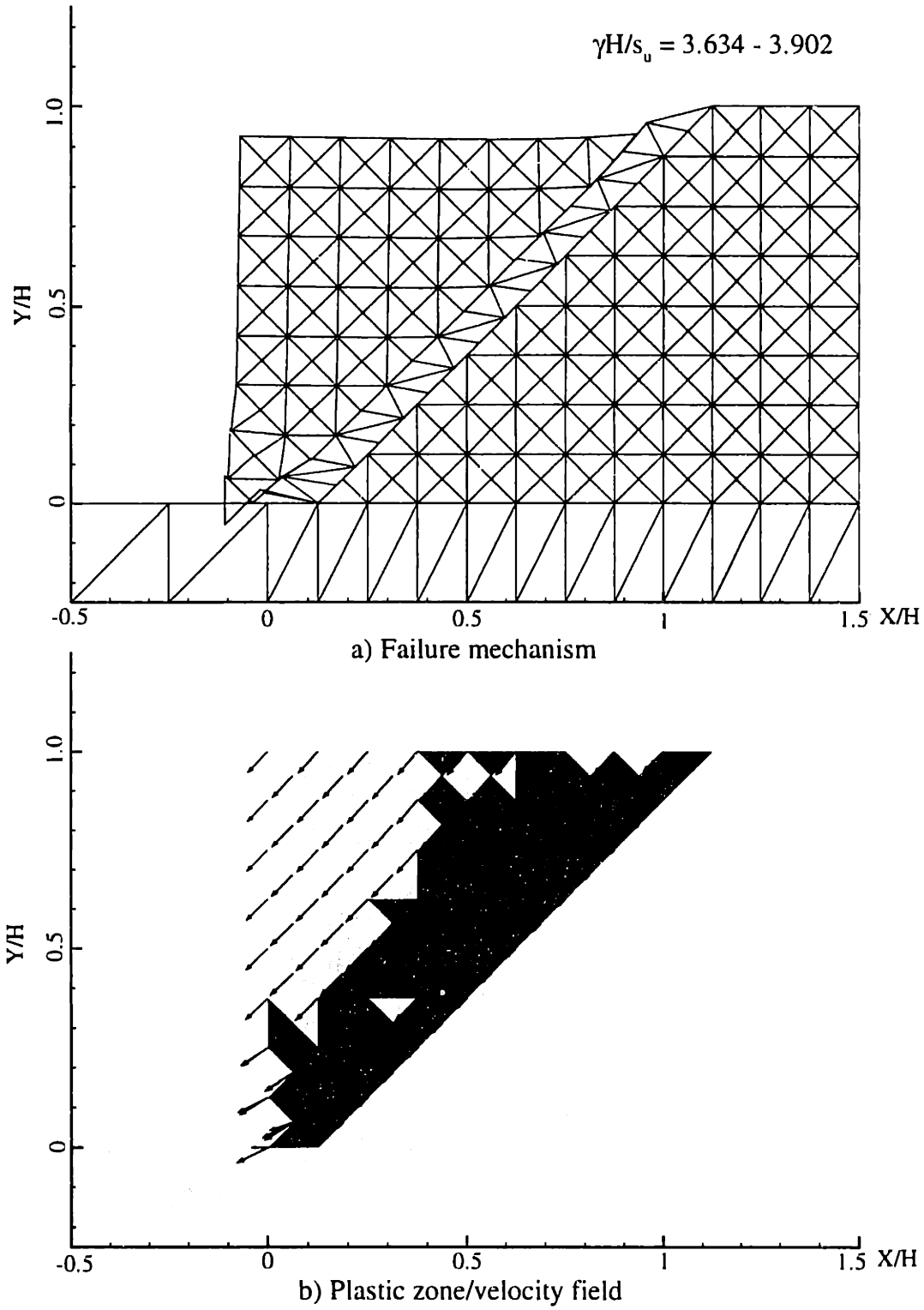

Figure 6.5 Upper bound results for a vertical cut in clay

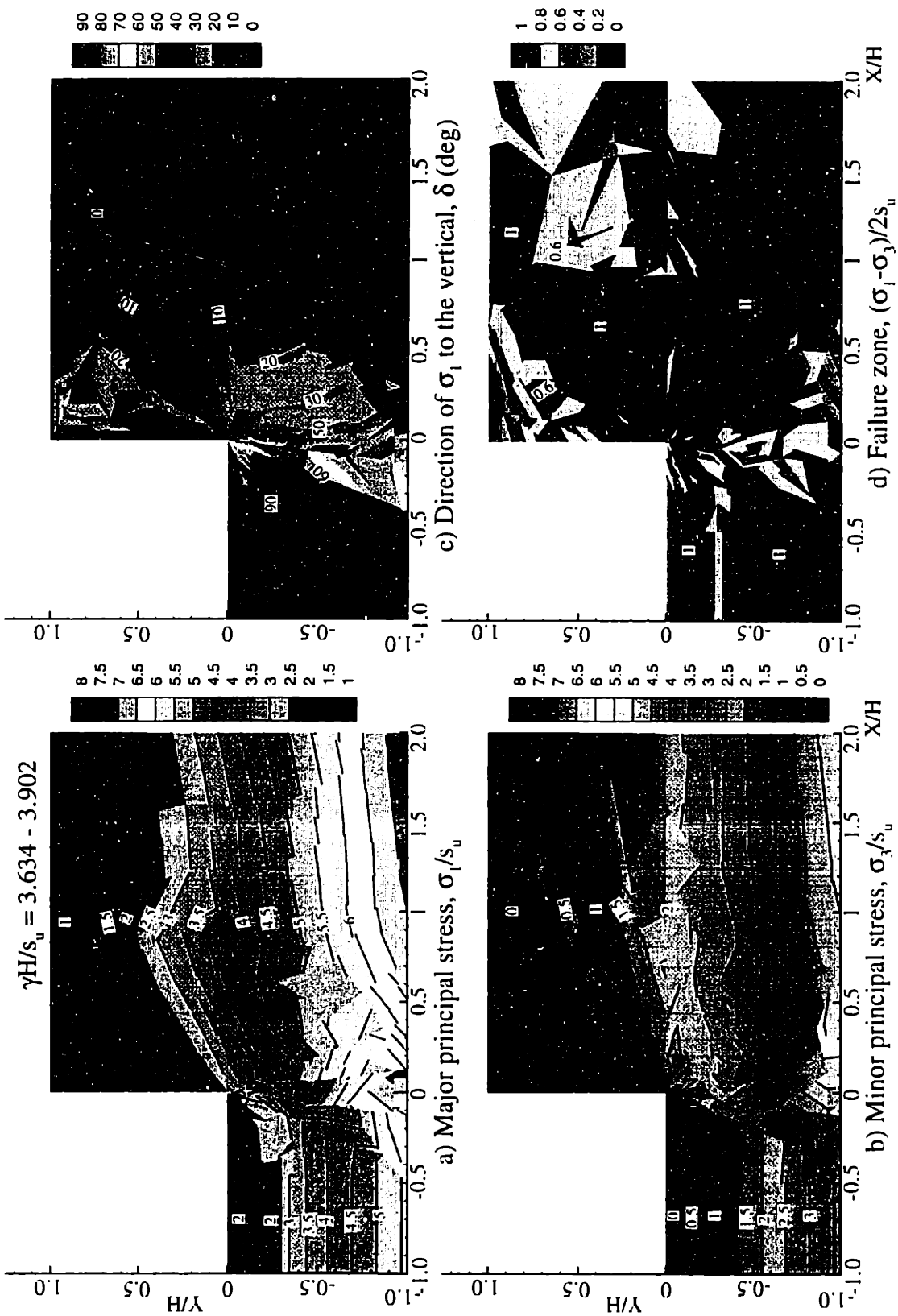

Figure 6.6 Lower bound results for a vertical cut in clay

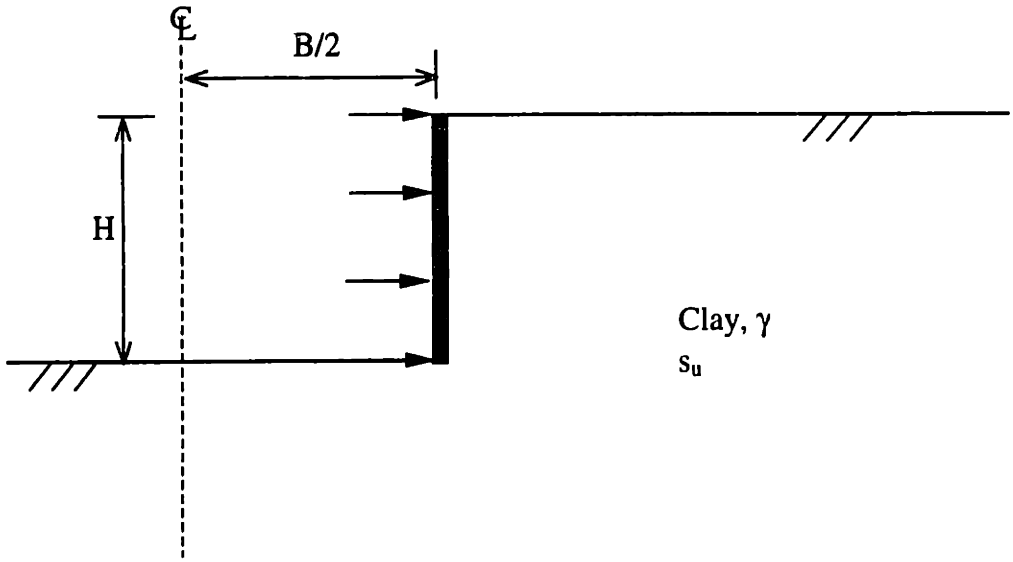

a) Without wall embedment

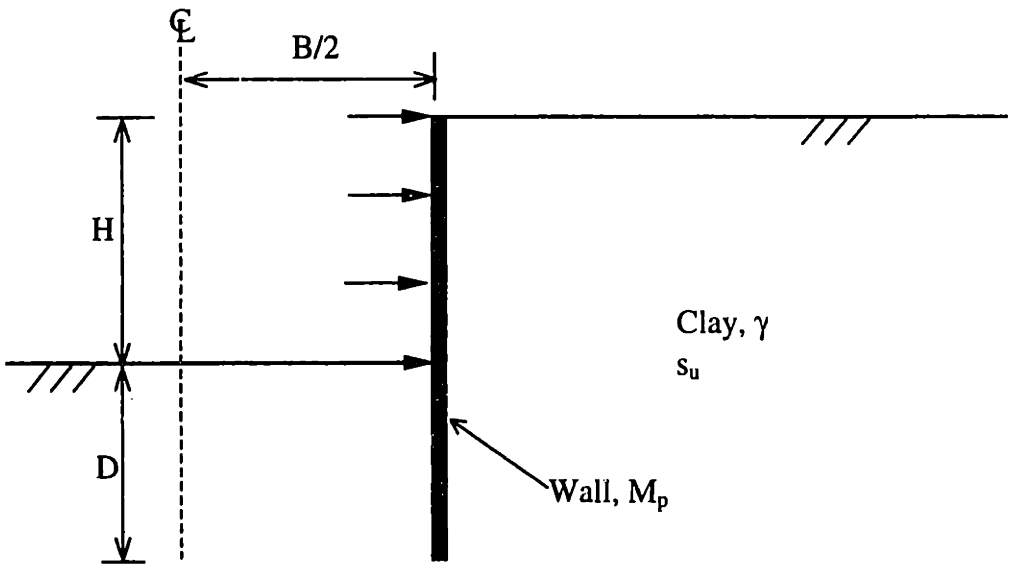

b) With wall embedment

Figure 6.7 Problem notations for braced excavations in clay

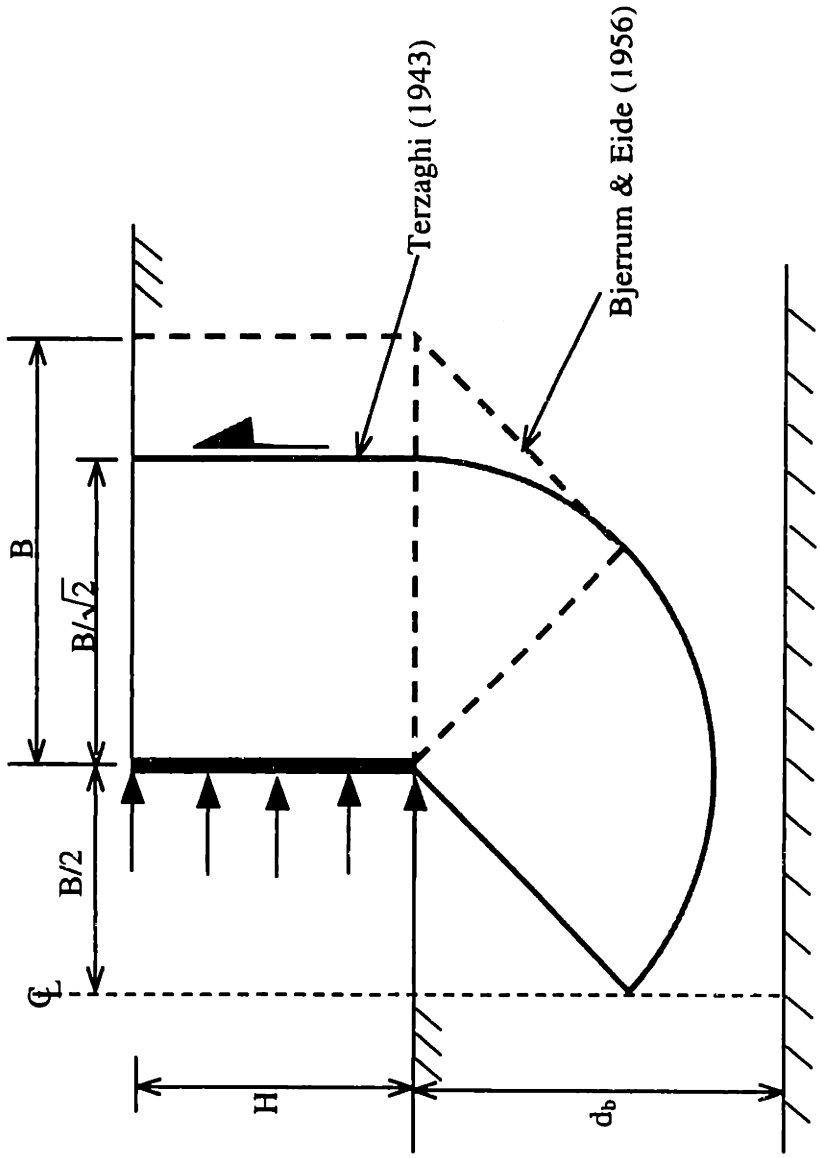

Figure 6.8 Standard basal heave calculations for braced excavations without wall embedment

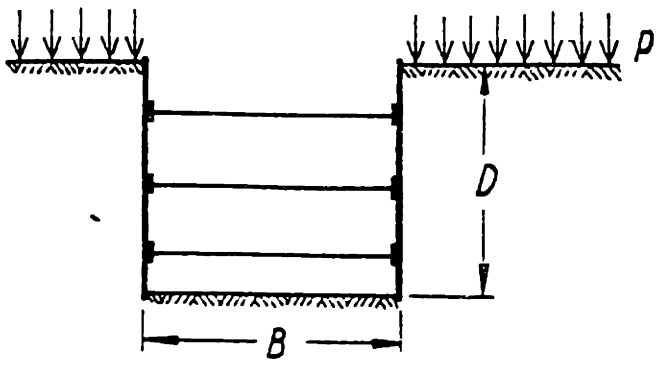

$$F = N_c \frac{s}{\gamma D + p}$$

D = depth of excavation
B = width of excavation
L = length of excavation
p = surcharge
s = undrained shear strength of clay
γ = density of clay
N_c = coefficient
F = safety factor

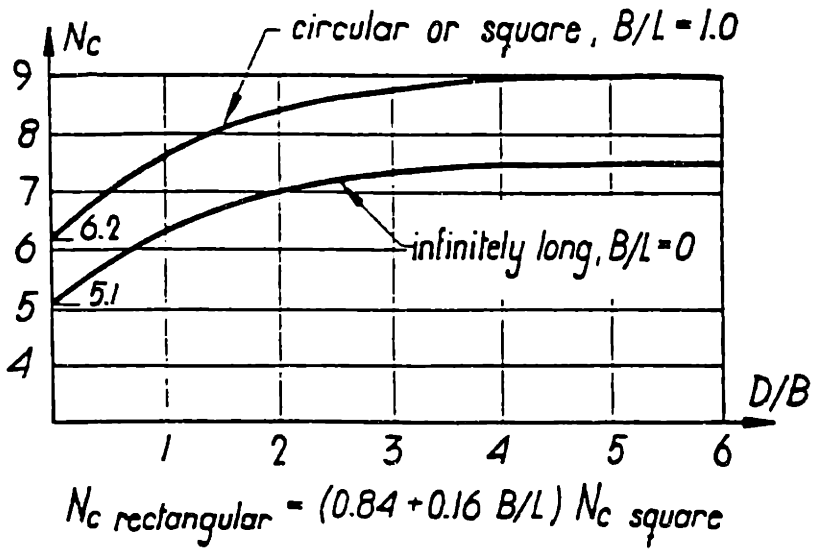

Figure 6.9 Stability number of braced excavation by Bjerrum and Eide (1956)

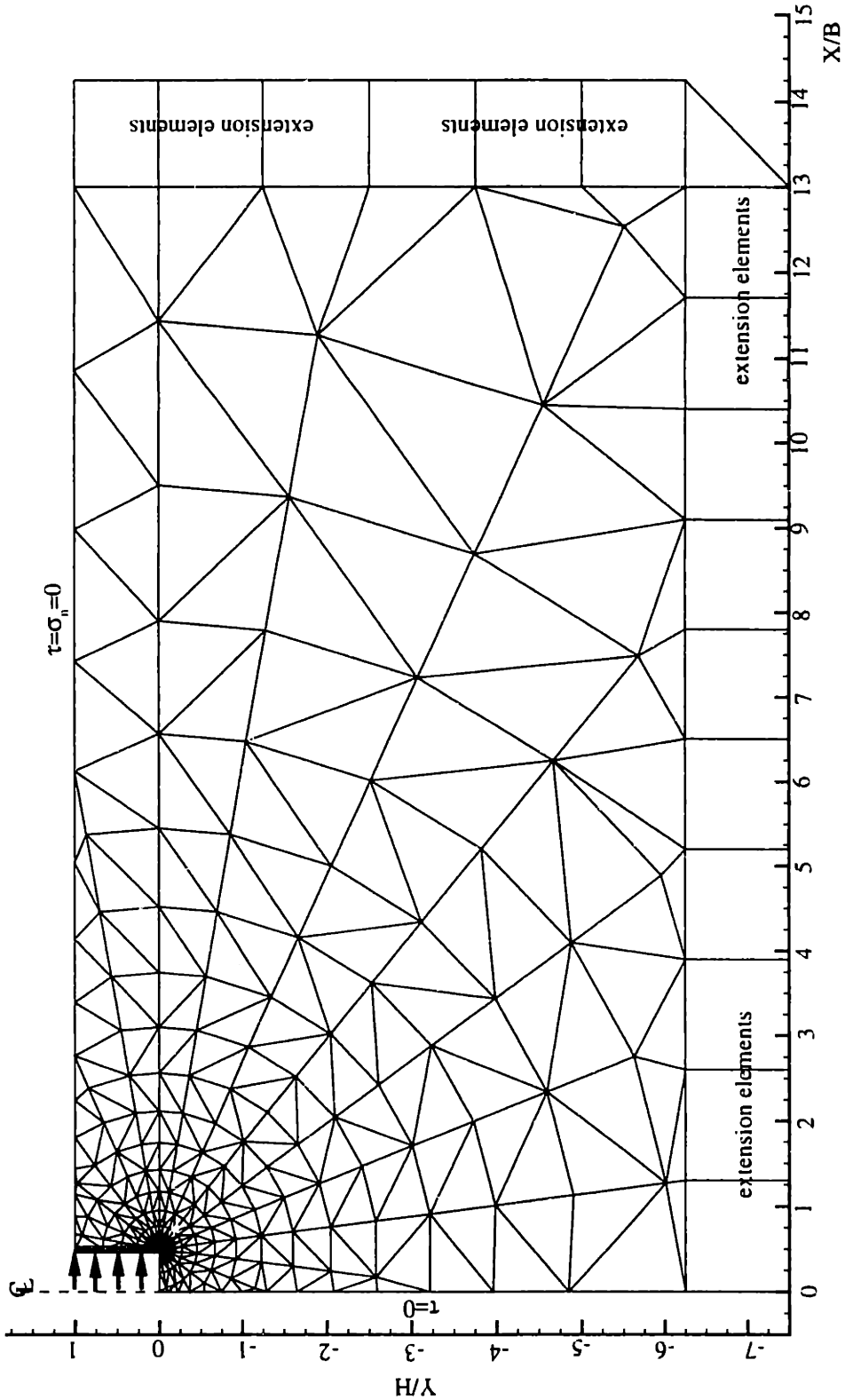

Figure 6.10 Typical lower bound mesh for a braced excavation in clay

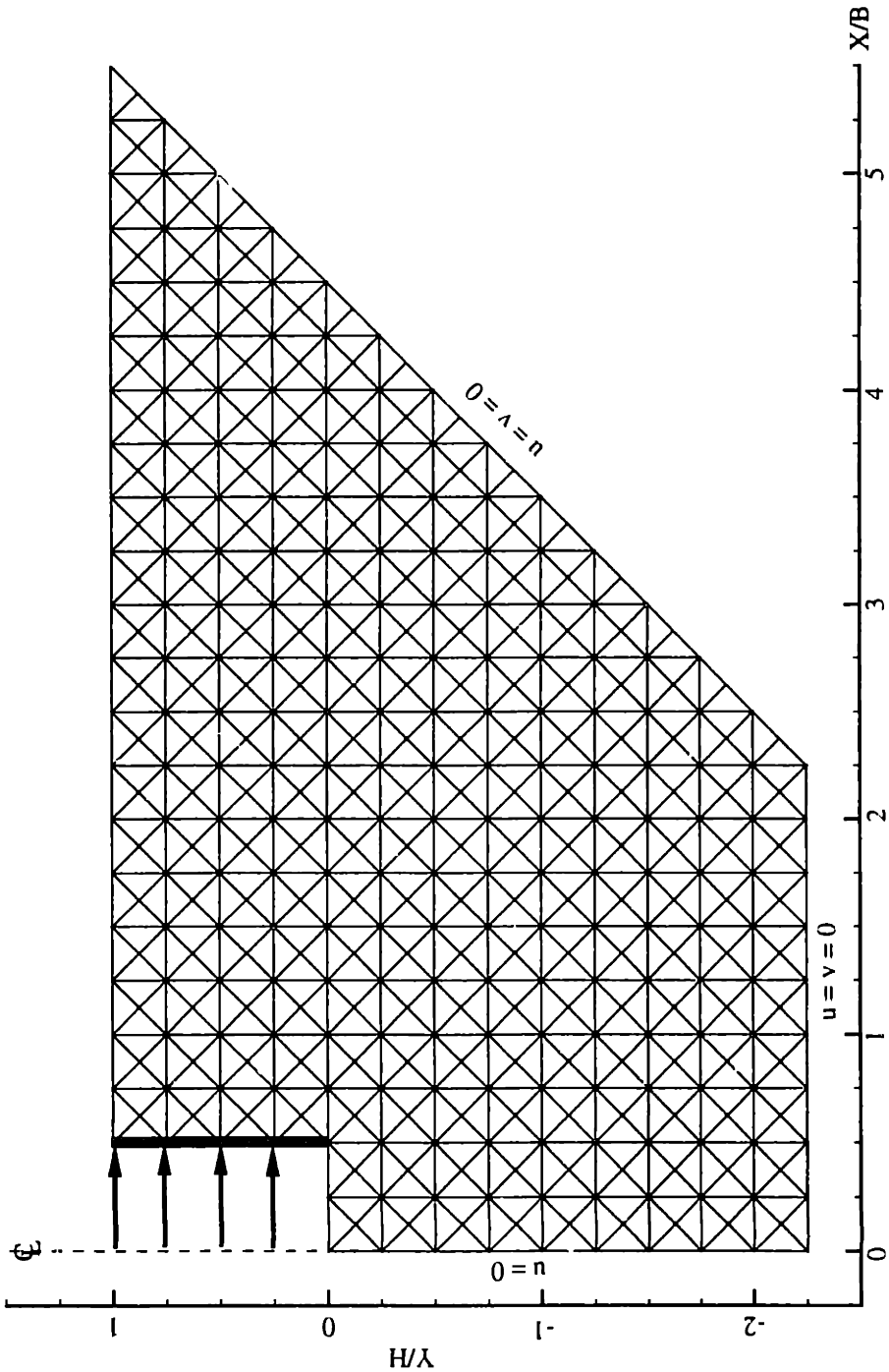

Figure 6.11 Typical upper bound mesh for a braced excavation in clay

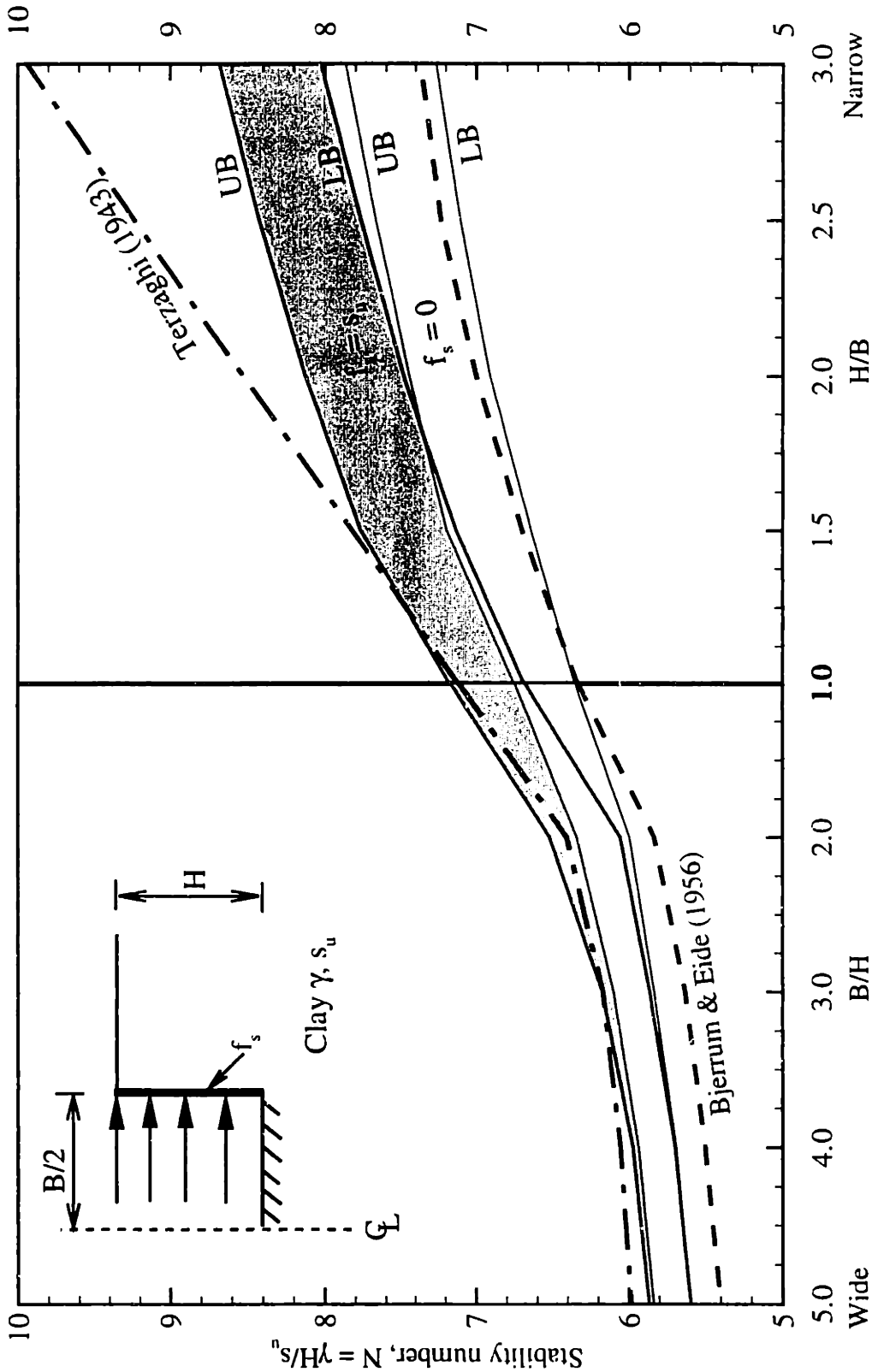

Figure 6.12 Undrained stability of a braced excavation in clay by numerical limit analyses

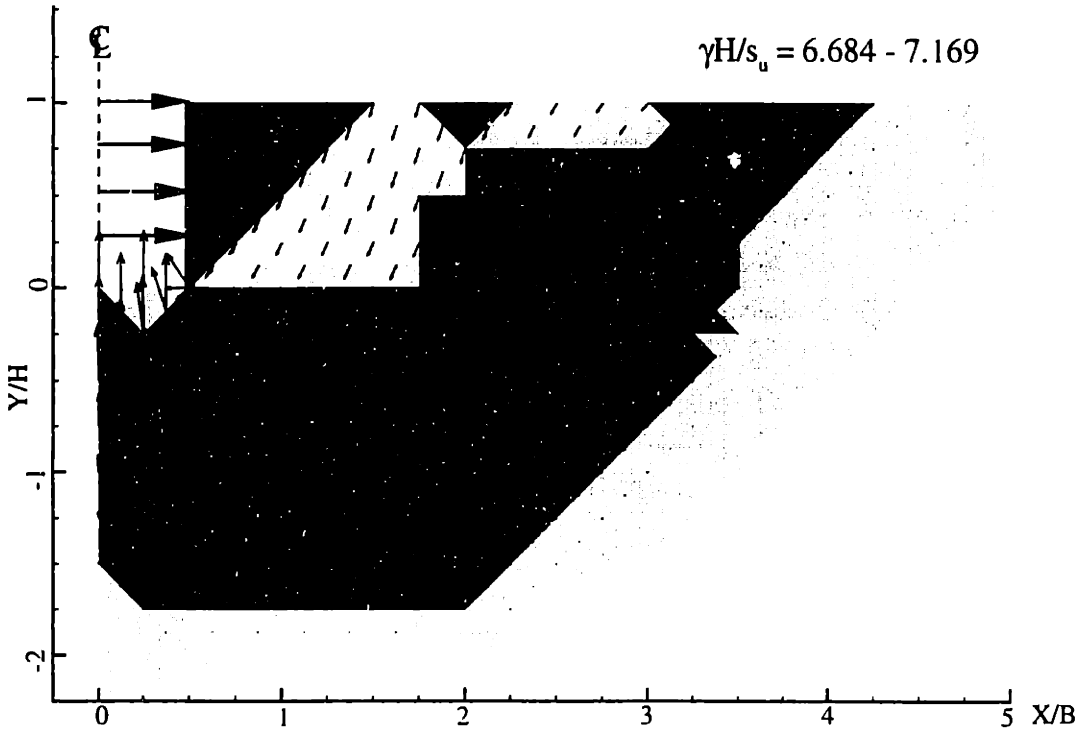

a) Plastic zone/velocity field

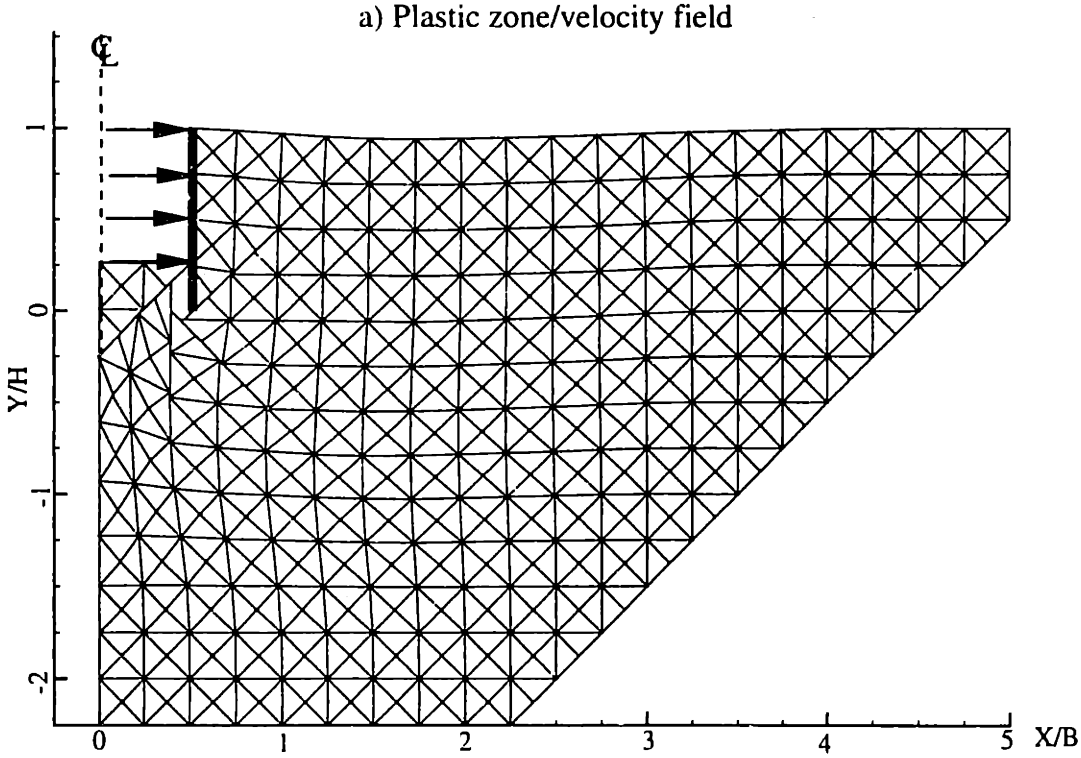

b) Failure mechanism

Figure 6.13 Upper bound results for braced excavation: Rough walls, H/B = 1.0

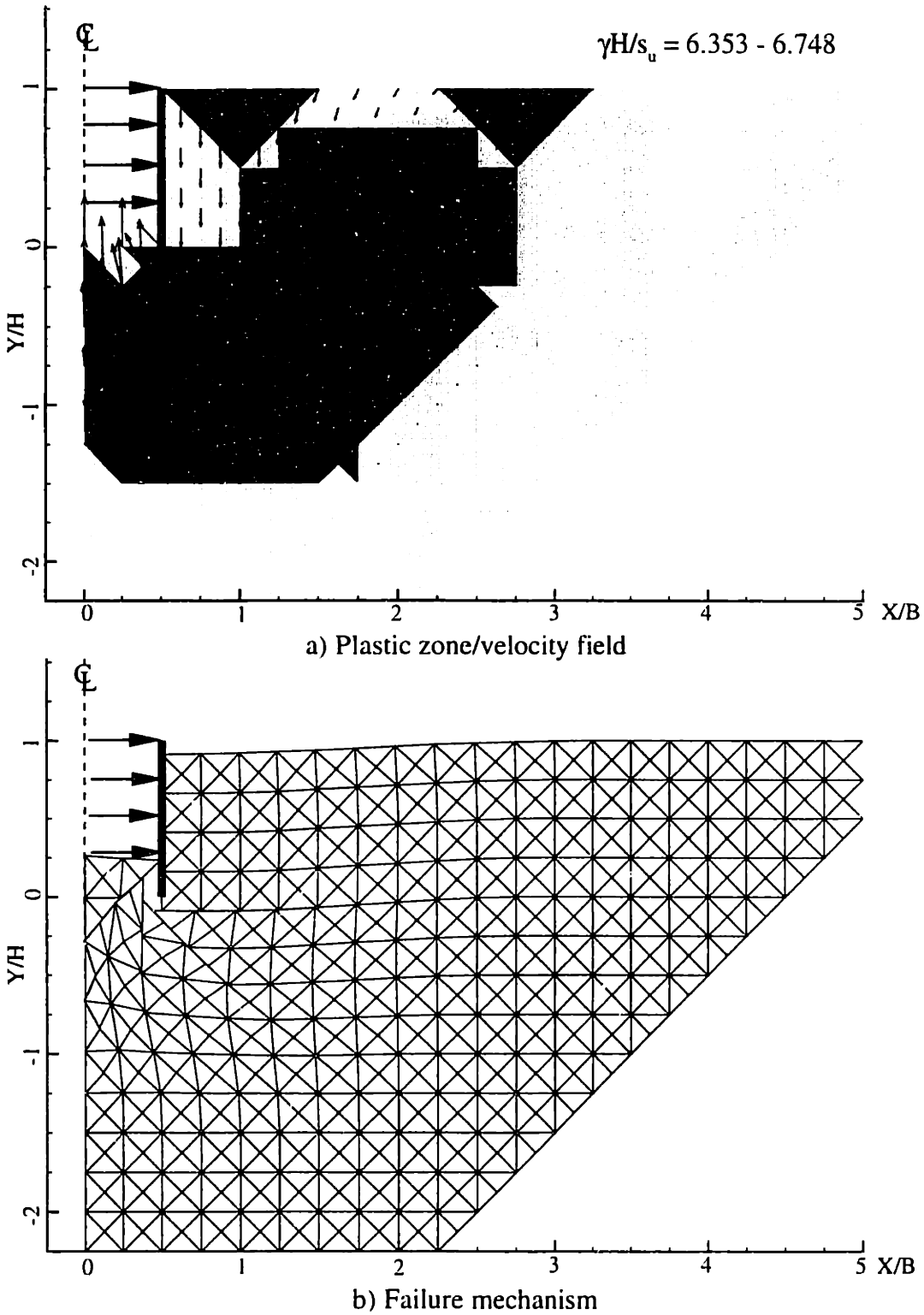

a) Plastic zone/velocity field

b) Failure mechanism

Figure 6.14 Upper bound results for braced excavation: Smooth walls, H/B = 1.0

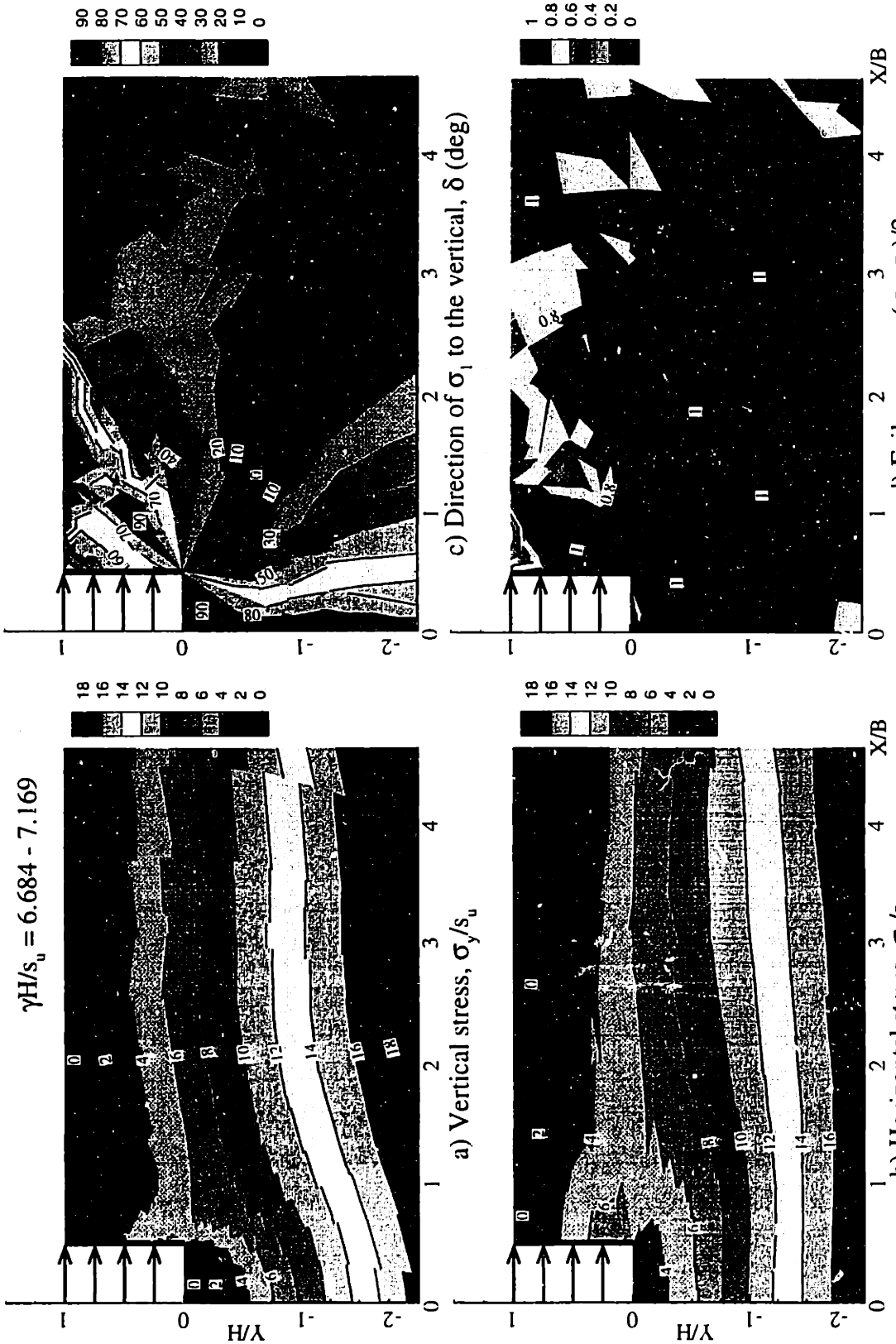

Figure 6.15 Lower bound results for braced excavations: Rough walls, H/B=1.0

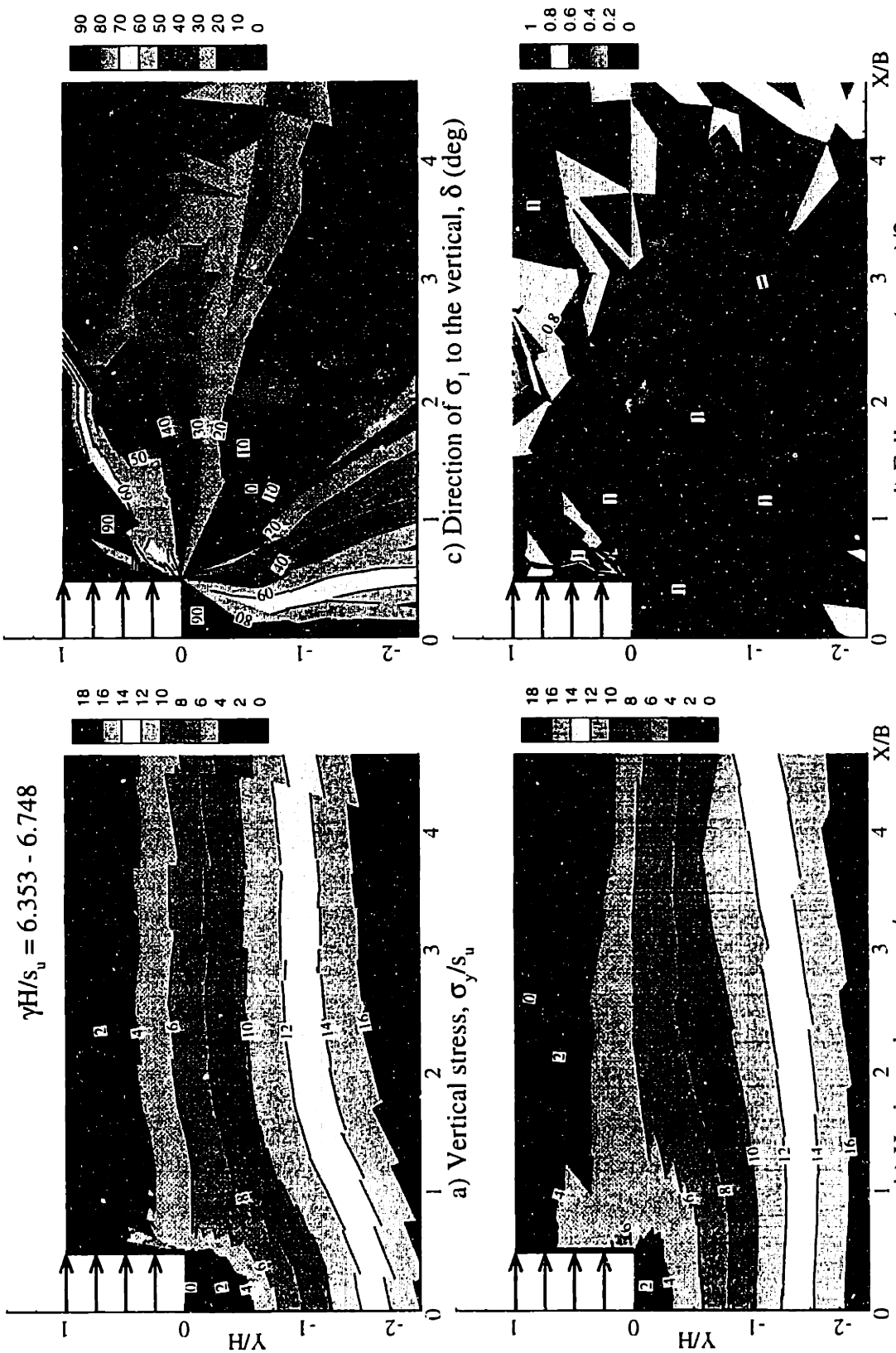

Figure 6.16 Lower bound results for braced excavations: Smooth walls, H/B=1.0

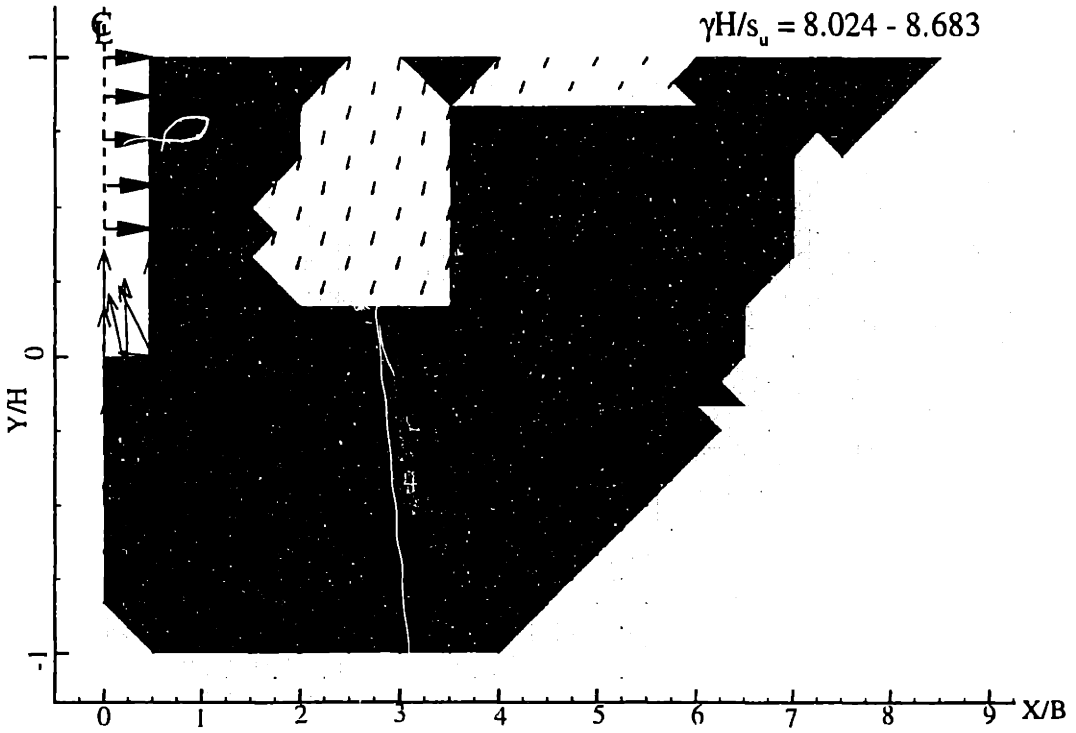

a) Plastic zone/velocity field

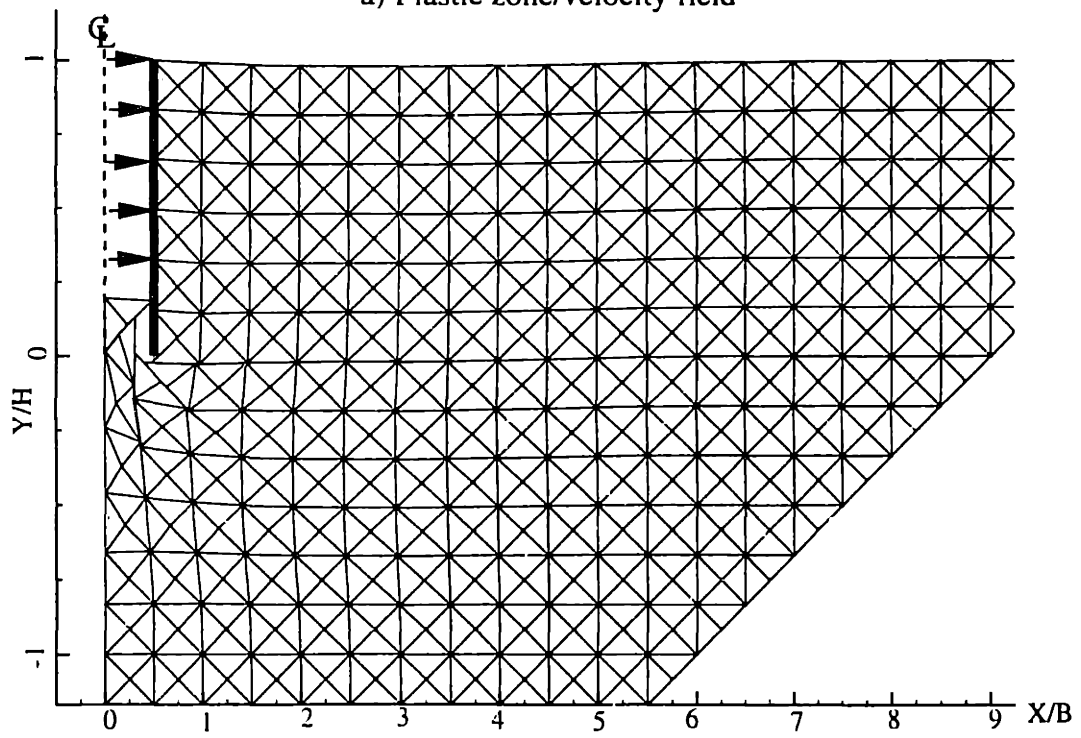

b) Failure mechanism

Figure 6.17 Upper bound results for braced excavation: Rough walls, H/B =3.0

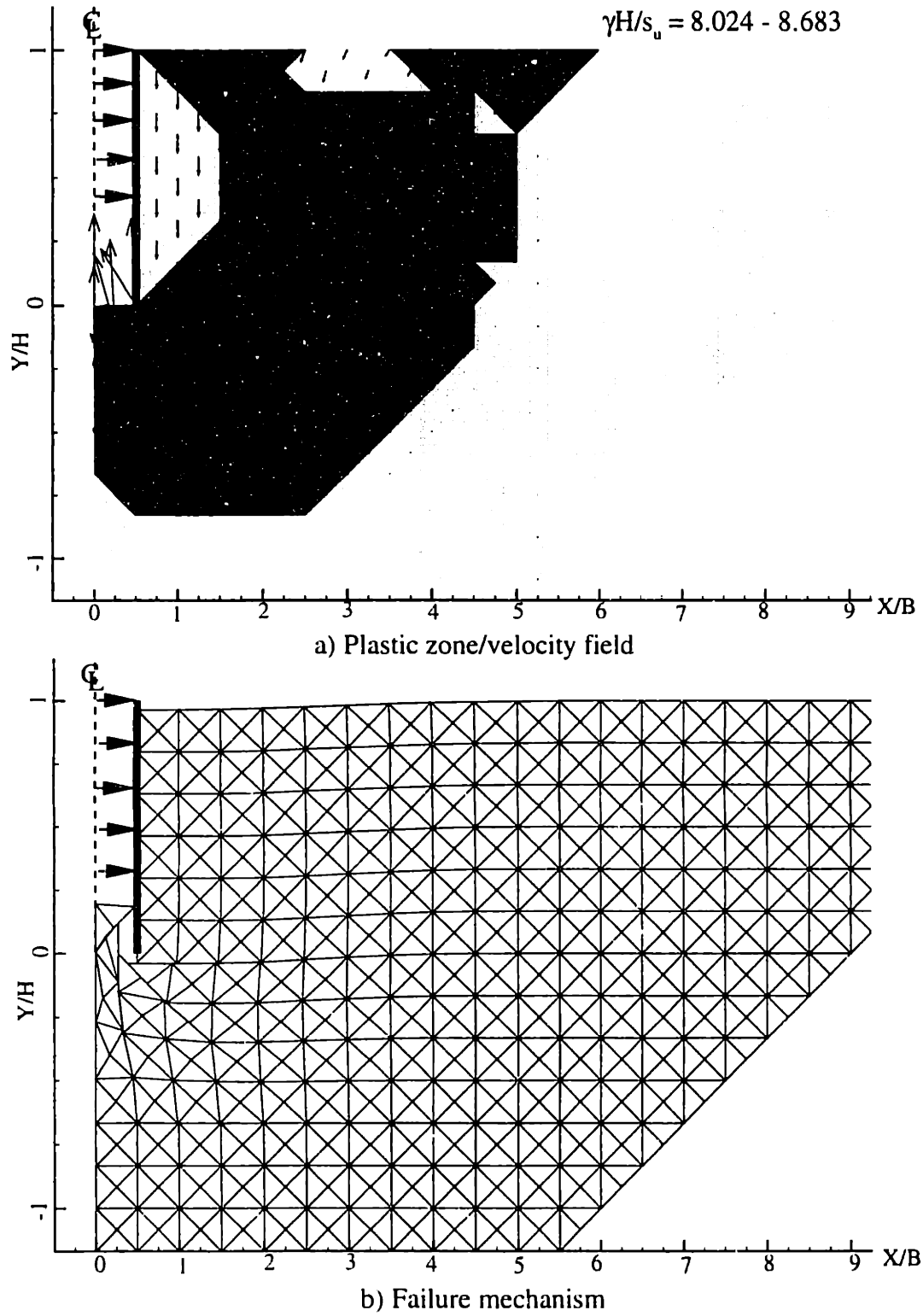

a) Plastic zone/velocity field

b) Failure mechanism

Figure 6.18 Upper bound results for braced excavation: Smooth walls, H/B =3.0

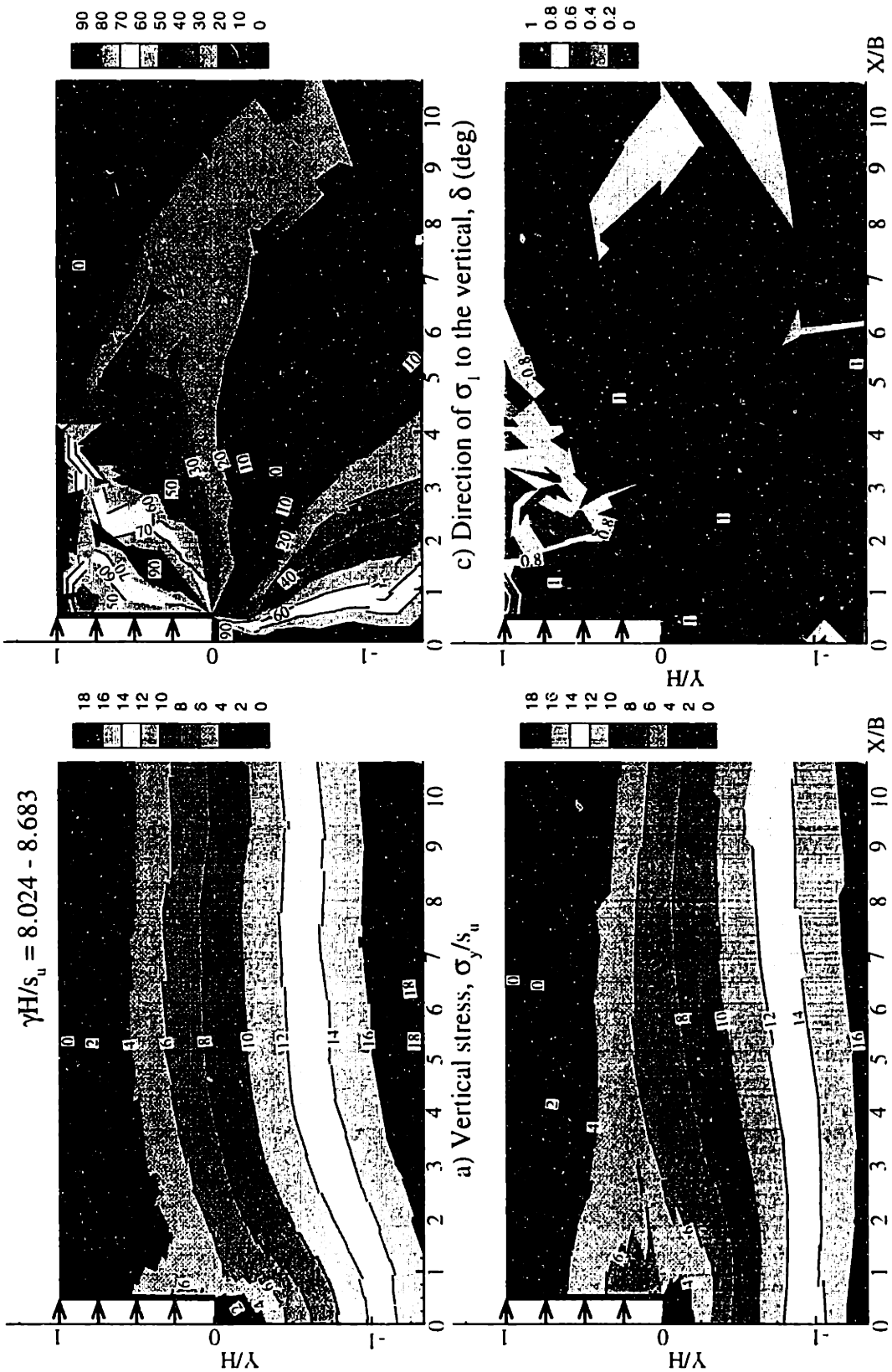

Figure 6.19 Lower bound results for braced excavations: Rough walls, H/B=3.0

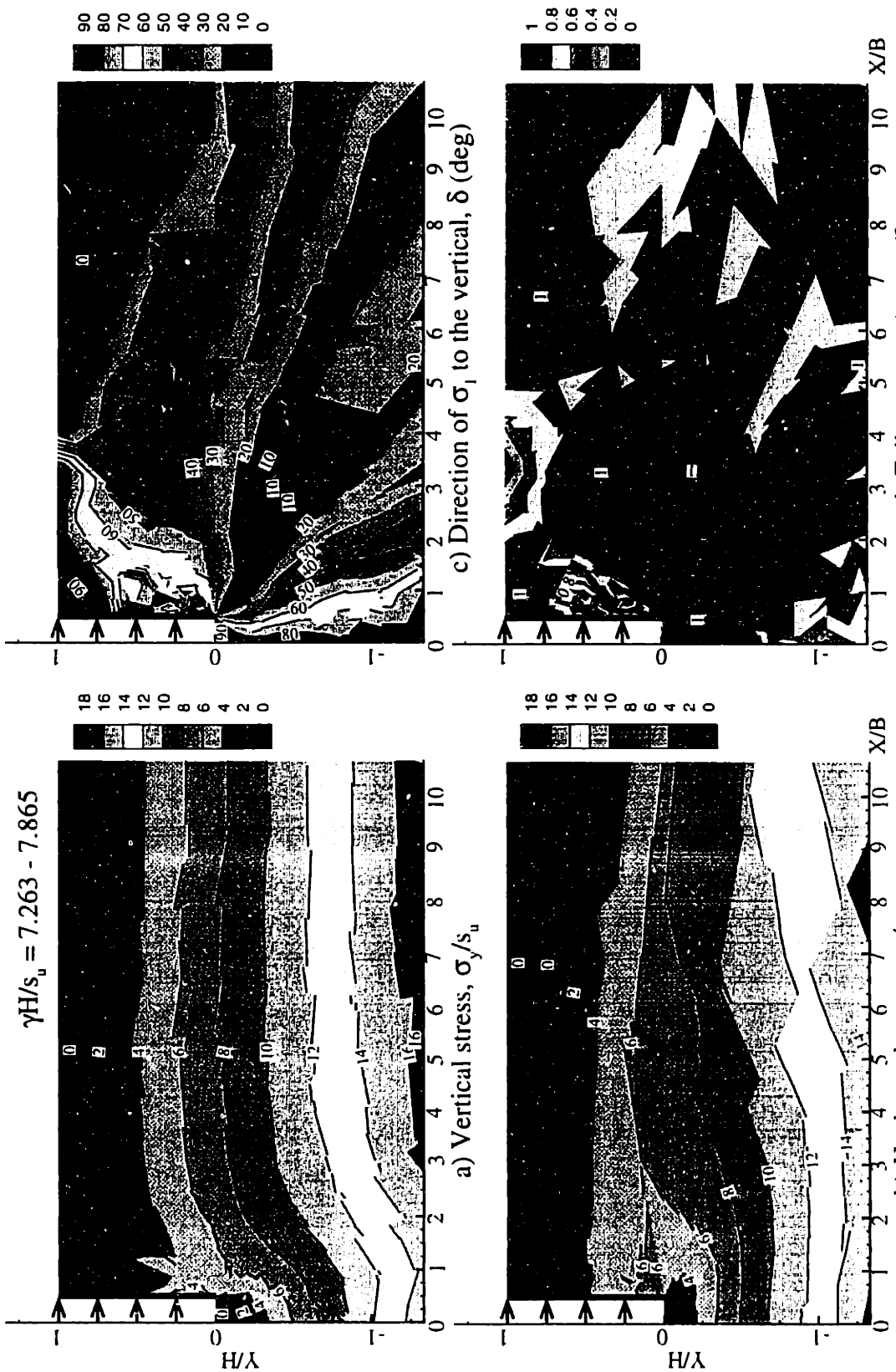

Figure 6.20 Lower bound results for braced excavations: Smooth walls, H/B=3.0

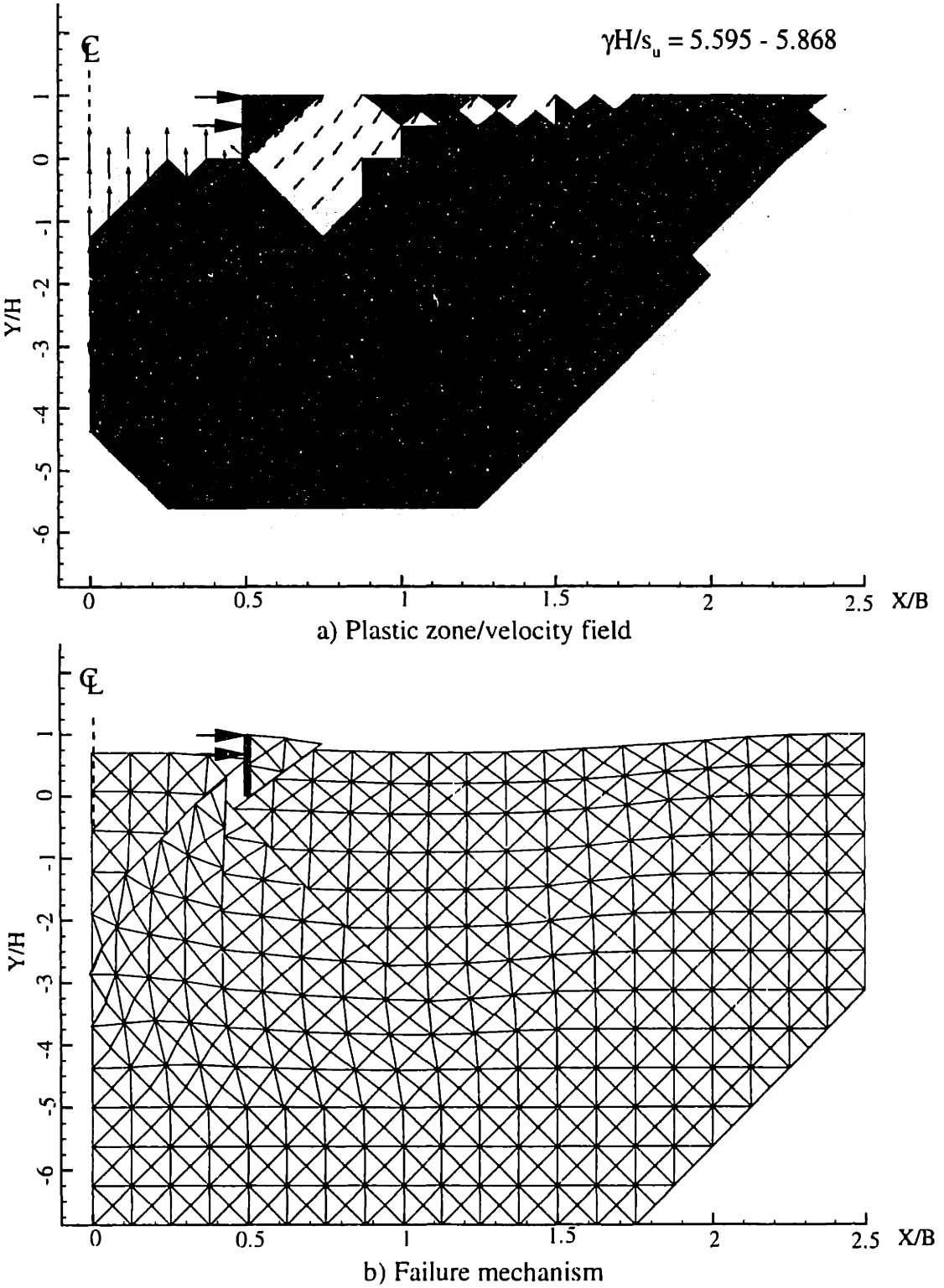

Figure 6.21 Upper bound results for braced excavation: Rough walls, B/H = 5

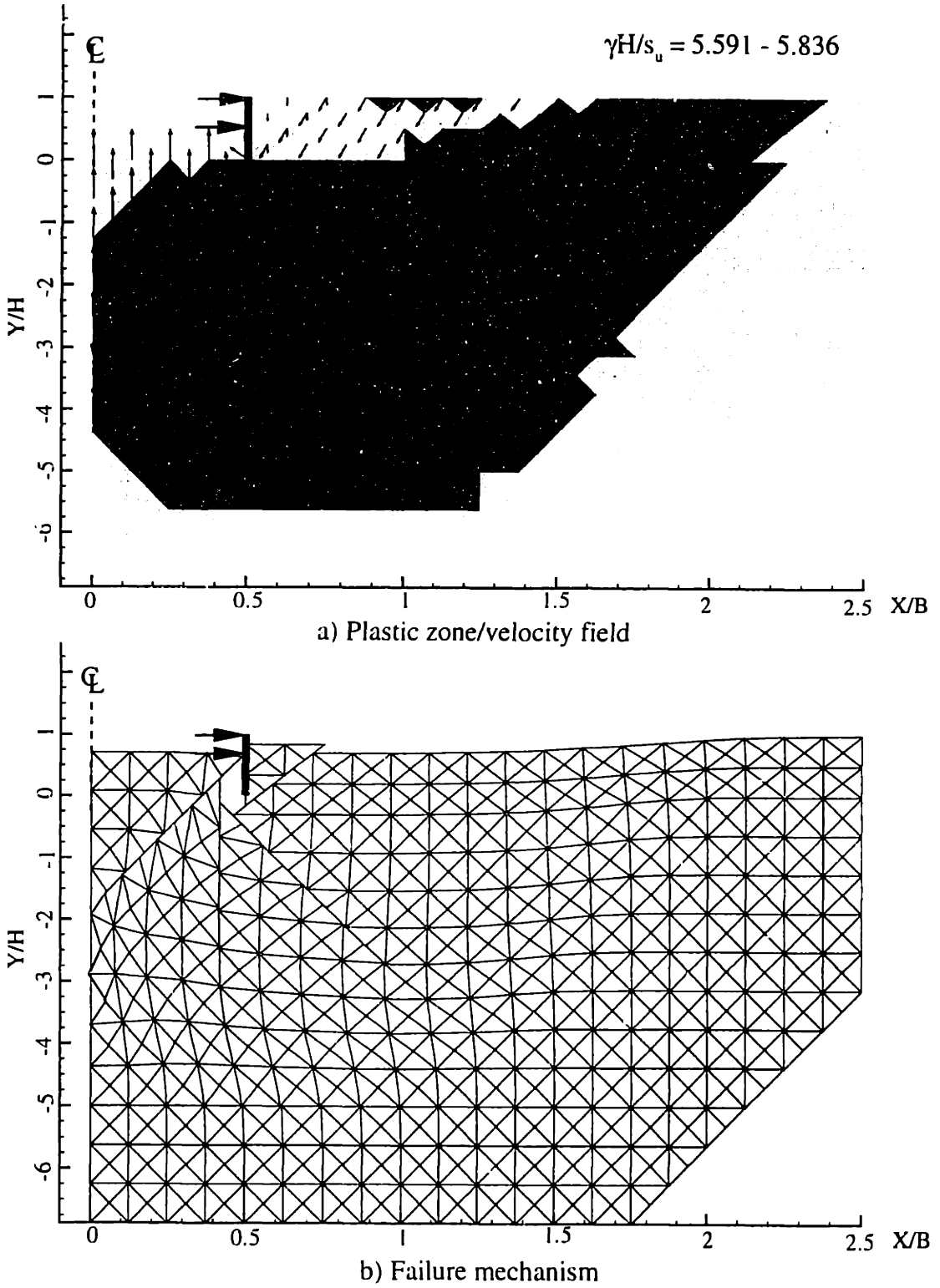

Figure 6.22 Upper bound results for braced excavation: Smooth walls, B/H = 5

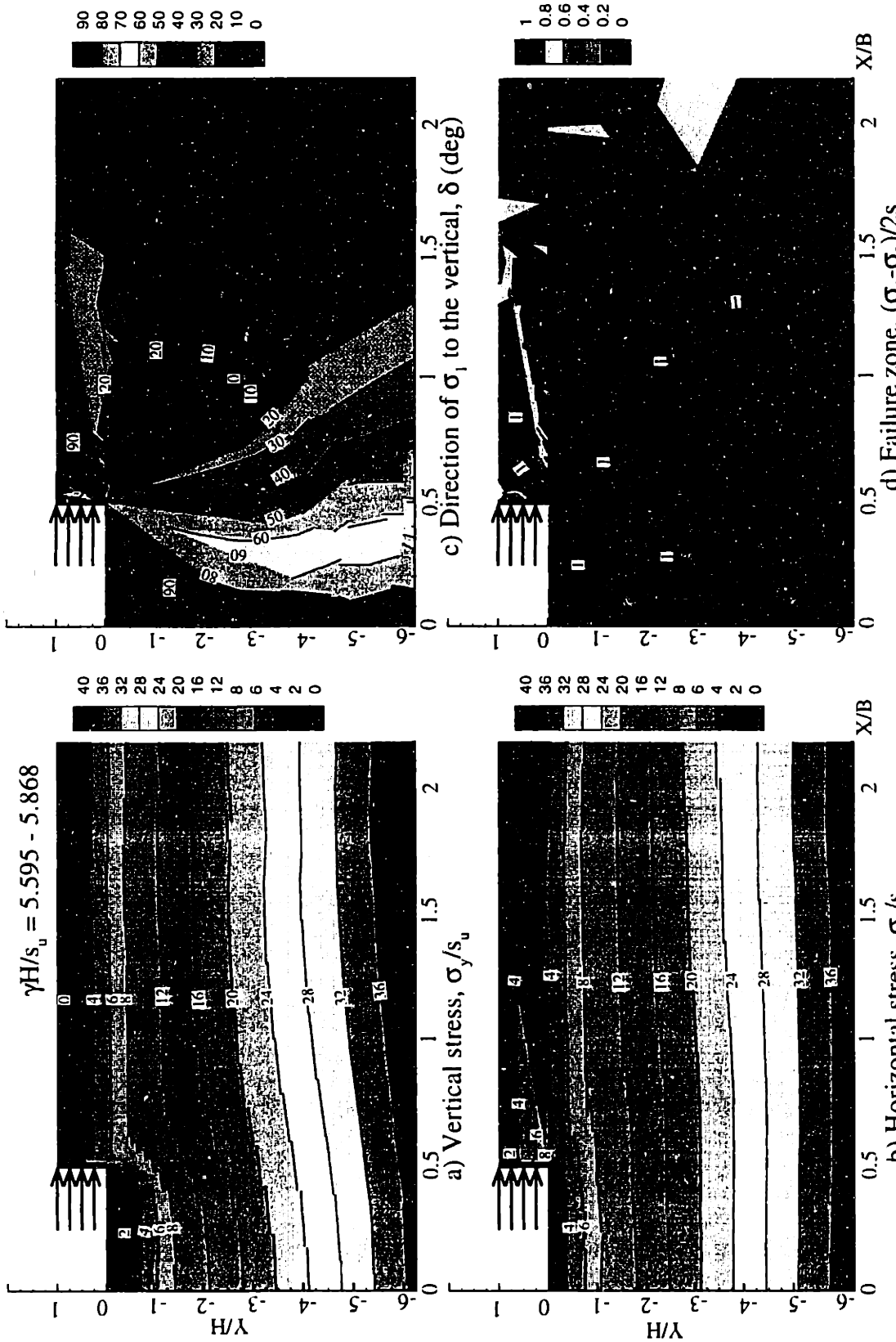

Figure 6.23 Lower bound results for braced excavations: Rough walls, B/H=5.0

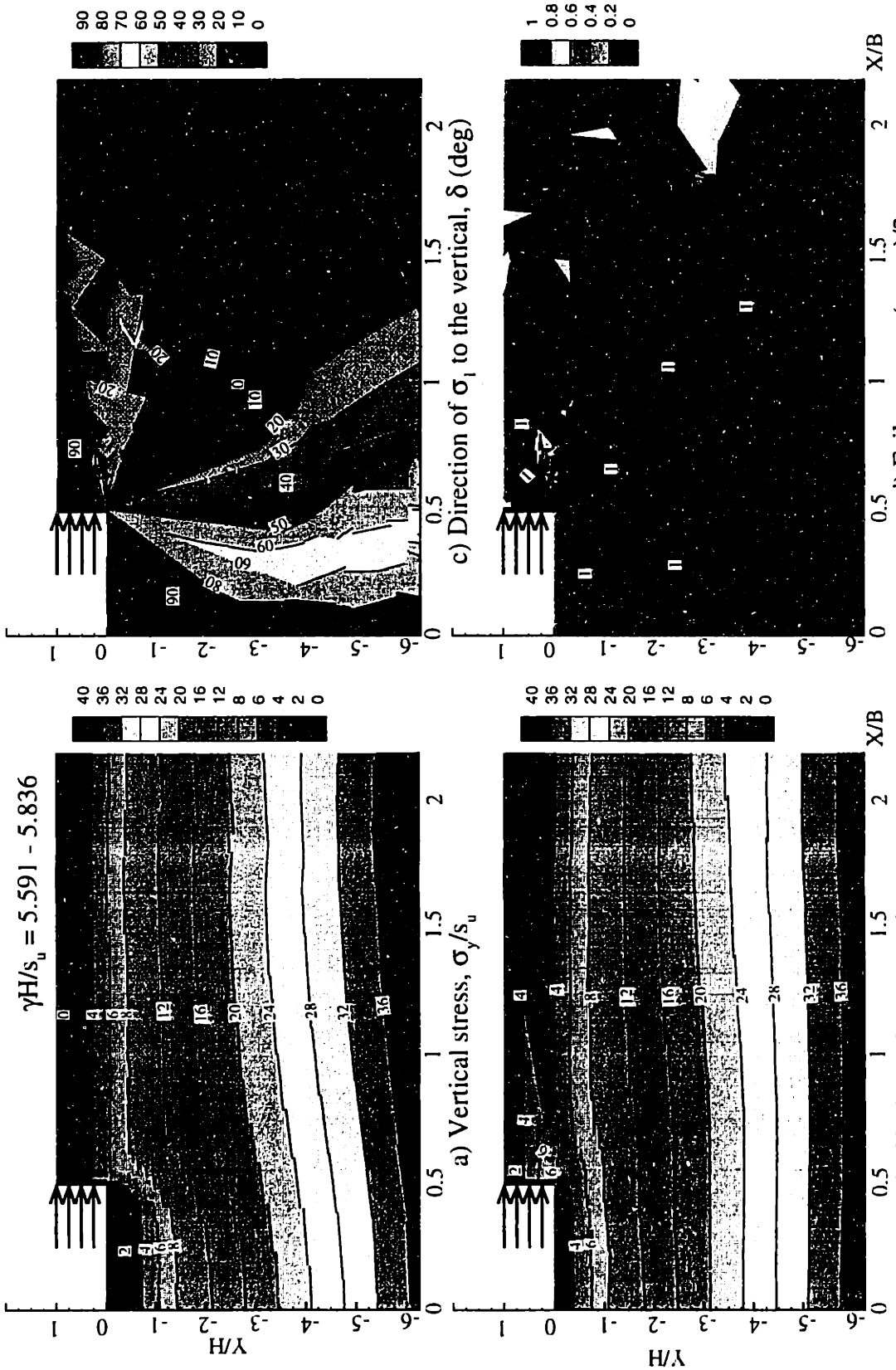

Figure 6.24 Lower bound results for braced excavations: Smooth walls, B/H=5.0

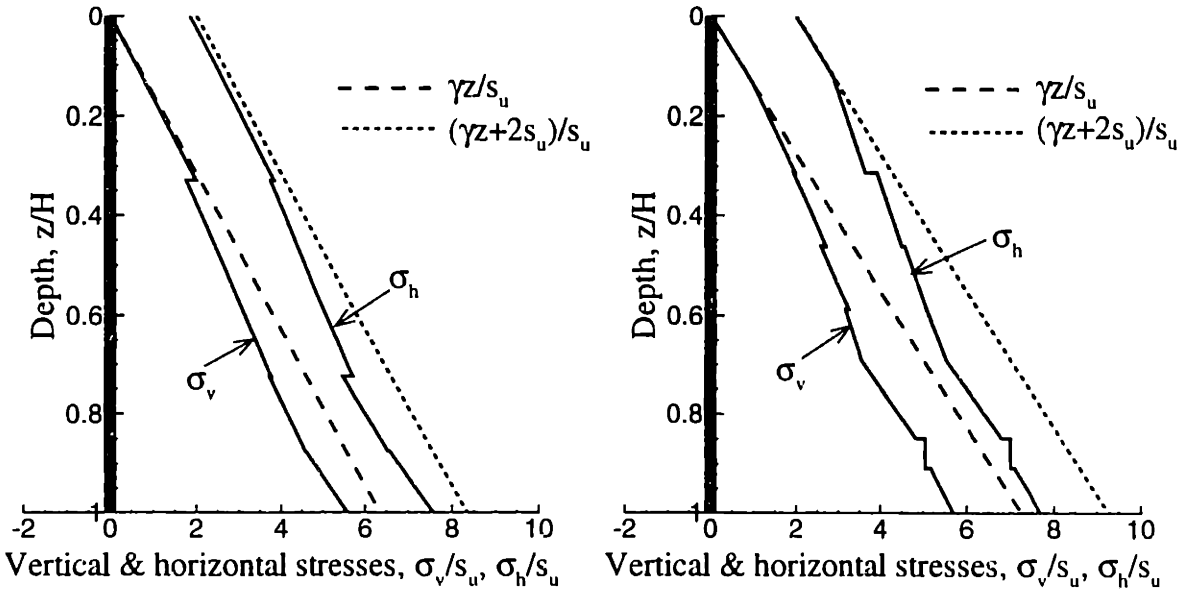

a) H/B = 1.0

b) Narrow excavation, H/B = 3.0

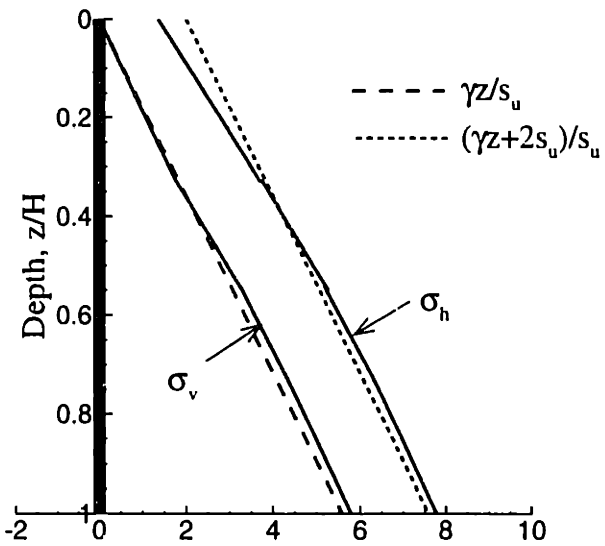

c) Wide excavation, B/H = 5.0

Figure 6.25 Vertical and horionzontal stresses along the wall for braced excavations (smooth wall interfaces)

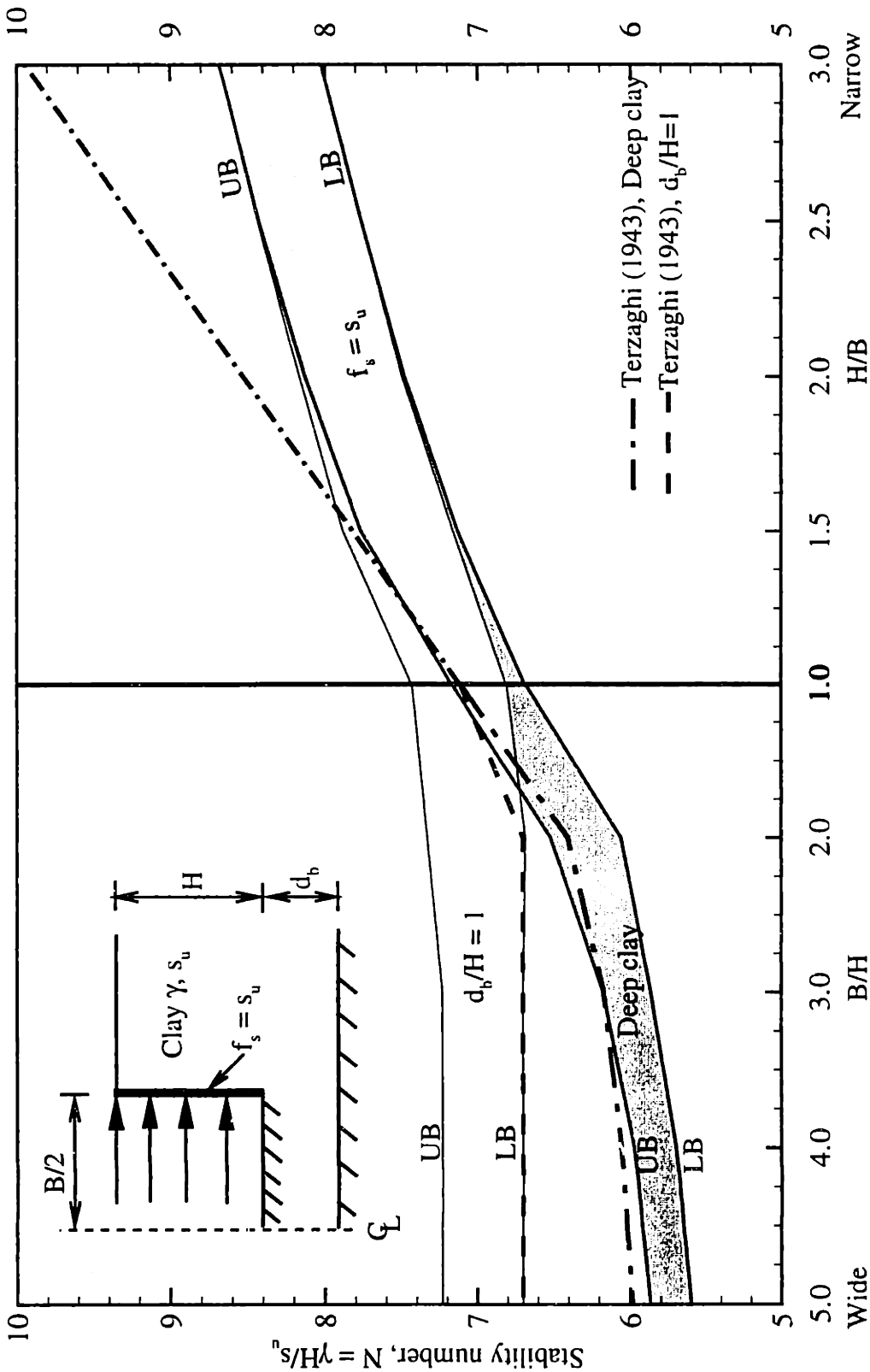

Figure 6.26 Undrained stability of a braced excavation in a finite depth of clay by numerical limit analyses

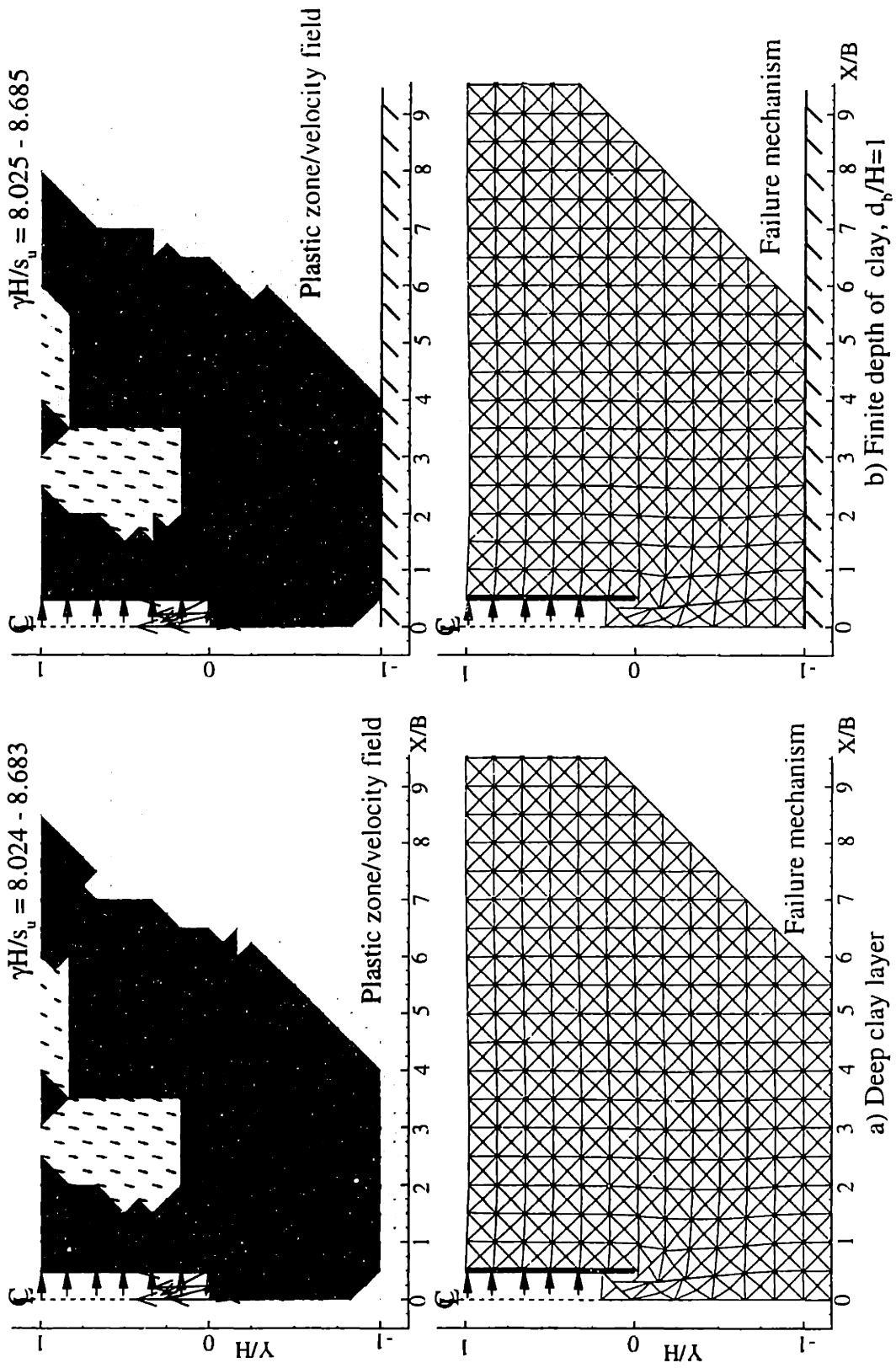

Figure 6.27 Comparisons of upper bound results for deep clay layer and finite depth of clay: H/B = 3

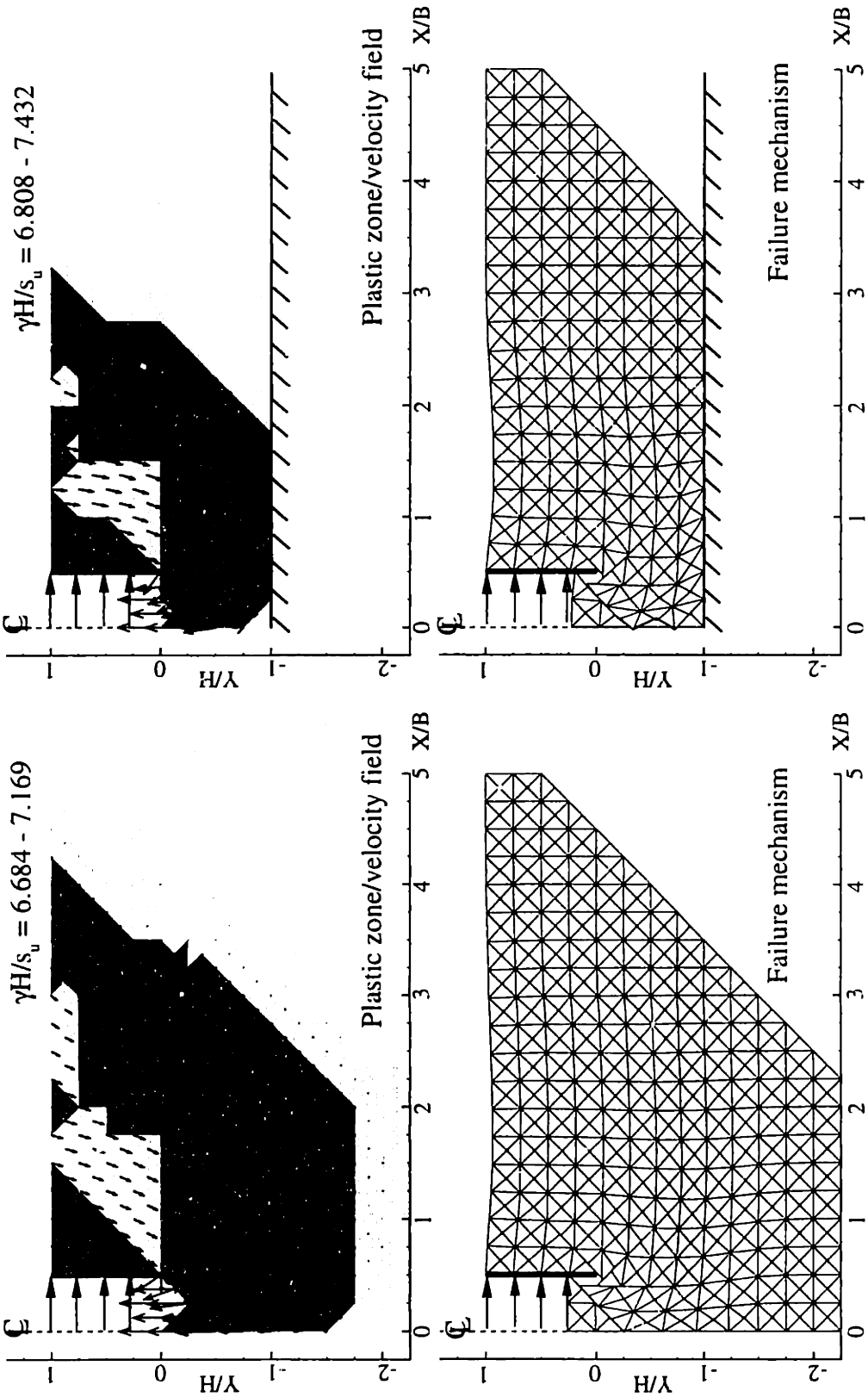

Figure 6.28 Comparisons of upper bound results for deep clay layer and finite depth of clay: H/B = 1

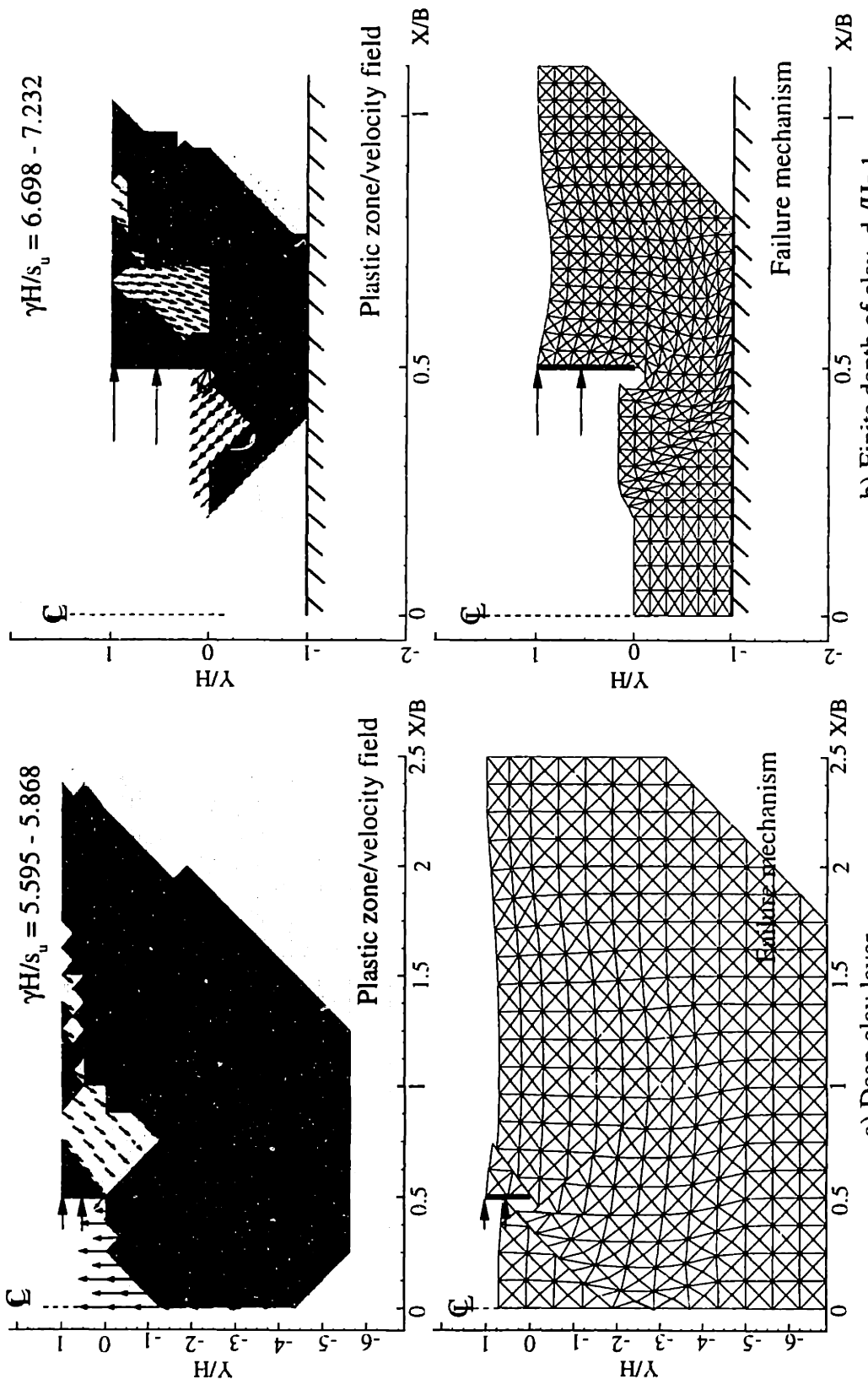

a) Deep clay layer

b) Finite depth of clay, $d_b/H=1$

Figure 6.29 Comparisons of upper bound results for deep clay layer and finite depth of clay: B/H = 5

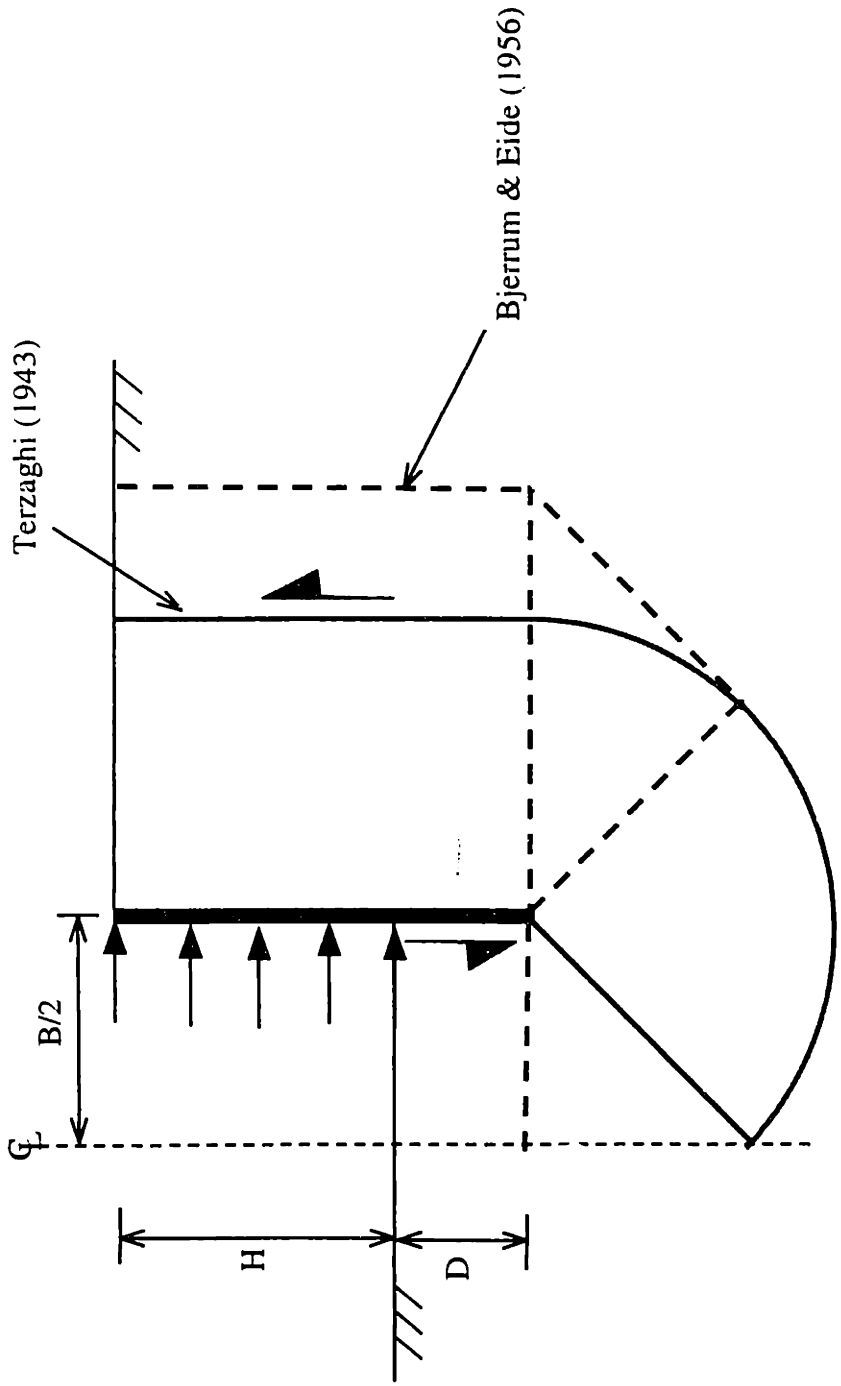

Figure 6.30 Conventional modifications of basal heave calculations for braced excavations with wall embedment

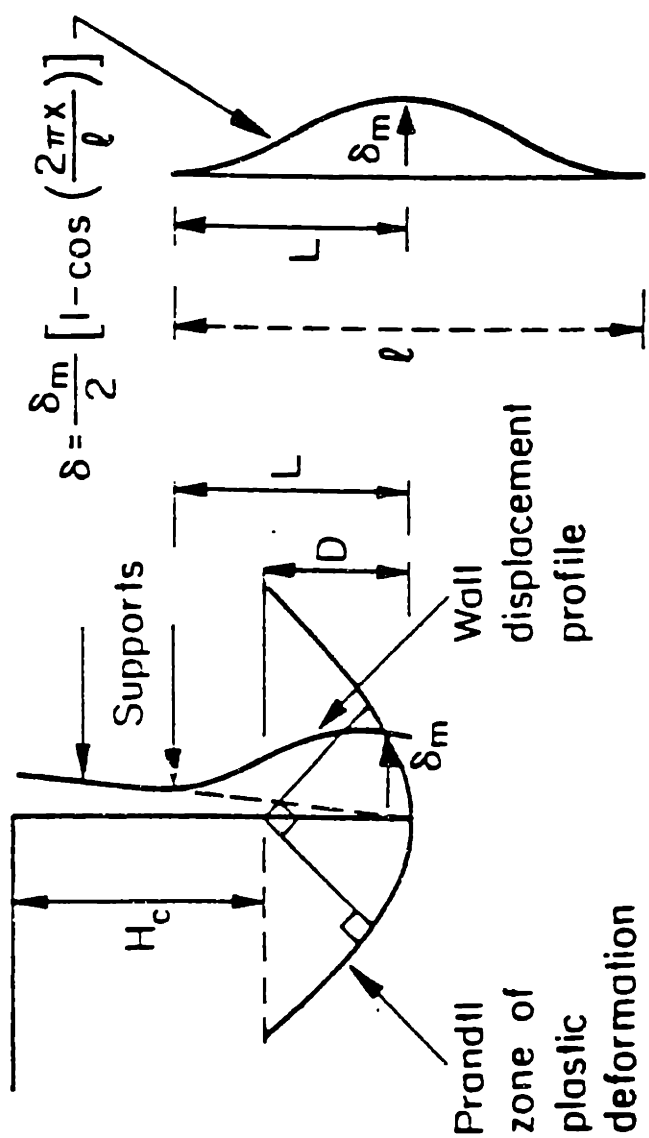

Figure 6.31 Modification of stability number with wall embedment by O'Rourke (1993)

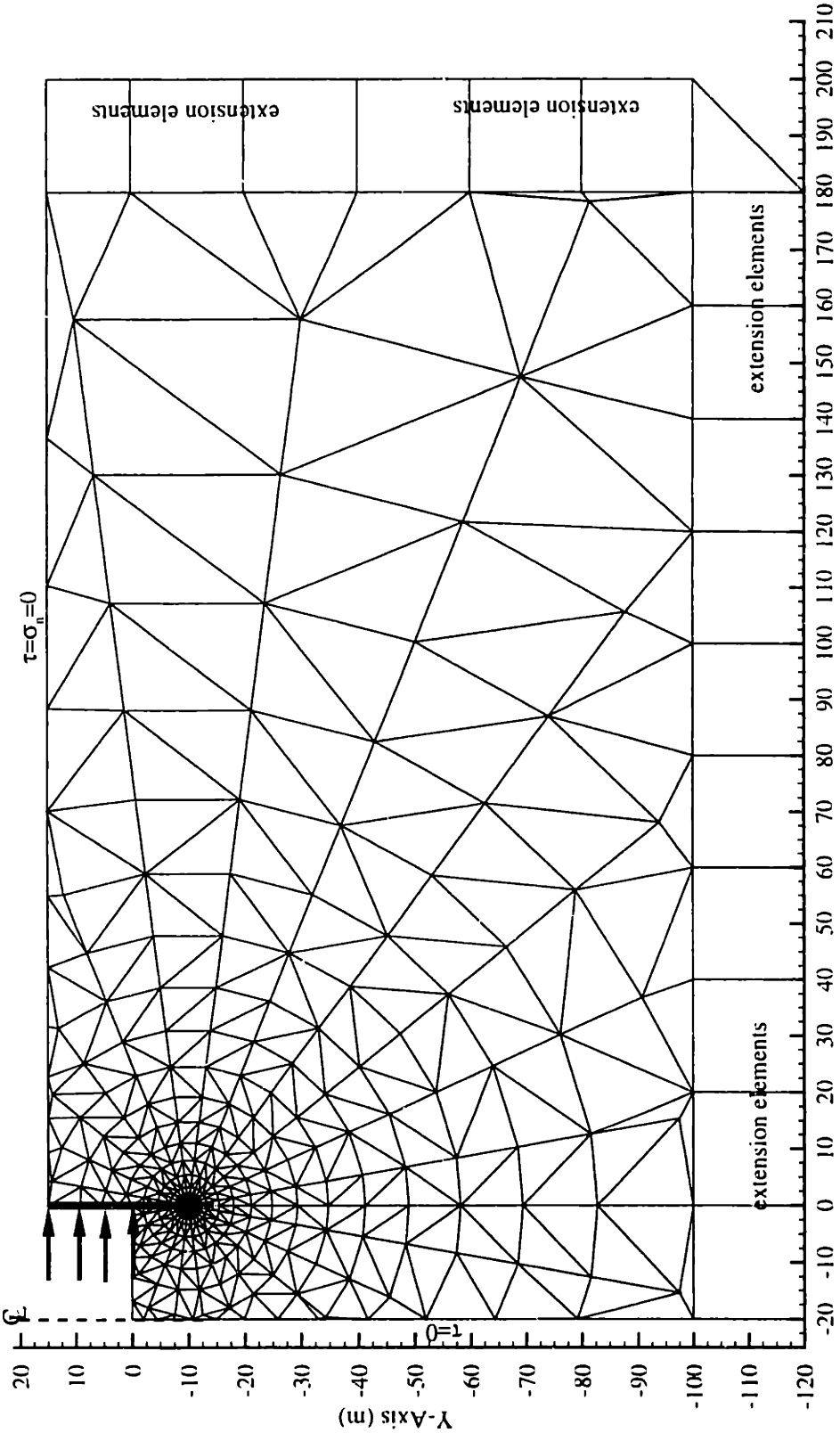

Figure 6.32 Lower bound mesh for a braced excavation with wall embedment

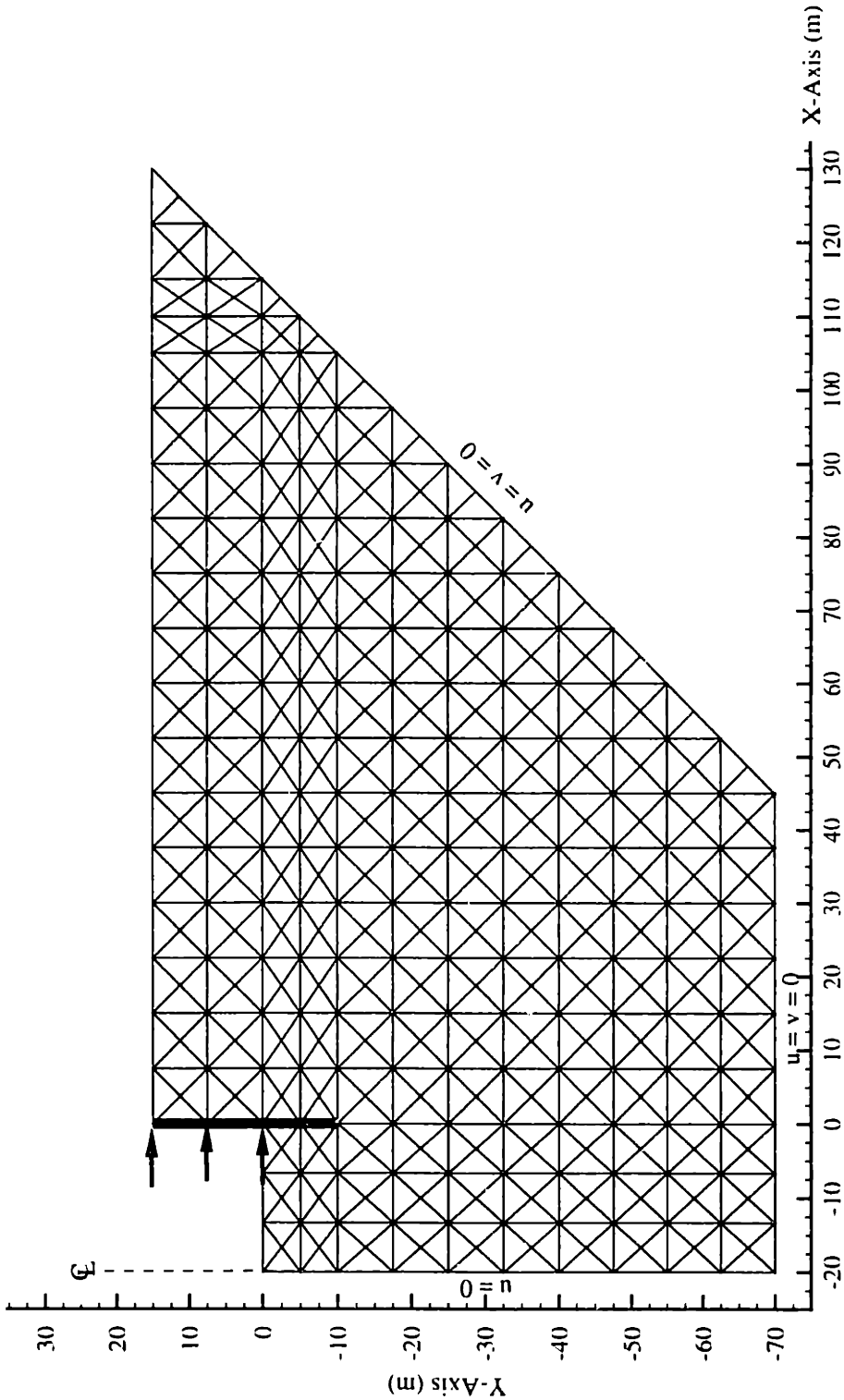

Figure 6.33 Upper bound mesh for a braced excavation with wall embedment

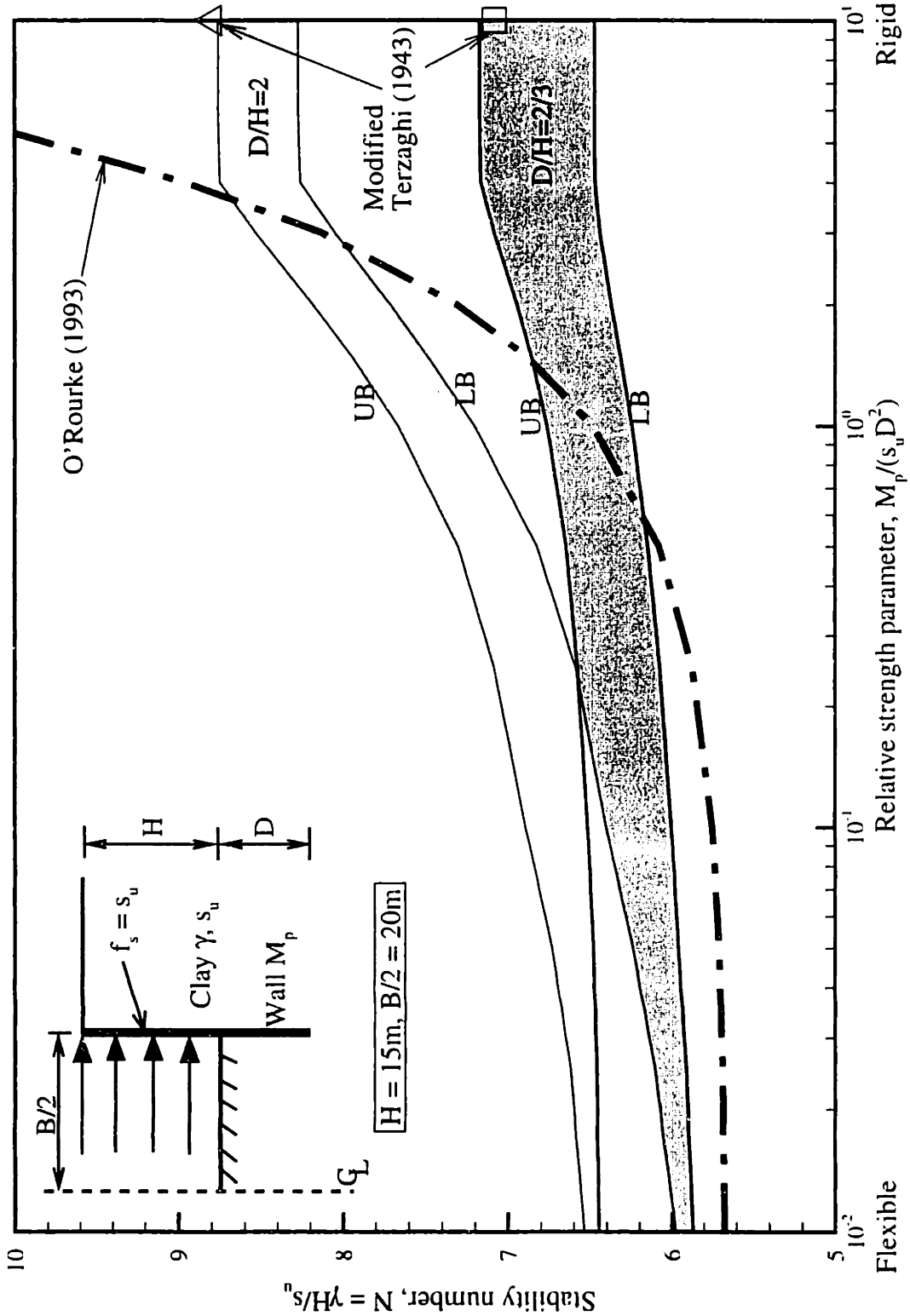

Figure 6.34 Undrained stability of braced embedded wall in clay by numerical limit analyses

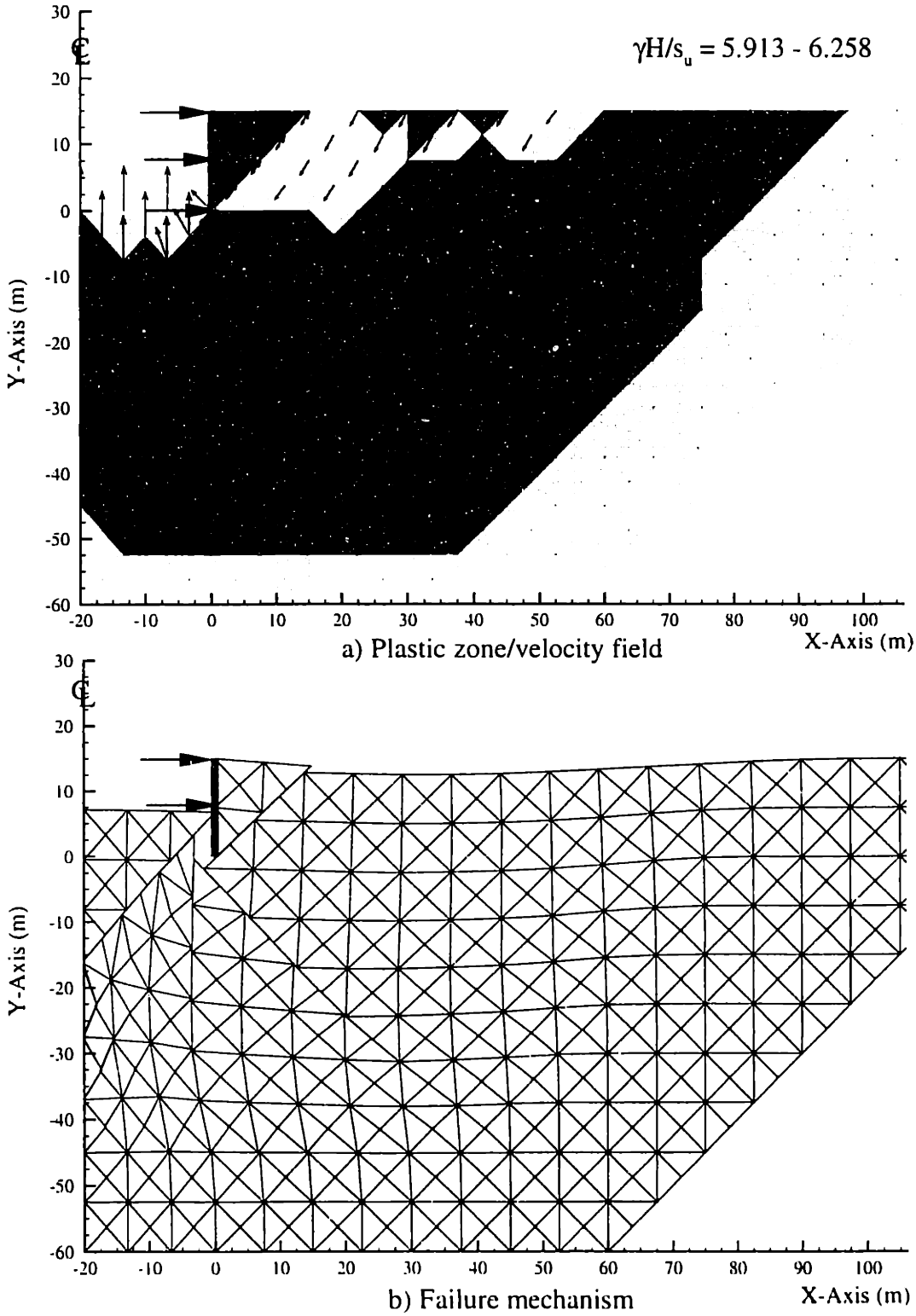

Figure 6.35 Upper bound results for braced excavation: Base case B=40m, H=15m

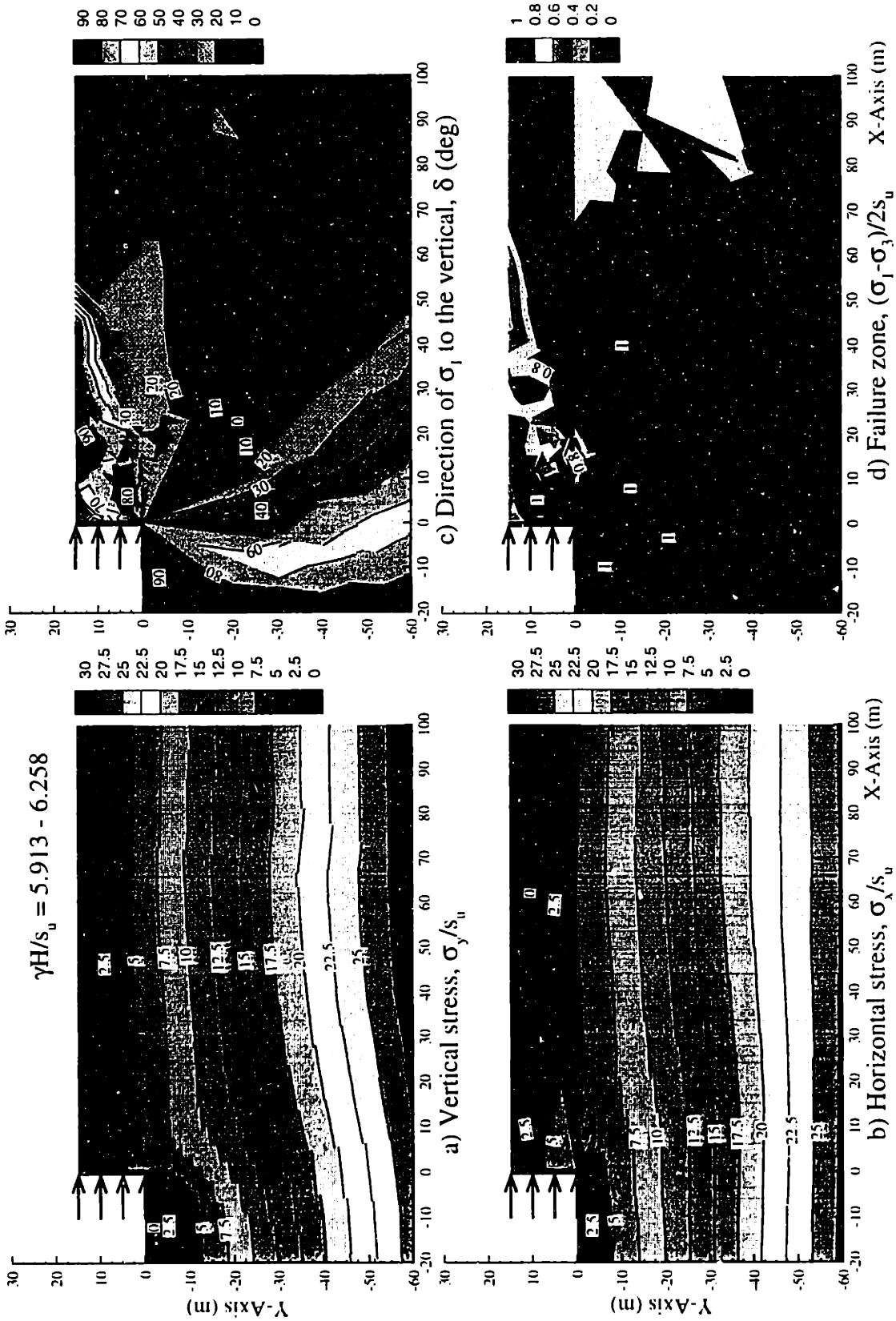

Figure 6.36 Lower bound results for braced excavations:Base case, B = 40m, H =15m

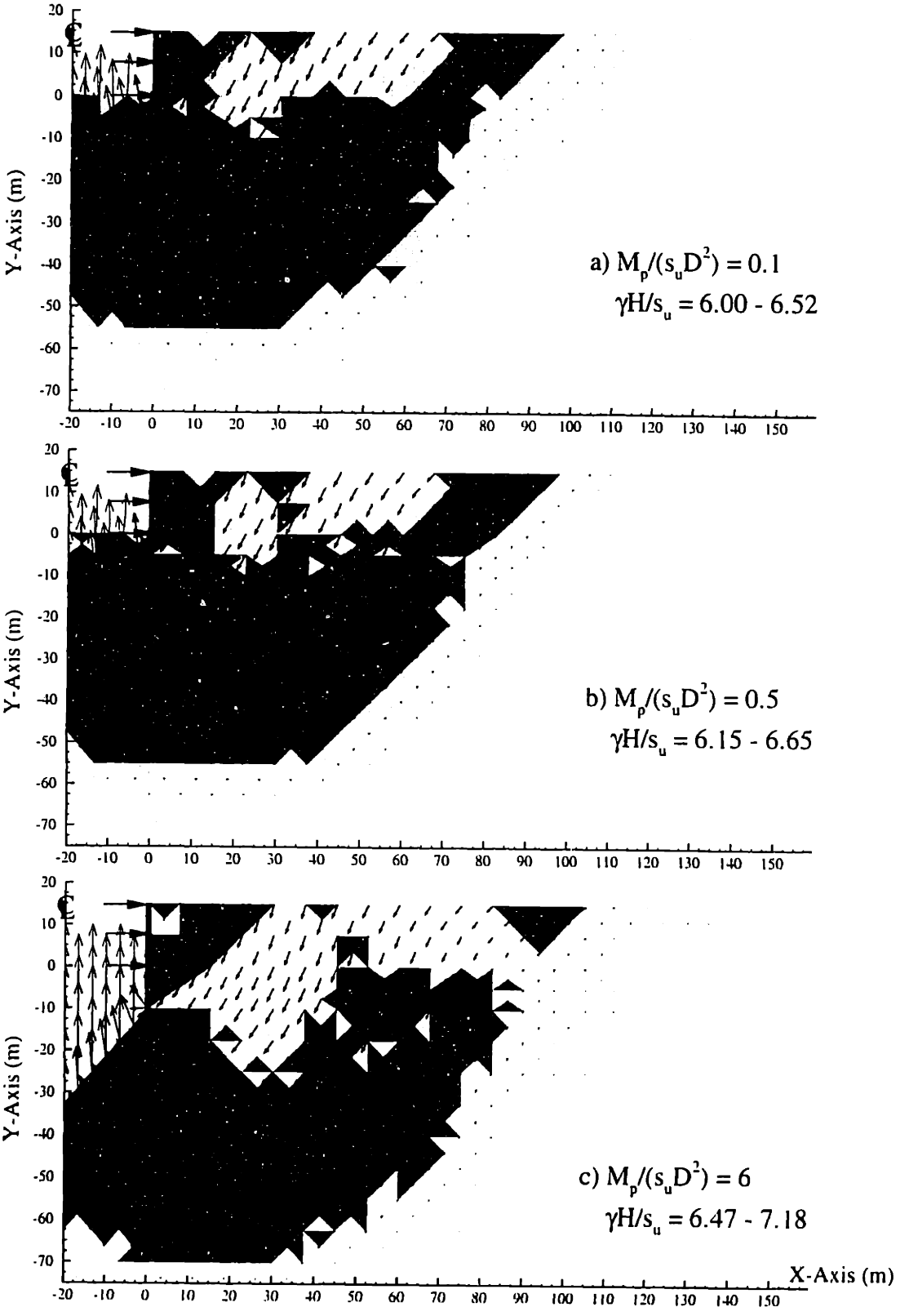

Figure 6.37 Comparisons of velocity field and plastic zone for different relative strength parameters, D/H = 2/3

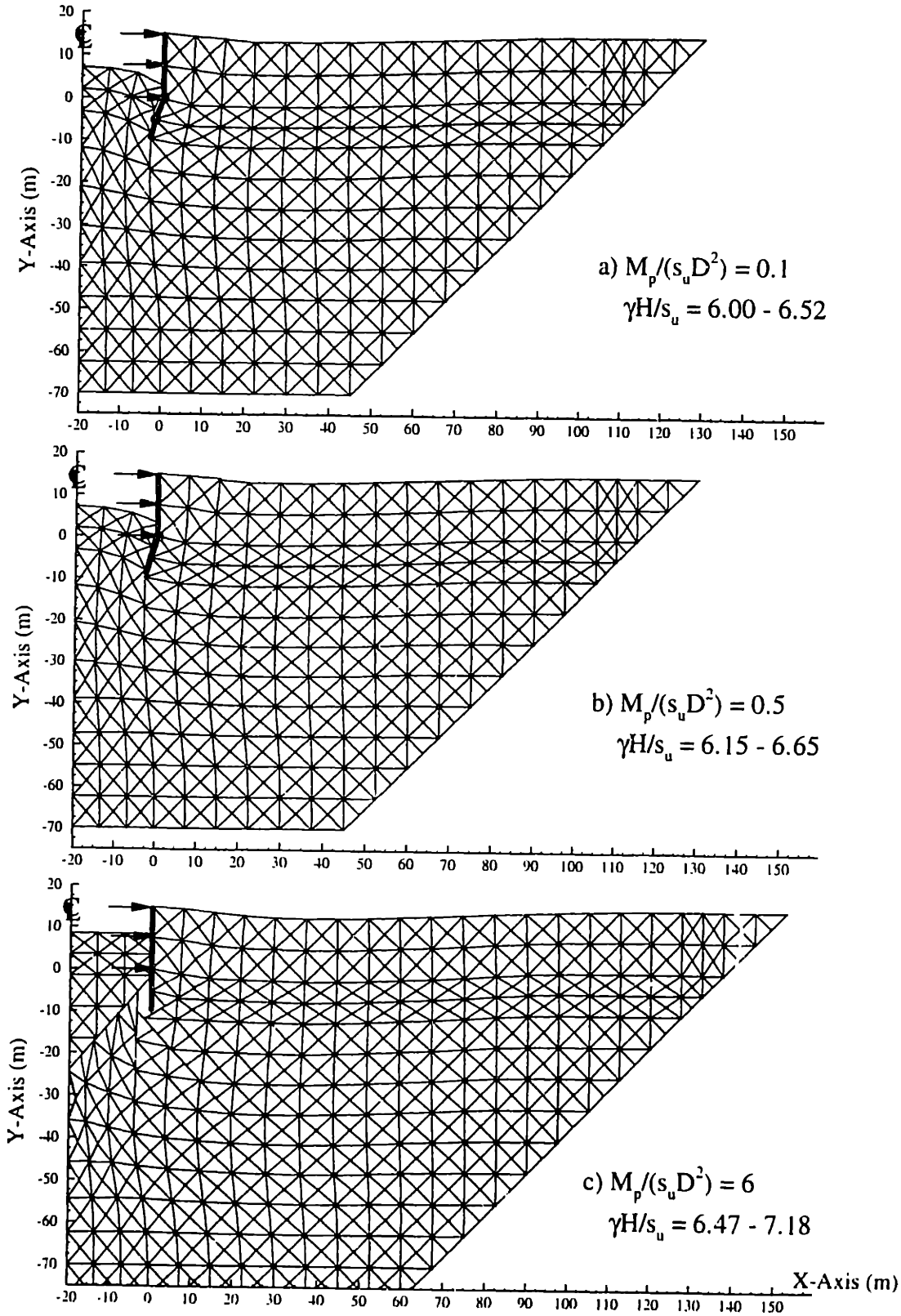

Figure 6.38 Comparisons of failure mechanism for different relative strength parameters, D/H = 2/3

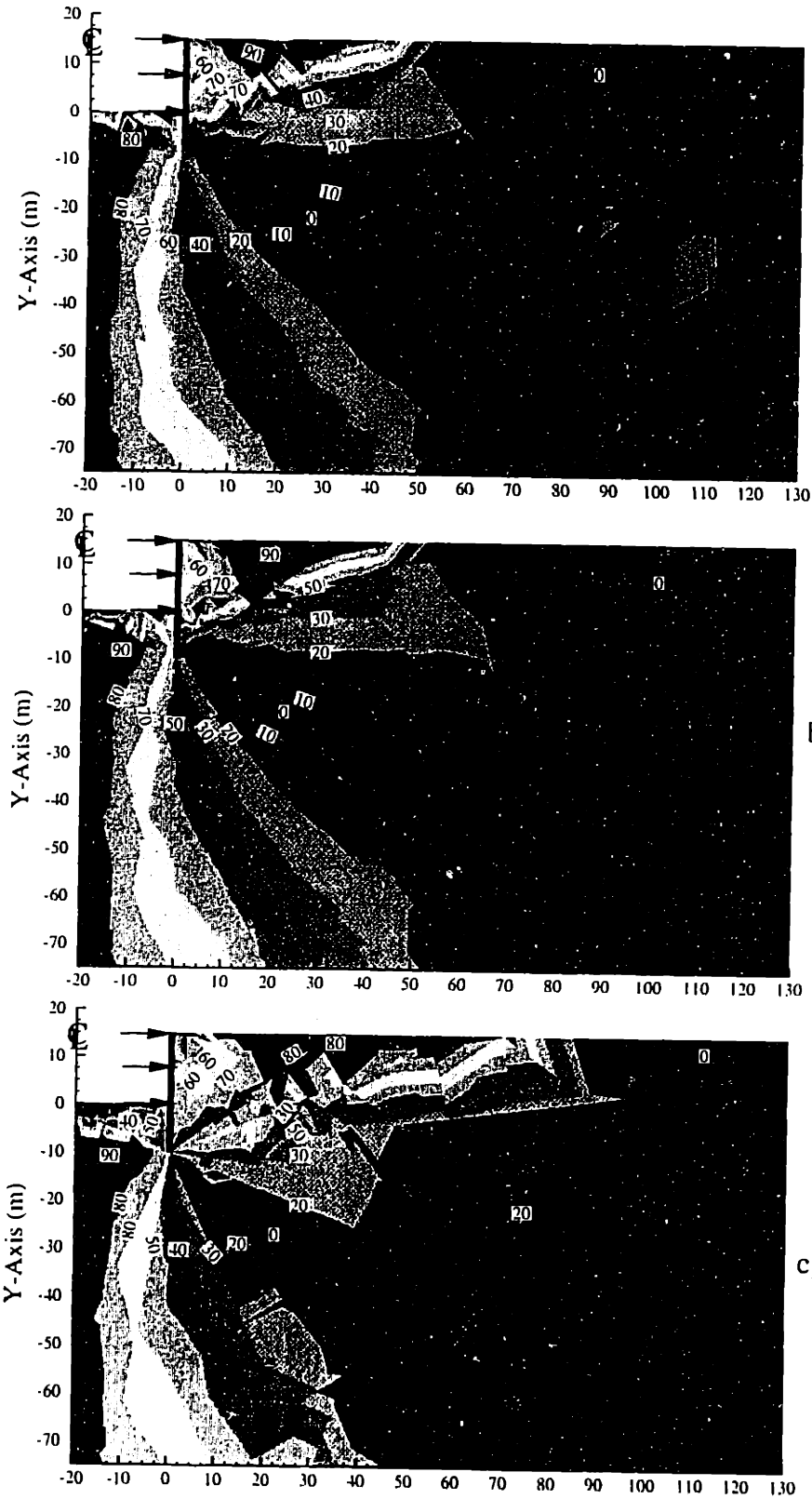

Figure 6.39 Comparisons of the direction of σ_1 to the vertical, δ (deg.) for different relative strength parameters, D/H=2/3

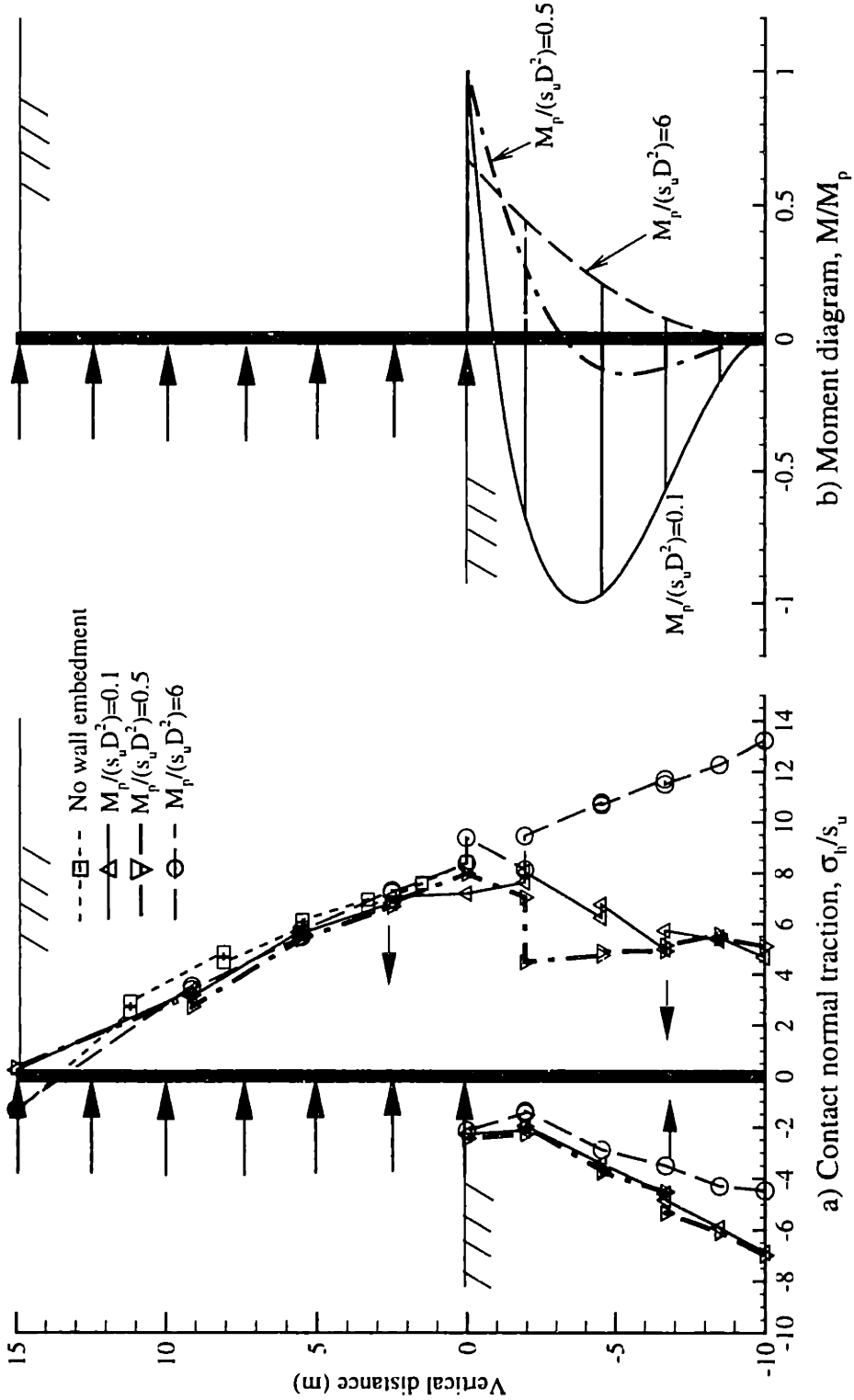

Figure 6.40 Contact pressure and moment diagrams along the wall, D/H = 2/3

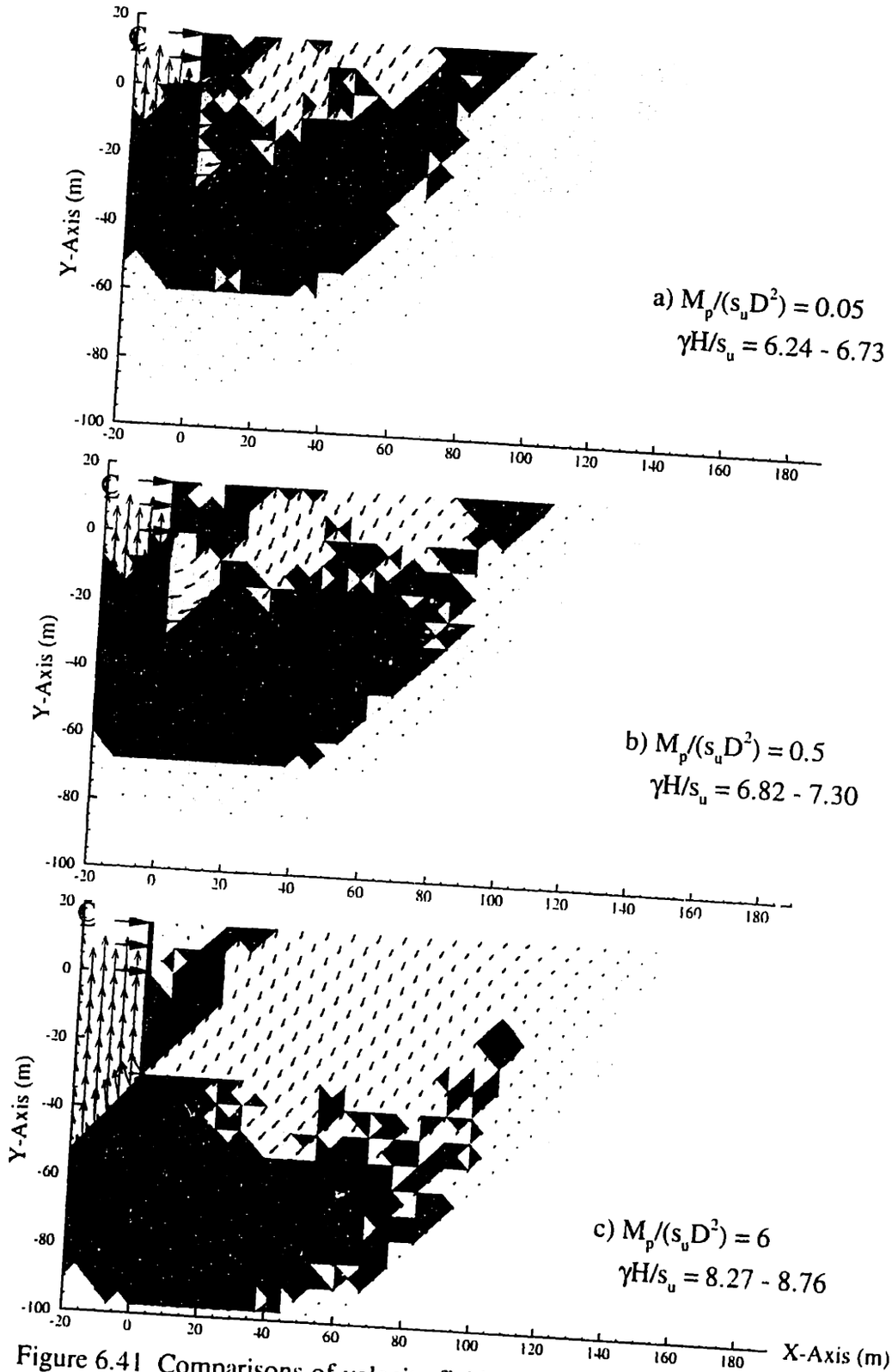

Figure 6.41 Comparisons of velocity field and plastic zone for different relative strength parameters, D/H = 2

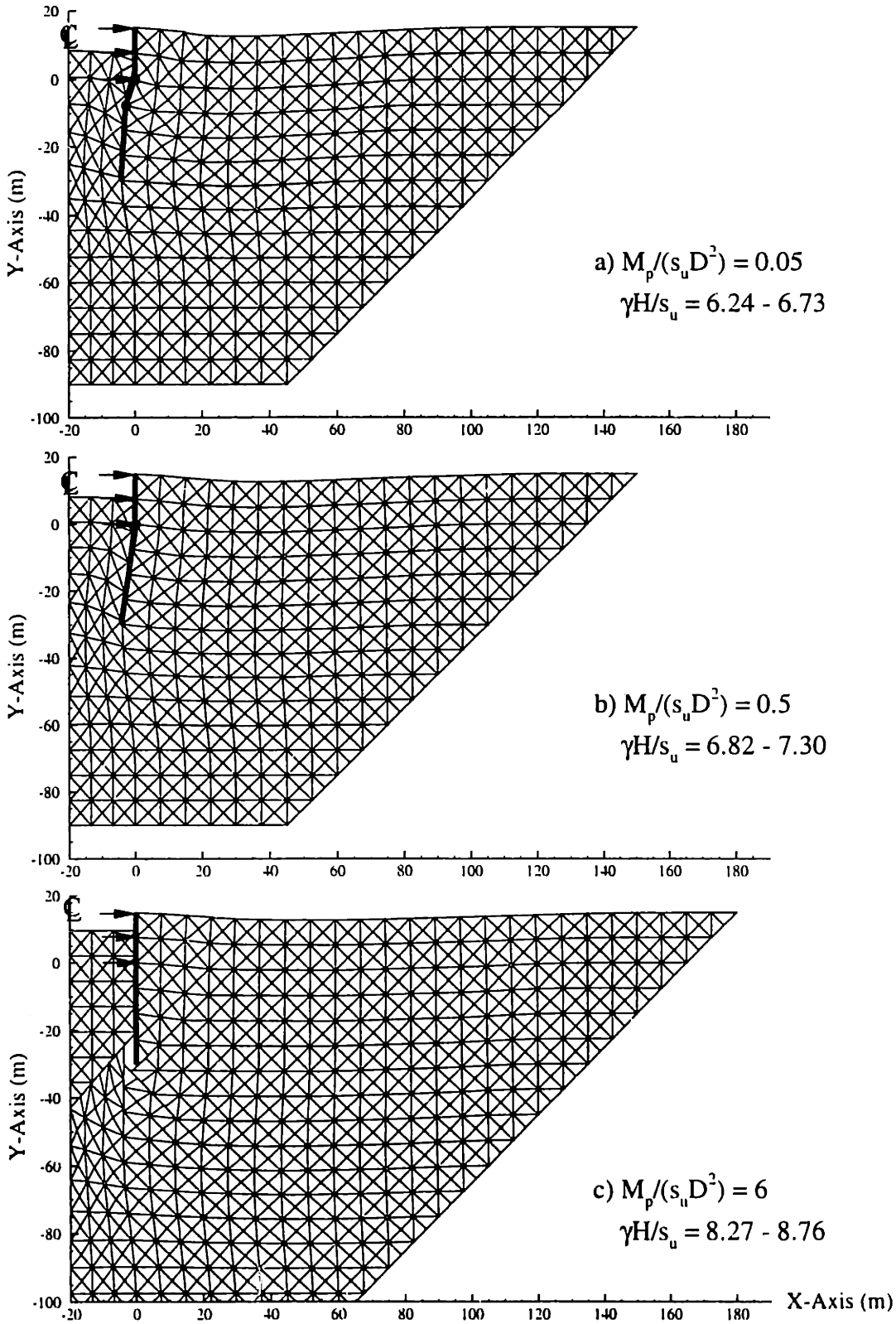

Figure 6.42 Comparisons of failure mechanism for different relative strength parameters, D/H = 2

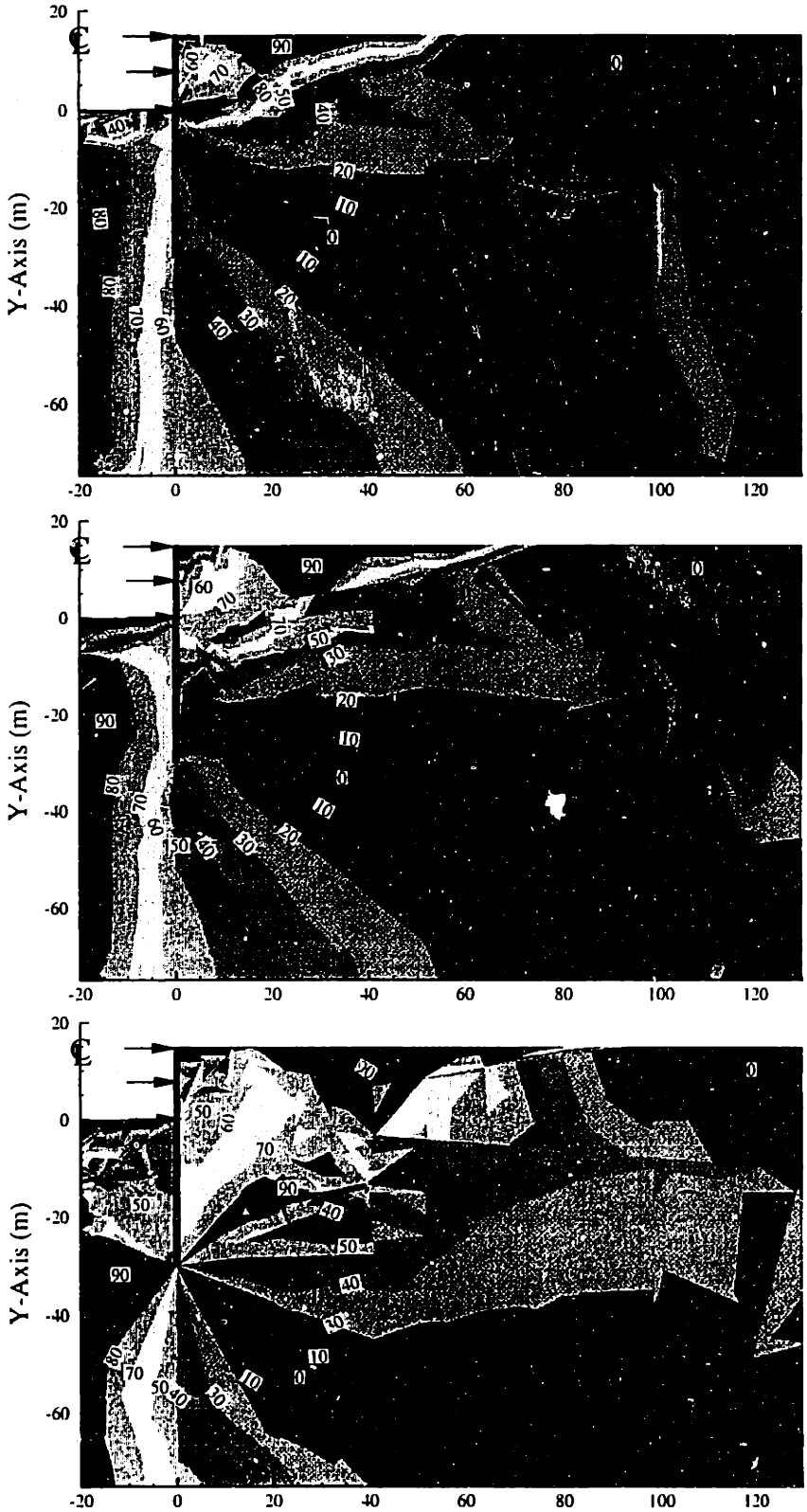

a) $M_p/(s_u D^2) = 0.05$
$\gamma H/s_u = 6.24 - 6.73$

b) $M_p/(s_u D^2) = 0.5$
$\gamma H/s_u = 6.82 - 7.30$

c) $M_p/(s_u D^2) = 6$
$\gamma H/s_u = 8.27 - 8.76$

Figure 6.43 Comparisons of the direction of σ_1 to the vertical (deg.) for different relative strength parameters, D/H = 2

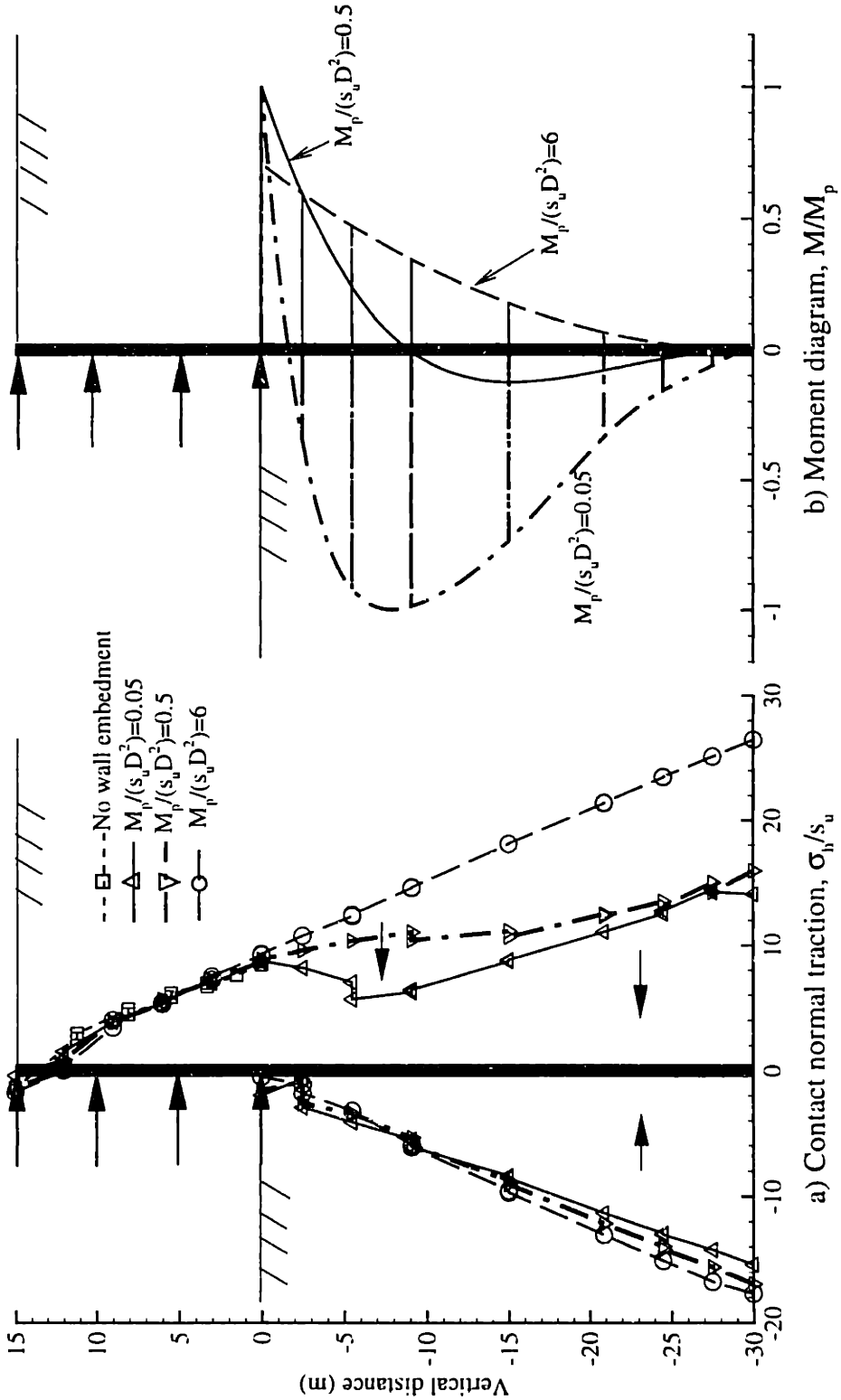

Figure 6.44 Contact pressure and moment diagram along the wall, D/H = 2

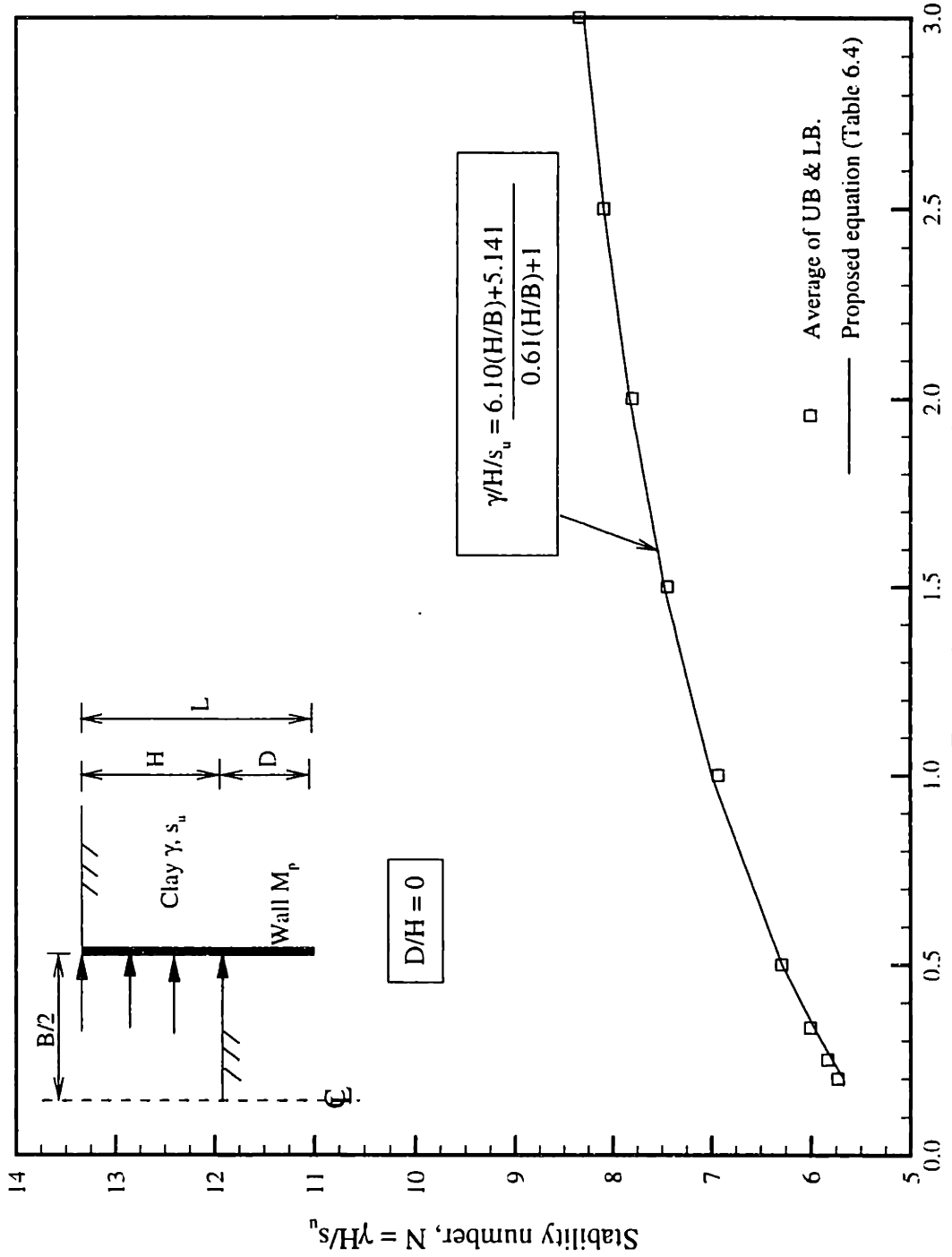

Figure 6.45 Evaluation of proposed equation for braced excavation in homogeneous clay with no embedment

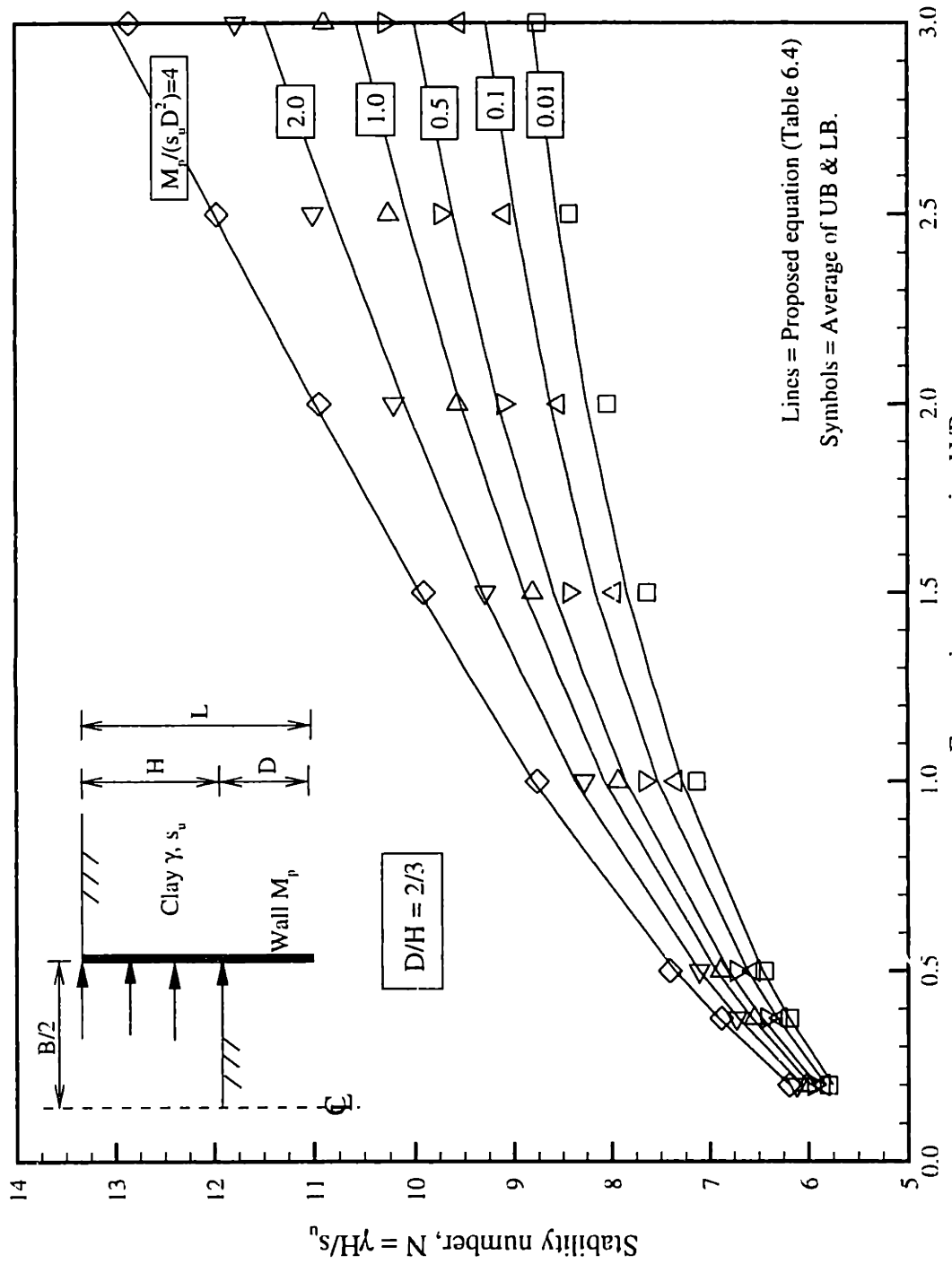

Figure 6.46 Evaluation of proposed equation for braced excavation in homogeneous clay, with embedment ratio D/H = 2/3

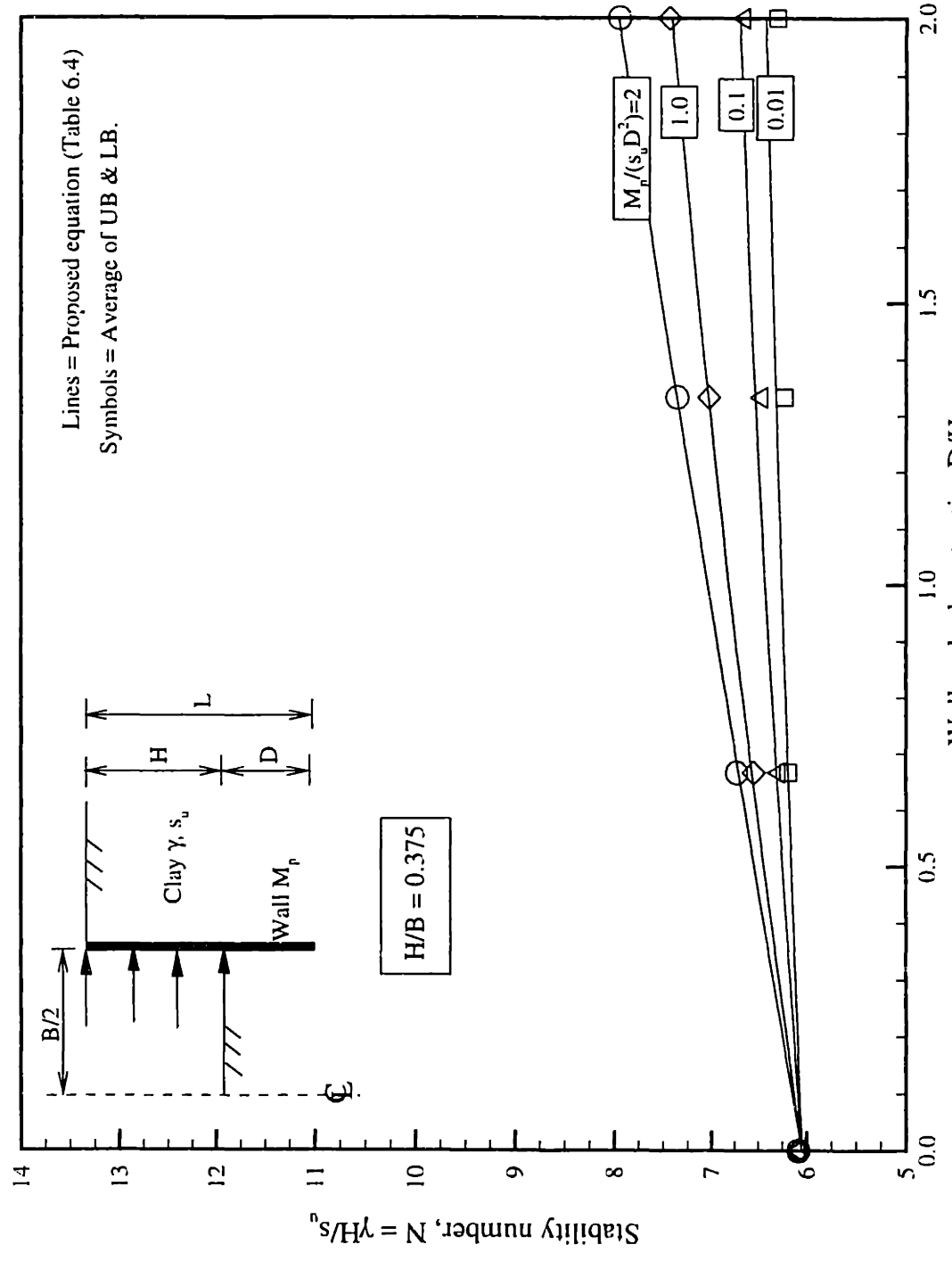

Figure 6.47 Evaluation of proposed equation for braced excavation in homogeneous clay, with aspect ratio H/B=0.375

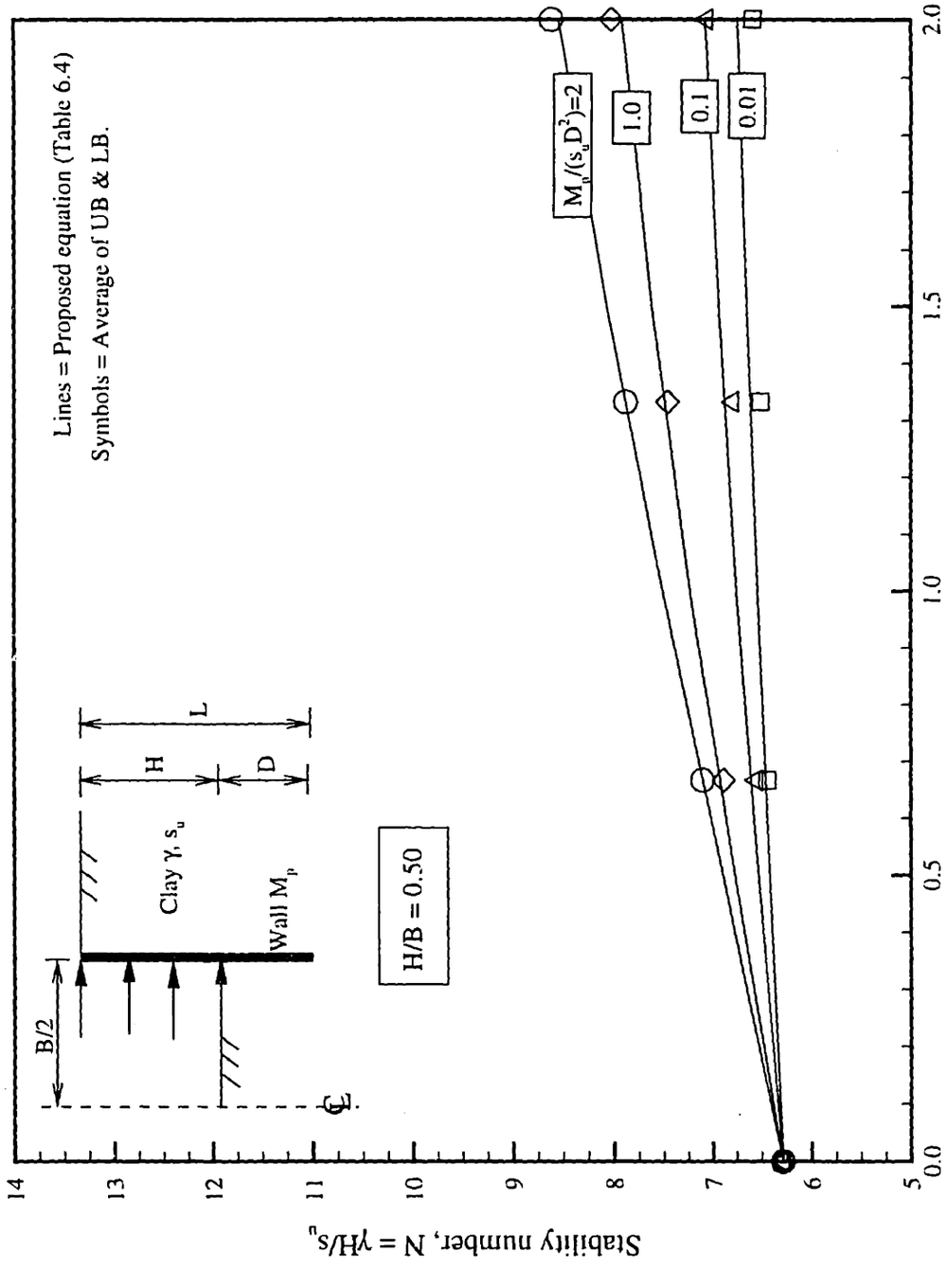

Figure 6.48 Evaluation of proposed equation for braced excavation in homogeneous clay, with aspect ratio H/B=0.5

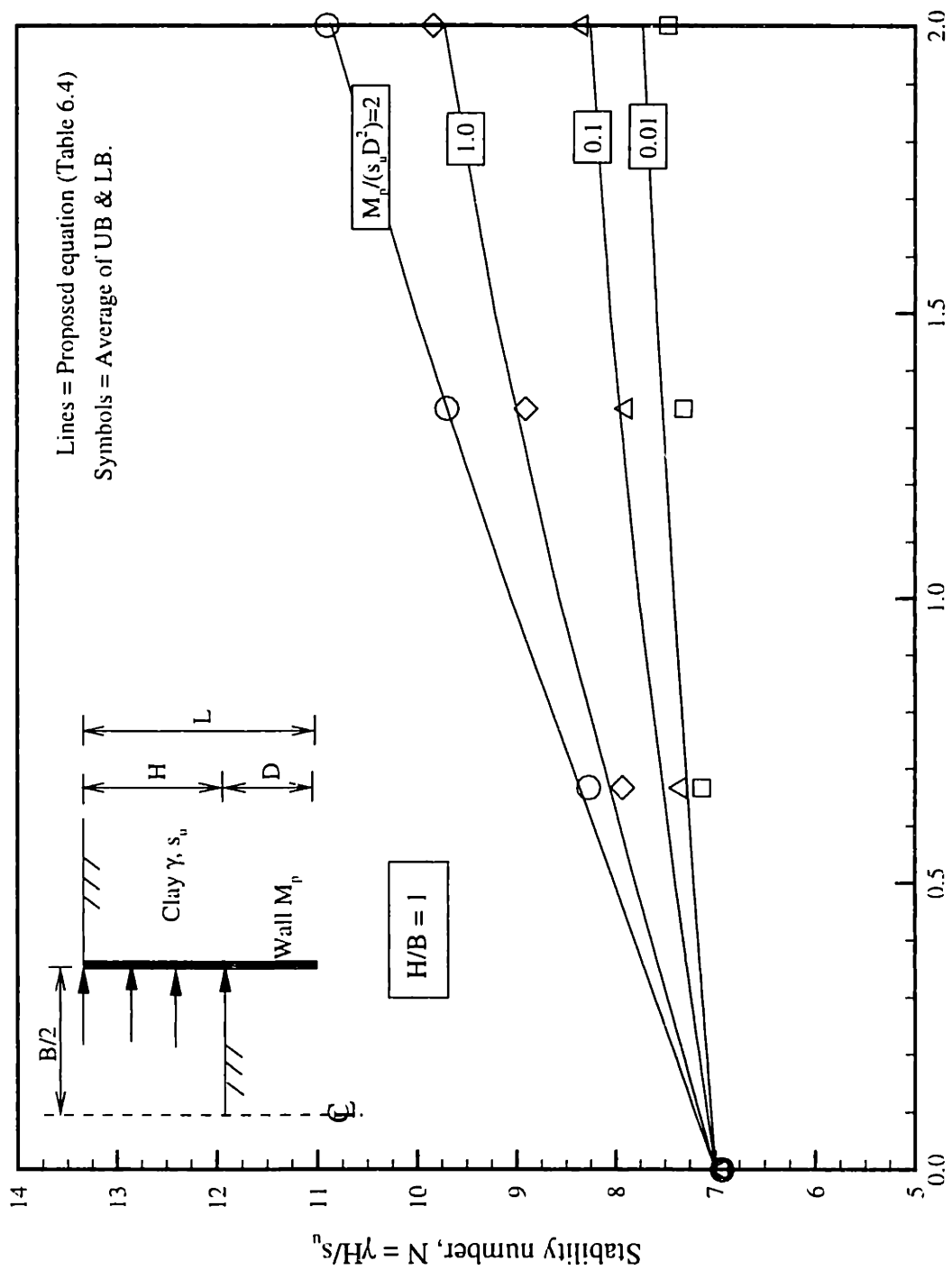

Figure 6.49 Evaluation of proposed equation for braced excavation in homogeneous clay, with aspect ratio H/B=1

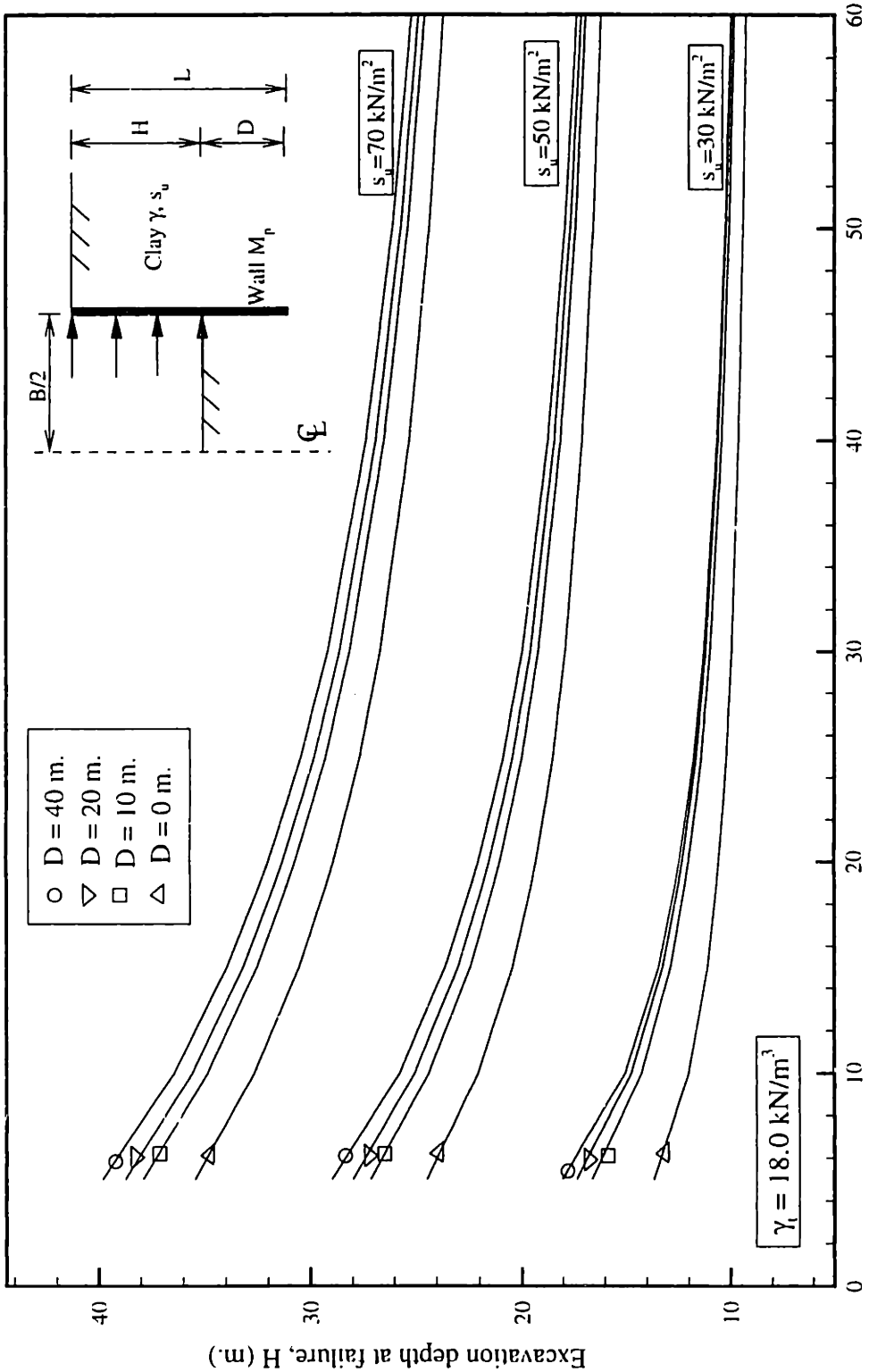

Figure 6.50 Design chart for braced excavation in homogeneous clay for M_p = 1 MNm/m

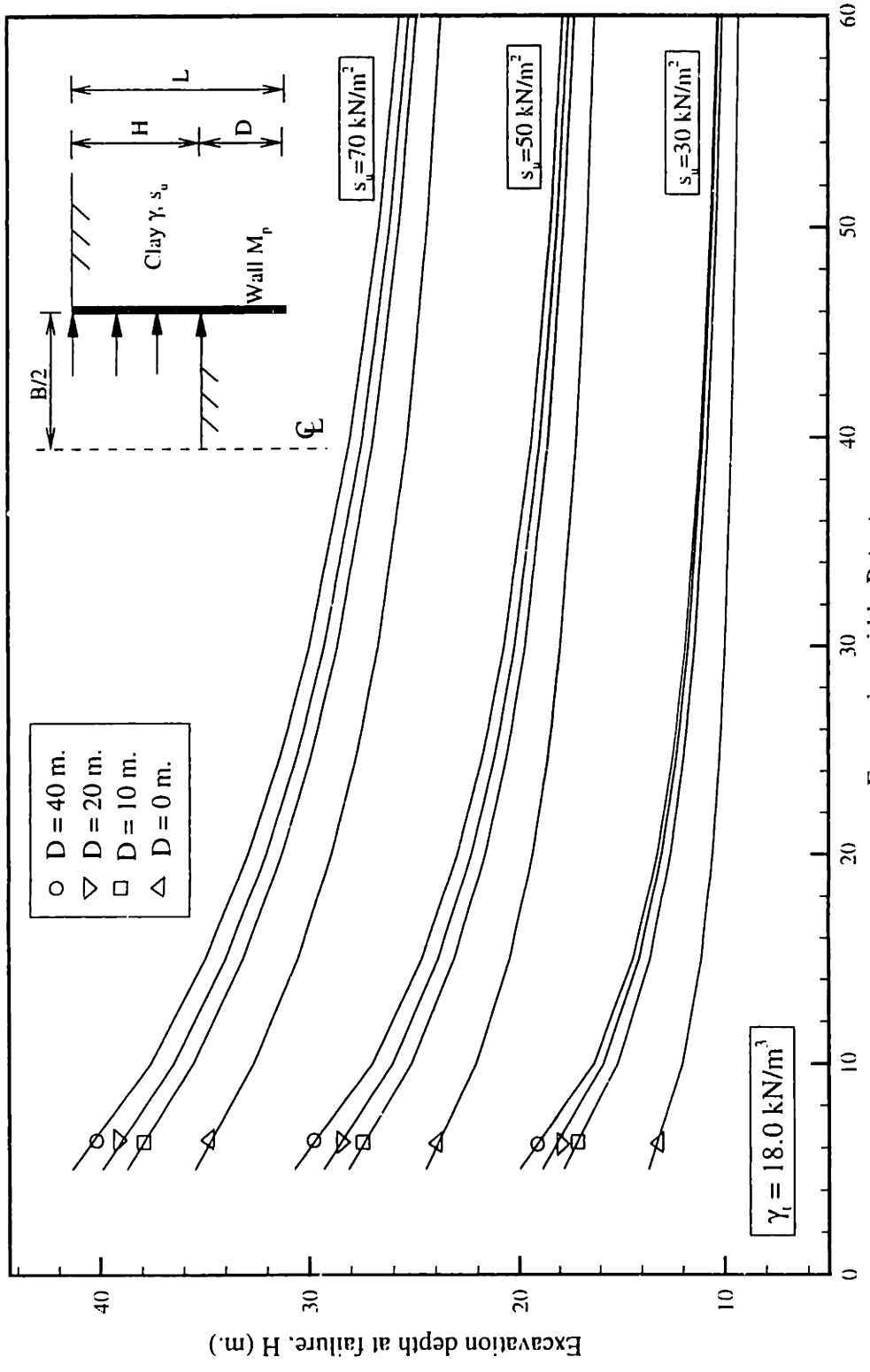

Figure 6.51 Design chart for braced excavation in homogeneous clay for M_p = 2.0 MNm/m

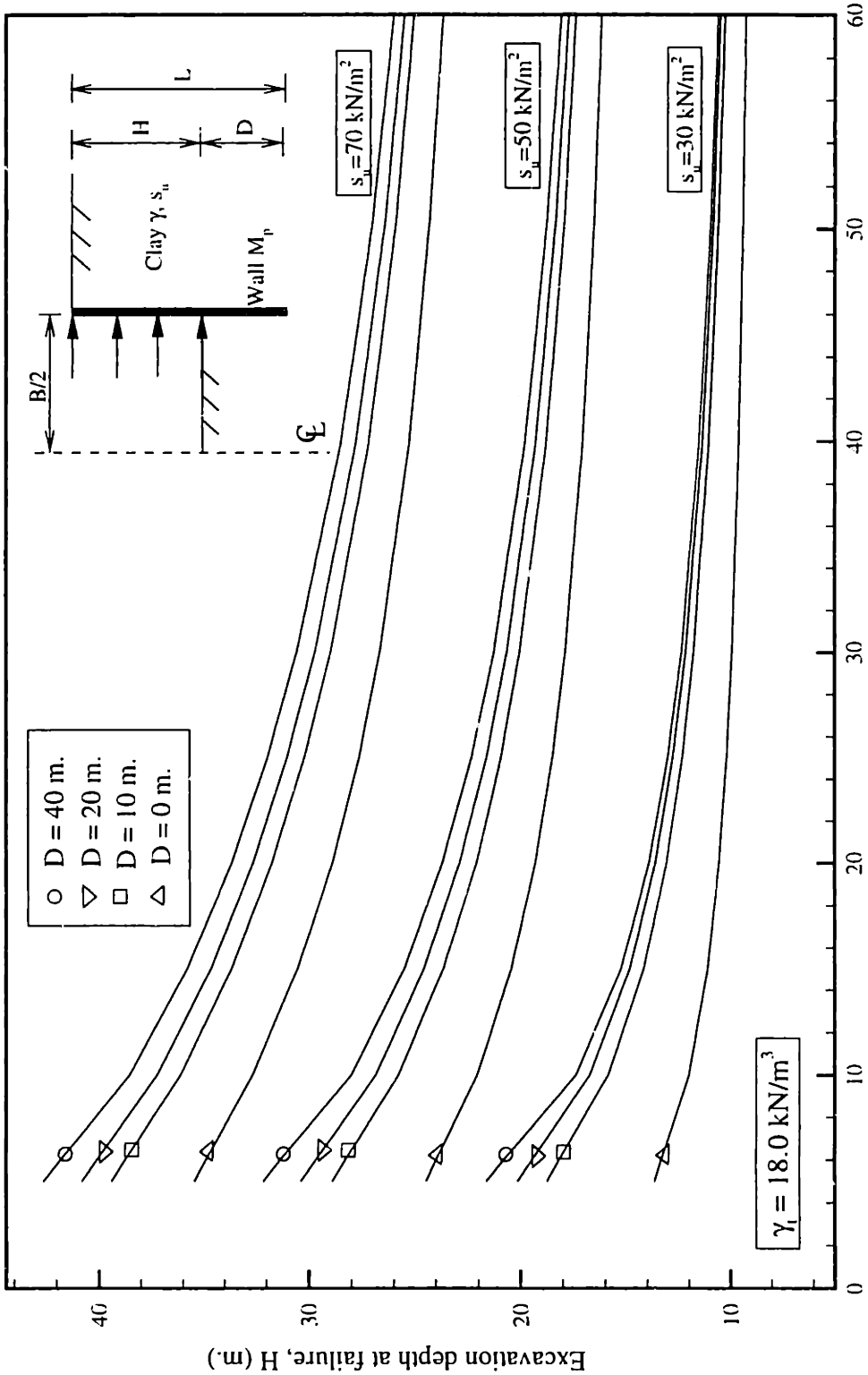

Figure 6.52 Design chart for braced excavation in homogeneous clay for M_p = 3.0 MNm/m

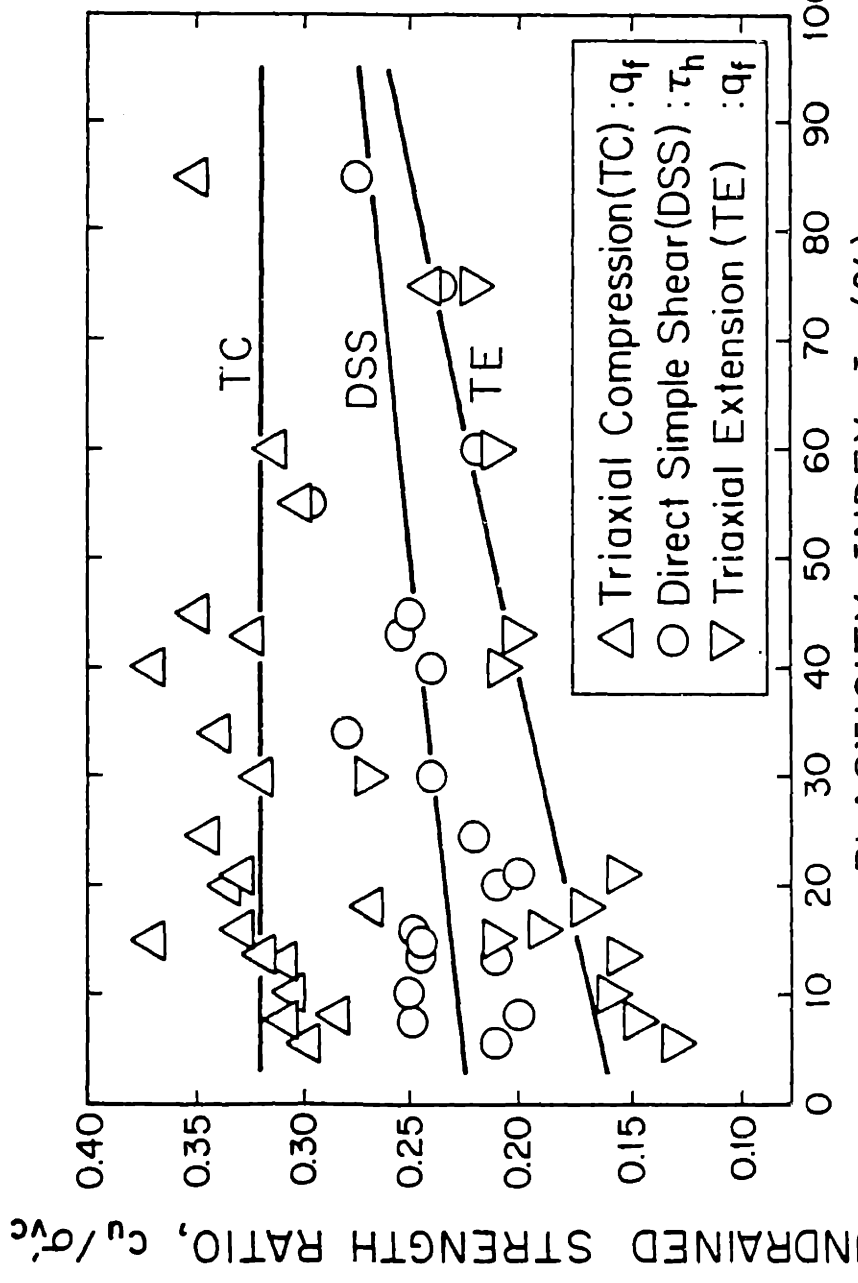

Figure 6.53 Undrained strength anisotropy from CK_0U Tests on Normally Consolidated Clays and Silts (after Ladd, 1991)

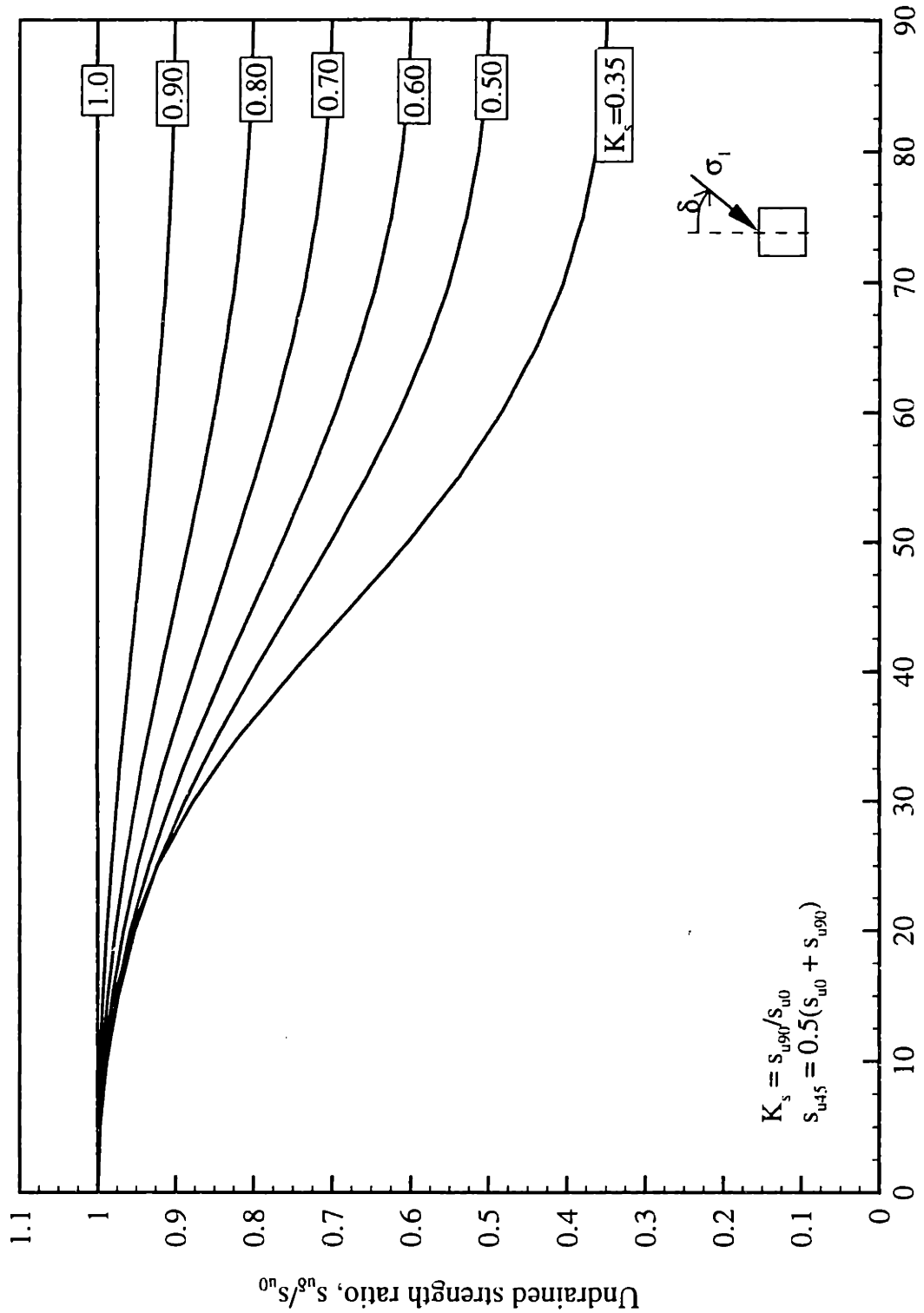

Figure 6.54 Variation of undrained strength with the direction of major principal stress using the strength envelope given by Davis & Christian (1971)

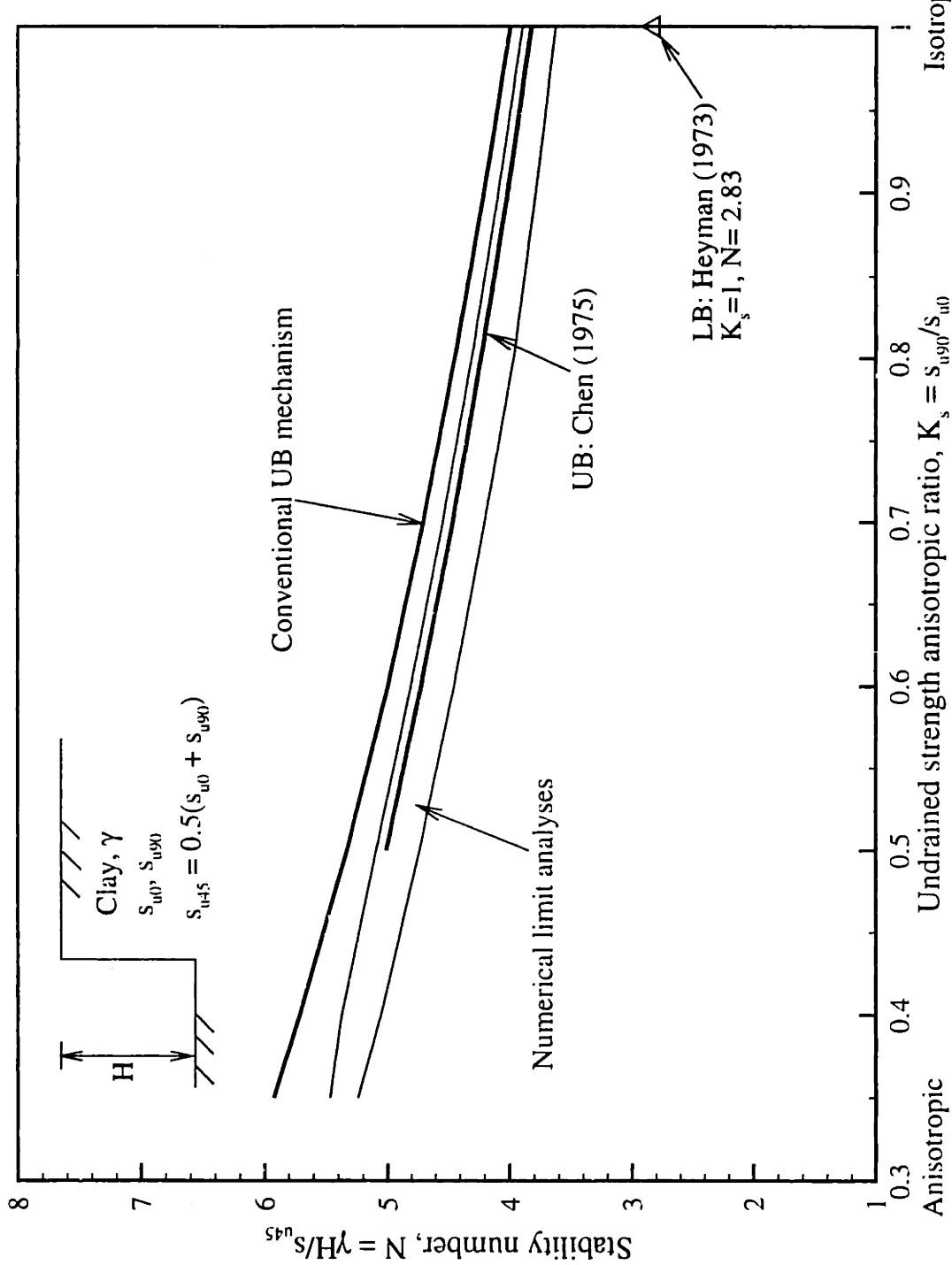

Figure 6.55 Stability number of a vertical cut in anisotropic clay, homogeneous strength (not including fissured clay, K_s>1)

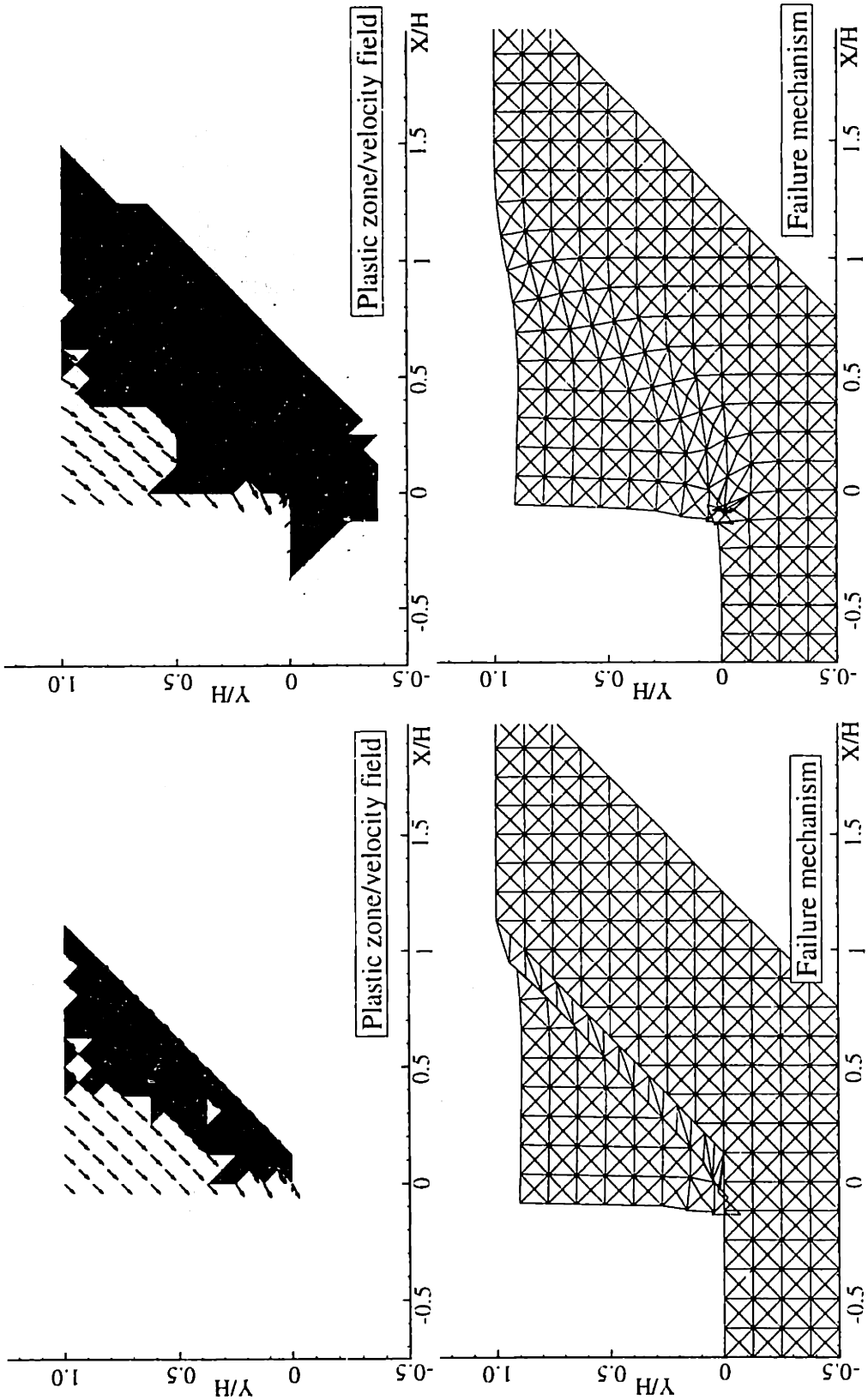

a) Isotropic strength, K_s=1: N = 3.634 - 3.902

b) Anisotropic strength, K_s=0.5: N= 4.736 - 5.096

Figure 6.56 Comparisons of upper bound results for vertical cut in isotropic and anisotropic clays with K_s=0.5

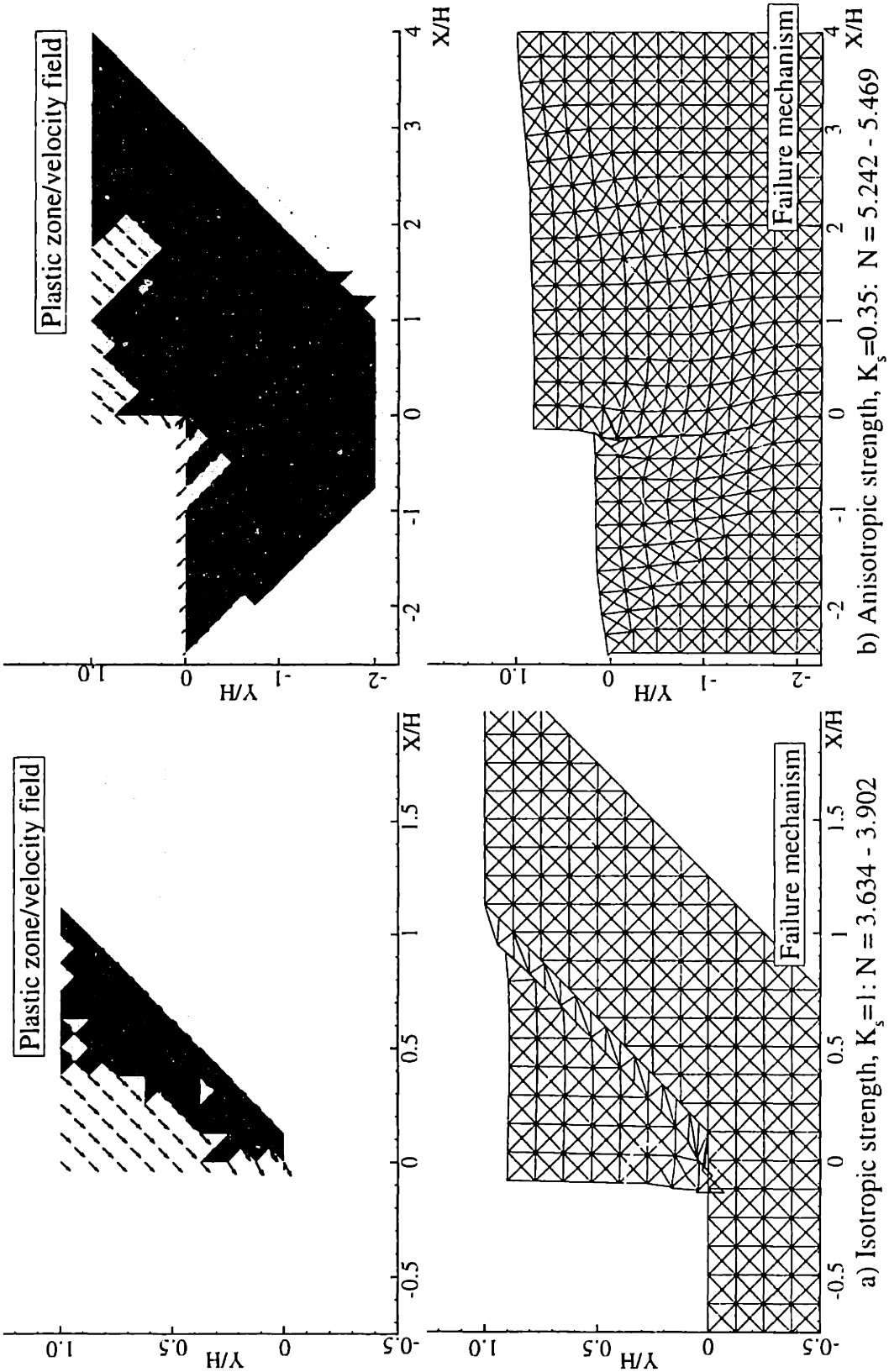

a) Isotropic strength, K_s=1: N = 3.634 - 3.902

b) Anisotropic strength, K_s=0.35: N = 5.242 - 5.469

Figure 6.57 Comparisons of upper bound results for vertical cut in isotropic and anisotropic clays with K_s=0.35

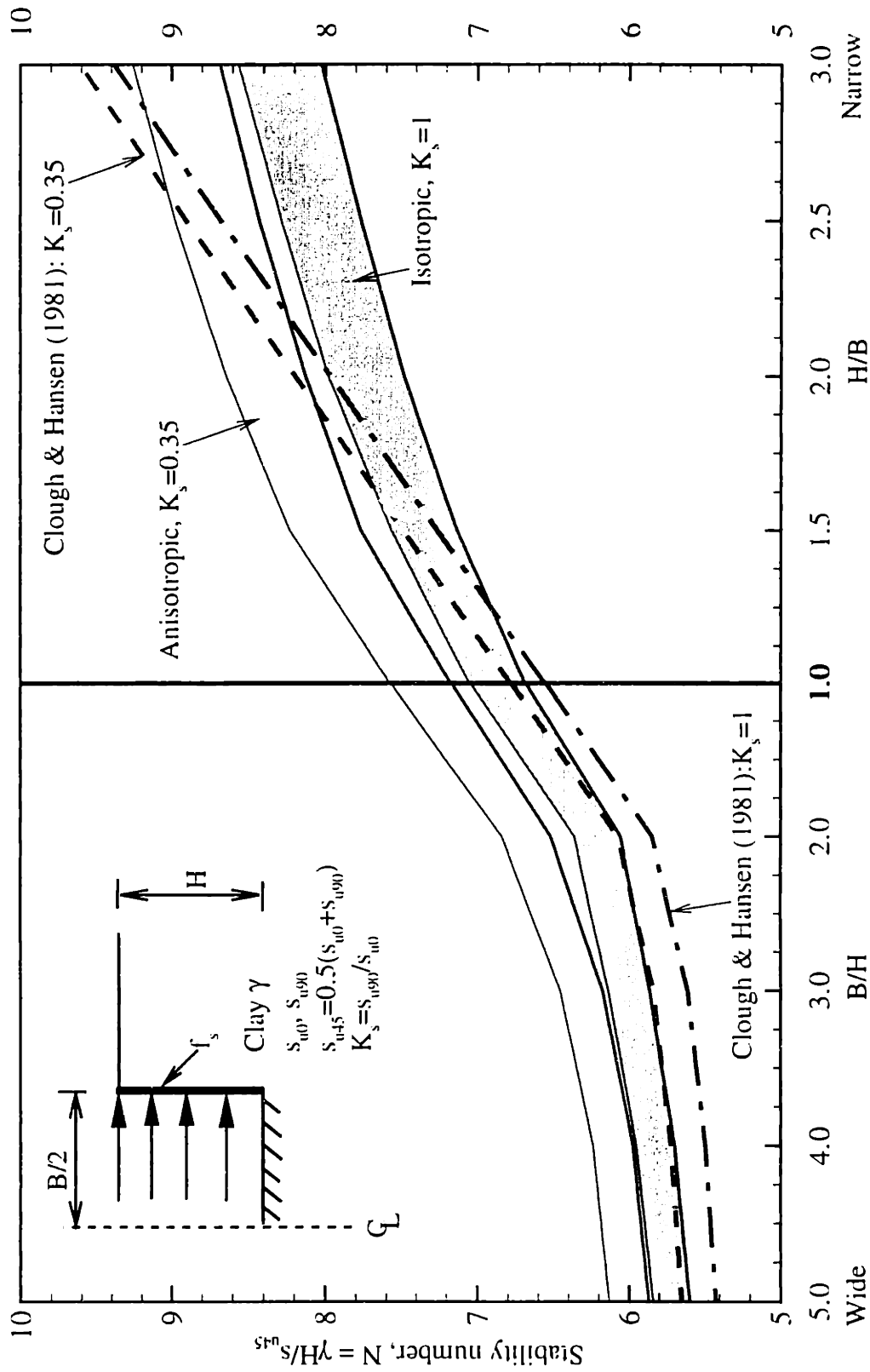

Figure 6.58 Undrained stability of a braced excavation in anisotropic clay, rough wall ($f_s=s_u$)

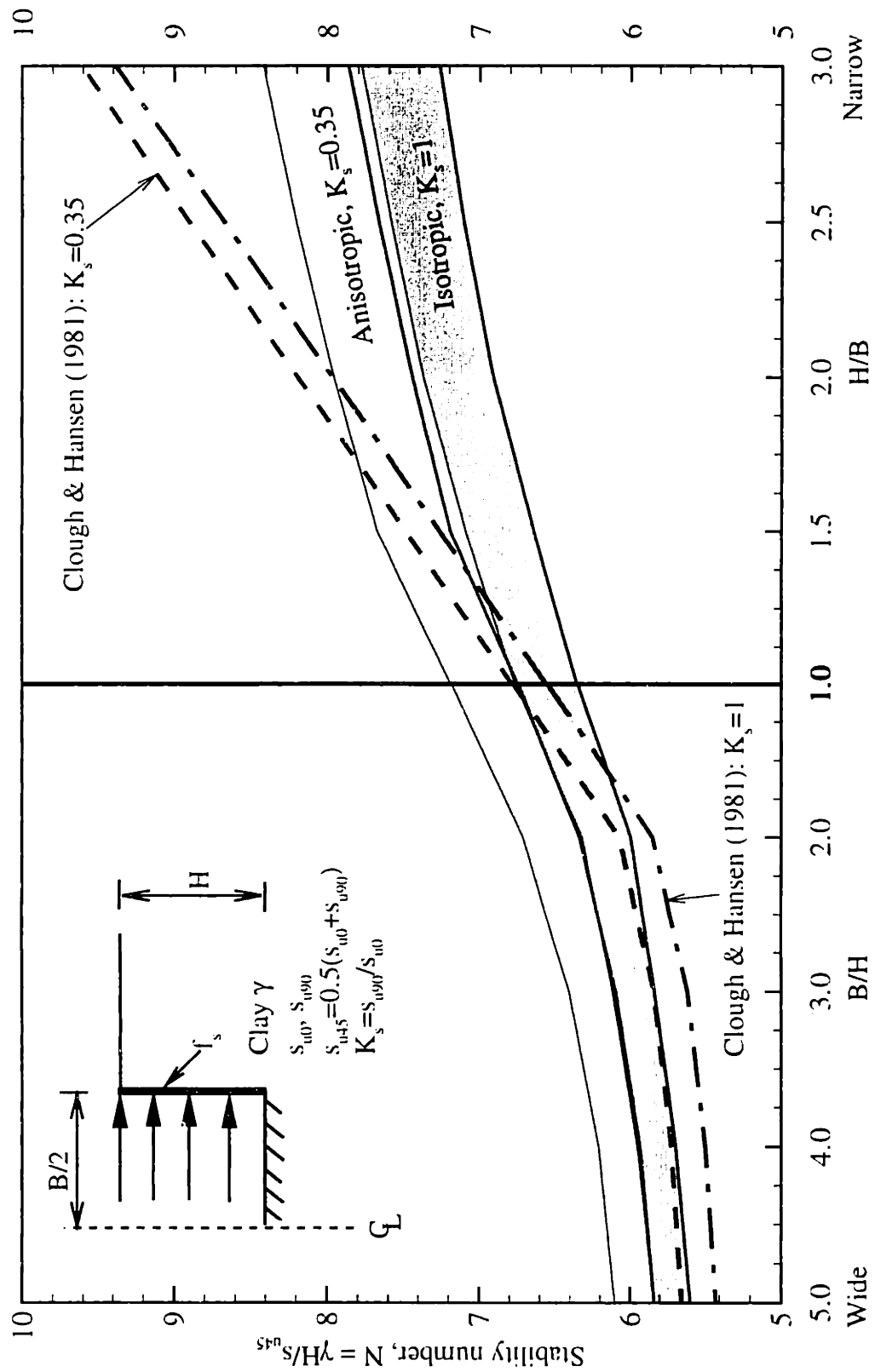

Figure 6.59 Undrained stability of a braced excavation in anisotropic clay, smooth wall (f_s=0)

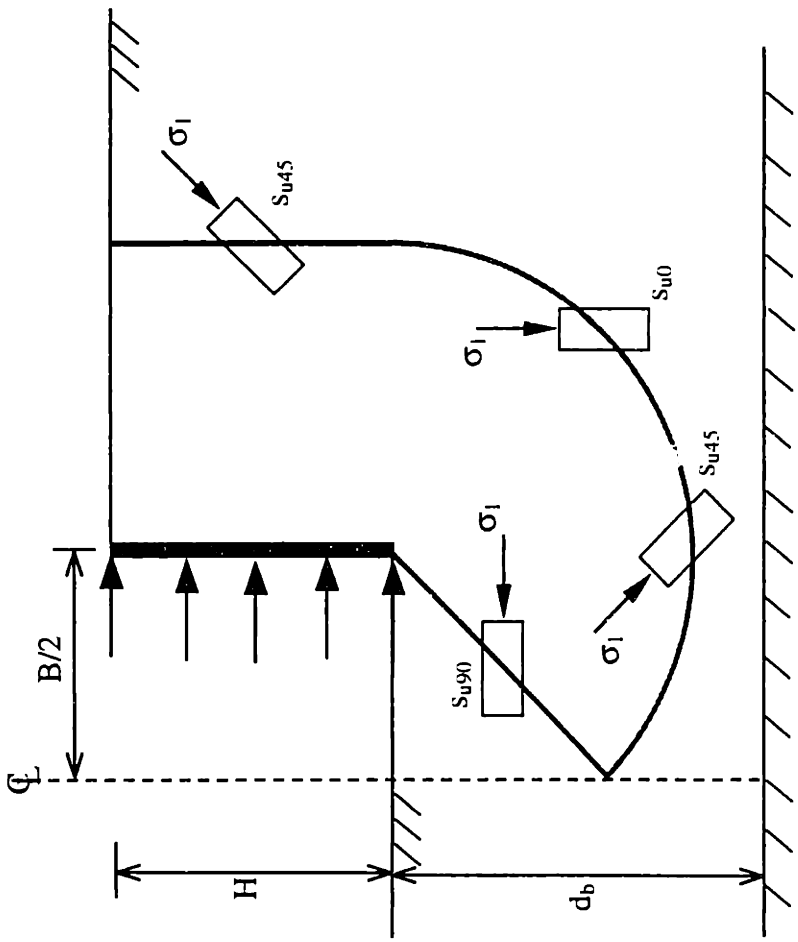

Figure 6.60 Modification of Terzaghi (1943)'s basal heave calculations for braced excavations in anisotropic clay (after Clough and Hansen, 1981)

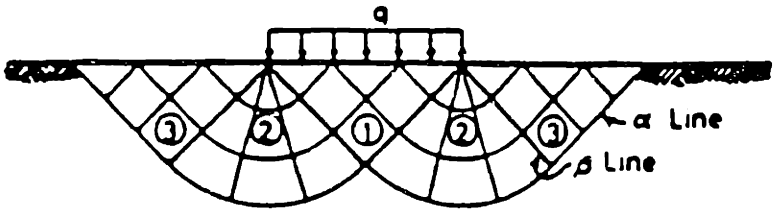

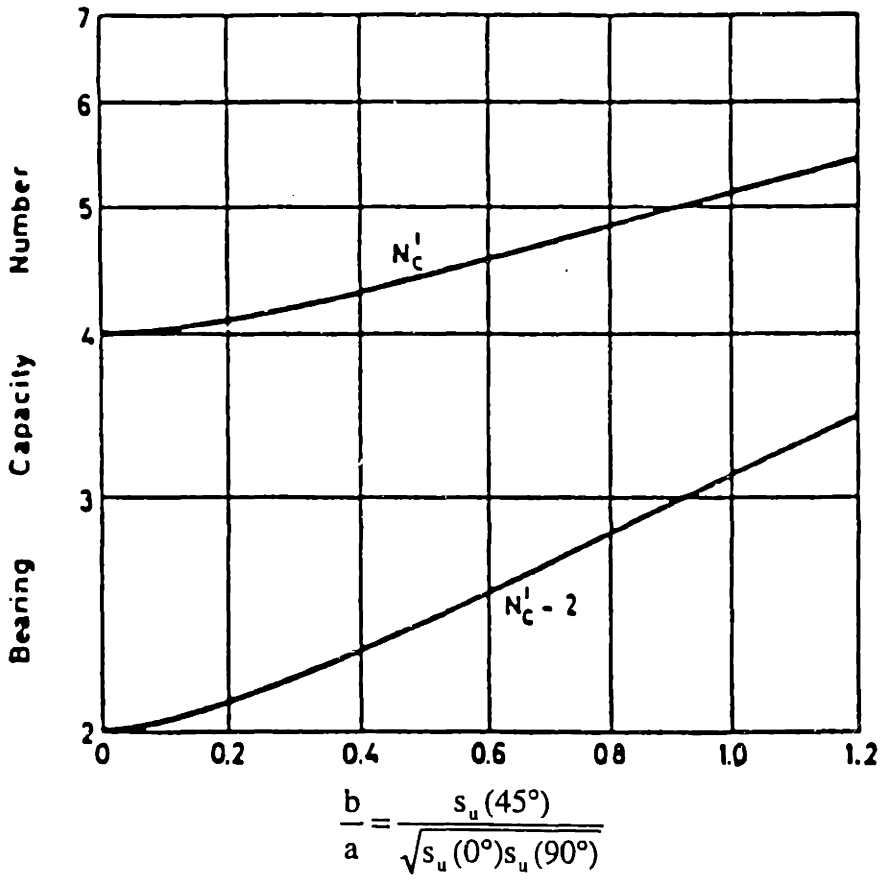

Figure 6.61 Davis and Christian (1971) solutions for ultimate bearing capacity of a rigid footing on anisotropic clay

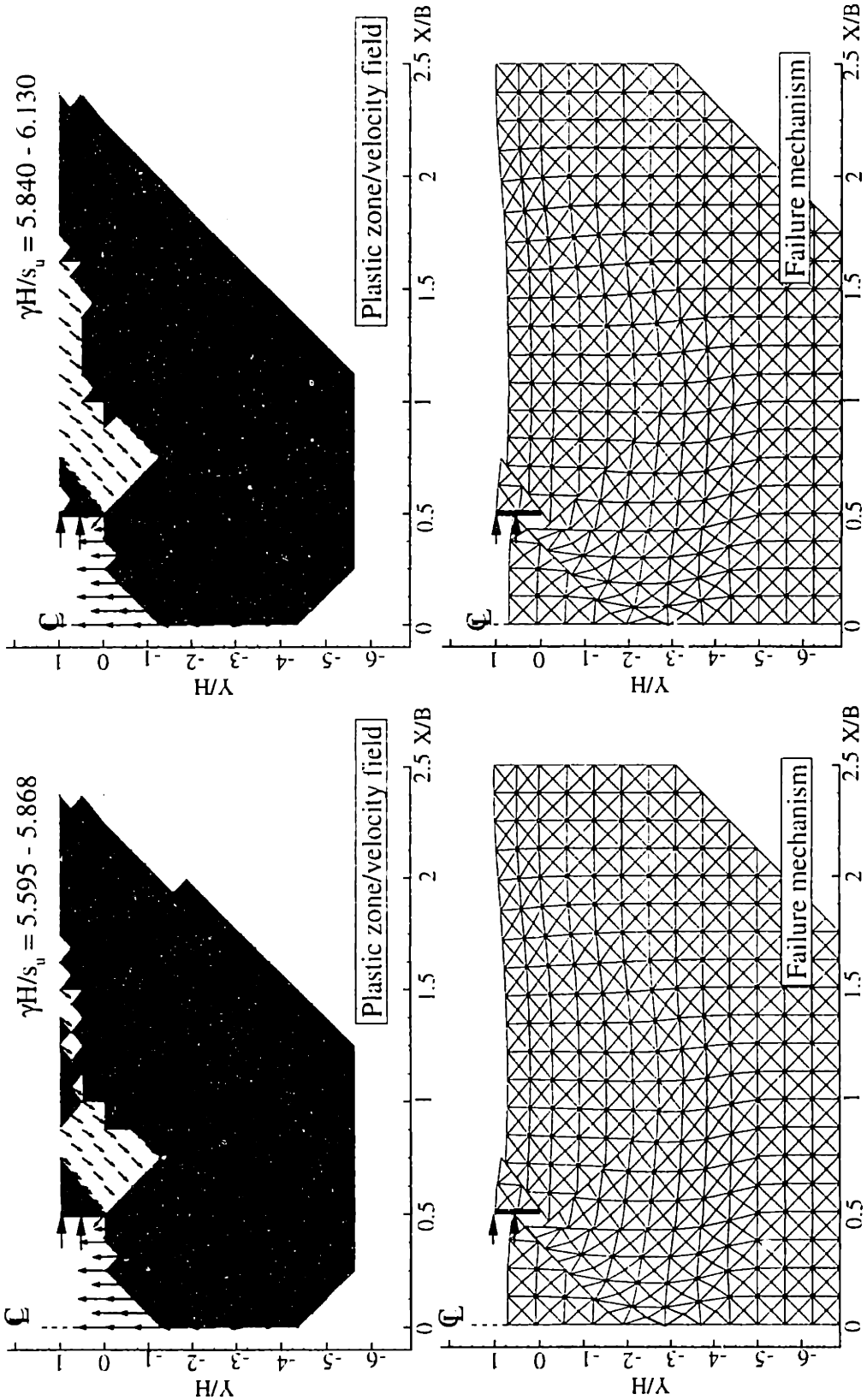

a) Isotropic strength, K_s=1

b) Anisotropic strength, K_s=0.35

Figure 6.62 Comparisons of upper bound results for isotropic and anisotropic strength: B/H = 5

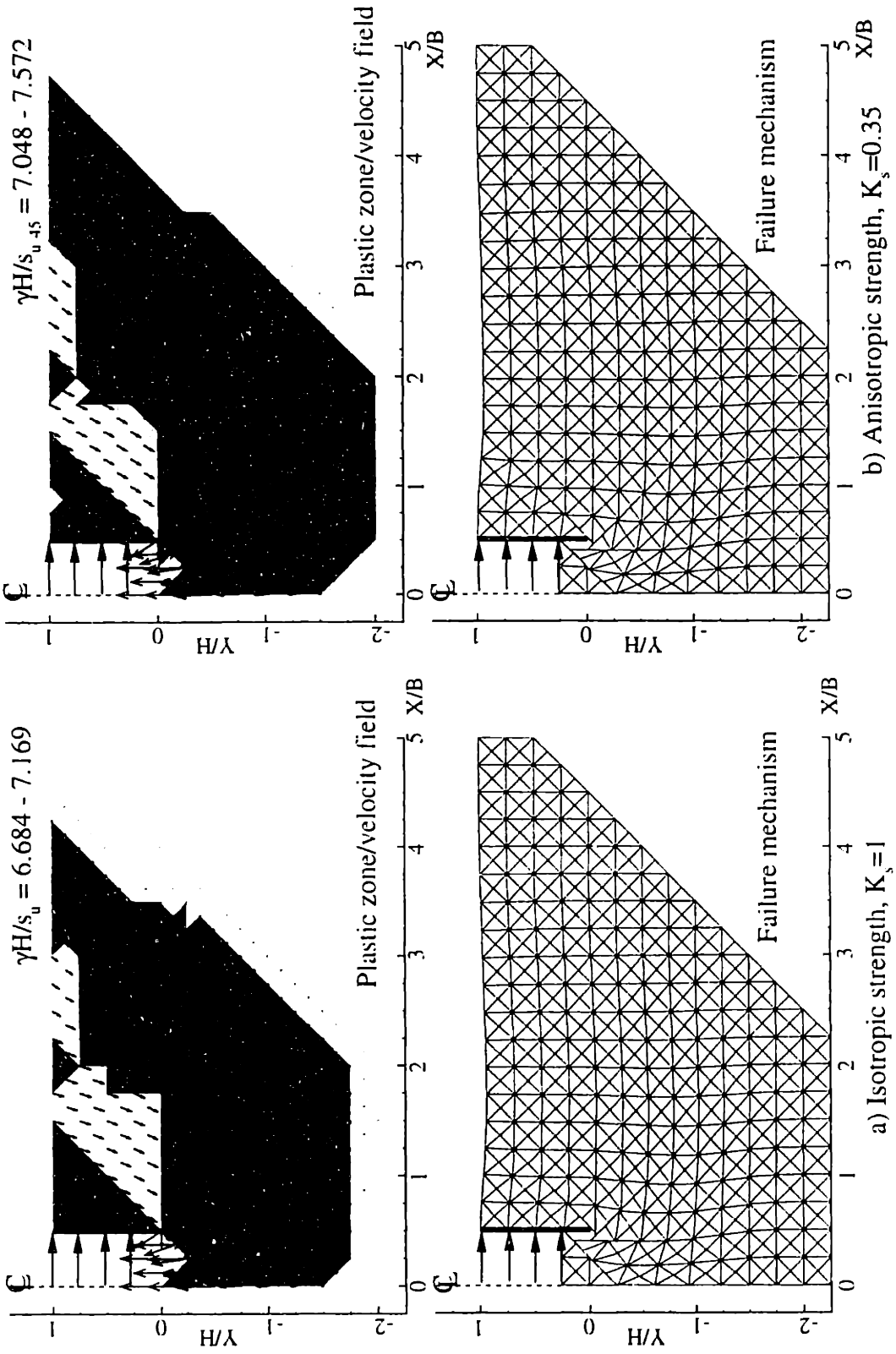

Figure 6.63 Comparisons of upper bound results for isotropic and anisotropic strength H/B = 1

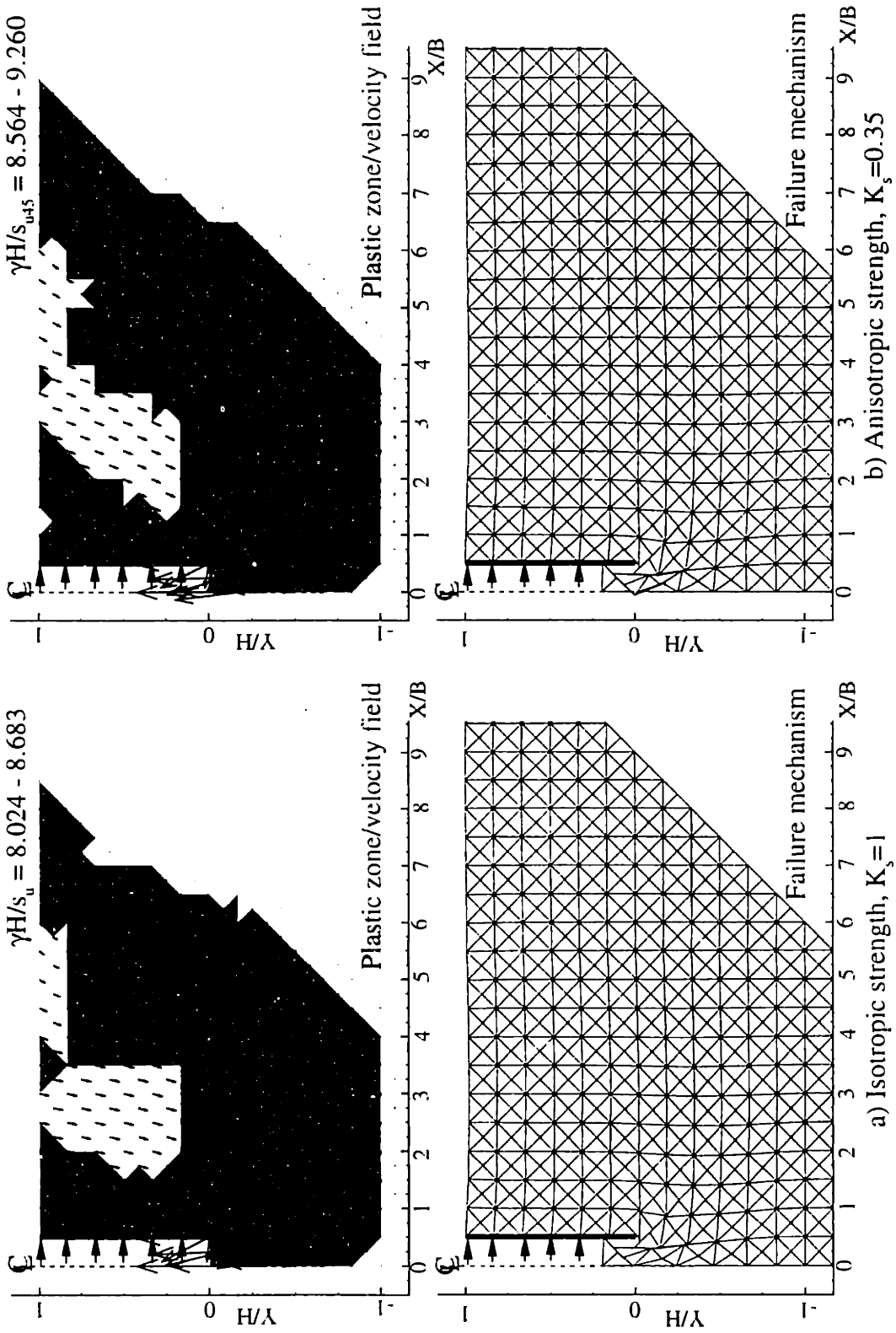

Figure 6.64 Comparisons of upper bound results for isotropic and anisotropic strength: H/B = 3

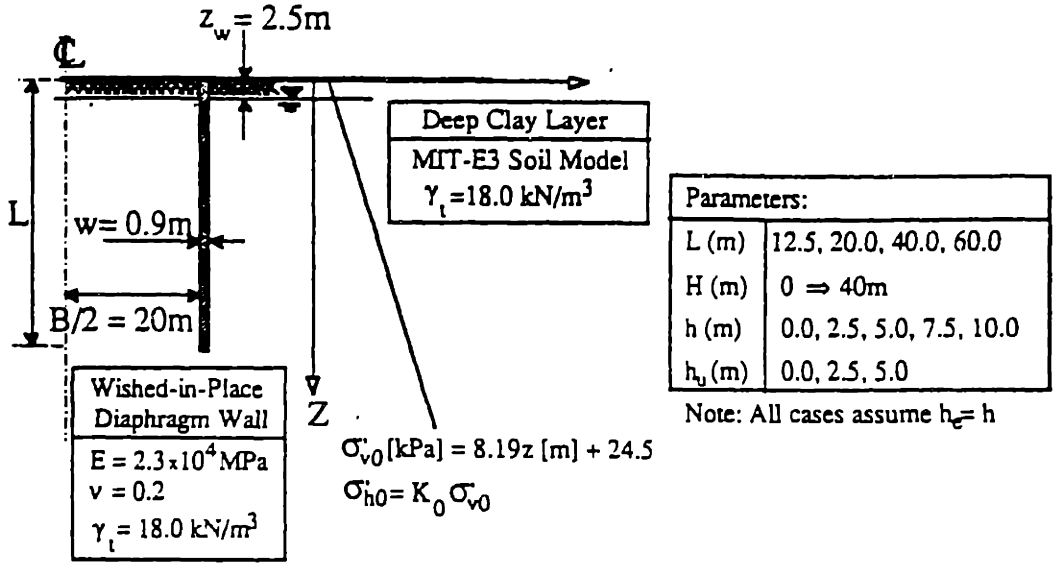

(a) Initial Conditions and Summary of Geometric Parameters

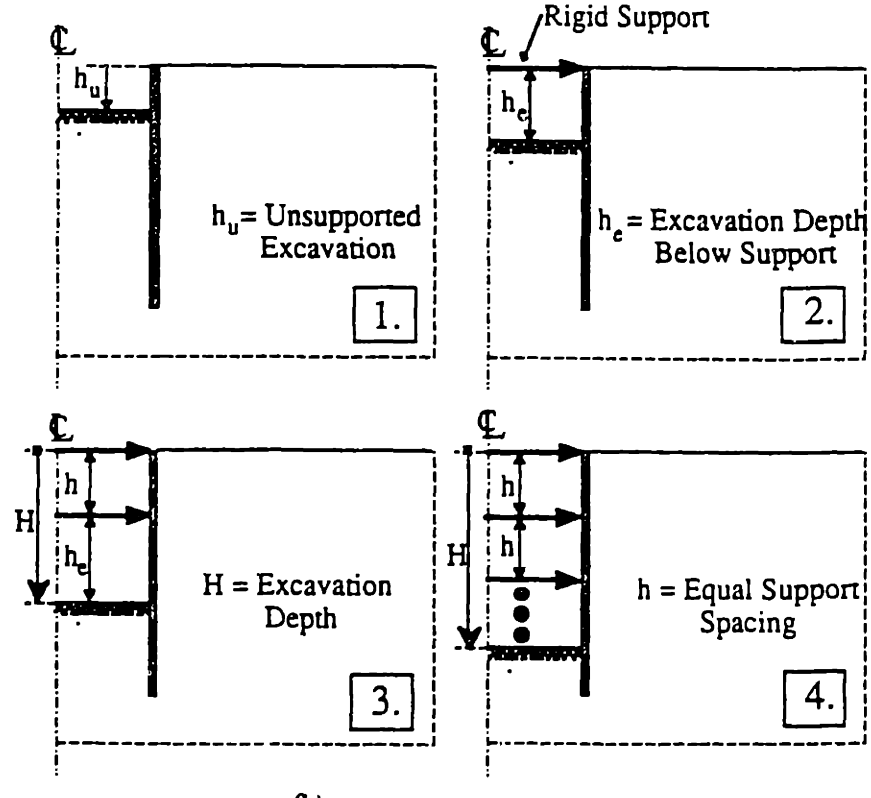

(b) Excavation Sequence

Figure 6.65 Finite element model excavation sequences by Hashash and Whittle (1996)

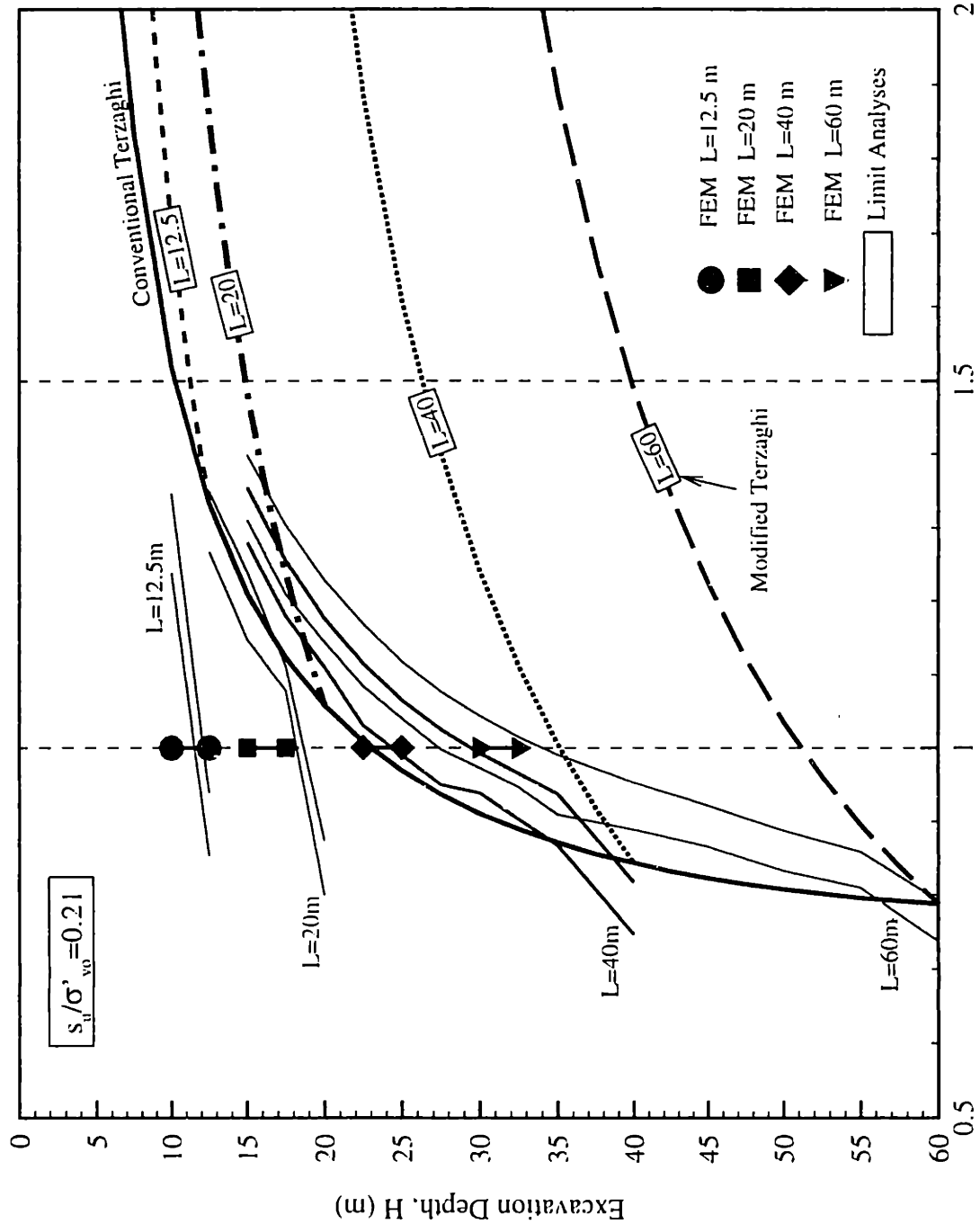

Figure 6.66 Basal heave stability by numerical limit analyses, using isotropic strength, s_u/σ'_{v0} = 0.21

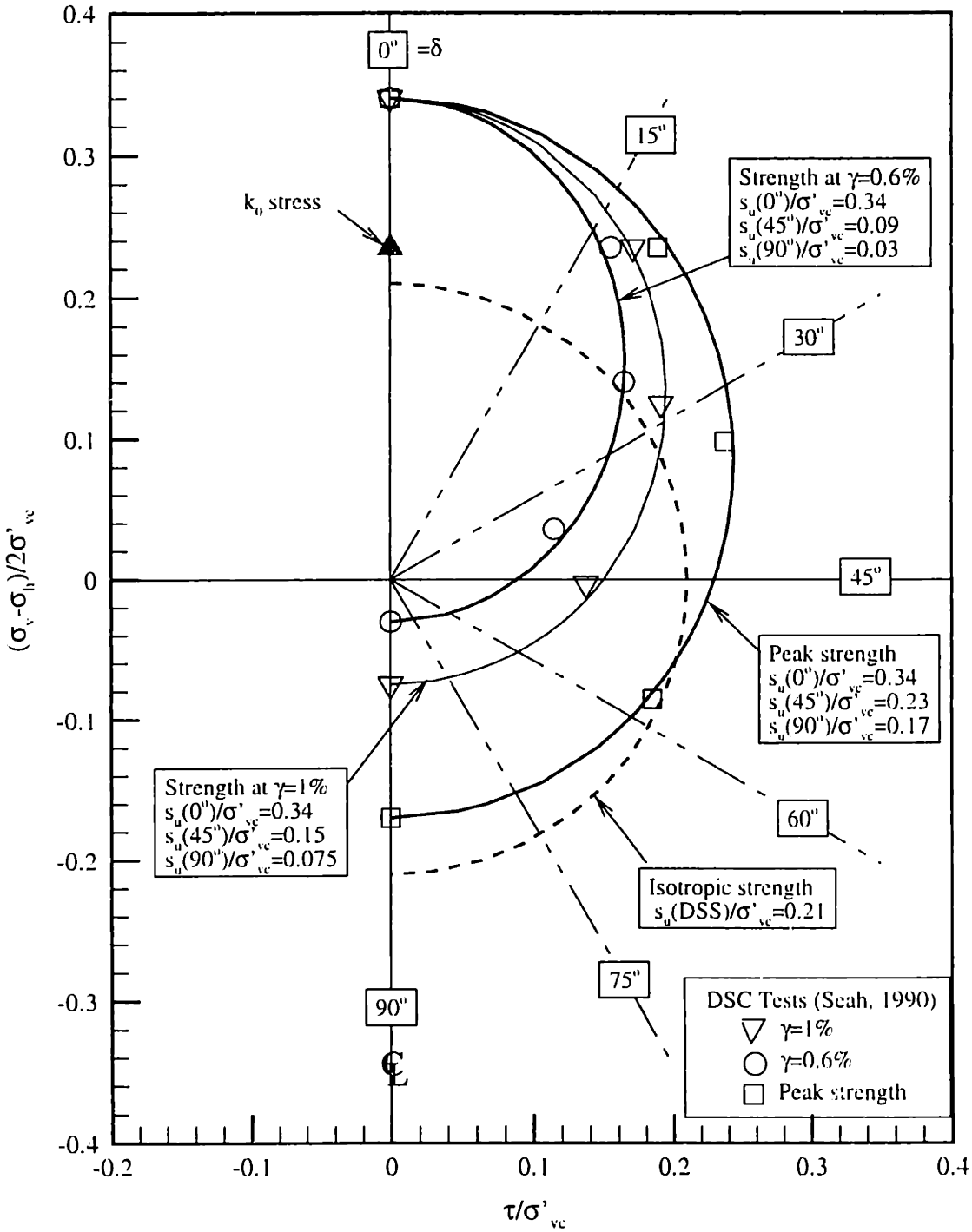

Figure 6.67 Anisotropic Yield Strength for Normally Consolidated BBC

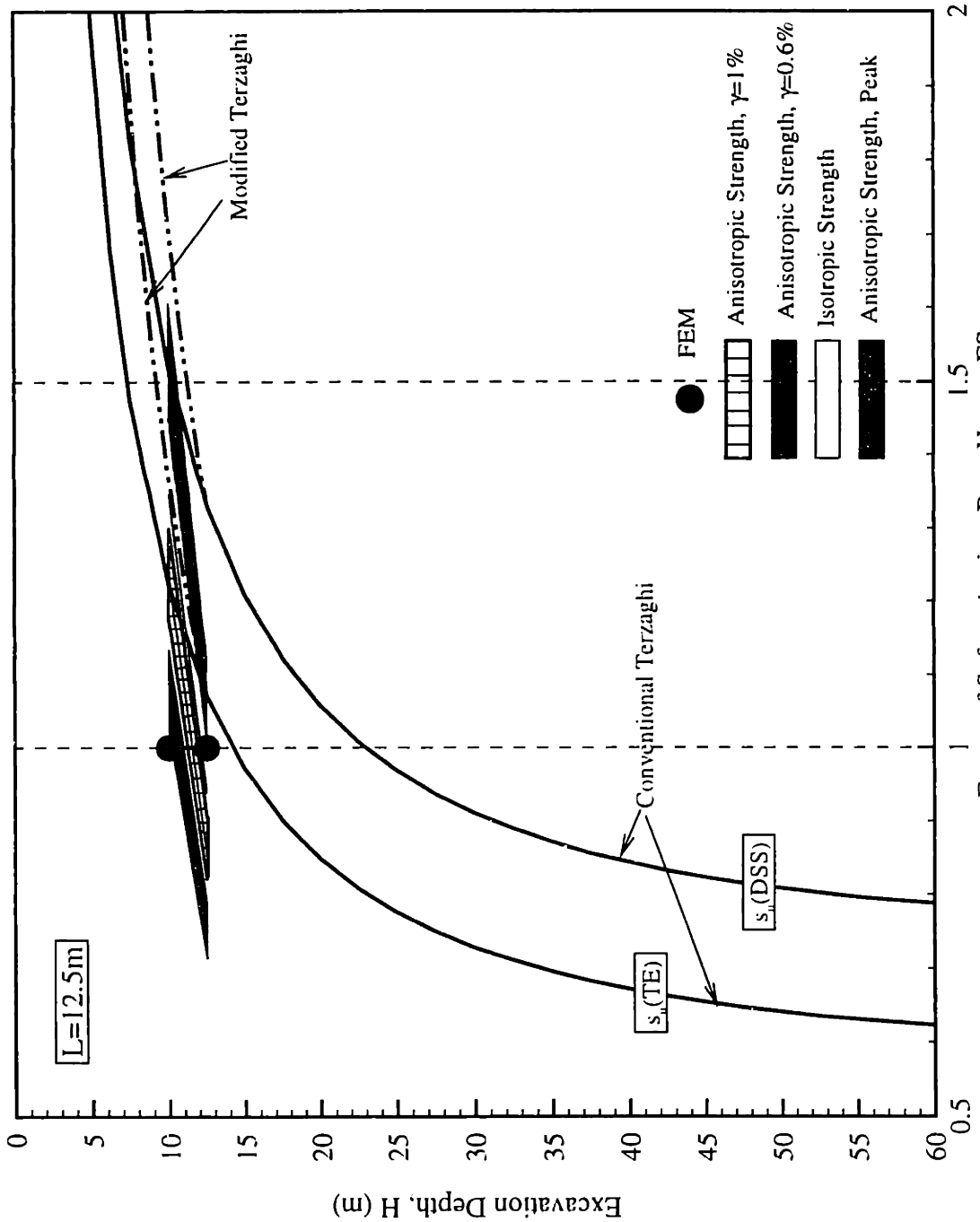

Figure 6.68 Effect of undrained strength anisotropy for stability of braced wall with L = 12.5 m

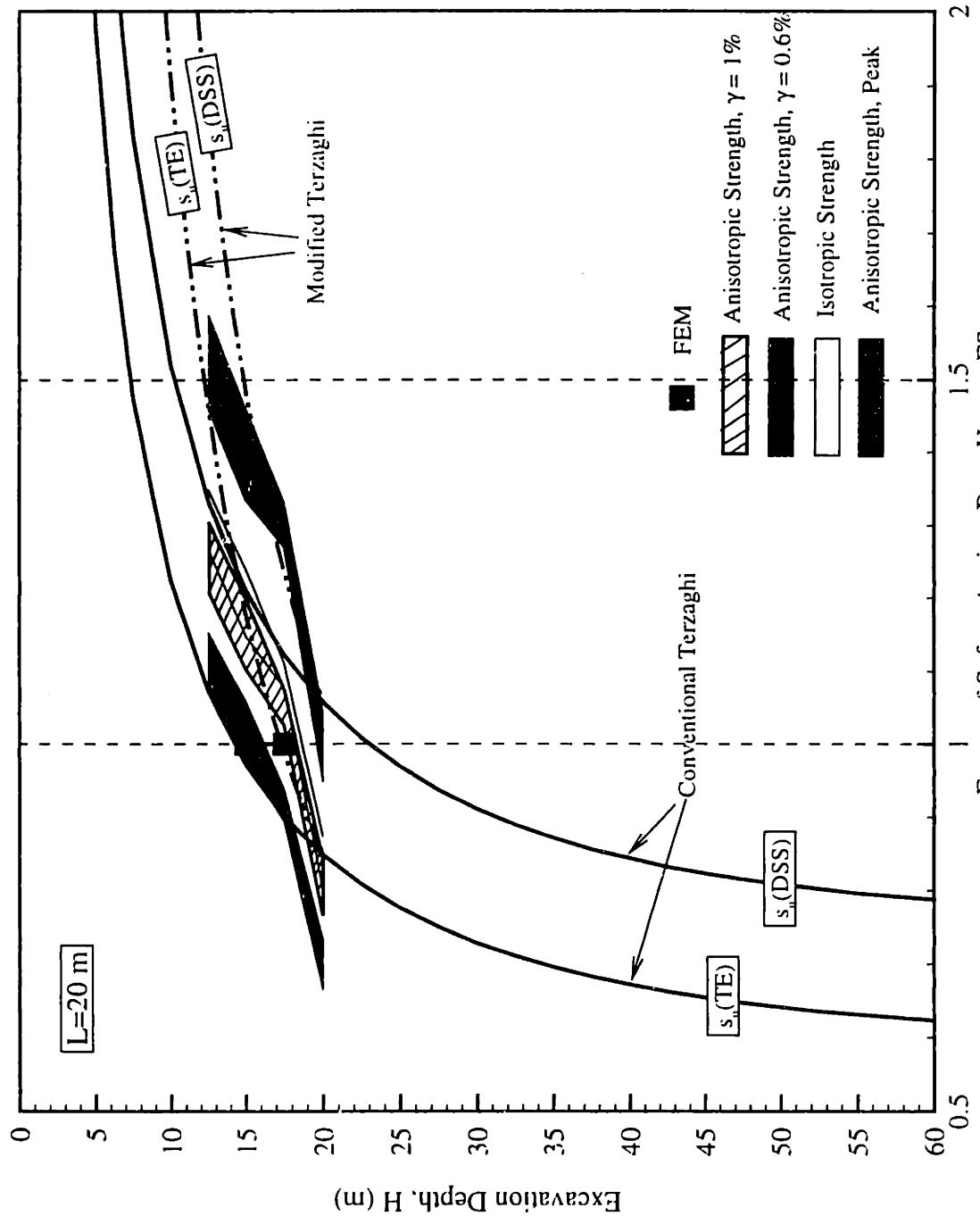

Figure 6.69 Effect of undrained strength anisotropy for stability of braced wall with L = 20 m

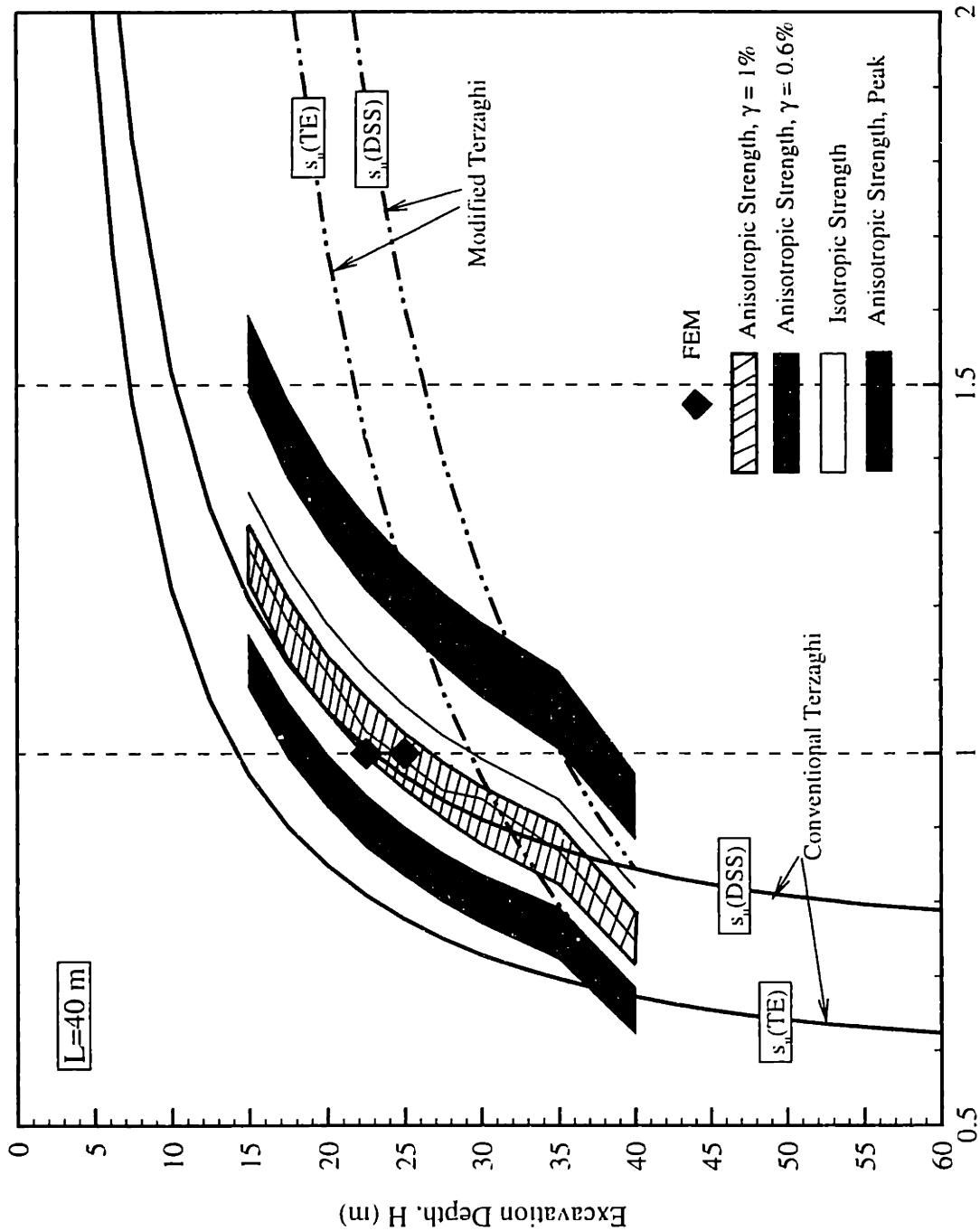

Figure 6.70 Effect of undrained strength anisotropy for stability of braced wall with L = 40 m

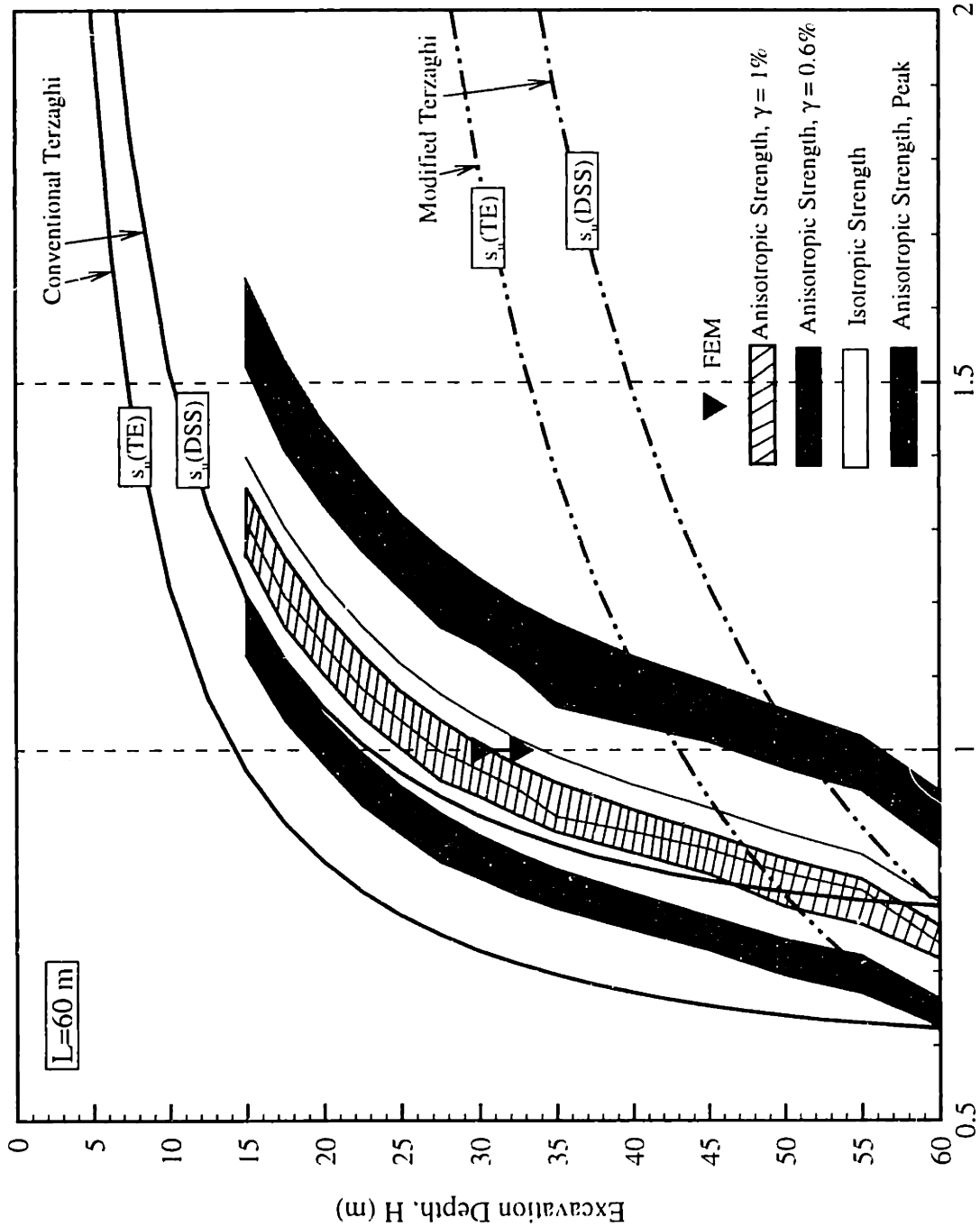

Figure 6.71 Effect of undrained strength anisotropy for stability of braced wall with L = 60 m

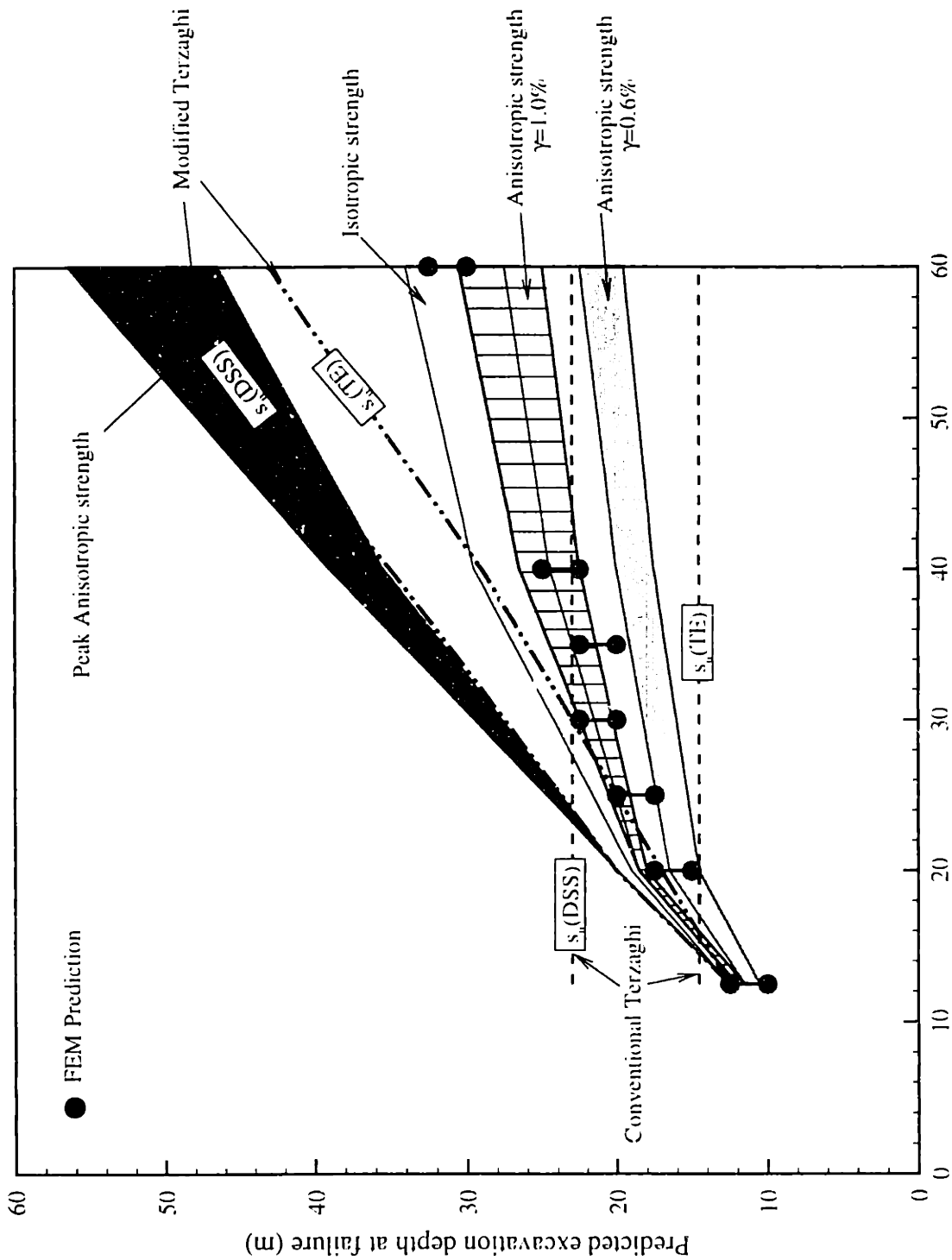

Figure 6.72 Effect of undrained strength anisotropy on predicted excavation depth at failure

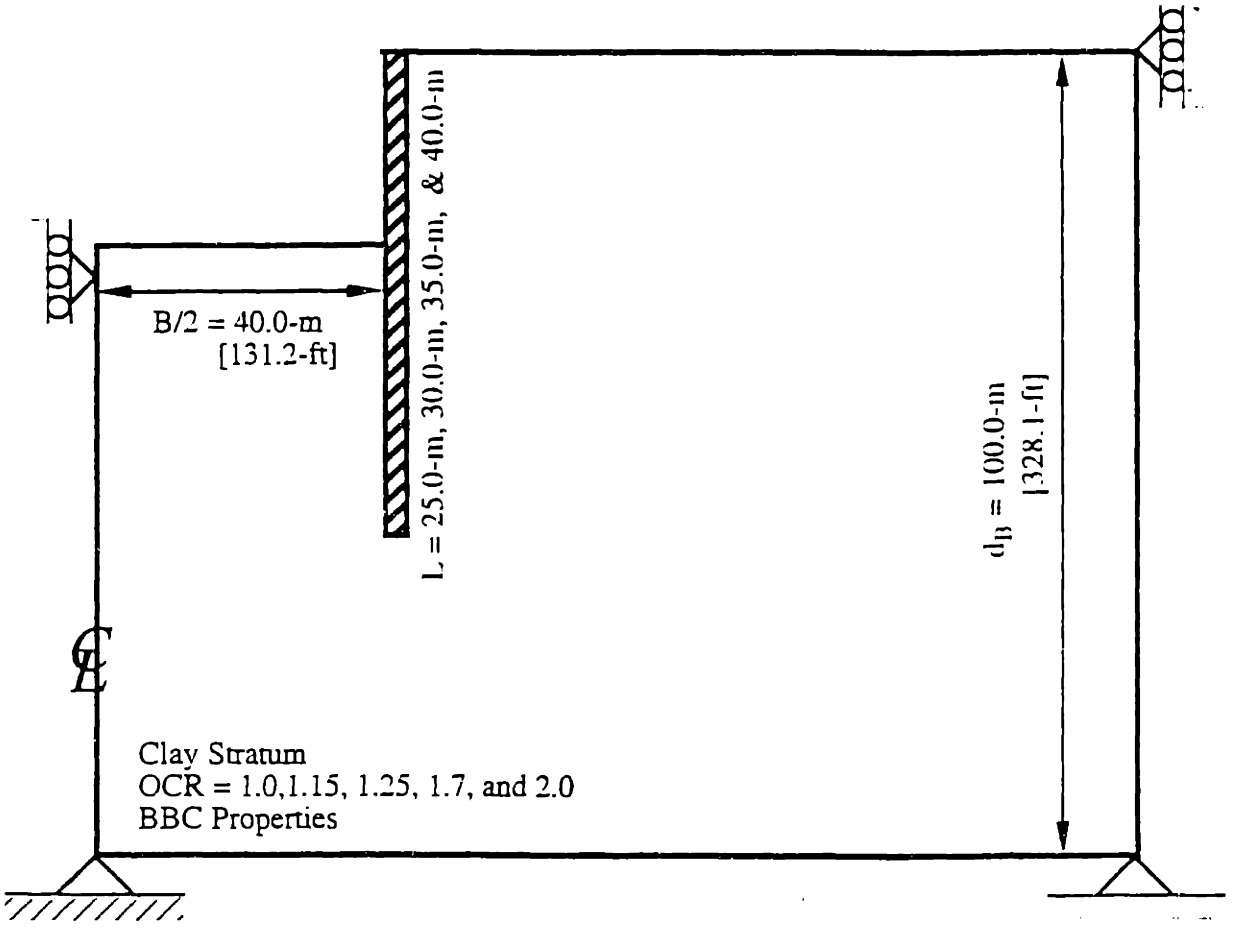

GROUP D: (16 cases)

Constant Parameters:

B	= 80.0-m	[262.5-ft]
d_B	= 100.0-m	[328.1-ft]
h	= 2.5-m	[8.2-ft]

Variables:

L	= 25.0-m	[82.0-ft]
	30.0-m	[98.4-ft]
	35.0-m	[114.8-ft]
	40.0-m	[131.2-ft]
OCR	= 1.0, 1.15, 1.25, 1.7, & 2.0	

Figure 6.73 Group D finite element analyses for evaluating the effects of clay stress history (After Jen, 1998)

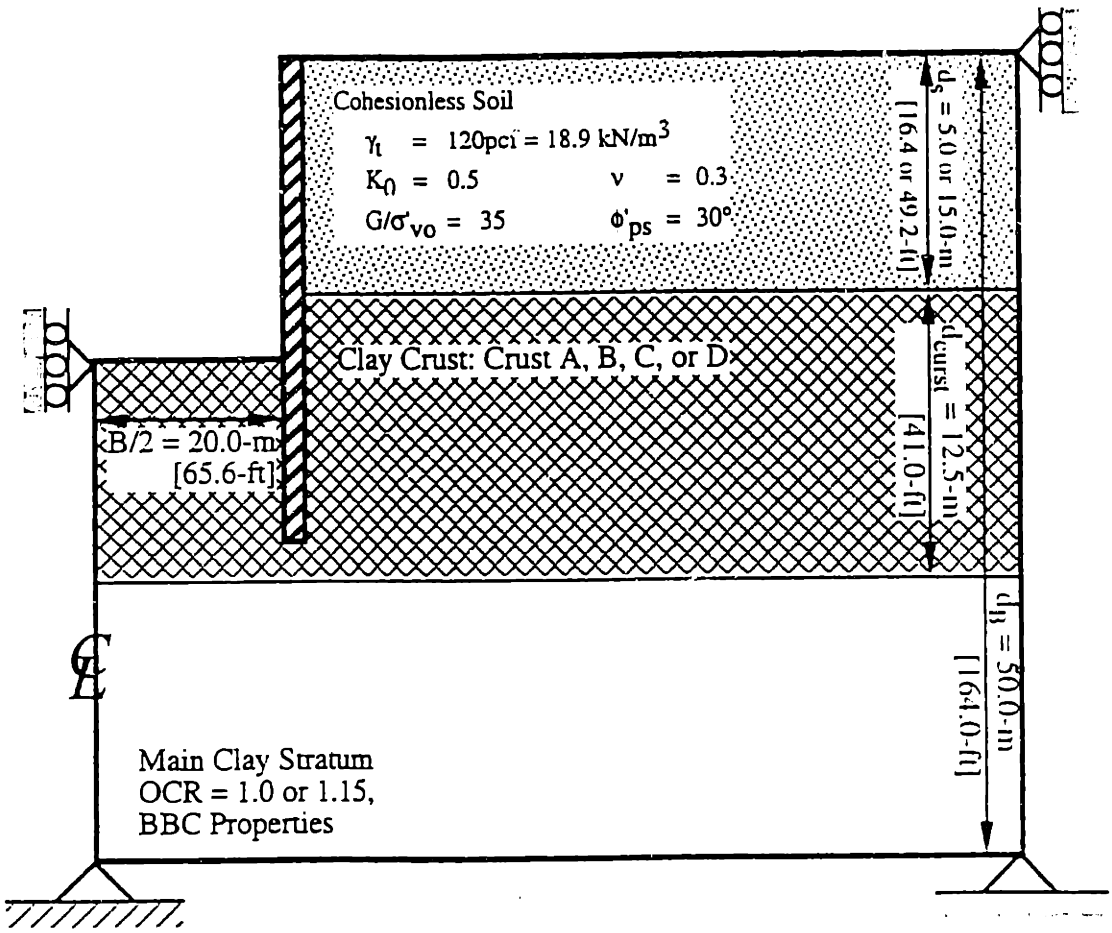

GROUP F: (4 cases)

Constant Parameters:

B	=	40.0-m	[131.2-ft]
d_B	=	50.0-m	[164.0-ft]
L	=	25.0-m	[82.0-ft]
h	=	2.5-m	[8.2-ft]

Variable: Soil Profile

Soil Profile	Profile F1	Profile F2	Profile F3	Profile F4
d_S	15.0-m	15.0-m	15.0-m	5.0-m
Clay Crust Depth	15 to 27.5m	15 to 27.5m	15 to 27.5m	5 to 17.5m
Main Clay Stratum	OCR=1	OCR=1.15	OCR=1	OCR=1

Figure 6.74 Group F finite element analyses for evaluating the effects of clay crust (After Jen, 1998)

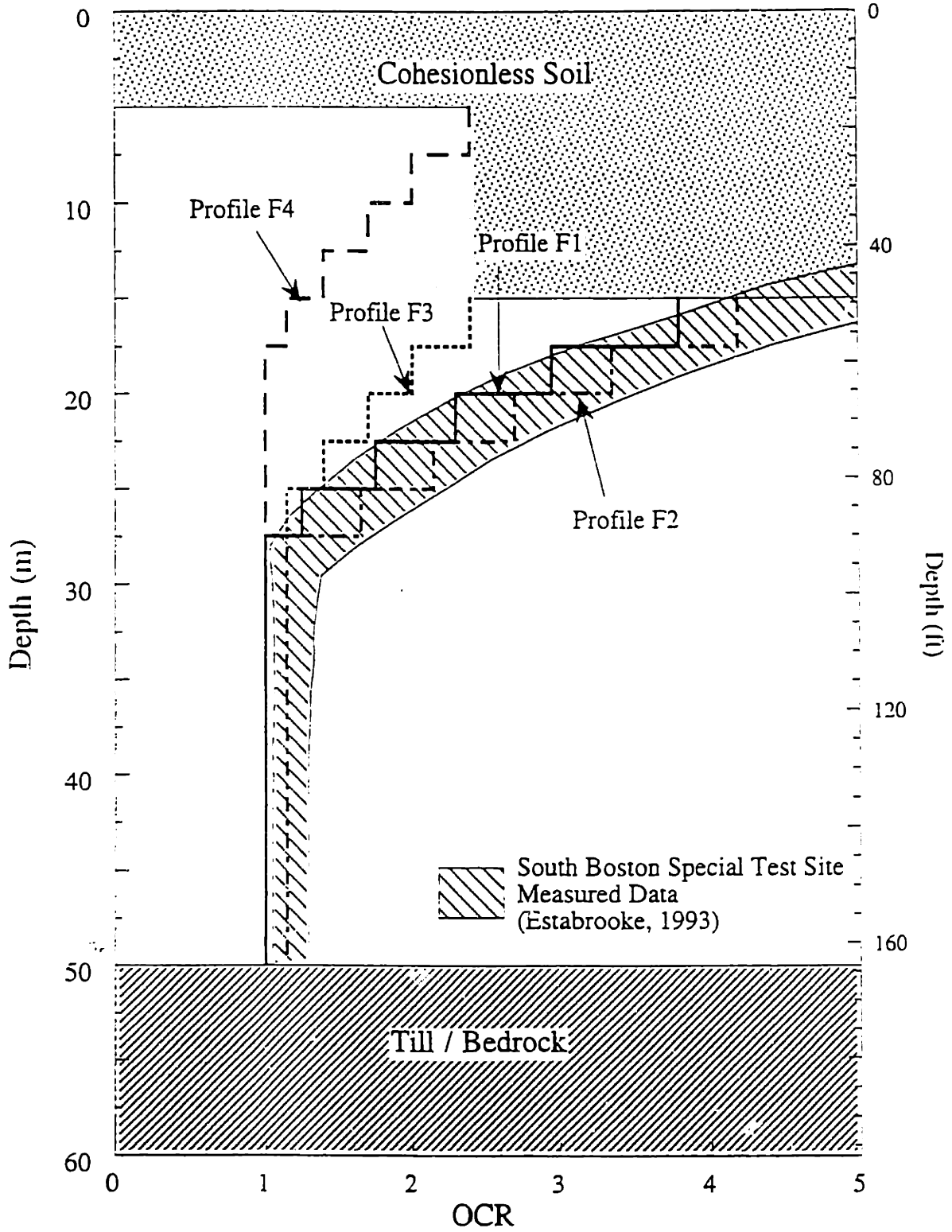

Figure 6.75 Stress history profiles (F1, F2, F3, F4) in Group F finite element analyses (After Jen, 1998)

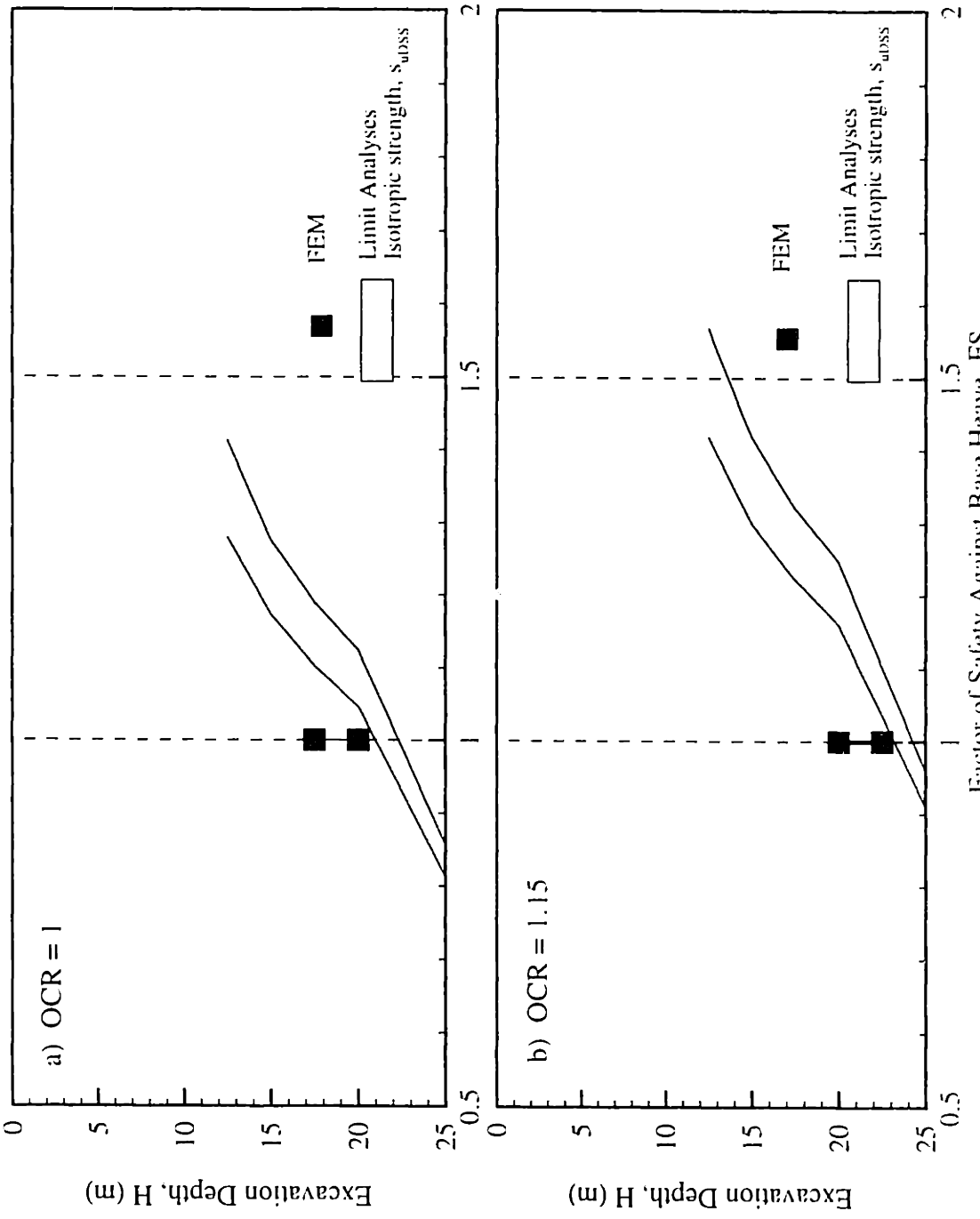

Figure 6.76 Comparisons of basal heave stability by numerical limit analyses and finite element method (FEM)
B = 80m, L = 25m, Diaphragm Wall

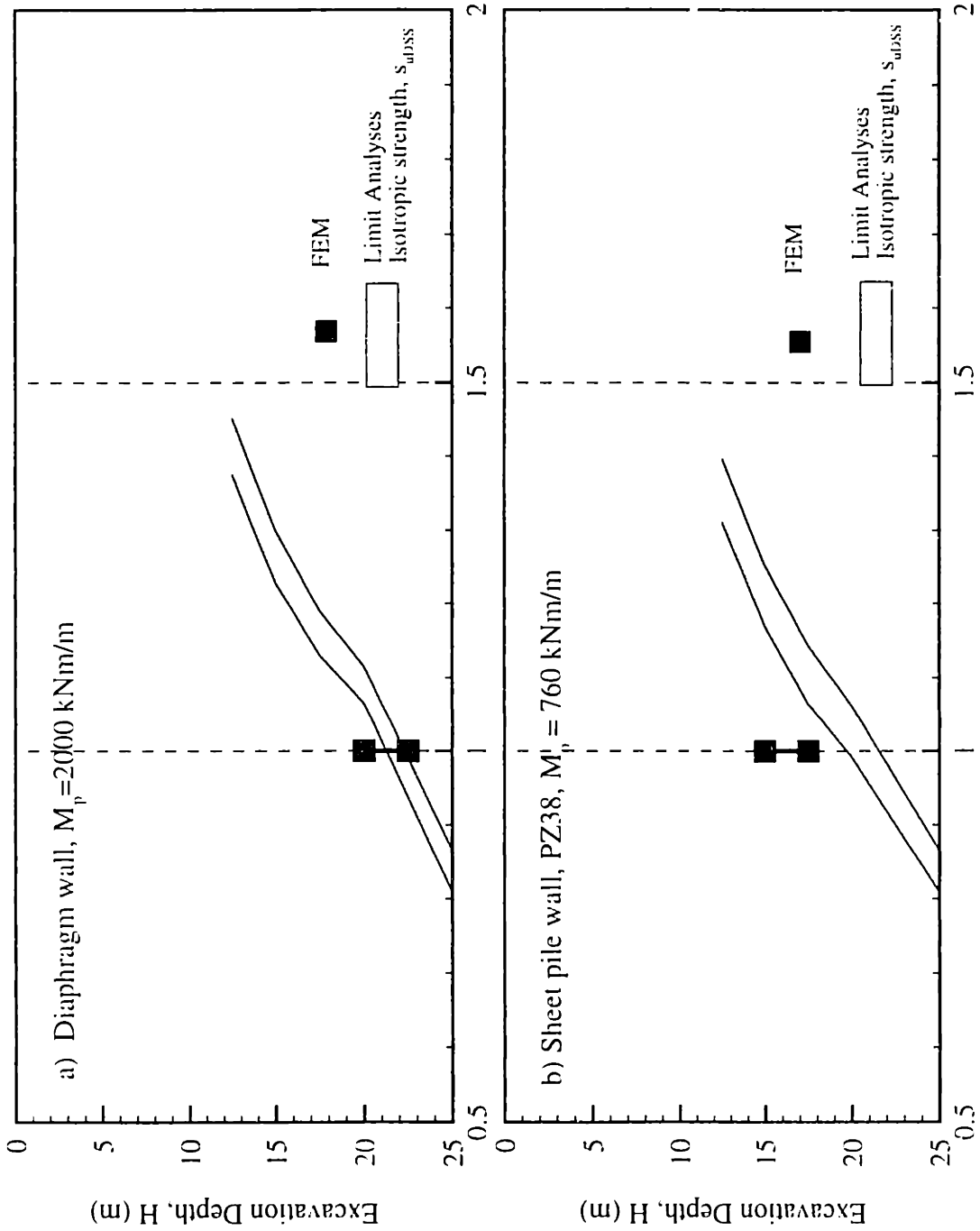

Figure 6.77 Comparisons of basal heave stability by numerical limit analyses and finite element method (FEM)
B = 40m, L = 25m, Soil Profile F4

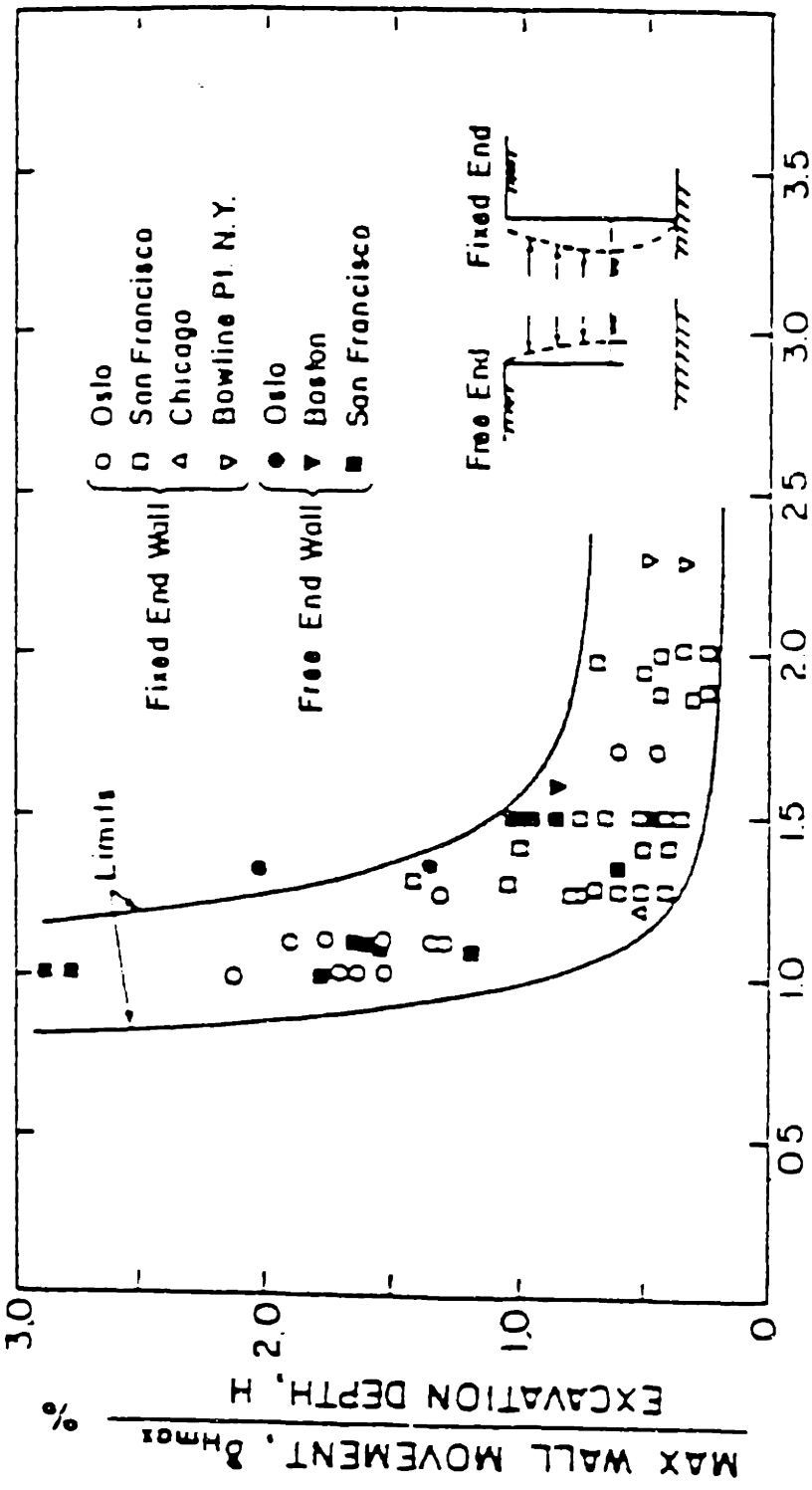

Figure 6.78 Relationship between factor of safety against basal heave and maximum wall deflections in soft to medium clay (After Mana and Clough, 1981)

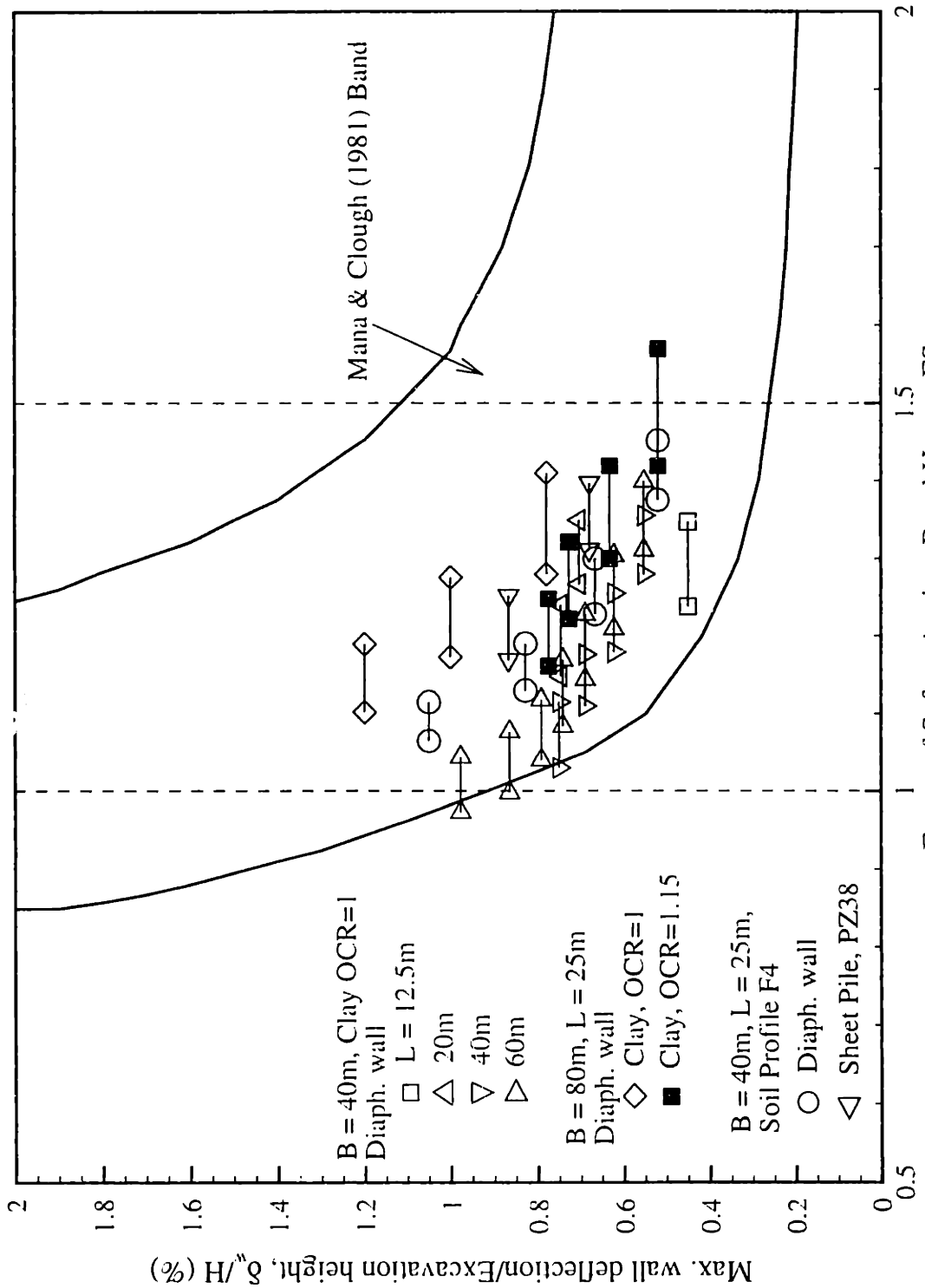

Figure 6.79 Predicted FS from numerical limit analyses and maximum wall deflections from FEM

Chapter 7. Case Study: Stability Analysis of Tieback Excavations in East Boston

7.1 Introduction

This chapter describes the application of numerical limit analyses to re-assess the stability of two tie-back walls, constructed to support excavations for section C07A of the Central Artery/Third Harbor Tunnel Project (CA/T) in East Boston. This case study is of particular interest as instability of the excavation support system caused a major delay in the construction program. The project was completed after the remaining excavations were stabilized using sub-grade buttresses constructed by deep soil mixing (DSM) and jet grouting. Even though the redesign was successful, significant lateral movement of the wall occurred during the final stage excavation. Details of this case study have been published by O'Rourke and O'Donnell (1997a, b) and O'Rourke et al. (1997)[1].

Section 7.1 and 7.2 summarize the site description and soil profiles in East Boston. Section 7.3 presents the results of stability analysis using numerical limit analysis for a typical cross section that failed (East wall, Section A-A′). The factors of safety calculated by limit analysis are compared with deep rotational stability calculations using the limit equilibrium method (O'Rourke and O'Donnell, 1997a). Reliability analysis with First Order Second Moment method (FOSM) were also carried out to investigate the uncertainty in the calculated factor of safety due to uncertainties in the soil properties, excavation, and support parameters. Independent design options are proposed to improve the stability of this section. Section 7.4 presents the results of analysis for a remediated wall section, where DSM and jet grouting were used (West wall Section B-B′). Numerical limit analyses are also applied to evaluate possible redesigns and other applications of DSM to improve the stability of Section B-B′.

Appendix 7A summarizes results for four short case studies of excavation stability based on data published in the literature.

---

[1] The MIT geotechnical group also compiled complete field performance data for this project, but were restricted from publishing this material.

7.2 Site Description

Figures 7.1 and 7.2 show the project location and a plan view of the excavation, respectively. The project involved the construction of approximately 915m of Interstate I-90 Highway in an area known as Bird Island Flats (BIF). The Mainline Tunnel at this site consists of a two-barrel reinforced concrete structure built by cut-and-cover techniques to depths ranging from 12.5m to 25.9m. The width of the constructed highway varies from approximately 24.4m to 53.3m.

Temporary support was provided by means of a soil mixed wall (SMW) with earth-anchor tiebacks. Taki and Yang (1991) discuss the design and construction principles pertaining to SMW, while Pearlman and Himick (1993) describe the application of the technology at the BIF site. Structural reinforcing for the wall was provided by steel sections (W21 x 50) on 1.2m spacing. Tiebacks were postgrouted typically 24 hours after initial grouting with a process similar to the tube-a-manchette method (e.g. Xanthakos et al., 1994). Proof tests were performed on all tiebacks, and performance tests were run on approximately 2% of all tiebacks, both in accordance with the recommended procedures of the Post Tensioning Institute (PTI) (1995).

The BIF project involved an extensive amount of instrumentation, including inclinometers, extensometers, settlement points, and observation wells, as shown in Figure 7.2. Also shown in this figure are two cross sections of the excavations considered in the papers by O'Rourke and O'Donnell (1997a, b): 1) East Wall, Section A-A′, where instability occurred during construction; and 2) West Wall, Section B-B′, which was stabilized with a remedial soil mix buttress. Stability calculations of these excavations are presented in Sections 7.4 and 7.5.

7.2.1 East Wall, Section A-A′

Figure 7.3 shows the East wall Section A-A′, where failure occurred when the excavation depth was approximately 13.4m[2]. The distance between the east and west walls was about 60m at this section. Two levels of tiebacks had been installed and post-grouted. The third level of tiebacks had been installed at elevation 22.5m, but only the

[2] Data compiled by the MIT geotechnical group show that the excavated depth at failure, H_f = 12.8m.

first stage of grouting had been applied when a maximum lateral movement of 215mm was recorded adjacent to the SMW. To stabilize the excavation, soil was backfilled to the elevation of the second-level tiebacks, at which time further wall deflections were arrested.

7.2.2 West Wall, Section B-B′

In order to prevent failure at Section B-B′, additional tieback anchors were installed, and the toe of the wall was stabilized by deep soil mixing (DSM) and jet grouting, to form a subgrade buttress, extending up to 20m across the excavation. Figures 7.4 and 7.5 show the plan and profile views of base stabilization scheme (West wall). The primary components of the system were a series of parallel DSM buttresses on 2.4m centers. The buttresses were composed of a single line of interlocking DSM columns connected near the wall to three rows of DSM columns. The combined DSM and jet grout made up 35% of the soil volume in the treated zone. Figure 7.6 shows the geometry of the West wall at Section B-B′ the final excavation grade, where the excavation depth is 15.4m. Note that the excavation height at Section B-B′ is 2m deeper than at Section A-A′ (13.4m). The SMW was supported by five levels of tieback anchors installed within the BBC[3]. At this location, the remedial buttress was 16.2 m long and extended 5m below the excavation grade.

O'Rourke and O'Donnell (1997b) describe field measurement of wall deflection after construction of the remedial buttress. The excavations were successfully stabilized, however maximum lateral wall movements of 170mm were measured at Section B-B′.

7.3 Soil Profiles

The soil conditions at the BIF site (see Figs. 7.3 and 7.6) consists of approximately 7 m of granular and cohesive fill underlain by a 1-m thick layer of organic silt and a 19m to 23-m thick deposit of Boston Blue Clay (BBC). Below this marine clay is 10-m thick deposit of stiff glaciomarine overlying argillite (bedrock). The ground water table is located about El. +31.5m and +33.0m for Section A-A′ and B-B′,

[3] A 6th level of tieback anchors were later installed in the bedrock.

respectively. Table 7.1 summarizes the characteristic and relevant properties of each soil layer as reported by O'Rourke and O'Donnell (1997a). The unit weights and strengths of each layer (except BBC) are consistent with recommendations of Haley and Aldrich (1991a, b).

The critical parameter that affects the stability of this excavation is the undrained shear strength profile of the marine clay (BBC). Figure 7.7 shows the stress history and undrained strength profile of BBC. The current stability analyses consider three strength profiles of clay:

1. Profile 1 is based on the stress history profile measured in 1-D compression tests at the East Boston special test site (Haley and Aldrich, 1992). This site (Fig. 7.1) is located approximately 0.5 km from the failure. The undrained strengths are derived from this data using normalized SHANSEP strength parameter[4] (Ladd and Foott, 1974), S = 0.19, m = 0.75, from undrained direct simple shear tests (CK_0UDSS).
2. Profile 2 was derived from the best estimate of pre-consolidation pressure (σ'_p) obtained in the original BIF site investigation (Haley and Aldrich, 1991b).
3. The profile labeled μs_{uFV} corresponds to correctted[5] field vane strengths interpreted by O'Rourke and O'Donnell (1997a, Table 7.1). These field vane data were obtained after the failure had occurred.

Even though there is much scatter in both μs_{uFV} and σ'_p data, Profile 2 gives strengths that are significantly higher than the field vane strength profile. The source of this discrepancy remains unknown, but may be related to changes in stresses caused by the excavation. Profile 1 can be considered a conservative strength profile based on pre-existing data and correlates surprisingly well with the field vane strengths.

---

[4] $s_u = \sigma'_{vo} S.(\sigma'_p/\sigma'_{vo})^m = S.\sigma'^{\,m}_p/\sigma'^{\,1-m}_{vo}$

[5] Correction factors according to recommendations of Bjerrum (1973).

7.4 Analyses of East Wall, Section A-A′

7.4.1 Input Parameters for Numerical Limit Analyses

Figure 7.8 shows the spatial discretization used in the numerical limit analyses for the East wall, Section A-A′. The soil mass is discretized using plane strain triangular elements. The strengths and unit weights of each soil layer are given in Table 7.1. The analyses consider drained failure of the granular fill, while that other layers are undrained. The analyses consider three undrained strength profiles of BBC (Profile 1, 2 and μs_{uFV}, Figure 7.7). The glaciomarine layer is treated as a rigid base in the analyses.

The soil-mix wall (SMW) is modeled using structural elements (beam and joint), which allow bending failure. The plastic moment M_p = 373 kNm/m, corresponding to the bending capacity of the W21x50 steel sections (LRFD, 1994) at 1.2 centers. The free lengths of tiebacks are simulated as 1-D pin-ended element, where failure is permitted in axial tension. The plastic limit load, F_p = 765.6 kN/m is computed for 5 strands of ½-inch seven-wire strand (Schnabel, 1991). Note that the free length does not physically connect to soil elements. Fixed anchors are modeled as structural elements that can also fail in axial tension (same F_p as the free length).

Soil-structure interfaces are used along SMW and fixed anchors. The analyses assume that SMW-soil interfaces are rough with shear resistance, f_s, controlled by the undrained shear strength of the surrounding soil.

However, it is difficult to estimate the shear resistance of soil-anchor interface, since the anchors are post-grouted to the surrounding clay. As a result, the interface strength may have a higher capacity due to post-grouting. According to Ostermayer (1974), the lowest values of shear resistance are 30-80 kPa, recorded in clay with medium to high plasticity (I_c = 0.8 – 1.0). Reported successful applications of postgrouting show increase in shear resistance along the interface from 120 to 300 kPa. Such results have also been reported by Jorge (1969). Using these data, the analyses assume that the soil-anchor interface, $f_s = ns_u$, where n = 2. This uncertainty is considered in the reliability analysis in Section 7.4.4.

The other difficulty for estimating the soil-anchor strength is that the analysis assumes a plane strain geometry, while the fixed anchors are actually cylindrical and spaced at 1.2m intervals. To account for the differences in the surface area of fixed

anchor lengths between plane strain and cylindrical geometry, the soil-anchor strength, $f_{s,ps}$ for plane strain calculations can be estimated as:

$$f_{s,ps} = A_{cylin} n s_u / A_{ps} \quad (7.1)$$

where $A_{cylin} = \pi D$ is the surface area for cylindrical geometry/unit length

$A_{ps} = 2s$ is the surface area for plane strain geometry/unit length

D = diameter of fixed anchor

n = strength factor due to postgrouting (assume = 2)

s = anchor spacing (1.2m)

The analyses assume D = 0.20m. For the first level of anchor located in organic silts, it follows from eqn 7.1 that $f_{s,ps}$ = 22.5 kPa (s_u = 43 kPa, Table 7.1). For anchors located in BBC, the undrained strength corresponding to Profile 1, 2, or μs_{uFV} are used to calculate $f_{s,ps}$ instead[6].

The excavation height at Section A-A′ is another uncertainty in the calculations. Data compiled by Jameson (pers. comm., 1996) show that the excavation height of this section at failure $H_f \approx 12.8$ m, instead of 13.4m. Thus, the analyses for H = 12.8m are also included for comparison purposes.

7.4.2 Predictions for Isotropic Strengths of BBC

Table 7.2 summarizes results of numerical limit analyses for the East wall, Section A-A′, at H = 13.4m. The analyses use isotropic strength for three undrained strength profiles of BBC (Profile1, 2, μs_{uFV}, see Figure 7.7). Upper and lower bound estimates of the factor of safety range from FS = 0.93 – 1.04, based on the corrected field vane strength profile, μs_{uFV}. These results compare very closely with the range of FS quoted by O'Rourke and O'Donnell (1997a), using limit equilibrium calculations (FS = 0.99 – 1.04) with the same strength parameters. Similar results are also obtained using a conservative strength Profile 1 (FS = 0.93 – 1.04), based on σ'_p from East Boston Special Test Site. However, much higher factors of safety are computed using the stress history data from the BIF site, as indicated by results for the best estimate strength Profile 2, with FS = 1.27 – 1.44.

---

[6] For BBC, $f_{s,ps}$ = 41.9 kPa.

Figure 7.9 shows the predicted upper bound (UB) failure mechanism for Profile 1. The velocity arrows indicate directions of plastic slip along the interfaces between elements in the mesh, while plastic shear distortion of individual elements is indicated by dark shading. The UB analysis predicts a failure zone that extends to the base of the clay layer (El. +7.5m) and intersects the ground surface in the retained soil up to 40m behind the wall. Bending failure of the wall occurs just below the elevation of the excavation grade (shown most clearly by plastic hinges marked in Figure 7.10b). The results in Figure 7.9 are broadly similar to the deep-seated rigid body rotational mechanism assumed in the limit equilibrium calculations by O'Rourke and O'Donnell (1997a), as shown in Figure 7.10.

Figure 7.11 shows contours of major principal stress direction (δ, relative to the vertical) and mobilized shear strength (q/q_f) from the lower bound analysis of Profile 1. Figure 7.11a shows that the soil below the base of the excavation fails in a passive mode of shearing ($\delta = 90°$), while the retained soil fails in an active shearing ($\delta = 0°$). Between these two zone, there is a radial shear zone, where $\delta = 90°$ -> $0°$. Figure 7.11b shows the full shear strength is mobilized at all points in the soil mass ($q/q_f \approx 1.0$), indicating a high quality lower bound collapse load.

Figure 7.12 shows the LB predictions of net shear and normal tractions, and bending moment and axial force along SMW and tiebacks. The lower bound analysis predicts that the bending failure of SMW occurs at the excavation grade ($M = M_p$), which fits in very well with the predicted UB failure mechanism (Figure 7.9b). The axial force along free and fixed lengths is less than its plastic axial load ($F < F_p$).

Similar upper and lower bound results for H = 12.8m are illustrated in Figures 7.13 through 7.15. Table 7.2 shows that the computed factors of safety for H = 12.8m are approximately 3 – 6% lower than those for H = 13.4m for all three undrained strength profiles.

7.4.3 Results for Anisotropic Strength of BBC

This section evaluates the effects of undrained strength anisotropy of BBC on the factor of safety of the East Wall, Section A-A′. (Note that the depth of excavation for these anisotropic strength analyses, H = 12.8m.)

The analyses consider two sets of anisotropic strength parameters for BBC using the Davis and Christian (1971) yield function (c.f. Section 4.3) defined as follow:

1) Parameter set AN1 (Ladd, pers. comm., 1998)

These parameters are based on experience of stability during staged construction, and include effects of strain compatibility as discussed by Ladd (1991).

Compression mode: $S_c = 0.26$; $m_c = 0.68$

DSS mode: $S_d = 0.20$; $m_d = 0.775$ (same ratios as to Profile 2)

Extension mode: $S_e = 0.14$; $m_e = 0.90$

where

$$s_u = S\sigma'^{m}_{p}\sigma'^{1-m}_{vo} \tag{7.2}$$

2) Parameter set AN2

These mobilized strength parameters are obtained by fitting the anisotropic yield function directly to laboratory data (DSC, CK_0UC, CK_0DSS, CK_0UE) at a shear strain, $\gamma = 0.6\%$ at different initial OCR's, as shown in Figure 7.16. The selected shear level represents an average strain predicted at failure in non-linear finite element analyses using the MIT-E3 soil model (after Hashash and Whittle, 1996)[7]. The SHANSEP parameters for set AN2 are:

Compression mode: $S_c = 0.32$; $m_c = 0.47$

DSS mode: $S_d = 0.09$; $m_d = 0.943$

Extension mode: $S_e = 0.03$; $m_e = 1.245$

Figure 7.17 compares the undrained strength ratios as a function of overconsolidation ratio (OCR) for parameter sets AN1 and AN2. The figure shows significant differences in undrained strength ratios for different direction of shearing. The compression strength ratio for set AN2 is higher than parameter AN1 for OCR $\leq$ 3. However, the strengths in DSS and extension modes for AN1 are substantially larger than AN2 (for the same range of OCR's). Figures 7.18 compares strength profiles derived

[7] For short wall cases, L = 12.5m, 25m.

from parameter sets AN1 and AN2 based on the best estimate of stress history measured at the BIF site. There is only a small range of undrained strength anisotropy using parameter set AN1, similar in magnitude to uncertainties in the reference strengths (shaded band). In contrast, set AN2 generates very low mobilized strengths in DSS and extension modes. Note that Figure 7.19 shows anisotropic strength profiles derived from parameter sets AN1 and AN2 based on the stress history Profile 1 (East Boston Special Test Site).

Table 7.3 summarizes the results of numerical limit analyses for anisotropic strength profiles of BBC at East wall, Section A-A′. For all stress history profiles (Profile 1 or 2), anisotropic parameter AN1 generates a higher factor of safety than AN2 by 25 – 35%. These differences result from the different assumptions of normalized strength parameters used to characterize the BBC (sets AN1, AN2). Parameter set AN2 (mobilized strength at $\gamma = 0.6\%$) predicts failure for stress history Profile 1 and also for Profile 2 using lowest estimate of σ'_p, while the best estimate σ'_p results generate FS = 1.08 – 1.16. In contrast, results for parameter set AN1 are comparable to (or slightly higher than) results presented previously assuming isotropic (DSS) strengths of BBC.

Figure 7.20 and 7.21 illustrate the upper bound results for analyses with undrained strength anisotropy using sets AN1 and AN2 and stress history Profile 1 (East Boston Special Test Site). It is clear from these results that there is small difference in predicted failure mechanisms for isotropic (Figure 7.13) and anisotropic strength parameters (AN1, or AN2.

Figures 7.22 and 7.23 show the corresponding lower bound results for anisotropic strength analyses. The contours of the direction of major principal stress to the vertical for two anisotropic strengths (Figure 7.22a, 7.23a) are similar to that of isotropic strength (Figure 7.15a). The results show an active failure in the retained soil, radial shear failure below the tip of the wall, and a passive failure below the bottom of excavation.

7.4.4 Reliability Analyses with First Order Second Moment Method

Numerical limit analyses have also been performed to evaluate the uncertainty in the calculated factor of safety using the First Order Second Moment method (FOSM). This procedure is similar to that described by Christian et. al (1992). Table 7.4 lists the

variables to be considered in the reliability analyses, the best estimates of their mean values, $E[X_i]$, as well as their uncertainties expressed in terms of standard deviation, $SD[X_i]$. There are 3 main sets of variables in the analyses:

1) Geometry:

The uncertainties in the geometry of excavations include the depth of excavation, the elevation of Glaciomarine deposits, and the free length of the second tier of tiebacks. The analyses assume the standard deviation for the height of excavation = 0.6m. Construction data of East Boston available at MIT (Jameson R, 1996) show that the free length of 2nd level of tieback ranges from 9m to 15m at Section A-A′. Assuming that these limits of 2nd free length correspond to 99% of all data (i.e. 6SD), the standard deviation of the 2nd level, SD ≈ 1m.

2) Properties of Overlying Soils:

All best estimates of unit weight, undrained strength, and the standard deviation for overlying soils are based on the site investigation reported by Haley and Aldrich (1991b).

3) Properties of BBC:

The undrained strength profile of BBC is the major concern in this analysis. Figure 7.24 shows the best estimate and standard deviation in the preconsolidation pressure (σ'_p) and the undrained strength profiles (assuming isotropic strengths from DSS mode of shearing). The lines $E[\sigma'_p]$, $E[\sigma'_p]$-SD, and $E[\sigma'_p]$+SD are derived from the laboratory data of σ'_p at the BIF site using linear regression analyses. The best estimate of SHANSEP strength profile $E[s_u]$ and its coefficient of variation (COV) can be estimated based on Christian et al. (1992) as:

$$E[s_u] = \sigma'_{v0} E[S] \left(\frac{E[\sigma'_p]}{\sigma'_{v0}} \right)^{E[m]} \tag{7.3}$$

and

$$COV^2[s_u] = COV^2[S] + E^2[m].COV^2[\sigma'_p] + \ln^2\left(\frac{E^2[\sigma'_p]}{\sigma'_{v0}}\right)SD^2[m] \qquad (7.4)$$

where E[S] = 0.20, E[m] = 0.775 (same as Profile 2)

SD[S] = 0.012, SD[m] = 0.05 (Ladd, Pers. comm., 1998)

It can be seen that the linear regression line for laboratory data of σ'_p gives rise to a prediction of E[s_u] profile similar to the best estimate strength Profile 2. The profiles of E[s_u]-SD, and E[s_u]+SD also bound the band of SHANSEP strength Profile 2.

4) Others Uncertainties:

Other variables include the plastic tieback load (F_p), the plastic moment of SMW (M_p), and the skin friction of fixed anchors (f_s). The analyses assume that the uncertainty in F_p, and M_p results from the yield stress of steel tendon and sections. For uncertainty in f_s, the data from Ostermayer (1974) show that post grouting can increase the capacity of skin friction as high as 5 times of the undrained strength of the clay (n = 5). However, the post grouting may give adverse effects, which assumes n = 0.4. Assuming that these limits on n correspond to 99% of all tiebacks responses, then SD[n] = 0.77.

Based on the best estimate of all parameters in Table 7.4, the lower and upper bound factors of safety for Section A-A′ are FS = 1.253 – 1.379.

Sensitivity analyses are performed for each variables and the corresponding factor of safety are listed in Table 7.5. Using FOSM approximation, the variance components of factor of safety generated by each variable can be estimated as follows (Christian et. al, 1992):

$$V[FS] = \sum_{i=1}^{k}(V[FS_i]) \quad ; \quad V[FS_i] = \left(\frac{\Delta FS}{\Delta X_i}\right)^2 V[X_i] \qquad (7.5)$$

where V[FS] = total variance of factor of safety

$V[FS_i]$ = variance components generated by variable X_i

$\Delta FS/\Delta X_i$ = sensitivity of FS

$V[X_i]$ = variance of $X_i = SD^2[X_i]$

k = numbers of variables

Tables 7.6 and 7.7 summarize the lower and upper bound calculations of the variance in factor of safety, respectively. The results show that the undrained strength of BBC generates the largest uncertainty, approximately 90% of the total variance. This uncertainty results from the scatter data of laboratory of preconsolidation pressure at the BIF sites as well as the standard deviation of SHANSEP strength parameters. The second important variable is the depth of excavation, which constitutes 7% of the total uncertainty. The variance components due to other individual variables are negligible.

The lower and upper bound calculations for reliability analyses with FOSM give rise to the factor of safety and its standard deviation as follows:

Lower Bound: FS = 1.253 ± 0.255 (SD)

Upper Bound: FS = 1.379 ± 0.265 (SD)

Based on Christian et. al. (1992), the reliability index, β can then be calculated as:

$$\beta = \frac{E[FS] - 1.0}{SD[FS]} \tag{7.6}$$

Lower Bound analyses: $\beta = (1.253 - 1.0)/0.255 = 0.992$

Upper Bound analyses: $\beta = (1.379 - 1.0)/0.265 = 1.430$

The reliability index gives rise to the probability of failure, P_f, of the East wall, Section A-A′ as follows:

Lower Bound analyses: $P_f = 16.1\%$

Upper Bound analyses: $P_f = 7.6\%$

Hence, based on these calculations, the probability of failure for Section A-A′ ranges from 8 – 16%.

7.4.5 Proposed Redesign Options for Section A-A′

This section evaluates the stability of possible re-design options for Section A-A′ as follows:

1. Strengthen the wall

In this case, the plastic moment of the wall, M_p increases from 373 kNm/m (SMW) to 2000 kNm/m, which is a typical value for a moderate to heavily reinforced, 1-m wide diaphragm wall.

2. Extend tip of wall into Glaciomarine layer

There are two boundary conditions at the tip of the wall. If the wall tip is driven deeply enough into Glaciomarine deposits, the end condition can be considered as fixed ended, with zero rotation at the tip. If the toe is not fully embedded, the end condition corresponds to a pin ended condition. Both cases have been considered in conjunction with SMW and diaphragm walls.

3. Extend the free length of tiebacks

Figure 7.25 shows the proposed new locations of tiebacks. The free length of both levels at tiebacks is extended by 11m, while the fixed anchor length remains constant at 12m.

The base case in this section corresponds to the SHANSEP undrained strength Profile 1 of BBC, where the excavation height, H = 12.8m. The reference factor of safety for this case, FS = 0.99 – 1.10 (with upper and lower bound results in Figs. 7.13 and 7.15, respectively).

Table 7.8 summarizes the factor of safety corresponding to the three proposed redesign options evaluated by numerical limit analyses. The results show the followings:

1. Strengthen the wall

There is no change in the factor of safety by strengthening the plastic moment of the wall (M_p = 2000 kN/m). Figures 7.26 and 7.27 show the corresponding upper and lower bound results. The upper bound analysis predict no bending failure in the wall (Figure 7.26), while the failure mechanism is very similar to the reference SMW case (see Fig. 7.13). The lower bound analysis shows that the moment along the wall is less than M_p (Figure 7.27c).

2. Extend tip of wall into Glaciomarine deposits

The results in Table 7.8 show that extending wall tip into Glaciomarine deposits does improve the stability of this section. The improvement in factor of safety ranges from 7% to 21%, depending on the end conditions of the wall and its plastic moment. Typically, the fixed end provides higher stability than the free end (by 2-5%). Unlike the first option, strengthening the strength of the wall in this case significantly improve the stability (by more than an additional 8%). Figure 7.28 through 7.35 summarize upper and lower bound results for these alternatives. The upper analysis predict that bending failure of the wall occurs along the embedded section (shown by several plastic hinges) when the tip of the wall is extended into glaciomarine (e.g. Figure 7.28). The lower bound analysis also shows that, $M = M_p$ along the embedded sections (e.g. Figure 7.29). Notice that for the case of fixed end, both lower and upper bound calculations also predict the plastic hinges occurring at the tip of the wall. (e.g. UB-Figure 7.30, LB-Figure 7.31).

3. Extend free length of tiebacks

The results show that the stability can be improved about 7% by extending the free length of tiebacks. Figures 7.36 and 7.37 show corresponding upper and lower bound results for this option. The upper bound results show that extending the free length of tiebacks cause the plastic zone in the retained soil to move further from the wall (Figure 7.36). Failure of excavation still corresponds to a deep rotational mechanism. Plastic bending failure of the wall occurs at the excavated grade and at the middle point of the embedded wall section.

In summary, improving the bending strength of the wall has minimal effect on the stability of this section, while extending the wall to the glaciomarine deposits is beneficial. However, there will be significant extra cost in installing the wall an extra +5m into the hard stratum. Extending the lengths of the tieback is also beneficial and much easier to perform in the field. The practical difficulties with this design may be

related to achieving the design preload forces of fixed anchors located within the clay crust.

7.5 Analyses of West Wall, Section B-B′

7.5.1 Input Parameters

Similar stability calculations have been performed for the West wall at Section B-B′ (Fig. 7.6), where DSM and jet grouting were used to construct a remedial buttress. Figure 7.38 shows the spatial discretization used for numerical upper and lower bound limit analyses of this excavation. The calculations use properties of overlying soil layers from Table 7.1, and consider three undrained strength profiles of BBC (Profiles 1 and 2, and μs_{uFV}, see Figure 7.7). Parameters for the soil-mixed wall, tieback, and anchors at Section B-B′ are modeled in the same way as Section A-A′.

The jet grout columns and deep soil-mix buttress are modeled by 2-D plane strain triangular elements, similar to the soil mass. The analyses assume that the unit weight of the buttress is the same as BBC. Undrained shear strength parameters of the soil-mix material[8], s_u = 1915 kPa, are quoted from laboratory data reported by O'Rourke and O'Donnell (1997b). Effects of uncertainties in unit weight and strength of the buttress are examined in Section 7.5.4.

7.5.2 Results for Isotropic Strength of BBC

Table 7.9 summarizes predicted factor of safety by numerical limit analyses for West wall Section B-B′ for the three isotropic undrained strength profiles. The analyses also evaluate the stability of this section without DSM buttress. The results show the following:

1. For Profile 1 and μs_{uFV}, the limit analyses predict that failure should have occurred at Section B-B′ if the section had not been stabilized with a DSM buttress. In contrast, analyses of best estimate of undrained strength Profile 2 suggest a stable of excavation even without the stabilizing buttress (FS = 1.06 – 1.22).

[8] This initial calculation assumes that the soil buttress is continuously along alignment of the wall.

2. Similarly, for Profile 1 and μs_{uFV}, limit analyses predict that failure will occur and hence the remedial buttress is inadequate. Results for Profile 2 shows an adequate margin of safety similar to the results of East wall, Section A-A′.
3. For all undrained strength profiles, the DSM buttress improves the stability of the cross section approximately 15 – 21%.

Figure 7.39 shows the predicted failure mechanism from the upper bound analysis of Section B-B′ using undrained strength Profile 1 (FS = 0.92 – 1.00). The results show a rigid body rotation of the DSM buttress relative to the tieback wall with a plastic hinge forming in the wall above the excavated grade. This mechanism was not considered in the limit equilibrium calculations, and can explain why O'Rourke and O'Donnell (1997b) obtain significantly higher factors of safety from the field vane strength (FS = 1.08 – 1.13, see Figure 7.40) compared to numerical limit analyses with similar undrained strength profile (FS = 0.98 – 1.08). This implies that limit equilibrium calculations based on rigid body rotation mechanisms considered by O'Rourke and O'Donnell (1997b) can give misleading estimates of the factor of safety for tieback excavations in clay.

Figure 7.41 shows corresponding lower bound results for contours of the direction of major principal stress to the vertical (δ, deg.), and the contour of mobilized shear strength (q/q_f). The lower bound analysis in Figure 7.41a predicts an active failure in the retained soil ($\delta = 0°$), while the radial shear failure zone occurs in the soil underneath tieback and buttress ($\delta = 0° \rightarrow 90°$). The clay next to the buttress fails in an extension mode of shearing ($\delta = 0°$).

Figure 7.42 shows the upper bound results for Section B-B without DSM buttress for undrained strength Profile 1 of BBC. Comparisons of excavations with basal stabilization in Figure 7.39 show that the buttress forces the plastic zone further towards the center of the excavation. There are also significant differences in velocity field and the failure mechanism of the entire system. Figure 7.43 shows lower bound results without DSM buttress. Clearly, the radial shear fan ($\delta = 0° \rightarrow 90°$) for the case without buttress occurs right at the tip of SMW (Figure 7.43a). With buttress, this zone is spread out and occurs below the buttress with a smaller passive failure zone ($\delta = 90°$) (see Figure 7.41a).

7.5.3 Results for Anisotropic Strength of BBC

The stability of Section B-B′ has also been examined using the mobilized undrained strength anisotropy parameter sets AN1 and AN2 (see Figure 7.17, Section 7.4.3). Table 7.10 summarizes the results of anisotropic strength analyses of BBC for the West wall, Section B-B′ with the remedial DSM buttress. As expected, the results show similar trends to those previously for the East wall Section A-A′ in Table 7.3). Parameter set AN1 generates factors of safety that are slightly higher than isotropic predictions, while AN2 gives corresponding low values of FS due to the low strength ratios mobilized in extension and simple shear modes.

Figures 7.44 and 7.45 show the upper bound results for undrained strength anisotropy with sets AN1 and AN2 (and the stress history Profile 1), respectively. There is no difference in UB results for the two anisotropic analyses, and both are similar to isotropic strength results (Figure 7.39), which show a deep-seated failure together with a rigid body rotation of the buttress.

The corresponding lower bound solutions (Figures 7.46 and 4.47) show some differences in directions of major principal stresses between AN1 and AN2. Both anisotropic analyses generate larger zones of active failure ($\delta = 0°$) in the retained soil than the isotropic case (Fig. 7.41a).

7.5.4 Effect of Unit Weight and Shear Strength of the Buttress

Numerical limit analyses were also carried out to assess the effect of unit weight and shear strength of the buttress. (Note that these analyses use the undrained strength Profile 1 with isotropic strength.)

1) Unit weight of buttress

According to Japanese design methods (Takenaka & Takenaka, 1995), the total unit weight of saturated soil cement is similar to the unit weight of the untreated soil, and hence unit weight variations are not considered. Jameson (1996) shows that that the unit weight of untreated soil and soil-cement are very similar if the soil has a high initial water content ($w > 100\%$). In soils with lower initial water contents and high water/cement ratios, the soil cement unit weight (γ_{sc}) may be up to 20% less than the untreated material.

The effects of the unit weight of the soil-cement buttress can then be summarized as follows:

$\gamma_{sc} = \gamma_{BBC}$: FS = 0.915 – 1.005

$\gamma_{sc} = 0.8\gamma_{BBC}$: FS = 0.887 – 0.982

It can be seen that the factor of safety reduces by 3 – 4% if the unit weight of soil cement reduces to 80% of the unit weight of the untreated material/parent BBC.

2) Shear strength of buttress

The analyses in Section 7.5.2 assume an undrained shear strength of the soil-mix buttress, s_u = 1915 kPa, which is about 40 times the average strength of BBC for Profile 1 (s_{uave} = 50 kPa). Table 7.11 and Figure 7.48 summarize calculations of factor of safety for selected ratios s_{uB}/s_{uave}, where s_{uB} is the undrained shear strength of the bulk buttress material. The results show that the maximum factor of safety can be achieved by increasing the mass strength of the buttress by just five times the strength of the surrounding soil.

7.5.5 Proposed Redesigns for Section B-B′

Table 7.12 summarizes the results of numerical limit analysis which evaluate other possible designs of the buttress geometry at Section B-B′. Note that all of the analyses use undrained (isotropic) strength Profile 1 for BBC.

1) Reduce thickness of buttress

The first redesign considers three smaller depths of buttress below the final excavated grade, 2.2m, 1.0m and 0m (using only jet grout column). The results in Table 7.12 show that the thickness of buttress can be reduced from 4.9m (original design) to 2.2m, without any reduction in factor of safety. As a result, construction cost of buttress could be reduced significantly. However, the factor of safety would have been reduced by 6 – 8% if the stabilization program used only jet grout column (zero thickness of buttress). Figures 7.49 and 7.50 show the upper bound results for thickness of buttress = 2.2m, and 0m, respectively. The

failure mechanism for buttress thickness = 2.2m (Figure 7.49) is similar to that of 4.9m (Figure 7.39), which involves a rigid body rotation of the jet grout and buttress. For zero thickness of buttress (Figure 7.50), the upper bound analysis predicts a rigid body rotation of the jet grout column and a passive wedge of material behind it.

2) Extend jet grout column into glaciomarine

The second redesign considers how much the stability can be improved by extending jet grout column into the underlying glaciomarine layer. The results in Table 7.12 show that the factor of safety can be increased by approximately 30% for this stabilization scheme. Figure 7.51 shows the corresponding upper bound results. The failure mechanism involves a rigid body rotation of the buttress, while the jet grout column fails by plastic shearing at the base elevation of the buttress. The deformed shape of jet grout column is similar to the failure of a laterally loaded fixed cantilever wall. Plastic shearing in the soils also occurs underneath the buttress.

3) Extend length of buttress across width of excavation

The third redesign considers the stabilization by constructing the buttress across the full width of excavation. The results in Table 7.12 show that the stability improves significantly by about 90% for this option. Figure 7.52 shows the corresponding upper bound results. The predicted failure mechanism of this option significantly differs from the original design at Section B-B′ (Figure 7.39). The jet grout column and buttress form a rigid structural element and prevents deep-seated failure in the underlying clay. As a result, the SMW wall becomes the weak point in the system and failure occurs by lateral movement of the wall relative to the buttress. The upper bound analysis predicts axial (tensile) failure of the 5^{th} tieback, while the lower bound analysis predicts that the force in this tieback, $F \approx 0.8F_p$, where F_p = plastic limit load of tieback.

4) Use a grid of jet grout column

The final redesign considers the use of a grid of jet grout columns with 1m diameter, spaced at 5m centers, as shown in Figure 7.53. Each column is driven into the underlying glaciomarine deposits. For practical purposes, separate calculations have also been performed assuming there is no jet grout column next to the SMW wall (for ease of construction). Results in Table 7.12 show that this new stabilization without a column of jet grout next to the SMW generates a factor of safety 3% higher than the original design. If a column of jet grout is constructed next to the SMW, the stability of excavation improves further by 17%. Figures 7.54 and 7.55 show the corresponding failure mechanisms for both cases. The jet grout columns curtail the extent of the failure zone inside the base of the excavation, but cause vertical squeezing of the soil against the first row of grout columns (Fig. 7.54) or between the first two columns (Fig. 7.55). Failure in the retained soil does not extend to the base of the clay layer. Both upper and lower bound analyses predict axial (tensile) failure of the 5th tieback for the case, where there is a jet grout column next to SMW (Fig. 7.55).

7.6 Summary

Uncertainties in undrained shear strength profiles of BBC are the major issue in this case study. The strength profile 2, derived from the best estimate of the stress history at the BIF site is 20% higher than the field vane strength, $\mu s_u(FV)$, and profile 1 based on the stress history of the East Boston Special Test Site. Stability analyses for Profile 2 suggest an adequate margin of safety for both excavations, East wall, Section A-A′ (FS = 1.27 – 1.44), and West wall, Section B-B′ (FS = 1.27 – 1.41). In contrast, the analyses for the conservative strength, Profile 1 indicates that both sections should have failed (FS < 1). In practice, the wall did not fail at Section B-B′ although relatively large ground movements were measured during excavation (17cm). Hence, the predictions based on Profile 1 are inconsistent with the observed stability at West wall. One possible explanation why the excavation at the West wall was stable is that other aspects of the re-design, such as excavation in short length segments may have increased the actual stability of this section.

Results of anisotropic strength analyses based on parameter set AN2 can be interpreted such that shear strain, $\gamma = 0.6\%$ are assumed to be mobilized in the soil mass. These imply that lateral wall deflections can occur at both sections as:

Section A-A′: $\delta_w \approx 0.6\%L = (0.6)(22) = 13$ cm

Section B-B′: $\delta_w \approx 0.6\%L = (0.6)(20) = 12$ cm

where L is the total length of soil-mix wall

Maximum lateral movement of 21.5cm (before failure) and 17cm were recorded at Section A-A′, and B-B′, corresponding to the shear strain approximately $\gamma \approx 1\%$ (= 21.5/22) and 0.9% (= 17/20), respectively. Thus, factors of safety for set AN2 (Table 7.3, 7.10) should be considered as conservative predictions for both excavations. On the other hand, the parameter set AN1 corresponding to very large shear strain (assuming $\gamma > 5\%$) does not provide realistic mobilized shear resistance of BBC for both sections.

Reliability analyses with First Order Second Moment methods show that the probability of failure (P_f) for Section A-A′ ranges from 8-16%. In practice, all foundations and earth works are typically designed to experience very small failure probability, $P_f < 0.1\%$. Thus, those results can be interpreted such that this section is likely to become unstable, and the parameter which generates the largest uncertainties is the undrained shear strength of BBC.

7.7 Reference

Bjerrum, L. (1973). "Problems of soil mechanics and construction on soft clay: SOA Report. "Proc. 8th Int. Conference on Soil Mech. and Found. Engrg., Moscow, U.S.S.R., 3, 111-159.

Christian, J. T., Ladd, C. C., and Baecher, G. B. (1994). "Reliability and probability in stability analysis." J. Geotech. Engrg. Div., ASCE, 120(12), 763-786.

Clough, G. W. and Reed, M. W. (1984). "Measured behavior of braced wall in very soft clay." J. of Geotech. Engrg., ASCE, 110(1), 1-19.

Finno, R. J., Atmatzidis, D. K., and Perkins, S. B. (1989) "Observed performance of a deep excavation in clay." J. of Geotech. Engrg, ASCE, 115(8), 1045-1064.

Haley and Aldrich. (1991a). "Final geotechnical data report, Central Artery (I-93)/Tunnel (I-90) project, design section D007A, Boston, MA." Rep. Prepared For the Massachusetts Dept. of Public Works, File No. 10360-54, Cambridge, Mass., Vols. 1-2.

Haley and Aldrich. (1991b). "Final geotechnical data report, Central Artery (I-93)/Tunnel (I-90) project, design sections D007A and D007C, Boston, MA." Rep. Prepared For the Massachusetts Dept. of Public Works, File No. 10360-74, Cambridge, Mass., Vols. 1-2.

Haley and Aldrich. (1992). "Report on special laboratory and in-situ testing program, Central Artery (I-93)/Tunnel (I-90) project, design sections D007A and D007C, Boston, MA." Rep. Prepared For the Massachusetts Hwy. Dept., File No. 10360-40, Cambridge, Mass., Vols. 1-2.

Hashash, Y. M. A., and Whittle, A. J. (1996). "Ground movement prediction for deep excavations in soft clay.". J. of Geotech. Engrg, ASCE, 122(6), 474-486.

Jameson R. N. J. (1996). "Mechanical properties of soil cement and applications in excavation support.". M.S. Thesis, Dept. of Civil and Environmental Eng., Massachusetts Institute of Technology, Cambridge, MA.

Jorge, G. R. (1969). "The re-groutable IRP anchorage for soft soils, low capacity or Karstic rocks." Proc. 7th Int. Conf. on Soil Mech. and Found. Eng., Specialty Session No. 15, Mexico City, 159-163.

Ladd, C. C., and Foott, R. (1974). "New design procedure for stability of soft clays." J. Geotech. Engrg. Div., ASCE, 100(7), 763-786.

Ladd, C. C. (1991). "Stability evaluation during staged construction." The Twenty-Second Terzaghi Lecture, J. of Geotech. Engrg. Div., ASCE, 117(4), 537-615.

Load and Resistance Factor Design (LRFD) (1994). Manual of steel construction, Vol. 1, American Institute of Steel Construction, Chicago.

Post Tensioning Institute (PTI). (1995). Post tensioning manual, 5th Ed., Phoenix, Ariz.

O'Rourke, T. D., and O'Donnell C. J. (1997a). "Deep rotational stability of tieback excavations in clay." J. Geotech. And Geoenvir. Engrg., ASCE, 123(6), 506-515.

O'Rourke, T. D., and O'Donnell C. J. (1997b). "Field behavior of excavation stabilized by deep soil mixing." J. Geotech. And Geoenvir. Engrg., ASCE, 123(6), 516-524.

O'Rourke, T. D., McGinn, A. J., Dewsnap, J., and Stewart, H. E. (1997). "Performance of excavations stabilized by deep soil mixing." Rep. Prepared For Bechtel/Parsons Brinckerhoff., Cornell Univ., Ithaca, N. Y.

Ostermayer, H. (1974). "Construction carrying behavior and creep characteristics of ground anchors." ICE Conf. on Diaphragm Walls and Anchorages, London, 141-151.

Pearlman, S. L., and Himick, D. E. (1993). "Anchored excavation using soil mixed wall." Rep. Presented at Deep Found. Inst. 18th Annu. Conf. and Meeting, Deep Foundation Inst., Englewood Cliffs, N.J.

Rodriguez, J. M. and Flamand, C. L. (1969). "Strut loads recorded in a deep excavation in clay." Proc. 7th Int. Conf. on Soil Mech. and Found. Engg., Mexico City, Vol. II, 1969, 459 – 467.

Schnabel, H. (1982). Tiebacks in foundation engineering and construction. Mc-GrawHill, New York.

Takenaka, D. and Takenaka, K. (1995). "Deep chemical mixing method using cement as hardening agent" included in Haley and Aldrich (1995).

Norwegian Geotechnical Institute. "Measurements at a strutted excavation, Oslo Subway, Vaterland 3", Techical Report 8, Blindern, Norway, 1962.

Xanthakos, P., Abramson, L. W., and Bruce, D. A. (1994). Ground control and movement. John Wiley & Sons, Inc., New York, N.Y.

Soil type (1)	Description (2)	Unit weight (kN/m³) (3)	Drained angle of shearing resistance (4)	Undrained shear strength (kN/m²) (5)
Granular fill	Brown coarse to fine sand, trace of silt, and cinders with fragments of brick, wood, and concrete.	18.9	30°	—
Cohesive fill	Pebble to head-size clay fragments with infilling of subangular to angular coarse sand and gravel.	18.0	30°	$0.3-0.4\sigma'_{vo}$[a]
Organic silt	Slightly to moderately overconsolidated medium stiff dark brown to black organic silt, little fine sand, trace of shells, and clay.	17.3	30°	33–53[b]
Marine clay	Gray clay and silt with seams and partings of fine sand.			
	Overconsolidated crust	18.5	—	119
	Upper zone	18.5	—	119–41[c]
	Middle zone	18.5	—	46
	Lower zone	18.5	—	48–56[b]
Glaciomarine deposits	Gray silt, little coarse to fine sand, and clay with trace of fine gravel with cobbles.	23.1	—	—

[a] S_u expressed as a function of vertical effective stress σ'_{vo}.
[b] Average strength ± one standard deviation.
[c] Linearly decreasing with depth.

Table 7.1 Summary of soil characteristics and properties at the BIF sites (after O'Rourke and O'Donnell, 1997a)

Factor of Safety (FS) by Numerical Limit Analyses

Undrained Strength Profile of BBC	**H = 13.4 m LB – UB**	**H = 12.8 m LB – UB**
SHANSEP Profile 1 (EB Special Test Site)	0.934 – 1.043	0.992 – 1.101
SHANSEP Profile 2 (BIF site)		
Lower Limit, σ'_p	1.065 – 1.195	1.132 – 1.261
Best Estimate, σ'_p	1.270 – 1.435	1.351 – 1.515
Corrected Field Vane, μs_u(FV)	0.937 – 1.036	0.991 – 1.067

Notes:
1.) H = Excavated height
2.) For H = 13.4 m., FS(LEM) = 0.99-1.04 based on μs_u(FV) by O'Rourke & O'Donnell (1997a)

Table 7.2 Factor of safety for East wall Section A-A′ with isotropic strength of BBC

Factor of Safety (FS) by Numerical Limit Analyses

Stress History	**Isotropic Strength** **LB – UB**	**Anisotropic Strength Parameter AN1** **LB – UB**	**Anisotropic Strength Parameter AN2** **LB – UB**
Profile 1 (EB Special Test Site)	0.992 – 1.101	1.123 – 1.215	0.864 – 0.932
Profile 2 (BIF site)			
Lower Limit, σ'_p	1.132 – 1.261	1.200 – 1.298	0.941 – 1.013
Best Estimate, σ'_p	1.351 – 1.515	1.435 – 1.552	1.081 – 1.164
Corrected Field Vane, μs_u(FV)	0.991 – 1.067	–	–

Table 7.3 Factor of safety for East wall Section A-A′ with anisotropic strength of BBC, H = 12.8m

Geometry

Parameter, X_i	E[X_i]	SD[X_i]	Remarks for SD
1. Depth of excavation, H	13.4m	0.6m	Based on reported differences in H at failure in Section A-A′
2. El. of Glacio. location	+7.5m	2.5m	Haley and Aldrich (1991b)
3. Free length of 2nd tieback	12.0m	1.0m	Data available at MIT

Properties of Overlying Soils

Parameter, X_i	E[X_i]	SD[X_i]	Remarks for SD
1. Cohesive Fill			
Unit Weight, γ_t (kN/m^3)	18.0	0.6	Haley and Aldrich (1991b)
Undrained Strength, s_u (kPa) = 0.3-0.4σ'_{v0}	19.1	3.2	Haley and Aldrich (1991b)
2. Organic Silt			
Unit Weight, γ_t (kN/m^3)	17.3	0.9	Haley and Aldrich (1991b)
Undrained Strength, s_u (kPa)	43	10	Haley and Aldrich (1991b)

Properties of BBC

Parameter, X_i	E[X_i]	SD[X_i]	Remarks for SD
1. Unit Weight, γ_t (kN/m^3)	18.5	0.5	Haley and Aldrich (1991b)
2. Undrained strength profile (kPa)	See Figure 7.24	See Figure 7.24	C. C. Ladd (Pers. Comm., 1998) SHANSEP Parameters: SD[S] = 0.012, SD[m] = 0.05

Others

Parameter, X_i	E[X_i]	SD[X_i]	Remarks for SD
1. Tieback failure load (kN/m)	765.6	38.3	Assume SD = 5% in yield stress
2. Plastic moment of SMW (kNm/m)	372.9	18.6	Assume SD = 5% in yield stress
3. Skin friction of fixed anchor in Organic Silt, f_s (kPa)	22.5	8.7	$f_s = ns_u$, n = 0.4 – 5.0 due to post grouting (Ostermayer, 1974)
4. Skin friction of fixed anchor in BBC, f_s (kPa)	41.9	16.1	$f_s = ns_u$, n = 0.4 – 5.0 due to post grouting (Ostermayer, 1974)

Table 7.4 Parameters for sensitivity analysis of East wall Section A-A′

Geometry

Parameter, X_i	X_i-SD LB – UB	X_i+SD LB – UB
1. Depth of excavation, H	1.320 – 1.462	1.186 – 1.306
2. El. of Glacio. location	1.232 – 1.349	1.279 – 1.412
3. Free length of 2nd tieback	1.250 – 1.372	1.256– 1.386

Properties of Overlying Soils

Parameter, X_i	X_i-SD LB – UB	X_i+SD LB – UB
1. Cohesive Fill		
Unit Weight, γ_t (kN/m^3)	1.271 – 1.399	1.236 – 1.360
Undrained Strength, s_u (kPa) = 0.3-0.4σ'_{v0}	1.248 – 1.373	1.259 – 1.385
2. Organic Silt		
Unit Weight, γ_t (kN/m^3)	1.264 – 1.391	1.243 – 1.367
Undrained Strength, s_u (kPa)	1.245 – 1.370	1.261 – 1.388

Properties of BBC

Parameter, X_i	X_i-SD LB – UB	X_i+SD LB – UB
1. Unit Weight, γ_t (kN/m^3)	1.263 – 1.390	1.243 – 1.368
2. Undrained strength profile	1.006 – 1.114	1.495 – 1.641

Others

Parameter, X_i	X_i-SD LB – UB	X_i+SD LB – UB
1. Tieback failure load (kN/m)	1.253 – 1.379	1.253 – 1.379
2. Plastic moment of SMW (kNm/m)	1.253 – 1.379	1.253 – 1.379
3. Skin friction of fixed anchor in Organic Silt, f_s (kPa)	1.252 – 1.377	1.254 – 1.380
4. Skin friction of fixed anchor in BBC, f_s (kPa)	1.237 – 1.367	1.260 – 1.384

Notes: E[FS] = 1.253 – 1.379

Table 7.5 Factor of safety obtained from sensitivity analyses for East wall Section A-A′

Parameter, X_i	Best. Est. $E[X_i]$	Std. Dev. $SD[X_i]$	Sensitivity $\Delta FS/\Delta X_i$ x 10^{-3}	$V[FS_i]$ $(\Delta FS/\Delta X_i)^2.V[X_i]$ x 10^{-6}
1. Excavated depth, H (m)	13.4	0.6	-116.67	4489
2. El. of Glacio. Location (m)	+7.5	2.5	9.40	552
3. Free length of 2nd tieback	12.0	1.0	3.00	9
4. Cohesive Fill, γ_t (kN/m^3)	18.0	0.6	-29.17	306
5. Cohesive Fill, s_u (kPa)	19.1	3.2	1.72	30
6. Organic Silt, γ_t (kN/m^3)	17.3	0.9	-11.67	110
7. Organic Silt, s_u (kPa)	43.0	10.0	0.80	64
8. BBC, γ_t (kN/m^3)	18.0	0.5	-20.00	100
9. Undrained Strength Profile of BBC (kPa)	74.97[1]	14.5[1]	16.80	59329
10. Tieback load (kN/m)	765.6	38.3	0.0	0
11. M_p of SMW (kNm/m)	372.9	18.6	0.0	0
12. Fixed Anchor f_s in Organic Silt, (kPa)	22.5	8.7	0.11	1
13. Fixed Anchor f_s in BBC (kPa)	41.9	16.1	0.71	132
			V[FS] =	65123

[1] average value

SD[FS] = 0.255

Summary of Lower Bound Analyses:

FS = 1.253 ± 0.255 (SD)

Table 7.6 Uncertainty in calculated factor of safety for lower bound analyses of East wall Section A-A′

Parameter, X_i	Best. Est. $E[X_i]$	Std. Dev. $SD[X_i]$	Sensitivity $\Delta FS/\Delta X_i$ x 10^{-3}	$V[FS_i]$ $(\Delta FS/\Delta X_i)^2.V[X_i]$ x 10^{-6}
1. Excavated depth, H (m)	13.4	0.6	-130.00	6084
2. El. of Glacio. Location (m)	+7.5	2.5	12.60	992
3. Free length of 2nd tieback	12.0	1.0	7.00	49
4. Cohesive Fill, γ_t (kN/m^3)	18.0	0.6	-32.50	380
5. Cohesive Fill, s_u (kPa)	19.1	3.2	1.88	36
6. Organic Silt, γ_t (kN/m^3)	17.3	0.9	-13.33	144
7. Organic Silt, s_u (kPa)	43.0	10.0	0.90	81
8. BBC, γ_t (kN/m^3)	18.0	0.5	-22.00	121
9. Undrained Strength Profile of BBC (kPa)	74.97[1]	14.5[1]	17.21	62278
10. Tieback load (kN/m)	765.6	38.3	0.0	0
11. M_p of SMW (kNm/m)	372.9	18.6	0.0	0
12. Fixed Anchor f_s in Organic Silt, (kPa)	22.5	8.7	0.17	2
13. Fixed Anchor f_s in BBC (kPa)	41.9	16.1	0.53	72
[1] average value			V[FS] =	70240

SD[FS] = 0.265

Summary of Uower Bound Analyses:

FS = 1.379 ± 0.265 (SD)

Table 7.7 Uncertainty in calculated factor of safety for upper bound analyses of East wall Section A-A′

Redesign Options	**Factor of Safety LB – UB**	**Average Improvement**
As-Built	0.992 – 1.101	–
Strengthen wall (M_p = 2000 kNm/m, Diaphragm wall)	0.994 – 1.104	+0.25%
Extend wall into bedrock		
1) M_p = 373 kNm/m, SMW wall		
1.1 Pin support at tip of wall	1.071 – 1.175	+7.3%
1.2 Fixed support at tip of wall	1.084 – 1.194	+8.8%
2) M_p = 2000 kNm/m, Diaphragm wall		
2.1 Pin support at tip of wall	1.151 – 1.261	+15.2%
2.2 Fixed support at tip of wall	1.208 – 1.325	+21.0%
Extend free length of tiebacks by 11m	1.075 – 1.179	+7.7%

Notes:
1.) Excavated depth, H = 12.8m
2.) All cases assume undrained (isotropic) strength Profile 1

Table 7.8 Proposed redesign options for East wall Section A-A′

Factor of Safety (FS) by Numerical Limit Analyses

Undrained Strength Profile of BBC	**Without Remedial Buttress LB – UB**	**With Remedial Buttress LB – UB**	**Average Improvement**
SHANSEP Profile 1 (EB Special Test Site)	0.789 – 0.883	0.915 – 1.005	14.8%
SHANSEP Profile 2 (BIF site)			
Lower Limit, σ'_p	0.887 – 1.003	1.042 – 1.146	15.8%
Best Estimate, σ'_p	1.060 – 1.218	1.267 – 1.408	17.4%
Corrected Field Vane, μs_u(FV)	0.784 – 0.903	0.976 – 1.078	21.8%

Notes:

1.) FS(LEM) = 1.08 – 1.13 based on μs_u(FV) by O'Rourke & O'Donnell (1997b)

Table 7.9 Factor of safety for West wall Section B-B′ with isotropic strength of BBC

Factor of Safety (FS) by Numerical Limit Analyses

Stress History	**Isotropic Strength** **LB – UB**	**Anisotropic Strength Parameter AN1** **LB – UB**	**Anisotropic Strength Parameter AN2** **LB – UB**
Profile 1 (EB Special Test Site)	0.915 – 1.005	1.042 – 1.117	0.824 – 0.877
Profile 2 (BIF site)			
Lower Limit, σ'_p	1.042 – 1.146	1.112 – 1.192	0.900 – 0.957
Best Estimate, σ'_p	1.267 – 1.408	1.370 – 1.466	1.056 – 1.124
Corrected Field Vane, μs_u(FV)	0.976 – 1.078	–	–

Table 7.10 Factor of safety for West wall Section B-B′ (Remedial buttress) with anisotropic strength of BBC

s_{uB}/s_{uave}	Factor of Safety, FS. LB – UB
1	0.789 – 0.883
1.5	0.818 – 0.925
2	0.838 – 0.946
4	0.886 – 0.989
5	0.899 – 1.000
8	0.910 – 1.004
19.15	0.914 – 1.004
38.3 (original design)	0.915 – 1.005

Notes: 1) s_{uB} = undrained shear strength of buttress
2) s_{uave} = 50 kPa (average)
3) BBC Profile 1, Isotropic strength

Table 7.11 Effect of shear strength of buttress to factor of safety of West wall Section B-B′

Redesign Options	Factor of Safety LB – UB	Average Improvement
As-Built	0.915 – 1.005	–
Reduce depth of buttress below final grade		
1) 2.2m	0.914 – 1.002	-0.2%
2) 1.0m	0.909 – 1.002	-0.5%
3) 0m	0.843 – 0.945	-6.8%
Extend jet grout column into bedrock	1.172 – 1.321	+30%
Extend buttress across full width of excavation	1.648 – 1.964	+88%
Use grid of jet grout column (Fig. 7.53)		
1. Without column next to SMW	0.920 – 1.058	3%
2. With column next to SMW	1.074 – 1.263	17%

Notes:
1.) Undrained (isotropic) strength Profile 1 of BBC

Table 7.12 Proposed redesign options for West wall Section B-B'

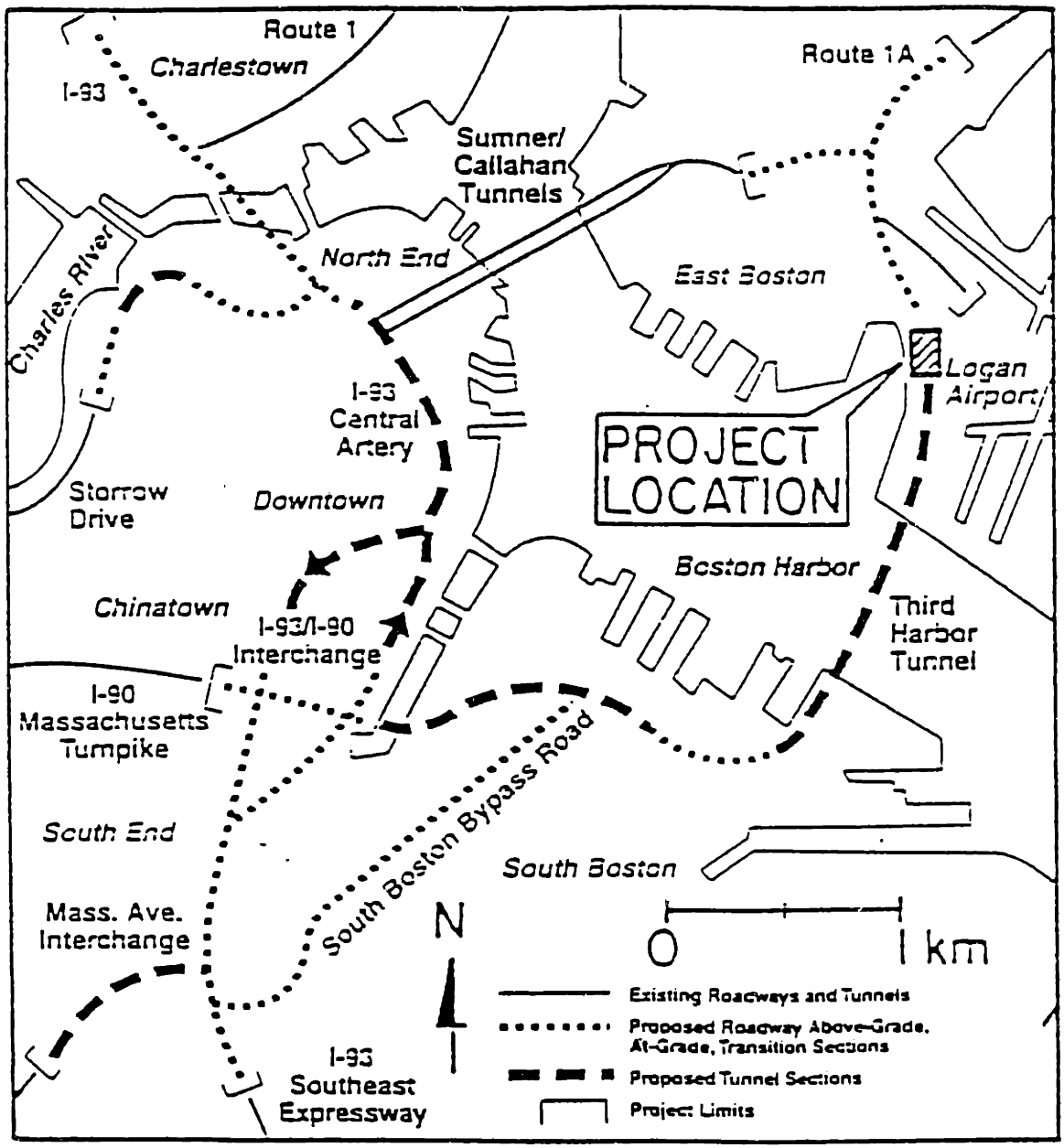

Figure 7.1 Plan view of Boston CA/T project with location of case history site (after O'Rourke and O'Donnell, 1997a)

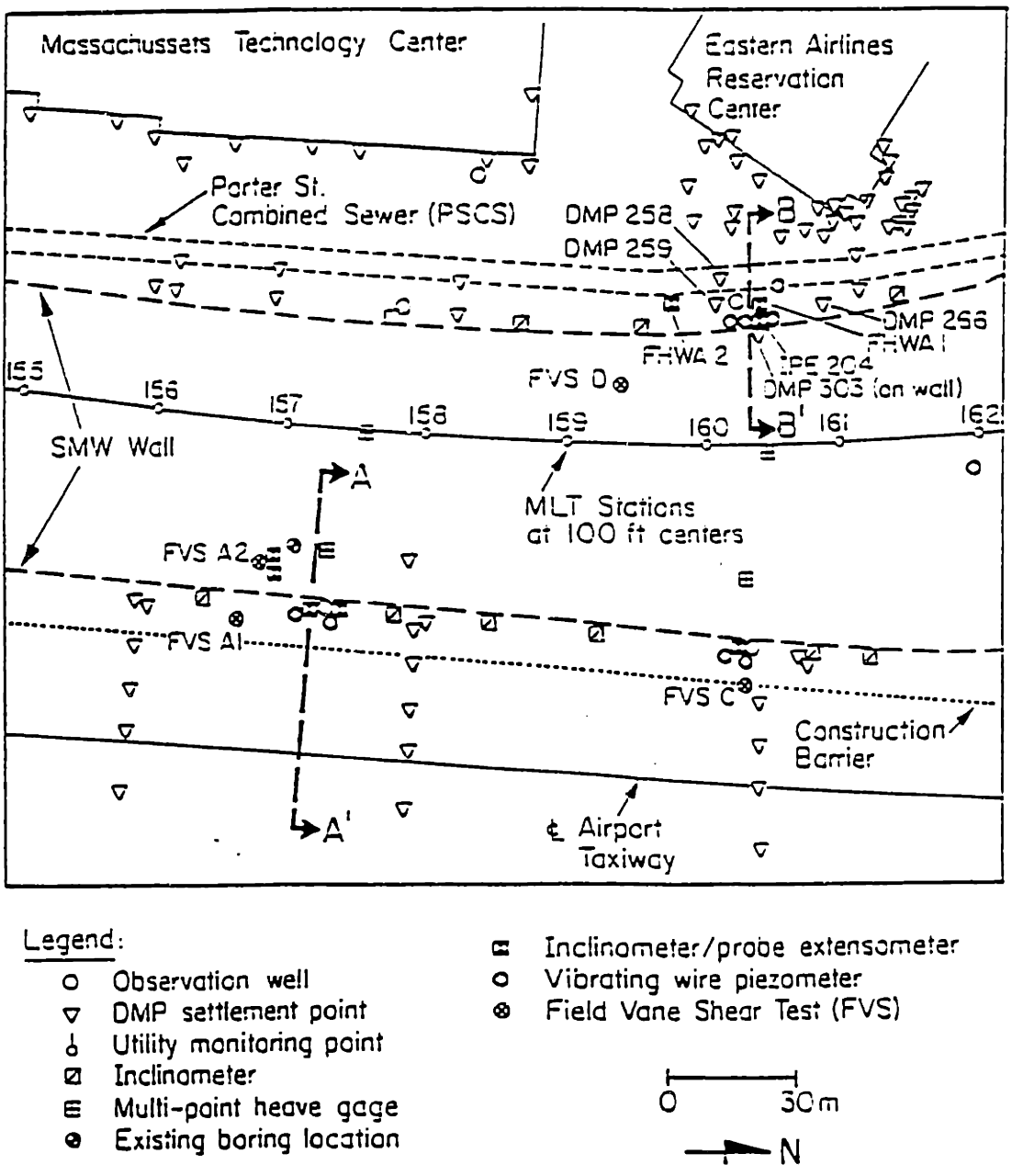

Figure 7.2 Plan view of case history area on BIF project
(after O'Rourke and O'Donnell, 1997a)

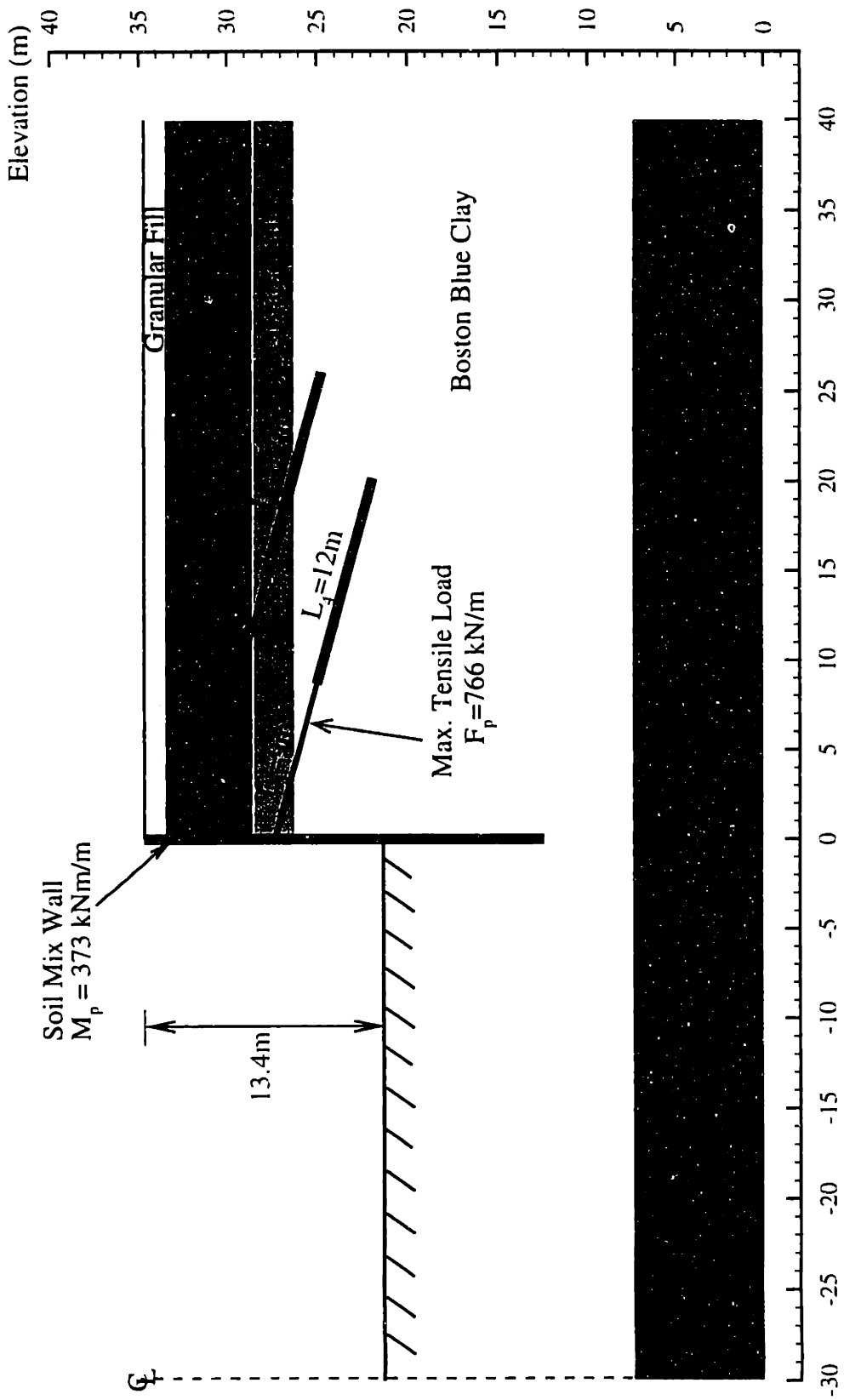

Figure 7.3 Cross section of East wall Section A-A' (Failure)

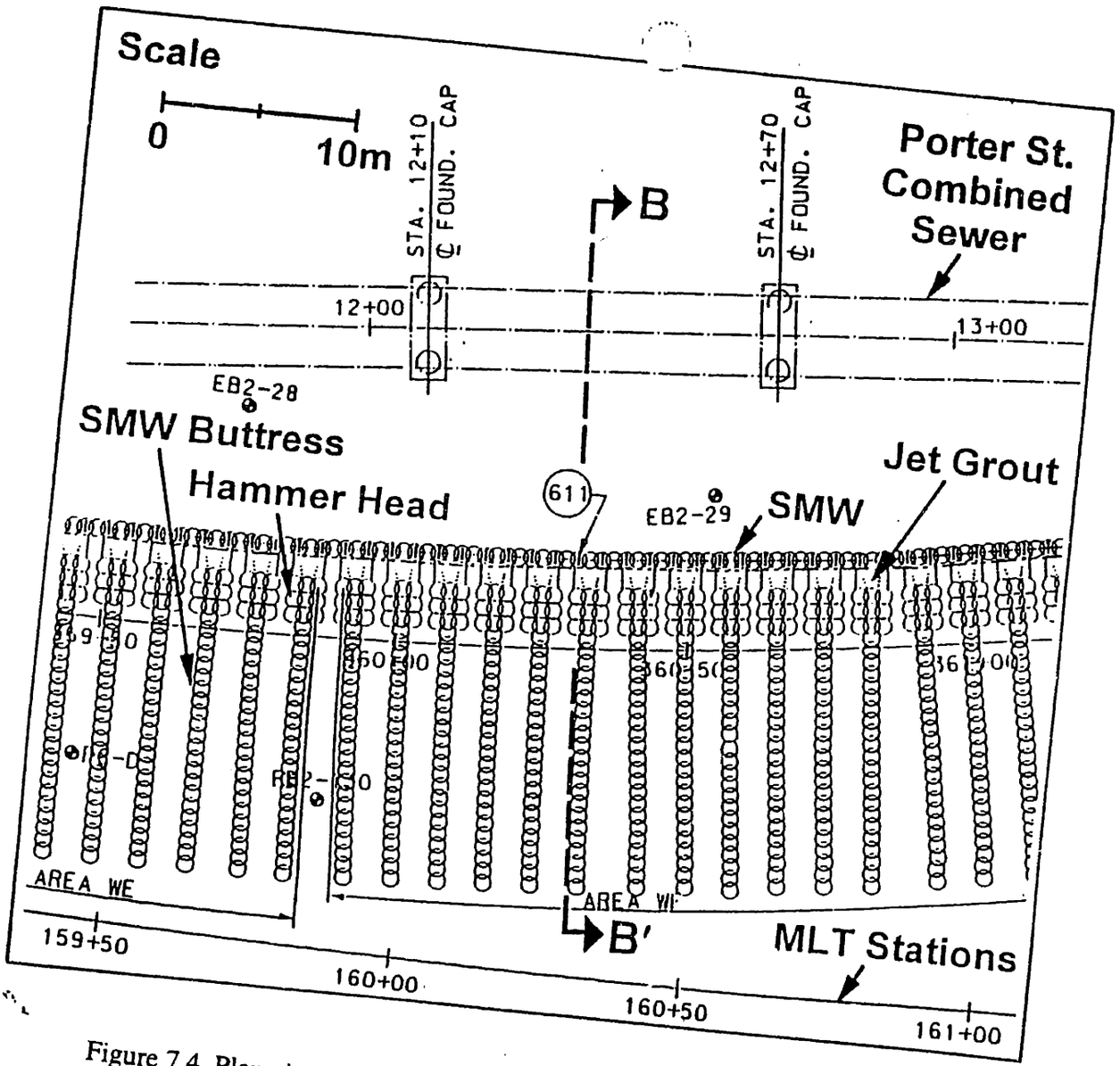

Figure 7.4 Plan view of basal stabilization scheme at West wall, Section B-B'
(after O'Rourke and O'Donnell, 1997b)

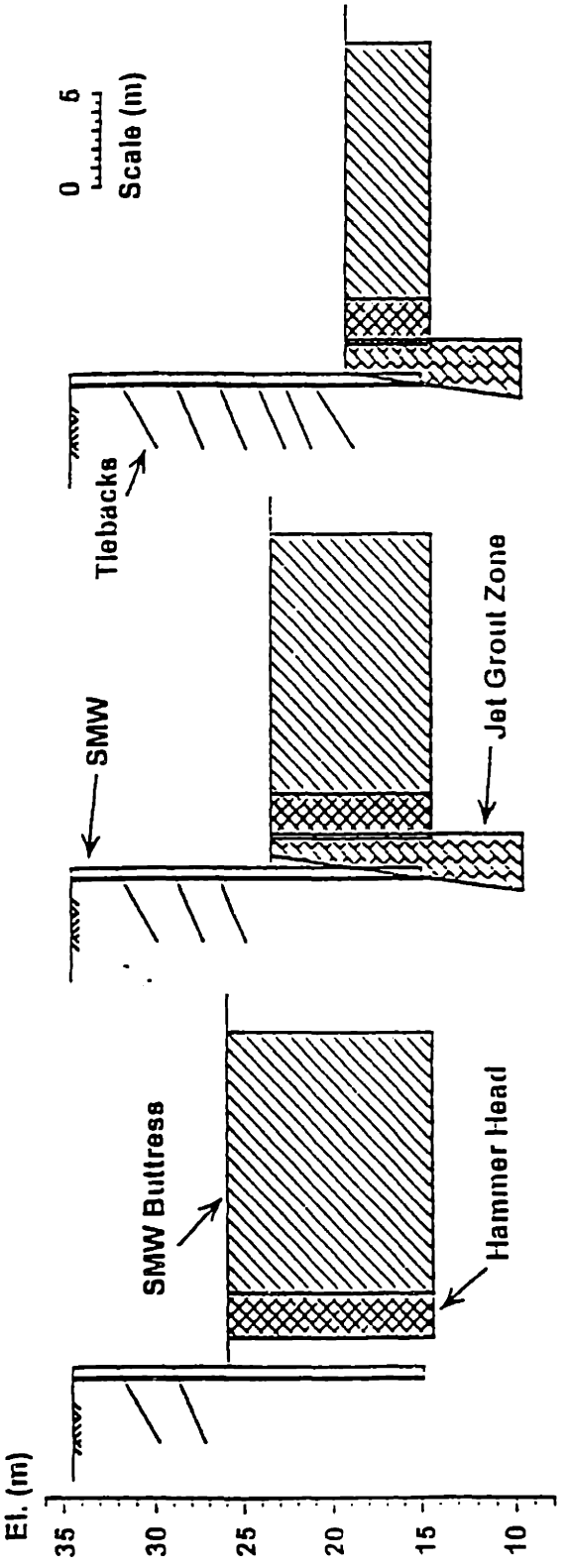

Figure 7.5 Profile view of basal stabilization scheme at West wall, Section B-B'
(after O'Rourke and O'Donnell, 1997b)

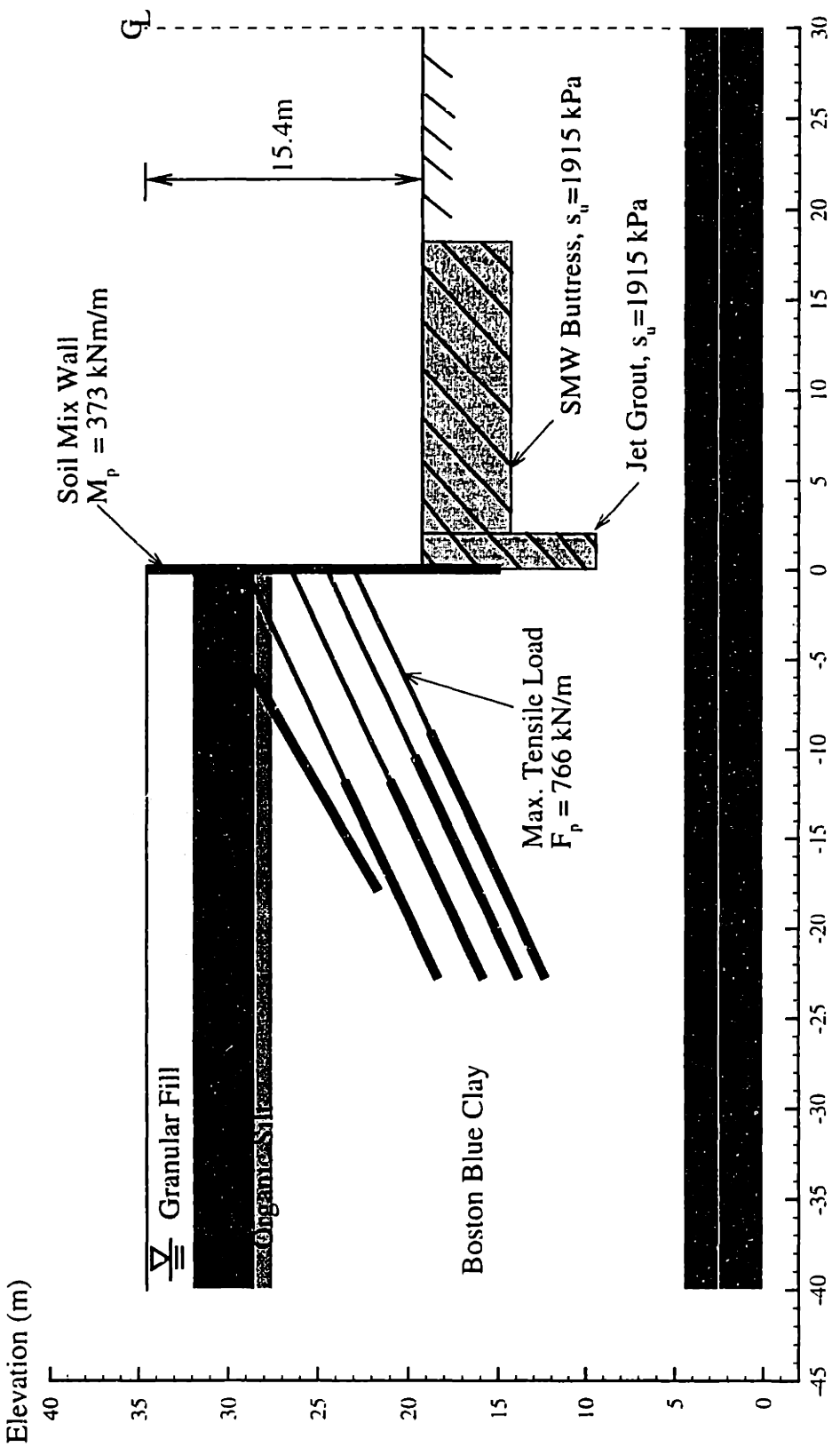

Figure 7.6 Cross section of West wall Section B-B': Remedial buttress

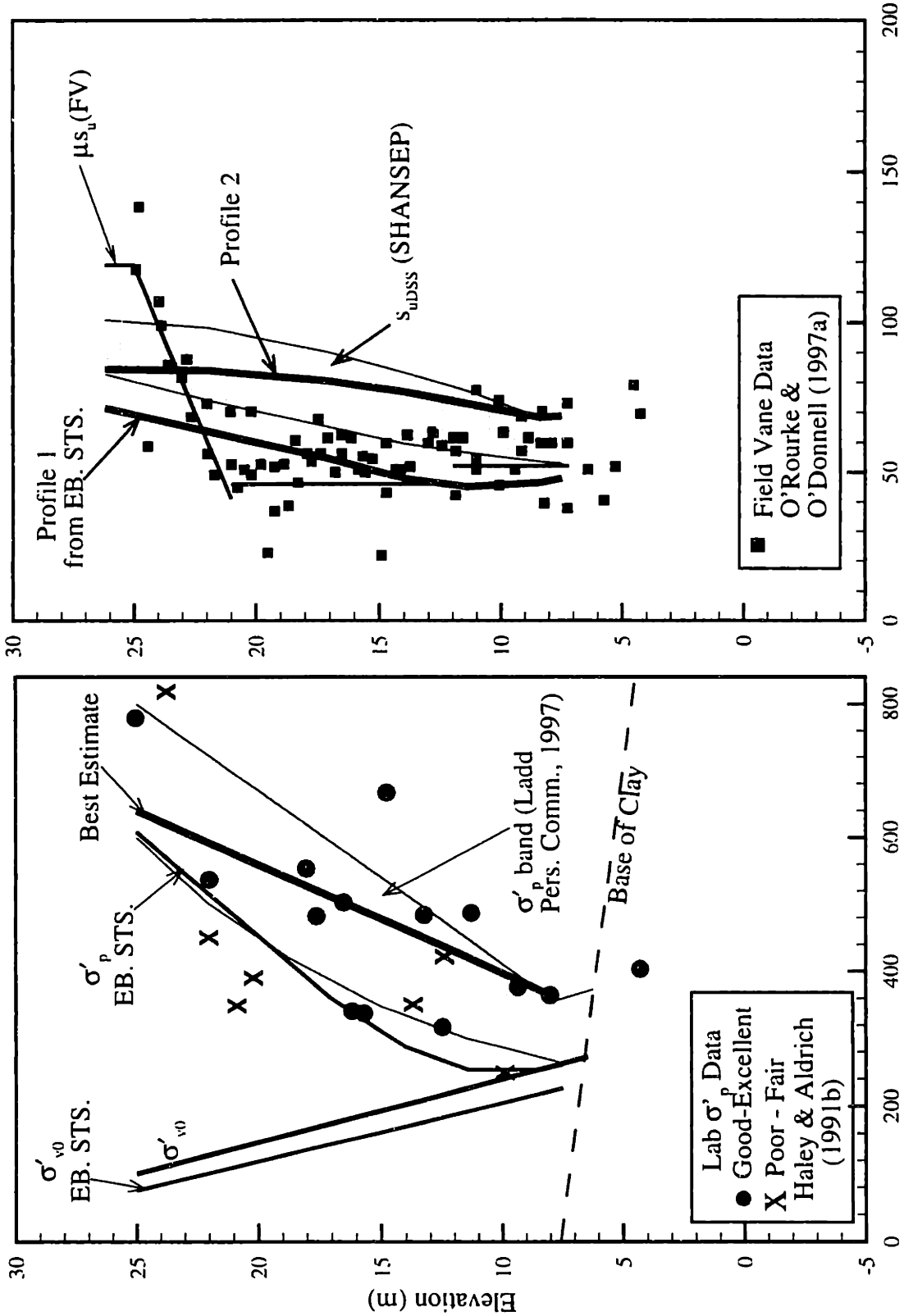

Figure 7.7 Stress history and undrained strength profiles for BIF case study

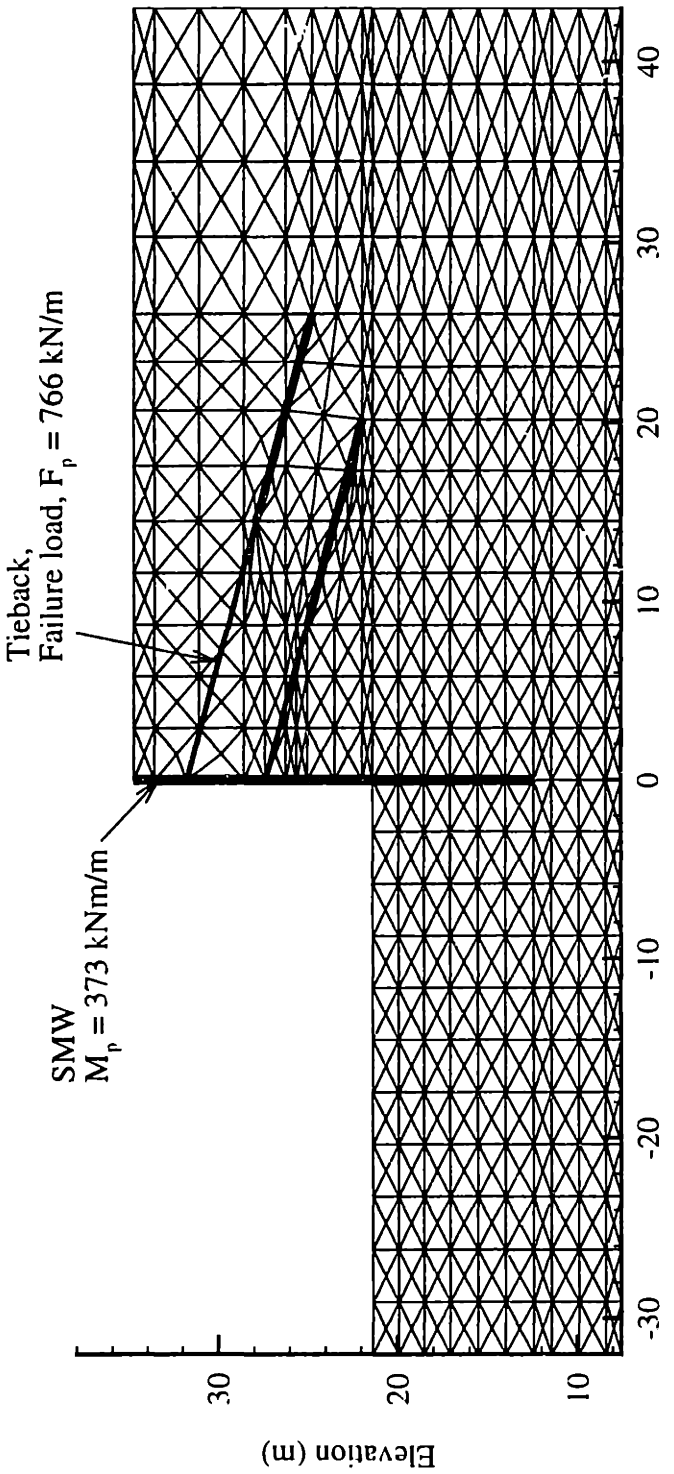

Figure 7.8 Spatial discretization of numerical limit analyses for East wall Section A-A′

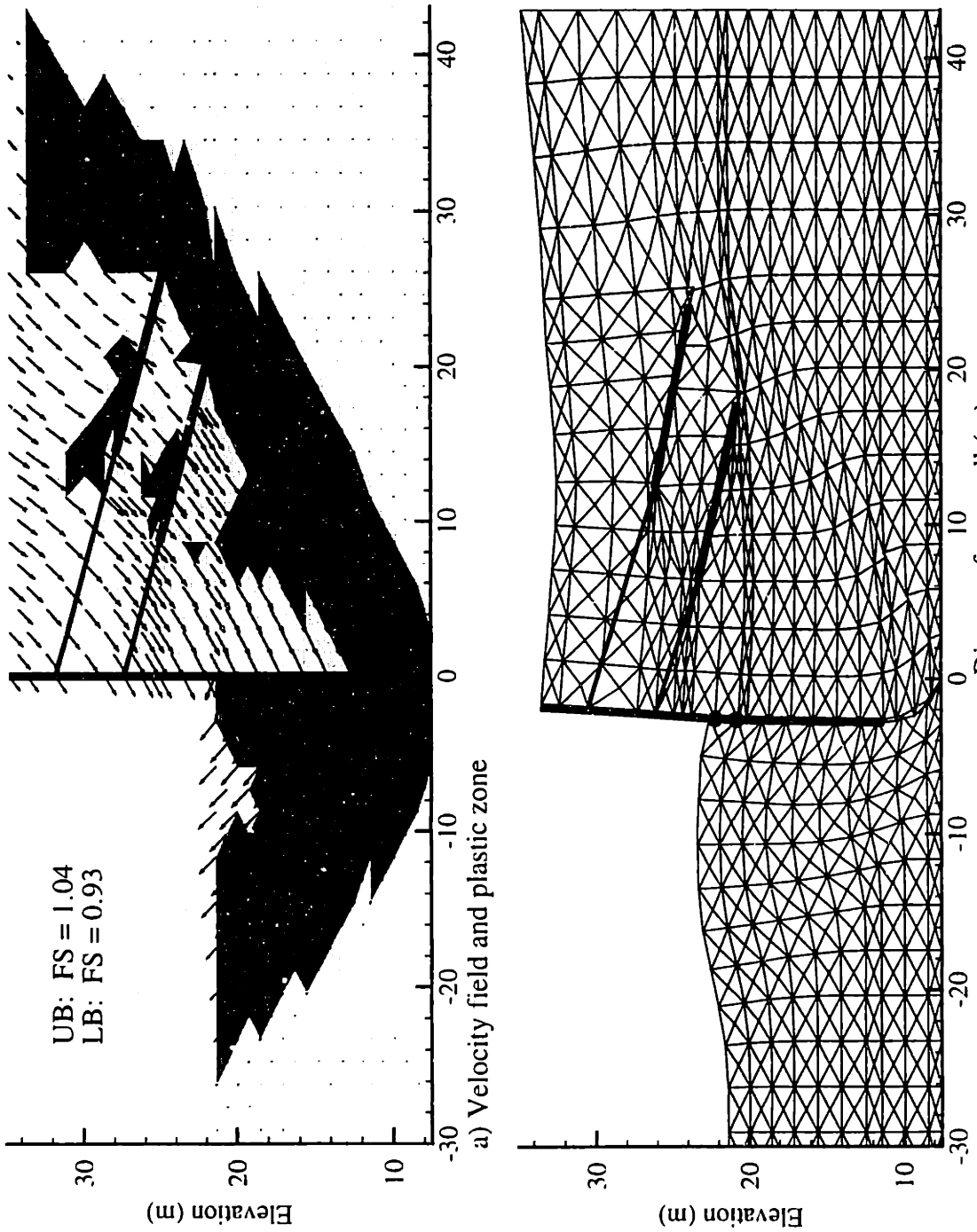

Figure 7.9 Upper bound results for East wall Section A-A', (BBC Profile 1, isotropic strength, H = 13.4m)

H	13.4 m	D/H	0.67	x_o	0.04
γ	18.3 kN/m^3	W/H	1.5	y_o	1.41
B/H	1.48	θ	10°	N_s	5.57

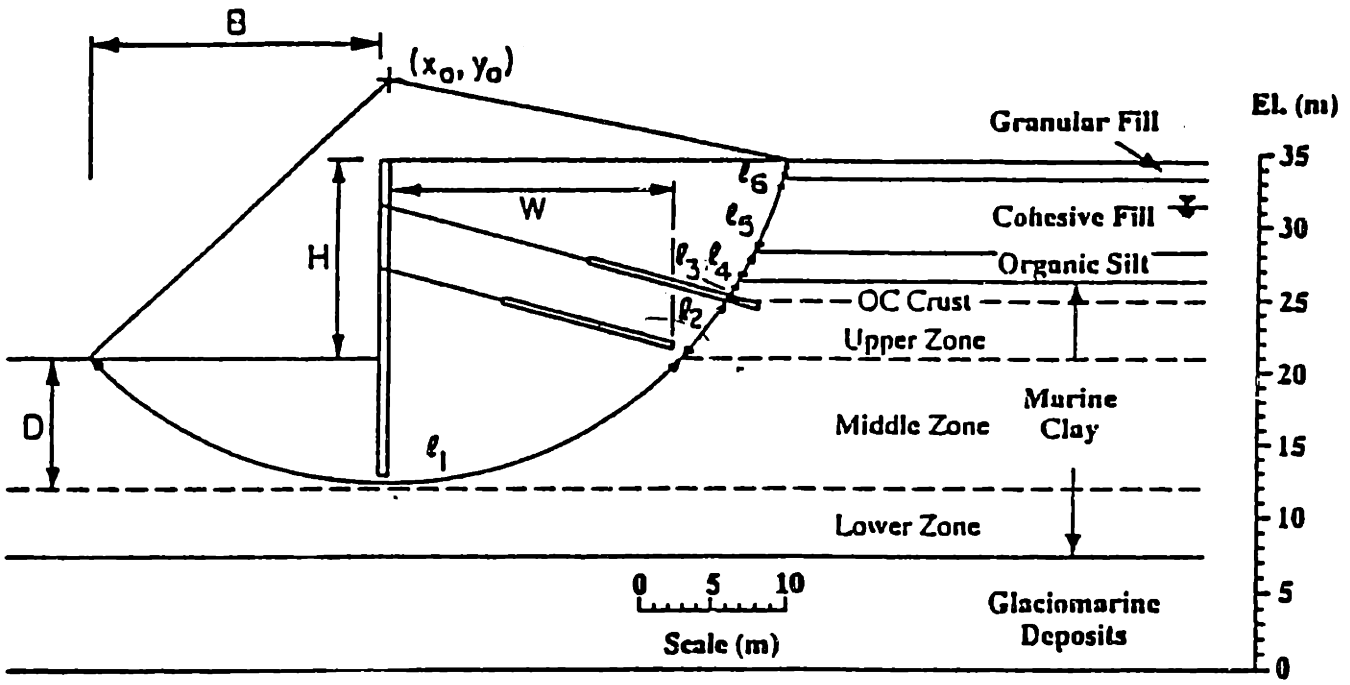

Figure 7.10 Limit equilibrium calculation for East wall, Section A-A′ by O'Rourke and O'Donnell (1997a)

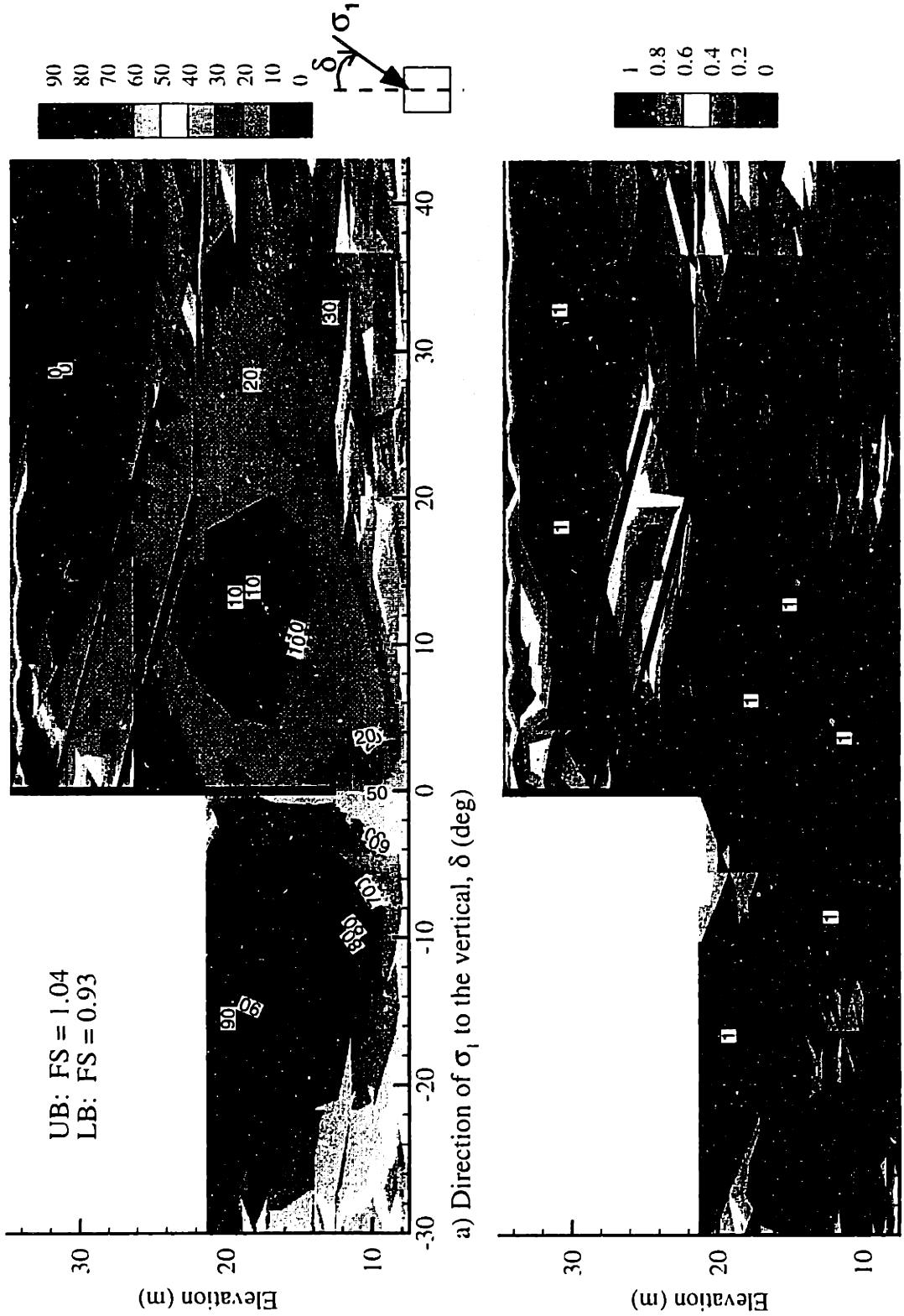

Figure 7.11 Lower bound results for East wall Section A-A' (BBC Profile 1, isotropic strength, H =13.4m)

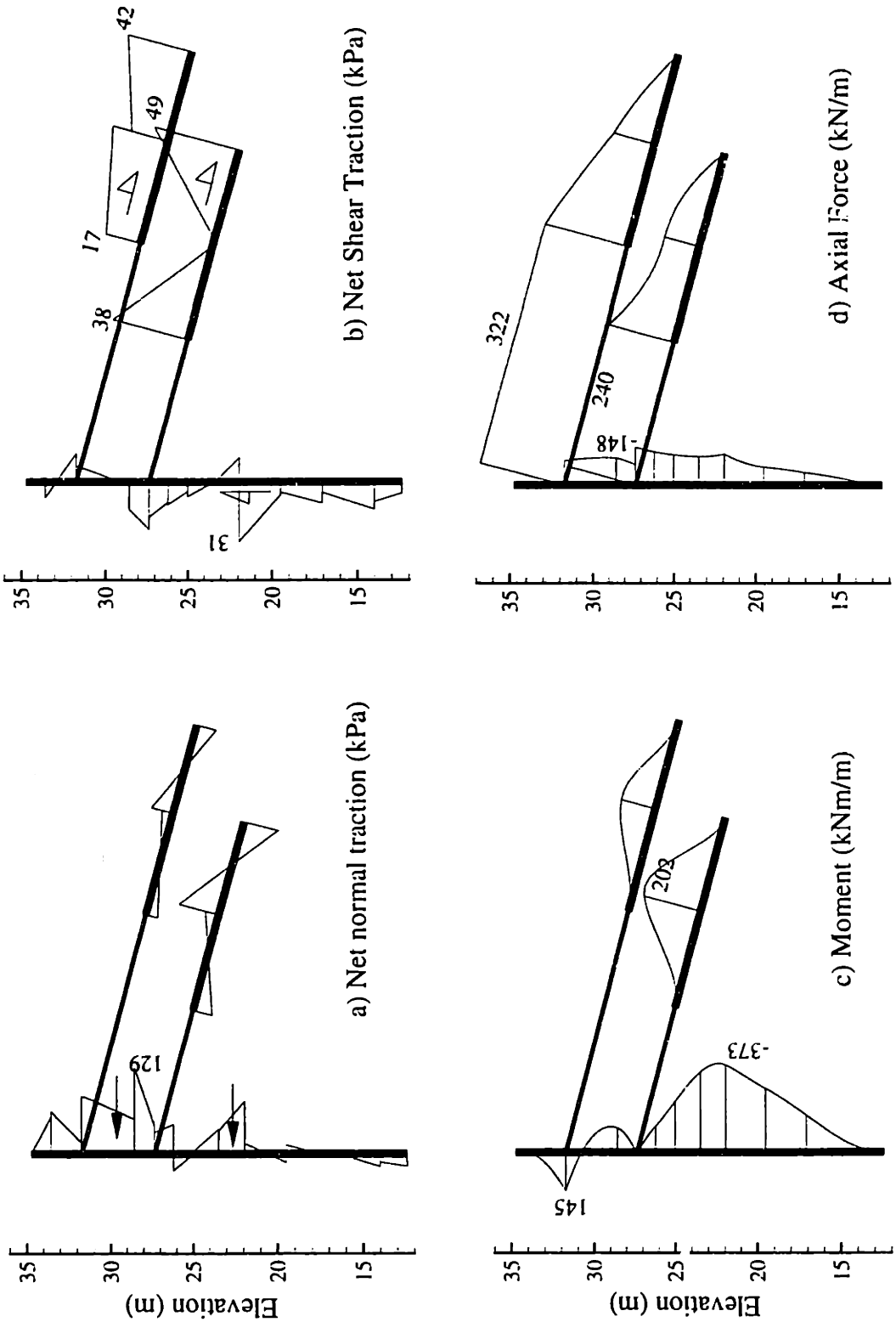

Figure 7.12 Net tractions, force and moment diagrams along SMW and tiebacks from LB analyses of East wall Section A-A' (BBC Profile 1, isotropic strength, H = 13.4m)

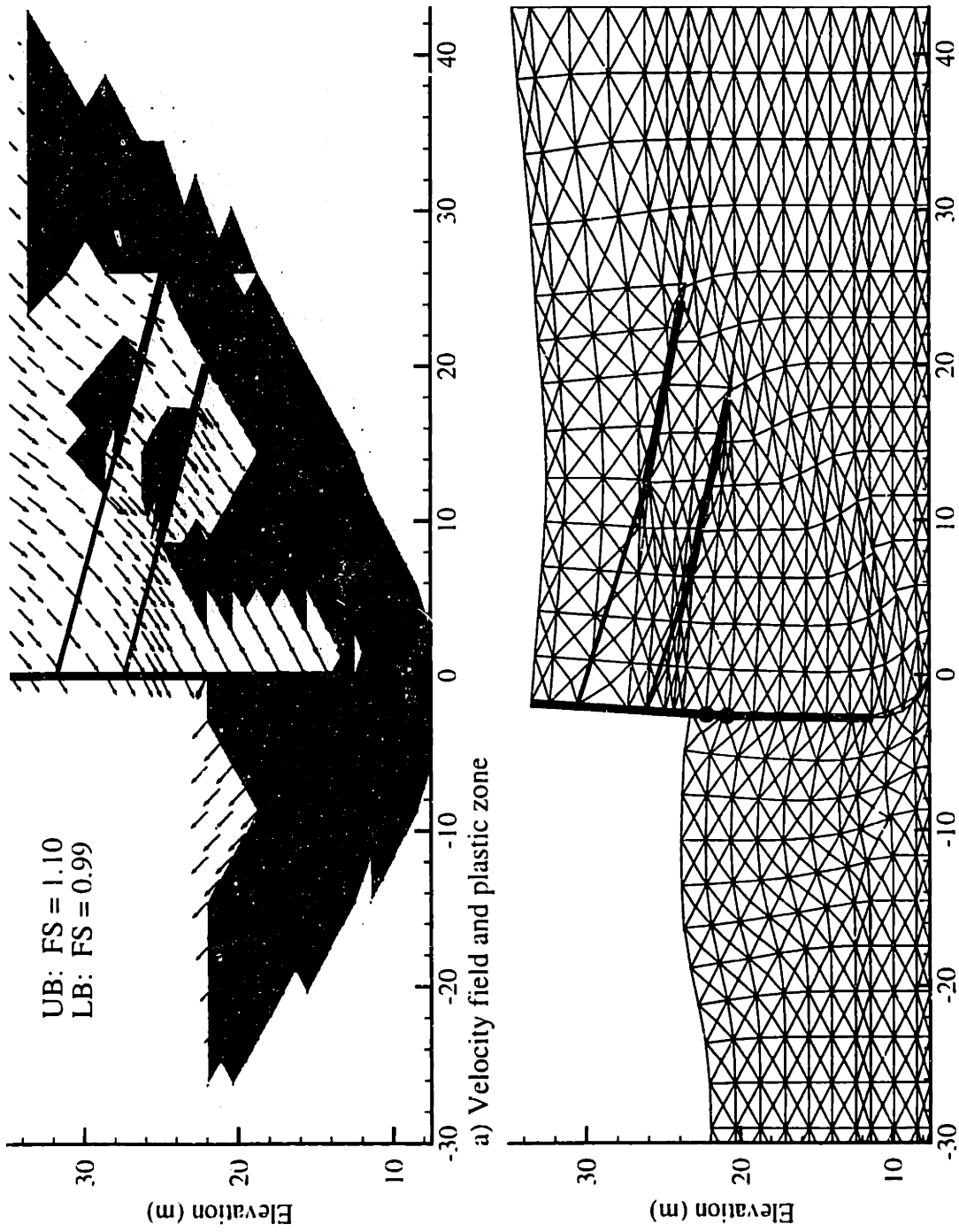

Figure 7.13 Upper bound results for East wall Section A-A' (BBC Profile 1, Isotropic strength, H = 12.8m)

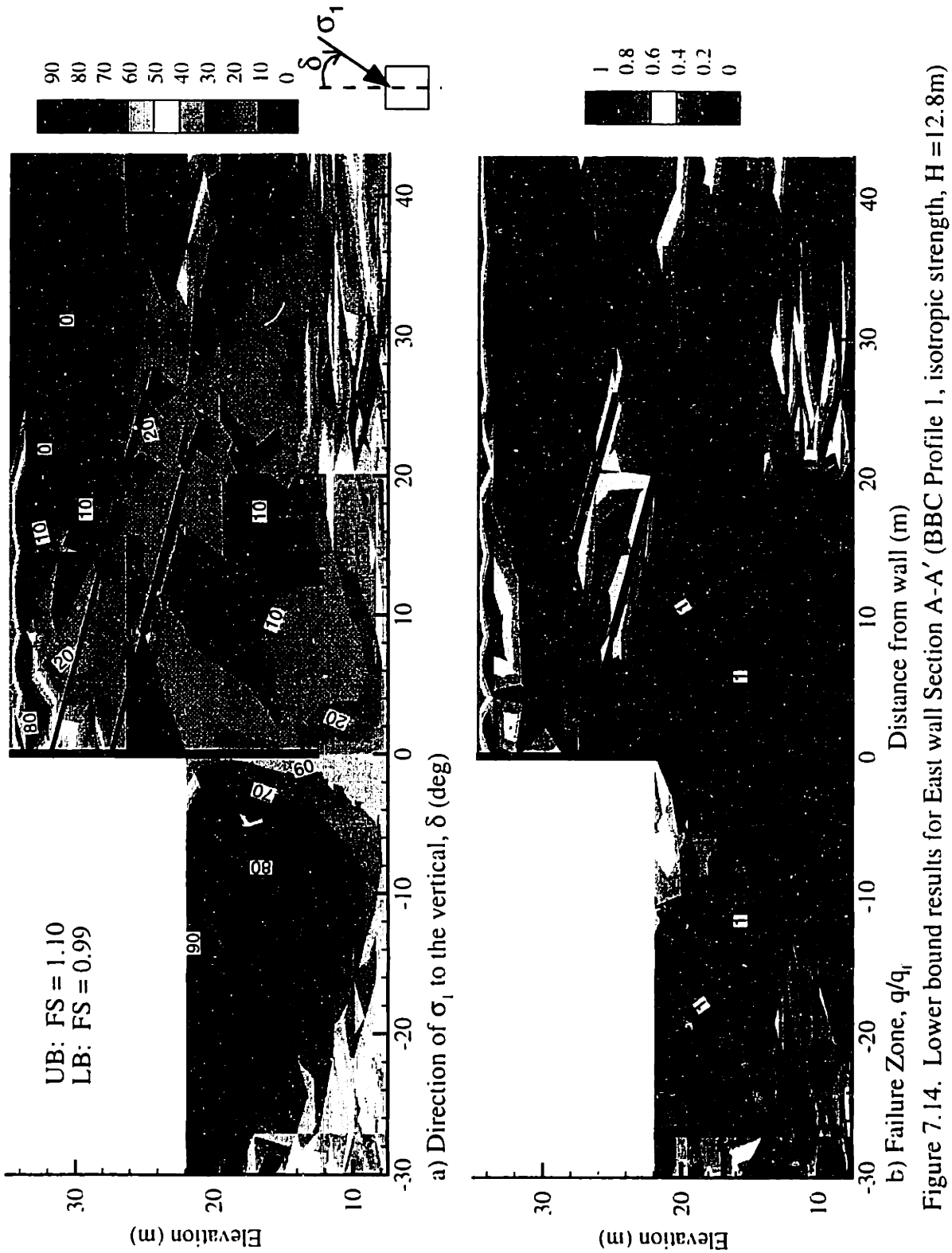

Figure 7.14. Lower bound results for East wall Section A-A′ (BBC Profile 1, isotropic strength, H =12.8m)

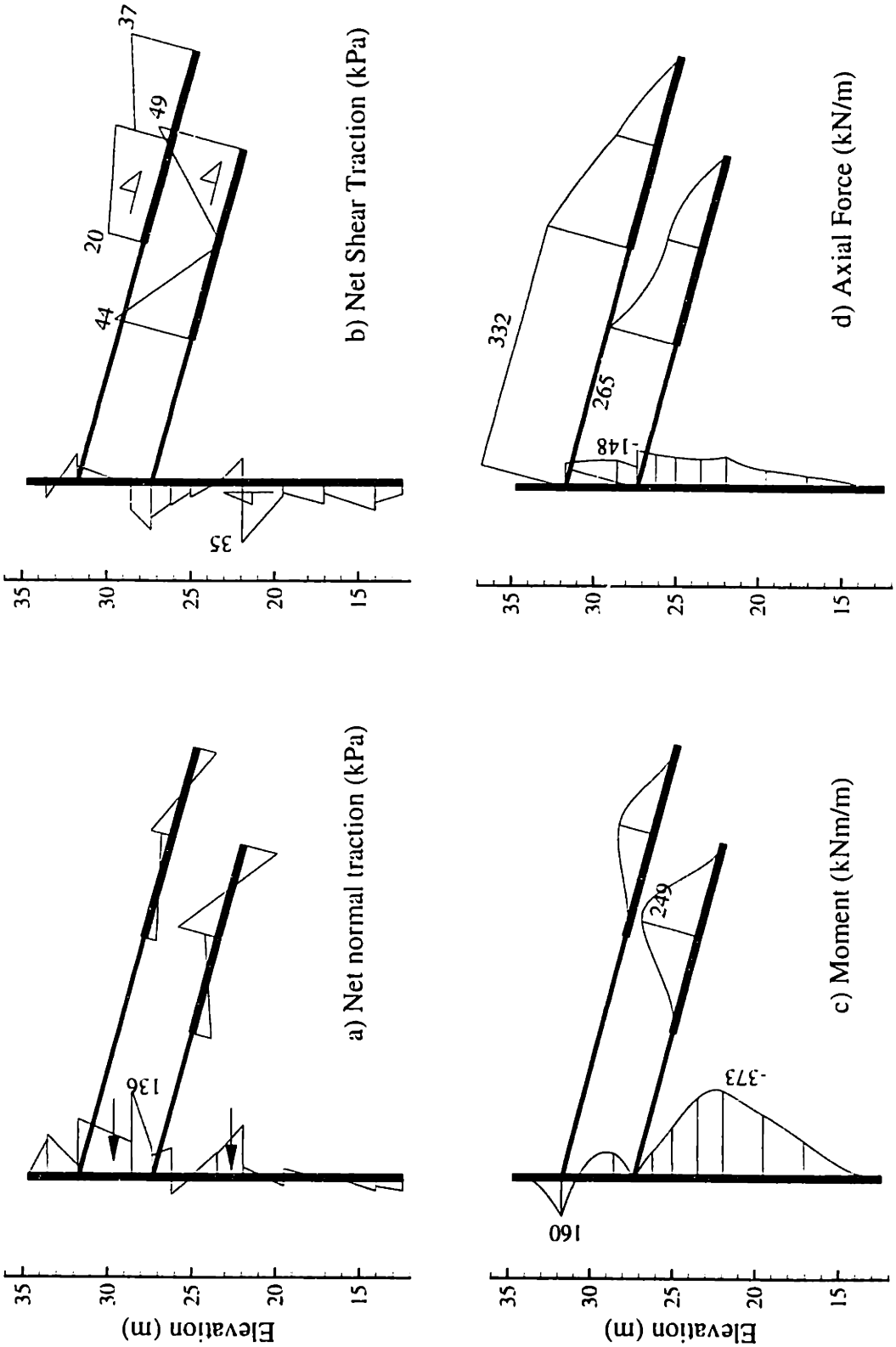

Figure 7.15 Net tractions, force and moment diagrams along SMW and tiebacks from LB analyses of East wall Section A-A' (BBC Profile 1, isotropic strength, H = 12.8m)

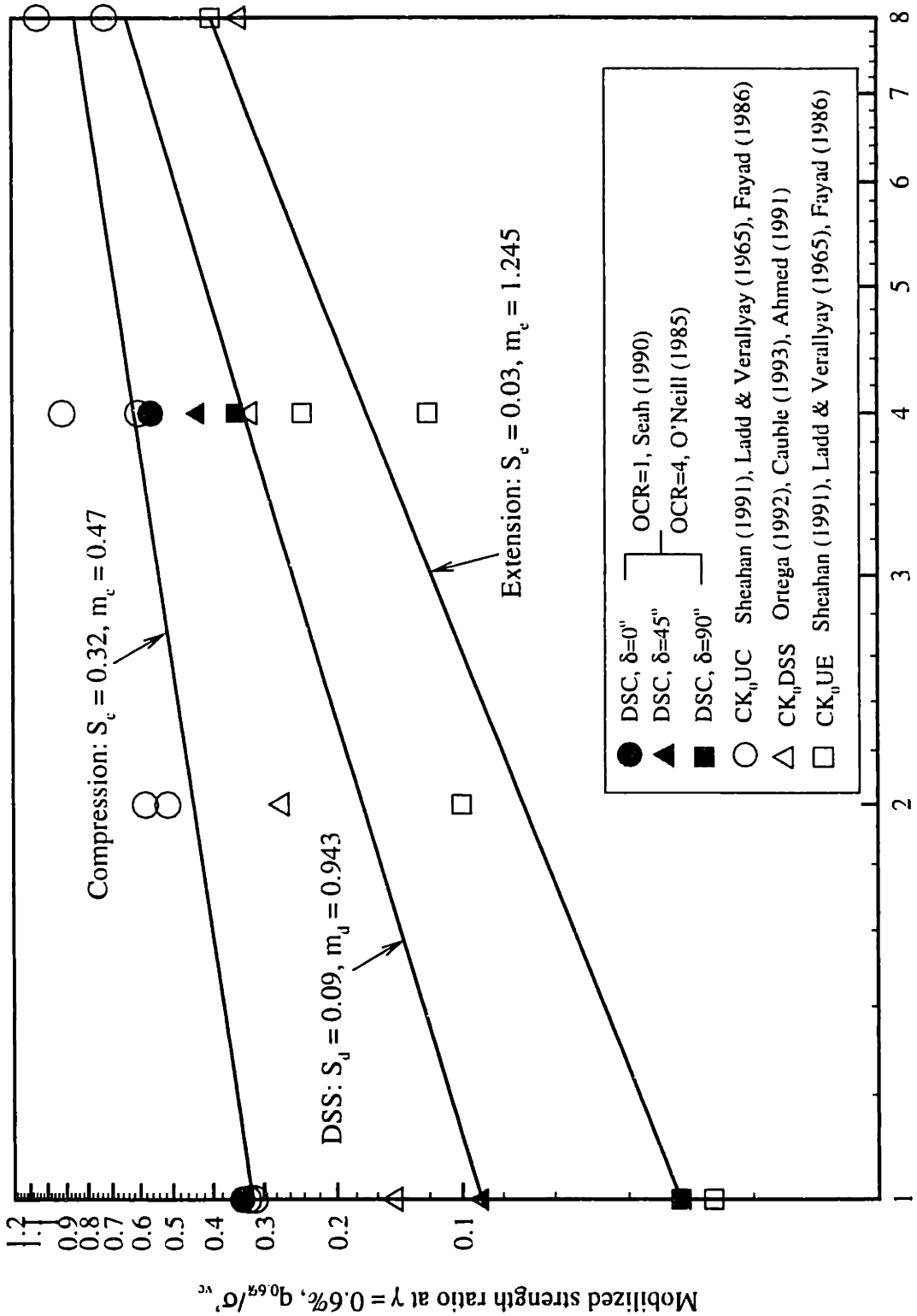

Figure 7.16 Mobilized anisotropic undrained strength ratios for BBC at γ = 0.6%, parameter set AN2

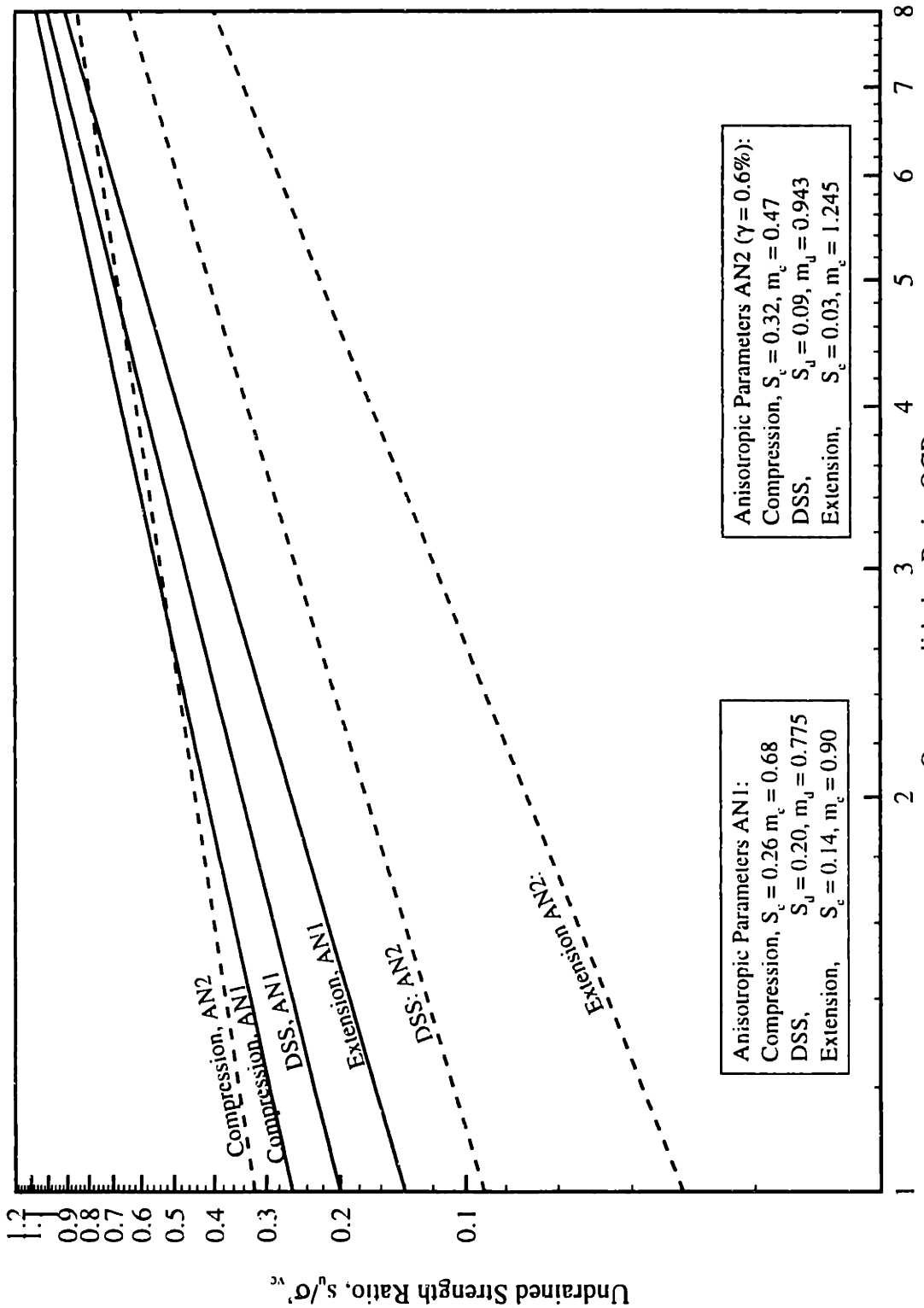

Figure 7.17 Comparisons of mobilized anisotropic strength ratios for BBC using parameter sets AN1 and AN2

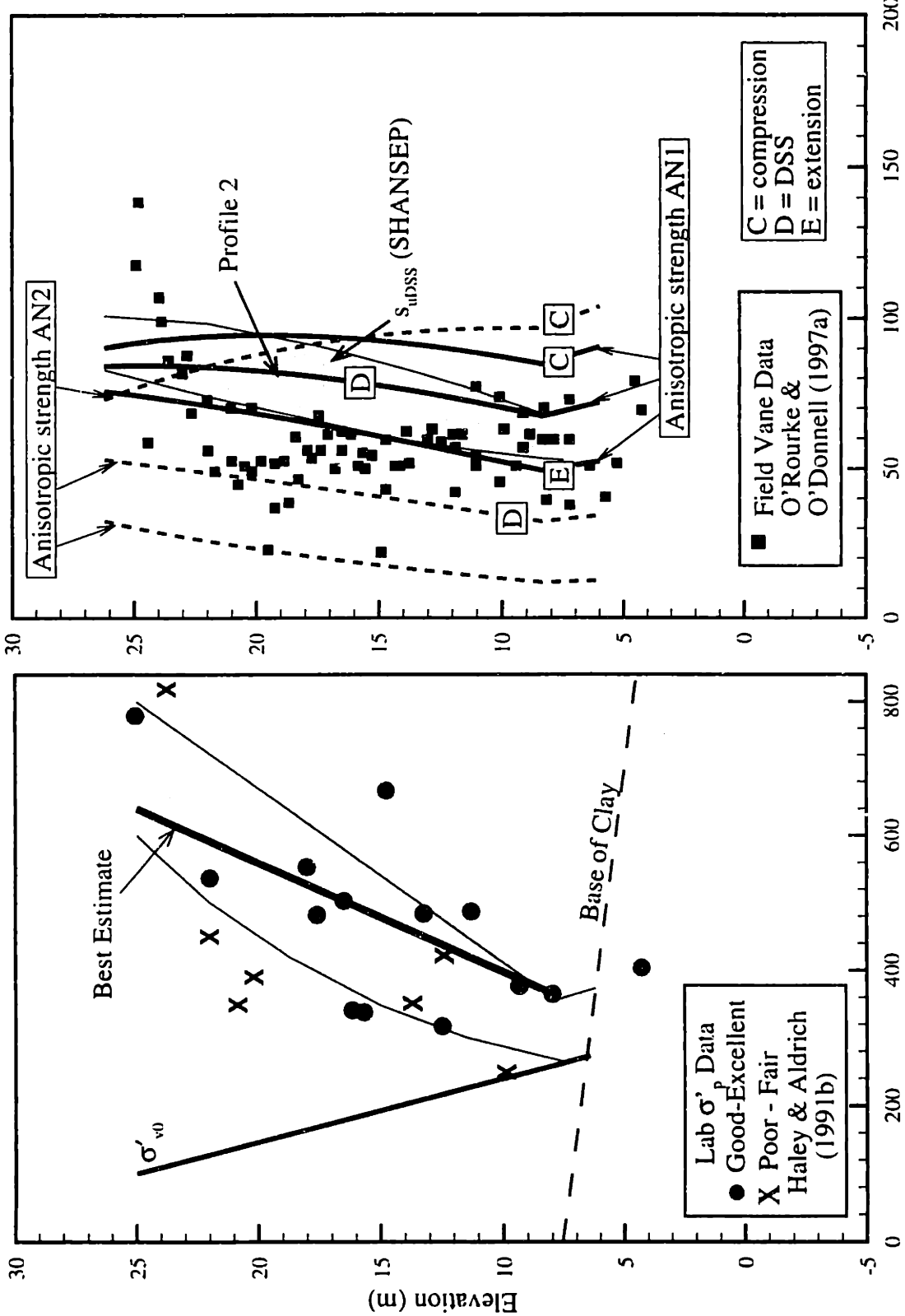

Figure 7.18 Comparisons of mobilized anisotropic strength profiles derived from stress history of original BIF site

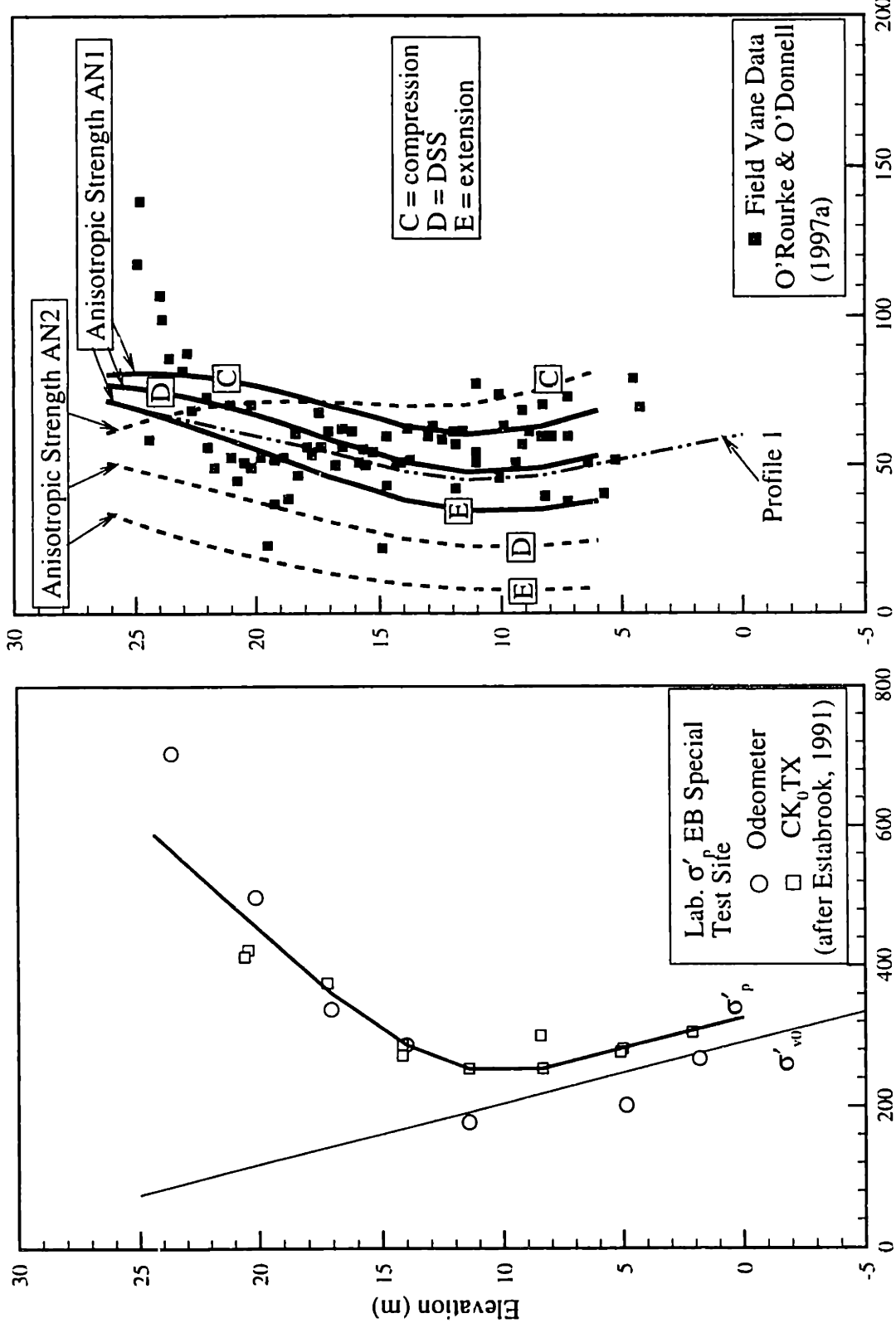

Figure 7.19 Comparisons of mobilized anisotropic strength profiles derived from stress history of EB Special Test Site

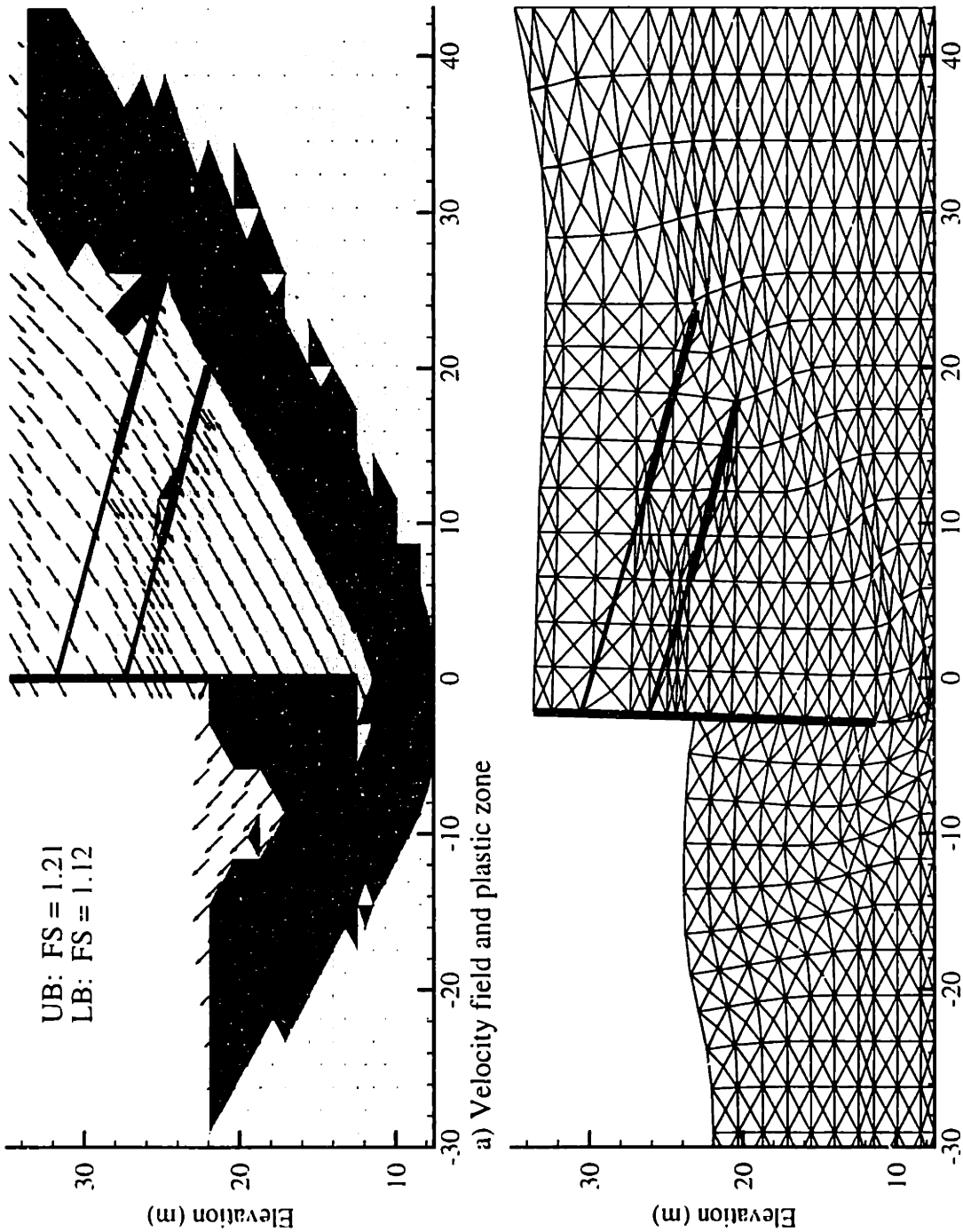

Figure 7.20 Upper bound results for East wall Section A-A' (stress history Profile 1, Anisotropic strength AN1)

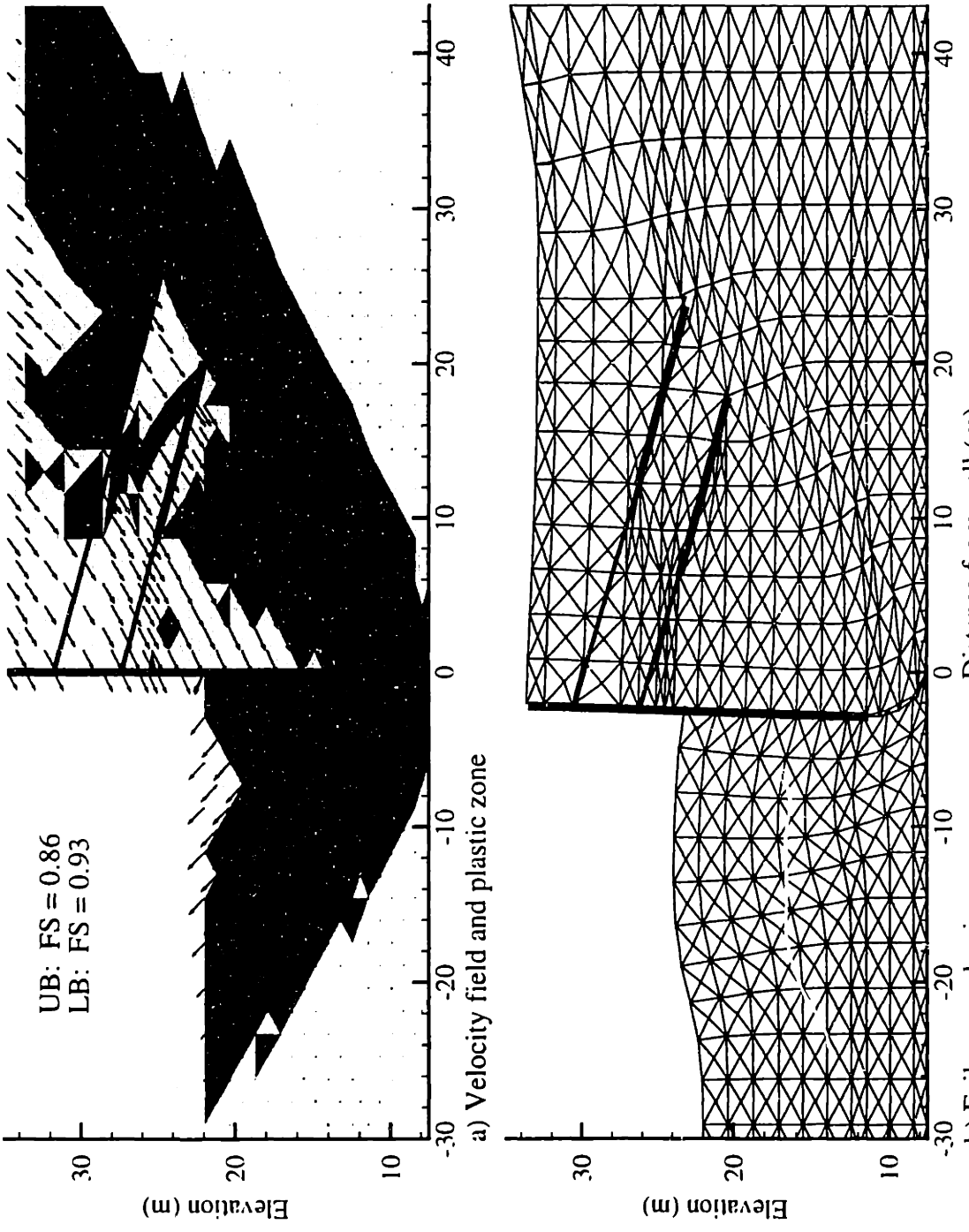

Figure 7.21 Upper bound results for East wall Section A-A' (stress history Profile 1, anisotropic strength AN2)

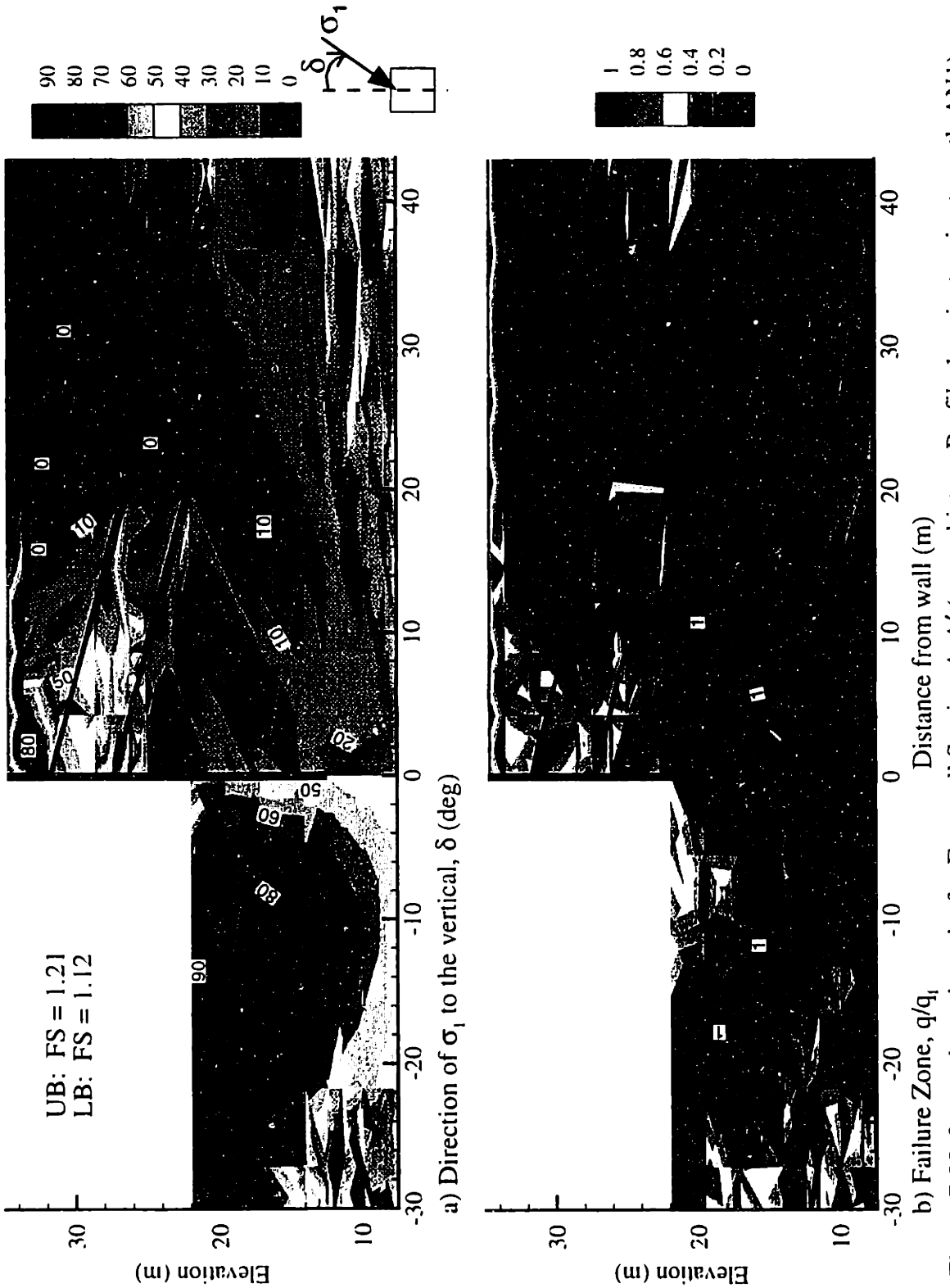

Figure 7.22 Lower bound results for East wall Section A-A′ (stress history Profile 1, anisotropic strength AN1)

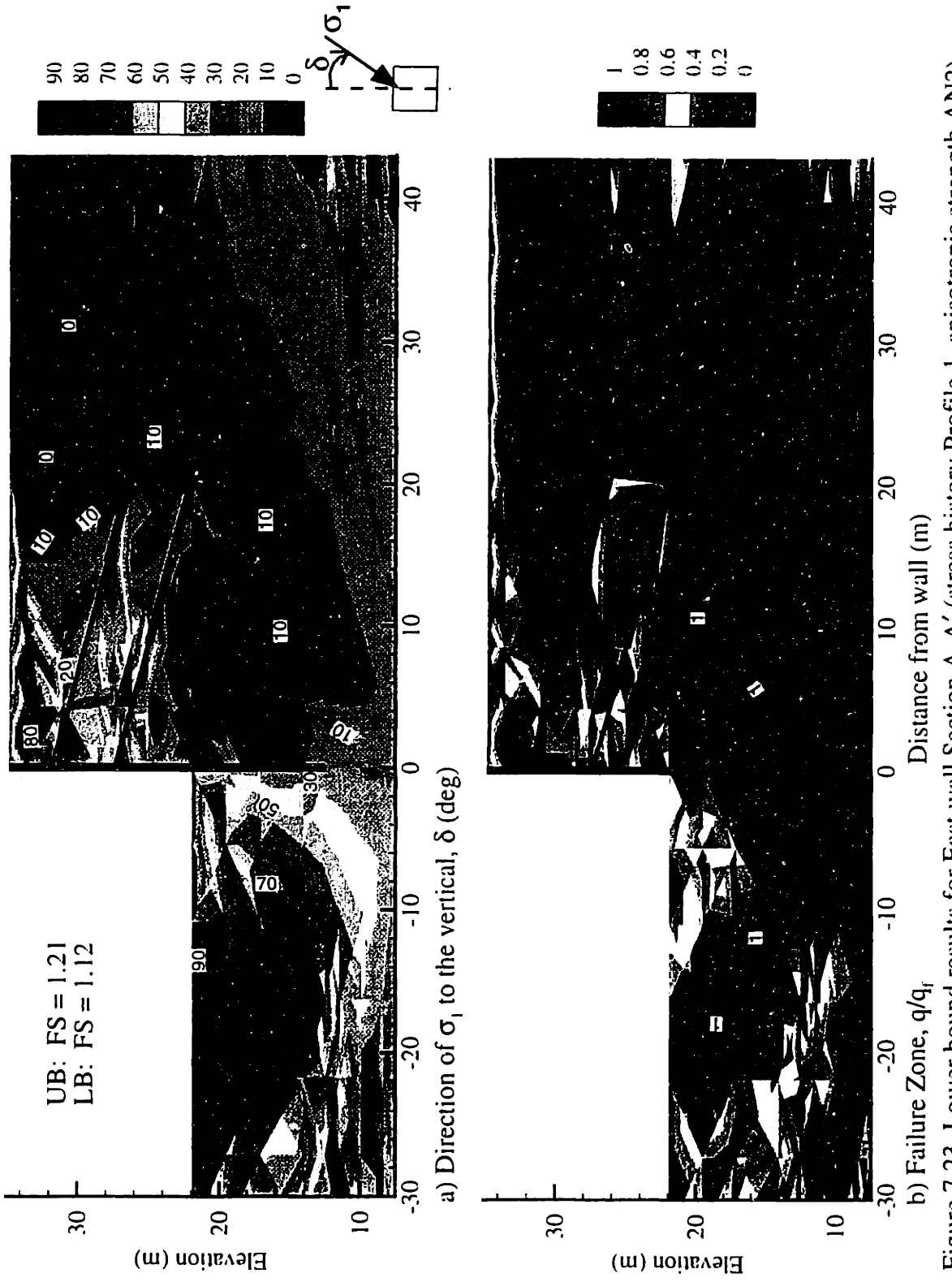

Figure 7.23 Lower bound results for East wall Section A-A′ (stress history Profile 1, anisotropic strength AN2)

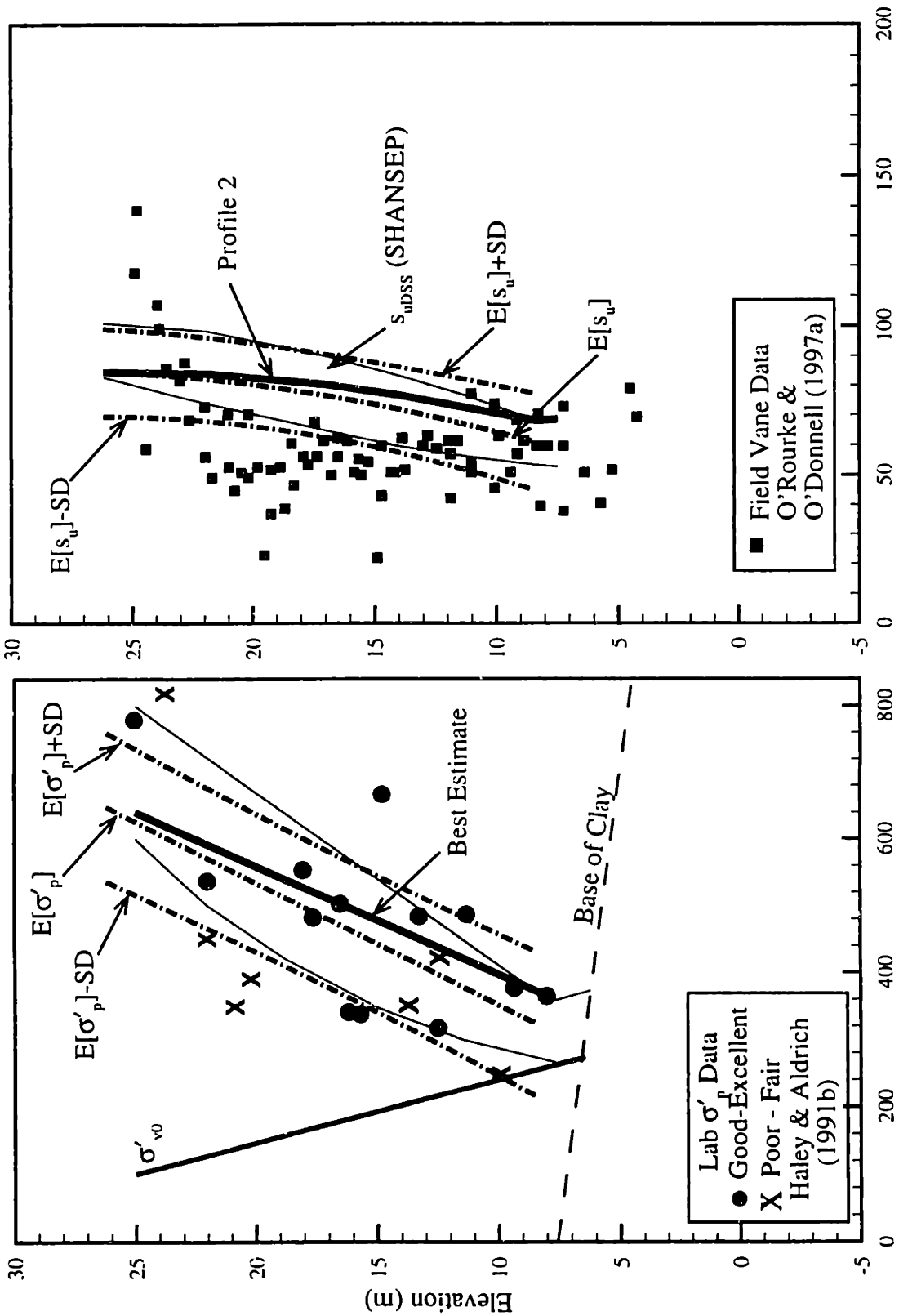

Figure 7.24 Undrained strength profiles for sensitivity analyses

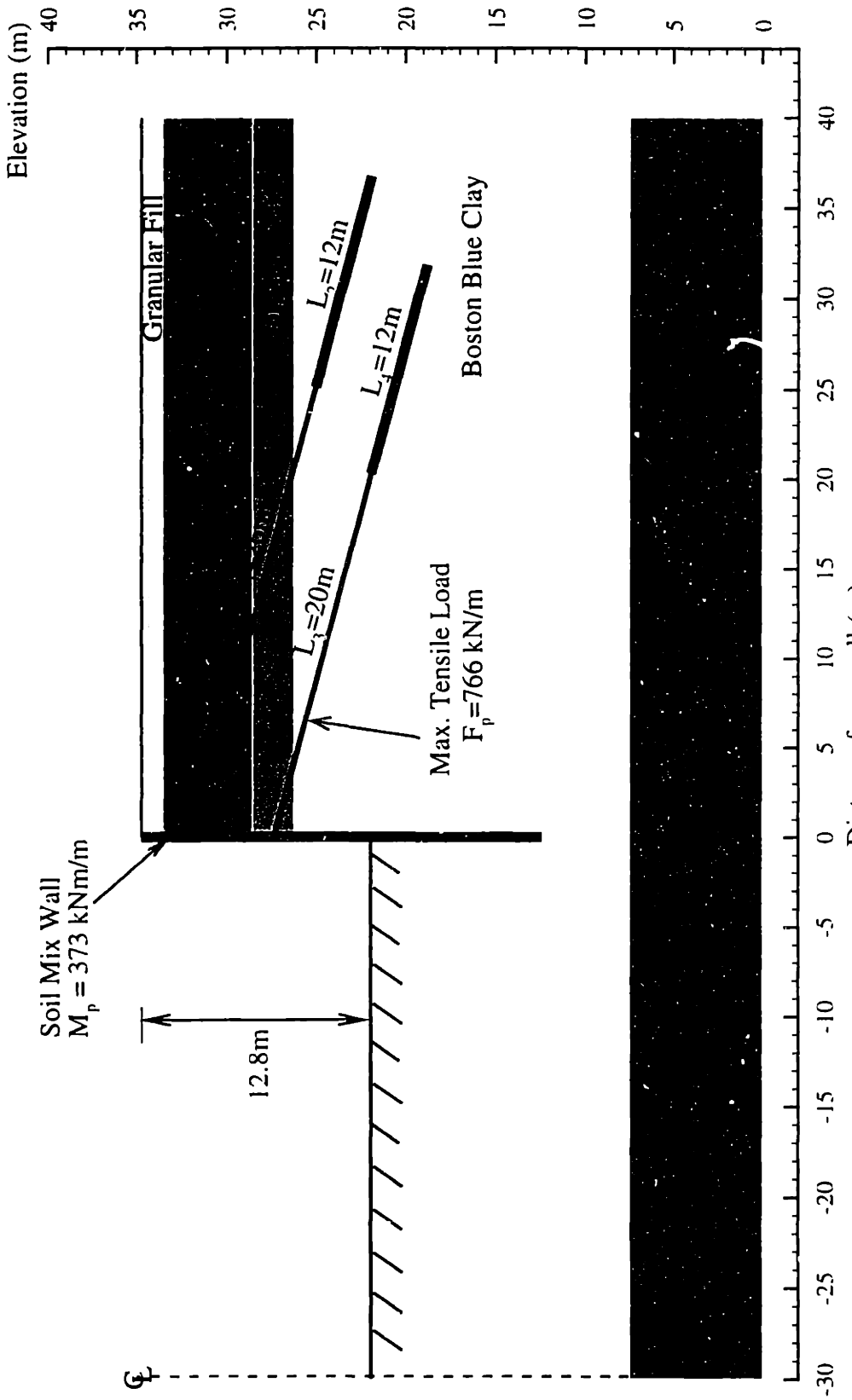

Figure 7.25 Proposed new locations of tiebacks for East wall Section A-A′

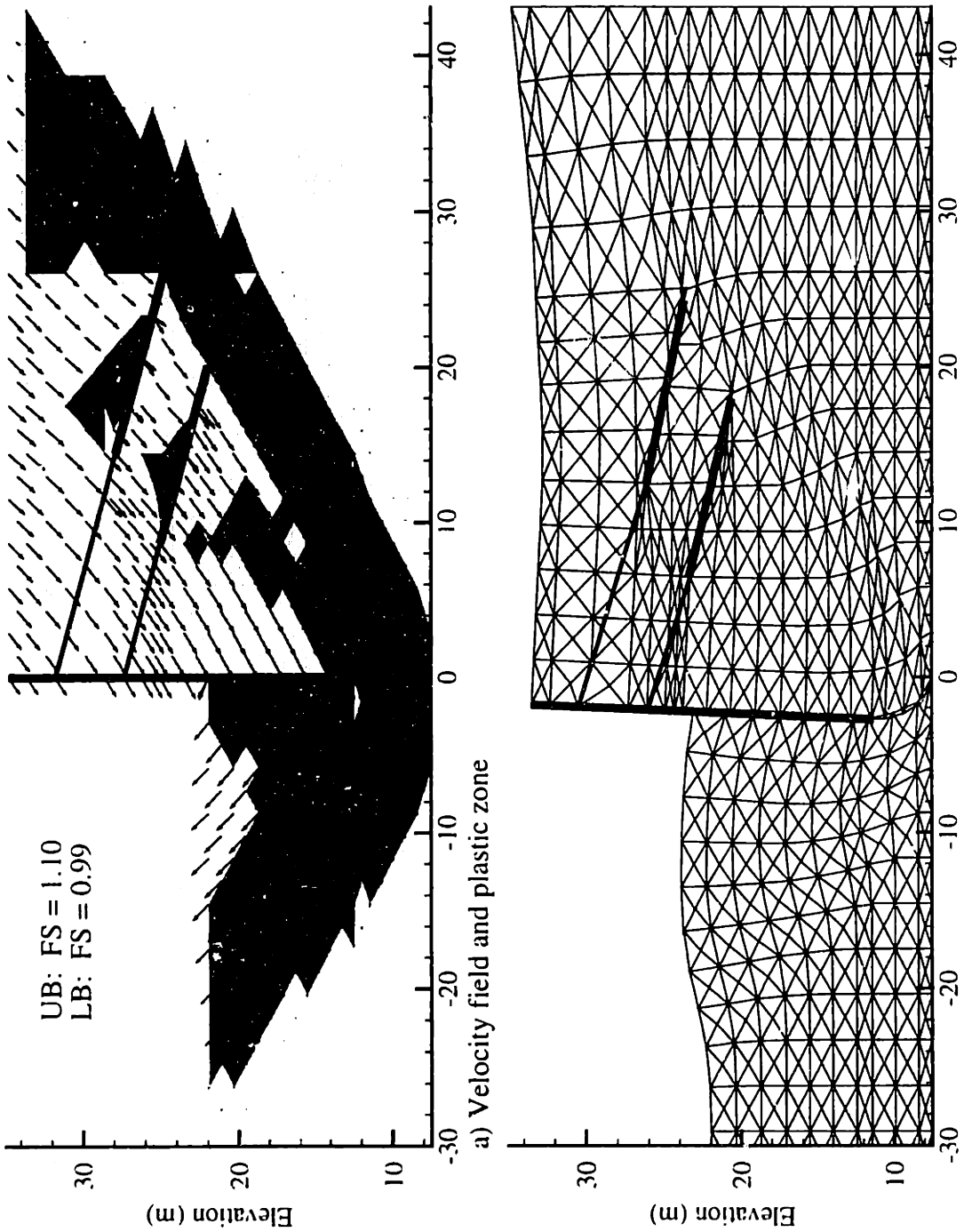

Figure 7.26 Upper bound results of Section A-A' for strengthening the wall, M_p = 2000 kNm/m

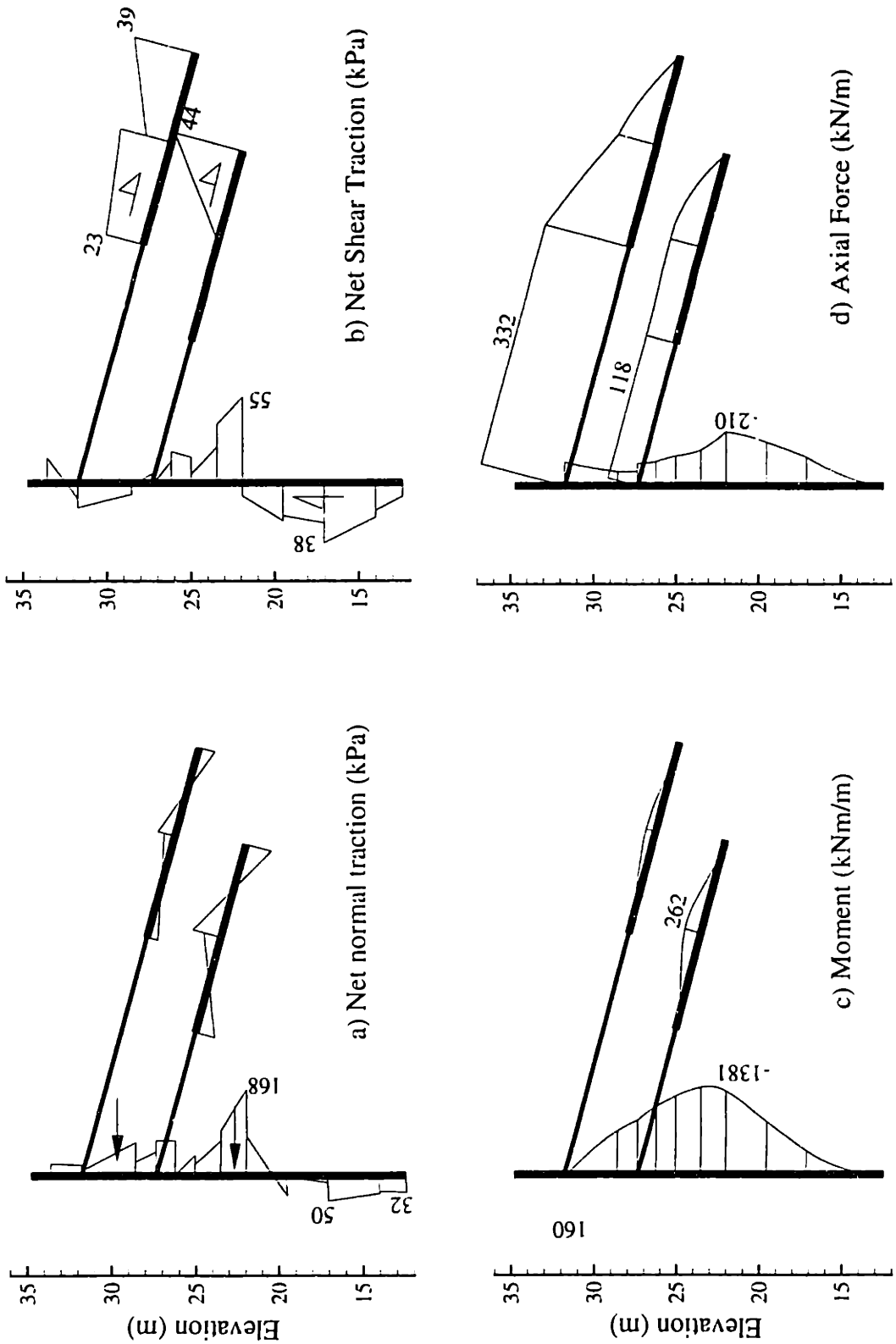

Figure 7.27 Lower bound results of Section A-A' for strengthening the wall, M_p = 2000 kNm/m

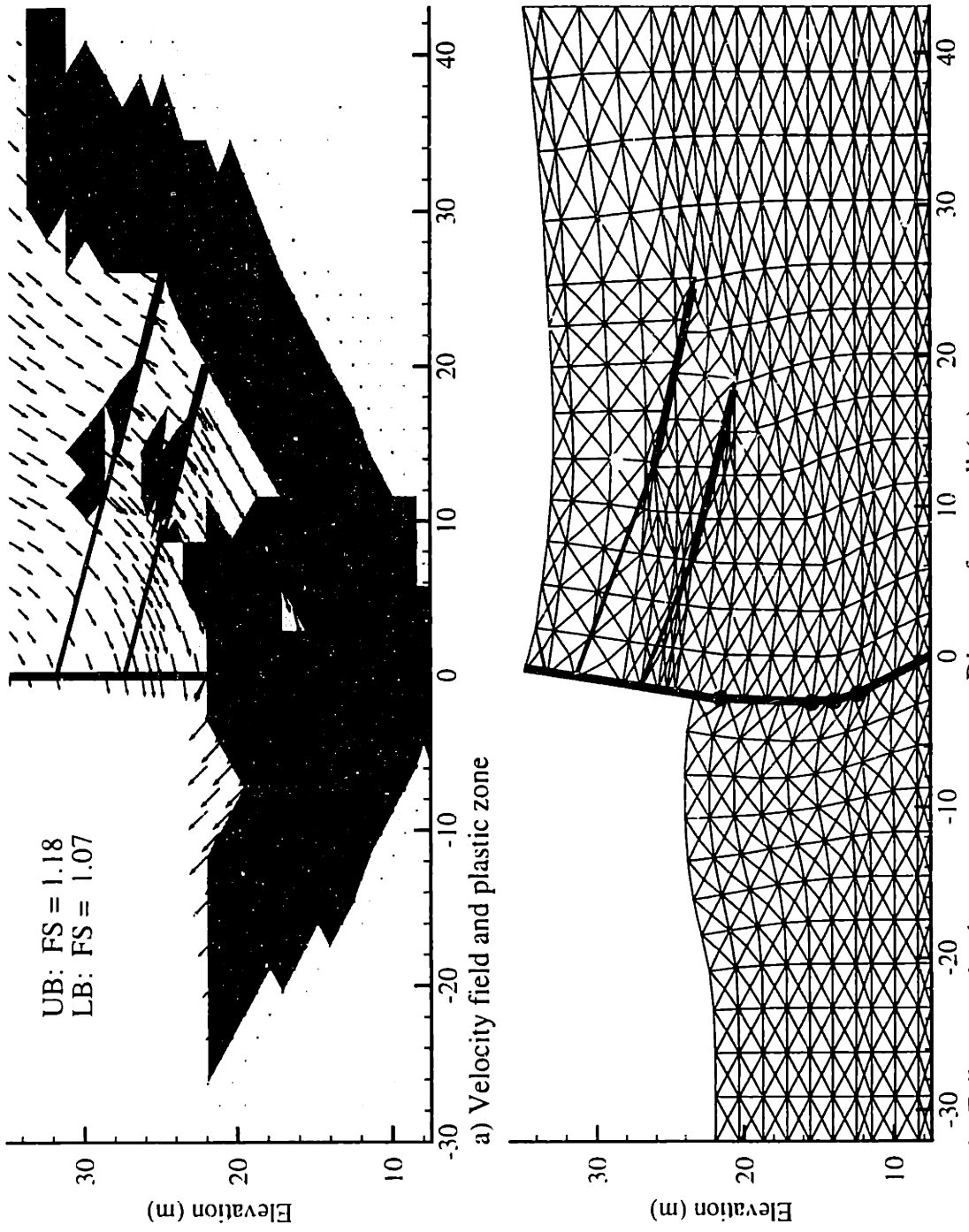

Figure 7.28 Upper bound results of Section A-A': extending the wall into bedrock, pin support, M_p=373 kNm/m

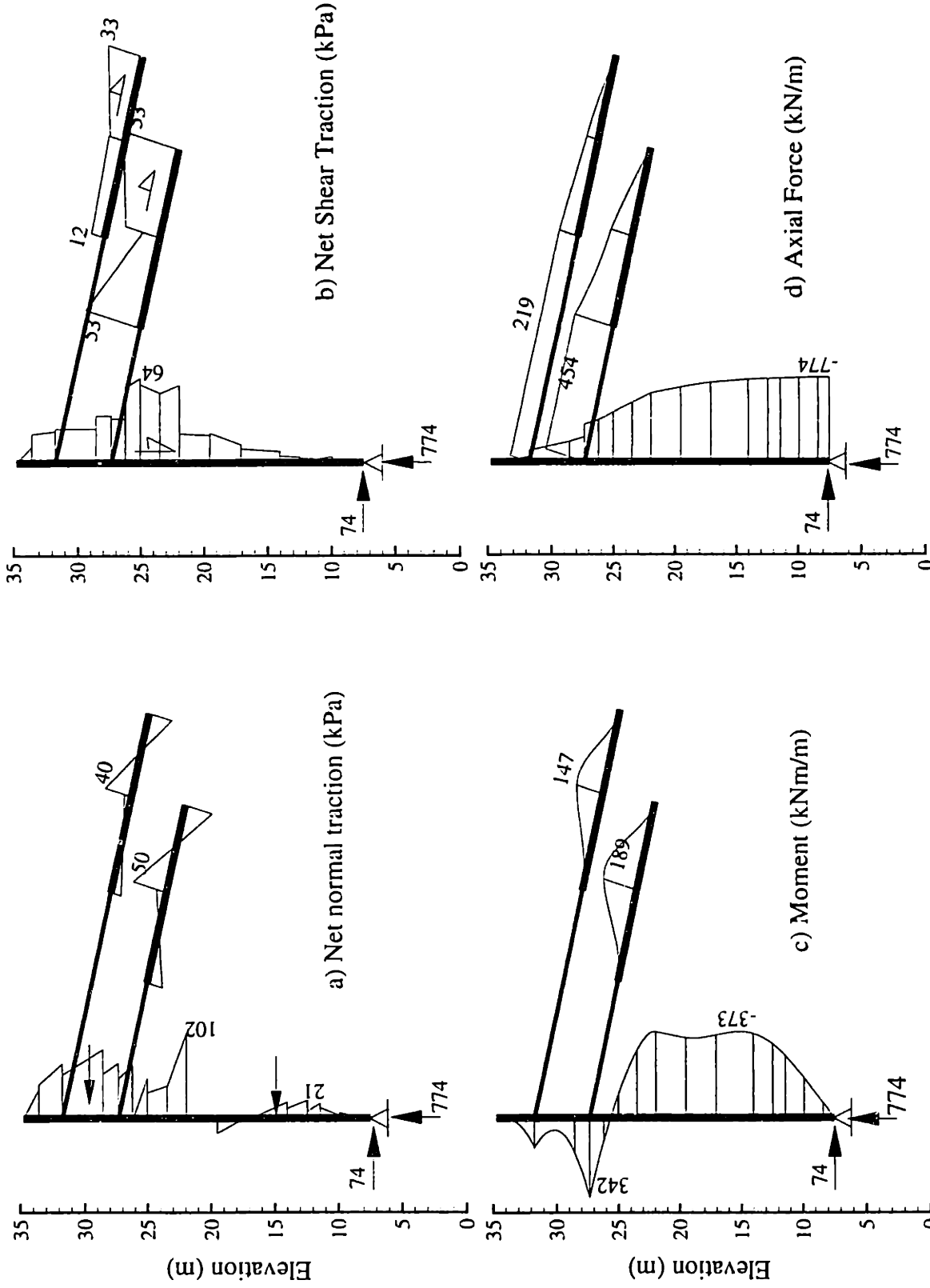

Figure 7.29 Lower bound results of Section A-A': extending the wall into bedrock, pin support, M_p = 373 kNm/m

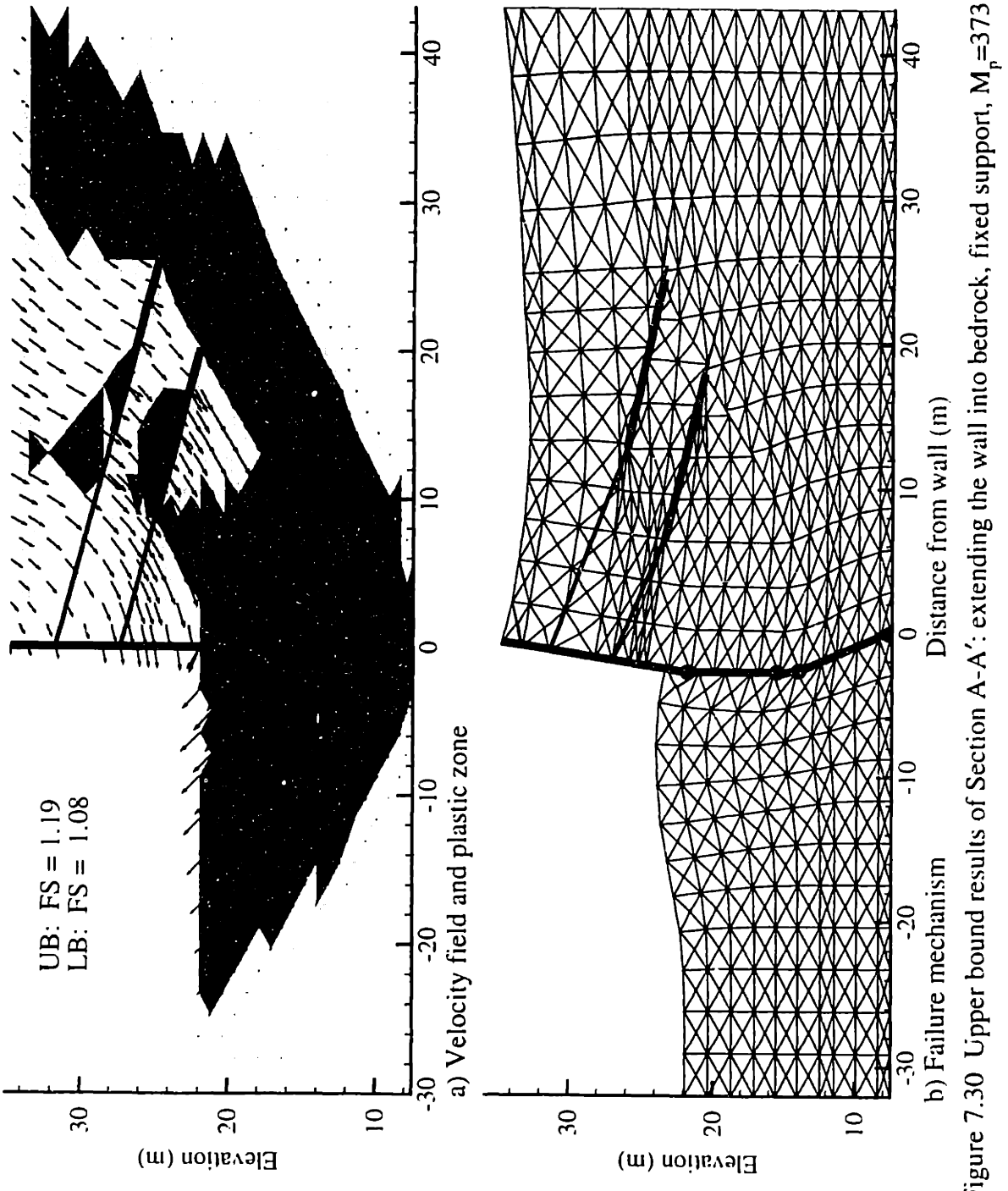

Figure 7.30 Upper bound results of Section A-A': extending the wall into bedrock, fixed support, M_p=373 kNm/m

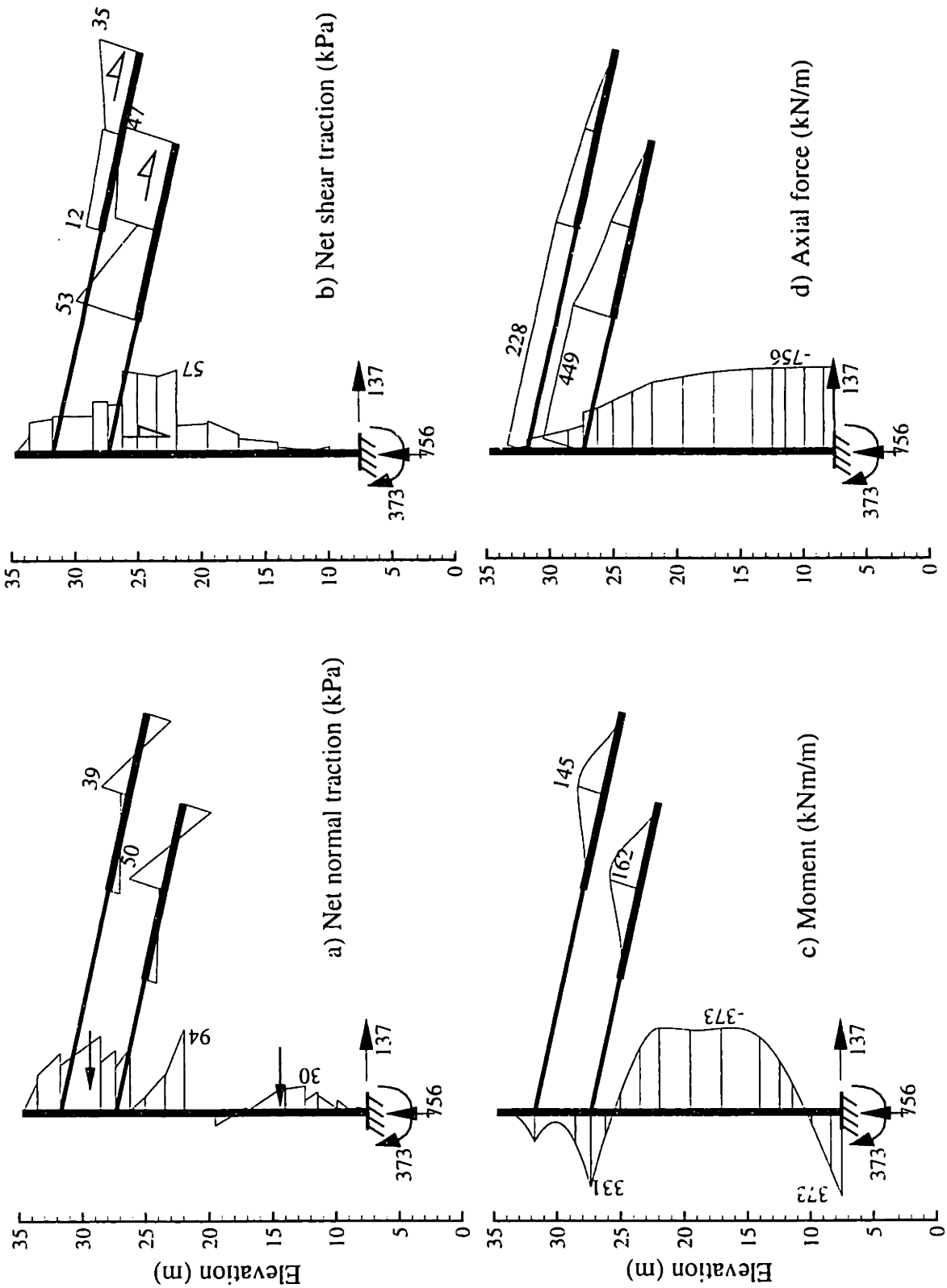

Figure 7.31 Lower bound results of Section A-A′: extending the wall into bedrock, fixed support, M_p=373 kNm/m

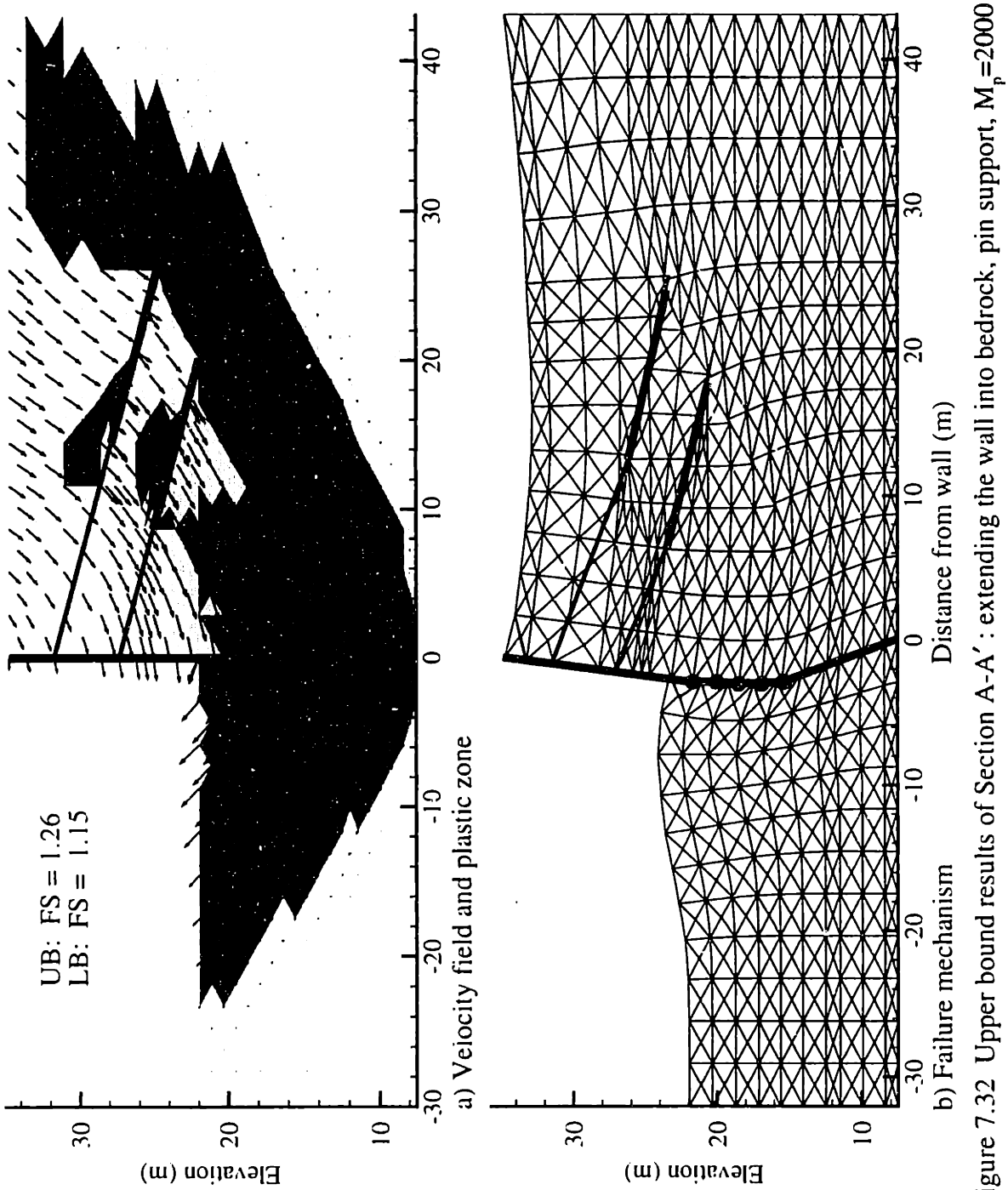

Figure 7.32 Upper bound results of Section A-A' : extending the wall into bedrock, pin support, M_p=2000 kNm/m

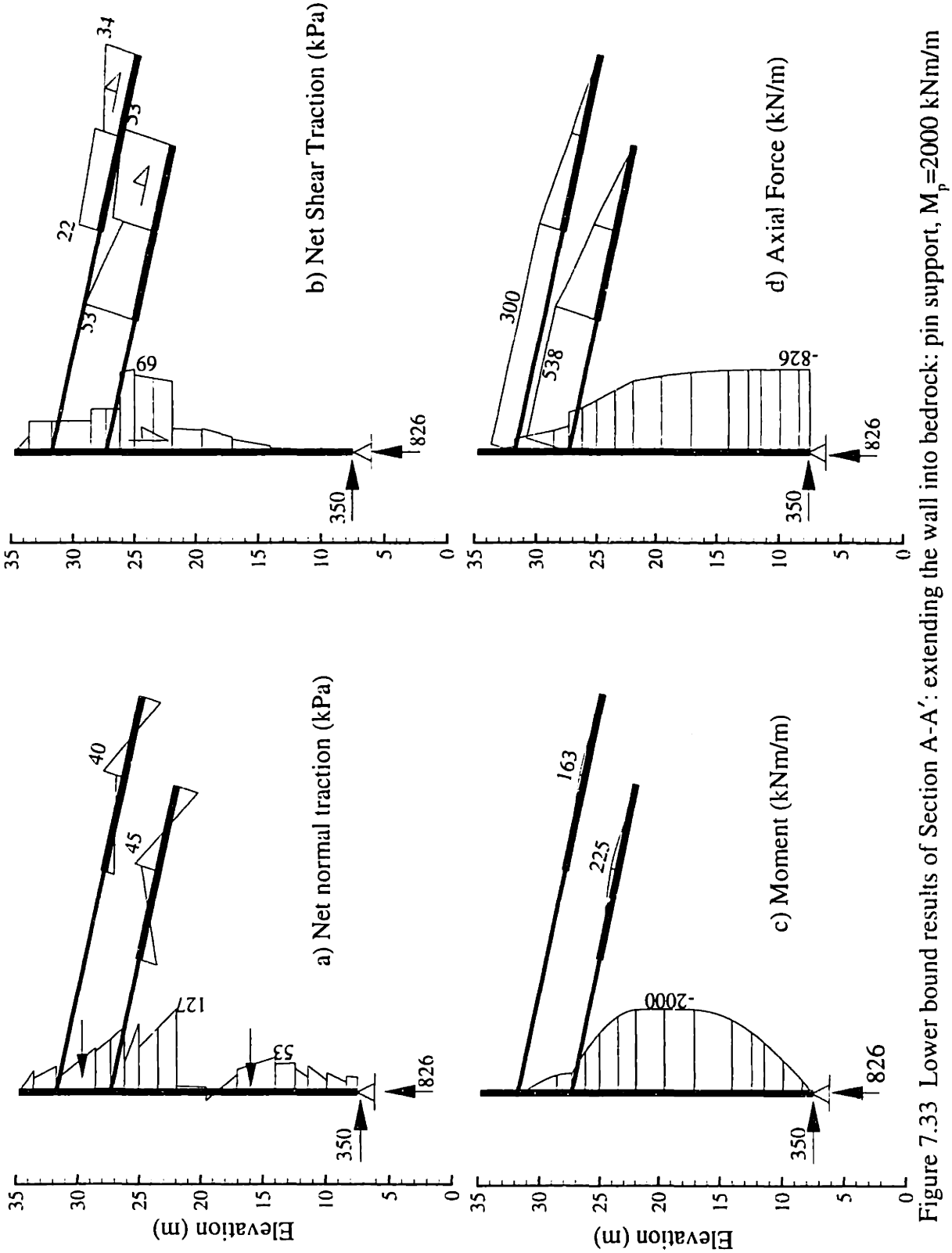

Figure 7.33 Lower bound results of Section A-A': extending the wall into bedrock: pin support, M_p=2000 kNm/m

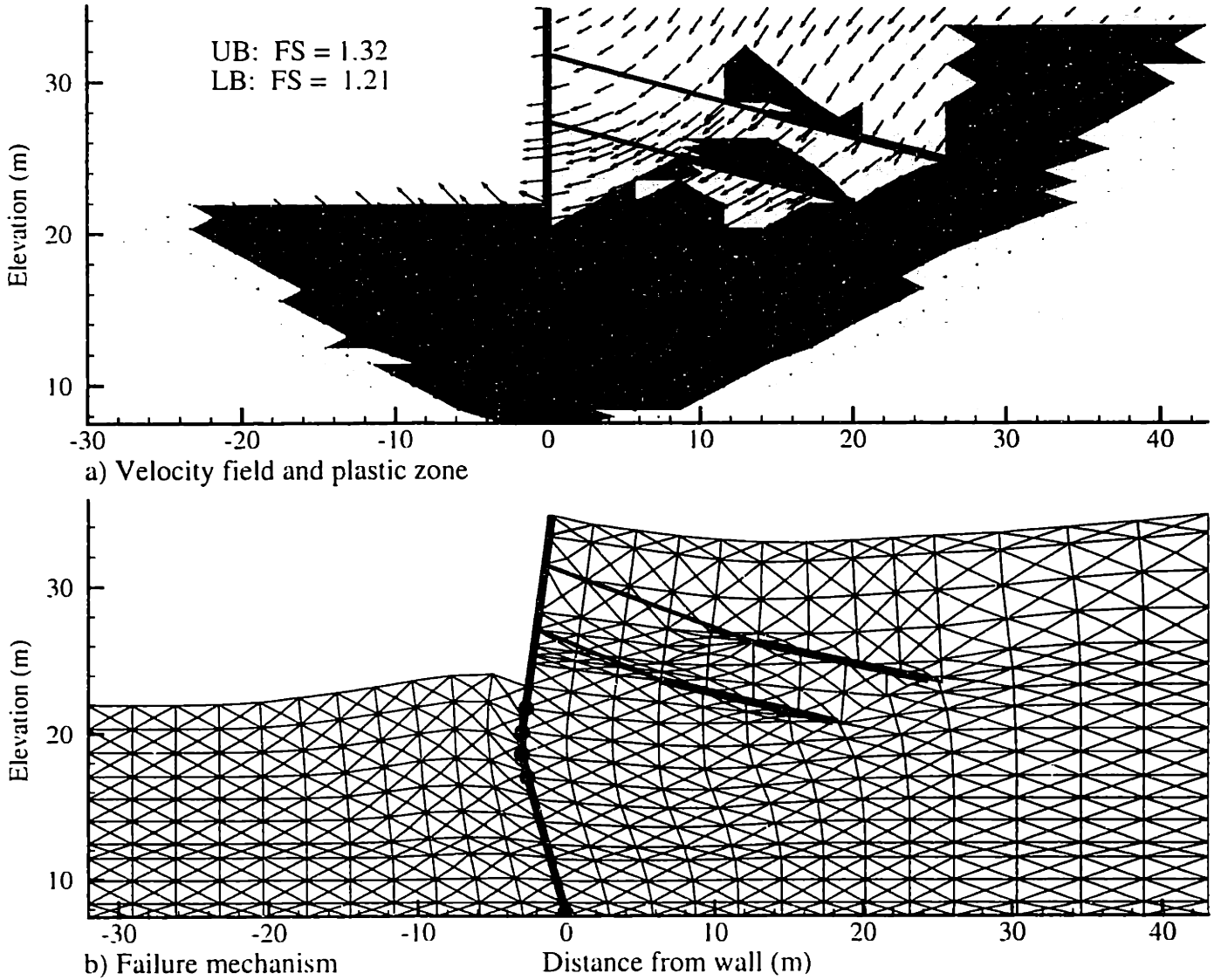

Figure 7.34 Upper bound results of Section A-A′: extending the wall into bedrock, fixed support, M_p=2000 kNm/m

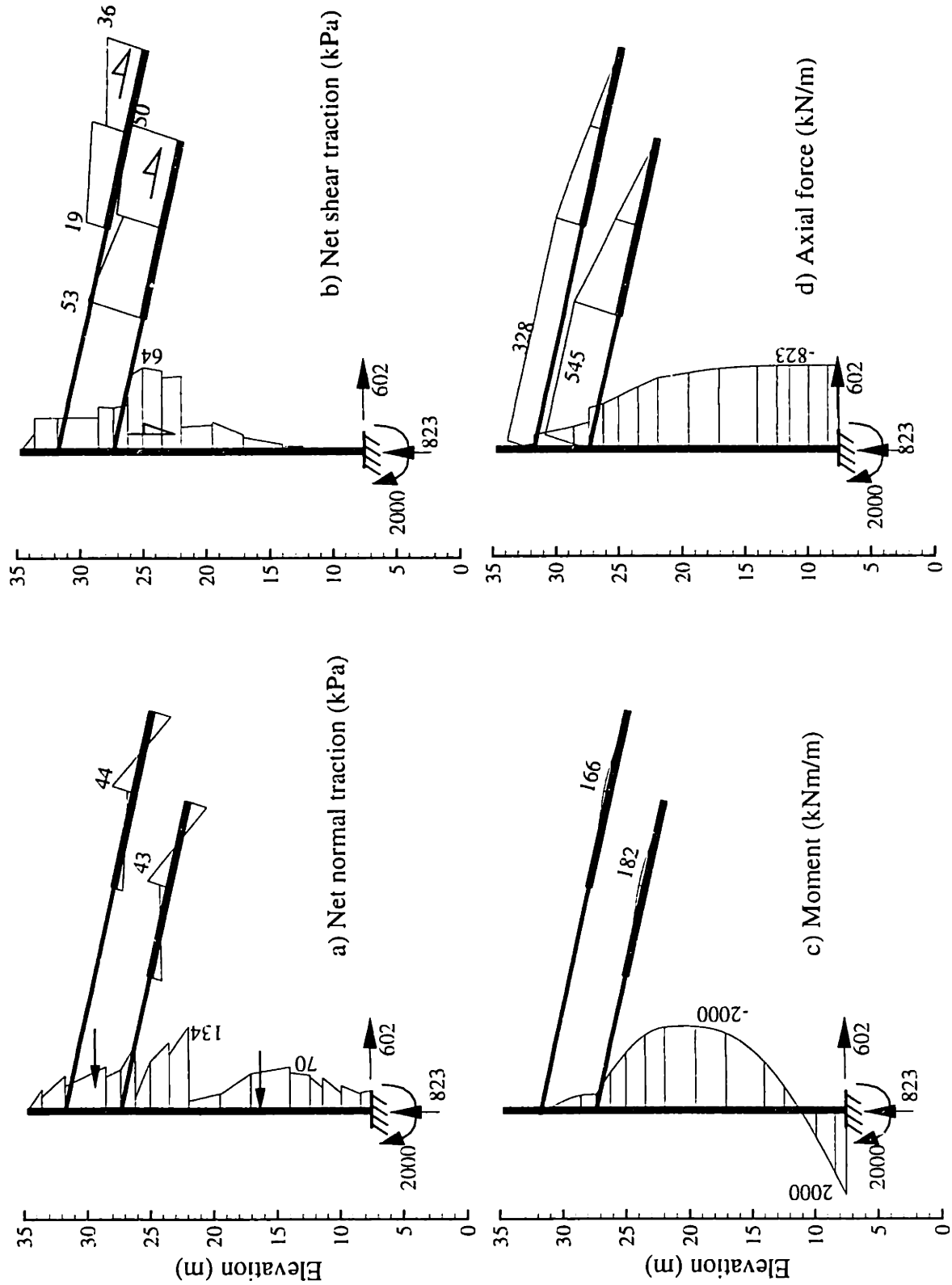

Figure 7.35 Lower bound results of Section A-A′: extending the wall into bedrock: fixed support, M_p=2000 kNm/m

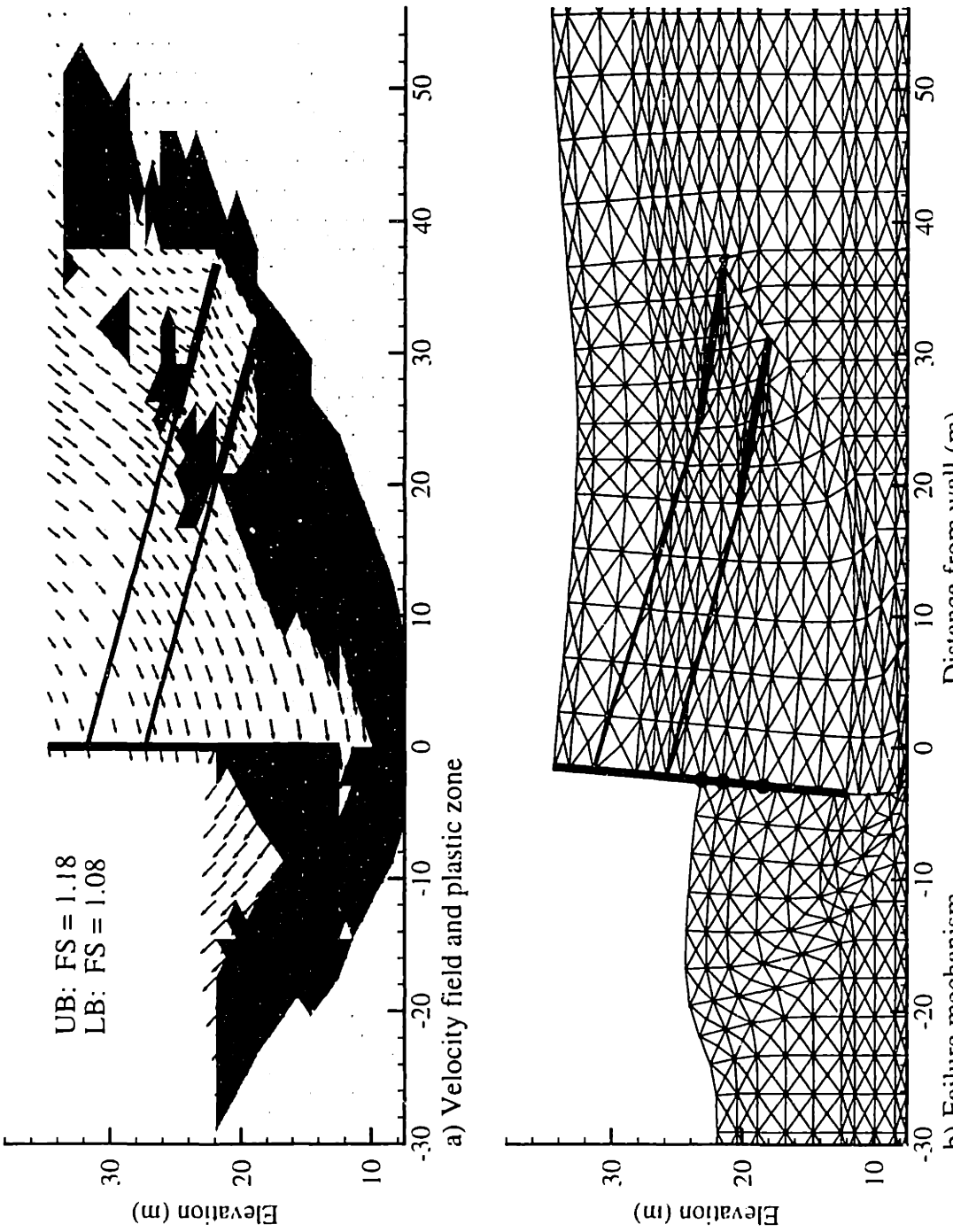

Figure 7.36 Upper bound results of Section A-A′ for new locations of tiebacks

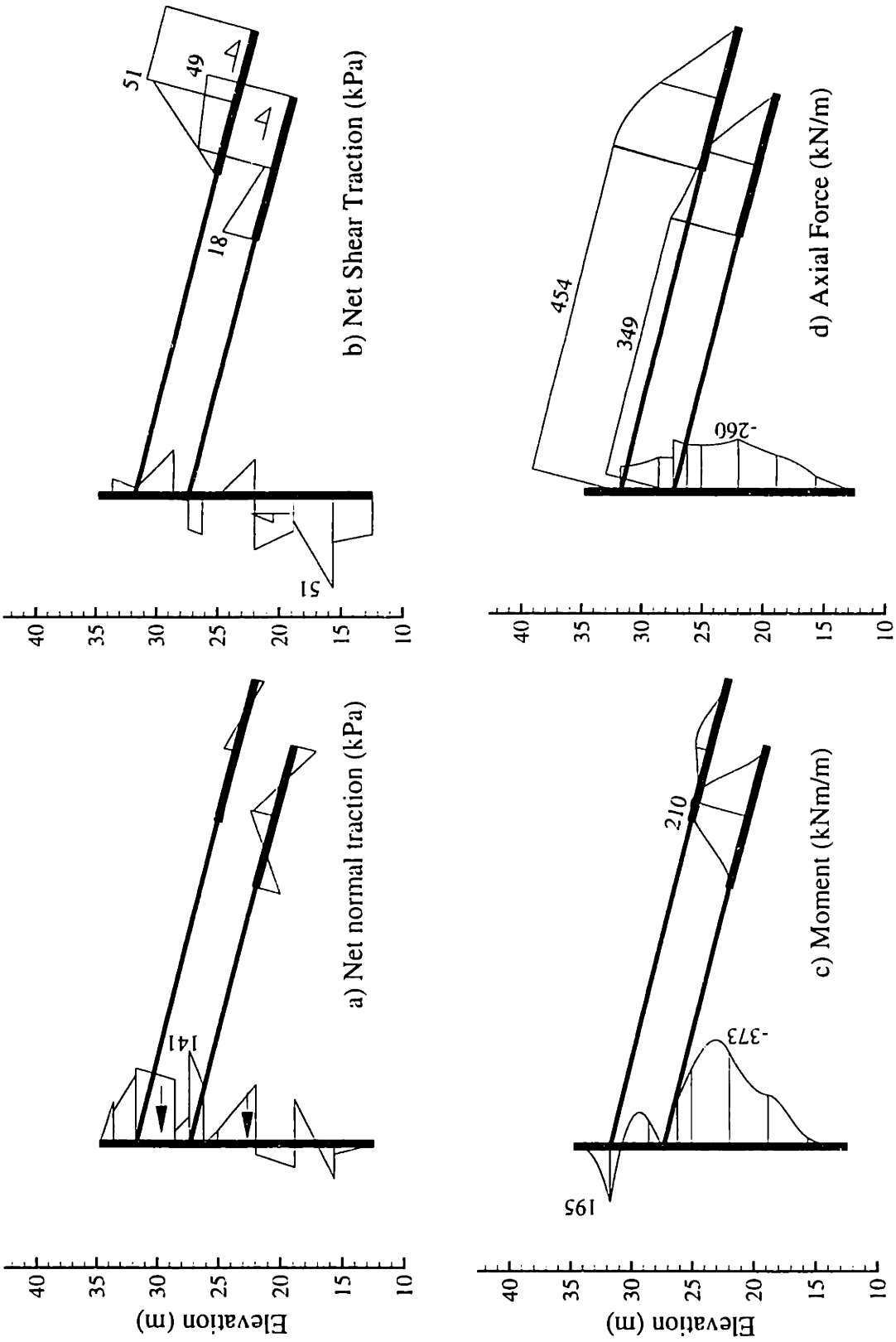

Figure 7.37 Lower bound results of Section A-A′ for new locations of tiebacks

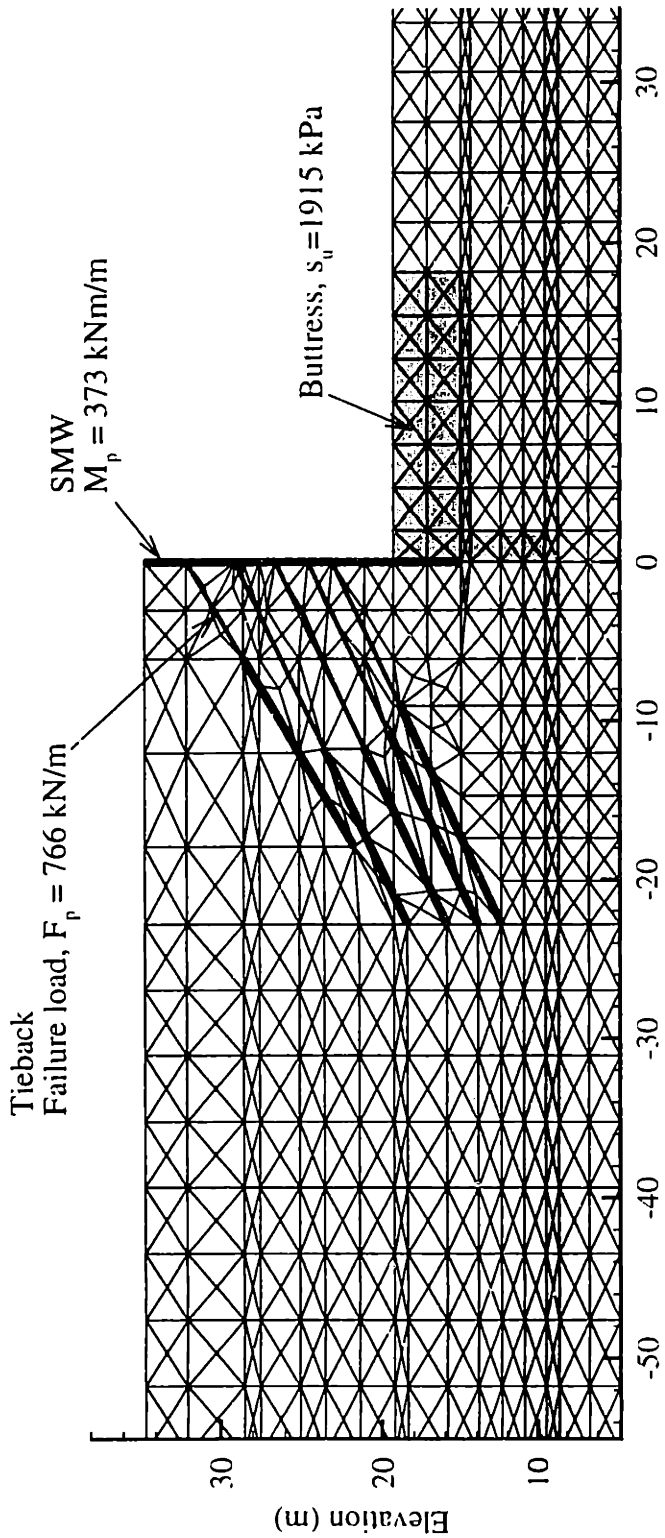

Figure 7.38 Spatial discretization used for numerical limit analyses of West wall Section B-B′

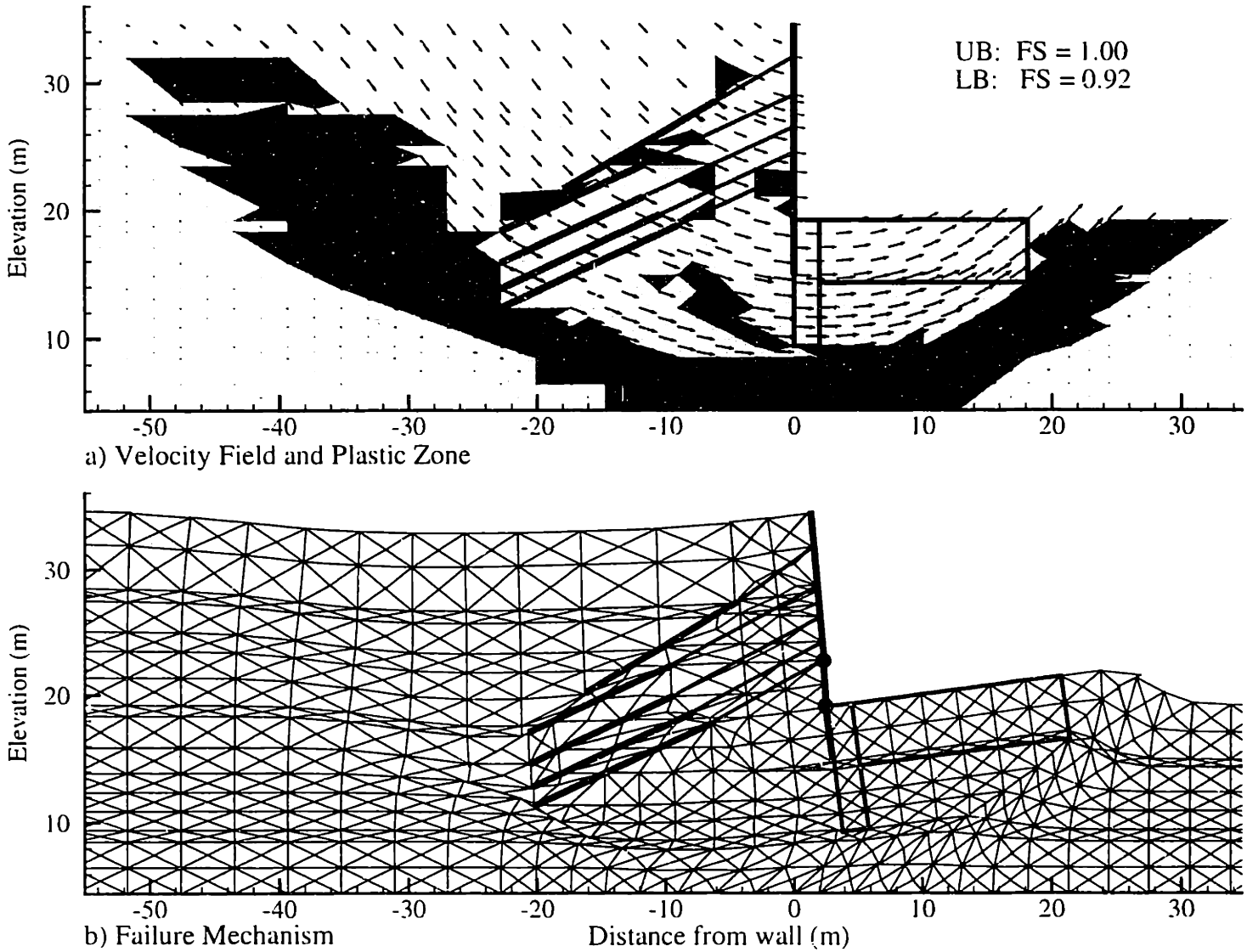

Figure 7.39 Upper bound results for West wall Section B-B′ with remedial buttress, BBC Profile 1

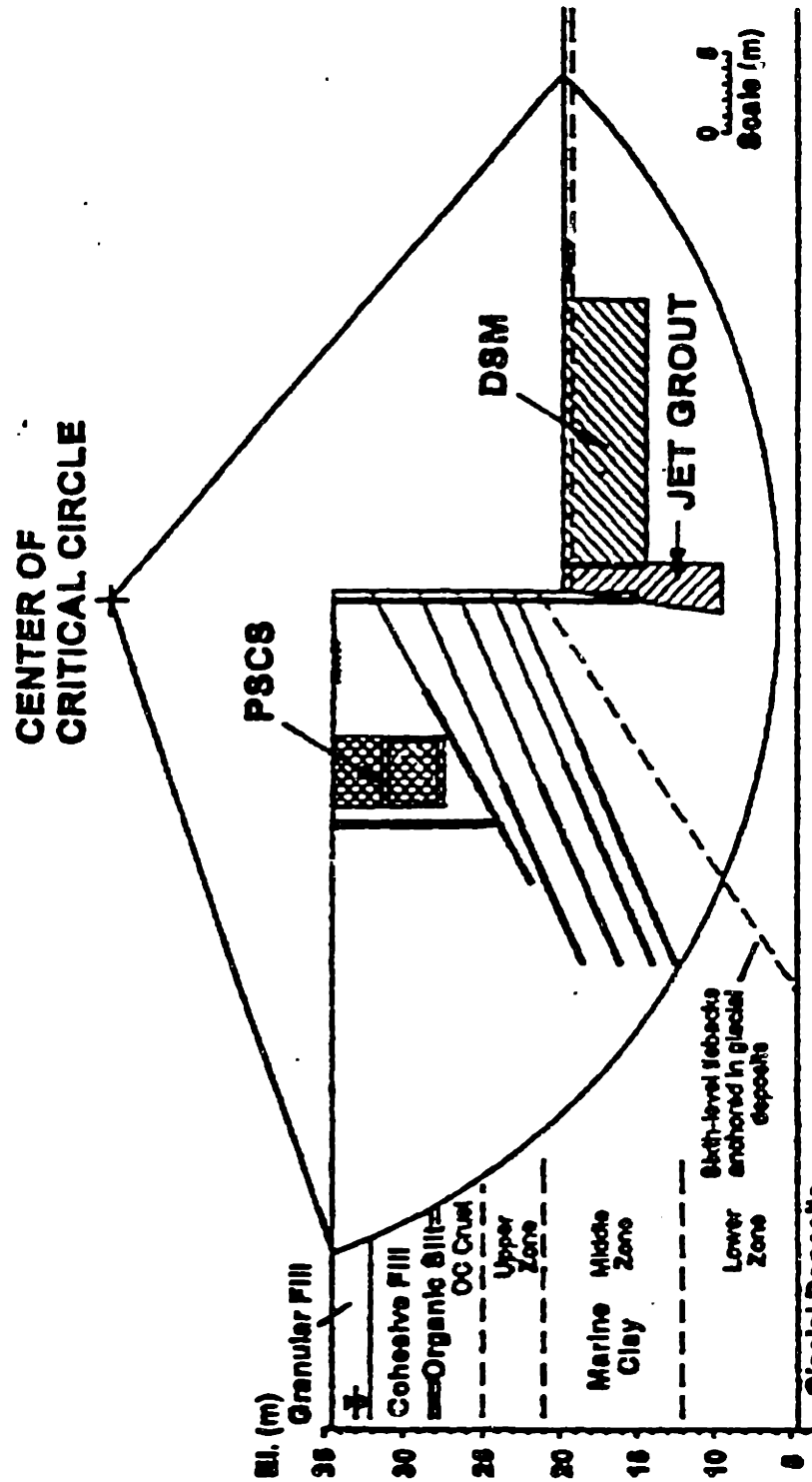

Figure 7.40 Limit equilibrium calculation for West wall, Section B-B' by O'Rourke and O'Donnell (1997b)

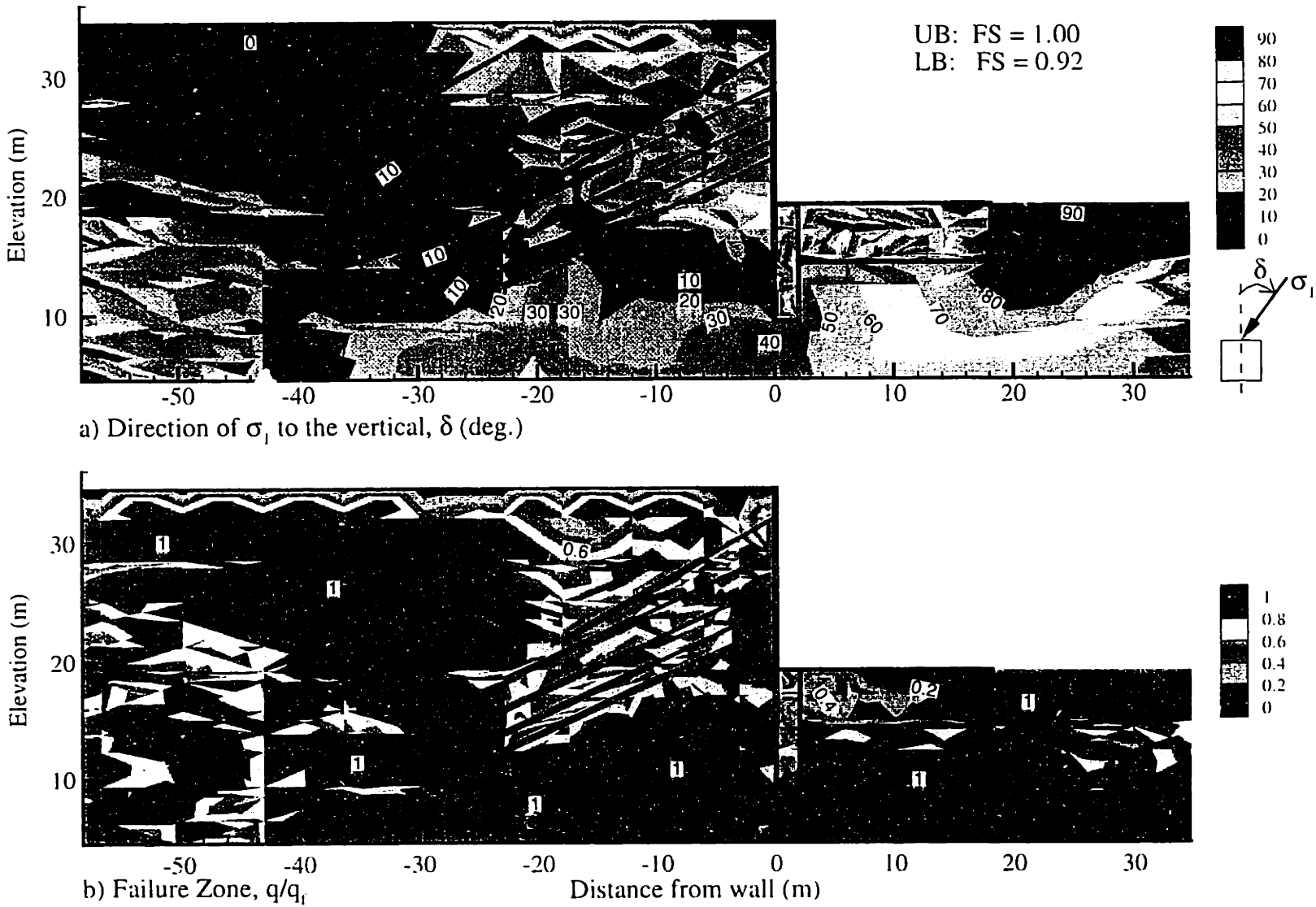

Figure 7.41 Lower bound results for West wall Section B-B′ with remedial buttress, BBC Profile 1

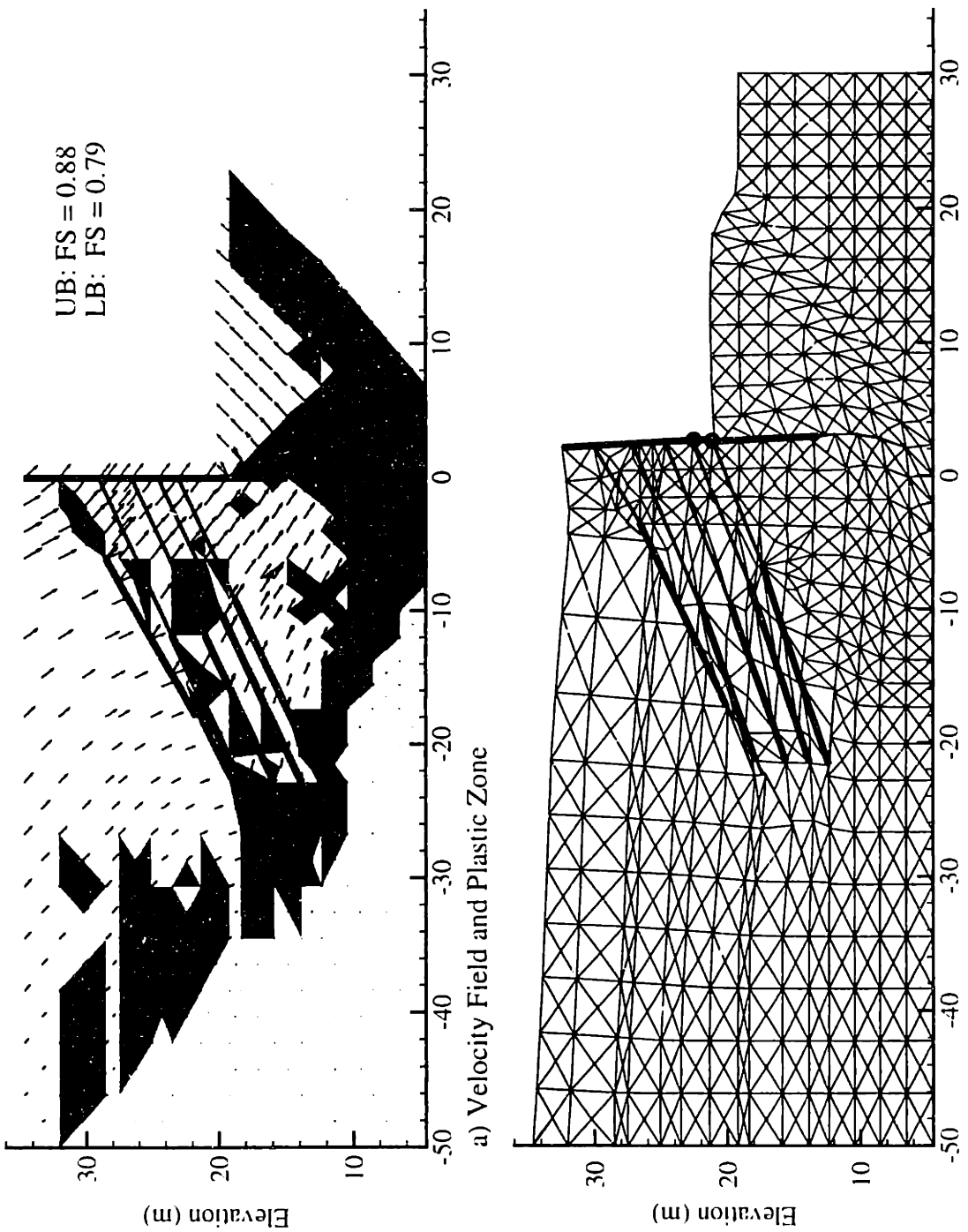

a) Velocity Field and Plastic Zone

b) Failure Mechanism

Figure 7.42 Upper bound results for West wall Section B-B′ without remedial buttress, BBC Profile 1

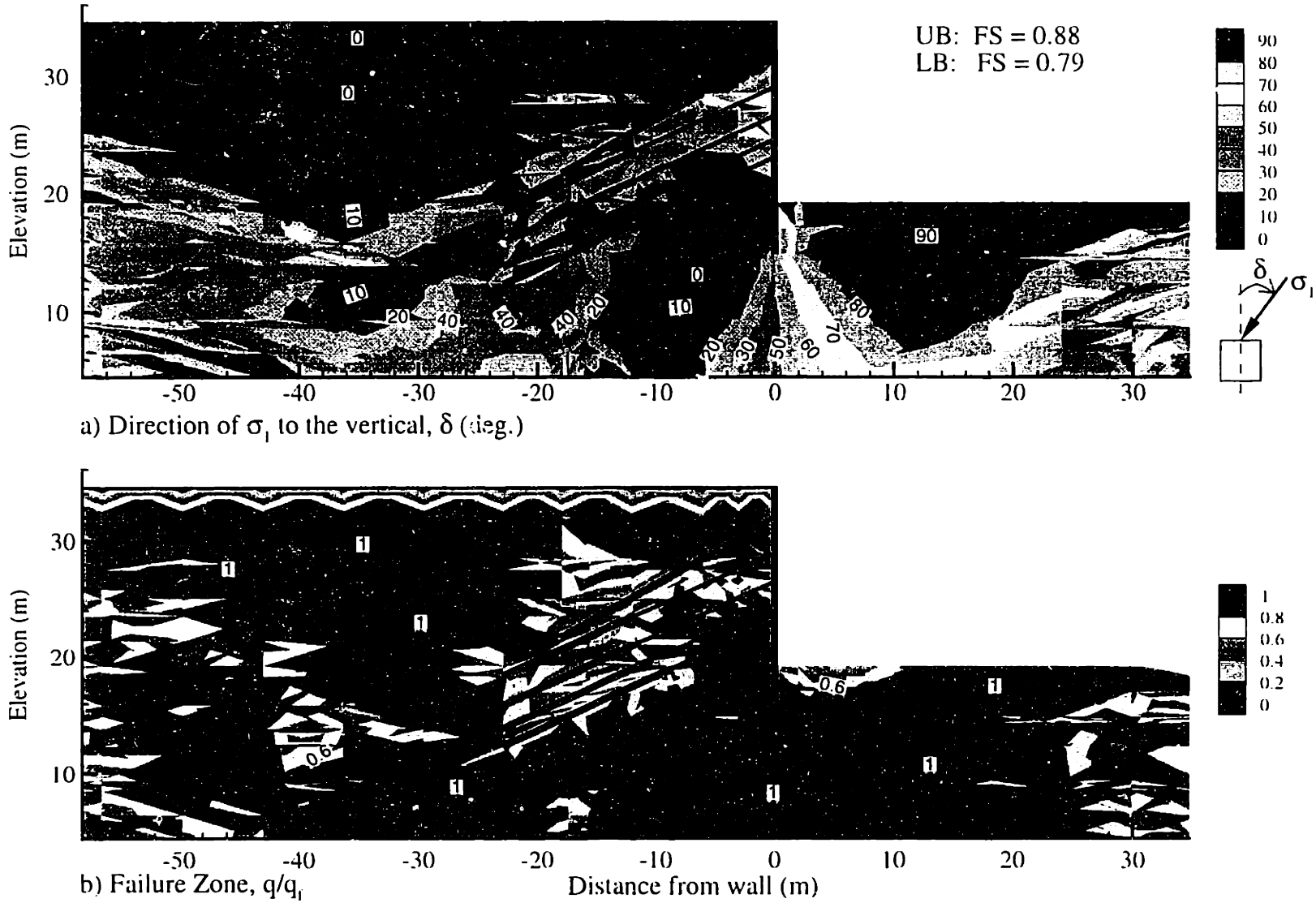

a) Direction of σ_1 to the vertical, δ (deg.)

b) Failure Zone, q/q_l

Figure 7.43 Lower bound results for West wall Section B-B′ without remedial buttress, BBC Profile 1

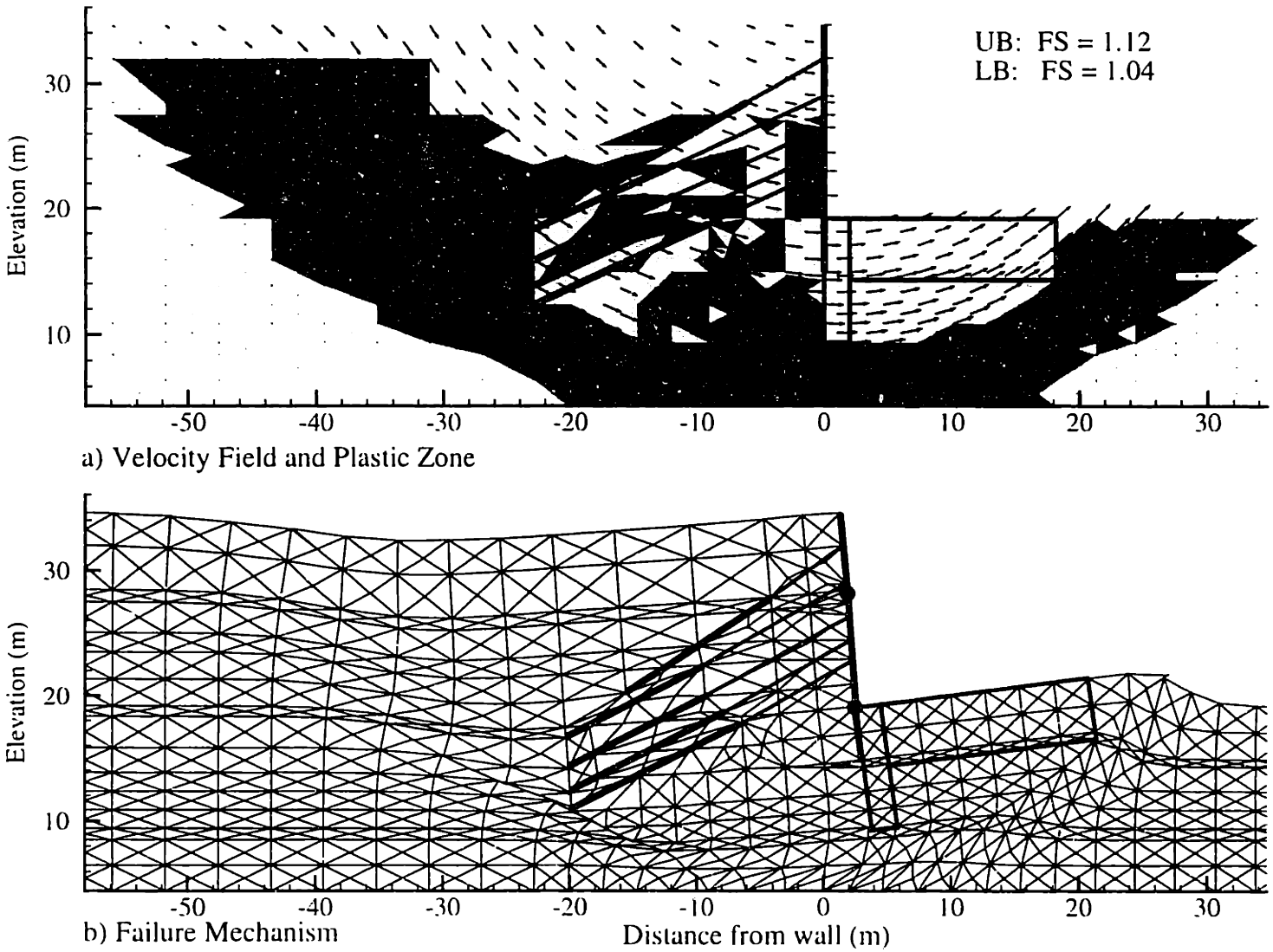

Figure 7.44 Upper bound results for West wall with anisotropic strength parameter AN1, stress history Profile 1

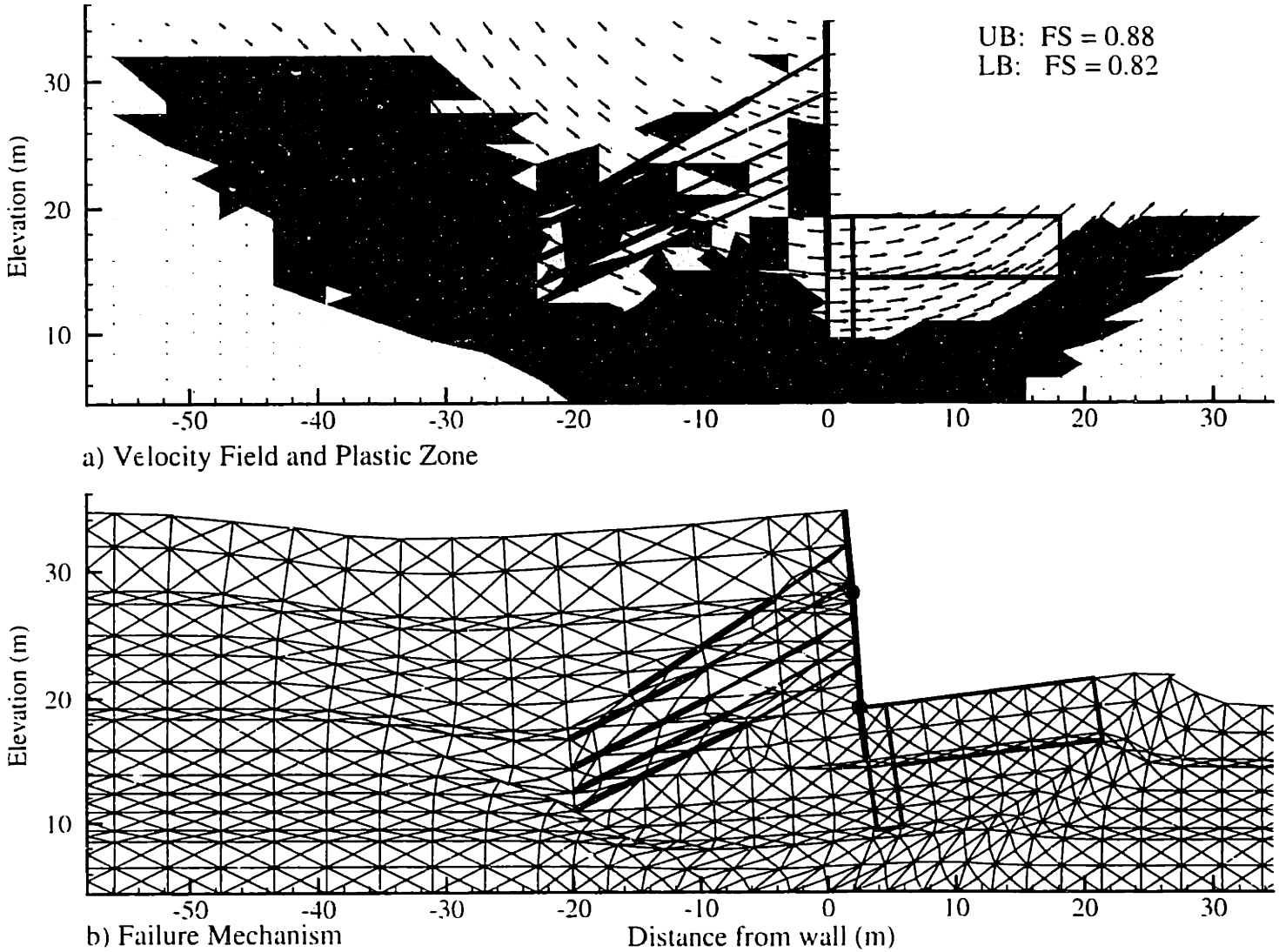

Figure 7.45 Upper bound results for West wall with anisotropic strength parameter AN2, stress history Profile 1

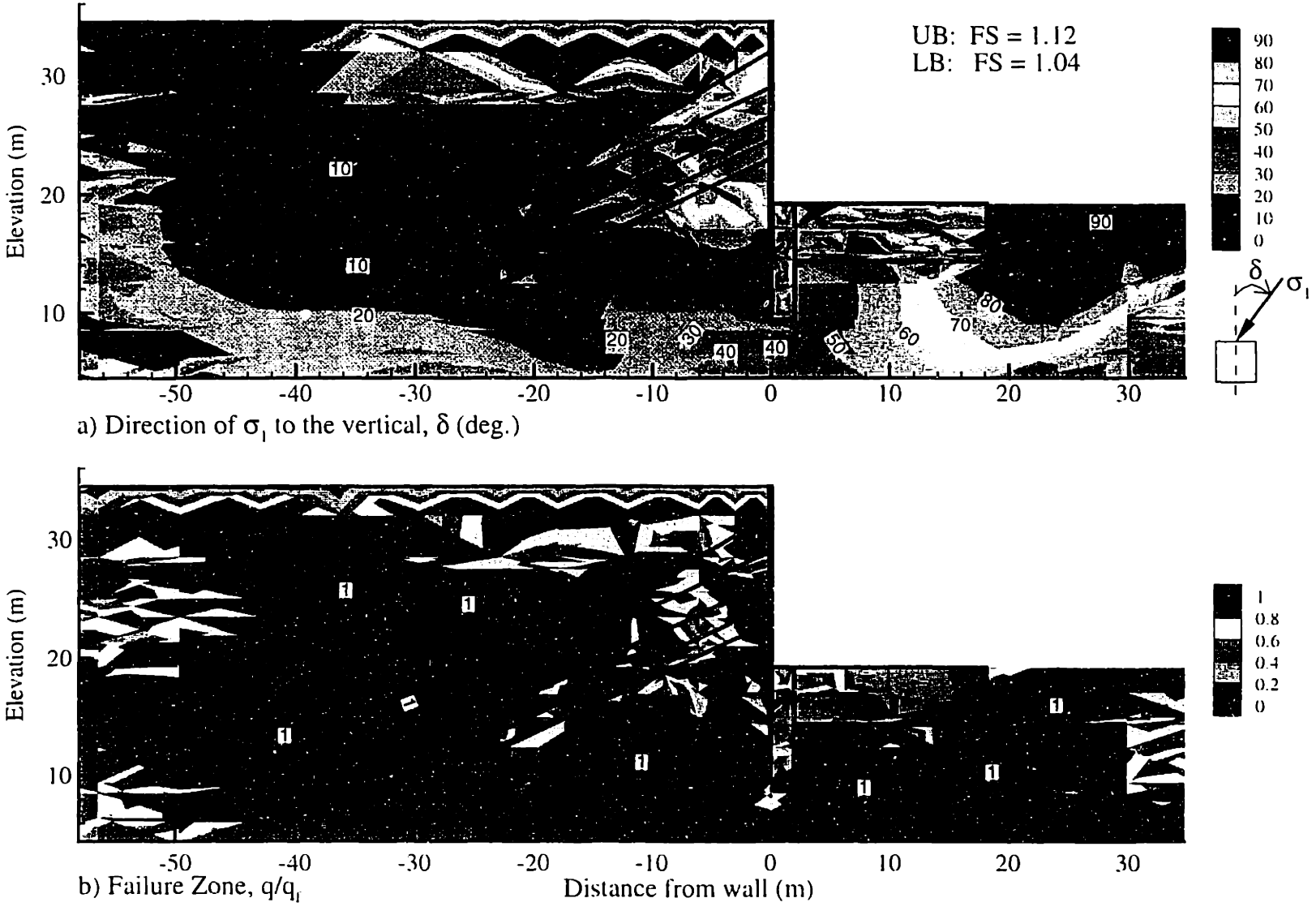

Figure 7.46 Lower bound results for West wall with anisotropic strength parameter AN1, stress history Profile 1

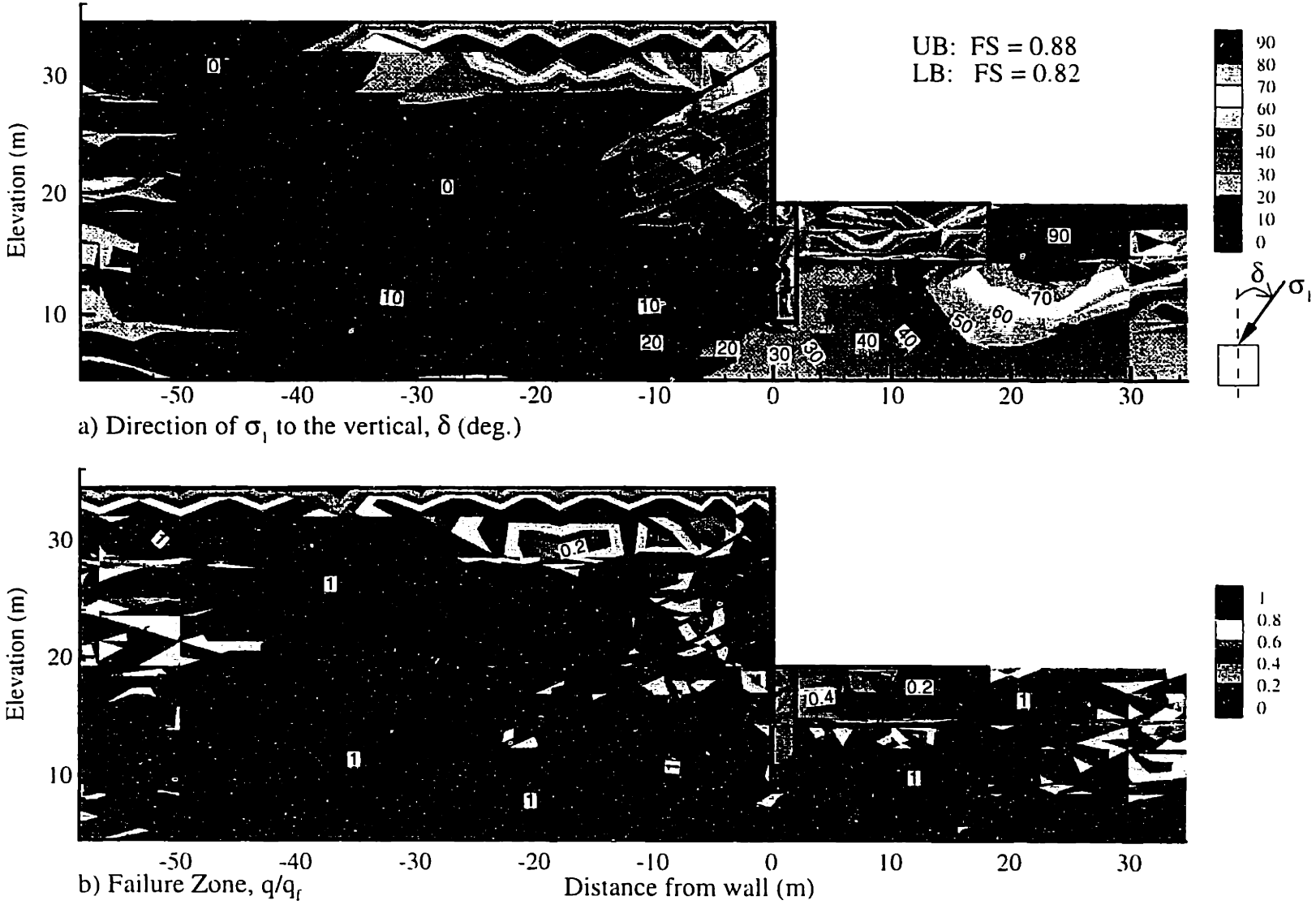

Figure 7.47 Lower bound results for West wall with anisotropic strength parameter AN2, stress history Profile 1

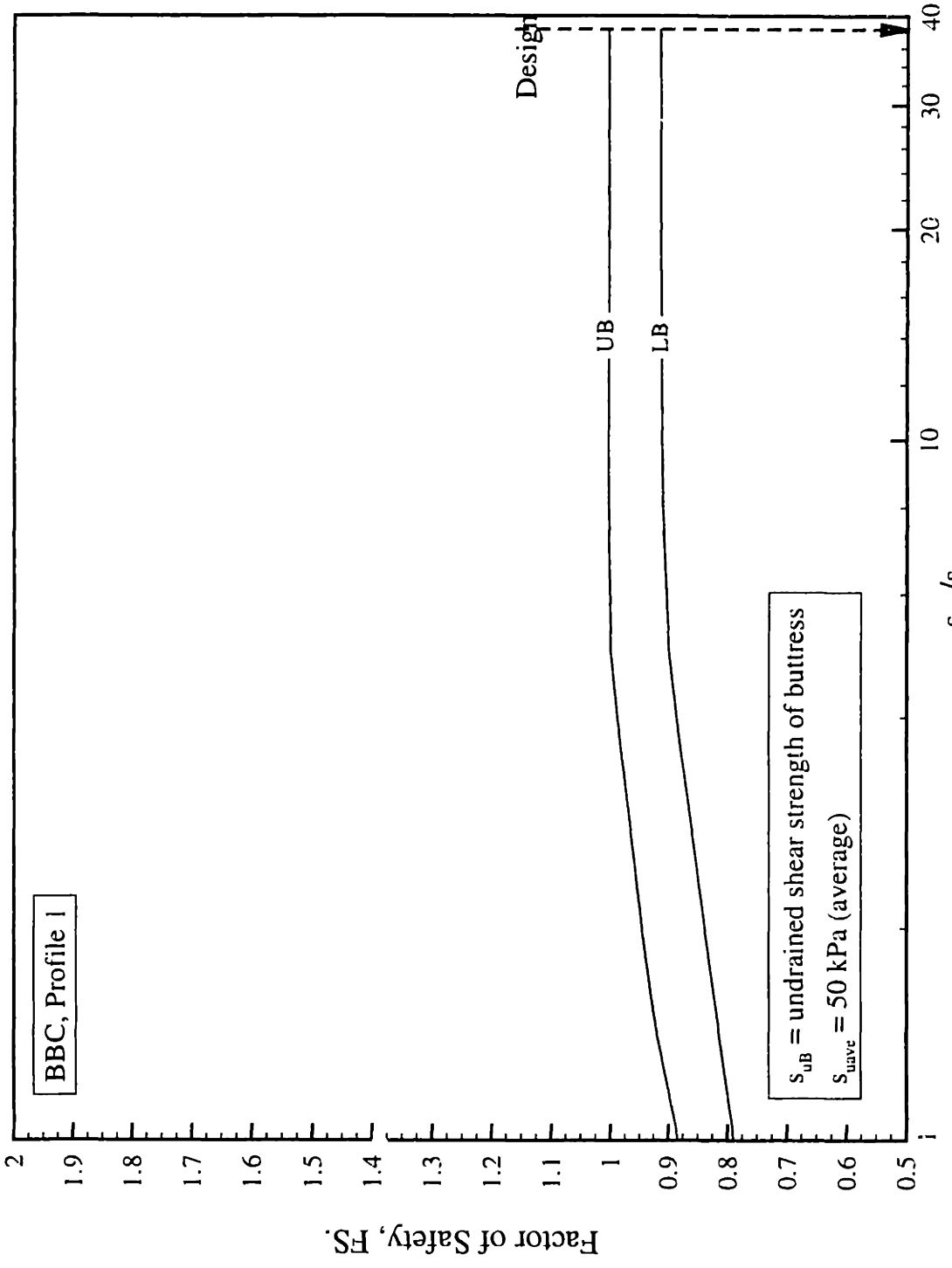

Figure 7.48 Effect of shear strength of buttress to factor of saftety of West wall Section B-B′

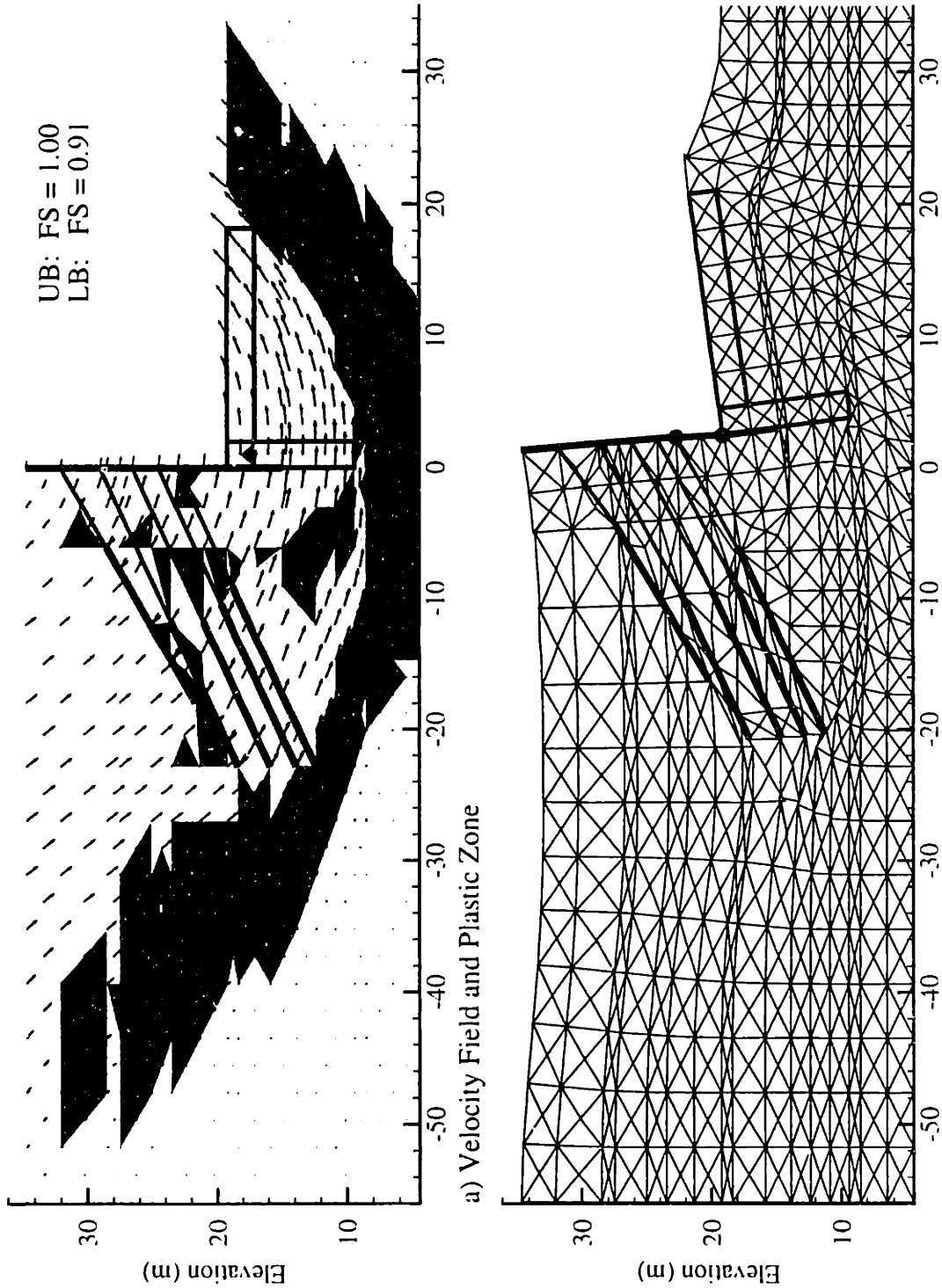

Figure 7.49 Upper bound results of West wall Section B-B′ for 2.2m thick buttress

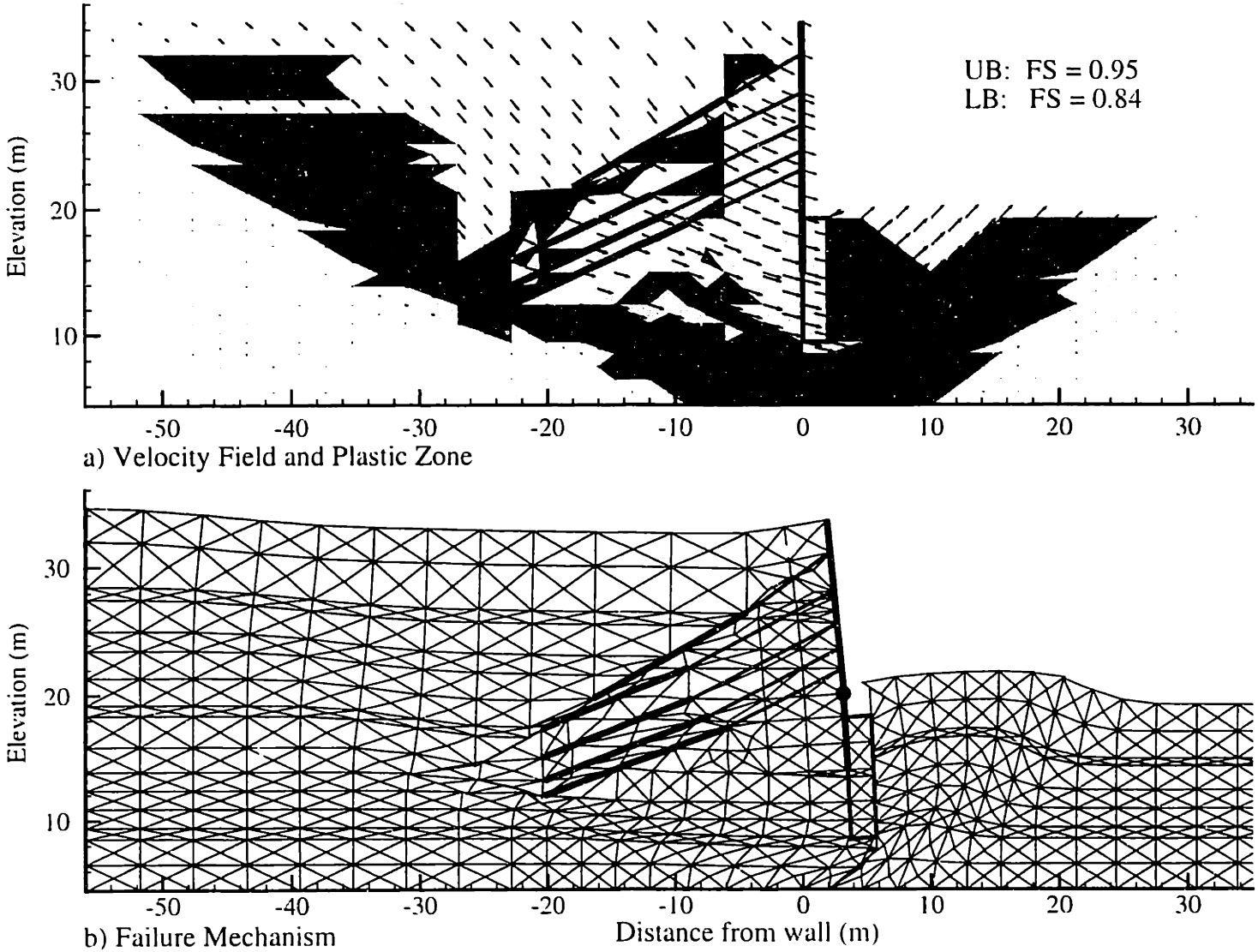

Figure 7.50 Upper bound results for West wall Section B-B′ with no DSM buttress

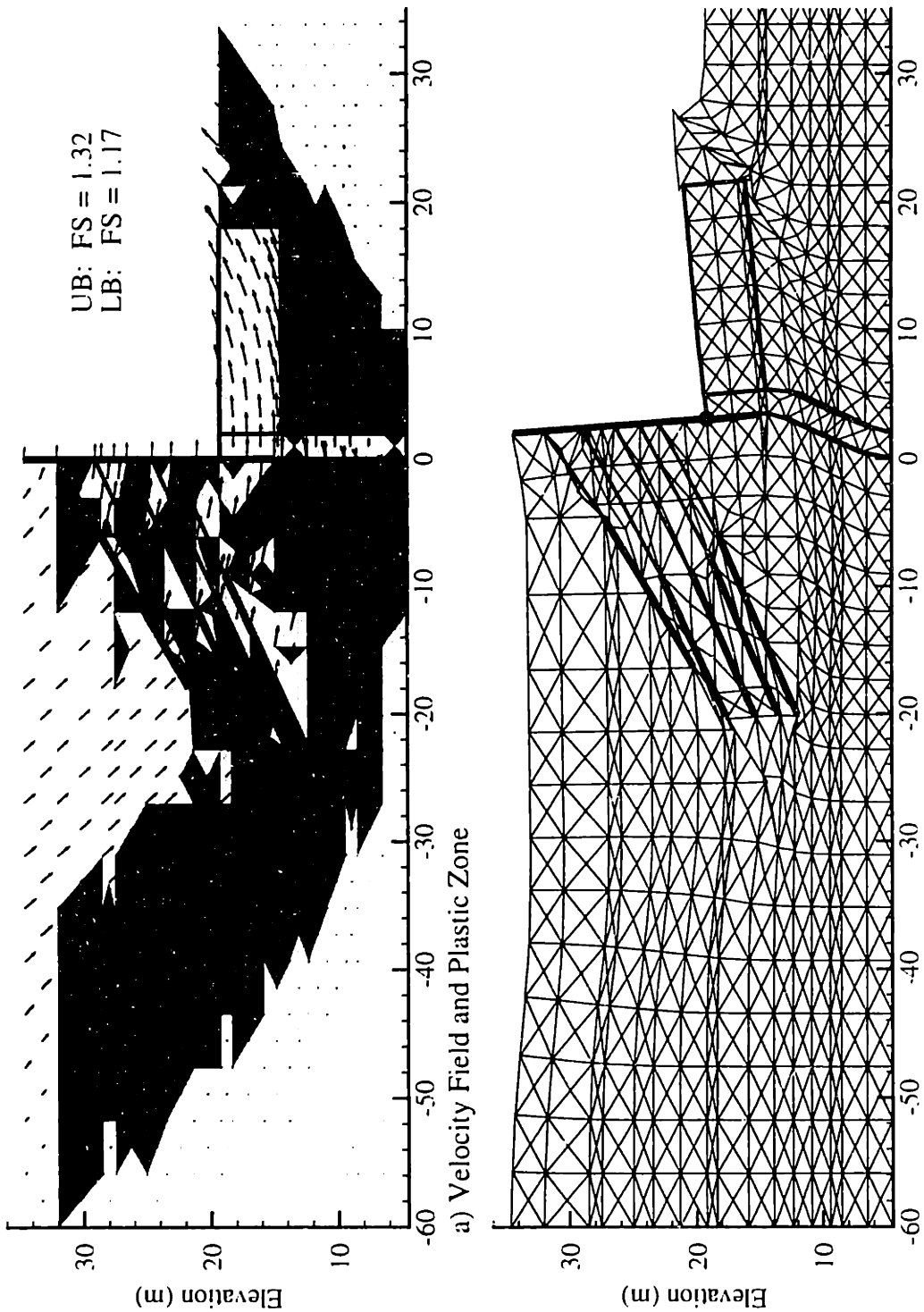

Figure 7.51 Upper bound results for West wall Section B-B′ for extending jet grout column to Glaciomarine

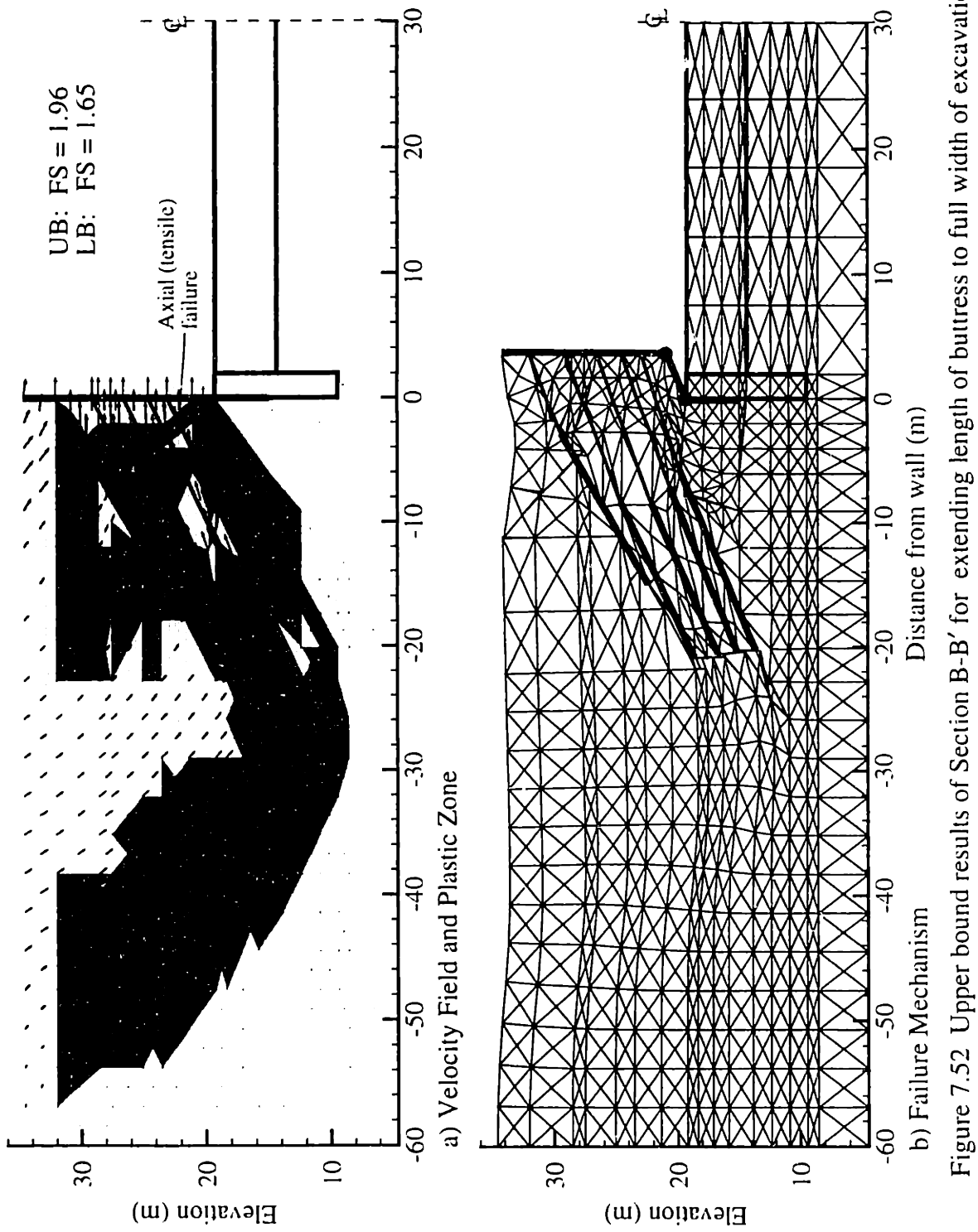

Figure 7.52 Upper bound results of Section B-B′ for extending length of buttress to full width of excavation

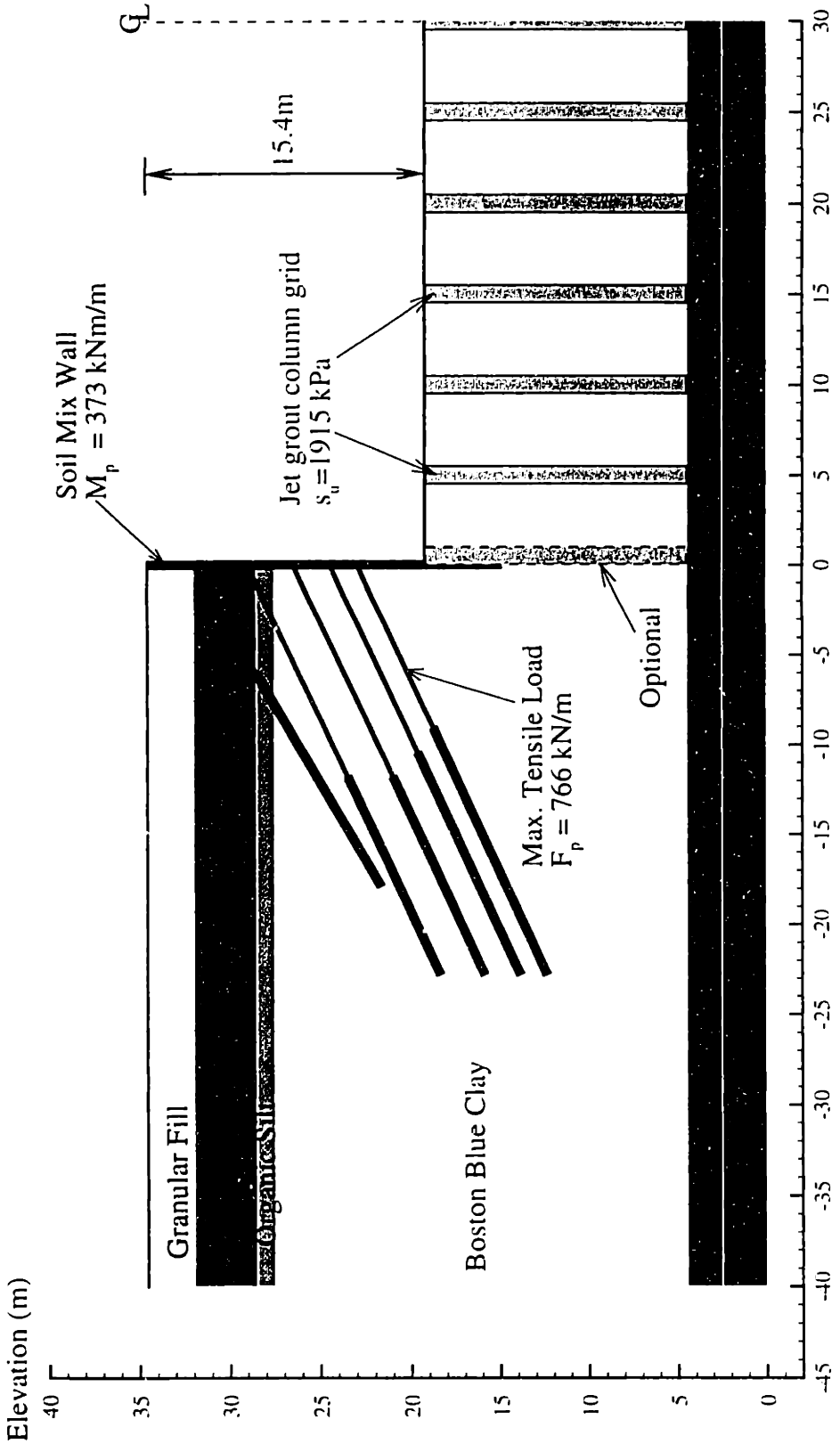

Figure 7.53 Proposed redesign West wall Section B-B′ with a grid of jet grout column

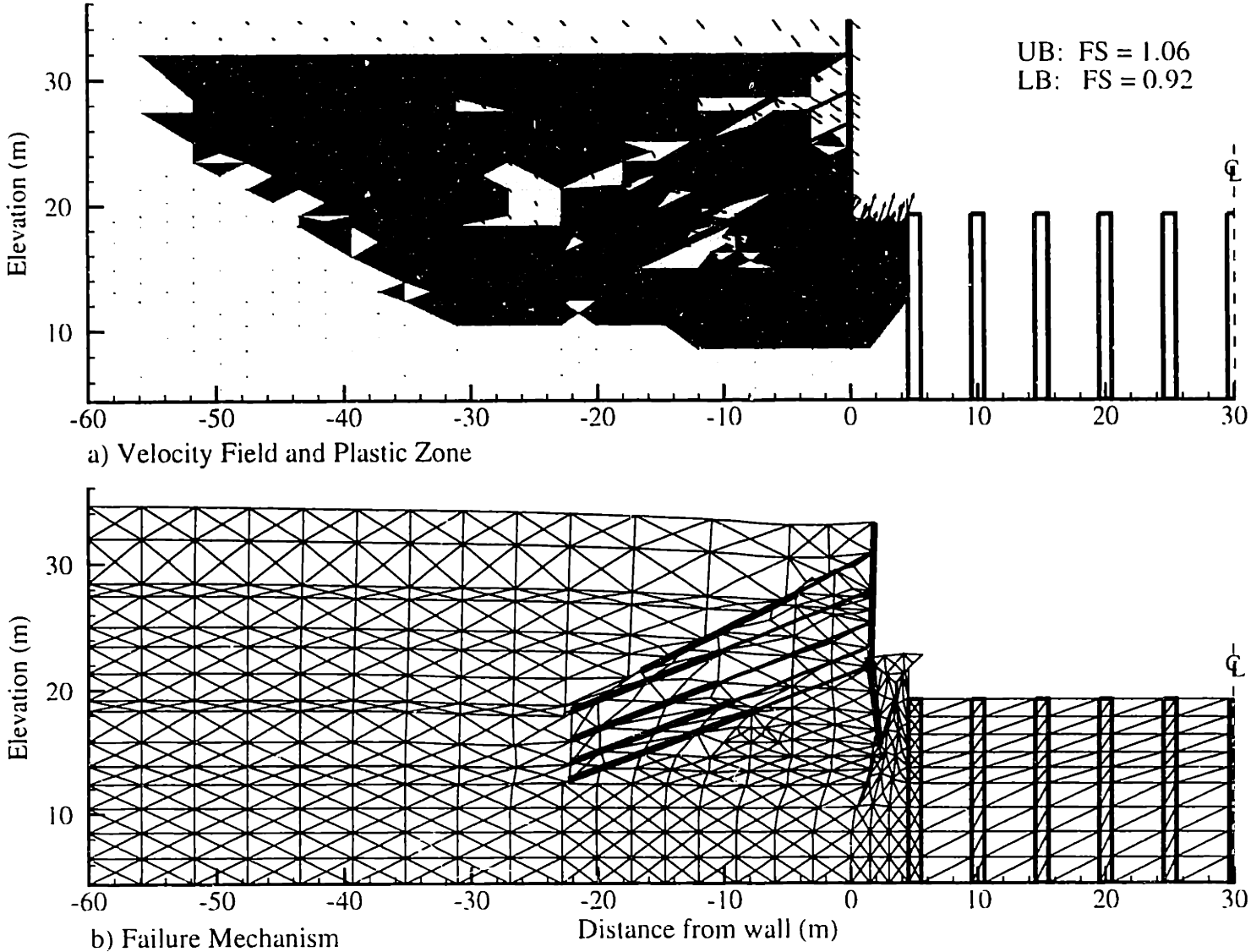

Figure 7.54 Upper bound results for Section B-B′ using a grid of jet grout column: without column next to SMW

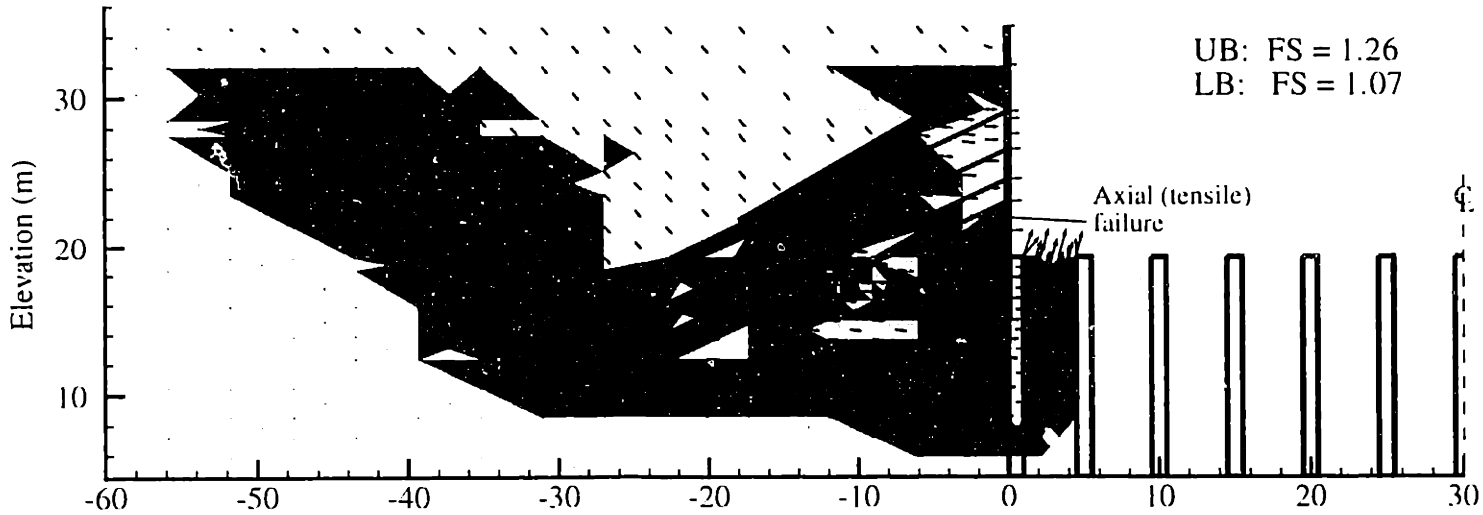

a) Velocity Field and Plastic Zone

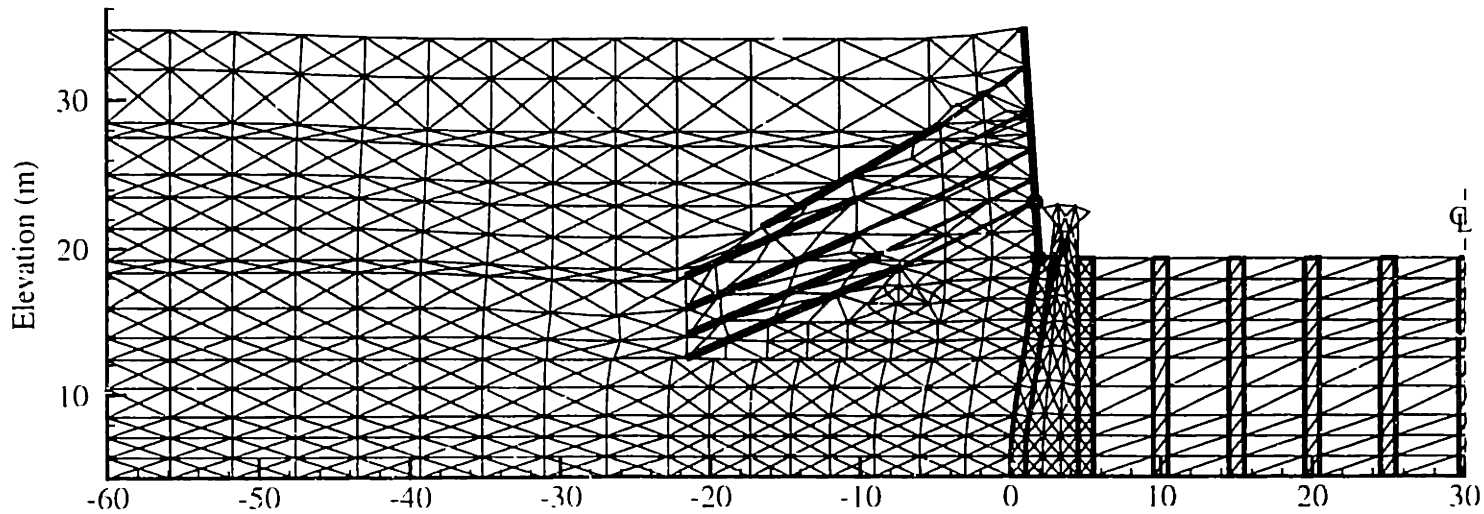

b) Failure Mechanism

Figure 7.55 Upper bound results for Section B-B′ using a grid of jet grout column: with column next to SMW

Appendix 7A. Case Studies of Excavations

Numerical limit analyses have been applied to evaluate the stability of four excavations that are well documented in the literature: 1) Vaterland 3 (NGI, 1962); 2) Mexico City (Rodriguez and Flamand, 1969); 3) Davidson Ave. (2 sections; Clough and Reed, 1984); and 4) HDR-4 Chicago (at CD 152, CD 164; Finno et al., 1989).

Table 7A.1 summarizes the results of these analyses, while details of excavation support, geometry, soil profile, and predicted failure mechanisms (upper bound analyses) are presented in Figures 7A.1 to 7A.16. The factors of safety from numerical limit analyses are compared with limit equilibrium calculations reported by O'Rourke (1993). The latter approximates the effects of wall embedment based on elastic strain energy in bending.

All calculations from numerical limit analyses assume isotropic shear strength of the clay. For the case of HDR-4 Chicago, the analysis also uses the anisotropic peak strength (since the data were available). The results of stability analysis from Table 6.9 show the following:

For all excavations, numerical limit analyses predict factors of safety that are consistent with observed behavior. For the cases, where no failure occurred, (i.e. Vaterland 3, Mexico City, Davidson Ave. (section #1), and HDR-4 excavation), the predicted FS > 1.0. In contrast, the analyses do predict FS < 1.0 at Davidson Ave. (section #2), where failure was observed.

At the Davidson Ave., section #2, a slope failure inside the excavation exposed a section of wall to an unsupported depth of H = 7.3m. This resulted in large inward deformation of the wall, which caused the second level wales to rotate, popping the braces at this level upward. As a result, the wall was propped only by the upper level of struts (Fig. 7A.8). Inclinometer measurements of this section showed a cumulative horizontal movement of 400m, and the excavation was temporarily backfilled to prevent massive failure. Thus, it is reasonable to assume that this section had experienced failure. Numerical limit analyses predict FS = 0.88-0.96.

Even though there is no visible failure observed in excavations for Davidson Ave at Section #1, and HDR-4 Chicago at construction day 152, maximum wall deflection, δ_{vmax}/H as high as 2% were measured. In these excavations, numerical limit analyses do

show a small safety margin, where FS = 1.1-1.2, which agrees the observed excavation performance of large wall movement.

Stability of excavations at Vaterland 3, Mexico city, and HDR-4 Chicago at construction day 164 is adequate, according to predictions of numerical limit analyses. The predictions correspond with their actual excavation performance, where no failure was observed.

Excavations	Vaterland #3	Mexico city	Davidson Ave #1	Davidson Ave #2	HDR-4 Chicago CD 152	HDR-4 Chicago CD 162
H (m)	9.0	9.0	9.1	7.3	7.9	12.2
B (m)	11.0	7.0	7.6	7.6	12.2	12.2
L (m)	11.0	18.2	13.7	13.7	19.2	19.2
Wall	SheetPile PZ32	SheetPile Z-section	SheetPile PZ32	SheetPile PZ32	SheetPile PZ40	SheetPile PZ40
Factor of Safety by Numerical Limit Analyses (LB – UB)	1.27 – 1.38	1.20 – 1.31	1.15 – 1.12	0.88 – 0.96	ISO: 1.09 – 1.18 AN: 1.12 – 1.21	ISO: 1.12 – 1.22 AN: 1.13 – 1.23
Factor of Safety* O'Rourke (1993)	1.38	1.12	1.38	1.00	AN: 1.1	AN: 1.3
Observed behavior δ_{wall} (cm) δ_{wall}/H (%)	No Failure 10 – 13 cm 1.1 – 1.4%	No Failure 10 – 15 cm 1.1 – 1.7%	No Failure 10 – 25 cm 1.1 – 2.7%	Failure	No Failure 15 – 17 cm 1.9 – 2.1%	No Failure 15 – 17 cm 1.2 – 1.4%
Supporting Material	Figs. 7A.1-7A.3	Figs. 7A.4-7A.6	Figs. 7A.7-7A.11		Figs. 7A.12-7A.16	
References	NGI, 1962	Rodriguez & Flamand, 1969	Clough & Reed, 1984		Finno et al., 1989	

Notes:
H = Height of excavation, B = Width of excavation, L = Total length of sheetpile wall
LB = Lower Bound; UB = Upper Bound; CD = Construction Day
ISO = Isotropic Strength; AN = Peak Anisotropic Strength
*All values of FS, except HDR-4 Chicago are reported by O'Rourke (1993). For HDR-4 Chicago, FS is calculated using Clough and Hansen's method (1981) accounting for strength anisotropy.

Table 7A.1 Summary of stability analyses for case studies of braced excavations

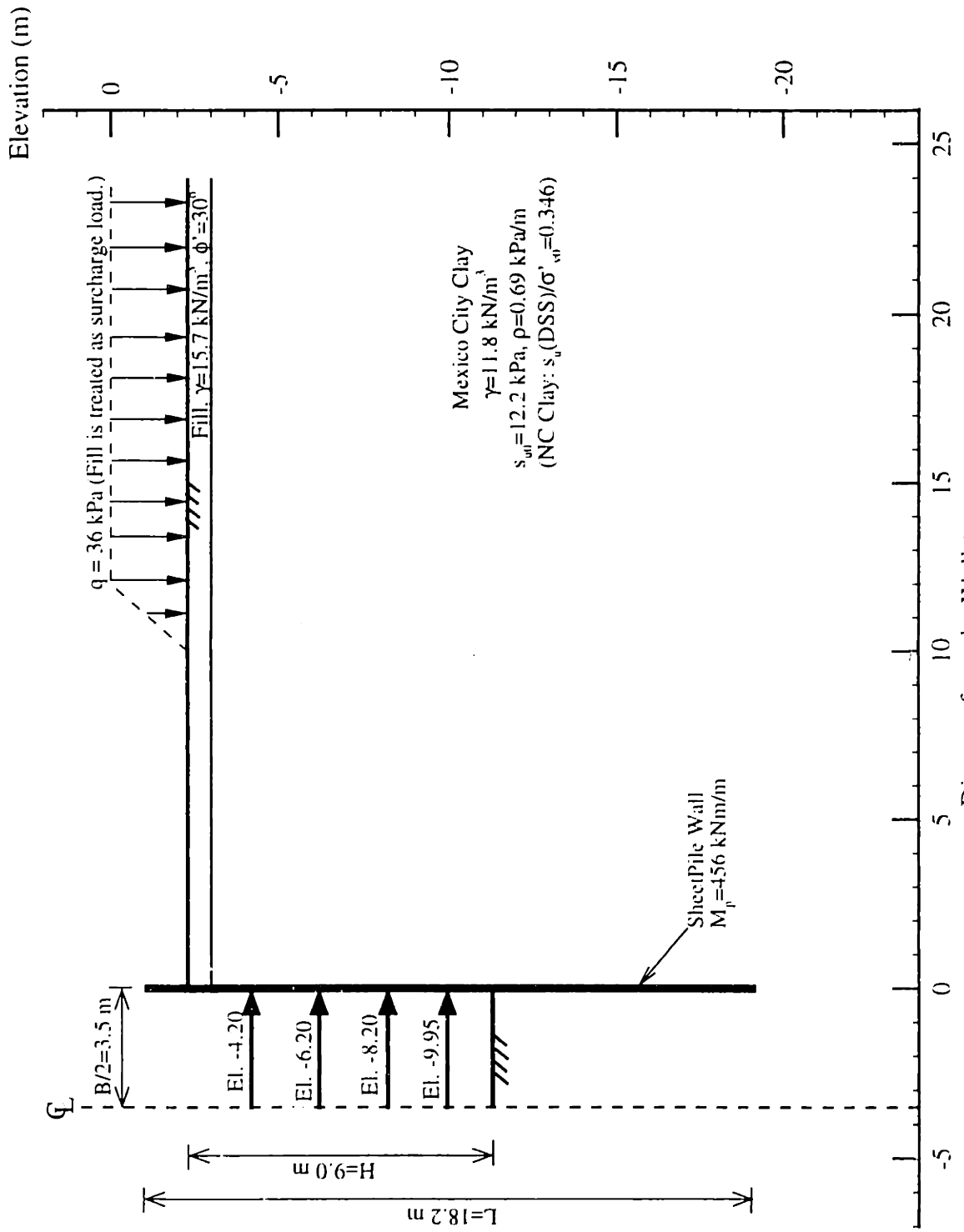

Figure 7A.1 An Excavation in Mexico City (Rodriguez and Flamand, 1969)

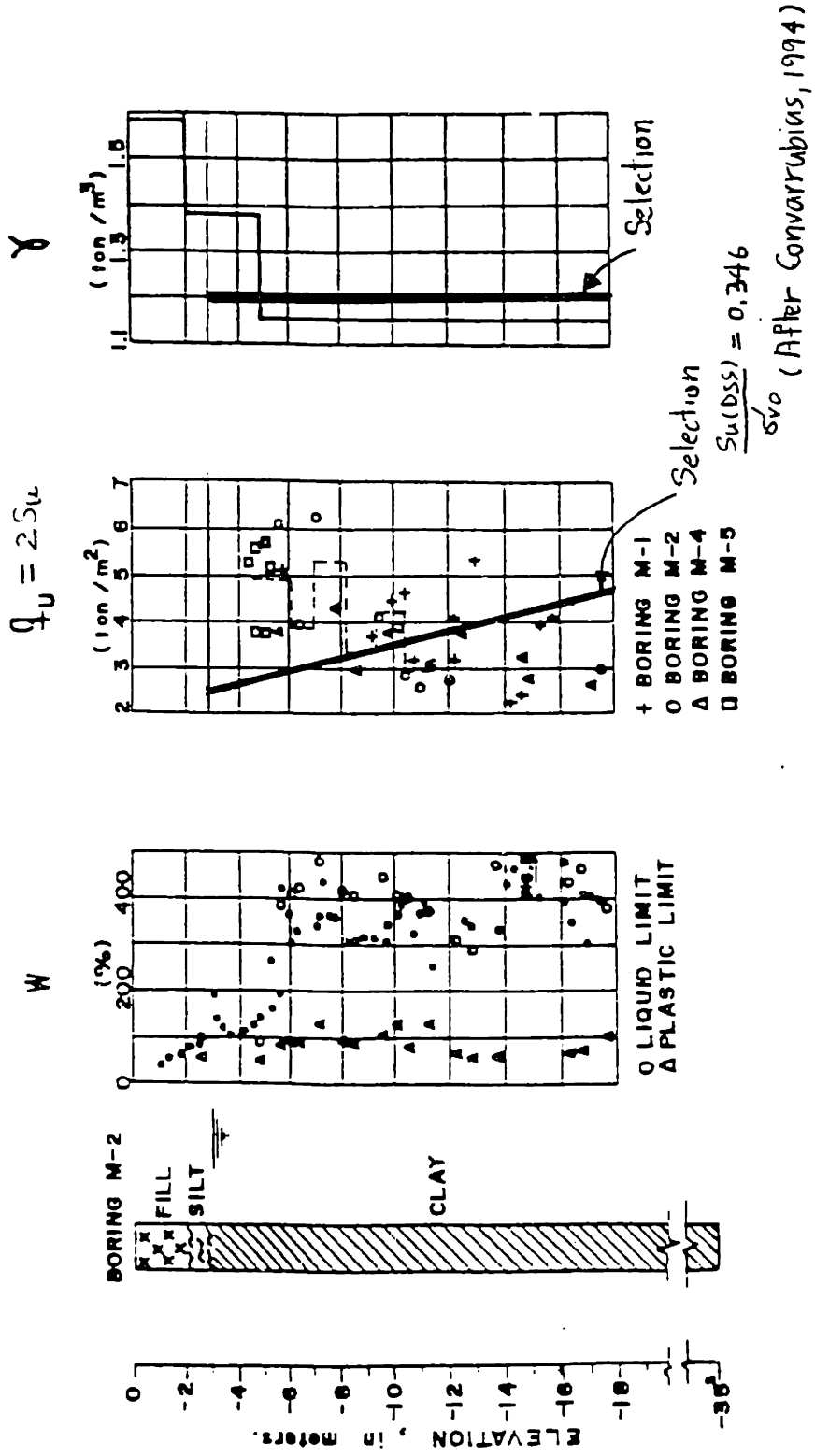

Figure 7A.2 Soil profile and properties for an excavation in Mexico city (After Rodriguez and Flamand, 1969)

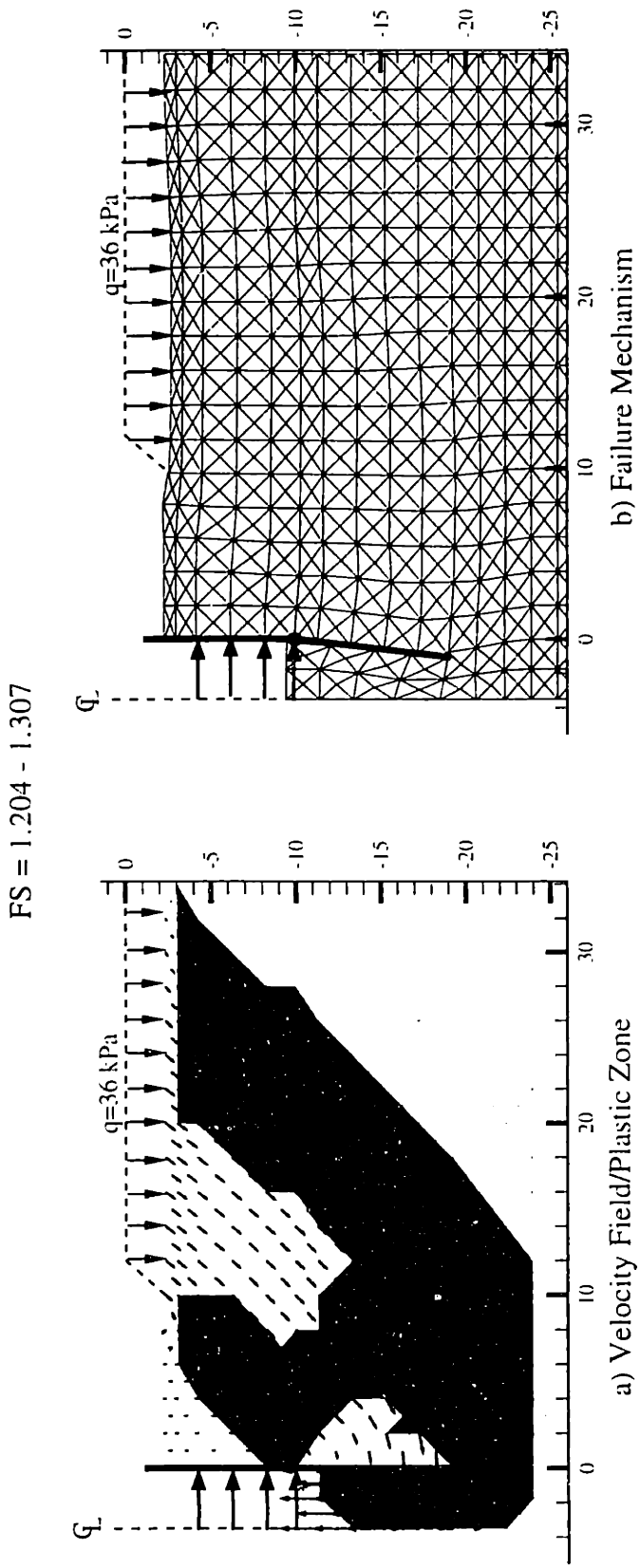

a) Velocity Field/Plastic Zone

b) Failure Mechanism

Figure 7A.3 UB Results: An Excavation in Mexico City

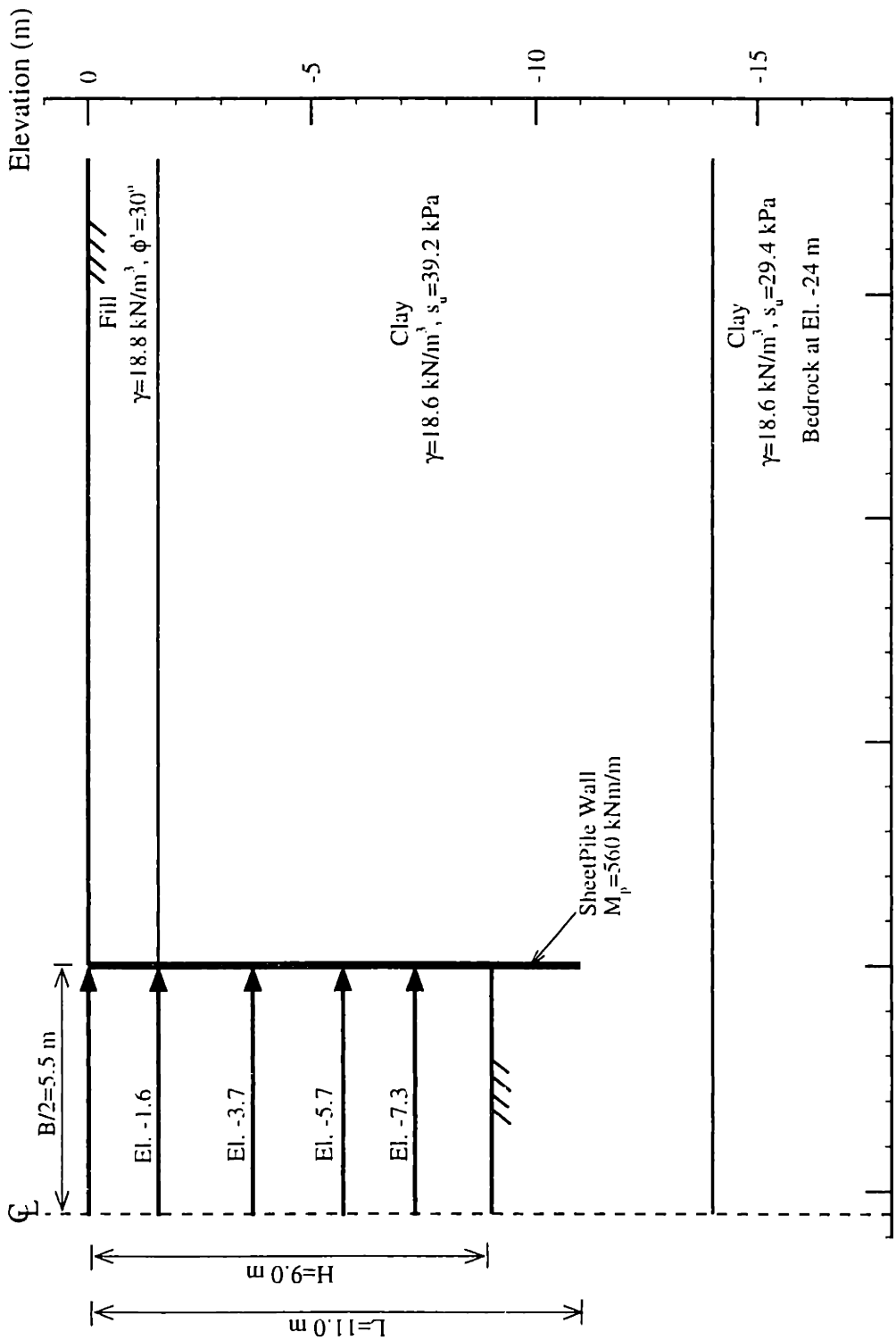

Figure 7A.4 Excavation Geometry at Vaterland 3. (NGI, 1962)

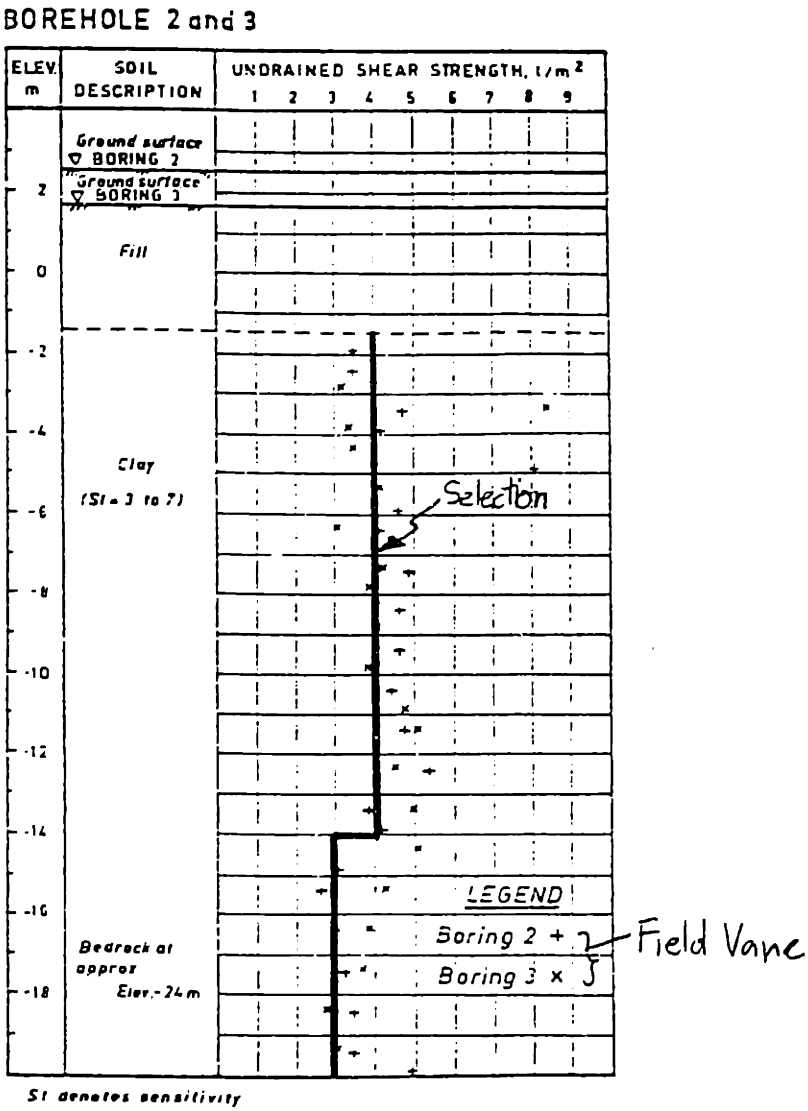

Figure 7A.5 Undrained shear strength profile of clay at Vaterland 3 (After NGI, 1962)

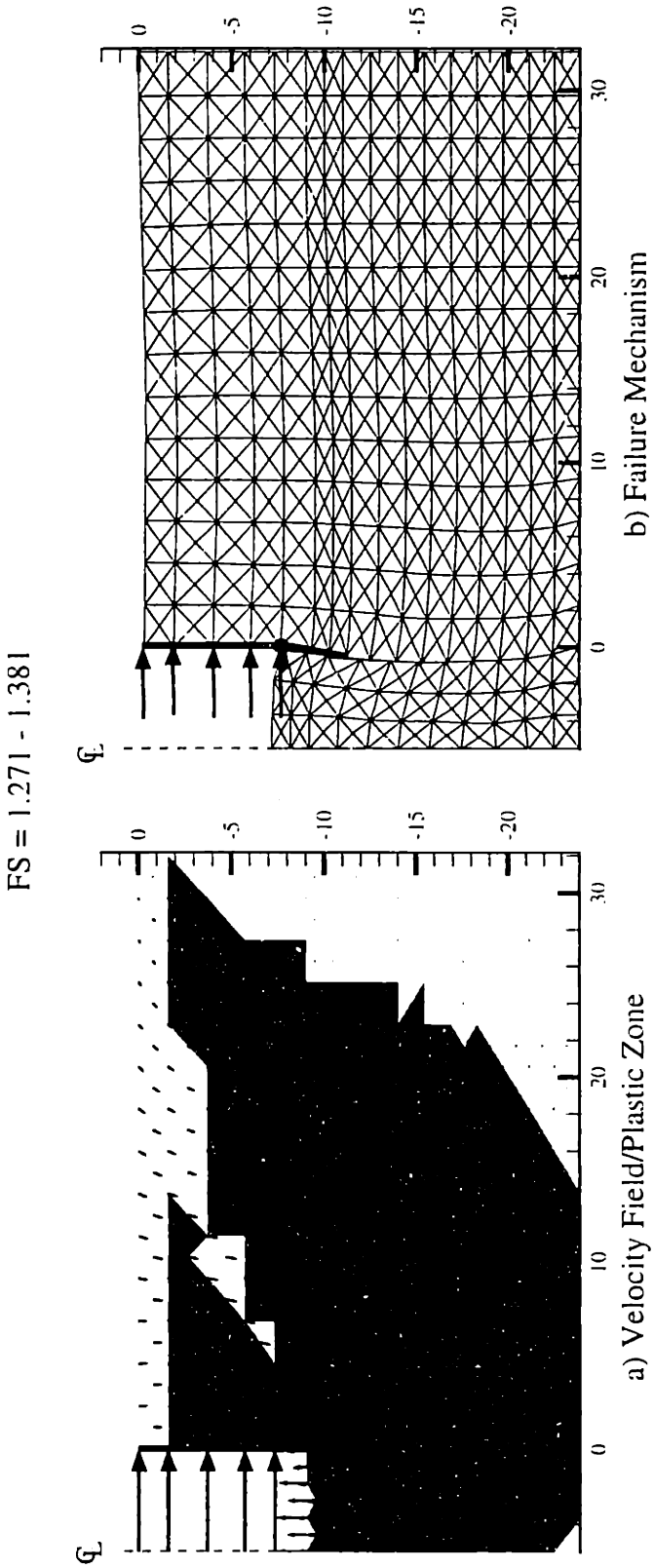

Figure 7A.6 UB Results for an Excavation at Vaterland 3

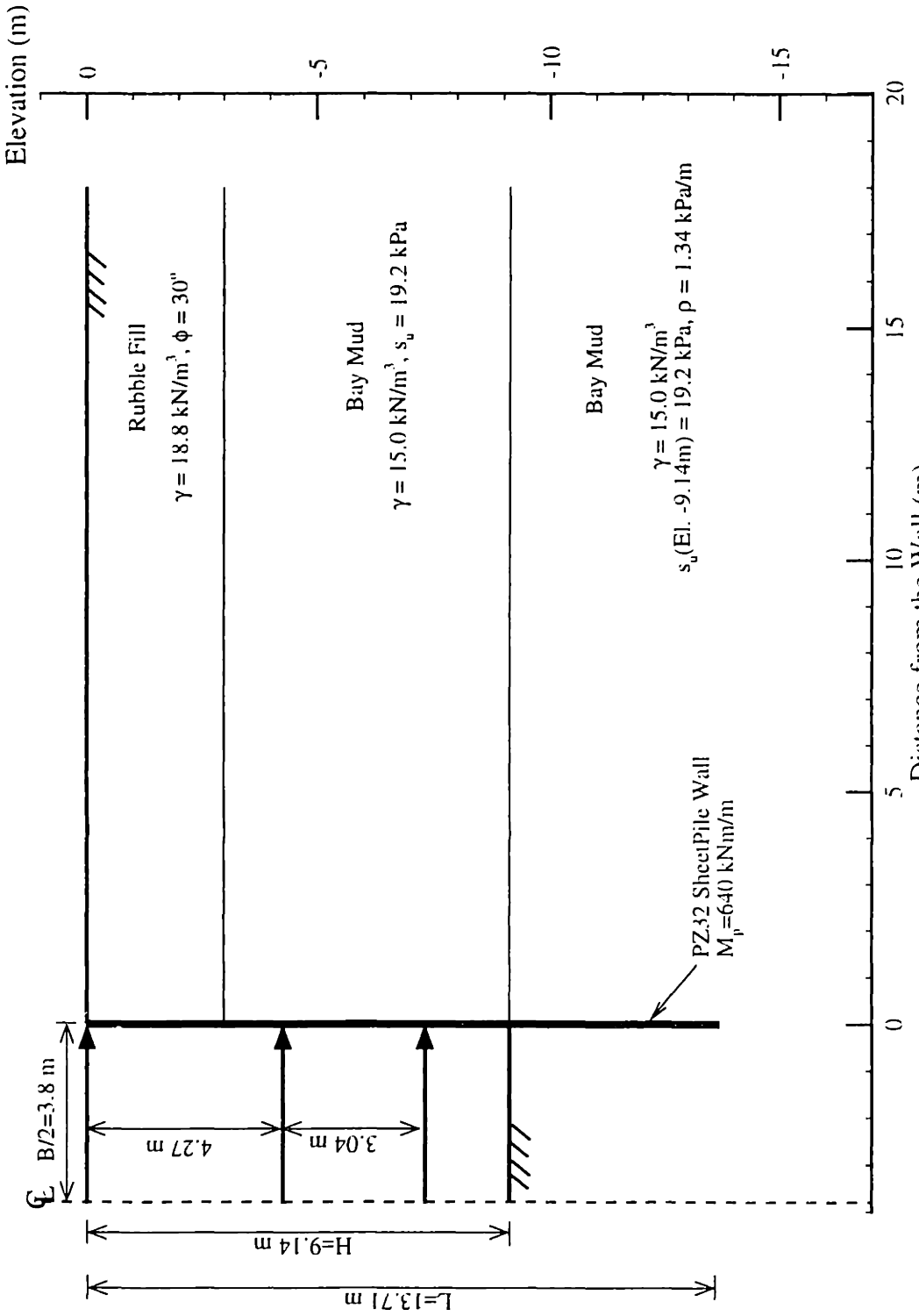

Figure 7A.7 Excavation Geometry at Davidson Avenue #1 (Clough & Reed, 1984)

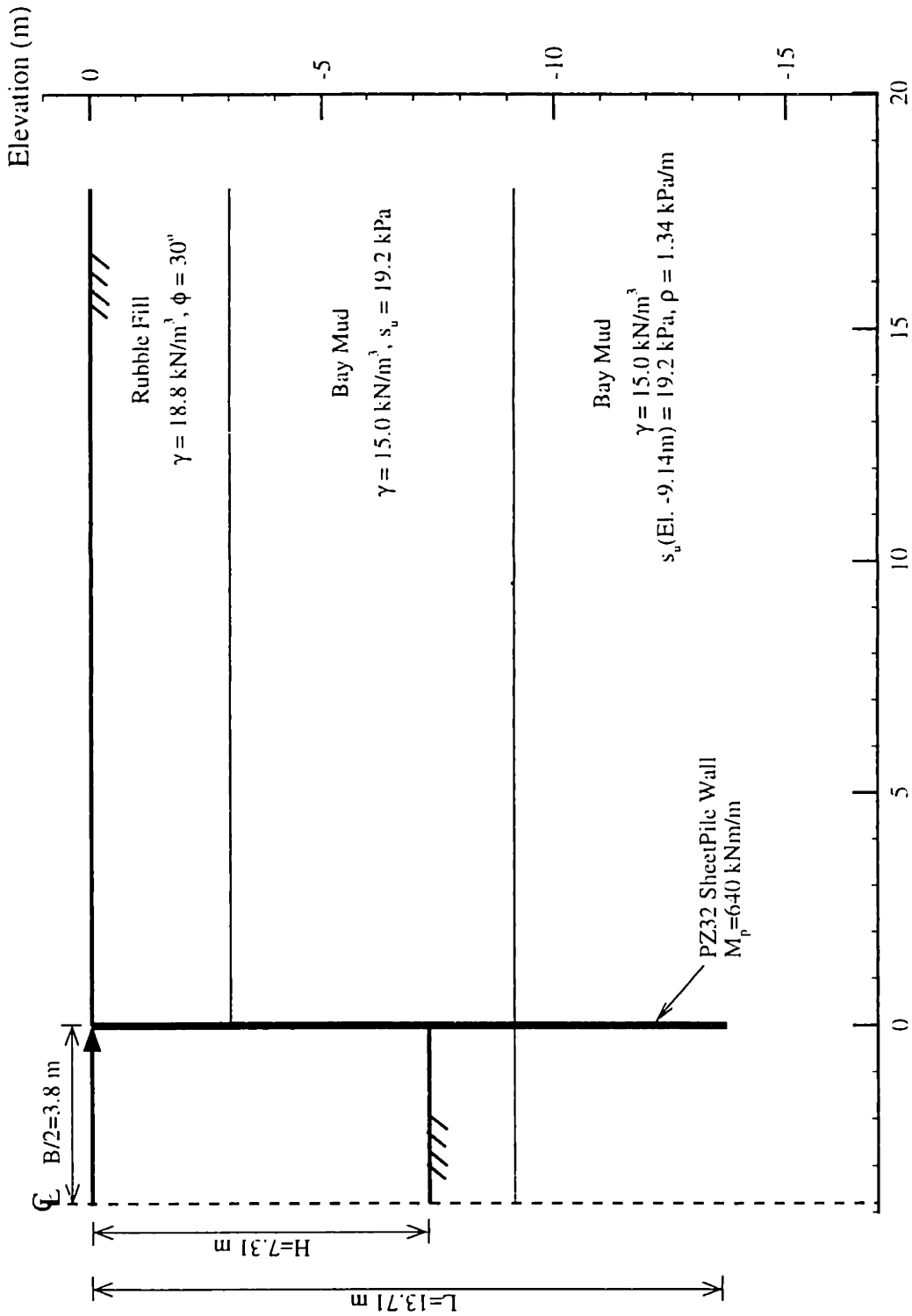

Figure 7A.8 Excavation Geometry at Davidson Avenue #2 (Clough & Reed, 1984)

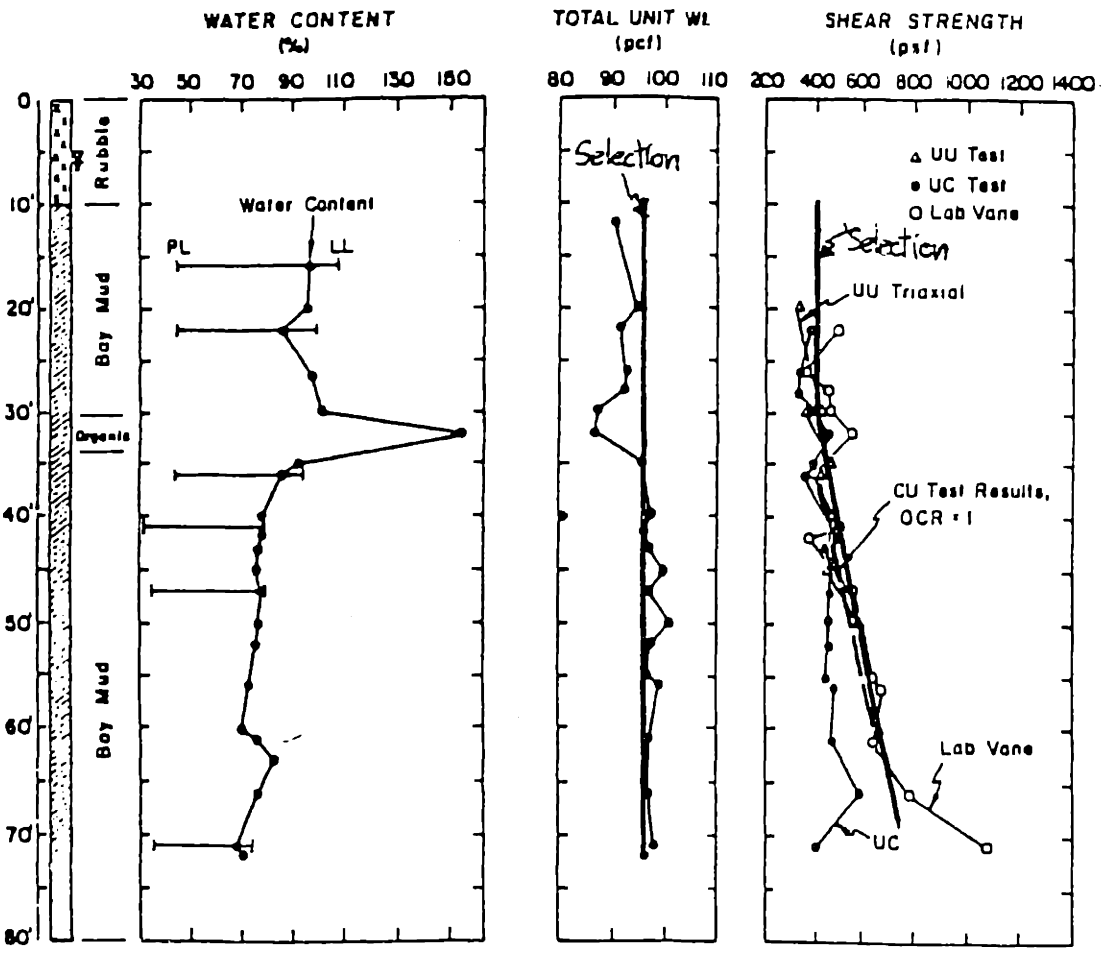

Figure 7A.9 Undrained shear strength profile of Bay Mud at Davidson Ave. (After Clough and Reed, 1984)

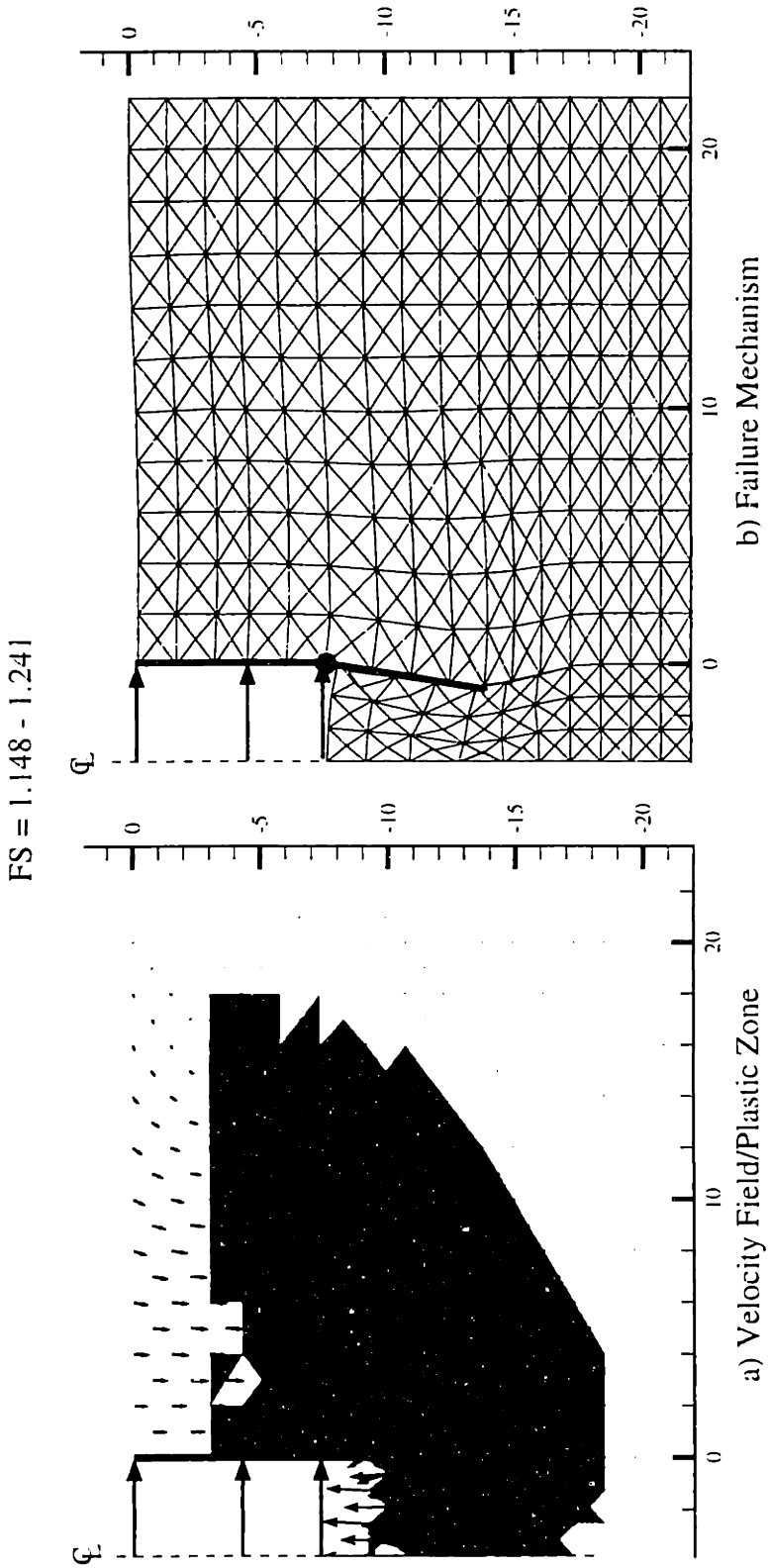

Figure 7A.10 UB Results for an Excavation at Davidson Ave. #1

FS = 0.882 - 0.960

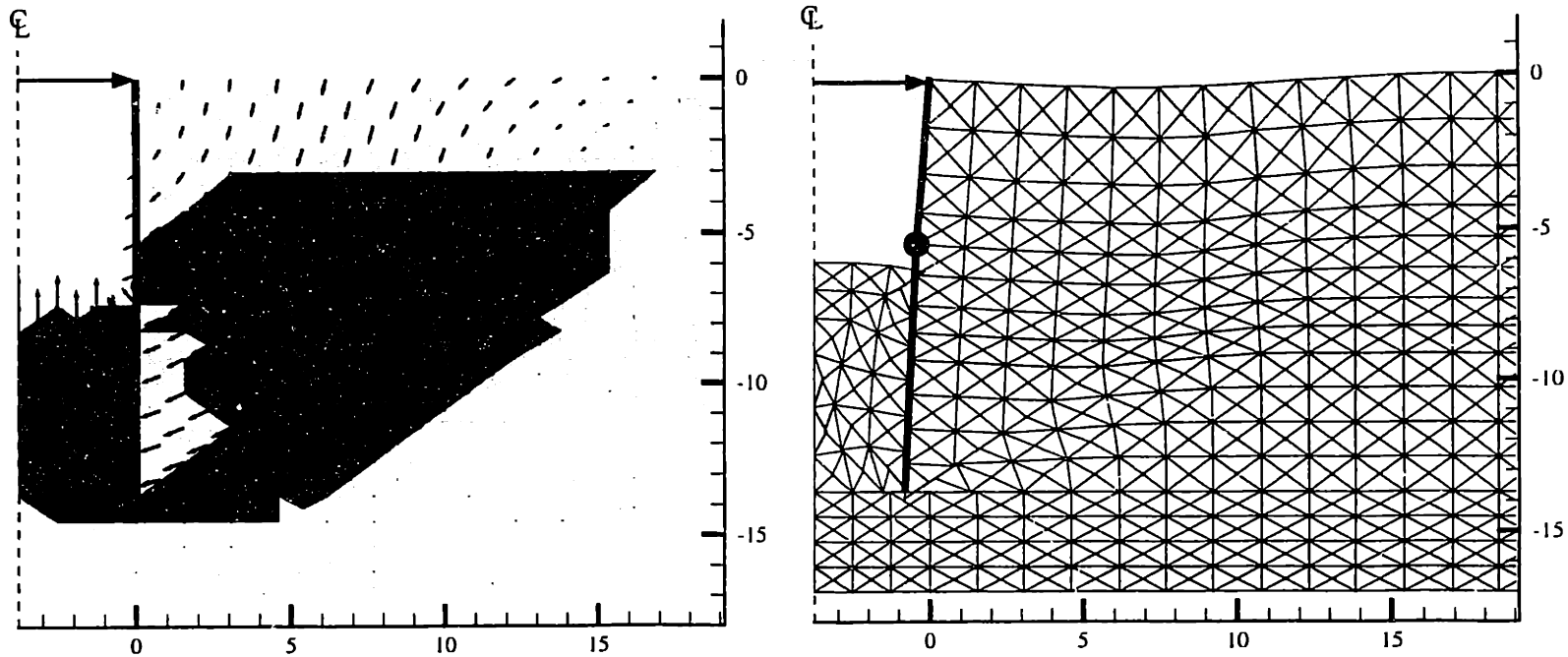

a) Velocity Field/Plastic Zone

b) Failure Mechanism

Figure 7A.11 UB Results for an Excavation at Davidson Ave. #2

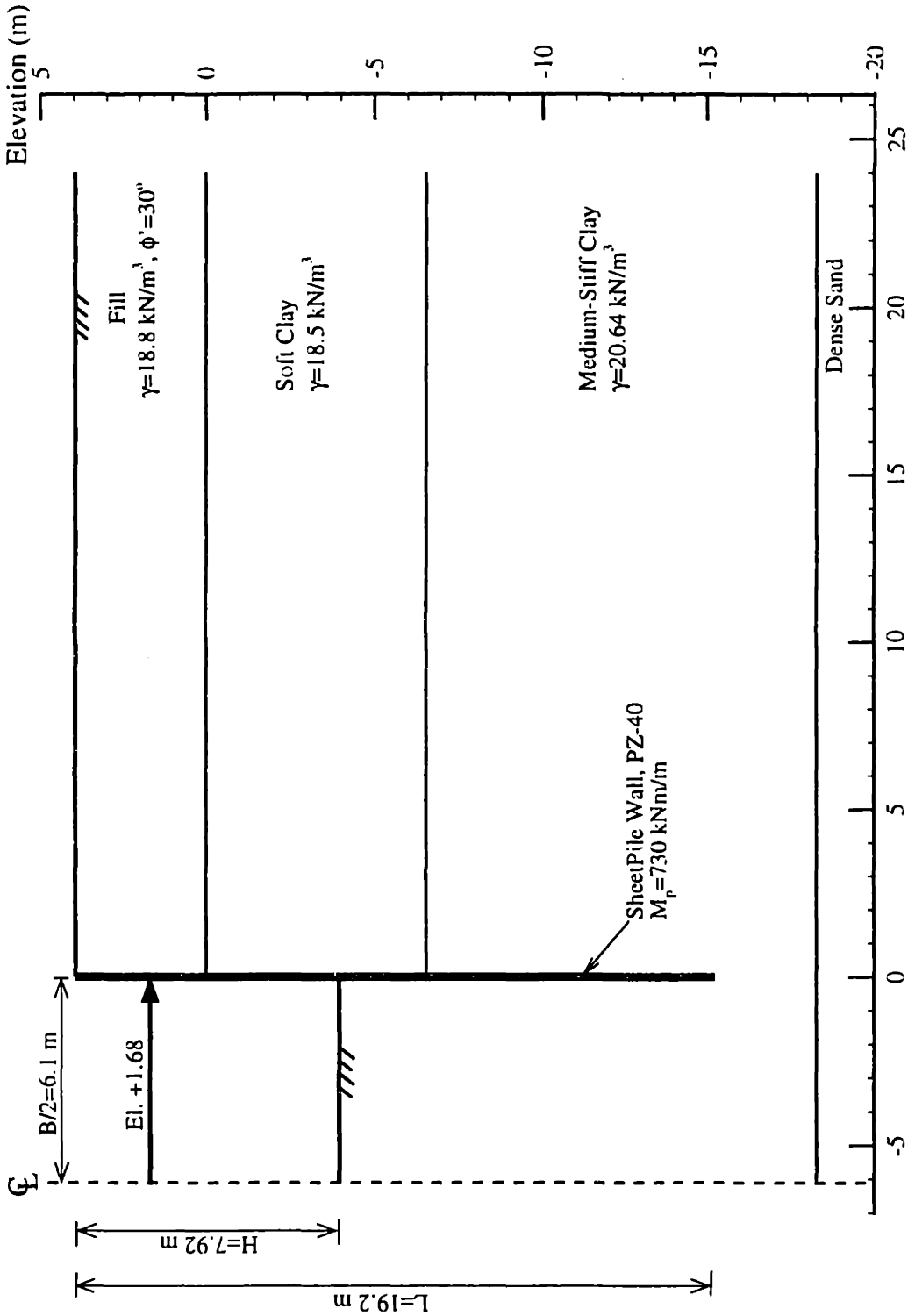

Figure 7A.12 HDR-4 Excavation in Chicago: Construction Day 152 (Finno et. al, 1989)

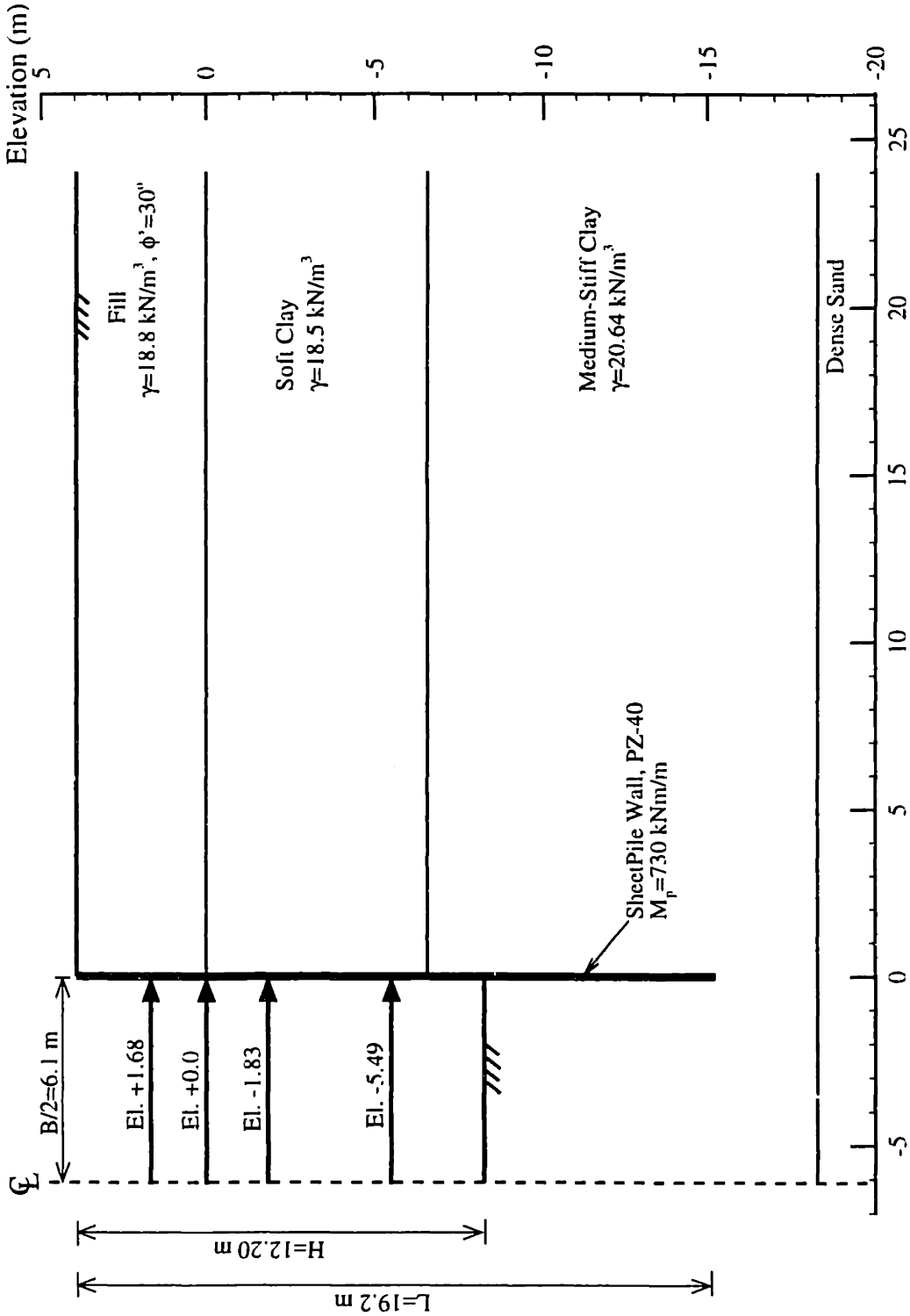

Figure 7A.13 HDR-4 Excavation in Chicago: Construction Day 164 (Finno et. al, 1989)

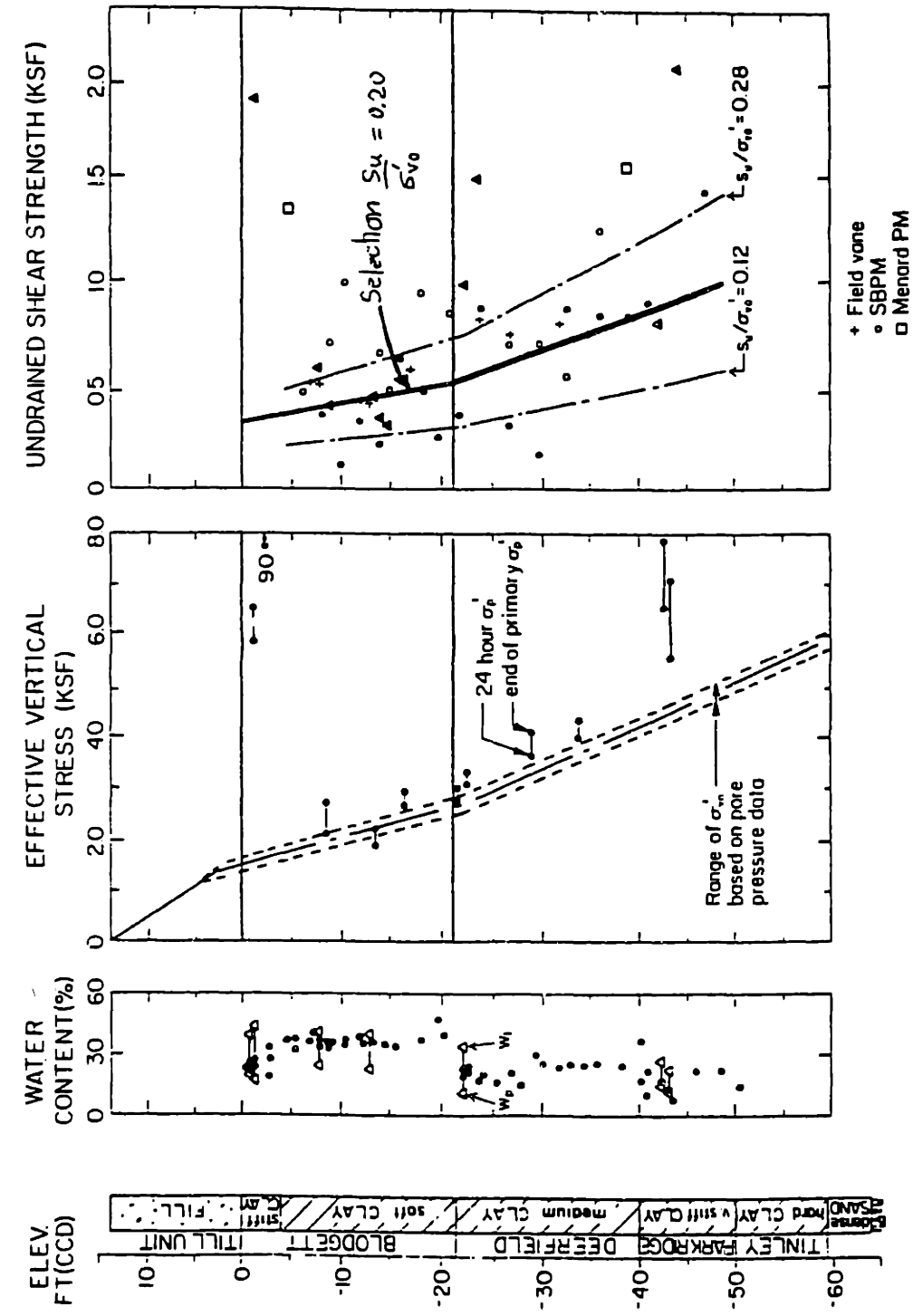

Figure 7A.14 Stress history and undrained shear strength at HDR-4 Chicago
(After Finno et. al. 1989)

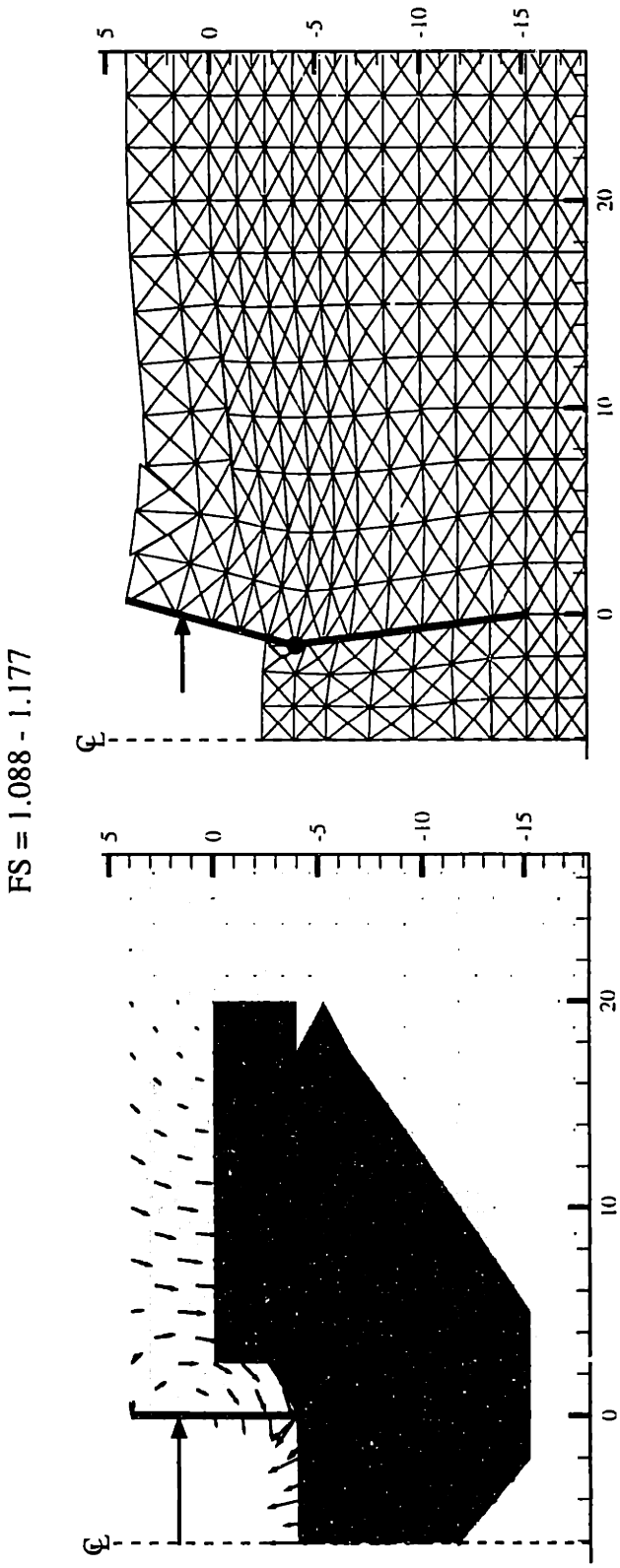

Figure 7A.15 UB Results for HDR-4 Excavation: Construction day 152, Isotropic Strength

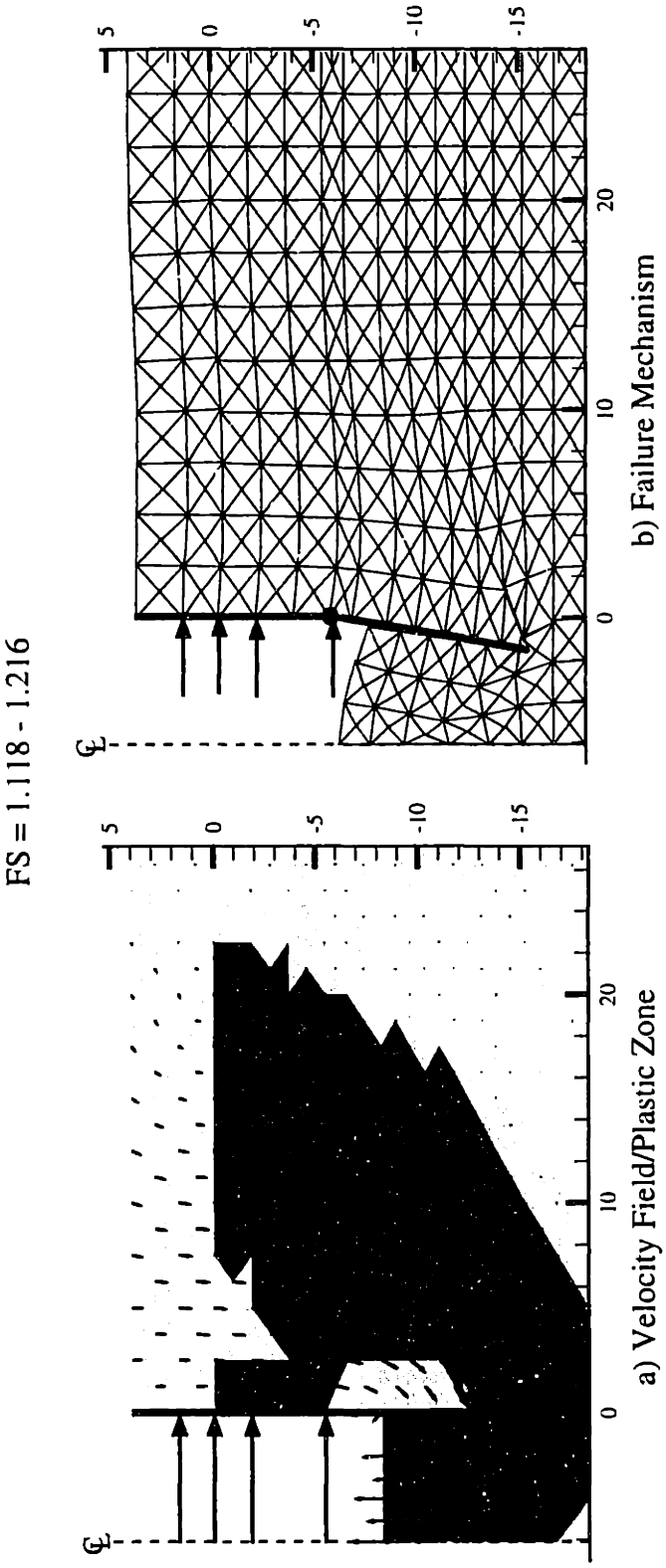

Figure 7A.16 UB Results for HDR-4 Excavation: Construction day 164, Isotropic Strength

Chapter 8. Implementation and Validation of Pore Water Pressure into Numerical Limit Analyses

8.1 Introduction

This chapter describes modifications of the numerical limit analyses to include pore pressure and effective stress strength parameters (Sections 4.2, 4.3). The proposed formulation is evaluated by comparisons with analytical upper bound solutions and limit equilibrium calculations for homogeneous slopes: 1) subject to uniform ratios of pore pressure to total overburden stress; and 2) submerged under water (Section 4.4). Section 4.5 applies the new formulation to predict upper and lower bounds on the stability of an offshore breakwater in Brazil. The case study of this Reinder failure was documented in previous research at MIT (Lee, 1995; Ladd and Lee, 1993; Ladd et al., 1993).

8.2 Lower Bound Implementation

In the numerical lower bound formulation for plane strain problems, the soil mass is discretized into 3-noded triangular elements, assuming a linear variation of the unknown stresses (σ_x, σ_y, τ_{xy}) within each element:

$$\sigma_x = \sum_{i=1}^{3} N_i \sigma_{xi} \quad ; \quad \sigma_y = \sum_{i=1}^{3} N_i \sigma_{yi} \quad ; \quad \tau_{xy} = \sum_{i=1}^{3} N_i \tau_{xyi} \qquad \text{(2.2; bis)}$$

where N_i = standard linear shape function (e.g. Zienkiewicz, 1983)

(σ_{xi}, σ_{yi}, τ_{xyi}) = unknown total stresses at node i

It should be noted that these unknowns are total, not effective stresses.

The proposed formulation assumes that pore water pressures are known at each node in the mesh. These pressures can be either static or correspond to steady flow conditions (steady seepage). These conditions are modeled by allowing pore water pressures (p_w) to vary linearly within each triangular element:

$$p_w = \sum_{i=1}^{3} N_i p_{wi} \qquad (8.1)$$

where p_{wi} = known pore water pressure at node i

Since total stresses are unknown variables for each node, there is no modification required for: 1) the equilibrium with triangular elements; 2) equilibrium of normal and shear traction across stress discontinuities; or 3) stress boundary conditions.

However, modifications of the lower bound analyses are necessary to incorporate the pore pressures in the yield criterion. For plane strain conditions with positive stresses in tension, the Mohr-Coulomb yield criterion can be expressed in terms of effective stress parameters as follows:

$$F = (\sigma'_x - \sigma'_y)^2 + (2\tau_{xy})^2 - (2c'\cos\phi' - (\sigma'_x + \sigma'_y)\sin\phi')^2 = 0 \qquad (8.2)$$

where c', ϕ' = effective cohesion intercept and frictional angle

σ'_x, σ'_y = effective normal stresses in x and y directions

The lower bound linearization of this single non-linear yield function follows Sloan (1988)'s formulation, resulting in a series of linear inequality which describes the convexity of linearized yield criterion as:

$$F_k = A_k\sigma'_x + B_k\sigma'_y + C\tau_{xy} - D_k \leq 0 \quad , k = 1,2,...,n \qquad (8.3a)$$

where $A_k = \cos(2\pi k/n) + \sin\phi'\cos(\pi/n)$ (8.3b)

$B_k = \sin\phi'\cos(\pi/n) - \cos(2\pi k/n)$

$C_k = 2\sin(2\pi k/n)$

$D_k = 2\, c'\cos\phi'\cos(\pi/n)$

n = the number of linearized planes

The effective stresses can be expressed in terms of total stresses by using the Terzaghi's effective stress equation:

$$\sigma'_x = \sigma_x - p_w \;\; ; \sigma'_y = \sigma_y - p_w \qquad (8.4)$$

Substituting equation 8.4 into equation 8.3a leads to the linearized yield criterion in terms of total stresses:

$$F_k = A_k\sigma_x + B_k\sigma_y + C_k\tau_{xy} - D_k - p_w(A_k + B_k) \leq 0 \quad , k = 1,2,...,n \qquad (8.5)$$

As the stresses, effective cohesion intercept, and pore water pressure vary linearly within the element, the yield condition can be satisfied by enforcing a series of linear inequality constraints on the nodal point total stresses, cohesion intercept and pore pressure:

$$F_{ki} = A_k\sigma_{xi} + B_k\sigma_{yi} + C_k\tau_{xyi} - D_{ki} - p_{wi}(A_k + B_k) \leq 0 \quad , k = 1,2,...,n \qquad (8.6)$$

where F_{ki} = the k^{th} side of the linearized yield function at node i

$D_k = 2c'_i\cos\phi'\cos(\pi/n)$

c'_i = effective cohesion intercept at node i

The term $p_{wi}(A_k + B_k)$ in equation 8.6 represents the only modification of the lower bound formulation that is necessary to incorporate pore pressures in the soil. To model undrained shearing of a clay, the effective stress parameters become total stress parameters assuming:

$$\phi' = \phi = 0 \text{ (total stress)} \qquad (8.7)$$
$$c' = s_u$$

It follows from equation 8.3b that the term $(A_k + B_k) = 0$, when $\phi' = 0$. This means that the presence of pore pressure will not influence the shear resistance of incompressible (undrained) materials.

8.3 Upper Bound Implementation

Conceptual modifications of the upper bound formulation include adding the work done by pore water pressures in the calculation of internal power dissipation within triangular elements and along velocity discontinuities.

Like the lower bound formulation, the pore water pressure in the upper bound formulation is assumed to be a known quantity at all nodes in the mesh and can vary linearly within each triangular element.

The upper bound linearization of Mohr-Coulomb yield criterion in equation 8.2 gives rise to the external linearized yield function (after Sloan and Kleeman, 1995):

$$F_k = A_k\sigma'_x + B_k\sigma'_y + C_k\tau_{xy} - D_k = 0 \quad , k = 1,2,...,n \qquad (8.8a)$$

where $A_k = \cos(2\pi k/p) + \sin\phi'$ (8.8b)

$B_k = \sin\phi' - \cos(2\pi k/n)$

$C_k = 2\sin(2\pi k/n)$

$D_k = 2c'\cos\phi'$

n = the number of linearized planes

The plastic flow within triangles is associated with the linearized yield function derived in terms of effective stresses as follows:

$$\dot{\varepsilon}_x = \sum_{k=1}^{p} \dot{\lambda}_k \frac{\partial F_k}{\partial \sigma'_x} = \sum_{k=1}^{p} \dot{\lambda}_k A_k \tag{8.9}$$

$$\dot{\varepsilon}_y = \sum_{k=1}^{p} \dot{\lambda}_k \frac{\partial F_k}{\partial \sigma'_y} = \sum_{k=1}^{p} \dot{\lambda}_k B_k$$

$$\dot{\gamma}_{xy} = \sum_{k=1}^{p} \dot{\lambda}_k \frac{\partial F_k}{\partial \tau_{xy}} = \sum_{k=1}^{p} \dot{\lambda}_k C_k$$

where $\dot{\lambda}_k$ is the non-negative plastic multiplier rates associated with F_k

The internal energy dissipated within each element is expressed as the product of total stresses with plastic strain rates as follows:

$$W_{ele} = \int_A (\sigma_x \dot{\varepsilon}_x + \sigma_y \dot{\varepsilon}_y + \tau_{xy} \dot{\gamma}_{xy}) dA \tag{8.10}$$

where A = the area of triangular element

Substituting Terzaghi's definition of effective stresses (eqn. 8.4) in equation 8.10 leads to the following:

$$\begin{aligned} W_{ele} &= \int_A [(\sigma'_x + p_w)\dot{\varepsilon}_x + (\sigma'_y + p_w)\dot{\varepsilon}_y + \tau_{xy}\dot{\gamma}_{xy}] dA \\ &= \int_A [\sigma'_x \dot{\varepsilon}_x + \sigma'_y \dot{\varepsilon}_y + \tau_{xy}\dot{\gamma}_{xy} + p_w(\dot{\varepsilon}_x + \dot{\varepsilon}_y)] dA \end{aligned} \tag{8.11}$$

It should be noted that $(\sigma'_x \dot{\varepsilon}_x + \sigma'_y \dot{\varepsilon}_y + \tau_{xy}\dot{\gamma}_{xy})$ represents the plastic strain energy for distortion of the soil skeleton, while $p_w(\dot{\varepsilon}_x + \dot{\varepsilon}_y)$ represents the work done by the water pressure in expanding the volume of the element.

By substituting for the plastic flow in equation 8.9, the effective stress terms can be eliminated from the energy equation as follows:

$$\begin{aligned} W_{ele} &= \int_A \sum_{k=1}^{n} [\dot{\lambda}_k (A_k \sigma'_x + B_k \sigma'_y + C_k \tau_{xy} + p_w (A_k + B_k))] dA \\ &= \int_A \sum_{k=1}^{n} [\dot{\lambda}_k (D_k + p_w (A_k + B_k))] dA \\ &= \int_A \sum_{k=1}^{n} [\dot{\lambda}_k D_k] dA + \int_A \sum_{k=1}^{n} [\dot{\lambda}_k p_w (A_k + B_k)] dA \\ &= \sum_{k=1}^{n} [\dot{\lambda}_k] \int_A 2c' \cos\phi' dA + \sum_{k=1}^{n} [\dot{\lambda}_k (A_k + B_k)] \int_A p_w dA \end{aligned} \tag{8.12}$$

Note that the second term in equation 8.12 expresses the modification due to work done by pore water pressure within the element. For an incompressible material, where $\phi' = \phi = 0$ (total stress), this term vanishes ($A_k + B_k = 0$, equation 8.8b), and there is no work done by the pore pressure.

Since the effective cohesion intercept and pore pressure are assumed to vary linearly throughout the element, the terms in equation 8.12 can be evaluated analytically as:

$$W_{ele} = 2A\cos\phi' \frac{(c'_1 + c'_2 + c'_3)}{3} \sum_{k=1}^{p} [\dot{\lambda}_k] + A \frac{(p_{w1} + p_{w2} + p_{w3})}{3} \sum_{k=1}^{p} [\dot{\lambda}_k (A_k + B_k)] \tag{8.13}$$

where c'_1, c'_2, c'_3 = effective cohesion at node 1, 2, and 3, respectively

p_{w1}, p_{w2}, p_{w3} = pore pressures at node 1, 2, and 3, respectively

The second modification is to include the work done by pore pressure in plastic shearing along velocity discontinuities, which can be done as follows:

For shearing along velocity discontinuities, the Mohr-Coulomb yield criterion can be written in terms of effective normal and shear stresses as two yield functions:

$$F_1 = \tau + \sigma'_n \tan\phi' - c' = 0 \tag{8.14}$$
$$F_2 = -\tau + \sigma'_n \tan\phi' - c' = 0$$

where τ, σ'_n = shear and effective normal stresses

These yield envelopes can be conveniently rewritten as:

$$F_k = A_k \sigma'_n + B_k \tau - c' = 0 \; ; \; k = 1, 2 \tag{8.15a}$$

where $A_1 = \tan\phi', B_1 = 1 \quad ; \quad A_2 = \tan\phi', B_2 = -1$ (8.15b)

The tangential and normal velocity jumps associated with the yield functions are then:

$$\Delta u_t = \sum_{k=1}^{2} \dot{\lambda}_k \frac{\partial F_k}{\partial \tau} = \sum_{k=1}^{2} \dot{\lambda}_k B_k$$
$$\Delta u_n = \sum_{k=1}^{2} \dot{\lambda}_k \frac{\partial F_k}{\partial \sigma'_n} = \sum_{k=1}^{2} \dot{\lambda}_k A_k \tag{8.16}$$

where Δu_t, Δu_n = tangential and velocity jumps

$\dot{\lambda}_k$ = non-negative plastic multiplier rates associated with the yield envelope at velocity discontinuities

The dissipation of power along discontinuity is expressed in terms of total stresses by the following:

$$W_{dis} = \int_L (\tau \Delta u_t + \sigma_n \Delta u_n) dL \tag{8.17}$$

where L = length of velocity discontinuity

Pore pressures can then be brought into this work equation by introducing effective stresses as follows:

$$\begin{aligned} W_{dis} &= \int_L (\tau \Delta u_t + (\sigma_n' + p_w) \Delta u_n) dL \\ &= \int_L (\tau \Delta u_t + \sigma_n' \Delta u_n + p_w \Delta u_n) dL \\ &= \int_L (\tau \Delta u_t + \sigma_n' \Delta u_n) dL + \int_L p_w \Delta u_n dL \end{aligned} \tag{8.18}$$

The first term $(\tau \Delta u_t + \sigma_n' \Delta u_n)$ represents the energy of the soil skeleton dissipated due to plastic shearing along the velocity discontinuity, while $p_w \Delta u_n$ represents the energy due to pore pressure when there is dilation along discontinuities (normal velocity jumps).

The shear and effective normal stresses can be removed from the work equation by substituting the flow rule equation 8.14 as follows:

$$\begin{aligned} W_{dis} &= \int_L \sum_{k=1}^{2} \dot{\lambda}_k (A_k \sigma_n' + B_k \tau + p_w A_k) dL \\ &= \int_L \sum_{k=1}^{2} \dot{\lambda}_k (c' + p_w A_k) dL \\ &= \int_L [c'(\dot{\lambda}_1 + \dot{\lambda}_2) + p_w \tan\phi'(\dot{\lambda}_1 + \dot{\lambda}_2)] dL \end{aligned} \tag{8.19}$$

It should be noted that for undrained soils, where $\phi' = \phi = 0$ (total stress), the terms $p_w \tan\phi'(\dot{\lambda}_1 + \dot{\lambda}_2) = 0$, which shows no influence of pore pressure at velocity discontinuities.

The velocity discontinuity between two elements is characterized by two nodal pairs (1,2) and (3.4), as shown in Figure 8.1. Since the velocity jumps vary linearly along the discontinuity, the terms $\dot{\lambda}_1$, and $\dot{\lambda}_2$ also follow the same linear variation and can be expressed as:

$$\dot{\lambda}_1 = \dot{\lambda}_{(1,2)1}(1-t/L) - \dot{\lambda}_{(3,4)1}(t/L) \tag{8.20}$$

$$\dot{\lambda}_2 = \dot{\lambda}_{(1,2)2}(1-t/L) - \dot{\lambda}_{(3,4)2}(t/L)$$

where $\dot{\lambda}_{(1,2),1}$, $\dot{\lambda}_{(1,2),2}$= plastic multiplier rates associated with F_1, and F_2 at nodal pairs (1,2), $\dot{\lambda}_{(3,4),1}$, $\dot{\lambda}_{(3,4),2}$= plastic multiplier rates associated with F_1, and F_2 at nodal pairs (3,4).

The effective cohesion intercept and pore water pressure are also assumed to vary linearly along the discontinuity as:

$$c' = c'_{(1,2)}(1-t/L) - c'_{(3,4)}(t/L) \tag{8.21}$$

$$p_w = p_{w(1,2)}(1-t/L) - p_{w(3,4)}(t/L)$$

where $c'_{(1,2)}$, $c'_{(3,4)}$ = cohesion at nodal pairs (1,2) and (3,4), respectively

$p_{w(1,2)}$, $p_{w(3,4)}$ = pore pressure at nodal pairs (1,2) and (3,4), respectively

Substituting equations 8.20 and 8.21 into 8.19 and integrating, the power dissipated in each velocity discontinuity can be found as:

$$W_{dis} = \frac{L}{6}\left(2c'_{(1,2)} + c'_{(3,4)} + \tan\phi'(2p_{w(1,2)} + p_{w(3,4)})\right)\left(\dot{\lambda}_{(1,2),1} + \dot{\lambda}_{(1,2),2}\right) + \frac{L}{6}\left(c'_{(1,2)} + 2c'_{(3,4)} + \tan\phi'(p_{w(1,2)} + 2p_{w(3,4)})\right)\left(\dot{\lambda}_{(3,4),1} + \dot{\lambda}_{(3,4),2}\right) \tag{8.22}$$

Equations 8.13 and 8.22 represent the two modifications of the upper bound formulation necessary to include pore water pressures and effective stress strength parameters.

8.4 Validation of Implementation of Pore Water Pressure

This section evaluates the implementation of pore water pressure by analyzing the stability of a homogeneous slope in a cohesive-frictional soil with various pore pressure conditions. Figure 8.2 shows the selected slope with 45° inclination to the horizontal. The

soil has an effective friction angle, $\phi' = 20°$ and cohesion intercept, c'. The first example considers the slope subjected to constant ratio of pore water pressure to total overburden stress (Fig. 8.1):

$$r_u = \frac{p}{\gamma h} \tag{8.23}$$

where p = pore water pressure at any point

γ = total unit weight of soil

h = depth of the point in the soil mass below the ground surface (see Figure 8.2)

The following analyses consider three values of r_u = 0, 0.25, and 0.5. The first case ($r_u = 0$) corresponds to a dry slope.

Table 8.1a summarizes the numerical lower and upper bound predictions of the stability number, $\gamma H/c'$ for the three selected pore pressure ratios, r_u. In all three cases, the lower and upper bound solutions bracket the true stability number within an accuracy of ±5%. The table shows a significant reduction in stability as r_u increases. These results are expected due to the corresponding reduction in effective stress in the soil. Table 8.1 also compares the results of the numerical limit analyses with upper bound solutions obtained by Michalowski (1995a, 1995b), using a rotational mechanism to solve stability factors for a wide range of slope geometries, pore pressures ratios and frictional angles. Michalowski's upper bound solutions are more accurate than the results of the proposed numerical upper bound analyses (stability numbers are 6-8% lower in Table 8.1). However, his solutions are also consistent with the range of stability numbers predicted by the numerical lower and upper bound analyses.

It should be noted that Bishop and Morgenstern (1960) also presented design charts for homogeneous slopes with constant r_u. Unfortunately, their solutions are only available for slope inclination angles less than 27°.

The author performed limit equilibrium calculations of stability using conventional method of slices, as implemented in the commercial UTEXAS3 software (Wright, 1991). The program includes both circular and non-circular searches together with different methods for computing the factor of safety (e.g. Simplified Bishop, 1955; Spencer, 1967). Table 8.1a summarizes stability numbers computed by UTEXAS3 using circular and non-circular shear surfaces with Spencer's method. For all three values of r_u,

LEM predicts stability numbers lower than either numerical upper bound solutions or results of Michalowski (1995). In the case, where r_u = 0.50, the non-circular search generates a stability number equal to the numerical lower bound calculation.

It is difficult to evaluate the accuracy of limit equilibrium calculations due to approximations made in the assumptions of interslice forces. Whitman and Bailey (1967) offered two guidelines for assessing whether limiting equilibrium mechanisms are reasonable:

1) The locations of the thrust line should not fall outside the sliding mass, but should instead pass through the slices at approximately 1/3 the height of each slice (based on the classical theory of earth pressure problem).
2) Interslice shear forces should not exceed the available shear resistance of the soil.

Following these recommendations, the author found that all of the LEM solutions in Table 8.1a (with Spencer method) fail these validation criteria (for both circular and non-circular shear surfaces). In all cases, the locations of the thrust line at some slices which falls outside the sliding mass (see Figure 8.3). Thus, they can be considered as unreasonable solutions; and hence explains why UTEXAS3 generates lower stability numbers than numerical upper bound and Michalovski's solutions.

The second example considers a 45° submerged slope shown in Figure 8.2b, with computed stability numbers presented in Table 8.1b. Numerical limit analyses again bracket the exact solution for this problem within ±5%. It can be seen that the submerged slope has a higher stability than the dry slope (r_u = 0) by 40 – 50%, due to the resistance from water pressure along the side slope. Table 8.1b also shows LEM solutions using UTEXAS3 with circular and non-circular searches (Spencer method). Although the predicted stability numbers from these calculations are within the range of the numerical bound solutions, they should again be regarded with caution as the thrust line for some slices are located outside the failed mass.

Figures 8.4 and 8.5 compare the predicted upper bound failure mechanism for the dry slope (r_u = 0) with the case where r_u = 0.5, and with the case of the submerged slope, respectively. In all three examples, the upper bound mechanism is contained above the

toe of the slope. When pore pressures exist in the soil ($r_u = 0.5$), the predicted failure zone extends further into the soil mass (Figure 8.4). There is no difference in failure mechanism between dry and submerged slopes (Figure 8.5). Critical failure surfaces from circular and non-circular LEM calculations are also superimposed in these figures. These results show small difference between circular and non-circular shear surfaces and are in reasonable (1^{st} order approximation) zones of failure in the predicted upper bound calculations.

8.5 Case study: Stability Analysis of Reinder Failure of Brazil Breakwater

This section describes the application of the proposed stability analyses for assessing the failure of an offshore breakwater in Brazil. This case study is of particular interest as the slope failure has been extensively analyzed using limit equilibrium calculations (with the UTEXAS3 software; Ladd et al., 1993). Full details of the case study have been presented by Ladd et. al (1993). The project, called Terminal Portuario Sergipe (TPS), includes a combined access bridge-conveyor system extending to a loading dock and harbor protected by a rockfill breakwater. Figure 8.6 shows the plan view of the TPS Breakwater. The breakwater is located in a water depth of 10m and is underlain by 4m of sand and 8m of soft, plastic Sergipe clay, as shown in Figure 8.7. The so-called Reinder design (Ladd et. al, 1993) of the 800m-long breakwater consisted of, 1) placing 100-120m wide, 5m high geotechnical berm, 2) allowing the soft clay to consolidate and strengthen under the weight of this berm, and 3) placement of a central rockfill portion to El. 6 m above sea level. A massive failure occurred on placement of the first 100m length of the central rockfill to El. 5m. The failure passed through the underlying Sergipe clay and extended more than 100m along the alignment (Fig. 8.6).

Ladd et al. (1993) performed stability analyses using UTEXAS3 for several embankment geometries, considering two different thickness of Sergipe clay. This chapter presents numerical limit analyses for cross section D of the Reinder Failure (see Figure 8.7), which is the most representative of the central portion of the breakwater and subsurface conditions at the location of the failure. At this site, the sea level is at El. +0.0m, and the soil profile consists of the mudline located at El. –10.2m with 4m of upper sand and 8m of Sergipe clay terminating at El. –22.2m. Note that although the failure occurred on both sides of the breakwater, the stability analyses focus on the

seaside, since the embankment crest was lower on the landside and the access bridge inhibited failure in that direction.

Table 8.2 lists the best estimates of soil properties used in the limit equilibrium stability analyses (Ladd et. al., 1993). These same properties will also be used for numerical limit analyses. Note that the rockfill and geotechnical berm have very high friction angles ($\phi' = 53°$), compared to the upper sand ($\phi' = 35°$). The analyses consider three distributions of undrained strength profiles for the Sergipe Clay, as shown in Figures 8.8.

1) Field vane strength profile (Themag, 1992). This is based on field vane data obtained from the original site investigation (Heerema, 1987) and assumes no lateral variation in undrained strengths within the clay.
2) SHANSEP strength of the virgin clay. These are based on stress history data and normalized strength parameters based on laboratory tests (Ladd and Lee, 1993). Effects on undrained strength anisotropy are included using strength parameters from triaxial compression, $s_u(C)$, extension $s_u(E)$, and direct simple shear $s_u(D)$ tests (as discussed below)[1]. This set of strength parameters assumes no consolidation of the clay prior to the Reinder failure.
3) Revised SHANSEP strengths for partial consolidation. This set of anisotropic strength parameter assumes partial consolidation of the clay beneath the geotechnical berm (zone A, Figure 8.6) and no consolidation (i.e. virgin clay) in zone B beyond the berm. The strength parameters for zone A are based on 1-D consolidation analyses described by Ladd et al. (1993). Note that shear strengths gained due to partial consolidation occur in the top and the base of the clay layer.

Figure 8.8 also compares the strength profiles in direct simple shear mode for three analysis cases. Below El. –15, $s_u(FV)$ is approximately 15 % higher than revised and virgin SHANSEP strengths. There is also a significant difference in $s_u(D)$ between Revised and Virgin profiles at El. –21.2 to –22.2, and in $s_u(C)$ at El. –14.2 to –16.2.

[1] These parameters are based on strain compatibility methods proposed by Ladd (1991).

Figure 8.9 shows the spatial discretization of the breakwater for the numerical limit analyses. The soil is discretized into three-noded triangular plane strain elements. The water table is at El. +0.0. Pore water pressures are considered in the rockfill geotechnical berm, and upper sand layers. The unit weights and effective friction angles of these layers are listed in Table 8.2. The top layer of lower sand is treated as a rigid boundary in the analyses. The limit analyses consider three sets of undrained strength parameters for the Sergipe clay. Undrained strength anisotropy is simulated using the yield function of Davis and Christian (1971) (c.f. Chapter 4, Section 4.4). The analyses assumed that $s_u(0°) = s_u(C)$, $s_u(45°) = s_u(D)$, and $s_u(90°) = s_u(E)$, where $s_u(\delta°)$ = undrained strength corresponding to the major principal stress rotating, $\delta°$, relative to the vertical.

There are some differences in handling the anisotropic strength of clay between numerical limit analyses and limit equilibrium (UTEXAS3) analyses. UTEXAS3 program models anisotropy by inputting shear strength as a function of inclination of the shear surface, α ($s_{u\alpha}$). Figure 8.10 compares the undrained strength ratio, $s_{u\alpha}/s_u(D)$ used for the virgin and revised SHANSEP profiles as function of α (after Ladd et al., 1993). The parameter $s_{u\alpha}$ can also be derived from anisotropic strength function of Davis and Christian (1971) used in the numerical limit analyses (c.f. Chapter 4, Section 4.4.2, equation 4.25):

$$s_{u\alpha} = |\tau_1| = \left| h\sin 2\alpha - \sqrt{\frac{a^2 + b^2 - a^2\cos 4\alpha + b^2\cos 4\alpha}{2}} \right| \qquad (8.24)$$

where $h = [s_u(0°) - s_u(90°)]/2$

$a = [s_u(0°) + s_u(90°)]/2$

$$b = \frac{a \times s_u(45°)}{\sqrt{s_u(0°) \times s_u(90°)}}$$

and $s_u(0°)$, $s_u(45°)$, $s_u(90°)$ are undrained shear strengths at δ = 0°, 45°, 90°, respectively.

Figure 8.10 shows that $s_{u\alpha}$ used in the limit equilibrium calculations is piecewise linear, while the limit analyses correspond to a sinusoidal function of α. The results show that the anisotropic strength criterion used in the limit analyses corresponds to higher

values of $s_{u\alpha}$ than those used by Ladd et al. (1993) for all inclination angle, $-90° \leq \alpha \leq 90°$.

The definition of factor of safety (FS) used in numerical limit analyses of Reinder failure is based on the conventional definition of FS which assumes the same degree of mobilization for cohesion intercept and friction angle as:

Drained materials: $$FS = \frac{c'}{c'_m} = \frac{\tan\varphi'}{\tan\varphi'_m} \tag{8.25}$$

Undrained materials: $$FS = \frac{s_u}{s_{um}}$$

where c'_m, ϕ'_m = mobilized effective cohesion intercept and friction angle

s_{um} = mobilized undrained shear strength

Note that this definition is also used in the limit equilibrium calculations of UTEXAS3 program.

Table 8.3 summarizes the results of numerical limit analyses for the Reinder failure. For all strength profiles, numerical lower and upper bound calculations bound the factor of safety within an error of ±5%. The results show that the isotropic field vane strength profile, s_u(FV) predicts factor of safety 10% higher than the revised SHANSEP s_u (profile 3) and 4% higher than the virgin SHANSEP s_u. The limit analyses predict failure (FS < 1.0) both virgin and revised strength profiles, while field vane strength data suggest the section is stable.

Also shown in this table are the results of limit equilibrium calculations using UTEXAS3 with Spencer's method (Spencer, 1967) for circular, wedge, and non-circular shear surfaces[2]. The factor of safety corresponding to the non-circular shear surface is reported as the best estimate of stability for Reinder breakwater (Ladd et. al, 1993). The results of UTEXAS3 also show similar trends among the three strength profiles as the numerical limit analyses (i.e. $FS_1 > FS_3 > FS_2$). In addition, results using non-circular shear surfaces predict that stability of breakwater is inadequate for all three strength profiles, with factor of safety approximately 15% lower than circular shear surfaces.

[2] The author has replicated the original LEM results of non-circular shear surfaces.

There is a significant difference in the factor of safety computed by numerical limit analyses and UTEXAS3 with non-circular shear surfaces. For all strength profiles, the non-circular shear surfaces predict factors of safety that are approximately 13-15% lower than the numerical upper bound, and 7-8% lower than numerical lower bound solutions. Figure 8.11 summarizes the results of the limit equilibrium analyses with non-circular shear surfaces. The results show a failure surface extending beyond the toe of the geotechnical berm with a steep ($\alpha \approx 70°$) backscarp through the rock fill close to the centerline of the breakwater. The surfaces exhibit an unusual double hump curvature close to the base of the Sergipe clay.

Figures 8.12 – 8.14 show the predicted upper bound failure mechanisms for the Reinder breakwater with the three undrained strength profiles. The darker shading (e.g. Figure 8.12a) shows the plastic shearing zone in the soil. Generally, the upper bound analysis predicts a deep seated failure in the Sergipe clay. The plastic zone intersect the rockfill about 5m beyond the centerline axis (x = 100m), and emerges in the upper sand layer beyond the geotechnical berm. Results of critical failure surfaces predicted by UTEXAS3 for circular, wedge, and non-circular shear searches are also superimposed on those figures. The comparisons show the following:

1.) The limit analyses and limit equilibrium solutions predict similar zones of failure in the toe region, but limit equilibrium calculations show a much smaller failure zone within the rockfill (for all three strength cases).

2.) Neither the wedge nor circular shear surfaces match the predicted plastic zone from the upper bound analyses even though they produce relatively similar magnitudes of safety factor.

3.) It is interesting to note that the shape of wedge and non-circular shear surfaces differs only in the rockfill layer, but the factor of safety of the latter decreases approximately by 12%.

Table 8.4 summarizes the results of a new stability calculation using UTEXAS3 (with non-circular shear surface) with anisotropic undrained strength that matches the yield criterion of Davis and Christian (1971) used in limit analyses (sinusoidal $s_{u\alpha}$ in Fig. 8.10). It can be seen that $s_{u\alpha}$ has a very small effect on the computed factor of safety (within 2%). These results confirm that differences between numerical limit analyses and

limit equilibrium calculations are due mainly to approximation associated with methods of slices.

Further analyses have been carried out to explain why UTEXAS3 (non-circular shear surface) predicts a lower factor of safety than the upper bound analyses. These analyses focus on the field vane strength, s_u(FV). Figure 8.15 compares the factor of safety of selected non-circular shear surfaces (computed by UTEXAS3) with results of the upper bound analysis. Note that these shear surfaces differ only in the backscarp through the rock fill (i.e. x > 80m). It can be seen a non-circular shear surface with similar failure zone to the upper bound calculation produces a very similar factor of safety. This result confirms that the low factor of safety from UTEXAS3 is directly linked to the location of the backscarp. The next step of the diagnosis assesses why the upper bound analyses do not predict the same zone of failure as limit equilibrium calculations.

Referring to Figure 8.12, it can be seen that there are small differences between the shape of non-circular and wedge surfaces. In order to answer the above question, the author performed upper bound calculations on the pre-assumed wedge surfaces in Figure 8.12. The results of these analyses are illustrated in Figure 8.16 and 8.17 for different mesh refinements. The upper bound analyses predict a very small difference in factor of safety between two meshes (FS = 1.248 vs. 1.245). It can be seen that the factor of safety for the upper bound wedge mechanism in Figure 8.17 (FS = 1.245), is higher than that of upper bound mechanism in Figure 8.12 (FS = 1.124). Accordingly, the reason why the upper bound analyses does not match the failure backscrap of UTEXAS3 is that this mechanism is not critical (the critical upper bound mechanism found corresponds to Figure 8.12). Since UTEXAS3 gives a factor of safety for wedge surface, FS = 1.105, which is lower than the upper bound predictions of 1.245, it can be concluded that the results of wedge surface from UTEXAS are misleading. Furthermore, the calculation of FS = 0.981 for the non-circular shear surface (failure zone very similar to the wedge mechanism in Figures 8.16, 8.17) is not reasonable. It appears that there is a significant error associated with non-circular shear surface in the limit equilibrium calculations (similar conclusions can be drawn for the results of anisotropic revised and virgin strength profiles).

The validity of limit equilibrium (method of slice) calculaitons can be assessed by considering the thrust line locatior and orientation. For the non-circular shear surfaces, the thrust line lies within the soil mass (see Figure 8.18). However, the resultant force inclination (using Spencer's method) is almost horizontal for all cases of strength profiles and shear surfaces (wedge, non-circular). This means that the magnitude of interface shear on each slice is very small, and thus one would obtain similar results with the simplified Bishop's method (1955)[3]. The shear force on each slice may have small influence on the clay layer, but should have significant effect for frictional materials, such as the rockfill and geotechnical berm ($\phi' = 53°$). Hence, the author believes that the limit equilibrium calculation mobilizes unreasonably small interface shear forces in these intervals and this may explain the very low factor of safety obtained for the Reinder failure.

It can not be concluded from this study that limit equilibrium calculations with Spencer method and non-circular shear surfaces always give a conservative factor of safety. Instead, the direction and magnitude of error are unknown due to the assumption of a constant orientation of interslice forces, search procedure to locate the most critical failure surface, and the shape of failure surface. Recent studies by Yu et. al. (1998) and Michalowski (1995a,b) have used limit analyses to check the accuracy of limit equilibrium calculations for slope stability problems. For small slope inclinations in clay (strength increasing with depth), Yu et. al (1998) find that the simplified Bishop's method can produce a much lower stability number than numerical lower bound solutions. Michalowski (1995a,b) has also shown that the simplified Bishop's method generates lower stability numbers than his upper bound mechanism for cases of very steep slopes, while other slope geometries give similar or higher values of FS. It is clear that without rigorous solutions from limit analyses, it is difficult to assess the accuracy of limit equilibrium methods.

---

[3] In simplified Bishop (1955), the interface shear force is assumed to be zero for all slices. A useful checking for Spencer method is to plot the factor of safety by force and moment equilibrium as a function of the inclination of side force resultant. Unfortunately, UTEXAS3 does not have a capability to check that. The program reports only the sum of force and moment equations for a trial factor of safety.

8.6 References

Bishop, A. W. (1955). "The use of the slip circle in the stability analysis of slopes." Géotechnique, 5, 7-17.

Bishop, A. W., and Morgenstern, N. R. (1960). "Stability coefficients for earth slopes." Géotechnique, 10(4), 129-150.

Davis, E. H., and Christian, T. J. (1971). "Bearing capacity of anisotropic cohesive soil". J. Soil Mech. Found. Div., ASCE, 97(5), 753-769.

Ladd, C. C. (1991). "Stability evaluation during staged construction." The Twenty-Second Terzaghi Lecture, J. of Geotech. Engrg. Div., ASCE, 117(4), 537-615.

Ladd, C. C., and Lee, S-M. (1993). "Engineering properties of the Sergipe Clay." TPS Progress Report No. 4, Research Report 93-07, March 19, 1993, Dept. of Civil and Environmental Engineering, MIT, Cambridge, MA.

Ladd, C. C, Lee, S-M, and Whelan, M. P. (1993). "Backanalyses of the Reinder Failure." TPS Progress Report No. 5, Research Report 93-10, May 29, 1993, Dept. of Civil and Environmental Engineering, MIT, Cambridge, MA.

Lee, S-M (1995). "Stability and deformation during staged construction of an offshore breakwater on soft clay." PhD thesis, Dept. of Civil and Environmental Eng., Massachusetts Institute of Technology, Cambridge, MA.

Michalowski, R. L. (1995a). "Slope stability analysis: a kinematic approach." Géotechnique, 45(2), 283-293.

Michalowski, R. L. (1995b). "Stability of slopes: Limit analysis approach." Reviews in Engineering Geology, 10, 51-62.

Wrigth, S. G. (1991). "UTEXAS3, A computer program for slope stability calculations." Shinoak Software, Austin, TX, Revised Sept. 1991.

Sloan S. W. (1988). "Lower bound limit analysis using finite elements and linear programming." Int. J. Numer. Anal. Methods in Geomech., 12(1), 61-77.

Sloan S. W., and Kleeman, P. W. (1995). "Upper bound limit analysis using discontinuous velocity fieids." Computer Methods in Applied Mechanics & Engineering, 127, 293-314.

Spencer, E. (1967). "A method of analysis of the stability of embankments assuming parallel interslice forces" Géotechnique, 17, 11-26.

Whitman, R. V., and Bailey, W. A. (1967). "Use of computers for slope stability analysis." J. Soil. Mech. Found. Div, ASCE, 93(SM4), 475-498.

Yu, H. S., Salgado, R., Sloan, S. W. (1998). "Limit analysis versus limit equilibrium for slope stability." J. of Geotech. Engrg., ASCE, 124 (1), 1-11.

Stability number, $\gamma H/c'$

Slope with r_u	Numerical Limit Analyses LB – UB	Michalowski (1995) UB Rotational Mechanism	Limit Equilibrium Calculation UTEXAS3 W/ Spencer Method	
			Circular Search	Non-Circular Search
$r_u = 0$ (no pore pressure)	14.95 – 17.60	16.16	16.02*	15.84*
$r_u = 0.25$	10.54 – 11.65	10.94	10.80*	10.68*
$r_u = 0.50$	7.74 – 8.36	7.99	7.87*	7.74*

*Locations of thrust line at some points are located outside sliding mass

a) Example1: Slope with constant pore water pressure ratio (slope angle = 45°, $\phi' = 20$)

Stability number, $\gamma H/c'$

Numerical Limit Analyses LB – UB	Limit Equilibrium Calculation UTEXAS3 with Spencer's Method	
	Circular Search	Non-Circular Search
22.44 – 25.09	23.52*	23.14*

*Locations of thrust line at some points are located outside sliding mass

b) Example 2: Slope submerged under water (slope angle = 45°, $\phi' = 20$)

Table 8.1 Validation of pore water pressure formulation for numerical limit analyses

Soil	Unit Weight (kN/m^3)	Strength
Rockfill	Dry, $\gamma_d = 18.0$ Total, $\gamma_t = 20.0$	Effective frictional angle, $\phi' = 53°$
Berm	Total, $\gamma_t = 20.0$	Effective frictional angle, $\phi' = 53°$
Upper Sand	Total, $\gamma_t = 18.0$	Effective frictional angle, $\phi' = 35°$
Sergipe Clay	Total, $\gamma_t = 16.0$	Profile 1, Field Vane, s_u(FV) (isotropic) Profile 2, SHANSEP Virgin, s_u (anisotropic) Profile 3, SHANSEP Revised, s_u (anisotropic)

Table 8.2 Soil properties for stability analyses of Reinder breakwater

Factor of Safety (FS)

Soil Profile	Numerical Limit Analyses LB – UB	Limit Equilibrium Calculations using UTEXAS3		
		Circular (Bishop's Method)	Wedge (Spencer's Method)	Non-circular (Spencer's Method)
Profile 1, Isotropic strength Field Vane s_u Themag (1992)	1.046 – 1.124	1.175	1.105	0.981
Profile 2, Anisotropic strength SHANSEP Virgin s_u	0.921 – 0.985	1.069	0.961	0.843
Profile 3, Anisotropic strength SHANSEP Revised s_u	0.955 – 1.021	1.086	0.987	0.876

Note:

1) Geometry of Section D
2) UTEXAS3 anisotropic strength analyses use $s_{u\alpha}$ step-function (Ladd et. al, 1993).

Table 8.3 Summary of stability analyses of Reinder breakwater

Factor of Safety (FS)

Soil Profile	Numerical Limit Analyses LB – UB	UTEXAS3 Non-circular shear surface (Spencer's Method)	
		$s_{u\alpha}$ Step-Function (Ladd et. al., 1993)	$s_{u\alpha}$ from UB Limit Analyses
Profile 2, Anisotropic Strength SHANSEP Virgin s_u	0.921 – 0.985	0.843	0.858
Profile 3, Anisotropic Strength SHANSEP Revised s_u	0.955 – 1.021	0.876	0.895

Note:
1) Geometry of Section D

Table 8.4 Effect of anisotropic strength $s_{u\alpha}$ in UTEXAS3 stability analyses of Reinder breakwater

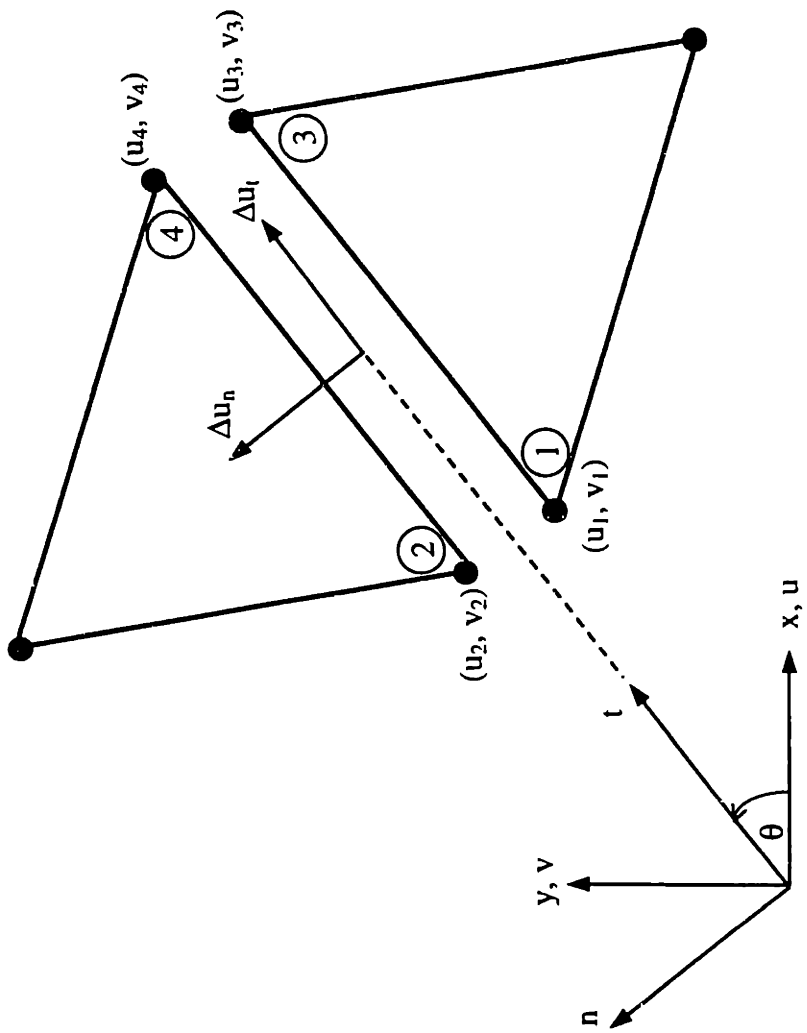

Tangential velocity jump, $\Delta u_t = (u_j - u_i)\cos\theta + (v_j - v_i)\sin\theta$

Normal velocity jump, $\Delta u_n = -(u_j - u_i)\sin\theta + (v_j - v_i)\cos\theta$

Figure 8.1 Velocity discontinuity for the upper bound calculation

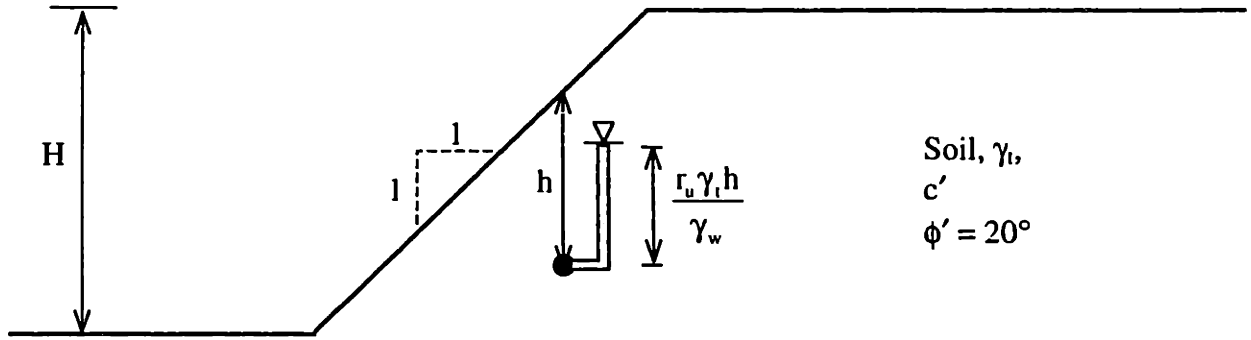

a) Example 1: Slope subjected to constant pore water pressure ratio, $r_u = 0, 0.25, 0.5$

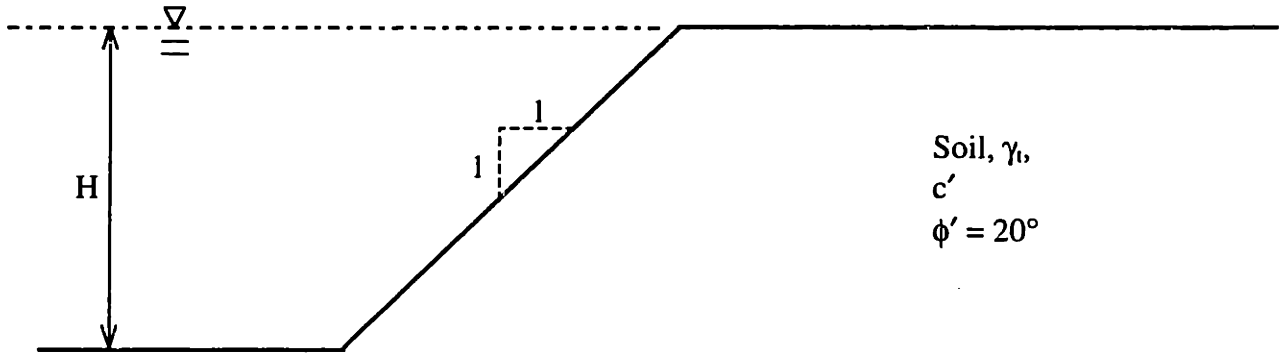

b) Example 2: Slope submerged under the water

Figure 8.2. Problems of homogeneous slopes with pore water pressure

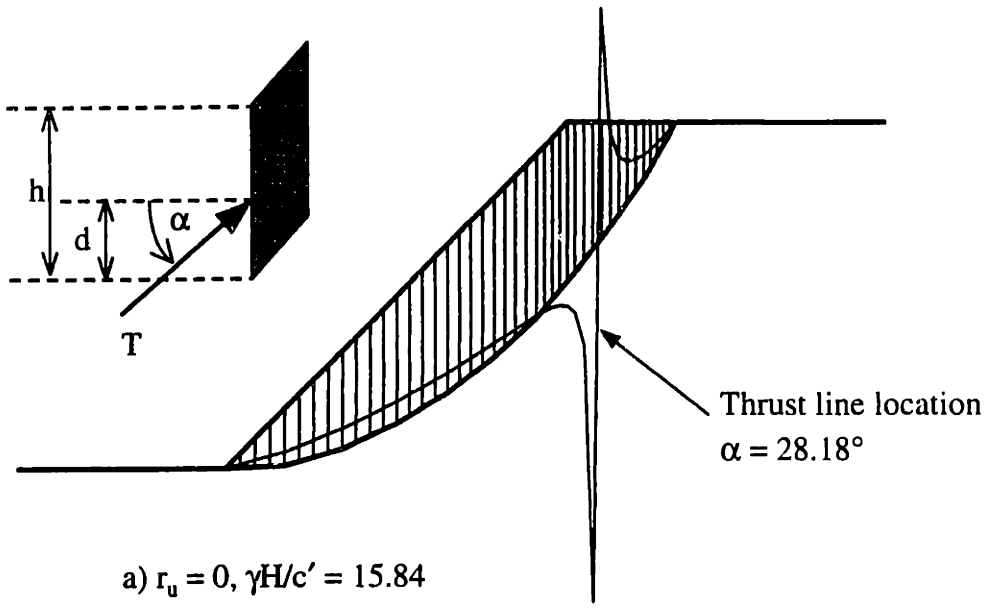

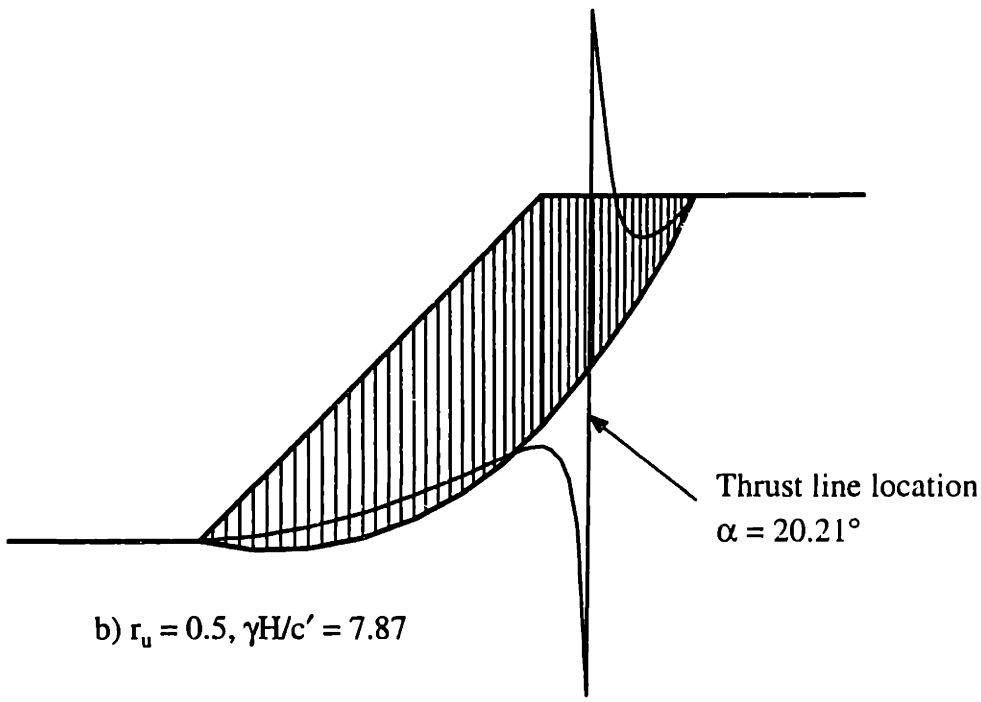

Figure 8.3 Results of UTEXAS3 with non-circular searches (Spencer's method) for slopes subjected to pore pressure, r_u (ϕ' = 20°, slope angle = 45°)

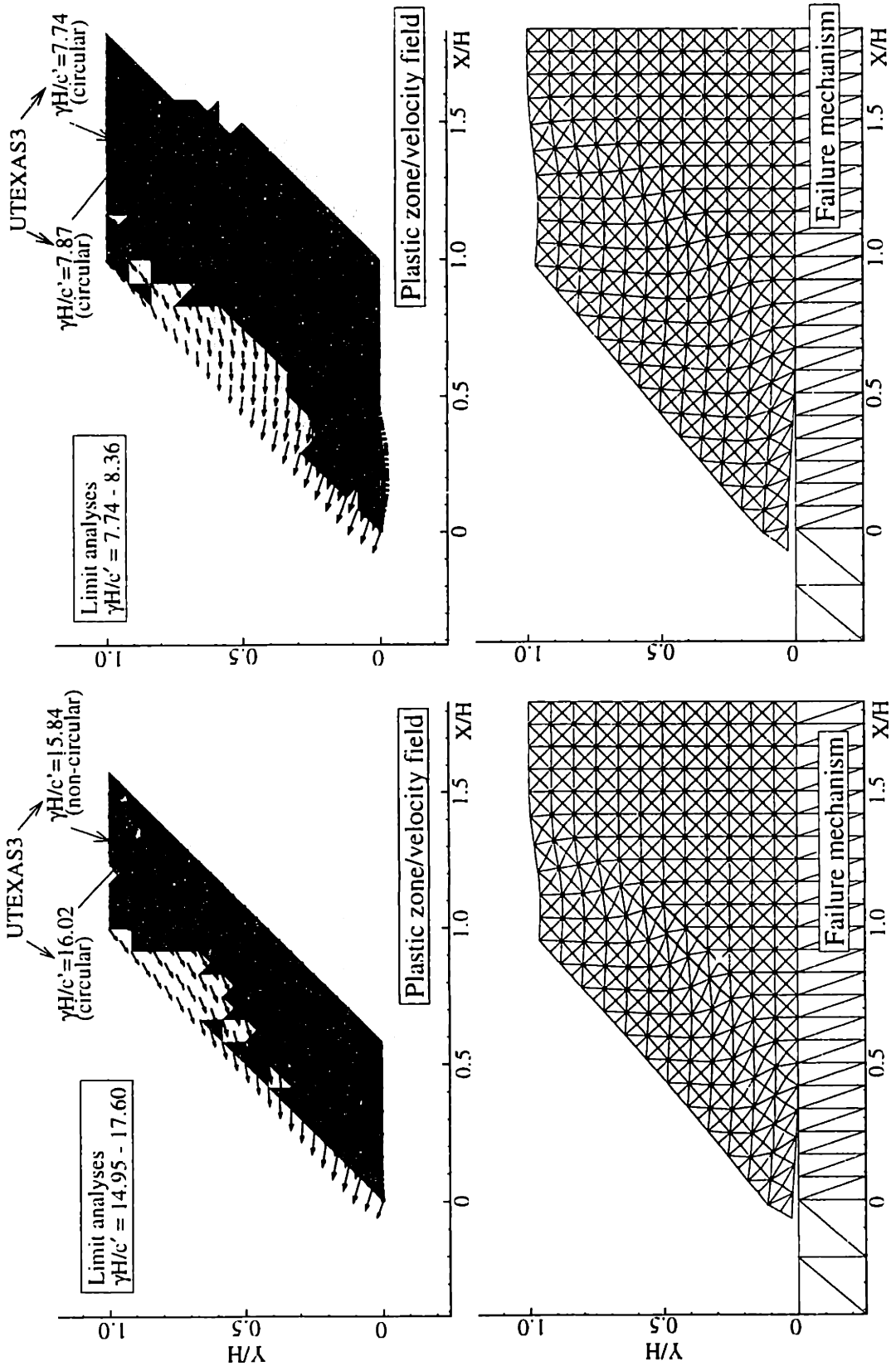

Figure 8.4 Upper bound results for slopes subjected to pore water pressure ratio, r_u ($\phi' = 20^o$, slope angle = 45^o)

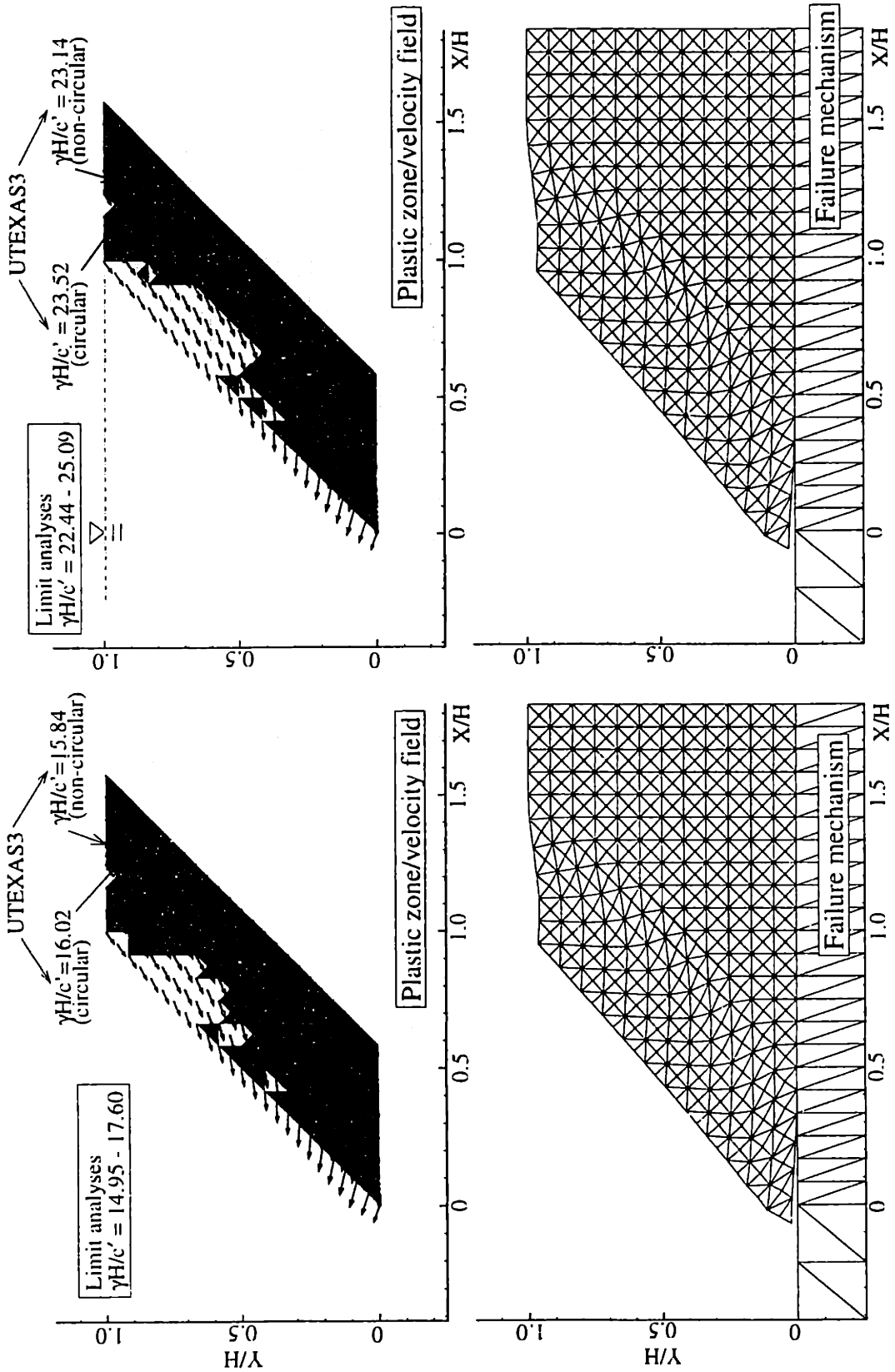

a) Dry slopes

b) Submerged slopes

Figure 8.5 Upper bound results for dry and submerged slopes ($\phi' = 20°$, slope angle = 45°)

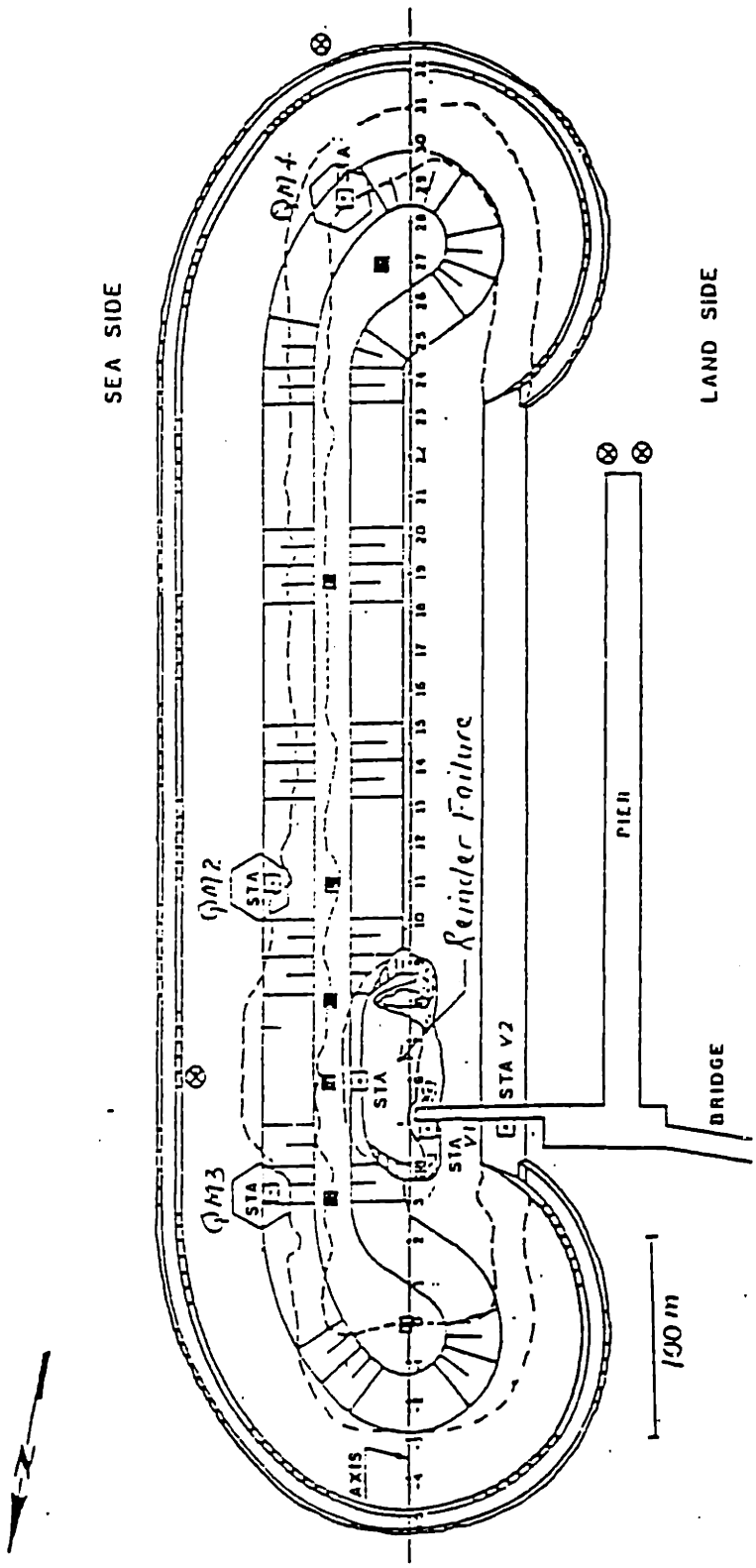

Figure 8.6 Plan view of TPS Reinder breakwater (after Ladd et al., 1993)

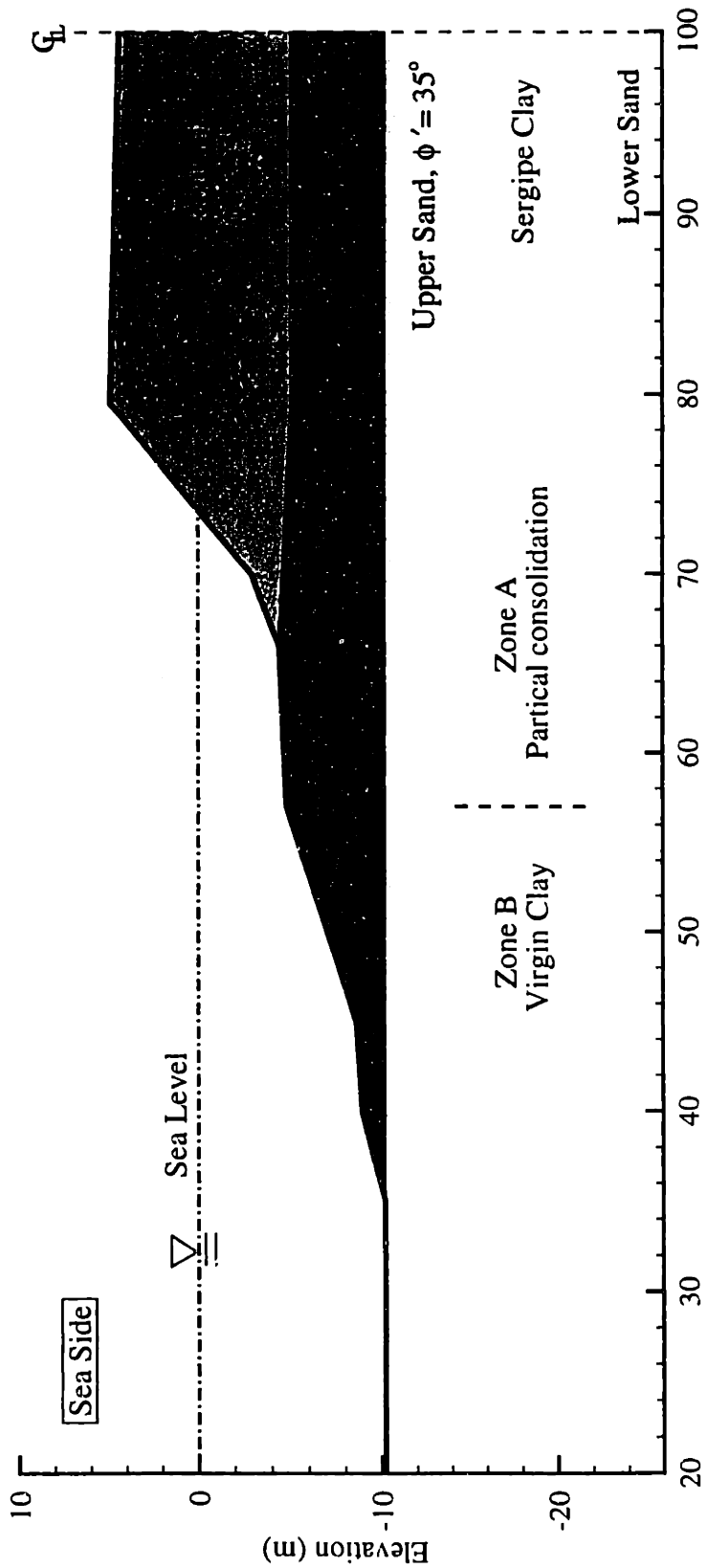

Figure 8.7 Cross sections of the Reinder breakwater, Section D (after Ladd et al., 1993)

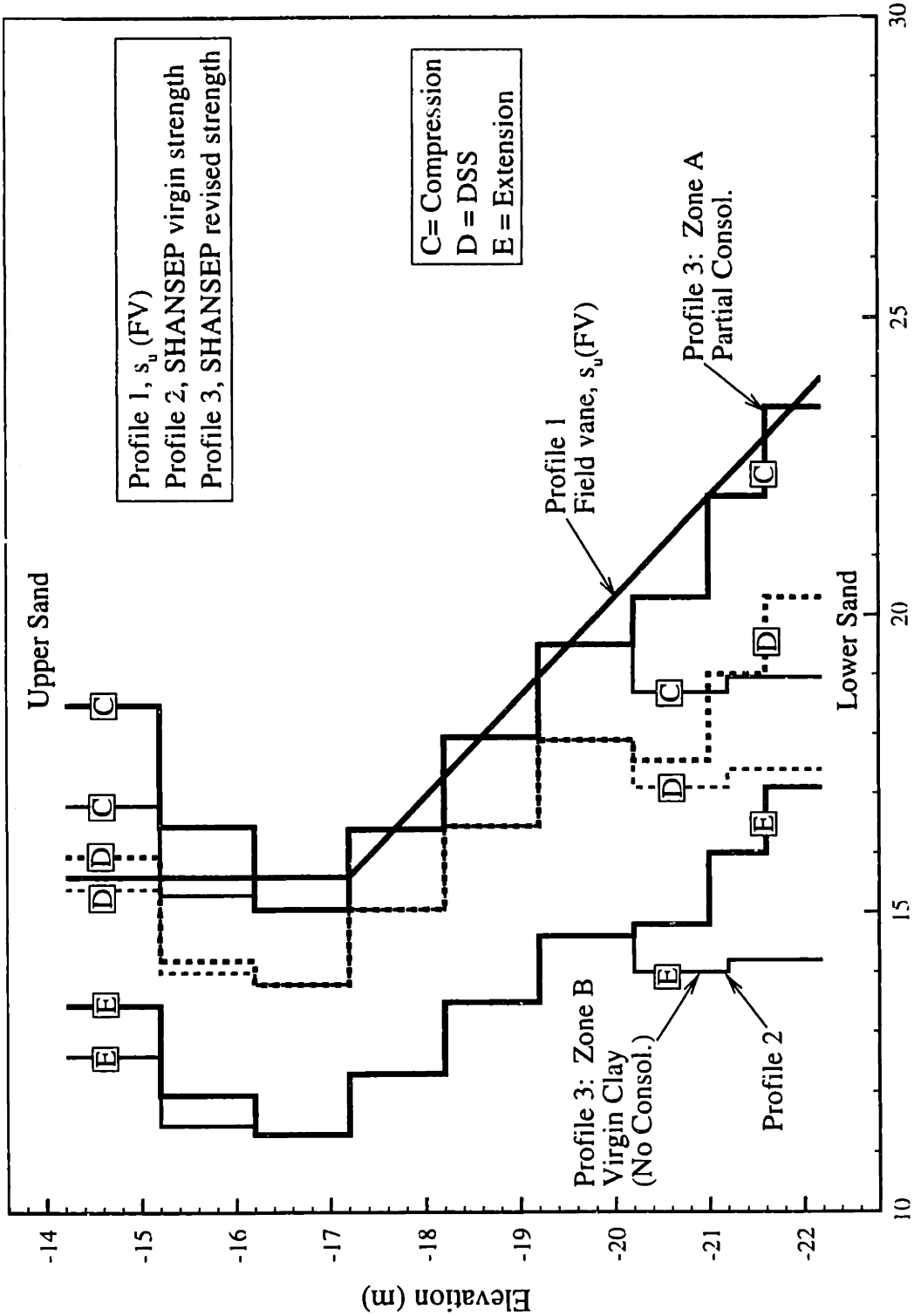

Figure 8.8 Undrained strength profiles of Sergipe clay for the Reinder failure (after Ladd et al., 1993)

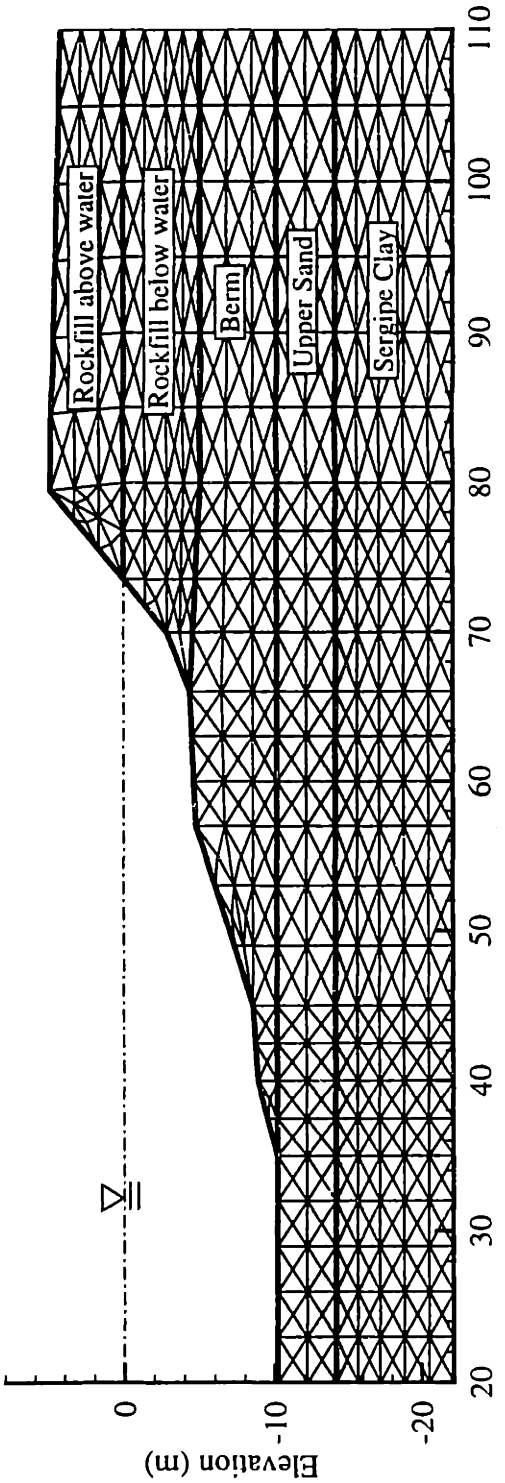

Figure 8.9 Spatial discretization of Reinder breakwater used for numerical limit analyses

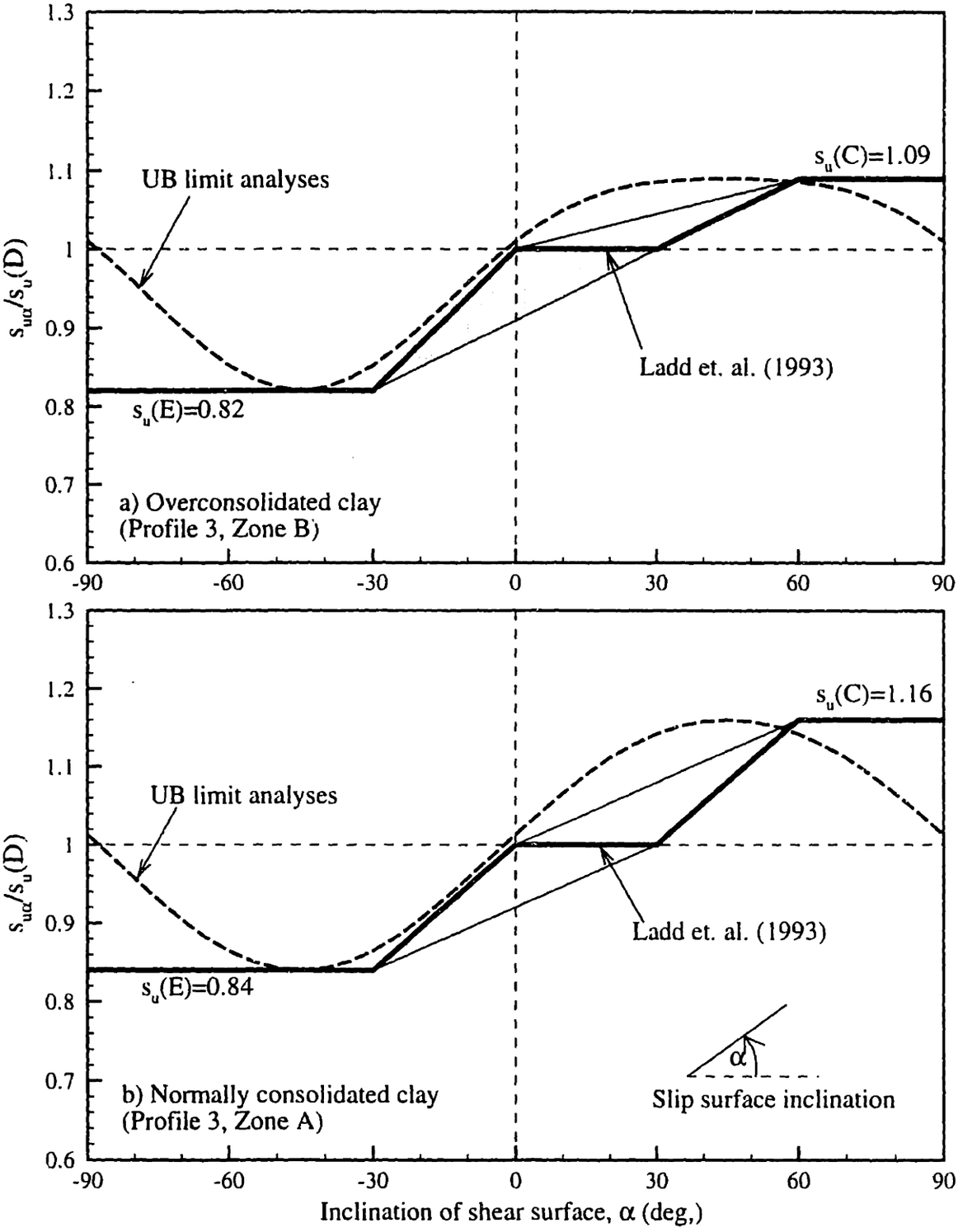

Figure 8.10 Comparison of undrained strength anisotropy for limit analyses and limit equilibrium (UTEXAS3) calculations

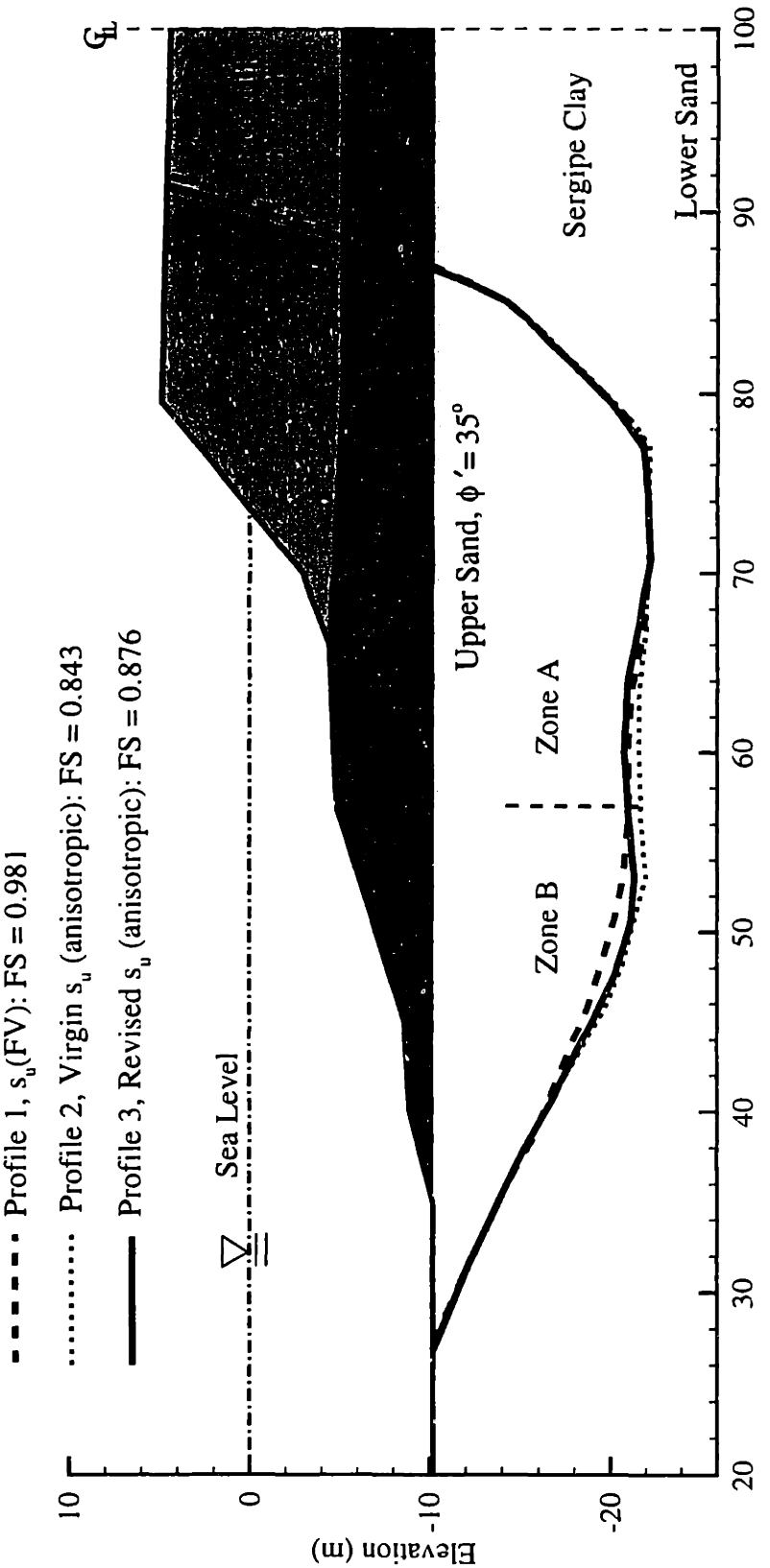

Figure 8.11 Critical non-circular shear surfaces from UTEXAS3 for the Reinder faiure (after Ladd et al. 1993)

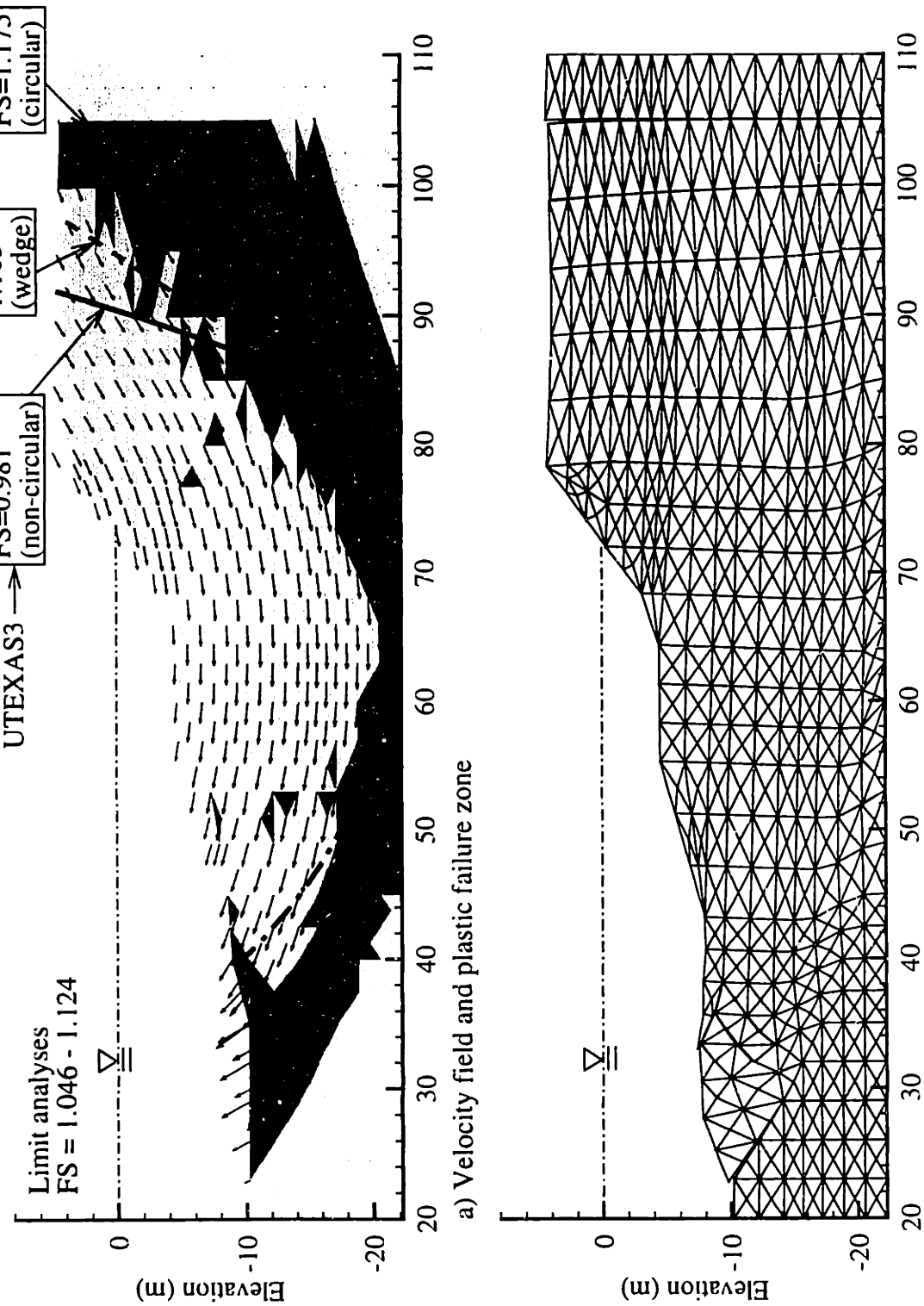

a) Velocity field and plastic failure zone

b) Failure mechanism

Figure 8.12 Upper bound results for Reinder failure for field vane strength s_u(FV)

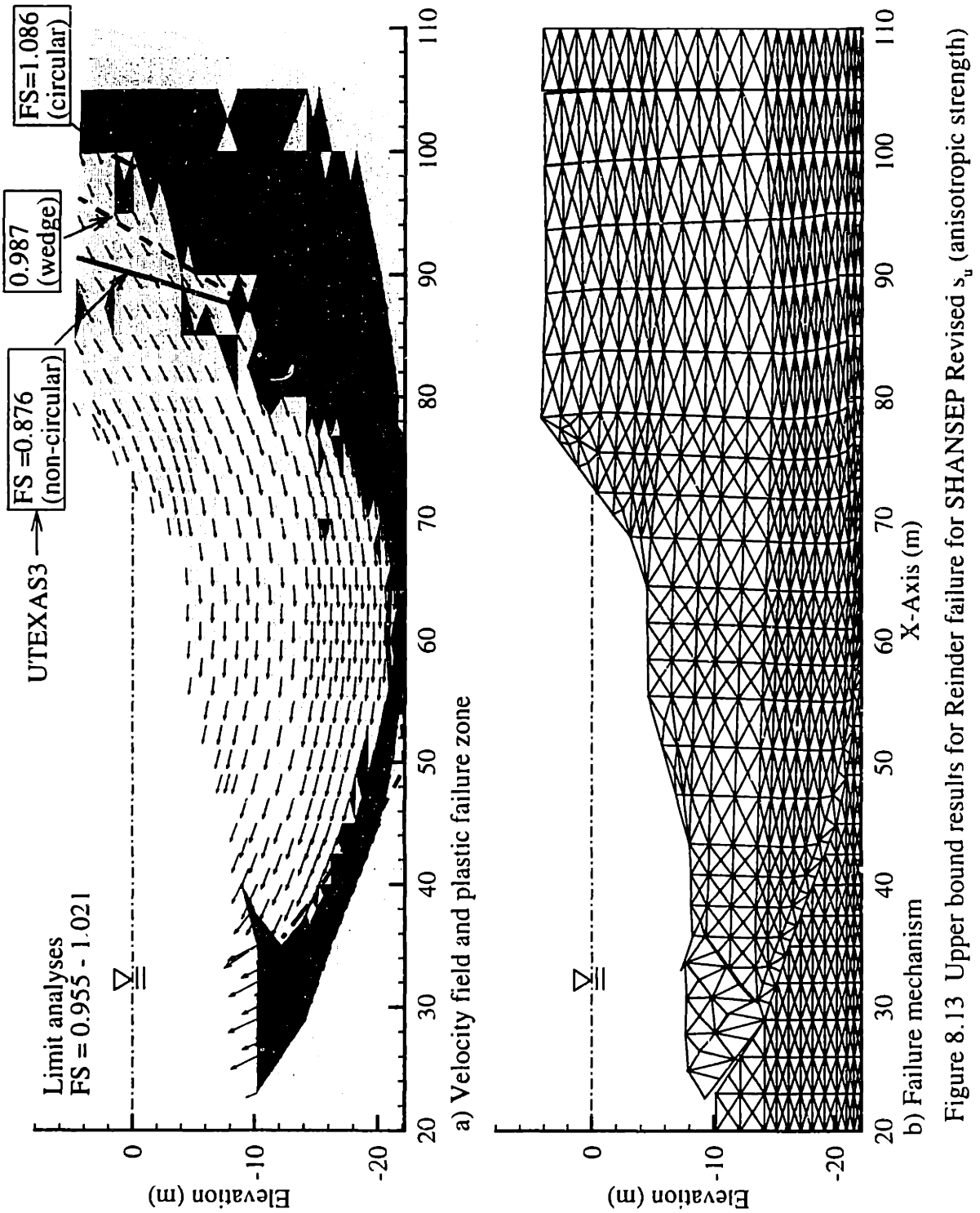

a) Velocity field and plastic failure zone

b) Failure mechanism

Figure 8.13 Upper bound results for Reinder failure for SHANSEP Revised s_u (anisotropic strength)

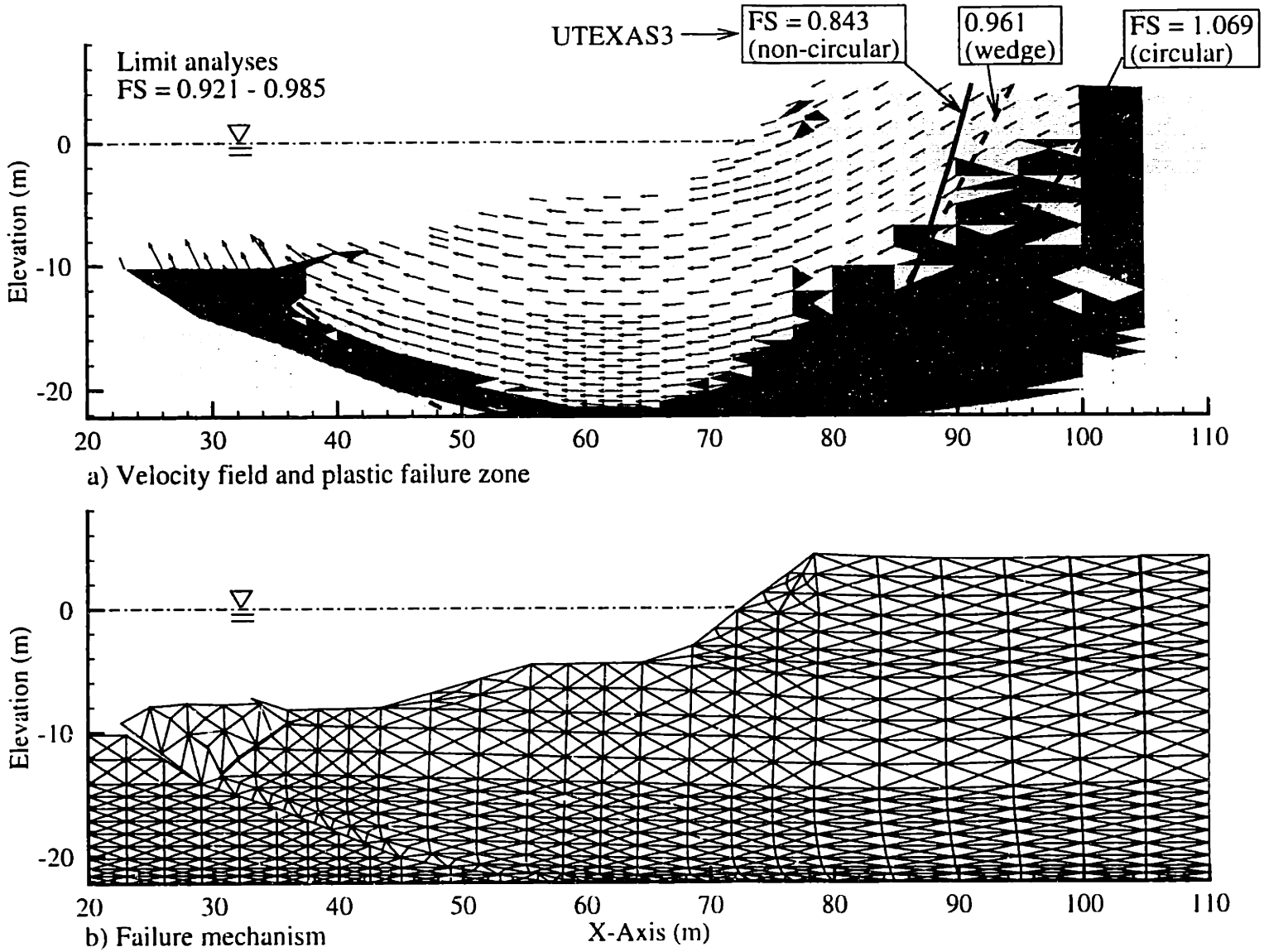

Figure 8.14 Upper bound results for Reinder failure for SHANSEP Virgin s_u (anisotropic strenght)

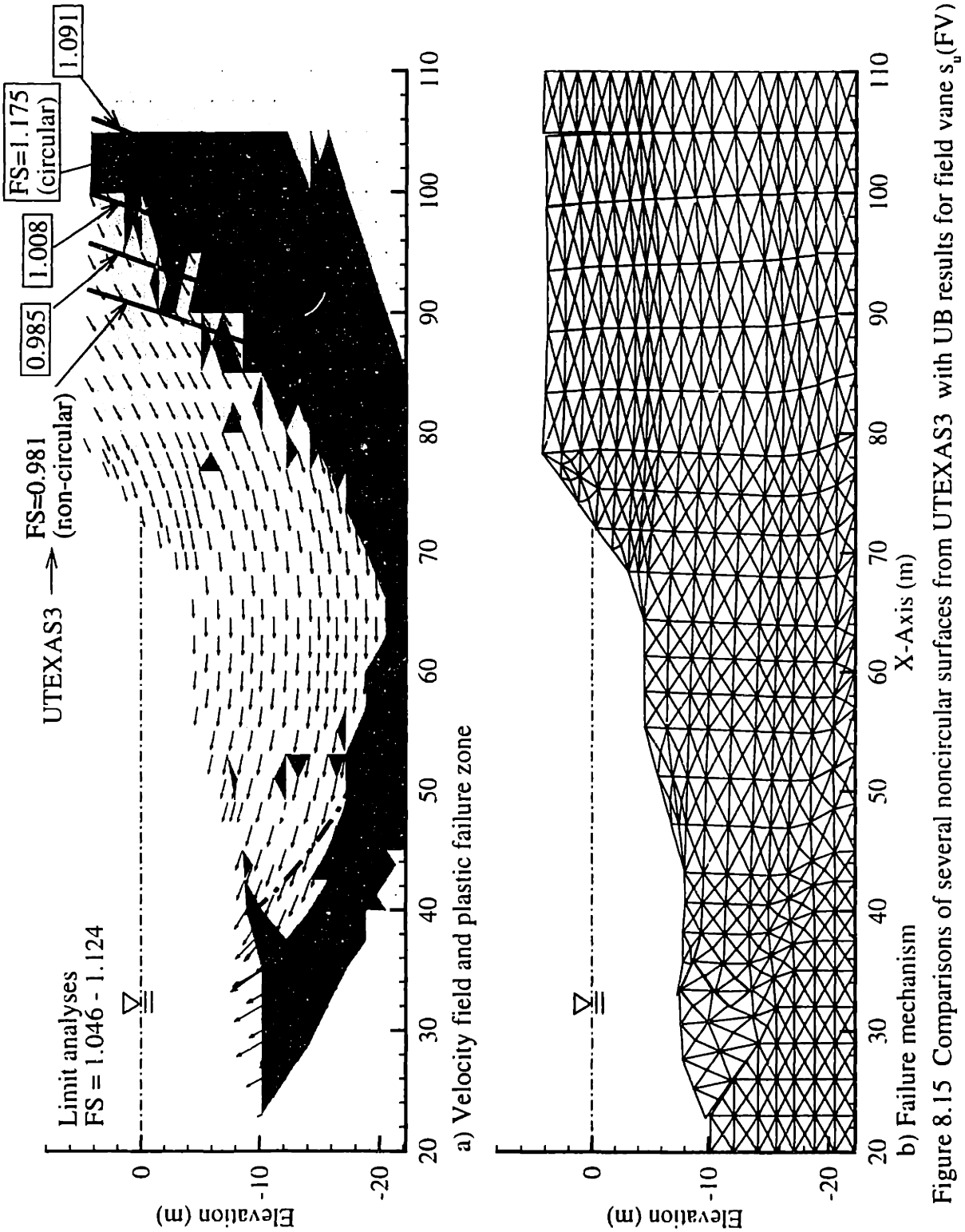

a) Velocity field and plastic failure zone

b) Failure mechanism

Figure 8.15 Comparisons of several noncircular surfaces from UTEXAS3 with UB results for field vane s_u(FV)

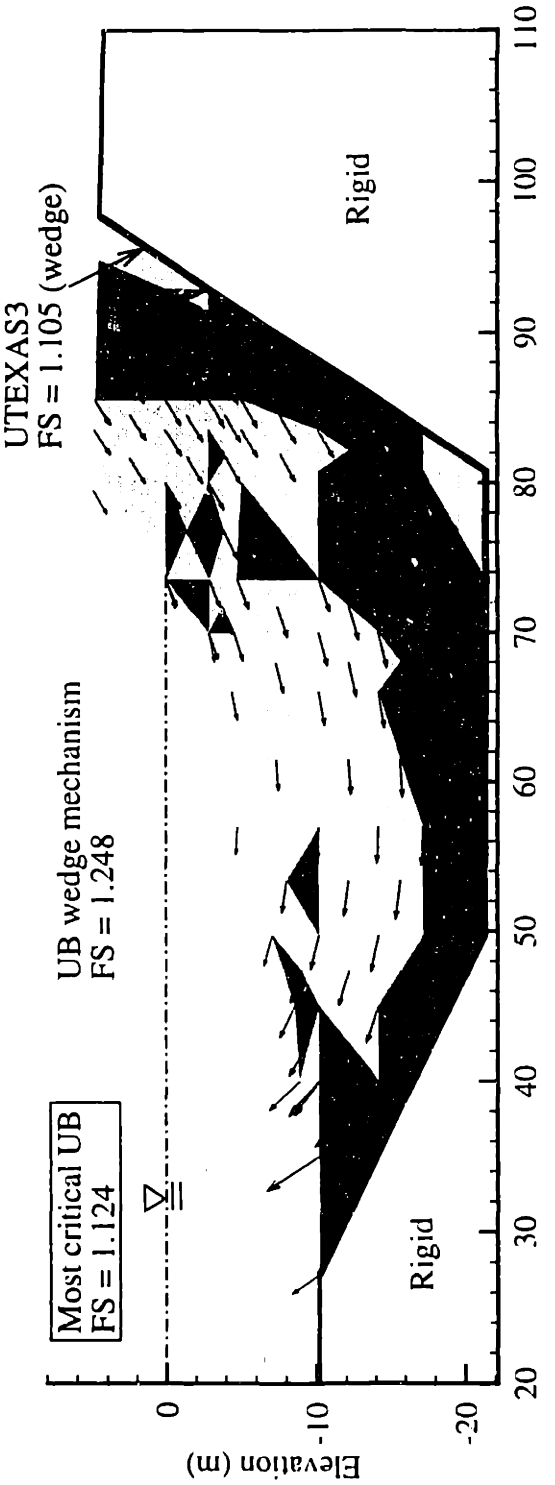

a) Velocity field and plastic failure zone

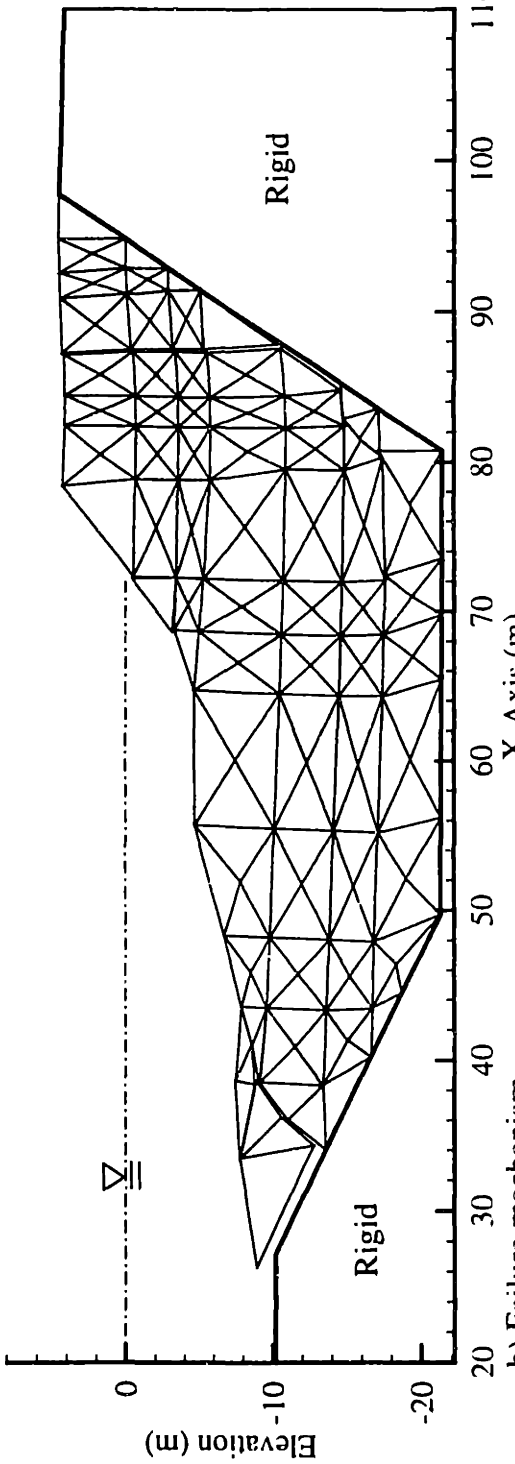

b) Failure mechanism

Figure 8.16 Upper bound results of wedge mechansim with small refinement, field vane strength s_u(FV)

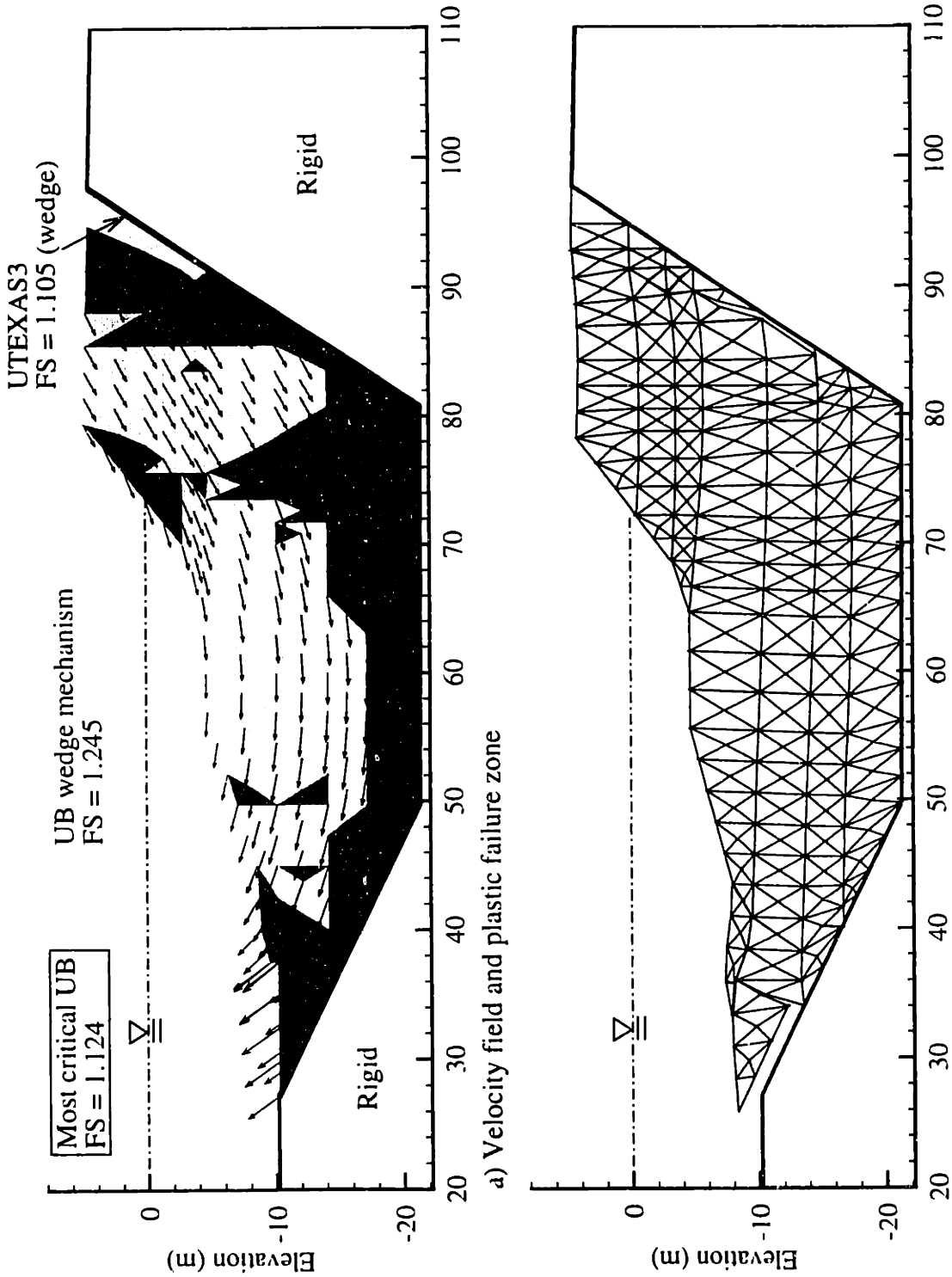

a) Velocity field and plastic failure zone

b) Failure mechanism

Figure 8.17 Upper bound results of wedge mechansim with more refinement, field vane strength, s_u(FV)

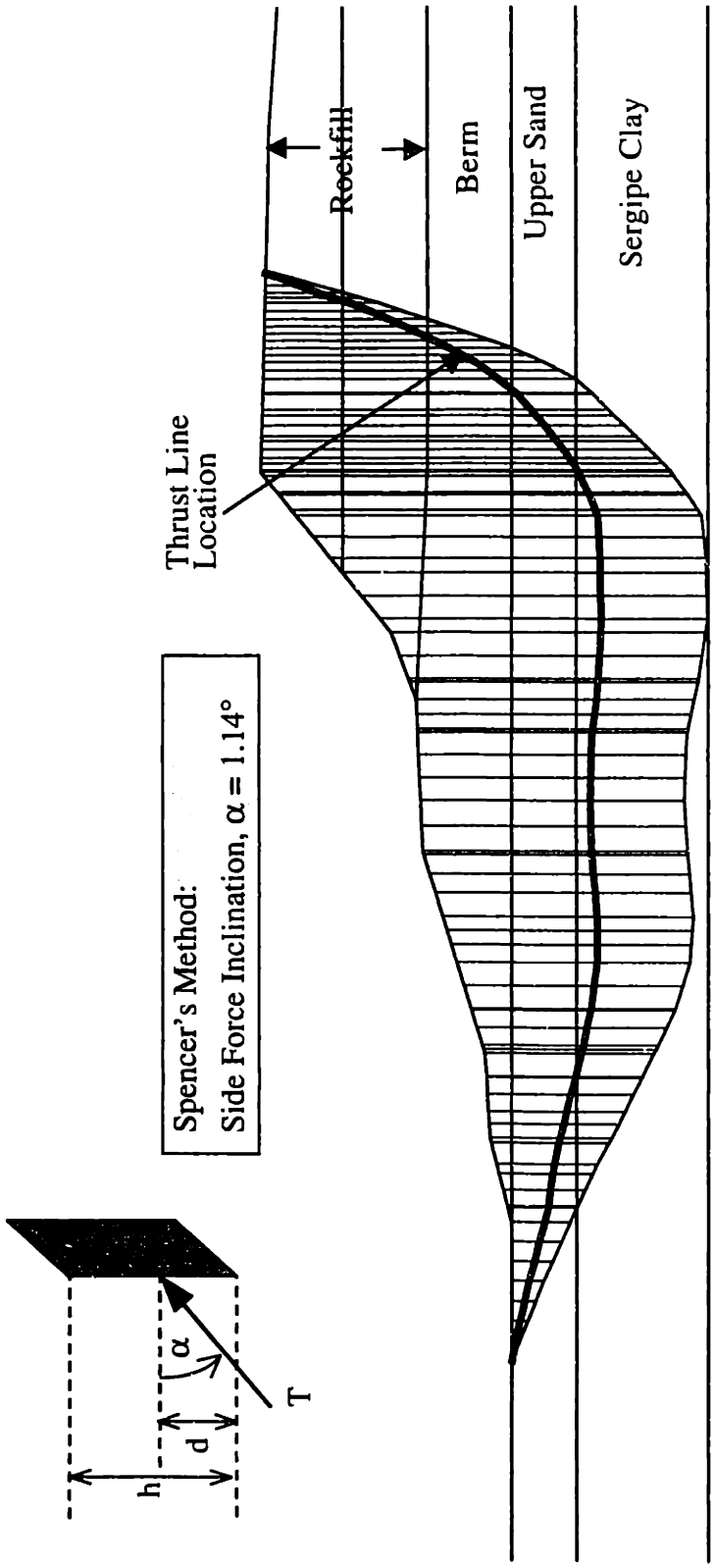

Figure 8.18 Results of UTEXAS3 for the Reinder failure, Profile 3 Revised SHANSEP s_u, FS = 0.876

Chapter 9. Summary, Conclusions and Recommendations

Recent developments of efficient numerical methods of limit analyses (Sloan, 1988a; Sloan and Kleeman, 1995), which satisfy rigorous lower and upper bound theorem, offer a new approach to solve stability problems in geotechnical engineering more accurately and efficiently. This thesis has described further development and application of these analyses for undrained stability problems in clay. Sections 9.1 – 9.7 summarize the principal achievements of this research, while Section 9.7 gives recommendations for further study.

9.1 Undrained Limit Analyses for Combined Loading of Strip Footings on Clay

Chapter 2 applies numerical limit analyses to evaluate the undrained stability of surface footings on non-homogeneous and layered clay deposits under the combined effects of vertical, horizontal and moment (V, H, M) loading. The chapter also presents a brief summary of the formulation of numerical lower and upper bound limit analyses for plane strain problems based on Ukritchon (1996), Sloan (1988a) and Sloan and Kleeman (1995).

In the lower bound formulation (Sloan, 1988a), the soil mass is discretized into 3-noded triangular elements (Fig. 2.2). The analyses solve the unknown nodal stress components (σ_x, σ_y, τ_{xy}), which are assumed to vary linearly within each element. Stress discontinuities are allowed to occur at the interface between adjacent elements. Statically admissible stress fields are obtained by satisfying the constraints of static equilibrium, stress boundary conditions and Mohr-Coulomb yield criterion. The non-linear Mohr-Coulomb yield criterion is approximated by a series of linear constraints on the stresses, which ensure that the solutions do not exceed the yield criterion. The lower bound load is obtained by maximizing the applied load subject to the constraints of static-admissibility.

In the upper bound formulation (Sloan and Kleeman, 1995), the soil mass is also discretized into triangular elements with unknown nodal velocities (u_x, u_y). The analyses assume that the velocities vary linearly within each element. Linearization of the non-linear yield criterion results in additional sets of unknown variables, the plastic multiplier rates associated with each element. Plastic deformation is allowed to occur within the

elements, while velocity discontinuities can occur along all interfaces between adjacent element triangles. A kinematically admissible velocity field is defined by the constraints of compatibility, velocity boundary conditions, and associated flow. The non-linear yield criterion is linearized by using a polygonal approximation, which circumscribes the original yield surface. The upper bound collapse load is obtained by maximizing the applied load subject to the constraints of kinematic admissibility.

The original numerical limit analyses are modified to include interactions between a rigid footing and the underlying soil (Fig.2.3). In lower bound formulation, the rigid footing are represented by the equilibrium of vertical, horizontal, and moment loading on the interface normal and shear tractions. The upper bound formulation represents a rigid footing by two unknown velocities, u_c, v_c and an angular rotation, ω_c, defined about a fixed reference point at the center of the base, and treats soil-footing interfaces as velocity discontinuities. In order to simulate separation between the soil and footing (zero under base suction), the analyses introduce a modified Tresca yield criterion with a no-tension cutoff (Fig. 2.5).

For all cases presented in this chapter, the analyses are able to resolve the true collapse loads of combined loading to within ±5% by computing rigorous upper and lower bound solutions. The analyses compare the stability for cases of zero underbase suction (allowing separation) and full underbase suction (typically occurring for offshore short-term storm loading). Lower bound calculations confirm that the reduction in footing capacity for vertical eccentric loading is related to the loss of contact pressure at the trailing edge of the footing (Fig. 2.10a). At an eccentricity e/B = 0.25, approximately 50% of the footing remains in contact with the soil. Similarly, upper bound solutions for the same problem show a physical separation between the base of footing and underlying soil (Fig. 2.11d). Analyses of concentric loads at large inclination angle, $\alpha > 45^{\circ}$, generate sliding failure along the surface (Fig. 8.11c), while lower bound analyses show full mobilization of the shear traction beneath the footing. For combined loading, the results show significant differences in failure mechanisms between zero base suction and full underbase suction for Mode I loading (i.e., backward eccentricity, Figs. 2.17a, b), while the results for Mode II (forward eccentricity) are not affected by the underbase

suction (Fig. 2.17c). The analyses are able to replicate the full range of failure mechanisms expected under combined inclined and eccentric loading.

The calculations for combined vertical, horizontal, and moment loading are summarized in the form of convex failure envelopes for: 1) homogeneous clay (Fig. 2.15); and 2) profiles where the undrained shear strength increases linearly with depth (Fig. 2.18). The results focus on the geometry of the three-dimensional failure envelope of combined loading of footings and illustrate the effect of underbase suction (Fig. 2.14). Comparisons in cross sections of the failure surface at H-M planes (constant values of V/V_0, where $V_0 = (2+\pi)s_u$) clarify differences in failure mechanism between two modes of combined loading (Fig. 2.1). Underbase suction preserves the moment capacity of the footing at low vertical load ratio, V/V_0, but has no effect on the predicted failure conditions for $V/ > 0.65$. The results indicate the additional stability provided by underbase suction (which can be mobilized for offshore shallow foundations). For non-homogeneous profiles, the yield surface remains non-symmetric as the profile parameter, $\rho B/s_{u0}$ rises, while increases in the moment capacity are more pronounced for Mode II than for Mode I (Fig. 2.18).

Bearing capacity factors computed from numerical limit analyses have been compared with existing solutions (Meyerhof, 1953; Vesic, 1975). For eccentric, vertical loading, the effective width concept proposed by Meyerhof (1953) is a lower bound solution on the true collapse load (Fig. 2.13a). The existing empirical bearing capacity factors for inclined, eccentric loading are conservative, often underestimating the exact collapse solutions for footings on homogeneous clay by more than 25% (Fig. 2.13). However, the same correction factors are completely unreliable (and non-conservative) for situations where undrained strength increases linearly with depth (Fig. 2.19). The undrained stability for combined loading of surface foundations can be either estimated directly from results presented in this chapter or computed using the proposed curve fitting functions, based on dimensional analysis.

9.2 Development and Validation of Numerical Limit Analyses for Structural Element

Chapter 3 describes the formulation of numerical upper and lower bound limit analyses for structural elements. The proposed formulation is evaluated through: i) comparisons with analytical solutions for a series of 2-D structural frame problems; and ii) analyses of a laterally loaded wall embedded in clay.

In the lower bound formulation, the structure is discretized into beam and joint elements (Fig. 3.1). The beam element has two nodes (one at each end), while the joint element has one node. Each node has three unknown degrees of freedom: 2 forces, F_x (x-dir.), F_y (y-dir.), and one moment F_z (z-dir), and is unique to each particular element. Joint elements do not have any physical dimension. The formulation assumes that the beam elements carry only distributed tractions (normal and shear), while joint elements carry only point forces, including moments. The static constraints include equilibrium of the beam and joint elements, traction and force boundary conditions, and require that the yield criterion is not violated. The proposed formulation allows failure of structural elements to occur in combined axial, shear, and bending. The lower bound analysis is formulated as linear programming problem whose objective function is the maximization of the external applied load subject to the constraints of a static admissibility. Finally, the lower bound load is solved by the method of linear programming problem using the active set algorithm (Sloan, 1988b).

The upper bound formulation also discretizes the structure into 2-noded beam and 1-noded joint elements (Fig. 3.5). Each node of a beam element has two unknown velocities, u (x-dir), v (y-dir), whereas a joint element has three unknown velocities, u (x-dir), v (y-dir), and w (angular velocity). The beam element is assumed to be a rigid element, while plastic failure is permitted to occur at adjacent nodes of beam and joint elements. Linearization of the non-linear yield criterion results in addition sets of unknown variables, the plastic multiplier rates, associated with each linearized yield constraint. Kinematically admissible solutions are defined by the constraints of rigid movement of beam elements, associated plastic flow at adjacent nodes of beam and joint elements, and velocity boundary conditions. The upper bound formulation leads to a linear programming problem whose objective function is the minimization of the external

applied load subject to the constraints of kinematic admissibility. Finally, the upper bound load is solved by applying the active set algorithm of linear programming (Sloan, 1988b).

The lower bound analyses model soil-structure interfaces by applying contact shear and normal tractions to adjacent beam elements. The upper bound analyses treat soil-structure interfaces as velocity discontinuities, which allow tangential and normal jumps to occur across interfaces. Separation between soil and beam elements is modeled by modifying the yield criterion with a zero tension-cutoff. Interface roughness is controlled by specifying the ratio of shear traction to undrained shear strength of the surrounding soil.

Five examples of two dimensional frame structures were analyzed with the proposed formulation. The analyses consider only the failure due to plastic moment. In all cases, the upper and lower bound analyses bracket the true collapse load very accurately (<< 1% error, Table 3.1). The predicted collapse mechanisms from upper bound analyses are in excellent agreement with the exact solutions (Figs. 3.9-3.18).

The numerical limit analyses of structural and plane strain elements can be applied to analyze a wide range of stability problems involving soil-structure interaction. This chapter presents the first application of this combined formulation to analyze a laterally loaded wall embedded in a homogeneous clay layer. This problem is a good test of the proposed formulation as failure of the system can occur due to shear distortion in the soil mass and/or plastic collapse of the structural wall. The results show that the capacity of the laterally loaded wall, $H/(s_u L)$ is a function of the relative strength parameter, $M_p/(s_u L^2)$, where H = horizontal load applied at the top of the wall, L = wall length, M_p = plastic moment of the wall, and s_u = undrained shear strength of clay. The analyses are able to simulate correctly three failure mechanisms of "short", "intermediate", and "long" piles for free and fixed head walls as proposed by Broms (1964) (Figs. 3.30, 3.31 3.41, 3.42).

The analyses generate the failure envelopes of free-head walls with combined horizontal load and moment (Figs. 3.43-3.45). The results clearly show that the size of failure envelope reduces significantly with relative strength parameters. The differences between failure envelopes of smooth and rough surfaces appear for the case of rigid

walls, indicating that the wall capacity for a rough interface is higher than a smooth interface (Fig. 3.47). Failure envelopes for the case of rigid walls, generated by numerical limit analyses, do tie in with approximate solutions of Davis (1961). The results of free-head wall are summarized in the form of design chart for a practical range of relative strength parameters, and eccentricity ratios of horizontal load (Fig. 3.52).

9.3 Development and Validation of Anisotropic Undrained Strength

Chapter 4 describes the formulation of the yield function for representing the anisotropic undrained strength of clay in numerical limit analyses. The formulation selects the yield function proposed by Davis and Christian (1971) as this matches very closely with results from laboratory directional shear cell (DSC) on K_0-consolidated Boston Blue Clay (BBC).

Modification of the lower bound analysis requires linearization of the anisotropic yield function and enforces a set of inequality constraints that ensure stresses to lie inside the linearzied functions.

In the upper bound formulation, modifications are required to describe the plastic flow and internal work dissipation associated with the linearized anisotropic yield criterion in the triangular elements and along velocity discontinuities between elements. In triangular elements, this is accomplished by applying linear coefficients from the exterior linearization of the yield function in the compatibility and associated flow equations, and to calculations of internal power dissipation. Along velocity discontinuities, the associated flow of incompressible material results in two linear anisotropic yield envelopes, each of which corresponds to different rates of plastic shear dissipation and slip directions. Finally, dissipation of energy along velocity discontinuities corresponding to slip directions is added in the internal energy equation.

Implementation of the anisotropic undrained strength envelope is evaluated through prediction of the bearing capacity of a vertically-loaded rigid strip footing on anisotropic clay. For all anisotropic strength ratios, results of numerical limit analyses match very well with the exact solutions given by Davis and Christian (1971) (Table 4.2). There are very small differences in the predicted upper bound failure mechanisms, velocity field and plastic zone for isotropic and anisotropic yield criteria (Fig. 4.28-4.31).

This chapter also demonstrates the application of numerical limit analyses for computing the undrained lateral resistance of deeply-embedded sections in clay. The analyses consider three cross sections: 1) centrally-loaded flat plate; 2) diagonally-loaded square section; and 3) a pipe section. For all sections, the lower and upper bound solutions bracket the true collapse load to within ±5%. The results of numerical limit analyses matches very well with analytical slip-line solutions given by Broms (1964) for flat plat and square sections, and Randolph and Houlsby (1984) for pipe sections (Tables 4.3, 4.4). The load factor of pipe sections increases by about 30% as the interface strength ratio, f_s/s_u increases from 0 (smooth) to 1 (rough, fully adhesive) (Fig. 4.38). There are important differences in the predicted failure mechanism due to interface roughness. Rough surfaces generate a much larger zone of plastic soil distortion than the smooth cases (Figs 4.39, 4.43, 4.47). The contact normal and shear tractions along sections from lower bound analyses show clearly that the higher lateral capacity of rough interfaces results from the presence of shear tractions, which is mobilized to the undrained strengths of the clay (e.g. Figs. 4.50). However, peak anisotropic strength generates a 20% increase in the load resistance factor, $N = P/(Ds_{uDSS})$ for all three cross-sectional geometries. In contrast, there is practically no difference in predicted upper bound failure mechanisms between isotropic and anisotropic strengths (e.g. Figs. 4.57, 4.58).

9.4 Undrained Tensile Loading for a Rigid-Planar Caissons

Chapter 5 describes the application of the numerical limit analyses for computing the undrained tensile capacity of rigid-planar caissons in non-homogeneous clay, where undrained shear strength increases linearly with depth. The chapter also proposes a simple method for applying the solutions for the planar caisson geometries to estimate the capacity of axisymmetric caissons. The scaled results are then compared with displacement-based finite element analyses (FE) using the MIT-E3 soil model (Whittle et al., 1996). Numerical limit analyses are also carried out to make predictions of axial pullout for: 1) miniature caissons in laboratory element tests (Cauble, 1996); 2) the centrifuge model caissons performed by EPR (Clukey and Morrison, 1993); and 3) field experiments performed by NGI (Andersen et. al., 1993). The centrifuge and field experiments include data for inclined loading.

Results of numerical limit analyses are compared with conventional limit equilibrium calculations (LEM) by Clukey and Morrison (1993) for planar caissons. For length to width aspect ratios, L/B = 1.0, 3.0, the upper bound calculations (Figs. 5.5, 5.8) show that there is no failure within the soil plug. These results correspond with the LEM assumption of a reverse end bearing failure mechanism. However, this LEM assumption is not valid for shallow, wide caissons, where upper bound analyses show a failure occurring inside the soil plug (Fig. 5.11). The pullout capacity estimated from LEM is conservative for only deep planar caissons, where L/B > 1 (Fig. 5.17).

Results of FE analyses (Whittle et al., 1996) are compared with numerical limit analyses (scaling from planar caisson) for two series of simulation for full size prototype showing: 1) effects of wall length, where L = 10, 20, 30, 40, 60m for a diameter, B = 20m; and 2) effect of cap diameter, B = 10, 20, 40 for L = 20m. The comparisons of wall length effect show that the lower bound calculation predict much higher wall forces than FE analyses for L = 60m (Fig. 5.22). One possible explanation is that the wall forces from FE analyses are not fully mobilized at L = 60m (Fig. 5.21). However, there is consistent agreement between the lower bound calculations and the FE analyses of limiting cap resistance. The comparisons of cap diameter effect show that the limit analyses predict the wall force in the same range as FE analyses, but suggest that the caisson can sustain much higher cap forces for B > 30m (Fig. 5.23).

Predictions of pullout capacity using the limit analyses (scaled to axisymmetric geometries) match very closely with the measured capacities in all three sets of experiments (laboratory 1-g, centrifuge, and field). Of particular interest are the results of a field experiment by NGI (Andersen et al., 1993), where the experiment used a 4 cell caissons unit subjected to a static load inclined at 10° from the vertical (Fig. 5.49). The predicted upper bound failure mechanism involves a rigid body rotation of the caisson about a point located at the base of the caisson (Fig. 5.54). This mechanisms show reasonable agreement with the estimated locations of the failure surface based on measured distortions of epoxy columns with the clay (Fig. 5.53).

Section 5.2 describes a generalized design chart for estimating the undrained pullout capacity of single caisson. However, the results are strictly limited to planar all geometries, and require approximate scaling to estimate the capacity of axisymmetric

caisson. Another limitation of this method can be seen from comparisons with CET caissons, where scaling results of planar analyses fail to match the measured distribution of wall and cap forces, while still achieving a good estimate of the total capacity. The other limitation is that the method can not take into account of the effect of caisson installation, which is likely to be an important parameter in practice.

9.5 Undrained Stability of Braced Excavations

Chapter 6 describes the application of numerical limit analyses for computing undrained stability of braced excavations in clay.

The first example considers the stability of a well braced vertical cut. The results are reported in terms of stability number, $N = \gamma H/s_u$, where H = depth of excavation, γ = total unit weight of clay, s_u = undrained shear strength of clay. For all cases presented in this chapter, numerical limit analyses bound the true stability number within ±5%. The results of supported vertical cut show that the interface roughness causes a 15% increase in the predicted value of N, but has minimal effect of the stability of wide excavation (Fig. 6.12). The basal stability mechanism proposed by Terzaghi (1943) corresponds to an upper bound on the actual stability of wide excavations, but significantly overestimates the stability of narrow excavations. In contrast, the empirical mechanism of Bjerrum and Eide (1956) is conservative for all excavation width ratios, B/H. The typical upper bound failure mechanism comprises a rigid wedge of soil that is pushed upward inside the excavation together with a rotational shear zone passing below the wall (e.g. Figs. 6.13, 6.14). Wall roughness increases the zone of plastic failure in the retained soil. The typical lower bound result (e.g. 6.15c) shows that the soil below the bottom of excavation fails in an extension mode of shearing ($\delta = 90°$), together with a radial shear zone below the tip of the wall ($\delta = 90° \rightarrow 0°$). The retained soil behind the wall fails between the direct simple shear and a passive shearing ($\delta = 45°$-$90°$).

The second example considers the effects of wall embedment, D, on the stability of a well braced excavation of depth, H = 15m and width, B = 40m. In this case, the strength of the wall is limited by its plastic bending moment capacity, M_p. Dimensional analysis shows that the stability number of the excavation can be written as a function of the relative strength parameter, $M_p/(s_u D^2)$, and the embedment to excavation depth ratio,

D/H. The results show that stability number increases with the embedment ratio, D/H and with the relative strength parameter, but remains constant for $M_p/(s_uD^2) > 4$. This limiting condition corresponds to the case where there is no bending failure of the wall. There is an error in proposed methods of analysis that incorporates the elastic strain energy of an assumed wall deflection (O'Rourke, 1993). This approach underestimates the stability of flexible walls, while greatly overestimating stability for rigid wall cases. In addition, it fails to identify the increase in stability of excavations due to the embedment ratio, D/H. Stability calculations using Terzaghi modified base heave (which include the weight of soil plug and assume the rigid embedded wall) are in very good agreement with upper bound stability numbers for the case of rigid wall. The upper bound results show that for small values of $M_p/(s_uD^2)$, the predicted failure mechanism corresponds to a subgrade bulging mode, where plastic hinges form at excavated grade and within embedded wall section (Fig. 6.41a). For intermediate values of $M_p/(s_uD^2)$, the mechanism (Fig. 6.41b) corresponds to rotational failure of the wall (one plastic hinge at the excavated grade). For very large value of $M_p/(s_uD^2)$, the wall is rigid and the soil behind the wall has to flow underneath it causing a massive failure zone (Fig. 6.41c). The predicted upper bound mechanisms correspond very well bending moments of the wall computed from lower bound analyses (Fig. 6.44).

Numerical limit analyses are also carried out to assess the stability for combinations of parameters, D/H, H/B, $M_p/(s_uD^2)$. Results are summarized in the form of empirical curve fitting equation using dimensional analysis. Stability numbers can be estimated from the proposed empirical equation or design charts generated by this equation for practical values of B, D, H, M_p, s_u. Design charts clearly show that the undrained shear strength of the clay is the dominant parameter affecting stability, while the parameters, B, D, M_p all have secondary effects.

The influence of undrained strength anisotropy is evaluated through examples considered the stability of unsupported and supported vertical cuts. These analyses assumed $s_{u45} = 0.5(s_{u0} + s_{u90})$. For unsupported vertical cuts, the stability number, $N = \gamma H/s_{u45}$ shows good agreement between numerical limit analyses and solutions given by Chen (1975). while conventional mechanisms with planar surface overestimate the true stability number (Fig. 6.55). The results show that the analysis using s_{u45} with isotropic

strength gives a conservative estimate of stability number for actual vertical cuts in anisotropic clay. In contrast to the isotropic case where plastic shear distortion occurs in a band extending at 45° from the toe of the slope, failure of anisotropic clay extends below the toe of the cut. The zone of plastic failure below toe is more pronounced for smaller value of anisotropic strength ratio, $K_s = s_{u90}/s_{u0}$.

For supported vertical cuts, the results show that the stability number of anisotropic strength ratio of $K_s = 0.35$ is approximately 5% higher than for isotropic strength ($K_s = 1$) for all geometric aspect ratios, H/B (Figs. 6.58, 6.58). Solutions given by Clough and Hansen (1981), that accounting for anisotropic shear strength, are conservative for B/H ≥1, but can overestimate the stability of narrow excavations with H/B > 2.

This chapter also shows comparisons of predicted failure height between numerical limit analyses and non-linear finite element analyses using the MIT-E3 soil model (Hashash and Whittle, 1996). The base case considers an excavation of width, B = 40m, supported by diaphragm wall of length, L = 12.5, 20, 40, 60m, with cross-lot bracing. The soil profile corresponds to Boston Blue Clay at a constant OCR = 1.0, such that undrained shear strength increases linearly with depth. Predictions from numerical limit analyses using isotropic strength tend to overestimate the finite element analyses for all wall lengths (L ≤ 40m). Improved matching can be achieved by including undrained strength anisotropy in the limit analyses. Input parameters for these calculations are based on the mobilized shear resistance at shear strain levels observed in the finite element calculations.

9.6 Case study: Stability of Tieback Excavation in East Boston

Chapter 7 presents applications of numerical limit analyses to analyze the stability of tie-back walls at the Bird Island Flats (BIF) site in East Boston.

The study considers two sections: 1) East wall, Section A-A′, where the excavation became unstable during construction (Fig. 7.3); and 2) West Wall, Section B-B′ (Fig. 7.6), where deep soil mixing and jet grouting were used to construct buttresses that stabilize the base of the excavation. Uncertainties in the undrained shear strength profiles of the marine clay (BBC) are the major concern in the analyses (Fig. 7.7). The

calculations consider three profiles: 1) a conservative strength based on pre-consolidation pressure data (σ'_p) and normalized strength parameters from the nearby East Boston Special Test Site (Haley and Aldrich, 1992); 2) the best of undrained shear strength using the stress history data measured at the BIF site; 3) field vane shear strength, μs_{uFV} (O'Rourke and O'Donnell (1997a) using data obtained after the failure occurred). Comparisons show that profile 2 generates undrained strengths that are up to 20% larger than the field vane in the lower soft clay (where OCR < 2). Numerical limit analyses predict that the East wall Section A-A′, and West wall Section B-B′ should both have failed if either strength profile 1 and or 3 (μs_{uFV}) are valid. In contrast, the analyses indicate that both sections should have an adequate safety margin (FS > 1.27) for strength profile 2. There is no evidence to suggest differences in the in situ undrained strengths between these two sections. One possible explanation why the excavation remained stable at Section B-B′ are differences in construction procedures (excavation in short length segments).

For the East wall, the predicted upper bound failure involves a deep-seated rotational mechanism (Fig.7.9) with bending failure of the wall occurring just below the excavated grade. This result is similar to the limit equilibrium calculations using rigid body circular arc analyses by O'Rourke and O'Donnell (1997a) who obtained the same range of FS using field vane strengths (Fig. 7.10). For West wall, Section B-B′, the upper bound analysis predicts a rigid body rotation of the DSM buttress relative to the main wall, as well as deep-seated failure in the clay (Fig. 7.39). This mechanism is not considered in the limit equilibrium calculations by O'Rourke and O'Donnel (1997b) (Fig. 7.40), who obtains a misleading FS = 1.08 – 1.13, that is significantly higher than the upper bound analysis for the same strength profile.

This chapter also demonstrates the application of reliability analyses (First Order Second Moment methods, FOSM) in conjunction with the proposed limit analyses to estimate the uncertainty of the calculated factor of safety. The analyses consider East wall, Section A-A′, using stress history data measured at the BIF site (profile 2). Best estimates and standard deviations are selected for the principal geometric and material properties at Section A-A′. These uncertainties are then propagated into calculations of FS by performing sensitivity analyses. The results show that the undrained strength of

BBC generates the largest uncertainty, accounting for approximately 90% of the total variance (Tables 7.6, 7.7). The uncertainty in strength Profile 2 results from the scatter data of stress history at the BIF site as well as uncertainties in the normalized (SHANSEP) strength parameters. The second important variable is the excavation depth, but this constitutes only 7% of total uncertainty.

This chapter also demonstrates the application of numerical limit analyses to evaluate other design strategies for improving the stability of both sections, A-A′ and B-B′. For East wall, the analyses consider three options: 1) strengthening the wall; 2) extending wall into bedrock; and 3) extending the free length of tiebacks. The results show that there is no improvement achieved by strengthening the wall (using a diaphragm wall as opposed to a soil-mix wall), while extending the wall into bedrock and extending free length of tieback show an increase in stability about 7%. For the West wall, the analyses consider four options: 1) reducing the vertical thickness of the soil-mix buttress; 2) extending the jet grout columns into bedrock; 3) extending the length of the buttress across the full width of the excavation (60m); and 4) using a regular grid of jet grout columns (Fig. 7.53). The results show that the thickness of buttress can be reduced from 4.9m (original design) to 2.2m, without any reduction in FS. Of the other schemes, the most effective is option 3 (full width mat).

9.7 Implementation and Validation of Pore Water Pressure in Numerical Limit Analyses

Chapter 8 describes the implementation and validation of pore water pressure in numerical limit analyses, and presents its application in the re-analysis of the failure of an offshore breakwater in Brazil (Reinder failure; Ladd et. al, 1993).

For both lower and upper bound analyses, the proposed formulation assumes that pore water pressures are defined at all nodes in the mesh (either geostatic or steady flow conditions). Pore pressures, p_w, are assumed to vary linearly within each triangular elements.

In the lower bound analyses, the unknown nodal variables (σ_x, σ_y, τ_{xy}) are total stresses, and there is no modification required for the equilibrium within triangular elements, equilibrium of normal and shear tractions across stress discontinuities, or stress

boundary conditions. Modifications are necessary to express the Mohr-Coulomb yield criterion in terms of effective stresses. Hence, pore pressures are brought into the linearized yield function (Eqn 8.6). For undrained materials (incompressibility), the lower bound formulation shows no influence of pore water pressures.

In the upper bound formulation, the plastic flow within triangular elements and along velocity discontinuities are associated with the linearized Mohr-Coulomb yield function defined in terms of effective stress (eqns 8.9, 8.14). The upper bound modifications require additional internal dissipation of energy due to pore water pressures within elements and in plastic shearing along velocity discontinuities (eqns 8.13, 8.22). For undrained materials, there is again no influence of the pore water pressures.

The implementation of the proposed pore water pressure formulation is evaluated through predictions of stability of homogeneous slopes (in cohesive-frictional soils) with pore water pressure. The first example considers the case of slope subjected to constant pore water pressure ratios, r_u = 0, 0.25, 0.5; while the second considers a submerged slope. For all cases, numerical limit analyses with pore water pressure are able to bracket the stability numbers within ±5% (Table 8.1). In the first example, stability numbers from numerical limit analyses correspond very well with analytical upper bound solutions by Michalowski (1995a, b). The stability calculations are also compared with limit equilibrium calculations using conventional slope stability software (UTEXAS3, Wright, 1991) and Spencer's method of slices. Although stability numbers from these LEM calculations (circular and non-circular shear surfaces) do fall within the range of the numerical limit analyses, detailed interpretation shows that the location of thrust lines located outside the failure mass, and are not considered physically realistic (Fig. 8.3).

Numerical limit analyses have been carried out to re-assess the Reinder failure, using undrained strength profiles for the Sergipe clay derived in previous research (Ladd et al., 1993; Ladd and Lee, 1993). In all cases, the lower and upper bound analyses bracket the factor of safety within ±5% (Table 8.2). The results of limit analyses indicate that the stability of breakwater is inadequate using (SHANSEP) strength profiles (with and without partial consolidation of the soil). Previous LEM calculations (using Spencer's method) predict factors of safety that are approximately 15% lower than the numerical upper bound, with a steep backscarp in the overlying rockfill (Figs. 8.12, 8.13,

8.14). The underestimation of factor of safety from LEM calculations is surprising and suggests serious limitations of stability analyses using method of slices.

Limit analyses of homogeneous slopes with pore pressure and the Reinder case study confirm the limitations of existing slope stability calculation methods. However, it is difficult to check the accuracy of the latter due to assumptions of orientation and location of interslice forces. As a result, the sign of the error remains indeterminate.

9.8 Recommendations

Further research on numerical limit analyses should be pursued in two general area: 1) improvement and development of the predictive capabilities of the current numerical limit analyses; and 2) applications of this approach to analyze other geotechnical problems.

9.8.1 Development and Improvement

The capabilities of numerical limit analyses should be improved in the following areas:

1. It is well-known that the Mohr-Coulomb yield criterion with associated flow predicts much higher rates of dilation than is observed in laboratory tests on sands. Thus, the current numerical limit analyses should also be modified to include a more realistic yield criterion for sands in which the peak friction angles varies with the confining pressure and density (e.g. Pestana, 1994).

2. The current formulation is limited to plane strain problems. Further development can be carried out to generalize the formulation in three-dimensional problems. New formulation strategies are necessary to improve the computational efficiency for 3D cases. Recent works by Lyamin and Sloan (1996) have formulated numerical lower limit analyses into non-linear programming problem. In addition, non-linear stress and velocity distributions within elements may be necessary in order to achieve accurate predictions. In order to apply 3-D numerical limit analyses to general stability problems in

practice, implementation of pore pressure is also necessary. This represents a straightforward extension of the work in Chapter 8.

9.8.2 Application of numerical limit analyses

The inclusion of structural elements, undrained strength anisotropy, and pore water pressures in the numerical limit analyses provides many possible applications for stability problems in geotechnical engineering. These practical applications include:

1.) Collapse loads of shallow foundations

Bearing capacity of shallow foundations is one of the most important stability problems encountered in soil mechanics. Analytical solutions exist for plane strain footings with relatively simple soil profile (Davis and Booker, 1973). Chapter 2 demonstrates an application of this method to solve more complicated loading of plane strain surface footings. The method can also be used to solve the bearing capacity of footings for generalized soil profiles, including undrained strength anisotropy of clay (contribution of Chapter 4). The first application of three dimensional numerical limit analyses should address the collapse of other footing geometries such as circular, square, or rectangular shapes. Existing solutions of these geometries are based on empirical shape factors. Inclined and eccentric load of these footings is of particular interest in practice.

2.) Collapse loads of deep foundations and embedded sections

Most deep foundations and embedded sections require three dimensional numerical limit analyses. The method can be used to check existing solutions of end bearing for cylindrical piles and update the tensile pullout load of caissons in Chapter 5. Other stability of embedded sections includes lateral loaded piles and pullout load of anchor block or plates. Application of 2-D plane strain limit analyses can be used to estimate collapse loads of those problems, but these calculations require to scaling approximation.

3.) Stability of slopes and embankment

Slope stability problems commonly occur in geotechnical practice. Implementation of pore water pressures has extended the capabilities of numerical limit analyses to handle real problems involving layers of sands and clays as well as ground water flows. Chapter 8 demonstrates the first application of this method to check to failure of embankment. Numerical limit analyses have several advantages over existing limit equilibrium method (LEM) in estimating slope stability: i) they provide a rigorous self-checking bound on the true solutions; and ii) they eliminate the ad-hoc search procedures used in LEM calculations using methods of slices. The method can also be applied to analyze the stability of earth dams and embankments as well. The influence of 3-D geometry of slopes can be investigated with 3-D numerical limit analyses. Progressive failure in slope stability problems can be represented approximately in limit analyses using the strain compatibility technique (Ladd, 1991), where mobilized shear resistance is selected at an allowable shear strain for anisotropic strength analyses.

4.) Stability of braced excavations

Chapters 6 and 7 demonstrate the application of numerical limit analysis to solve stability of braced excavations very effectively. The supporting systems can be included cross-lot bracing or tieback anchors. The major advantage of this method is that it can simulate the failure of soil, structural wall and bracing. This flexibility should enable the method to achieve widespread use in these soil-structure interaction problems.

5.) Stability of ground improvement

Ground improvement with geosynthetic material is becoming popular in soil engineering to increase the stability of foundation. The current numerical limit analyses with structural elements (Chapter 3) can be applied to analyze such problems, including slopes, embankments or retaining walls with reinforcement, bearing capacity of soil reinforcement, etc. The method can

also be used to check other possible soil improvements to increase factor of safety of foundations, such as soil mixing with cement or soil jet grouting as demonstrated in Chapter 7.

6.) Reliability analyses

For all stability problems, numerical limit analyses can be used together with reliability analyses using First Order Second Moment method (FOSM) to propagate uncertainties in geometric and soil parameters to predicted solutions, as demonstrated in Chapter 7. The major advantage of this technique is that it provides insight into the probability of failure, which is a useful concept for design practice.

9.9 References

Andersen, K.H., Dyvik, R., Schroder, K., Hansteen, O.E. and Bysveen, S. (1993). "Field tests of anchors in clay. II: Predictions and interpretation" J. of Geotech. Engrg., ASCE, 119(10), 1532-1549.

Bjerrum, L., and Eide, O. (1956). "Stability of strutted excavations in clay." Géotechnique, 6, 115-128.

Broms, B. B. (1964). "Lateral Resistance of Piles in Cohesive Soils." J.S.M.F.D., ASCE, Vol. 90, SM2, 27-63.

Cauble, D.F. (1996). "Experimental measurements for a model suction caisson" PhD Thesis, Dept. of Civil Engrg., MIT, Cambridge, MA.

Clough, G. W. and Reed, M. W. (1984). "Measured behavior of braced wall in very soft clay." J. of Geotech. Engrg., ASCE, 110(1), 1-19.

Clough, G. W., and Hansen, L. A. (1981). "Clay anisotropy and braced wall behavior." J. of Geotech. Engrg., ASCE, 107(7), 893-913.

Clukey, E.C. and Morrison, M.J. (1993) "A centrifuge and analytical study to evaluate suction caissons for TLP applications in the Gulf of Mexico." Design and Performance of Deep Foundations: Piles and Piers in Soil and Soft Rock, ASCE, NY, 141-156.

Davis, E. H. (1961). "The Application of the Theory of Plasticity to Foundation Problem - Limit Analysis." Post-Grad. Course on Fndn. Eng., Univ. of Sydney, Aust.

Davis, E.H. and Booker, J.R. (1973). "The effect of increasing strength with depth on the bearing capacity of clays." Géotechnique, 23(4), 551-563.

Davis, H. E., and Christian, T. J. (1971). "Bearing capacity of anisotropic cohesive soil". J. Soil Mech. Found. Div., ASCE, 97(5), 753-769.

Finno, R. J., Atmatzidis, D. K., and Perkins, S. B. (1989) "Observed performance of a deep excavation in clay.". J. of Geotech. Engrg, ASCE, 115(8), 1045-1064.

Geer, M. (1996). "Analysis of pile and suction caisson behavior in axial loading." PhD Thesis in progress, MIT, Cambridge, MA.

Haley and Aldrich. (1992). "Report on special laboratory and in-situ testing program, central artery (I-93)/tunnel (I-90) project, design section D007A and D007C,

Boston, MA." Rep. Prepared For the Massachusetts Hwy. Dept., File No. 10360-40, Cambridge, Mass., Vols. 1-2.

Hashash, Y. M. A., and Whittle, A. J. (1996). "Ground movement prediction for deep excavations in soft clay.". J. of Geotech. Engrg, ASCE, 122(6), 474-486.

Ladd, C. C., and Lee, S-M. (1993). "Engineering properties of the Sergipe Clay." TPS Progress Report No. 4, Research Report 93-07, March 19, 1993, Dept. of Civil and Environmental Engineering, MIT, Cambridge, MA.

Lyamin, A. V., and Sloan, S. W. (1996). "A comparison of linear and nonlinear programming formulations for lower bound limit analysis." Research Report, The University of Newcastle, Australia.

Ladd, C. C, Lee, S-M, and Whelan, M. P. (1993). "Backanalyses of the Reinder Failure." TPS Progress Report No. 5, Research Report 93-10, May 29, 1993, Dept. of Civil and Environmental Engineering, MIT, Cambridge, MA.

Michalowski, R. L. (1995a). "Slope stability analysis: a kinematic approach." Géotechnique, 45(2), 283-293.

Michalowski, R. L. (1995b). "Stability of slopes: Limit analysis approach." Reviews in Engineering Geology, 10, 51-62.

Meyerhof, G. G. (1953). "The bearing capacity of foundation under eccentric and inclined loads." Proc. Third International Conference on Soil Mechanics and Foundation Engineering, Zurich, 1, 440-445.

Norwegian Geotechnical Institute. "Measurements at a strutted excavation, Oslo Subway, Vaterland 3", Techical Report 8, Blindern, Norway, 1962.

O'Rourke, T. D. (1993). "Base stability and ground movement prediction for excavations in soft clay." Proc. ICE Conf. on Retaining Structures, Cambridge, Thomas Telford, 131-139.

O'Rourke, T. D., and O'Donnell C. J. (1997a). "Deep rotational stability of tieback excavations in clay." J. Geotech. And Geoenvir. Engrg., ASCE, 123(6), 506-515.

O'Rourke, T. D., and O'Donnell C. J. (1997b). "Field behavior of excavation stabilized by deep soil mixing." J. Geotech. And Geoenvir. Engrg., ASCE, 123(6), 516-524.

Pestana-Nascimento, J. M. (1994). "A unified constitutive model for clays and sands." ScD thesis, Dept. of Civil and Environmental Eng., Massachusetts Institute of

Technology, Cambridge, MA.

Randolph and Houlsby (1984). "The limiting pressure on a circular pipe loaded laterally in cohesive soil." Géotechnique, 34(4), 613-623.

Rodriguez, J. M. and Flanmand, C. L. (1969). "Strut loads recorded in a deep excavation in clay." Proc. 7th Int. Conf. on Soil Mech. and Found. Engg., Mexico City, Vol. II, 1969, 459 – 467.

Sloan S. W. (1988a). "Lower bound limit analysis using finite elements and linear programming." Int. J. Numer. Anal. Methods in Geomech., 12(1), 61-77.

Sloan S. W. (1988b). "Lower bound limit analysis using finite elements and linear programming." Int. J. Numer. Anal. Methods in Geomech., 12(1), 61-77.

Sloan S. W., and Kleeman, P. W. (1995). "Upper bound limit analysis using discontinuous velocity fields." Computer Methods in Applied Mechanics & Engineering, 127, 293-314.

Terzaghi, K. (1943). Theoretical Soil Mechanics, John Wiley & Sons, New York.

Ukritchon, B. (1996). "Evaluation of numerical limit analyses by finite elements and linear programming." MS Thesis, Department of Civil & Environmental Engineering, MIT, Cambridge, MA.

Vesic, A. S. (1975). "Bearing capacity of shallow foundations." *Foundation Engineering Handbook*, H. F. Winterkorn and H. Y. Fang (Ed.) Van Nostrand Reinhold Company, 121-145.

Whittle, A. J., Germaine, J. T., Cauble, D. F., Geer, M. A. (1996). "Behavior of suction caisson foundations: Final Report." report submittted to MIT Sea Grant and Joint Oil Industry Consortium, Cambridge , MA.

Wrigth, S. G. (1991). "UTEXAS3, A computer program for slope stability calculations." Shinoak Software, Austin, TX, Revised Sept. 1991.